PATA DAYS 2018 GREECE

9th International INQUA Workshop on Paleoseismology, Active Tectonics and Archeoseismology

Possidi, Greece, 25-27 June 2018

PROCEEDINGS

Editors: Olga Koukousioura and Alexandros Chatzipetros

The 9th International INQUA Workshop on Paleoseismology, Active Tectonics and Archeoseismology

25-27 June 2018
Possidi, Greece

ON THE OCCASION OF THE 40TH ANNIVERSARY OF THE M 6.5 THESSALONIKI EARTHQUAKE.
COVER: SURFACE RUPTURE AT STIVOS VILLAGE
BACKCOVER: SURFACE RUPTURE AND ASSOCIATED DAMAGE AT STIVOS VILLAGE
(PHOTO CREDIT: GEORGE SYRIDES)

Proceedings of the 9th International INQUA Workshop on Paleoseismology, Active Tectonics and Archeoseismology

25 - 27 June 2018
Possidi, Greece

Editors
Olga Koukousioura
Alexandros Chatzipetros

Organizing Committee

Honorary Chair
Spyros Pavlides (Greece)

Chair
Alexandros Chatzipetros (Greece)

Members
Olga Koukousioura (Greece)
Triantaphyllos Kaklis (Greece)
Efi Thomaidou (Greece)
Ioannis Papanikolaou (Greece)
Christoph Grützner (Germany)
Ilias Lazos (Greece)
Dominikos Vamvakaris (Greece)

PROCEEDINGS VOLUMES OF PATA DAYS:

Vol. 9: Proceedings of the 9th International INQUA Meeting on Paleoseismology, Active Tectonics and Archeoseismology *(Koukousioura O. & Chatzipetros A., Eds.),* 25-27 June 2018, Possidi (Greece).

Vol. 8: Proceedings of the 8th International INQUA Meeting on Paleoseismology, Active Tectonics and Archeoseismology. Handbook and Programme. (Clark KJ, Upton P, Langridge R, Kelly K, Hammond K.), 13 16 November 2017. Lower Hutt (NZ): GNS Science. 441 p. (GNS Science miscellaneous series 110). doi:10.21420/G2H061.

Vol. 7: Proceeding of the 7th International INQUA Meeting on Paleoseismology, Active Tectonics and Archeoseismology (*J.P. McCalpin & C. Gruetzner, eds*.). ISBN 978-0-9974355-2-8, 2016. Published digitally by the Crestone Science Center, Crestone, CO 81131 USA, Guidebook No. 12; 7th International INQUA Meeting on Paleoseismology, Active Tectonics and Archeoseismology, Crestone (USA).

Vol. 6: Abstracts Volume, 6th International INQUA Meeting on Paleoseismology, Active Tectonics and Archeoseismology (*Blumetti, A.M., Cinti, F.R., De Martini, P.M., Galadini, F., Guerrieri, L., Michetti, A,M., Pantosti, D. and Vittori, E., eds.)*, 19-24 April 2015, Pescina, Fucsino Basin, Italy: Miscellanea INGV, Anno 2015_ Numero 27, ISSN 2039-6651, printed in Italy by Instituto Nazionale di Geofisica e Volcanologia, Rome, Italy, 545 p.

Vol. 5: Proceeding of the 5th International INQUA Meeting on Paleoseismology, Active Tectonics and Archeoseismology (*C. Grutzner, J.-H. Choi, P. Edwards & Y.-S. Kim, eds*.). ISBN 9791195344109 93450. Printed in Korea, 2014. 5th International INQUA Meeting on Paleoseismology, Active Tectonics and Archeoseismology, Busan (Korea).

Vol. 4: Seismic Hazard, Critical Facilities and Slow Active Faults (*C. Grutzner, A. Rudersdorf, R. Perez-Lopez & K. Reicherter, eds.*). ISBN 978-3-00-0427-96-1. Printed in Germany, 2013. 4th International INQUA Meeting on Paleoseismology, Active Tectonics and Archeoseismology, Aachen (Germany).

Vol. 3: Earthquake Geology and Archeoseismology: Society and Seismic Hazard (*R. Perez-Lopez, P.G. Silva, M.A. Rodriguez Pascua, V.H. Garduno Monroy, G. Suarez & K. Reicherter, eds*.) Printed in Mexico, 2012. 3rd INQUA-IGCP 567 International Workshop on Earthquake Geology, Paleoseismology and Archeoseismology, Morelia (Mexico).

Vol. 2: Earthquake Geology and Archeoseismology: Society and Seismic Hazard (*C. Grutzner, R. Perez-Lopez, T. Fernandez-Steeger, I. Papanikolaou, K. Reicherter, P.G. Silva & A. Vott, eds.*) ISBN: 978-960-466-093-3. Printed in Greece, 2011. 2nd INQUA-IGCP 567 International Workshop, Corinth (Greece).

Vol. 1: Archaeoseismology and Paleoseismology in the Alpine-Himalayan Collisional Zone (*R. Perez-Lopez, C. Grutzner, J. Lario, K. Reicherter & P.G. Silva, eds.*) ISBN: 978-84-7484-217-3. Printed in Spain, 2009. 1st INQUAIGCP 567 International Workshop, Baelo Claudia, Cadiz (Spain).

INTRODUCTION

Dear colleagues,

Welcome to the 9th International INQUA Meeting on Paleoseismology, Active Tectonics and Archeoseismology (PATA Days 2018). The Organizing Committee and the supporting team of the Department of Geology, Aristotle University of Thessaloniki, is honored and happy to be your host in Greece. PATA Days 2018 is the next in a series of very successful annual meetings that bring together the global community of earthquake geologists. We hope that this will be a fruitful and stimulating event as well. The programme consists of 95 presentations (55 oral and 40 poster ones) covering a very broad spectrum of subjects relevant to earthquake geology. Geographically, they cover a variety of tectonically diverse parts of the world. The associated Summer School targets students and early career researchers and gives them the opportunity to attend lectures by some of the top experts in the field.

June 2018 also marks the 40th anniversary of the M 6.5 Thessaloniki earthquake of June 20th, 1978. This earthquake caused extensive damage and fatalities. It was a landmark event for Greek seismology, as it was the first major earthquake that hit a modern Greek city. The damages in Thessaloniki, the second largest city in Greece, and the subsequent socioeconomic reverberations, led to the understanding of the importance of solid scientific knowledge. It was the beginning of the modern era of earthquake research in Greece. It was also one of the first cases where earthquake geology methods were applied in the field. Some of the first detailed surface rupture maps were produced at the aftermath of this event. Subsequent research, based on these early efforts, has contributed to better understanding of the active tectonic regime and the interaction of faults in the area. Seismic hazard assessment was significantly assisted by earthquake geology findings and subsequent improvements to building codes helped mitigating possible effects.

Finally, we would also like to thank the sponsors of this meeting, whose assistance has been invaluable in organizing the events and providing support to young scientists. We hope you enjoy this meeting and have the opportunity to engage in interesting discussions on the latest in earthquake geology research.

On behalf of the Organizing Committee,

Alexandros Chatzipetros, Spyros Pavlides

CONTENTS

INQUA Focus Group Earthquake Geology and Seismic Hazards

paleoseismicity.org

A New Design Wave Simulator for Realistic Earthquake Experiments: Usage of the One Wave Actuator as a Sequential Source of P and S-Type Waveforms

Acar, Dursun (1,7), Önder, Şebnem (2), Alpar, Bedri (3), İşseven, Turgay (4), Demirbağ, Emin (4), Kurt, Hülya (4), Özeren, Sinan (5), Postacıoğlu, Nazmi (6), Imren, Caner (4), Okut, Nigar Gözde (4)

(1) Istanbul Technical University, EMCOL, Istanbul, Turkey, dursunacaracar@hotmail.com
(2) Çanakkale Onsekiz Mart University, Geophysical Engineering Department, 17100 Çanakkale, Turkey, selbek@comu.edu.tr
(3) Istanbul University, Institute of Marine Sciences and Management, 34134, Fatih, İstanbul, Turkey, alparb@istanbul.edu.tr
(4) Istanbul Technical University, Department of Geophysical Engineering, Istanbul, Turkey, isseven@itu.edu.tr
(5) Istanbul Technical University Eurasia Institute of Earth Sciences, Istanbul, Turkey, ozerens@itu.edu.tr
(6) Istanbul Technical University Faculty of Science and Letters, Physics Engineering, Istanbul, Turkey, nposta@itu.edu.tr
(7) Anadolu University Faculty of Open Education Philosophy Eskişehir, Turkey

Abstract: *Realistic wave generator model experiments can develop our knowledge about fault fracture mechanisms. Especially for seismographic data resolve and its interpretations for multi- surface fractured fault generated earthquakes can be model subject with their data records. Mechanical instrument based earthquake wave forming can characterize separately for each broken segment before quake design for understand integrated and propagated complex seismograph data how occurred about self composition. Briefly, examination of single source or multi- source born body waves will be possible at time- dependent wave conduction experiments which simulations to based multi actuator direction. Hereby real seismograph observation with correlations other seismograph data will be more clear about how many segment is component and result of each segment's wave forms how interference at far points. This is first step of starting multi-vector acting experiment set series at earthquake simulations. We are thinking that shake mechanisms with arranged source directions will help to models focused to geologic substances-seismic frequency bandpass relationships. Experiment set is able to product real directional P- and S-waves as coming from one broken segment, unlike to simulations of random placed P-wave actuator user conventional shake tables.*

Keywords*: earthquake, simulator experiment, P and S waves, data processing*

INTRODUCTION

We designed a new mechanic experiment system at a laboratory-scale to be used in realistic earthquake simulations. Present well-known systems exist with separate waveform generators for body wave sources. The wave propagations during these operations can be predictable easily because of their accorded phase and spreading direction shifts. The production of P and S wave forms is rather difficult with two mechanic sources which are placed separately, as they makes cross-obstacles with continuous artificial act cuts. Our system, however, is designed to generate P-wave and S-waves sequentially. Two types of elementary waves existed at the planning stages of experiment. Experiment design is using only one actuator and providing one way focused seismic waves with 85 cm conductor rod fixed to the far center of the flywheel (7cm in diameter) to accomplish push and pull movements of the sample carrier table (Figure 1).

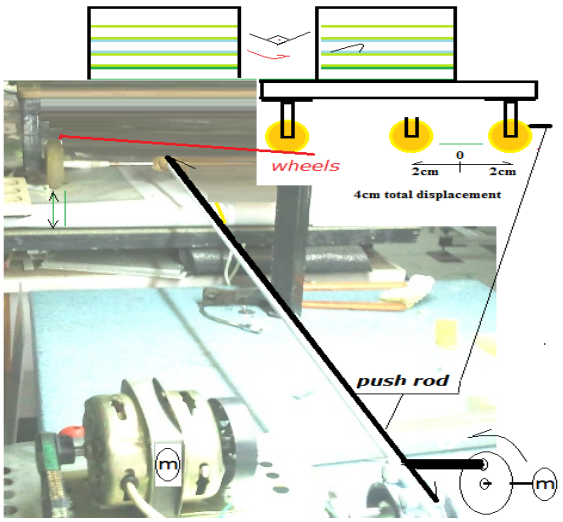

Figure 1: General design characteristics illustrated with 90° turned panoramic view.

Design based to benefits of long axial rod's longtitutional elastic movements between both fixing points of shake table and the far centered flywheel with some restrictions which can be changed manually. Vertical displacement restriction ratios of the wave conductor rod is directly related to the adjusting of wave amplitudes and the length of specs used for simulating earthquake waves (Figure 2).

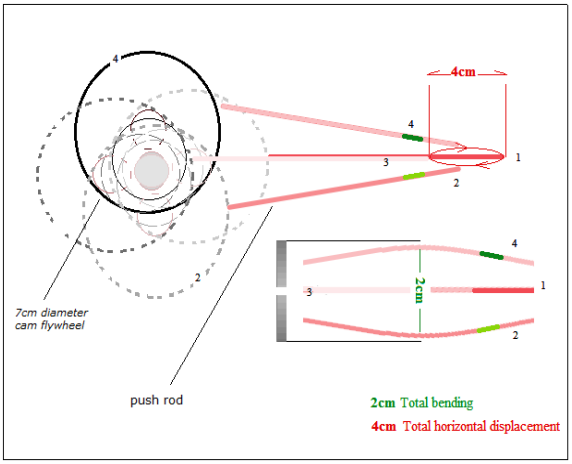

Figure 2: Experiment push rod mechanism horizontal displacement and bending characteristics.

The shake table has four ball bearing wheels with low friction for accord to S type wave actuator movements. Acceleration controllers were not use in the experiments because the linear actuator needs far basin-fault experiment set. Using only one actuator for different wave forms eliminates undesirable wave propagation of the multi actuator without mechanical hesitations. We have performed successful experiments with Kelvin- Helmholtz interphase irregularities in artificial biogenic sediments (Figure 3).

Figure 3: Experiment materials before and after the shaking processes: (P-Wave and S- Wave provided as naturel earthquake by mechanical system. You tube Video link https://www.youtube.com/watch?v=7TILOS42Hhg).

During the earlier applications of the experiment we used unbalanced weight fixed rotor driven electric motors in generating P-Wave separately by using different P-wave motors. Unfortunately we were not successful in P-wave to S-wave switching because P-wave spread direction was not convenient with the S wave generator due to mechanical wave interferences. Irregular wave propagation loads prevent randomly to normal movements of centric axial S-wave generator. Dimension of the P-wave actuator needs always heavy construction too. But light motor application weight gets more convenient with experiment sets for all types of earthquakes representing various tectonic settings.

Experiment accepts stable acceleration constant with today's circumstances related which fault broken at one fault line. Secondly; multi line broken faults not simulated for complexity of acceleration calculation.

In future we will use second stage experiment sets for a different purpose closed basin-fault seismic interactions about deformations.

DISCUSSION

Especially accelerometer installations will help to research and development stages of explained subjects below. Accelerometer group 1 are observing to quality and direction of artificial P- and S-wave about table. Group 2 is related with sediment material on experiment about paleoseismic events and other records. Paleoseismic structures in sediments still has question about their generation related with the seismic wave conditions (Figure 4). We will continue to work with our model type experiments under two main subjects.

1-Signal interference or data filtration and resampling or noise cancelling

2- Interpretation of integrated signals related to multi segmental fractures on with the purpose of separation of each segment on seismograms (Figure 5).

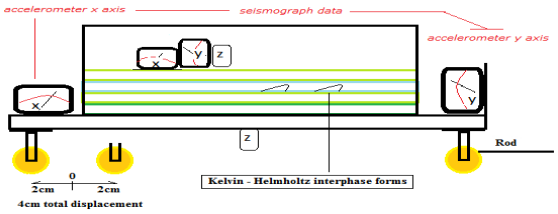

Figure 4: Experiment and accelerometer deployments; For experiment material; accelerometers at X,Y,Z axis, for rigid shake tables X,Y and for non rigid tables Z axis accelerometers can be used.

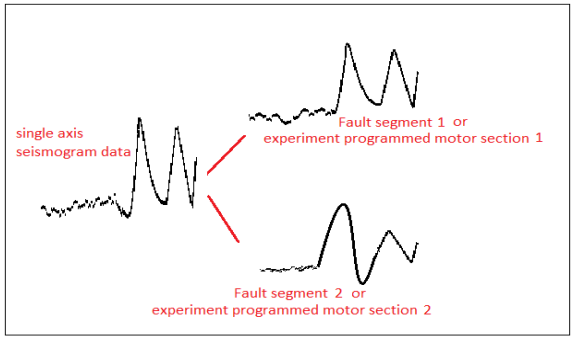

Figure 5: Multi segment broken earthquake seismo-signal and its separated segment signals (illustration).

Acknowledgements: Authors thanks to Prof. Dr. Namık Çağatay and Prof. Dr. Kadir Eriş for their permission to use EMCOL Laboratories of ITU. We also thanks to the researchers at the neighbour laboratories for their patience for our experiments.

INQUA Focus Group Earthquake Geology and Seismic Hazards

paleoseismicity.org

Assessing the intensity values of Iranian earthquake using EMS98 and ESI2007 intensity scale

Amini, Hamed (1)

(1) Postdoc at Institute of Geophysics of Tehran University, Tehran, Iran, hiamini@ut.ac.ir

Abstract: *Iran is a country located in convergence of Arabian and Eurasia plates. According to its high seismic activity, completing the catalog of its earthquakes as much as possible is necessary. Assessing the intensity values of all earthquakes is a way to improve the earthquake catalog. In this study, firstly, EMS98 scale, the resent macroseismic intensity scale used to assess the intensity values. There are not complete descriptions on building damage for all earthquakes, but some descriptions reported on environmental effects for some earthquakes; then, ESI2007 scale is also selected to assess more reliable intensity values. Comparing the results of two scales for the earthquakes with more complete descriptions, show that they are consistent to each other. Then, their maximum value can be used for final intensity values, and in the lack of description of one scale, the value of another one can be consider estimating the intensity values.*

Keywords*: Intensity value, ESI and EMS scale, Iranian earthquake*

INTRODUCTION

Iran is located in convergence of Arabian and Eurasia plates. According to its high seismic activities and lots of occurred earthquakes in various period of the time in this region, improving its earthquake dataset by completing the information is necessary. Considering the earthquake intensity values is a way to improve the earthquake dataset. The main propose of this study is to assess the intensity values using the earthquake descriptions.

Firstly, the most recent macroseismic intensity scale, EMS scale (Grünthal, 1993, 1998), based on different categories of building damage and also effects on people, objects, and natural environment was selected as a basic scale to assess the intensity values. For several Iranian earthquakes especially historical ones, it is not possible to assess their reliable intensities only based on this scale. As there are some reports of the environmental effects for some of the earthquakes, the ESI scale (Michetti et al., 2004 and 2007 and Guerrieri et al., 2015), based on environmental effect descriptions considering comparison of three most diffused intensity scales (MCS, MSK, and MM), are also used to assess the more reliable intensity values of the earthquakes.

Using the earthquakes with more complete descriptions, their intensity values assessed in both EMS and ESI scales. In the following, the final intensity values of both scales for each of these earthquakes are compared to find the best earthquake intensity values.

DATASET

Description of 136 Iranian earthquakes was collected from available books, articles, and reports of different Iranian research centers (i.e. International Institute of Earthquake Engineering and Seismology (IIEES), Building and Housing Research Center (BHRC), Geological Survey of Iran (GSI), and National Geoscience Database of Iran (NGDIR)). Moreover, most earthquake descriptions of this region were reported by Berberian (1976a, 1976b, 1976c, 1977, 1981, 2005), Zare & Memarian (2003), Ambraseys (2001), and Ambraseys & Moinfar (1977).

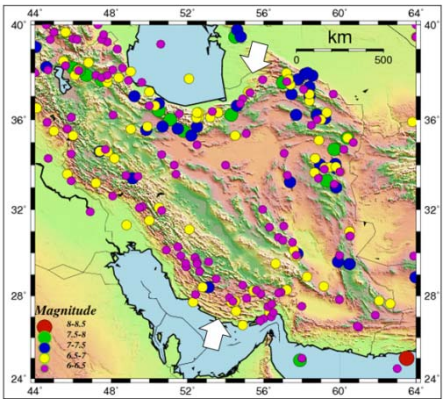

Figure 1: Location of Iran and its earthquakes with magnitude more than 6; the vectors show the convergence of Arabian-Eurasia which according to Vernant et al. (2004) is between 22-25 mm/yr for Iran region.

IRANIAN EARTHQUAKE INTENSITIES

In various period of the time, many earthquakes occurred in different parts of Iran. To assess the Iranian earthquake intensities, four intensity scales have been applied depend on their introducing time to the world. They consist of one 5-degree scale introduced by Ambraseys & Melville (1982) (AMS) and three 12-degree intensity scales consist of Modified Mercalli (MM: MMI; Richter, 1958; Wood & Neumann, 1931), the Medvedev-Sponheuer-Karnik (MSK; Medvedev, 1964), and the European Macroseismic Scale (EMS98; Grünthal, 1993, 1998).

In this study, ESI2007 scale is also used to assess the intensity values. On the other hand, to consider all reported descriptions on building damage and environmental effects of the earthquakes, the definition of two EMS98 and ESI2007 scales are applied at the same time to assess more reliable value of the intensities. To show using these two scales, the final unified intensity values of the earthquakes are called EMS-ESI scale.

DISCUSSION

A collection of 136 earthquakes with more complete descriptions on both building damage and environmental effects considered to assess their intensity values in both EMS and ESI scales. According to their assessed intensity values, in most cases, the values are the same or their differences are in one degree (Fig. 2) (Table 1).

In 2 and 14 cases, the differences are in 3 and 2 units, respectively; which is because of their less description on these earthquakes. Then, by increasing the descriptions of each earthquake, its intensity values can be assessed with more accuracy.

In some cases, such as 1058.12.08, 1483.02.18, 1780.01.08, 1936, 06.30, 2013.04.09, and so on, the assessed value of ESI is larger; conversely in other ones, such as 856.12.24, 1316. 01.05, 1890.07.11, 1900.02.24, 1968.05.30, and so on, the value of EMS is larger. According to Michetti et al. (2007) for these earthquakes with different assessed intensity values in the EMS or/and the ESI scale, the maximum values between two assessment are selected as their final intensity value.

To improve more information of earthquakes, field studies using paleoseismology and dating, geology, geotectonic and other related investigation can be useful; therefore, such studies suggested improving the earthquake information and then, their intensity and parameter dataset.

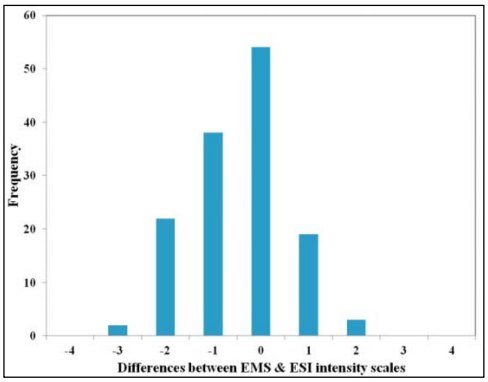

Figure 2 Histogram of differences between the intensity values of ESI2007 and EMS98 scales assessed for a set of 136 earthquakes of this study.

Table 1: List of 136 earthquakes with more complete descriptions and their intensity values assessed in EMS, ESI, and this study (EMS-ESI) scales.

Y	M	D	EMS	ESI	EMS-ESI
856	12	22	X	IX	X
872	6	22	VIII	IX	IX
893	12	24	IX	VIII	IX
956	…	…	VII	VIII	VIII
958	2	23	XI	XI	XI
958	4	…	IX	IX	IX
1052	6	2	IX	IX	IX
1058	12	8	VIII	IX	IX
1066	5	…	X	IX	X
1127	…	…	X	X	X
1130	2	27	IX	IX	IX
1135	7	25	IX	IX	IX
1150	4	1	IX	IX	IX
1177	5	…	X	IX	X
1179	4	29	X	IX	X
1194	3	…	VII	VIII	VIII
1226	11	18	X	IX	X
1304	11	7	VII	VIII	VIII
1316	1	5	XI	VIII	XI
1344	…	…	VIII	VIII	VIII
1364	2	10	IX	IX	IX
1459	…	…	VI	VIII	VIII
1470	…	…	IX	IX	IX
1483	2	18	VIII	IX	IX
1485	8	15	X	IX	X
1493	1	10	X	IX	X
1503	…	…	IX	IX	IX
1549	2	15	X	IX	X
1550	…	…	VII	VIII	VIII
1591	…	…	VIII	VIII	VIII
1593	…	…	X	IX	X
1593	9	…	X	XI	XI
1608	4	20	IX	IX	IX
1622	10	4	VIII	VIII	VIII
1641	2	5	IX	IX	IX
1666	…	…	IX	IX	IX
1673	7	30	X	IX	X
1677	…	…	IX	IX	IX
1679	6	4	IX	VIII	IX
1695	5	11	X	IX	X
1696	4	14	X	IX	X
1703	…	…	VII	VIII	VIII
1715	3	8	X	IX	X
1721	4	26	IX	IX	IX
1778	12	15	IX	VIII	IX
1780	1	8	X	XI	XI
1786	10	…	IX	VIII	IX
1804	…	…	VIII	VIII	VIII
1805	…	…	IX	VIII	IX
1807	7	11	IX	VIII	IX
1808	6	26	VIII	VIII	VIII
1808	12	16	IX	VIII	IX
1809	…	…	IX	IX	IX
1824	6	2	IX	VIII	IX
1824	6	25	IX	IX	IX
1825	…	…	IX	IX	IX
1827	…	…	VIII	VIII	VIII
1830	3	27	IX	IX	IX
1833	…	…	IX	IX	IX
1834	…	…	IX	VIII	IX
1837	6	…	VII	VIII	VIII
1838	…	…	IX	IX	IX
1840	7	2	X	X	X
1843	4	18	VIII	VIII	VIII
1844	5	12	X	IX	X
1844	5	13	X	IX	X
1851	6	…	IX	IX	IX
1853	5	5	X	VIII	X

1862	**12**	**21**	VIII	IX	IX
1863	**12**	**30**	IX	VIII	IX
1864	**1**	**17**	VIII	VIII	VIII
1871	**12**	**23**	X	VIII	X
1875	**5**	**…**	IX	VIII	IX
1879	**3**	**22**	XI	IX	XI
1880	**7**	**4**	X	IX	X
1884	**5**	**19**	VIII	VIII	VIII
1890	**7**	**11**	X	IX	X
1893	**11**	**17**	X	X	X
1894	**2**	**26**	X	VIII	X
1895	**1**	**17**	X	IX	X
1896	**1**	**4**	X	IX	X
1897	**5**	**27**	IX	VIII	IX
1900	**2**	**24**	IX	VIII	IX
1903	**9**	**25**	IX	VIII	IX
1909	**1**	**23**	X	X	X
1911	**4**	**18**	X	IX	X
1923	**5**	**25**	X	VIII	X
1923	**9**	**17**	IX	IX	IX
1923	**9**	**22**	X	IX	X
1927	**7**	**22**	IX	IX	IX
1929	**5**	**1**	XI	XI	XI
1929	**7**	**15**	IX	IX	IX
1930	**5**	**6**	XI	XI	XI
1930	**10**	**2**	X	VIII	X
1933	**11**	**28**	X	IX	X
1935	**3**	**5**	IX	VIII	IX
1935	**4**	**11**	IX	IX	IX
1936	**6**	**30**	VIII	IX	IX
1941	**2**	**16**	XI	X	XI
1945	**11**	**27**	XI	XI	XI
1947	**9**	**23**	XI	X	XI
1957	**7**	**2**	X	VIII	X
1953	**2**	**12**	X	X	X
1957	**7**	**2**	XI	IX	XI
1962	**4**	**1**	IX	VIII	IX
1962	**9**	**1**	XI	XI	XI
1962	**11**	**6**	VIII	VIII	VIII
1965	**6**	**21**	VIII	VIII	VIII
1968	**4**	**29**	IX	VIII	IX
1968	**5**	**30**	IX	VIII	IX
1968	**8**	**31**	XI	X	XI
1968	**9**	**1**	X	IX	X
1968	**9**	**14**	X	VIII	X
1968	**11**	**15**	VIII	VIII	VIII
1969	**1**	**3**	IX	IX	IX
1970	**7**	**30**	VIII	VIII	VIII
1971	**4**	**12**	VIII	VIII	VIII
1971	**11**	**8**	VIII	VIII	VIII
1972	**4**	**10**	XI	XI	XI
1975	**3**	**7**	X	VIII	X
1977	**4**	**6**	X	VIII	X
1977	**12**	**19**	X	X	X
1978	**9**	**16**	XI	XI	XI
1979	**11**	**27**	IX	X	X
1980	**12**	**19**	VIII	VIII	VIII
1981	**7**	**28**	X	IX	X
1988	**8**	**11**	X	X	X
1990	**6**	**20**	XI	XI	XI
1994	**2**	**23**	VIII	X	X
1997	**2**	**4**	X	IX	X
1997	**5**	**10**	XI	XI	XI
1998	**3**	**14**	VII	X	X
2005	**2**	**22**	X	X	X
2012	**8**	**11**	X	X	X
2013	**4**	**9**	VII	IX	IX

CONCLUSION

The description of 136 Iranian earthquakes collected from different references (e.g. books, articles, documentation and websites) used to assess the intensity values of these earthquakes in both EMS98 and ESI2007 scales. In this study, consistency of the EMS and ESI scales for Iranian earthquakes was tested using the dataset of these earthquakes with more complete descriptions with the possibility of assessing their intensity values in both EMS and ESI scales.

Comparing the results of two scales for the earthquakes with more complete descriptions, show that they are consistent to each other. In about 80% cases, the assessed intensity values by two scales differed by one degree or less. So that according to Michetti et al. (2007), for the earthquakes with different assessed intensity values in the EMS or/and the ESI scale, the maximum values between them were selected as their final intensity values (Called EMS-ESI scale in this study).

Therefore, for other Iranian earthquakes in the lack of information of one scale, the value of another one can be used to consider for the final intensity values. Moreover, field studies using paleoseismology and dating, geology, geotectonic and other related investigation suggested improving the earthquake information to improve their intensity and parameter dataset.

Data and Resources: International Institute of Earthquake Engineering and Seismology (IIEES) with searching on http://www.iiees.ac.ir/fa/eqreports/, Building and Housing Research Center (BHRC) with searching on http://bhrc.ac.ir/, Geological Survey of Iran (GSI) with searching on http://www.gsi.ir/General/Lang_fa/, and National Geoscience Database of Iran (NGDIR) with searching on http://www.ngdir.com/Downloads/PDownloadList.asp.

Acknowledgements: Thanks to Prof. Mehdi Zare, Prof. Paolo Gasperini and Prof. Alessandro Maria Michetti for their help and suggestion.

REFERENCES

Ambraseys, N.N., 2001. Reassessment of earthquakes, 1900-1999, in the Eastern Mediterranean and the Middle East. *Geophysical Journal International* 145, 471-485.

Ambraseys, N.N., & Moinfar, A.A., 1977. Iran earthquake 1968. vol. Publication No. 69. Tehran, Iran. Technical Research and Standard Bureau, Plan and Budget Organization.

Ambraseys, N.N., & Melville, C.P., 1982. A History of Persian Earthquakes. Cambridge Univ. Press, New York, pp. 219.

Berberian, M., 1976a. Documented earthquake faults in Iran. *Geol Surv Iran* 39, 143-186.

Berberian, M., 1976b. Contribution to the Seismotectonics of Iran (Part II): in Commemoration of the 50th Anniversary of the Pahlavi Dynasty. Tehran: Geological Survey of Iran.

Berberian, M., 1976c. Quaternary faults in Iran. *Geological Survey of Iran* 39, 187-258.

Berberian, M., 1977. Contribution to the seismotectonics of Iran (Part III): In Commemoration of the 50th Anniversary of the Pahlavi Dynasty. Ministry of Industry and Mines. Geological Survey of Iran, Tectonic and Siesmotectonic Section.

Berberian, M., 1981. Active Faulting and Tectonics of Iran.

Berberian, M., 2005. The 2003 Bam urban earthquake: A predictable siesmotectonic pattern along the western margin

of the rigid Lut Block, southeast Iran. *Earthquake Spectra* 1 (S1), 35-99.

Grünthal, G., 1993. European macroseismic scale 1992: updated MSK scale. European Seismological Commission, Subcommission on Engineering Seismology, Working Group Macroseismic scale.

Grünthal, G., (ed.), 1998. European Macroseismic Scale 1998, Cahiers du Centre Europèen de Gèodynamique et de Seismologie. *Conseil de l'Europe, Conseil de l'Europe* 15, 99.

Guerrieri, L. Michetti, A.M., Reicherter, K., Serva, L., Silva, P.G., Audemard, F., Azuma, T., Baiocco, F., Baize, S., Blumetti, A.M., Brustia, E., Clague, J., Comerci, V., Esposito, E., Gurpinar, A., Grutzner, C., Jin, K., Kim, Y.S., Kopsachilis, V., Lucarini, M., McCalpin, J., Mohammadioun, B., Morner, N.A., Okumura, K., Ota, Y., Papathanassiou, G., Pavlides, S., Perez López, R., Porfido, S., Rodríguez Pascua M.A., Rogozhin, E., Scaramella, A., Sintubin, M., Tatevossian, R., & Vittori, E., 2015. Earthquake Environmental Effect for seismic hazard assessment: the ESI intensity scale and the EEE Catalogue. *Memorie descrittive della Carta Geologica d'Italia* V, XCVII.

Medvedev, S., Sponheuer, W., & Karnik, V., 1964. Neue seismische Skala Intensity scale of earthquakes, 7. Tagung der Europaischen Seismologischen Kommission vom 24.9. bis 30.9. *Veroff Institut für Bodendynamik und Erdbebenforschung in Jena* 77, 69-76.

Michetti, A.M., Esposito, E., Gurpinar, A., Mohammadioun, B., Mohammadioun, J., Porfido, S., Rogozhin, E., Serva, L., Tatevossian, R., Vittori, E., Audemard, F., Comerci, V., Marco, S., MaCalpin, J., & Morner, N.A., 2004. The INQUA Scale, An innovative approach for assessing earthquake intensities based on seismically-induced ground effects in natural environment. *Memorie descrittive della Carta Geologica d'Italia* 67.

Michetti, A.M., Esposito, E., Guerrieri, L., Porfido, S., Serva, L., Tatevossian, R., Vittori, E., Audemard, F., Azuma, T., Clague, J., Comerci, V., Gurpinar, A., Mc Calpin, J., Mohammadioun, B., Mörner, N.A., Ota, Y., & Roghozin, E., 2007. Intensity scale ESI 2007. In: *Mem. Descr. Carta Geologica d'Italia, Servizio Geologico d'Italia* (Guerrieri, L., Vittori, E. ed), Dipartimento Difesa del Suolo, APAT, Rome, 74p.

Richter, C., 1958. *Elementary Seismology*. San Francisco: W.H. Freeman.

Wood, H.O., & Neumann, F., 1931. *Modified Mercalli Intensity Scale of 1931.* California: Seismological Society of America.

Zare, M., & Memarian, H., 2003. Macroseismic intensity and attenuation laws: A study on the intensities of the Iranian earthquakes of 1975-2000. *Four the International Conference of Earthquake Engineering and Seismology*, 12-14.

INQUA Focus Group Earthquake Geology and Seismic Hazards

paleoseismicity.org

Foraminiferal assemblage analysis of beach samples and drill cores from the Northwest coast of Crete

Anh, Thu Vu (1), Mathes-Schmidt, Margret (1), Vött, Andreas (2), Reicherter, Klaus (1)

(1) Inst. of Neotectonics and Natural Hazards, RWTH Aachen University, Lochnerstrasse 4-20, D - 52056 Aachen, Germany, t.vu@nug.rwth-aachen.de
(2) Natural Hazard Research and Geoarchaeology Institute for Geography, Mainz University, Johann-Joachim-Becher-Weg 21, D - 55099 Mainz, Germany, voett@uni-mainz

Abstract: *At the coasts around Crete beach samples were collected in order to characterize foraminiferal assemblages and identify their distribution patterns as function of environmental and local conditions. In addition, samples from two drill cores near Kissamos and near Falarsana (NW Crete) were examined. Cluster analysis and the Principal component analysis (PCA) show approximately the same three groups of foraminifera assemblages: (Ia) Peneroplis pertusus, (Ib) Cibicides pseudolobatulus, (II) Ammonia beccarii; (III) Globigerina bulloides-Globigerinoides rubra. The cluster analysis computed for group (1) two subcategories. Two groups appear locally limited. Group (Ib) is typical for the north western coast and the core from Falarsana. Group III characterizes Kissamos core samples and the eastern Kissamos beach samples. Biotic indices show the original habitats of the foraminifera from inner shelf areas to bathyal water depth.*

Keywords*: Crete, coastal environment, foraminiferal assemblages, multivariate statistics*

INTRODUCTION

Crete is highly affected by tectonics which is associated with relative sea level changes, earthquakes and also tsunamis. During the July AD 365 earthquake the western part of Crete was uplifted by approximately 9 m and further hit by the associated tsunami (Stiros, 2001, 2010; Shaw et al., 2008). Foraminifera are one of the useful microfossil groups applied as a significant and sufficient tool in environmental characteristic in coastal areas (Buosi et al., 2013). The changes in foraminifera assemblages in terms of diversity, species composition, abundance as well as test morphology can be used for determining ecosystem conditions (Buosi et al., 2013) and for reconstruction of paleoenvironmental changes because they quickly respond to changes in eg temperature, salinity and bathymetry (Murray, 1991, 2006). Aim of the study was to map typical foraminifera assemblages for coastal areas of Crete as a tool for recognition of high energy events, climate and relative sea level changes.

STUDY AREA

The island of Crete is situated in the Eastern Aegean Sea in the middle part of the Hellen arc, near the southern limit of the Ionian Trench, within an active extensional regime of the Aegean (Pirazzoli, 1992; Mason et al., 2016). The study area is divided into three subareas (fig. 1), because of the different styles of the coast. Here we focus on the western area (fig. 1). Sampling was concentrated on the northwestern coast north- and southward of the ancient harbor of Falarsana and within the U-shaped Bay of Kissamos which opens to the North (Fig. 1). More samples were taken further east.

METHODS

As statistical techniques cluster analysis (Q and R mode), principal component analysis (PCA) and ordination analysis were used as well as calculation of biotic indices: species richness (Murray, 1991), the alpha-index of Fisher (Fisher et al., 1943), Simpson's index (Simpson, 1949), the Shannon-Wiener index [H(s)] (Shannon & Weaver, 1963) and the percentage dominance (Walton, 1964). The grain size distribution was determined for all beach samples by wet sieving.

RESULTS AND DISCUSSION

A total of 65 samples were examined, whereof 36 gave enough material for statistical analysis. Foraminifera assemblages are rich and diverse containing a total of 66 species of benthic and planktonic foraminifera which belong to the orders Miliolida (32.30%), Rotaliida (66.53%), Lituolida (0.009%), Textulariida (0.21%) and Lagenida (0,95%).

Group Ia (5 samples) is named after *Peneroplis pertusus* (Fig. 2), the dominant species. Other typical foraminifera of this group are: *Asterigerinata mammilla* and *Cibicides pseudolobatulus*. *Peneroplis pertusus* lives epifaunal in lagoons and on the innermost shelf (Murray, 1973, 1991, 2006; Phleger, 1960; Hohenegger, 2003). This environment is characterized by sands with a significant contribution of medium sand.

Group Ib (18 samples) is dominanted by *Cibicides pseudolobatulus* (Fig. 2), subsidiary species are *Asterigerinata mamilla, Miniacina miniace* and agglutinanted species.

Cibicides pseudolobatulus lives epifaunal in cold to warm water environments or on hard substrates in high energy environments of the shelf zone (Murray, 1991). Grain size of the samples is normally fine sand.

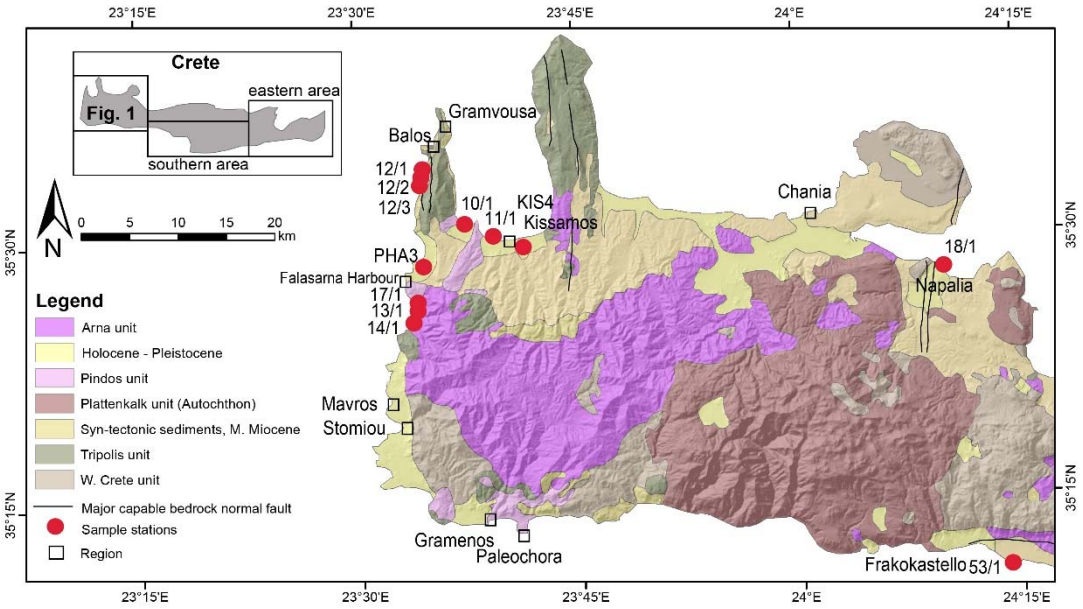

Figure 2: Geological map (based on Sheet Palaiokhora, 1972, scale 1:50.000) of the western investigation area.

.

Group Ia and Ib occur in samples on the west coast in beach samples as well as in core samples. This part of the coast is wind and wave affected especially in winter (Koletsis et al., 2010; Soukissian et al., 2011). Particularly *Cibicides* is adapted to high energy environments (Murray, 2006).

Group II (two samples) is identified by a high amount of *Ammonia beccarii* together with a fewer amount of *Amphistegina lobifera*, *Quinqueloculina seminula*, and *Elphidium cripsum* (Fig. 2). *Ammonia beccarii* prefers muddy sand, brackish and hypersaline lagoons and is also common in inner to middle shelf areas (Murray, 1991). Coarse sand is an environmental characteristic of this cluster.

Group III (11 samples) is dominated by *Globigerina bulloides* and *Globigerinoides rubra*. *Cibicides pseudolobatulus* and *Neoconorbina terquemi* occur with minor individuals (fig. 2). *Globigerina bulloides* and *Globigerinoides rubra* live commonly in the epipelagic, outer-bathyal zone (Szczechura, 1984; Murray, 1973). Wave action in the Bay of Kissamos is low throughout the year (Koletsis et al., 2010; Soukissian et al., 2011). Prevailing winds in winter are coming from the north (Pyökäri, 1999). The sheltered position against strong wave action in the inner Bay allows the accumulation of thin-shelled foraminifera like *Globigerina* and *Globigerinoides* which are probably brought in by winds from the north and surface currents.

CONCLUSIONS

The foraminifera assemblages of the beaches of West Crete are divided in three main groups by statistical methods wherefrom the cluster analysis reveals the best results. The composition of foraminifera species can be correlated with the environment: Group I (Ia, Ib) assemblages are typical for environments which are exposed to high wave and wind energy. A good proxy of this group is *Cibicides pseudolobatulus.*

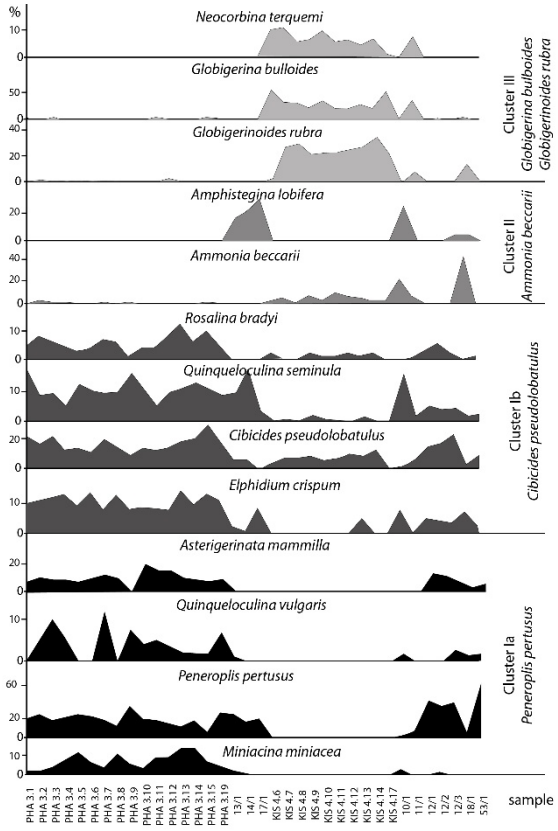

Figure 2: Assemblage clusters with typical and abandon species of foraminifera in percentage proportion of all individuals of a sample.

Only two samples plot in Group II, an interpretation would not be well founded at the moment. A correlation with samples of the southern and eastern areas is in progress.

Group III is characterized by a high amount of planktonic species which was not expected for beach sediments here. The U-shaped form of the Bay of Kissamos seals off high waves and strong winds and allows the preservation of a diverse fauna of foraminifera. Planctonic foraminifera like *Globigerina bulloides* and *Globigerinoides rubra* which are carried into the Bay by northern winds and currents, occur with benthic forms in the same beach sediment. For this the exclusive occurrence of planctonic species is not a sufficient characteristic for a high energy event in the Bay of Kissamos.

Together with the upcoming results from the southern and eastern coasts on Crete the knowledge of common foraminifera assemblages may serve as a tool to evaluate changes in ecosystems, sea level, climate and high energy deposits of Cretan coastal areas.

Acknowledgements: Financial support by DFG Projects RE 1361/19-1 and VO 938/12-1 (Tracing the spatial and temporal variabilities of tsunamites on Crete Island (Greece) by sedimentological, geophysical and geodetical methods) is gratefully acknowledged.

REFERENCES

Buosi, C., Cherchi, A., Ibba, A., Marras, B., Marrucci, A., & Schintu, M., 2013. Preliminary data on benthic foraminifera assemblages and sedimentological characterization from some polluted and unpolluted coastal areas of Sardinia (Italy). *Paleontological Italiana* 52 (1), 35-44.

Fisher, R.A., Corbet, A.S., & William, C., 1943. The relationship between the number of species and the number of individuals in a random sample of animal population. *Journal of Animal Ecology* 12, 42-58.

Hohenegger, J., & Baal, C., 2003. Protisten (Mikroalgen und Protozoen)-Klasse Foraminifera d'Orbigny, 1826. In: *Das Mittelmeer-Fauna, Flora, Ökologie - Allgemeiner Teil* (Hofrichter, R., ed) (2003), Spektum Akademischer Verlag. Heidelberg and Berlin, 102-195.

Koletsis, I., Lagouvardos, K., Kotroni, V., & Bartzokas, A., 2010. The interaction of northern wind flow with the complex topography -of Crete Island - Part 2: Numerical study. *Nat. Hazards Earth Syst. Sci.* 10, 1115-1127, doi: 10.5194/nhess-10-1115-2010.

Mason J., Schneiderwind S., Pallikarakis, A., Wiatr, T., Mechernich, S., Papanikolaou I., & Reicherter, K., 2016. *Tectonophysics* 683, 216-232.

Murray, J.W., 1973, *Distribution and ecology of living Benthic Foraminiferids*. Heinemann. London. 744 pp.

Murray, J.W., (ed) 1991. *Ecology of Benthic Foraminifera*. Longman Group UK Limited. London. 402 pp.

Murray, J.W., 2006. *Ecology and Applications of Benthic Foraminifera*. Cambridge University Press. 426 pp.

Phleger, F.B., 1960. *Ecology and distribution of recent Foraminifera*. The Johns Hopkins Press. 297 pp.

Pirazzoli, P.A., Ausseil-Badie, J., Giresse, P., Hadjidaki, E., & Arnold, M., 1992. Historical environmental changes at Phalasarna harbor, West Crete. *Geoarchaeology* 7, 371-392.

Pyökäri, M., 1999. Beach sediments of Crete: Texture, Composition, Roundness, Source and Transport. *Journal of Coastal Research* 15 (2), 537-553.

Shaw, B., Ambrayses, N.N., England, P.C., Floyd, M.A., Gorman, G.J., Highham, T.F.G., Jackson, J.A., Nocquet, J. M., Pain, C.C., & Piggott, M.D., 2008. Eastern Mediterranean tectonics and tsunami hazard inferred from the AD 365 earthquake. *Nature Geoscience* 1, 268-276.

Shannon, C.E., & Weaver, W.W., 1963. *The mathematical theory of communication*. University of Illinois Press. Urbana. 125 pp.

Simpson, E.H., 1949. Measurement of diversity. *Nature* 163, 688.

Soukissian, T., Prospathopoulos, A., Hatzinaki, M., & Kabouridou, M., 2008. Assessment of the Wind and Wave Climate of the Hellenic Seas Using 10-Year Hindcast Results. *The Open Ocean Engineering Journal* 1, 1-12.

Stiros, S.C., 2001. The AD 365 Crete Earthquake and possible seismic clustering during the fourth to sixth centuries AD in the Eastern Mediterranean: a review of historical and archaeological data. *Journal of Structural Geology* 23, 545-562.

Stiros, S.C., 2010. The 8.5+ magnitude, AD365 earthquake in Crete: Coastal uplift, topography changes, archaeological and historical signature. *Quaternary International* 216, 54-63.

Szczechura, J., 1984. Morphologic variability in the Globigerinoides-Orbulina Group from the Middle Miocene of the Central Paratethy. *Acta Paleontological Polonica* 29 (1-2), 3-27.

Walton, W.R., 1964. Recent foraminiferal ecology and paleoecology. In: *Approaches to Paleoecology* (Imbrie, J., Newell, N.D., eds.), Wiley, New York, 151-237.

INQUA Focus Group Earthquake Geology and Seismic Hazards

paleoseismicity.org

Storytelling Technologies for Dissemination of Scientific Information of Natural Disasters: The June 12, 2017, Mw 6.3 Lesvos (Northeastern Aegean, Greece) earthquake story map

Antoniou, Varvara (1), Mavroulis, Spyridon (2), Spyrou, Nafsika-Ioanna (2), Bardouli, Pavlina (2), Andreadakis, Emmanouil (2), Skourtsos, Emmanuel (2), Kaviris, George (3), Sakkas, Vasilios (3), Carydis, Panayotis (4), Lekkas, Efthymios (2)

(1) National and Kapodistrian University of Athens, School of Sciences, Faculty of Geology and Geoenvironment, Department of Geography-Climatology, Panepistimiopolis, 15784, Athens, Greece, vantoniou@geol.uoa.gr
(2) National and Kapodistrian University of Athens, School of Sciences, Faculty of Geology and Geoenvironment, Department of Dynamic Tectonic Applied Geology, Panepistimiopolis, 15784, Athens, Greece, smavroulis@geol.uoa.gr
(3) National and Kapodistrian University of Athens, School of Sciences, Faculty of Geology and Geoenvironment, Department of Geophysics-Geothermy, Panepistimiopolis, 15784, Athens, Greece
(4) National Technical University of Athens, Greece

Abstract: *On June 12, 2017, a shallow crustal strong earthquake with magnitude 6.3 occurred offshore, south of Lesvos (12:28 GMT), 35.8 km SSW of the capital of Lesvos Island, Mytilene, causing one fatality, extensive earthquake environmental effects and severe structural damage in the SE part of the island. A set of the scientific data acquired in the field and the preliminary scientific results obtained by the aforementioned research has been presented not only to the scientific community but also to the general public and to much broader audiences by using a recently developed and introduced tool: the story telling through story maps. The 2017 Lesvos earthquake story map is presented and emphasis has been given to the used scientific data, its structure as well as the accessibility and sharing.*

Keywords*: story maps, storytelling, dissemination, presentation, natural disasters, earthquakes*

INTRODUCTION

The effective communication of scientific research to different audiences and the accurate dissemination of scientific information shared with both the public and the scientific community is one of the most crucial points of the effective management of the destructive impact of a natural disaster on human, nature, buildings and infrastructure.

As regards the dissemination of information within the scientific community, the majority of scientists present their materials and methods, their results and conclusions in papers presented in various meetings including conferences, workshops and congresses and published in scientific journals. This way of dissemination enable scientists to inform the community about their research, to expose their ideas to criticism by other scientists, and, of course, to stay abreast of scientific developments around the world.

As regards the dissemination of scientific information to the public and especially to non-technical audiences, various tools of representation and dissemination have been developed. Maps have been used to tell stories for thousands of years due to the fact that they can contain and convey a large amount of information in a small amount of space. One of the recently developed and introduced tools in this direction is the story telling through story maps.

Story maps are simple web applications that allow to tell a story about the world. They combine interactive maps, multi-media content such as photos and videos, simple interactive elements that control or enhance aspects of the map, descriptive text providing context, summarizing the aim of the map, and explaining its components as well as credit and source information [Environmental Systems Research Institute (ESRI), 2012]. Story maps are hosted by ESRI in the cloud and may be suitable for presenting and describing various stories and subjects about the world (https://storymaps.arcgis.com/en/gallery/#s=0) including natural disasters among others.

Some components commonly found in story maps are authoritative and well-organized data, clear and useful pop-ups, simple cartography, time-enabled data and dynamic legends. They can be built not only by highly-trained specialists, graphic designers and journalists but also by anyone with a basic familiarity with web and mobile platforms. They can serve not only the general public, but also communities and organizations.

The process of the development and publication of a story map including the following steps (ESRI, 2012): (a) development of a storyboard, (b) collection of information, (c) creation of a web map or maps, (d) selection of a basemap, (e) assembling the map, (f) adjustment and refinement of the map, (g) configuration of pop-ups, (h) adjustment of symbols, (i) saving the map, (j) sharing the map, (k) publication of the map as an app, using a story map template or other means.

As regards natural disasters, story maps represent a new capability of GIS, expanding its typical use for planning, analysis, and decision support and making its products accessible to much broader audiences which will be educated, informed and inspired (ESRI, 2012).
The aim of this paper is the presentation of the story map created for the dissemination of scientific information related to the June 12, 2017, Mw 6.3 Lesvos (Northeastern Aegean, Greece) earthquake.

THE STUDIED 2017 LESVOS EARTHQUAKE

On June 12, 2017, a shallow crustal strong earthquake with magnitude 6.3 occurred offshore, south of Lesvos (12:28 GMT), 35.8 km SSW of the capital of Lesvos Island, Mytilene, causing one fatality and severe structural damage in the SE part of the island (Papadimitriou et al., 2017, 2018). The southeastern part of Lesvos Island suffered the most by the earthquake in its natural environment, building stock and infrastructure (Lekkas et al., 2017a, 2017b).

The earthquake environmental effects comprised ground cracks, slope movements and a small-scale tsunami (Lekkas et al., 2017). Building damage was observed in the southeastern part of Lesvos. Very heavy structural damage was limited in the traditional village of Vrissa (Lekkas et al., 2017a, 2017b; Papadimitriou et al., 2018). Taking into account that Vrissa is located inland, further from the epicenter than other settlements with less damage, this village looks like an earthquake impact paradox. For interpreting this paradox, a rapid field macroseismic reconnaissance was conducted performing not only classical methods of earthquake damage assessment (e.g. building-by-building inspection), but also modern and innovative techniques, which comprise the use of Unmanned Aircraft Systems (UAS) and Geographic Information Systems (GIS) online applications as the basis of a rapid post-earthquake damage assessment before any intervention was made in the settlement (Antoniou et al., 2017; Mavroulis et al., 2017). Thus, all earthquake effects on the natural environment and the building stock of Vrissa were collected and saved with maximum accuracy for further processing and analysis. All data and critical information collected were freely accessible from link (https://goo.gl/v9vaQQ) to all ministries, state authorities, agencies competent in civil protection and disaster management as well as in the direction and coordination of the executive and operational forces at central, regional and local level in order to rapidly and effectively respond to the emergency needs of the affected population raised from the earthquake disaster. Moreover, this data went public through the social networks and media during not only the emergency phase but also during the post-disaster phase. Shortly after the data acquisition and the first analysis and interpretation, preliminary scientific reports were published online in seismological centers and earth science related blogs. The scientific results of this interdisciplinary and multiparametric research conducted by geologists, seismologists, engineers and geographers not only in the field during the emergency phase but also in laboratory during the post-disaster phase were published in scientific journals (Papadimitriou et al., 2018), international workshops (Antoniou et al., 2017; Lekkas et al., 2017a, 2017b) and congresses (Mavroulis et al., 2018a, 2018b, 2018c; Antoniou et al., 2018).

THE 2017 LESVOS EARTHQUAKE STORY MAP

A set of the scientific data acquired in the field and the preliminary scientific results obtained by the aforementioned research has been further presented by using the ESRI Story Map web templates (https://storymaps.arcgis.com/en/). The use of ESRI Story Maps has grown tremendously since being introduced about two years ago, with over 1000 Story Maps now being created each day. Story Maps give the researchers the possibility to authoritative maps with narrative text, images, and multimedia content to help visualize information, and new functionality is being added and improved regularly.

In the case of the 2017 Lesvos earthquake, a story map has been created in order to present this seismic disaster. The story map is accessible at the following link: https://goo.gl/i237Um and is available in both Greek and English language. Various scientific data, maps and videos were combined: (a) the parameters of the earthquake comprising magnitude, focal depth, epicenter location, focal mechanism, aftershocks, number of affected people (fatalities and injured) and damage on buildings and infrastructures, (b) the results of the source parameter determination, the coulomb stress analysis and the application of differential interferometry techniques, (c) the geological setting of Lesvos Island in general and of the earthquake-affected area in particular, (d) data on historical and instrumentally recorded seismicity of Lesvos Island, (e) the earthquake environmental effects induced by the 2017 Lesvos earthquake including ground cracks, slope failures and tsunamis, (f) the non-structural and structural damage induced by the 2017 Lesvos earthquake on residential buildings, monumental structures and industrial facilities of Vrissa, (g) information about the National and Kapodistrian University of Athens, the Environmental Disaster Crisis Management Strategies (EDCM) post-graduate studies program supporting the scientific research on the 2017 Lesvos earthquake and (h) the scientific team comprising members of National and Kapodistrian University of Athens, the National Technical University of Athens and the National Observatory of Athens.

The 2017 Lesvos earthquake story map comprises the following tabs entitled (a) general info, (b) seismic sequence, (c) geological setting, (d) historic data, (e) earthquake environmental effects, (f) building damage, (g) Vrissa settlement and (h) about (https://goo.gl/gKQHoY). All users interested not only in the characteristics and the impact of the 2017 Lesvos earthquake, but also in various aspects of earth sciences, civil and earthquake engineering and natural disasters have the opportunity to remain on any given tab for as long as required and navigate freely between them at their pace. Moreover, they have the possibility to expand or hide explanatory legends, quickly switch between slides, open or close pop-up photos and maps, view properties and attributes of selected geometries such as date, latitude, longitude, magnitude and depth of earthquake epicenters presented as point

geometries, view the dominant types of buildings in the affected area and the earthquake-induced damage in the traditional settlement of Vrissa classified into 4 categories (green color: no to slight structural damage, slight to moderate non-structural damage, blue color: moderate structural damage, heavy non-structural damage, purple color: heavy structural damage, very heavy non-structural damage, red color: very heavy structural damage, partial or total collapse).

(a)

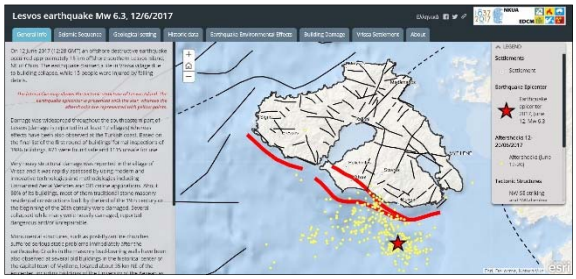

(b)

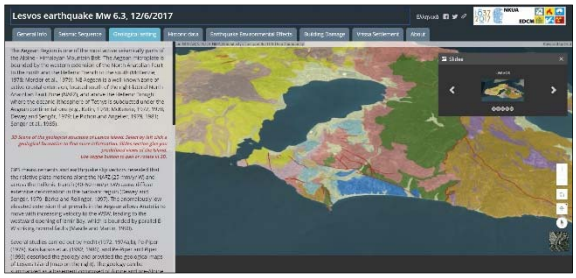

(c)

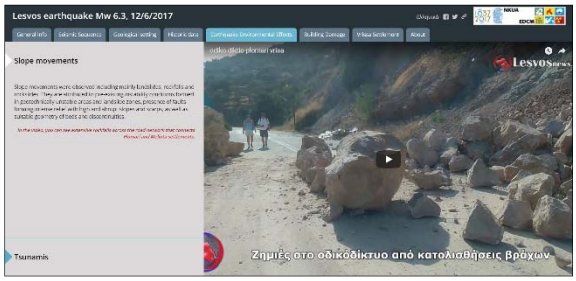

(d)

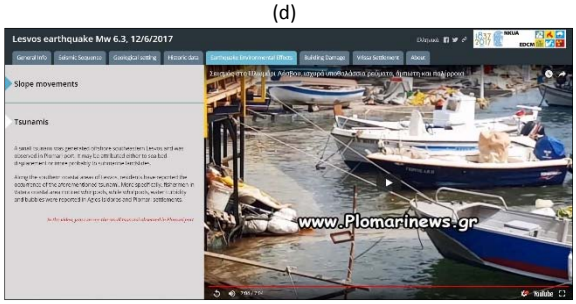

(e)

(f)

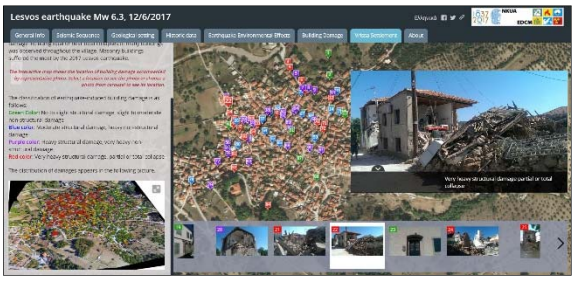

(g)

Figure 3: Screen captures of the (a) Introduction, (b) "General info", (c) "Geological setting", (d, e) "Earthquake Environmental Effects", (f) "Building Damage" and (g) "Vrissa Settlement" tabs of the story map for the 2017 Lesvos earthquake.

As far as the accessibility of this story map is concerned, users of smart phones and devices operating on all systems are now able to open this story map and use all of its features. Moreover, they can share the story map in social media and beyond by easy-to-use share links/buttons.

CONCLUSIONS

The creation of story maps contributes to the exploitation of the scientific knowledge gained by the scientific community and the information of the general public. This aims to the effective communication and cooperation in such an important issue as the generation of a strong earthquake with destructive impact on the local population, the natural and built environment as well as in the effective prevention and management of earthquake disasters in earthquake prone areas.

REFERENCES

Antoniou, V., Andreadakis, E., Mavroulis, S., Spyrou, N.-I., Skourtsos, E., Lekkas E., & Carydis, P., 2017. Post-earthquake rapid assessment using Unmanned Aircraft Systems (UAS) and GIS online applications: the case of Vrissa settlement after the 2017 June 12, Mw 6.3 Lesvos earthquake (North Aegean Sea, Greece). In: PATA DAYS 2017: 8th International Workshop on Paleoseismology, Active Tectonics and Archeoseismology, Blenheim, New Zealand, 13-16 November, (Clark, K.J., Upton, P., Langridge, R., Kelly, K., Hammond, K., eds), *GNS Science Miscellaneous Series* 110, 22-25.

Antoniou, V., Andreadakis, E., Mavroulis, S., Spyrou, N.-I., Skourtsos, E., Carydis, P. & Lekkas, E., 2018. Earthquake-induced building damage assessment using Unmanned Aircraft Systems (UAS): the case of Vrissa settlement after the 2017 Lesvos earthquake (Northeastern Aegean, Greece). *Geophysical Research Abstracts* 20, EGU2018-9671.

Environmental Systems Research Institute (ESRI) 2012. Storytelling with Maps: Workflows and Best Practices,

http://storymaps.esri.com/downloads/building%20story%20maps.pdf.

Environmental Systems Research Institute (ESRI). Story Maps, https://storymaps.arcgis.com/en/.

Lekkas, E., Carydis, P., Skourtsos, E., Mavroulis, S., Andreadakis, E., Antoniou, V., & Spyrou, N.-I., 2017a. Factors controlling the distribution of building damage in the traditional Vrissa settlement induced by the 2017 June 12, Mw 6.3 Lesvos (Northeastern Aegean Sea, Greece) earthquake. In PATA DAYS 2017: 8th International Workshop on Paleoseismology, Active Tectonics and Archeoseismology, Blenheim, New Zealand, 13-16 November, (Clark, K.J., Upton, P., Langridge, R., Kelly, K., Hammond, K., eds), *GNS Science Miscellaneous Series* 110, 232-235.

Lekkas, E., Mavroulis, S., Skourtsos, E., Andreadakis, E., Antoniou, V., Kranis, C., Soukis, K., Lozios, S., & Alexoudi, V., 2017b. Earthquake environmental effects induced by the 2017 June 12, Mw 6.3 Lesvos (North Aegean Sea, Greece) earthquake. In PATA DAYS 2017: 8th International Workshop on Paleoseismology, Active Tectonics and Archeoseismology, Blenheim, New Zealand, 13-16 November, (Clark, K.J., Upton, P., Langridge, R., Kelly, K., Hammond, K., eds), *GNS Science Miscellaneous Series* 110, 228-231.

Lesvos earthquake Mw=6.3 12/6/2017. Esri Story Map, https://goo.gl/gKQHoY.

Mavroulis, S., Andreadakis, E., Antoniou, V., Skourtsos, E., Carydis, P., & Lekkas, E., 2018a. Factors controlling the distribution of building damage in the traditional Vrissa settlement induced by the 2017 June 12, Mw 6.3 Lesvos (Northeastern Aegean Sea, Greece) earthquake. *Geophysical Research Abstracts* 20, EGU2018-9317.

Mavroulis, S., Andreadakis, E., Antoniou, V., Skourtsos, E., & Lekkas, E., 2018b. Geodynamic phenomena and ESI 2007 intensities of the 2017 June 12, Mw 6.3 Lesvos (North Aegean Sea, Greece) earthquake. *Geophysical Research Abstracts* 20, EGU2018-9254.

Mavroulis, S., Andreadakis, E., Spyrou, N.-I., Antoniou, V., Skourtsos, E., Carydis, P., Voulgaris, N., & Lekkas, E., 2018c. Building damage induced by the 2017 June 12, Mw 6.3 Lesvos (North Aegean Sea, Greece) earthquake and application of the European Macroseismic Scale 1998. *Geophysical Research Abstracts* 20, EGU2018-9129.

Mavroulis, S., Spyrou, N.-I., Andreadakis, E., Antoniou, V., Skourtsos, E., Lekkas, E., & Carydis, P., 2017. Damage assessment mapping with the use of UAS and Web GIS: The case of Vrissa settlement after the June 12, 2017 Mw 6.3 Lesvos Earth-Quake (Northeastern Aegean Sea). International Conference "GeoArch-Hazards - New Technologies, Hazards and Geoarchaeology", Athens, Greece 2017.

Papadimitriou, P., Tselentis, G.-A., Voulgaris, N., Kouskouna, V., Lagios, E., Kassaras, I., Kaviris, G., Pavlou, K., Sakkas, V., Moumoulidou, A., Karakonstantis, A., Kapetanidis, V., Sakkas, G., Kazantzidou, D., Aspiotis, T., Fountoulakis, I., Millas, C., Spingos, I., Lekkas, E., Antoniou, V., Mavroulis, S., Skourtsos, E., & Andreadakis, E., 2017. Preliminary report on the Lesvos 12 June 2017 Mw=6.3 earthquake. Euro-Med Seismological Centre (EMSC).

Papadimitriou, P., Kassaras, I., Kaviris, G., Tselentis, G.-A., Voulgaris, N., Lekkas, E., Chouliaras, G., Evangelidis, C., Pavlou, K., Kapetanidis, V., Karakonstantis, A., Kazantzidou-Firtinidou, D., Fountoulakis, I., Millas, C., Spingos, I., Aspiotis, T., Moumoulidou, A., Skourtsos, E., Antoniou, V., Andreadakis, E., Mavroulis, S., & Kleanthi, M., 2018. The 12th June 2017 Mw=6.3 Lesvos earthquake from detailed seismological observations. *Journal of Geodynamics* 115, 23-42, https://doi.org/10.1016/j.jog.2018.01.009.

INQUA Focus Group Earthquake Geology and Seismic Hazards

paleoseismicity.org

Holocene deformation along the Liquiñe - Ofqui Fault Zone, southern Chile: Field observations and geomorphic analysis

Astudillo, Luis (1,3), Cortés-Aranda, Joaquín (1,3), Melnick, Daniel (2,3), Tassara, Andrés (1,3)

(1) Departamento de Ciencias de la Tierra, Facultad de Ciencias Químicas, Universidad de Concepción, Víctor Lamas 1290, Barrio Universitario, Casilla 160-C, Concepción, Chile
(2) Instituto de Ciencias de la Tierra, Universidad Austral de Chile, Valdivia, Chile
(3) Millennium Nucleus: The Seismic Cycle Along Subduction Zones, Valdivia, Concepción, Chile

Abstract: *We present evidence of Holocene deformation along the northern Liquiñe-Ofqui Fault Zone (LOFZ). We studied four sites: Lonquimay, Palguín, Liquiñe and Maihue (A, B, C and D in Figure 1A). All the sites exhibit deformed tephra-bearing fluvial, glacial and lacustrine deposits. Tephra deposits were used to constrain the timing of deformation by correlations with formerly dated tephra deposits; our presented evidence is younger than ca. 11 ka. We then performed a geomorphic analysis of the fluvial network to link our punctual observations with fault traces. This revealed that NNE and ENE kilometric branches of the LOFZ have conducted Holocene deformation. We suggest that, during the Holocene, deformation is represented by both horizontal and vertical displacements that range from tens of centimeters to hundreds of meters; this deformation is at least partially due to earthquakes. Millennial slip rates (13-28 mm/yr) are higher than GPS velocities, suggesting the occurrence of slip deficit.*

Keywords*: LOFZ, geomorphology, southern Chile, GIS*

INTRODUCTION

In several oblique subduction margins worldwide, the convergence-induced deformation is partitioned among the megathrust and crustal strike-slip faults (Allen, 1965). These latter have proven to be capable to nest moderate to large earthquakes with important effects in society. Examples of this are given by the earthquakes of Kobe in 1995 (Mw 6.9) and Kumamoto in 2016 (Mw 7), along the Japan Subduction Zone. Both events occurred at shallow depths (<20 km) and involved an important toll of casualties. In general, the seismic hazard linked to the occurrence of megathrust earthquakes is often better appraised than that associated to strike-slip structures. One of the main reasons for this disparity is given by the fact that the earthquake size, geometry of the causative faults, recurrence interval and, in a broader, sense their neotectonic signature are, in general, less constrained. The Southern Chile subduction zone, between 37°S and 46°S (Figure 1A), constitutes a tectonic domain in which deformation induced by the convergence of the Nazca and South American plates, oriented N78°E, is significantly partitioned. There, the Liquiñe-Ofqui Fault Zone (LOFZ), a dextral-transpressive intra-arc fault zone (e.g. Lavenu & Cembrano, 1999), partially absorbs the parallel-to-the-trench component of the convergence (Cembrano, Hervé, & Lavenu, 1996). Slip rates along this structure have been estimated for the very long-term (last 6 Ma) and very-short term (instantaneous velocities). For the long-term (Rosenau et al. 2006), kinematic models indicate slip rates of 32+6 mm/yr for its southern portion (46°S and 42°S) and 13+3 mm/yr for its northern portion (42°S and 38°S).

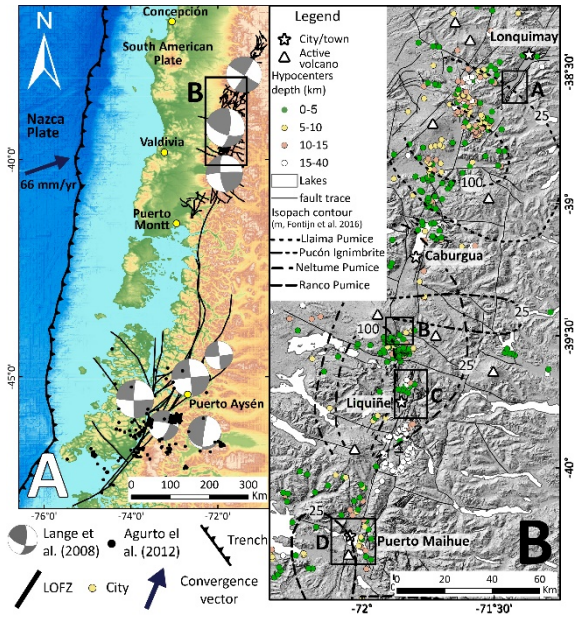

Figure 4: Location of the LOFZ and the study sites. A) Tectonic context for the southern Chile Andes and crustal seismicity related to the LOFZ. B) Study sites along the northern part of the LOFZ. Seismicity according to depth and isopach contours from Fontijn et al. (2016) are also depicted.

For the short-term, using geodetic data, Wang et al. (2007) estimate a slip rate of 6.5 mm/yr for the southern end of the LOFZ, which decreases northwards tapering to zero at the northern termination of the LOFZ. Evidence of earthquakes in this structure are given by the Ms 5.3 Lonquimay earthquake (Barrientos & Acevedo-Aránguiz,

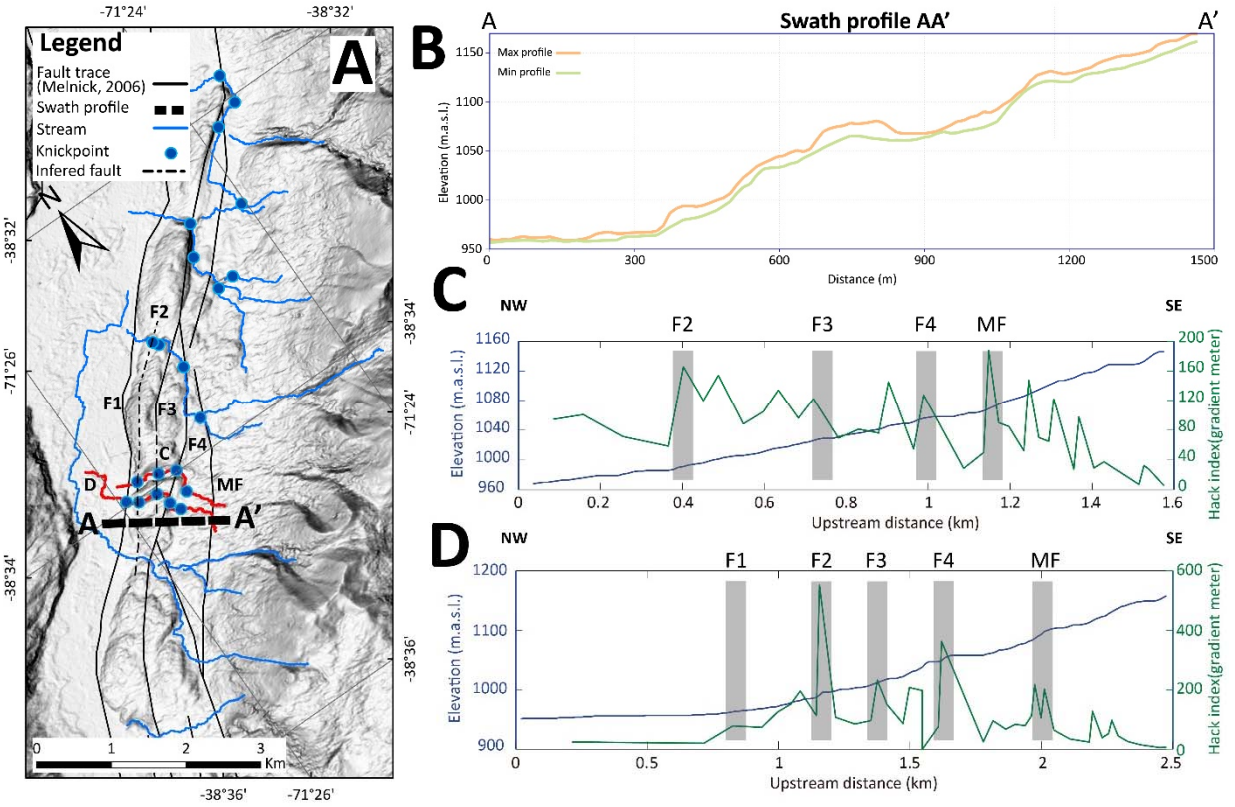

Figure 5: Lonquimay site. A) Shaded relief map of the site showing part of the drainage network and its relationship with the structures published by Melnick et al. (2006) and those interpreted herein. B) Swath profile AA' showing the staircase topography controlled by fault activity. C and D correspond to thalweg profiles for the red streams in A. The grey rectangles correspond to peaks of SL index that are spatially related to knickpoints (blue dots in A).

1992) and the Mw 6,2 Hudson earthquake (Chinn & Isacks, 1983). However, Lange et al. (2008) reported the first robust evidence of earthquakes along this intra-arc fault zone, showing the localization of 75 seismic events along this structure occurred between December 2004 and November 2005 (Figure 1A). Then, the Aysén Seismic Crisis, which lasted three months between January and April of 2007, culminated with two large seismic events of Mw 6.1 and Mw 6.2. This demonstrated the capacity of this structure to produce earthquakes with significant impact for the Southern Chile Region. Despite the instrumental evidence attesting for its activity, several questions relative to its seismic potential remain open: Has this structure produced moderate to large earthquakes comparable to those of 1965, 1989 or 2007, formerly during the Holocene? What is the evidence of these events? At which rate deformation has been conducted for the millennial timespan? These and other unsolved questions define a gap with respect to the seismic hazard assessment linked to this structure, in a region in which this aspect is mostly evaluated from the perspective of the megathrust earthquakes. To start filling this gap, we are currently undertaking a project devised, among other tasks, to identify and characterize evidence of Holocene deformation along branches of the LOFZ between 38°S and 40.5°S (Figure 1B). Herein, we present novel field evidence of Holocene sediments deformed according to different kinematic styles by LOFZ and secondary faults strands at four locations, which are, from north to south: a) Lonquimay; b) Palguín; c) Liquiñe and d) Maihue (A-D in Figure 1B, respectively). In general, the outcrops at each site consist of alluvial, fluvial, lacustrine and/or pyroclastic deposits. Most of the pyroclastic layers can be spatially correlated to those defined and dated by Fontijn et al. (2016) for the southern Chile Lake District; this allow us constraining the age of the deformation. Our punctual observations are then linked to new interpreted or already mapped fault traces of meso/megascopic extent. Then, to assess the influence of these fault traces in the drainage network developed over homogeneous rocks, we have performed a geomorphic analysis using SL index (Stream Length gradient index; Hack, 1973) to highlight potentially tectonic knickpoints.

RESULTS

- **Lonquimay site** (A in Figure 1B) is located at the northern end of the LOFZ; this area has been structurally characterized by Melnick (2006). In the Lonquimay river valley, NE-ENE trending lineaments have developed a positive topography interpreted as a shutter ridge (Figure 2A). This shutter ridge is limited to the east by a ca. 50 m height scarp (Figure 2A-B). The shutter ridge is incised by several drainages draining towards the Lonquimay River. Some drainages are dextrally displaced by LOFZ branches; horizontal offsets of around 250-300 m were measured along a fault trace of the LOFZ (F4 in Figure 2A). The right flank of the river depicted in figure 2C exhibits a pumice layer covering alluvial deposits; this pumice layer may be correlated with the Llaima Pumice dated in 10.45+0.13 ka BP (Fontijn et al. 2016). Considering the drainage offset and the age of the Llaima Pumice, we estimate a local horizontal slip rate of 23.8 to 28.6 m/ka for this part of the LOFZ. The thalweg profiles of two deflected drainages

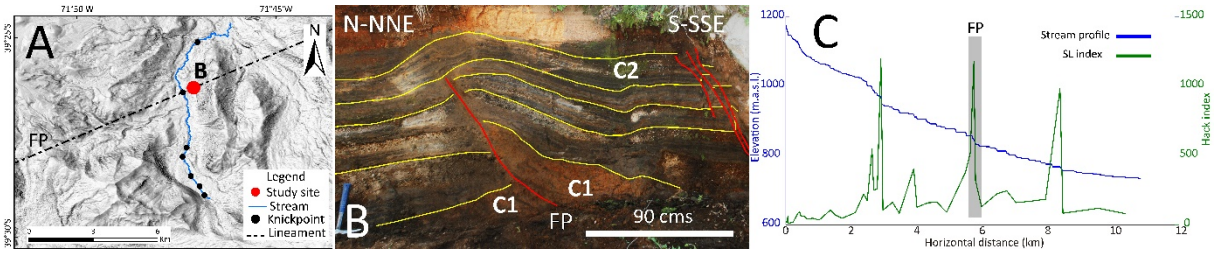

Figure 6: Palguín site. A) Shaded relief map of the Palguín site B) Roadcut next to the Palguín river exhibits a NE striking south dipping reverse fault affecting a sequence of pyroclastic deposits. C) Palguín river thalweg profile together with the SL index calculated for the river.

show knickpoints spatially related to previously suggested (Melnick et al., 2006) and newly interpreted faults controlling the western margin the Lonquimay Valley; these knickpoints correlate with SL peaks (Figure 2C-D).

- **Palguín site** (B in Figure 1B) is located nearby the NW trending Lanín-Quetrupillán-Villarrica lineament, 3 km southward the Palguín Village (B in Figure 1B). At this site, we identified a roadcut exhibiting a NE striking-south dipping reverse fault affecting a sequence of layered pyroclastic deposits (FP in Figure 3A-B). This fault offsets by 0.5 m an orange pumice layer at the base of the sequence (C1 in Figure 3B). A second non-deformed pumice layer atop of the exposed sequence seals the fault (C2 in Figure 3B). The pumice layers can be spatially correlated with the Neltume Pumice (11.40±0.81 ka) and with the Pucón Ignimbrite (4.00±0.05 ka), respectively (Fontijn et al. 2016). Considering the possible age of the pumice deposits we calculate a minimum vertical slip rate of ca. 0.05 m/ka for the last ca. 11 ka; most of this rate would be due to an event occurred between ca. 11 ka and 4 ka. Given the subvertical geometry of the interpreted fault trace, we do not discard the occurrence of horizontal slip during the interpreted causative event. Figure 3C shows the thalweg profile of the Palguín River with several slope breaks along its course. The slope break at ca. 6 km fits with a peak of the SL index and with the projection of the fault identified in B (FP in Figure 3C).

- **Liquiñe site** (C in Figure 1A), located in the periphery of the Liquiñe town (white star in Figure 4A), is characterized by several NNW to NNE subparallel lineaments that control the steepened local topography (Figure 4A, C). 2 km eastward the Liquiñe Town, Jara and Melnick (2009) report a dextral displacement of the Liquiñe River by one branch of the LOFZ (F2 in Figure 4). At this site, we measured ca. 156 m of dextral offset. At the northern flank of the river, fluvial conglomerates with an interbedded pumice layer are exposed (Figure 4B). The pumice layer may be correlated with the 11.4+/-0.81 ka Neltume Pumice (Fontijn et al, 2016). Considering the drainage offset and the age of the Neltume Pumice, it is possible to estimate a local slip rate of ca. 13.6 m/ka for the LOFZ. Furthermore, the thalweg profile of the Liquiñe River shows several knickpoints that fit with peaks of SL index and the position of the NNE trending lineaments defining locally the LOFZ (Figure 4D); this suggests that, in addition to horizontal offsets, vertical displacements may also take place along the LOFZ strands. These faults can be followed by several kilometres both northward and southward from the river trend (Figure 4A).

- **Maihue site** (D in Figure 1B) is located at the southern border of the Maihue Lake (Figure 5A); in general, the periphery of the Maihue Lake exhibits several NNE trending lineaments, some of them controlling glacio-fluvial valleys. At the study site (D in Figure 5A), a NS-NNE fault promotes thrusting of moraine deposits over lacustrine deposits (LGF in Figure 5). This fault may be continued northward the Maihue Lake where it defines the western border of the valley depicted in Figure 5C. This valley flank shows a staircase topography given by the occurrence of fluvial terraces; this may be also related to fault activity. A conspicuous incision draining to the east the Carrán-Los Venados Volcano shows some breaks in its thalweg profile; at ca. 3 km, a subtle break in the thalweg slope fits with a peak of SL index and with the projection of the fault verified in site B of figure 5D.

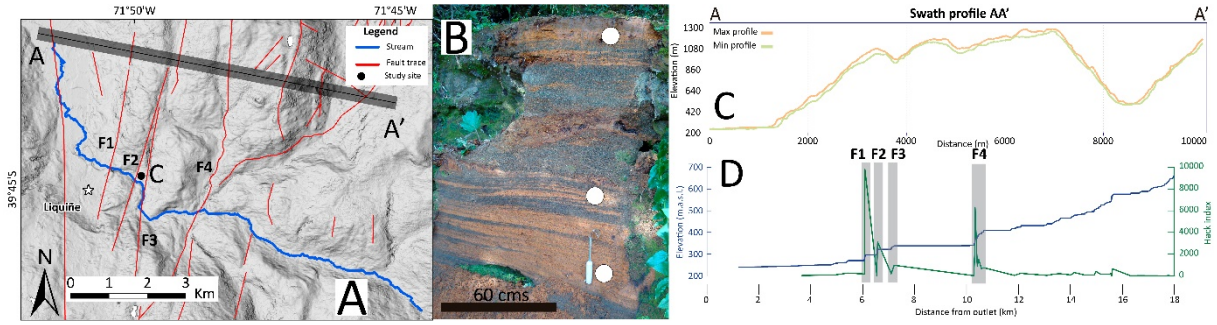

Figure 7: Liquiñe site. A) Shaded relief map of the Liquiñe area with mapped traces of the LOFZ and the Liquiñe River studied segment. B) Fluvial deposits on the northern flank of the river. The orange pumice layer were sampled (white dots) to better constrain the age of deformation. C) Swath profile AA' shows a staircase topography controlled by the LOFZ. The profile is crossed by several branches that are spatially consistent with the topographic scarps. D) Thalweg profile of the Liquiñe River segment depicted in A. Fault related knickpoints showing vertical displacements are highlighted with grey rectangles.

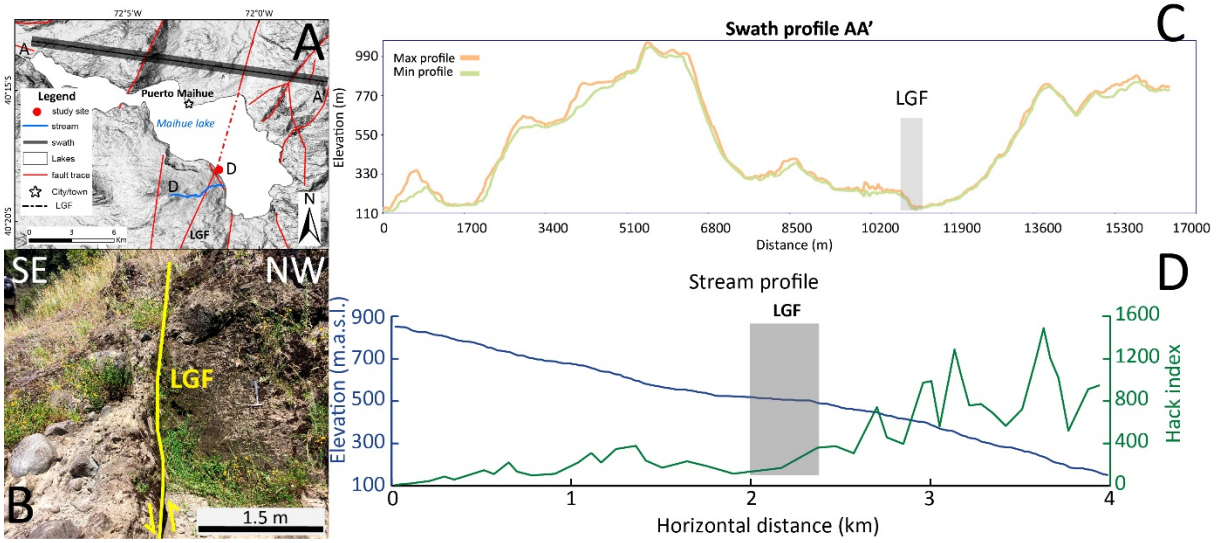

Figure 8: Maihue Lake site. A) Shaded relief map of the lake showing the location of the study site, swath and thalweg profiles along with the LOFZ traces. B) Outcrop at the south border of the Maihue Lake. A NNE-NS striking-subvertical LOFZ branch (LGF) thrusts moraine deposits over a lacustrine deposit. C) Swath profile AA'. The profile shows a fluvio-glacial valley (Pillanleufu river valley) with terraces.

DISCUSSION

We have documented neotectonic evidence of Holocene activity in the LOFZ. This evidence corresponds to offset drainages, deformed Holocene deposits and knickpoints in river thalwegs. The kinematic styles attest for both horizontal and vertical movements along its branches. We argue that at least part of the herein documented deformation is seismic; this is because our targeted sites lie on zones with significant instrumental seismicity (Figure 1B). Further, this interpretation is supported by recent findings in the southern portion of this structure, where mass transport deposits in the bottom of the Aysén Fjord have been interpreted as caused by earthquakes related to the LOFZ (Wills et al., 2018). (Figure 1B). We highlight that millennial slip rates estimates at Lonquimay and Liquiñe sites are similar in to those reported by Rosenau et al. (2006); however, they increase northwards. Further, millennial slip rates are higher than those provided by Wang et al. (2007) for the northern LOFZ, insinuating that some slip deficit may be currently occurring at this portion of the LOFZ. Ongoing work is focused on better determining millennial slip rates and finding appropriate sites to undertake paleoseismological surveys.

Aknowledgements: This study has been supported by Iniciativa Científica Milenio (ICM) through grant NC160025 'Millennium Nucleus CYCLO: The Seismic Cycle along Subduction Zones' and VRID (UdeC) project Field evidence as a first-order tool for assessing seismic hazard along the northern LOFZ (38°S-40.5°S).

REFERENCES

Allen, C.R., 1965. Transcurrent Faults in Continental Areas. *Philosophical Transactions of the Royal Society A: Mathematical, Physical and Engineering Sciences* 258 (1088), 82-89.

Cembrano, J., Hervé, F., & Lavenu, A., 1996. The Liquiñe Ofqui fault zone: a long-lived intra-arc fault system in southern Chile. *Tectonophysics* 259 (1-3), 55-66.

Chinn, D.S., & Isacks, B.L., 1983. Accurate source depths and focal mechanisms of shallow earthquakes in western South America and in the New Hebrides Island Arc. *Tectonics* 2 (6), 529-563, https://doi.org/10.1029/TC002i006p00529.

Fontijn, K., Rawson, H., Van Daele, M., Moernaut, J., Abarzúa, A. M., Heirman, K., & Moreno, H., 2016. Synchronisation of sedimentary records using tephra: A postglacial tephrochronological model for the Chilean Lake District. *Quaternary Science Reviews* 137, 234-254.

Hack, J., 1973. Stream-profile analysis and stream-gradient index. *Journal of Research of the U. S. Geological Survey* 1 (4), 421-429.

Lange, D., Cembrano, J., Rietbrock, A., Haberland, C., Dahm, T., & Bataille, K., 2008. First seismic record for intra-arc strike-slip tectonics along the Liquiñe-Ofqui fault zone at the obliquely convergent plate margin of the southern Andes. *Tectonophysics* 455 (1-4), 14-24.

Lavenu, A., & Cembrano, J., 1999. Compressional- and transpressional-stress pattern for Pliocene and Quaternary brittle deformation in fore arc and intra-arc zones (Andes of Central and Southern Chile). *Journal of Structural Geology* 21 (12), 1669-1691.

Lomnitz, C., 2004. Major Earthquakes of Chile: A Historical Survey, 1535-1960. *Seismological Research Letters* 75 (3), 368-378.

Melnick, D., Rosenau, M., Folguera, A., & Echtler, H., 2006. Neogene tectonic evolution of the Neuquén Andes western flank (37-39°S). In Special Paper 407: Evolution of an Andean Margin: A Tectonic and Magmatic View from the Andes to the Neuquén Basin (35°-39°S lat) (Vol. 407, pp. 73-95). Geological Society of America.

Rosenau, M., Melnick, D., & Echtler, H., 2006. Kinematic constraints on intra-arc shear and strain partitioning in the southern Andes between 38°S and 42°S latitude. *Tectonics* 25 (4), https://doi.org/10.1029/2005tc001943.

Wang, K., Hu, Y., Bevis, M., Kendrick, E., Smalley, R., Vargas, R.B., & Lauría, E., 2007. Crustal motion in the zone of the 1960 Chile earthquake: Detangling earthquake-cycle deformation and forearc-sliver translation. *Geochemistry, Geophysics, Geosystems* 8 (10), https://doi.org/10.1029/2007gc001721.

Wils, K., Van Daele, M., Lastras, G., Kissel, C., Lamy, F., & Siani, G., 2018. Holocene event record of Aysén Fjord (Chilean Patagonia): An interplay of volcanic eruptions and crustal and megathrust earthquakes. *Journal of Geophysical Research: Solid Earth* 123, 324-343, https://doi.org/10.1002/.

INQUA Focus Group Earthquake Geology and Seismic Hazards

paleoseismicity.org

Soft-sediment deformation structures induced by earthquakes in front of the advancing Scandinavian Ice Sheet on Rügen Island (NE Germany)

Belzyt, Szymon (1), Pisarska-Jamroży, Małgorzata (1), Börner, Andreas (2), Hoffmann, Gösta (3), Hüneke, Heiko (4), Kenzler, Michael (4), Obst, Karsten (2), Rother, Henrik (5), van Loon, A.J. (Tom) (6, 7)

(1) Institute of Geology, Adam Mickiewicz University, B. Krygowskiego 12, 61-680 Poznań, Poland, szymon.belzyt@amu.edu.pl
(2) State Authority of Environment, Nature Conservation and Geology Mecklenburg-Western Pomerania, Goldberger Strasse 12, 18273 Güstrow, Germany
(3) Steinmann Institute - Geology, Bonn University, Nussallee 8, 53115 Bonn, Germany
(4) Institute of Geography and Geology, University of Greifswald, F.-L. Jahn Strasse 17a, 17487 Greifswald, Germany
(5) Landesamt für Geologie und Bergwesen, Sachsen Anhalt / Geologischer Dienst, Dezernat Landesaufnahme und Analytik, Köthener Strasse 38, 06118 Halle, Germany
(6) Geocom Consulting, Valle del Portet 17, 03726 Benitachell, Spain
(7) College of Earth Science and Engineering, Shandong University of Science and Technology, Qingdao 266590, Shandong, China

Abstract: *Two layers deformed by seismicity-related processes in a glaciolacustrine silty-sandy succession are exposed in a coastal cliff near Dwasieden on Rügen Island, NE Germany. These layers, with abundant soft-sediment deformation structures such as load structures, fluid-escape structures and small-scale faults, extend continuously over a length of at least 150 m. They are separated by undeformed sediments and are classified as seismites formed as a result of seismically-induced liquefaction. Based on the stratigraphic position and optically stimulated luminescence dating, these two seismites must have formed in front of the advancing Pleistocene Scandinavian Ice Sheet that reached the study area during the Last Glacial Maximum. Regarding the fact that there are no known active faults in the vicinity of the study area, such intraplate seismic activity must have been triggered by reactivation of pre-existing faults, caused by changes in the regional stress field as a consequence of increased loading by the thickening ice masses.*

Keywords*: glacio-isostatic loading; intraplate earthquakes; seismites; soft-sediment deformation structures; liquefaction*

INTRODUCTION

Observations by Hoffmann & Reicherter (2012), Brandes & Winsemann (2013), Brandes et al. (2015), Van Loon & Pisarska-Jamroży (2014), and Van Loon et al. (2016) suggest that the relatively rapidly fluctuating extent of thick ice masses can affect the local stress field and trigger intraplate earthquakes. Consequently, susceptible layers of unconsolidated, water-saturated fine-grained sediments on the surface or at shallow depths can undergo liquefaction, forming laterally extensive deformed layers - seismites (see Seilacher, 1969; Allen, 1982; Owen & Moretti, 2011; Moretti & Van Loon, 2014).

Hitherto, seismic activity was linked to the response of the Earth's crust to unloading, because glacio-isostatic rebound during deglaciation takes place faster than during glaciation. This is supported by calculations of stress-state changes under different tectonic regimes during glacial cycles (Grollimund & Zoback, 2001; Brandes et al., 2015). However, recent investigations near Dwasieden unexpectedly provided data that indicate that earthquakes can also be triggered by ice-sheet loading during glacial ice advance.

The Dwasieden coastal cliff is situated on Rügen Island (NE Germany) in the south-western part of the Baltic Sea, 2 km SW of the Sassnitz town (Figs 1 and 3). During the Quaternary, the study area was reached several times by the Scandinavian Ice Sheet, reaching its maximum extent during the Late Weichselian. Traces of successive stages of

Figure 9: Location map of the Rügen Island. Dashed and dotted lines present maximum extent of Scandinavian Ice Sheet during Brandenburgian, Pomeranian and Frankfurt phases of Weichselian Glaciation (MIS 2-5d).

the Saalian Glaciation (MIS 6), succeeded by traces of the Weichselian Glaciation (MIS 2-5d, Brandenburg, Frankfurt, Pomeranian and Mecklemburg phases) have been investigated in NE Germany for many years (Fig. 1).

The sedimentary succession of the cliff, which has an overall height of 20 m, is composed of Late Cretaceous (Early Maastrichtian) limestone overlain by five unlithified Quaternary (late Pleistocene) units: three glacial diamictic layers, separated from each other by glaciofluvial and glaciolacustrine silts, sands and gravels. Within the sandy silts, three deformed layers with abundant soft-sediment deformation structures are present.

RESULTS

Two of the deformed layers have been recognized as seismites, meeting most of criteria for such levels (Owen et al., 2011; Moretti & Van Loon, 2014) including (1) a large spatial extent - deformations are present over the whole horizontal extent of the exposure, (2) lateral continuity of the deformations in these levels, (3) vertical repetition of layers separated by non-deformed sediments - the two seismites are separated by undisturbed sediments (so called sandwich-like distribution) and (4) the presence of soft-sediment deformation structures comparable with structures described from recent earthquake-affected

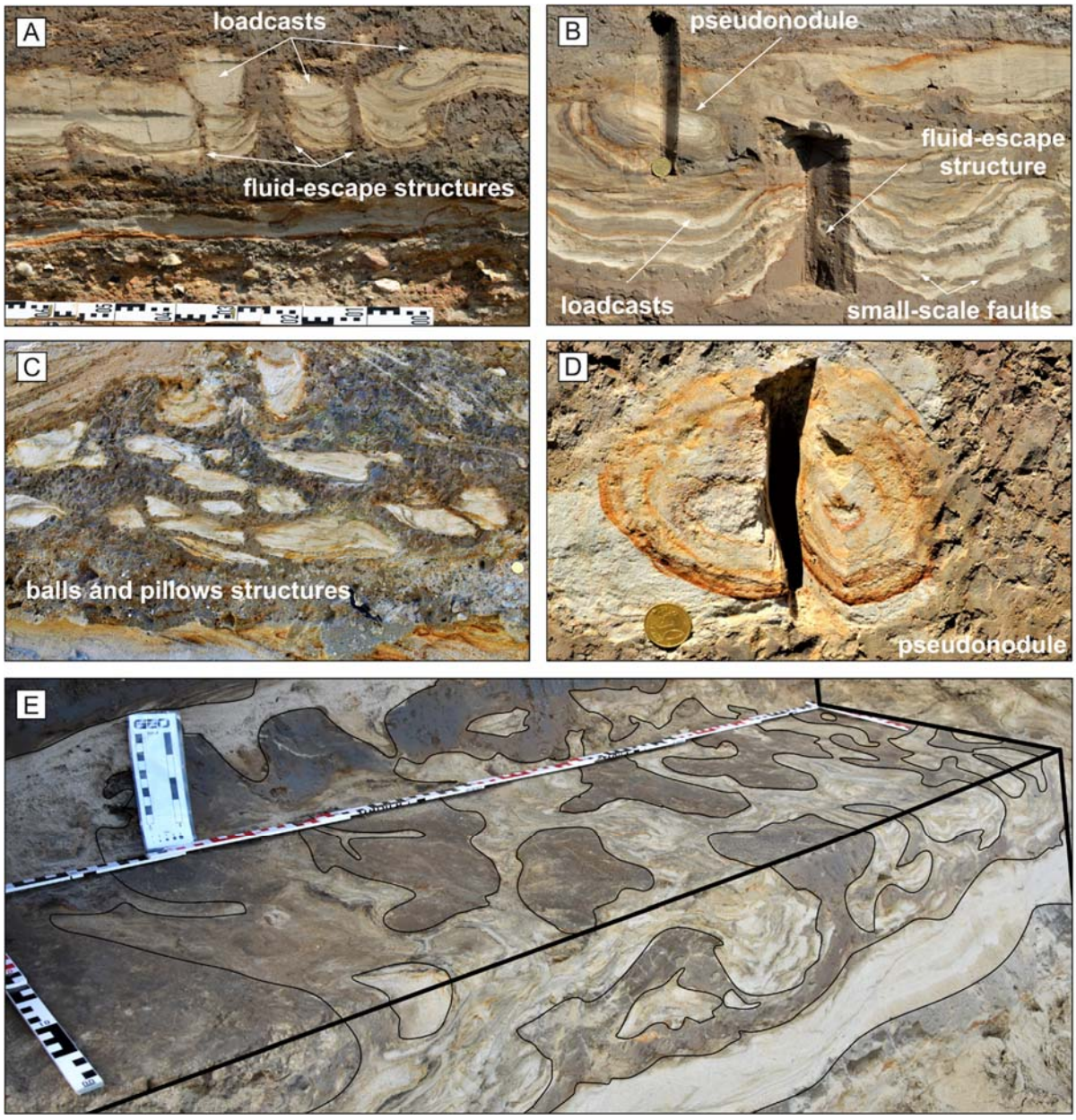

Figure 2: Liquefaction-induced soft-sediment deformation structures within the studied seismites. A-B: Load structures - load casts and pseudonodules, fluid-escape structures indicating vertical sediment movement and small-scale faults. C-D: 3D view of load structures.

layers (load structures e.g., load casts, pseudonodules, flame structures, ball-and-pillow structures; fluid-escape structures and brittle deformations like small-scale faults; Fig. 2.). The stratigraphic position of both seismites between two layers of till (glacial diamictons) suggests that the deformation occurred either during a phase of ice-sheet retreat or during a phase of ice advance. Optically stimulated luminescence dating of three samples collected

from the section indicate that the sediments with the seismites were deposited between 22.7±1.9 ka and 19.0±1.8 ka. This result corresponds to the age of the maximum extent of the Scandinavian Ice Sheet in the SW Baltic Sea area (Last Glacial Maximum; see Houmark-Nielsen, 2010). Comparison with the regional stratigraphy thus implies that the deformed sediments must have been deposited shortly before the ice sheet covered the study area during the Brandenburgian phase of ice advance.

DISCUSSION

Sedimentological, stratigraphical and geochronological investigation lead to the conclusion that earthquakes with magnitudes of over 4.5 (cf. Ambraseys, 1988) must have occurred in NE Germany during the late Pleistocene. Such seismic activity was induced by the increasing load caused by the advancing ice mass during the late Weichselian glaciation.

Neither evidence of Neogene seismic activity, nor the occurrence of major surface faults in the study area have been reported. Reactivation of deeply-rooted structures influenced by fluctuating masses of thick ice-sheet must therefore be held responsible.

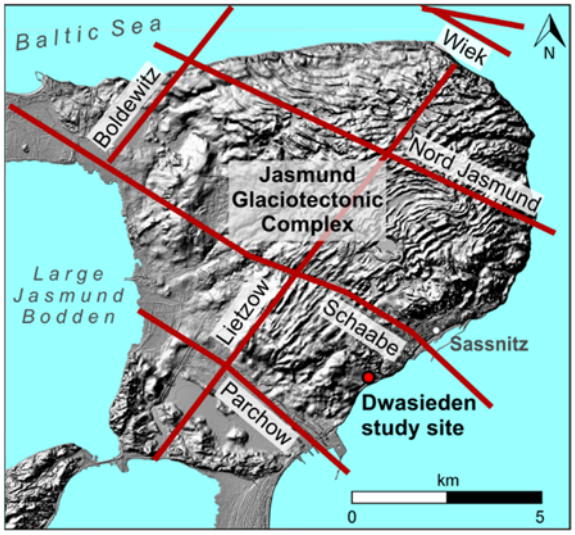

Figure 3: Location of Dwasieden study site on the digital elevation model of Jasmund peninsula (NE part of Rügen Island; based on LiDAR data from @GeoBasis-DE/M-V 2015 by J. Hartleib). Reddish lines represent interpreted major subsurface faults.

Looking into the geological structure of Rügen Island, the most interesting subsurface faults that exist in the Middle Rügen Block of the Torqnquist Fan (Thybo, 2000) are of second order: these are the Nord Jasmund, Schaabe, Lietzow, Parchow, Granitz and Rappin Faults (Fig. 3). Having been primarily developed under an extensional regime, they were reactivated during the Carboniferous and Mesozoic, changing the normal faults into reverse faults.

Regarding the strike direction and the angle between the strike and the direction of the ice-sheet front, the tectonic regime, recent horizontal stress directions and the distance from the study site, the NW-SE trending Schaabe Fault is the most likely to have become reactivated, causing the earthquakes that led to the formation of the two seismites. Located at 2 km away from the Dwasieden site, it also seems to underlie a surficial valley visible on a 5-m DEM (Fig. 3.).

Acknowledgements: The study has been financially supported by a grant for the GREBAL project (No. 2015/19/B/ST10/00661) from the National Science Centre Poland.

REFERENCES

Ambraseys, N.N., 1988. Engineering seismology. *Earthquake Engineering and Structural Dynamics* 17, 1-105.

Brandes, C., Steffen, H., Steffen, R., & Wu, P., 2015. Intraplate seismicity in northern central Europe is induced by the last glaciation. *Geology* 43, 611-614.

Hoffmann, G., & Reicherter, K., 2012. Soft-sediment deformation of Late Pleistocene sediments along the southwestern coast of the Baltic Sea (NE Germany). *International Journal of Earth Sciences* 101, 351-363.

Houmark-Nielsen, M., 2010. Extent, age and dynamics of Marine Isotope Stage 3 glaciation in the southwestern Baltic Basin. *Boreas* 39, 343-359.

Moretti, M., & Van Loon, A.J., 2014. Restrictions to the application of "diagnostic" criteria for recognizing ancient seismites. *Journal of Palaeogeography* 3, 162-173.

Owen, G., & Moretti, M., 2011. Identifying triggers for liquefaction-induced soft-sediment deformation in sands. *Sedimentary Geology* 235, 141-147.

Seilacher, A. 1969. Fault-graded beds interpreted as seismites. *Sedimentology* 13, 155-159.

Thybo, H., 2000. Crustal structure and tectonic evolution of the Tornquist Fan region as revealed by geophysical methods. *Bulletin of the Geological Society of Denmark* 46, 145-160.

Van Loon, A.J., Pisarska-Jamroży, M., Nartišs, M., Krievāns, M., & Soms, J., 2016. Seismites resulting from high-frequency, high-magnitude earthquakes in Latvia caused by Late Glacial glacio-isostatic uplift. *Journal of Palaeogeography* 5, 363-380.

INQUA Focus Group Earthquake Geology and Seismic Hazards

paleoseismicity.org

The Bar and Katërkolle Faults, Southern Montenegro: Structure and deformation rate estimates

Biermanns, Peter (1), Schmitz, Benjamin (2), Ustaszewski, Kamil (2), Mechernich, Silke (3), Onuzi, Kujtim (4), Reicherter, Klaus (1)

(1) Institute of Neotectonics and Natural Hazards, RWTH Aachen University, Lochnerstr. 4-20, 52064 Aachen, Germany, p.biermanns@nug.rwth-aachen.de
(2) Institute of Geosciences, Structural Geology, Friedrich-Schiller-Universität Jena, Burgweg 11, 07749 Jena, Germany
(3) Institute of Geology and Mineralogy, University of Cologne, Zülpicher Strasse 49b, 50674 Köln, Germany
(4) Institute of Geosciences, Energy, Water and Environment, Polytechnic University of Tirana, Rruga Don Bosko 60, Tirana, Albania

Abstract: *We report the existence of considerable extensional tectonics in the per-se contractional domain of the Southern External Dinarides, S Montenegro and N Albania. Two pronounced fault scarps, the Bar and Katërkolle fault scarps, traverse the Rumija mountain chain SW of the town of Bar for ≥13 km. Geomorphic appearance of the scarps and their surroundings as well as indicators on fault planes prove active normal faulting. From scarp profiling, we derive minimum slip rates of 0.37 ± 0.06 - 0.49 ± 0.08 mm/yr. Magnitude estimates based on surface rupture length and displacement markers yield associated magnitudes between c. 5.5 and 6.5. We interpret the fault scarps as tectonic, co-seismic features. Hence, it remains enigmatic how instrumental signals of extensional earthquakes are hitherto missing. We propose the existence of normal faults to be related to rollback-related extensional tectonics that are well-recognized further inland.*

Keywords*: Tectonic geomorphology, fault scarps, Dinarides, Montenegro*

INTRODUCTION

General setting

The Dinarides - Hellenides transition in S Montenegro and N Albania represents an area of enhanced seismicity hosting earthquakes up to Mw = 7.1 (Montenegro 1979, e.g. Benetatos & Kiratzi, 2006). In the coastal stripe of the External Dinarides, seismicity is largely related to NE-ward continental subduction of the Adria microplate below Eurasia. Instrumental records show exclusively contractional signals, with focal mechanisms indicating earthquakes along shallow thrusts (Fig. 1). We report outcrop-based evidence that in the same area considerable extensional tectonics co-exist, apparently without leaving any imprint in instrumental records so far. The question arises if the observed structures are (a) associated with the well-recognized roll-back-induced extension further inland (e.g. Dumurdzanov, 2005) or (b) explicable as syn-convergence features. To gain further inferences on deformation style and kinematics in that regard, we characterize two major fault scarps of normal faults SW of Bar (Montenegro): The Bar Fault Scarp (BFS) and Katërkolle Fault Scarp (KFS).

Bar and Katerkolle fault scarps: Morphology & structure

Two sections of large-scale fault scarps, BFS and KFS, dissect the SW and S slopes of the Rumija mountain chain between Bar and Katërkolle (Montenegro). The W - NW section (BFS, Fig. 1a) has a length of c. 5 km, the E section (KFS) measures c. 7.5 km. A c. 4 km long gap between BFS and KFS shows no distinct fault plane outcrops but a penetrative step in terrain steepness, making an interconnection between both sections arguable. BFS transects Upper Triassic bedded limestones and dolomites; KFS traverses Middle Triassic and Cretaceous bedded and massive limestones; both located in the Budva-Cukali zone and showing shallow (c. 25-35°) NW-dipping beds (Geol. Map of Montenegro, 1971, Fig. 4).

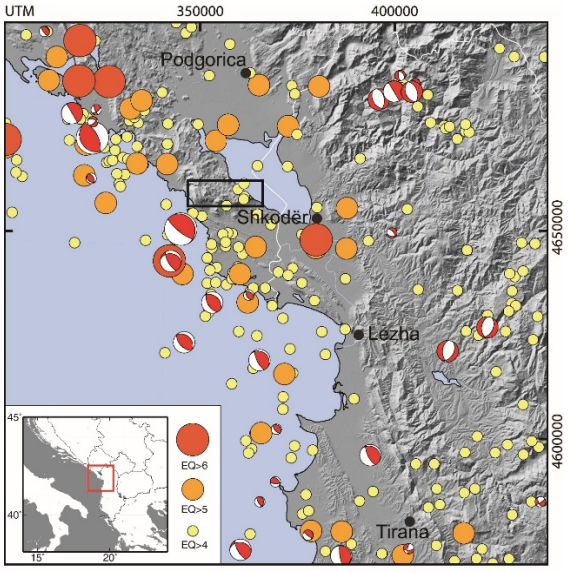

Figure 10: Overview map of S Montenegro and N Albania showing instrumentally recorded earthquakes with intensities ≥ 4. Where available, focal mechanisms are shown. Data compiled from SVI, EMEC and Global CMT catalogues, Aliaj (2006) and Benetatos & Kiratzi (2006). Black box: Study area with fault scarp locations.

Figure 2: Field photographs – (a) Overview of the N section of BFS. (b) Fault plane showing corrugations on fault plane. Total height of outcrop wall reaches c. 50 m due to erosion through gully in footwall. (c) Representative outcrop of fault plane at BFS_S, Person for scale. (d) Horizon on fault plane indicating exposure during seismic event.

Across the faults, bedrock limestone in the footwall is juxtaposed against carbonatic, partly cemented colluvial sediments in the hangingwall, consisting of cm- to m-scale cobbles. Mean fault plane strike bends from c. NNW-SSE in the N of BFS to c. E-W in the S of BFS and KFS (Fig. 4). This is accompanied by a general steepening of fault planes from c. 55° to 70°. Based on fault plane strike and dip, BFS may be subdivided into two subsections, BFS_N and BFS_S. Fault planes show a self-similar undulated pattern with corrugations (Fig. 2b). Fault plane dip, striations, occasional slickenfibres and Riedel shears prove normal fault movement. The general trend of striations follows the mean fault plane trend, preserving a predominant dip-slip movement. On short distances, striations only vary insignificantly, yielding local strike-slip components, particularly towards the ends of scarp sections.

METHODS

Mapping of fault plane and earthquake horizons

To characterize BFS and KFS as extensional structures in a contractionally dominated region, we mapped the associated fault planes to record their overall structure and surficial habit. We compiled an extensive dataset of fault plane and striation measurements and mapped horizontal stripes indicative of single earthquake events (see also Mechernich et al., this volume). Based on the obtained results and additional remote sensing studies, we estimated possible magnitudes based on empirical correlations (Wells & Coppersmith, 1994).

Scarp profiling

Following the examples of e.g. Papanikolaou (2005) or Mason (2016), we selected three representative sites (Fig. 4) at key sections within BFS_N, BFS_S and KFS to derive slip rate estimates from scarp profiling. The technique is based on the assumption that pronounced fault scarps only form after the LGM (c. 18 ± 3 kyr ago in the Mediterranean region, e.g. Benedetti, 2002). To obtain conservative and maximum long-term slip rates, free face height and vertical throw are averaged over the stated time period. Profiles were measured by ruler and clinometer.

RESULTS & INTERPRETATION

Earthquake horizons

Horizontal along-strike ribbons of distinct colour, roughness properties (e.g. micro-karstification features), markedness of slickensides, characteristic solution flutes and lichen growth occur at several locations along the fault planes of BFS and KFS (Fig. 2d). The boundaries between single ribbons are non-gradual and sharp. Two horizons of 15 ± 3 cm and 25 ± 2.5 cm pervasively re-appear along the full scarp length, so that we conclude an exhumation of single horizons during particular seismic events (see also Mechernich et al., this volume).

Magnitude estimates

Magnitude estimates after Wells & Coppersmith (1994) are based on (a) surface rupture length and (b) slip per event derived from the above described horizons. Results strongly depend on the presumption which of the introduced sections rupture simultaneously. Considered scenarios cover different combinations between sole rupture of BFS_N, BFS_S or KFS and combined rupture of all of these segments plus the intermittent distance between BFS and KFS. Magnitudes derived from surface rupture lengths range between $M_W = 5.3 \pm 0.43$ and $M_W = 6.5 \pm 0.52$ comparing the smallest (BFS_S) with the largest (BFS, KFS + intermittent part) possible rupture length. Magnitudes derived from slip per event (i.e. earthquake marker horizons) amount to $M_w \approx 6.0$ - 6.4.

Scarp profiling

Two sets of long-term (i.e. post-LGM) slip rates were calculated from the constructed scarp profiles (Fig. 3): (a) based on a conservative approach by only considering the free face height and (b) based on the full amount of vertical throw. Both sets of slip rate values differ by almost factor two: The conservative method yields rates of 0.49 ± 0.08 (BFS_N), 0.39 ± 0.07 (KFS) and 0.37 ± 0.06 mm/yr (BFS_S), while the throw-based estimate yields rates of 1.022 ± 0.15 mm (BFS_N), 0.53 ± 0.075 mm (BFS_S) and 0.91 ± 0.12 mm (KFS). Contemplating (a) the applicability of the applied method, (b) common fault scarp morphology (e.g. McCalpin, 2009) (c) representative rates obtained in comparable settings, (d) the possible influence of non-tectonic factors on our sites and (e) published vertical movement rates for the concerned region (c. 1 mm/yr, e.g. Serpelloni, 2013), we propose slip rates, if at all, to only insignificantly exceed the conservatively generated values.

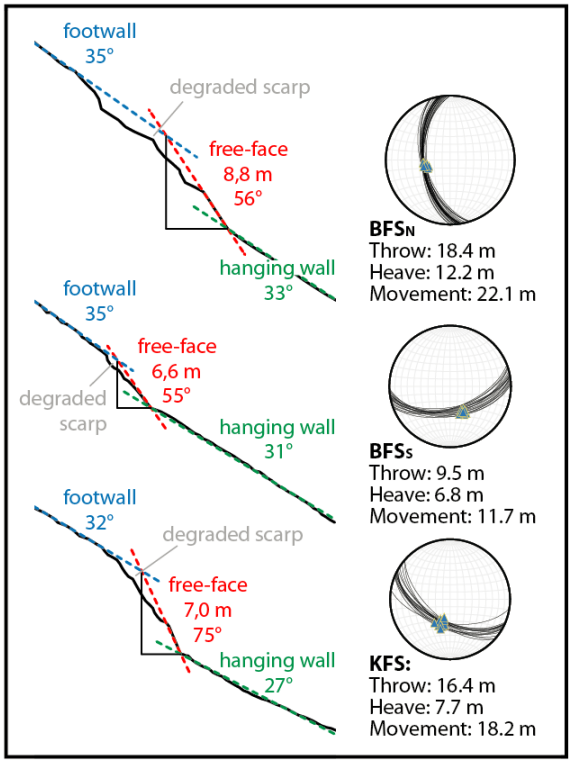

Figure 3: Profiles across three the fault scarps at three selected representative sampling locations.

DISCUSSION

For the Bar and Katërkolle fault scarps we generated outcrop-based first slip rate and magnitude estimations. All of the generated values match amongst themselves and appear to be realistic when compared with anticipatory dimensions in the broader region. Largest error sources in the presented work include (a) the presumed surface rupture lengths for magnitude calculation, hinging on the combination of simultaneously rupturing sections and (b) the interpretation of degraded scarps when calculating post-LGM slip rates from scarp profiles. For the calculations based on surface rupture length, different scenarios of simultaneously rupturing sections and the resulting magnitudes (M_W = 5.3 ± 0.43 and M_W = 6.5 ± 0.52) are realistic and compatible with slip-based estimates. Scarp profile-based slip rate estimations by contrast yield a wide range of possible rates, depending on the incorporation of the degraded scarp portion in respective calculations. Owed to above listed considerations, we favour a conservative approach with slip rates ranging between 0.37 ± 0.06 and 0.49 ± 0.08 mm/yr.

Genesis of extensional structures in a region in which exclusively compressional earthquakes have hitherto been instrumentally recorded remains partly enigmatic. We consider (i) action of tensile stresses during contractional deformation, (ii) recurrence intervals of extensional earthquakes exceeding the period in which seismicity has been instrumentally recorded (iii) 'slow earthquakes' (e.g. Crescentini, 1999) or (iv) gravitational processes. We rate (i) as relatively unlikely due to geometrical relations between fault planes, regional sedimentary bedding and possible (back-) thrusts. Three arguments also speak against (iv): (a) Gravitational and / or erosional processes would not explain the observed uniform exhumation of horizontal horizons on fault planes. (b) Striations on fault planes are independent of the local fall line. (c) Analogue examples of normal faulting are observed in locations close-by (e.g. Mali i Rrencit anticline, Albania) where potential energy contrast would not allow for gravitationally driven evolution. We rather expect the formation of normal faults to be connected to an ongoing W-ward migration (since late Eocene) of extensional tectonics related to slab rollback along the Aegean arc (e.g. Dumurdzanov, 2005; Burchfiel, 2008) and clockwise rotation of the Hellenides around a pivot falling immediately into theconcerned study area (Handy, 2004, 2018).

CONCLUSIONS

We report normal faults to be recently active in a domain that is per-se governed by purely contractional seismicity. We propose a tectonic, co-seismic origin of these structures, based on structural, geomorphological and qualitative observations made on bedrock fault scarps on the Rumija mountain chain (S Montenegro). The emergence of extensional structures during per-se compressive events is equally rated unlikely so that alternative solutions for a missing extensional signal in instrumentally measured seismicity have to be found. The age of fault scarps, i.e. their morphological expression, is proposed to post-date the LGM, (c. 18 ka, e.g. Benedetti, 2002) so that long-term slip rates may be estimated from the contemporaneous amount of free-face exhumation (compare e.g. Papanikolaou, 2005; Mason, 2016). For three selected sites we calculated minimum slip-rates of 0.49 ± 0.08 (BFS_N), 0.39 ± 0.07 (KFS) and 0.37 ± 0.06 mm/yr (BFS_S) with a conservative method. As the interpretation of the degraded scarp section has a large effect on according calculations, slightly increased rates are discussible. After the empirical relations methods by Wells & Coppersmith (1994), we additionally estimated earthquake magnitudes based on present surface rupture lengths and slip per event (derived from mentioned earthquake horizons). Depending on the presumption which fault segments rupture simultaneously, magnitudes range between $M_w \approx$ 5.5 ± 0.43 and 6.5 ± 0.52. Slip-based estimates reach $M_w \approx$ 6.0 - 6.4. In the context of anticipatory magnitudes in the region, these values appear realistic. We attribute the genesis of extensional structures to processes related to

slab-roll-back and consequent clockwise rotation of the Hellenides with respect to the Dinarides around rotational pivots in the immediate study area (Dumurdzanov, 2005; Burchfiel, 2008; Handy, 2014, 2018).

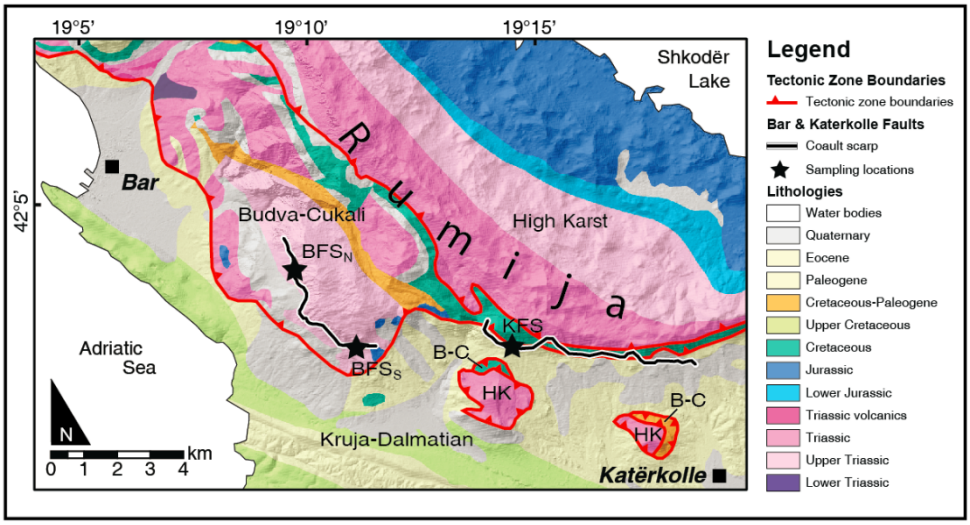

Figure 4: Fig. 3: Localization of the Bar and Katërkolle fault scarps superposed on a geological map including lithological as well as large-scale tectonic units. Sites for scarp-profiling (Figure 4) are indicated by black stars. Underlying map based on Geological Survey of Montenegro (1971).

Acknowledgements: We cordially thank Kristijan Sokol (University of Belgrade) and Martin Đaković (Geological Survey of Montenegro) for their help in the field as well as numerous fruitful discussions. We also thank our B.Sc. students from RWTH Aachen and FSU Jena for helping with data acquisition in the frame of their thesis. Project ALMOND is financed by Deutsche Forschungsgemeinschaft (DFG) which is gratefully acknowledged.

REFERENCES

Aliaj, S., 2006. The Albanian orogen: convergence zone between Eurasia and the Adria microplate. In: *The Adria Microplate: GPS Geodesy, Tectonics and Hazards* (Pinter, N., Grenerczy, G., Weber, J., Stein, S., Medak, D., eds), NATO Science Series IV: Earth and Environmental Sciences, Springer, 133-149.

Benedetti, L., Finkel, R., Papanastassiou, D., King, G., Armijo, R., Ryerson, F., Farber, D., & Flerit, F., 2002. Post-glacial slip history of the Sparta fault (Greece) determinedby36Cl cosmogenic dating: Evidence for non-periodic earthquakes. *Geophysical Research Letters* 29 (8), 87-1-4.

Benetatos, C., & Kiratzi, A., 2006. Finite-fault slip models for the 15 April 1979 (Mw 7.1) Montenegro earthquake and its strongest aftershock of 24 May 1979 (Mw 6.2). *Tectonophysics* 421, 129-143.

Burchfiel, B.C., Nakov, R., Dumurdzanov, N., Papanikolaou, D. Tzankov, T., Serafimovski, T., King, R.W., Kotzev, V., Todosov, A., & Nurce, B., 2008. Evolution and dynamics of the Cenozoic tectonics of the South Balkan extensional system. *Geosphere* 4, 919-938.

Crescentini, L., Amoruso, A., & Scarpa, S., 1999. Constraints on slow earthquake dynamics from a swarm in central Italy. *Science* 286 (5447), 2132-2134.

Dumurdzanov, N., Serafimovski, T., & Burchfiel, C.B., 2005. Cenozoic tectonics of Macedonia and its relation to the South Balkan extensional regime. *Geosphere* 1, 1-22.

Geological Survey of Montenegro, 1971. Basic geological map sheet of Yugoslavia 1:100.000 sheet Bar. Federal geological Institute, Beograd.

Grunthal, G., Wahlstrom, R., & Stromeyer, D., 2013. The SHARE European Earthquake Catalogue (SHEEC) for the Time Period 1900-2006 and Its Comparison to the European-Mediterranean Earthquake Catalogue (EMEC). *Journal of Seismology* 17, 1339-1344.

Handy, M.R., Giese, J., Onuzi, K., Pleuger, J., Schmid, S.M., Spakman, W., & Ustaszewski, K., 2018. Transfer and rotational normal faulting at the Dinarides-Hellenides junction - their relation to tearing and retreat of the Adriatic slab. 17th TSK Symposium on Tectonics, Structural Geology and Crystalline Geology, 19-25 March 2018, Jena, Germany, p. 55.

Handy, M.R., Ustaszewski, K., & Kissling, E., 2014. Reconstructing the Alps-Carpathians-Dinarides as a key to understanding switches in subduction polarity, slab gaps and surface motion. *Int J Earth Sci (Geol Rundsch)*, doi:10.1007/s00531-014-1060-3.

Mason, J., Schneiderwind, S., Pallikarakis, A., Wiatr, T., Mechernich, S., Papanikolaou, I., & Reicherter, K., 2016. Fault structure and deformation rates at the Lastros-Sfaka Graben, Crete. *Tectonophysics* 683, 216-232.

McCalpin, J.P., editor 2009. *Paleoseismology*, volume 95 of International geophysics series. Elsevier Acad. Press, Amsterdam, 2. ed. Edition.

Papanikolaou, I.D., Roberts, G.P., & Michetti, A.M., 2005. Fault scarps and deformation rates in Lazio-Abruzzo, Central Italy: Comparison between geological fault slip-rate and GPS data. *Tectonophysics* 408, 147-176.

Pondrelli, S., Salimbeni, S., Ekström, G., Morelli, A., Gasperini, P., & Vannucci, G., 2006. The Italian CMT dataset from 1977 to the present. *Physics of the Earth and Planetary Interiors* 159, 286-303.

Serpelloni, E., Facenna, C., Spada, G., Dong, D., & Williams, S.D.P., 2013. Vertical GPS ground motion rates in the Euro-Mediterranean region: New evidence of velocity gradients at different spatial scales along the Nubia-Eurasia plate boundary. *J. Geophys. Res. Solid Earth* 118, 6003-6024.

Wells, D.L., & Coppersmith, K.J., 1994. New empirical relationships among magnitude, rupture length, rupture width, rupture area, and surface displacement. *Bulletin of the Seismological Society of America* 84 (4), 974-1002.

INQUA Focus Group Earthquake Geology and Seismic Hazards

paleoseismicity.org

Attenuation of distributed faulting during thrust earthquakes: implications for fault displacement hazard

Boncio, Paolo (1), Nurminen, Fiia-Charlotta (2), Pace, Bruno (1), Valentini, Alessandro (1), Visini, Francesco (3)

(1) CRUST-DISPUTer, Università "G. d'Annunzio" di Chieti-Pescara, Chieti, Italy, paolo.boncio@unich.it
(2) Oulu Mining School, University of Oulu, Oulu, FI-90014, Finland
(3) Istituto Nazionale di Geofisica e Vulcanologia, L'Aquila, Italy

Abstract: *We compile data on distributed faulting (DF) from 11 well-studied surface faulting thrust earthquakes occurred globally since 1971 and we analyse statistically the distribution of DF ruptures in terms of distance to the trace of the principal fault (PF). The displacement on DF, normalized by the displacement on PF, is analysed as a function of distance to PF, as well. We obtain regressions that help in estimating the attenuation of DF with distance during surface-rupturing thrust/reverse earthquakes, with implications for earthquake fault zoning and fault displacement hazard assessment.*

Keywords*: Fault displacement hazard, thrust fault, distributed faulting*

INTRODUCTION

Fault Displacement Hazard (FDH) is a localized hazard due to rupture of the ground surface during moderate-to-large earthquakes caused by slip along the main seismogenic fault (principal fault, PF) and/or along secondary faults connected to or triggered by the PF (distributed faulting, DF). FDH can be faced by strategies of fault zoning and avoidance or by (or together with) strategies of probabilistic estimates of FDH (Youngs et al., 2003). Both strategies need to know the trace of the PF, the expected displacement on PF, the deformation close to the PF trace, and the distribution of DF away from PF. While the general fault geometry and the expected displacement on the main fault can be obtained through detailed earthquake geology aided by empirical relationships, the occurrence of DF is particularly difficult to predict. Direct observations from well-documented case studies may help significantly (e.g. shape and size of rupture zones, attenuation relationships for DF).

The distribution of DF and the width of the rupture zone for normal and strike-slip earthquakes (e.g. Youngs et al., 2003; Petersen et al., 2011) is much more studied than for thrust earthquakes.

The objectives of this work are: 1) to compile the data from well-studied surface-faulting, non-subduction, thrust earthquakes globally; 2) to analyse statistically the distribution of DF and the variation of the normalized displacement on DF as a function of distance from PF; and 3) to discuss the implications for earthquake fault zoning and FDH analysis.

DATA

Surface faulting data were compiled from the literature for 11 well-studied historic thrust earthquake ruptures occurred globally from 1971 to 2014 ($5.4 \leq M \leq 7.9$). Several different types of coseismic fault scarps characterise the analysed earthquakes, depending on the topography, fault geometry and near-surface materials (simple and hanging wall collapse scarps; pressure ridges; fold scarps and thrust or pressure ridges with bending-moment or flexural-slip secondary faults due to large-scale folding). For all the earthquakes, the distance of DF from the PF (r), the width of the rupture zone and the displacement on the DF were measured systematically in GIS-georeferenced published maps or compiled directly from the literature.

RESULTS

Surface ruptures can occur up to very large distances from PF: ca. 2,000 m on the footwall (FW) and 3,000 m on the hanging wall (HW). The farthest ruptures (>900 m on the FW and >2,000 m on the HW) are ruptures isolated from the main fault, interpreted here as triggered slip on pre-existing faults not directly connected with the primary seismogenic fault (sympathetic ruptures, Sy). Sympathetic ruptures are a small percentage of the total DF ruptures. Apart from Sy ruptures, DF occurs within ~750 m on the FW and ~1,600 m on the HW. Most DF occurs on the HW, preferentially in the vicinity of the main fault trace (< 50 m). The widest rupture zones are recorded where bending-moment (B-M) or flexural-slip (F-S) secondary faults, associated with large-scale folds (hundreds of meters to kilometres in wavelength), are present.

The distribution of surface ruptures is fitted with probability density functions. We obtained two couples

of fitting functions (Fig. 1), two for the HW and FW of the entire database ("all DF") and two for HW and FW of the "simple thrust" database (excluding B-M, F-S and Sy).

The highest hazard is concentrated in a narrow zone, ca. 60 m in width that should be considered as a fault avoidance zone. The fault zones should be asymmetric compared to the trace of the principal fault. The average FW:HW ratio is close to 1:2.

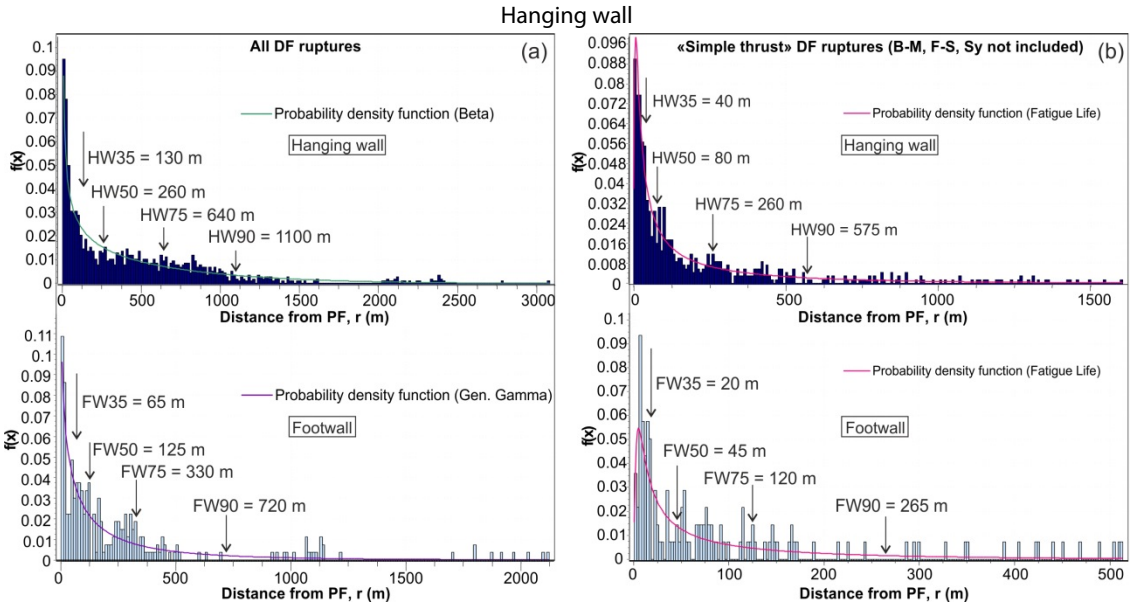

Figure 1: Probability density functions of distributed faulting DF for surface-faulting thrust earthquakes for the hanging wall (HW) and footwall (FW) of the entire database of DF (a) and for a subset of data obtained by excluding B-M, F-S and Sy ruptures (b). For the equations of the fitting functions see Boncio et al. (2018). The widths of the rupture zone for different percentiles in the HW and FW are indicated (e.g., HW50 is the 50th percentile in the hanging wall).

The attenuation relationship for displacement (d) on DF is obtained by analysing the correlation between d, normalized to the displacement D on PF, versus the distance from PF.

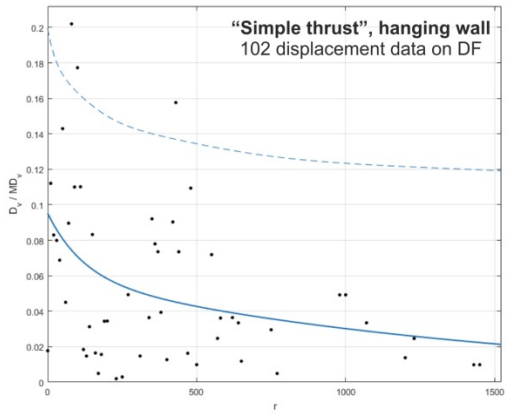

Figure 2: Attenuation curve of normalized displacement on DF (d/MD, vertical component) in the hanging wall ("simple thrust" database of DF) versus distance (r) from PF. Dashed line indicates the 95% upper bound. Each point is an average of all the data lying within a 10 m-wide bin.

Different normalization values were tested (average, AD and maximum, MD displacement for both net slip and vertical component of slip). The most complete database is that considering the vertical component of displacement. An example of fitting function for normalized vertical displacement versus distance from PF is illustrated in Figure 2. The results from this study and the obtained regressions, partly published in Boncio et al. (2018), can help in shaping and sizing fault zones against FDH, as well as for estimating the likelihood of having DF at varying distances from PF during probabilistic studies of fault displacement hazard.

REFERENCES

Boncio, P., Liberi, F., Caldarella, M., & Nurminen, F. C., 2018. Width of surface rupture zone for thrust earthquakes: implications for earthquake fault zoning. *Natural Hazards and Earth System Sciences* 18 (1), 241-256.

Petersen, M., Dawson, T.E., Chen, R., Cao, T., Wills, C.J., Schwartz, D.P., & Frankel, A.D., 2011. Fault displacement hazard for strike-slip faults. *Bull. Seismol. Soc. Am*. 101 (2), 805-825.

Youngs, R.R., Arabasz, W.J., Anderson, R.E., Ramelli, A.R., Ake, J.P., Slemmons, D.B., McCalpin, J.P., Doser, D.I., Fridrich, C.J., Swan III, F.H., Rogers, A.M., Yount, J.C., Anderson, L.W., Smith, K.D., Bruhn, R.L., Knuepfer, P.L.K., Smith, R.B., dePolo, C.M., O'Leary, D.W, Coppersmith, K.J., Pezzopane, S.K., Schwartz, D.P., Whitney, J.W., Olig, S.S., & Toro, G.R., 2003. A methodology for probabilistic fault displacement hazard analysis (PFDHA). *Earthq. Spectra* 19, 191-219.

INQUA Focus Group Earthquake Geology and Seismic Hazards

paleoseismicity.org

Parameters of the 2016 central Italy earthquake surface faulting (M 6.5, normal fault) and comparison with global data

Boncio, Paolo (1), Testa, Alessio (1), Di Donato, Michele (1), Mataloni, Giovanni (2), Palumbo, Donato (2), Le Donne, Lucio (2)

(1) CRUST-DISPUTer, Università "G. d'Annunzio" di Chieti-Pescara, Chieti, Italy, paolo.boncio@unich.it
(2) Dipartimento di Architettura, Università "G. d'Annunzio" di Chieti-Pescara, Pescara, Italy

Abstract: *We present the parameters of the surface faulting that formed during the 2016 earthquakes in central Italy (maximum magnitude = 6.5), obtained thanks to direct field survey. The obtained parameters (SRL, AD calculated with different methods, MD, D/MD, D/AD, AD/MD) are compared with global data compiled and analysed in various works in the literature. A comparison with the values predicted by well-established empirical regressions is performed as well. The differences are open to discussion.*

Keywords*: 2016 earthquakes, central Italy, normal fault, coseismic surface faulting, rupture parameters*

INTRODUCTION

The Central Italy 2016 seismic sequence started on August 24 with a Mw 6.0 shock located 9 Km NW of the Amatrice town. Two Mw 5.4 and Mw 5.9 earthquakes occurred on October 26, 25 km further N. The largest shock (Mw 6.5) occurred on October 30, between the 24 August and 26 October events, close to the Norcia town. All of them are normal faulting earthquakes, reactivating NW-SE striking, SW-dipping normal faults. The first event nucleated between the M. Gorzano and M. Vettore - M. Bove faults, and ruptured up to the surface along the southern section of the M. Vettore - M. Bove fault for a surface rupture length (SRL) of nearly 6 km (Lavecchia et al., 2016). The 26 and 30 October shocks ruptured up to the surface the M. Vettore - M. Bove fault, reactivating the fault section previously faulted by the 24 August event as well. As a result, surface faulting effects occurred for nearly 30 km (Fig. 1). The international research group Open EMERGEO (Civico et al., 2018; Villani et al., 2018) performed the survey of coseismic effects starting few hours after the main events. The northern area of the fault system was only partially surveyed by Open EMERGEO. Therefore, we decided to perform additional field work in order to fill in the gaps of rupture mapping/measuring and obtain more complete estimates of the surface displacement.

The obtained parameters are compared with global data of normal faulting surface-rupturing earthquakes and with empirical relationships between magnitude and rupture parameters.

DATA AND RESULTS

The M. Bove- M. Vettore fault was divided into several fault sections during the survey: Cupi - Ussita section, M. Bove section, M. Porche section, and Redentore - Vettoretto section.

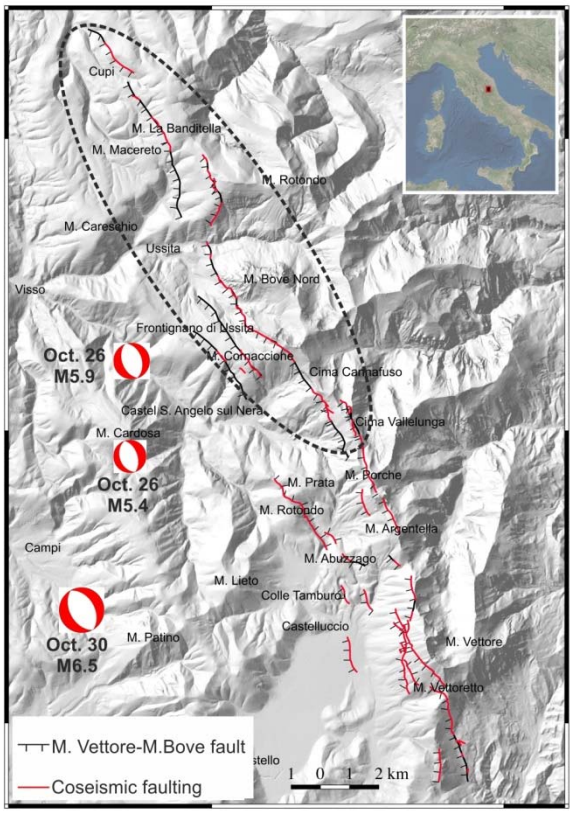

Figure 1: Map of the 2016 surface faulting along the M. Vettore – M. Bove fault in central Italy. Ellipse indicates the area where the Open EMERGEO database (Civico et al., 2018; Villani et al., 2018) was integrated by additional field mapping in this work.

The collected data allowed us to reconstruct the along-strike displacement profile (Fig. 1) and the main rupture parameters. These parameters are the Average Displacement (AD), the Maximum Displacement (MD) and the Surface Rupture Length (SRL). The results are: SRL = 30 km (32 km if a 2 km-long uncertain rupture at the southern end of the M. Vettore fault is considered);

Arithmetic AD: 37 cm; Integral AD: 36 cm; and maximum cumulative displacement MD = 240 cm (MD = 222 cm for the 30 October event).

These parameters are compared here with global normal faulting rupture data and empirical relationships from the literature. The comparison shows that the AD is lower than the expected value, the MD is higher than the expected value and, finally, the AD/MD ratio is lower than global data.

A possible explanation for the very low value of AD is an attenuation of coseismic displacement toward the surface, possibly due to the high segmentation of the fault system.
The long-term (post-Late Glacial Maximum) AD/MD ratio is more close to the global coseismic data, suggesting that the AD/MD ratio is recovered during the long-term, possibly due to moderate-magnitude earthquakes on single fault sections, or creep processes or both of them. The anomalously high value of MD might be due in part by localized tectonic phenomena, such as back-tilting as suggested by high-resolution topographic scarp analysis (terrestrial LiDAR) in the area of Dmax.

The realization of high-resolution topographic profiles allowed us to compare the topographic displacement profile with the coseismic displacement profile along the fault. The good correlation between the coseismic MD and topographic MD suggests that the maximum displacement recurs systematically in the same section of the fault (Redentore - Vettoretto section).

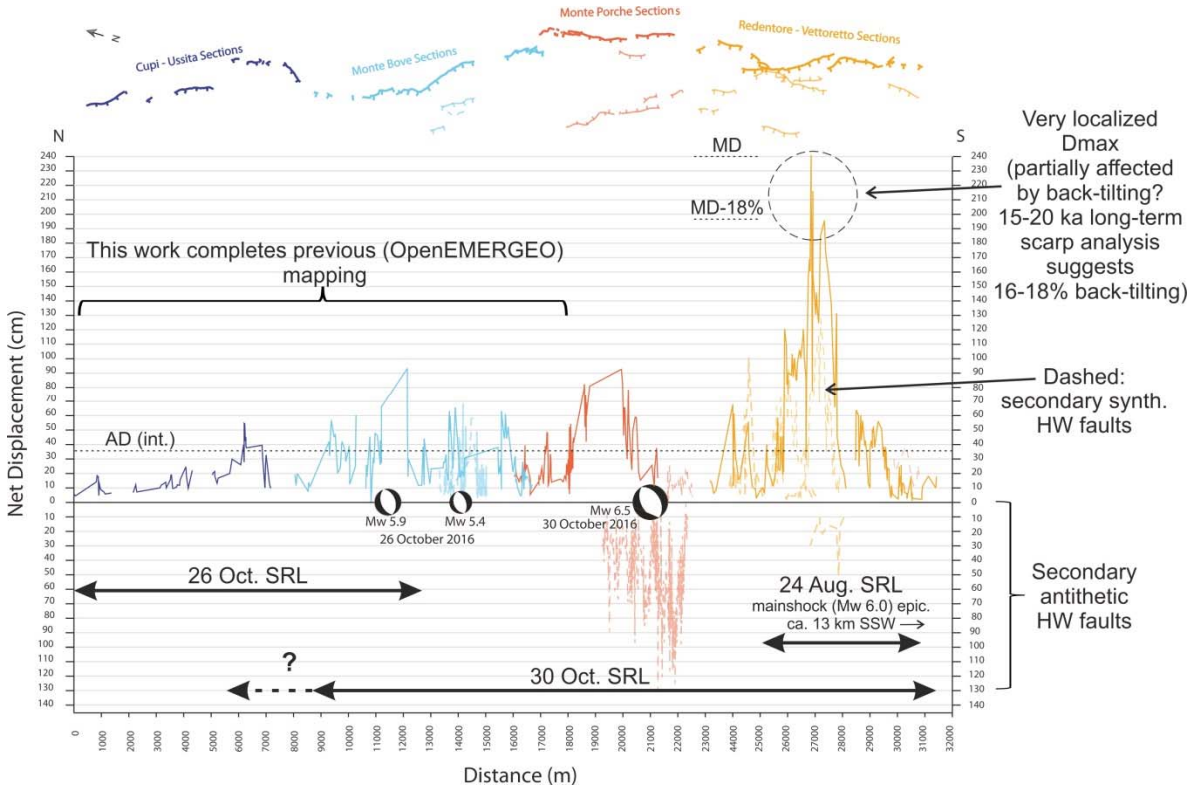

Figure 1: Cumulative net displacement of the 2016 earthquakes along-strike the M. Vettore - M. Bove normal fault.

REFERENCES

Civico, R., Pucci, S., Villani, F., Pizzimenti, L., De Martini, P.M., Nappi, R., & the Open EMERGEO Working Group, 2018. Surface Ruptures following the 30 October 2016 Mw 6.5 Norcia 645 earthquake, Central Italy. *Journal of Maps* 14 (2), 151-160, doi: 10.1080/17445647.2018.1441756.

Villani, F., Civico, R., Pucci, S., Pizzimenti, L., Nappi, R., De Martini, P.M., & the Open EMERGEO Working Group, 2018. A database of the coseismic effects following the 30 October 2016 Norcia earthquake in Central Italy. *Scientific Data* doi: 10.1038/sdata.2018.49.

Lavecchia, G., Castaldo, R., De Nardis, R., De Novellis, V., Ferrarini, F., Pepe, S., Brozzetti, F., Solaro, G., Cirillo, D., Bonano, M., Boncio, P., Casu, F., De Luca, D., Lanari, R., Manunta, M., Pepe, A., Zinno, I., & Tizzani, P., 2016. Ground deformation and source geometry of the 24 August 2016 Amatrice 670 earthquake (Central Italy) investigated through analytical and numerical modeling of DInSAR measurements and structural-geological data, *Geophys. Res. Lett*. 43,12,389-12,398, 672, doi: 10.1002/2016GL071723.

INQUA Focus Group Earthquake Geology and Seismic Hazards

paleoseismicity.org

Late Quaternary marine terraces along the Tyrrhenian coast of northern Calabria (southern Italy): New morphostratigraphical and geochronological data

Cerrone, Ciro (1), Ascione, Alessandra (1), Balassone, Giuseppina (1), Mormone, Angela (2), Robustelli, Gaetano (3), Soligo, Michele (4), Tuccimei, Paola (4)

(1) Department of Earth, Environmental and Resources Science - DiSTAR, University of Naples "Federico II", via Cinthia 21, 80126 Naples, Italy, ciro.cerrone@unina.it, alessandra.ascione@unina.it, giuseppina.balassone@unina.it
(2) IstitutoNazionale di Geofisica e Vulcanologia - INGV, OsservatorioVesuviano, Via Diocleziano 328, 80124 Naples, Italy, angela.mormone@ingv.it
(3) Department of Biology, Ecology and Earth Science - DiBEST, University of Calabria, Via P. Bucci, Cube 15b, 87036 Rende (CS), Italy, gaetano.robustelli@unical.it
(4) Department of Science, Roma Tre University, Largo San Leonardo Murialdo 1, 00146 Rome, Italy, paola.tuccimei@uniroma3.it, michele.soligo@uniroma3.it

Abstract: *A study of marine terraces has been carried out in a key area of the Tyrrhenian coast of the southern Apennines. The investigated area is located between the Campania coastal belt, in the north, which is substantially stable since the last interglacial, and southern Calabria, in the south, where the late Quaternary shorelines are strongly uplifted. In the study area, marine terraces stand up to ~170 m a.s.l. Particular attention has been devoted to the analysis of shorelines standing few tens of m a.s.l., which have been investigated by geomorphological-stratigraphical analyses and U-series dating of both corals (Cladocora caespitosa), and speleothems either predating or postdatingsea-level markers. The new data have allowed identifying recent sea-level fluctuations. The first age determinations allow correlating paleoshorelines in the 15-20 m a.s.l. elevation range to the youngest peaks of MIS 5, and point to recent uplift of the investigated area.*

Keywords*: Marine terraces, U-series dating, uplift, late Quaternary, southern Apennines*

INTRODUCTION

Impressive flights of marine terraces occur along the Tyrrhenian coastal area of southern Italy, from Campania to Calabria. In these regions, the uppermost marine terraces testify to long-term Quaternary uplift of the southern Apennines mountain belt in the order of hundreds of metres (e.g., Dumas et al., 1982; Carobene & Dai Pra, 1990; Westaway, 1993; Ascione & Romano, 1999; Filocamo et al., 2009). However, variable amount of uplift has been characterizing the Tyrrhenian margin of the southern Apennines during the Quaternary, with the sounthernmost segment (southern Calabria) recording larger uplift (e.g., Damiani, 1970; Dumas et al., 1982; Westaway, 1993; Ascione & Romano, 1999). Such an uplift trend has been maintained in late Quaternary times, as it is shown by the elevation of the last interglacial marine terraces, which increases southwards from southern Campania, where the last interglacial markers are uplifted by a very few metres (Esposito et al., 2003), to southern Calabria. In southern Calabria, uplift rates ~1 mm/yr for the last interglacial to present time span have been estimated (Dumas et al., 1982, 1987b; Cosentino & Gliozzi, 1988; Miyauchi et al., 1994; Tortorici et al., 2003; Dumas & Raffy, 2004; Ferranti et al., 2006), and related to the summation of a regional component, associated with the subducted Ionian slab, and a local component, which is associated to activity of large normal faults (Cosentino & Gliozzi, 1988; Westaway, 1993; Miyauchi et al., 1994; Tortorici et al., 2003). The northwards transition, or boundary, of the fast uplifting sector of the Apennines is poorly defined, due to the lack of outcrops in a ~100 km long coastal segment (Ferranti et al., 2006).

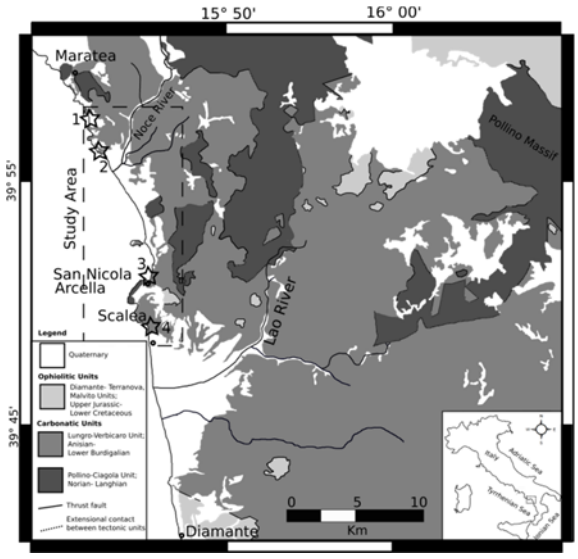

Figure 1: Simplified geological map of northern Calabria (after Iannace et al., 2005, modified). The dashed rectangle indicates location of the study area; stars indicate sites mentioned in the text: (1) Marina di Maratea; (2) Castrocucco; (3) Grotta del Prete; (4) Scalea.

Within such a framework, the region encompassing the Basilicata to northern Calabria sector, which is considered by several authors as a slowly uplifting area since the late Middle Pleistocene (e.g. Damiani, 1970; Carobene & Dai Pra, 1990, 1991; Filocamo et al., 2009), and by Westaway (1993) as an area of fast uplift, appears as a key area to unravel the recent tectonic behaviour of the entire southern Apennines Tyrrhenian margin.

With the aim to get new constraints on late Quaternary sea-level markers from this key area, we are investigating the marine terraces and deposits outcropping along the coastal belt of the Basilicata to northern Calabria sector of the Tyrrhenian margin. Our work is based on a combined geomorphological-stratigraphicalstudy, which is integrated by mineralogical and geochronological (U-series dating) analyses.

GEOLOGICAL BACKGROUND

The study area is located in the coastal margin of the Tyrrhenian back-arc basin, and spans from Marina di Maratea (Basilicata region), in the north, and Scalea (northern Calabria), in the south (Fig. 1). Back-arc extension and opening of the Tyrrhenian Sea were coeval with Neogene to Early Pleistocene thrusting of the southern Apennines mountain belt (e.g., Butler et al., 2004, and references therein).

Rocky headlands and bays formed in Triassic to Miocene carbonates that are tectonically overlain by ophiolitic units (Iannace et al., 2005; Fig. 1) characterise the coastof the northern and southern segments of the study area, which in the central part hosts the Noce River coastal plain (Fig. 1).

A flight of marine terraces reaching elevations ranging from ~130 m, in the north, to ~170 m a.s.l., in the south (Filocamo, 2007; Filocamo et al., 2010), dominates the landscape of the area investigated with this study. Relative sea-level markers consisting of small-size marine terraces and tidal notches are identified down to few m a.s.l. Most of marine terraces are undated, and both the chronological framework of relative sea-level markers and the Quaternary uplift rate of the study region are debated. For instance, the highest marine terrace has been associated with MIS 5.5 by Westaway (1993), who estimated an uplift rate around 1 mm/yr for the last ~100 ka. On the other hand, such a terracehas been related to the late part of the Early Pleistocene based on the chronological framework reconstructed for marine terraces from the nearby Lao River coastal area (Filocamo, 2007; Filocamo et al., 2009; location in Fig. 1). On the other hand, ages of marine terraces at lower elevations from the northern sector of the area investigated with this study (i.e., the Marina di Maratea to Castrocucco coastal strand; location in Fig. 1) and from one of the studied sites were constrained by geochronolgical data, i.e., $^{230}Th/^{234}U$ measurements on coral *Cladocora caespitosa*and D/L measurements on bivalves(Carobene & Dai Pra, 1990; 1991).Based on such data, marine terraces located in the ~12-19 m elevation range were related to the late MISs of the Middle Pleistocene. Based on D/L measurements, marine terraces in the ~5-9 m elevation range from the Basilicata coastal sector were related to MIS 5.5, and shorelines at ~2-5 m a.s.l. to either MIS 5.3 or MIS 5.1 (Carobene & Dai Pra, 1991).Collectively, available data have allowed estimating an uplift rate in the order of 0.05-0.03 mm/yr in the last interglacial to present time span (Ferranti et al., 2006).

MATERIALS AND METHODS

The study herein was carried out through the combination of geomorphological and Quaternary stratigraphy analyses, mineralogical analyses and U-series disequilibria dating.

The geomorphological and Quaternary stratigraphy analysis was carried out through the analysis of detail-scale maps (1:5.000 scale map edited by Regione Calabria and Regione Basilicata, and LiDAR data) and field surveys. The field surveys were focused on analysis of erosional landforms and shallow marine and continental deposits associated with the marine terraces and tidal notches, and blanketing the sea-cliffs. Particular attention was devoted to detailed analysis of the more recent markers of paleo-sea levels, i.e., those standing within few tens of m a.s.l. Elevations of paleo-sea level indicators were measured by a laser distance meter.

In order to constrain ages of paleo-sea level markers, corals (*Cladocora caespitosa*) and calcite concretions were sampled for U-series dating. Speleothems and corals are considered excellent samples to be dated with U-series disequilibria methods because in most cases they consist of pure calcium carbonate, free from a detrital component that makes problematic the dating of dirty carbonates. For corals it is important to verify their original aragonitic nature and check for the eventual presence of calcite. The occurrence of relevant calcite indicates that weathering processes have affected the coral after its burial, with consequent opening of the chemical system. Therefore, a mineralogical characterization of coral samples was carried out through the XRD method.

For routine mineralogical characterization of each coral sample a GE-Seifert MZVI automated diffractometer (XRD) has been used, with CuKα radiation, 40 kV and 30 mA, 5s per step and a step scan of 0.05° 2θ in the 3-70° 2θ interval. The software package RayfleX (GE Inspection Technologies, 2004) was used for data processing, and phase identification was made by means of the ICDD-PDF2 database. For quantitative XRD phase analysis, i.e. calculation of percentages of aragonite, calcite and all the other associated minerals, we have used both the GE-Seifert MZVI instrument (counting 18s per step, step scan 0.02° 2θ) and a PANalytical diffractometer (equipped with a high speed PIXcel detector, Ni-filtered, CuKα radiation, pyrolytic graphite crystal monochromator, 40 kV and 40 mA, step size of 0.02° and scanning time 8 s/step). The data were refined using the Rietveld method (Bish & Post, 1993, and references therein); the XRD spectra were elaborated with multiple refinements by the GSAS package (General Structure Analysis System; Larson & Von Dreele, 2000) and its graphical interface EXPGUI (Toby, 2001), as well as with HighScore Plus software. The Rietveld structural models were based on the American Mineralogical Crystal Structure Database (AMCSD).

The $^{230}Th/^{234}U$ method is the most widely used dating technique applied to continental carbonate deposits and corals and is based on the extreme fractionation of the parent isotopes ^{238}U and ^{234}U from their long-lived daughter ^{230}Th in the hydrosphere. Uranium, markedly more soluble than Th in the surface and near-surface environments, is readily mobilised as the highly soluble uranyl ion (UO_2^{2+}) and its complexes, whereas Th is easily hydrolyzed and precipitated or adsorbed on detrital particles. Uranium is co-precipitated with $CaCO_3$ on exsolution of CO_2, while Th is generally negligible. In the absence of detrital Th, ^{230}Th only forms in situ by radioactive decay of co-precipitated U. In a closed system the extent to which the $^{230}Th/^{234}U$ activity ratio has returned towards unity is a function of time, taking into account also the state of disequilibrium between ^{234}U and ^{238}U (Kaufman & Broecker, 1965).

About 3 g of corals and 40 g of continental carbonates were selected and dissolved in nitric acid. Few millilitres of hydrogen peroxide were added and heated at 100 °C in order to destroy organic matter. Isotopic complexes of uranium and thorium were extracted according to the procedure described in Lawrence Edwards et al., 1987 and alpha-counted using high resolution ion implanted Ortec silicon surface barrier detectors. The ages were calculated by means of Isoplot/Ex (version 3.0), a plotting and regression program designed by Ludwig (2003) for radiogenic-isotope data.

DISCUSSION AND CONCLUDING REMARKS

The study that is being conducted provides new data on late Quaternary sea-level markers in the Tyrrhenian coastal belt of the southern Apennines spanning from Basilicata to northern Calabria.

Both a revision, and reinterpretation, of outcrops reported in the literature, and new findings were performed with the field surveys. Among the analysed outcrops, those shown in Fig. 1 are characterised by distinct sea-level markers, e.g., wave-cut platforms, tidal notches and lithophaga hole bands. Several outcrops (e.g., sites shown in Fig. 1) are characterised by the occurrence of *Cladocora caespitosa* bioconstructions located at various elevations, however within the 2.5-15 m elevation range. In addition the field surveys allowed identification of calcite concretions associated with paleoshorelines, i.e. calcite concretion that either cover and postdate, or predate sea-level markers. Both the corals and speleothems have been sampled and are being analysed for geochronology.

X-ray diffractometry analysis has allowed selection of corals sampled for U-series dating. Based on XRD results some of the samples with relatively high calcite content (20-30%) were discarded, while the aragonitic nature of corals sampled in the sites 1, 3 and 4 shown in Fig. 1, with moderate calcite amount that is always below 3%, has been assessed.

U-series analyses have shown that $^{230}Th/^{232}Th$ activity ratios are always higher than 80, indicating that samples do not contain a significant detrital fraction. Furthermore, the uranium content of corals, about 2-3 ppm, approaches the average value of uranium abundance in living corals and the initial $^{234}U/^{238}U$ activity ratio ($^{234}U/^{238}U_i$) of marine carbonates generally approach that of the marine water. These data are an evidence of the general good quality of obtained ages.

To date, geochronological data are available for two of the investigated outcrops, i.e.outcrops in the Castrocucco and Grotta del Prete sites (sites 2 and 3 in Fig. 1, respectively). In the Castrocuccosite (site 2 in Fig. 1) lithophaga hole bands reaching ~20 m a.s.l. are exposed along the sea cliff. Along the sea cliff, speleothems some cm thick covering the carbonate rocks are preserved. The calcite concretions are affected by lithophaga holes at ~15 m a.s.l., filled with calcarenites (Fig. 2). In the Grotta del Prete site, a wave-cut platform located ~20 m a.s.l. (inferred elevation of the abrasion platform inner edge) crops out. The wave-cut platform is mantled by beach conglomerates, which pass upwards to biocalcarenites bearing *Cladocora caespitosa* bioconstructions. The biocalcarenite deposit is eroded by potholes, which may be related witha sea-level fall. The potholes are buried by arenites that testify to a younger sea-level rise.

U-series dating of a speleothem sample (CSC8) from the Castrocucco site and of a coral sample (GRP2) from the Grotta del Prete outcrop have provided ages of 151±11 ky and 84±4yr, respectively.

By U-series dating of sample CSC8 correlation of the speleothem from the Castrocucco site with MIS6 may be inferred. Based on such a correlation, the relative sea-level rise, which is testified by the lithofaga holes that postdate the speleothem, may be related with MIS5.

U-series dating of sample GRP2 constrains age of the coral-bearing deposits from the Grotta del Prete site to MIS 5.1. Such a correlation, coupled with field evidence, suggests the occurrence of sea-level fluctuations during MIS 5.1, consistent with findings by Dumas et al. (2005) from southern Calabria.

Figure 2: Close-up view of the sea cliff in the Castrocucco site (site 2 in Fig. 1), showing, in the right part, a calcite concretion affected by lithophaga holes that are filled with calcarenites (in the rectangle).

The new findings provide evidence for late Pleistocene sea-level fluctuations, and allow a better definition of both the elevation and age of relative sea-level markers in the investigated area. For instance, age determination of sample GRP2 updates dating of the *Cladocora*-bearing deposits from the Grotta del Prete site, previously related to the late part of the Middle Pleistocene by Carobene & Dai Pra (1991).

The new data on elevation and age of the analysed deposits and shorelines point to recent (late Quaternary - Holocene?) uplift of the investigated coastal sector of one order of magnitude greater than that assessed with former studies, and suggest a thoroughly revision, and reinterpretation, of the chronological framework for late Quaternary sea-level markers in the Tyrrhenian coastal belt of northern Calabria.

REFERENCES

Ascione, A., & Romano, P., 1999. Vertical movements on the eastern margin of the Tyrrhenian extensional basin. New data from Mt. Bulgheria (Southern Apennines, Italy). *Tectonophysics* 315 (1-4), 337-356.

Bish, D.L., & Post, J.E., 1993. Quantitative mineralogical analysis using the Rietveld full pattern fitting method. *American Mineralogist* 78, 932-940.

Butler, R.W.H., Mazzoli, S., Corrado, S., Donatis, M.D., Di Bucci, D., Gambini, R., Naso, G., Nicolai, C., Scrocca, D., Shiner, P., & Zucconi, V., 2004. Applying Thick-skinned Tectonic Models to the Apennine Thrust Belt of Italy-Limitations and Implications. In: *Thrust Tectonics and Hydrocarbon System: American Association of Petroleum Geologists Memoir* (McClay, K.R., ed), 82, 647-667.

Carobene, L., & Dai Pra, G., 1990. Genesis, Chronology and Tectonics of the Quaternary marine terraces of the Tyrrhenian coast of northern Calabria (Italy). Their correlation with climatic variations. *Il Quaternario* 3 (2), 75-94.

Carobene, L., & Dai Pra, G., 1991. Middle and Upper Pleistocene sea level highstands along the Tyrrhenian coast of Basilicata (Southern Italy). *Il Quaternario*, 4 (1a), 173-202.

Cosentino, D., & Gliozzi, E., 1988. Considerazioni sulle velocità disollevamento di depositi eutirreniani dell'Italia Meridionale e dellaSicilia. *Memorie della Società Geologica Italiana* 41, 653-665.

Damiani, A.V., 1970. Terrazzi marini e sollevamenti differenziali fra i Bacini del Lao e del Corvino (Calabria settentrionale). *Italian Journal of Geosciences* 89 (1), 145-158.

Dumas, Gueremy, P., Lhenaff, R., & Raffy, J., 1982. Le soulèvement quaternaire de la Calabrie méridionale. *Revue de Géologie Dynamique et de Géographie Physique* 23, 27-40.

Dumas, B., Guérémy, P., Lhénaff, R., & Raffy, J., 1987. Rates of uplift as shows by raised Quaternary shorelines in Southern Calabria (Italy). *Zeitschrift für Geomorphologie, N.F.*, Supplementband 63, 119-132.

Dumas, B., Guérémy, P., & Raffy, J., 2005. Evidence for sea-level oscillations by the "characteristic thickness" of marine deposits from raised terraces of Southern Calabria (Italy). *Quaternary Science Reviews* 24 (18-19), 2120-2136.

Esposito, C., Filocamo, F., Marciano, R., Romano, P., Santangelo, N., Scarciglia, F., Tuccimei, P., 2003. Late Quaternary shorelines in southern Cilento (Mt. Bulgheria): morphostratigraphy and chronology. *Italian Journal of Quaternary Science* 16 (1), 3-14.

Ferranti, L., Antonioli, F., Mauz, B., Amorosi, A., Dai Pra, G., Mastronuzzi, G., Monaco, C., Orrù, P., Pappalardo, M., Radtke, U., Renda, P., Romano, P., Sansò, P., & Verrubbi, V., 2006. Markers of the last interglacial sea-level high stand along the coast of Italy: Tectonic implications. *Quaternary International* 145-146, 30-54.

Filocamo, F., 2007. Evoluzione quaternaria del margine tirrenico dell'Appennino meridionale tra il golfo di Sapri e la foce del fiume Lao: studio stratigrafico e geomorfologico. PhD Thesis, Federico II University, Napoli, Italy, 340 pp. Available at http://www.fedoa.unina.it.

Filocamo, F., Romano, P., Di Donato, V., Esposito, P., Mattei, M., Porreca, M., Robustelli, G., & Russo Ermolli, E., 2009. Geomorphology and tectonics of uplifted coasts: New chronostratigraphical constraints for the Quaternary evolution of Tyrrhenian North Calabria (southern Italy). *Geomorphology* 105 (3-4), 334-354.

Filocamo, F., Ascione, A., Romano, P., 2010. The marine terraces of the Policastro Gulf: new insights on the evolution of the Southern Apennines Tyrrhenian margin. *Rendiconti Online Società Geologica Italiana* 11, 44-45.

Iannace, A., Bonardi, G., D'Errico, M., Mazzoli, S., Perrone, V., & Vitale, S., 2005. Structural setting and tectonic evolution of the Apennine Units of northern Calabria. *Comptes Rendus Geoscience* 337 (16), 1541-1550.

Kaufman, A., & Broecker, W., 1965. Comparison of Th230 and C14 ages for carbonate materials from Lakes Lahontan and Bonneville. *Journal of Geophysical Research* 70 (16), 4039-4054.

Larson, A.C., & Von Dreele, R.B., 2000. GSAS. Report LAUR 86-748. Los Alamos National Laboratory, New Mexico, USA.

Lawrence Edwards, R., Chen, J.H., & Wasserburg, G.J., 1987. 238U234U230Th232Th systematics and the precise measurement of time over the past 500,000 years. *Earth and Planetary Science Letters* 81 (2-3), 175-192.

Ludwig, K.R., 2003. *User's Manual for Isoplot 3.00: A Geochronological Toolkit for Microsoft Excel*.

Miyauchi, T., Dai Pra, G., & Sylos Labini, S., 1994. Geochronology of Pleistocene marine terraces and regional tectonics in the Tyrrhenian coast of South Calabria, Italy. *Il Quaternario* 7 (1), 17-34.

Toby, B.H., 2001. EXPGUI, a graphical user interface for GSAS. *Journal of Applied Crystallography* 34, 210-213.

Tortorici, G., Bianca, M., De Guidi, G., Monaco, C., & Tortorici, L., 2003. Fault activity and marine terracing in the Capo Vaticano area (Southern Calabria) during the Middle-Late Quaternary. *Quaternary International* 101/102, 269-278.

Westaway, R., 1993. Quaternary uplift of southern Italy. *Journal of Geophysical Research* 98, 21741-21772.

INQUA Focus Group Earthquake Geology and Seismic Hazards

paleoseismicity.org

Reinterpretation of evolution process of Wonwonsa fault near Ulsan fault zone in southeast region of Korean Peninsula

Cho, Sung-il (1), Gwon, Sehyeon (1), Choi, Weon-hack (1), Inoue, Daiei (2)

(1) Central Research Institute, Korea Hydro & Nuclear Power Co., Ltd. Daejeon 305-343, Korea, chosi4476@khnp.co.kr
(2) Central Research Institute of Electric Power Industry 1-6-1, Otemachi, Chiyoda-ku, Tokyo, Japan

Abstract: *According to the pre-existing studies, the Wonwonsa fault is a thrust fault with a low angle that is almost horizontal, and the Quaternary sedimentary layer that covers granite with unconformity is distributed with a wedge shape in the upper and lower parts of the fault. However, the extended distribution of the fault was not clear so that a possibility of having a secondary factor such as landslide was raised, but an accurate analysis through an additional investigation was not presented. In this study, to establish the developing characteristics of the Wonwonsa fault, the geometric characteristics and extended distribution of the fault through the comprehensive analysis of the lineament and site investigation, and the correlation between the sedimentary layer and fault were analysed. Through this study, the evolution process of the Wonwonsa fault was explained with three models of the fault using unconformity, landslide and active fault movement. The extended distribution of the Wonwonsa fault was not confirmed, and in consideration of the irregular continuity of the fault gauge zone, distribution status of the terrace sedimentary layer and altitude difference, it is judged that the secondary sliding caused by a landslide after a reverse fault movement in the past seems more reasonable.*

Keywords*: Wonwonsa fault, Lineament, Terrace, Landslide, Joint*

INTRODUCTION

Because the largest earthquake (M_L 5.8, September 12th, 2016) in Gyeongju-si and second largest earthquake (M_L 5.4, November 15th, 2017) occurred in the southeast region of the Korean Peninsula since the instrumental earthquake data were being collected, there have been active reevaluation studies on the fault activities. In the entire southeast region of the Korean Peninsula, the Yangsan and Ulsan fault zones are distributed (Fig. 1), and in the nearby outcrop, about 60 faults that have been active after the Quaternary period have been reported (Choi et al., 2011).

The Wonwonsa fault was confirmed in the nearby outcrop of the Ulsan fault zone in the southeast region of the Korean Peninsula, and there are more than 10 active fault outcrops that are exposed to the east side of the Ulsan fault zone. Also, the main direction of the faults is mostly south-north direction, and except some faults, they indicate the reverse fault movement that moved from east to west (Chang, 2001). According to the pre-existing studies (Chang, 2001; Choi, 2003), they are thrust faults with low angle whose direction is N5°E/12°SE, which is almost horizontal, and the Quaternary sedimentary layers that covers the Mesozoic granite with unconformity are distributed with a wedge shape in the lower part. The creation period of the fluvial terrace was analysed to be 34 ~ 33 ka (Cheong et al., 2001) by the OSL (Optically Stimulated Luminescence) method and 33,270 ± 230 yBP (KIGAM, 1998) by the ^{14}C method using charcoal. The ESR (Electron Spin Resonance) analysis result using the fault gauge showed that the Wonwonsa fault had multiple fault movements during about 13,000 ~ 70,000 years ago (Yang, 2006). The extension of the fault was reported that continuing up to about 50 m in the upstream direction of the valley from the outcrop (Chang, 2001).

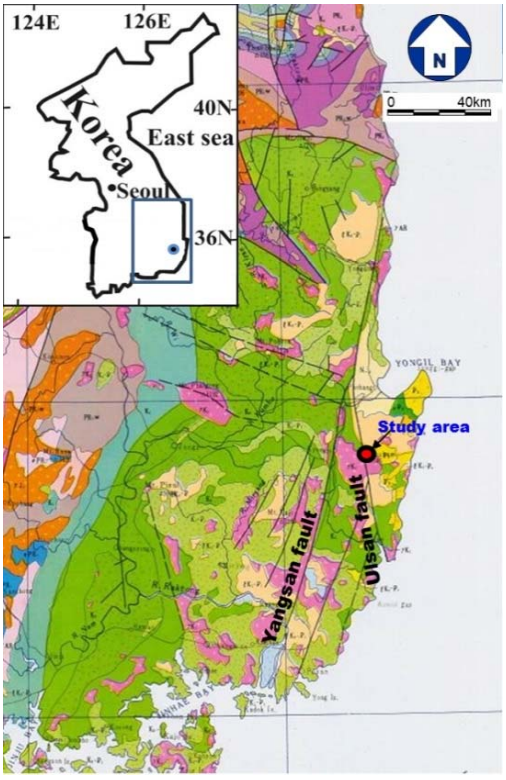

Figure 1: Geological map of the Korean Peninsula and the location of the study area (modified after KIGAM, 1995).

However, the extended distribution of the Wonwonsa fault was not clear so that a possibility of having a secondary factor such as landslide was raised (KIGAM, 1998), but an accurate analysis through an additional investigation was not presented. Therefore, in this study, the comprehensive analysis of the lineament and fault distribution using aerial photographs was carried out, the geometric characteristics and extended distribution of the Wonwonsa fault were thoroughly investigated, and the correlation between the fault and sedimentary layer was analysed to reinterpret the fault movement history.

RESULT OF LINEAMENT ANALYSIS

For the accurate analysis of the fault extension and terrace distribution characteristics, aerial photographs with the scale of 1:10,000 were used to interpret the lineament, and it was classified using the lineament activity rank and terrace classification criteria suggested by Inoue & Choi (2006). The classification of the lineament grade was made as La (terrace was cut and the active fault was certain), Lb (lower terrace was cut but the active fault was less certain), Lc (higher terrace was cut but the active fault was not certain), Ld (lineament was interpreted, but activity is suspicious), or Le (lineament was not active but nontectonic). The characteristics of the terrace were classified based on the divided degree of the valley dissection flatness and smoothness of the surface, altitude, and chronological characteristics found by the isotope analysis. As the result of the lineament analysis, the lineament with Ld rank whose lineament was clearly developed in the rock was confirmed, and in both sides of the lower part of the Mohwa River, lower terraces were developed (Fig. 2).

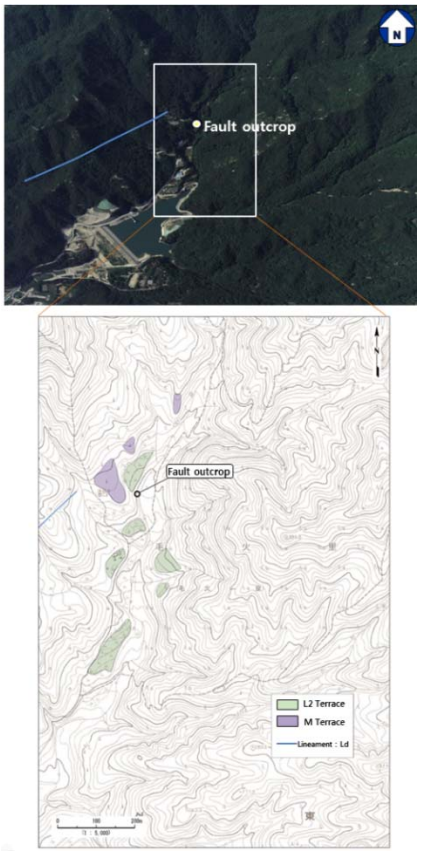

Figure 2: Lineament and terrace map by aerial photos interpretation.

The fluvial terraces were composed of low terraces and middle terraces, and lower terraces were developed at the height of 20 m and middle terraces were distributed at the height of 50 m from the river bed.

EXTENTION OF FAULT

The Wonwonsa fault extension status following the river in the north-northeast direction which was the main direction of the fault was carefully investigated. About 25 m of the Wonwonsa fault surface was confirmed from the outcrop, and the extended distribution following the main upstream direction was not confirmed. However, at a location of 30 m away from the fault outcrop in the north-northeast direction, sub-parallel joints with the direction of N20°E/15°NW were observed. These joints were not long and distributed with the regular space of about 1 m. Also, they were judged to be sheeting joints whose internal filling materials received differential weathering (Fig. 3). Also, some shear joints with the direction of N10°W/45°SW were confirmed, but since there was a large tilt angle difference compared with the Wonwonsa fault, it was difficult to judge them to be a fault extension (Fig. 4).

Figure 3: Sheeting joint confirmed following the main upstream direction from the outcrop.

Figure 4: Shear joints confirmed following the main upstream direction from the outcrop.

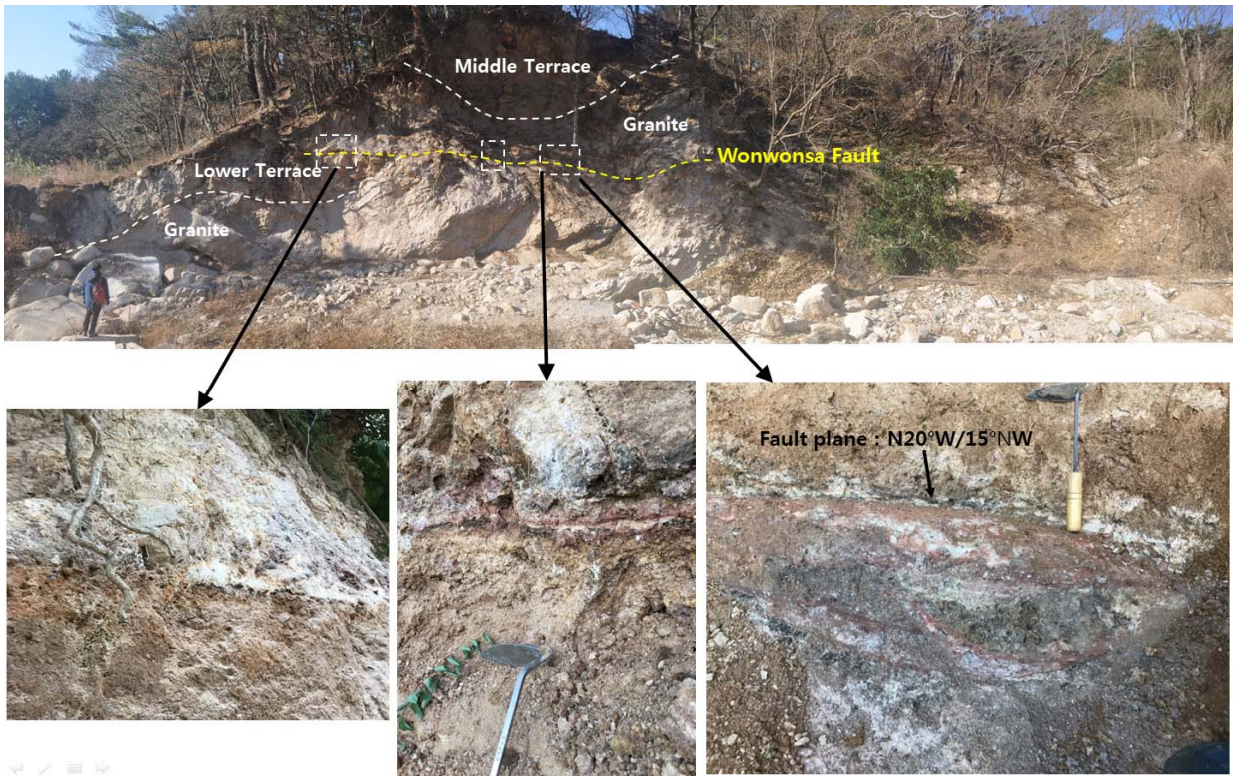

Figure 5: Characteristics of Wonwonsa fault plane in the outcrop.

In addition, the part where the boundary surface of the fault had a close contact with the low terrace in the lower part had the thickness of about 1 cm, and the part that had a close contact with the granite had the thickness of about 30 cm, thereby showing an uneven distribution of the parts that had a close contact with the fault (Fig. 5). Therefore, the continuity of the fault gauge zone was not clear.

CHARACTERISTICS OF SEDIMENTARY DEPOSITES

In the sedimentary layer of the river bed that was distributed near the Wonwonsa fault outcrop, many boulders with the diameter of 2 ~ 3 m were observed, and such boulders were judged to be deposited because of a large flood (Fig. 6). The lower terraces in the lower part of the Wonwonsa fault were mostly composed of pebbles that were smaller than somewhat weathered cobbles, and no bigger pebbles were observed. The diameter of the largest pebble of the middle terrace in the upper part of the Wonwonsa fault was about 30 cm, and the pebbles were more weathered than those of the lower terrace. Furthermore, weathered sand-like granite covered the uneven pebble layer evenly. Near the Wonwonsa at the top of the fault outcrop, another pebble layer was confirmed at a position whose altitude was about 10 m higher than the middle terrace of the upper part of the fault. The sedimentation status was very similar to that of the middle terrace so that it was very difficult to classify it as a different terrace layer based on the altitude difference.

Figure 6: Characteristics of terrace in the outcrop. (a) Middle terrace, (b) Lower terrace.

DISCUSSION AND CONCLUSION

In this study, three models are suggested as follows in consideration of the extension status of the Wonwonsa fault, irregular distribution of the fault gauge zone, and the sedimentation status and altitudinal distribution of the fluvial terrace.

1. Unconformity model: To explain the evolution process of the Wonwonsa fault with the unconformity model, the terrace layer in the upper part of the bed rock and the granite bed rock must be composed of gravel layers of boulders. However, the sedimentation status is different from a generally distributed sedimentation, and the size of gravel is too large so that it would be very difficult to observe this as a part of the sedimentation layer.

2. Active fault model: In consideration of the development status of the fault gauge zone, the Wonwonsa fault can be interpreted as a reverse fault that was originated by a geological structural movement. However, the fault did not extend from the outcrop, and if the age dating using ESR is believable, it must have reactivated multiple times intermittently, but the continuity of the fault gauge zone was not clear so that it was difficult to interpret it as the fault model. Furthermore, if the terraces distributed in the upper and lower parts of the fault are presumed to be the same deposited layers unrealistically large displacement of the fault have to imagine because the fault surface is developed with a very low angle.

3. Landslide model: There is an altitude difference of about 10 m between the middle terrace in the upper part of the Wonwonsa fault and the highest terrace layer near the Wonwonsa. If these two terraces were assumed to be located in the identical layer, it can be presumed that the middle terrace layer in the highest part must have slid by a landslide (Fig. 7). If the landslide model is certain, there must be traces of the landslide scarp caused by the landslide near the fault outcrop, and it is possible for them to extend into the sub-horizontal fault surface. However, the fault outcrop is covered with talus and soil so that the landslide scarp could not be confirmed. Therefore, the landslide scarp must be found in the future, and if these two terrace layers should be proven to be deposited at the same period based on the age dating, or facies analysis etc., the evolution process of the Wonwonsa fault can be explained by the landslide model.

The extension status of the Wonwonsa fault and the continuity of the fault gauge zone were not clear, and in consideration of the distribution and altitude difference of the terrace sedimentation layer, it is presumed that the secondary sliding caused by a landslide after a reverse fault movement in the past seems more reasonable. However, to secure the credibility of the landslide model, it is necessary to confirm the landslide scarp caused by the landslide and secure a basis by performing an age dating to find out whether the middle terrace whose altitude difference is about 10 m came from the sedimentary layer with the same origin.

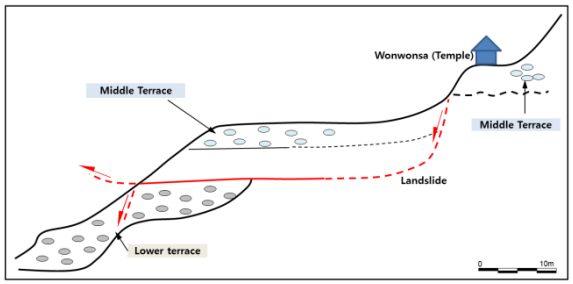

Figure 7: Landslide model for the evolution of Wonwonsa fault.

REFERENCES

Chang, T.W., 2001. Quaternary Tectonic Activity at the Eastern Block of th Ulsan Fault. *Journal of the Geological Society of Korea* 37 (3), 431-444.

Cheong, C.S., Lee, S.H. Kim, J., Im, C.B., Chang, B.U., Jeong, G., & Chang, H.W., 2001. Rb-Sr and K-Ar dating of fault gouges from the Ulsan fault zone, southeastern Korea. European Union of Geosciences, 595 p.

Choi, W.H., 2003. Neotectonics of the Gyeongju-Ulsan area in the southeastern part of Korean Peninsula. Doctoral dissertation. Seoul National University, 205 p.

Inoue, D., & Choi, W.H., 2006. The Activity of the Ulsan Fault System Based on Marine Terrace Age Study at the Southeastern Part of Korean Peninsula. CRIEPI report: N 05012.

KIGAM (Korea Institute of Geoscience and Mineral Resources), 1998. Final report of the re-evaluation of design earthquake based on the Yangsan fault. 435 p.

KIGAM (Korea Institute of Geoscience and Mineral Resources), 2011. Active Fault Map and Seismic Hazard Map. 688 p.

Lee, H.-K., & Schwarcz, H.P., 2001. ESR dating of the subsidiary faults in the Yangsan faults systems, Korea. *Quaternary Science Reviews* 20, 999-1003.

Yang, J.S., 2005. Quaternary fault activity in the southeastern part of the Korea Peninsula. Doctoral dissertation. Kangwon National University, 595 p.

INQUA Focus Group Earthquake Geology and Seismic Hazards

paleoseismicity.org

Rapid Late Pleistocene uplift in the Mejillones Peninsula, northern Chile subduction zone (23.5°S): Insights from ^{10}Be dated marine abrasion terraces

Cortés-Aranda, Joaquín (1,2), González, Gabriel (3), Martinod, Joseph (4), Regard, Vincent (4), Pousse, L. Lea (6), Astudillo, Luis (1,2)

(1) Universidad de Concepción, Chile, joacortes@udec.cl
(2) Núcleo Milenio Cyclo
(3) Universidad Católica del Norte, Chile
(4) Université Savoie-Mont Blanc, France
(5) Geoscience Environment Toulouse (GET), France
(6) Centre Européen de Recherche et d'Enseignement des Géosciences de l'Environnement (CEREGE), France

Abstract: *We present Late Pleistocene apparent uplift rates for the Mejillones Peninsula, in the northern Chile subduction zone. Our estimates are made from a flight of marine abrasion terraces dated with cosmogenic ^{10}Be; we determine a fast and slightly variable uplift rate during the last ca. 500 ka, which ranges between ca. 0.47 and ca. 0.58 m/ka. These values are markedly higher than surrounding coastal areas. Terrace configuration and Late Pleistocene uplift history is controlled by sea level changes, coastal uplift due to the megathrust earthquake cycle and normal faulting. We highlight the importance of the normal Mejillones Fault, which we interpret as the direct responsible for promoting rapid uplift in this zone of the Nazca-South America convergent margin.*

Keywords*: Northern Chile, Marine abrasion terraces, 10Be dating, coastal uplift, normal faulting*

INTRODUCTION

The northern Chile subduction zone (18°S-24°S) is characterized by the convergence between the Nazca and South America plates. There, the convergence-induced deformation is significantly balanced among the stages of the subduction cycle; two linked consequences of this cycle are the occurrence of megathrust earthquakes and coastal uplift. In this context, the Mejillones Peninsula (23.5°S, MP, Fig. 1a) occurs as an anvil-shaped promontory disrupting the N-S coast-line. This peninsula has been proposed as a long-term barrier for the propagation of subduction earthquakes (Victor et al. 2011); further, it experiences higher uplift rates than surrounding areas (Casanova et al., 2006; Victor et al., 2011, Binnie et al., 2016). Its first-order morphological configuration is represented by a horst-halfgraben geometry conducted by N-S normal faults (Fig. 1b). Marine abrasion terraces atop of the horst (Fig. 1b-c, 2a-d) and shoreline ridges atop of the halfgraben (Fig. 1b-c, 2a-d) attest for the interaction between Late Pleistocene sea level changes, coastal uplift and normal faulting. In the northern MP, atop of the Morro Mejillones Horst (MMH), an outstanding flight of marine abrasion terraces occurs (Fig 1c). In previous studies, these terraces have been mapped and dated to quantify rates of coastal uplift (Marquardt, 2005, Casanova et al., 2006, Cortés, 2012, Binnie et al., 2016). However, these studies, mainly because of methodological limitations, have not accurately considered the maximum inundation level (shoreline angle) linked to the construction of each abrasion terrace. This is a critical issue when considering the classical approaches to calculate uplift rates.

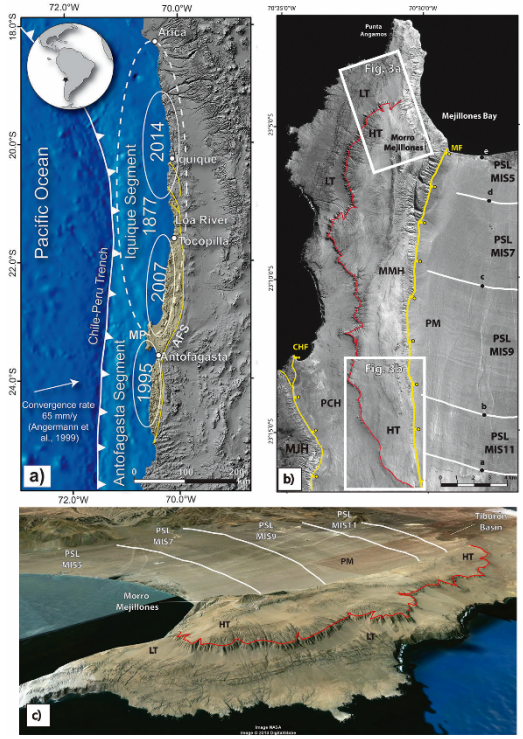

Figure 11: a) Location of the Mejillones Peninsula MP in the seismotectonic setting of northern Chile. Ellipses are megathrust earthquake ruptures. b) Map view of the main morphostructural units in the northern MP. MF and CHF are Mejillones and Caleta Herradura faults, respectively. PCH and PM are Caleta Herradura and Mejillones halfgraben, respectively. MMH and MJH are Morro Mejillones and Morro Jorgino horst, respectively. HT and LT are Higher and Lower terraces, respectively. c) Inclined view of Higher (HT) and Lower (LT) in the Morro Mejillones Horst (MMH).

Further, previous numerical ages obtained for these terraces, mainly by TCN's (^{10}Be) measurements, have never discussed the possible influence of erosion in age calculations. In this contribution, we present the results of a study that addresses the aforementioned issues to unravel the neotectonic significance of the terraces atop of the MMH in the northern MP. First, we employ a Pleaides DEM (1.5 m of spatial resolution) to generate a semi-automatic (field controlled) surface map of the terraces at the northern MP (Fig. 3a-b). This map shows the distribution of all the surfaces with slopes lesser than 15° according to their elevation above the sea level. This map was useful to identify marine terraces but not for accurately determining the elevation of their shoreline angles. For identifying the shoreline angle elevations, we have used the same high resolution DEM to perform and process swaths profiles (Fig. 4a-b) with the TerraceM software (Jara-Muñoz et al., 2015). In addition, we provide new cosmogenic ^{10}Be measurements, obtained both in surface and along one vertical profile, to suggest a terrace chronology. In depth concentrations were modelled according to the Hidy's method (Hidy et al., 2010) to obtain the best (the less xchi value result) minimum age/minimum erosion rate and the best (the less xchi value result) maximum age/maximum erosion results. Finally, we calculate apparent uplift rates for the MMH and discuss their significance in terms of the eustatic and neotectonic processes operating in the area.

Terrace distribution. The MMH presents two major groups of marine abrasion platforms that are referred as higher (HT) and lower (LT) terraces (Fig. 1b-c, 2a-d, 3a-b). They are separated by a hectometre-scale marine paleocliff (Fig 1b-c, 2a). Combining our surface map and analysis of swath profiles using TerraceM software (Jara-Muñoz et al., 2015), we have determined:

-The HT (Fig. 3a-b) define a ca. 2 km width degraded surface with subtle vestiges of at least four terraces both at the northern and southern MMH (Fig. 3a-b). They have been named, from older to younger, T1 to T4. Their shoreline angles are depicted in Fig. 4a-b.

- The LT (Fig 3a) correspond to at least five levels that have been named, from older to younger, T6 to T10. T6 is a 5 km width degraded surface, preserved only at the northern MMH (Fig. 3a). Terraces T7 to T10 are all narrower than 300 m and are disposed in a staircase pattern at the northern MMH (Fig. 3a). The shoreline angles of terraces T6 to T10 are depicted in Fig. 4a.

Terrace ages

- HT ages. Samples for ^{10}Be analysis have been collected from HT both at the northern (three samples of quartz-rich bedrock) and southern MMH (five amalgamated samples of quartz clasts; Fig. 2b, d). The resulting ages are very different among them and much younger than any marine terraces located at similar elevations everywhere along the northern Chile-southern Peru Coastal Forearc. Further, marine deposits over which T2 has been constructed preserve rests of Pliocene TAMAs fauna (*Glycymeris ovatus and Trachycardium*); these molluscs has been dated in 1.1 to 1.6 Ma at the southern MP (Victor et al., 2011). We thus consider that ^{10}Be measurements from HT are strongly affected by erosion and hence not useful to perform age calculations. Alternatively, ^{10}Be results were employed to calculate a mean erosion rate of 2.64±0.13 m/Myr with the Cronus Earth online calculator.

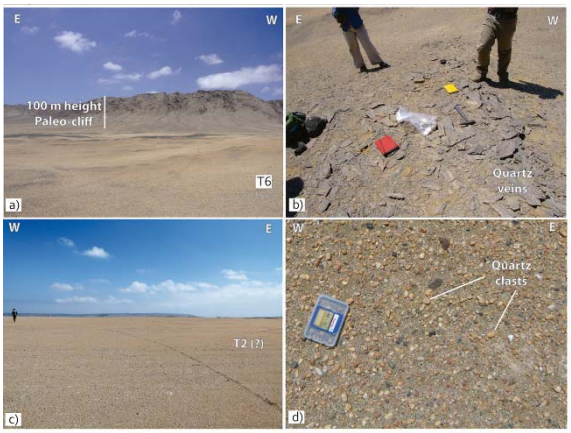

Figure 2: a) View of T6 limited to its inner part by the 100 m height paleo-cliff. b) T6 sample site in bedrock. c) View of the HT at the southern MMH. d) Sample site (amalgamated samples) at the southern MMH.

- LT ages. Surficial and vertical profile samples were collected. Three surface samples of quartz-rich bedrock were collected from T6 at the northern MMH (Fig. 2a-b); for terraces T8 to T10, one quartz-rich bedrock sample per level was collected. In addition, three vertical profiles were performed in the northern MMH. Samples of these profiles were employed to independently obtain a maximum admissible erosion rate for surficial ^{10}Be concentrations. The best (xchi value 13) inversion for depth concentrations was obtained in sample H3 (Fig 3a); this results in a maximum erosion rate of 2 m/Myr. In this way, we bracket the age of the LT taking into account null erosion (minimum age) and a maximum erosion (maximum age). Age calculations were performed with the Cronus Earth online calculator.

For T6, surficial 0 erosion ages vary between 329±31 ka and 398±38 ka. When considering the maximum erosion rate ages range between 441±94 ka and 743±324 ka.

For T7, no ages are available.

For T8, a surficial 0 erosion age of 325±25 ka was determined. Considering the maximum erosion rate for LT, the age of T8 is 424±90 ka.

For T9, a surficial 0 erosion age of 405±41 ka was obtained. With the maximum erosion rate for LT, the age for T9 is 779±397 ka. Since samples come from bedrock, inheritance does not explain such an old age.

For T10, a surficial 0 erosion age of 254±25 ka was obtained. With the maximum erosion rate for LT, the obtained age for T10 is 273±42 ka.

DISCUSSION

Our ^{10}Be dating strategy allowed us to propose a new terrace chronology considering both null and maximum erosion rates. We have demonstrated that an erosion rate of ca. 2 m/Ma considerably affects terrace age determination and MIS assignations. We highlight that formerly published ^{10}Be ages considering 0 erosion rates (e.g. Binnie et al., 2016) may have resulted, at least in some cases, in underestimated ages and thus in overestimated uplift rates.

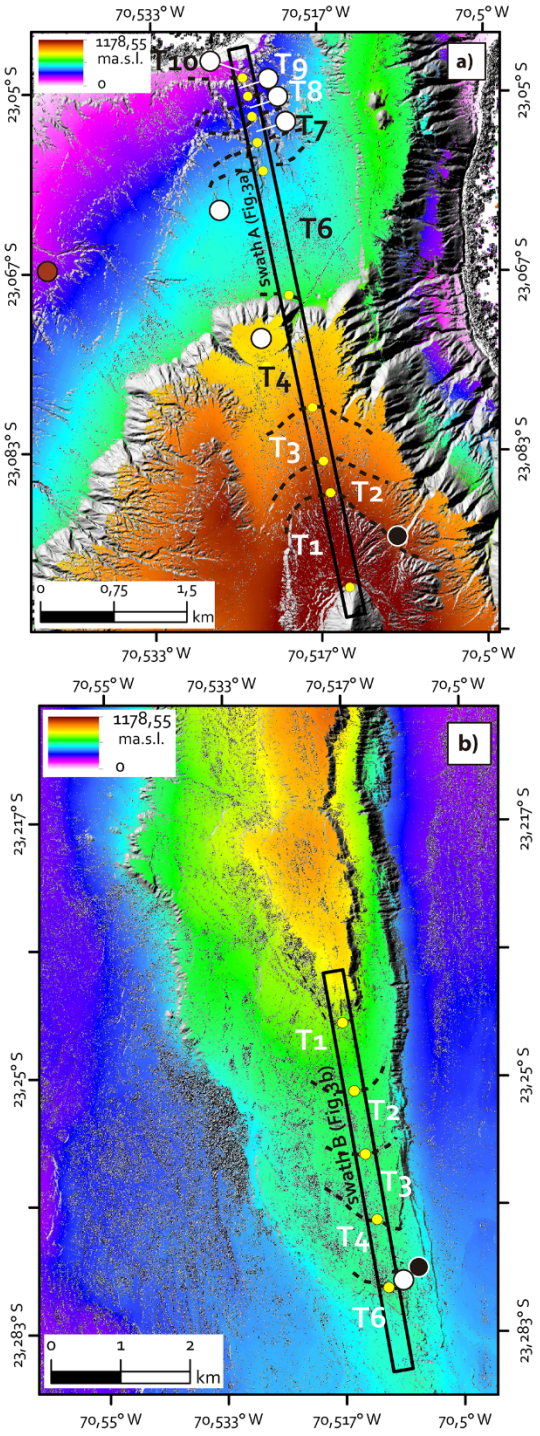

Figure 3: Surface maps referred in text a) northern MMH. b) southern MMH. b) northern MJH. Yellow circles are shoreline angles determined from swath profiles (black rectangles) using TerraceM software. Black and white circles are TAMA and 10Be samples sites, respectively. Red circle is the site where vertical sample H3 was collected.

The main parameters defined in this contribution are synthetized in Table 1. Despite the significant uncertainties in the age determinations, we interpret that **T6** was likely formed between ca. 441 ka and ca. 743 ka. Given its width (around 1.5 km) and position in the terrace flight, we infer that **T6** is a polygenetic surface formed before MIS-13 (487±15 ka, after Siddall et al., 2006), during MIS-15 (589±30 ka, after Siddall et al., 2006) and older highstands. Binnie et al. (2016) assign this terrace to MIS-13 based on their 0 erosion age of ca. 486 ka. **T7**, because its position in the flight, is assigned to MIS-13 highstand (487±15 ka, after Siddall et al., 2006). This terrace was not identified by Binnie et al. (2016). For **T8**, based on the calculated ages, we suggest that it was built during the MIS-11 highstand (405±10 ka, after Siddall et al., 2006). Binnie et al. (2016) assign this terrace to MIS-11a(?).**T9**, according to its position in the terrace flight, is assigned to MIS-9c highstand (321±6 ka, after Siddall et al., 2006). This is in agreement with the interpretations of Binnie et al. (2016). Finally, **T10** is interpreted as built during MIS-9a highstand (310±6 ka, after Siddall et al., 2006). This is in agreement with the interpretations of Binnie et al. (2016).

With our data, we cannot calculate reliable uplift rates from HT; Marquardt (2005), from an ash layer occurring at around 600 ma.s.l. on the MMH, calculated a long term uplift rate of 0.11±0.01 m/ka from these terraces. However, if the TAMAs fauna reported herein for the HT is more representative of their age, a faster uplift rate may be estimated for the last 1.5 Ma. Conversely, we have calculated uplift rates for the northern from LT. **From T6**, if we assume that it was formed at least during MIS-15, we can estimate an uplift rate of 0.51±0.03 m/ka. **From T7, T8, T9 and T10**, we obtained uplift rates of 0.47±0.01 m/ka, 0.52±0.01 m/ka, 0.58±0.01 m/ka, and 0.53±0.01 m/ka, respectively. From our calculations, we suggest that a slightly variable ca. 0.47 m/ka to ca. 0.58 m/ka uplift rate has occurred at the northern Mejillones Peninsula since at least the MIS-15 highstand; these rates are faster than surrounding regions in northern Chile. The marked staircased pattern of the LT in the northern MMH is in agreement with this rapid uplift rate. Previously, following the construction of the HT at ca. 1.5-1.03 Ma, uplift rate must have been considerably slower; this is reflected in the construction of the 100 m height paleocliff at the northern MMH.

Marine terrace distribution and the calculated uplift rates reflects a complex interaction between sea level variations, coastal uplift and normal faulting. As interpreted in previous studies (e.g. Binnie et al., 2016), rapid uplift may be related to both a higher recurrence of subduction earthquakes and/or normal faulting. The eastern border of the MMH is given by the Mejillones Fault. The Mejillones Fault has produced a Pliocene cumulative scarp of 400 m at its northern tip that progressively diminishes in height towards its southern tip; its post-35 ka scarp follows a similar trend (Cortés et al., 2012). Interestingly, the general topography of the MMH is tilted to the south and to the west; in particular, at the northern MMH, it is evident that the shoreline angle elevations of the LT diminish towards west. This tilting is consistent with the geometry and kinematics of the Mejillones Fault. Even considering that the activity of the Mejillones and other normal faults in the Coastal Forearc may be directly controlled by megathrust earthquakes, we suggest a direct control of the Mejillones Fault in the Late Pleistocene uplift history of the Morro Mejillones Horst (MMH). Ongoing work is focused in mapping and dating marine terraces atop of the Morro Jorgino Horst; this horst is limited to the east by the Caleta Herradura Fault. This fault, although more segmented than the Mejillones Fault, has constructed a geometrical-similar scarp. If the first-order control exerted by the CHF on the Late Pleistocene uplift of the CHH is proved, normal faulting would be the first-order control in explaining rapid coastal uplift rates and its variations throw time.

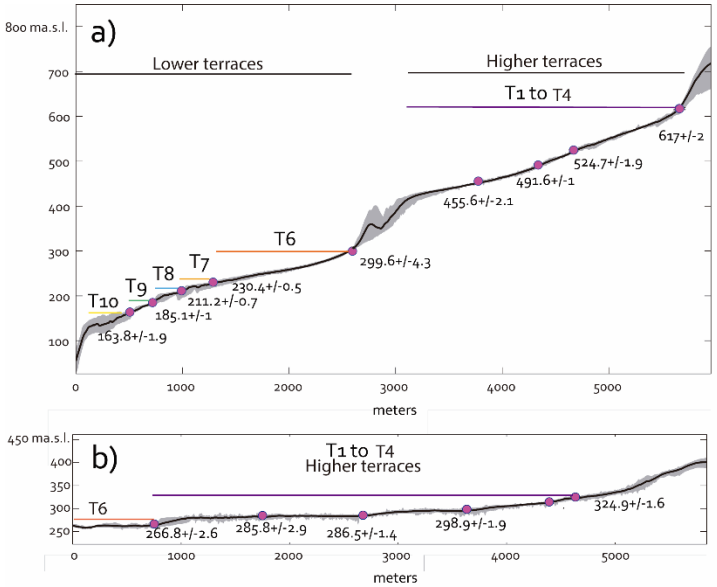

Figure 4: Swath profiles and shoreline angles from TerraceM software. Purple circles are shoreline angles for each terrace (T1 to T10) determined with TerraceM software. In each profile, black lines are the mean topography. The surrounding grey area limits the maximum and minimum topography. a) Swath A (Fig 3a) b)Swath B (Fig3b).

Terrace	Terrace group	SA (ma.s.l.)	Age	MIS	Uplift rate (m/ka)
T1	Higher	617+/-2 (N); 324,9+/-1.6 (S)	Pliocene	?	-
T2	Higher	524+/-1.9 (N); 298,9+/-1.9 (S)	Pliocene	?	-
T3	Higher	491.6+/1 (N); 286,5+/-1.4 (S)	Pliocene	?	-
T4	Higher	455.6+/-2.1 (N); 285,8+/-2.9 (S)	Pliocene	?	-
T6	Lower	299.6+/-4.3 (N); 266.8+/-2.6 (S)	ca. 441-743 ka	15 (589+/-30 ka) and older	0.51+/-0.03
T7	Lower	211.2+/-0.7	-	13 (487+/-15 ka)	0.47+/-0.01
T8	Lower	224.7+/-0.3	ca. 325-424 ka	11 (405+/-10)	0.52+/-0.01
T9	Lower	185.1+/-1	ca.405-779 ka	9c (321+/-6 ka)	0.58+/-0.01
T10	Lower	163.8+/-1.9	ca. 254-273 ka	9a (310+/-6 ka)	0.53+/-0.01

Table 1. Synthesis of the terrace parameters. SA are the shorelines angle elevations determined for terraces at the northern (N) and southern (S) Morro Mejillones Horst with TerraceM. The provided numerical ages come from 10Be analysis and were calculated both for 0 erosion and maximum erosion rates.

REFERENCES

Binnie, A., Dunai, T., Binnie, S., Victor, P., González, G., & Bolten, A., 2016. Accelerated late quaternary uplift revealed by 10Be exposure dating of marine terraces, Mejillones Peninsula, northern Chile. *Quaternary Geochronology* 36, 12-27.

Casanova, C., Pinter, N., & Radtke, U., 2006. New elevation data and ages from late-Neogene coastal terrace sequences in Mejillones peninsula northern Chile: Reconstructing the morphotectonic evolution along a segment of the Nazca subduction Zone. *Geophys. Res. Abstr.* 8, 09951.

Cortés, J., 2013. Activité des failles de la plaque supérieure dans l'avant-arc côtier du nord du Chili (~23°30'S): Paléosismologie, implications néotectoniques et relation avec le cycle de subduction, Ph. D. Thesis, Université Toulouse 3 Paul Sabatier, Toulouse, France.

Cortés, A.J., González, L.G., Binnie, S., Robinson, R., Freeman, S.P.H.T., & Vargas, E.G., 2012. Paleoseismology of the mejillones fault, northern Chile: Insights from cosmogenic 10Be and optically stimulated luminescence determinations. *Tectonics* 31, 1-21, doi: 10.1029/2011TC002877.

Hidy, A.J., Gosse, J.C., Pederson, J.L., Mattern, J.P., & Finkel, R.C., 2010. A geologically constrained Monte Carlo approach to modeling exposure ages from profiles of cosmogenic nuclides: An example from Lees Ferry, Arizona. *Geochemistry, Geophysics, Geosystems* 11 (9).

Jara-Muñoz, J., Melnick, D., & Strecker, M., 2016. "TerraceM: A MATLAB® tool to analyze marine and lacustrine terraces using high-resolution topography. *Geosphere* 12 (1), 176-195.

Marquardt, C., 2005. Deformationes néogènes le long de la cote nord du Chile (23°-27°S). Univ. Paul Sabatier, Toulouse.

Siddall, M., Chappell, J., & Potter, E.-K., 2006. Eustatic Sea Level During Past Interglacials. In: *The Climate of Past Interglacials* (Sirocko, F., Litt, T., Claussen, M., Sanchez-Goni, M.-F., Eds), Elsevier, Amsterdam, pp. 75-92.

Victor, P., Sobiesiak, M., Glodny, J., Nielsen, S.N., & Oncken, O., 2011. Long-term persistence of subduction earthquake segment boundaries: evidence from Mejillones Peninsula, northern Chile. *Journal of Geophysical Research: Solid Earth* 116 (B2).

INQUA Focus Group Earthquake Geology and Seismic Hazards

paleoseismicity.org

Finding Maymyo 1912: the search of a Nineteenth Century earthquake along and around the Kyaukkyan Fault, Myanmar

Crosetto, Silvia (1), Watkinson, M. Ian (1), Falcucci, Emanuela (2), Gori, Stefano (2), Min, Soe (3)

(1) Royal Holloway University of London, Egham, UK, silvia.crosetto.2013@live.rhul.ac.uk
(2) Istituto Nazionale di Geofisica e Vulcanologia, Rome, Italy
(3) Department of Geology, Taungoo University, Bago Division, Myanmar

Abstract: *In May 1912 a magnitude 7-8 earthquake focused near Maymyo (Pyin Oo Lwin) struck the Northern Shan State, eastern Myanmar. Contemporary evaluation of damage distribution led to a correlation between the earthquake and the topographically prominent Kyaukkyan Fault near the western margin of the Shan Plateau. Paleoseismic investigations in the epicentral area revealed evidence of a fault rupture younger than 1270 ± 30 BP. The presence of pottery and charcoal in the younger faulted stratigraphy demonstrates Kyaukkyan Fault activity within human times with a possible correlation to the 1912 Maymyo earthquake, although uncertainty about the causative fault of that earthquake still remains. We here evaluate the reliability of the historic information that led to the attribution of the Maymyo earthquake to the Kyaukkyan Fault, compare it with a similar case-study, and discuss possible alternative scenarios by considering other faults in the area surrounding the reported epicentre of the 1912 event.*

Keywords*: strike-slip, paleoseismology, active tectonics, Shan Plateau, causative fault*

INTRODUCTION

The Kyaukkyan Fault is a N-S-trending, ~500 km long strike-slip fault that traverses the western Shan Plateau, an elevated region averaging >1 km straddling eastern Myanmar and part of northern Thailand (**Σφάλμα! Το αρχείο προέλευσης της αναφοράς δεν βρέθηκε.**). The Kyaukkyan Fault, together with the Shan Scarp fault system and other N-S-trending faults of the western Shan Plateau, is part of a 250 km wide system of splays at the north-western end of the Mae Ping fault in NW Thailand (e.g. Morley, 2004). The fault is widely considered to have been the origin of a large earthquake that hit northern Myanmar on the 23rd May 1912, known as the Maymyo (currently Pyin Oo Lwin) earthquake. The earthquake was initially estimated at magnitude 8 (Gutenberg & Richter, 1954), and more recently revised to Ms 7.7 to 7.6 (e.g. Abe & Noguchi, 1983; Pacheco & Sykes, 1992). Either way, it remains the strongest known earthquake in Myanmar. The Kyaukkyan Fault is considered to be the origin of the Maymyo earthquake because of the distribution of isoseismals mapped soon after the seismic event, and because of its prominent topographic expression (Coggin Brown, 1917).

TECTONIC SETTING

The modern setting of this region is the result of the tectonic evolution of SE Asia, ultimately driven by the northward movement of India toward Eurasia, whose accommodation caused extensive internal deformation within the Eurasian margins (e.g. Tapponnier et al., 1982; Morley, 2009).

The broad strike-slip fault network in Thailand and Myanmar is characterised by right-lateral, N-S-trending faults, and left-lateral, E-W-trending faults that underwent shear reversal in the latest Paleogene (e.g. Holt et al., 1991; Lacassin et al., 1998; Socquet & Pubellier, 2005), before deformation became localised along the Sagaing Fault after about 22-16 Ma (e.g. Searle et al., 2007).

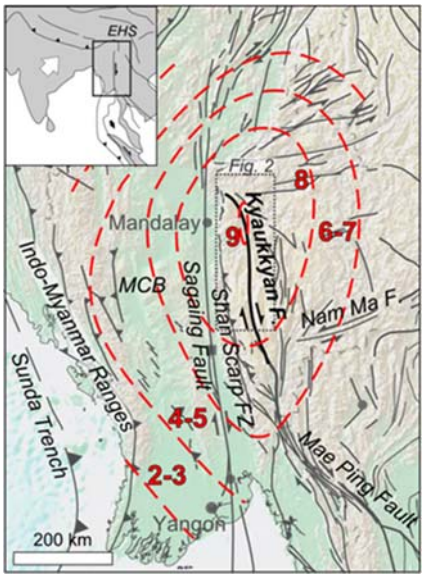

Figure 12: Schematic tectonic map of Myanmar showing the isoseismal distribution related to 1912 Maymyo (Pyin Oo Lwin) earthquake as reported by Coggin Brown (1917). EHS: Easter Himalayan Syntaxis.

Currently, the relative motion between India and Sundaland, the stable SE Asia promontory, is 35-36 mm/yr. Inboard of the Sunda Trench, partitioned strike-slip motion is dominated by the Sagaing Fault, which accommodates 18-20 mm/yr (Vigny et al., 2003); the remainder may be distributed in the Indo-Myanmar Ranges (Gahalaut & Gahalaut, 2007; Rangin et al., 2013) and possibly further east in Myanmar. NE-SW- to E-W-trending left-lateral faults of eastern Myanmar and northern Thailand accommodate the differential motion between Sundaland and China, expressed by GPS vectors' rotation around the Eastern Himalayan syntaxis (e.g. Shen et al., 2005; Rangin et al., 2013). The Quaternary activity of the Kyaukkyan Fault has been recently documented (Crosetto et al., 2018). Fault activity in historic times is testified by the Pawritha city wall, which straddles the fault north of Inle Lake (**Σφάλμα! Το αρχείο προέλευσης της αναφοράς δεν βρέθηκε.**) and is apparently offset to the right by 12.2 ± 1.8 m (Soe Min et al., 2017); by the smooth bend of the Mandalay-Lashio railway where it crosses the fault at Kyaukkyan village (Coggin Brown, 1917); and by records of historic and instrumental-era seismicity (Crosetto et al., in prep).

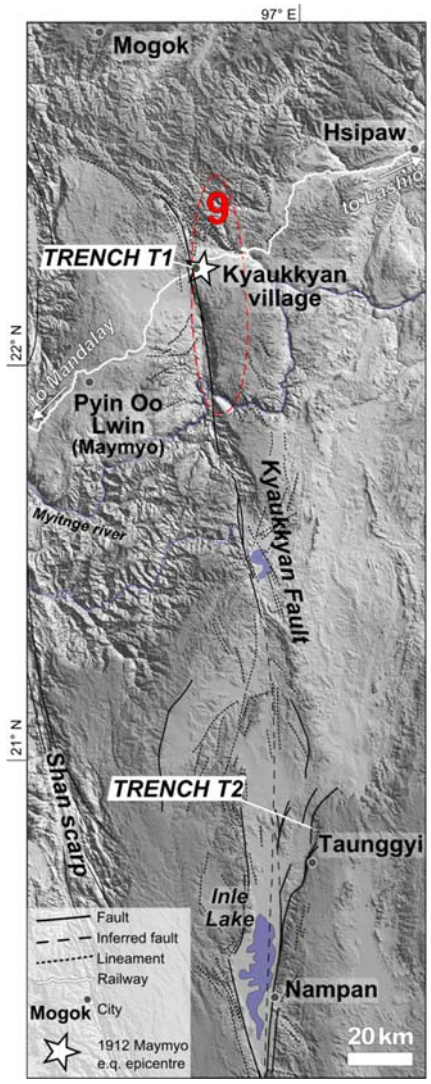

Figure 13: Tectonic setting of the northern part of the Kyaukkyan Fault with a greyscale shaded Shuttle Radar Topography (SRTM) 90 m base DEM.

METHODS

Extensive mapping of Quaternary geomorphic features, and remote sensing observations and analysis led to the identification of potential paleoseismic trenching sites.
AMS ^{14}C radiocarbon dating of charcoals provided absolute age control on the stratigraphy of trench T1, at Kyaukkyan village. BetaCal3.21 and the INTCAL13 curve (Reimer et al., 2013) were used for AMS ^{14}C ages calibration.

RESULTS & DISCUSSION

A total of five trenches were dug, although only two of them intercepted features we interpreted to be surface ruptures.

Trench T1, located at Kyaukkyan village, was dug perpendicular to the N-S-trending lineament crossing the railway bend reported by Coggin Brown (1917), allegedly considered as epicentre of the 1912 earthquake. The trench exposed a succession of alternating clay and calcrete layers cross-cut by four main N-S-trending faults (Figure 14). Two rupturing events were identified based on the relation between the stratigraphic succession and their deformation, and constrained by radiocarbon ages: Event 1, associated to the activity of faults *F1* and *F2* and constrained between 1270 ± 30 BP to 4660 ± 30 BP, and Event 2, associated to the activity of faults *F3* and *F4* and younger than 1270 ± 30 BP. This younger event may correspond to the 1912 earthquake, but may also be related to an older event.

Trench T2, located north of Taunggyi, was dug across a subtle N-S-trending scarp that separates a terrace capped by a red clay formation *terra rossa* from the basin-filling sediments. The scarp was interpreted as the expression of a fault synthetic to the basin-bounding fault in the shallow subsurface (Crosetto et al., 2018).

The clay succession exposed in the trench was deformed along discrete planes interpreted as the result of activity along N-S-trending faults. Despite the lack of datable material within the trench, the observed deformation immediately below the agricultural layer is evidence of recent activity along the fault and far from the main basin-bounding fault of Inle Lake basin. We cannot exclude that this deformation is related to the 1912 earthquake.

Review of the historical information
The contemporary report of Coggin Brown remains the first and most important line of evidence for attributing the 1912 Maymyo earthquake to the Kyaukkyan Fault. Without it, it is unlikely that modern studies (e.g. Wang et al., 2014; Soe Min et al., 2017) would have focused on the Kyaukkyan fault, and would perhaps have linked the 1912 event to the Sagaing Fault instead.

Coggin Brown (1917) reported that buildings in the town of Pyin Oo Lwin (Maymyo) were not as severely damaged as in cities lying close to the Sagaing Fault. These cities were not included in a higher intensity isoseismal due to the possibility of ground-shaking amplification caused by the alluvium underlying them, and because of the condition of the cities' old buildings, which he considered

to be more prone to damage than the newer ones in Pyin Oo Lwin. The landscape, on the contrary, appeared to have experienced the most severe damage in the area around Kyaukkyan village, although the very low population density of the area has to be acknowledged when accounting for such data.
Furthermore, geometric and estimated delineation of isoseismal 9 (maximum intensity) was based on sparse observations and hence biased by the interpretation that the Kyaukkyan Fault was the source, as conceded by Coggin Brown himself.

It also has to be taken into account that intensity estimation for historical earthquakes suffers from reporting and sampling biases that can lead to an overestimation of up to two intensity units (Hough, 2013).

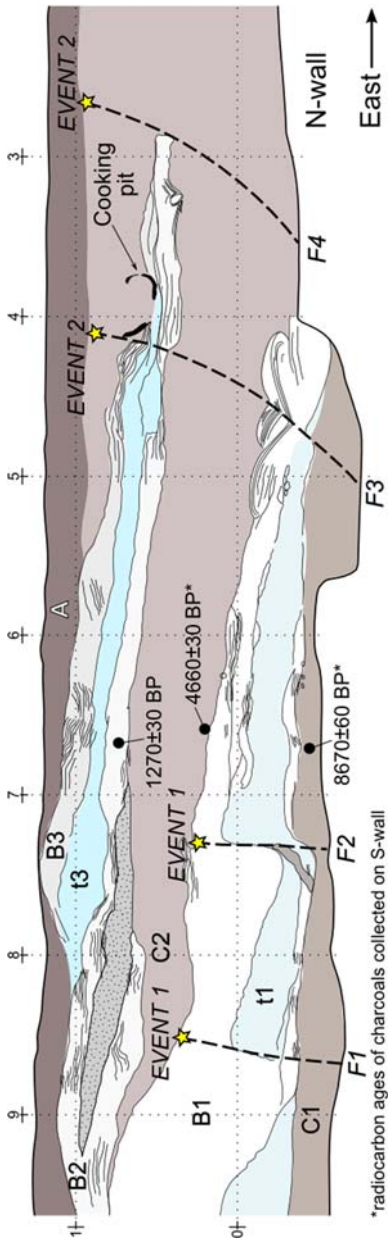

Figure 14: Interpretative log of the northern wall of trench T1, at Kyaukkyan village. Black dots locate the position of the charcoals collected for radiocarbon dating. Dotted lines indicate the position of the 1x1 m grid; dashed lines indicate fault (F1, F2, F3, F4) positions; stars indicate tip points of faulting events. Lithologic units: A, agriculture layer; B3, platy calcrete; t3, chalky-nodular transition layer; B2, platy calcrete; C2, upper clay; B1, chalky calcrete; t1, transition layer; C1, lower clay.

Alternative faults
Given the uncertainty associated with attributing the rupture identified in the trenches to the 1912 earthquake, it is necessary to consider alternative scenarios for that seismic event, including a non-Kyaukkyan Fault source. These are listed below.

1) The **Sagaing Fault** lies at a linear distance of 40 km west of Pyin Oo Lwin (Figure 15). The Sagaing segment of the fault, passing through Mandalay district, has generated numerous earthquakes larger than magnitude 7 (e.g. Engdahl & Villaseñor, 2002), suggesting that a Mw 7.6-7.7 earthquake like the 1912 Maymyo event along this fault would not be unusual.

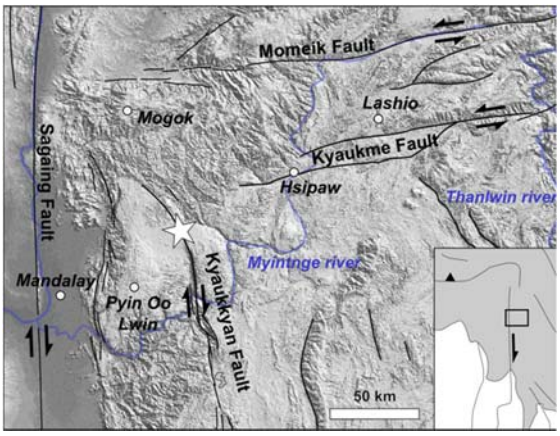

Figure 15: Schematic fault map of the area surrounding the inferred epicentre of the 1912 Maymyo earthquake (white star).

2) The left-lateral, E-W-trending **Kyaukme Fault** (western strand of the Lashio Fault) is situated 20 km north-east of Kyaukkyan village, the inferred 1912 epicentre. Although the Kyaukme Fault does not account for major instrumental seismicity, the town of Hsipaw experienced serious damage to the railway medical store and other buildings in 1912 (Coggin Brown, 1917).

3) About 70 km north of Kyaukkyan village, the **Momeik** (Nantinghe in China) **Fault** is a prominent E-W-trending, left-lateral fault extending for at least 400 km from the Sagaing Fault, to the west, almost to the Red River Fault zone, to the east. The recent activity of the Momeik Fault has been demonstrated (Sun et al., 2017) and a M≈7 event in 1941 in the central part, and moderate (4<M<5) instrumental seismicity in its westernmost part makes it a potential candidate as alternative source of the 1912 earthquake.

A similar case: Chilik earthquake
The Ms 8.3 Chilik earthquake occurred in 1889 in the Tien-Shan region of Kazakhstan, and is an example of historical earthquakes with dubious causative fault attribution. The main tool of investigation of the earthquake was a questionnaire about the damage and subjective description of the seismic shock, sent to the local population two months after the earthquake. The outcome of the questionnaire was then used to build a map of the isoseismals (Rossi-Forel scale) where the peak isoseismal of X was geometrically determined as the centre of maximum intensity (Mushketov, 1891; Krüger et al.,

2017). This also defined Chilik city as the epicentre of the earthquake. Of the many faults identified in the epicentral area, Abdrakhmatov et al. (2016) proposed the Saty Fault as causative fault of Chilik earthquake, although a direct relation between the fault and the earthquake has yet to be confirmed.

This controversy is analogous to the 1912 Maymyo earthquake concerning: absence of reported fault rupture, approximation of isoseismals, unknown 'true' magnitude, sparse human development used as control points in generating an isoseismal map, and the presence of alternative potential causative faults in the area of the historical earthquake.

CONCLUSIONS

- It is clear that a large earthquake occurred in central Myanmar on May 23rd 1912.
- A Kyaukkyan Fault source is broadly consistent with contemporary damage reports, but paleoseismological evidence is only just coming to light.
- There is evidence for recent surface rupturing events along the mapped trace of the Kyaukkyan Fault, including one dated to ≤ 1270 ± 30 BP.
- If the Kyaukkyan Fault did cause the 1912 earthquake, a historical overestimation of the magnitude assigned could explain the lack of geomorphic rupture features (e.g. Wang et al., 2011; Crosetto et al., 2018, In prep.).
- An alternative scenario, whereby a nearby fault caused the 1912 earthquake cannot be excluded; further investigations along the Kyaukkyan Fault as well as objective consideration of alternative seismic sources might lead, as for the Chilik earthquake, to a more reliable attribution of the 1912 Maymyo event.

Acknowledgements: This project was funded by the RHUL Reid scholarship, and by other smaller grants of Royal Holloway University of London and the SE Asia Research Group. We are grateful to Dr Myo Thant, Dr Lin Thu and the Myanmar Earthquake Committee for their critical support in organising field campaigns.

REFERENCES

Abdrakhmatov, K.E., Walker, R.T., Campbell, G.E., Carr, A.S., Elliott, A., Hillemann, C., Hollingsworth, J., Landgraf, A., Mackenzie, D., & Mukambayev, A., 2016. Multisegment rupture in the 11 July 1889 Chilik earthquake (Mw 8.0-8.3), Kazakh Tien Shan, interpreted from remote sensing, field survey, and paleoseismic trenching. *J. Geophys. Res. Solid Earth* 121, 4615-4640.

Abe, K., & Noguchi, S.I., 1983. Revision of magnitudes of large shallow earthquakes, 1897-1912. *Phys. Earth Planet. Inter*. 33, 1-11.

Coggin Brown, J., 1917. The Burma Earthquake of May 1912. *Mem. Geol. Surv. India* 42, 1-147.

Crosetto, S., Watkinson, I.M., Soe Min, Gori, S., Falcucci, E., & Nwai Le Ngal, 2018. Evidence of Quaternary and recent activity along the Kyaukkyan Fault, Myanmar. *J. Asian Earth Sci*. 156, 207-225.

Engdahl, E.R., Villaseñor, A., 2002. Global Seismicity: 1900-1999, In: *International Handbook of Earthquake and Engineering Seismology* (W.H.K., Lee et al., eds),. Boston, Mass., pp. 665-690.

Gahalaut, V.K., & Gahalaut, K., 2007. Burma plate motion. *J. Geophys. Res. Solid Earth* 112.

Gutenberg, B., & Richter, C.F., 1954. *Seismicity of the Earth and Associated Phenomena*, 2nd ed. Princeton University Press, Princeton, N.J., USA.

Holt, W.E., Ni, J.F., Wallace, T.C., & Haines, A.J., 1991. The active tectonics of the Eastern Himalayan Syntaxis and surrounding regions. *J. Geophys. Res*. 96, 14595-14632.

Hough, S.E., 2013. Spatial Variability of "Did You Feel It?" Intensity Data: Insights into Sampling Biases in Historical Earthquake Intensity Distributions. *Bull. Seismol. Soc. Am*. 103, 2767-2781.

Krüger, F., Kulikova, G., & Landgraf, A., 2017. Instrumental magnitude constraints for the 11 July 1889, Chilik earthquake. In: *Seismicity, Fault Rupture and Earthquake Hazards in Slowly Deforming Regions* (Landgraf, A., Kübler, S., Hintersberger, E., Stein, S., eds),. Geological Society, London, Special Publications, pp. 41-72.

Lacassin, R., Replumaz, A., & Leloup, P.H., 1998. Hairpin river loops and slip-sense inversion' on southeast Asian strike-slip faults. *Geology* 26, 703-706.

Morley, C.K., 2009. Evolution from an oblique subduction back-arc mobile belt to a highly oblique collisional margin: the Cenozoic tectonic development of Thailand and eastern Myanmar. *Geol. Soc. London, Spec. Publ.* 318, 373-403.

Morley, C.K., 2004. Nested strike-slip duplexes, and other evidence for Late Cretaceous-Palaeogene transpressional tectonics before and during India-Eurasia collision, in Thailand, Myanmar and Malaysia. *J. Geol. Soc. London* 161, 799-812.

Mushketov, I.V, 1891. *Materials for investigation of earthquakes in Russia*. Annex to 27th Vol. tidings Imp. Russ. Geogr. Soc.

Pacheco, J.F., & Sykes, L.R., 1992. Seismic moment catalogue of large shallow earthquakes, 1900 to 1989. *Bull. Seismol. Soc. Am*. 82, 1306-1349.

Rangin, C., Maurin, T., & Masson, F., 2013. Combined effects of Eurasia/Sunda oblique convergence and East-Tibetan crustal flow on the active tectonics of Burma. *J. Asian Earth Sci.* 76, 185-194.

Reimer, P.J., Bard, E., Bayliss, A., Beck, J.W., Blackwell, P.G., Ramsey, C.B., Buck, C.E., Cheng, H., Edwards, R.L., & Friedrich, M., 2013. IntCal13 and Marine13 radiocarbon age calibration curves 0–50,000 years cal BP. *Radiocarbon* 55, 1869-1887.

Searle, M.P., Noble, S.R., Cottle, J.M., Waters, D.J., Mitchell, A.H.G., Hlaing, T., & Horstwood, M.S., 2007. Tectonic evolution of the Mogok metamorphic belt, Burma (Myanmar) constrained by U-Th-Pb dating of metamorphic and magmatic rocks. *Tectonics* 26.

Shen, Z.K., Lü, J., Wang, M., & Bürgmann, R., 2005. Contemporary crustal deformation around the southeast borderland of the Tibetan Plateau. *J. Geophys. Res. Solid Earth* 110, 1-17.

Socquet, A., & Pubellier, M., 2005. Cenozoic deformation in western Yunnan (China-Myanmar border). *J. Asian Earth Sci.* 24, 495-515.

Soe Min, Watkinson, I.M., Soe Thura Tun, & Win Naing, 2017. The Kyaukkyan Fault. In: Geological Society (Ed.), Myanmar: Geology, Resources and Tectonics. London.

Sun, H., He, H., Wei, Z., Shi, F., & Gao, W., 2017. Late Quaternary paleoearthquakes along the northern segment of the Nantinghe fault on the southeastern margin of the Tibetan Plateau. *J. Asian Earth Sci*. 138, 258-271.

Tapponnier, P., Peltzer, G., Le Dain, A.Y., Armijo, R., & Cobbold, P.R., 1982. Propagating extrusion tectonics in Asia: New insights from simple experiments with plasticine. *Geology* 10, 611-616.

Vigny, C., Socquet, A., Rangin, C., Chamot-Rooke, N., Pubellier, M., Bouin, M., Bertrand, G., & Becker, M., 2003. Present-day crustal deformation around Sagaing fault, Myanmar. *J. Geophys. Res. Solid Earth* 108.

Wang, Y., Sieh, K., Soe Thura Tun, Kuang Yin Lai, & Than, Myint, 2014. Active tectonics and earthquake potential of the Myanmar region. *J. Geophys. Res. Solid Earth* 119, 3767-3822.

Wang, Y., Sieh, K., Thura Aung, Soe Min, Saw Ngwe Khaing, Soe Thura Tun, 2011. Earthquakes and slip rate of the southern Sagaing fault: Insights from an offset ancient fort wall, lower Burma (Myanmar). *Geophys. J. Int.* 185, 49-64.

INQUA Focus Group Earthquake Geology and Seismic Hazards

paleoseismicity.org

Earthquake CAT Risk model for the Region of Attica, Greece, based on a fault specific hazard module

Deligiannakis, Georgios (1), Papanikolaou, Ioannis (1), Zimbidis, Alexandros (2), Kakouris, Iraklis (3)

(1) Mineralogy-Geology Laboratory, Department of Natural Resources Development and Agricultural Engineering, Agricultural University of Athens, 75 Iera Odos Str., 11855 Athens, Greece, gdeligian@aua.gr
(2) Department of Statistics, Athens University of Economics and Business, 76 Patission Str., 10434, Athens
(3) Prudential Actuarial Solutions Ltd, 148, Momferatou Str., 11475, Athens

Abstract: *The new Solvency II EU directive for the insurance and reinsurance undertakings has increased the use of Earthquake Catastrophe models in the European insurance industry. Existing models, as well as the European Insurance and Occupational Pensions Authority Standard Formula (EIOPA SF), inherit deficits related to the incompleteness and inhomogeneity of the historical records and are characterized by low spatial resolution. This paper presents a new Earthquake CAT Risk Model, based on a fault specific hazard module which utilizes geological data, for a more accurate Solvency Capital Requirements (SCR) calculation. The comparison of the model outputs with the SF reveals an overall 15% overestimation by EIOPA of the SCR for the Region of Attica. Nevertheless, variations for individual CRESTA zones within Attica include both overestimation in 7 out of 10 zones ranging from 3 to 57%, and underestimation of the SCR in the remaining 3 zones from 19% up to 49%.*

Key words*: Attica, Solvency, insurance, earthquake, SCR.*

INTRODUCTION

Earthquake Catastrophe (CAT) models have been extensively used by insurance and re-insurance companies for pricing, structuring and management of reinsurance treaties, risk assessment and future losses estimation. As of January 2016, the Solvency II EU Directive demands for the Solvency Capital Requirements (SCR) to be accurately calculated for every insurance company (European Commission, 2009). According to this regulatory framework, each insurance company specifies the required capital K, in order to ensure that it will be able to meet its obligations over the following year, with a probability of at least 99.5%. In other words, the insurance company would be insolvent (thus the capital K would be insufficient for full damage coverage of its own retention) with a probability of 0.5%, which is equivalent to capital K inefficacy once every 200 years.

In order to accurately calculate the SCR, insurance companies have the option to use either the standard approach which utilizes the Standard Formula (SF) as defined in technical papers, such as QIS4 (European Commission, 2008) and QIS5 (European Commission, 2010) provided by the European Insurance and Occupational Pensions Authority (EIOPA), or a full internal model if approved by supervisors of private insurance in each EU country. Other combinational methods, such as the use of the standard approach with a partial internal model, with undertaking-specific parameters, or with simplifications, are also feasible. Regarding the Greek insurance companies, the most widespread practice is to use the SF for the SCR calculations, or a combination of the SF and the existing vendors models for reinsurance contracts. The existing models consist of 4 major modules: Hazard, Vulnerability, Exposure and Loss. The Hazard modules are usually based on worldwide seismicity and insured loss data, downscaled to the Greek territory. The SF is no exception, as it is based on past events and their corresponding insured losses, thus inheriting problems related to the incompleteness and the inhomogeneity of the historical records and lower spatial resolution of hazard (e.g. Papanikolaou et al., 2015; Deligiannakis et al., 2018). Furthermore, it incorporates rough assumptions so that it can fit every insurance company in EU, only by adjusting the country factor, the risk zone weights and the correlation matrix for all Catastrophe Risk Evaluation and Standardising Target Accumulations (CRESTA) zones in each country (European Commission, 2010).

This paper addresses a newly developed Synthetic Stochastic Earthquake Catastrophe model based on a fault specific Hazard Module, which offers high spatial and temporal resolution. It is applied in the Region of Attica, Greece, which hosts more than 40% of the total value for the Greek insured portfolios.

METHODOLOGY

The Synthetic Stochastic Model consists of four basic modules: Hazard Module, Vulnerability Module, Exposure Module and Loss Module.

Hazard Module

Earthquake Catastrophe Models are mainly based on the Hazard Modules outputs. The scope of the Hazard Module is to identify the hazard that could potentially cause losses to insured portfolios, looking at the physical characteristics

of potential disasters. We use a fault specific seismic hazard assessment approach for the region of Attica (see also Deligiannakis et al., 2018). The fault specific approach is utilized in order to address problems related to the incompleteness of historical records, aiming on the reconstruction of a more complete earthquake catalogue over a larger period of time (~15,000 years, i.e. during the Holocene), obtain higher spatial resolution and calculate realistic source locality distances, since seismic sources are very accurately located. The method of seismic hazard mapping from geological fault throw-rate data was firstly introduced by Papanikolaou (2003) and Roberts et al. (2004). It consists of the combination of the following four major factors:

1. Compilation of a fault database, that includes the identification of active seismic sources, determination of fault lengths and their characteristics regarding their kinematics and slip rates.
2. Empirical data which combine fault rupture lengths, earthquake magnitudes and coseismic slip relationships (Wells and Coppersmith, 1994; Pavlides & Caputo, 2004).
3. The radiuses of VI, VII, VIII, and also IX isoseismals on the Modified Mercalli (MM) intensity scale, within which horizontal ground accelerations exceed 500cm/sec^2 in the Greek territory (Theodulidis and Papazachos, 1992) causing damage even to well-constructed buildings (Rieter, 1990).
4. Attenuation - amplification functions for seismic shaking on bedrock compared to basin filling sediments (Sauter & Shah, 1978; Degg 1992).

In general, two types of sources were used for the active fault determination and the compilation of the fault database for the Attica Region; a) published literature (i.e. scientific articles, onshore and offshore neotectonic maps) regarding location and fault activity and b) Fieldwork with in situ geomorphological interpretations. The active faults database contains 24 faults, only 4 of which have ruptured in historical times, that are long enough to produce surface ruptures and can sustain damage in the Attica mainland in case of earthquake rupture (see also Deligiannakis et al., 2018) (Fig. 1). Moreover, for the expected macroseismic intensities caused by faults with no surface trace, or from intermediate and deep earthquakes, we integrated information based on the historic and recorded seismicity from NOA-UOA and AUTH catalogues. The fault specific modeled epicenters, along with the instrumentally recorded events were stochastically simulated in order to assess the future earthquake events. These simulations include the location, magnitude, depth and recurrence for each event. Attenuation relationships were applied for each of these events in order to assess their MM Intensity spatial distribution. The modeled intensities were then attenuated/amplified according to the surface geologic conditions, providing the expected intensities for each geological formation. The input data for the surface geology were extracted from: a) the 1:25,000 Earthquake Planning and Protection Organization (E.P.P.O.) detailed geotechnical map for the Athens Metropolitan Area (Marinos et al., 1999), b) by 12 geological maps of 1:50,000 scale by IGME (Fig. 2). Figure 3 displays a simulated earthquake event related to an active fault offshore eastern Attica.

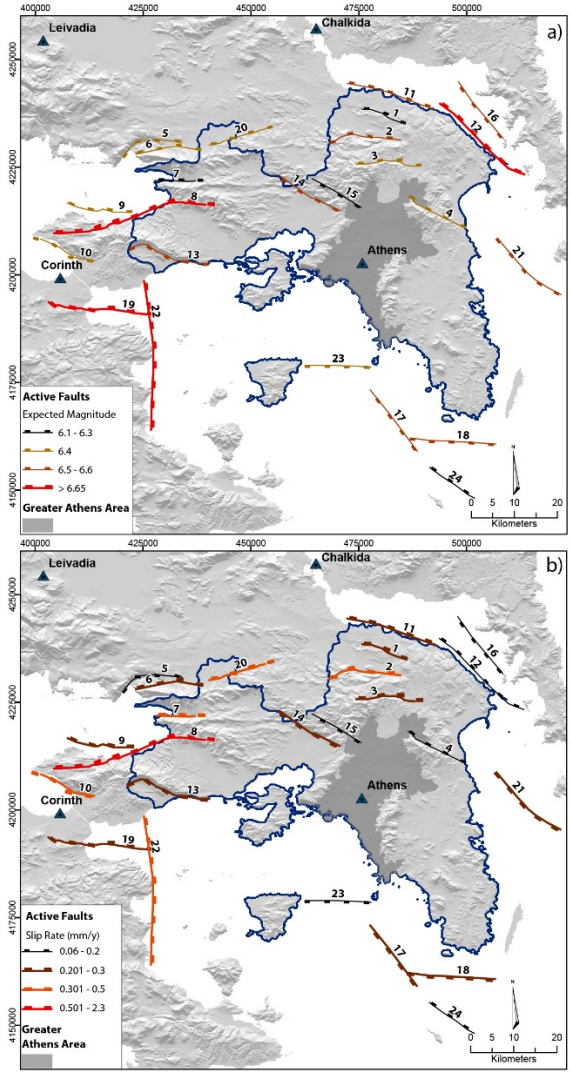

Figure 1: Map of active faults that can sustain damage within the region of Attica. Different fault symbols represent the maximum expected magnitude (a) and different slip-rate categories (b).

Vulnerability Module

The structural damage in buildings and the corresponding loss that occurred due to the simulated earthquake events is computed using the Vulnerability Module. The extent to which a building will be damaged during an earthquake depends on certain characteristics, such as the building construction type, the age, the number of floors, the use of the building, etc. The Building Vulnerability Tables display the average value of the expected building damage E[Xi], depending on the seismic intensity and the building characteristics. The total damage X_i corresponding to the i_{th} building is calculated as follows:

$$X_i \approx U(E(X_i)-\alpha\%E(X_i),\ E(X_i)+\alpha\%E(X_i)),\ \text{where } \alpha=20$$

The actual values that are used in this module are based on existing tables (e.g. Sauter & Shah, 1978; Degg, 1992), modified by already published vulnerability curves and tables (e.g. Kappos et al., 1998; Kappos et al., 2006; Kappos & Panagopoulos, 2009), which represent the Greek building inventory in a more accurate way. The corresponding vulnerability curves for 8 different construction types for Adobe, Concrete, Wooden and Steel buildings that were used in the model are displayed in Figure 4.

Exposure Module

Each insurance company adopts an individual database architecture, which includes the insured buildings locations and details, along with other policy features, such as the coverage types and limits. As a result, the insured portfolio database is redesigned in a way that can be incorporated into the Vulnerability Module and then transferred into the Loss Module.

Loss Module

We assume that the insured portfolio consists of n buildings and X_i is a random variable, representing the amount of the annual own retained loss for the i_{th} building, where i=1,2,…,n. The total annual own retained loss amount S for the insurance company can be described as follows:

$$S= X_1+X_2+\cdots X_n \qquad (1)$$

The Solvency II requirement is typically described by the following equation:

$$Pr[S<K]=99.5\% \qquad (2)$$

S is a random variable, as it represents a sum of random variables. Equation (2) could be solved for K if the distribution of the S random variable could be computed by an analytical formula. As this is not feasible, we use special simulation techniques for the definition of the random variable S.

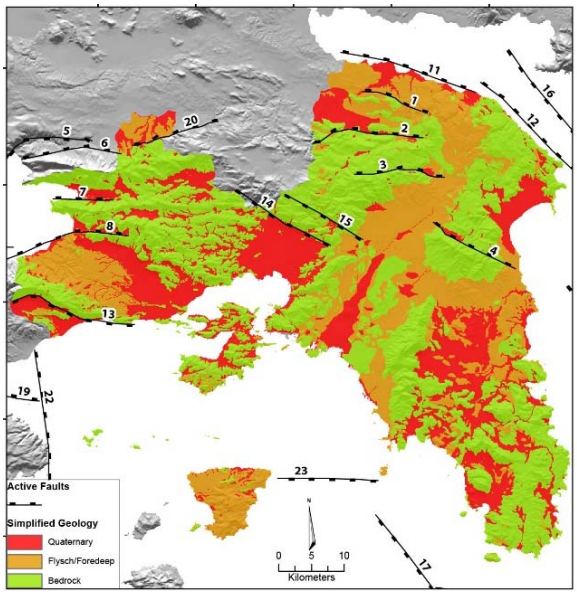

Figure 2: Detailed geological map of the broader Attica region, based on the 1:50,000 scale geological maps of IGME. A more detailed 1:25,000 scale soil map (E.P.P.O.) was used for the broader Athens area, where the majority of the insured value is located.

We develop a synthetic stochastic model that reproduces a large number (e.g. N, where N=10,000) of different values for the random variable S (e.g. S_1, S_2,...$S_{9,999}$, $S_{10,000}$). Two options are available for the calculation of the capital K:

a) We sort the random variable S values in descending order (e.g. $S_{(1)}$, $S_{(2)}$,...$S_{(9,999)}$, $S_{(10,000)}$), then select the N_o ω arranged value, where:

$$\omega=N\times0.05 \qquad (3)$$

and calculate capital K based on the corresponding value from the sorted random variables S, that is:

$$K= S_{(\omega)} \qquad (4)$$

b) A theoretical distribution is fitted to the initial sample of the random variable S, (S_1, S_2, …. $S_{9,999}$, $S_{10,000}$) and then the capital K is calculated using the mathematical formula of the corresponding cumulative distribution or cumulative probabilities tables, so as the equation (2) is solved.

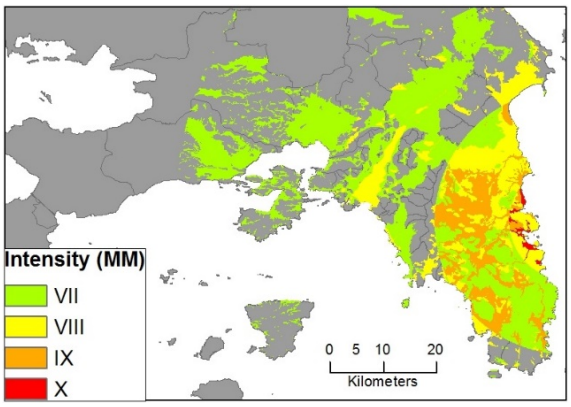

Figure 3: Spatial distribution of MM intensity after a simulated earthquake event. The modelled epicentre of the M6.6 event is related to an active fault offshore eastern Attica.

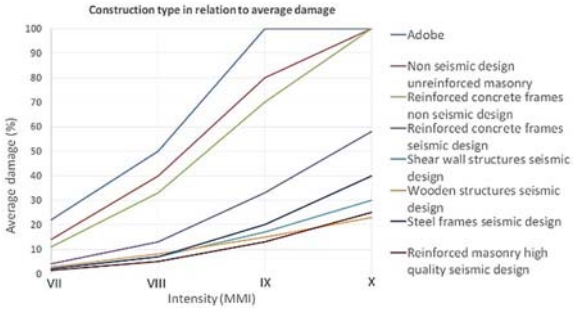

Figure 4: Vulnerability curves for different construction types, in relation to the Modified Mercalli intensity scale.

We tested our model in order to compare the calculated SCR with the outputs of the EIOPA's standard approach. For this reason, we developed a €100bn demo portfolio for the whole Greek market, which was then distributed to each CRESTA zone based on the share of the exposure that is attributed to each particular zone, according to the actual industry exposure distribution data for the year 2017. Regarding the vulnerability, it was assumed that the majority of the buildings are made of reinforced concrete, under new, old, or no seismic design. This distribution was also made using aggregated insurance companies' data, so that we could emulate the Greek insured buildings distribution in the most accurate way. The demo portfolio was then split in Postal Codes level, in order to fit our model algorithm. However, the SF algorithm only uses aggregated information in CRESTA zone level. Furthermore, for the whole Attica region and the individual CRESTA Zones calculations, we assumed zero relativity values for the rest of Greece using the SF.

RESULTS - DISCUSSION

Overall, for the whole Attica Region buildings inventory, the SCR calculated using the SF is overestimated by 15% compared to the hereby presented EQ CAT Risk Model.

However, larger variations result when modelling separate CRESTA Zones within Attica. In 7 out of 10 Cresta Zones the SCR calculated by the SF was 3 - 57% higher, while in the remaining 3 cases it was 19 - 49% lower. These variations result from differences on the spatial analysis, the local site conditions and the variations in seismic intensity recurrences throughout the same CRESTA Zone. The SF zonal weights and relativities refer to the 10 CRESTA zones of Attica, instead of using the 291 Postal Codes for a more granular analysis. The following example (Fig. 5) shows the high spatial resolution, even in sub-Postal Code level, of the Earthquake CAT Risk Model for the MM Intensity VIII distribution over the last 15000 years for the northern suburbs of Athens. It is evident that the biggest part of Cresta Zone '14' is not expected to experience such intensities.

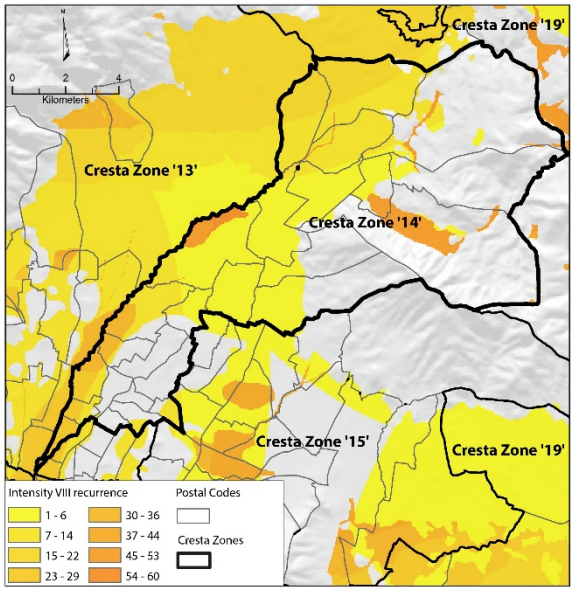

Figure 5: EQ CAT Risk Model outputs for the SCR calculation, compared with the current SF outputs for each CRESTA zone in Attica.

Moreover, several postal codes within this zone will not experience Intensity VIII at all, while others will be shaken at such intensities, but with a very low recurrence. In this CRESTA Zone, the postal codes with low or zero intensity VIII recurrence are the ones with the largest insured values and thus the Earthquake CAT Model estimates a 57% lower SCR than the SF.

CONCLUSIONS

An Earthquake CAT model for the Attica Region is developed, based on a detailed fault specific Hazard Module with a catalogue of stochastically simulated future earthquake events. This module is the primary asset in comparison to the existing CAT models and the EIOPA standard approach, as it does not suffer from the incompleteness and the inhomogeneity of the historical records that the existing CAT models use, as well as the lower spatial resolution of seismic hazard. Compared to the SF, this model yields a more realistic representation of hazard, which is analysed more effectively both spatially and in terms of recurrence. The differences between the two models suggest that the zone relativities and aggregation matrices of the SF should be recalibrated for the Region of Attica.

Acknowledgements: We would like to thank the Bank of Greece for their support during the model development.

REFERENCES

Degg, M.R., 1992. *The ROA Earthquake Hazard Atlas project: recent work from the Middle East*. In: Geohazards: Natural and man-made, McCall, G.J.H., Laming, D.J.C., Scott, S.C. (eds). Chapman and Hall, London, pp. 93-104.

Deligiannakis, G., Papanikolaou, I.D., & Roberts, G., 2018. Fault Specific GIS Based Seismic Hazard Maps for the Attica Region, Greece. *Geomorphology* 306, 264-282.

European Commission, 2008. QIS4 technical specifications, MARKT/2505/08.

European Commission, 2009. Directive 2009/138/EC of the European parliament and of the council of 25 November 2009 on the taking-up and pursuit of the business of insurance and reinsurance, Solvency II, Official Journal of the European Union, p. L335.

European Commission, 2010. QIS5 technical specifications - Calibration Paper. CEIOPS-SEC-40-10, p. 92.

Kappos, A.J., Stylianidis, K.C., & Pitilakis, C., 1998. Development of Seismic Risk Scenarios Based on a Hybrid Method of Vulnerability Assessment. *Natural Hazards* 17, 177-192.

Kappos, A.J., Panagopoulos, G., Panagiotopoulos, C., & Penelis, G., 2006. A hybrid method for the vulnerability assessment of R/C and URM buildings. *Bulletin of Earthquake Engineering* 4, 391-413.

Kappos, A.J., & Panagopoulos, G., 2009. Fragility curves for reinforced concrete buildings in Greece. *Structure and Infrastructure Engineering* 6 (1), 39-53.

Marinos, P., Boukovalas, G., Tsiambaos, G., Protonotarios, G., & Sabatakakis, N., 1999. *Preliminary geological - geotechnical study of the disaster area (of Athens earthquake of Sept 7th, 1999) in NW Athens Basin (in Greek)*. E.P.P.O., Athens, 13 pp.

Papanikolaou, I.D., 2003. *Generation of high resolution seismic hazard maps through integration of earthquake geology, fault mechanics theory and GIS techniques in extensional tectonic settings*. Ph.D. Thesis, University of London, London, United Kingdom, 437 pp.

Pavlides, S., & Caputo, R., 2004. Magnitude versus faults' surface parameters: quantitative relationships from the Aegean Region. *Tectonophysics* 380, 159-188.

Reiter, L., 1990. *Earthquake Hazard Analysis. Issues and Insights*. New York: Columbia University Press 254 pp.

Roberts, G.P., Cowie, P., Papanikolaou, I., & Michetti, A.M., 2004. Fault scaling relationships, deformation rates and seismic hazards: An example from the Lazio-Abruzzo Apennines, central Italy. *Journal of Structural Geology* 26, 377-398.

Sauter, F., & Shah, H.C., 1978. Studies on earthquake insurance. Proceedings of the Central American Conference on Earthquake Engineering, San Salvador.

Theodulidis, N.P., & Papazachos, B.C., 1992. Dependence of strong ground motion on magnitude-distance, site geology and macroseismic intensity for shallow earthquakes in Greece: I, Peak horizontal acceleration, velocity and displacement. *Soil Dynamics and Earthquake Engineering* 11, 387-402.

Wells, D.L., & Coppersmith, K., 1994. New Empirical Relationships among Magnitude, Rupture Length, Rupture Width, Rupture Area, and Surface Displacement. *Bulletin of the Seismological Society of America* 84, 974-1002.

INQUA Focus Group Earthquake Geology and Seismic Hazards

paleoseismicity.org

Geometric and kinematic characteristics of the normal fault system in Neogene-Quaternary Ptolemais Basin, NW Greece; Insights from the opencast lignite mines

Delogkos, Efstratios (1, 2), Manzocchi, Tom (1, 2), Childs, Conrad (1, 2), Pavlides, Spyros (3), Walsh, John (1, 2)

(1) Fault Analysis Group, UCD School of Earth Sciences, University College Dublin, Belfield, Dublin 4, Ireland
(2) Irish Centre for Research in Applied Geosciences, UCD School of Earth Sciences, University College Dublin, Belfield, Dublin 4, Ireland
(3) Department of Geology, Aristotle University of Thessaloniki, Thessaloniki, Greece

Abstract: *Extensive opencast lignite mining in Ptolemais Basin, NW Greece has exposed a plethora of outcrops within a neotectonic and active normal fault system. During the last eight years, we have been working on data derived from our frequent visits to these mines with the aim to get a better understanding on the controls of fault zone structure and evolution. In this presentation, we discuss some of our findings that relate to the structure, timing, and neotectonic activity of the faults.*

Keywords*: Normal faults, Fault geometry, fault growth, Ptolemais Basin*

INTRODUCTION

The Florina-Ptolemais-Servia Basin in western Macedonia, NW Greece (Fig. 1), is affected by two normal fault systems related to two extensional episodes (Pavlides & Mountrakis, 1987; Mercier et al., 1989). The first, Late Miocene episode resulted in the formation of the basin following the Alpine orogenic cycle when the continental crust failed under a NE-SW extensional regime due mainly to postorogenic collapse (Pavlides, 1985; Pavlides & Mountrakis, 1987). The second episode, with a NW-SE direction of extension took place during the Quaternary and resulted in the subdivision of the large basin into several sub-basins along NE-SW trending faults (Pavlides, 1985).

The present topography within the basin is dominated by the NE-SW trending normal faults formed during the second extensional episode and exhibits typical geomorphological characteristics of recent neotectonic or either active faults (Pavlides & Mountrakis, 1987; Goldsworthy and Jackson, 2001). Although this region had been considered to have relatively low seismic activity (Papazachos & Papazachou, 2003), on 13 May 1995, a devastating earthquake (Mw= 6.5) occurred at the southern limit of the basin associated with the Aliakmon Fault Zone (Fig. 1; Pavlides et al., 1995; Mountrakis et al., 1998, Papazachos et al., 1998).

Unlike previous studies that are based on large active faults with a topographic expression (e.g. Goldsworthy & Jackson, 2001), this study focuses on smaller faults of the same fault system (e.g. Fig. 2). We examine the geometric and kinematic characteristics of this fault system by using a three-dimensional dataset derived from repeated mapping in the four active lignite mines in the Ptolemais Basin (Fig. 1).

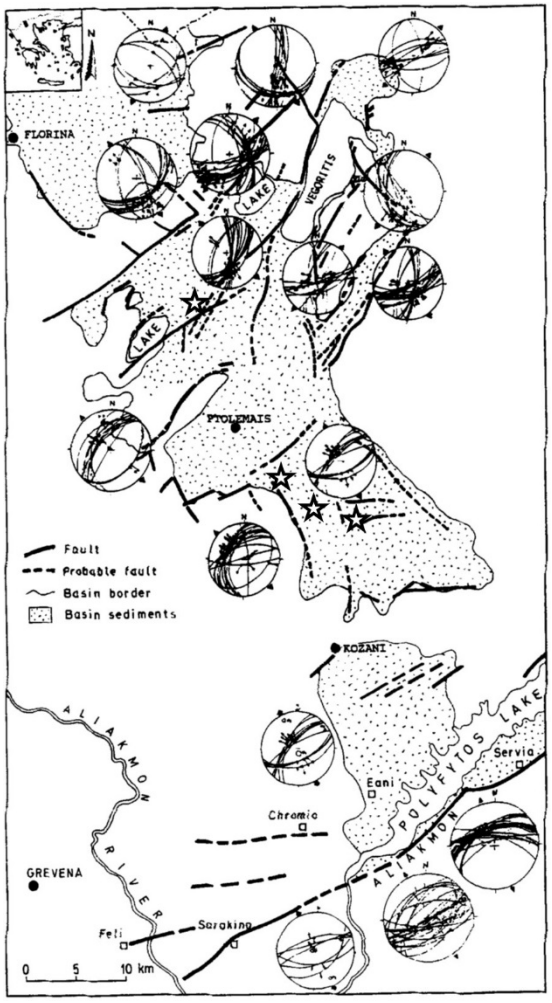

Figure 16: Neotectonic map of the Florina-Ptolemais-Servia Neogene-Quaternary basin showing the main faults, the equal-area projections of measured striated faults and the resulting directions of extension (after Mountrakis et al., 1995). The locations of the four active lignite mines are shown by stars.

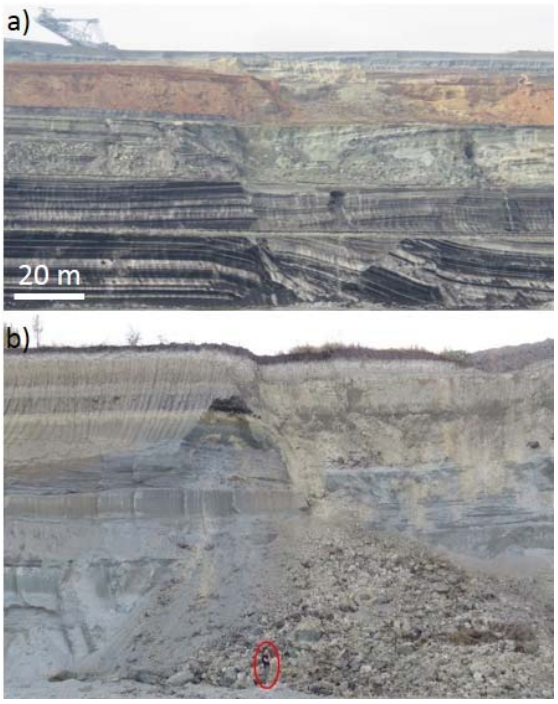

Figure 2: a) Panoramic view of a normal fault zone exposed in Amynteon Lignite Mine. b) Outcrop photograph of the same fault zone exposed at the uppermost mining face showing offsets of the Quaternary deposits.

DATA AND METHODOLOGY

This study is based on data collected from the four active lignite mines in Ptolemais Basin, at 3-month intervals in the period from 2010 to 2017. The mines operate on ca. 7 principal benches using the continuous surface mining method with bucket-wheel excavators, belt conveyors and stackers (Fig. 3).

Figure 3: a) Oblique view of Kardia mine, showing the main mining faces associated conveyor belts and some subsidiary faces between them. b) A closer view of the mining faces showing a bucket-wheel excavator used for the selective mining of the multi-layered lignite deposits in Ptolemais Basin.

The ca. 20 m high mining faces are on average 2.5 km long and step back from the bottom to the top, separated by benches that have widths of ca 50 - 100 m (Fig. 3). During each mapping interval, each face was taken back between 20 and 50 m. The data collected during each fieldwork campaign are photographs at various resolutions and accurate GPS locations, structural measurements and interpretations for all exposed faults and related structures observed in each mine, such as normal or reverse drag. Mapping of successive 20 m high mine faces on several benches over a vertical stratigraphic interval of ca. 100 m provides detailed 3D maps of fault displacements and fault zone structure (e.g. Fig. 4; Delogkos et al., 2016).

This work has mostly concentrated on faults in the Early Pliocene Ptolemais Formation, which has a thickness of approximately 110 m and consists of a rhythmic alternation of m-scale lignite and lacustrine marl beds, with intercalated fluvial sands and silts and some 20 volcanic ash beds (Steenbrink et al., 1999).

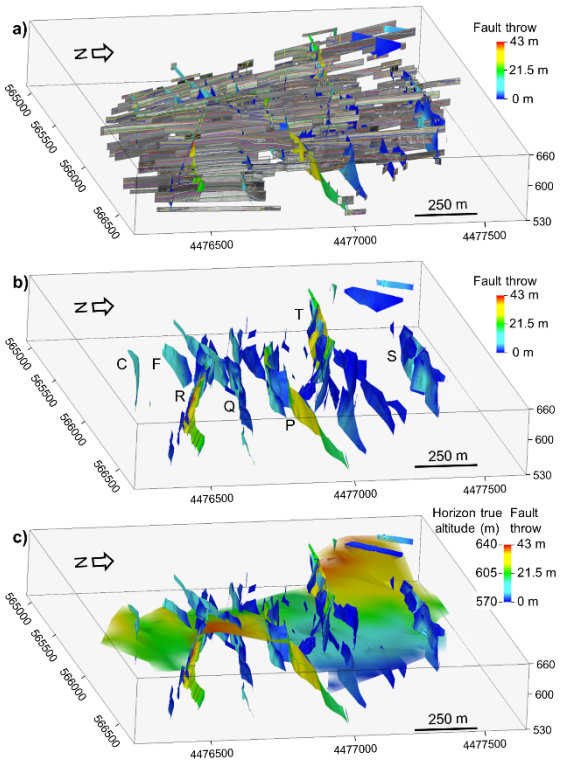

Figure 4: Oblique view of a 3D model of Kardia Mine showing (a) all the mining faces imported into a 3D structural interpretation package, including the interpretation of seven fault zones which displace the lignite-marl sequence by up to 50 m. The colours on the fault surfaces are contours of throw. (b) As (a), but excluding the imported mining faces. (c) As (b), but including one of the interpreted horizons, which is located near the middle of the exposed stratigraphic sequence. The horizon is coloured for height above sea level. After Delogkos et al., 2016.

RESULTS AND DISCUSSION

Three-dimensional mapping of the normal faults reveals high variability in their internal structure. At the largest scale, the faults comprise a few main soft- or hard-linked but interacting slip-surfaces with a zone of associated normal drag occupying a total width of about 100m (Figs.

5, 6). The degree of segmentation and connectivity between fault segments progressively increases with finer scales of inspection (Fig. 6). Continuous deformation constitutes an integral element of the fault structure in all stages of fault growth.

The distribution of the aggregate throw along a fault zone resembles that of a single isolated fault, demonstrating geometrically and kinematically coherent arrays of fault segments. Furthermore, the distributions of throws on individual fault surfaces along a fault zone appear to depend on the size, throw distribution and the 3D arrangement of the other fault zone components.

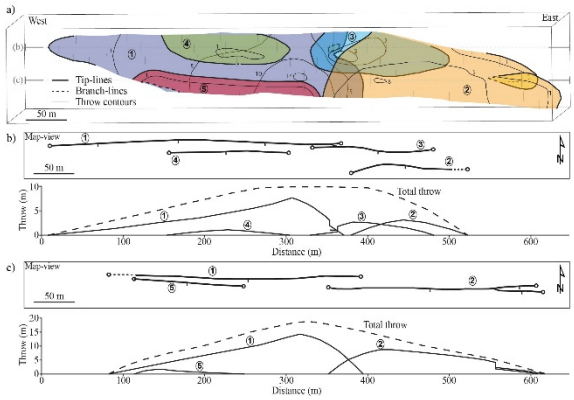

Figure 5: a) Oblique 3-D view of the mapped fault surfaces along a normal fault zone in Prolemais Basin. Fault tip-lines are shown with heavy black lines and branch-lines are heavy black dashed lines. The fault surfaces are contoured for throw (m). The upper and lower edges of the fault surfaces are end of the data unless a tip-line or branch-line is shown. (b) and (c) Map views of the fault segments at the levels indicated in (a). The corresponding throw profiles are also including; dashed lines show the total throw along the fault including throw by continuous deformation and smaller fault segments.

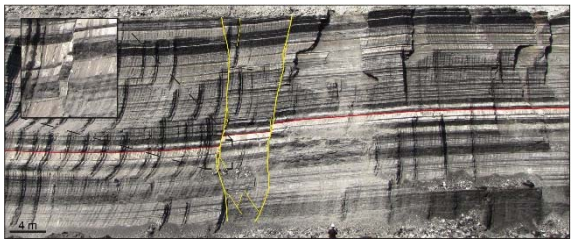

Figure 6: Outcrop through the normal fault zone shown in Fig. 5.

In one of the mines, Kardia, mutually cross-cutting relationships between the normal faults and contemporaneous bed-parallel slip-surfaces provide insights into their growth history (Delogkos et al., 2017 and in press). This analysis indicates that fault interactions restrict fault propagation early during the fault growth history and increase displacement gradients (Fig. 7).

In terms of fault timing, most of the fault displacement occurred after the deposition of the Ptolemais Formation with only a few examples suggesting synchronous faulting during the sedimentation of the Lower Pliocene Ptolemais Formation. In two of the mines, Amynteon and Notio, where most of the overlying sequence is preserved (including Quaternary), the frequency of faulting appears to decrease upwards with only relatively few faults offsetting the most recent deposits. In the other two mines, Kardia and Mavropigi, where the Ptolemais Formation is overlain unconformably by characteristic Pleistocene red-beds, only a few faults propagate and offset this sequence. Displacement differences between the faults above and below this unconformity suggest that most of the throw of these faults predates the unconformity, and generally only the larger faults were still active in the Pleistocene (e.g. Figs. 2, 8).

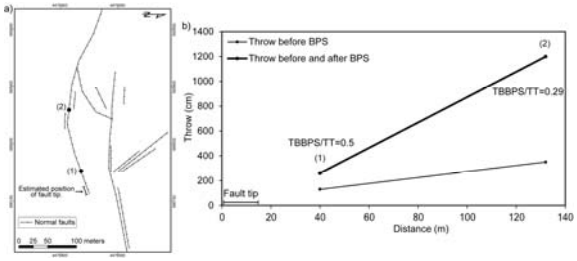

Figure 7: a) Fault map showing the locations (1 and 2) of the recorded bed-parallel slip (BPS) that displaces the footwall fault of a north-dipping normal fault zone in Kardia Lignite Mine. (b) Profiles of the throw before the bed-parallel slip (TBBPS) and the total throw (TT) of the normal fault which has been displaced by the bed-parallel slip, showing the increase in throw gradient with increasing throw along this relay bounding, fault segment. The range of the estimated position of the fault tip is based on the available outcrops. (After Delogkos et al. accepted)

Figure 8: Photograph of the Proastio normal fault exposed at the northwest limit of Mavropigi Mine. The estimated displacement is ca. 350 m based on boreholes. Note that this fault is included as a Seismogenic Source in the GreDaSS database.

Our research to date has mostly focused on fault exposures within the Ptolemais Formation because its fine sequence allows detailed displacement analysis that is essential for understanding fault zone geometry and growth which has been the principal aim of our research. However, we believe that future work on the numerous blind faults that propagated into the overlying sediments could potentially provide information of the fault growth history on shorter time-scales.

Acknowledgements: The work has funded by the multi-company QUAFF project, sponsored by Anadarko, BG, BP, ConocoPhillips, ENI, ExxonMobil, Marathon, Statoil, Total and Woodside. This presentation has also emanated from research supported in part by a research grant from Science Foundation Ireland (SFI) under Grant Number 13/RC/2092 and is co-funded under the European Regional Development Fund and by PIPCO RSG and its member companies. C. Childs is funded by Tullow Oil. The authors would like to thank the Public Power Corporation (ΔΕΗ/ΛΚΠΑ) for permission to work in the mines and the corporation's employees

for their hospitality and assistance in the field. The authors would also like to thank Badley Geoscience Ltd for the use of the T7 software. Thanks to the other members of the Fault Analysis Group for the field assistance and useful discussions.

REFERENCES

Delogkos, E., Manzocchi, T., Childs, C., Sachanidis, C., Barbas, T., Schöpfer, P.J.M., Chatzipetros, A., Pavlides, S., & Walsh, J.J., 2016. Throw partitioning across normal fault zones in the Ptolemais Basin, Greece. In: Geometry and Growth of Normal Faults (Childs, C., Holdsworth, R.E., Jackson, C.A.-L., Manzocchi, T., Walsh, J.J., Yielding, G., eds.), Geological Society, London, Special Publications, 439.

Delogkos, E., Childs, C., Manzocchi, T., Walsh, J.J., & Pavlides, S., 2017. The role of bed-parallel slip in the development of complex normal fault zones. *Journal of Structural Geology*.

Delogkos, E., Childs, C., Manzocchi, T., & Walsh, J.J. (in press). The nature and origin of bed-parallel slip in Kardia Mine, Ptolemais Basin, Greece. *Journal of Structural Geology*.

Goldsworthy, M., & Jackson, J., 2001. Migration of activity within normal fault systems: examples from the Quaternary of mainland Greece. *Journal of Structural Geology* 23, 489-506.

Mercier, J.L., Sorel, D., & Vergely, P., 1989. Extensional tectonic regimes in the Aegean basins during the Cenozoic. *Basin Res*.

Mountrakis, D., Pavlides, S. Zouros, N., Astaras, Th., & Chatzipetros, A., 1998. Seismic fault geometry and kinematics of the 13 May 1995 western Macedonia (Greece) earthquake. *J. Geodyn. Spec. Issue* (Pavlides, King, eds) 26, 2-4, 175-196.

Papazachos, B.C., & Papazachou, C.B., 2003. *Earthquakes of Greece*. Ziti Publ. Co., Thessaloniki.

Papazachos, B.C., Karakostas, V.G., Kiratzi, A.A., Papadimitriou E.E., & Papazachos, C., 1998. A model for the 1995 Kozani-Grevena seismic sequence. *J. Geodynamics* 26 (2-4), 217-231.

Pavlides, S., 1985. Neotectonic evolution of the Florina-Vegoritis-Ptolemais basins. PhD thesis. University of Thessaloniki Greece, 256 pp.

Pavlides, S.B., & Mountrakis, D.M., 1987. Extensional tectonics of northwestern Macedonia, Greece, since the late Miocene. *J. Struct. Geol.* 9 (4), 385-392.

Pavlides, S., Zouros, N., Chatzipetros, A. Kostopoulos, D., & Mountrakis, D., 1995. The 13 May 1995 western Macedonia, Greece (Kozani - Grevene) earthquake; preliminary results. *Terra Nova* 7, 544-549.

Steenbrink, J., Van Vugt, N., Hilgen, F.J., Wijbrans, J.R., & Meulenkamp, J.E., 1999. Sedimentary cycles and volcanic ash beds in the Lower Pliocene lacustrine succession of Ptolemais (NW Greece): Discrepancy between 40Ar/39Ar and astronomical ages. *Palaeogeography, Palaeoclimatology, Palaeoecology* 152, 283-303.

INQUA Focus Group Earthquake Geology and Seismic Hazards

paleoseismicity.org

The attenuation of ESI and traditional seismic intensity with distance: preliminary results from Greek earthquakes

Ferrario, M. Francesca (1), Melaki, Maria (2), Papanikolaou, Ioannis (2), Livio, Franz (1), Serra Capizzano, Stefano (1), Michetti, M. Alessandro (1)

(1) Università degli Studi dell'Insubria, Dipartimento di Scienza e Alta Tecnologia, Como, Italy, francesca.ferrario@uninsubria.it
(2) Agricultural University of Athens, Department of Natural Resources Development and Agricultural Engineering, Athens, Greece

Abstract: *We analyze traditional (MM and EMS) and environmental intensity (ESI scale) of 10 earthquakes that hit Greece between 1894 and 2015. We compute the macroseismic epicenter and the intensity-distance attenuation for each event. We find that the adopted macroseismic scale has a primary role in the intensity-distance regression, as expected; and that the ESI scale has a steeper regression than MM scale.*
ESI regressions are consistent with those obtained for a dataset of 14 events occurred in the Central Apennines (Italy) and confirm that earthquake environmental effects occur consistently through time in different tectonic settings. We suggest that the integration of MM/EMS and ESI scales can better describe the intensity field of strong earthquakes, especially in the epicentral region.

Keywords*: macroseismic intensity; ESI scale; intensity attenuation*

INTRODUCTION

Strong earthquakes, and earthquake-related phenomena, pose a huge societal challenge because they may affect large populations and cause significant loss of lives and economic properties. Greece is located in a complex tectonic setting characterized by the subduction of the African plate beneath the Eurasian plate, and by the relative motion of the Aegean Sea and Anatolian microplates. As a consequence, Greece hosts an intense seismic activity, and strong earthquakes (Mw 6 to 7) are frequent: since 2000, earthquakes affected more than 80.000 people and caused over 500 million € of economic losses (EM-DAT, 2017).

Macroseismic intensity is a critical parameter for assessing seismic hazard and improve mitigation of earthquake risk. Traditionally, intensity is assessed from the effects on humans and the built environment as well as the natural environment. The intensity scale historically adopted in Greece is the MM (Modified Mercalli intensity), which has recently been flanked by the EMS (European Macroseismic Scale) and by the ESI scale (Environmental Scale Intensity). EMS is based mainly on the effects on man-made structures, and environmental effects are overlooked. On the contrary, the ESI scale is based on Earthquake Environmental Effects (EEEs) only (Michetti et al., 2007; Serva et al., 2016). Since the introduction of the ESI scale is very recent, a quantitative assessment of ESI behavior is still lacking.

Here we analyze 10 Greek historical and instrumental events, where intensity data point (IDPs) are available for both ESI and traditional scales. Our analyses aim at (i) evaluating the decay of seismic intensity with distance for the ESI scale for each event and (ii) comparing the ESI dataset with traditional intensity. Then, we compare our results with a similar analysis performed on Italian Apennines events.

DATABASE

We gathered data for macroseismic intensities from published literature and from the Monthly Bulletins of the Geodynamic Institute of the National Observatory of Athens (NOA) concerning 10 events that occurred in Greece between 1894 and 2015 (Table 1). In addition, we extracted data regarding the ESI 2007 (Papanikolaou & Melaki (2017) and references therein; for the 2015 Lefkada event: Papathanassiou et al., 2017). Overall, intensity ranges from 1 to 10 for MM/EMS and from 4 to 10 for the ESI. We consider intensity equal or higher than 4 only, for a total of 1911 and 211 IDPs for MM and EMS, respectively, and 219 IDPs for ESI scale. The events include normal and strike-slip mechanisms, and the magnitude range is Mw 5.7 - 6.8.

MM points have mean and maximum epicentral distances of 86 and 359 km, whereas values for the EMS scale are of 36 and 144 km, and for the ESI scale are of 8 and 72 km, respectively (Figure 1).

METHODS AND DATA ANALYSIS

Firstly, we calculate the macroseismic epicenter as the barycenter of IDPs with highest intensity, using the Boxer algorithm (Gasperini et al., 2010). We calculate separately the macroseismic epicentre for traditional intensity (MM or EMS), and for the ESI scale.

Then, we compute the epicentral distance for each IDP. We choose a method widely adopted for the traditional scales, i.e., the one proposed by Bakun & Wenthworth

(1997). It is an intensity-binning approach, which uses median values of distance to calculate attenuation relationships. A least square method is adopted to extract a linear regression, in the form:

$$I = a * D + b \qquad [1]$$

Where *I* is the intensity, *D* the epicentral distance (in km), *a* and *b* are free parameters.

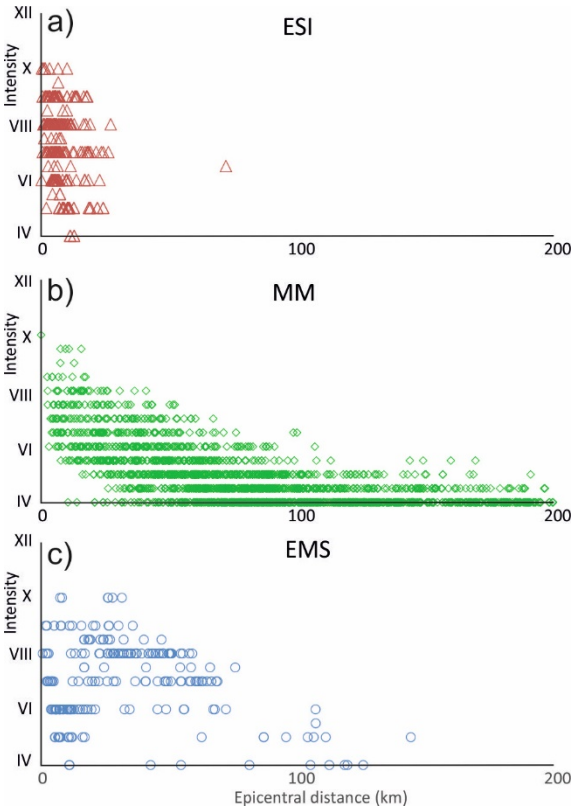

Figure 17: Observed ESI (a), MM (b) and EMS (c) intensity as a function of distance for the 10 analyzed earthquakes.

RESULTS

The location of instrumental and macroseismic epicentre is in good agreement: the average distance between the two is of 11.5 km for the MM scale and of 8.6 km for the ESI scale.

A direct comparison between MM and ESI can be performed at 65 sites, where both intensities are available: in 58.5% of the occurrences the two scales are in agreement (intensities are equal or have a difference of half degree); in 30.7% of the cases ESI is higher and in the remaining 10.8% MM is higher.

When analyzing intensity-distance attenuations for single events, ESI regressions show a lower coefficient of determination (r^2) in respect of traditional intensity, possibly due to insufficient observations or uneven spatial distribution. Nevertheless, both the slope (coefficient *a* in equation [1]) and intercept (coefficient *b* in equation [1], i.e., intensity predicted at the epicenter) computed from traditional intensity are typically lower than the ones obtained from ESI data.

Traditional intensity has a slope of -0.11±0.17, corresponding to a decrease of one degree of intensity every 9 km and an intercept of 8.30±1.16, whereas ESI (excluding Kalamata 1986 and Thessaloniki 1978) has slope of -0.26±0.18, corresponding to a decrease of one degree of intensity every 4 km and an intercept of 9.55±1.62. Figure 2 shows an example for the 1993 Pyrgos event.

When comparing all the events, we found that the primary driver ruling the intensity-distance relation is the adopted macroseismic scale, irrespective of maximum intensity. ESI regressions have a very steep attenuation in the first 20 km from the epicenter, MM regressions are much more gradual and EMS shows two distinct behaviors: Lefkada 2015 and Cephalonia 2014 events have the steepest regressions, whereas the Atalanti case history is the less steep.

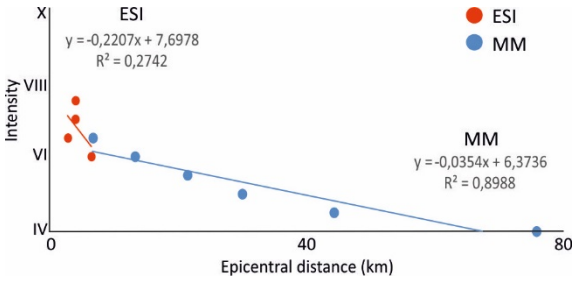

Figure 18: Regressions obtained with the intensity-binning approach for the 1993 Pyrgos event.

We compare the results obtained for Greek earthquakes with a similar research performed on 14 normal faulting events occurred in the Italian Apennines (Ferrario et al., 2017). We find that i) in the near field, ESI intensity is higher than traditional intensity and ii) the intensity attenuation of Greek events is steeper than Italian ones, both for traditional and ESI scales.

CONCLUSIONS

Our results suggest that traditional scales might be inappropriate to fully describe seismic effects in the epicentral area, due to saturation phenomena, as demonstrated by the lower intensity expected at the epicenter computed with MM in respect of ESI scale. We argue that the ESI scale complements information obtained with damage-based scales.

Traditional intensity is closely linked to earthquake shaking, but we argue that a comprehensive depiction of intensity fields must include the full spectrum of earthquake effects, and all possible scenarios. We believe that the integration of traditional intensity and the ESI scale can improve the effectiveness of hazard studies, which are nowadays based on relationships derived from damage-based scales only.

REFERENCES

Bakun, W.H., & Wentworth, C.M., 1997. Estimating earthquake location and magnitude from seismic intensity data. *Bull. Seismol. Soc. Am.* 87, 1502-1521.

EM-DAT, 2017. The Emergency Events Database - Universite catholique de Louvain (UCL) - CRED, D. Guha-Sapir - www.emdat.be, Brussels, Belgium.

Ferrario, M.F., Michetti, A.M., & Livio, F., 2017. Intensity-attenuation relationships for strong Apennines earthquakes: questioning the stability of regression coefficients over time and space based on MCS and ESI scales. 36° GNGTS congress, Trieste, 14-16 november 2017, pp. 30-34.

Gasperini, P., Vannucci, G., Tripone, D., & Boschi, E., 2010. The location and sizing of historical earthquakes using the attenuation of macroseismic intensity with distance. *Bull. Seismol. Soc. Am.* 100 (5A), 2035-2066.

Michetti, A.M., Esposito, E., Guerrieri, L., Porfido, S., Serva, L., Tatevossian, R., Vittori, E., Audemard, F., Azuma, T., Clague, J., Comerci, V., Gürpinar, A., McCalpin, J., Mohammadioun, B., Mohammadioun, J., Mörner, N.A., Ota, Y., & Roghozin, E., 2007. Environmental Seismic Intensity Scale - ESI 2007. *Memorie Descrittive della Carta Geologica d'Italia*, 74, 7-54, Servizio Geologico d'Italia - Dipartimento Difesa del Suolo, APAT, Roma, Italy.

Monthly Bulletin of the Geodynamic Institute, National Observatory of Athens", Kozani (1995), Sofades (1954), Pyrgos (1993), Thessaloniki (1978), Andravida (2008), Kalamata (1986), Lefkada (2003).

Papanikolaou, I., & Melaki, M., 2017. The Environmental Seismic Intensity Scale (ESI 2007) in Greece, addition of new events and its relationship with magnitude in Greece and the Mediterranean; preliminary attenuation relationships. *Quat. Int.* 451, 37-55.

Papathanassiou, G., Valkaniotis, S., Ganas, A., Grendas, N., & Kollia, E., 2017. The November 17th, 2015 Lefkada (Greece) strike-slip earthquake: Field mapping of generated failures and assessment of macroseismic intensity ESI-07. *Engineering Geology* 220, 13-30.

Serva, L., Vittori, E., Comerci, V., Esposito, E., Guerrieri, L., Michetti, A.M., Mohammadioun, B., Porfido, S., & Tatevossian, R.E., 2016. Earthquake hazard and the environmental seismic intensity (ESI) scale. *Pure and Applied Geophysics* 173 (5), 1479-1515.

Table 1: Number of IDPs and maximum intensity for the 10 studied events.

Event	Date	Epicenter	Magnitude	Scale	N° IDPs trad. intensity	I max trad. intensity	N° IDPs ESI	I max ESI
1	17/11/2015	Lefkada	Mw 6.4	EMS	26	VIII	20	VIII – IX
2	26/01/2014 - 03/02/2014	Cephalonia	Mw 5.9 Mw 6.0	EMS	18 (26/01) + 18 (03/02)	VII IX	26	VIII
3	08/01/2008	Andravida	Mw 6.4	MM	171	VIII – IX	24	VIII
4	14/08/2003	Lefkada	Ms 6.4	MM	149	VII – VIII	17	VIII – IX
5	13/05/1995	Kozani-Grevena	Ms 6.6	MM	514	IX – X	19	IX
6	26/03/1993	Pyrgos	Ms 5.5	MM	122	VI - VII	11	VII – VIII
7	13/09/1986	Kalamata	Ms 6.0	MM	241	X	21	IX
8	20/06/1978	Thessaloniki	Ms 6.5	MM	585	VIII – IX	22	IX
9	30/04/1954	Sofades	Ms 6.8	MM	129	IX – X	10	IX – X
10	20/04/1894 – 27/04/1894	Atalanti	Ms 6.4 Ms 6.8	EMS	96 (20/04) + 59 (27/04)	X X	19	X

INQUA Focus Group Earthquake Geology and Seismic Hazards

paleoseismicity.org

On-going Holocene slip-rates analysis for the Banning strand of the San Andreas Fault: Challenges with estimating slip-rates along a rapidly moving fault

Figueiredo, M. Paula (1), McGill, Sally (2), Owen, A. Lewis (1), Gontz, Allen (3)

(1) Department of Geology, University of Cincinnati, USA, paula.figueiredo@uc.edu.
(2) Department of Geological Sciences, California State University San Bernardino, USA
(3) Department of Geological Sciences, San Diego State University, USA

Abstract: *The Banning fault is the southern strand of the San Andreas Fault system (SAF), south of San Gorgonio Pass, in the Coachella Valley of Southern California. This area has a complex tectonic setting where the slip-rate along the SAF is being transferred from the San Bernardino strand though two branches onto the Indio strand, north of the Salton Sea. Despite evidence of Holocene tectonic activity, slip-rate for SAF strands are not fully understood, neither how slip is partitioned between them. Along the Banning strand, a paleochannel wall of Mission Creek is incised into an offset alluvial fan surface; LiDAR analysis suggest a 148 ± 9 m maximum displacement. Samples for dating were collected (OSL, TCN Be and C-14) and initial results indicated unrealistically high slip-rates. This result, redirected the research to a sub-surface analysis and to a reassessment of the slip-rate methods that are usually applied in these types of studies.*

Keywords*: Southern San Andreas, Banning, Geochronology, Morphotectonics, Ground-Penetration-Radar*

INTRODUCTION

The complexity of the San Andreas Fault system (SAFS) increases south of the San Bernardino strand, across the San Gorgonio Pass Fault zone (SGP; Fig. 1). Here, the San Bernardino and the San Jacinto Mountains converge and the deformation is partially accommodated by uplift and folding through a complex system of strike-slip and thrust faults. South of the SGP and towards the northern Coachella Valley, the SAFS splays into two branches: a northern (Mill Creek-Mission Creek strands) and a southern one (Banning and Garnet Hills strands), both converging close to Biskra Palms, to become the Indio strand. Despite evidence of Holocene tectonic activity, slip-rate for SAFS strands are not fully understood, neither how slip is partitioned between faults. The slip rate of the southern SAFS decreases from ~25 mm/yr at Cajon Pass (Weldon & Sieh, 1985) to 11.6 ±1mm/yr at Badger Canyon (McGill et al., 2016) and 7-16 mm/yr at Plunge Creek (McGill et al., 2013) towards SGP, but increases southwards to Coachella Valley as much as 12-22 mm/yr at Biskra Palms (Behr et al., 2010; Fletcher et al., 2010) and 17-24 mm/yr at Pushawalla Canyon (Blisniuk et al., 2012, 2013) (Fig.1).

At the SGP, geodetic modelling of strain suggests 2 mm/yr of northwest oriented dextral shear in the vicinity of the SAF (Rangel & McGill, 2016). A low Pleistocene slip rate of 1-2 mm/yr is defined for the Mill Creek strand (Sieh et al., 1994; Weldon, 2010) and might even have had periods of tectonic quiescent due to an inter-play with Pinto Mountain Fault (Kendrick et al., 2015). Heermance & Yule (2017), at Millard Canyon, presented evidence for a Holocene combined slip of ~5 mm/yr for the Banning strand and San Gorgonio thrust strand, and Gold et al. (2015) characterized a similar 4-5 mm/yr Holocene slip for the Banning strand, about 15 km westward, close to Whitewater Canyon. No slip rates are known for the Garnet Hill strand. Farther SE, and across the Coachella Valley at the Indio and Edom hills, Scharer et al. (2016) estimated 2-6 mm/yr of Holocene slip for the Banning, fault suggesting that for this strand, the slip is efficiently transferred along the Coachella Valley. However, this also suggests that a significant amount of

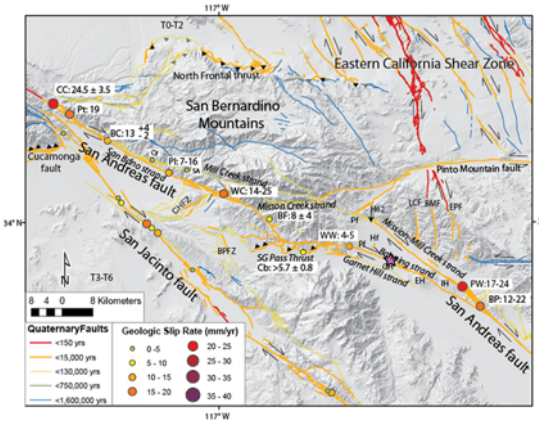

Figure 1: Quaternary faults and slip rates in the San Gorgonio Pass and north Coachella Valley region (adapted from McGill et al., 2017). Purple star indicates location of our study. CC, Cajon Creek; Pt, Pitman Canyon; BC, Badger Canyon; Pl, Plunge Creek; WC, Wilson Creek; BF,Burro Flats; Cb, Cabezon; WW, Whitewater - Gold et al. (2015); PW, Pushawalla Canyon-Blisniuk et al. (2012); BP, Biskra Palms - Behr et al. (2010), Fletcher et al. (2010).

the slip along the singular strand of the SAF in Coachella Valley (south of Indio, 12-22 mm/yr; 17-24 mm/yr) could be transferred onto other fault strands farther north. Another hypothesis is that the slip-rate might be larger in the central Banning and decreasing towards the extremes. All of these views carry different consequences for seismic

hazard, and geological slip-rate sites are still too sparse to investigate how the slip is in fact transferring between the San Gorgonio Pass area and the southern Coachella Valley strand of the SAFS.

The southern section of SAF is the only section that has not ruptured historically. Paleoseismic data of Castillo et al. (2018) corroborates the existence of prehistorical seismicity along the Banning strand, and reinforces it as a relevant and active strand of the SAF. These authors studied a paleoseismic trench, close to North Palm Springs, where they identified 5 prehistoric earthquakes and provide possible evidence for another 4 events. The most recent event occurred before746-626 cal yr BP and after 1119-864 cal yr BP, and at least 3-4 earthquakes occurred since ~2.7 ka. From the compilation of all data, and assuming at 3 or 4 complete earthquake cycles, Castillo et al. (2018) propose a maximum average interval of 720 yr or a minimum average interval of 330 yr. Compared with other paleoseismic sites in the region, the Banning strand seems to have intermediate to shorter intervals than the SGP, but longer than the Mission Creek and the Indio strands.

DISCUSSION: BANNING STRAND SLIP-RATE STUDY

Our study focuses close to the North Palm Springs, where the Mission Creek Fault crosses the Banning strand, ~12 km east of Gold et al.'s (2015), 22 km west of Scharer et al.'s (2016) site and 2 km east of Castillo et al.'s (2018) sites. Here, the Mission Creek channel is incised into a distal alluvial fan (arroyo) surface; both are displaced by the Banning strand and a minor scarp in the alluvial deposits is partially covered by dunes (Fig.2). A terrace riser ~1.2 m high was interpreted to be an ancient channel wall of Mission Creek, incised into an older Qal2 surface and displaced ~148 ± 9m. This riser separates a higher surface Qal2 from an incised lower and broad Qal1. This morphology is evident on B4 LiDAR imagery and we later confirmed it during a field survey. The site characteristics, with a perpendicular angle between the Mission Creek and the fault, fault zone and creek channel are well defined, and a general scarcity of well-defined linear geomorphic markers along the Banning strand, lead to select this site to define Holocene to late Pleistocene slip rates. Since the site is located in a conservation area, no exploratory trenches are allowed to investigate for evidence of channels and other piercing points and instead we choose to open 3 pits: two 2-m-deep pits on the old fan surface (Qal2) and one 1.5-m-deep pit was excavated into the alluvial deposits that post-date the incision (Qal1). Our goal was to collect samples for geochronology to define the timing of the incision of the offset channel wall, to estimate the slip rate for this part of the Banning fault. Samples from two depth-profiles for ^{10}Be Terrestrial Cosmogenic Nuclide (TCN) (7 samples per profile) and 12 samples for Optically Stimulated Luminescence (OSL) (4 samples per pit) were collected and then processed in the Quaternary Geochronology Laboratories at the University of Cincinnati; TCN Be measurements were conducted at the Lawrence Livermore National Laboratory. In addition, C-14 samples were also collected and dated at the Keck-Carbon Cycle Accelerator Mass Spectrometer at University of California-Irvine.

Preliminary results:

Results from the geochronology were inconsistent between methods. The ^{10}Be TCN depth profiles were challenging: one profile did not exhibit the expected decay in ^{10}Be/ ^{9}Be ratio, suggesting that it could be a young surface, while the other provided an age of ~12ka. This would suggest a slip rate in the order of 12-13 mm/yr for the ~150m displacement (McGill et al., 2016). However, results from OSL and C-14 ages were consistent between themselves and indicated a much younger age for the surfaces than initially predicted (~2 ka) which would imply an unrealistic slip-rate of ~75 mm/yr. The young age of the sediments was also corroborated by the absence of soil development. Thus, based on the OSL, C-14 results and lack of soil development, the age of 2 ka was considered reliable and the TCN older ages, were interpreted as result of ^{10}Be inheritance.

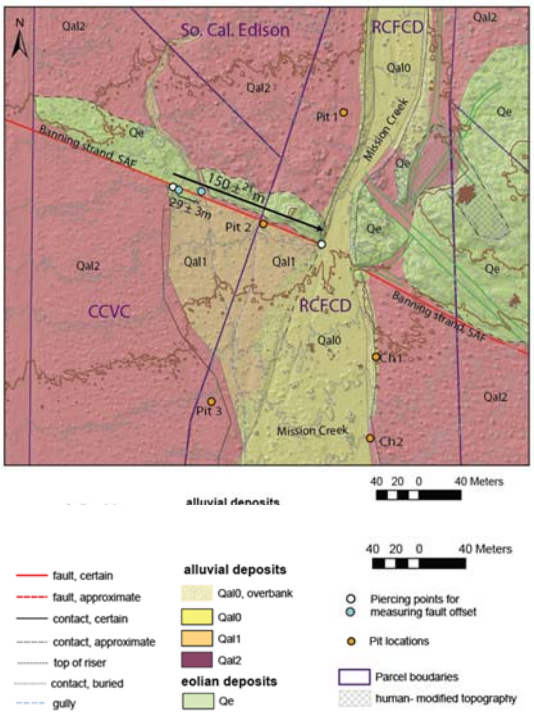

Figure 2: Geologic Interpretation of the Mission Creek at the Banning fault study site showing the location of pits. Piercing points for the two displacements considered. Explanations in the text.

The problem and further analysis:

To test the hypothesis that the sequence of young deposits dated to 2-3 ka were exposed in the pits are not overbank deposits covering an older surface, OSL samples were collected at new pits farther from the active channel as well as two samples from a natural exposure of Qal2 in the east bank of Mission Creek, south of the fault. Preliminary results indicate that the age at the base of a 2m-deep-pit is 2.8 ka and that the deposits in the eastern bank are also quite young (1-2 ka), corroborating the ~2 ka as the timing for the abandonment of the surface, which is consistent with the age of the sediments characterized by Castillo et al. (2018), for a nearby location.

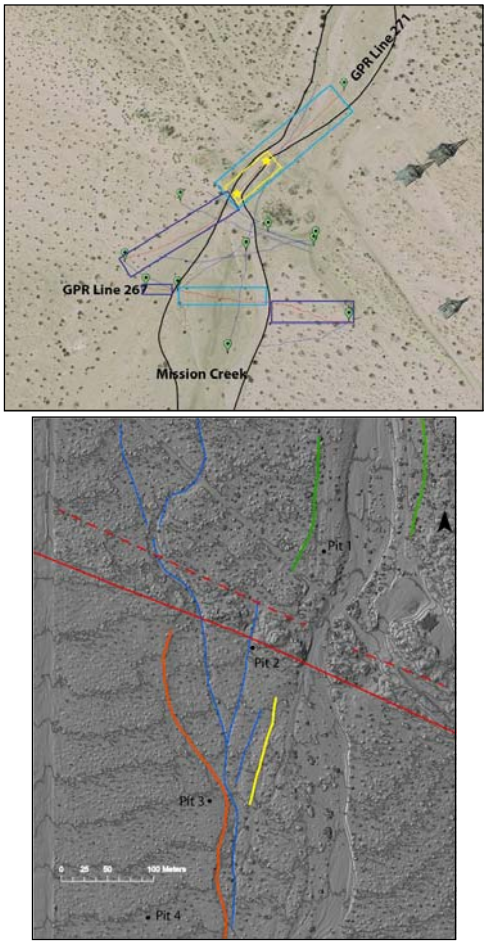

Figure 3: Details of study sites a) Location of the GPR lines on an aerial photograph; b) Geomorphology interpretation of the Mission Creek area across the Banning on Lidar. Location of pits provided. Green lines are risers north of the fault, orange and yellow lines are risers south of the fault.

A new correlation was proposed for the truncated terrace riser south of the fault with the west edge of a gully north of the fault and west of the Mission Creek, with a right-lateral separation of 29 ± 3 m (Fig.2), which implies a more realistic slip rate of ~14.5 mm/yr (McGill et al., 2017). However, this alternate correlation is also problematic, since it is difficult to explain the lack of preservation of the Qal2 surface south of the fault, east of the gully and west of the active channel of Mission Creek. Questions remain, since the width of the gully does not seem to be able to account for the erosion and deposition pattern observable at that location. No other gullies or channels are recognized at the surface, which is partially covered by dunes. Further analysis in the high-resolution topography using LiDAR lead to the recognition of smaller channel risers, poorly preserved and with a smooth expression: one very smooth present north of the fault and another one present at the lowered surface previously considered as Qal1. However, it was not possible to establish a correlation between them.

New methodology:

Because trenching is not allowed, to investigate relationships between older channels that are now buried, we conducted a ground-penetration radar (GPR) survey to determine the effectiveness of the system in this location for identifying palaeochannels (Fig. 3). Reconnaissance-level lines were acquired using a MALA GX 450 MHz system with a vertical resolution of ~8 cm and horizontal resolution, controlled by wheel-firing, of ~5 cm. The lines were run parallel (6 lines) to the surface expression of the fault in and adjacent to the arroyo of Mission Creek. Lines were also acquired perpendicular (2 lines) to the fault along the arroyo axis. Line 267, acquired parallel to the fault, revealed one major paleochannel buried at the Qal1 area with numerous smaller cut and fill structures that are associated with periods of arroyo activity (Fig. 4a). Line 271, acquired perpendicular to the fault, reveals various structures associated with braided channel bar migration and a clear difference between the active channel and flood plain depositional structure. At the fault zone, in depth, there is stratigraphic disturbance which correlates with the fault scarp at the surface. Additionally, an ~35-40 m wide complex fault zone is revealed with a northern fault that clearly displaces horizons in depth, but that has no significant surface expression (Fig.4). The study area was already inferred as a likely small push-up structure during previous field surveys, but this was not possible to confirm due to the aeolian cover.

Our Goals:

The dense grid of GPR lines will allow us to test two alternative questions for the offset of the ~2 ka distal fan surface, which include:(1) Are there channels north of the fault and west of Mission Creek, now covered by the aelioan cover that could have erode the Qal2 surface and generate the Qal1 south of the fault, between the truncated terrace riser and the modern channel of Mission Creek? (2) Is it possible that the channel that appears to be offset 29 ± 3 m from the truncated terrace riser could in fact have intersected the fault closer to that riser, with the original channel subsequently being buried by aeolian deposits? If so, the GPR may allow us to document the buried channel that was responsible for carving the truncated terrace riser and to locate the piercing point beneath the dune. This could yield an even smaller offset and a slip rate of 5.2-6.4 mm/yr, which would be more compatible with published rates of ~ 5 mm/yr for the Banning strand.

CONCLUSION

Our study demonstrates the benefits of cross-correlating techniques, applied to a tectonic slip-rate investigation. The cross-correlation of several geochronology methods revealed to be a key factor to evaluate the suitability of each method for this site. If we only had used ^{10}Be TCN depth profiles, we would have estimated a slip-rate of ~10-12 mm/yr, and assumed the ~150 m displacement as correct. However, the OSL and C-14 results consistency lead us to conclude that the surface age was younger and therefore, that the Mission Creek displacement had to be smaller. Since the observations at the surface are not sufficiently robust to understand the past surface processes and solve the displacement hypothesis, we are conducting sub-surface analysis to complement them.

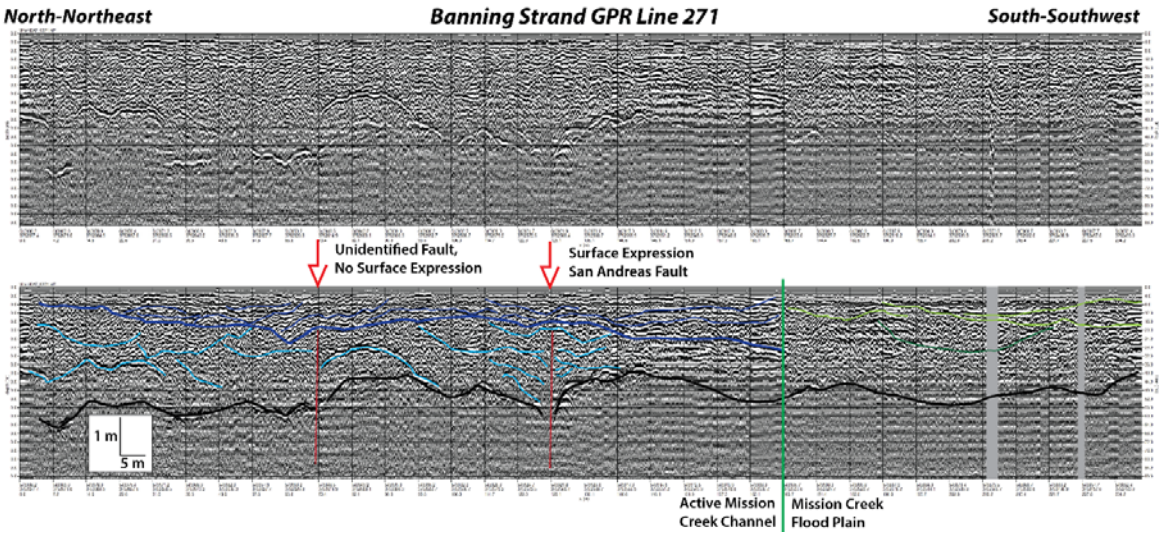

Figure 4: Banning Strand GPR Line 271, perpendicular to the SAF and axial along Mission Creek. GPR Line 271 was acquired along the dry bed of Mission Creek with a nearly perpendicular crossing of the SAF. Red Lines and Red Arrows indicate the location of interpreted faults. Dark blue reflectors are interpreted as channels and channel deposits (bars) in the most recently active episodes of Mission Creek; no vertical offset or significant disturbance is observed for the upper 1 m, which is consistent with the lack of a fault scarp, deposition after the most recent event. Light blue reflectors are interpreted as channels and channel deposits below the most recently active Mission Creek; offset and disturbance is observed where faults are present. Light green reflectors are interpreted as overbank flood deposits related to flooding. Dark green reflectors are interpreted as former channels beneath the modern flood plain of Mission Creek. Black Line indicates radar basement and is not interpreted with respect to geology.

Acknowledgements: This work was funded by Southern California Earthquake Centre (SCEC) award # 15182.

REFERENCES

Behr, W.M., Rood, D.H., Fletcher, K.E., Guzman, N., Finkel, R., Hanks, T.C., Hudnut, K.W., Kendrick, K.J., Platt, J.P., Sharp, W.D., Weldon, R.J., & Yule, J.D., 2010. Uncertainties in slip-rate estimates for the Mission Creek strand of the southern San Andreas Fault at Biskra Palms Oasis, southern California. *Geological Society of America Bulletin* 122, 1360-1377, doi:10.1130/B30020.1.

Blisniuk, K.D., Scharer, K., Burgmann, R., Sharp, W., Rymer, M., Rockwell, T., & Williams, P, .2012. A new slip rate estimate for the San Andreas fault zone in the Coachella Valley at Pushawalla Canyon. *SCEC Annual Meeting, Abstract* #129.

Blisniuk, K.D., Scharer, K., Sharp, W.D., Burgmann, R., Rymer, M.J., & Williams, P., 2013. New geological slip rate estimates for the Mission Creek strand of the San Andreas fault zone. *SCEC 2013 Annual Meeting*, Abstract #032.

Bryan, A., Castillo, B., McGill, S., Scharer, K., Yule, D., McNeil, J., & McPhillips, D., 2018. Preliminary ages of prehistoric earthquakes on the Banning Strand of the San Andreas Fault, near North Palm Springs, California. *114th Corileran Anual Section Meeting* Abstr #313451.

Fletcher, K.E.K., Sharp, W.D., Kendrick, K.J., Behr, W.M., Hudnut, K.W., & Hanks, T.C., 2010, Th/U dating of a late Pleistocene alluvial fan along the southern San Andreas fault. *Geological Society of America Bulletin* 122, 1347-1359.

Gold, P., Behr, W., Rood, D., Sharp, W., Rockwell, T., Kendrick, K., & Salin, A. 2015. Holocene geologic slip rate for the Banning strand of the southern San Andreas Fault, southern California. *Journal of Geophysical Research*120 (I.8), 5639-5663.

Heermance, R., & Yule, D., 2017. Holocene slip rates along the San Andreas Fault system in the San Gorgonio Pass and implications for large earthquakes in southern California, *Geophysical Research Letters* 44 (11), 5391-5400.

Kendrick, K.J., Matti, J.C., & Mahan, S.A., 2015. Late Quaternary slip history of the Mill Creek strand of the San Andreas in San Gorgonio Pass, southern California: The role of a subsidiary left-lateral fault in strand switching. *Geol. Soc. Am. Bull*.127, 1-26.

McGill, S., Owen, L., Weldon, R.J., & Kendrick, K., 2013. Latest Pleistocene and Holocene slip rate for the San Bernardino strand of the San Andreas fault, Plunge Creek, Southern California: Implications for strain partitioning within the southern San Andreas fault system for the last ~35 k.y. *Geological Society of America Bulletin* 125 (1/2), 48-72.

McGill, S, 2016. Fault at Badger and Pitman Canyons, Southern California. *Geological Society of America*, *Abstracts with Programs.* Vol. 48, No. 4, doi: 10.1130/abs/2016CD-274681.

McGill, S.F., Figueiredo, P.M., & Owen, L.A., 2016. Work in progress to estimate a Latest Pleistocene slip rate for the Banning Strand of the San Andreas Fault near North Palm Springs. Poster presentation, *2016 SCEC Annual Meeting*.

McGill, S., Figueiredo, P.M, & Owen, L.A., 2017. Puzzling results in a slip rate study for the Banning Strand of the San Andreas Fault near North Palm Springs. Poster 2017, *SCEC Annual Meeting*.

Rangel, T., & McGill, S., 2016 Low slip rate for San Gorgonio Pass section of the San Andreas Fault inferred from Geodesy. *Geological Society of America, Abstracts with Programs,* Vol. 48, No. 4 , doi: 10.1130/abs/2016CD-274567.

Scharer, K.M. 2016. Slip transfer and the growth of the indio and Edom Hills, Southern San Andreas fault, *Geological Society of America*, Cordilleran Section, 112th Annual Meeting.

Sieh, K., Grant, L.B., & Freeman, S.T., 1994, Late Quaternary slip rate of the North Branch of the San Andreas fault at City Creek, California. *Geological Society of America*, Abstracts with Programs, v. 26, p. 91.

Weldon, R., 2010, Slip rate for the North Branch of the San Andreas fault. San Bernardino Valley, annual report to the Southern California Earthquake Center.

Weldon, R.J., & Sieh, K.E.,1985. Holocene rate of slip and tentative recurrence interval for large earthquakes on the San Andreas fault, Cajon Pass, southern California. *Geol. Soc. Am. Bull.* 96.

INQUA Focus Group Earthquake Geology and Seismic Hazards

paleoseismicity.org

Revisiting late Pleistocene uplifted marine terraces at South Portugal: new geochronology data and its implications

Figueiredo, M. Paula (1), Owen, A. Lewis (1), Rockwell, K. Thomas (2)

(1) Department of Geology, University of Cincinnati, USA paula, figueiredo@uc.edu
(2) Department of Geological Sciences, San Diego State University, USA

Abstract: *A sequence of marine terraces and coastal landforms is present at the southwest of Portugal. Those are interpreted to be uplifted, with ages from late to middle Pleistocene. The best preserved terrace was interpreted to correspond to MIS 5e (circa 120 ka) and a lower terrace to be MIS 5a (circa 80 ka), however without a geochronology calibration. Later, a beach deposit assumed to be MIS 5a was dated through pIRIR (K-feldspar) and OSL (quartz), providing a MIS 5c age, which could imply a lower uplift rate than previously interpreted. New luminescence data, for the same beach deposit and other coastal deposits through OSL with quartz, indicate the presence of a MIS 5a high stand, which reworked older sediments. This, corroborates the initial interpretation, and the estimated uplift rate of circa 0.11 ± 0.01 mm/yr.*

Keywords*: Portugal, marine terraces, Optical Stimulated Luminescence, Pleistocene*

INTRODUCTION

The littoral section of southwest Portugal is located close to eastern Atlantic sector of the Eurasia-Nubia plate boundary, that converges obliquely with a WNW-ESE direction at a rate of 4-5 mm/yr. It corresponds to the most seismic region in Portugal, with a higher seismic hazard. In the onshore, several tectonic structures with Plio-Quaternary activity are present, with low slip-rates, generally lower than 0.2 mm/yr (Cabral et al., 2012) and no Holocene or historical earthquakes with surface rupture was identified. However, at the offshore, significant earthquakes have occurred such as the 1755 Mw>8 and tsunami or the 1969 Mw 7.9 earthquakes. Historical accounts described additional large magnitude historical seismicity inferred to be located in the offshore followed by tsunami inundation during years 382 AD and 60 BC (Andrade et al., 2016). In fact, Large historical and paleo-earthquakes generated in the Gulf of Cadiz were also recognized by the identification of correlative tsunami deposits and turbidites suggesting a 1300-1800 yr recurrence interval for a regional earthquake with magnitude larger than 8 (Figueiredo et al., 2013 and references within).

Uplift along the southern Portugal was previously recognized as the result of a regional Plio-Pleistocene long term uplift, with rates in the range 0.1-0.2 mm/yr (Cabral et al., 1995). However, at the coastline no marine terraces were characterized or the age of the sediments or landforms constrained, so there was not enough control on the variability of vertical motions through time. In addition, no relationship was established between uplift and active crustal structures, namely the off-shore ones, or efforts were conducted to investigate co-seismic effects and recent vertical motions that could be associated to large Holocene earthquakes such as the 1755 or the 382 AD. Figueiredo and co-authors (2013) presented the first study about uplifted marine terraces, recognized a late Pleistocene marine terrace sequence, poorly preserved but with constant elevations regionally. These authors, based on the interpretation that the two lower terraces present in the region corresponded to the MIS 5a and MIS 5e, estimated an uplift rate of 0.11± 0.01 mm/yr since late Pleistocene to present (Fig. 1), and suggested that the southwest Portugal was experiencing higher uplift rates than the rest of the country. In fact, Ressureição et al. (2012), estimated a 0.04 mm/yr uplift rate for a coastal section circa 100 km north of Figueiredo et al. (2013) study. This difference in regional uplift is also supported by a thorough morphotectonic analysis that verifies a higher incision along the southwest which is assumed to be correlative to a higher uplift rate (Figueiredo, 2015; Figueiredo et al., in press).

DISCUSSION

In a rising coastline with a steady uplift, the preservation of marine terraces for the last interglacial, MIS 5, depends

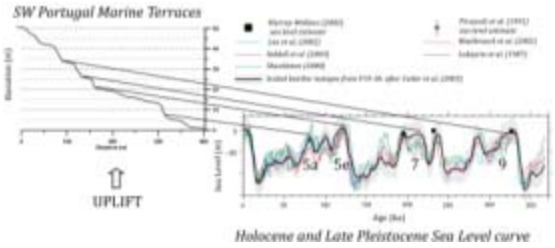

Figure 1: SW Portugal lower marine terrace sequence and correlation with Pleistocene sea level curve adapted from Siddal et al., 2006 (Figueiredo et al., 2013).

mostly on the uplift rate; MIS 5e high-stand was higher than the present msl and therefore it is generally preserved and present. The position of the MIS 5c and the younger MIS 5a high-stands regarding the present msl are very similar; in a rising coast with uplift rates >0.2 mm/yr, such as in Southern California, MIS 5c is preserved and was emerged during the MIS 5a. For lower uplift rates, MIS 5a reoccupies the previous MIS 5c terrace. This being said, in a coastline under a steady uplift, the 3 MIS 5 high stands will be preserved or 2, the oldest and the youngest.

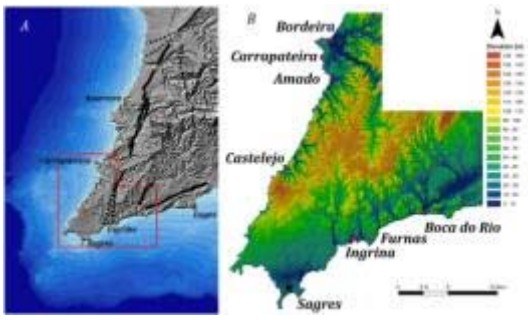

Figure 2: Digital terrain model of southwestern Portugal: (A): Regional Geomorphology and continental shelf bathymetry; (B) DEM with marine terrace locations (Red dots) and toponomy (black dots).

The marine terraces at southwest Portugal are poorly preserved, generally absent of sediments and difficult to date. The only place where geochronology was applied was at one site where the lowest marine terrace was characterized, at Castelejo (Fig. 2 and 3).

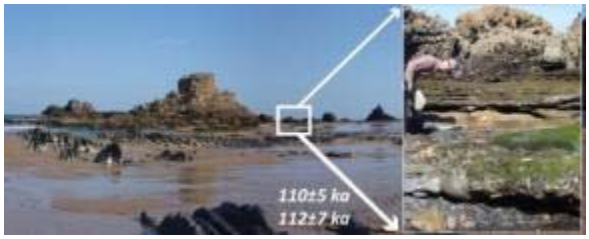

Figure 3: Marine terrace at Castelejo and sampling beach sands for OSL dating. Age results are indicated.

Here, a remnant of beach sand deposit was sampled for luminescence dating and dated in Nordic Laboratory for Luminescence, providing an age of 112 ± 7 ka (quartz, OSL) and 110 ± 5 ka (feldspar, PiRIR) which corresponds to the MIS 5c (Figueiredo, 2015). This did not change the uplift rate significantly, but it raised many questions on why MIS 5c was preserved and MIS 5a absent. Could it mean that the uplift rate was higher for MIS 5e and 5c and then decreased since MIS 5a?

Can it be that the age obtained is in fact representative of the age of the sediment? Dating sediments, such as the marine/ coastal ones that might have not completely bleached is a constrain recognized by several authors (Lamonthe, 2016; Murray et al., 2012).

The way to test these hypotheses is to re-evaluate this sediments age and in addition, applied geochronology techniques to other sites.

Where to collect data:

Portuguese coastal area is a very dynamic system, with a maximum meso tidal range of 4 m, and a maximum high-tide of circa 2 m. The area is frequently subject to a high energy wave and frequent storms with significant height and long wavelength periods. The average wave energy input for a representative site along the west facing coast reaches 40 to 45 kWm^{-1}/yr, significantly higher than sheltered location along the south facing coast that have values < 10 kWm^{-1}/yr (Figueiredo et al., 2013 and references within). This has two immediate consequences:
- one is that the identification of references for characterizing the vertical movement needs to be done more carefully, taking into account some of the problematic presented by Rovere et al. (2016); features such as storm benches, notches, and sea-caves, have larger dimensions than the ones forming at micro-tidal ranges.
- the second is that sediments from paleo marine terraces are easily eroded, and are missing. Rare exceptions correspond to too thin sediment cover or sediments preserved from erosion, if covered by dunes or colluviums.

Nevertheless, at some locations, some deposits were preserved and were sampled for luminescence. We revisited the sites previously described, and sampled at Castelejo site again and two additional sites: Amoreira and Furnas (see locations at Fig. 2, Amoreira is north of Bordeira and outside this map).

At Amoreira beach, one of the major exhorreic drainage in the area (Aljezur River) outflows to the Atlantic Ocean. Here, overlaying the abrasion platform trimmed on the Palaeozoic bedrock, a deposit of beach sand with some coarser pebbles is assumed to correspond to a marine/fluvial sediment, that is interpreted to correspond to the paleo outflow of Aljezur River. Overlaying this deposit, cemented aelionites covered these sediments (Fig. 4).

Figure 4: Marine/fluvial sediments at Amado beach.

The Furnas site (Fig. 5), is located in the bottom of a cliff, along the southern coast. The features interpreted on this site, lead to interpret this terrace as a very narrow terrace, close to the msl, with sub-aerial and submerged features, such as the presence of a small surge channel. Due to correlation with other sites elevations (all measured with GPS-RTK), this site was interpreted to be MIS 5a (despite evidences of a submerged section).

Figure 5: Furnas terrace: general perspective, shells and beach sand sampled.

New results:

All the samples were chemically processed and prepared for quartz and the equivalent doses were measured by a Riso Automated OSL Dating system, in the Luminescence Laboratory of the University of Cincinnati. To calculate the dose-rates, crushed bulk rock were sent to ACTLAbs for chemical analysis of the U, Th, K and Rb and later calculated through DRAC calculator (Aberystwyth University).

Two samples were collected at the Castelejo site, with the references "Cast –B" and "Cast-4". One sample was collected for Amoreira with the reference "Amor" and one sample for Furnas with the reference "Furnas".

To conduct an analysis of the equivalent doses for the grain populations, we are measuring a large number of aliquots (n), which will allow us to determine how well bleached the sediment was. The quality of the measurements is also tested through acceptance criteria. For example, for sample Cast -B, we measured 40 aliquots, and considered only 30 valid for Equivalent dose calculations. We then conducted an analysis of the equivalent doses for the grain population (Fig.6) following the mixture modeling algorithm of Galbraith and Green, through the method developed by Vermeesch (2009):

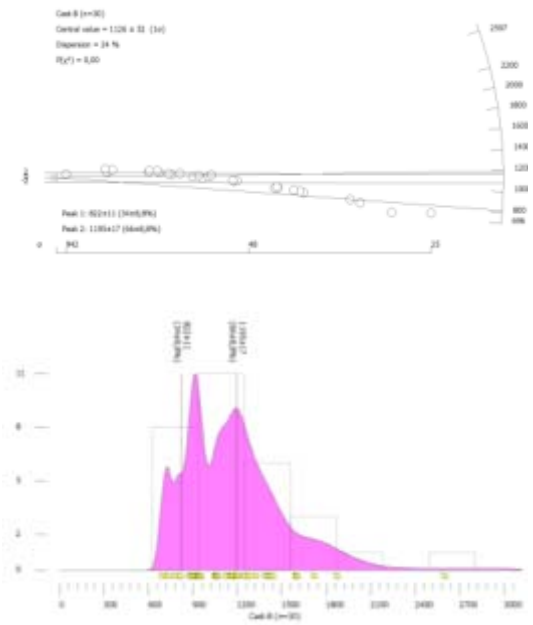

Figure 6: Analysis of equivalent dose distribution for sample Cast-B.

The analysis indicate that the sample, has a dispersion of 24%; the mixture modelling provides 2 larger peaks, a peak with the smaller equivalent dose with a value of 822 ± 11, and a second and higher peak with a value of 1195 ± 17. We consider that the smaller peak corresponds to the last time the sediment was exposed to sunlight and bleached, and therefore to be representative of the sediment age. In this case, an equivalent dose of 822 ± 11 along with a dose-rate of 1.054 ± 0.045, allows us to calculate an age of 85.09 ± 3.81.

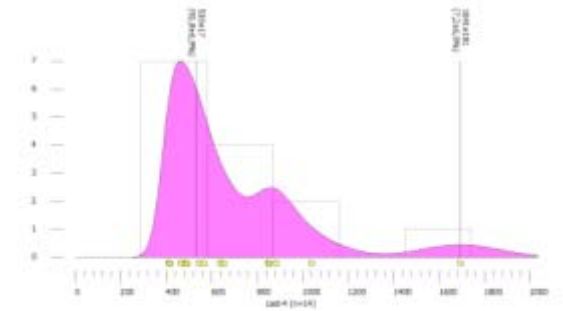

Figure 7: Density distribution for sample Cast-4 (smaller peak 530±17).

The same analysis can be conducted at Cast-4: although for both samples the dispersion is not high, the presence of grains with higher equivalent doses, probably corresponding to not fully bleached grains, can still be detected.

Sample Amor, has a really low dispersion (17%) and a narrow distribution (Fig. 8). We consider this to be a well-bleached sediment.

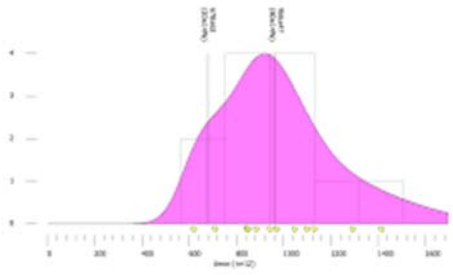

Figure 8: Density distribution for sample Amor (smaller peak 678±62).

Preliminary results for these 4 samples are presented in Table 1:

Sample	n	Weighted mean			Minimum age model		
Cast-B	30	95,85	±	4,2	85,09	±	3,81
Cast-4	14	80,61	±	8,12	78,99	±	7,97
Amor	12	71,66	±	7,75	82,19	±	9,36
Furnas	2	124,21	±	6,03		±	

Table 1: Preliminary results of the OSL ages, for SW Portugal.

CONCLUSION

New samples for luminescence dating were collected at marine terraces sediments at the southwest Portugal. The aim was to further investigate the sediments ages and infer uplift rates.

Although preliminary (we are still reading more aliquots), the results suggest that the sediment present at Castelejo beach, can correspond to the MIS 5a high-stand. The presence of grains with older equivalent doses can be an indicative of partial bleaching, and should be tested.

The correlative sediments located north at Amoreira beach, seem to correspond to younger than Castelejo, although still in the range of the MIS 5a high-stand time frame.

The Furnas paleo beach sand, only has a few reading and it is premature to make any conclusion. However, initial reading suggest that this could correspond to a older terrace, MIS 5e or even older.

Acknowledgements: This work was supported by Research Funds of the Department of Geology and the Quaternary Geochronology Laboratories of the University of Cincinnati.

REFERENCES

Cabral, J., 1995. Neotectónica em Portugal Continental. *Mem. Nº31, Inst.Geol.Min.*, 265 pp.

Cabral, J., 2012. Neotectonics of mainland Portugal: state of the art and future perspectives. *Journal of Iberian Geology* 38 (1), 71-74.

Figueiredo, P.M., 2015. *Neotectonic and Seismotectonic Studies along the Southwest Portugal sector: Implications for the regional seismicity*, Doctoral Thesis, Lisbon University.

Figueiredo, P.M., Cabral, J., & Rockwell, T.K., 2013. Recognition of Pleistocene marine terraces in the Southwest of Portugal (Iberian Peninsula): Evidences of regional Quaternary uplift. *Annals of Geophysics* 56 (6), *Special Issue Earthquake Geology,* S0672, doi: 10.4401/ag-6276.

Figueiredo, P.M., Rockwell, T.K., Cabral, J., & Ponte Lira, C., (in press). Morphotectonics in a low tectonic area: Analysis of the southern Portuguese Atlantic coastal region, *Geomorphology.*

Ressureição, R., Cabral, J., & Dias, R., 2012. Plio-Pleistocene marine terraces at the Melides-Vila Nova de Milfontes (Alentejo, SW, Portugal): neotectonic implications. In: *7th Symposium about the Iberian Atlantic Margin Book of Abstracts*, Lisbon.

Rovere, A., Raymo, M., Vacchi, M., Lorscheid, T., Stocchi, P., Gómez-Pujol, L., harris, D., Casella, E., O'Leary, M., & Hearty, P., 2016. The analysis of Last Interglacial (MIS 5e) relative sea-level indicators: Reconstructing sea-level in a warmer world. *Earth Science Reviews* 159, 404-427.

Siddall, M., Chappell, J., & Potter, E.-K., 2006. Eustatic Sea Level During Past Interglacials. In: The climate of past interglacials (Sirocko, F., Litt, M., Claussen, M., Sanchez-Goni, F., eds), Elsevier, Amsterdam.

Vermeesch, P., 2009. Radial Plotter: a Java application for fission track, luminescence and other radial plots. *Radiation Measurements* 44 (4), 409-410.

INQUA Focus Group Earthquake Geology and Seismic Hazards

paleoseismicity.org

Quaternary differential vertical motion at SW Iberia inferred by Plio-Pleistocene marine terraces and morphotectonics. Is there a new kid in the block?

Figueiredo, M. Paula (1), Rockwell, K. Thomas (2), Cabral, João (3), Cunha, P. Pedro (4), Rood, Dylan (5)

(1) Department of Geology, University of Cincinnati, USA, paulafigueiredo@uc.edu
(2) Department of Geological Sciences, San Diego State University, USA
(3) Instituto Dom Luiz, Faculdade de Ciências, Universidade de Lisboa, Portugal
(4)...Departamento de Ciências da Terra ,Universidade de Coimbra, Portugal
(5)...Department of Earth Science & Engineering, Imperial College London, UK

Abstract: *SW Iberia region is the closest onshore area to the complex setting of the Southwest Iberian Margin and Gulf of Cadiz, a part of the Eurasia-Nubia plate boundary. Here, a sequence of late Pleistocene marine terraces is present allowing to estimate an uplift rate of circa 0.11 mm/yr, higher than for neighboring regions. However, the long-term uplift rate for the same region is about 0.04 mm/yr based on dating of an early Pleistocene (2Ma) terrace, and using an MPWP geomorphic reference. This suggests an increase in the uplift rate sometime after early Pleistocene time. A detailed morphotectonic analysis highlights some active structures and corroborates the region with higher uplift. This, does not appear to be directly associated with a known active structure, although the uplift margin partially correlates with the São Marcos-Quarteira Fault. We infer the existence of an active structure that likely initiated or accelerated activity during the Pleistocene.*

Keywords*: SW Iberia, Pleistocene, marine terrace, morphotectonic, geochronology*

INTRODUCTION

Southern Portugal, located in SW Iberia, corresponds to the closest inland region to the Southwest Iberian Margin (SWIM) (Fig.1). SWIM is located NW of the Gulf of Cadiz, and has a complex tectonic setting, with NNE-SSW thrusts and interference with long WNW-ESE strike slip faults. The entire region hosts the eastern Atlantic section of the Eurasia-Africa plate boundary, with a NW-SE to WNW-ESE convergence at 4-5 mm/yr. It is also the locus of significant earthquake generation, such as the 1755 Mw>8 and the 1969 Mw 7.9 earthquakes.

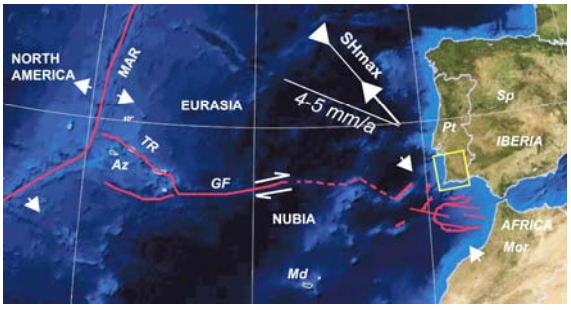

Figure 1: Geodynamic setting of SW Iberia. The study area is highlighted by the yellow rectangle.

Inland, several tectonic structures with Plio-Quaternary activity are known (Fig.2), mainly strike-slip faults with reverse components (corroborating a transpressive tectonic regime). Their activity rates are low, generally lower than 0.2 mm/yr (Cabral et al., 2012) and despite relevant historical seismicity and moderate instrumental seismicity, no Holocene or historical earthquakes with surface rupture have been identified.

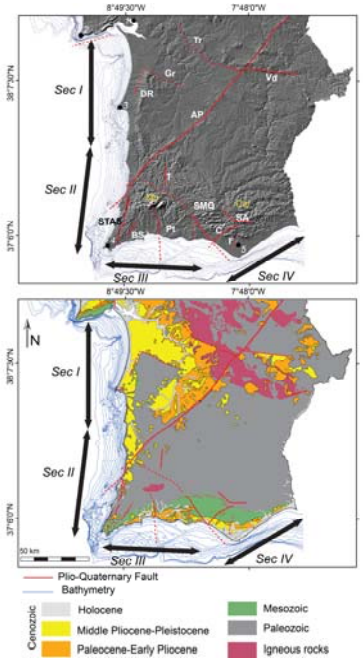

Figure 2: Main Plio-Quaternary tectonic structures at south Portugal, with a shaded relief DEM and geological map (Adpated from Figueiredo et al., in press).

DISCUSSION

Marine terraces

Efforts to characterize and quantify Pleistocene deformation in SW Portugal were conducted, in particular during the past decade (Dias, 2001; Figueiredo et al., 2010, 2013, 2016; Figueiredo, 2015). A sequence of poorly preserved marine terraces was recognized at consistent elevations along the entire SW region coast, and was inferred to be late Pleistocene in age (Figueiredo et al., 2013; Figueiredo, 2015). At one location, Castelejo, paleo beach sands were dated through OSL techniques, in the Nordic Laboratory for Luminescence Dating,providing an age of 112 ± 7 ka (quartz, OSL) and 110 ± 5 ka (feldspar, PiRIR) (Fig.3). These ages suggest a MIS 5c age for that terrace, as well as an uplift rate of 0.11 ± 0.01 mm/ yr. However, Ressureição et al. (2012), at a coastal section circa 100 km northwards estimated an uplift rate of 0.04 mm/yr based on geomorphology analysis, suggesting that the southern area is uplifting at higher rates.

Figure 3: Marine terrace at Castelejo and sampling beach sands for OSL dating. Age results are PiRIR for K feldspar.

Detailed topographic surveys and LiDAR analysis showed that marine terrace elevations are consistent along the western and southern coastlines of the south-westernmost region. A sequence of terraces was recognized from 2 to 40/45 m elevation, and inferred to correspond to global highstands ranging from MIS 5 to MIS 11/ 13 ((Siddal et al., 2006), assuming the same uplift rate recognized for the late Pleistocene (Fig 4).

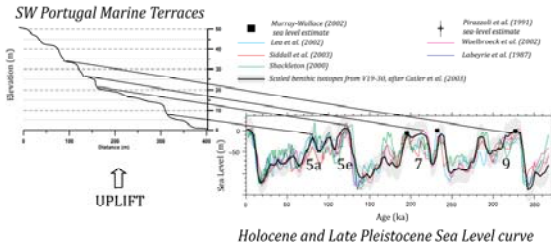

Figure 4: SW Portugal lower marine terrace sequence and correlation with Pleistocene sea level curve (Figueiredo et al., 2013).

Higher marine terraces are less preserved and more eroded. At Telheiro, a well preserved terrace with rounded boulders overlaying an abrasion platform trimmed across Triassic bedrock and covered by a thick marine sand cover, has an inner edge at circa 80 m elevation. In order to obtain an age for this landform, we sampled the basal unit, collecting quartz rich sand and gravel, to which we applied TCN Be^{10} and Al^{26}burial dating. Samples were processed at the Cosmogenic laboratories at the University of Glasgow and we obtained a preliminary age of 2.0 Ma $^{+0.3}/_{-0.2.}$ (Fig.5).

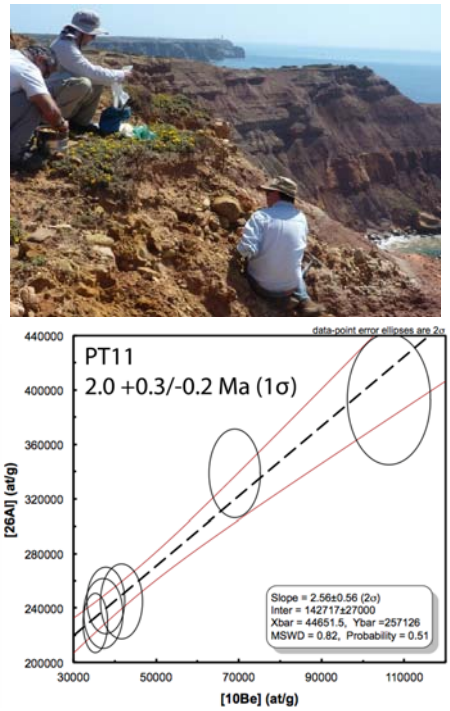

Figure 5: Sampling and age modelling for the Telheiro terrace, applying Terrestrial Cosmogenic Nuclide Be^{10} and Al^{26} burial dating.

The age obtained at Telheiro, provides an uplift rate of ~0.04 mm/yr, less than the uplift rate estimated for the late Pleistocene sequence. This lower and older vertical motion is also supported by additional evidence. At about 160 m elevation, there is a regional break in slope, between a broad regional abrasion platform and steeper relief. This is interpreted as corresponding to the mid-Pliocene Warm Period (3-3.3 Ma), a major reference during the Pliocene when the sea-level was higher than today by 20 to 25 m. If so, then the uplift rate inferred for this geomorphologic marker is also 0.04-0.05 mm/yr.

Altogether, these observations suggest that a regional uplift rate of 0.04-0.05 mm/a may have persisted from mid-Pliocene to early Pleistocene time, but sometime after that and likely before 400-500 ka (MIS 11/13), increased to an uplift rate of circa 0.11 mm/yr.

Morphotectonic analysis

A detailed morphotectonic analysis was conducted not only in the SW region, but for the entirety of southern Portugal, with two goals in mind. First, to investigate Quaternary active structural controls in the landscape and associated rates of deformation; and second, to investigate differential vertical motions and where they occur (Figueiredo, 2015; Figueiredo et al., 2018). For this, a total of nine morphotectonic indices were applied to a total of 77 catchments flowing to the Atlantic, along 460 km of coastline. The cross correlation of results highlighted the São Teotónio- Aljezur- Sinceira, a left-lateral fault system and São Marcos Quarteira, a right lateral strike slip

fault with a wide and complex fault zone, as major active structures in the SW region.

The cross correlation of geomorphic indices, as the valley-floor width and the terminal basin shape, along with other information, allowed confirmation of a change in the type of incision and valley shape, as well as changes in the shape of the catchment basin. Those changes were identified to occur south of Sines Cape southwards along the western coastline and east of the São Marcos-Quarteira Fault (Fig. 6). These are interpreted as responses to an increase in the uplift rate, and are shown to be consistent with the marine terrace observations (Figueiredo, 2015).

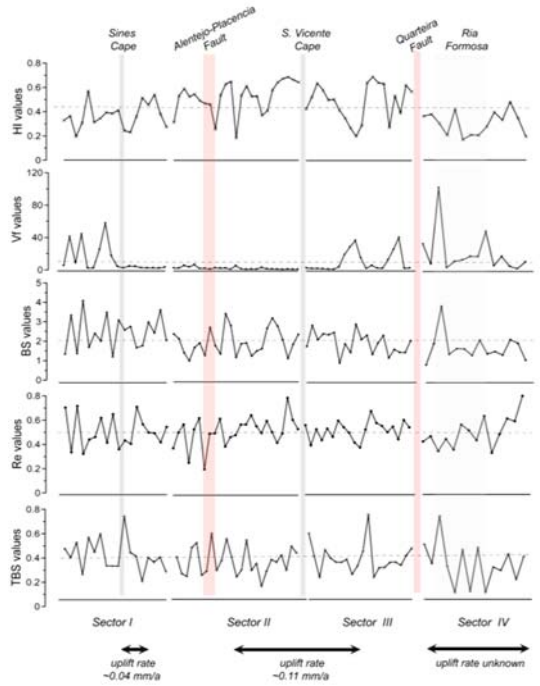

Figure.6 .Graphical plots of the HI values, basin shape indices and valley-floor width. Each point corresponds to one catchment. Overlapping the plots, the location of the main active faults that cross the coastline and geomorphic references are provided. In addition, information concerning uplift rates is also provided. (from Figueiredo et al., in press)

Based on these observations, it appears that the area corresponding to a higher uplift rate can be demarcated as a block. Additional analysis of further indices, such as basin asymmetries and the stream-length gradient, indicate that along this area, there are higher gradients and an absence of regional asymmetries. This suggests that the area is uplifting at a uniform rate, without any topographic surface tilting.

Although this higher uplift area seems to be limited to the SE by the São Marcos-Quarteira Fault, there is no known active structure that limits it the uplift region to the northwest. Moreover, the gradual southward increase in the uplift rate along the western coastline cannot be associated with any Quaternary structures that cross the coastline.

If there is a block with distinct geomorphology that is rising at a higher rate, as appears to be the case, what is driving this differential uplift behaviour and how is it express at the surface? What mechanisms and structures may be driving these processes?

Geodesy survey

Cabral et al. (2017) presented a regional crustal velocity analysis, based on the record of a network of campaign-style GPS stations established in southern Portugal almost 20 years ago, and complemented with younger permanent stations. These authors detected a difference in the horizontal velocities between the SW region and the remaining southern territory of Portugal. Thus, they inferred the presence of abroad right-lateral shear zone that partially coincides with the São Marcos Quarteira Fault. A prolongation of this structure is proposed, although its presence in the topography has not yet been recognized. Despite the presence of a distinct lineament in the landscape, this has been interpreted as resistant relief controlled by Devonian quartzite and Variscan structures.

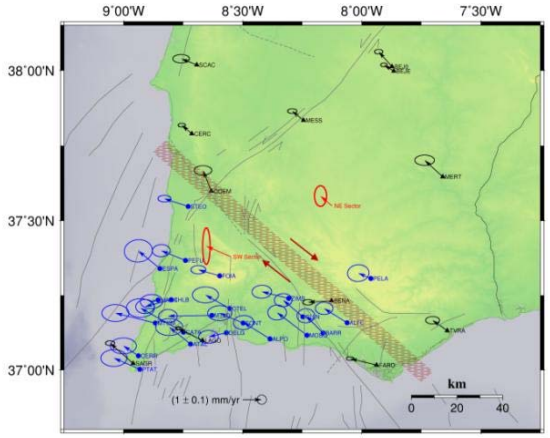

Figure 7: Proposed deformation zone, interpreted to be a right-lateral shear zone by Cabral et al. (2017). The map indicates estimated geodetic horizontal velocities, relative to Eurasia (ITR2008-PMM model). Black velocities refer to permanent stations, blue ones are GPS stations campaigns, and the weighted average velocities are in red colour; error ellipses at 95% confidence level. From Cabral et al. (2017).

Relationship with active offshore sources

The process that is driving the differential uplift of the SW Portuguese coast has not been attributed to any onshore structures that cross the coastline. Long wave length crustal deformation has been considered as a possibility, to justify the observations. However, the spatial variations point to a likely correlation with the São Marcos-Quarteira Fault inland. Nonetheless, it is still unknown whether there is a relationship with any active offshore structures. Modelling the expected surface deformation with the Coulomb software (Toda et al., 2011) for a rupture along the Marquês de Pombal and Horseshoe thrusts, assuming a vertical and horizontal displacement of 5 m and 2 m, respectively, and a fault dip of 30°, there is no vertical displacement expected for the onshore region (Fig.8). Modelling an increase in the displacements will only increase deformation closer to the fault zone and still cause no deformation inland. Therefore, we suggest that other structures, closer to coastline and not yet

characterized, might be responsible for accommodating this differential vertical motion.

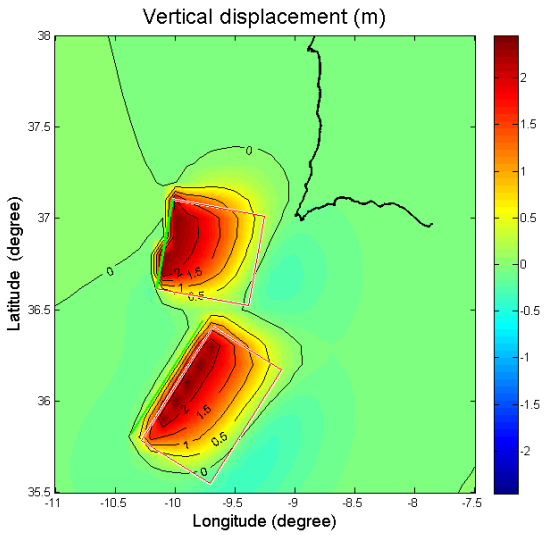

Figure 8: Modeling of the surface deformation for a combined rupture of Marquês de Pombal and Horseshoe thrusts, assuming a vertical displacement of 5 m and 2 m horizontal, and a fault dip of 30°.

Implications for seismic hazard

The onshore São Marcos Quarteira Fault has about 40 km and extends south-eastward into the offshore, where it continues for an additional 70 km (Fig.1). Considering that it also probably extends to the northwest, as a structure with a recent re-activation, we can add an additional 45 km potential fault length, making for a total of 155 km for this major fault zone. Considering scaling relationships in Wells & Coppersmith (1994), and using length and probable kinematics of this fault zone, this major regional fault zone may have the capacity to generate an earthquake with surface rupture with magnitudes ranging from Mw 6.9 to 7.5, depending if it ruptures one or more segments. There is no historical seismicity known for this structure, nor is there any paleoseismology data to suggest how often such ruptures may occur.

CONCLUSION

The combination of different data, analyses and geodetic surveys leads to the recognition of an area in SW Portugal that is behaving and most likely accommodating deformation differently than that of the remaining southern Portuguese territory. In addition, preliminary geochronology results suggest that there was an increase in the deformation rates during the Pleistocene. Characterized as a Plio-Quaternary structure, the São Marcos Quarteira Fault appears to correspond to a larger and regionally active structure with a relevant role in the morphological control of the landscape in southern Portugal. This structure is most likely a broad and complex zone of deformation, with low tectonic rates, which hinders its recognition and characterization at the surface. Nevertheless, the combination of all observations indicates its existence as a potential seismogenic source and, consequently, increases the seismic hazard for the region.

Further studies are being conducted to investigate this structure.

Acknowledgements: This work was funded by Fundação para a Ciência e Tecnologia, through a PhD scholarship (SFRH/BD/36892/2007) attributed to Paula Marques Figueiredo and and through project PTDC/GEO-GEO/2860/2012 (FASTLOAD).

REFERENCES

Cabral, J., 2012. Neotectonics of mainland Portugal: state of the art and future perspectives, *Journal of Iberian Geology* 38 (1), 71-74.

Cabral, J., Mendes, V., Figueiredo, P.M., Silveira, A.B., Pagarete, J., Ribeiro, A., Dias, R., & Ressureição, R., 2017. Active tectonics in Southern Portugal (SW Iberia) inferred from GPS data. Implications on the regional geodynamics. *Journal of Geodynamics* 112, 1-11.

Dias, R., 2001. *Neotectónica da Região do Algarve*, Ph.DDissertation, Univ. of Lisboa, 369 pp.

Figueiredo, P.M., 2015. *Neotectonic and Seismotectonic Studies along the Southwest Portugal sector: Implications for the regional seismicity*, Doctoral Thesis, Lisbon University.

Figueiredo, P.M., Cabral, J., & Rockwell, T., 2010. Southwest Portugal Plio-Pleistocene Tectonic Activity Studies: The S.Teotónio- Aljezur - Sinceira Fault System and Coastal Tectonic Uplift Evidences, Abstract book for the *1st Iberfault, Active Tectonics and Paleoseismology Iberian Meeting, Sigüenza, España*.

Figueiredo, P.M., Cabral, J., & Rockwell, T.K., 2013. Recognition of Pleistocene marine terraces in the Southwest of Portugal (Iberian Peninsula): Evidences of regional Quaternary uplift. *Annals of Geophysics* 56 (6)*, Special Issue Earthquake Geology,* S0672, doi: 10.4401/ag-6276.

Figueiredo, P.M., Rockwell, T.K., Cabral, J., & Ponte Lira, C., (in press). Morphotectonics in a low tectonic area: Analysis of the southern Portuguese Atlantic coastal region, *Geomorphology.*

Ressureição, R., Cabral, J., & Dias, R., 2012. Plio-Pleistocene marine terraces at the Melides-Vila Nova de Milfontes (Alentejo, SW, Portugal): neotectonic implications. *7th Symposium about the Iberian Atlantic Margin Book of Abstracts*, Lisbon.

Siddall, M., Chappell, J., & Potter, E.-K., 2006. Eustatic Sea Level During Past Interglacials. In: *The climate of past interglacials* (Sirocko, F., Litt, M., Claussen, M., Sanchez-Goni, F., eds), Elsevier, Amsterdam.

Toda, Shinji, Stein, R.S., Sevilgen, Volkan, & Lin, Jian, 2011. Coulomb 3.3 Graphic-rich deformation and stress-change software for earthquake, tectonic, and volcano research and teaching-user guide. *U.S. Geological Survey Open-File Report 2011–1060*, 63 pp.

Wells, D., & Coppersmith, K., 1994. New empirical relationships among magnitude, rupture length, rupture width, rupture area and surface displacement. *Bulletin of the Seismological Society of America* 84 (4), 974-1002.

INQUA Focus Group Earthquake Geology and Seismic Hazards

paleoseismicity.org

Active deformation between the Campania Plain and the Apennines based on integration of geological, geomorphological and seismological data

Forlano, Serena (1), Ferranti, Luigi (1), Milano, Girolamo (2)

(1) Dipartimento di Scienze della Terra, delle Risorse e dell'Ambiente, Università Federico II, Napoli, Italy, serena.forlano@unina.it
(2) Istituto Nazionale di Geofisica e Vulcanologia, Osservatorio Vesuviano, Napoli, Italy

Abstract: *We illustrate the preliminary results of a multidisciplinary investigation of the active deformation pattern along a NE-SW trending crustal transect in southern Italy between the Tyrrhenian margin and the Campania Apennines. This region encompasses two different tectonic domains of recent and active deformation. The Tyrrhenian margin to the west is a subsiding sector, and shows ~N-S trending Quaternary extension, a low-rate historical and instrumental seismicity, and the interplay between volcanic and tectonic processes. In contrast, NE-SW trending Middle Pleistocene-current extension and high-rate seismicity dominates the uplifting mountain chain to the east.*
We present the preliminary analysis of background seismicity and field geological-structural analysis, which have provided a first definition of the geometry and kinematics connected to major tectonic processes and of the structural transition between the western and eastern sectors.

Keywords*: Seismotectonics Campanian Plains Southern Apennines*

INTRODUCTION

Joint analysis of geological and geophysical data provides a valid approach to the characterization of active deformation in both volcanic and tectonic areas. Geological-structural and geomorphological observations can be used to characterize exposed or shallowly buried structures that have been active in the recent past, whereas background seismicity analysis provides information on the current activity of deeper structures. Integration of the two sets of observations allows bridging the gap between short and long-term deformation processes and mechanisms.

Active deformation in the Campania region of southern Italy occurs both at a local scale due to the presence of volcanic processes in the Tyrrhenian margin, and at a regional scale where it is expressed by extensional and transtensional tectonics that created the transition between the Tyrrhenian margin and the Apennines (Fig. 1).

The Tyrrhenian margin includes a submerged shelf, the volcanic areas around Naples, and the Campania Plain, which is a sector of high-rate Quaternary subsidence where a levelled, up to ~3.5 km thick extensional basin fill rests above a domino-block faulted substratum (Milia et al., 2003). Quaternary NNW-SSE trending extension was accommodated by E-W and ENE-WSW striking, listric-shaped normal faults (Fig. 1), which created major offshore and coastal depocenters segmented by buried ridges (Acocella & Funiciello, 2006; Milia et al., 2013). Although some of these faults are supposedly active and control the Late Pleistocene-Holocene volcanism, they are not associated to large earthquakes.

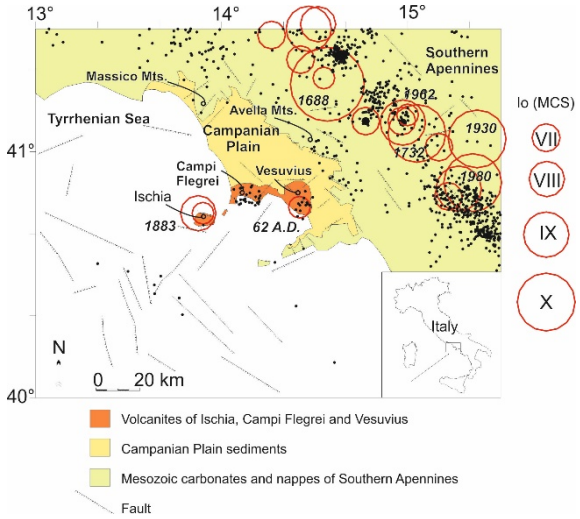

Figure 19: Schematic structural map of the northern Campania region (slightly modified from Milano et al., 2004). Open circles represent the large historical earthquakes that have occurred in the area. Black dots represent earthquake locations for events between 1983 and 2002 (from ING-GNDT, 2001).

Conversely, the nearby Apennines chain to the east is characterized by Pleistocene uplift and by NW-SE striking left-transtensional faults active under a ~NNW-SSE extension axis, similar to the one that in the Tyrrhenian margin is still active today. Since the Middle-Late Pleistocene, NE-SW extension on the same or newly formed faults, some of which are associated to large earthquakes that nucleate at 10-12 km depth (Ferranti et al., 2014), overprinted the earlier left transtension in the Apennines. Finally, active right-transtensional, E-W striking faults exist in the frontal-foreland domain east of the

Apennines, and recent studies have documented they also extend at higher crustal depths under the Apennines. However, to what extent the right-transtensional faults continue to the west and how they interact with the overlying extensional crustal panel are not yet clear.

The seismicity of the study area is very articulated (Fig. 1). The strongest historical earthquakes that have occurred in the Campanian portion of the Apennines were related to NW-SE normal faults. The most recent destructive earthquakes occurred in 1930 (Ms 6.7), 1962 (Ms 6.2) and 1980 (Ms 6.9). The focal mechanism of the latter event (Gasparini et al., 1985) show normal solutions with a NE–SW trending T-axis, in agreement with the strain regime acting in the Southern Apennines (Montone & Mariucci, 2016). In the last 30 years, seismicity is characterized by isolated event with M<3.5 and by the occurrence of low energy seismic sequences and swarms (MD max 4.6) (e.g. the 1990, 1996 and 1997-98 sequences; Alessio et al., 1996; Milano et al., 2002) with hypocentres within the first 15 km of the crust. In the Campanian Plain, the strongest events occurred at Ischia (1883 AD; Io VIII MCS; 2017, MD 4.0) and Vesuvius (62 AD, Io VII MCS). With the exception of the local seismicity of Vesuvio and Campi Flegrei volcanic areas, characterized by single and/or swarm-type activity of low energy (M<2.5), the background seismicity in the Campanian plain is characterized by temporally and spatially isolated events with magnitudes of less than 3.0. Seismic clusters are located close to the Massico mountain ridge, in the north-western sector of the plain, and along the Avella mountain ridge (Gaudiosi et al., 2012). Relatively to the Avella ridge, a low magnitude seismic swarm (M<3.5) occurred in 2005. The location of this swarm falls on the first Apennines spurs in the same place where in 1981 an M=4.9 event occurred. Recently (2017), a M_w=3.90 event occurred at Ischia and affect the same area of the 1883 destructive event. Offshore, isolated events occur (M max 3.7) at a depth not exceeding 13 km (Milano et al., 2004).

To better understand the structural interaction between the subsiding margin and the uplifting chain, and how active and seismogenic deformation is expressed in each sector, we started a multidisciplinary study along a NE-SW trending transect spanning the submerged shelf, the volcanic areas, the Campania Plain, the margin between the chain and the plain, and the axis of the mountain belt.

Analysis centres on merging different approaches and datasets including: a) geometric and kinematic characterization of structures responsible for major tectonic processes at the border between the margin and the chain and within the chain; b) characterization of the background seismicity in order to identify active seismogenic volumes. Section a) of the project uses structural and geomorphological data on-land, and interpretation of high-resolution seismic reflection profiles offshore, whereas point b) relies on the accurate epicentral and hypocentral relocation of last ~10 yr events and on the valuation of the fault plane solutions to retrieve information on the present-day kinematics of the active structures.

DISCUSSION

We show here preliminary results of the seismicity and subordinately of the geological-structural analysis, focusing on the boundary between the northern Campania Plain and the flank of the Apennines ridge.

Preliminary work on the exposed faults along the flank of the Apennines has shown a complex structural transition between the uplifting and subsiding areas, where the NW-SE striking faults are segmented by E-W striking faults, which control development of local, relatively deep local basins. Structural analysis revealed the existence of two sets of differently oriented slip lineations on the major faults, which we relate to two different kinematic regimes. A first set trends ~NNW-SSE and is associated to left-transtensional slip on the E-W striking faults. Instead, a second set trends ~NE-SW and is associated to normal to right-transtensional slip on the same faults. Whether the two are coeval or temporally superposed is not yet established using available data. Notably, the depth projection of the faults that have both normal and strike-slip motion broadly overlaps with the focal depth of events, which have a strike-slip focal mechanism.

The preliminary results on the analysis of the background seismicity that occurred in the last 4 years in the study area show that seismic activity in the Campanian Plain, with the exception of those related to the volcanic areas, is virtually lacking. The few seismicity localizes along the eastern border of the plain on the first outcrop of the Apennine Chain. Few low magnitude events, localized along the WNW-ESE lineament of the Avella Ridge, show kinematics that seem compatible with transtensional motion.

Future work at the transition between the margin and the chain will be devoted at a better definition of the kinematic of these faults and of the link between exposed boundary faults and background seismicity. Besides, we also aim at better characterizing active deformation in the chain where uncertainties on location and kinematics of major seismogenic structures persist.

REFERENCES

Acocella, V., & Funiciello, R., 2006. Transverse systems along the extensional Tyrrhenian margin of central Italy and their influence on volcanism. *Tectonics* 25, TC2003, doi: 10.1029/2005TC001845.

Alessio, G., Gorini, A., Vilardo, G., & Iannaccone, G., 1996. Low energy sequences in areas with higth seismic potential: Benevento (Sourthern Apennines), April 1990. In: Earthquake Hazard and Risk (Schenk, V., ed), 3-16.

Ferranti, L., Palano, M., Cannavò, F., Mazzella, M.E., Oldow, J.S., Gueguen, E., Mattia, M., & Monaco, C., 2014. Rates of geodetic deformation across active fault in southern Italy. *Tectonophysics* 621, 101-122.

Gasparini, C., Iannaccone, G., & Scarpa, R., 1985. Fault-plane solutions and seismicity of the Italian peninsula. *Tectonophysics* 117, 59-78.

Gaudiosi, G., Alessio, G., Cella, F., Fedi, M., Florio, G., & Nappi, R., 2012. Multiparametric data analysis for seismic source identification in the Campanian area: merging of seismological, structural and gravimetric data. *Bollettino di Geofisica Teorica ed Applicata* 53 (3), 283-298, doi: 10.4430/bgta0050.

Milano, G., Ventura, G., & Di Giovambattista, R., 2002. Seismic evidence of longitudinal extension in the Southern Appennines chain (Italy): The 1997-1998 Sannio-Matese seismic sequence. *Geophysical Research Letters* 29 (20), doi: 10.1029/2002GL015188.

Milano, G., Petrazzuoli, S., & Ventura, G., 2004. Effect of the hydrothermal circulation on the strain field of the Campanian Plain (southern Italy). *Terra Nova* 00 (0), 1-5, doi: 10.1111/j.1365-3121.2004.00556.x.

Milia, A., Torrente, M.M., Russo, M., & Zuppetta, A., 2003. Tectonics and crustal structure of the Campania continental margin: relationships with volcanism. *Mineral. Petrol*. 79 (1-2), 33-47.

Milia, A., Torrente, M.M., Massa, B., & Iannace, P., 2013. Progressive changes in rifting directions in the Campania margin (Italy): New constrains for the Tyrrhenian Sea opening. *Glob. Planet. Change* 109, 3-17.

Montone, P., & Mariucci, M.T., 2016. The new release of the Italian contemporary stress map. *Geophys. J. Int*. 205 (3), 1525-1531.

INQUA Focus Group Earthquake Geology and Seismic Hazards

paleoseismicity.org

Paleoseismology of the Western Garlock Fault at Campo Teresa, Tejon Ranch, Southern California

Gath, Eldon (1), Rockwell, Thomas (2)

(1) Earth Consultants International, Santa Ana, California, USA, gath@earthconsultants.com
(2) San Diego State University, San Diego, California, USA

***Abstract**: The 250-km-long northeast-trending Garlock fault in southern California bounds extension on the north from right-laterally slipping blocks to the south. Multiple paleoseismic sites have been published for the central and eastern segments of the fault, but only Twin Lakes on the western segment. A geotechnical investigation at Campo Teresa, 25 km west of Twin Lakes generated data for the timing of the last 2-4 rupture events. Two trenches exposed the northern and southern fault traces within a narrow stepover. The exposures allowed us to constrain displacements and ages based on two radiocarbon dates from colluvial deposits; two events since 1710±40 ybp and likely two events 1710 - 4100±40 ybp. The MRE and penultimate events appear to be similar 4-m left-lateral events on the southern fault, each with about 2 m of vertical separation on the northern fault.*

***Keywords**: Tectonic geomorphology, Paleoseismology, Garlock fault*

INTRODUCTION

The 250-km Garlock fault, one of the principal active faults in southern California, separates the Basin-and-Range extensional terrane to the north from the Mojave strike-slip faulting (Eastern California Shear Zone) to the south (Fig. 1). The fault appears to have initiated movement about 9 to 10 million years ago (Carter, 1987; Loomis & Burbank, 1988) and has since accumulated 56±8 km of sinistral displacement (Smith, 1962; Davis & Burchfield, 1973), providing a Miocene to present average slip rate of 5-7 mm/yr.

McGill & Sieh (1991) divide the Garlock fault into western, central and eastern segments. The western segment extends 100 km from the fault's intersection with the San Andreas fault near Frazier Park, eastward to the 3.5 km-wide Koehn Lake stepover. The central segment extends from Koehn Lake 105 km eastward to near Quail Mountain (Fig. 2), where the fault makes a distinct 15° bend. The eastern segment extends to the southern end of Death Valley.

Evidence for late Quaternary and Holocene activity is abundant along the length of the fault. Offset and deflected streams, offset alluvial fans, scarps, sag ponds, and linear valleys are well documented (Clark, 1973). Several studies have determined Holocene slip rates and event chronologies across the three segments (Fig. 2). At Searles Lake, McGill & Sieh (1993) determined a Holocene slip rate of 4-9 mm/yr, with a best estimate of 5-7 mm/yr, which is consistent with a rate of 5.3 +1/-2 by Ganev et al. (2012). These late Pleistocene-Holocene rates are similar to the Miocene-to-present rate, although almost double the current geodetic rate, leading to speculation that there are discrete cycles of strain along the Garlock fault (Dolan et al., 2016).

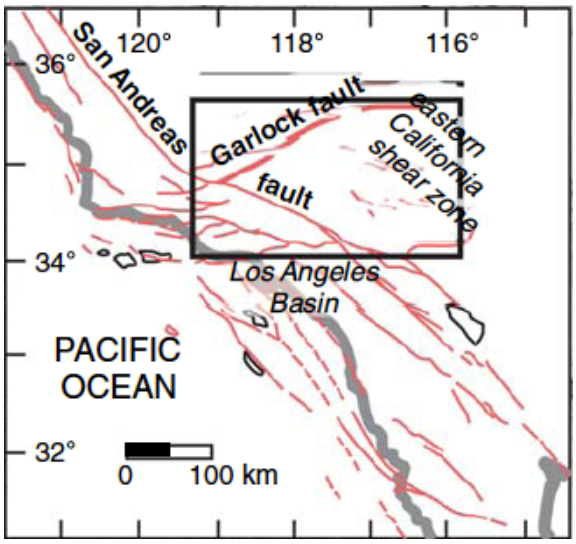

Figure 1: Location of the Garlock fault in southern California. Inset box represents the area shown in Fig. 2.

The slip rate of the western segment is constrained between 5.3-10.7 mm/yr (McGill et al., 2009). Considering the continuity of the fault and the absence of major structures that could decrease the average rate determined for the central section of the fault, this rate is unlikely to be correct.

Historically, the Garlock fault has been characterized by low levels of background seismicity, and the fault has not produced any large earthquakes with surface rupture, but the historical record in this area only goes back to the early to mid 1800s. Tectonic, geomorphic and paleoseismic investigations, in contrast, demonstrate that the Garlock has repeatedly failed in large surface-rupturing

earthquakes throughout the Holocene (Burke, 1979; McGill & Sieh, 1991, 1993; McGill et al., 2009; LaViolette et al., 1980; McGill & Rockwell, 1998; Dawson et al., 2003; Madugo et al., 2012).

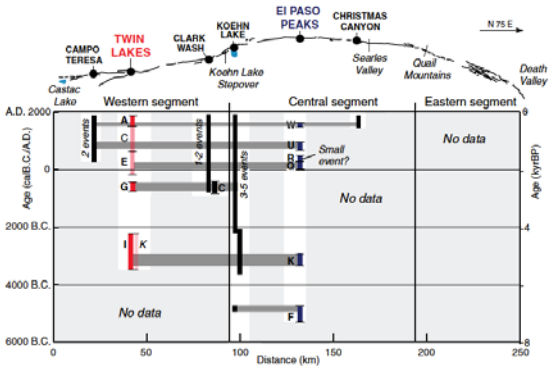

Figure 2: Earthquake chronologic correlations along the Garlock fault (Madugo et al., 2012). The Campo Teresa site is the westernmost paleoseismic site.

McGill & Sieh (1991), using offset gullies, terrace risers, channel walls, shutter ridges and other geomorphic features, determined that the central Garlock fault typically fails in large earthquakes with 3-7 m of slip. The past three earthquakes on the central segment near El Paso Peaks, all of which occurred in the past 1800 years, appear to have produced 18 m of slip (McGill & Rockwell, 1998; McGill & Sieh, 1991). Deeper trenching at the same site (Dawson et al., 2003) showed that six large earthquakes occurred during the past 7000 years along the central Garlock fault, with four of them during the past 2000 years. From this, they speculated that strain release was not cyclic, but rather occurred in clusters that may correlate to seismic activity in the Eastern California Shear Zone (Rockwell et al., 2001; Dolan et al., 2016). This is consistent with earlier work by Burke (1979) that demonstrated 9-17 events during the past 15,000 years near Koehn Lake, yielding a longer-term average recurrence rate of 860-1600 years.

Along the western segment, Stepp et al. (1980) found evidence for two Holocene surface ruptures at the Twin Lakes site, with the most recent occurring less than 890 $\pm$ 195 radiocarbon years BP. Later at Twin Lakes, Madugo et al. (2012) interpreted up to six events in the last ~5600 years through the site, including new timing constraints on the past two events (Fig. 2). McGill & Sieh (1991) identified geomorphic evidence for large slip events, with up to 7 m of displacement per event west of Koehn Lake. These observations suggest that the western Garlock fails about as frequently as the central Garlock, and may even fail together in very large earthquakes, as initially suggested by McGill & Sieh (1991). Fig. 2 illustrates the earthquake chronologies at each of the paleoseismic sites along the Garlock fault, and suggests that many of them can be correlated across multiple sites. The Campo Teresa site is the westernmost site with event data that have been used for event correlations. These data were generated during a geotechnical fault hazard study for planning of the Tejon Ranch (Fig. 3), and details of the event evidence at the site have never before been published. This paper provides the documentation for that site.

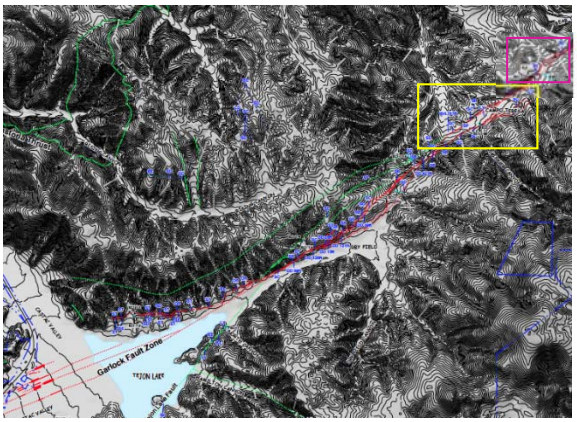

Figure 3: Geomorphic mapping of the Garlock fault along the extreme western segment across Tejon Ranch. Rattlesnake Canyon (Fig. 4) is shown by the pink box and the Campo Teresa site (Fig. 5) by the yellow box.

FAULT MORPHOLOGY ON TEJON RANCH

Across Tejon Ranch, the Garlock fault has tectonic geomorphology similar to the more easterly sections of the fault. The fault is readily expressed across the landscape by left-laterally deflected drainages, shutter ridges, and side-hill benches (Fig. 4).

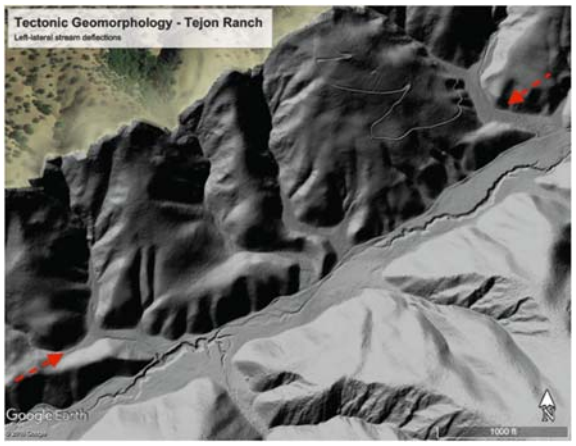

Figure 4: Tectonic geomorphology along Rattlesnake Canyon on Tejon Ranch, about 1 km NE of the Campo Teresa trenching site. The main Garlock fault trace is shown by the red arrows. The canyons are all left-laterally deflected about 125 m.

TRENCHING RESULTS

The Garlock fault is well expressed in the Campo Teresa area. Trenches T-9a and T-9b were located on the southern part of a linear valley, Trench T-10 was extended across a linear fault scarp on the north side of the valley (Fig. 5). Trenches T-9a and T-10 (Fig. 5) exposed fault strands that bound both sides of the linear valley. Below we discuss the findings in trench T-10 followed by T-9a and b.

Trench T-10 was placed across a linear scarp on the north side of the Campo Teresa valley. The excavation was 24 m long and up to 4 m deep. Limestone bedrock forms the hillside in the northern portion of the trench with colluvium and alluvium present in the central and southern portions, respectively (Fig. 7). The colluvium in this trench consists of friable, massive silty sand with scattered

pebbles but no large limestone clasts. The limestone in this area is highly fractured and locally sheared within the fault zone.

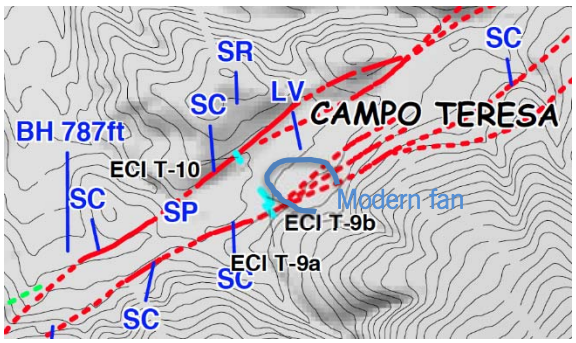

Figure 5: Campo Teresa trenching site showing the geomorphic mapping (SC-scarp, SR-sidehill ridge, SP-spring, LV-linear valley, BH-beheaded drainage) and the sites for trenches 9a&b and 10. Modern fan margin shown by blue line; with channel along western margin offset ~8 m through trench 9a.

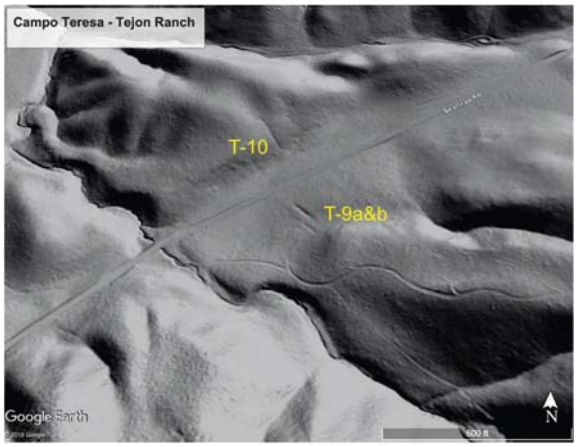

Figure 6: LiDAR image of the Campo Teresa area of Fig. 5 with the trench depressions still visible. Note the left-lateral stream deflection to the left of the T-9 trenches, but the lack of a similar deflection across the lineament trenched by T-10.

Two primary fault traces, about a meter apart, trending northeast and dipping to the south were observed within the bedrock. Both faults deform the overlying colluvium, and both vertically deform the base of the modern topsoil horizon similar amounts. A piece of detrital charcoal from the faulted colluvium yielded a radiocarbon age of 1710± 40 BP (Fig. 7). Based on its stratigraphic position immediately beneath a buried, weakly developed paleosol (buried A horizon), we interpret that this sample has experienced two rupture events, as follows. The penultimate event occurred when the paleosol was at the ground surface, down-dropping it at least 1 m vertically against the limestone and rotating it to subhorizontal.

The paleosol and scarp were subsequently buried by 2 m of colluvial sediments reestablishing the slope. The most recent event generated an additional 0.7-1 m of vertical separation on the same southernmost fault, with the formation of a minimum of a 0.5-0.7m surface scarp on both faults. The total vertical rupture separation, summed across the fault zone, is ~2 m in the penultimate event and ~1.5-2 m in the MRE. Lateral slip, if any, cannot be determined from this exposure.

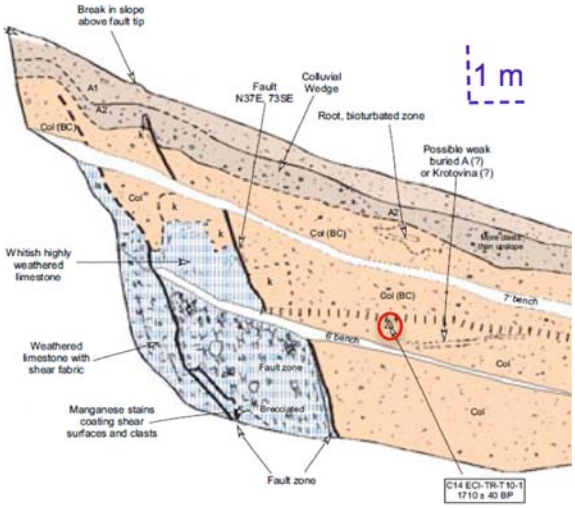

Figure 7: Graphic log of east wall of Trench T-10. Limestone is in blue, colluvium in orange, and colluvium-derived modern A-soil horizon, in brown. Red circle indicates the location of the 1710 ybp radiocarbon date from within the colluvium.

Trench T-9a was located at the gentle break in slope along the southern margin of the valley and was approximately 30 m long by 3 m deep (Fig. 6). The geologic units exposed in this trench included a surficial layer of colluvium underlain by granitic bedrock in the southeast (up-slope) portion of the trench and younger alluvium at the northwest end of the trench (Fig. 7). The bedrock is composed of friable, highly weathered Tejon Lookout granite. The colluvium consists of friable pebbly silty sand with weak soil development and a notable absence of granitic clasts.

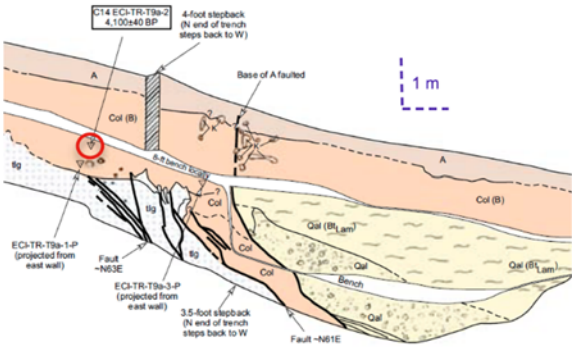

Figure 8: Graphic log of west wall of Trench 9a. Granite in white, colluvium in orange, alluvium in yellow, and modern colluvium-derived A soil horizon in brown. Red circle indicates the location of the 4100 ybp radiocarbon date from within the older colluvium, capped by younger colluvium above the bench.

A piece of detrital charcoal within the colluvium yielded a radiocarbon age of 4,100 ± 40 BP. This colluvium overlies several prominent faults within the bedrock as well as a fault that juxtaposes bedrock and older colluvial wedges faulted between the bedrock and the alluvial channel (Fig. 8). The alluvium is comprised of weakly stratified pebbly sand atop a clast-supported pebble gravel derived from an alluvial fan to the east (Fig. 5). Soil formation within the

sandy alluvium is limited to argillic (Bt) lamellae. The dated colluvium is overlain by another colluvial deposit, correlated to the 1710 ybp unit in T-10, that also overlies the alluvial deposits. The northernmost fault truncates the older colluvium against the alluvial units, continues through the overlying colluvium, and displaces the base of the A soil developed on the youngest colluvial deposit (Fig. 8). We interpret the truncation of the 4300 ybp colluvium as representing an earlier event pre-1710 ybp, and the offset, but undated, colluvial wedges within the fault zone suggest the possibility of more than one event in the time interval between 4300 and 1710 ybp.

The faults trend ~N62E and dip variably to the north. The fault exposed in Trench T-9a has a dominant lateral component and is along strike with the strand that beheads and left-laterally deflects a third-order drainage ~240 m (BH 787 ft on Fig. 5). Based upon field measurements of the fan margins, the fault has translated the alluvial fan deposits exposed in the trench (Fig. 8) a minimum of 8 m left-laterally, and up to 1 m vertically (Fig. 5). This alluvial channel deposit is stratigraphically equivalent to the paleosol in T-10 (Fig. 7) implying it is also about 1710 ybp and would have experienced two displacement events [see discussion of T-10].

Trench T-9b was located north of Trench T-9a to look for additional faults basinward (Figs 5 & 6). The trench measured approximately 38 m long by 4.5 m deep and exposed younger alluvium consisting of crudely bedded, friable, silty pebbly sand and sandy gravel with weak soil development similar in age to the uppermost soils in T-9a. No faults or fractures were observed within this trench indicating that the principal faults are on the margins of the valley.

CONCLUSIONS

The Campo Teresa site provides documentation for at least two western Garlock fault ruptures within the past 1700 years, and at least one additional event (likely two) between 1700 and 4100 ybp. The MRE is expressed by the 1.5-2 m vertical displacement of the modern surface soils overlying buried colluvial and alluvial units in T-10 (Fig. 8). Those colluvial deposits, and capping weak soil, were previously down-dropped a similar 2 m post-1700 ybp (Fig. 8). The 4100 ybp colluvial unit overlies several fault traces, but is truncated by a fault that pre-dates the penultimate event of about 1700 ybp (Fig. 7). The younger alluvial fan deposits exposed in T-9a were left-laterally offset about 8 m in 2 events. Those same two events likely generated the 2-m/event vertical separations in T-10. The two post-1710 ybp events were used by Madugo et al. (2012) in the along-fault event correlation (Fig. 2). Given that the data support the occurrence of at least one and probably two or more events between 1710 and 4100 ybp, these events may well correlate with the third and fourth events at the Twin Lakes site (Fig. 2).

Acknowledgements: This work was undertaken by Earth Consultants International as part of a multi-year geologic hazards investigation of Tejon Ranch for planning of their Mountain Village development project. The entire report can be accessed at http://www.co.kern.ca.us/planning/pdfs/eirs/TMV/TejonMountainVillage_App_G1.pdf. The trenches were logged by Aaron Meltzner, Chris Walls, Altangerel Orgil, and Molly Zorba. Tania Gonzalez and Chris Madugo provided valuable review of the paper.

REFERENCES

Burke, D.B., 1979. Log of a trench in the Garlock fault zone, Fremont Valley, California, U.S. *Geol. Survey Misc. Field Studies Map* MF-1028.

Clark, M.M., 1973. Map showing recently active breaks along the Garlock and associated faults, California, U.S. *Geol. Survey Map* I-741.

Dawson, T.E., McGill, S.F., & Rockwell, T.K., 2003. Irregular recurrence of paleoearthquakes along the central Garlock, near El Paso Peaks, California. *J. Geoph. Res.* 108, 2356-2385.

Dolan, J.F., McAuliffe, L.J., Rhodes, E.J., McGill, S.F., & Zinke, R., 2016. Extreme multi-millennial slip rate variations on the Garlock fault, California: Strain super-cycles, potentially time-variable fault strength, and implications for system-level earthquake occurrence. *Earth and Planetary Sci. Letters* 446, 123-136.

Ganev, P.N., Dolan, J.F., McGill, S.F., & Frankel, K.L., 2012. Constancy of geologic slip rate along the central Garlock fault: Implications for strain accumulation and release in southern California. *Geophysical J. Int*. 190 (2), 745-760.

LaViolette, J.W., Christenson, G.E., & Stepp, J.C., 1980. Quaternary displacement on the western Garlock fault, southern California. In: *Geology and Mineral Wealth of the California Desert, Santa Ana, California*, (Fife, D.L., Brown, A.R., eds), South Coast Geol. Soc., 449-456.

Madugo, C.M., Dolan J.F., & Hartleb R.D., 2012. New Paleoearthquake ages from the Western Garlock Fault: Implications for regional earthquake occurrence in Southern California. *B. Seism. Soc. of America* 102 (6), 2282-2299.

McGill, S.F., & Rockwell, T.K., 1998. Ages of late Holocene earthquakes on the central Garlock fault near El Paso Peaks, California. *J. Geophysical Res*. 103 (B4), 7265-7279.

McGill, S.F., & Sieh, K., 1991. Surficial offsets on the central and eastern Garlock fault associated with prehistoric earthquakes. *J. Geophysical Res*. 96, 21,597-21,621.

McGill, S.F., & Sieh, K., 1993. Holocene slip rate of the central Garlock fault in southeastern Searles valley, California. *J. Geophysical Res.* 98, 14,217-14,231.

McGill, S.F., Wells, S.G., Fortner, S.K., Kuzma, H.A., & McGill, J.D., 2009. Slip rate of the western Garlock fault, at Clark Wash, near Lone Tree Canyon, Mojave Desert, California. *Geol. Soc. Am. Bull.* 121, 536-554, doi: 10.1130/B26123.1.

Stepp, J.C., LaViolette, J.W., & Christenson, G.E., 1980. Seismic hazard of the western portion of the Garlock fault. *U.S. Geol. Survey, Open-File Rep*., OF 80-1172.

INQUA Focus Group Earthquake Geology and Seismic Hazards

paleoseismicity.org

Previewing tsunami risk in coastal zone of southern Aegean Sea

Gogou, Marilia (1), Andreadakis, Emmanuel (1), Nomikou, Paraskevi (1), Lekkas, Efthimios (1)

(1) National and Kapodistrian University of Athens, Faculty of Geology and Geoenvironment, Panepistimiopolis, Zografou, Athens, Greece, mgogou@geol.uoa.gr

Abstract: *This paper attempts to assess the tsunami risk in the area of the southern Aegean Sea as well as to preview this hazard in the present coastal areas of Folegandros, Sikinos, Irakleia, Schinoussa, Koufonisia, Keros, Amorgos, Astypalea, Anafi and Santorini. The risk zonation of these coastal zonesis based on measured run up values recorded in the last historical tsunami, after the Amorgos earthquake in 1956. The risk zones are overlain in current land uses of the islands and satellite imagery, highlighting the impacts of a potential tsunami in southern Aegean Sea in residential, tourist, industrial and agricultural areas. According to the risk assessment Matrix (using probability, frequency and intensity of tsunami) ,the study area requires organizational measures on the allocation of responsibilities and response, whereas, Santorini, Amorgos, Folegandros, Astypalea require immediate action, detailed planning and distribution of responsibilities at local and national level, as well as monitoring of tsunami.*

Keywords*: Tsunami, risk assessment, South Aegean Sea, coastal zone*

INTRODUCTION

The coastal zones are popular areas with high population density, tourist destinations, major business areas and natural crossing points due to their beauty, wealth and productivity. At the same time, coastal zones are among the most vulnerable areas to climate change and natural hazards. One of the potential hazards to the well-being of the population and to the economic sustainability of many businesses and activities is the risk of tsunami. There is a high potential for the generation of large tsunamis around the North and South Aegean Sea, as well as for destructive local events in near-shore zones (Theilen-Willige, 2008). The historic record shows that parts of both the Turkish and Greek coastlines were struck by destructive tsunamis (Yalciner et al., 2001, 2004). The wider region of the southern Aegean Sea is characterized by a particular geodynamic structure which, combined with the composition and morphology of the seafloor and the intense seismicity of the area, lead to a high-level and intermediate-level tsunami risk towards the shores of the islands (Papadopoulos et al., 2005; Papadopoulos et al., 2007). The ancient and modern history, provides significant examples of disasters caused by tsunami waves, with latest occurrence the one in Amorgos Island just 60 years ago, in 1956 (Okal et al., 2009), followed in size and extent by the Kos/Bodrum earthquake and tsunami of July 21st 2017 (Ocakoğlu et al., 2018).

In this study (Fig. 1), we analysed and processed all the testimonials, historical and scientific data, highlighting the magnitude and severity of the tsunami hazard in the coastal zone of the bustling islands of the southern Aegean Sea, in an attempt to answer a critical question: What would happen nowadays if a tsunami hit the area. This question is posed to emphasize the final conclusion which allocates the risk management which is needed in reference to the risk distribution on the study area.

Figure 20: Study area.

The aim of this study is to identify the coastal areas that could be affected by tsunami and not to calculate the potential tsunami magnitudes in the southern Aegean Sea. Hence, the risk zoning of the coastal areas is based on possible run-up value, which is probably the most basic feature for estimating the tsunami risk, as it indicates the height at which the water eventually manages to climb, entering the land. Taking into account the historical events that have already occurred on a global scale and the very distinctive coastal zone morphology and bathymetry of the southern Aegean Sea (Nomikou et al., 2012, 2013; Hooft et al., 2017), the coastal region of the islands are divided in 7 risk zones depending on how they could be affected by a future tsunami.

METHODS

In order to preview the seismic hazard in the coastal zone, ArcGIS applications were used, creating the risk zoning on the altitude maps of each area. This zoning was then overlain to satellite imagery, highlighting exactly the areas in which an upcoming tsunami would hit nowadays at all probable run-up ranges of 0-3, 3-5, 5-10, 10-20,20-30,30-50 ,> 50 meters. This gives an initial picture of the coastal areas in need of further attention in the case of this future risk, as the low-gradient coasts would allow the tsunami waves to penetrate both deeper and higher inland (inundation and higher inundation) and thus to have an extensive flooding. Furthermore, we importeddata from the latest recorded tsunami event in the area, in Amorgos in 1956, so as to be able to carefully exclude areas that are considered to be safer and protected and to isolate the most vulnerable ones. More specifically, the witnessed or recorded run-up values are pointed out on the risk zone maps. In addition, the coastal morphology was taken into account; where the zoning is virtually unobtrusive and looks uniform, it involves the presence of steep gradient shores that create rocky cliffs. The available 1956 tsunami run-up values of Folegandros, Amorgos, Astypalea, Anafi and Santorini are coincide with the implementation of the zoning in this study.

RESULTS

As a first result of the implementation of the risk zoning, is that some of the coastal zones of these islands could be characterized as naturally protected areas against tsunamis. Steep slopes along most of their coastlines, serve as a natural "wall" towards large waves. By concentrating the majority of their inhabitants, their infrastructure and their activities in the mainland, they are at very low hazard risk. But this does not exclude the risk to their port facilities and the small number of bathing beaches, especially during the summer period. Such islands are Anafi, Folegandros, Sikinos, as well as some parts of Amorgos.

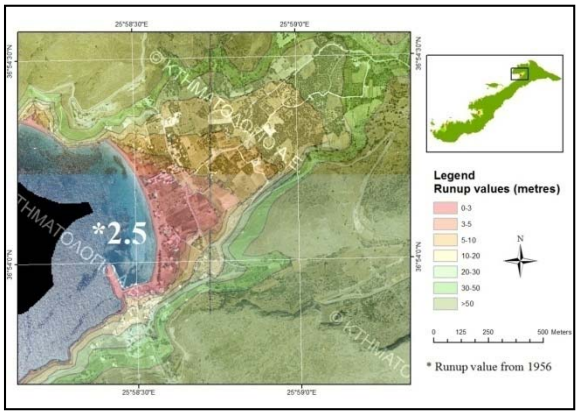

Figure 2: Aigiali, Amorgos.

The coastal zone of Amorgos is characterized by both high risk and low risk areas. The southern side of the island consists of steep, rocky high-altitude coastlines, while the northern part is characterized by mild slopes, allowing the water to penetrate several meters into the coastal zone. Nevertheless, the risk in the southern side cannot be ignored for two reasons: firstly, because in the last tsunami of 1956 (Okal et al., 2009) the highest run-ups were recorded due to its short distance and relative position to the Amorgos fault zone (Nomikou et al., 2018) and secondly, on the basis of satellite imagery, the presence of beaches used by bathers is evident, during the summer months. On the northern side of the island, Rachidi and Aigiali bay (Fig. 2), the inhabited areas with high touristic development and the presence of the two largest ports of the island, appear to be most affected.

The distinctive morphology of the island of Astypalea, combined with low altitudes in the center of the island, constitutes an area rather vulnerable to tsunamis. In Astypalea several run ups from the 1956 tsunami were recorded, ranging in size from 2.5 to 10m (Okal et al., 2009). Zoning of the risk in the coastal zone of the island seems to be in line with the distribution of these values. The center of the island in the form of a thin line of land, presents the greatest risk. As the main road network passes through it, water with moderate run-ups (≥ 10) can cover, in some places, the entire breadth of the land, cutting off the island in two. The island's airport, although located in the center of the island, is at an altitude that can be affected by run ups exceeding 20 meters. The areas with the highest risk are: a) Livadia, where it seems that even with minimum run up values (first and second risk zones 0-5 meters) water appears to affect most of the settlement (Fig. 3), b) the main town of Astypalea c) the area of Analipsi, d) the area of Agios Ioannis and e) the whole bay in Vathy.

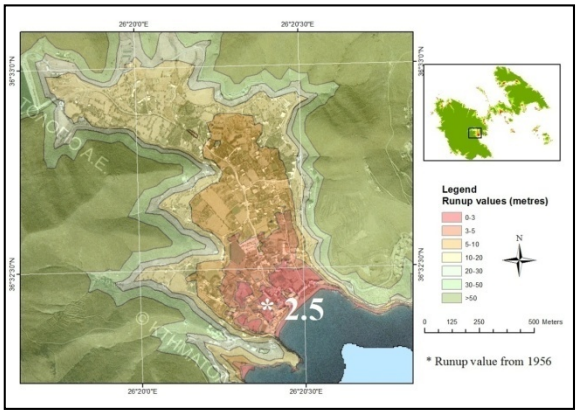

Figure 3: Livadia, Astypalea.

The implementation of the zoning shows that even with minimum wave action, coastal infrastructure, road networks, housing, tourist activities and port facilities are affected.

Anafi and Sikinos are among the islands with a steep rise in altitude on their coastline. Residential areas, towns and villages are mainly located at the most central points of the islands and in general outside the coastal zone. As a result, they escape the devastating impact of a potential tsunami in the area. However, their port facilities are vulnerable, as well as the tourist infrastructure and activities covered by the most vulnerable zone of 0 to 3m. In Sikinos, the only residential area located within the coastal zone is the Alopronia area, at the eastern part of the island. In this area, apart from the port facilities, it seems that coastal dwellings, some of which are tourist accommodation situated opposite the jetty and tangentially oriented along

the coastline, actually touch the sea, with a nearly zero altitude difference from its level, thus increasing the risk.

In Folegandros, the depiction of the zoning presents similar effects to those of Anafi and Sikinos. Due to the coastline's steep slopes, it is considered generally protected. However, in the southern part of the island, large run ups were recorded in 1956, which if they were to occur today, they would jeopardize the entire Agkali settlement and the beaches on the southern coastline (Fig. 4).

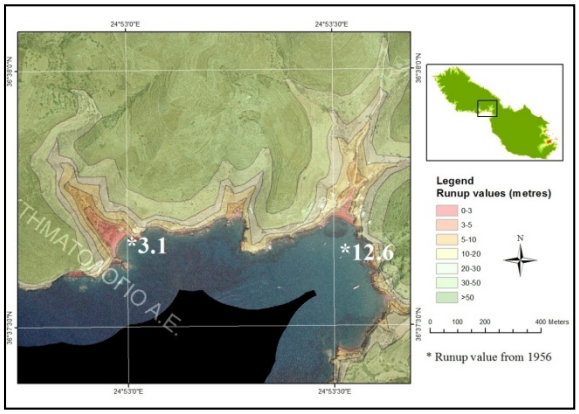

Figure 4: Agkali, Folegandros.

In Ios, in the area of the island's main town (Fig. 5), where the harbor is located, the altitude gradients are mild, thus permitting the 0 to 3m run up zone to inundate up to a distance of about 300m, the 3 to 5m zone up to a distance of about 600m and the 5 to 10m zone over one kilometer inland. In that area, there is a large number of residential and tourist accommodation, part of the town's road network and port facilities. In Ios, the region of Mylopotas is also at risk. It is characterized by extensive tourist development with many recreational businesses, tourist accommodation and campsite facilities at an altitude of less than 5 meters above sea level, therefore within the 3 to 5m run up zone.

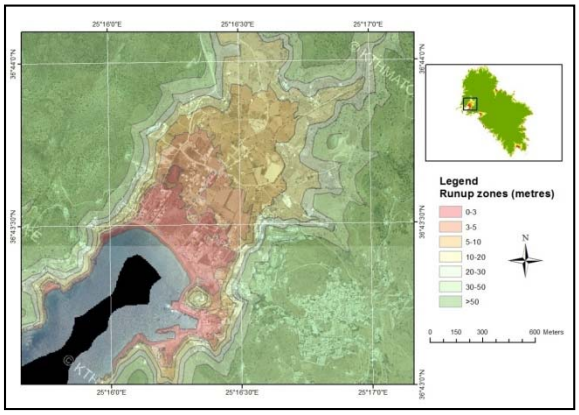

Figure 5: Main town of Ios.

Santorini is the island identified with the highest risk in the event of a tsunami amongst all the islands of the current study where the risk zoning was applied. That is mainly due to the very mild slope gradients throughout the eastern coastal zone. This risk is further increased due to the island's location, since it is very close to the active offshore fault zones (Nomikou et al., 2018) but also due to the existence of active submarine volcanic cones, north-east of the island (Nomikou et al., 2012). In the area of Monolithos, apart from houses located in the 0-3, 3-5 and 5-10m run up zones, there is also the main power supply unit of the island, which could be hit, should run up exceed 3m. Approximately 150m to the hinterland is located the northern part of the airport, which at this point is affected by run up values > 20m (Okal et al., 2009). The southern part of the airport, which is affected by quite low values > 2m, is considered more vulnerable. The area of Kamari, located a little further south, is a region with great tourist development. Leisure and tourist facilities such as sun loungers, umbrellas, special platforms along the coastline and alongside the coastal road network occupy an area within the 0-3m run up zone. In the following two risk zones of 3-5 and 5-10m run ups, houses, tourist accommodation, catering establishments, convenience and other stores, entertainment centers are lined up. The same applies for the Perissa area, which is located even further to the south. The risk zoning becomes even more visible and evenly positioned on the map (Fig. 5). This area hosts, most of the year, a population 10 times the size of the permanent residents'. Particularly in the summer months, the number of people enjoying Perissa's coastal zone or people active in local businesses is very large, heightening the risk in the event of a hazardous phenomenon. At the same time, in this area, the 0-3 m zone can refer to inundation values > 200m, which means that even with the smallest action of a tsunami wave, a large part of the area will be affected.

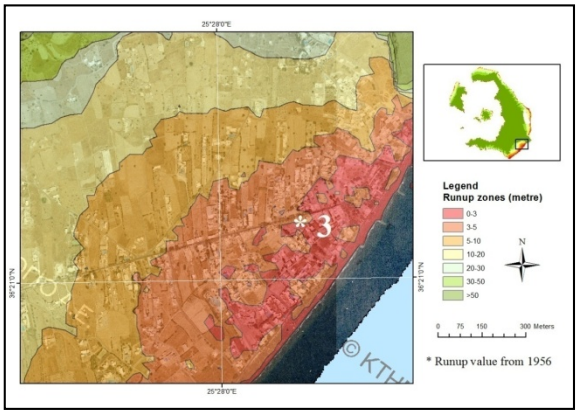

Figure 6: Run up zoning, Perissa area, Santorini.

The preview of the run-up values which is presented in this study, highlights the impact of a potential tsunami of almost any intensity occurring in the region of the southern Aegean islands, nowadays.

However, in order to approach and resolve the real risk of these coastal areas, we also account the data relating to the probability, frequency and possible starting point of the tsunami. In addition to the starting points of the tsunami, the connection of all remaining data (probability, frequency, intensity) was carried out with the help of a risk matrix. A risk matrix is a table consisting of various "probability" or "frequency" categories in its rows or columns (X or Y axis) and various "severity" or "impact" categories on the other axis, respectively (Louis, 2008).

For this risk matrix, at axis X: frequency, South Aegean tsunami history days and at axis Y: impacts, tsunami phenomena that have been recorded in the area, for which there are sufficient data to classify them according to the 12-grade Tsunami Intensity Scale ITIS 2012 (Papadopoulos, 2007; Lekkas et al., 2011, 2013).

With the help of this matrix, the risk was assessed for each coastal zone of the islands, in order to create a tool for setting priorities for both the monitoring of the natural phenomenon and for the process of taking preview and response measures (Louis A, 2008). Except the zoning areas, this risk matrix also includes the very recent events of Lesvos (2017) (Papadopoulos et al., 2017; Papadimitriou et al., 2017) and Kos (2017) (Ocakoğlu et al., 2018; Kiratzi & Koskosidi, 2018), the Amorgos (1956) event (Okal et al., 2009) and the event of the tsunami triggered from the eruption of the volcano of Santorini (1600 BC) (Novikova et al., 2011).

The results of the risk matrix show that most of the studied islands in the southern Aegean Sea are consideredin High Risk areas or areas in need of Direct Measures. As we refer to impacts, these areas in the 60s clearly did not have the same residential and anthropogenic development as nowadays. Thus this study is an attempt to highlight the risk of a potential tsunami of corresponding intensity of today, for the islands with recorded data from the 1956 tsunami. Additionally, risk zoning as described above, has been applied to recent satellite imagery based on the run up range.

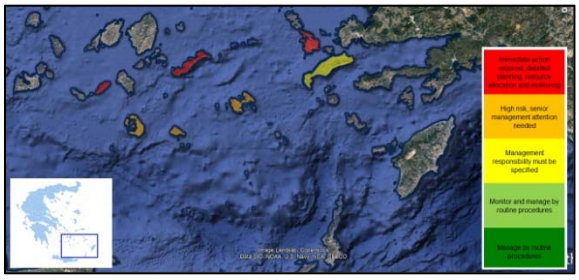

Figure 7: Tsunami risk in south Aegean Sea. Red: Immediate action required, Orange: High risk, senior management attention needed, Yellow: Management responsibility must be specified, Light Green: Monitor and manage by routine procedures, Green: Manage by routine procedures.

CONCLUSIONS

South Aegean region has a history of tsunami events, both in antiquity, in the historic and very recent past, showing the existence of a real threat to the coastal zone of its islands. From historical records, it seems that he latest huge tsunami in 1956, did not have such a big impact on local society mainly because residential and touristic development had not yet flourished in the 1950s. Today, on the same islands, the development of anthropogenic activities is high enough, to consider low value run-up as highly hazardous. They could cause severe impact, especially in the summer months when the population is concentrated near the coastline. Furthermore, the large number of tourists during the summer months and their safety is under the responsibility of the Greek Civil Protection. Summarizing the results of the preview of the tsunami risk in the coastal zone of the southern Aegean islands nowadays and in the future, the study highlights the urgent need of preventive and protective measures that could be considered as part of the implementation of the Integrated Coastal Zone Management in this region.

The distribution of these actions and the priority for the design of strategies for the protection of the southern Aegean Sea from a tsunami incident can be based on the Risk Matrix of the current study, which is also a useful tool for future risk assessment for any area deemed necessary.

REFERENCES

Hooft, E.E.E., Nomikou, P., Toomey, D.R., Lampridou, D., Getz, C., Christopoulou, M-E., O'Hara, D., Arnoux, G.M., Bodmer, M., Gray, M., Heath, B.A., & VanderBeek, B.P., 2017. Backarctectonism, volcanism, and mass wasting shape seafloormorphology in the Santorini-Christiana-Amorgos region of theHellenic Volcanic Arc. *Tectonophysics* 712-713, 396-414.

Kiratzi, A.A., & Koskosidi, A., 2018. Constrains on the year source motions of the Kos-Bodrum 20 July 2017 MW6.6 earthquake. 16th European Engineering. Thessaloniki 18-21 June 2018.

Lekkas, E., Andreadakis, E., Kostaki, I., & Kapourani, E., 2011. Critical Factors for Run-up and Impact of the Tohoku Earthquake Tsunami. *International Journal of Geosciences* 2, 310-317.

Lekkas, E., Andreadakis, E., Kostaki, I., & Kapourani, E., 2013. A Proposal for a New Integrated Tsunami Intensity Scale (ITIS-2012). *Bulletin of the Seismological Society of America* 103 (2B), 1493-1502.

Louis A., 2008. What's wrong with Risk Matrices. *Risk Analysis* 28, No. 2.

Nomikou, P., Carey, S., Papanikolaou, D., Croff Bell, K., Sakellariou, D., Alexandri, M., & Bejelou, K., 2012. Submarine Volcanoes of the Kolumbo volcanic zone NE of Santorini Caldera, Greece. *Global and Planetary Change* 90-91, 135-151.

Nomikou, P., Papanikolaou, D., Alexandri, M., Sakellariou, D., & Rousakis, G., 2013. Submarine volcanoes along the Aegean volcanic arc. *Tectonophysics* 597-598, 123-146.

Novikova, T., Papadopoulos, G.A., & McCoy, F.W., 2011. Modelling of tsunami generated by the giant Late Bronze Age eruption of Thera, South Aegean Sea, Greece. *Geophys. J. Int*. 186, 665-680.

Okal, E.A., Synolakis, C.E., Uslu, B., Kalligeris, N., & Voukouvalas, E., 2009. The 1956 earthquake and tsunami in Amorgos, Greece. *Geoph. J. Int*. 178, 1533-1554.

Ocakoğlu, N., Nomikou, P., İşcan, Y., Loreto, M.F., & Lampridou, D., 2018. Evidence of extensional and strike-slip deformation in the offshore Gökova-Kos area affected by the July 2017 Mw6.6 Bodrum-Kos earthquake, eastern Aegean Sea, doi: 10.1007/s00367-017-0532-4, GMLE-D-17-00084.1.

Papadopoulos, G.A., & Fokaefs, A., 2005. Strong Tsunamis in the Mediterranean Sea: A re-evalucation. *ISET, Journal of Earthquake Technology* 42 (4), 159-170.

Papadopoulos, G.A., 2007. *Quantification of Tsunamis: The New 12-Point Tsunami Intensity Scale.* Intrernational Center for Theoretical Physics.

Theilen-Willige, B., 2008. Tsunami hazard assessment in the Northern Aegean Sea. *Science of Tsunami Hazards* 27 (1), 1-16.

Yalciner, A.C., et al., 2001. *Field surveys and modeling of the 1999, Izmit tsunami*, 4-6.

INQUA Focus Group Earthquake Geology and Seismic Hazards

paleoseismicity.org

The hidden part of the fault activity in the landscape evolution of the Mejillones Peninsula northern Chile, what does it tell us for fault growth and fault-hazard assessment?

Gonzalez, Gabriel (1), González, Yerko (1), Cortes, Joaquin (2), del Rio, Ian (1)

(1) CIGIDEN (Centro para la investigación y gestion integrada de desastres naturales), Universidad Católica del Norte, Antofagasta, Chile
(2) Departamento de Geología, Universidad de Concepción, Chile.

Abstract: *In this contribution is discussed the role of normal faulting in the morphology of the Mejillones Peninsula (22ºS). We document the contribution of two major faults (Mejillones Fault and Caleta Herradura Fault) in the position of flying marine terraces. This aspect is a key element to understand the kinematic link between these two major normal faults and to unravel how these faults have accumulated vertical displacement since Pliocene to the Present. In order to provide constrain for fault-hazard assessment we estimate slip rates for these two faults. Our main conclusion is that Caleta Herradura Fault and Mejillones Faults are Quaternary active faults, kinematically linked, the reduction in south direction of the vertical slip in the Mejillones Fault is balanced by the increase in the vertical slip along the Caleta Herradura Fault. Slip rates on the fault are similar, by with strong variation along strike.*

Keywords*: Quaternary Normal faulting, marine terraces, tectonic morphology, Mejillones Peninsula, northern Chile*

INTRODUCTION

The Mejillones Peninsula, located in the northern part of Chile, is a key place for understanding the interlink among fault activity, surface uplift and landscape evolution. Horst and half-graben topography in this peninsula gives clear evidence for active normal faulting during the Quaternary. Two major horsts configure the first order topography of the Mejillones Peninsula (Armijo & Thiele, 1990; Niemeyer et al., 1996; González et al., 2003; Marquardt, 2005; Victor et al., 2011). The most significant faults are the Mejillones Fault and Caleta Herradura Fault. These faults have accumulated vertical displacement greater than 500 m since the Miocene producing two prominent NS elongated fault scarps (Allmendinger & González, 2011), which separate marine sediments in the lowland areas (Pampa Mejillones-Pampa Herradura and Pampa Aeropuerto, Fig. 1) from Palaeozoic and Mesozoic metamorphic and igneous rocks. The prominent horst structures are located to the western side of these two faults. Abandoned beach ridges ornament the surface of the two down-going blocks indicating sea regression and net uplift of the hangingwall. From the concave to the sea arc pattern of these beach ridges it is possible to infer that sea retreated from the central part of the Mejillones Peninsula to the north and to the south. The horsts contain several flying marine terraces and paleo-sea cliffs formed in metamorphic and igneous rocks. A (up to 100 m high) major paleo-cliff is conspicuously visible in satellite images of the area (Fig.1). This cliff separates high lying Pliocene marine terraces from low-lying Pleistocene marine terraces. In this contribution we discuss the role of fault activity in configuring the morphology of the horsts, particularly in the vertical position of marine terraces and the along horst variation of the altitude of paleo-shoreline angles. By this analysis we recovered the tectonic signal induced by normal faulting in the landscape configuration at hectometric scale. Furthermore, we estimated how fault displacement varies along fault strike and how these faults have grown since the Pliocene to the Present. Our work is based on a detailed field characterization of marine stratigraphic markers, the use of a 5 m resolution Digital Elevation model and topographic levelling of marine terraces and shoreline angles using dual GPS. In order to identify shoreline angle, we analyse swath profiles with the matlab script TerraceM (Jara-Muñoz et al., 2016). The accuracy in altitude of shoreline angles given by this method is ca 3 m. In order to increase the accuracy we use dual GPS to measure the altitude of shoreline angles. In this case instrumental accuracy is below 1 cm. Because of erosion and partial covering of wave cut notches the exact position of shorelines remain in the order of 1 m. To constrain the age of marine terraces we use paleontological determination of malacofauna association included in remnant marine sediments and tephra geochronology based on single crystal Ar^{40}/Ar^{39} determinations.

MARINE TERRACE CONFIGURATION

The two horsts expose a conspicuous Paleocoastal Cliff, which separates the high lying marine terraces from low lying marine terraces. This Paleocostal Cliff can be delineated surrounding the highest part of the Morro Mejillones horst and Morro Jorgino horst. A relevant aspect is that the high lying marine terraces contains malacofauna association of Pliocene age including a large number of *Trachycardium procerum, Anomia Peruviana and Dosinia ponderosa, which are* mixed with Pliocene taxa such as *Chlamys Vidali, Chama pellucida* and *Glycymeris ovatus*. According to Ortlieb et al. (1996) the first three species represent particular pale-oceanographic condition dictated

by elevated sea surface temperature. Presently this type of association is living in the Pananic Provincia and in the Paita Transition Zone (4-6 ºS). An Ar^{40}/Ar^{39} of 3.67 ± 0.02 Ma obtained in a single-crystal of Sanidine extracted from an ash layer interbedded with marine sediments exposed at southern tip of the Morro Mejillones Horst and covering the highest marine abrasion platform indicates that these high lying marine terraces are Pliocene in age. This observation confirms the Ar^{40}/Ar^{39} age of 3.25 ± 0.17 Ma obtained in ash layer covering the highest marine terrace surrounding the summit of the Morro Mejillones horst (Marquardt, 2005). In the low-lying marine terraces malacofauna association preserve a great number of *Argopecten purpuratus* and *Concholepas concholepas*, which indicate a Pleistocene age. In the central part of the Mejillones graben (Tiburon Basin) an ash bed dated in 672.7 ± 43.9 Ky by Ar^{40}/Ar^{39} in biotite separates an underlying section containing the Pliocene fauna association from shallow marine conglomerate including Pleistocene taxa. This relationship clearly shows that shallow marine coastal deposits covering the Mejillones graben are Pleistocene. Along the eastern flank of the Morro Jorgino we have mapped the same reworked ash layer and dated at two points by using Ar^{40}/Ar^{39} in single crystal of sanidine. This layer was deposited on top of the low-lying marine terrace group and at the foot of the Paloeocoastal cliff. In the highest marine terrace of this group, the ash layer is interbedded in colluvial sediments covering this terraces, however in the following lower lying marine terrace this reworked ash was deposited on top of shallow marine sediments, which cover the abrasion platform of this terrace. This field relationship indicates clearly that the prominent Paleocostal Cliff was formed between the Pliocene and Pleistocene. The height of this Paleocoastal Cliff in the Morro Mejillones Horst decreases 140 m from north to south. In the same direction, the elevation of the shoreline angle, separating the high lying marine terraces from the low-lying marine terraces, decreases 33 m. This systematic variation is clear evidence that the northernmost part of this horst has attained higher amount of uplift than the south. Because of the sharp difference between north-south variation of Paleocoastal Cliff height and the north-south altitudinal variation of shoreline angle of this cliff it is possible to conclude that high lying marine terraces have accumulated more latitudinal variation than the low lying marine terraces. Thus, most the documented latitudinal variation of Paleocoastal Cliff height was generated before the Pleistocene, probably during the Pliocene. Consequently, latitudinal variation of shoreline angle position accumulated during the Pleistocene-Holocene.

In the northernmost part of Morro Jorgino Horst the paleocoastal cliff recovers its height reaching 120 m. The cliff height decreases 84 m from north to south. In the same direction the vertical position of shoreline angle decrease progressively to the south from 254 ± 1 m to 243 ± 1 m. In the western border of this horst there are ten marine terraces, which conform the group of low lying marine terraces. For all of these terraces we measured the altitude of shoreline angle by using dual GPS. Vertical position of each shoreline angle was used to estimate along strike temporal variation of surface uplift on the western part of the horst. The result of this analysis is summarized in the Fig. 2.

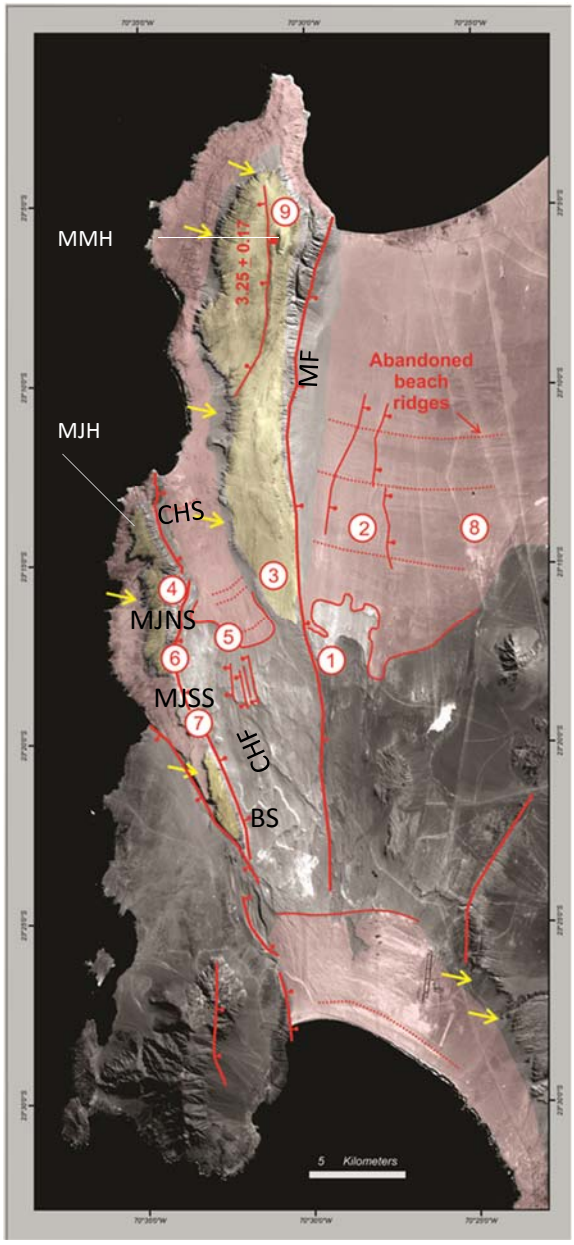

Figure 21: Satellite images showing main structural and morphological features of the Mejillones Peninsula. MF= Mejillones Fault; CHF= Caleta Herradura Fault. Yellow colour represents high lying marine terraces of Pliocene ages and pink colour marine terraces of Pleistocene age. Yellow arrows indicate the position of paleocoastal cliff preserved in the Morro Mejillones Horst (MMH) and Morro Jorgino Horst (MJH). CHS=Caleta Herradura segment; MJNS=Morro Jorgino north segment; MJSS= Morro Jorgino south segment and BS= Bandurrias segment. MMH=Morro Mejillones Horst; MJH=Morro Jorgino Horst.

STRUCTURAL ANALYSIS OF FAULT DISPLACEMENT

The surface expression of the cumulative fault scarp in the Mejillones Fault shows that this structure has accumulated larger vertical displacement in the north than the south. In fact, in the north the cumulative fault scarp reaches 450 m in height, whereas in the south this scarp attains just 65 m in height. Surface mapping reveals that this structure is not segmented and probably larger cumulative displacement in the north relates to a regular pattern of fault-slip accumulation in this fault position.

The Caleta Herradura Fault shows a more complex pattern of fault slip than Mejillones Fault. The detailed geological and structural mapping of the trace of this fault allows identifying the occurrence of four segments in a 20 km long fault line (Fig. 1). The northernmost segment (CHS=Caleta Herradura segment) has formed a cumulative fault scarp, which reaches 265 m in height. By using the vertical offset of the reworked ash layer dated in 672.7 ± 43.9 Ky (located in the middle part of the cumulative fault scarps) we estimate a slip rate of 0.21 + 0.02 mm/yr for this segment. The two central segments (MJNS=Morro Jorgino North Segment and MJSS=Morro Jorgino South Segment) are shorter than the northernmost one. In the MJNS segment the Caleta Herradura Fault is branched in six discrete faults, which have tilted and uplifted Miocene-Pliocene marine sediments. The slip rate in the easternmost fault of the MJSS based in the position of the same ash layer is 0.12 + 0.01 mm/yr. Cumulative fault scarps in these segments reach 206 m in the north and 180 m in the south. The last and southernmost segment (BS) has produced a cumulative fault scarp, which reaches 276 m in height. This segment is formed by a single fault.

DISCUSSION

The described variation in height of the prominent paleocoastal cliff and the altitudinal variation of shoreline angle correlate with cumulative fault displacement along the Mejillones and Caleta Herradura faults. In the Mejillones Fault has been clearly documented that this variation is related with larger vertical offset accumulated in the northernmost part of the fault. The along strike reduction in cumulative vertical displacement in the Mejillones Fault geographically coincides with the large cumulative vertical displacement in the Caleta Herradura Fault. It suggests that both structures are linked kinematically.

The figure 2 shows the vertical variation through time of shoreline angles of four marine terraces of the Morro Jorgino Fault. It clearly illustrates that a most irregular pattern of surface uplift has occurred in this horst in comparison with Morro Mejillones Horst. This pattern is probably related with the observed fault segmentation. Whereas Bandurrias Segment accumulated continuous vertical offsets the other segments probably alternated fault slip through time. Presently we have not dated these marine terraces. Therefore, the absence of numerical ages does not allow to constrain slip rate variation.

Calculated slip rate in the Caleta Herradura fault indicates that recurrence time of earthquakes along this fault is probably at the thousands of years scale. We observed discrete vertical offset in alluvial fans forming 2 m fault scarps. It suggests that probably Mw 7.0 earthquake represent a characteristic earthquake in this fault. This type of paleo-earthquake is similar than those proposed for the Mejillones Fault. Thus fault-hazard assessment in this peninsula is mainly related to these two faults. The most critical question how this upper plate faults relate with subduction earthquakes.

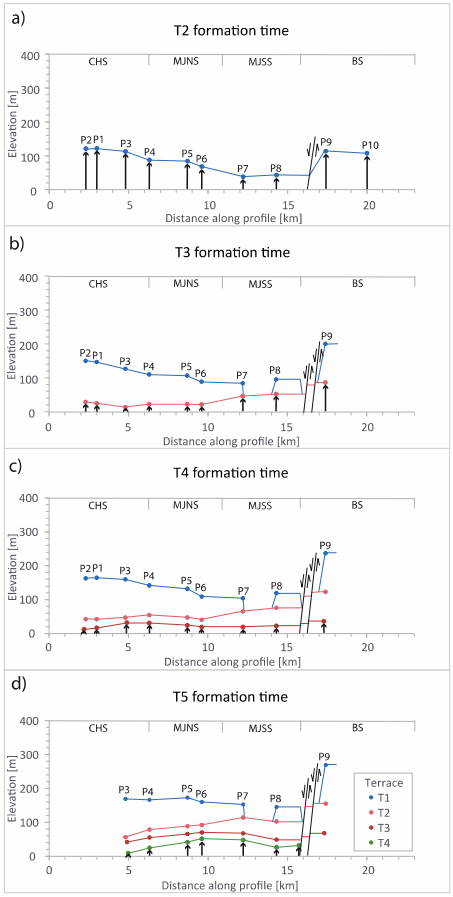

Figure 2: Along fault strike profile showing the variation in altitude of shoreline angle of marine terraces in the western side of Morro Jorgino Fault. Elevation is measured with respect to the sea level using dual GPS. T1 are the oldest terrace and highest marine terrace and T5 is the youngest marine terrace represented in this structural section. Figure 2d represent the marine terrace configuration the formation time T5. The comparison of figures 2a and 2d reveals that the southward tilting of T1 was counterbalanced by increase of fault-slip in the MJNSS and MJSS segments. Normal faults represented in the section separate the BS segment from the other segments.

Acknowledgements: We thank FONDECYT project 1140846 and the FONDAP project 15110017 for funding support for field work and doctoral thesis.

REFERENCES

Armijo, R., & Thele, R., 1990. Active faulting in northern Chile: ramp stacking and lateral decoupling along a subduction plate boundary? *Earth and Planetary Science Letters* 98, 40-61.

Allmendinger, R., & González, G., 2010. Invited Paper: Neogene to Quaternary Tectonics of the Coastal Cordillera, northern Chile. *Tectonophysics* 495, 93-110.

González, G., Cembrano, J., Carrizo, D., Macci, A., & Schneider, H., 2003. Link between forearc tectonics and Pliocene-Quaternary deformation of the Coastal Cordillera, Northern Chile. *Journal of South American Earth Sciences* 18, 321-342.

Jara-Muñoz, J., Melnick, D., & Strecker, M., 2016. TerraceM: A MATLAB® tool to analyze marine and lacustrine terraces using high-resolution topography. *Geosphere* 12 (1), 176-195.

Marquardt, C., 2005. Déformations néogènes le long de la côte nord du Chile (23º-27ºS). Avanta-arc des Andes Centrales. PhD thèses, Université Toulose III Paul Sabatier, Toulouse France, 212 pp.

Niemeyer, H., González, G., & Martinez, E., 1996. Evolución tectónica cenozoica del margen continental activo de

Antofagasta, norte de Chile. *Revista Geológica de Chile* 23 (2), 165-186, SERNAGEOMIN Chile.

Ortlieb, L., Diaz, A., & Guzman, N., 1996. Interglacial stage episode during oxygen isotope stage 11 in northern Chile. *Quaternary Science Review* 15, 857-871.

Victor, P., Sobiesiak, M., Glodny, J., Nielsen, N., & Oncken, O., 2011. Long-term persistence of subduction earthquake segment boundaries: Evidence from Mejillones peninsula, N-Chile. *Journal of Geophysical Research* 116, B02402.

INQUA Focus Group Earthquake Geology and Seismic Hazards

paleoseismicity.org

Quantification of mass wasting volume associated with the giant landslide Maleh-Kabood induced by the 2017 Kermanshah earthquake by InSAR technique

Goorabi, Abolghasem (1)

(1) Faculty of Geography, University of Tehran, Enqlab Avenue, Tehran, Iran, goorabi@ut.ac.ir

Abstract: *InSAR is employed to retrieve and calculate the spatial characteristics of the largest coseismic landslide Maleh-Kabood, induced by the Ms 7.3 Azgleh earthquake in Kermanshah Province, Iran. The seven interferometric pairs selected from the Sentinel 1, 2 imageries data covering the NW-Zagros mountainous area are used in the study. The post-seismic topographic change relative to the pre-seismic over the landslide area is spatially mapped. The quantitative estimation of associated with the landslide suggests that the giant landslide is characterized by a major sliding length of 3570 m along the NW–SE directions with an extension width of 2270 m perpendicular to Maleh-Kabood to Ghorchi-Bashi axis, and a peak height change of about 20 m in the vertical direction. The depth of fissures caused by landslides is measured about 50-100 m. The affected area of landslide mass movement reaches 6.0 km^2 (577 Hectares) with the volume up to 450 million m^3.*

Keywords*: Mass wasting volume, Maleh-Kabood landslide, Earthquake 7.3 of Azgleh (Kermanshah), InSAR*

INTRUDUCTION

The earthquake with high magnitude usually triggers massive coseismic landslides, even large-scale giant landslides with a volume up to several millions of m3 while occurring in steep mountainous areas (Gallen et al., 2017; Wang et al., 2016; Vega & Hidalgo, 2016; Setiawan et al., 2016; Goorabi, 2009). The earthquake-induced landslide is one of the most significant geological hazards, which can result in enormous human casualties and serious property damages, even more than what is directly caused by the earthquake itself (Chen et al., 2014).

The quantitative knowledge of earthquake-induced landslides may aid in analysing the type, size, geomorphology, morphotectonics and motion features of seismic landslides. The characterization of seismic landslides is also essential for better understanding of causal mechanisms (Faulting or folding) and improvement of earthquake-induced landslide prediction and early warning system. To reduce the landslide induced damages, detection and monitoring of slope deformation are critical. It is however very challenging to detect and monitor the often slow deformation of a great number of slopes In situ observations with, e.g., GPS, spirit levelling, and geotechnical instrumentation, are sometimes less effective or practical due to their poor spatial resolution and deployment difficulties. In addition, field measurements can be rather labour intensive and costly (Sassa & Canuti, 2009). The interferometric synthetic aperture radar (InSAR) technique has great advantages for geological hazard observation due to its large ground coverage and high spatial resolution under all weather conditions. InSAR can overcome the aforementioned limitations as the method can remotely sense a large number of slopes in an area while offering good observation accuracy (Yin et al., 2010; Carnec, Massonnet & King 1996). Although InSAR has been successfully used in mapping surface deformations associated with earthquakes it is often challenging to employ the conventional InSAR technique for landslide monitoring due to the usual dense vegetation coverage and rugged terrain features in landslide prone areas that often lead to both temporal and spatial decorrelation and geometric distortions. Other factors such as atmosphere artifacts are also a matter of concern (Colesanti & Wasowski, 2006).

The detailed knowledge of the giant landslide has a major significance for a better understanding of complicated interplay of slope failure, seismic parameters (e.g. the earthquake magnitude, surface rupture, fault plane geometry, coseismic slip), and terrain parameters related to geomorphology (E.g. slope angle, orientation, altitude and slope curvature). Some immediate investigations following the seismic event, including field geological and geophysical surveying as well as optical remote sensing investigation, have been carried out to retrieve the feature of the giant landslide. The geographic location and affected extent of landslide have been determined by landslide inventory mapping. However, it is quite challenging to detail the spatial characteristics related to topographic change, mass wasting volume and depositing thickness due to the rugged terrain and its large coverage.

A devastating earthquake measured at a magnitude of Ms 7.3 struck Sarpol-e-Zahab area (near Azgleh village) on the western of the Kermanshah Province, western Iran on 12 Nov 2017 (USGS, 2017). The earthquake originated in the Zagros fault zone at the north-western margin of the Zagros Mountain. The Ezgeleh earthquake was the country's largest seismic event in more than 50 years and

caused more than 505 fatalities, 1 persons missing, 12385 injured and more than 1 million people left homeless (IIEES[1]).

The intense ground shaking caused by the seismic event triggered many coseismic landslides in a steep terrain range covering an area of almost 41,750 km2. Fortunately, the seismic landslides directly resulted had not fatalities. The largest coseismic landslide, referred to as Maleh-Kabood landslide, triggered by the earthquake occurred upper and between the villages of Ghorchi-Bashi and Maleh-Kabood. We studied the deformation of the slopes over a period of about 12 days before and after of the landslide (Earthquake 7.3 of Azgleh) by InSAR technique with 6 ascending sentinel images.

MATERIAL AND METHODS

The 2017 Azgleh earthquake struck the Kermanshah region at the western of the Iran, adjacent to the Iran-Iraq borders. The area is characterized by an elevation between 800- 4000 m and a topographic relief of more than 3000 m over a distance of more than 100 km. From the southwest to the northeast, the western margin of the Zagros is composed of three major tectonic units including the Khuzestan plain, Zagros fold belt, and the Zagros thrust belt. It terminate to Sanandaj-Sirjan Zone (**Σφάλμα! Το αρχείο προέλευσης της αναφοράς δεν βρέθηκε.**). In the same direction, there are three large faults, the Zagros foredeep fault (MFF), high Zagros thrust fault (HZF) and Morvareed-Dinvar-Kermanshah fault. These faults accommodated a significant crustal shortening during the late Quaternary, which has led to the identification of the Sarpol-e-Zahab region as a major thrust zone that was reactivated in the Arabian-Iran plate collision (IIEES).

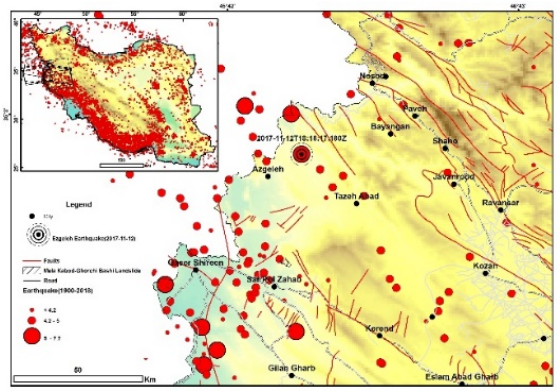

Figure 22: Simplified topographic (derivative from SRTM90) and faults map of study area. Inset show distribution of earthquakes in Iran (1900–2018).

The Azgleh earthquake initiated close to the base of the Zagros foredeep fault (MFF) with a focal depth of almost 18 to 25 km and propagated upwards (USGS). The seismological record data indicates that the rupture initiated in the north eastern Sarpol-e-Zahab and propagated unilaterally toward the southwest, along a northeast dipping fault. The largest coseismic surface motion is found near Sarpol-e-Zahab about a 0.90 m. The earthquake triggered many landslides that some of them blocked the road (IIEES).

The largest seismic landslide Azgleh triggered by the Kermanshah earthquake is located on the limb of Maleh-Kabood syncline (Figure 23). Its central geographic location is N34°32'26", E45°54'13", which is almost 8-9 km away from the surface rupture of the Zagros foredeep fault (MFF). The pre-seismic Azgleh slope is an isolated ridge with its three sides cut. The rock strike of slope is almost perpendicular to the slope surface and has a perfect extension. The free surface of slope and surface connectivity of limestone bedding plane compose together the base of the seismic mega-landslide formation. The intensive surface motion, recorded with the maximum peak ground acceleration (PGA) 680 cm/s2 and long duration of about 11s near the focus, but a number of researchers believe has a greater impact on the failure of the structures was around 700 in the Sarpol-e Zahab accelerogram(away from the epicenter around 40 km). This ground acceleration can forms the radical triggering factors of the mega-landslide (IIEES).

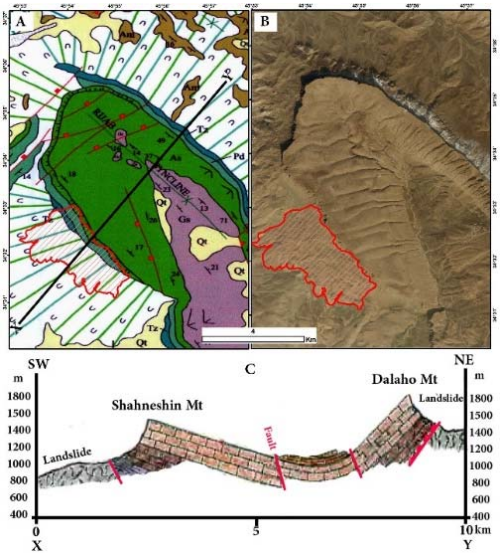

Figure 23: Morphotectonics map (A, B) and base structure of Maleh-Kabood landslide.

In order to detail the spatial characteristics of the seismic landslide, this study employs twelve scenes of post-seismic SAR imagery data, which were collected by the C-band (radar wavelength of 5.6 cm) Sentinel-1, 2 sensor on-board the satellite ESA from track 6 along the ascending orbits between Octobers to November 2017. Among these images, four were acquired in the fine beam single-polarization (FBS) (i.e. VV) mode, and the others were acquired in the fine beam double-polarization (FBD) (i.e. VH + VV) mode. The VV polarization data of the FBD images were extracted and utilized in subsequent interferometric analysis. The pixel spacing of these images is 4.3 m in the azimuth direction and 1.7 m in the slant range direction, respectively, while the central look-angle is ~34.2°. The Hashes square marked in **Σφάλμα! Το αρχείο προέλευσης της αναφοράς δεν βρέθηκε.** shows

- International Institute of Earthquake Engineering and Seismology(IIEES)1

the Maleh-Kabood landslide area with a ground extent of about 4 km ×3 km.

All of the Sentinel images were co-registered and resampled to a same pixel grid space. Seven interferometric pairs with high coherence quality were selected for data reduction from the full combination of Sentinel images with the assistance of visual inspection of fringe clarity. *Table 2* lists the information of selected interferometric pairs and image acquisitions. The temporal baseline is between 12 and 24 days, and the spatial baseline from 4 to 50 m. It should be noted that we set image of per-seismic (before of earthquake) as a master and post-seismic as slave.

Table 2: Sentinels interferometric pairs over the Maleh-Kabood landslide area.

InSAR Pairs	Master Date (D/M/Y) Time	Slave Date (D/M/Y) Time	T (Days)	Baseline (m)	Track
1	31-OCT-2017 03:01:49	-	0	0	79
2	-	12-NOV-2017 03:01:49	-12	-52.46	79
3	-	24-NOV-2017 03:01:49	-24	-6.65	79
4	07-NOV-2017 02:53:49	-	0	0	6
5		19-NOV-2017 02:53:48	-12	14.83	6
6	31-OCT-2017 03:01:49	-	0	0	79
7	-	12-NOV-2017 03:01:48	-12	-49.55	79
8	-	24-NOV-2017 03:01:48	-24	-6.32	79
9	06-NOV-2017 14:51:46	-	0	0	174
10	-	18-NOV-2017 14:51:46	-12	-1.18	174
11	11-NOV-2017 15:00:04	-	0	0	72
12	-	23-NOV-2017 15:00:04	-12	-33.53	72

DISCUSSION

Interferograms formation

The initial interferograms corresponding to all the selected interferometric pairs are firstly computed from the conjugate multiplication of co-registered complex SAR images with the SNAP Software. The derived interferometric phases are contributed by flat-earth trend, topography, ground motion, atmospheric delay, and decorrelation noise (*Equation 1*) therefore, the phase value at each pixel in the interferogram can be modelled as a sum of the following components:

φint =φflat+φtop+φdef+þφatm+ φnoi (*Equation 1*)

$$= \frac{4\pi}{\lambda}.B \parallel + \frac{4\pi}{\lambda}.\frac{B\perp}{R.sin\theta}.\left(H_{pre\_seis} + \varepsilon_{seis\_cha}\right) + \frac{4\pi}{\lambda}.r + \phi atm + \phi noi$$

where λ is the radar wavelength, R is the sensor-target distance, θ is the radar incident angle, B|| and B⊥ are the parallel and perpendicular components of spatial baseline, respectively, H_{pre_seis} and ε_{seis_cha} are the pre-seismic DEM elevation and its change caused by the seismic event, respectively, and r is the possible ground displacement along the radar line of sight (LOS) direction (Chen et al. 2014). The flat-earth trend and pre-seismic topographic effects can be determined and removed from each of initial interferograms by using the satellite orbital state vectors and pre-seismic DEM. In this study, the DEM 30m generated from Shuttle Radar Topography Mission (SRTM) is used. The residual interferometric phase φdint after the removal of topographic component phase at each pixel can be written as:

$$\phi_{d\,int} = \frac{4\pi}{\lambda}.\frac{B\perp}{R.sin\theta}.\varepsilon_{seis\_cha}(x,y) + \frac{4\pi}{\lambda}.T.v(x,y) + \phi atm + \phi res \quad (Equation\ 2)$$

where (x,y) are the azimuth and range coordinates of pixel, where (x,y) are the azimuth and range coordinates of pixel, T is the temporal baseline, v is the mean deformation velocity along the LOS direction, and φres is the residual phase possibly from noise, atmospheric phase screen (APS) (Ferretti, Prati, و Rocca 2001) and nonlinear ground deformation. The time series of interferograms after removing the flat-earth and pre-seismic topographic phase was then generated. In order to obtain unwrapped interferometric phases, the Snaphu software package developed by Stanford University was subsequently applied.

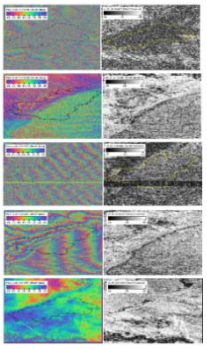

Figure 24: Interferograms and related coherence maps over the study area.

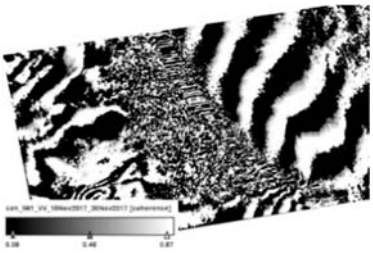

Figure 25: Coherence map of landslide area

RESULTS

Figure 27 shows the maps of topographic elevation change (before and after) caused by the earthquake 7.3 of Azgleh (Kermanshah) and overlaid boundary of Maleh-Kabood landslide. The subtraction of the two DEMs (After-Before) shows that some areas move up and some move down. The negative values in the map (differential map) indicate that the elevation is decreasing, i.e., the Maleh-Kabood slope collapsing, and the positive values indicate that the elevation is increasing, i.e., the valley sediments filling in the Maleh-Kabood to Ghorchi-Bashi gully. It can be seen

that the maxima of height increase related to the landslide mass deposit reach about 20m. The total number of SAR image pixels over the landslide area is about 8200000, thus the quantitative estimate of the affected area is approximately six km^2. The elevation change on two maps (frequency in elevations pixels) (Figure 27) show the height of the upper landslide has decreased. Then towards the villages of Maleh-Kabood and Ghorchi-Bashi (toe of landslide), the height consecutively has risen and dropped.

Based on the derived height change data and affected extent, the mass wasting volume of the landslide could be quantitatively estimated up to 450 billion m^3. *Figure 27* shows the post-seismic deformation volume over the landslide area during the time span of 12 days after the seismic event (24 November 2017), which is a by-product derived from the InSAR methods. The post seismic deformation field indicates a different displacement pattern within the landslide range (Figure 28).

Figure 26: Histogram of elevation change Pre and post-seismic earthquake within Maleh-Kabood landslide.

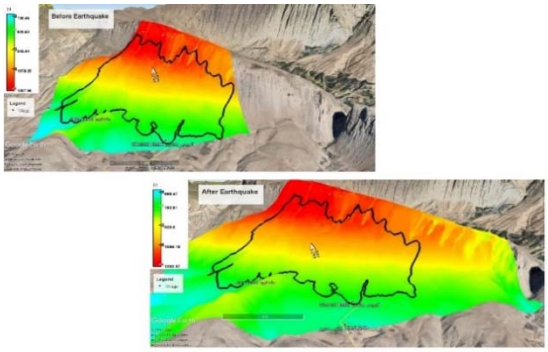

Figure 27: Pre- (Up) and post-seismic (Down) terrain model of the Maleh-Kabood area with border of landslide.

CONCLUSIONS

The seven interferometric pairs from post-seismic Sentinel imagery data were utilized to perform the investigation on the largest seismic landslide triggered by the Kermanshah earthquake (7.3 Ms, 12 Nov 2017). The resulting local topographic change suggests that the giant landslide is characterized by a spatial sliding length of 4500 m along the N-S directions with an extension width of 2500 m along the Mala-Kabood gully, and 50 m peak height change in the vertical direction (Figure 28).

The affected area caused by the mega-landslide reaches 6.0 km2 with a mass wasting volume up to 1.28 billion m3. The mass emplacement process was further inferred from the combination of the derived geomorphic characteristics and field observations including initial sliding, opposite colliding and mass sedimentation associated with the landslide event (Fig. 7).

Figure 28: fieldwork photos from Maleh-Kabood landslide.

This demonstrated that InSAR technique has the potential to qualify the mass wasting volume and map topographic change of earthquake-induced giant landslides.

REFERENCES

Carnec, C., Didier, M., & King, C., 1996. Two Examples of the Use of SAR Interferometry on Displacement Fields of Small Spatial Extent. *Geophysical Research Letters* 23 (24), 3579-3582.

Chen, Q., Haiqin, C., Yinghui, Y., Guoxiang, L., & Liu, L., 2014. Quantification of mass wasting volume associated with the giant landslide Daguangbao induced by the 2008 Wenchuan earthquake from persistent scatterer InSAR. *Remote Sensing of Environment* 152, 35-125.

Colesanti, C., & Wasowski, J., 2006. Investigating landslides with space-borne Synthetic Aperture Radar (SAR) interferometry. *Engineering Geology* 88 (3), 173-199.

Ferretti, A., Prati, C., & Rocca, F., 2001. Permanent scatterers in SAR interferometry. *IEEE Transactions on Geoscience and Remote Sensing* 39 (1), 8-20.

Gallen, S.F., Clark, M.K., Godt, J.W., Roback, K., & Niemi, N.A., 2017. Application and evaluation of a rapid response earthquake-triggered landslide model to the 25 April 2015 Mw 7.8 Gorkha earthquake, Nepal. *Tectonophysics*, Special Issue on the 25 April 2015 Mw 7.8 Gorkha (Nepal) Earthquake, 714–715 (C), 173-187.

Goorabi, A., 2009. *Effect of Neotectonics on Evolution of Quaternary landforms in Central Iran (Case Study on Dehshir and Anar Faults)*. University Of Tehran.

Sassa, K., & Canuti, P., 2009. *Landslides - Disaster Risk Reduction*. Berlin, Heidelberg: Springer Berlin Heidelberg.

Setiawan, H., Sassa, K., Takara, K., Miyagi, T., & Fukuoka, H., 2016. Initial Pore Pressure Ratio in the Earthquake Triggered Large-scale Landslide near Aratozawa Dam in Miyagi Prefecture, Japan. *Procedia Earth and Planetary Science, the Fourth Italian Workshop on Landslides* 16 (C), 61-70.

Vega, J.A., & Hidalgo, C.A., 2016. Quantitative risk assessment of landslides triggered by earthquakes and rainfall based on direct costs of urban buildings. *Geomorphology* 273 (C), 217-235.

Wang, Y., Song, C., Lin, Q., & Li, J., 2016. Occurrence probability assessment of earthquake-triggered landslides with Newmark displacement values and logistic regression: The Wenchuan earthquake, China. *Geomorphology* 258 (C), 108-119.

Yin, Y., Zheng, W., Liu, Y., Zhang, J., Li, D., 2010. Integration of GPS with InSAR to Monitoring of the Jiaju Landslide in Sichuan, China. *Landslides* 7 (3), 359-365.

INQUA Focus Group Earthquake Geology and Seismic Hazards

paleoseismicity.org

Coseismic deformation analysis of the 1996 Ston-Slano (southern Croatia) M_L 6.0 earthquake: preliminary results using DInSAR and geological investigations

Govorčin, Marin (1), Matoš, Bojan (2), Herak, Marijan (3), Pribičević, Boško (1), Vlahović, Igor (2)

(1) University of Zagreb, Faculty of Geodesy, Department of Geomatics, Kačićeva 26, HR-10 000 Zagreb, Croatia
(2) University of Zagreb, Faculty of Mining, Geology and Petroleum Engineering, Department of Geology and Geological Engineering, Pierottijeva 6, HR-10 000 Zagreb, Croatia, bojan.matos@rgn.hr
(3) University of Zagreb, Faculty of Science, Department of Geophysics, Horvatovac 95, HR-10 000 Zagreb, Croatia

Abstract: *The Dinarides, a NW-striking mountain chain along the eastern margin of the Adriatic plate, is the most seismically active zone in Croatia. Historical and instrumental records indicate ongoing tectonics concentrated within southern Dalmatia. Results of the DInSAR analysis of coseismic deformation and fault kinematics for the Ston-Slano 1996 M_L 6.0 earthquake are presented. Constructed interferograms suggest concentric fringe pattern of coseismic ground displacements, with maximum uplift of 26 cm and subsidence of c. 8 cm in the Podimoć area, approximately 8 km NW of 1996 Ston-Slano earthquake epicentre. The kinematic analysis of shear joint/fault data indicate compressional/transpressional stress field with NE-SW and locally NW-SE trending S_{Hmax}, coinciding with the present stress field. Considering the location of microseismic epicentre, analyzed interferograms and fault kinematics suggest that the earthquake rupture probably started near Slano, and proceeded towards NW along a reverse fault situated in the Adriatic offshore.*

Keywords*: Ston-Slano earthquake, Croatia, DInSAR, interferogram, compressional stress field*

INTRODUCTION

The Dinarides are a fold and thrust belt oriented NW–SE along the eastern margin of the Adriatic microplate. Tectonically uplifted during Late Eocene to Oligocene (Pamić et al., 1998) it is still active due to ongoing convergence between the Adriatic and the European plate (≤4.17 mm/yr; Bennett et al., 2008). Recent seismic activity accommodated within collisional zone of the undeformed part of the Adriatic microplate and the Central Dinarides yields the most seismically active zone in Croatia, the area of southern Dalmatia (Markušić & Herak, 1999; Ivančić et al., 2001; Kastelic et al., 2013). Seismogenic sources are dominantly NW striking thrust faults (S_{Hmax} is NE-SW trending compression) with earthquakes confined to shallow crustal levels (≤20 km in depth; Herak & Herak, 1990; Tomljenović et al., 2009). Beside historical seismicity (*e.g.* the Dubrovnik earthquake of 1667), instrumentally recorded earthquakes (e.g. the 1996 Ston-Slano earthquake, M_w = 6.0) indicate ongoing tectonic activity along the mapped faults that represent potential seismogenic sources along the Dalmatian coastline.

In this work we address preliminary results of the DInSAR and geo-structural investigations in the region of the 1996 earthquake (the Ston-Slano area in southern Croatia) which could provide important insights into the local seismogenic assemblage. The Ston-Slano earthquake series, with the mainshock of September 5, 1996 (M_L = 6.0, I_{max} = VIII MSK), is the most important and the largest one in this epicentral area after the catastrophic Dubrovnik earthquake of 1667 (I_o = IX MSK). Described in detail by Markušić et al. (1998) and Herak et al. (2001), the mainshock caused devastation at several localities in the greater epicentral area, with maximum observed damage of VIII MSK in Ston, and Podimoć and Mravinca villages (Fig. 1). Herak et al. (2010) reported peak horizontal ground acceleration of 0.64 g in Ston. The sequence lasted for over a year, with more than 1800 aftershocks within 50 km from the mainshock's epicentre.

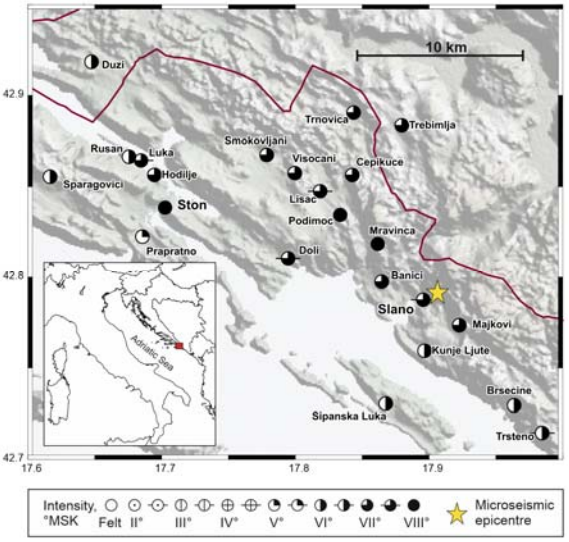

Figure 1: Observed intensities (°MSK) in the greater epicentral area of the Ston-Slano mainshock. The microseismic epicentre is shown by a yellow star. A small red rectangle in the overview map shows the geographical location of the area.

METHODS

InSAR data analysis

The ground displacements caused by the 1996 Ston-Slano earthquake sequence were analyzed with the Differential SAR Interferometry (DInSAR) technique applied on the ERS2 data scenes of descending track 451 (see Massonnet & Feigl, 1998). The ERS2 data were obtained by satellite launched by ESA that was equipped with SAR instrument operating at C-band (5.66 cm wavelength) under the look angle of 23°. The first scene was acquired on 9th of August 1996, before the earthquake sequence, whereas the second one was acquired afterwards, on 25th of July 1997. For ERS2 data processing, we used the InSAR Scientific Computing Environment (ISCE) software developed at NASA's JPL and Caltech (Rosen et al., 2012). The software processing flow comprises focusing, coregistration, interferogram generation, flat earth and topographic correction, phase unwrapping and geocoding. Moreover, an external DEM SRTM 1 arc second (30 m x 30 m) was used for topographic correction, whereas coseismic interferogram phase noise reduction was achieved by adaptive Goldsten-Werner filter (Goldstein & Werner, 1998). The phase unwrapping, reconstruction of the full interferogram waveform, was performed with a minimum cost flow (MCF), statistical-cost, network-flow (SNAPHU) algorithms (Chen & Zebker, 2001), which finally resulted in wrapped and unwrapped coseismic interferograms. Afterwards, unwrapped phase values were converted to one-dimensional "line-of-sight" (LOS) displacements.

Field investigation and geo-structural analysis

To address fault kinematics in relation to the past and the present stress fields, geological and structural investigations in the Ston-Slano area were focused along the mapped faults (Fig. 2), which mark tectonic contacts between the Mesozoic and Eocene deposits. In an area about 25 km long and 5 km wide structural data on outcrop-scale shear joint/fault planes were collected. Structural survey addressed measurements of dip direction and dip angle of shear joint/fault planes, orientation of slickensides defined by azimuth and plunge, and sense of movement. During initial campaign, we gathered about 100 shear joint/fault plane data within the three mapped fault zones. Collected structural data were separated into kinematically homogeneous pair datasets and processed through software Tectonics FP inversional method (Ortner et al., 2002). Using the P-T axis method (Turner, 1953; Marrett & Allmendinger, 1990) the theoretical maximum (σ1), intermediate (σ2) and minimum stress axes (σ3) were calculated, whereas by applying Right Dihedra Method (Angelier & Mechler, 1977) we derived the synthetic focal mechanisms for the analyzed fault segments, i.e., paleo-synthetic focal mechanisms representative of the paleostress field.

RESULTS

InSAR results and ground coseismic displacement

The DInSAR wrapped interferogram shows surface displacements in radar LOS represented as phase changes from -π to π radians. The coseismic ground displacements caused by an earthquake event are visible as the concentric fringe pattern (Fig. 3a). The absolute surface displacements were reconstructed during the phase unwrapping step, which followed conversion of angular LOS surface displacements to metric values in vertical direction. The unwrapped interferogram (Fig. 3b) shows maximum uplift of 26 cm and subsidence of -8 cm within around 10 km wide zone between two NW-striking faults in the area of Podimoć, NW of the Ston-Slano earthquake microseismic epicentre (Figs. 1 & 3b).

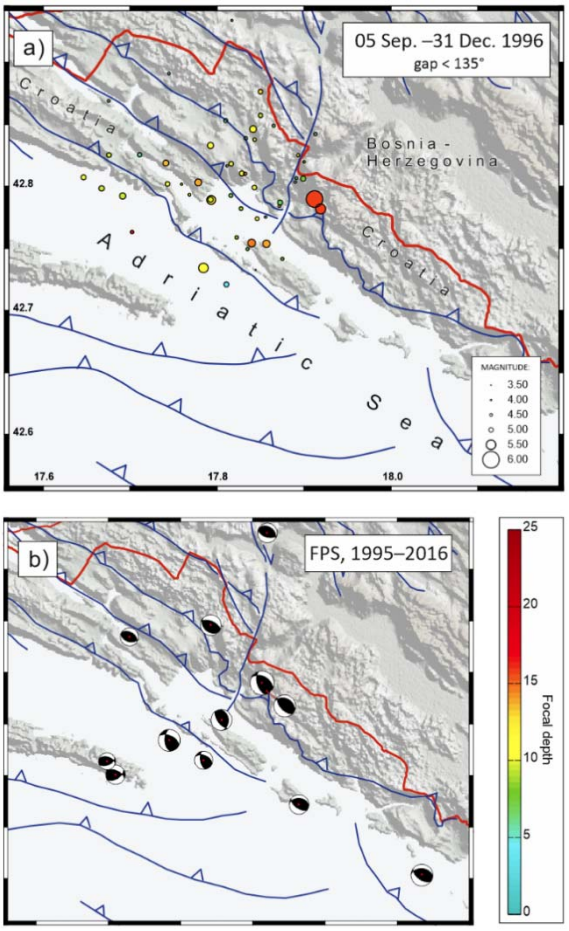

Figure 2: a) Reliably located epicentres of the 1996 Ston-Slano earthquake sequence. b) Fault-plane solutions (FPS; lower hemisphere stereographic projection, compressive quadrants are black) for the earthquakes in the period 1995–2016. Surface traces of faults (after Raić et al., 1980; Tomljenović et al., 2009 with references therein) are shown by blue lines, with barbs on the hanging wall of reverse faults.

Fault-slip analysis and paleostress field

The collected shear joint/fault plane data within the three mapped NW-striking fault zones in the Ston-Slano area characterize fault segments with mostly reverse NNE-dipping fault planes (Fig. 3b) and tectonic transport towards SSW. Additionally, both reverse NW- and SE-dipping planes were observed. The kinematic analysis according to computed stress axes (Fig. 3b) indicate dominant compressional/transpressional stress field with NE-SW and locally NW-SE trending S_{Hmax}.

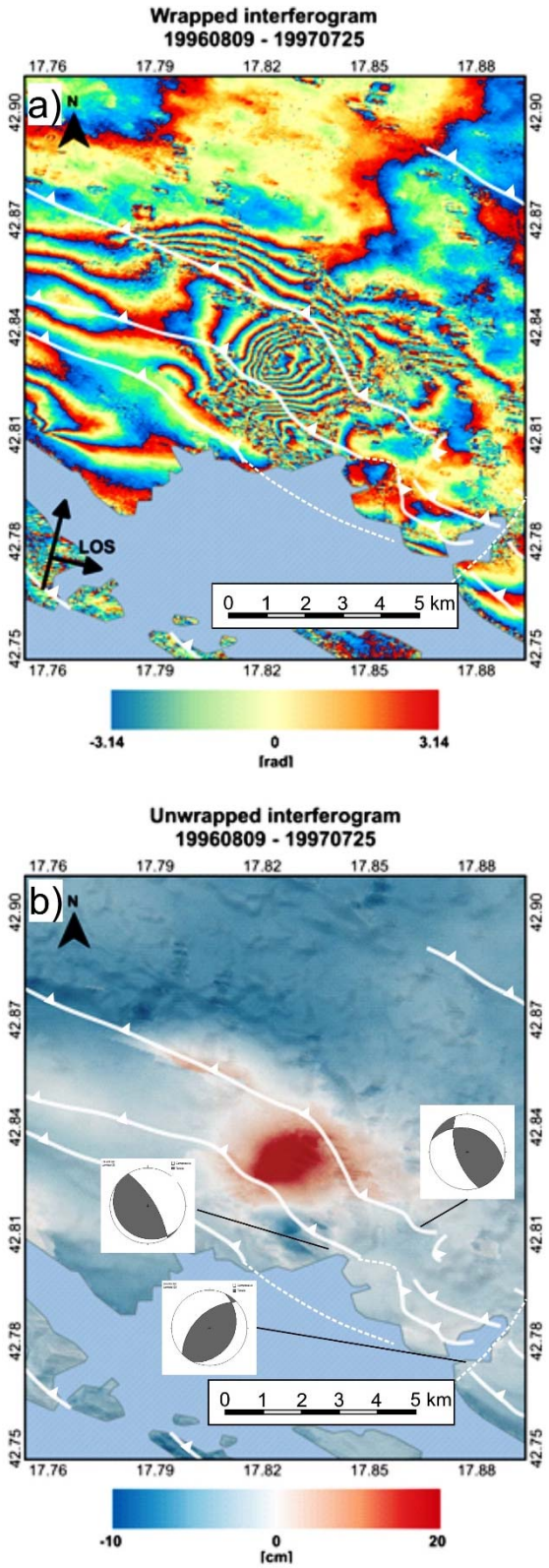

Figure 3: a) Wrapped interferogram of the 1996 Ston-Slano earthquake sequence. b) Unwrapped interferogram of the 1996 Ston-Slano earthquake sequence with scale of coseismic deformation. Based on structural data we derived paleo-synthetic focal mechanisms, a representative of the paleostress fields. Lower hemisphere stereographic projection, compressive quadrants are grey. Surface traces of faults (after Raić et al., 1980; Tomljenović et al., 2009 with references therein) are shown by white lines, with barbs on the hanging wall of reverse faults.

Beside compressional/transpressional stress field, a few collected structural fault kinematic data also indicate local NE–SW oriented extension as well as dextral and sinistral motion along the NNE–SSW striking planes.

DISCUSSION

From Figs. 1 and 2 it is seen that the most damaged area was around Podimoć, coinciding with the zone of maximum observed coseismic displacement, which is located about 8 km to the NW from the Slano microseismic epicentre (where the rupture had started). The preliminary structural data analyses indicate that observed shear joint/fault plane groups were formed within compressional/transpressional paleostress field with NE–SW and locally NW-SE trending S_{Hmax}. This implies positive correlation between observed paleostress field and the present stress field (compare Figs. 2b and 3b), which favor possibility of structural reactivation and neotectonic activity of observed fault segments in the study area.

The Ston-Slano mainshock rupture started near Slano at the depth of 15-20 km, most probably on a reverse fault with a surface trace located further to the SW, in the Adriatic offshore. As the average expected fault-length for a magnitude 6.0 earthquake on a reverse fault of about 9 km (Wells & Coppersmith, 1994) closely matches the distance between the epicentre and the area of the largest coseismic displacement, we propose that, due to source geometrical properties, strata thickness and rheological heterogeneities, coseismic rupture propagated mostly unilaterally about 8 km towards NW, to the Podimoć area, where a bulk of accumulated seismic energy was released.

Acknowledgement: This research was financially supported by the Croatian Science Foundation, Grant no. IP-2014-09-9666.

REFERENCES

Angelier, J., & Mechler, P., 1977. Sur une methode graphique de recherche des contraintes principales egalement utilisables en tectonique et en seismologie: la methode des diedres droits. *Bull. Soc. Géol. France* 19, 1309-1318, doi:10.2113/gssgfbull.S7-XIX.6.1309.

Bennett, R.A., Hreinsdóttir, S., Buble, G., Bašić, T., Bačić, Z., Marjanović, M., Casale, G., Gendaszek, A., & Cowan, D., 2008. Eocene to present subduction of southern Adria mantle litosphere beneath the Dinarides. *Geology* 35, 3-6.

Chen, C.W., & Zebker, H.A., 2001. Two-dimensional phase unwrapping with use of statistical models for cost functions in nonlinear optimization. *Journal of the Optical Society of America* 18, 338-351.

Goldstein, R.M., & Werner, C.L., 1998. Radar interferogram filtering for geophysical applications. *Geophys. Res. Lett.* 25, 4035-4038, doi: 10.1029/1998GL900033.

Herak, D., & Herak, M., 1990. Focal depth distribution in the Dinara Mt. region, Yugoslavia. *Gerlands Beitrage zur Geophysik* 99, 505-511.

Herak, M., Herak, D., Markušić, S., & Ivančić, I., 2001. Numerical modelling of the Ston-Slano (Croatia) aftershock sequence. *Studia geophysica et geodaetica* 45, 251-266.

Herak, M., Allegretti, I., Herak, D., Kuk, K., Kuk, V., Marić, K.,Markušić, S., & Stipčević, J., 2010. HVSR of ambient noise in Ston (Croatia) - comparison with theoretical spectra and with the damage distribution after the 1996 Ston–Slano earthquake. *Bulletin of Earthquake Engineering* 8 (3), 483-499.

Ivančić, I., Herak, D., Markušić, S., Sović, I., & Herak, M., 2001. Seismicity of Croatia in the period 1997–2001. *Geofizika* 18-19, 17-29.

Kastelic, V., Vannoli, P., Burrato, P., Fracassi, U., Tiberti, M.M., & Va-Lensise, G., 2013. Seismogenic sources in the Adriatic Domain. *Mar. Petrol. Geol*. 42, 191-213. doi: 10.1016/j.marpetgeo.2012.08.002.

Markušić, S., Herak, D., Ivančić, I., Sović, I., Herak, M., & Prelogović, E., 1998. Seismicity of Croatia in the period 1993-1996 and the Ston-Slano earthquake of 1996. *Geofizika* 15, 83-101.

Markušić, S., & Herak, M., 1999. Seismic zoning of Croatia. *Natural Hazards* 18, 269-285.

Marrett, R., & Allmendinger, R.W., 1990. Kinematic analysis of fault-slip data. *Journal of Structural Geology* 12, 973-986. doi:10.1016/0191.

Massonnet, D., & Feigl, K.L., 1998. Radar interferometry and its application to changes in the Earth's surface. *Reviews of geophysics* 36(4), 441-500.

Ortner, H., Reiter, F., & Acs, P., 2002. Easy handling of tectonic data: The programs TectonicVB for Mac and Tectonics FP forWindows™.

Pamić, J., Gušić, I., & Jelaska, V., 1998. Geodynamic evolution of the Central Dinarides. *Tectonophysics* 297, 251-268.

Raić, V., Papeš, J., & Ahac, A., 1980. Basic geological map of Yugoslavia, M 1:100 000, sheet Ston (K33-48). Geological Survey Zagreb, published by Federal Geological Institute Beograd.

Rosen, P.A., Gurrola, E., Sacco, G.F., & Zebker, H., 2012. The InSAR scientific computing environment. In Synthetic Aperture Radar, 2012. EUSAR. 9th European Conference on VDE, 730-733.

Tomljenović, B., Herak, M., Herak, D., Kralj, K., Prelogović, E., Bostjančić, I., & Matoš, B., 2009. Active tectonics, seismicity and seismogenic sources of the Adriatic coastal and offshore region of Croatia. In: 28 Convegno Nazionale "Riassunti Estesi delle Comunicazioni", Eds: Slejko, D. & Rebez, A., Trieste. *Stella Arti Grafice*, 133-136.

Turner, F.J., 1953. Nature and dynamic interpretation of deformation lamellae in calcite of three marbles. *American Journal of Science* 251, 276-298.

Wells, D.L., & Coppersmith, K.J., 1994. Empirical relationships among magnitude, rupture length, rupture width, rupture area, and surface displacement, *Bulletin of the Seismological Society of America* 84 (4), 974-1002.

INQUA Focus Group Earthquake Geology and Seismic Hazards

paleoseismicity.org

Active faulting in NW Slovenia and NE Italy - first results from field studies and tectonic geomorphology

Grützner, Christoph (1)

(1) Friedrich Schiller University Jena, Institute for Geological Sciences, Burgweg 11, 07749 Jena, Germany, christoph.gruetzner@uni-jena.de

Abstract: *The eastern Southern Alps-Dinarides region marks the transition from head-on thrusting on E-W thrust faults in Italy to right-lateral strike-slip faulting on NW-SE striking structures mainly in Slovenia. We investigate the major active faults, their sense of motion, their Quaternary tectonic history, and how they drive erosion using a set of interdisciplinary tools: (i) high-resolution digital elevation models; (ii) near-surface geophysical surveys to image the sub-surface structure of active faults; (iii) paleoseismological trenching to determine long-term slip rates, earthquake recurrence intervals, and paleo-magnitudes; and (iv) the erosional response to active faulting using catchment-wide erosion rates from in situ cosmogenic ^{10}Be in river sediment. Here I report results from field work and remote sensing studies. I document landscape features that indicate Late Quaternary tectonic activity along some of the main faults. These sites will be subject to geophysical investigations to check their suitability for later trenching studies.*

Keywords*: Dinarides, Southern Alps, tectonic geomorphology, paleoseismology, erosion rates*

INTRODUCTION

In the framework of SPP 2017 'Mountain building processes in 4D' we started the project 'Earth surface response to Quaternary faulting and shallow crustal structure in the eastern Adria-Alpine collision zone and the Friulian plain. A consortium of geologists, geophysicists, and geochemists will investigate the geometry of major active faults, their sense of motion, and how they drive erosion using (i) high-resolution digital elevation models from airborne LiDAR surveys and drones; (ii) georadar and electric resistivity tomography to image surface traces and the sub-surface structure of active faults; (iii) paleoseismological trenching to determine long-term slip rates, earthquake recurrence intervals, and paleo-magnitudes; (iv) the erosional response to active faulting using catchment-wide erosion rates from *in situ* cosmogenic ^{10}Be in river sediment.

Research questions

- Which faults in Friuli and W Slovenia accommodate the present-day convergence of Adria and Eurasia? Is active tectonic deformation confined to a few major structures or is it widely distributed?
- What is the Quaternary faulting history of the active faults? What is the length of their earthquake recurrence intervals and what are the maximum magnitudes? Can we tie historical earthquakes to their causative faults?
- What is the mechanism of faulting? Is/was there slip-partitioning? Do some of these faults creep?
- How much does catchment-averaged erosion change in vicinity to seismically active faults (relative to an endmember scenario not affected by faulting) and what are the differences in erosion rates, for a given rock erodibility, for different fault types?
- Can we use erosion rates to identify regions of active tectonics where little is known about actual faults?
- How does the tectonic driver of erosion in the study area compare to the climatic driver elsewhere in the Alps?

Figure 29: In the Alps-Dinarides transition zone the style of faulting changes from thrusting on E-W striking faults in Italy to right-lateral strike slip and transpression on NW-SE striking faults in Slovenia. Black lines are the main faults of interest (Moulin et al., 2016, and own mapping). Historical and instrumental seismicity are from the SHEEC database (Stucchi et al., 2012; Grünthal et al., 2013); the 1511 Idrija EQ is marked (note that the location is uncertain, the earthquake probably occurred on the Idrija Fault). Beachballs with black outlines are derived from p-wave arrivals (Herak et al., 1995); those with blue outlines are from quakes M>5 determined from first arrivals used in the Italian RCMT catalogue 1997-2017 (Pondrelli et al., 2002, and updates thereof); red outlines mark data from teleseismic body waveform inversion 1953-1984 (Anderson & Jackson, 1987). Topography is from SRTM1 data.

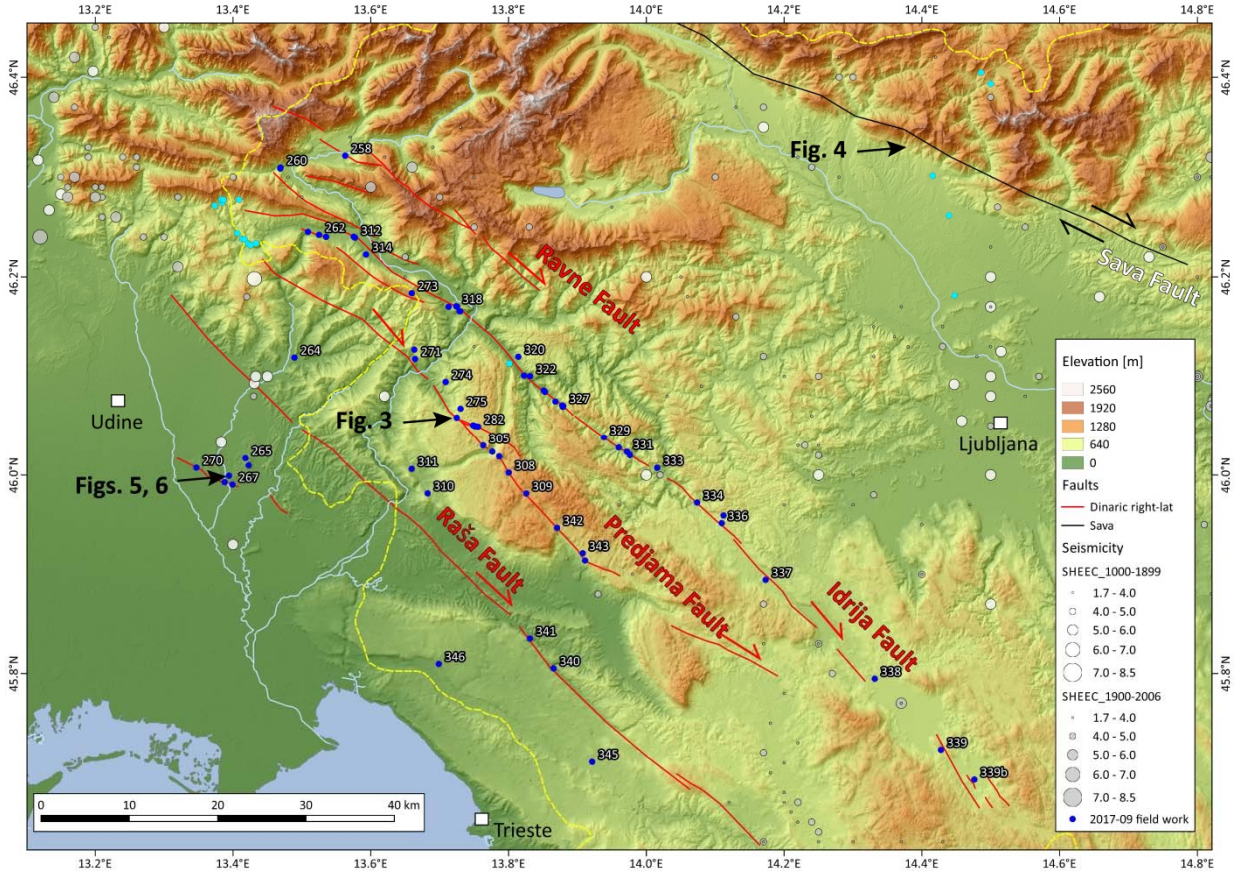

Figure 30: Map of the working area. The four main Dinaric Faults are labelled in red; the Sava Fault bounding the Ljubljana Basin is labelled in white. Light and dark blue dots are 2017 field work sites. Black arrows mark the sites discussed in the text. Topography: SRTM1 data.

The team

- Friedrich-Schiller-Universität Jena: C. Grützner (PI), K. Ustaszewski
- RWTH Aachen University: K. Reicherter (PI)
- GFZ Potsdam: F. von Blanckenburg (PI), H. Wittmann-Oelze
- Geological Survey of Slovenia: P. Jamšek
- University of Ljubljana: M. Vrabec

FIRST RESULTS

In the following I present first results from the analysis of high-resolution topography data (1 m LiDAR DEM of Slovenia and 0.1 m DEMs derived from drone imagery using Structure-from-Motion photogrammetry, SfM) and field work in 2017. The aim of the work presented here is to define sites for future near-surface geophysical investigations (georadar, electrical resistivity tomography) that will be used to precisely locate active fault traces and to image subsurface structure and sediment thickness. The most promising sites will then be subject to paleoseismological trenching.

I focussed on the four most prominent right-lateral faults in W Slovenia, the Idrija, Predjama, Raša, and Ravne Faults (Fig. 1). Preliminary data were also gathered from a short fault in Italy and the Sava Fault north of the Ljubljana Basin (Fig. 2).

In a first step I used the 1 m Lidar DEM to identify lineaments that may be related to large earthquakes. Although none of the historical earthquakes is known to have ruptured the surface, fault scarps may be preserved in the landscape for hundreds or thousands of years, even in moderate climate.

Predjama Fault

The Predjama Fault runs through hilly terrain along most of its length, which complicates geomorphological analyses. Long-term (Quaternary time scale) offsets were studied by Moulin et al. (2016), but so far no evidence for strong single earthquakes has been published.

Near the Čepovan canyon, I discovered a lineament in Late Quaternary talus slopes and basin sediments (Fig. 3). In the field, the lineament appeared to coincide with a tractor track on a pasture, but was barely visible with the naked eye. I collected several hundreds of aerial photographs with a drone and produced a 10 cm-DEM using the SfM technique. Topographic profiles perpendicular to the fault reveal a systematic vertical offset of the slope of about 0.5 m.

This observation indicates that the offset is due to coseismic displacement and not caused by terracing or road excavation (cf. Copley et al., 2018). I have identified similar features at other sites along the Predjama Fault, and at the Idrija Fault (cf. Moulin et al., 2016).

In the 1 m LiDAR DEM a clear horizontal displacement can be identified, although mass movements at the edges of the fan complicate the estimation of offset. Topographic profiles reveal a vertical offset across the fault that must post-date fan formation. This site will be analysed with near-surface geophysics in a future campaign and sampled for dating. Together with the amount of offset the abandonment age of the fan will allow for calculating a Late Quaternary slip rate.

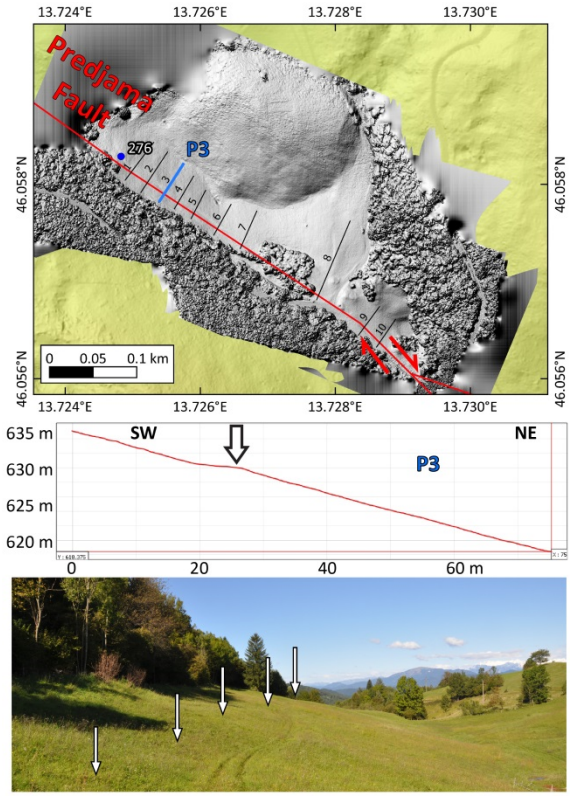

Figure 31: Drone-based DEMs reveal that the break in slope at the Predjama Fault is not related to the tractor track, but the entire slope is offset - very likely due to a surface-rupturing earthquake not that long ago (Holocene). View direction of the field photo is towards NW along the fault.

Sava Fault

The Sava Fault has a very clear imprint on the large-scale morphology. Rivers are offset by several kilometers right-laterally, and the topographic relief across the fault is in the order of 1 km along most of its length. Jamšek Rupnik (2013) studied this fault and documented Quaternary horizontal and vertical offsets. In order to estimate the fault slip rate and to date the last surface-rupturing earthquakes I concentrated on an alluvial fan that crosses the fault (Fig. 4).

Faults near Udine, Italy

A series of WNW-striking hills with a linear mountain front points to active tectonics in the eastern Friulian plain near Udine (Fig. 2). The hills have dissected, rather flat tops and die out towards the north.

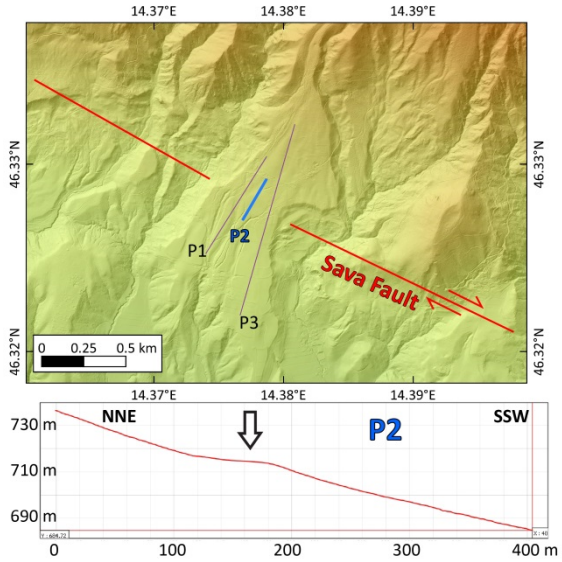

Figure 32: The Sava Fault offsets rivers all along its strike by several kilometers. Smaller right-lateral offsets and vertical displacement were also found in an alluvial fan surface of Late Quaternary age.

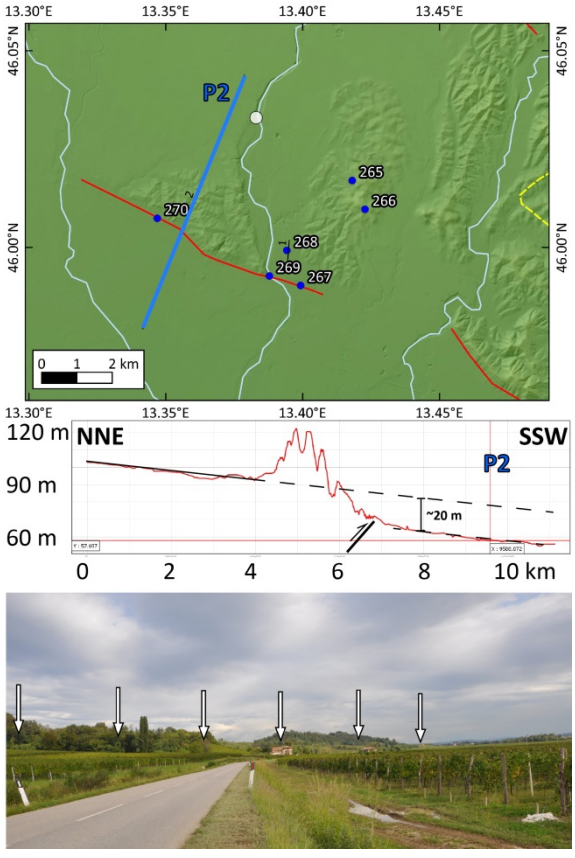

Figure 33: Around 20 m vertical offset can be observed across the gentle hills in the eastern Friulian plain. The photo shows the 15 - 20 m high scarp at the southern edge of the hills, photo location is at the intersection of the fault and profile 2.

The cumulative scarp at their base is up to 20 m high, which is also the amount of vertical offset of the basin fill on

either side of the hills (Fig. 5). This suggests that the hills are hanging wall uplifts on top of a N-dipping blind thrust.

Near Manzano I visited a 5-8 m high, apparently relatively young, 500 m long scarp that offsets a Late Quaternary river terrace (Fig. 6). The scarp is located 700 m north of the main fault trace and can only be observed on the eastern side of the river, but not in the present-day flood plain in the west of the little valley. However, it aligns with the mountain front further west and with lineaments that can be identified in the uplifted hills (1 m LiDAR data of the Regione Autonoma Friuli Venezia Giulia). I interpret the scarp as the surface expression of the youngest vertical movements on a N-dipping thrust fault. This site is a good candidate for more detailed investigations of the earthquake history of this fault system and bears the potential for paleoseismological trenching.

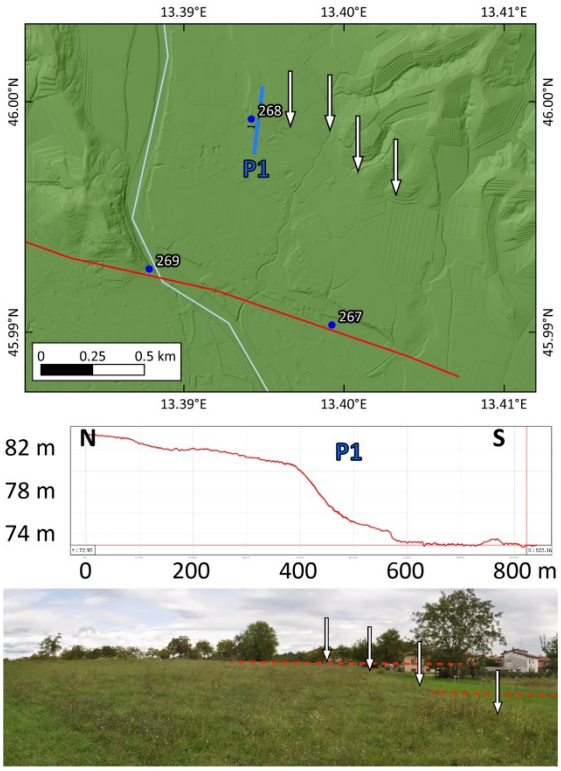

Figure 34: In Italy, some faults turn towards more westerly directions. Consequently, reverse mechanisms seem to prevail. I found a young fault scarps that has probably recorded only a few earthquakes. Field photo shows the scarp, looking to the east.

CONCLUSIONS

Several faults in NE Italy and NW Slovenia bear the geomorphological signature of recent large earthquakes that may have broken the surface. While there is already a body of literature on the long-term deformation on Plio-Quaternary timescales, only few studies so far have looked at single pre-historic events.

My investigation makes use of the new high-resolution topographic datasets that are available nowadays and allow for the detection of even subtle geomorphological features. The places that I have identified will be subject to detailed geophysical studies in order to select the most promising trench sites. First field studies have shown that there is potential to conduct paleoseismological trenching. Although the results are promising thus far, I am well aware of potential problems:

- The study region is the type locality of karst. While rivers usually are a tectonic geomorphologist's best friend, underground drainage systems do not record the effects of active tectonics on the surface drainage pattern.
- In a karst landscape, classical targets for paleoseismological trenching such as river terraces and alluvial fans may be rare.
- The sediment cover is usually rather thin in the mountainous parts of Slovenia, which is why it may be hard to find suitable archives.
- Large parts of the study area underwent intense anthropogenic modification in the past millennia.
- OSL dating on quartz and feldspars may be impossible due to the abundance of limestones in the better part of the study area.

REFERENCES

Anderson, H.A., & Jackson, J.A., 1987. Active tectonics of the Adriatic region. *Geophys. J. R. Astron. Soc.* 91, 937-983.

Copley, A., Grützner, C., Howell, A., Jackson, J., Penney, C., & Wimpenny, S., 2018. Unexpected earthquake hazard revealed by Holocene rupture on the Kenchreai Fault (central Greece): Implications for weak sub-fault shear zones. *Earth and Planetary Science Letters* 486, 141-154.

Grünthal, G., Wahlström, R., & Stromeyer, D., 2013. The SHARE European Earthquake Catalogue (SHEEC) for the time period 1900-2006 and its comparison to the European-Mediterranean Earthquake Catalogue (EMEC). *Journal of Seismology* 17 (4), 1339-1344.

Herak, M., Herak, D., & Markušić, S., 1995. Fault plane solutions for earthquakes (1956-1995) in Croatia and neighboring regions. *Geofizika* 12 (1), 43-56.

Jamšek Rupnik, P., 2013. Geomorphological evidence of active tectonics in the Ljubljana basin. PhD thesis, University of Ljubljana.

Moulin, A., Benedetti, L., Rizza, M., Jamšek Rupnik, P., Gosar, A., Bourles, D., Keddadouche, K., Aumaître, G., Arnold, M., Guillou, V., & Ritz, J. F., 2016. The Dinaric fault system: Large-scale structure, rates of slip, and Plio-Pleistocene evolution of the transpressive northeastern boundary of the Adria microplate. *Tectonics* 35 (10), 2258-2292.

Pondrelli, S., Morelli, A., Ekström, G., Mazza, S., Boschi, E., & Dziewonski, A.M., 2002. European-Mediterranean regional centroid-moment tensors: 1997-2000, *Phys. Earth Planet. Int.* 130, 71-101.

Stucchi, M., Rovida, A., Capera, A.G., Alexandre, P., Camelbeeck, T., Demircioglu, M.B., Gasperini, P., Kouskouna, V., Musson, R. M.W., Radulian, M., Sesetyan, K., Vilanova, S., Baumont, D., Bungum, H., Fäh, D., Lenhardt, W., Makropoulos, K., Martinez Solares, J.M., Scotti, O., Živčić, M., Albini, P., Batllo, J., Papaioannou, C., Tatevossian, R., Locati, M., Meletti, C., Viganò, D., & Giardini, D., 2013. The SHARE European earthquake catalogue (SHEEC) 1000–1899. *Journal of Seismology* 17 (2), 523-544.

INQUA Focus Group Earthquake Geology and Seismic Hazards

paleoseismicity.org

Preliminary analysis of a trench investigation in the central Yangsan Fault, SE Korea

Gwon, Sehyeon (1), Cho, Sung-il (1), Choi, Weon-hack (1), Inoue, Daniei (2)

(1) Central Research Institute, Korea Hydro & Nuclear Power. Co., Ltd. 1312-70 Yuseong-daero, Yuseong-gu, Daejeon, Korea.
(2) Central Research Institute of Electric Power Industry 1-6-1, Otemachi, Chiyoda-ku, Tokyo 110-0015, Japan, sehyeon.gwon@khnp.co.kr

Abstract: *A trench investigation at Wolsan-ri, Naenam-myeon, Gyeongju was conducted to evaluate the paleo-earthquake in central part of the NNE-striking Yangsan fault, SE Korea. Based on field survey, we selected and excavated two trenches (WS-1 and 2) at the Wolsan-ri site. The preliminary analysis of the trenches suggests that the fault was active at least once in the Quaternary, where the timing of the paleo-earthquake was probably before the deposition of unit WC1 and soon after that of unit WC2. To determine the timing of the faulting, samples for OSL and radiocarbon dating are collected from the trenches, and the age-dating is in progress. With geochronological analysis, a quantitative age of the faulting event will be resolved.*

Keywords*: Paleoseismology, Strike-slip fault, Yangsan fault, trench, fault activity*

INTRODUCTION

In the early 1990s, paleoseismological analysis began with an instrumental microseismicity in SE Korea, and many Quaternary faults were reported (Figure 1). As the Korean peninsula is located in a stable intra-plate region, geomorphic features associated with active tectonics is not clearly identified. Therefore, the potential activity of the faults has been relied on various age dating techniques.

The earthquake in Gyeongju (M_L 5.8, 14 Sept 2016) was occurred at the west of the Yangsan fault, which caused a debate about its relevance of the Yangsan fault. The Yangsan fault is about 200 km long dextral fault and has been subdivided into three section (Lee & Jin, 1991; Chang & Chang, 2009; Choi et al., 2017). However, the paleo-seismogenic activity for the fault around the Gyeongju city, located in the central part of the Yangsan fault, is not fully understood.

We conducted a paleoseismological analysis along the central Yangsan fault to investigate the fault activity with field survey, trench excavation and numerical dating. The aim of this study is to determine the timing of the paleo-earthquake in the central Yangsan fault. Our result provides an essential information to understand seismic fault behavior of the Yangsan fault.

THE WOLSAN-RI TRENCH SITE

The Wolsan-ri site is a few paleoseismological site to examine the most recent paleo-earthquake of the central part of the Yangsan fault in the southern region of Gyeongju city (Figure 2). A highway passing through the NNE-striking Yangsan fault and widely distributed alluvium around the Wolsan-ri area site can be a significant challenge to site the trench excavation. At the Wolsan-ri trench site, on the Yangsan fault, the fault exposed in a small river, where a fault zone with approximately 1 m width is developed within the Cretaceous basement rock.

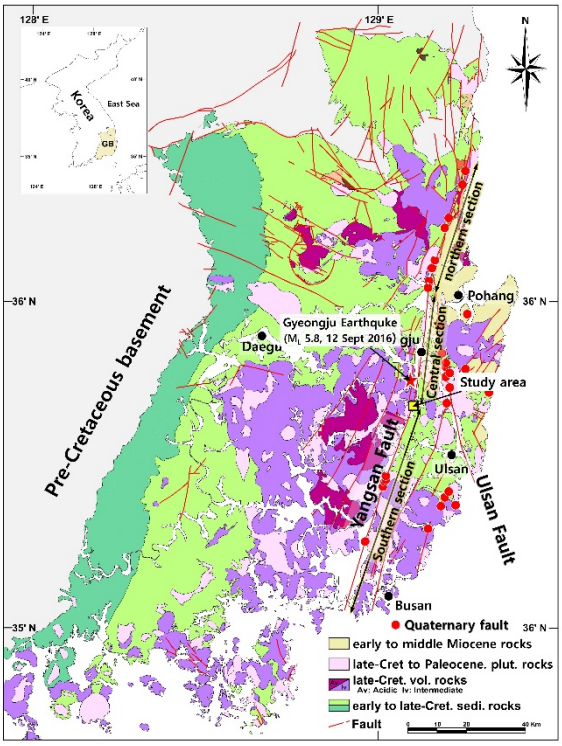

Figure 35: Geological map of the Gyeongsang basin, SE Korea (modified from Lee et al, 2000). Segmentation of the Yangsan Fault proposed by Choi et al. (2017).

We opened two trenches at the Wolsan-ri site, where the trench WS-1 was for locating the fault and paleo-channel and the trench WS-2 was for proving the horizontal offset of fluvial deposit across the fault. Unfortunately, the paleo-channel in the trenches was parallel to the fault. But stratigraphic correlation between two trenches allows to constraint the timing of the paleo-earthquake at the site along the Yangsan fault.

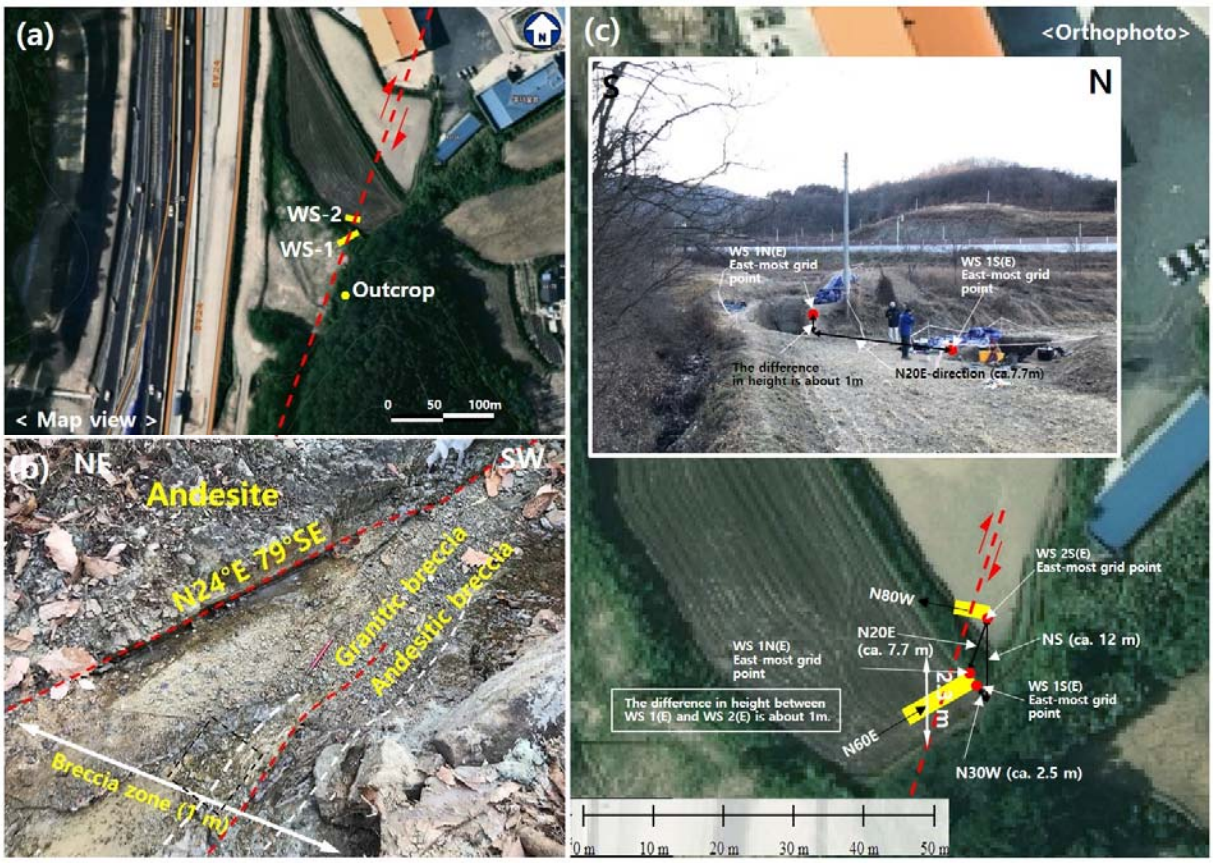

Figure 36: (a) Annotated aerial photograph of the Wolsan-ri trench site. (b) photograph of fault outcrop showing NNE-striking fault zone in small river adjacent to the trench site. (c) Schematic map of the trench site showing the spatial relationship between trenches.

STRATIGRAPHY

The trenches at the Wolsan-ri site exposed sediments of deformed gravel and silty sand layer, where the stratigraphy was classified by 8 units in descending order. Unit WA is a cultivated land and unit WB is a backfill layer (Figure 3). Unit WC1, which is the youngest sedimentary layer in the trench WS-1, is a bluish gray silty sand and it forms the soil wedge on the upper part of WC2. Unit WC2 is a yellowish brown gravelly sand with sub-angular andesitic pebbles. Unit WC3 is mainly composed of gravelly silt with dark, organic-rich silty clay at the lower part. The Units WC4 is a yellowish brown sand-supported gravels. Unit WC5 is clast-supported gravels, which is probably fluvial origin.

In trench WS-2, the youngest Quaternary unit is yellowish brown gravelly sand which is very similar to unit WS2 in trench WS-1. The gravelly sand is laterally replaced by sediments composed of gravelly silt and organic-rich silty clay. The units described above are probably correlated with the units of WC2 and 3 in trench WS-1, respectively. Moreover, the clast-supported gravel (WS5 in trench WS-1) is overlain by unit WC3, means that the stratigraphic correlation between the two trenches is reasonable. A yellowish brown silt- or sand-supported gravel where the sub-angular gravel with 2~5cm diameter is similar to unit WC4. The unit WC6 is yellow silty sand.

AGE OF DEPOSITS

To determine the age of the sediments exposed in the trenches, we collected four samples for OSL dating and five detrital charcoals for radiocarbon dating. The geochronological analysis on the samples is in progress.

EVIDENCE OF PALEO-EARTHQUAKE

In trench WS-1, the fault zone consists of dark gray and pale gray fault gouges near the center of the trench, the former is cut by the latter. The young fault (N20°E/85°SE) localized along the narrow fault gouge zone in width of 5~10 cm. The S-C fabric and gently plugging fault striation (10°~15°) within fault zone indicate the dextral movement of the fault. In contrast, the old fault zone is distributed within highly weathered basement rocks.

A faulting event is significantly indicated by the young fault that deforms unit WC2 and earlier fault rock but is covered by undisturbed soil-wedge unit of WC1. To the west of the fault, a disturbed unit composed of sediment and pre-existing fault materials aligns with the fault and is integrated progressively into unit WC2, which could be interpreted as the result of deformation along the young fault. Therefore, the faulting event could be occurred before unit WC1 and after unit WC2.

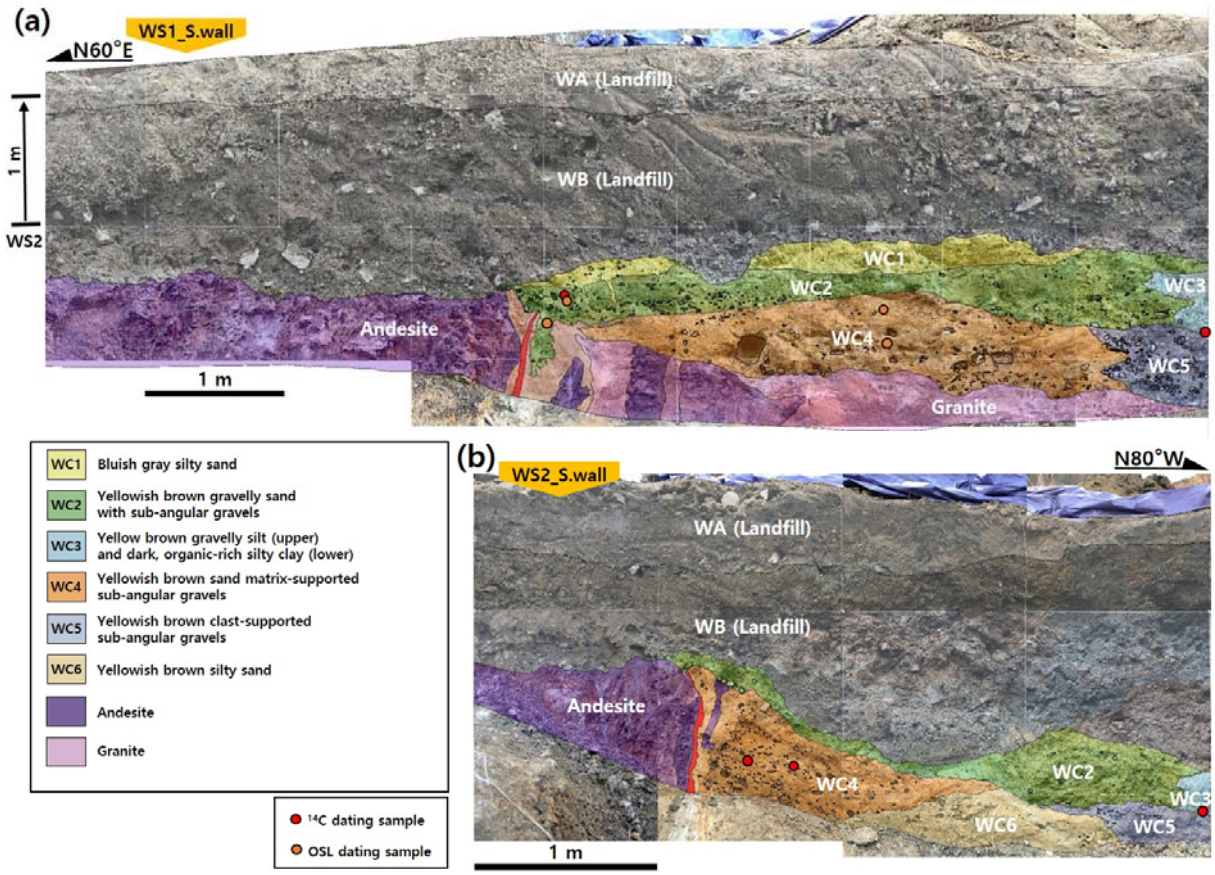

Figure 37: Log of the Wolsan-ri trench WS-1 (a) and WS-2 (b).

The old fault zone seems to be associated with earlier faulting event that occurred in basement rocks. The old fault zone is composed with a massive, dark gray fault gouge and associated breccia zone. Fractured andesitic dyke is incorporated into the fault zone. The fault zone is sealed by quartz that also observed along small faults within the andesitic rock. Also, the fault gouge is re-deposited into unit WC4, indicates that the fault zone was exposed for a considerable geological time on the surface before sedimentation of the WC4 layer. These evidence indicates that the fault zone could be occurred before the uplift of the basement rock.

In trench WS-2, the youngest pale gray fault cut unit WC4 and is covered by unit WC2 that is cut by the fault in trench WS-1. Adjacent to the young fault, a sediment composed of unit WC4, fault gouge and fragmented andesitic dykes are accumulated in the fault zone. The disturbed sediment is not penetrated into WC2 underlain by WC4, suggests that the deformation of unit WC4 was occurred before deposition of unit WC2.

DISCUSSION AND CONCLUSION

Two trenches at the Wolsan-ri site were excavated to clarify the paleo-earthquake in the central part of the Yangsan fault that is a major dextral strike-slip fault in SE Korea. The preliminary analysis of the trenches suggests that a faulting event has been occurred in the Quaternary, The timing of the event is probably before the deposition of unit WC1 and immediately after that of unit WC2. To determine the timing of the faulting, OSL dating for silty sand and radiocarbon dating for detrital charcoal are in progress.

In this study, the lacking of paleo-channel (WS5) across the fault in the trench is not allowed to estimate the horizontal displacement of the fault. It is required to evaluate the potential maximum magnitude of the earthquake and to understand the seismic fault behavior in the central Yangsan fault, SE Korea.

REFERENCES

Chang, C.J., & Chang, T.W., 2009. Behavioral characteristics of the Yangsan Fault based on geometric analysis of fault slip. *The Journal of Engineering Geology* 19 (3), 277-285 (in Korean with English abstract).

Choi, J.-H., Young-Seog Kim, Y.-S., & Klinger, Y., 2017. Recent progress in studies on the characteristics of surface rupture associated with large earthquakes. *Journal of the Geological Society of Korea* 53 (1), 129-157.

Lee, J.I., 2000. Provenance and thermal maturity of the lower Cretaceous Gyeonsang Supergroup, Korea. Ph.D. thesis, Seoul National University, Seoul, 129 pp.

Lee, K., & Jin, Y.G., 1991, Segmentation of the Yangsan fault system: Geophysical studies on major faults in the Kyeongsang Basin. *Journal of the Geological Society of Korea* 27 (4), 434-449.

INQUA Focus Group Earthquake Geology and Seismic Hazards

paleoseismicity.org

Late Quaternary slip rate of the Yushu Batang Fault and its strain partitioning role in Yushu area, central Tibet

Huang, Xuemeng (1), Du, Yi (1), He, Zhongtai (1), Ma, Baoqi (1), Xie, Furen (1)

(1) Key Laboratory of Crustal Dynamics, Institute of Crustal Dynamics, China Earthquake Administration, Beijing 100085, China, huangmeng00000@163.com

Abstract: *The late Quaternary activity of Yushu segment is poorly understood compared with other segments within Ganzi-Yushu Fault system in central-eastern Tibet. Interpretation of remote sensing images and field investigations reveals that the Yushu Batang fault has a clear geomorphic expression which is characterized by prominent fault escarpment and systematically offset gullies, fluvial terraces and alluvial fans along strike. Morphotectonic mapping, combined with optically stimulated luminescence (OSL) and radiocarbon ($_{14}C$) data, suggest that the Batang Fault is a late Holocene active left-lateral strike-slip fault, along with some reverse component. The average left-lateral slip rate of this fault is 2-4 mm/yr and vertical slip rate is 0.2–0.6 mm/yr since Late Pleistocene. Comparison with the slip rates of other faults within the Ganzi-Yushu Fault system demonstrates that the Batang Fault partitioned nearly a third of the strike slip deformation within Yushu segment.*

Keywords*: Yushu Batang fault, Ganzi-Yushu fault system, morphotectonic mapping, late Pleistocene slip rate*

INTRODUCTION

The Ganzi-Yushu fault system is the northwestward continuation of Xianshuihe fault and they jointly accommodate the relative motion between Bayan Har block and Qiangtang-Chuandian block (Fig. 1). Based on the geometry and historic earthquakes, Ganzi-Yushu fault has been divided into Ganzi, Manigange, Dengke, Yushu and Dangjiang segment (Zhou et al., 1996). Compared with other segments, the Yushu segment is geometrically more complex with some branches, among which the Batang fault is a major one. The Yushu segment mainly consists of Yushu fault to the north and Batang fault to the south. The Batang fault, about 10km south of Yushu, didn't record any surface ruptures in the 2010 Ms7.1 Yushu earthquake.

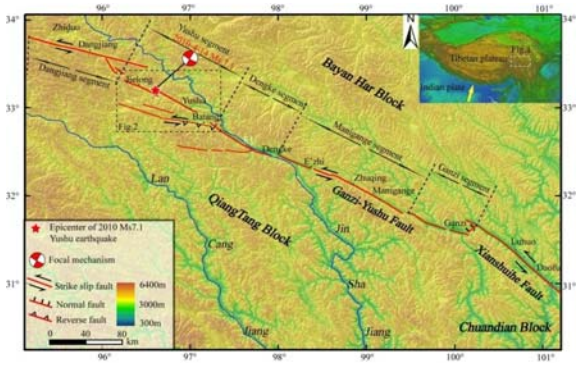

Figure 1: Satellite image showing active blocks and the location of Ganzi-Yushu fault system. (a) Satellite image showing the location of the Ganzi-Yushu fault system within central-eastern Tibet Plateau. (b) Segmentation and rupture of history earthquakes of Ganzi-Yushu fault. Background is Shuttle Radar Topographic Mission (STRM, resolution of 90m) shaded relief map.

Moderate historic earthquakes have occurred on the west segment of this fault, such as the earthquakes of 2006 M5.0, M5.4 and M5.6 in Balongda. Seen from remote sensing images, this fault has a clear expression in the geomorphology, and yet its geometry and late Quaternary slip-rate are still unknown.

RESULTS

In this contribution, we employ the methods of interpretation of remote sensing images, morphotectonic mapping, section analysis, optically stimulated luminescence(OSL) and radiocarbon(14C) dating to study the Late Quaternary slip rate of the Batang fault, and explore its strain partitioning role this fault has played in the Yushu segment of Ganzi-Yushu fault system. Based on the geomorphic mapping and dating of offset terraces and fluvial fans at Zhada, Xiabatang, Shangabatang sites, the late Pleistocene left lateral slip rate was estimated to be 2.2-3.0 mm/a and vertical slip rate of about 0.2-0.6 mm/a (Fig. 2).

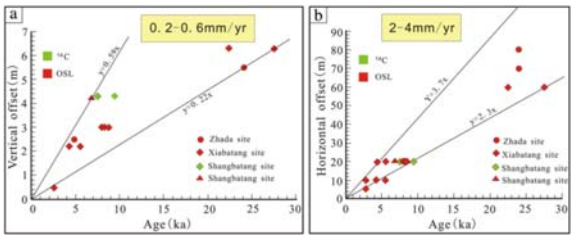

Figure 2: Ages of features versus offsets that constrain late Quaternary slip rate of Yushu Batang fault. (a) Vertical slip rate; (b) Left lateral strike slip rate.

DISCUSSION

Ganzi-Yushu fault is the northwestward continuation of Xianshuihe fault, and the two faults form the boundary between Bayan Har block and Qiangtang-Chuandian block. Late Quaternary slip rate of the Ganzi-Yushu fault system based on geological evidences is about 5-7.3 mm/a(Li et al., 1995; Zhang et al., 1996), 3.3-8 mm/a (Peng et al., 2006), 3.4-7.3 mm/a (Zhou et al., 1996), 12 mm/a (Wen et al., 2003) and 14 mm/a (Xu et al., 2003), among which the slip rate of 12-14 mm/a may be an overestimation because they used the ages of the lower terrace as the inception time of the offset of terrace risers(Cowgill, 2007). Global Positioning System (GPS) researches show that Bayan Har block moves eastward at a rate of 15-19 mm/yr, the Qiangtang block moves eastward at a rate of 22-28 mm/yr (Zhang et al., 2004; Shen et al., 2005). The relative slip rate of 7-10mm/yr means that Qiangtang block extrudes eastward faster than Bayan Har block along the Ganzi-Yushu fault. GPS velocity profile revealed that the slip rate on the Ganzi-Yushu fault system is about 6.6±1.5 mm/a (Wang et al., 2013). Overall, the slip rate of about 7-10 mm/a on the Ganzi-Yushu fault system may be relatively more reliable.

Compared with other segments, the Yushu segment is geometrically more complex with a few branches, within which the Batang fault south of Yushu is the major one. According to the recurrence interval of 450-680a and the coseismic offset of 1.5-2.0 m in the 2010 Yushu Ms7.1 earthquake, Lin et al (2011) estimated that the average slip rate of the Yushu fault is about 2-5 mm/a. Compared with the slip rate on the Yushu fault, the Batang fault partitioned nearly a third of the strike slip deformation in Yushu segment (Fig. 3).

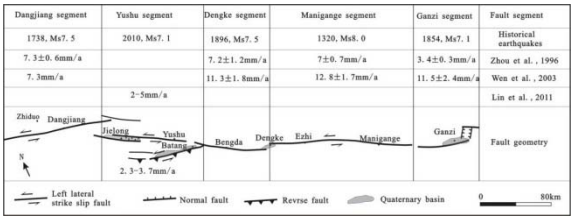

Figure 3: Historical earthquakes, fault segments and slip rates along the Ganzi-Yushu fault.

Acknowledgments: This research was supported by the China Earthquake Administration Research Fund (Grant Number ZDJ2012-03). We are grateful to the graduate (Zhang Zhi) from Jiangxi Normal University for his field work. We also thank the drivers (Cairen Nima and He Haiqing) for their careful logistic arrangement.

REFERENCES

Cowgill, E., 2007. Impact of riser reconstructions on estimation of secular variation in rates of strike-slip faulting: Revisiting the Cherchen River site along the Altyn Tagh Fault, NW China. *Earth and Planetary Science Letters* 254, 239-255.

Li, M., Xing, C., Cai, C., Guo, W., Wu, S., Yuan, Z., Meng, Y., Tu, D., Zhang, R., & Zhou, R., 1995. Research on activity of Yushu fault. *Seismology and Geology* 17, 218–224.

Lin, A., Jia, D., Rao, G., Yan, B., Wu, X., & Ren, Z., 2011. Recurrent Morphogenic Earthquakes in the Past Millennium along the Strike-Slip Yushu Fault, Central Tibetan Plateau. *Bulletin of the Seismological Society of America* 101, 2755-2764.

Shen, Z.-K., Lü, J., Wang, M., & Bürgmann, R., 2005. Contemporary crustal deformation around the southeast borderland of the Tibetan Plateau. *Journal of Geophysical Research* 110, B11409.

Wang, Y., Wang, M., Shen, Z.-K., Ge, W., Wang, K., Wang, F., & Sun, J., 2013. Inter-seismic deformation field of the Ganzi-Yushu fault before the 2010 Mw 6.9 Yushu earthquake. *Tectonophysics* 584, 138-143.

Wen, X., Xu, X., Zheng, R., Xie Y., & Wang, C., 2003. Average slip-rate and recent larth earthquake ruptures along the Ganzi-Yushu fault. *Science in China Series* D 33 (l), 199-208.

Xu, X., Wen, X., Zheng, R., Ma, W., Song, F., & Yu, G., 2003. Pattern of latest tectonic motion and dynamics of active blocks in Sichuan Yunnan region, China. *Science in China* (SerD) 33 (l), 151-162 (in Chinese).

Zhang, P.-Z., Shen, Z., Wang, M., Gan, W., Bürgmann, R., Molnar, P., Wang, Q., Niu, Z., Sun, J., & Wu, J., 2004. Continuous deformation of the Tibetan Plateau from global positioning system data. *Geology* 32, 809-812.

Zhang, Y., Li, M., Meng, Y., et al., 1996. Research on fault activity in the Bayan Har Mountain region and the seismic and geologic implications. *Research on Active Faults* 5, 154-171.

Zhou, R., Ma, S., & Cai, C., 1996. Late Quaternary active features of the Ganzi-Yushu fault zone, *Earthquake Research in China* 12 (3), 250-260.

Zhou, R., Wen, X., Chai, C., & Ma, S., 1997. Recent earthquakes and assessment of seismic tendency on the Ganzi-Yushu fault zone. *Seismology and Geology* 19 (2), 115-124.

INQUA Focus Group Earthquake Geology and Seismic Hazards

paleoseismicity.org

Paleoseismogenerating structures Kharaulakh segment of Arctic-Asian seismic belt

Imaeva, Lyudmila (1), Imaev, Valeriy (1, 2)

(1) Institute of the Earth's Crust, Siberian Branch, Russian Academy of Sciences, 128 Lermontov st., Irkutsk 664033, Russia
(2) Institute of Diamond and Precious Metals Geology, Siberian Branch, Russian Academy of Sciences, 39 Lenin pr., Yakutsk 677077, Russia, imaev@crust.irk.ru

Abstract: *For active structures Kharaulakh segment of Arctic Asian seismic belts were the subject of our complex study aimed at reconstructing the stress-strain state of the crust and defining the types of seismotectonic deformation (STD) in the study area. Based on the degrees of activity of geodynamic processes, the regional principles for ranking neotectonic structures were constrained, and the corresponding classes of the discussed neotectonic structures were substantiated. We analyzed the structural tectonic positions of the modern structures, their deep structure parameters, and the systems of active faults and paleoseismogenerating structures in the Kharaulakh segment. From the earthquake focal mechanisms, we calculated the average seismotectonic strain tensors. Using the geological, geostructural, geophysical and the corresponding average tensors, we determined the directions of the principal stress axes and revealed a regularity in the changes of tectonic settings in the Northeast Arctic.*

Keywords: *Kharaulakh segment, active faults, kinematic types, Late Cenozoic deformation, earthquake mechanism, paleoseismogenerating structures*

The Kharaulakh segment is the northern flank of the Verkhoyansk fold-thrust belt (Fig. 1). It originated from the Riphean in the reworked margin of the Siberian platform and developed as a passive continental margin that accumulated a thick layer of sediments. Its origin and long-term development influenced the structure and character of the observed dislocations. During the Cenozoic, the rotation pole of the North American and Eurasian plates changed its position several times. This may explain the alternation of the epochs of extension and compression revealed from the structural-tectonic data (Imaev et al., 2000; Parfenov et al., 2001; Imaeva et al., 2016).

In the Kharaulakh segment, the Cenozoic megacomplex is represented mainly by the Paleocene-Eocene continental deposits that occur with the sharp angular unconformity at different horizons of the dislocated Precambrian-Mesozoic megacomplex. These deposits fill a series of sublongitudinally oriented depressions, such as Kengdei, Kunga, and Nyaiba (Fig. 1), which were formed in the Paleogenic during the earliest rifting stage in the zone of the continental continuation of the spreading Gakkel Ridge. At some locations, the Paleogenic deposits are folded and faulted to form thrusts and reverse faults. All the above observations provide evidence of compression in the Cenozoic. Special structural studies show that the compression axis was oriented sublatitudinally. It is dated as the Middle Miocene, according to interpretations of the Cenozoic profiles of the Kharaulakh segment and its adjacent areas (Drachev, 2002).

The next episode of the Cenozoic evolution of the study region was the extension phase in the Pliocene-Quaternary. Young normal faults that displaced the Neogene weathering crust are observed along the coast of the Buor-Khaya Bay (Fig. 1). The extension axis was oriented in either the sublatitudinal or northeastern direction The Quaternary evolution of the southern zone of the Laptev Sea shelf, as well as of the Lena river delta, was sharply different from that of the continental part of the Kharaulakh segment. In this zone, tectonic movements were mainly caused by normal faulting, which defined the block structure of this territory, as shown by the distinct differences in hypsometric positions of the Late Quaternary and Holocene deposits. In the center of the Lena River delta, the base of the Holocene alluvial deposits is traced at the current river level, according to (Galabala, 1987). However, that base was not reached by a 25-m borehole drilled at the northeastern termination of this delta. In the western part of this delta did not reach the base. In the western part of this delta, Zyryanian-Sartanian layers are shifted by 30 m along the fault plane. Normal faulting in this area gives evidence of the extension phase, with the axes supposedly oriented in the sublatitudinal and northeastern directions.

In our seismotectonic study of the Kharaulakh segment, we analyzed the geostructural data on active faults in combination with the information on tectonic stress fields reconstructed by the tectonophysical analysis of the Late Cenozoic faults and folds. Having consolidated the geological and geophysical data on this area, we identified the systems of regional faults and revealed seismogenerating structures of different scales in the zones of dynamic influence of these faults. Such structures correlate with seismic events (M = 6.0-7.0) that have occurred at different times.

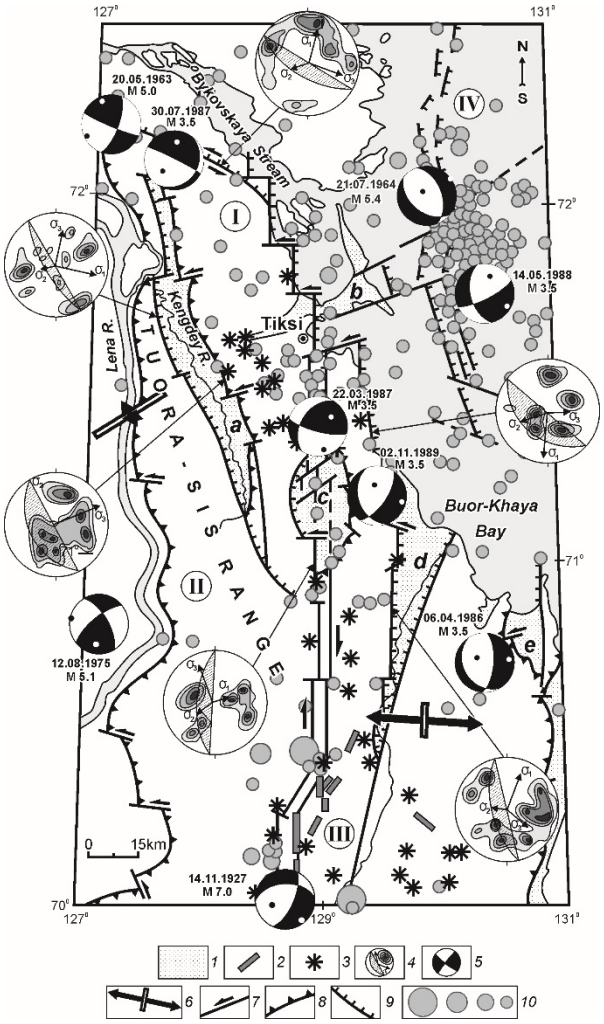

Figure 1: Seismotectonics of the Kharaulakh segment. 1 – Cenozoic depression: a – Kengdey, b – Khorogor, c – Kunga, d – Kharaulakh, e – Nyaybinskaya; 2 – seismodislocations; 3 – seismic features; 4 – rock fracturing diagrams, positions of vectors of the principal stress axes and fault planes; 5 – focal mechanisms, dates and magnitudes of earthquakes (lower hemisphere; the axes of the principal comressional and extensional stresses are marked by black and white dots); 6 – horizontal projections of the principal strain axes (extension, compression); kinematics of active faults: 7 – strike-slip faults, 8 – thrusts, 9 – normal faults; 10 – earthquake hypocenters sized by magnitude: ≥ 6.8, 6.7–5.0, 4.9– 4.0, ≤ 3.9 (data published by the Geophysical Survey of the Russian Academy of Sciences (GS RAS) and its Yakutian branch). Systems of active faults: I – Primorskaya, II – West Verkhoyansk, III – Kharaulakh, IV – Buorkhainskaya.

The most active area is the Kharaulakh zone of strike-slip faults with normal component. This zone is represented by the system of closely spaced sub-parallel longitudinal faults arranged en echelon to each other. The activity of the Kharaulakh faults is morphologically expressed in aerial photographs - these faults are associated with numerous troughs, ditches, landslides and avalanches. The seismic potential of the Kharaulakh fault zone is the highest. Five strong earthquakes (M = 5.8-7.0) took place at its southern termination in Bulunin 1927 and 1928, and more than 20 seismodislocations of the gravitational and tectonic genesis were identified in this area (Fig. 1, 2). Some of them, located south of the Kharaulakh depression, are observed as outcropped segments of active faults. The recent instrumental observations show seismic activity through the entire length of the Kharaulakh fault zone, from the cluster of the Bulun earthquakes to the Kunga depression in the north.

In an earlier structural-dynamic study (Imaeva et al., 2016), several zones witch different types of the crustal stress-strain state in the Kharaulakh segment of the Verkhoyansk fold system were identified. Each of such zones was characterized by a specific parageneses of faults, including normal, strike-slip and thrust faults or their combinations. The proposed zoning was supported by the geostructural field observations, as well as by the calculated STD parameters (Imaeva et al., 2017).

According to the STD data, the Kharaulakh segment includes two zones with transitional deformation settings, from the vertical strain to compression and extension. One zone is located within the Chekurov anticline in the northwestern flank of the Verkhoyansk-Kolyma fold system. The direction of compressive forces in this region influenced the formation of the strong earthquake source (M_w = 5.2). Another zone is the southern part of the Kharaulakh fault zone, wherein seismotectonic deformation shows the transition from the vertical strain to extension. In this area, compression is sublongitudinal, while extension is sublatitudinal (Fig. 2), which is not consistent with the parameters of the $M \geq 7.0$ Bulun earthquake focal mechanism. This discrepancy may arise as the focal mechanism determined for this seismic event is uncertain (Fujita et al., 2009).

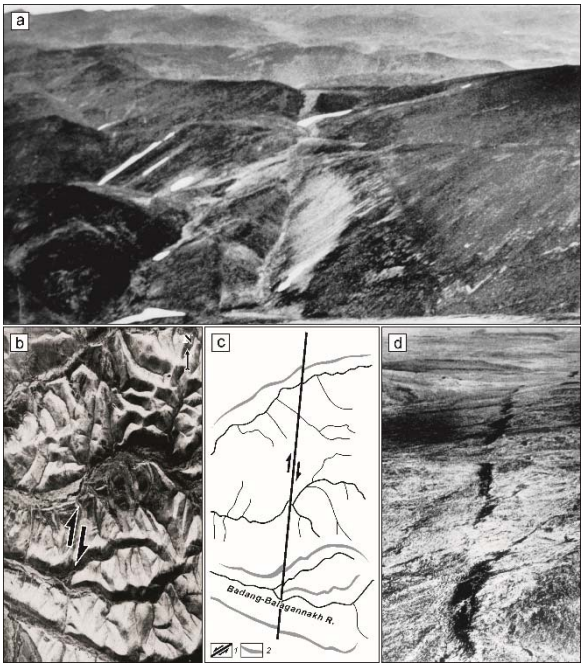

Figure 2: The Beris seismodislocation: (a) photo image of trenches exposed at the surface after Bulun earthquakes of 1927–1928 (M ≥ 7.0); (b) aerial image of Beris seismodislocation, with arrows indicating displacement direction along the fault plane; (c) fragment of aerial image interpretation: 1 – strike-slips, 2– axial parts of watersheds; (d) photo of seismogenic tension cracks in zone of Kharaulakh faults (location of Beris seismodislocation).

Thus, the analysis of the crustal stress state in the Kharaulakh segment verifies the existence of a unique transition region wherein the mid-oceanic and continental

crust structures are conjugated, and the tectonic stress field change, such that extension is replaced with compression.

Acknowledgements: Our studies were supported by the Russian Science Foundation Project 15-17-20000 – Seismogeodynamic Analysis and Seismic Zoning of the Eastern Segment of the Coastal Shelf Zone in the Russian Arctic Region and by the Russian Foundation for Basic Research 18-05-60009 - Seismogeodynamics and Potential Seismicity of the Arctic Sector of the Siberian Craton, and also project of DPMGI SB RAS (N 0381-2616-0001).

REFERENCES

Drachev, S., 2002. On the base tectonics of the Laptev Sea shelf. *Geotectonics* 6, 60-76 (in Russian).

Fujita, K., Kozmin, B.M., Mackey, K.G., Riegel, S.A., Imaev, V.S., & McLean, M.S., 2009. Seismotectonics of the Chersky seismic belt, eastern Russia (Yakutia) and Magadan district, Russia. *Geology, Geophysics and Tectonics of Northeastern Russia: a Tribute to Leonid Parfenov. Stephan Mueller,* Spec. Publ. Ser. 4, 117-145. doi: 10.5194/smsps-4-117-2009

Galabala, R.O., 1987. New data on the structure of the Lena river delta (Quaternary), Northeastern Asia. NEISRI FEB, *USSR Acad. Sci.*, Magadan, 152-172 (in Russian).

Imaev, V.S., Imaeva, L.P., & Koz'min, B.M., 2000. *Seismotectonics of Yakutia*. GEOS, Moscow, 226 (in Russian).

Imaeva, L.P., Imaev, V.S., & Koz'min, B.M., 2016. Dynamics of seismogenic structures of the frontal zone of the Kolyma-Omolon superterrane. *Geotectonics* 50 (4), 349-365. doi: 10.1134/S001685211604004X

Imaeva, L.P., Gusev, G.S., Imaev, V.S., & Mel'nikova, V.I., 2017. Neotectonic activity and parameters of seismotectonic deformations of seismic belts in the Northeast Asia. *Journal of Asian Earth Sciences* 148, 254-264. http://dx.doi.org/10.1016/j.jseaes.2017.09.007

Parfenov, L.M., Oksman, V.S., Prokopiev, A.V., Timofeev, V.F., Tretyakov, F.F., Trunilina, V.A., & Deikunenko, A.V., 2001. Collage of terranes in the Verkhoyansk-Kolyma orogenic area. In: *Tectonics, Geodynamics and Metallogeny of the Republic of Sakha (Yakutia)*. Nauka, Moscow, 199-254 (in Russian).

INQUA Focus Group Earthquake Geology and Seismic Hazards

paleoseismicity.org

Terrestrial Lidar surveying of active normal faults: Preliminary results from The Pidima fault scarp, Messinia, Greece

Karamitros, Ioannis (1), Ganas, Athanassios (1), Chatzipetros, Alexandros (2)

(1) National Observatory of Athens, Institute of Geodynamics, yannis_karam@yahoo.com
(2) Aristotle University of Thessaloniki, Department of Geology

Abstract: *The Geometrical and morphological features (azimuth, dip-angle, roughness etc.) of the active fault scarp in Pidima village (Messinia, Greece) were measured with the use of Terrestrial Laser Scanner (TLS) data. The fault scarp was surveyed during May 2015 and was supplemented with field data collected during the years 2014 and 2017. An extensive research was made on TLS applications on structural geology and fault scarps and a number of methods/algorithms were tested and applied. The result point cloud is of millimetre accuracy with its geometrical characteristics displayed with different textures. The TLS results are in close agreement with data collected in the field.*

Keywords*: Lidar, TLS, Fault, Pidima, Messinia, Geometry, Tectonics*

INTRODUCTION

The studied fault segment is located near Pidima village in the South Messinia basin, in Southern Greece. The basin is covered by post orogenic sediments of Pliocene to Quaternary age, unconformably overlying the basement (alpine) rocks of the tectonic zones of Gabrovo - Tripolis and Olonos - Pindos (Mariolakos & Spyridonos, 2010; Mountrakis, 2010). The fault is part of the Eastern Messinia Fault Zone (EMFZ; Valkaniotis et al., 2015) and its trace is located in the western side of the Taygetus mountain range (Fig. 1). The area is one of the most tectonically and seismically active in the Hellenic Arc, mostly because it is located about 60 km from the Hellenic trench, where the African plate subducts below the Eurasian one (Ganas & Parsons, 2009; Mariolakos & Spyridonos, 2010). The neotectonic structure of SW Peloponnesus is characterised by the presence of tectonic grabens and horsts striking NNW-SSE and E-W (Mariolakos & Spyridonos, 2010). The Pidima active fault has a N-S orientation and dips towards WSW.

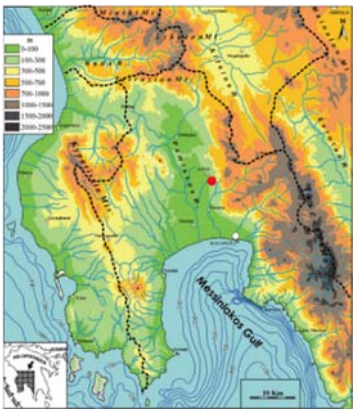

Figure 38: The area of SW Peloponnesus with the borders of the Messinia basin in the centre. The red dot indicates the area around Pidima village where the Fault Plane is located (modified from Fountoulis et al., 2014).

METHODS

The fault scarp data was collected in the field with the use of Lidar technology and onsite measurements. Lidar is a remote sensing system and is an acronym of "Light Detection and Ranging". The instrument operates by emitting intense, focused beams of light to a target, in order to measure the time it takes for the reflected light to be detected by the sensor and finally compute where the object is located in three dimensions (Schmid et al., 2012). The ground based laser is called TLS (Terrestrial Laser Scanner) and can be mobile or stationary. The resulting product is a densely spaced network of elevation points based on the Cartesian coordinates (x, y, z) of the reflected points, called point cloud. These three-dimensional coordinates of the target objects are computed from the time difference between the laser pulse being emitted and returned in association with the starting angle of the pulse and the absolute location of the sensor. The measure of the reflection strength of the laser pulse upon returning to the laser scanner is called Intensity. This value is dependent on the reflectivity of the target material, range to the target and atmospheric conditions (Hodgetts, 2013). The primary goal of the research was to use TLS to identify the geometric characteristics of the Pidima fault surface such as the distribution of the dip direction change across its surface.

DATA ACQUISITION

The survey of the fault plane was carried out during May 2015 using the ILRIS-(3D-HD) laser scanner by Optech. We performed a static close-range scanning, in the distance of 10m normal to the fault plane, essential for millimetre accuracy. Due to extreme weather conditions the survey of south upper part of the fault surface was not completed (Fig. 2). The fault plane data is in the form of four overlapping scans along the length of the plane, aligned together, with a total of 10582758 (ten and a half million) points.

Figure 39: Panoramic view of the fault plane near Pidima. The area of the surface surveyed is enclosed in the red box. View to the East.

The removal of remaining vegetation and noise points was made manually and the removal of eroded points, Semi-Automated. Afterwards the data was subsampled for computational purposes at 3621287 cloud points.

RESULTS AND DISCUSSION

The initial data was imported on the CloudCompare software and consists of the coordinates of each point and its intensity values. At this processing stage it represents an accurate depiction of the fault surface and the difference in the surface materials is evident even without color (Fig. 3). From the 3D model the maximum length of the fault surface was calculated at 27.84 m and the maximum width (that is top to bottom) at 7.981 m. The Dip Direction and Dip angle of every point was then calculated and illustrated with different colors across the surface, as shown in figures 4 and 5.

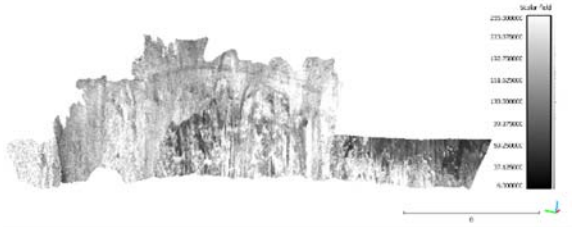

Figure 40: The Pidima fault 3D model, cleaned and subsampled, giving a visual comparison of the intensity value of the surface materials in greyscale.

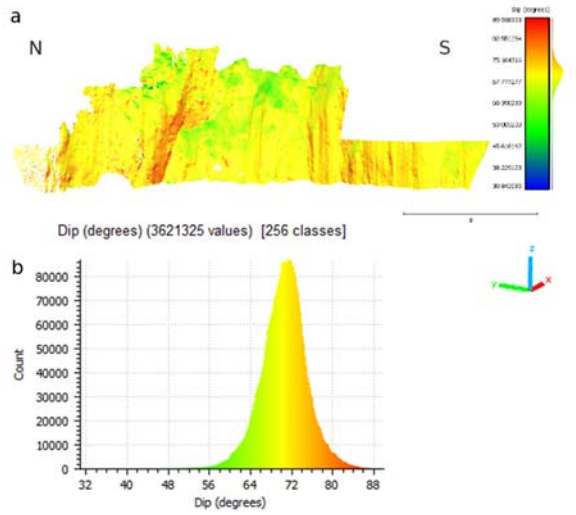

Figure 41: a) Cleaned scarp image showing distribution of dip-angles along strike (see scale on the right; n=3.6 million points) and b) histogram of dip-angle values.

In conclusion, the TLS data of Pidima Fault plane gave many useful and interesting results. The image analysis of the fault plane allowed for a detailed logging of some of its geometrical characteristics.

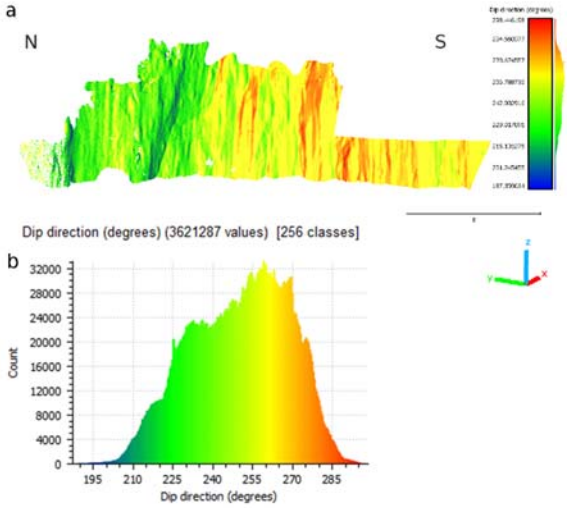

Figure 42: a) Cleaned scarp image showing distribution of dip directions along strike (see scale on the right; n=3.6 million points) and b) histogram of dip-direction values.

The fault plane demonstrates significant changes along its surface, such as lower dip-angles in its upper part (Fig. 4) and a difference in dip direction in its northern part (Fig. 5). For more conclusive results a complete survey of the fault plane is required with the addition of photogrammetry survey for comparison and to complement the results. It is important to mention that a digital image integration would improve the analysing methods immensely and even allow for more advanced methodologies.

Acknowledgements: This research was funded by project ASPIDA "Infrastructure Upgrade for Seismic Protection of the Country and Strengthen Service Excellence through Action", project MIS-448326, implemented under the Action "Development Proposals for Research Bodies-KRIPIS.". We acknowledge Sotiris Valkaniotis, Konstantina Betzelou and Elena Partheniou for field support. Use of CloudCompare software.

REFERENCES

Fountoulis, I., Mariolakos, I., & Ladas, I., 2014. Quaternary basin sedimentation and geodynamics in SW Peloponnese (Greece) and late stage uplift of Taygetos Mt.

Ganas, A., & Parsons, T., 2009. Three-dimensional model of Hellenic Arc deformation and origin of the Cretan uplift. *Journal Geophysical Research* 114, B06404, doi: 10.1029/2008JB005599.

Hodgetts, D., 2013. Laser scanning and digital outcrop geology in the petroleum industry: A review. *Mar. Pet. Geol*. 46, 335-354.

Karamitros, I., 2016. Applications of Terrestrial Laser Scanning technology in structural geology (MSc thesis).

Mariolakos, I., & Spyridonos, E., 2010. Remarks on the karstification in the wider area of the Upper Messinia closed hydrogeological basin (SW Peloponnesus, Greece). Bull. Geol. Soc. Greece 43, 1785-1791.

Mountrakis, D.M., 2010. *Geology of Greece*.

Schmid, K., Waters, K., Dingerson, L., Hadley, B., Mataosky, R., Carter, J., & Dare, J., 2012. Lidar 101: An introduction to lidar technology, data and applications.

Valkaniotis, S., Betzelou, K., Zygouri, V., Koukouvelas, I., & Ganas, A., 2015. Late Quaternary tectonic activity and paleoseismicity of the Eastern Messinia Fault Zone, SW Peloponessus (Messinia, Greece), *Geophysical Research Abstracts*, Vol. 17, EGU2015-13215-1, 2015, EGU General Assembly 2015.

INQUA Focus Group Earthquake Geology and Seismic Hazards

paleoseismicity.org

Mechanism of Earthquake migration: Case study Lut block area, Eastern Iran

Khatib, Mohammad Mahdi (1), Zarei, Saeed (1)

(1) Department of Geology, University of Birjand, Birjand, Iran, mkhatib@birjand.ac.ir

Abstract: *The Lut block (LB) in the eastern part of Iranian plateau bordered by large strike-slip faults which concentrated an intercontinental deformation due to convergence the Afro-Arabian and Eurasian plates. Several large earthquakes occurred in the LB. The mechanism of the earthquake sequences in the LB studied by using of the variation functions and major earthquake epicentre movements, thickness of earth crust, it's underneath viscosity, Momentum, and variation stresses analysis investigated and by fuzzy logic were analysed. Ratio of the geodetic moment rate to the seismic moment rate obtained more than 3.07 which ratio reflects the important role of the inter-seismic deformation in this area. The results indicate that south-eastern part of LB has a highest potential of seismicity. Geostatistics process show whole faults have seismic migration, in addition to earthquake migration on the strike of maximum regional stress, large part of migration observed on the south and south-eastern of LB.*

Keywords*: Lut Block, earthquake migration, Seismic Moment, Coulomb stress changes, Fuzzy logic*

INTRODUCTION

Earthquakes interact with each other presented in many different ways. Coulomb stress calculations on successive earthquake on north of Lut block is a good evidence for this matter that earthquakes cannot be treated as individual independent events. The Lut block is located on the eastern part of Iranian plateau and bordered by large strike-slip faults to the east and west[1, 2, 3] which concentrated an intercontinental deformation due to convergence the Afro-Arabian and Eurasian lithospheric plates. Several large earthquakes have influenced the settlements in the Lut block in the past causing heavy damage in the region (Fig. 1).

This research contains three part of our study in Lut block: Evaluation of seismicity triggering, Estimation of the seismicity potential based on Geodetic, seismic and geological moment rate, and earthquake migration using the Fuzzy logic parameters.

THE COULOMB STATIC STRESS CHANGES ON DAHST-EBYAZ AND ZIRKUH AREA

The stress change maps would be useful for earthquake hazard to foresee the most likely locations of the upcoming aftershocks [4-7]. Generally, the changes in Coulomb stress range 0.1 to 1 bar, which are considered enough to trigger the future earthquakes. We perceive that the successive events on the Dasht-e-Bayaz areas have characteristic spatial distribution patterns and the seismicity after the main shocks is consistent with the Coulomb stress change. For all the computations, we used the shear modulus(G) of 3.2 × 105 bars, in a uniform elastic half-space with Poisson's ratio(v) of 0.25, Young modulus (E) 8 × 105 bar and an effective coefficient of friction which is include the effect of pore fluid pressure and has been postulated to vary in the range 0.2–0.8. With an average value of μ'= 0.4 often used. Coulomb 3.3 software is used to calculate Coulomb failure stress changes [10]. The rupture parameters (strike, dip, rake and depth) and source faults of the earthquakes after the 1968 W, Dasht-e-Bayaz earthquakes are defined from the published studies [2-3].

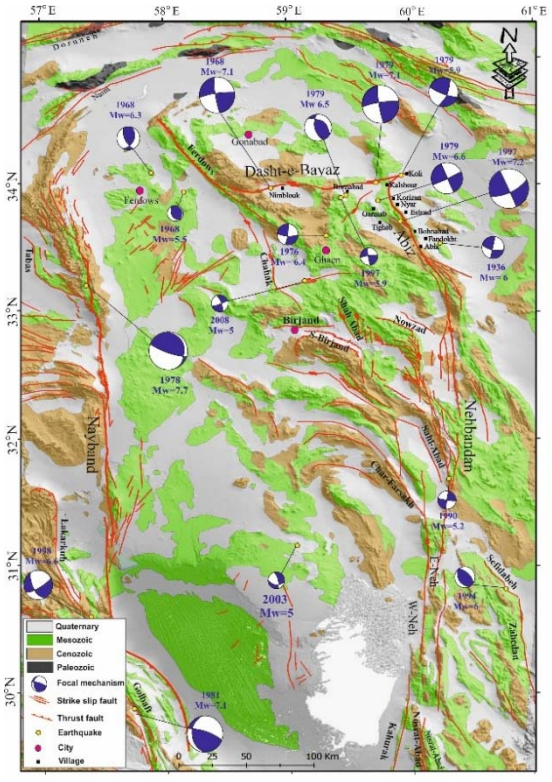

Figure 1: Earthquake-fault map of the eastern Iranian plateau between Dasht-e- Bayaz and northern Makran on the south (Lut block), showing major faults and Fault-plane solutions for 1968-1997 earthquake sequence with Mw>5.

The empirical relationships proposed by Leonard have been used to calculate the width, length and slip of the source faults and assuming homogeneous fault slip. The calculated the Coulomb stress change indicated that the 1968 Dasht-e-Bayaz main shock can "trigger" the second one or more of the Ferdows thrust fault (1968.09.01, Ferdows earthquake) and the eastern section of the Dasht-e-Bayaz segment (1979.11.27, Koli-Buniabad earthquake) into the failure regime by showing a positive increase (≥0.5bar) in coulomb stress(Fig.2).

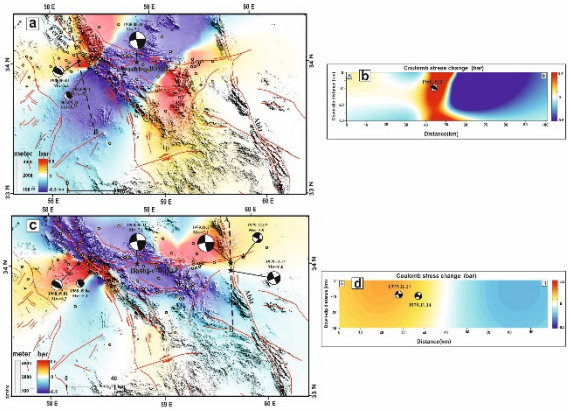

Figure 2: (a) The Coulomb stress change associated with the 1968 Dasht-e-Bayaz earthquake. Red colours indicate an increase in ΔCFS, and Blue colours indicate a decrease. The source fault that includes the western part of Dasht-e-Bayaz strike-slip and the assumed receiver fault that include the Ferdows are shown. (a and b) map and Cross-sectional view of the Coulomb stress change due to the Dasht-e-Bayaz earthquake through the 1968 Ferdows event along the dashed line AB. The occurrence of the 1968 Ferdows earthquake in the positive Coulomb stress change lobe shows that it was triggered Due to the transfer of stress increase from the co-seismic slip of the 1968 Dasht-e-Bayaz earthquake. (c) Map of the Cumulative Coulomb stress changes imparted by the 1968 Dasht-e-Bayaz and Ferdows earthquakes to the E; Dasht-e-Bayaz receiver fault. (d) The cross-sectional view of the fault traces are shown based on the A–B dashed line. Beach balls show the main shock locations. The focal mechanisms are taken from the Global Centroid Moment Tensor.

The 18 years later, damaging Zirkuh earthquake (Mw 7.2) occurred on a conjugate right-lateral Abiz Fault that was inconsistent with the stress-change field calculated for preceding large earthquakes on the Dasht-e-Bayaz Fault. Thus, we examined the triggering effect of previous events of the Abiz fault including those segments that had ruptured during the 30 June 1936 Abiz, 14 November 1979 Korizan, and 7 December 1979 Kalat-e Shur earthquakes (Fig. 3). Our results suggest that a Zirkuh earthquake is occurred in enhanced Coulomb stress zone which is confirmed by the cross sections drawn perpendicular to the Abiz fault plane.

Also, we modelled the Coulomb stress changes due to the 1997 Zirkuh earthquake on the surrounding faults to expand insights as to which fault segments are now more hazardous (closer to failure) than they were before the Zirkuh earthquake. Stress map view on optimum oriented fault shows positive increased stress zones that transfer stress at some sites located at the ruptures tips and off the fault regions from north to south of Abiz Fault. It is documented that southern parts of Abiz Fault are candidate for occurrence the next events (Fig. 4).

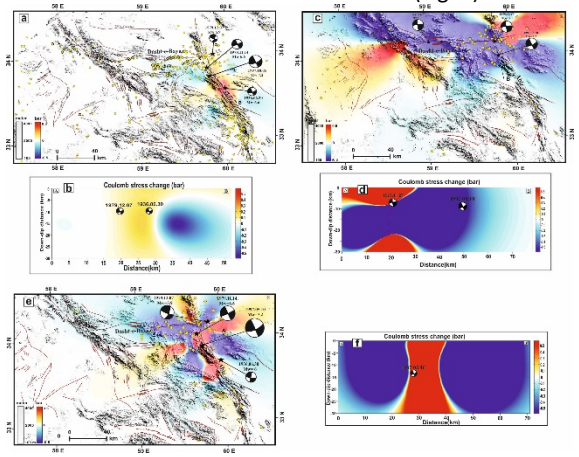

Figure 3: (a) Map of Coulomb stress changes caused by the 1936 Abiz earthquake and its triggering effect on later Abiz earthquake. (b) Cross-sectional view of the Coulomb stress change due to the 1936 Abiz earthquake through the 1979 Korizan and Kalat-e-shur earthquakes along the dashed line AB. (c) Map view and cross section of Cumulative Coulomb stress change (in bars) from the 1968 Aug 31 earthquake and 1979 Nov 27 to the Abiz receiver fault. Considering coefficient of friction is 0.4. (e and f) Coulomb stress changes associated with Abiz earthquake sequence (1936-1979). The occurrence of Zirkuh main shock doublet (Mw=7.2) in positive Coulomb stress shows that it was triggered due to transfer of positive Coulomb stress from co-seismic slip of earlier events on the Abiz fault. Figure of cross sections show the cross sectional view of Coulomb stress change along line AB.

To validate the Coulomb stress calculations, we plotted the earthquakes after the main shocks on the each stress changes map and good correlations between the main shock stress changes and the spatial pattern of the seismicity were observed at the terminate part of strike slip faults. However, these results suggest that the majority of earthquakes occurred at zones of larger stress increased zones; the effects of regional stress field should be considered.

GEODETIC, SEISMIC AND GEOLOGICAL MOMENT RATE IN THE LB

Estimate of moment rate is comparatively reckoned as a new method for dealing with tectonic activities rate in different regions and it prepares the way for putting together different methods. Depending on the type of deformation and geometry of fault, the study area divided to the 5 zones (Fig.4). Then we compare value of three type of moment rate in these zones to each other. The most moment rate in the Lut block belongs to geodetic approach (1.2119×10^{18} Nm/yr) and then seismic moment rate (3.9455×10^{18} Nm/yr) and finally the least quantity belongs to geologic moment rate (2.4882×10^{16} Nm/yr).

The most of seismic moment rate was obtained respectively in Zone 3, 1, 4, 5 and 2. According to seismic map, maximum seismic moment is along Abiz, Dasht-e- Bayaz and Tabas Faults. These faults are responsible for large earthquake in the study area. Maximum geologic moment rate is related to west-Neh, East-Neh, Kahoorak, Abiz and Nosrat-abad Faults. According to values of geological and geodetic moment rates in the south-eastern of Lut area and based on

the value of the release seismic energy in the north and western part of Lut area, it seems that in the next time, the most of seismic potential and seismic hazard are in the south-eastern part of study area.

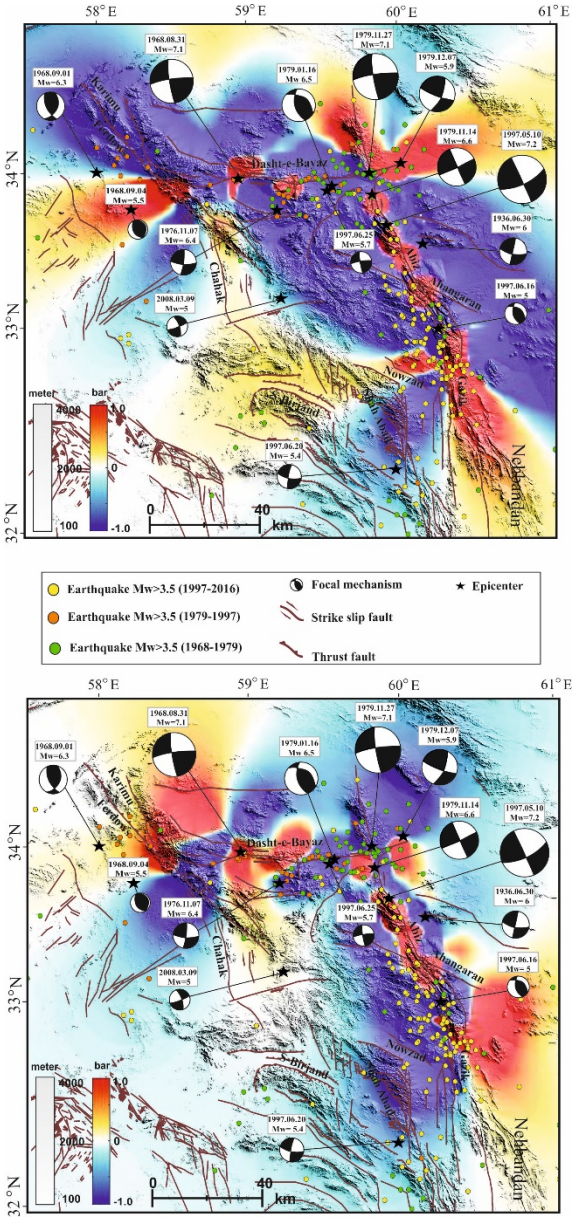

Figure 4: Cumulative stress changes (in bars) on optimally-oriented strike slip (a) and thrust (b) fault caused by major earthquakes in the Dsht-e-Bayaz and Zirkuh area. The source planes are Dasht-e Bayaz and Zirkuh faults, the main earthquakes are indicated by the black stars. Most aftershocks or small earthquakes with Mw ≥ 3.5 (White circles: 1997-2016 and grey circles: 1968-1997) shows events that occur in the study area. Yellow circles during 1997 Zirkuh earthquake to 2016 occur in regions where the stress change on optimally oriented Dasht-e-Bayaz and Abiz faults was raised by the 1936-1997 Earthquakes. It is observed that maximum number of events falls in the southern parts of Abiz fault. The potential active faults represented in southern parts of the Abiz fault (Nehbandan fault and its segments), North and North East part of the Abiz fault and in west of the Dasht-e-Bayaz area like Karimu thrust fault.

Ratio of the geodetic moment rate to the seismic moment rate obtained more than 3.07 which ratio reflects the important role of the inter-seismic deformation in this area. Ratio of seismic moment rate to geological moment rate is 0.63 %. This value indicates that 0.63 % potential of the faults for seismic energy has been released as significant part of the elastic energy in the area at the future.

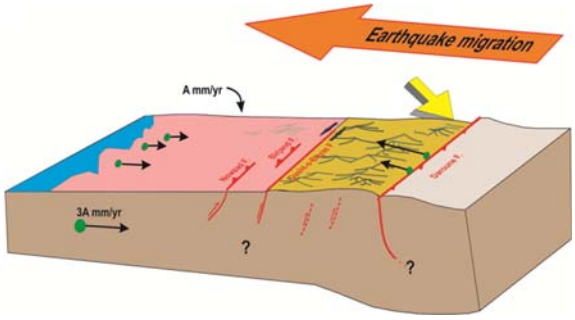

Figure 5: Proposed seismotectonic pattern for Lut block based on earthquake migration analysis on this study.

FUZZY LOGIC AND EARTHQUAKE MIGRATION

In this study the mechanism of the earthquake sequences in the Lut block tectonic history by using of the variation functions and major earthquake epicentre movements, thickness of earth crust, it's underneath viscosity, Momentum, and variation stresses analysis investigated and by fuzzy logic were analysed. Our results indicate that south-eastern part of Lut block has a highest potential of seismicity. Geostatistics process of hot point migration (points with high seismic moment) in yearly ranges show whole faults have seismic migration but in the study area, in addition to earthquake migration on the strike of maximum regional stress(NE-SW), large part of migration observed on the south of Lut block. This migration vergence is important for seismicity risk analysis.

In other word, north Lut block locking was observed following the stress increasing from the convergence of afro-Arabian plate and Makran subduction zone. Earthquake will migrated toward south and south-eastern part of Lut block as a result of tectonic stress (Fig.5). These results consistent with Coulomb stress calculations and moments rate comparisons.

CONCLUSION

In this research revealed that earthquake-induced stress increases of several bars triggered the sequential earthquake in the Dasht-e-Bayaz (1968-1979) and Abiz (1936-1997) faults, each earthquake raising the probability of future events at the site of the next-to-strike. Distribution map of earthquake(1997-2017) and cumulative stress changes (in bars) on optimally-oriented strike slip and thrust fault caused by major earthquakes in the Dasht-e-Bayaz and Zirkuh area show positive increased stress zones that transfer stress at some sites located at the ruptures tips and off the fault regions from north to south of Abiz Fault. It is documented that southern parts of Abiz Fault such as Abgarm, Avaz, north of Ardekul, Dastjerd, Zeidan and Ahangaran fault are candidate for occurrence the next events.

This value shows seismic energy that has been released as a significant part of the elastic energy in the area at the future.

Acknowledgements: We would like give thanks to University of Birjand for support this Project.

REFERENCES

Tirrul, R., Bell, I.R., Griffis, R.J., & Camp, V.E., 1983. The Sistan Suture Zone of eastern Iran. *Geol. Soc. Am. Bull.* 94, 134-150.

Nowroozi, A.A., & Mohajer-Ashjai, A., 1985. Fault movements and tectonics of eastern Iran:boundaries of the Lut plate. *Geophys. J.Royal Astron. Soc*. 83, 215-237.

Walker, R., & Jackson, J., 2002. Offset and evolution of the Gowk fault, S E Iran:A major intracontinental strike-slip system. *J. Struct. Geol*. 24, 1677-1698.

Steacy, S., Gomberg, J., & Cocco, M., 2005. Introduction to special section: stress transfer, earthquake triggering and time-dependent seismic hazard. *J Geophy Res* 110 (B05S01), doi: 10.1029/2005JB003692.

Steacy, S., Marsan, D., Nalbant, S.S., & McCloskey, J., 2004. Sensitivity of Static Stress Calculations to the Earthquake Slip Distribution. *J Geophy Res* 109 (B04303), doi: 10.1029/2002JB002365.

McCloskey, J., Nalbant, S.S., & Steacy, S., 2005. Indonesian earthquake: Earthquake risk from co-seismic stress. *Nature* 434, 291, doi: 10.1038/434291.

Sarkarinejad, Kh., & Ansari, Sh., 2014. The Coulomb stress change and sesimicity rate due to the 1990 Rudbar M 7.3 earthquake. *Bull Seismol Soc Am*, doi: 10.1785/0120130314.

INQUA Focus Group Earthquake Geology and Seismic Hazards

paleoseismicity.org

The Hellenides: A complicated, multiphase deformed Alpine orogenic belt. Compression vs extension, the dynamic peer for the orogen making

Kilias, Adamantios (1)

(1) Department of Geology, Aristotle University of Thessaloniki, 54124-Thessaloniki, Greece, kilias@geo.auth.gr

Abstract: *We present the main geological structure and architecture of the Hellenic orogenic belt, as well as the new aspects for its geotectonic evolution during the Alpine orogeny, based on our recent studies and experience about the deformational history of the Hellenides but also on the more modern views, published from others colleagues, concerning the Alpine geotectonic reconstruction of the Hellenides. From the Jurassic to present day compression alternated progressively with extension leading to the making of the Hellenic orogen, while the Axios/Vardar suture zone should be traced along the northern boundary of the Rhodope nappe stack with the Strandja/Sredna Gora massifs.*

Keywords*: Hellenides, compression, extension, orogeny, deformation*

INTRODUCTION

The Hellenides, as a branch of the broader Alpine orogenic belt in Laurasia were resulted from the convergence and final continental collision of Europe and Apulia (Africa) plates in a complicated, multiphase deformational regime, with the question around the existence of one or more Tethys ocean basins between Europe and Apulia continents to remain under debate until today (Fig. 1; Gawlick et al., 2008; Kilias et al., 2010; Robertson, 2012).

The goal of this work was to present the main geological structure and architecture of the Hellenic orogenic belt, as well as the new aspects for its geotectonic evolution during the Alpine orogeny. We based on our recent studies and experience about the deformational history of the Hellenides but also on the more modern views, published from others colleagues, concerning the Alpine geotectonic reconstruction of the Hellenides.

GEOLOGICAL SETTING

According to the traditional subdivision of the Hellenides in isopic zones they are, from the West to the East the following (Fig. 1, 2): **I.** Paxos zone, Ionian zone, Gavrovo zone, Parnassos zone and Pindos zone (including the Koziakas unit) forming the External Hellenides and **II.** Pelagonian zone (or nappe), Sub-Pelagonian zone, Axios/Vardar zone, Circum-Rhodope belt, Serbo-Macedonian massif, Rhodope massif and Attico-Cycladic massif belonging to the Internal Hellenides.

In a general view the Internal Hellenides are tectonically emplaced onto the External Hellenides during the Tertiary (Fig. 1). A Paleocene-Eocene age's high-pressure metamorphic belt marks the tectonic contact between the Internal and External Hellenides in the Olympos-Ossa and Cyclades area (Fig. 1; Okrusch & Broecker, 1990; Schermer, 1993; Kilias et al., 2002). While in the Olympos-Ossa area an Oligocene-Miocene isothermal decompression metamorphic path is recognized associated with rapid exhumation of the high-pressure rocks, in the Cycladic blue schists unit the exhumation was followed during the Oligocene-Miocene by a decompression path with an initially increasing temperature gradient, migmatization and granitoide intrusions (Okrusch & Broecker, 1990; Schermer, 1993; Kilias et al., 2002, 2010). A younger high-pressure/low-temperature (HP/LT) metamorphic belt of Oligocene-Eocene age is also recorded in between the tectonostratigraphic domains of the External Hellenides in the southern Peloponnese and Crete island. Isothermal decompression path during the Early-Middle Miocene has been described for the southern Peloponnese and Crete island (Seidel et al., 1982). Furthermore, in the Serbo-Macedonian and Rhodope massifs Tertiary high- to ultrahigh-pressure metamorphic rocks have been also described. They are strongly affected by medium- to high-temperature retrogressive metamorphism, partly reaching migmatization conditions until granitoide intrusions. Decompression evolved through an increasing temperature gradient (Liati & Gebauer, 1999). Early Jurassic and Cretaceous ages have been also dated for high-pressure parageneses in the Serbo- Macedonian/Rhodope metamorphic province (Wawrzenitz & Mposkos, 1997; Jahn-Awe et al., 2010; Froitzheim et al., 2014).

STRUCTURAL EVOLUTION

The Alpine structural evolution starts with the continental rifting of the Pangaia Super-continent during the Permo-Triassic and the opening of the Neotethyan ocean. Bimodal magmatism and A-type granitoide intrusions associate the initial stages of the continental rifting (Mountrakis et al., 1983; Koroneos et al., 2013). Subsequently, deformation history and metamorphism are recorded in six main deformational events from the Middle-Jurassic to present day (D1-D6) showing in the Table I and Fig. 1,2 (Kilias et al., 2010, 2013; Katrivanos et al., 2013). Older Paleozoic deformational events have been strongly overprinted by the Alpine deformation. They are recognized only as rests in some places in the Paleozoic basement rocks of the Internal Hellenides.

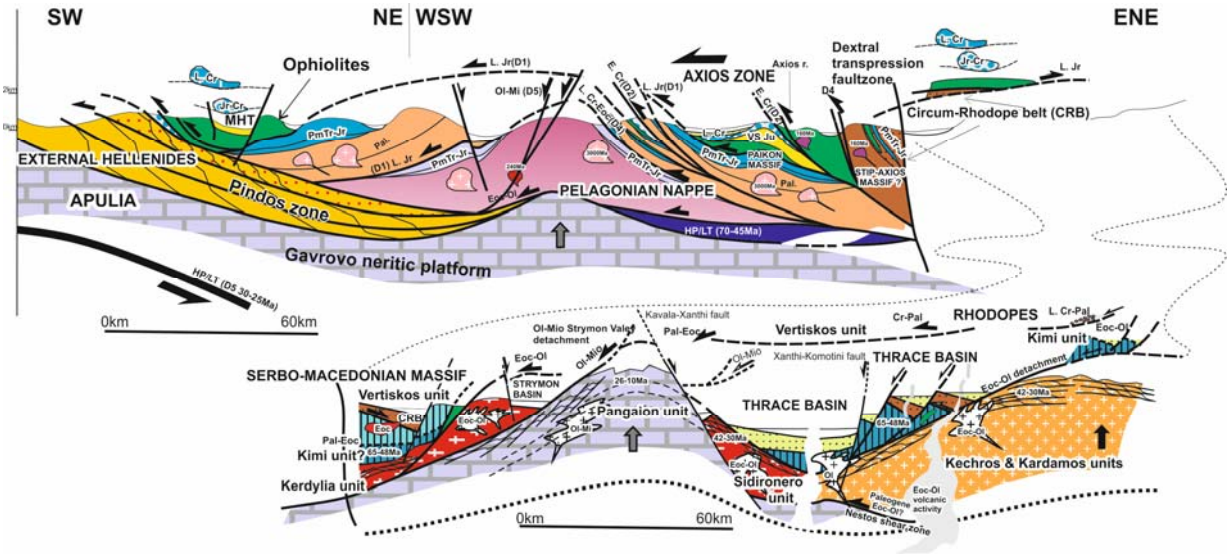

Figure 43: Geological cross-section through the northern Hellenides. The D1 to D6 deformational events are shown (modified after Kilias et al., 2013).

Table 1: Summarized the structural evolution of the Internal Hellenides during the Alpine orogeny.

1. **Permo-Triassic**, continental rifting, bimodal magmatism and A-type granite intrusion.
2. **Triassic-Jurassic**, passive margins extension and sedimentation.
3. **Middle Jurassic**, intraoceanic subduction, amphibolite sole, ophiolite mélanges, island arc magmatism.
4. **Mid-Late Jurassic**, ophiolite obduction, high-pressure metamorphism, retrogression from greenschist to amphibolite facies conditions metamorphism, W-ward sense of movement and imbrication. E-ward sense of movement? **D1.**
   Deposition during extension? of the **Upper Jurassic-Lower Cretaceous** sediments above the obducted ophiolite belt or at the front of the obducted ophioites.
5. W-ward imbrication during the **Albian-Aptian (Early Cretaceous)**, syn-tectonic metamorphism, **D2.**
6. **Upper Cretaceous** extension, carbonate transgression terminated in the Paleocene internal Hellenides flysch, **D3.** Subduction of the Axios/Vardar ocean remnants under the Europa margin.
7. **Tertiary** compression **(Paleocene-Eocene)**, W-ward sense of movement, HP/LT metamorphism and building of the Internal Hellenides high pressure belt of Paleocene-Eocene age, progressively, emplacement of the Pelagonian nappe together with the HP/LT internal metamorphic belt on the External Hellenides, **D4**. Syn-orogenic extension associated with high-temperature metamorphism, migmatization and magmatism in the Serbo-Macedonian/Rho-dope metamorphic province.
8. HP/LT metamorphism and building of the External Hellenides high pressure belt of **Oligocene-Miocene** age associated with compression and nappe stacking in the External Hellenides. Syn-orogenic extension, high-temperature metamorphism and magmatism in the Internal Hellenides (**D5;** Olympos-Ossa, Kyklades and Serbo-Macedonian/Rhodope metamorphic province).
9. **Neogene-Quaternary**, active Hellenic subduction, extension and intramontagne basin formation, **D6**. Recent neo-tectonic activity.

During the Alpine orogeny in the Hellenides compression, nappe stacking and high-pressure metamorphism alternated progressively through time with extension, orogenic collapse and medium- to high-temperature metamorphism that was leading to uplift and exhumation of deep crustal levels. The deformation during the extensional stages were progressively evolving from ductile to brittle conditions. An S- to SW-ward migration of the dynamic peer compression vs extension is clearly recognized during the Alpine orogeny in the Hellenides. In any case extension and crustal uplift follow compression and nappe stacking (Kilias et al., 1999; Burg, 2012; Kilias et al., 2013).

The kinematic pattern of extension and compression tectonics appears to be complicated, but nevertheless for both stages, compressional and extensional, the recognized stretching lineation is roughly perpendicular to the Hellenic arc; that is NE-SW trending in the west and N-S trending in the center, with a main movement direction, at least for the compressional tectonics, SW- and S-ward, respectively (Kilias, 1991; Kilias et al., 1999, 2002, 2010; Jolivet et al., 2004; Papanikolaou, 2013). The sense of shear during the extensional stages of deformation and the nappes' collapse appears in many places bivergent, indicating an important component of bulk coaxial deformation during extension (Fig. 1,,2; Kilias et al., 1999, 2002).

GEOTECTONIC RECONSTRUCTION

According to our more recent structural works (Kilias et al., 2010, 2013; Katrivanos et al., 2013; Michail et al., 2016), as well as a lot of studies from others researchers, concerning the geodynamic evolution of the Hellenides (e.g. Jolivet et al., 2004; Gawlick et al., 2008; Jahn-Awe et al., 2010; Froitzheim et al., 2014), we suggest that all ophiolite belts in the Hellenides, as well as the Middle-Late Jurassic island

arc magmatic products during the Neotethyan intra-oceanic subduction (Michard et al., 1998; Michail et al., 2016), subsequently incorporated in between the AxiosVardar zone units and the Circum-Rhodope belt, were originated from a single source and this was the Neotethyan Axios/Vardar ocean basin. The latter closed finally during the Late Cretaceous-Paleocene subducted under the European continental margin, including the Serbo-Macedonian and Strandja/ Sredna Gora massifs (Fig. 2). In this content, the ophiolite nappes and the island arc magmatic products should be considered as far-travelled nappes on the Hellenides continental parts (Pelagonian nappe and Serbo-Macedonian massif), associated with deposition of Mid- to Late Jurassic ophiolite mélanges in basins at the front of the ophiolite thrust sheets (Fig. 1, 2; Gawlick et al., 2008; Kilias et al., 2010; Kostaki et al., 2013). Furthermore, the deposition of the Upper Jurassic sedimentary carbonate series (Gawlick et al., 2008; Robertson, 2012; Kostaki et al., 2013) on the top of the obducted ophiolite nappe clearly determine the upper limit of the ophiolite emplacement (?Kimmeridgian/Tithonian; Fig. 1, 2). In this scenario we assume that the Vardar/Axios ophiolites are also allochthones and they do not mark a typical suture zone (Fig. 1, 2).

The suture zone between the Pelagonian nappe and External Hellenides (Apulia plate) was dated coeval in time with the suturing taken place during the Tertiary along the Nestos thrust between the Rhodopes nappes, in detail, between the lower carbonate Pangaion unit and the Sidironero unit (Fig. 2; Schermer, 1993; Kilias, 1995; Dinter, 1998; Jahn-Awe et al., 2010; Froitzheim et al., 2014; Gautier et al., 2017). It is also supported by the existence of the Paleocene-Eocene high- to ultrahigh pressure metamorphic belt recognized in the Rhodope units (Liati & Gebauer, 1999; Froitzheim et al., 2014), as this Paleocene-Eocene age`s high-pressure metamorphism has been already described for the suture zone between Pelagonian nappe and the Gavrovo carbonate platform of the External Hellenides (Fig. 2, 3; Schermer, 1993; Kilias, 1995). The main difference is that the Rhodope units are under higher metamorphic conditions metamorphosed than the Pelagonian nappe and its suturing with the External Hellenides. It can be easy explained due to their geotectonic position in deeper and more internal structural levels of the Hellenic orogen.

Regarding the above described structural architecture, the lower-most Pangaion Rhodope unit should be the marginal part of the Apulia plate, which was unterthrusted below the Internal Hellenides, i.e. the Pelagonian and Serbo-Macedonian massifs. The latter be supposed as the European margin at the eastern part of the Neothethyan Ocean realm (Fig. 2; Jahn-Awe et al., 2010; Froitzheim et al., 2014; Gautier et al., 2017). Therefore, the lower most Pangaion Rhodope unit should be equivalent to the Olympos-Ossa carbonate unit and the External Hellenides Gavrovo zone. The higher, compared to the latter, metamorphic conditions affected the Rhodope Pangaion unit can be explained by the fact that the Pangaion unit corresponded to the deeper buried, towards the East, parts of the same Apulia carbonated platform under the internal Hellenides nappe stack. The same Apulia carbonate platform is also exhumed in the Attico-Cycladic massif and in the same geotectonic position but here, was metamorphosed during the Paleocene-Eocene under high-pressure conditions. Additionally, in the Cyclades area is exhumed the Paleozoic basement of the Apulia plate as metamorphic core complexes under the carbonate platform and the overlain Internal Hellenides nappe stack but with the latter to be appear only as rests or as deposited erosional material in the Neogene basins (Jolivet et al., 2004).

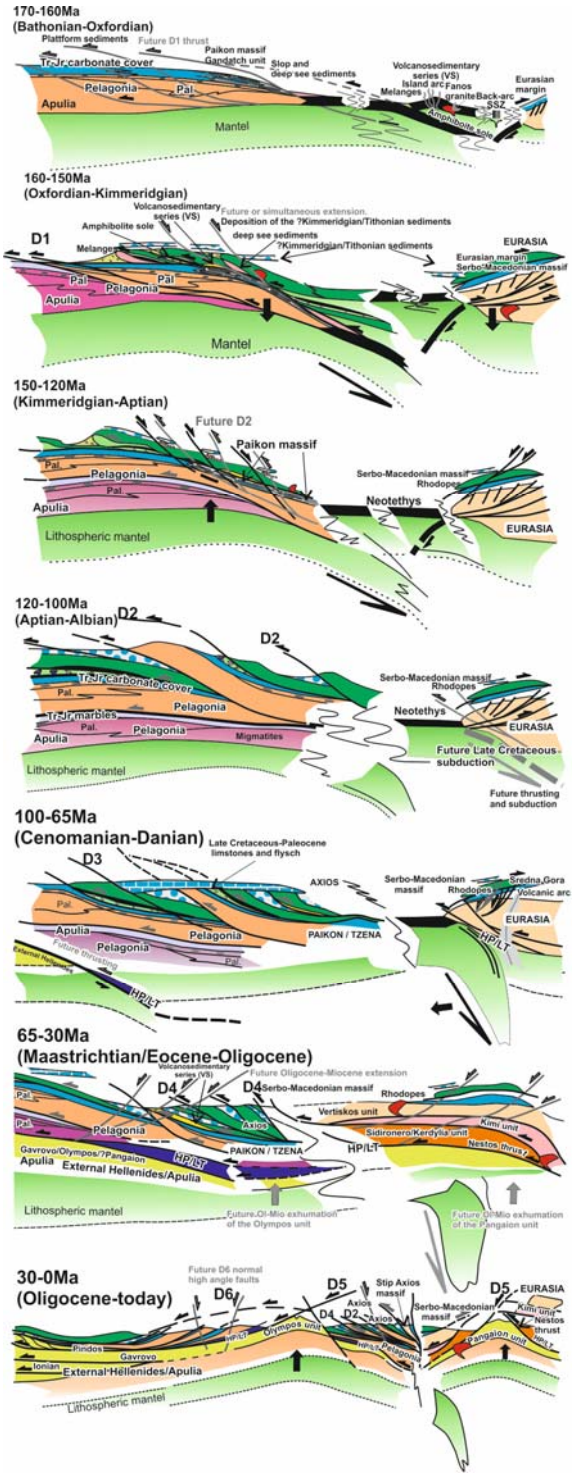

Figure 2: The structural evolution of the Hellenides during the Alpine orogeny (D1 to D6 events). Without scale (modified after Kilias et al. 2010, Katrivanos et al. 2013, Froitzheim et al. 2014).

In this scenario, the Internal Hellenides thrust stack (Serbo-Macedonian/Rhodope metamorphic province) should be rooted along the northern boundary of the Rhodope massif, at its tectonic contact with the Strandja and Sredna Gora massifs (suture zone). Cretaceous-Tertiary nappe stacking and crustal thickening in the Internal Hellenides were followed by syn-to late-orogenic extension, crustal thinning and exhumation of the deeper structural units as tectonic windows or metamorphic core complexes (Fig. 2; Marchev et al., 2005; Burg, 2012; Kilias et al., 2013; Froitzheim et al., 2014). High-temperature metamorphism, partly migmatization and intense magmatism associated the Tertiary extensional tectonic regime (Kilias & Mountrakis, 1998; Liati & Gebauer, 1999; Marchev et al., 2005; Burg, 2012; Gautier et al., 2017). Extension occurred simultaneously with compression and westward-verging nappes' stacking in the External Hellenides (Jolivet et al., 2004; Kilias et al., 2010; Froitzheim et al., 2014). As a result External and Internal Hellenides are constructed from the same thrust sheets, being progressively younger to the W-SW but with higher metamorphic grade conditions in the Serbo-Macedonian and Rhodope Internal Hellenides (Jahn-Awe et al., 2010; Liati & Gebauer, 1999; Dinter, 1998).

A retreating subduction zone and roll back of the subducted lithospheric slab, under the Pelagonian and the other Internal Hellenides nappes stack related to orogenic collapse of the overthricken crust or mantel delamination (Marchev et al., 2005; Burg, 2012) could explain well the extensional tectonics in the Internal Hellenides taken place simultaneously with compression in the External Hellenides and the Hellenic vorland.

CONCLUSIONS

I. The Alpine structural evolution of the Hellenides starts with the continental rifting of the Pangaea Super-continent during the Permo-Triassic and the opening of the Neotethyan ocean.

II. Deformation and metamorphism are recorded in six main deformational stages from the Middle-Jurassic to present day (D1-D6). Compression, nappe stacking and high-pressure metamorphism alternated progressively through time with extension, orogenic collapse and medium- to high-temperature metamorphism partly migmatization, that was leading to uplift and exhumation of deep crustal levels as tectonic windows or metamorphic core complexes. An S- to SW-ward migration of the dynamic peer compression vs extension is clearly recognized during the Alpine orogeny in the Hellenides. In any case extension and crustal uplift follow compression and nappe stacking.

III. The ophiolite belts in the Hellenides are considered as far travelled nappes, originated from a single source and this was the Neotethyan Axios/Vardar ocean basin. The latter closed finally during the Late Cretaceous-Paleocene subducted under the European continental margin. The upper limit of the ophiolite emplacement is the Kimmeridgian/Tithonian.

IV. The lower-most Pangaion Rhodope unit should be the marginal part of the Apulia plate, which was unterthrusted below the Internal Hellenides, i.e. the Pelagonian and Serbo-Macedonian massifs. The latter be supposed as the European margin at the eastern part of the Neothethyan Ocean realm.

V. The Vardar/Axios Neotethyan ophiolites are allochthonnes and the Axios/Vardar suture zone is traced in between the Rhodopes nappes. The Internal Hellenides thrust stack are rooted along the northern boundary of the Rhodope massif with the Strandja and Sredna Gora massifs, being progressively younger to the W-SW until the External Hellenides thrust sheets.

VI. A retreating subduction zone and roll back of the subducted lithospheric slab, under the Pelagonian and the other Internal Hellenides nappes stack related to orogenic collapse of the overthickened crust or mantel delamination could explain well the Tertiary extensional tectonics in the Internal Hellenides taken place simultaneously with compression in the External Hellenides and the Hellenic vorland.

REFERENCES

Burg, J.P., 2012. Rhodope: From mesozoic convergence to cenozoic extension. Review of petro-structural data in the geochronological frame. *J. Virtual Explor.* 42.

Dinter, D.A., 1998. Late Cenozoic extension of the Alpine collisional orogen, northeastern Greece: Origin of the north Aegean Basin. *Bull. Geol. Soc. Am.* 110, 1208-1230.

Froitzheim, N., Jahn-Awe, S., Frei, D., Wainwright, A.N., Maas, R., Georgiev, N., Nagel, T.J., & Pleuger, J., 2014. Age and composition of meta-ophiolite from the Rhodope Middle Allochthon (Satovcha, Bulgaria): A test for the maximum-allochthony hypothesis of the Hellenides. *Tectonics* 33, 1477-1500.

Gautier, G., Bosse, V., Cherneva, Z., Didier, A., Gerdjikov, I., & Tiepolo, M., 2017. Polycyclic alpine orogeny in the Rhodope metamorphic complex: the record in migmatites from the Nestos shear zone (N. Greece). *Bull. Soc. géol. Fr.* 188 (36).

Gawlick, H.J., Frisch, W., Hoxha, L., Dumitrica, P., Krystyn, L., Lein, R., Missoni, S., & Schlagintweit, F., 2008. Mirdita Zone ophiolites and associated sediments in Albania reveal Neotethys Ocean origin. *Int. J. Earth Sci.* 97, 865-881.

Jahn-Awe, S., Froitzheim, N., Nagel, T.J., Frei, D., Georgiev, N., & Pleuger, J., 2010. Structural and geochronological evidence for Paleogene thrusting in the western Rhodopes, SW Bulgaria: Elements for a new tectonic model of the Rhodope Metamorphic Province. *Tectonics* 29, 1-30.

Jolivet, L., Rimmele, G., Oberhansli, R., Goffe, B., & Candan, O., 2004. Correlation of syn-orogenic tectonic and metamorphic events in the Cyclades, the Lycian nappes and the Menderes massif. Geodynamic implications. *Bull. Soc. Geol. Fr.* 175, 217-238.

Katrivanos, E., Kilias, A., & Mountrakis, D., 2013. Kinematics of deformation and structural evolution of the Paikon Massif (Central Macedonia, Greece): A Pelagonian tectonic window? *Neues Jahrb. für Geol. und Paläontologie - Abhandlungen* 269, 149-171.

Kilias, A., 1991. Transpressive tektonik in den zentralen Helleniden, Aenderung der translationspfade durch die transpression (Nord-zentral Griechenland). *Neues Jahrb. für Geol. und Paläentologie, Monatshefte* 20, 291-306.

Kilias, A., 1995. Emplacement of the blueschists unit in eastern Thessaly and exhumation of Olympos-Ossa carbonate dome as a result of Tertiary extension (central Greece). *Miner. Wealth* 96, 7-22.

Kilias, A., Falalakis, G., & Mountrakis, D., 1999. Cretaceous-

Tertiary structures and kinematics of the Serbomacedonian metamorphic rocks and their relation to the exhumation of the Hellenic hinterland (Macedonia, Greece). *Int. J. Earth Sci.* 88, 513-531.

Kilias, A., Falalakis, G., Sfeikos, A., Papadimitriou, E., Vamvaka, A., & Gkarlaouni, C., 2013. The Thrace basin in the Rhodope province of NE Greece - A tertiary supradetachment basin and its geodynamic implications. *Tectonophysics* 595-596, 90-105.

Kilias, A., Frisch, W., Avgerinas, A., Dunkl, I., Falalakis, G., & Gawlick, H.-J., 2010. Alpine architecture and kinematics of deformation of the northern Pelagonian nappe pile in the Hellenides. *Austrian J. Earth Sci.* 103, 4-28.

Kilias, A., & Mountrakis, D., 1998. Tertiary extension of the Rhodope massif associated with granite emplacement (Northern Greece). *Acta Vulcanol.* 10, 331-337.

Kilias, A., Tranos, M.D., Orozco, M., Alonsochaves, F.M., & Soto, J.I., 2002. Extensional collapse of the Hellenides: A review. *Rev. la Soc. Geol. Espana* 15, 129-139.

Koroneos, A., Kilias, A., & Avgerinas, A., 2013. Hercynian plutonic rocks of Voras Mountain, Macedonia, Northern Greece: their structure, petrogenesis, and tectonic significance. *Int. Geol. Rev.* 55, 994-1016.

Kostaki, G., Kilias, A., Gawlick, H.-J., & Schlagintweit, F., 2014. Component analysis in the vardar/axios zone of northern greece reveals an eroded late jurassic carbonate platform comparable to those of the Eastern Alps/Western Carpathian, Dinarides, Albanides and Hellenides. *Bul. Shk. Gjeol.* 1, 85-88.

Liati, A.L., & Gebauer, D.G., 1999. Constraining the prograde and retrograde P-T-t path of Eocene HP rocks by SHRIMP dating of different zircon domains: Inferred rates of heating, burial, cooling and exhumation for central Rhodope, northern Greece. *Contrib. to Mineral. Petrol.* 135, 340-354.

Marchev, P., Kaiser-Rohrmeier, M., Heinrich, C., Ovtcharova, M., von Quadt, A., & Raicheva, R., 2005. 2: Hydrothermal ore deposits related to post-orogenic extensional magmatism and core complex formation: The Rhodope Massif of Bulgaria and Greece. *Ore Geol. Rev.* doi:10.1016/j.oregeorev.2005.07.027

Michail, M., Pipera, K., Koroneos, A., Kilias, A., & Ntaflos, T., 2016. New perspectives on the origin and emplacement of the Late Jurassic Fanos granite, associated with an intra-oceanic subduction within the Neotethyan Axios-Vardar Ocean. *Int. J. Earth Sci.* 105, 1965-1983.

Michard, A., Feinberg, H., & Montigny, R., 1998. Supra-ophiolitic formations from the Thessaloniki nappe (Greece), and associated magmatism: An intra-oceanic subduction predates the Vardar obduction. *Comptes Rendus l'Academie Sci. - Ser. IIa Sci. la Terre des Planetes* 327, 493-499.

Okrusch, M., & Broecker, 1990. Eclogites associated with high-grade blueschists in the Cyclades archipelago, Greece: a review. *Eur. J. Mineral.* 2, 451-478.

Papanikolaou, D., 2013. Tectonostratigraphic models of the Alpine terranes and subduction history of the Hellenides. *Tectonophysics* 595-596, 1-24.

Robertson, A.H.F., 2012. Late Palaeozoic-Cenozoic tectonic development of Greece and Albania in the context of alternative reconstructions of Tethys in the Eastern Mediterranean region. *Int. Geol. Rev.* 54, 373-454.

Schermer, E.R., 1993. Geometry and kinematics of continental basement deformation during the Alpine orogeny, Mt. Olympos region, Greece. *J. Struct. Geol.* 15, 571-591.

Seidel, E., Kreuzer, H., & Harre, W., 1982. A Late Oligocene/Early Miocene high pressure belt in the external Hellenides. *Geol. Jahrb.* 23, 165-206.

Wawrzenitz, N., & Mposkos, E., 1997. First evidence for Lower Cretaceous HP/HT-Metamorphism in the Eastern Rhodope, North Aegean Region, North-East Greece. Eur. *J. Mineral*. 9, 659-664.

INQUA Focus Group Earthquake Geology and Seismic Hazards

paleoseismicity.org

Quaternary activity patterns of the Keumwang Fault in the South Korea

Kim, Man-Jae (1), Yu, Tae-Gwang (1), Lee, Hee-Kwon (1)

(1) Department of Geology, Kangwon National University, Chuncheon-si, Gangwon-do, 200-701, South Korea, heekwon@kangwon.ac.kr

Abstract: *Although the southern Korean peninsula located in intra-plate regions has been known tectonically stable, paleo-seismological studies show that large earthquakes have occurred in the Quaternary period. The Keumwang fault is the strike-slip fault which cut the Korean peninsula with NE-SW strike. We analysed ESR (Electron Spin Resonance) dates of fault gouge bands collected from 3 fault cores along the Keumwang fault. ESR ages show temporal clustering into active and inactive periods since 520 ka. Recurrence intervals between active periods range from 10 to 80 ka. Results from this study suggest that long-term cyclic fault movements of the Keumwang fault have occurred in the study area.*

Keywords*: Keumwang fault, Fault gouge, ESR dating, Fault movement, Activity patterns of active fault*

INTRODUCTION

Although the southern Korean peninsula located in the intra-plate regions has been known tectonically stable, paleo-seismological studies show that large earthquakes have occurred in the Quaternary period. Most of earthquakes have occurred in the active faults at irregular intervals ranging from a few hundred years to a few million years. Because fault movements in the active faults have long recurrence intervals, it is difficult to predict when faults will reactivate using only instrumental and historical records. Dating of prehistoric fault movements can be used in evaluation of long-term activity patterns of the active faults.

The Keumwang fault that NE segment of the Kongju fault system is the strike-slip fault which cut the southern Korea peninsula with NE-SW strike (Fig. 1). The fault core consists of a 2~50 m thick fault gouge bounded by 30~100 m thick fault damage zone. The Keumwang fault underwent at least six distinct stages of fault activities based on deformation environment, time and mechanism (e.g. Kim & Lee, 2016). ESR dates of fault gouges collected from the Keumwang fault show temporal clustering during the Quaternary period (e.g. Kim & Lee, 2016). We studied the Quaternary activity patterns of the Keumwang fault in the Inje-gun area, Gangwon-do, South Korea (Fig. 1), using ESR dating method. We collected fault gouge bands samples from the fault cores along the Keumwang fault.

ESR dating method can be used determining the time of fault activity of the fault. The basic assumption of ESR dating method is that ESR signals of quartz grains within fault gouges are reset by grain boundary frictional sliding, frictional heating and lattice deformation during fault movement (e.g. Lee and Schwarcz, 1994a, 1995). After fault movement, ESR signals increase again by natural radiation of U, Th, K. Buhay et al. (1988) suggested the grain size plateau criterion can be used to evaluate complete resetting of ESR signals during fault movement. A graph of grain sizes versus ESR ages would generate an age plateau in low ages which indicate the last activity of a volume of given fault gouge (e.g. Lee & Schwarcz, 1994b).

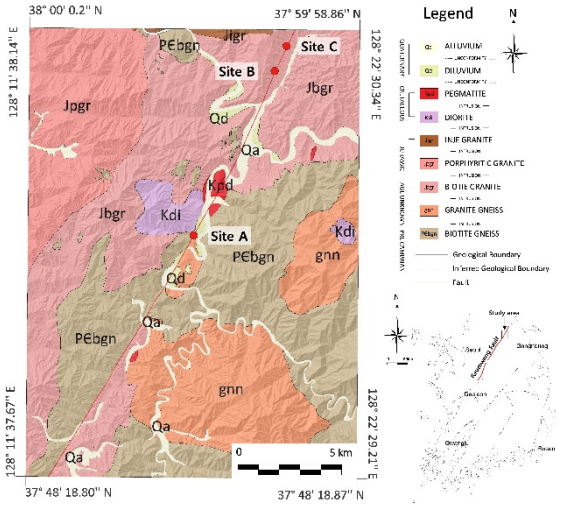

Figure 44: Geological map of the study area showing the locations of sampling sites along the Keumwang fault (modified from Kang & Jin, 1972; Kim et al., 1975; Shin et al., 1975; Lee et al., 1975).

ANALITICAL METHOD OF ESR DATING

The samples were soaked in a mixture of hydrochloric acid and nitric acid to remove organic matters, carbonate and clay minerals. After washing, the 25~45 μm, 45~75 μm, 75~100 μm, 100~150 μm and 150~250 μm size fractions were extracted by wet- and dry-sieving. Magnetic minerals were removed using a magnetic separator. Fine particles attached to quartz grain were removed using ultrasonic cleaner. 10 aliquots of 100 mg for each size fraction were weighed. Aliquots of each grain size were irradiated with a ^{60}Co gamma ray source with a dose rate of 0.11~0.33 mGy/s. To remove effects of counterfeit E' signal, heat the

samples at 170 ℃ for 15 min (e.g. Toyoda & Schwarcz, 1997).

Measurements of all the samples were carried out with an ESR spectrometer JEOL JES-TE 200 at Central laboratory of Kangwon National University. The E' signal was measured at room temperature and Al signal was measured at 77 K with liquid nitrogen. Instrumental settings for E' and Al signals were: microwave power = 100 μW for E' signal and 2 mW for Al signal, scan width = 5 mT for E' signal and 2.5 mT for Al signal, scan time = 1.5 min, modulation frequency = 100 KHz, modulation amplitude = 5, time constant = 0.03 sec.

Equivalent doses of fault gouge were determined by the additive dose method using an exponential function (e.g. Yokoyama et al., 1985). Radioactive elements (U, Th and K) contents in the samples were measured by gamma spectrometry using a HPGe Gamma spectrometer at Central laboratory of Kangwon National University. The data were processed using the DATA program of Grün (2009).

LINEAMENT ANALYSIS

Shaded-relief images created from digital elevation model (DEM) can enhance the lineament of fault at different orientations by simulating imaginary light under varied directions (e.g. Oguchi et al., 2002). We carried out lineament analysis using shaded-relief images and aerial photograph to identify the Keumwang fault (Fig. 2). In study area, lineament of the fault is predominantly developed in the range of N25° ~ 35°E. We found 3 fault cores (Site A, B and C) along the lineament by detailed geological mapping.

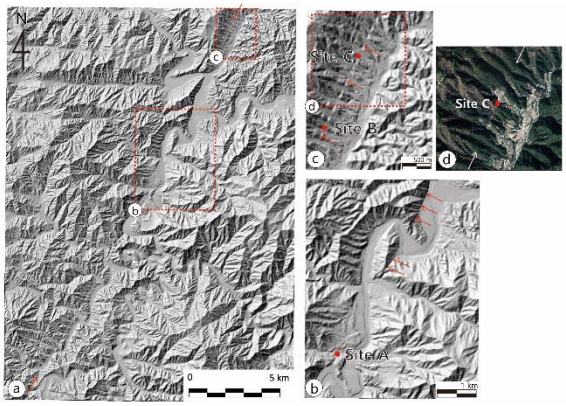

Figure 45: Shaded-relief images with an azimuth of 315° and an altitude of 45° (a, b, c) and aerial photograph (d) of the study area. The red dots represent location of fault cores. The red and white arrows represent lineament developed in study area.

STRUCTURAL FEATURES AND RESULTS OF ESR DATING

Site A (MJ002)

The approximately 23 m wide fault core is developed in biotite gneiss (Fig. 1). It is composed of grey fault gouge bands, dark fault gouge bands, fault breccia and relics of host rock alternating with each other (Fig. 3). The thickness of fault gouge bands are various from approximately 2 cm to a few m. The boundaries between fault core and host rocks are the distinguishable fault planes strike N15°~38°E and dip to the SE at 74°~87°. The fault core is characterized by numerous shear planes, shear bands, quartz veins, relics of host rocks. The P-foliations developed in the boundary gouge band in the northwest of the fault core show the dextral strike-slip movement. Fragments of host rock and quartz veins cut by shear planes indicate dextral shear sense.

A total of 14 fault gouge samples were collected across the fault core (Fig. 3). The ESR signals of 8 samples (MJ002-4, MJ002-5, MJ002-7, MJ002-8, MJ002-9, MJ002-11, MJ002-12, MJ002-15) from the 14 samples are saturated. 6 of 14 fault gouge gave us ESR ages. E' signal of MJ002-1(dark fault gouge) gave us an ESR age of 250±30 ka. E' and Al signals of MJ002-2 (grey fault gouge) gave us a plateau ESR age of 230±30 ka. E' and Al signals of MJ002-3(dark fault gouge) gave us a plateau ESR ages of 200±20 ka. Al signal of MJ002-10(grey fault gouge) gave us an ESR age of 450± 70 ka. E' signal of MJ002-13 (dark fault gouge) gave us a plateau ESR age of 270±30 ka. Al signal of MJ002-14(grey fault gouge) gave us a plateau ESR age of 520±40 ka.

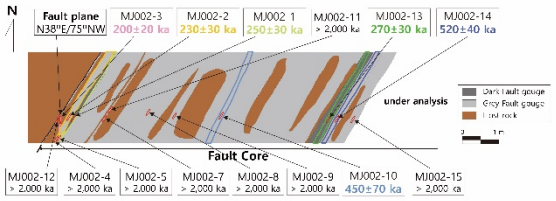

Figure 46: Schematic diagram across the fault core (Site A) and ESR ages of the Keumwang fault. Red ellipses represent sampling locations for ESR dating.

Site B (MJ014)

The approximately 11 m wide fault core is developed in biotite granite (Fig. 1). It is composed of grey fault gouge bands and relics of host rocks alternating with each other (Fig. 4). The thickness of fault gouge bands are various from approximately 2 cm ~ 5 m. The fault core is bounded by distinguishable fault planes strike N30°~32°E and dip to the SE at 78°~84°. A 8~9 cm thick grey fault gouge band is developed between fault core and host rocks in the northwest of the fault core. A 4~5 cm thick grey gouge band is developed between the fault core and foliated cataclasite derived from granite in the southeast of the fault core.

A total of 16 samples were collected across the fault core (Fig. 4). The ESR signals of 9 samples (MJ014-2, MJ014-5, MJ014-6, MJ014-8, MJ014-9, MJ014-11, MJ014-12, MJ014-13, MJ014-14) from the 16 samples are saturated. 7 of 16 fault gouge gave us ESR ages. E' signal of MJ014-1 gave us an ESR age of 210±30 ka. E' signal of MJ014-3 gave us an ESR age of 190±30 ka. E' and Al signals of MJ014-4 gave us a plateau ESR age of 430±50 ka. E' and Al signals of MJ014-7 gave us a plateau ESR age of 260±20 ka. E'

signal of MJ014-10 gave us a plateau ESR age of 260±30 ka. E' signal of MJ014-15 gave us an ESR age of 140±30 ka. ESR E' signal of MJ014-16 gave us a plateau ESR age of 140 ±10 ka.

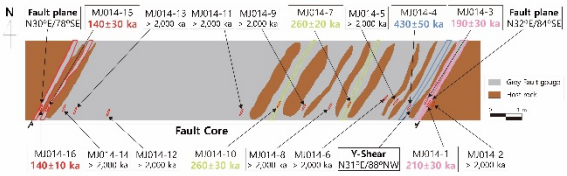

Figure 47: Schematic diagram across the fault core (Site B) and ESR ages of the Keumwang fault. Red ellipses represent sampling locations for ESR dating.

Site C (MJ031)

The approximately 17 m wide fault core is developed in biotite granite (Fig. 1). It is composed of dark grey gouge, grey gouge and relics of host rocks (Fig. 5). Among them, the dark grey gouge occupies most of fault core. The thickness of fault gouge bands are various approximately 2 cm ~ a few m. The fault core is bounded by distinguishable fault planes strike N20°E and dip to the NW at 86°. A few cm thick dark grey gouge band is developed in the northwest of the fault core. A 30 cm thick dark grey gouge band is developed in the southeast boundary of fault core

A total of 13 fault gouge samples were collected across the fault core (Fig. 5). The ESR signals of 4 samples (MJ031-2, MJ031-10, MJ031-11, MJ031-13) from the 13 samples are saturated. 9 of 13 fault gouge gave us ESR ages. E' signal of MJ031-1(grey fault gouge) gave us an ESR age of 490±40 ka. E' and Al signals of MJ031-3 (grey fault gouge) gave us a plateau ESR age of 520±40 ka. E' signal of MJ031-4 (dark fault gouge) gave us an ESR age of 480±80 ka. Al signal of MJ031-5 (grey fault gouge) gave us an ESR age of 320±50 ka. E' and Al signals of MJ031-6(dark fault gouge) gave us a plateau ESR age of 440±40 ka. E' signal of MJ031-7 (grey fault gouge) gave us a plateau ESR age of 270±30 ka. E' signal of MJ031-9 (dark fault gouge) gave us a plateau ESR age of 210±20 ka. E' signal of MJ031-12 (grey fault gouge) gave us a plateau ESR age of 220±20 ka. E' and Al signals of MJ031-14 (dark fault gouge) gave us a plateau ESR age of 220±20 ka.

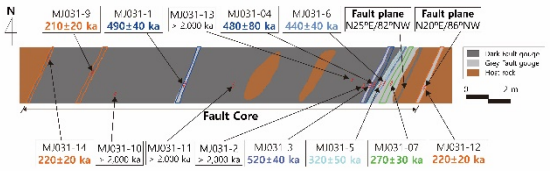

Figure 48: Schematic diagram across the fault core (Site C) and ESR ages of the Keumwang fault. Red ellipses represent sampling locations for ESR dating.

CONCLUSION

ESR ages of fault gouge collected from the 3 fault cores developed along the Keumwang fault in study area show temporal clustering into active and inactive periods since 520 ka (Fig. 6 & 7). The fault cores are reactivated at 140, 200, 220, 230, 260, 270, 320, 440, 490, 520 ka. Recurrence intervals between active periods in Quaternary period range from 10 to 80 ka. The important points in this study are that 1) the fault cores consist of fault gouge bands which were generated before the Quaternary period, and only a very small part of them were reactivated in the Quaternary period, 2) records of active period older than 520 ka have presumably been obliterated by later fault movements (Lee & Schwarcz, 1996), 3) the ESR data also suggest the presence of synchronous activity over 3 fault core along the Kemwang fault in the study area. 4) Samples collected from boundary gouge bands developed between the fault core and host rocks show consistent ESR age estimates (about 20 ka) within the ranges of error.

Acknowledgements: This work is financially supported by Ministry of the Interior and Safety as Earthquake Disaster Prevention Human resource development Project.

REFERENCES

Buhay, W.M., Schwarcz, H.P., & Grün, R., 1998. ESR dating of fault gouge: The effect of grain size. *Quaternary Science Reviews* 7, 515-522.

Grün, R., 2009. The DATA program for the calculation of ESR age estimates on tooth enamel. *Quaternary Geochronology* 4, 231-232.

Kang, P.C., & Jin, M.S., 1972. Geological report of the Pung Am sheet (1:50,000). Korea Institute of Energy and Resources, 34 pp. (in Korean with English abstract).

Kim, B.K., Chi, J.M., Lee, D.Y., & So, C.S., 1975, Geological report of the Hyeon Ri sheet (1:50,000). Korea Institute of Energy and Resources, 21-27 pp. (in Korean with English abstract).

Kim, M.J., & Lee, H.K., 2016, Internal structure and movement history of the Keumwang Fault. *Journal of the Petrological Society of Korea* 25, 210-230 (in Korean with English abstract).

Lee, D.S., Yun, S., & Kim, J.J., 1975, Geological report of the Changchon sheet (1:50,000). Korea Institute of Energy and Resources, 21-22 pp. (in Korean with English abstract).

Lee, H.K., & Schwarcz, H.P., 1994a. Criteria for complete zeroing of ESR signals during faulting of the San Gabriel fault zone, Southern California. *Tectonophysics* 235, 317-337.

Lee, H.K., &Schwarcz, H.P., 1994b. ESR Plateau dating of fault gouge. *Quaternary Science Review* 13, 629-634.

Lee, H.K., & Schwarcz, H.P., 1995. Fractral clustering of fault activity in California. *Geology* 23, 377-380.

Lee, H.K., & Schwarcz, H.P., 1996. Electron spin resonance plateau dating of periodicity of activity on the San Gabriel fault zone, Southern California. *Journal of Geological Society of America Bulletin* 108, 735-746.

Oguchi, T., Aoki, T., & Matsuta, N., 2002. Identification of an active fault in the Japanese Alps from DEM-based hill shading. *CSIS Discussion Paper* 49, 1-13.

Shin, B.W., Hong, M.S., Lee, Y.D., & Bak, B.S., 1975. Geological report of the Jaeon sheet (1:50,000). Korea Institute of Energy and Resources, 18-19 pp. (in Korean with English abstract).

Toyoda, S., & Schwarcz, H.P., 1997. The hazard of the counterfeit E′ signal in quartz to the ESR dating of fault movement. *Quaternary Science Reviews* 16, 483-486.

Yokoyama, Y., Falguères, C., & Quaegebeur, J.P., 1985. ESR dating of quartz from quaternary sediments: first attempt. *Nuclear Tracks* 10, 921-928.

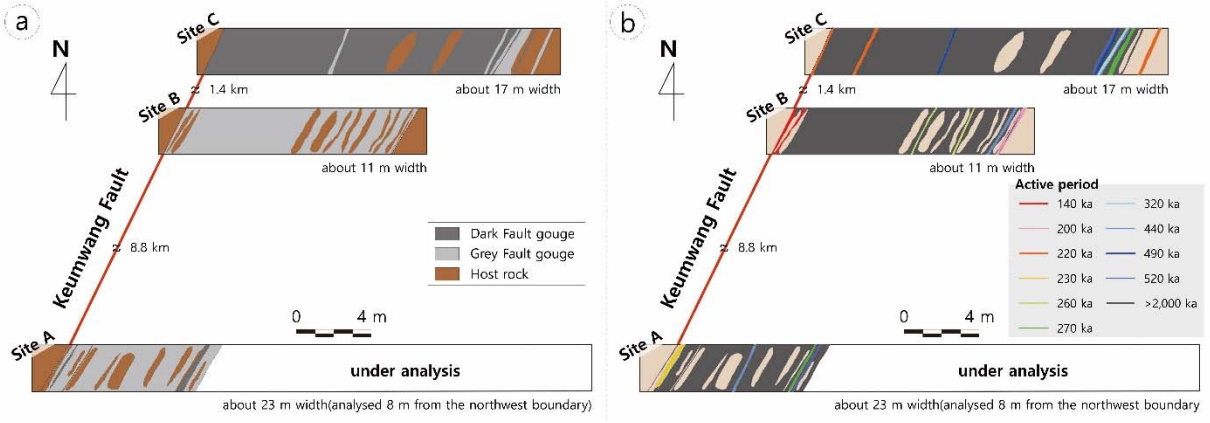

Figure 49: (a) Schematic diagram across the 3 fault cores, (b) Quaternary activity pattern of the 3 fault core.

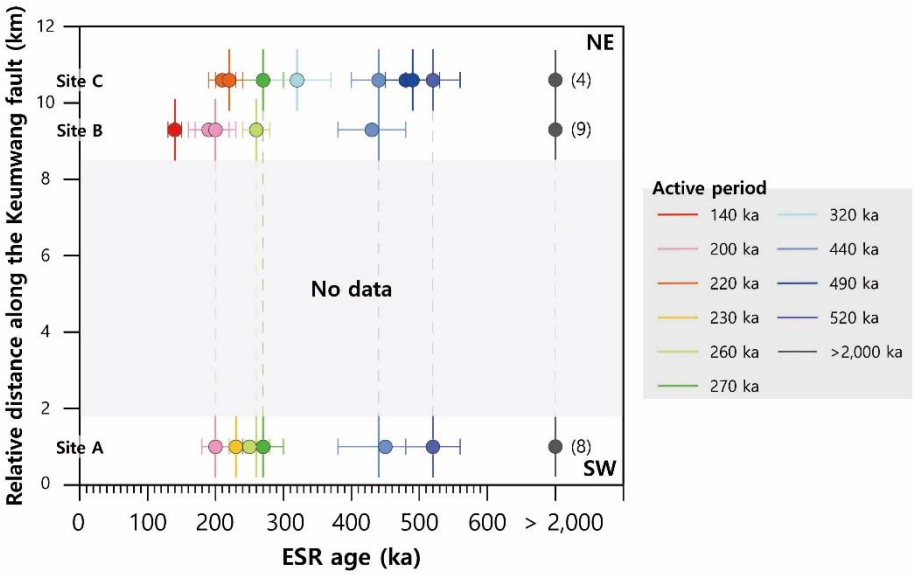

Figure 7: Temporal of activity pattern of the Keumwang fault during the Quaternary period.

INQUA Focus Group Earthquake Geology and Seismic Hazards

paleoseismicity.org

Related fault and deformation mechanism based on structural damage patterns from Pohang Earthquake (Mw=5.4), SE Korea

Kim, Taehyung (1), Naik, Sambit Prasanajit (1), Jeong, Su Ho (1), Shin, Hyeonjo (1), Kim, Young-Seog (1)

(1) Department of Earth & Environmental Sciences, Pukyong National University, 45 Yongso-ro, Nam-gu, Busan, S.Korea, goth4453@naver.com

Abstract: *The Pohang Earthquake (M_W=5.4), occurred on 15th of November, 2017, was the second biggest instrumental earthquake in the Korean Peninsula, which destroyed many structures producing several side effects such as liquefaction and lateral spreading. The Pohang basin is one of the Paleogene basins located in the south-eastern part of the Korean Peninsula, which is composed of Paleogene to Quaternary sedimentary rocks and covers the Cretaceous igneous rocks. We classified damage patterns of buildings into three classes based on their characteristics such as simple cracking, tilting, and conjugate fracturing. Based on our analysis, we inferred several potential factors of these damages such as 1) shaking, 2) surface deformation caused by liquefaction or ground motions, 3) structural loading and direction of the buildings. These damages are caused by surface deformation of the NE-striking (blind) fault, which might be generated as a normal fault and later have been reactivated as reverse fault (inversion).*

Keywords*: Pohang earthquake, Structural damage, InSAR, Blind fault, Inversion*

INTRODUCTION

The Pohang Earthquake (M_W=5.4) occurred on 15th of November 2017 at the southeastern part of the Korean Peninsula. Focal depth of the earthquake is relatively shallow (4.37 km) and NE striking reverse fault plane was inferred based on focal mechanism (Fig. 1).

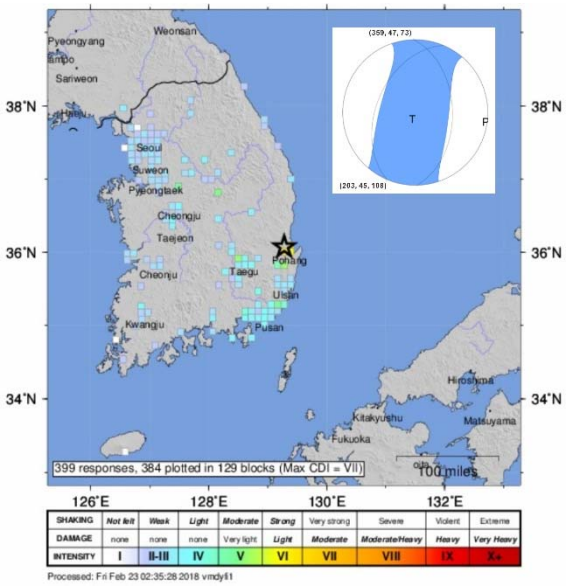

Figure 50: Intensity map of the Pohang Earthquake (M_W=5.4) and the fault plane solution (USGS).

Although surface ruptures have not been reported in the study area, many structural damages and several side effects related with the earthquake, such as liquefaction and lateral spreading, were reported. Especially, relatively many different types of building damages compared with the magnitude are observed in the study area. Thus, we classified the patterns of damaged buildings and make the distribution map of structural damages in Pohang city to understand the relationship between geological features or seismic characteristics and damage patterns.

TECTONIC AND GEOLOGICAL SETTINGS

Korean peninsula is located in the Eurasian plate, which is surrounded by the Pacific plate, the Philippine Sea plate, and the Indian plate (Fig. 2a). The ENE-WSW to E-W trending maximum principal stress has been produced based on the interaction between these plates, which is well matched with the current tectonic stress pattern of this region (e.g. Lim & Lee, 1991; Kim, 2002; Haimson et al., 2003; KRNA, 2006; Lee & Chang, 2007; Bae et al., 2008; Choi et al., 2008; Kim et al., 2016).

The study area is a part of the Gyeongsang Basin, and has mainly NNE-SSW trending major structural features such as the Yangsan fault (mainly strike-slip) and other sub-parallel faults (i.e. Ilgwang, Dongnae, Moryang, Milyang, and Jain). Apart from these strike-slip faults, another NNW-SSE to NW-SE trending reverse dominant oblique-slip fault namely 'Ulsan fault' makes a complex fault system around the study area. More than 60 Quaternary fault sites have been reported along the Yangsan and Ulsan Fault System, a major tectonic feature in the SE part of Korea (Fig. 2b; e.g., Kyung, 1997; KIGAM, 1998; Okada et al., 1998; Kyung & Chang, 2001; Lee & Schwarcz, 2001; KOPEC, 2002; Cheong et al., 2003; Choi et al., 2003a, b; Ree et al., 2003; Lee & Yang, 2005; Choi et al., 2012).

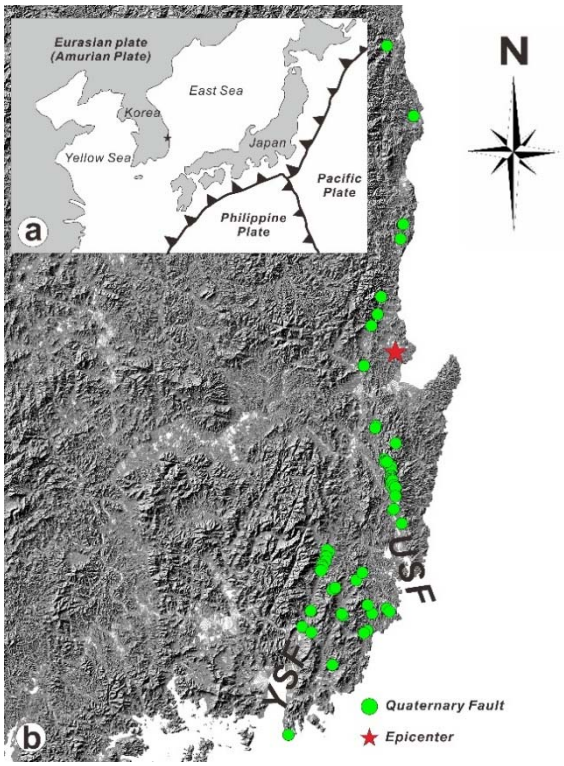

Figure 51: Tectonic map around the Korean Peninsula (a) and locations of the epicentre of the Pohang Earthquake and reported Quaternary faults in Korea (b).

The Pohang basin is one of the Paleogene basins located in the south-eastern part of the Korean Peninsula, which is composed of Paleogene to Quaternary sedimentary rocks covering the Cretaceous igneous rocks (Fig. 3). Several NE striking normal faults related to basin development were developed around this area (i.e. Gokgang fault).

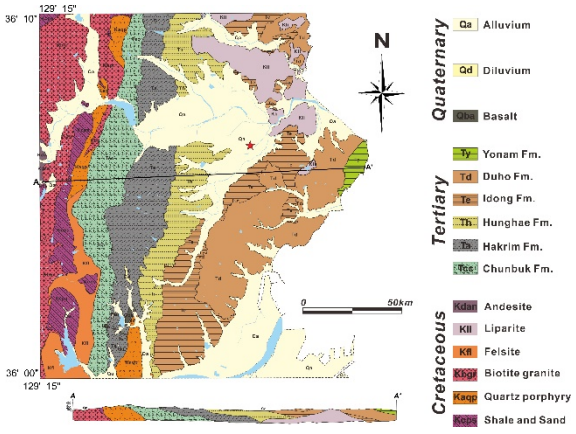

Figure 52: Geological map of the study area (modified from Um et al., 1964). Star marks the epicentre of the main shock.

ANALYSIS OF DAMAGE PATTERNS OF BUILDINGS

We classified structural damage patterns into three classes based on their characteristics such as simple cracking, tilting, and conjugate fracturing (Figs. 4-6). We separately analyzed these different damage patterns to understand the controlling factors. Simple crack type is mostly composed of tensile fractures, which is developed along structural discontinuities such as brick or tile boundaries. Some bricks are collapsed toward free surfaces (Fig. 4). Shaking might have weakened brick boundaries, because they could be behavior as discontinuities within buildings during earthquakes. Some buildings are tilted after the event. Most of tilting types are observed along fences with few degrees (less than 2°), but some buildings are severely tilted (Fig. 5). This type of serious damage could be due to ground subsidence related with shaking or liquefaction, but we need further study to comfirm the relationship between liquefaction and subsidence direction.

Last type is conjugate shear fracture damage, which is generally developed in pillar/wall of buildings (Fig. 6). Most of them show around 60° of dip and normal slip sense. It may indicate that vertical stress is the maximum principal stress direction effected to buildings. Measured conjugate fractures also indicate vertical maximum stress, although minimum stress directions are variable. Interestingly, most of the strikes of conjugate fractures are parallel to the long/short axis of damaged buildings, indicating the effect of building orientation. Although we need more detailed quantitative or statistical analyses to confirm this idea, building orientation may be an important controlling factor as well as vertical ground motion

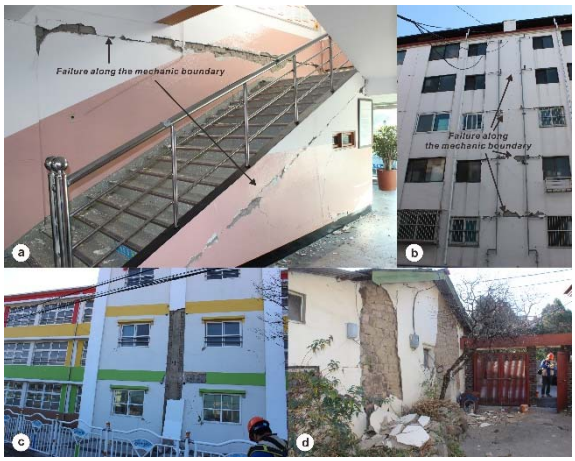

Figure 53: Simple crack type damages such as cracks along brick boundaries and collapsing of wall tiles.

Figure 54: Tilting type damages of wall and/or buildings.

Figure 55: Conjugate fracture type damages in buildings. This type of damages are mainly developed in pillars. Conjugate normal slip sense of shear fractures indicates vertical maximum stress.

DISCUSSION AND CONCLUSIONS

Although the data is not enough to trace the tendency, the distribution map of damaged buildings shows NE-SW trending slightly higher intensity of damage around the Pohang city (Fig. 7a). This higher intensity trend is well matched with the trend of uplifted area on the InSAR (Fig. 7b). It indicates that the main damages are closely related with the uplift of the area. The inferred σ1(vertical), based on the crack patterns, indicates strong vertical displacement or stress. The result strongly support this interpretation, though there are no reported surface rupture. Based on seismic records, the NE striking/NW dipping fault is activated (Fig. 7c). InSAR data also represented ±5cm uplift/subsidence along the NE trending lineament (Fig. 7b). It means that the vertical ground motion/deformation was caused by the NE strike (blind) fault, which affect the building damages. We conclude that the vertical motion was caused by the NE striking revers faulting, which was reactivated from a normal fault developed from the Paleogene basin rifting (inversion) under the E-W maximum principal stress (Fig. 8).

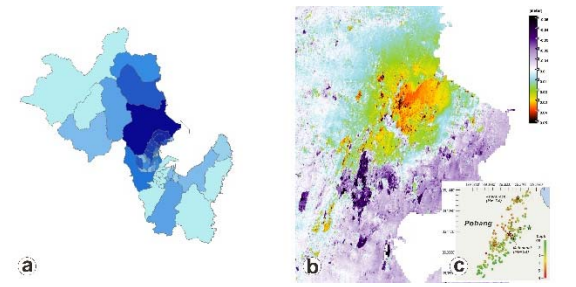

Figure 56: (a) Distributions of damaged building (red star marks the epicentre of the Pohang Earthquake). (b) LOS (Line of Sight) displacement map. Positive values indicate uprising/easting of the land surface while negative values are subsidence/westing. (c) Aftershocks distribution of the Pohang Earthquake (modified from KMA. Seismic fault is dipping to the NW direction.

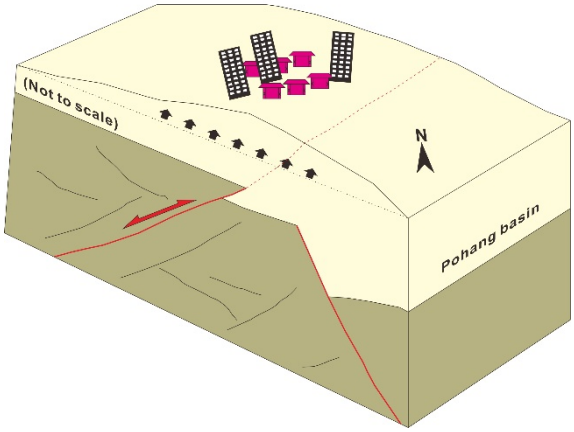

Figure 57. Schematic diagram for surface deformation and building damages related with the reverse faulting.

Acknowledgements: This research was supported by a grant (2017-MPSS31-006) of Fundamental Technology Development Program for Extreme Disaster Response funded by Ministry of Interior and Safety(MOIS, Korea) and the BK21 plus Project of the Graduate School of Earth Environmental Hazard System.

REFERENCES

Bae, S., Jeon, S., Kim, J., & Kim, J., 2008. Characteristics of the regional rock stress field at shallow depth in the Kyungsang Basin with In-situ rock stress measurements. Tunnel & Underground Space. *Journal of Korean Society for Rock Mechanics* 18, 149-161 (in Korean with English abstract).

Cheong, C.S., Hong, D.G., Lee, K.S., Kim, J.W., Choi, J.H., Murray, A.S., Chwae, U., Im, C.B., Chang, C.J., & Chang, H.W., 2003. Determination of slip rate by optical dating of fluvial deposits from the Wangsan fault, SE Korea. *Quaternary Science Reviews* 22, 1207-1211.

Choi, J.H., Murray, A.S., Cheong, C.S., Hong, D.G., & Chang, H.W., 2003b. The resolution of stratigraphic inconsistency in the luminescence ages of marine terrace sediments from Korea. *Quaternary Science Reviews* 22, 1201-1206.

Choi, J.H., Murray, A.S., Jain, M., Cheong, C.S., & Chang, H.W., 2003a. Luminescence dating of well-sorted marine terrace sediments on the southeastern coast of Korea. *Quaternary Science Reviews* 22, 407-421.

Choi, S.-J., Jeon, J.-S., Song, K.-Y., Kim, H.-C., Kim, Y.-H., Choi, P.-Y., Chwae, U.C., Han, J.-G., Ryoo, C.-R., Sun, C.-G., Jeon, M.S., Kim, G.-Y., Kim, Y.-B., Lee, H.-J., Shin, J.S., Lee, Y.-S., & Kee, W.-S., 2012. Active faults and seismic hazard map. NEMA, Seoul, 882 pp. (in Korean with English abstract).

Choi, S.-O., Park, C., Synn, J.-H., & Shin, H.-S., 2008. A decade's experiences on the hydro fracturing in-situ stress measurement for tunnel construction in Korea. *Proceedings of the Korean Society for Rock Mechanics Conference Spring 2008*, 79-88 (in Korean with English abstract).

Haimson, B.C., Lee, M.Y., & Song, I., 2003. Shallow hydraulic fracturing measurements in Korea support tectonic and seismic indicators of regional stress. *International Journal of Rock Mechanics and Mining Sciences* 40, 1,243-1,256.

Kim, M.-C., Jung, S., Yoon, S., Jeong, R.-Y., Song, C.W., Son, M., 2016. Neotectonic Crustal Deformation and Current Stress Field in the Korean Peninsula and Their Tectonic Implications: A Review. *Jour. Petrol. Soc. Korea* 25 (3), 169-193 (in Korean with English abstract).

Kim, S.J., 2002. A Study on the estimation of design parameters appropriate to Korean rock masses. Thesis of Ph.D., Kyungpook National University, Korea, 320 pp. (in Korean with English abstract).

Korea Institute of Geology, Mining and Materials (KIGAM), 1998. An Investigation and Evaluation of Capable Fault: Southeastern Part of the Korean Peninsula. 301 pp. (in Korean with English abstract).

Korea Power Engineering Company (KOPEC), 2002. The Preliminary Site Assessment Report (PSAR) for the new Weolsung Reactors 1 and 2. Unpublished Report, Yongin.

KRNA, 2006. Joint report on the environmental impact from the Wonhyo Tunnel, Gyeongbu Express Line. Korea Rail Network Authority.

Kyung, J.B., 1997. Paleoseismological study on Mid-northern part of the Ulsan Fault by trench method. *Journal of Engineering Geology* 7, 81-90.

Kyung, J.B., & Chang, T.W., 2001. The Latest Fault Movement on the Northern Yangsan Faultt Zone around the Yugye-Ri Area, Southeast Korea. *Journal of the Geological Society of Korea* 37, 563-577 (in Korean with English abstract).

Lee, H.-K., & Schwarcz, H.P., 2001. ESR dating of the subsidiary faults in the Yangsan fault system, Korea. *Quaternary Science Reviews* 20, 999-1003.

Lee, H.-K., & Yang, J.-S., 2005. ESR dating of the Ilkwang fault. *Journal of the Geological Society of Korea* 41, 369-384 (in Korean with English abstract).

Lee, J.B., & Chang, C., 2007. Current state of Stress in south-east Korea. *The Journal of Engineering Geology* 17, 299-307 (in Korean with English abstract).

Lim, H.U., & Lee, C.I., 1991. The trends and variations of natural stresses in rock masses with depth. Tunnel & Underground Space. *Journal of Korean Society for Rock Mechanics* 1, 91-101 (in Korean with English abstract).

Okada, A., Watanabe, M., Suzuki, Y., Kyung, J.B., Jo, W.R., Kim, S.K., & Oike, K., 1998. Active fault topography and fault outcrops in the central part of the Ulsan fault system, southeast Korea. *Journal of Geography* 107, 644-658 (in Japanese).

Ree, J.-H., Lee, Y.-J., Rhodes, E.J., Park, Y., Kwon, S.-T. Chwae, U., Jeon, J.-S., & Lee, B., 2003. Quaternary reactivation of Tertiary faults in the southeastern Korean Peninsula: Age constraint by optically stimulated luminescence dating. *The Island Arc* 12, 1-12.

Um, S.H., Lee, D.W., & Bak, B.S., 1964. Explanatory text of the Geological map of Pohang sheet (1/50,000). Geological survey of Korea.

INQUA Focus Group Earthquake Geology and Seismic Hazards

paleoseismicity.org

Lefkos Basin, Karpathos: Transtensional forearc neotectonics, Early Byzantine geoarchaeology and historical seismicity in the southeastern Aegean region, Greece

Kleinspehn, L. Karen (1)

(1) Department of Earth Sciences, University of Minnesota, 116 Church Street SE, Minneapolis, MN 55455-0231, USA, klein004@umn.edu

Abstract: *Quaternary sedimentary basins yield critical insight into active subduction dynamics and seismic hazards in the Hellenic forearc. Structural mapping of Lefkos Basin, a forearc basin on Karpathos's west coast, suggests multiphase deformation spanning late Early Pleistocene to historical time. Oblique faulting impacted multiple Early Byzantine buildings, including a partially submerged 6th century basilica. Terracotta fragments incorporated into gouge along a restraining-bend thrust also signify faulting during human occupation. Pervasive hydraulic fracturing with fluidized sediment injected along fault planes records discreet rupture events. Lefkos Basin represents the onshore exposed eastern margin of the offshore Karpathos Basin suggesting they are linked kinematically and share similar seismic hazards.*

Keywords: *Karpathos Island, Leukos, Historical seismicity, Early Byzantine, Forearc transtension*

INTRODUCTION

Important recent advances have been made in understanding subduction dynamics globally and their associated hazards, particularly intermediate-to-deep seismicity along the subduction interface (e.g. Bebout et al., 2018). As part of that effort, substantial consideration has been directed toward intermediate-to-deep subduction-zone earthquakes and their potential seismic and/or tsunami hazards along the Hellenic plate boundary (e.g. Yolsal-Çevikbilen & Taymaz, 2012; England et al., 2015; Kkallas et al., 2018). In contrast, deformation of the overriding plate and forearc seismicity can also be significant but has attracted less attention. Forearc basins faithfully record deformation and active faulting in the overriding plate that can be utilized as valuable predictors of seismic hazard.

The late Early Pleistocene to Holocene Lefkos Basin, a forearc basin on the west coast of the Dodecanese island of Karpathos (Fig. 1), constitutes the exposed eastern margin of the offshore Karpathos Basin (Fig. 1a), whose approximately 2.5 km depth represents the deepest sector in the Aegean Sea (Sakellariou et al., 2005). Structural mapping suggests the onshore Lefkos basin records a multiphase deformational history spanning late Early Pleistocene to historical time. This contribution focuses on the youngest deformation phase and its historical seismicity in relation to the Early Byzantine settlement within the Lefkos Basin, designated as Leukos in archaeological studies (e.g. Nelson et al., 2015).

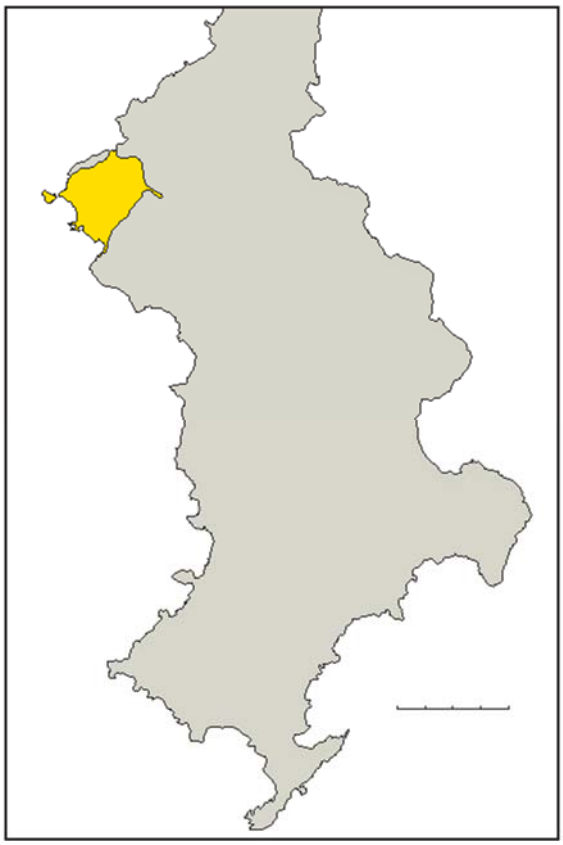

Figure 58a: Location of the study area in Lefkos Basin (rectangle) in western Karpathos adjacent to the Karpathos Basin (KB). Bathymetry at https://maps.ngde.noaa.gov/viewer/bathymetry/. 1b: Simplified geologic map of southern Karpathos showing locations of the Lefkos Basin (heavy yellow pattern), other Neogene-Holocene sedimentary basins (light pattern), and Hellenide basement units (grey). Modified from Christodoulou (1963).

Figure 2: Early Byzantine buildings now partially submerged below sea level on the shoreline, Lefkos. Archaeological interpretation from Nelson et al. (2015). 59a: The semi-circular apse of the nave of a 6th century CE basilica in the swash zone. 2b: A two-story structure with only its first-story, barrel-vaulted ceiling and the floor of the second story remaining above sea level. 2c: Walls of an edifice of unknown function constructed of grey blocks laid in double courses that were bonded and sealed on the inside with terracotta fragments (red-orange), thick mortar, and a cocciopesto lining. Structure sits in the swash zone partially covered with beach sand and marine debris. Meter stick for scale.

BASIN HISTORY

Quaternary forearc basins yield vital insight into active subduction dynamics, and Lefkos Basin is well poised to reveal active tectonism in an obliquely convergent sector of the Hellenic forearc (Sakellariou et al., 2005). $^{87}Sr/^{86}Sr$ isotopic ratios of planktonic foraminifera indicate Calabrian filling of the basin was actually initiated prior to 1.85 ± 0.015 Ma in latest Gelasian time. Syn-depositional faulting, seismicity and slope failure below storm wave base are recorded in the initial basin fill in the form of weakly lithified deep-marine carbonate marls, gravity-driven mass-flow calcirudites, syn-depositional fault displacements that diminish and die out stratigraphically upward, fluid-expulsion pipes, natural hydraulic fracturing, and clastic dikes. Debris slides transported ≤15-m blocks of pre-Neogene (Hellenide) brecciated meta-dolostone down a northeast-facing paleoslope. These slides may have been seismically triggered but importantly record dispersal from the southwest signifying sediment sources in areas that are now well below sea level.

Sedimentary lithofacies of the subsequent phase attest to basin shoaling with a transition stratigraphically upward to large lower-to-middle shoreface bars and hummocky cross-strata with wavelengths up to 10 m that are capped by 20-m high, gravelly marine fan-delta clinoforms and finally non-marine alluvial-fan calcarenites and debris-flow calcirudites. A cool-water ahermatypic coral, *Lobelia pertusa*, yielded a $^{230}U/^{234}Th$ age of 0.596 ± 0.057 Ma (Ionian stage = MIS 15d) for the youngest fully marine strata (shoreface facies). The overlying fan-delta to alluvial-fan facies record a transition to coarse non-marine gravels derived from Karpathos to the east, suggesting the regression can be attributed to tectonic uplift of Karpathos island rather than exclusively to eustatic sea-level fall.

Lefkos Basin, which had been raised above sea level, was subsequently dissected by steep oblique-slip faults, dipping dominantly ≥75°, that down-faulted major portions of the basin back down to or below sea level. Oblique faulting continued into historical time impacting multiple, 4th-6th century CE, Early Byzantine architectural remains within the basin and is the focus of this contribution.

RELATIONSHIP AMONG FAULTING AND EARLY BYZANTINE STRUCTURES

During the 4th-6th century CE a sizable settlement flourished at Lefkos (Nelson et al., 2015). Several stone archaeological structures were clearly not constructed at their present elevation as they are now partially submerged at the shoreline. A basilica, ascribed to the 6th century CE (Kollias, 1970, Nelson et al., 2015), now sits partially underwater (Fig. 2a). Although the apse of the nave is all that is currently visible in the swash zone on the modern beach (Fig. 2a), the rectangular nave of the basilica was previously excavated and measures ~21 m wide and >35 m long (Kollias, 1970), suggesting that the Early Byzantine population of Lefkos was large enough to support a significant congregation at that time.

Approximately 150 m to the northwest, another Early Byzantine building is also partially submerged below sea level on a tombolo where waves often lap at its base (Fig. 2b). The building had two stories with a barrel-vaulted ceiling capping the first story (Nelson et al., 2015). Most of the first story is buried below sea level by modern beach sands and has not been properly excavated. The vault is projected to have been ~3.5 m high of which only the upper part is exposed (Nelson et al., 2015), leaving several meters of the first story extending below sea level. A second course of blocks and a wall fragment sit above the ceiling vault suggesting that the floor and a portion of a second story is also preserved (Fig. 2b). Most of the blocks are roughly-hewn, intrabasinal bioturbated granule-pebble calcirudites as well as rounded boulders from local meta-carbonate units but a few exotic boulders, such as porphyritic vesicular basalt, were also used. A coarse, sandy carbonate mortar with terracotta fragments was applied between blocks on their outer side. The building's function has been the topic of speculation with interpretations ranging from a bathhouse to an industrial purpose or a role in port activities (Nelson et al., 2015). Because the building materials and mode of construction are similar to other dated Early Byzantine structures throughout the Lefkos settlement, this building is included in the assemblage of the 4th-6th-century CE structures (Nelson et al., 2015).

Several other structures near this arched example also sit in the modern swash zone along the beach. For example, approximately 90 m along the shoreline to the northeast, one edifice of unknown function had walls constructed of sedimentary blocks laid in double courses that were bonded and sealed on the inside with terracotta fragments, thick mortar and a cocciopesto lining (Fig. 2c). Most of this structure lies below sea level, and the structure is frequently buried and subsequently uncovered as modern beach sand migrates in response to different wave regimes.

Importantly, eustatic sea-level rise alone is insufficient to have submerged these buildings. Eustacy in the last 1.5 millennia can account for only <1.5-2 m of sea-level rise (Stanford et al., 2011; Murray-Wallace & Woodroffe, 2014). Thus, a significant component of tectonic subsidence must have driven the submergence of these Byzantine structures.

In addition to submerged Byzantine buildings, evidence exists to suggest that faulting occurred during human occupation of the area. For example, a thrust fault contains dark red-brown, ceramic shards (terracotta) within its fault gouge (Fig. 3). These shards are likely not dateable, and whether they represent shards of pottery, roof tiles, plinfa fragments or other architectural elements, is indeterminate. However, similar terracotta-type fragments were used as chinking stones or as components together with mortar in several walls throughout the Early Byzantine settlement (Fig. 2c; Nelson et al., 2015). One shard within the fault zone appears to have sandy mortar still attached (Fig. 3c). The shards are clearly exotic, and presumably anthropogenic, as no natural red-brown clay deposits exist within the basin, and none of the conglomerate clasts in the adjacent fault blocks consists of natural red-brown clay clasts (Fig. 3b). Additional evidence for faulting during human occupation includes an extensional fault that cross-cuts blocks emplaced in an Early Byzantine cistern wall, and notably, other faults that have ceramic and glass shards that were incorporated into their fault gouge.

AGE AND STYLE OF ACTIVE FAULTING

The fault activity that impacted archaeological remains may have occurred while the Early Byzantine Lefkos settlement was occupied and therefore contributed to the village's demise. If that scenario is correct, the maximum age of faulting would be 6th century CE.

Archaeological studies suggest that the population had decreased substantially by the early 7th century CE (Nelson et al., 2015), consistent with intermittent seismic events. However, a smattering of artifacts from the early 7th century CE have been recovered indicating continued occupation but with a greatly diminished population until the village was finally abandoned in the early 7th century CE at the latest (Christendom, 2013; Nelson et al., 2015). Because no direct dating of the faults has been accomplished, faulting could also be younger and have occurred in later Byzantine, medieval or more recent time.

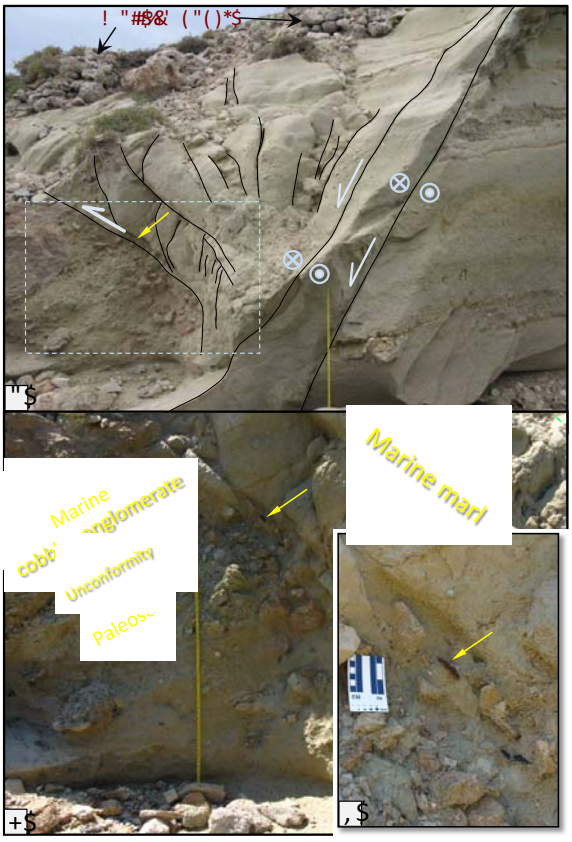

Figure 60a: Ceramic shards (arrow in a, b, c) are incorporated into gouge along a thrust fault on the north side of Akrotiri Pounta Liani, Lefkos within an 30-m wide obliquely extensional shear zone. Rectangle denotes area covered by photograph in b. Meter stick for scale in a and b. 3b: Marine marl was thrust over a marine cobble conglomerate that lies unconformably on a paleosol. 3c: Inset is close-up photo of one ceramic shard in 3a-b.

Several of the impacted archaeological remains (Figs. 2b-c, 3) sit within a ~30-m wide shear zone trending roughly north-south in which faults record dextral-oblique shear. Strain appears to have been partitioned into dextral strike slip (Fig. 4) with extensional faults providing the dip-slip component that partially submerged several buildings within the broader shear zone (Figs. 2b-c). Localized thrusts represent shortening along restraining bends within the broader shear zone (Fig. 3). Faults, regardless of their sense of slip, display pervasive hydraulic fracturing with injection of sandy to pebbly fluidized sediment, sometimes fossiliferous, along the fault planes. The prevalence of hydraulic fracturing with injection of fluidized sediment suggests the faults did not creep but failed in discreet rupture events, some of which may have been catastrophic. This shear zone and others in the basin strike into deep offshore areas, and their displacements would have ruptured the sea floor raising the prospect that some events, particularly large dip-slip events, could have been tsunamigenic.

Figure 61: Fault plane with subhorizontal slickenlines that record dextral slip within a 30-m wide transtensional shear zone that affected the structure in Fig. 2b.

DISCUSSION

Archaeological remains and observed faults attest to significant fault activity in the Lefkos Basin within the last 1500 years. The basin records a long history of intermittent faulting in the midst of which Early Byzantine Lefkos was settled and thrived for two to three centuries. Stress orientations derived from faults that displaced archaeological remains and those that penetrated the modern calcrete soils in Lefkos Basin will be compared to stress fields interpreted from upper-crustal, earthquake moment tensor solutions in an effort to evaluate the degree to which Lekfos Basin is potentially active and should be incorporated into seismic-hazard assessments.

Because Lefkos Basin comprises the eastern margin of the offshore Karpathos basin, these results from the onshore basin raise the question of the degree to which Karpathos island and Karpathos Basin are linked and share Quaternary kinematic histories. Understanding that relationship is a goal of this study and should help illuminate regional-scale Hellenic forearc geodynamics.

Acknowledgements: This project was partially supported by a Grant-in-Aid of Research, Artistry and Scholarship from the University of Minnesota. The Institute of Geology and Mineral Exploration, Athens kindly provided permission to conduct fieldwork on Karpathos. Michael Nelson and his colleagues on the Leukos Survey Project provided invaluable discussions as well as low-altitude aerial photographs of the archeological sites. Geochronologic results relied on the vital assistance of Larry Edwards, Jacob Donlin and Akemi Berry at the University of Minnesota Isotope Laboratory. Thanks go to Nikita and Maria Mastrogiannis, Niko and Tina Mastrogiannis and their families for their unending support and hospitality.

REFERENCES

Bebout, G.E., Scholl, D.W., Stern, R.J., Wallace, L.M., & Agard, P., 2018. Twenty years of subduction zone science: Subduction Top to Bottom 2 (ST2B-2). *GSA Today* 28 (2), 10.1130/GSATG354A.1.

Christidou, E., 2013. Uncovering an Early Christian center on Karpathos, Greece. *Bible History Daily,* Online access at https://www.biblicalarchaeology.org/daily/biblical-topics/post-biblical-period/uncovering-an-early-christian-center-on-karpathos-greece/

Christodoulou, G., 1963. Geologic Map of Greece, 1:50.000, Karpathos. Institute for Geology and Subsurface Research, Athens.

England, P., Howell, A., Jackson, J., & Synolakis, C., 2015. Palaeotsunamis and tsunami hazards in the Eastern Mediterranean. *Philosophical Transactions Royal Society* A373, 20140374, doi: 10.1098/rsta.2014.0374.

Kkallas, C., Papazachos, C.B., Boore, D., Ventouzi, C., & Margaris, B.N., 2018. Historical intermediate-depth earthquakes in the southern Aegean Sea Benioff zone: Modeling their anomalous macroseismic patterns with stochastic ground-motion simulations. *Bulletin of Earthquake Engineering*, 1-30, https://doi.org/10.1007/s10518-018-0342-8.

Kollias, E. 1970. Λευκός, Γιαλού χωράφι Καρπάθου και η παλαιοχριστιανική Βασιλική του Λευκού, *Αρχαιολογική Εφημερίς* 1-15.

Murray-Wallace, C.V., & Woodroffe, C.D., 2014. *Quaternary Sea-Level Changes: A Global Perspective.* Cambridge University Press. 484 p.

Nelson, M.C., Kelly, A., Begg, D.J.I., & Brenningmeyer, T., 2015. The Early Byzantine settlement at Leukos, Karpathos. *The Annual of the British School at Athens* 110, 321-367, http://dx.doi.org/10.1017/S0068245415000040.

Sakellariou, D., Lykousis, V., Karageorgis, A., Anagnostou, C., & Perissoratis, C., 2005. Geomorphology and tectonic structure. In: *State of the Hellenic Marine Environment* (Papathanassiou, E., Zenetos, A., eds), Hellenic Center for Marine Research Publications, Athens, 16-20.

Stanford, J.D., Hemingway, R., Rohling, E.J., Challenor, P.G., Medina-Elizalde, M., & Lester, A.J., 2011. Sea-level probability for the last deglaciation: A statistical analysis of far-field records. *Global and Planetary Change* 79, 193-203, doi:10.1016/j.gloplacha.2010.11.002.

Yolsal-Çevikbilen, S., & Taymaz, T., 2012. Earthquake source parameters along the Hellenic subduction zone and numerical simulations of historical tsunamis in the Eastern Mediterranean. *Tectonophysics* 536–537, 61-100, https://doi.org/10.1016/j.tecto.2012.02.019.

INQUA Focus Group Earthquake Geology and Seismic Hazards

paleoseismicity.org

Mapping the Gyrtoni Fault (Thessaly, Central Greece) using an Unmanned Aerial Vehicle

Kremastas, Evaggelos (1), Pavlides, Spyros (2), Chatzipetros, Alexandros (2), Koukouvelas, Ioannis (3), Valkaniotis, Sotiris (4)

(1) Arkadiou Str. 119 Larisa 41336 Greece, ekremast@geo.auth.gr
(2) Department of Geology, Aristotle University of Thessaloniki, Thessaloniki, 54124 Greece, pavlides@geo.auth.gr, ac@geo.auth.gr
(3) Department of Geology, Division of Marine Geology and Geodynamics, University of Patras, Patras 26500 Greece, iannis@upatras.gr
(4) Koronidos Str. 9, Trikala, 42131 Greece, valkaniotis@yahoo.com

Abstract: *Gyrtoni Fault is an active normal fault located at the Larisa Basin, Thessaly and near the major city of Larisa. A UAV survey has been performed in order to map in detail the topographic expression of the fault, especially the visible morphological scarp. Results from the UAV survey present a detailed morphotectonic map of the fault and the ability to accurately measure fault scarp profiles.*

Keywords*: morphotectonic, normal fault, digital elevation model, UAV*

INTRODUCTION

Gyrtoni Fault (GF) is an ESE-WNW-trending, normal fault that defines the northeastern boundary of the Quaternary Larisa Basin (Caputo et al., 1994). The fault is at close proximity, distance of ~13 km, from Larisa that is a major city of Greece (Fig-1 A). GF was initially described by Schneider (1968) as an important morphological feature (Gyrtoni terrace) affecting the northern Larisa Plain. It was recognized as an active tectonic structure by Caputo (1990) and Caputo and Pavlides (1993). The surface expression of the fault is composed of two right stepping en-echelon fault segments (Caputo, 1995; Caputo et al., 1994, Fig-1 B). In this area two paleoseismological trenches have been recently excavated showing that the fault is characterized by high slip-rate in the order of 0.4 mm/yr (Tsodoulos et al., 2016a, b). The two paleoseismological trenches provide evidence of at least three, and possibly four faulting events (with ages ranging 2.16-1.42 ka, 3.77-2.80 ka, 5.59-3.77 ka, and <5.59 ka).

DATA AND METHODS

UAV mapping is progressively gain applicability as efficient and accurate solutions within a very short time compared to conventional techniques (Nikolakopoulos & Koukouvelas, 2017). In the present contribution aerial mapping has been performed using a DJI Phantom 4 UAV, a commercial tetra copter mounted with a 4K camera. The camera sensor has a focal length of 3.6 mm, 12 M effective pixels, and field of view 94^{o} (Fig.2 a). Flight planning and grid coverage was performed using the Pix4D software, and a 9.7" tablet was used for flight control.

The focus of the project was to produce a morphotectonic map of the GF scarp. In order to complete this map the study area was divided in 16 sub-areas, in which individual flights were performed. A total of 37 flights and 10.714 images were acquired to cover the study area. Two differed modes of UAV surveying have been performed one more detailed and one for wider coverage.

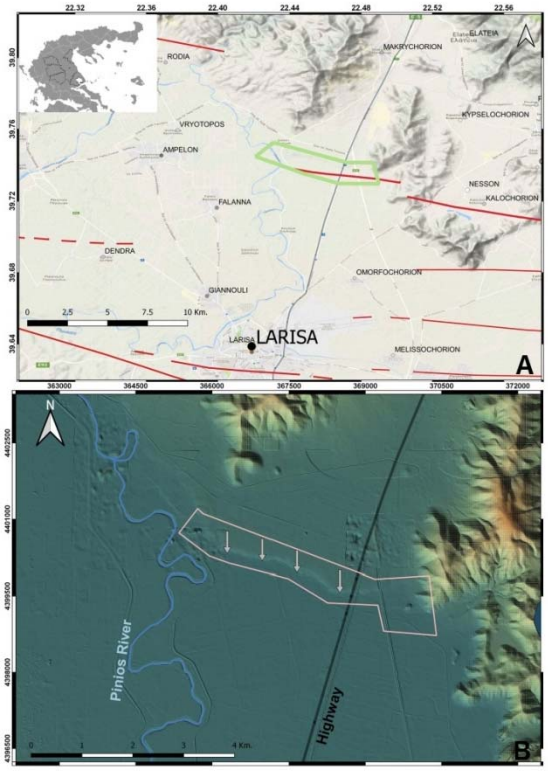

Figure 1: A) Location of GF and its proximity to Larisa city, east Thessaly. Other major active faults are shown as red lines, RF: Rodia Fault, TF: Tyrnavos Fault, AF: Asmaki Fault, LF: Larisa Fault. With the green polygon is the study area. B) Shaded relief map from Hellenic Cadastre orthophotomaps, of GF location. Fault scarp is marked by arrows. Box marks the extent of scarp high measurement displayed in figure5.

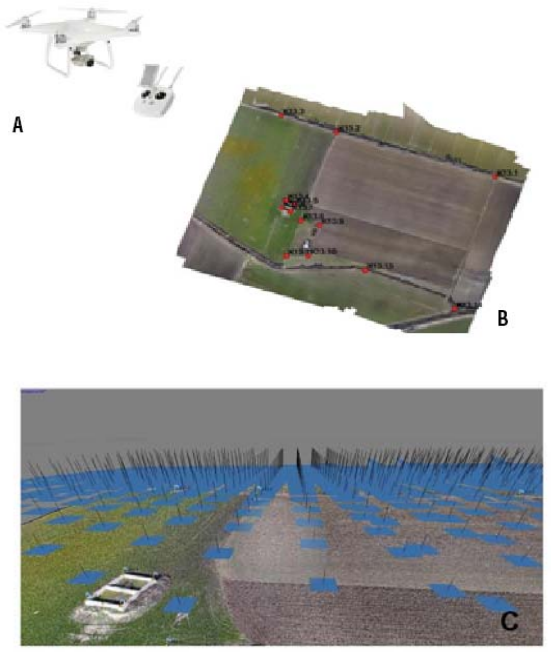

Figure 2: A) DJI Phantom 4 UAV used for aerial survey in the study area. B) Example of GCP use for a single flight path coverage. C) SfM processing of UAV imagery in Agisoft Photoscan.

Detailed mapping was used around the sites of the paleoseismological trenches (Tsodoulos et al., 2016), a relatively low flight height was applied, which allowed image acquisition with very high resolution. Some specifics for the detailed survey flights:

- Average flight height 39m, with a maximum altitude at the take-off point of 35m.
- Number of images: 368.
- Coverage area: 0.0554 Km^2.
- Coverage perimeter: 928 m
- Optimal ground resolution: 1.46 cm / pix.

The rest of GF area was mapped at a higher altitude, in order to achieve larger coverage. Although the flight height was twice the previous one, accuracy still was sufficient enough for the project purposes for specific parameters of the wide coverage survey flights see below:

- Average flight height of 67.7m, with a maximum altitude at the take-off point of 60m.
- Number of images: 941.
- Coverage area: 0.301 Km2.
- Coverage perimeter: 2.176 m
- Optimal ground resolution: 2.51 cm / pix.

All images from each flight were processed using Agisoft PhotoScan software, in order to create a detailed surface model of the area. Because the built-in GPS sensor of the UAV has not sufficient accuracy, there are large errors if only camera location used for processing, especially concerning surface altitude.

Therefore, the initial model must be corrected with the help of ground control points (GCP). Most GCP were selected from Hellenic Cadastre orthophotomaps, with a 1-1.5 m horizontal accuracy. In parts of the sites where no distinguishable features could be located with accuracy (e.g. agricultural fields) some additional GCP were manually picked using a hand-held GPS receiver and custom made ground targets (Fig.2 B). Elevation values for the GCP were extracted from Hellenic Cadastre 5m Digital Surface Model - DSM (with a vertical accuracy of 3.7 m). GCP were added at the Agisoft PhotoScan project and a corrected model was produced.

Using SfM processing in Agisoft Photoscan we get two main products:

- the point cloud dataset
- the orthophoto mosaic

From the point cloud dataset, a DSM raster file is extracted, while further processing and classification of the original point cloud enables the further extraction of a DTM raster. Figure 3 and 4 shows an example of DSM product in a part of GF scarp. The Figure 5 shows the along-strike fault scarp height measurements indicating that our UAV mapping is covering an entire fault segment. Fault scarp heights vary from 6,20m to 13,13m. In detail this profile of measurements, presented in Figure 5, suggests that the segment can be further separated into three smaller segments.

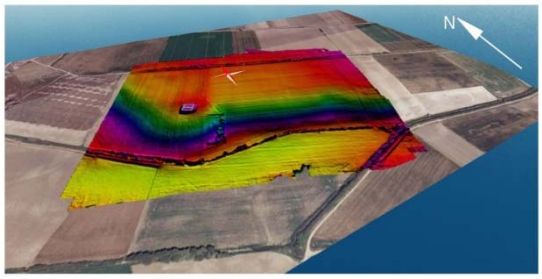

Figure 3: 3D view of a singular survey site, relief overlay on aerial imagery.

All the individual files from each flight were merged in a mosaic dataset covering the full extent of the surveyed area along GF. The DSM raster files were mosaicked using GDAL and QGIS. The full elevation model is presented in Figure 6. Total survey includes:

- Photos 10.714.
- Perimeter 12.618 Km.
- Surface: 3.0492 Km^2.

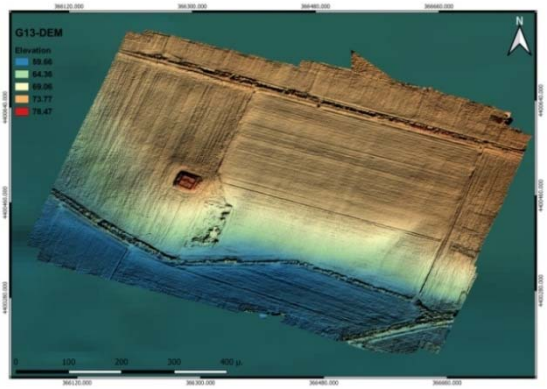

Figure 4: Shaded relief elevation output from a singular UAV flight.

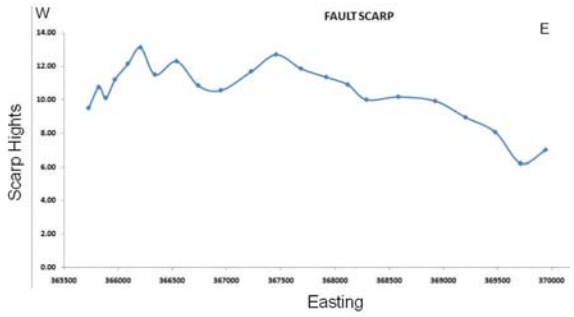

Figure 5: Fault scarp heights along GF. Scarp height measured using the high resolution DSM.

DISCUSSION

We performed a UAV mapping of GF in order to create a high resolution morphotectonic map. Multiple surveys were needed in order to cover the full length of the GF scarp in high resolution. Results are in agreement with previous paleoseismological results (Tsodoulos et al. 2016); GF is expressed through a continuous, fault scarp that is locally sinuous but in a general of WNW-ESE orientation. Scarp height values range between 6-12 m for most of the length of the fault. The morphological scarp that is interpreted as being formed by multiple events, with a mean displacement of ~0.5 m per event (Tsodoulos et al. 2016) can be further separated in smaller segments.

REFERENCES

Caputo, R., 1990. Geological and structural study of the recent and active brittle deformation of the Neogene-Quaternary basins of Thessaly (Greece). In: *Scientific Annals*, Vol. 12, Aristotle University of Thessaloniki, Thessaloniki.

Caputo, R., & Pavlides, S., 1993. Late Cainozoic geodynamic evolution of Thessaly and surroundings (central-northern Greece), *Tectonophysics* 223, 339-362.

Caputo, R., Bravard, J.-P., & Helly, B., 1994. The Pliocene-Quaternary tecto -sedimentary evolution of the Larisa Plain (Eastern Thessaly, Greece), *Geodyn Acta* 7, 57-85.

Caputo, R., 1995. Inference of a seismic gap from geological data: Thessaly (Central Greece) as a case study, *Ann Geofisica* 38, 1-19.

Nikolakopoulos, K., & Koukouvelas, I., 2017. Commercial vs professional UAVs for mapping. Proc. SPIE 10444, 5th International Conference on Remote Sensing and Geoinformation of the Environment (RSCy2017), 1044409 doi: 10.1117/12.2279409.

Schneider, H.A., 1968. Zur Quartargeologischen Entwicklungsgeschichte Thessaliens (Griechenland), R. Haber Verlag, 127 pp., 65 tabs., Berlin.

Tsodoulos, I., Pavlides, S., Chatzipetros, A., Koukouvelas, I., Caputo, R., Stamoulis, K., Gallousi, C., Papachristodoulou, C., & Ioannides, K., 2016a. Middle-Late Holocene earthquake history of the Gyrtoni Fault, Central Greece: Insight from optically stimulated luminescence (OSL) dating and paleoseismology. *Tectonophysics* 687, 14-27.

Tsodoulos, I., Pavlides, S., Chatzipetros, A., Koukouvelas, I., Caputo, R., Stamoulis, K., Gallousi, C., Papachristodoulou, C., Ioannides, K., Belesis, A., Kremastas, E., & Kalyvas, D., 2016b. Palaeseismological investigation of the Gyrtoni Fault (Thessaly, Central Greece), *Bulletin of the Geological Society of Greece* L (1), 2016.

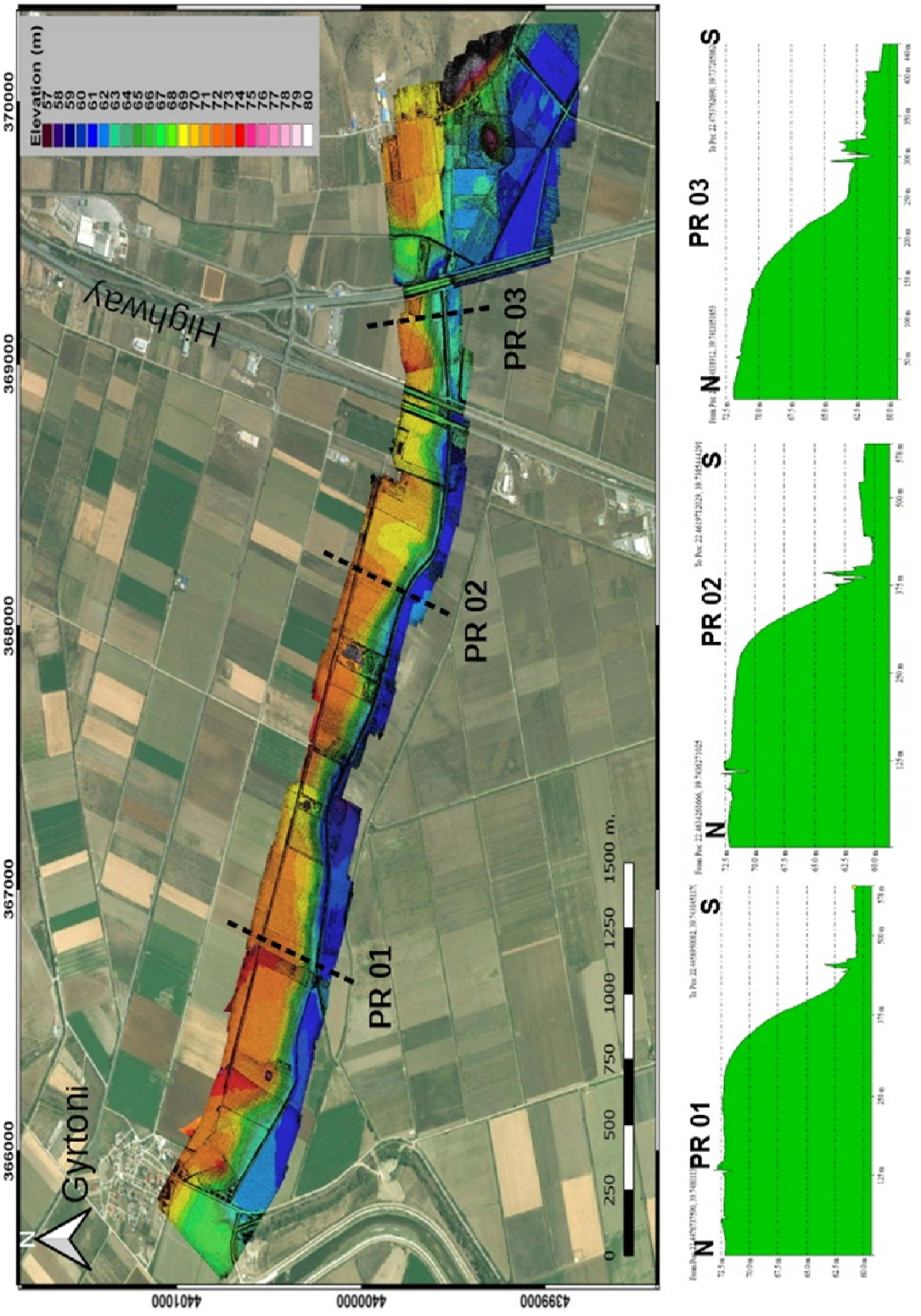

Figure 6: Overview of GF UAV survey. Slope map (0-20 degrees) mosaic created by merging multiple survey tiles. Below: Topographic profiles across the fault scarp, using the final DSM file.

INQUA Focus Group Earthquake Geology and Seismic Hazards

paleoseismicity.org

Shallow slip and fault geometry of the 2010 El Mayor-Cucapah (Mexico) earthquake from differential lidar

Lajoie, Lia (1), Johnson, Kendra (2), Nissen, Edwin (3)

(1) Department of Geophysics, Colorado School of Mines, 1500 Illinois St, Golden, CO 80401, USA, llajoie@mines.edu
(2) Global Earthquake Model, Via Ferrata 1, 27100 Pavia, Italy
(3) School of Earth and Ocean Sciences, University of Victoria, Victoria, B.C., V8P 5C2, Canada, enissen@uvic.ca

Abstract: *We investigate shallow slip in the 2010 M_w 7.2 El Mayor-Cucapah (Mexico) earthquake using three-dimensional surface deformation computed from pre- and post-event airborne light detection and ranging (lidar) topography (Glennie et al., 2014). By profiling the displacement field at densely-sampled (~300 m) intervals along the multi-segment rupture, and computing fault offsets in the E-W, N-S and vertical components, we map out the surface slip vector distribution. A principal goal is to resolve the discrepancy between field observations that are interpreted to reflect widespread low angle normal slip, and geodetic and/or seismological models which support rupture of sub-vertical faults. Since the computed slip vectors must lie in the plane of the fault, whose strike is known, we can calculate the dip (and rake) of the fault along strike and thus test these models explicitly. Along most of the fault trace, we find that coseismic faulting is steeply-dipping. However, a short (~5 km) section of the Paso Superior fault hints at local reactivation of a low-angle (<30°) structure.*

Keywords*: high resolution topography, differential lidar, earthquake deformation, low angle detachment faulting*

INTRODUCTION

We investigate fault zone surface deformation and subsurface fault geometry of the 4 April 2010 M_w 7.2 El Mayor-Cucapah earthquake in northern Baja California, Mexico (Figure 1). This earthquake incorporated several discrete dextral and dextral-normal faults with differing structural characteristics and ruptured through a variety of surface lithologies, enabling us to investigate the factors that control the surface expression of fault slip. It is also characterized by an exceptional wealth of field data and airborne and satellite imagery, providing new perspectives on the shallow slip in a large earthquake (e.g. Wei et al., 2011; Oskin et al., 2012; Gold et al., 2013; Fletcher et al., 2014, 2016; Barišin et al., 2015; Teran et al., 2015).

We build on earlier work by Glennie *et al*. (2014) by analyzing three-dimensional (3-D) coseismic surface displacements computed from pre- and post-earthquake airborne lidar topography. Discord between fault offsets surveyed in the field (Fletcher et al., 2014; Teran et al., 2015) and those determined over larger apertures using remote sensing data may reflect distributed strain within the fault zone and/or a shallow slip deficit (e.g. Dolan & Haravitch, 2014; Nissen et al., 2014). However, high-resolution surface deformation fields from modern airborne or satellite imagery also provide the means to produce much denser fault offset datasets than fieldwork would normally permit (e.g. Milliner et al., 2015).

Moreover, 3-D surface displacements mapped with differential lidar provide a unique opportunity to test for the involvement within the El Mayor-Cucapah earthquake of a low-angle (~20°-dipping) detachment fault. Normal slip on gently-dipping fault planes is mechanically unfavourable (e.g. Anderson 1905, 1951; Jackson & White, 1995), yet field observations in the northern rupture zone have been interpreted as indicating widespread oblique normal slip on a low-angle detachment underlying the Sierra Cucapah (Fletcher et al., 2014; Teran et al., 2015). However, this interpretation is inconsistent with several independent earthquake source models based on space

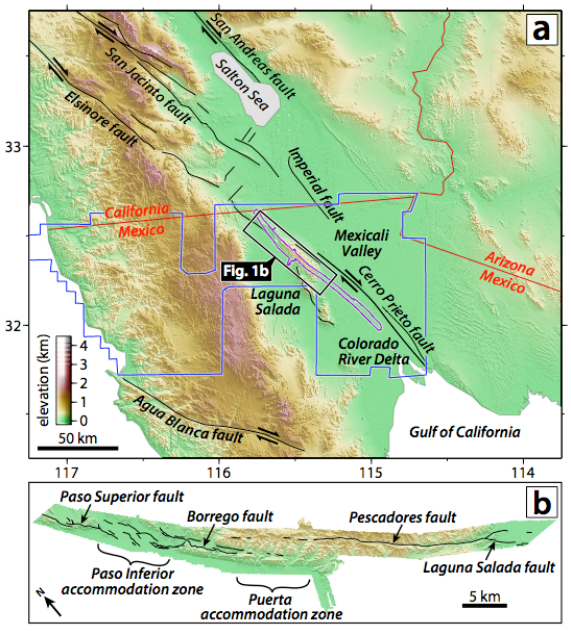

Figure 1: (a) Tectonic setting of the El Mayor-Cucapah earthquake showing other prominent regional faults. (b) The northern Sierra Cucapah section showing principal surface ruptures from Fletcher et al. (2014) plotted on post-earthquake lidar topography.

geodesy and/or seismology which all support steeply-dipping faulting (Fialko et al., 2010; Hauksson et al., 2011; Wei et al., 2011; Zheng et al., 2012; Uchide et al., 2013; Huang et al., 2017; Kyriakopoulos et al., 2017). A primary motivation of this study is to resolve this discrepancy.

DATA

The pre-event lidar data belong to a regional survey by the Instituto Nacional de Estadistica y Geografia (INEGI) in August 2006 (Figure 1a) and have an average density of ~0.013 points/m^2. The post-event data were collected by the National Center for Airborne Laser Mapping (NCALM) in August 2010, four months after the earthquake. They are much higher density, averaging ~10 points/m^2, but cover a relatively narrow ~3-5 km-wide swath centered on the surface rupture. This pair of datasets was first analyzed by Oskin et al. (2012) who mapped coseismic elevation changes by subtracting pre-event from post-event gridded digital terrain models (DTMs). However, this strategy does not account for lateral displacements and so cannot fully characterize the surface deformation field. Elevation changes are also of limited value in parts of the rupture zone containing rugged topography and where horizontal motions exceed vertical ones (e.g. Clark et al., 2017).

We instead used the 100 m-resolution 3-D surface deformation dataset of Glennie *et al.* (2014) (Figure 2) which was calculated by differencing pre- and post-event lidar point clouds using a windowed adaptation of the Iterative Closest Point (ICP) algorithm (Nissen et al., 2012, 2014). This has the advantage of capturing surface displacement vectors (as well as rotations) in each of the *x* (east-west), *y* (north-south) and *z* (vertical) dimensions. In practice there is too little relief within the Colorado River delta and Laguna Salada basin to resolve surface deformation in these areas, and initial results were also hampered by large N-S-trending artifacts related to errors in the pre-event survey data. Reprocessing of the pre-event lidar, described in Glennie et al. (2014), has reduced but not entirely eliminated these artifacts (Figure 2b, c).

METHODS

We developed a semi-automated procedure for measuring fault offsets from fault-perpendicular swath profiles through the *x*-, *y*-, and *z*-displacement fields. The swath profiles are centered at 300 m intervals along the fault surface trace (we use the published rupture map of Fletcher et al., 2014) and extend 1000 m orthogonally on either side of the fault. We use a swath width of 300 m, projecting all points within the swath onto the central profile line. Offsets are measured in each of the x, y and z displacement fields using straight-line, least-squares fits through the data points on each side of the fault, projecting to the fault, and computing the line separation at the fault (Milliner et al., 2015). In our implementation, the user cam define the limits for curve fitting on either side of the fault, allowing for some human discretion in removing artifacts and accounting for shorter-wavelength deformation.

The resulting *x*, *y* and *z* offsets at any point on the fault represent the local Cartesian slip vector; because this must lie in the plane of the fault, we can use knowledge of the local fault strike to compute the fault dip. Geometrically, this is done by projecting the slip vector onto a vertical plane orthogonal to the local fault strike and calculating its inclination. We also measure rake by taking the dot product of the strike and displacement vectors.

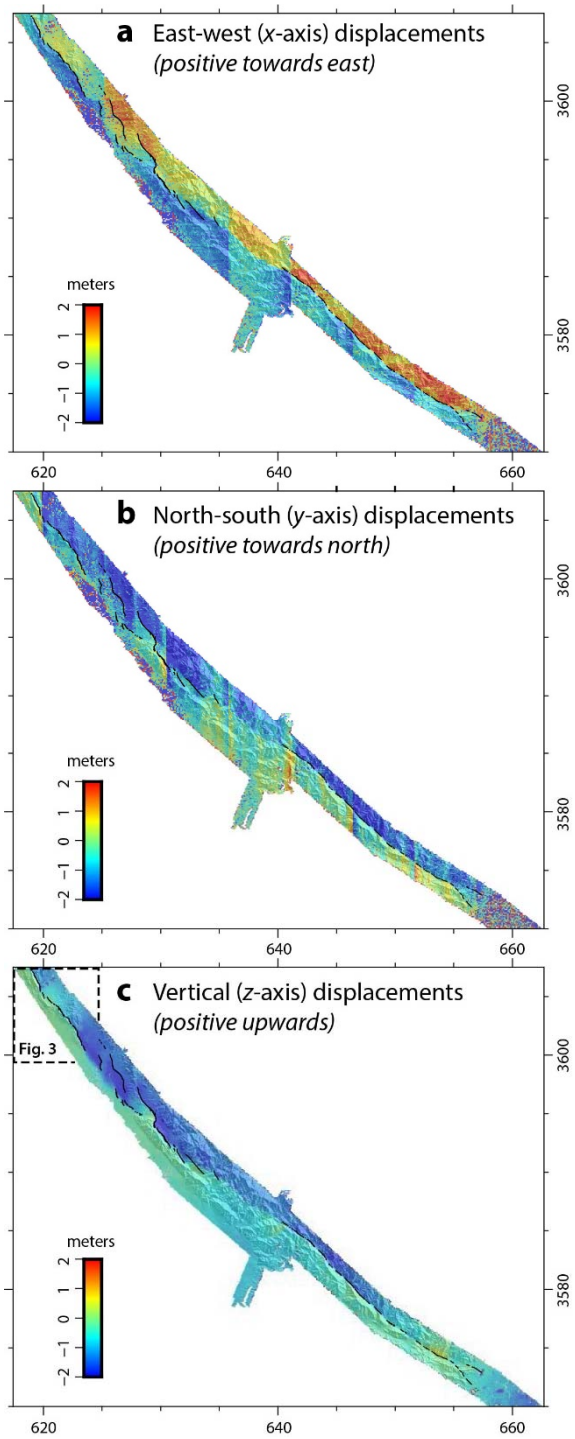

Figure 2: (a) East-west, (b) north-south and (c) vertical displacement field within the northern Sierra Cucapah section of the El Mayor-Cucapah rupture zone from application of our windowed adaptation to the Iterative Closest Point algorithm (Nissen et al., 2012, 2014; Glennie et al., 2014). Surface ruptures mapped in the field are shown by black lines (Fletcher et al., 2014; Teran et al., 2015). Coordinates are given in UTM Zone 11 kilometers.

RESULTS

To illustrate the type of data generated, Figure 3 shows profile locations and derived dip estimates along two segments of the Paso Superior fault in the northern rupture zone, plotted over the vertical displacement field (see Figure 2c for location). Figure 4 shows the same dip values, together with slip vector lengths (i.e. surface slip magnitudes), plotted as a function of distance along each fault segment. The Paso Superior fault is of particular interest as it encompasses some of the key field localities in which low-angle slip was observed on the ground (Fletcher et al., 2014; Teran et al., 2015).

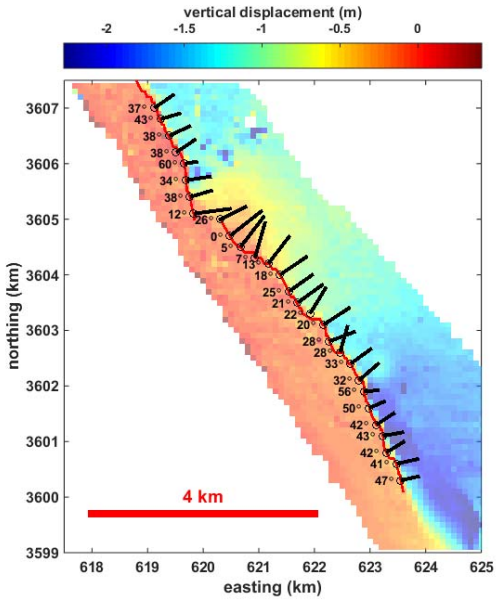

Figure 3: Calculated dip values for each profile location along the Paso Superior fault surface rupture (red line). Profile center points at 300 m intervals along the rupture are idicated by small circles. The black bars point down dip and are scaled by 90 - dip, such that longer arrows represent shallower dip angles. The background color map is the ICP vertical displacement field.

Along the southernmost Paso Superior fault, we estimate dip angles of 41° - 56°, reflecting the fact that fault throw is about equal to or slightly larger than heave. However, along the ~5 km middle part of the Paso Superior fault - close to the segment break - we calculate dips of 0° - 30°. These low angles can be confirmed visually from the raw displacement fields (Figure 2). The is only a faint discontinuity in the vertical displacement field at this location (reflecting small amounts of throw) but larger discontinuities in the horizontal displacement fields (reflecting larger amounts of heave). North of this central section, dips increase once again to values of ~40° at the northern edge of Figure 3.

Over a ~5 km section of the Paso Superior fault, the lidar data therefore support the field-based inferences of low-angle slip. Furthermore, the lidar displacement field hints that this slip extends over a distance of at least 2 km from the fault surface trace, and therefore probably several hundred meters into the subsurface. Existing seismological and geodetic models of the El Mayor-Cucapah earthquake therefore fail to capture important and genuine shallow-angle slip (Fialko et al., 2010; Hauksson et al., 2011; Wei et al., 2011; Zheng et al., 2012; Uchide et al., 2013; Huang et al., 2017; Kyriakopoulos et al., 2017). Instead, these models are likely to better characterize the deeper part of the fault zone, which is poorly sampled by the narrow (~3 km-wide) differential lidar footprint. We note that aftershock locations and mechanisms in this region appear inconsistent with deep slip on a NE-ward extension of the Paso Superior fault beneath the Mexicali Valley (Hauksson et al., 2011). We therefore envisage a scenario in which deep-seated slip on sub-vertical faulting transfers onto shallow, low-angle faulting only where no more favourably-oriented structure is available for reactivation.

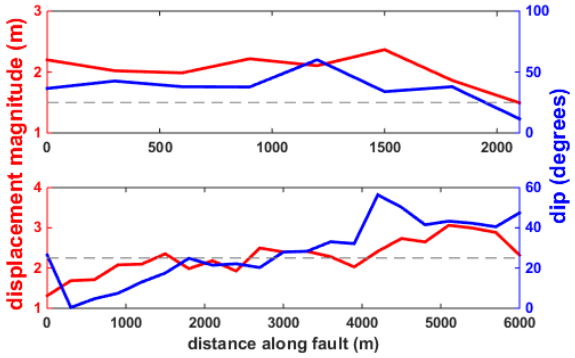

Figure 4: Surface slip magnitude (red) and fault dip (blue) calculated along strike for the northern (upper panel) and southern (lower panel) segments of the Paso Superior fault. Profiles are oriented N-S. Grey dashed lines delineate 25° dip.

This is further supported by the observed correlation between slip magnitude and fault dip along the Paso Superior fault, with correlation coefficients (R) of 0.57 for the northern segment (upper panel of Figure 4) and 0.64 for the southern segment (lower panel). Correlations for both fault segments are maximized at zero lag. This suggests that fault dip is providing a first-order control on displacement magnitude. For normal faults, with the maximum principal stress oriented vertically, Andersonian mechanics predicts optimally-oriented fault dip angles of ~60°; the less favorably-oriented the fault is, the less likely it is to slip (Anderson, 1905; Anderson 1951). The low-angle central Paso Superior fault appears to depress surface slip, whereas steeper sections of faulting to the north and south permit slip to break the surface relatively uninhibited.

CONCLUSIONS

Three-dimensional surface displacements in the 2010 El Mayor-Cucapah earthquake from differential lidar help resolve discrepancies between published fault models based on field measurements and those based on seismology and/or satellite geodesy. We do observe subsurface low-angle (0° - 30°) normal slip on a ~5 km section of the Paso Superior fault, consistent with local field measurements, but it is not pervasive throughout the wider Sierra Cucapah region as has been suggested. Furthermore, slip on the low-angle structure is depressed relative to adjacent, steeper sections of faulting.

Acknowledgements: We are grateful to all of the mapping and funding agencies involved in collecting and making available the lidar data. The Instituto Nacional de Estadistica y Geografia (INEGI) flew the pre-event survey, the National Center for Airborne Laser Mapping (NCALM) flew the post-earthquake survey, and the Open Topography facility (sponsored through NSF awards 1226353 and 1225810) curates both datasets. This research was supported primarily by the U.S. Geological Survey (USGS) through award G12AC20042, though we also acknowledge related support from the Southern California Earthquake Center (SCEC 14101) and the National Science Foundation (EAR 1461574). We thank Ramon Arrowsmith, Adrian Borsa, Alejandro Hinojosa Corona, Craig Glennie, Aravindhan Krishnan, Mike Oskin, and Sri Saripalli for many discussions of this work.

REFERENCES

Anderson, E.M., 1905. The Dynamics of Faulting. *Trans. Edinburch Geol. Soc*. 8 (3), 387-402.

Anderson, E.M., 1951. *The Dynamics of Faulting and Dyke Formation With Application to Britain*. 2nd ed., 206 pp., Oliver and Boyd, Edinburgh.

Barišin, I., Hinojosa-Corona, A., & Parsons, B., 2015. Co-seismic vertical displacements from a single post-seismic lidar DEM: example from the 2010 El Mayor-Cucapah earthquake. *Geophys. J. Int.* 202 (1), 328-346.

Clark, K.J., Nissen, E.K., Howarth, J.D., Hamling, I.J., Mountjoy, J.J., Ries, W.F., Jones, K., Goldstien, S., Cochran, U.A., Villamor, P., Hreinsdóttir, S., Litchfield, N.J., Mueller, C., Berryman, K.R., & Strong, D.T., 2017. Highly variable coastal deformation in the 2016 M_w 7.8 Kaikōura earthquake reflects rupture complexity along a transpressional plate boundary. *Earth Planet. Sci. Lett.* 474, 334-344.

Dolan, J.F., & Haravitch, B.D., 2014. How well do surface slip measurements track slip at depth in large strike-slip earthquakes? The importance of fault structural maturity in controlling on-fault slip versus off-fault surface deformation. *Earth Planet. Sci. Lett.* 388, 38-47.

Fialko, Y., Gonzalez, A., Gonzalez-Garcia, J.J., Barbot, S., Leprince, S., Sandwell, D.T., & Agnew, D.C., 2010. Static Rupture Model of the 2010 M7.2 El Mayor-Cucapah Earthquake from ALOS, ENVISAT, SPOT and GPS Data. *AGU Fall Meeting Abstr.*, T53B-2125.

Fletcher, J.M., Teran, O.J., Rockwell, T.K., Oskin, M.E., Hudnut, K.W., Mueller, K.J., Spelz, R.M., Akciz, S.O., Masana, E., Faneros, G., Fielding, E.J., Leprince, S., Morelan, A.E., Stock, J., Lynch, D.K., Elliott, A.J., Gold, P., Liu-Zeng, J., Gonzalez-Ortega, A., Hinojosa-Corona, A., & Gonzalez-Garcia, J., 2014. Assembly of a large earthquake from a complex fault system: Surface rupture kinematics of the 4 April 2010 El Mayor-Cucapah (Mexico) M_w 7.2 earthquake. *Geosphere* 10 (4), 797-827.

Fletcher, J.M., Oskin, M.E., & Teran, O.J., 2016. The role of a keystone fault in triggering the complex El Mayor-Cucapah earthquake rupture. *Nat. Geosci*. 9 (4), 303-307.

Glennie, C.L., Hinojosa-Corona, A., Nissen, E., Kusari, A., Oskin, M.E., Arrowsmith, J.R., & Borsa, A., 2014. Optimization of legacy lidar data sets for measuring near-field earthquake displacements. *Geophys. Res. Lett*. 41, 3494-3501.

Gold, P.O., Oskin, M.E., Elliott, A.J., Hinojosa-Corona, A., Taylor, M.H., Kreylos, O., & Cowgill, E., 2013. Coseismic slip variation assessed from terrestrial LiDAR scans of the El Mayor-Cucapah surface rupture. *Earth Planet. Sci. Lett.* 366, 151-162.

Hauksson, E., Stock, J., Hutton, K., Yang, W., Vidal-Villegas, J.A., & Kanamori, H., 2011. The 2010 M_w 7.2 El Mayor-Cucapah Earthquake Sequence, Baja California, Mexico and Southernmost California, USA: Active Seismotectonics along the Mexican Pacific Margin. *Pure. Appl. Geophys*. 168, 1255-1277.

Huang, M.H., Fielding, E.J., Dickinson, H., Sun, J., Gonzalez-Ortega, J.A., Freed, A.M., & Bürgmann, R., 2017. Fault geometry inversion and slip distribution of the 2010 M_w 7.2 El Mayor-Cucapah earthquake from geodetic data. *J. Geophys. Res.* 122, 607-621.

Jackson, J.A., & White, N.J., 1989. Normal faulting in the upper continental crust: observations from regions of active extension, *J. Struct. Geol.* 11, 15-36.

Kyriakopoulos, C., Oglesby, D.D., Funning, G.J., & Ryan, K.J., 2017. Dynamic Rupture Modeling of the *M*7. 2 2010 El Mayor-Cucapah Earthquake: Comparison With a Geodetic Model. *Journal of Geophysical Research: Solid Earth* 122 (12), 10263-10279.

Milliner, C.W.D., Dolan, J.F., Hollingsworth, J., Leprince, S., Ayoub, F., & Sammis, C., 2015. Quantifying near-field and off-fault deformation patterns of the 1992 M_w 7.3 Landers earthquake. *Geochem. Geophys. Geosyst*. 16, 1577-1598.

Nissen, E., Krishnan, A.K., Arrowsmith, J.R., & Saripalli, S., 2012. Three-dimensional surface displacements and rotations from differencing pre- and post-earthquake LiDAR point clouds. *Geophys. Res. Lett*. 39, L16301.

Nissen, E., Maruyama, T., Arrowsmith, J.R., Elliott, J.R., Krishnan, A.K., Oskin, M.E., & Saripalli, S., 2014. Coseismic fault zone deformation revealed with differential lidar: Examples from Japanese $M_w \sim 7$ intraplate earthquakes. *Earth Planet. Sci. Lett.* 405, 244-256.

Oskin, M.E., Arrowsmith, J.R., Corona, A.H., Elliott, A.J., Fletcher, J.M., Fielding, E.J., Gold, P.O., Garcia, J.J.G., Hudnut, K.W., Liu-Zeng, J., & Teran, O.J., 2012. Near-Field Deformation from the El Mayor-Cucapah Earthquake Revealed by Differential LIDAR. *Science* 335, 702-705.

Teran, O., Fletcher, J.M., Oskin, M.E., Rockwell, T.K., Hudnut, K.W., Spelz, R.M., Akciz, S.O., Hernandez-Flores, A.P., & Morelan, A.E., 2015. Geologic and structural controls on rupture zone fabric: A field-based study of the 2010 M_w 7.2 El Mayor-Cucapah earthquake surface rupture. *Geosphere* 11 (3), 899-920.

Uchide, T., Yao, H., & Shearer, P.M., 2013. Spatio-temporal distribution of fault slip and high-frequency radiation of the 2010 El Mayor-Cucapah, Mexico earthquake. *J. Geophys. Res*. 118, 1546-1555.

Wei, S., Fielding, E., Leprince, S., Sladen, A., Avouac, J.-P., Helmberger, D., Hauksson, E., Chu, R., Simons, M., Hudnut, K., Herring, T., & Briggs, R., 2011. Superficial simplicity of the 2010 El Mayor-Cucapah earthquake of Baja California in Mexico. *Nat. Geosci*. 4, 615-618.

Zheng, Y., Li, J., Xie, Z., & Ritzwoller, M.H., 2012. 5Hz GPS seismology of the El Mayor-Cucapah earthquake: estimating the earthquake focal mechanism. *Geophys. J. Int*. 190, 1723-1732.

INQUA Focus Group Earthquake Geology and Seismic Hazards

paleoseismicity.org

Preliminary results of seafloor exploration in the Western Saronic Gulf

Lampridou, Danai (1), Haase, Karsten (2), Nomikou, Paraskevi (1), Beier, Christoph (2), Wölki, Dominic (2), Storch, Bettina (2)

(1) Department of Geology and Geoenvironement, National Kapodistrian University of Athens, 15784, Greece, D.Lampridou@geol.uoa.gr, evinom@geol.uoa.gr
(2) GeoZentrum Nordbayern, Friedrich-Alexander Universität Erlangen-Nürnberg, Schlossgarten 5, D-91054 Erlangen, Germany, karsten.haase@fau.de, christoph.beier@fau.de, dominic.woelki@fau.de, bettina.storch@fau.de

Abstract: *We present here for the first time new high-resolution swath data and the resulting bathymetric map of the offshore area around Methana peninsula in the western Saronic Gulf acquired during cruise POS512 (2017) with R/V Poseidon. The Paphsanias volcanic field (NW of Methana) consists of 5 different volcanic cones situated at 170m up to 300m water depth. Elongated volcanic ridges and debris are concentrated at the northern part of the peninsula. Fault scarps cutting the seafloor, trending mainly NW-SE, E-W, SW-NE, may be interpreted to result from active tectonic activity and the western margin of the Epidavros basin is carved by three well-defined landslides.* The uneven and complex topography of the research area is mostly attributed to active tectonic and volcanic processes.

Keywords*: Methana Volcano, Pahpsanias, Bathymetry, Saronic Gulf*

INTRODUCTION

Here, we present, for the first time, new high-resolution swath data and the bathymetric map of the western Saronic Gulf acquired aboard R/V POSEIDON during the cruise POS512 in April-May 2017. Cruise POS512 was scheduled for ten working days in order to (1) obtain bathymetric data of the Epidavros Basin (Saronic Gulf) near the peninsula of Methana, (2) survey the volcanic structures of the Paphsanias Volcanic Field with the Remotely Operated Vehicle (ROV) PHOCA from GEOMAR Helmholtz Zentrum für Ozeanforschung Kiel, and (3) sample the volcanic rocks. During POS512, 427 nm of bathymetric survey were carried out (Haase et al., 2017), And 13 ROV dives recovered 163 samples including 131 fresh lavas from four different volcanoes of the Paphsanias Volcanic Field.

TECTONIC SETTING

The Hellenic volcanic arc belongs to the Hellenic orogenic zone, formed along the convergent plate boundary of the northwards subducting African plate underneath the active margin of the European plate (Le Pichon & Angelier, 1979; McKenzie, 1972). Tertiary volcanic rocks in the Aegean area indicate a southward migration of the volcanism from late Eocene by 300-350Km in the area internal to Crete (Papanikolaou, 1993; Royden & Papanikolaou, 2011). The present day active volcanic arc extends from the Saronic Gulf in the west up to Santorini and Nisyros islands, and dates back to the early Pliocene with a peak in activity during the Quaternary (Pe-Piper & Piper, 2002; Pe-Piper & Piper, 2005).

Apart from the onshore volcanic areas, submarine volcanism covers a significant area in the active Hellenic volcanic arc either in the form of independent volcanic edifices or as an offshore extention of the active volcanic islands. These volcanic structures are hosted within extensional neotectonic basins/grabens delineated by large marginal faults. The prevailing tectonic orientation is NE-SW in Santorini and Nisyros and NW-SE in Methana and Milos, following the general geometry of the volcanic arc (Nomikou et al., 2013).

REGIONAL SETTING

The peninsula of Methana is a complex andesite-dacite volcanic centre of approximately 35 km^2 surface area and has the longest recorded volcanic history of any volcanic centre in the South Aegean Arc (Fytikas et al., 1986). Volcanism started in the late Pliocene (Gaitanakis & Dietrich, 1995) and the most recent activity was an eruption in 230 BC erupting andesitic lavas at Kammeni Hora first described by the ancient geographer Strabo. Methana's volcanic evolution unravels eight volcanic phases, strongly influenced by the regional tectonic stress field. The Quaternary volcanic rocks on Methana consist of domes and flows radiating from the central part of the peninsula and many of them are elongated in an E-W or NW-SW direction (Pe-Piper & Piper, 2013).

The neotectonic structure of the Western Saronic Gulf comprises a succession of horst and graben structures formed by WNW-ESE trending normal faults (Papanikolaou et al., 1988, 1989). The larger graben correspond to two basins: a) the Epidavros Basin with a maximum water depth of 400 m and a Plio-Quaternary sediment thickness of 250-500 m, and b) the Megara Basin with a maximum water depth of 250 m and a Plio-Quaternary sediment thickness of more than 500 m.

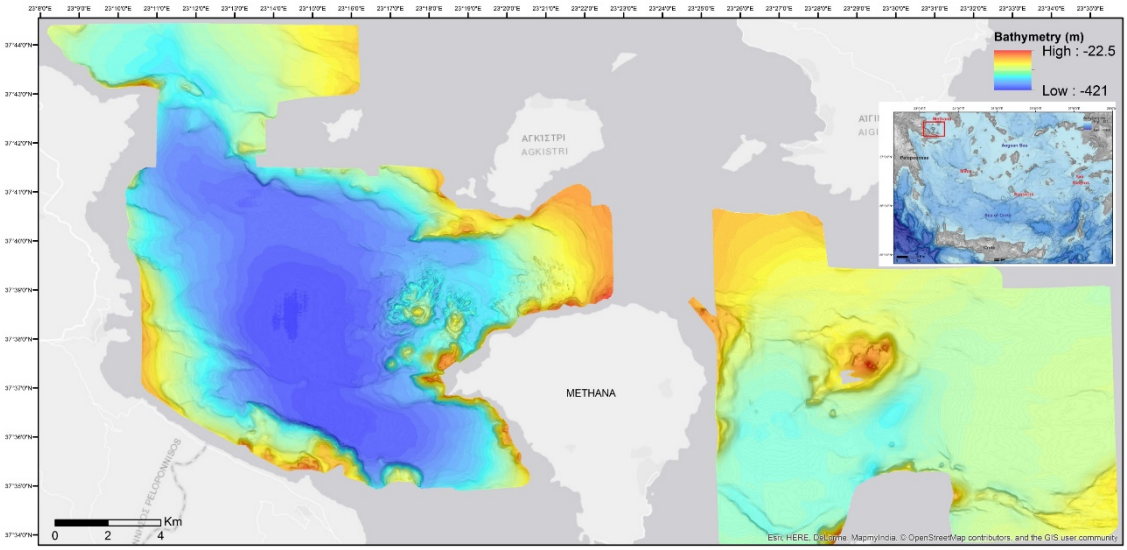

Figure 1: Bathymetric map of the Western Saronic gulf. Data collected with R/V Poseidon during POS 512.

The Paphsanias submarine volcano in the Epidavros Basin of the Western Saronikos Gulf was discovered in 1987 (Papanikolaou et al., 1988, 1989; Pavlakis et al., 1990). It is situated at a distance of 1.5-2 km to the NW of Methana peninsula cand covers an area of about 12 km^2 reaching a minimum water depth around 143m (Nomikou et al., 2013).

METHODOLOGY

Multibeam bathymetric data were collected by R/V POSEIDON using the hull mounted ELAC Nautik's SeaBeam 3050 multibeam (50kHZ). Acquisition was over a 140^o swath with a beam separation of 1.5^o and logged via HYPACK 2016. Multibeam data processing, was conducted with the open source package MB-SYSTEM and included pre-processing steps, editing of navigation, refraction correction, automatic filtering and manual beam-by-beam editing and finally generating a grid of 10m and spacing. Analyses and visualization of the produced DTM were carried out using the ArcGIS 10.3 and QPS Fledermaus software packages.

Rock sampling and the seabed survey were performed using the Remotely Operated Vehicle (ROV) PHOCA from GEOMAR Helmholtz Zentrum für Ozeanforschung Kiel. ROV Phoca is designed to operate up to 3000m water depth and carries various mounted HD cameras, two manipulators for sampling procedures and at the same time the digital telemetry system SubCan provides real time data transmission.

RESULTS

Our newly obtained high-resolution swath data reveal a complex seabed morphology (Figure1). Up until now little was known about the submarine area around Methana peninsula and our new map provides the first record of the submarine volcanism and tectonic features of the western Saronic Gulf.

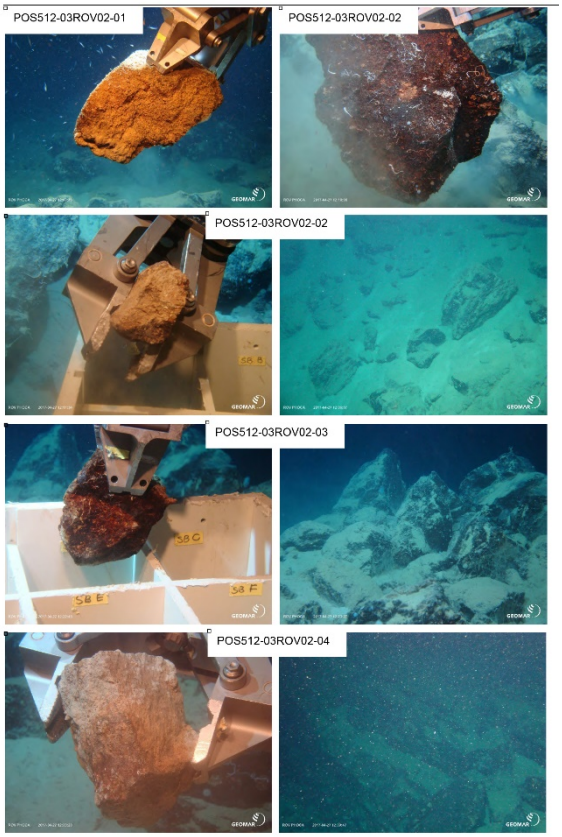

Figure 2: ROV sampling of the volcanic cones at Phasanias.

The Epidavros basin has maximum depth of 420m, while the flat bottom area lying eastwards of Methana is comparatively shallower, reaching a maximum depth of 280m.

Our new results show that the Paphsanias volcanic field consists of 5 volcanic edifices. Their base levels are located at 170m water depth up to 300m water depth and they are inclined towards the NW. Moreover, these cones show

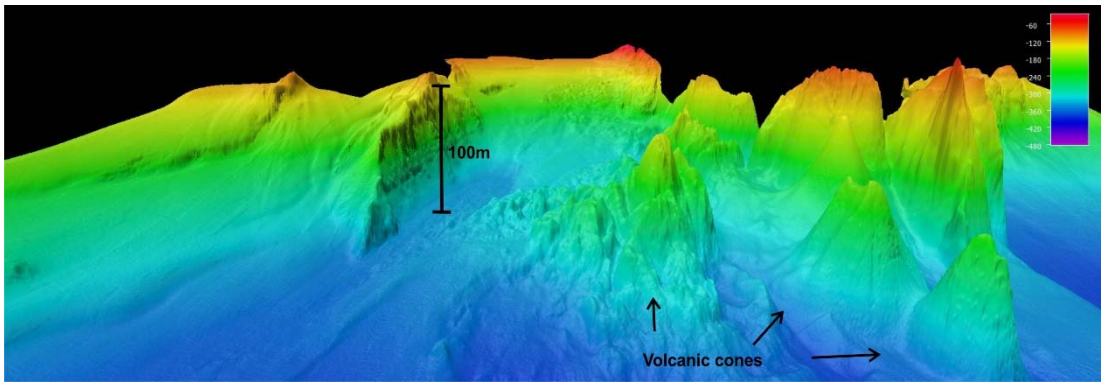

Figure 3: 3D reconstruction of the area depicting the Paphsanias volcanic field and the vertical 100m high fault scarp, trending W-E.

distinct morphological expressions. The ones closer to the shore are round pointy cones, while the ones situated at greater water depth are more complex crater-like structures including features that may represent lava domes. Based on the ROV imagery, cones at greater water depth also consist of lava flows with angular rocks, large debris fields and dispersed large boulders embedded into fine sediment (*Figure 2;* Haase et al., 2017). At the northern offshore area, between Methana and Agkistri, well-preserved elongated volcanic ridges trend NW-SE. Volcanic debris located close to the shore is possibly correlated with the Mavri Petra volcanic complex (Figure 4).

Several fault scarps are observed cutting the seafloor around Methana peninsula mainly oriented along NW-SE, E-W, SW-NE directions. The most distinctive feature is the one extending along the southern margin of Agkistri. This scarp is approximately 100 m high, forming an almost vertical steep cliff (Figure 3).

Noteworthy is the emergence of a semi-circular seamount up to the sea level (Figure 1), approximately 4km offshore Methana towards the east. According to the neotectonic map of the area (Papanikolaou et al., 1989) this outcrop should correspond to carbonate rocks likely Mesozoic in age.

The western slope of the Epidavros Basin is influenced by three major landslides. The landslide that extends from 37° 35' N 23°13'E up to 37°38'N 23°11'E is a complex landslide forming a 5 km along-slope and 3.5 km across-slope indentation in the margin (Figure 4). The main headwall scarp lies at 120 m water depth, while the secondary headwall is situated at 240m water depth. Narrow erosional gullies, confined to the main headwall area, dissect perpendicular to the shelf and open up a flat-bottom basin. The relatively flat-bottom basin may be interpreted as the depositional area of the landslide, because it has a smooth morphology and lacks the common rugged and crenulated topography produced by deposited debris.

DISCUSSION

Our new preliminary results provide insight into the complex seafloor topography of the western Saronic Gulf. A new high-resolution morpho-bathymetric map of the offshore area around Methana peninsula allows to identify the different volcanic, tectonic and erosional features. The seafloor around Methana appears to be characterised by active tectonics and volcanic processes. Further investigation is required to determine the interaction between tectonics and volcanism punctuated by the clustered volcanic features at the NW part of Methana.

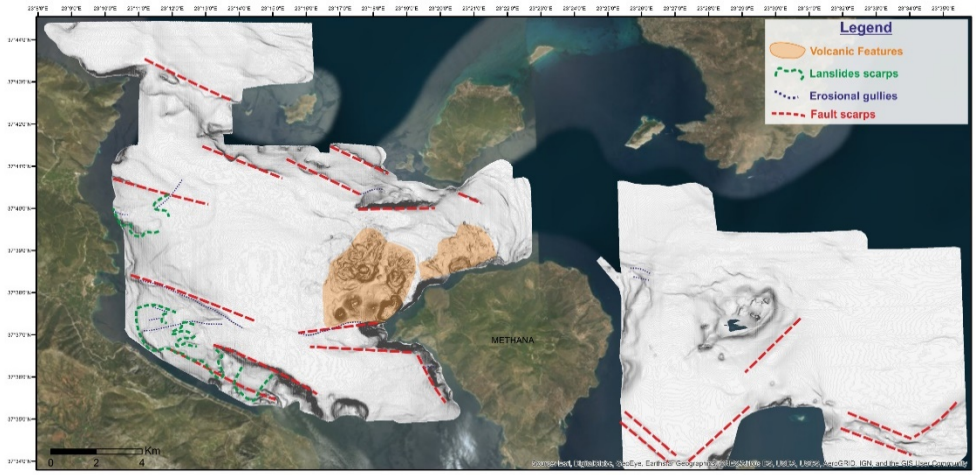

Figure 4: Greyscale slope shaded map and general geomorphologic interpretation of the offshore area around Methana peninsula.

Acknowledgements: We gratefully acknowledge the captain H. Volland and the crew of R/V Poseidon and the GEOMAR ROV team for their helpfulness and competence. We thank the Greek Authorities and in particular the Ephorate of Underwater Antiquities from the Greek Ministry of Culture (from which the observer Mr. Karagiannakis, E., has been on board from April 25 up May 6) for granting us permission to work in their territorial waters.

REFERENCES

Fytikas, M., Innocenti, F., Kolios, N., Manetti, P., & Mazzuoli, R., 1986. The Plio-Quaternary volcanism of Saronikos area (western part of the active Aegean volcanic arc). *Annales Geologiques des Pays Helleniques* 33, 23-45.

Gaitanakis, P., & Dietrich, A.D., 1995. Geological map of Methana peninsula, 1:25 000, Swiss Federal Institute of Technology, Zurich.

Haase, et al., 2017. Paphsanias Volcano. Poseidon-Berichte, Cruise 512.

Le Pichon, X., & Angelier, J., 1979. The Hellenic arc and trench system: a key to the neotectonic evolution of the eastern Mediterranean area. *Tectonophysics* 60, 1-42.

McKenzie, D.P., 1972. Active tectonics of the Mediterranean region. *Geophys. Journal of the Royal Astronomical Society* 30, 109-185.

Nomikou, P., Papanikolaou, D., Alexandri, M., Sakellariou, D., & Rousakis, G., 2013. Submarine volcanoes along the Aegean volcanic arc. *Tectonophysics* 597-598, 123-146.

Papanikolaou, D., Lykousis, V., Chronis, G., & Pavlakis, P., 1988. A comparative study of neotectonic basins across the Hellenic arc: the Messiniakos, Argolikos, Saronikos and Southern Evoikos Gulfs. *Basin Research* 1, 167-176.

Papanikolaou, D., Chronis, G., Lykousis, V., Pavlakis, P., Rousakis, G., & Syskakis, D., 1989. Submarine Neotectonic Map of Saronikos Gulf. EPPO/NCMR/University of Athens.

Papanikolaou, D., 1993. Geotectonic evolution of the Aegean. *Bulletin of the Geological Society of Greece* XXVII, 33-48.

Pe-Piper, G., & Piper, D., 2002. The igneous rocks of Greece. *Beitrage zur perionalen geologie der erde* 30. Gebruder Borntraeger (573 pp).

Pe-Piper, G., & Piper, D.J.W., 2005. The South Aegean volcanic arc: relationships between magmatism and tectonics. *Developments in Volcanology* 7, 113-133.

Pe-Piper, G., & Piper, D.J., 2013. The effect of changing regional tectonics on an arc volcano: Methana, Greece. *Journal of Volcanology and Geothermal Research* 260, 146-163, doi:10.1016/j.jvolgeores.2013.05.011.

Royden, L.H., & Papanikolaou, D., 2011. Slab segmentation and late Cenozic disruption of the Hellenic Arc. *G*^{3} 12 (3).

INQUA Focus Group Earthquake Geology and Seismic Hazards

paleoseismicity.org

Use of the Terrain Ruggedness Index for identifying individual neotectonic blocks: application to Heraklion basin, Greece

Lazos, Ilias (1), Chatzipetros, Alexandros (1)

(1) School of Geology, Aristotle University, 54124, Thessaloniki, Greece, ilialazo@geo.auth.gr, ac@geo.auth.gr

Abstract: *The objective of this paper is the determination of individual neotectonic blocks, based on lithological, geomorphological and tectonic features of the study area (Heraklion basin, Crete Island, Greece). The classification of the area into distinct crustal blocks estimates the successive deformation of each block, obtained during all deformation phases. Four steps were carried out, leading to blocks identification. The first step is the digitalization of the lithological and tectonic features of the study area in a semiautomatic GIS environment. During the second step, grouping of the digitalized geological formations takes place, based on their age. Afterwards, the determination of crustal blocks of the examined area is carried out, based on geological criteria. Finally, the Terrain Ruggedness Index (TRI) is estimated for the area and it is correlated to the identified classes. The TRI can be a significant indicator of neotectonic regime assessment, related to lithological, tectonic and geomorphological features.*

Keywords*: neotectonic blocks, GIS-based mapping, Terrain Ruggedness Index (TRI), active tectonics, Heraklion basin*

INTRODUCTION

Overview of the procedure

Determination of individual neotectonic blocks can be an essential and accurate tool for interpreting the tectonic regime of a study area. The division of the area into blocks is performed by taking into account both the tectonic structures (mainly faults and fault zones) and the lithological units of the study area. The block separation procedure is implemented by processing the tectonic and lithological features in a GIS environment, where both of them are digitized. In addition, the use of Digital Elevation Models (DEMs) is also supported in the same software environment. The combination of the processed data and the use of a specific methodology leads to the determination of the Terrain Ruggedness Index (TRI).

Geological setting

The Hellenic Subduction zone is the largest, fastest and most seismically active zone in the Mediterranean, where the African plate subducts beneath Crete at a rate of ~36 mm/year (McClusky et al., 2000; Reilinger et al., 2006; Gallen et al., 2014). Crete Island is located on the accretionary wedge of the Hellenic Arc and is characterized by remarkable neotectonic uplift due to its geotectonic position. This intense neotectonic activity is documented in the Heraklion basin, the largest basin of Crete Island (Figure 1). The tectonic regime of the Heraklion basin has been studied by various researchers (e.g. Fassoulas, 2001; Ganas et al., 2011; Kokinou et al., 2013). It is a fault-bounded Neogene basin that is also criss-crossed by neotectonic faults of various strikes. It has been developed over the alpine basement of Crete since Middle Miocene. The Heraklion Gulf submarine basin constitutes its prolongation to the north, where the tectonic boundary lies along the E - W coastline, as a result of Quaternary tectonism (Papanikolaou & Nomikou, 1998). Lithologically, the broader area is a part of the alpine basement that is subdivided into a series of tectonic units, their deformation dating mainly between Early Tertiary and Early Miocene, while the post-alpine sediments are also widespread.

Figure 62: Location map of the study area in Crete Island (red area) and location of Crete Island in Greece (red quadrilateral) (Google Earth).

MATERIALS AND METHODS

The primary materials used for the analysis of the study area are the geological maps of the Institute of Geology and Mineral Exploration (I.G.M.E). Five I.G.M.E. geological maps of 1:50,000 scale cover the study area and were used for the present paper. These five maps contain both lithological and tectonic features and they were digitalized in a GIS environment (first step). The scale of digitalization was 1:10,000 for the lithological formations and 1:5,000 for the tectonic features.

The result of the digitalization was the extraction of a large number of lithological formations, as shown in Figure 2. Furthermore, the ASTER/GDEM (Digital Elevation Model), generated by the TERRA satellite with resolution 3m × 3m, was used (Figure 3). In order for those lithological formations to be managed, they were classified into groups (second step). The criterion for this classification was exclusively their age, based on the assumption that rocks of similar age behave

similarly through time as far as their erosion processes are concerned, hence their morphotectonic signature would be similar. The classes are (Figure 4):

- Quaternary lithological formations
- Neogene lithological formations
- Paleogene lithological formations
- Bedrock (Paleozoic and Mesozoic formations)

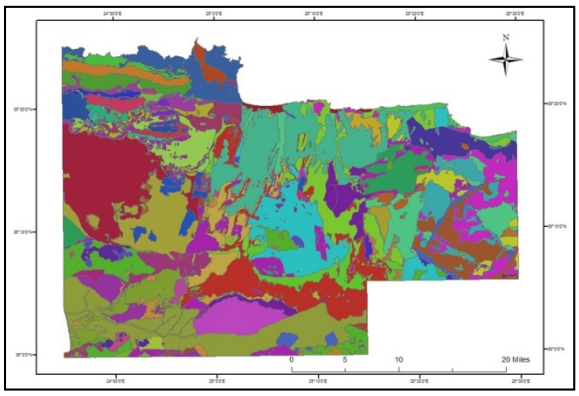

Figure 2: Digitalized lithological formations of the study area in a GIS environment.

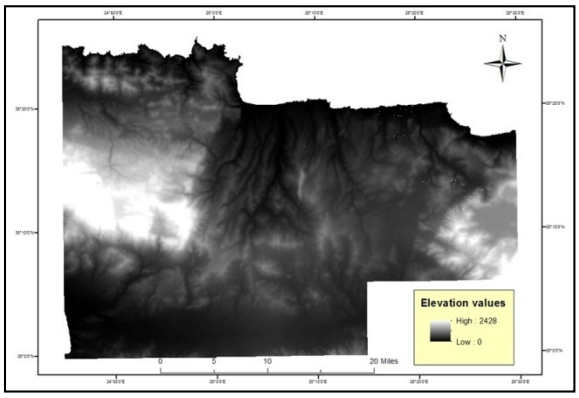

Figure 3: Digital Elevation Model (DEM) of the study area.

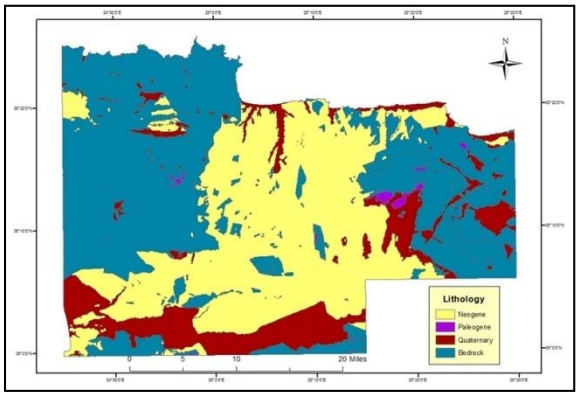

Figure 4: Grouped classes of lithological formations.

As shown in Figure 5, the study area contains a large number (2,095) of mapped tectonic features. The majority of those 2, tectonic features corresponds to normal faults and fault zones. The rest correspond mainly to probable normal faults or fault zones and a small percentage to thrusts, high-angle reverse faults and nappes.

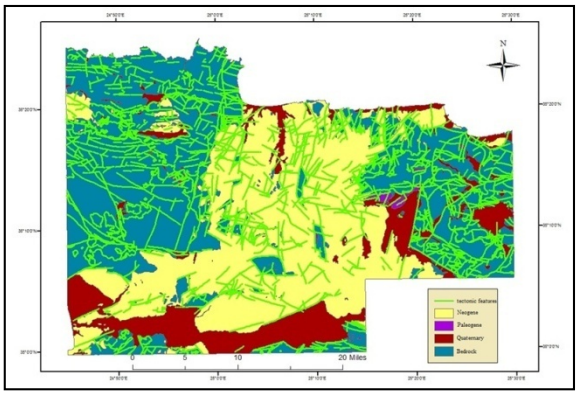

Figure 5: Grouped lithological formations and tectonic features of the study area.

Taking into account both the lithological and tectonic features, the study area was divided into 4 main neotectonic blocks (third step) (Figure 6). The blocks were defined as areas bounded by prominent fault zones, who are likely to have behaved mechanically uniformly during the neotectonic period. The first block (Block 1) consists mainly of bedrock formations, locally overlaid by Paleogene, Neogene and Quaternary formations. The second block (Block 2) is similar, in the sense that it mainly consists of bedrock formations covered in places by Quaternary sediments. The presence of Paleogene and Neogene formations is limited in this block. The third block (Block 3) is located between the first and the second block and consists of Neogene formations mainly, all Paleogene formations, bedrock nappes and a few Quaternary formations. The fourth block (Block 4) is located south of the third one and consists mainly of Quaternary formations. A small percentage of Neogene formations is also part of the fourth block.

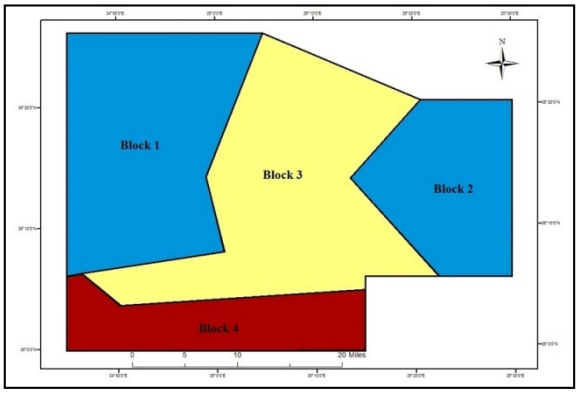

Figure 6: Distinct neotectonic blocks of the study area.

The classification of the study area into neotectonic blocks is followed by the estimation of the Terrain Ruggedness Index (TRI) (fourth step). The TRI is an objective indicator of the terrain heterogeneity (Riley et al., 1999), while it also identifies the different forms of the surface and determines the processes affecting it (Popit & Verbovšek, 2013). The basic principal of the TRI method is the estimation of relief ruggedness, estimated by the differences between the elevations in the cells in the window size of 3m × 3m, leading to the production of a raster map by using the DEM, including the maximum and minimum elevations. The TRI is calculated by the equation (Popit & Verbovšek, 2013):

$$TRI = \sqrt{\left| H_{\max}{}^2 - H_{\min}{}^2 \right|}$$

where TRI is the Terrain Ruggedness Index, H_{max} is the maximum elevations and H_{min} is the minimum elevations.

RESULTS AND DISCUSSION

The combination of this equation and the raster files resulted in the calculation of the Terrain Ruggedness Index (TRI) for the study area (Figure 7). The extracted TRI values are classified into three qualitative categories: high, medium and low. High TRI values are shown in green, medium TRI values in light green, white and light purple, and low values in purple. High TRI values correspond to rough morphologies, in contrast with low TRI values that indicate rather smooth surfaces. The TRI classes indicate significant differences among the neotectonic blocks. The first and the second block are characterized by medium TRI values, while both of them also show a quite large percentage of high values (especially the first block). The high values of these two blocks are the highest in the study area, while low TRI values are limited. In general, the TRI values of the first and the second block are characterized as medium to high.

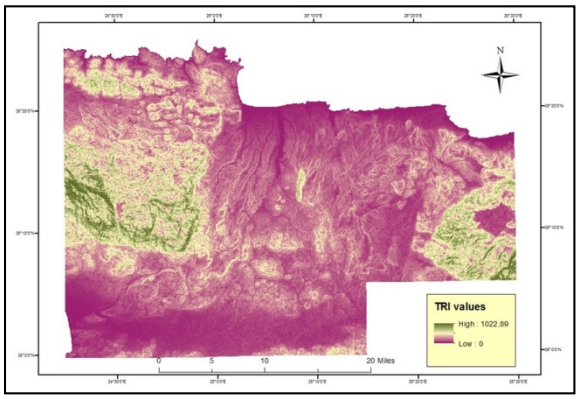

Figure 7: Terrain Ruggedness Index (TRI) of the study area.

The third block shows mainly medium TRI values. An insignificant percentage of low values appears in the north part of this block. The main characteristic of the third block is the presence of dispersed medium to high values and in some cases very high values. Nevertheless, this block is characterized as a medium TRI one. In the fourth block, mainly low and a small percentage of medium TRI values are observed. High TRI values are absent. Generally, the fourth neotectonic block is defined as a low TRI block.

CONCLUSIONS

The results show that the TRI values are directly connected to the lithology. The first and the second neotectonic blocks, which show medium to high TRI values, consist mainly of bedrock formations. The third block consists mainly of Neogene and Paleogene formations, showing medium TRI values. The dispersed medium to high TRI values are caused by the nappes that involve bedrock formations. The fourth block, characterized by low TRI values, consists almost exclusively of Quaternary formations. Consequently, the differentiation of the lithology is associated to the differentiation of the TRI values. TRI analysis also shows the important role of tectonic features. More than 50% of the mapped and digitalized tectonic features are in the first and second blocks. As shown in Figure 4, the lithological formations of Block 1 and Block 2, are deformed by a dense distribution of tectonic features. Fault presence is scarce in Block 3, in comparison compared with the first and second blocks, while tectonic features are virtually absent in Block 4. The distribution of tectonic features within the blocks shows that they are related to the TRI values. A wide distribution of tectonic features is related to medium to high TRI values, while in low TRI areas their occurrence is limited. This of course is correlated with the age of the geological material: older rocks are more deformed than younger ones, simply because of their longer exposure to deformation. Additionally, by comparing the Digital Elevation Model (Figure 3) and the calculated TRI values (Figure 7) an interdependency between elevations and TRI values is evident: high elevations are associated with high TRI values and low elevations with low ones.

In conclusion, Terrain Ruggedness Index (TRI) is affected by and can show differentiations in lithology, tectonics and elevation. TRI can be used as a tool to specify individual tectonic blocks, who can show differentiated behaviour (i.e. uplift or subsidence) during recent deformation phases.

REFERENCES

Fassoulas, C., 2001. The tectonic development of a Neogene basin at the leading edge of the active European margin: the Heraklion basin, Crete, Greece. *Journal of Geodynamics* 31, 49-70.

Gallen, S.F., Wegmann, K.W., Bohnenstiehl, D.R., Pazzaglia, F.J., Brandon, M.T., & Fassoulas, C., 2014. Active simultaneous uplift and margin-normal extension in a forearc high, Crete, Greece. *Earth and Planetary Science Letters* 398, 11-24.

Ganas, A., Palyvos, N., Mavrikas, G., Karastathis, V., Drakatos, G., & Makropoulos, K., 2011. Recognition and Characterisation of Neotectonic Faults in Heraklion City area (Crete, Greece): a multidisciplinary approach. *Geophysical Research Abstracts* 13, EGU2011-4824, 2011, EGU General Assembly 2011.

I.G.M.E. Geological Map of Greece, scale 1:50,000, sheets: Heraklion, Anoghia, Tymbakion, Ep. Arhanae, Mohos.

Kokinou, E., Skilodimou, H., & Bathrellos, G., 2013. Morphotectonic analysis in determining the impact of the tectonic activity in the geomorphology of the Heraklion basin (Crete, Greece). *Bulletin of the Geological Society of Greece, Proceedings of the 13th International Congress.*

McClusky, S., Balassanian, S., Barka, A., Demir, C., Ergintav, S., Georgiev, I., Gurkan, O., Hamburger, M., Hurst, K., Kahle, H., Kastens, K., Kekelidze, G., King, R., Kotzev, V., Lenk, O., Mahmoud, S., Mishin, A., Nadariya, M., Ouzounis, A., Paradissis, D., Peter, Y., Prilepin, M., Reilinger, R., Sanli, I., Seeger, H., Tealeb, A., Toksoz, M.N., & Veis, G., 2000. Global positioning system constraints on plate kinematics and dynamics in the eastern Mediterranean and Caucasus. *J. Geophys. Res., Solid Earth* 105, 5695-5719.

Papanikolaou D., & Nomikou P., 1998. Neotectonic blocks and planation surfaces in Iraklion basin, Crete, Greece. *Bull. Geol. Soc. Greece* XXXII/1, Patras, May 1998, 231-239.

Popit, T., & Verbovšek, T., 2013. Analysis of surface roughness in the Sveta Magdalena paleo-landslide in the Rebrnice area. *RMZ - Materials and Geoenvironment* 60, 197-204.

Reilinger, R., McClusky, S., Vernant, P., Lawrence, S., Ergintav, S., Cakmak, R., Ozener, H., Kadirov, F., Guliev, I., Stepanyan, R., Nadariya, M., Hahubia, G., Mahmoud, S., Sakr, K., ArRajehi, A., Paradissis, D., Al-Aydrus, A., Prilepin, M., Guseva, T., Evren, E., Dmitrotsa, A., Filikov, S.V., Gomez, F., Al-Ghazzi, R., & Karam, G., 2006. GPS constraints on continental deformation in the Africa-Arabia-Eurasia continental collision zone and implications for the dynamics of plate interactions. *J. Geophys. Res., Solid Earth* 111, B05411.

Riley, S.J., DeGloria, S.D., & Elliot, R., 1999. A Terrain Ruggedness Index that Quantifies Topographic Heterogeneity. *Intermountain Journal of Sciences* 5, 23-27.

INQUA Focus Group Earthquake Geology and Seismic Hazards

paleoseismicity.org

Rotation rates of the South Aegean region, Greece, based on primary geodetic data - Comparison between geodetic and palaeomagnetic results

Lazos, Ilias (1), Kondopoulou, Despina (2), Chatzipetros, Alexandros (1), Pavlides, Spyros (1), Bitharis, Stylianos (3), Pikridas, Christos (3)

(1) Department of Geology, School of Geology, Aristotle University of Thessaloniki, Greece, ilialazo@geo.auth.gr
(2) Department of Geophysics, School of Geology, Aristotle University of Thessaloniki, Greece
(3) Department of Geodesy and Surveying, School of Rural and Surveying Engineering, Aristotle University of Thessaloniki, Greece

Abstract: *In this paper the rotation rates of the South Aegean region are estimated, using the results extracted by primary geodetic data, collected by a wide network of permanently installed GPS stations into the study area. The geodetic data processing is based on the implementation of the GPS stations triangulation. The data of three different GPS stations, forming a triangle, are combined each time, leading to the calculation of the rotation rate of the triangle centroid, representing these three stations. Based on these rotation rate results, two rotation models are proposed (-5 Myr and -10 Myr period, respectively) and are compared to the recorded palaeomagnetic data of the study area. The combination of two different types of datasets (geodetic and palaeomagnetic) leads to the development of a general model, classifying the South Aegean region into distinct rotational blocks.*

Keywords*: rotations, geodetic data, palaeomagnetic data, GPS stations, South Aegean*

INTRODUCTION

South Aegean is one of the most tectonically active regions in the world. At the southern-southwestern part of the area, the Hellenic subduction zone is documented, associated to the convergence of the African plate beneath the Aegean - Anatolian plate (Figure 1) (Bocchini et al., 2018 and references therein). The geotectonic evolution of the South Aegean is interpreted by different theories, such as the back-arc extension (Le Pichon & Angelier, 1979; Mercier et al., 1989; Pavlides & Caputo, 1994), the westward tectonic escape (McKenzie, 1972; Dewey & Şengör, 1979) and the roll back related to tectonic escape (Armijo et al., 1999; Sternai et al., 2014).

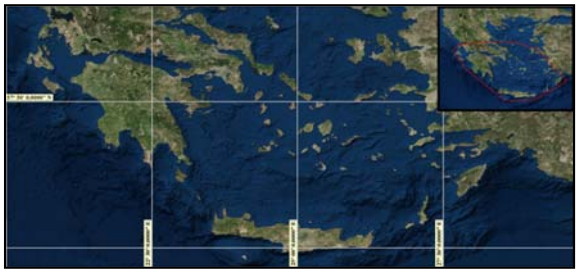

Figure 63: South Aegean region - Location in Greece (red polygon).

According to McClusky et al. (2000), the Aegean microplate velocity towards Africa is 40 mm/yr. The combination of this velocity and the aforementioned convergence leads to a significant uplift (~4 mm/yr) of Crete Island (accretionary wedge), while the volcanic arc, north of Crete Island, is also located into the South Aegean region.
The rotational regime of South Aegean is widespread, as both clockwise and counter-clockwise rotations have been documented, based mainly on palaeomagnetic data. Among the numerous palaeomagnetic studies published for the broader Aegean (including continental Greece and western Anatolia), a considerable amount has focused to the presently studied area (Kondopoulou, 2000; van Hinsbergen et al., 2005, 2010; Bradley et al., 2013, among others). The pattern arising from these studies for the last 10-12 Myr clearly defines a fast clockwise rotating block at the western part of the studied area and a counter-clockwise one at its eastern part (Figure 2). This pattern has been cross-checked by independent models (Walcott & White 1998) and is continuously strengthened by recent studies (Uzel et al., 2017 and references therein).

GPS DATA AND ANALYSIS SCHEME

The satellite geodetic methods such as GPS are valuable for the analysis and estimations of crustal deformation studies (Fotiou et al., 2003; Fotiou & Pikridas, 2012). Specifically, data of many permanent GPS stations and within seven years' time span were collected and processed in a previous study (Bitharis et al., 2016). Data analysis was mainly based on 30-sec daily GPS observations and elevation cut-off angle 10°.

The analysis was performed by GAMIT/GLOBK (Herring et al., 2010) software suite (release 10.5) at 24-h sessions, with three step approach as recommended. Firstly, the raw GPS data was processed to estimate daily loosely constrained solutions of site position coordinates. The Earth Orientation Parameters and GPS orbits were kept "fixed" (heavily constrained) using IERS Bulletin A values and IGS final orbits. In our strategy we estimate Zenith Total Delay (ZTD) adjusted every 2-hour interval and as a Mapping function the Vienna Mapping Function 1 (VMF1)

was selected. Concerning Solid Earth Tides the IERS2003 conventions were followed. Additionally, about Ocean Tide Loading and Tidal/non-Tidal atmospheric pressure loading corrections, recommended models were applied. More specifically, the stations which were located around the Greek network (i.e. IGS Network) were held as fixed with weights.

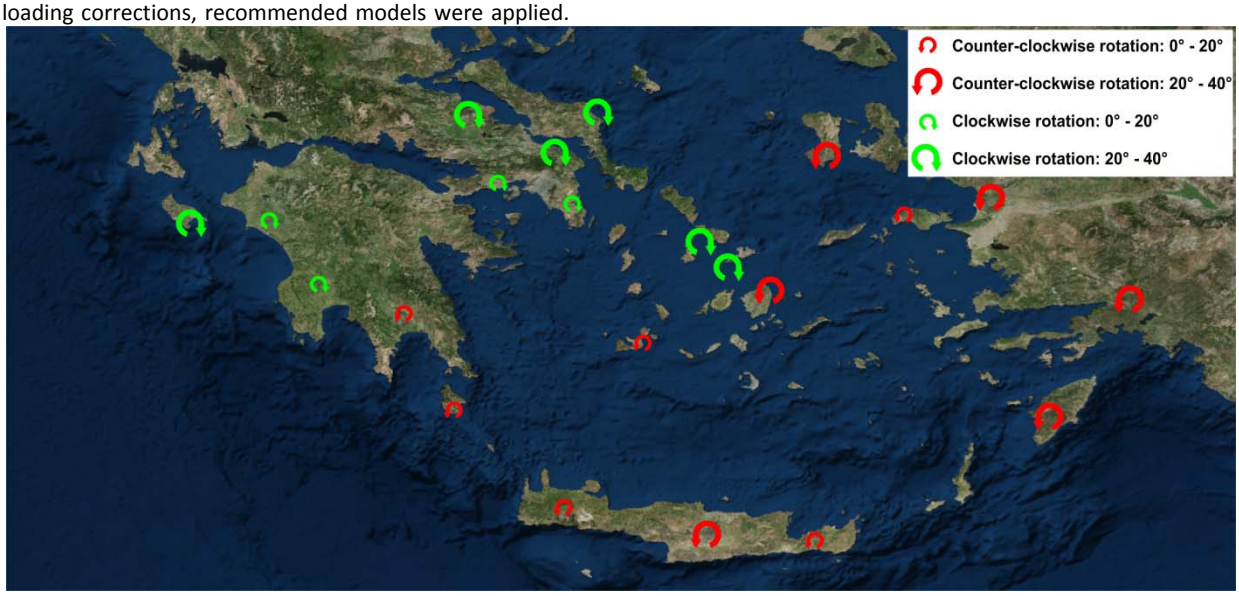

Figure 2: Rotations of the South Aegean region during the last 10 Myr period, based on recorded palaeomagnetic data.

METHODOLOGY

The calculation of the rotation rate is based on the methodology of triangulation of the permanently installed GPS stations, using the recorded primary geodetic data. The principle of this methodology is the combination of three different GPS stations each time, forming a triangle. GPS stations are located on the triangle vertices and are characterized by a specific East and North velocity component, extracted by processed raw data of each station. The combination of the East and North velocity component leads to the estimation of the total horizontal velocity vector of each GPS station. The centroid of the formed triangle is defined by the intersection of the three triangle medians, forming the starting point (0,0 point) of a new coordinate system, replacing the previous. Using the 0,0 point as centre, a circle is designed into the original, undeformed triangle and the average of the three total horizontal velocities is calculated for this point, constituting the translation vector. Moving each triangle vertex from the starting to the finishing point of the total horizontal velocity vector, the included circle is deformed into an ellipse. The translation vector connects the undeformed and the deformed triangle centres. Removing the translation vector of each deformed triangle vertex, the centroid of the deformed triangle can be relocated to the original 0,0 point, where the centroid of the undeformed triangle is located. Into the ellipse two perpendicular to each other axes (a major and a minor) are determined. The repositioning of the deformed triangle vertices into the original position, leads to the transformation of the ellipse into a circle, while the major and the minor axes of the circle remain perpendicular to each other. The angular divergence between the undeformed and the deformed axes shows the rotation rate during deformation. The implementation of the GPS triangulation process is carried out using the GPS triangular calculator software developed by the UNAVCO (http://www.unavco.org).

MODELLING

The construction of the proposed models, described below, was based on the primary raw data of 97 different permanently installed GPS stations, distributed throughout the South Aegean region (Figure 3), while the total of the rotation points taken into account in the study area is 3,084.

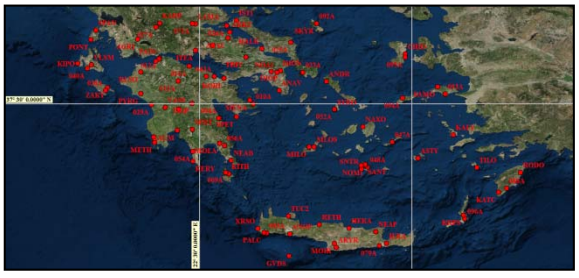

Figure 3: GPS stations of the study area.

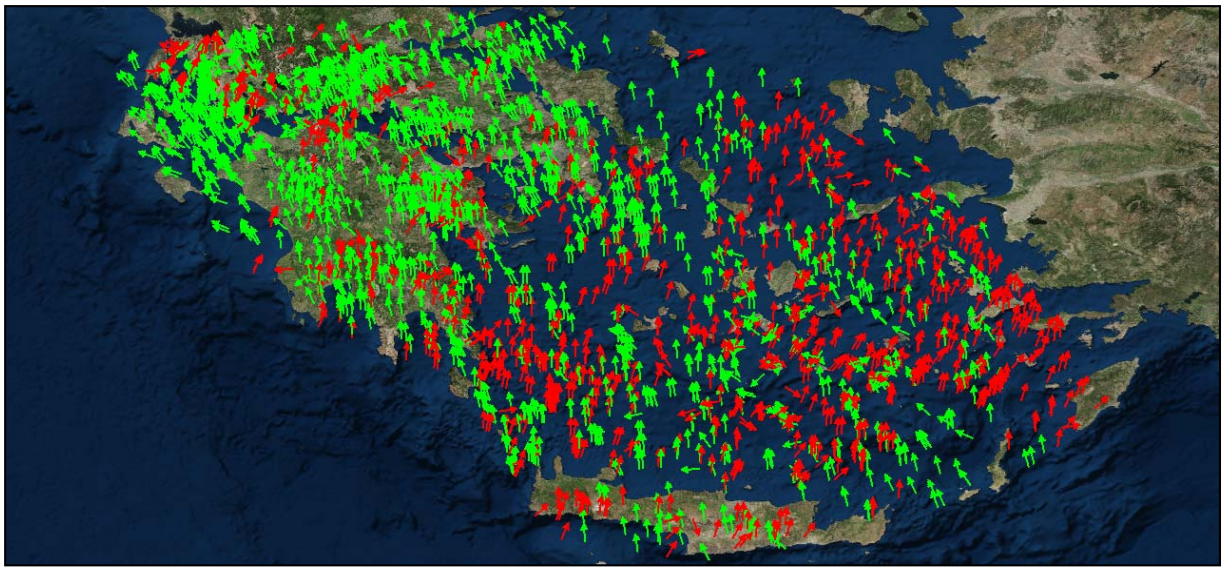

Figure 4: Clockwise (green) and counter-clockwise (red) rotation vectors of the study area for the -5 Myr period.

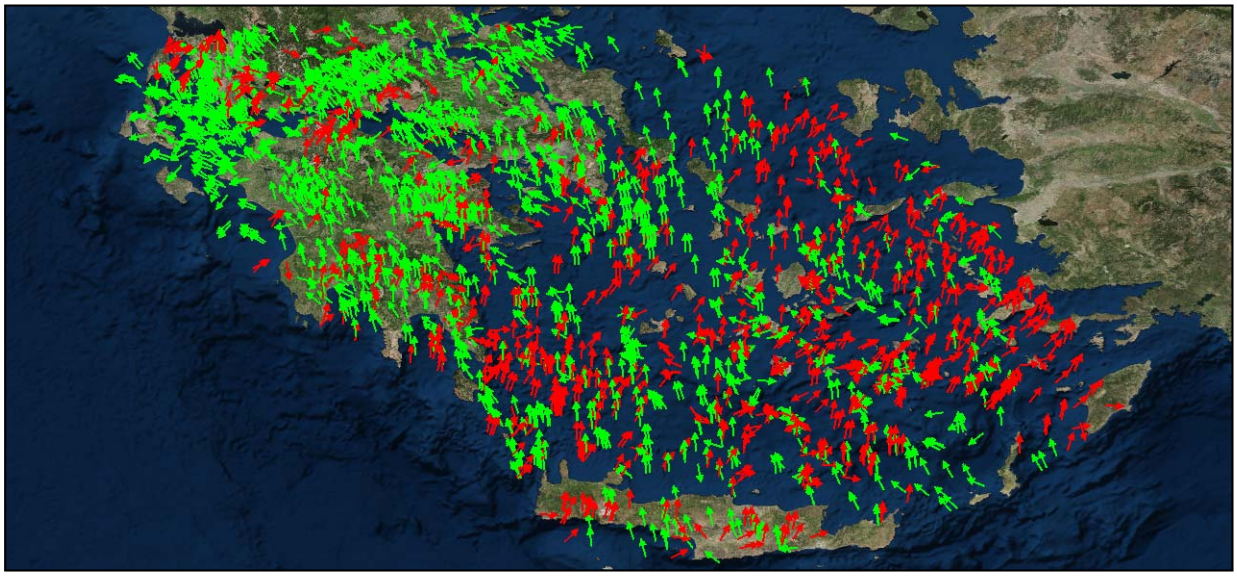

Figure 5: Clockwise (green) and counter-clockwise (red) rotation vectors of the study area for the -10 Myr period.

Based on the aforementioned triangulation process and the GPS triangular calculator software, the rotation rate (change in orientation) per year was calculated, as well as the direction of rotation (original orientation of an axis and orientation after deformation of the same axis). The annual observation of the rotation rate shows a limited rotation of the study area, while the visualization of the results cannot be imprinted due to low annual rotation rates. Based on these facts, the extracted rotation rates were extrapolated and modelled for the past 5 (Figure 4) and 10 Myr (Figure 5), respectively, assuming that the annual rotation rates are stable, leading to the estimation of the geodynamic evolution of the study area.

RESULTS – CONCLUSIONS

Based on both the spatial distribution of the clockwise and the counter-clockwise vectors, extracted by the geodetic data and the recorded palaeomagnetic data of the South Aegean region, a general model of rotation blocks is proposed (Figure 6).

The proposed model consists of two main blocks: a clockwise rotating block (Block 1) and a counter-clockwise rotating one (Block 2). Each of the two main blocks includes micro-blocks, showing regional rotation opposed to the general block rotation. The main clockwise block contains 8 micro-blocks of counter-clockwise rotation (Micro-blocks 1a, 1b, 1c, 1d, 1e, 1f, 1g and 1h), while the main counter-clockwise block contains 2 micro-blocks of clockwise rotation (Micro-blocks 2a and 2b).

Regional rotation differences between geodetic and palaeomagnetic data have been resolved by considering the regional tectonic setting and the geotectonic evolution of the area. The proposed model is a first result of a methodology underdevelopment to match and validate geodetic and paleomagnetic data.

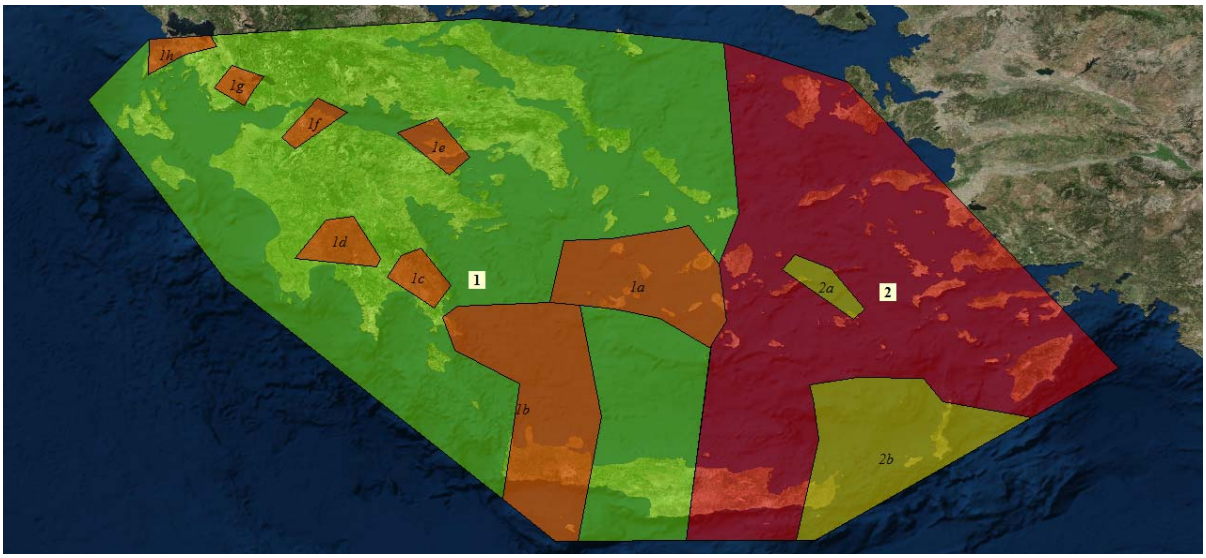

Figure 6: General model of rotation blocks of the South Aegean region (green shaded blocks: clockwise rotation, red shaded blocks: counter-clockwise rotation).

Ackowledgements: The Metrica S.A, National Cadastre and Mapping Agency S.A, National Observatory of Athens (Ganas et al., 2011) and National Technical University of Athens are acknowledged for providing GPS data.

REFERENCES

Armijo, R., Meyer, B., Hubert, A., & Barka, A., 1999. Westward propagation of the North Anatolian fault into the northern Aegean: Timing and kinematics. *Geology* 27, 267-270, doi:10.1130/0091-7613(1999)027<0267:WPOTNA>2.3.CO;2.

Bitharis, S., Fotiou, A., Pikridas, C., & Rossikopoulos, D., 2016. A New Velocity Field of Greece Based on Seven Years (2008-2014) Continuously Operating GPS Station Data. Springer Berlin Heidelberg, pp 1-9.

Bocchini, G.M., Brüstle, A., Becker, D., Meier, T., van Keken, P.E., Ruscic, M., Papadopoulos, G.A., Rische, M., & Friederich, W., 2018. Tearing, segmentation, and backstepping of subduction in the Aegean: New insights from seismicity. *Tectonophysics* 734-735, 96-118, doi: 10.1016/J.TECTO.2018.04.002.

Bradley, K.E., Vassilakis, E., Hosa, A., & Weiss, B.P., 2013. Segmentation of the Hellenides recorded by Pliocene initiation of clockwise block rotation in Central Greece. *Earth Planet. Sci. Lett.* 362, 6-19, doi: 10.1016/j.epsl.2012.11.043.

Dewey, J.F., & Sengör, A.M.C., 1979. Aegean and surrounding regions. Complex multiplate and continuum tectonics in a convergent zone. *Geol. Soc. Am. Bull*. 90, 84-92.

Fotiou, A., Kagiadakis, V., Pikridas C., & Rossikopoulos D., 2003. Geodetically derived displacements and crustal deformation analysis: Application in the Volvi area. *Proceedings of the 11th International Symposium on Deformation Measurements.* FIG commission 6, Santorini, Greece, 25 - 28 May.

Fotiou, A., & Pikridas, C., 2012. *GPS and Geodetic Applications*, Second Edi. Ziti Publishing.

Ganas, A., Chousianitis, K., Drakatos, G., Papanikolaou, M., Argyrakis, P., Kolligri, M., Petrou, P., Batsi, E., & Tsimi, C., 2011. NOANET: High-rate GPS Network for Seismology and Geodynamics in Greece. *Geophys. Res. Abstr*. EGU Gen. Assem. 13, 2011-4840.

Herring, TA., King, RW., & McClusky, SC., 2010. Documentation of the GAMIT GPS Analysis Software release 10.4. Dep Earth Planet Sci Massachusetts Inst Technol Cambridge, Massachusetts, 1-171.

Kondopoulou, D., 2000. Palaeomagnetism in Greece: Cenozoic and Mesozoic components and their geodynamic implications. *Tectonophysics* 326, 131-151, doi: 10.1016/S0040-1951(00)00150-5.

Le Pichon, X., & Angelier, J., 1979. The hellenic arc and trench system: A key to the neotectonic evolution of the eastern mediterranean area. *Tectonophysics* 60, 1-42, doi: 10.1016/0040-1951(79)90131-8.

McClusky, S., Balassanian, S., Barka, A., Demir, C., Ergintav, S., Georgiev, I., Gurkan, O., Hamburger, M., Hurst, K., Kahle, H., Kastens, K., Kekelidze, G., King, R., Kotzev, V., Lenk, O., Mahmoud, S., Mishin, A., Nadariya, M., Ouzounis, A., Paradissis, D., Peter, Y., Prilepin, M., Reilinger, R., Sanli, I., Seeger, H., Tealeb, A., Toksöz, M.N., & Veis, G., 2000. Global Positioning System constraints on plate kinematics and dynamics in the eastern Mediterranean and Caucasus. *J. Geophys. Res*. 105, 5695, doi: 10.1029/1999JB900351.

McKenzie, D., 1972. Active Tectonics of the Mediterranean Region. *Geophys. J. Int*. 30, 109-185, doi: 10.1111/j.1365-246X.1972.tb02351.x.

Mercier, J.L., Sorel, D., Vergely, P., & Simeakis, K., 1989. Extensional tectonic regimes in the Aegean basins during the Cenozoic. *Basin Res*. 2, 49-71, doi: 10.1111/j.1365-2117.1989.tb00026.x.

Pavlides, S., & Caputo, R., 1994. The North Aegean region: a tectonic paradox? *Terra Nov*. 6, 37-44, doi: 10.1111/j.1365-3121.1994.tb00631.x.

Sternai, P., Jolivet, L., Menant, A., & Gerya, T., 2014. Driving the upper plate surface deformation by slab rollback and mantle flow. *Earth Planet. Sci. Lett*. 405, 110-118, doi: 10.1016/j.epsl.2014.08.023.

Uzel, B., Sümer, Ö., Özkaptan, M., Özkaymak, Ç., Kuiper, K., Sözbilir, H., Kaymakci, N., İnci, U., & Langereis, C.G., 2017. Palaeomagnetic and geochronological evidence for a major middle miocene unconformity in Söke Basin (western Anatolia) and its tectonic implications for the Aegean region. *J. Geol. Soc. London.* 174, doi: 10.1144/jgs2016-006.

Van Hinsbergen, D.J.J., Dekkers, M.J., Bozkurt, E., & Koopman, M., 2010. Exhumation with a twist: Paleomagnetic constraints on the evolution of the Menderes metamorphic core complex, western Turkey. *Tectonics* 29, doi: 10.1029/2009TC002596.

Van Hinsbergen, D.J.J., Langereis, C.G., & Meulenkamp, J.E., 2005. Revision of the timing, magnitude and distribution of Neogene rotations in the western Aegean region. *Tectonophysics,* doi: 10.1016/j.tecto.2004.10.001.

Walcott, C., & White, S., 1998. Constraints on the kinematics of post-orogenic extension imposed by stretching lineations in the Aegean region. *Tectonophysics* 298, 155-175, doi: 10.1016/S0040-1951(98)00182-6.

http://www.unavco.org/

INQUA Focus Group Earthquake Geology and Seismic Hazards

paleoseismicity.org

Active tectonics (extensional regime and rotations) and Tertiary mineralization occurrences within Central Macedonia, Greece

Lazos, Ilias (1), Stergiou, Christos L. (2), Chatzipetros, Alexandros (1), Pikridas, Christos (3), Bitharis, Stylianos (3), Melfos, Vasilios (2)

(1) Department of Geology, School of Geology, Aristotle University of Thessaloniki, Greece, ilialazo@geo.auth.gr
(2) Department of Mineralogy-Petrology-Economic Geology, Aristotle University of Thessaloniki, 54124, Thessaloniki, Greece
(3) Department of Geodesy and Surveying, School of Rural and Surveying Engineering, Aristotle University of Thessaloniki, Greece

Abstract: *Since Tertiary the southwards migrating tectonic mechanisms of the broader Aegean region are repeatedly structurally controlling the formation of ore mineralization. In this contribution we present the spatial distribution of the Tertiary mineralization in comparison to the active tectonics of the Central Macedonia region. The multidisciplinary investigation used geodetic data in order to visualize the active extensional regime and the structural rotations, as well as accurate locality data of the regional ore mineralization. The combination of the active extensional regime and the mineralization localization highlights for some parts of the region the diachronic tectonic activity.*

Keywords*: active tectonics, Tertiary mineralization, geodetic data, Serbo-Macedonian Massif*

INTRODUCTION

The Central Macedonia, Greece, region consists geotectonically of the Vertiskos Unit of the Serbo-Macedonian Massif and the Kerdyllia Unit of the Rhodope Massif (Kydonakis et al., 2015). This region also hosts the southern part of the Serbo-Macedonian metallogenic belt and the western part of the Rhodope metallogenic province (Melfos & Voudouris, 2017).

Complex tectono-metamorphic events related to crustal stretching and unroofing, set in a back-arc environment, characterize the Cenozoic geotectonic evolution of the Central Macedonia region (Menant et al., 2018). As a result, numerous magmatic rocks were emplaced within the upper crust and several mineralizations were formed (Kockel et al., 1975). The structural mechanisms which favoured the fluid circulation related to these metallogenic events was characterized by initial ductile deformation expressed through detachment and supra-detachment faults (Eocene-Oligocene) and by subsequemt brittle deformation expressed through shear zones and normal and strike-slip faults (Oligocene-Miocene) (Kilias et al., 1999). During Pliocene-Holocene these structural mechanisms were evolved to the active tectonic regime (Koukouvelas & Aydin, 2002; Chatzipetros et al., 2013).

TERTIARY MINERALIZATIONS

In Central Macedonia region several ore mineralizations occur including mainly porphyry, epithermal, skarn, carbonate replacement, and intrusion-related vein types. Furthermore, these mineralizations are in close spatial association with the Oligocene-Miocene Tertiary magmatic rocks and tectonics (Kockel et al., 1975; Hahn et al., 2012; Siron et al., 2018; Melfos & Voudouris, 2017) (Fig. 1).

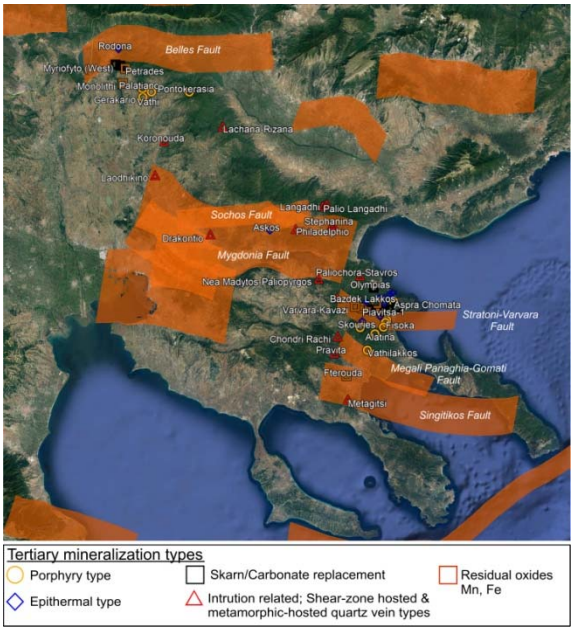

Figure 1: Satellite image depicting the major active fault zones (seismogenic sources) spatially related to the Tertiary mineralization of the Central Macedonia. Overall 50 ore deposits and mineralization occurrences are located in the region (fault data from Caputo et al., 2013; modified after Stergiou, 2016 and references therein).

In more detail, at the northern part of the region, south of Belles normal fault, the porphyry (Vathi, Palatiano, Gerakario, Pontokerasia, Doirani), skarn/carbonate replacement (East and West Myriofyto, Petrades, Monolithi) and epithernal (Rodonas) ore mineralizations are located (Frei, 1992; Mountrakis et al., 2006; Stergiou et al., 2016) (Fig. 1).

Throughout the central part of the region, shear-zone vein hosted type (Arethousa, Drakontio, Koronouda, Laodikino, Stephanina), metamorphic-hosted quartz vein type (Philadelphio, Rizana) and epithermal (Askos) ore mineralizations occur between the Sochos and Mygdonia faults. In the same region the shear-zone vein hosted type mineralization of Nea Madytos-Paliopyrgos and Stavros-Paliochora also appear (Goldsworthy et al., 2002; Bristol et al., 2015) (Fig. 1). These ore mineralizations are not related to any of the scarce magmatic rocks of the region. Their formation was controlled by strike-slip faulting and shearing mechanisms which induced the circulation of the hydrothermal fluids (Bristol et al., 2015).

At the southern part of the region, in an area of ~484 km^2, shear-zone vein hosted (Stanos, Chondri Rachi, Pravita, Metagitsi), porphyry (Aspra Chomata, Fisoka, Tsikara, Skouries, Dilofon, Alatina, Fisoka), epithermal (Aspres Gouves, Zepko, Vina, Papades, Gyftissa, Giannavos, Bazdek Lakkos) and skarn/carbonate replacement (Olympias, Varvara, Piavitsa, Mavres Petres, Madem Lakkos) ore types are located (Siron et al., 2018; Melfos & Voudouris, 2017 and references therein). In addition, several residual Fe-Mn oxides appear such as in Varvara-Kavazi and Fterouda (Fig. 1).

Geographically, these ore mineralizations are located mostly at the NE Chalkidiki region and were formed within a narrow, strongly structurally controlled belt (<10 km in width) (Hahn et al., 2012). The occurrence of this belt is closely associated to the Stratoni-Varvara, Megali Panaghia-Gomati and Singitikos normal to oblique faults (Chatzipetros et al., 2005; Hahn et al., 2012; Siron et al., 2018).

GPS DATA ANALYSIS

In the last two decades the GNSS measurements are widely used as a well-established tool in earth crustal deformation studies. Hence, the synergy between geodesy and geophysics can provide some very promising discussion about the Earth's crustal processes.

In this paper, we use a subset of the geodetic velocities which are provided by a previous study of Bitharis et al. (2016). We focus on the broader region of Central Macedonia, including 20 GPS permanent stations, in order to estimate the deformation parameters.

The geodetic velocities are referred on European Terrestrial Reference Frame 2000 (ETRF2000), which practically is coincident with the stable part of the Eurasian Plate. It should be mentioned that geodetic velocities were based on 7 years continuously 24-hourly operating GNSS data (2008-2014).

In our processing about the GNSS data analysis we apply all the recommendations from the analysis centres (e.g. EUREF). We use the Vienna Mapping Function 1 (VMF1), (Boehm et al., 2006), in order to estimate the Zenith Total Delay (ZTD) with two hours interval. Also, for the long-term analysis we follow the IERS2003 conventions, concerning to Solid Earth Tides. The whole GNSS processing has carried out with GAMIT/GLOBK (Herring et al., 2010) software suite (release 10.5).

METHODOLOGY - MODELLING

The estimation of the maximum horizontal extension values is based on the triangulation of the primary raw geodetic data of the permanent GPS stations. In more detail, sets of three GPS stations in the study area are combined, forming a triangle, while the recorded data of the three stations are taken into account in order to calculate the exact maximum horizontal extension value of the triangle. A dense network of GPS stations leads to the extraction of a significant number of triangle combinations and therefore to reliable results of the maximum horizontal extension.

For each set of three selected GPS stations, each one of them is placed on the triangle vertices. Each GPS station receives a unique East and North velocity component value, derived from the processing of each station raw data, while the total horizontal velocity vector is calculated based on the component vector addition.

The three medians of the triangle defines the triangle centroid, which is considered as the reference point (0, 0) of a new coordinate system. Initially, a circle is designed into the triangle (original and undeformed), while for the triangle centroid the translation vector value is extracted, taking into account the three total horizontal velocities. The location of triangle vertices changes, as each triangle vertex is relocated from the starting to the finishing point of each total horizontal velocity vector, leading to the transformation of the included circle into an ellipse, while the undeformed and the deformed triangle centers are connected by the translation vector. The subtraction of translation vector from each total horizontal velocity vector relocates the deformed triangle centroid to the original 0, 0 point, where the centroid of the undeformed centroid is also located.

This ellipse is defined by a major and a minor axis, perpendicular to each other. The relocation of the deformed triangle vertices into the original position causes the transformation of the ellipse into a circle, while the ellipse axes remain the same.

Based on this procedure, the maximum horizontal extension and the rotation rate of the triangle centroids are calculated. The maximum horizontal extension is measured along the longest axis of the ellipse and is defined as $\frac{l_f - l_0}{l_0}$, where l_f is the final length and l_0 is the original length. Taking into account the angular divergence between the undeformed and the deformed axes, the rotation rate during deformation is calculated. The application of the GPS triangulation process is carried out using GPS triangular calculator software, developed by the UNAVCO (http://www.unavco.org).

Regarding the modelling of the maximum horizontal extension and the rotation rate, the primary geodetic data were collected by 20 different permanently installed GPS stations, distributed into the study area. The combination of these stations led to the formation of 399 different triangles, while the maximum horizontal extension and the rotation rate were calculated for all 399 triangle centroids (Fig. 2).

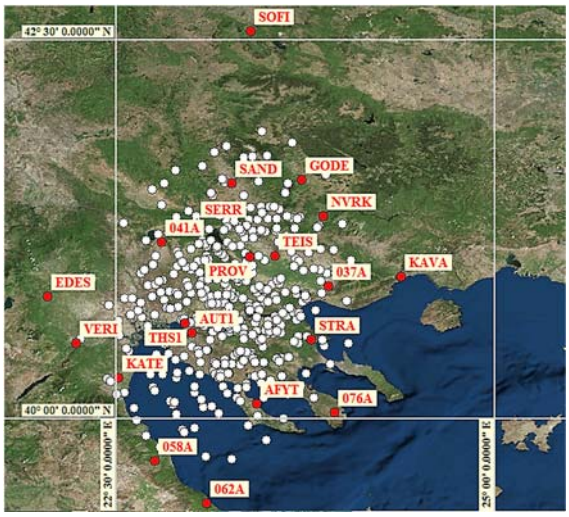

Figure 2: Satellite image showing the GPS stations (red dots) and triangle centroids (white dots) within the study area.

RESULTS AND DISCUSSION

By taking into account all maximum horizontal extension values, the contours of the study area were extracted. The contour step was 50 nano-strains, while the maximum and the minimum values were 543.5029 and 2.1114 nano-strains respectively (Fig. 3).

The overall spatial distribution of the ore mineralization appears almost perpendicular to the axial spatial distribution of the active maximum extension horizontal values. At the northern part the ore mineralization is located within areas with maximum extension horizontal values ranging between 50-200 nano-strains, while for the central and southern parts these values range between 100-300 nano-strains.

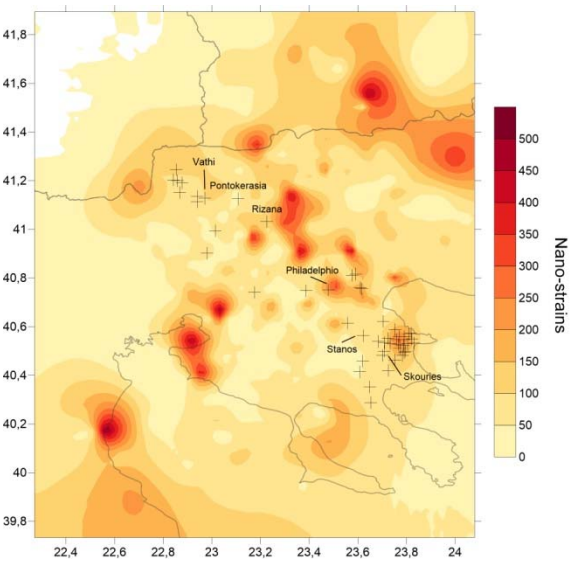

Figure 3: Interpolation map of the maximum extension horizontal values and the ore mineralization localities of the study area.

The rotation rate was calculated by constructing GPS data based rotation models. The annual rotation rates of the 399 triangle centroids were calculated and extrapolated for 5, 10 and 23 Myr BP periods, assuming that the rotation rate has been stable during these time frames (Fig. 4).

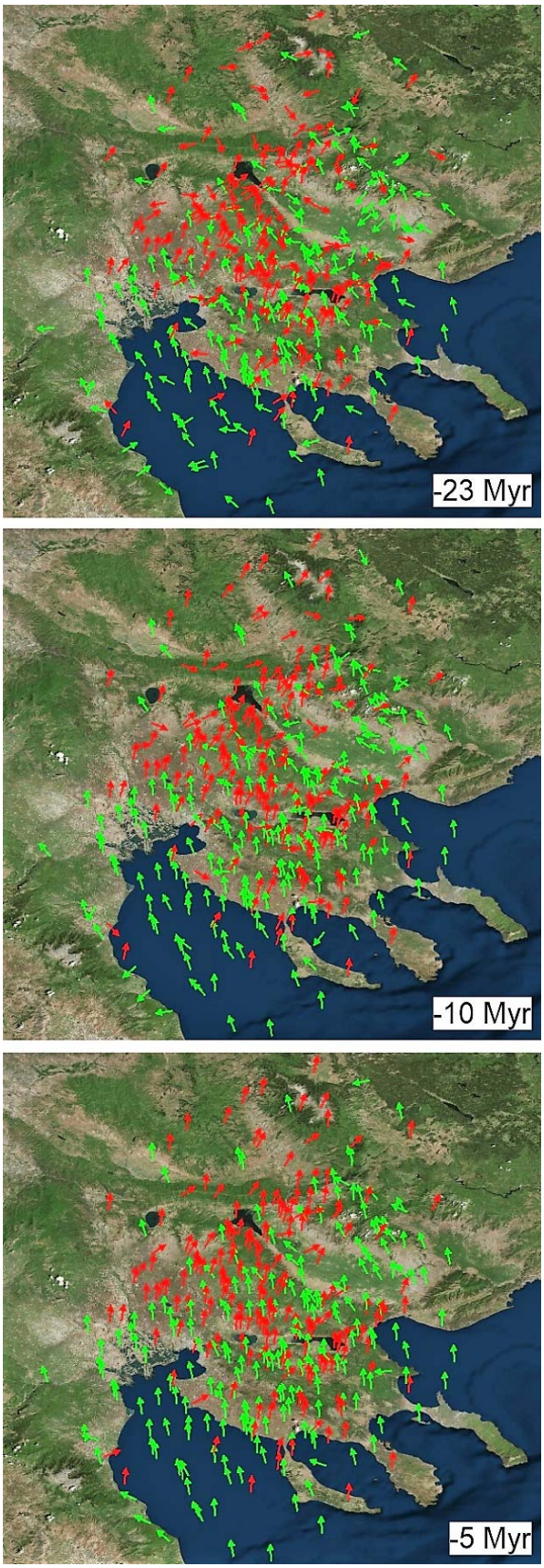

Figure 4: Rotation models for the study are for -5, -10 and -23 Myr periods. Red and green vectors indicate counter-clockwise and clockwise rotations respectively. Arrows indicate the calculated direction of the geographical North within these time periods.

These results lead to two main results: (a) the good correlation between the local maximum extension horizontal values and the ore mineralization occurrences in between Stratoni-Varvara and Megali Panaghia-Gomati faults and Sochos and Mygdonia faults, (b) the spatial relation between low maximum extension horizontal values and the occurrence of metamorphic-hosted quartz vein and shear-zone vein hosted ore mineralization (e.g. Stanos, Chondri Rachi, Pravita, Koronouda, Laodikino, Rizana).

These data highlight the dominant since Oligocene regional extensional regime, as well as the continuous activity of some tectonic structures. Most of the aforementioned ore mineralizations were formed between Oligocene-Miocene and their structural control mechanisms are still active today.

Regarding the rotation models of the study area, both clockwise and counter-clockwise rotations have been extracted. Based on the spatial distribution of rotation vectors, counter-clockwise rotation is more prominent at the northwestern part of the study area, while the southeastern part is subjected to mainly clockwise rotation. Between these two parts, there is a transition zone area, where both clockwise and counter-clockwise rotation vectors are observed, receiving zero (or close to zero) values, indicated that this part of the area is stable and have not been rotated. In general, the rotation models are in agreement with the published structural and paleomagnetic results of the region (Pavlides et al., 1988; Kilias et al., 1999). However a more detailed investigation is required. Future objectives of this research are the separation of the study area into distinct rotation micro-blocks of the upper crust for -5, -10 and -23 Myr periods and their correlation to the ore mineralization and the regional extensional regime.

Acknowledgements: The Metrica S.A, National Cadastre and Mapping Agency S.A, National Observatory of Athens (Ganas et al. 2011) and National Technical University of Athens are acknowledged for providing GPS data.

REFERENCES

Bitharis, S., Fotiou, A., Pikridas, C., & Rossikopoulos, D., 2016. A New Velocity Field of Greece Based on Seven Years (2008-2014) Continuously Operating GPS Station Data. *Springer Berlin Heidelberg,* 1–9.

Bristol, S.K., Spry, P.G., Voudouris, P.Ch., Melfos, V., Mathur, R.D., Fornadel, A.P., & Sakellaris, G.A., 2015. Geochemical and geochronological constraints on the formation of shear-zone hosted Cu-Au-Bi-Te mineralization in the Stanos area, Chalkidiki, northern Greece. *Ore Geology Reviews* 66, 266–282.

Caputo, R., Chatzipetros, A., Pavlides, S., & Sboras, S. 2013. The Greek Database of Seismogenic Sources (GreDaSS): state-of-the-art for northern Greece. *Annals of Geophysics* 55, 839-894.

Chatzipetros, A., Kiratzi, A., Sboras, S., Zouros, N., & Pavlides, S., 2013. Active faulting in the north-eastern Aegean Sea Islands. *Tectonophysics* 597, 106-122.

Chatzipetros, A., Michailidou, A., Tsapanos, T., & Pavlides, S., 2005. Morphotectonics and seismotectonics of the Stratoni-Barbara and Gomati-Megali Panagia active fault (Eastern Chalkidiki, Northern Greece). *Bulletin of the Geological Society of Greece* XXXVII, 127-142.

Frei, R., 1992. Isotope (Pb, Rb-Sr,S,O,C,U-Pb) geochemical investigations on Tertiary intrusives and related mineralizations in the Serbomacedonian Pb-Zn, Sb+Cu-Mo metallogenic province in Northern Greece. *Swiss Federal Institute of Technology (ETH) Zurich.* Switzerland. Ph.D. Thesis. 231 pp.

Ganas, A., Chousianitis, K., Drakatos, G. Papanikolaou, M., Argyrakis, P., Kolligri, M., Petrou, P., Batsi, E., & Tsimi, C., 2011. NOANET. High-rate GPS Network for Seismology and Geodynamics in Greece. In*: Geophysical research abstracts,* 13.

Goldsworthy, M., Jackson, J., & Haines, J., 2002. The continuity of active fault systems in Greece. *Geophysical Journal International* 148 (3), 596-618.

Hahn, A., Naden, J., Treloar, P.J., Kilias, S.P., Rankin, A.H., & Forward, P., 2012. A new time frame for the mineralization in the Kassandra mine district, N Greece: deposit formation during metamorphic core complex exhumation. *Journal of Earth Sciences* 96, 1079-1099.

Herring, T., King, R.W., & McClusky, S.C., 2010. Documentation of the GAMIT GPS Analysis Software release 10.4. *Department of Earth and Planetary Sciences, Massachusetts Institute of Technology, Cambridge, Massachusetts*, 1-171.

Kilias, A., Falalakis, G., & Mountrakis, D., 1999. Cretaceous–Tertiary structures and kinematics of the Serbomacedonian metamorphic rocks and their relation to the exhumation of the Hellenic hinterland (Macedonia, Greece). *International Journal of Earth Sciences* 88, 513-531.

Kockel, F., Mollat, H., & Gundlach, H., 1975. Hydrothermally altered and (copper) mineralized porphyritic intrusions in the Serbo-Macedonian Massif (Greece). *Mineralium Deposita* 10*,* 195-204.

Koukouvelas, I.K., & Aydin, A., 2002. Fault structure and related basins of the North Aegean Sea and its surroundings. *Tectonics* 21, 10-1.

Kydonakis, K., Brun, J.P., Sokoutis, D., & Gueydan, F., 2015. Kinematics of Cretaceous subduction and exhumation in the western Rhodope (Chalkidiki block). *Tectonophysics* 665, 218-235.

Melfos, V., & Voudouris, P., 2017. Cenozoic metallogeny of Greece and potential for precious, critical and rare metals exploration. *Ore Geology Reviews* 89, 1030-1057.

Mountrakis, D., Tranos, M., Papazachos, C., Thomaidou, E., Karagianni, E., & Vamvakaris, D., 2006. Neotectonic and seismological data concerning major active faults, and the stress regimes of Northern Greece. *Geological Society, London, Special Publications* 260 (1), 649-670.

Pavlides, S.B., Kondopoulou, D.P., Kilias, A.T., & Westphal, M., 1988. Complex rotational deformations in the Serbo-Macedonian massif (north Greece): structural and paleomagnetic evidence. *Tectonophysics* 145, 329-335.

Siron, C.R., Rhys, D., Thompson, J.F., Baker, T., Veligrakis, T., Camacho, A., & Dalampiras, L., 2018. Structural Controls on Porphyry Au-Cu and Au-Rich Polymetallic Carbonate-Hosted Replacement Deposits of the Kassandra Mining District, Northern Greece. *Economic Geology* 113 (2), 309-345.

Stergiou C.L., 2016. Mineralogical, geochemical and structural control study of the hydrothermal alterations and the ore mineralization at Vathi porphyry -Cu-Au±U±Mo, N. Greece., *Aristotle University of Thessaloniki*. Thessaloniki. M.Sc. Thesis. 120 pp.

Stergiou, C., Melfos, V., Voudouris, P., Michailidis, K., Spry, P., & Chatzipetros A., 2016. Hydrothermal alteration and structural control of the Vathi porphyry Cu-Au- Mo-U ore system, Kilkis district, N. Greece. In: *Scientific Annals of the School of Geology, Aristotle University of Thessaloniki, Honorary Publication in Memory of Professor A. Kasoli-Fournaraki* 105, 69-74.

UNAVCO, a non-profit university-governed consortium, facilitates geoscience research and education using geodesy. http://www.unavco.org.

INQUA Focus Group Earthquake Geology and Seismic Hazards

paleoseismicity.org

Palaeo-focal plane solution - a potential use of anisotropy of magnetic susceptibility (AMS) in palaeoseismology

Levi, Tsafrir (1), Weinberger, Ram (1), Issachar, Ran (1, 2), Marco, Shmulik (2)

(1) Geological Survey of Israel, Jerusalem, Israel
(2) Department of Geophysics, Tel Aviv University, Tel Aviv, Israel, shmulikm@tau.ac.il

***Abstract**: In many faulting events, not all the pre-seismic strain is released during by the rupture the elastic rebound. Some of it remains in the fault rocks as permanent deformation. Characterizing this deformation is helpful in reconstructing the full picture of seismic energy, stress in zones of active tectonics and earthquake-related deformation as well as ancient tectonic environments. Since it is often difficult to notice in massive non-layered rocks, we test the application of AMS analysis for detecting invisible strain (Levi et al., 2014). For validation, we choose laminated lacustrine rocks, in which the laminas are used as highly sensitive strain markers. We show that 'Depositional fabrics' prevails meters away from the fault planes. 'Deformation fabrics', which is detected up to tens of centimeters from the fault planes, is characterized by well-grouped AMS axes, in which one of the principal axes is parallel to the strike of the nearby fault. Variations in the AMS fabrics and magnetic lineations define the size of the inelastic damage zone around the faults. For characterizing the AMS in Eocene massive chalks near the Dead Sea Fault we had to separate the magnetic fabrics by combining measurements of room temperature and low-temperature anisotropy of magnetic susceptibility with anisotropy of anhysteretic remanence magnetization (AARM). This procedure reveal that the paramagnetic clay minerals preserve the original depositional fabric, whereas the diamagnetic minerals show tectonic fabrics (Issachar et al., 2018).*

The results demonstrate that the deformation-driven magnetic fabrics and the associated inelastic damage zones are compatible with coseismic dynamic faulting and the effects of the local strain field during earthquakes. Most of the AMS fabrics show a conspicuous similarity to that of the fault-plane solutions, i.e., the principal AMS axes and instantaneous strain ellipsoids are coaxial. These results suggest a novel application of the AMS method for defining the shape and size of the damage zones surrounding dynamic faults and determining the full tensor of the local strain field.

***Keywords**: Magnetic fabrics, AMS, Palaeoseismology, Palaeo-focal mechanism*

REFERENCES

Levi, T., Weinberger, R., & Marco, S., 2014, Magnetic fabrics induced by dynamic faulting reveal damage zone sizes in soft rocks, Dead Sea basin. *Geophysical Journal International* 199 (2), 1214-1229, https://doi.org/10.1093/gji/ggu300.

Issachar, R., Levi, T., Marco, S., & Weinberger, R., 2018, Separation of diamagnetic and paramagnetic fabrics reveals strain directions in carbonate rocks. *Journal of Geophysical Research: Solid Earth*, https://doi.org/10.1002/2017JB014823.

INQUA Focus Group Earthquake Geology and Seismic Hazards

paleoseismicity.org

Sub-bottom surveying in seismogenic Proval Bay (Lake Baikal) with ground-penetrating radar: application to study of Delta fault

Lunina, Oksana (1), Gladkov, Andrey (1), Denisenko, Ivan (1), Gladkov, Anton (1)

(1) Institute of the Earth's Crust, Siberian Branch of Russian Academy of Sciences, Lermontova street 128, Irkutsk 664033, Russia, lounina@crust.irk.ru

Abstract: *We carried out ground-penetrating radar (GPR) surveying in seismogenic Proval Bay formed during a devastating M ~7.5 Tsagan earthquake of 1862 - the largest event over the past 156 years on Lake Baikal. The GPR lines of 118-226 m in length were made in water area across the strike of the shoreline and the Delta fault between Oimur village and Oblom Cape. In the issue, we estimated possible throws on major seismogenic fault changing from 0.6 to 2.4 m, sediment thickness accommodated after 1862 seismic event, and sediment accumulation rate (SAR). The obtained results are consistent with the evidence of previous research obtained with using other approaches. Proval bay is still subsiding but SAR is slightly higher than the subsidence rate of this seismogenic structure. According to GPR data, the SAR near the shoreline varies from 1.37 to >2.16 cm/y with maximum value on the profile that is closest to the Selenga River.*

Keywords*: sub-bottom surveying, fault, ground-penetrating radar, parameters, Lake Baikal*

INTRODUCTION

Proval Bay with an area of ~200 km^2 formed during a devastating *M* ~7.5 Tsagan earthquake of 12 January 1862 that was the largest event over the past 156 years on Lake Baikal (Fig. 1). The earthquake is the best documented in terms of its macroseismic effects (Demin, 2005; Fitingof, 1865; Golenetsky, 1996; Lopatin, 1862; Lunina et al., 2012). The motion occurred under SW-NE extension on a stepped system of normal faults dipping mainly at 300-350°, ∠45-75°. These fracture system belongs to the 62-km-long Delta fault, which runs along the eastern shore of Lake Baikal.

The major NE-SW surface rupture of the 1862 earthquake was traceable along the sand hill from Kudara village to almost Oimur village disappearing in the Kharaus delta channel (Fitingof, 1865; Lopatin, 1862). The length of the fault scarp was estimated at 30 km, which is commensurate with the shoreline length of the newly formed Proval Bay from the Oblom Cape to Kudara village. A maximum vertical displacement obtained from a depth of Proval Bay near the Oblom Cape is 8 m (Kondorskaya & Shebalin, 1982), while vertical slip measured in a trench reached 2.8 m (Lunina et al., 2012). Since the time of Tsagan earthquake, the shoreline shortened down as the Selenga Delta boundary moved eastward (Vologina et al., 2010).

The aim of the present work was to find the seismogenic rupture of 1862 earthquake beneath water of Proval Bay and to try estimating vertical throw and thickness of sediments accommodated after the event using ground-penetrating radar (GPR). From the drilling data, we know that the soils of Thagan steppe (now the Proval Bay) are buried under sedimentary layer, thickness of which vary from 1.5 (Tulokhonov et al., 2006) to 3.5-4.3 m (Ladokhin, 1960).

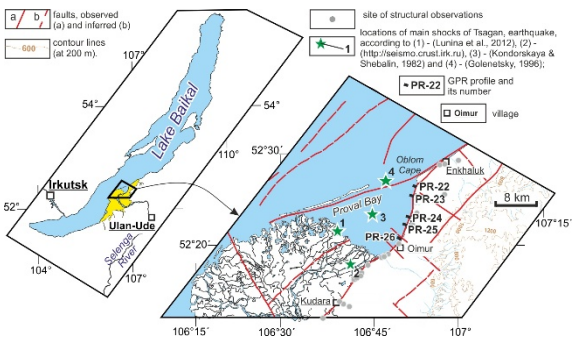

Figure 1: Location map of study area.

METHOD

The GPR lines of 118-226 m in length were surveyed in water area across the strike of the shoreline and the proposed Delta fault between Oimur village and Oblom Cape in summer 2015 (Fig. 1, Table). We used the Logis-Geotech OKO-2 radar (Russia) with an unshielded ABDL-Triton antenna with a 100 MHz dipole transmitter providing a penetration of 20 m and a resolution of 0.5 m, according to its technical specifications (Fig. 2). However, because of specific conditions of this first experimental work we reached only 4.5-5.0 m depth. After standard processing procedures, we assumed dielectric permittivity ε to be 56. The speeds of electromagnetic waves in the water-saturated layers were 4.5–5.05 cm/ns. According to electrometric research of Bashkuev et al. (2013), the Selenga River, delta of which borders Proval Bay from southwest has lower specific electric resistance (SER) than Lake Baikal at deepwater part, and SER in Proval Bay near

Oimur village is 12.4 m Ω·m. It is obvious that such low SER of water greatly decreased the penetration depth.

Figure 2: Example of work by OKO-2 radar with ABDL-Triton antenna on freshwater area.

RESULTS AND DISCUSSION

Three-four radar facies are distinguished from the change in the wave pattern on GPR sections within sedimentary sequence of Proval Bay (Fig. 3) where deposits are sands, silty pelite, and pelitic silt (Tulokhonov et al., 2006). Terrigenous material is predominant and consists of mineral grains and land plant remains admixed with diatom frustules and sponge spicules (Vologina et al., 2010).

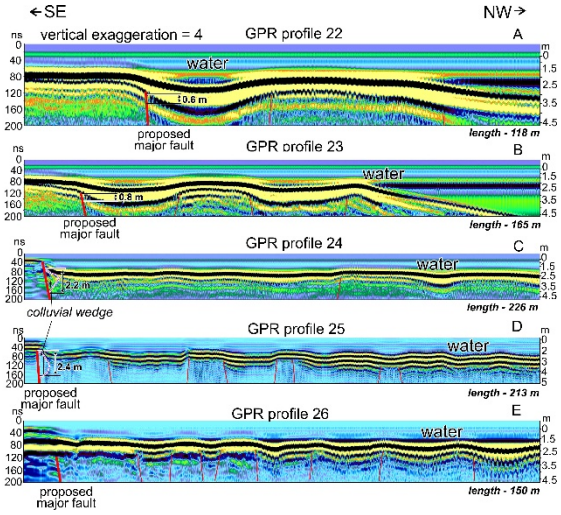

Figure 3. 100-MHz sub-bottom GPR profiles obtained by from Proval Bay (survey of 2015).

The georadar sections can be divided into three groups according to the structure. The GPR profiles 22 and 23 located near the Oblom Cape are very similar to each other (1 group). A clear displacement of the reflection events allow to map the major seismogenic fault and to measure throws (Fig. 3A and B, Table, see PR-23 and 24). The GPR profiles 24 and 25 in the area of Dulan village (second group) are obviously different in the structure of the sedimentary section from the GPR profiles 22 and 23 (Fig. 3C and d). The throw on the major fault is determined by the presence of proposed colluvial wedge and tilting a layer in the hanging wall (Table, see PR-24 and 25). The GPR profile 26 as a whole is similar to the GPR sections of the second group but vertical displacement can be only supposed as >1.8 (Fig. 3E, Table, see PR-26). Most likely, we have not reached an enough depth to reveal a possible throw.

Characteristics derived from analysis of the GPR profiles

GPR profile / characteristics	PR-26	PR-25	PR-24	PR-23	PR-22
Throw on major fault, m	>1.8	2.4	~2.2	0.8	0.6
Sediment thickness accommodated after 1862 event, m (±0.5 m)	>3.3	3.1	2.1	2.4	2.5
Speed of electromagnetic waves, cm/ns	4.7	5.05	4.73	4.5	4.5
Maximum water depth, m	1.5	2.2	1.9	1.5	1.6
SAR, cm/y (±0.32)	>2.16	2.03	1.37	1.57	1.63
Length of profile, m	150	213	226	165	118

There is a tendency that the vertical displacements of the layers decreases in direction of the Oblom Cape though depth survey performed by expedition of Russian Gegraphical Society in summer 1862 shows larger depths in the area of GPR sections 22 and 23 than in other places. It may be because of initially lower absolute marks of the terrain associated with the proximity of Lake Beloe, which existed before the earthquake of 1862 in the Tsagan steppe. More detailed depth survey in 1898 (Drizhenko, 1908) demonstrates depths varying from 2 to 11 foots (0.61-3.35 m) along the shore of Proval Bay, and the largest depth was measured in the area of GPR profile 25 that coincides with our results (Table). The subsided Lake Beloe also makes a figure on 1898 bathymetric map.

Maximum water depths on GPR profiles are commensurate with local depths indicated on 1898 bathymetric map. Tulokhonov et al. (2006) also noted that a depth of Proval Bay has not changed significantly since 1898 survey (Drizhenko, 1908). It should mean that the sediment accumulation rate (SAR) is approximately equal to rate of subsidence of seismogenic structure (Proval Bay). However, if we take into account a rise of the level of Lake Baikal on 1.1 m in 1958–1964 caused by construction of an Irkutsk hydroelectric power station we must conclude that accumulation rate is slightly higher than the subsidence of the bay. This immersion of the seismogenic structure after the 1862 earthquake may result from both tectonic and gravitational processes initiated by weak and moderate seismicity around Proval Bay and, as well as from compaction of sediments.

In general, the obtained sediment accumulation rates (Table) near the shoreline are in the regular correlation with the sediment accumulation rates established from drilling. In the different parts of central Proval bay it is 0.232 cm/y (sensu Vologina et al., 2010) and 1.07 cm/y (sensu Tulokhonov et al., 2006). In southern Proval bay near the delta of the Selenga River, it is ~1.98-2.27 cm/y, judging from data of Vologina et al. (2010).

CONCLUSIONS

This study shows that sub-bottom surveying by GPR in fresh water has a great informative value for estimation of the throws along the fault covered by water as well sediment thickness accommodated after a seismic event and even for SAR if we know date of an earthquake. Certainly, the method is more effective if one has drilling data directly on GPR profile. We plan to continue this research to try increasing a penetration during sub-bottom survey in summer as well as to carry out GPR research on ice at the same places at the end of March, 2018.

Acknowledgements: This work is supported by expeditionary grant of the Institute of the Earth's crust, SB RAS.

REFERENCES

Bashkuev, Yu.B., Khaptanov, V.B., Dembelov, M.G., & Buyanova, D.G., 2013. Results of electrometric researches of the water environment of the Selenga River, its inflows and Lake Baikal water area. *Siberian journal of science and technology* 51 (5), 127-132, (in Russian).

Demin, E.V., 2005. *Anthology of a Collapse: Historic Accounts of the Catastrophic Tsagan Earthquake of 1862 in Proval Bay, Lake Baikal*. Ulan-Ude, 296 p. (in Russian).

Drizhenko, F.K., 1908. Atlas of Lake Baikal. Compiled by Gydrophysical expedition under guidance of colonel F.K. Drizhenko. Main hydrogr. Administration press. St.-Pb. 31 p. (in Russian).

Fitingof, A.Kh., 1865. Description of the area at the Selenga Mouth, collapsed by earthquakes of 30 and 31 December 1861. *Gornyi Zhurnal* 3 (7), 95-101, (in Russian).

Golenetsky, S.I., 1996. Macro-seismic effects of the devastating Tsagan earthquake of 1862 on Lake Baikal. *Izv. RAN, Fizika Zemli* 11, 3-13, (in Russian).

Kondorskaya, N.V., & Shebalin, N.V., (Eds.), 1977. *New catalog of strong earthquakes in the USSR from ancient times through World Data Center A for Solid Earth Geophysics.* Colorado, USA: World Data Center A, 1982.

Ladokhin, N.P., 1960. Recent tectonic movement in Proval bay and methods of its study. *Izv. Ac. Sci. of USSR. Ser. geographical* 9 (1-2), 59-66.

Lopatin, I.A., 1862. On earthquakes at the Selenga mouth and nearby. *Amur, Newspaper of East Siberia*, No. 11, 7 February, 1862, (in Russian).

Lunina, O.V., Andreev, A.V., & Gladkov, A.S., 2012. The Tsagan earthquake of 1862 on Lake Baikal revisited: a study of secondary coseismic soft-sediment deformation. *Russian Geology and Geophysics* 53, 571-587.

Tulokhonov, A.K., Andreev, S.G., Batoev, V.B., Tsydenova, O.V., & Khlystov, O.M., 2006. Natural microchronicle of recent events in the basin of Lake Baikal. *Russian Geology and Geophysics* 47 (9), 1030-1034.

Vologina, E.G., Kalugin, I.A., Osukhovskaya, Yu.N., Sturm, M., Ignatova, N.V., Radziminovich, Ya.B., Dar'in, A.V., & Kuz'min, M.I., 2010. Sedimentation in Proval Bay (Lake Baikal) after earthquake-induced subsidence of part of the Selenga River delta. *Russian Geology and Geophysics* 51 (12), 1275-1284.

INQUA Focus Group Earthquake Geology and Seismic Hazards

paleoseismicity.org

Event deposits in the Eastern Thermaikos Gulf and Kassandra Peninsula (Northern Greece) and evidence of the 479 BC Herodotus - tsunami

Mathes-Schmidt, Margret (1), Papanikolaou, Ioannis (2), Reicherter, Klaus (1)

(1) Inst. of Neotectonics and Natural Hazards, RWTH Aachen University, Lochnerstrasse 4-20, 52056 Aachen, Germany, k.reicherter@nug.rwth-aachen.de
(2) Laboratory of Mineralogy & Geology, Department of Geological Sciences and Atmospheric Environment, Agricultural University of Athens, 75 Iera Odos Str., 118 55 Athens, Greece and Benfield-UCL Hazard Research Centre, University College London, UK

Abstract: *The world-wide first description of a tsunami and its effects in 479 BC were made by Herodotus. The wave hits the coast of Chalkidiki peninsula Greece where we investigated different areas from Angelochori down to Posidi (Kassandra peninsula) and the ruins of Mende. Ancient Mende was a quite important city in the classic Hellenistic period, already founded in the 12th cent. BC. However, the youngest parts of the city are situated close to the seaside (proasteion of the 6-5th cent. BC). Within the excavation of the proasteion, a high-energy layer has been encountered. Besides a vast amount of ceramics, the layer also contains shells of Acanthocardia sp. These have been dated as c. 2900 years BP by 14C, taking into account a reservoir effect of 400 years, which is a suitable candidate to the tsunami reported by Herodotus.*

Keywords*: Thermaikos Gulf, Kassandra peninsula, tsunami*

INTRODUCTION

The Herodotus Histories (Urania, Book 8, 129) report on a series of unundation by large waves and sea withdrawals occurring in winter 479 BC during the Persian-Greek war. Large portions of the Persian troops perished by drowning near Potidaea, western Chalkidiki peninsula (Greece), while sieging the Greek town. No earthquake was reported for this event, so a meterological effect or submarine slumping could be possible (Ambraseys, 2009). Herodotus's report is interpreted as the first of a historical tsunami (Bolt, 1978; Smid, 1970).

Modelling of the tsunami source along the western tip of the North Anatolian Fault Zone (NAFZ) in the North Aegean Basin revealed the possibility of high waves induced by seismicity (Reicherter et al., 2010) which may also effect Kassandra peninsula. The westernmost, 55 km long branch of the NAFZ is taken in account for the modelling because it can cause earthquakes with possible magnitudes around 7 or more (Papanikolaou & Papanikolaou, 2007). Wave heights dependent from coastal morphology may reach more than 2 meters with considerable run-up in flat coastal areas (Reicherter et al., 2010).

STUDY AREA

The investigation areas lie at the eastern coast of the Thermaikos Gulf (Fig.1). The climate is subtropical with dry and hot summers and mild and wet winters. The main wind directions in summer are from N and NE, so-called Etesians, but in April, May and July winds from S and SE are also common. Beaufort forces lie between 3 and 5, only occasionally rising to gale force. In winter wind stroms reach Beaufort up to 8.

From the Thessaloniki Bay the Gulf opens southward to the northern Aegean Sea. The sandy spit of Cap Epanomi marks the transition from the inner to the outer Gulf. Water depths increases from around 25 m in the Thessaloniki Bay to a maximum from c. 200 m in the Thermaikos Gulf and deepens rapidly at the shelf break to around 1200 m in the Sporades Basin (Fig.1). In its central part the shelf break is morphologically subdivided by a marginal plateau.

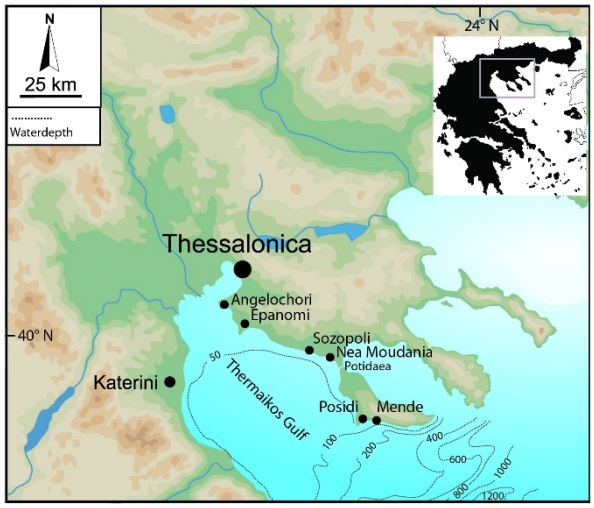

Figure 64: Investigation areas along the east coast of the Thermaikos Gulf: Angelochori, Epanomi, Sozopoli, Nea Moudania, Posidi and Mende.

Between Thessaloniki and Potidaea the coast has an almost low relief, flat and narrow beaches with beach ridges mostly not higher than 1 - 2 m and intercalated cliffy sections. Building and agricultural use range until the coast

but to some extent low vegetated dunes, more or less silted up lagoons and salines are present (eg Angelochori, Cap Epanomi). These areas are potential archives for tsunamites. The southern coastline of Kassandra peninsula is characterized by cliffs with more or less small beaches, getting more and more steeper towards its southern end.

During the field work in 2007 and 2008 percussion drilling was undertaken between Cap Angelochori and Posidi concentrating on areas sheltered from direct wave action such as lagoonal zones and smooth depressions behind the beach insofar there was no intense human use recognizable. Drilling locations were situated at different locations: Angelochori, Epanomi (North, West), Sozopoli, Nea Moudania and Posidi on the Kassandra peninsula (Fig. 1).

The saline and lagoon of Angelochori are located on a sandy spit bar at the transition of the Thessaloniki Bay to the Thermaikos Gulf. Neogene sands of the Messinian build the main geology. Cap Epanomi is built by a large spit bar with vegetated dunes and a central lagoon. It is situated at the transition from the inner to the outer Thermaikos Gulf. This position leads to substantial seasonal changes in wind and wave action in particular resulting in a higher amount of coarse sediments in the southern part. The northern part that is orientated to inner gulf shows chevron-like features on aerial images, which may be of aeolian or spillover origin. Aside from the lagoonal area more or less consolidated sandstones of Pliocene age with some intercalations of gravel, clayey and calcareous material crop out. Close to the village of Sozopoli behind a low beach berm a dried out lagoonal area beside a dune field is preserved. Nearby, Neogene sands form a huge cliff. The hinterland geology is built by Miocene to Pliocene sandstones and marls. At all sites Quaternary sand and sandy clays are the youngest sediments.

Kassandra peninsula (the ancient Pallene) is the westernmost prong of Chalkidiki peninsula and its west coast lies to the outer Thermaikos Gulf. The coastal area comprises mainly Neogene sands, conglomerates and marls of terrestrial and marine origin besides alluvium with sands, boulders and landslide masses.

METHODS

In September 2007 and 2008 we carried out 32 boreholes at 5 different areas using vibra-coring with an open window sampler along the coast of the Thermaikos Gulf. Field work comprises detailed core description and after a first appraisal additional drilling of overall 93 m of PVC-liners each of 1 m length were undertaken for investigation in the laboratory at the University of Aachen. The sedimentology and magnetic susceptibility of the most cores from Angelochori, Epanomi and Sozopoli were described in 2010 by Reicherter. A set of indicators are taken in account for determination of tsunami deposits as there are finning and thinning up sequences, rip up clasts, mud coated clasts, erosive bases, conservation status of biogens, unusual faunal associations, and the combination of sedimentological compound with magnetic susceptibility. To get more indications for the 479 BC tsunami of Herodot samples for radiocarbon dating and micropalaeontological investigations were taken from Ancient Mende.

INTERPRETATION AND DISCUSSION

At Ancient Mende the upper 20 - 30 cm consist of digging material from the excavation underlain by a rooted horizon. Marine sediments are intercalated in terrestrial sand layers. This marine layer consists in section 1a (fig. 2), at northwestern, landward side of the excavation, between c. 1.87 m and 2.30 m bgl. of fine sand and contains besides ceramics, charcoal and broken building materials complete and partly articulated shells of bivalves like *Acanthocardium* sp. In sect.1b, 1m left of section 1a, the same layer shows two fining up sequences between 1.75 m and 2.45 m bgl. The lower sequence starts with gravel showing an erosional contact in form of a channel. A similar deposit of gravel can be observed on the southwestern side of the excavation.

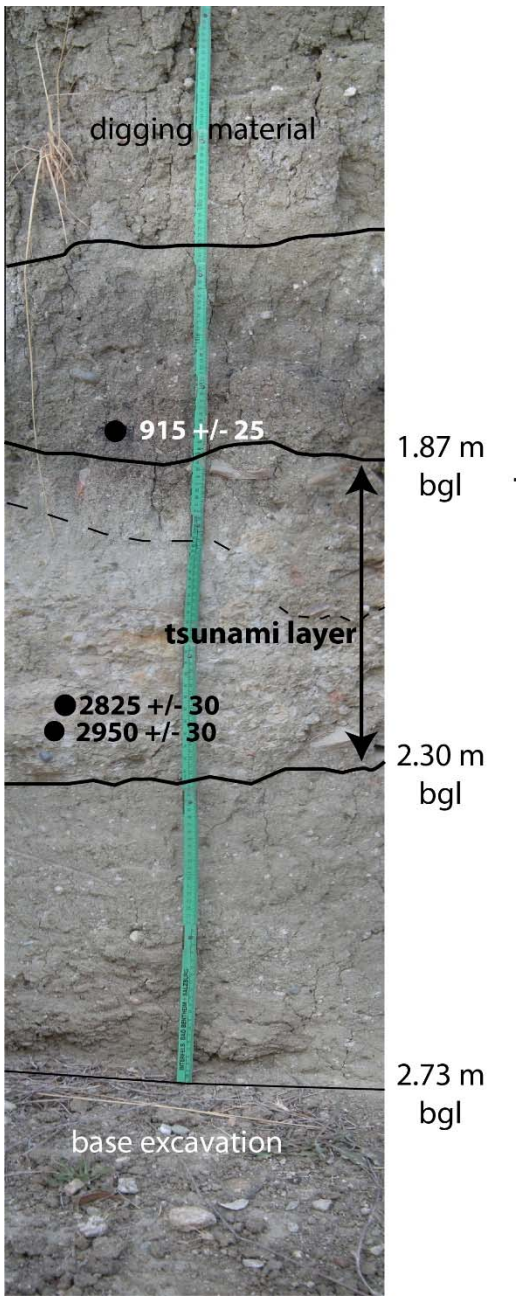

Figure 2: Profil of section 1a with radiocarbon ages.

All micropaleontological samples of the tsunami layer contain unidentified shell fragments, most likely small fragments of gastropods. Some samples show also fragments of agglutinated foraminifera and agglutinated worm tubes. In a sample of the upper part of the tsunami layer fragments of small, thin-shelled gastropods, assumed belonging to the marine species *Cylichna* sp., are found. These snails live as burrowers in the silty and muddy seafloor on the lower shore or deeper.

The top of the marine layer in sect. 1a is dated to 915 +/- 25 years whereas the radiocarbon dating near the base of the marine layers date to +/-2,900 yrs (Fig. 2).

CONCLUSIONS

The marine layer at the Ancient Mende excavation site is interpreted as an event layer. Fining up sequences, erosive contacts and the occurrence of a channel like bed with an imbricated gravel layer at its base occurring inside a building area indicate a tsunami. This consideration is confirmed by the occurrence of small gastropods from silty and muddy environments as can be found southward from the spit in deeper parts of the shelf. The small channel like form is interpreted as a backwash channel. Radiocarbon dates from above and from the base of the layer show ages that match the 479 BC tsunami described by Herodotus.

REFERENCES

Ambraseys, N., 2009. Earthquakes in the Mediterranean and Middle East - A multidisciplinary Study of Seismicity up to 1900. Cambridge University Press, Cambridge, 947 pp.

Bolt, B.A., 1978. Earthquakes. W.H. Friedman & Company, New York, 241 pp.

Papanikolaou, I.D., & Papanikolaou, D.I., 2007. Seismic hazard scenarios from the longest geological constrained active fault of the Aegean. *Quaternary International* 171-172, 31-44.

Reicherter, K., Papanikolaou, I., Roger, J., Mathes-Schmidt, M., Papanikolaou, D., Rössler, S., Grützner, C., & Stamatis, G., 2010. Holocene tsunamigenic sediments and tsunami modelling in the Thermaikos Gulf area (northern Greece). *Zeitschrift für Geomorphologie* 54 (3), 99-126.

Smid, T., 1970. Tsunamis in Greek Literature. *Greece and Rome* 17(1), 100-104. doi: 10.1017/S0017383500017393.

INQUA Focus Group Earthquake Geology and Seismic Hazards

paleoseismicity.org

Evaluation of seismic intensities of historical earthquakes in the southern and southwestern Peloponnese (Greece) based on the Environmental Seismic Intensity (ESI 2007) scale

Mavroulis, Spyridon (1), Lekkas, Efthymios (1)

(1) Department of Dynamic Tectonic Applied Geology, Faculty of Geology and Geoenvironment, School of Sciences, National and Kapodistrian University of Athens, Panepistimiopolis, 15784, Athens, Greece, smavroulis@geol.uoa.gr

Abstract: *The southern and southwestern Peloponnese is one of the most seismically and tectonically active areas in the Eastern Mediterranean. Based on historical and recent seismicity data, the area has been often struck by destructive earthquakes with significant impact on the natural and built environment. Taking into account various sources, the complete catalogue of destructive historical earthquakes from 550 BC to 1899 AD is presented for the first time with all induced earthquake environmental effects (EEE). Based on the application of the Environmental Seismic Intensity (ESI 2007) scale, the most susceptible areas to EEE are the Kalamata (Kato Messinia) basin followed by Sparta basin, the eastern slopes of Taygetos Mt, the Ionian coast of Messinia and the Kyparissia Mts. The maximum assigned local environmental seismic intensities are* $X_{ESI\ 2007}$ *for Sparta basin, VIII-IX*$_{ESI\ 2007}$ *for Kalamata basin, VIII*$_{ESI\ 2007}$ *for the Ionian coast of Messinia and VII for Kyparissia Mts.*

Keywords*: historical earthquakes, environmental effects, ESI 2007, Peloponnese, Greece*

INTRODUCTION

Earthquake environmental effects (EEE) are the effects induced by an earthquake on the natural environment (Michetti et al., 2007). They are classified into two types: (a) primary EEE, which include surface faulting, coseismic surface ruptures and permanent ground dislocations of tectonic origin and any other surface evidence of coseismic tectonic deformation (Michetti et al., 2007) and (b) secondary EEE classified into eight main categories: (i) hydrological anomalies, (ii) anomalous waves including tsunamis, (iii) ground cracks, (iv) slope movements, (v) trees shaking and vegetation damage, (vi) liquefaction phenomena, (vii) dust clouds and (viii) jumping stones (Michetti et al., 2007). The EEE can be used for the evaluation of the seismic intensity not only of recent but also of historical and palaeo- earthquakes and furthermore for the comparison among future, recent, historical and palaeo-earthquakes. The ESI 2007 scale has been already applied in historical earthquakes in various tectonic environments around the world, not only in individual events in order to enrich the existing database for countries [e.g. Greece (Papanikolaou & Melaki, 2017)], but also in a set of chosen historical events in the same region [e.g. southern Apennines in Italy (Serva et al., 2007)] in order to reassess the historical events in the region and to contribute to the reduction of the seismic risk. Although other efforts have been made to record the EEE of individual recent earthquakes in Greece and evaluate their ESI 2007 seismic intensity (e.g. Fountoulis & Mavroulis, 2013; Mavroulis et al., 2013; Lekkas & Mavroulis, 2015; Papanikolaou & Melaki, 2017; Lekkas et al., 2018), no one has focused on the complete seismic history of an area and the respective intensities based on the induced EEE. The southern and southwestern Peloponnese (Fig. 1) was considered appropriate for the development of this approach.

This study comprises the presentation of the complete catalogue of all destructive historical earthquakes covering a time period extending from 550 BC to 1899, generated in the southern and southwestern Peloponnese (Fig. 1), which is one of the most seismically and tectonically active areas of Greece. Furthermore, it includes the detailed and accurate description of all the available EEE induced by these earthquakes and the application of the ESI 2007 scale for these events based on the quantitative characteristics of their EEE.

The complete and detailed knowledge of the historical earthquakes, the past EEE and the respective seismic intensities serves as a valuable tool for revealing and highlighting subareas of significant earthquake-related hazards where no macroseismic damage data are available, testing the susceptibility and the vulnerability of the affected area to the same EEE and improving preparedness and land-use planning to cope with and overcome the changes that an earthquake induces on the natural environment of the affected area.

SEISMOTECTONIC SETTING

Onshore and offshore studies conducted by various researchers (Mariolakos et al., 1986; Papanikolaou et al., 1988; Papanikolaou et al., 2007) revealed that the southern and the southwestern part of Peloponnese is composed of major neotectonic macrostructures bounded by N-S and E-W trending fault zones (Fig. 1). These onshore macrostructures are from E to W the following: (a) the NW-SE striking Sparta basin, (b) the N-S striking Taygetos Mt mega-horst, (c) the Kalamata-Kyparissia mega-graben striking N-S in its southern part and E-W further to the north, (d) the very complex morphotectonic mega-structure of Kyparissia Mts-Lykodimo Mt striking N-S and

(e) the Gargallianoi-Pylos mega-horst located along the western coast of Messinia (Mariolakos et al., 1986; Fountoulis & Mavroulis, 2013) comprising smaller fault blocks (Fig. 1). These onshore structures are bounded by active fault zones and seismic faults (Fig. 1, e.g. the eastern marginal fault of Kato Messinia basin ruptured in 1986 Kalamata earthquake, the Sparta fault ruptured in 464 B.C. devastating Sparta). Offshore fieldwork in Messinian (Papanikolaou et al., 1988) and in Kyparissiakos Gulfs (Papanikolaou et al., 2007) demonstrated that active faults observed onshore continue in several cases offshore in the study area (Fig. 1).

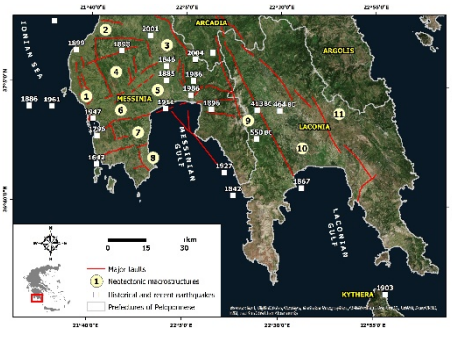

Figure 1: The southern Peloponnese along with the historical and recent earthquakes with impact on human, natural and built environment of the study area as well as the major onshore and offshore faults and the major neotectonic macrostructures: (1) Gargallianoi-Pylos mega-horst, (2) Kyparissia basin, (3) Ano Messinia basin, (4) Kyparissia Mts, (5) Kalamata (Kato Messinia) basin, (6) Vlahopoulo graben, (7) Lykodimo Mt horst, (8) Falanthi basin, (9) Taygetos Mt, (10) Sparta (Evrotas) basin, (11) Parnon Mt based on Mariolakos et al. (1986), Papanikolaou et al. (1988) and Fountoulis (1994).

METHODOLOGY

For the present study, data and information on historical and recent earthquakes and their EEE in the southern and southwestern Peloponnese were obtained from the following sources: (a) official earthquake catalogues from universities, seismological institutes and observatories, (b) books and scientific articles containing catalogues or information of earthquakes and their EEEs in Greece (e.g. Shebalin et al., 1974; Papazachos & Papazachou, 1989, 1997, 2003; Soloviev et al., 2000; Ambraseys, 2009) or in southwestern Peloponnese (e.g. Galanopoulos, 1947, 1981; Papadopoulos et al., 2014), (c) scientific articles referring to the impact of individual earthquakes in southwestern Peloponnese (e.g. Galanopoulos, 1940, 1941a, 1941b, 1949, 1960; Pirli et al., 2007; Ganas et al., 2012; Fountoulis & Mavroulis, 2013; Sakellariou & Kouskouna, 2014; Kouskouna & Kaviris, 2014), (d) official field survey and reconnaissance reports and (e) official reports of applied scientific research projects (e.g. Mariolakos et al., 1986; Plessa & Ganas, 2014).

HISTORICAL EARTHQUAKES, EEE & ESI 2007 INTENSITIES

The 550 BC and 464 BC Sparta earthquakes

The data referred to earthquakes from 550 BC to 1838 are limited to occurrence date and the most affected areas as well as limited information of secondary EEE comprising only slope movements including mainly landslides and rockfalls without any further quantitative information. The listed earthquakes occurred in (a) 550 BC causing the destruction of Sparta and the collapse of the Taygetos Mt. summit indicating rockfalls and landslides and (b) in 464 BC, when the most destructive earthquake of Sparta took place resulting in 20000 fatalities. The 464 BC Sparta earthquake triggered ground cracks and slope failures along the eastern slopes of Taygetos Mt. The exact geographic locations of the triggered effects are not available. Consequently, the areal distribution of the secondary effects cannot be extracted neither directly nor indirectly. Moreover, further quantitative information including either the volume of the mobilized materials or dimensions (length, width and frequency) of ground cracks are not available.

The 1842 April 18 earthquake

This earthquake generated ground cracks, slope failures, hydrological anomalies and tsunami waves were generated in and affected various sites. In Eva [previous name (p.n.) Naziri], located within the Pamisos River valley, ground cracks with width of 40 cm and depth of 7 m ($VIII_{ESI\ 2007}$) were observed close to geotechnically unstable areas and were related to coseismic landslide phenomena. Detachment of large rock masses and rockfalls occurred in Eva resulted in building damage and related fatalities. In Evrotas River valley, the earthquake caused detachment and fall of large rock masses in the archaeological site of Menelaion. Hydrological anomalies included water turbidity within the Pamisos River valley and more specifically water turbidity in Pamisos springs in Agios Floros ($VIII_{ESI\ 2007}$) and overflowing of wells. The flow of Pamisos River was disturbed and the river was locally overflowed. Liquefaction phenomena were reported in Analipsi (p.n. Tsitsori) ($VII_{ESI\ 2007}$). The coast close to Koroni was inundated and ships were washed on the shore by the earthquake-induced tsunami ($VIII\text{-}IX_{ESI\ 2007}$).

The 1846 June 11 Messinia earthquake

Liquefaction phenomena occurred in several sites in the form of ground cracks accompanied by ejection and flowing of sand-water mixture that covered large parts of fields ($VII_{ESI\ 2007}$). A large lake made of silt-water mixture was formed in Ammos (p.n. Mpaliaga) and sulfur odor was noticeable ($VIII_{ESI\ 2007}$). Ground cracks were observed in Mikromani within the post-alpine formations of Pamisos River valley with width varying from 5 to 8 cm along with the formation of craters with diameter of 10 cm with surging liquid material ($VII_{ESI\ 2007}$). Ground cracks with large width and partially filled with silt were also reported in the Pamisos River estuary ($VII_{ESI\ 2007}$). Hydrological anomalies were also observed in Messese area ($VII_{ESI\ 2007}$) and caused the outbreak of infectious diseases.

The 1867 September 20 earthquake

The earthquake severely affected the coastal areas of Laconian and Messinian Gulfs. It also affected the coast of Cephalonia Island (Ionian Sea) causing damage to Lyxouri port and the Cyclades complex in the Aegean Sea and especially Syros and Serifos Islands. They also reached the Italian coasts and affected Brindisi, Messina, Sicily and Catania coastal areas. Gytheio was destroyed by the waves, which had a significant impact on the Cape Pagania, on the western shore of the Laconian Gulf and on the Messinian Gulf. In Gytheio, changes to sea level were

observed. The sea initially receded from the shore and the sea bed was dried up. Afterwards, the sea rose for 6 m above its usual level and it looked like boiling ($X_{ESI\ 2007}$). In Kalamata located in the northern part of the Messinian Gulf, low and high water were similarly observed with the sea receding slowly from the coast approximately for 15 m ($IX_{ESI\ 2007}$). Lower values of sea level fall were observed in Petalidi coastal area, where then the sea water level rose up to 2m and caused inundation of the coastal area ($VIII_{ESI\ 2007}$). In Neapoli, the sea bed was also dried up causing boats touching the sea bed more than once ($VII_{ESI\ 2007}$).

The 1885 March 28 Messene earthquake

Rockfalls were triggered by the earthquake. No further information and details on the exact location and the areal distribution of the induced rockfalls and the volume of the mobilized geological material are available. Thus, the epicentral intensities and the local intensities cannot be estimated due to the absence of the exact location and the quantitative characteristics of the earthquake-induced rockfalls.

The 1886 August 27 Filiatra earthquake

The EEE include ground cracks, liquefaction phenomena, submarine landslides, tsunami waves and hydrological anomalies. Ground cracks were observed in the area between Katakolo and Gargalianoi ($V\text{-}VI_{ESI\ 2007}$). Ground cracks along with liquefaction phenomena (ejection of ground water) were observed in Marathopolis area ($VII_{ESI\ 2007}$). Submarine landslides resulted in disruption of submarine cables connecting Zakynthos and Crete. Tsunami waves were generated and affected a 35km long N-S coastal segment extending from Agrilos located north of Filiatra to the Pylos bay. The waves swept several boats onto the coast of Gialova ($VII\text{-}VIII_{ESI\ 2007}$) located north of Pylos, the sea close to Argilos, located to the north of Filiatra, advanced resulting in coastal inundation ranging from 10 to 15 m for a short time period ($VII\text{-}VIII_{ESI\ 2007}$). It was reported that the tsunami was observed up to Izmir. Hydrological anomalies comprised water turbidity in Evinos River, whose estuary is located north of Patras Gulf, in a distance of 120 km north of Filiatra. These hydrological anomalies in Evinos River were considered as an isolated effect of the 1886 earthquake generated in the far field. Thus, it has not been taken into account in the assessment of the environmetal seismic intensities.

The 1898 November 9 Kyparissia earthquake

Hydrological anomalies were observed in Aetos village located in Tryfillia province and included increased discharge and water turbidity (muddy water) in a spring ($VII_{ESI\ 2007}$).

The 1899 January 22 Kyparissia earthquake

Slope movements included mainly landslides and rockfalls located south of Kyparissia and east of Filiatra, more specifically in Perdikoneri and Rouzaki villages. Hydrological anomalies included water discharge variations in springs as far as Kalamata town ($VII_{ESI\ 2007}$), Varvitsa and Dimitsana villages. Liquefaction and slumping of geological material was induced along the Ionian coast of Messinia ($VII_{ESI\ 2007}$). In Messene marshes located west of Kalamata, extensive liquefaction phenomena occurred resulting in damage to railway embankments and telegraph lines ($VII_{ESI\ 2007}$).

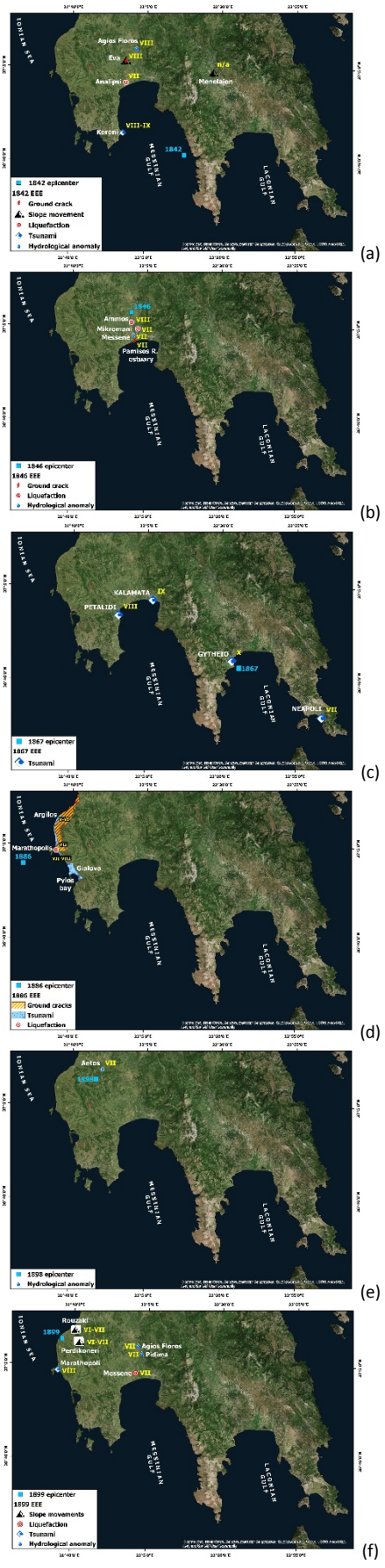

Figure 2: EEE induced by the (a) 1842, (b) 1846, (c) 1867, (d) 1886, (e) 1898, (f) 1899 earthquakes in southern and southwestern Peloponnese.

The subsequent earthquake-induced tsunami was about 1m high and resulting in inundation of Marathopolis coastal area ($VIII_{ESI\ 2007}$), while in Zakynthos Island was about 20-40 cm ($VII_{ESI\ 2007}$). The tsunami was possibly triggered by submarine slumps, but no damage occurred to the submarine cables between Zakynthos and Western Peloponnese. The hydrological anomalies observed in Varvitsa and Dimitsana villages located in Laconia and Arcadia prefectures respectively were also considered as far field effects of the earthquake and were not considered in the intensity assessment.

CONCLUSIONS

Based on the aforementioned data, slope movements were the most frequently reported EEE reported in 5 historical earthquakes followed by liquefaction phenomena, tsunami waves and hydrological anomalies reported in 4 historical earthquakes and ground cracks in 3 historical earthquakes. The most susceptible areas to the generation of EEE are the Kalamata (Kato Messinia) basin, which has been affected by EEE during 4 historical earthquakes, followed by Sparta (Evrotas) basin with EEE during 2 historical earthquakes, the eastern slopes of Taygetos Mt affected by slope movements during 2 historical earthquakes, the Ionian coast of Messinia suffered by EEE during 2 historical earthquakes, and the Kyparissia Mts also suffered by EEE during a historical event respectively. The maximum assigned local environmental seismic intensities are $X_{ESI\ 2007}$ for Sparta (Evrotas) basin, $VIII\text{-}IX_{ESI\ 2007}$ for Kalamata (Kato Messinia) basin, $VIII_{ESI\ 2007}$ for Ionian coast of Messinia and VII for Kyparissia Mts. These analysis is not only of historical interest, but significantly contribute to the completeness of the earthquake and the induced EEE catalogue, which is the very important for seismic hazard analysis and as such benefits all scientists and agencies competent to the prevention and management of natural disasters.

REFERENCES

Ambraseys, N., 2009. *Earthquakes in the Mediterranean and Middle East, a multidisciplinary study of seismicity up to 1900*. Cambridge University Press, Cambridge. 970 p.

Fountoulis, I.G., & Mavroulis, S.D., 2013. Application of the Environmental Seismic Intensity scale (ESI 2007) and the European Macroseismic Scale (EMS-98) to the Kalamata (SW Peloponnese, Greece) earthquake (Ms=6.2, September 13, 1986) and correlation with neotectonic structures and active faults. *Annals of Geophysics* 56 (6), 2013, S0675.

Fountoulis, I., Mariolakos, I., & Ladas, I., 2014. Quaternary basin sedimentation and geodynamics in SW Peloponnese (Greece) and late stage uplift of Taygetos Mt. *Bollettino di Geofisica Teorica ed Applicata* 55 (2), 303-324.

Galanopoulos, A.G., 1940. Das Schadenbeben Messeniens vom 28. Marz 1885. *Proceedings of the Athens Academy*, 1940.

Galanopoulos, A.G., 1941a. Das Riesenbeben der Messenischen Kuste vom 27 August 1886. *Proceedings of the Athens Academy*, 1941.

Galanopoulos, A.G., 1941b. Das Erdbeben von Messenien vom 22. Januar 1899. *Proceedings of the Athens Academy*, 1941.

Galanopoulos A.G., 1949. The Koroni, Messinia, earthquake of October 6, 1947. *Bulletin of the Seismological Society of America* 39, 33-39.

Galanopoulos, A.G., 1960. Tsunamis observed on the coasts of Greece from antiquity to present time. *Annali di Geofisica* 13, 369-386.

Kouskouna, V., & Kaviris, G., 2014. Seismic Hazard Study in Messinia (SW Peloponnese) area. In: *Second European Conference on Earthquake Engineering and Seismology*, Istanbul, 2014, doi: 10.13140/2.1.2196.4168.

Lekkas, E., Mavroulis, S., Carydis, P., & Alexoudi, V., 2018. The 17 November 2015 Mw 6.4 Lefkas (Ionian Sea, Western Greece) Earthquake: Impact on Environment and Buildings. *Geotechnical and Geological Engineering*, 2018.

Lekkas, E.L., & Mavroulis, S.D., 2015. Earthquake environmental effects and ESI 2007 seismic intensities of the early 2014 Cephalonia (Ionian Sea, Western Greece) earthquakes (January 26 and February 3, Mw 6.0). *Natural Hazards* 78, 1517-1544.

Mariolakos, I., Sabot, V., Alexopoulos, A., et al., 1986. *Microzonic study of Kalamata, (Geomorphology, Geology, Neotectonics)*. Earth Planning Protection Organization, Report, Athens, 110 p.

Papadopoulos, G.A., Baskoutas, I., & Fokaefs, A., 2014. Historical seismicity of the Kyparissiakos Gulf, western Peloponnese, Greece. *Bollettino di Geofisica Teorica ed Applicata* 55 (2), 389-404.

Papanikolaou, D., Chronis, G., Pavlakis, P., et al., 1988. *Submarine Neotectonic Map of Upper Messiniakos Gulf*. Applied Scientific Programm, Earthquake Planning and Protection Organization, National Center for Marine Research, Department of Dynamic, Tectonic, Applied Geology, National and Kapodistrian University of Athens, 31 p.

Papanikolaou, D., Fountoulis, I., & Metaxas, Ch., 2007. Active faults, deformation rates and Quaternary paleogeography at Kyparissiakos Gulf (SW Greece) deduced from onshore and offshore data. *Quaternary International* 171-172, 14-30.

Papanikolaou, I., & Melaki, M., 2017. The Environmental Seismic Intensity Scale (ESI 2007) in Greece, addition of new events and its relationship with magnitude in Greece and the Mediterranean; preliminary attenuation relationships. *Quaternary International* 451, 37-55.

Papazachos, B., & Papazachou, C., 1997. *The earthquakes of Greece*. Ziti Publications, Thessaloniki. 304 p.

Sakellariou, N., & Kouskouna, V., 2014. Assigning macroseismic intensities of historical earthquakes from late 19th century In SW Peloponnese (Greece). In: *Second European Conference on Earthquake Engineering and Seismology*, Istanbul, 2014, doi: 10.13140/2.1.2196.4168.

Serva, L., Esposito, E., Guerrieri, L., et al., 2007. Environmental effects from five hystorical earthquakes in Southern Apennines (Italy) and macroseismic intensity assessment: Contribution to INQUA EEE Scale Project. *Quaternary International* 173-174, 30-44.

Soloviev, S.L., Solovieva, O.N., Go, C.N., et al., 2000. *Tsunamis in the Mediterranean Sea 2000 B.C.-2000 A.D.* Springer Science+Business Media Dordrecht. 256 p.

INQUA Focus Group Earthquake Geology and Seismic Hazards

paleoseismicity.org

Local tsunamigenic earthquakes and subsequent tsunamis in the southern and southwestern Peloponnese and intensities based on the Integrated Tsunami Intensity Scale (ITIS 2012)

Mavroulis, Spyridon (1), Lekkas, Efthymios (1)

(1) Department of Dynamic Tectonic Applied Geology, Faculty of Geology and Geoenvironment, School of Sciences, National and Kapodistrian University of Athens, Panepistimiopolis, 15784, Athens, Greece, smavroulis@geol.uoa.gr

Abstract: *The southern Peloponnese has been affected by destructive historical and recent earthquakes with considerable effects on human, nature, buildings and infrastructures. Among other earthquake environmental effects, tsunamis were also induced and affected the coastal southern and southwestern Peloponnese. It is concluded that the most affected and vulnerable by tsunami generation areas are the northern and western coastal areas of the Messinian and the Laconian Gulfs and the Ionian coast of Messinia. The effects of the tsunamigenic earthquakes of 1842, 1867, 1886, 1899 and 1947 mainly included coastal inundation, washing of ships on the shore as well receding of the sea from the coast and subsequent sea level rise. Severe damage of buildings and infrastructures of the coastal area was limited. The maximum ITIS 2012 intensities were* $X_{ITIS\ 2012}$ *in Laconian Gulf,* $IX_{ITIS\ 2012}$ *in Messinian Gulf and* $VIII_{ITIS\ 2012}$ *along the Ionian coast of Messinia.*

Keywords*: earthquakes, tsunami, ITIS 2012, Peloponnese, coastal area*

INTRODUCTION

The Eastern Mediterranean region (Fig. 1) is one of the most rapidly deforming regions in the world and thus one of the most tectonically and seismically active. The maximum seismicity and the generation of tsunamis are observed along the Hellenic Arc (Papadopoulos, 2016). This activity is attributed to major geotectonic structures dominating the Eastern Mediterranean and producing earthquakes and subsequent tsunamis among other earthquake environmental effects (EEE). These structures include the Hellenic Arc, the Cyprus Arc and the Levantine Basin, while the most significant tsunami sources are observed along the western segment of the Hellenic Arc (offshore western Peloponnese, offshore western and northern Crete), along the tectonic rifts of Corinth and Evoikos Gulfs (Central Greece), within the Aegean Sea and along the North Aegean Sea trough (Fig. 1; Papadopoulos, 2016).

The study area is located in the southern and the southwestern part of Peloponnese. Onshore and offshore studies conducted by various researchers (Mariolakos et al., 1986; Papanikolaou et al., 1988; Mariolakos & Fountoulis 2004; Papanikolaou et al., 2007; Fountoulis & Mavroulis, 2013; Fountoulis et al., 2014) revealed that the study area is composed of major neotectonic macrostructures (megahorsts and megagrabens) bounded by N-S and E-W striking fault zones (Fig. 2). These onshore macrostructures are from E to W the following: (a) the NW-SE striking Sparta basin, (b) the N-S striking Taygetos Mt mega-horst, (c) the Kalamata-Kyparissia mega-graben striking N-S in its southern part and E-W further to the north, (d) the very complex morphotectonic mega-structure of Kyparissia Mts-Lykodimo Mt striking N-S and (e) the Gargallianoi-Pylos mega-horst located along the western coast of Messinia (Fig. 2; Mariolakos et al., 1986; Fountoulis & Mavroulis, 2013).

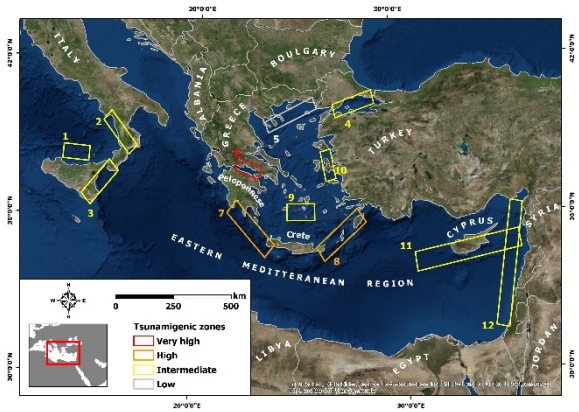

Figure 1: Generalized tsunamigenic zones of the Eastern Mediterranean Sea categorized by relative intensity and frequency of occurrence: 1: Calabria, 2: Aeolian islands, 3: Messina straits, 4: Marmara Sea, 5: North Aegean Sea, 6: Corinth Gulf, 7: West Hellenic Arc, 8: East Hellenic Arc, 9: Cyclades islands, 10: East Aegean Sea, 11: Cyprus Arc, 12: Levantine Sea (modified from Papadopoulos & Fokaes, 2005).

These onshore structures are bounded by active fault zones and seismogenic faults (Fig. 2; e.g. the eastern marginal fault of Kato Messinia basin ruptured in 1986 Kalamata earthquake, the Sparta fault ruptured in 464 B.C., devastating Sparta). Offshore fieldwork in Messinian Gulf conducted by Papanikolaou et al. (1988) and in Kyparissiakos Gulf by Papanikolaou et al. (2007) demonstrated that active faults observed onshore continue in several cases offshore in the study area (Fig. 2, e.g. the onshore eastern marginal fault zone of the Kato Messinia basin continues offshore in Messinian Gulf). These macrostructures have been repeatedly affected by

destructive earthquakes during the historical and recent times and suffered the impact of extensive EEE including the generation of tsunami waves.

The generation of the most significant and destructive tsunamis in the study area have been confirmed not only by several written and epigraphic sources (e.g. Galanopoulos, 1960; Soloviev et al., 2000; Ambraseys, 2009; Papadopoulos et al., 2014), but also by searching for palaeotsunami traces and especially for the Holocene tsunami imprint on the coastal part of the study area (Scheffers et al., 2008). It has been clearly shown that this part of Peloponnese is mainly affected by tsunamis strongly related to local earthquakes and coseismic submarine landslides generated in the western part of the Hellenic Arc and Trench system (HEAT) (Galanopoulos, 1960; Antonopoulos, 1980; Papazachos & Papazachou, 1997; Ambraseys, 2009; Papadopoulos, 2016; Papadopoulos et al., 2014). However, tsunami sources in other segments of the HEAT are capable to affect southern Peloponnese. More specifically, the seismic source that produce the 1303 AD earthquake and the subsequent tsunami is located at the eastern segment of HEAT between Crete and Rhodes and can be also considered as threatening the study area as it is concluded by geomorphological and sedimentological paleotsunami traces (Scheffers et al., 2008).

This study aims to the presentation of a complete list of the historical local tsunamigenic earthquakes that have greatly affected the southern part of Peloponnese and the subsequent tsunamis, the presentation of the tsunami quantitative characteristics where available, the detailed presentation of their impact on the coastal natural and built environment as well as the application of the Integrated Tsunami Intensity 2012 (ITIS 2012) scale for the evaluation of the tsunami intensity based on all the available tsunami information and data and the guidelines provided by Lekkas et al. (2013).

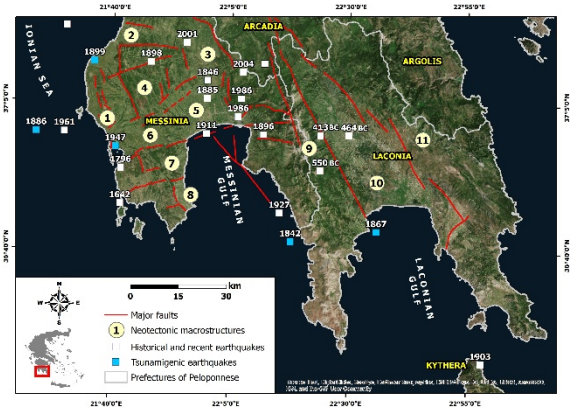

Figure 2: The southern Peloponnese along with the historical and recent earthquakes with impact on human, natural and built environment of the study area as well as the major onshore and offshore faults and the major neotectonic macrostructures: 1: Gargallianoi-Pylos mega-horst, 2: Kyparissia basin, 3: Ano Messinia basin, 4: Kyparissia Mts, 5: Kalamata (Kato Messinia) basin, 6: Vlahopoulo graben, 7: Lykodimo Mt horst, 8: Falanthi basin, 9: Taygetos Mt, 10: Sparta/Evrotas basin, 11: Parnon Mt based on Mariolakos et al. (1986), Papanikolaou et al. (1988) and Fountoulis (1994).

METHODOLOGY

For the present study, data and information on destructive earthquakes and subsequent tsunamis were obtained from verified catalogues and related scientific papers (e.g. Galanopoulos, 1941, 1947, 1949, 1950, 1960; Papazachos & Papazachou, 1997; Soloviev et al., 2000; Ambraseys, 2009; Papadopoulos, 2016; Papadopoulos et al., 2014). All derived data and information were used for the application of the ITIS 2012 scales for the evaluation of the seismic and tsunami intensities respectively.

ITIS 2012 is a recently introduced 12-grade scale ranging from I (not felt) to XII (completely devastating) and it is based on the assessment of a large number of objective criteria, grouped in six categories (physical quantities such as tsunami wave height, flow depth, and inundation extent, impact on humans, impact on mobile objects such as boats and cars, impacts on infrastructure, environmental effects and impact on structures) (Lekkas et al., 2013). This scale works well for modern events where large amounts of data are available (Lekkas et al., 2013; Barberopoulou & Scheele, 2015), while Reicherter (2015) argued that such scales are of limited use in paleotsunami science due to the small data sets, the absence of instrumental records and the difficulties in obtaining the minimum necessary parameters for the evaluation of intensity. In this frame, the ITIS 2012 is applied for the intensity evaluation of historical tsunamis in the study area in order to examine its applicability in utilizing tsunami historical information and its future in hazard assessments.

HISTORICAL EARTHQUAKES AND TSUNAMIS - ESI 2007 and ITIS 2012 INTENSITIES

The 1842 April 18 earthquake and tsunami

This earthquake was generated in the southwestern coast of Peloponnese (Fig. 3a) and caused very heavy structural damage in many settlements located within the Pamisos River valley, in the western part of Messinia and in Laconia (Ambraseys, 2009). As regards the tsunami generation and its impact, the coast close to Koroni was inundated and ships were washed on the shore by the tsunami (V-VI$_{ITIS\ 2012}$) (Fig. 3a).

The 1867 September 20 earthquake and tsunami

The 1867 earthquake generated tidal waves which affected the southern and western part of Peloponnese (Fig. 3b), the Ionian Islands, the Cyclades complex in the Aegean Sea and reached also the eastern Italian coasts (Soloviev et al., 2000; Papazachos & Papazachou, 1997; Papadopoulos et al., 2014). The waves rolled onto the southern and western shores of Peloponnese and had considerable impact on the funnel - shaped gulfs and bays opened towards the earthquake epicenter (Soloviev et al., 2000; Papazachos & Papazachou, 1997). Thus, they severely affected the coastal areas of Laconian and Messinian Gulfs (Fig. 3b). Oscillations of the sea level within the focal zone of the waves presented a long duration ranging from 5.5 up to 10 hours before the sea calmed down again.

Gytheion was destroyed by the waves, which had a significant impact on the Cape Pagania, on the western

shore of the Laconian Gulf and on the Messinian Gulf (Fig. 3b). In Gytheion, changes to sea level were observed. The sea initially receded from the shore and the sea bed was dried up. Afterwards, the sea rose for 6 m above its usual level and it looked like boiling ($X_{ITIS\ 2012}$ in Fig. 3b).

In Kalamata located in the northern part of the Messinian Gulf, low and high water were similarly observed with the sea receding slowly from the coast approximately for 15 m ($IX_{ITIS\ 2012}$ in Fig. 3b). Lower values of sea level fall were observed in Petalidi coastal area, where then the sea water level rose up to 2m and caused inundation of the coastal area ($VIII_{ITIS\ 2012}$ in Fig. 3b).

The 1886 August 27 Filiatra earthquake and tsunami

An earthquake occurred in the Ionian coast of Messinia (Fig. 3c; Galanopoulos, 1941, 1947). Tsunami waves were generated and affected a 35km long N-S coastal segment extending from Agrilos located north of Filiatra to the bay of Pylos. The waves washed several boats on the shore of Gialova (V-$VI_{ITIS\ 2012}$ in Fig. 3c) located north of Pylos. The sea close to Agrilos located to the north of Filiatra advanced resulting in coastal inundation ranging from 10 to 15 m for a short time period (VII-$VIII_{ITIS\ 2012}$ in Fig. 3c) (Galanopoulos, 1941a; Soloviev et al., 2000). It was reported that the tsunami was observed up to Izmir (Galanopoulos, 1960a; Karnik, 1971; Papazachos & Papazachou, 1997; Soloviev et al., 2000).

The 1899 January 22 Kyparissia earthquake and tsunami

This very strong earthquake occurred on January 22 causing no fatalities, many injuries and severe damage in many villages of Messinia (Galanopoulos, 1941b, 1947, 1955). The subsequent earthquake-induced tsunami was about 1m high and resulting in inundation of Marathopolis coastal area (VI-$VII_{ITIS\ 2012}$ in Fig. 3d), while in Zakynthos Island was about 20-40 cm ($VI_{ITIS\ 2012}$ in Fig. 3d) (Galanopoulos, 1941; Papazachos & Papazachou, 1997; Ambraseys & Jackson, 1990; Ambraseys 2009). Based on Galanopoulos (1941) the tsunami was possibly triggered by co-seismic submarine slumps, but no damage occurred to the submarine cables between Zakynthos and Peloponnese.

The 1947 January 6 Koroni earthquake and tsunami

On October 6, 1947, southwestern Peloponnese was hit by a strong earthquake that caused 3 casualties and 40 injured as well as severe damage in 54 villages of Pylia province (Galanopoulos, 1949). A tsunami was observed in Methoni coastal area (Fig. 3e) with inundation distance varying from 15m (Galanopoulos, 1949) to 60m (Ambraseys & Jackson, 1990) corresponding to $VIII_{ITIS\ 2012}$ intensity (Fig. 3e). This tsunami was attributed to submarine landslides generated along steep slopes of the seabed in a distance of 6 km SSW of the coast (Galanopoulos, 1949).

CONCLUSIONS

The southern Peloponnese has been affected by destructive historical and recent earthquakes with considerable effects on the local population, the natural environment, buildings and infrastructures.

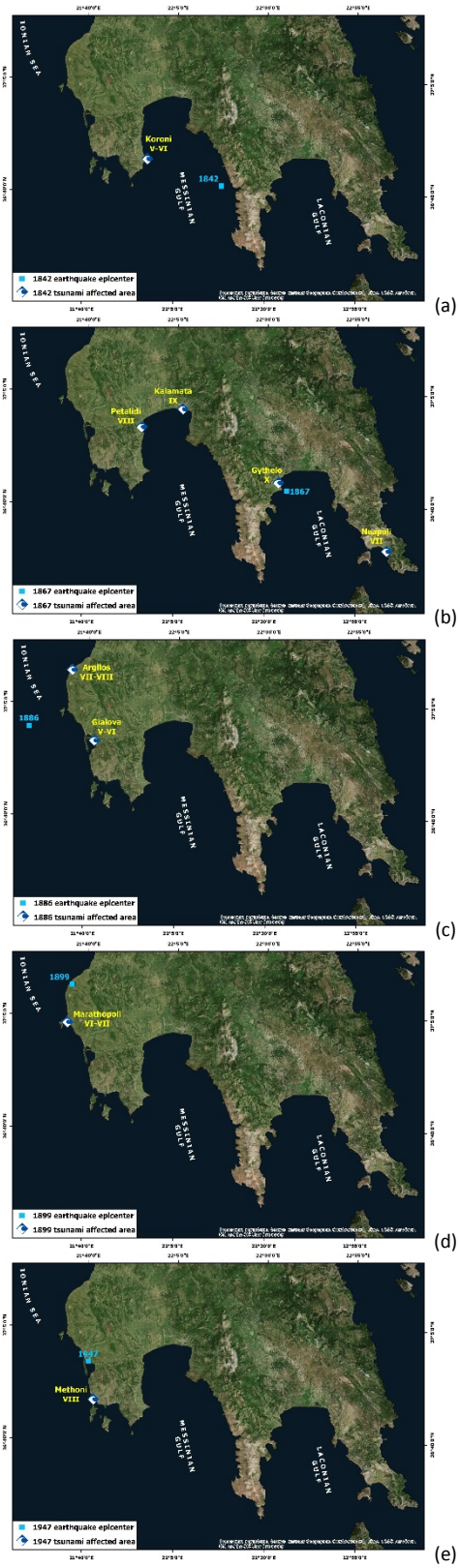

Figure 2: The local tsunamigenic earthquakes of (a) 1842, (b) 1867, (c) 1886, (d) 1899 and (e) 1947 with impact on the coastal areas of the southern and southwestern Peloponnese along with the assigned ITIS 2012 intensities.

Among other earthquake environmental effects, tsunamis were also induced and have affected the coastal southern and southwestern Peloponnese. This presentation supports earlier studies which suggest that post-disaster

assessments for historical events (>25 years old) are scarce or limited as regards the related information. Moreover, these limitations and difficulties in the case of the historical earthquakes are attributed to small data sets, absence of instrumental records and difficulties in obtaining the minimum necessary parameters for the evaluation of intensities. However, based on the quantitative data and information from various sources, the ESI 2007 and the ITIS 2012 were applied.

Based on these applications, it is concluded that the most affected and vulnerable by tsunami generation areas are the northern and western coastal areas of the Messinian (e.g. Kalamata, Petalidi, Koroni areas) and the Laconian (e.g. Gytheio area) Gulfs and the Ionian coast of Messinia in the southwestern Peloponnese (e.g. from Agrilos area to Pylos bay). The effects mainly included coastal inundation, washing of ships and boats on the shore as well receding of the sea from the coast and subsequent sea lever rise. Severe damage of buildings and infrastructures of the coastal area was limited. The maximum ITIS 2012 intensities were $X_{ITIS\ 2012}$ in Laconian Gulf, $IX_{ITIS\ 2012}$ in Messinian Gulf and $VIII_{ITIS\ 2012}$ along the Ionian coast of Messinia.

REFERENCES

Ambraseys, N., 2009. Earthquakes in the Mediterranean and Middle East, a multidisciplinary study of seismicity up to 1900. Cambridge University Press, Cambridge. 970 p.

Ambraseys, N.N., & Jackson, J.A., 1990. Seismicity and associated strain of central Greece between 1890 and 1988. *Geophysics Journal International* 101, 663-708.

Antonopoulos, J., 1980. Data for investigation on seismic sea-waves events in the eastern Mediterranean from the birth of Christ to 1980 A.D. *Annals of Geophysics* 33, 141-248.

Barberopoulou, A., & Scheele, F., 2016. Does the future of tsunami intensity scales lie in past events?. *Natural Hazards* 80, 401-424.

Fountoulis, I., 1994. *Neotectonic deformation of the Central-western Peloponnese*. PhD thesis, National and Kapodistrian University of Athens, GAIA 7, 386pp.

Fountoulis, I., Mariolakos, I., & Ladas, I., 2014. Quaternary basin sedimentation and geodynamics in SW Peloponnese (Greece) and late stage uplift of Taygetos Mt. *Bollettino di Geofisica Teorica ed Applicata* 55 (2), 303-324.

Fountoulis, I.G., & Mavroulis, S.D., 2013. Application of the Environmental Seismic Intensity scale (ESI 2007) and the European Macroseismic Scale (EMS-98) to the Kalamata (SW Peloponnese, Greece) earthquake (Ms=6.2, September 13, 1986) and correlation with neotectonic structures and active faults. *Annals of Geophysics* 56 (6), 2013, S0675.

Galanopoulos, A.G., 1941a. Das Riesenbeben der Messenischen Kuste vom 27 August 1886. *Proceedings of the Athens Academy*, 1941.

Galanopoulos, A.G., 1941b. Das Erdbeben von Messenien vom 22. Januar 1899. *Proceedings of the Athens Academy*, 1941.

Galanopoulos, A.G., 1947. The seismicity in Messinia province, *Annales Géologiques des Pays Hélléniques* 1, 38-59.

Galanopoulos, A.G., 1949. The Koroni, Messinia, earthquake of October 6, 1947. *Bulletin of the Seismological Society of America* 39, 33-39.

Galanopoulos, A.G., 1950. Die seismizität von Messenien. *Gerlands Beiträge zur Geophysik* 61, 144-162.

Galanopoulos, A.G., 1960. Tsunamis observed on the coasts of Greece from antiquity to present time. *Annali di Geofisica* 13, 369-386.

Karnik, V., 1971. Tsunamis. In: Seismicity of the European Area. Part II, D. Reidel Publ. Co., Dordrecht. 203-206.

Lekkas, E.L., Andreadakis, E., Kostaki, I., & Kapourani, E., 2013. A Proposal for a New Integrated Tsunami Intensity Scale (ITIS-2012). *Bulletin of the Seismological Society of America* 103 (2B), 1493-1502.

Mariolakos, I., & Fountoulis, I., 2004. The current geodynamic regime in the Hellenic area, In: *Neotectonic transect Moesia-Apulia. Field trip Guide book - B26* (Mariolakos, I., Zagorchev, I., Fountoulis, I., Ivanov, M. eds), 32nd International Geological Congress (Florence), 72 pp.

Mariolakos, I., Sabot, V., Alexopoulos, A., et al., 1986. *Microzonic study of Kalamata, (Geomorphology, Geology, Neotectonics)*. Earth Planning Protection Organization, Report, Athens, 110 p.

Michetti, A.M., Esposito, E., Guerrieri, L., et al., 2007 Intensity Scale ESI 2007. In: *Memorie descrittive della carta geologica d' Italia, vol. 74, Servizio Geologico d'Italia-Dipartimento Difesa del Suolo* (Guerrieri. L., Vittori, E., eds), APAT, Rome, Italy.

Papadopoulos, G.A., & Fokaefs, A., 2005. Strong tsunamis in the Mediterranean Sea: a re-evaluation. *ISET Journal of Earthquake Technology* 42 (4), 159-170.

Papadopoulos, G.A., 2016. *Tsunamis in the European-Mediterranean Region: From Historical Record to Risk Mitigation*. Elsevier publications, 280 p.

Papadopoulos, G.A., Daskalaki, E., Fokaefs, A., & Novikova, T., 2014. Tsunamigenic potential of local and distant tsunami sources threatening SW Peloponnese. *Bollettino di Geofisica Teorica ed Applicata* 55 (2), 469-484.

Papanikolaou, D., Chronis, G., Pavlakis, P., et al., 1988. *Submarine Neotectonic Map of Upper Messiniakos Gulf*. Applied Scientific Programm, Earthquake Planning and Protection Organization, National Center for Marine Research, Department of Dynamic, Tectonic, Applied Geology, National and Kapodistrian University of Athens, 31 p.

Papanikolaou, D., Fountoulis, I., & Metaxas, Ch., 2007. Active faults, deformation rates and Quaternary paleogeography at Kyparissiakos Gulf (SW Greece) deduced from onshore and offshore data. *Quaternary International* 171-172, 14-30.

Papazachos, B., & Papazachou, C., 1997. *The earthquakes of Greece*. Ziti Publications, Thessaloniki. 304 p.

Reicherter, K., 2015. Tsunamis as Paleoseismic Indicators. In: *Encyclopedia of Earthquake Engineering* (Beer M., Kougioumtzoglou I., Patelli E., Au IK., eds). Springer, Berlin, Heidelberg, https://doi.org/10.1007/978-3-642-36197-5_26-1.

Scheffers, A., Kelletat, D., Vött, A., et al., 2008. Late Holocene tsunami traces on the western and southern coastlines of the Peloponnesus (Greece). *Earth and Planetary Science Letters* 269, 271-279.

Soloviev, S.L., Solovieva, O.N., Go, C.N., et al., 2000. *Tsunamis in the Mediterranean Sea 2000 B.C.-2000 A.D.* Springer Science+Business Media Dordrecht. 256 p.

INQUA Focus Group Earthquake Geology and Seismic Hazards

paleoseismicity.org

Multiple Quaternary faults in the largest metropolitan area of the Rio Grande rift zone, western USA; the case of Albuquerque, New Mexico

McCalpin, James P. (1)

(1) GEO-HAZ Consulting, Inc., P.O. Box 837, Crestone, CO 81131 USA, mccalpin@geohaz.com

Abstract: *The largest metropolitan area within the Rio Grande rift zone (Albuquerque, New Mexico) lies in one of the most densely-faulted parts of the rift. Within 40 km of the urban center there are 27 named Quaternary faults. To date paleoseismic trenching has been performed on six of these faults, which has yielded displacement-per-events measurements at a single point on the fault (the trench site) and recurrence intervals for surface-rupturing earthquakes. However, it is not clear that all the of closely-spaced, parallel fault scarps are independent seismic sources. Deep geophysical cross-sections and precise dating of rupture events may be able to eliminate some possible rupture scenarios, but many will remain. At present the swarm-like fault zones are modelled as containing several discrete faults that generate earthquakes randomly in space and time.*

Keywords*: normal faults, rifts, trenching, geochronology*

INTRODUCTION

The Rio Grande rift is a 1000 km-long, up to 100 km-wide zone of horsts and grabens that extends from northern Mexico, northward through west Texas, New Mexico, and Colorado. The largest metropolitan area in the rift is the Albuquerque (New Mexico) Metropolitan Statistical Area, containing a population of 910,000 (2016 estimate). Within 40 km of downtown Albuquerque there are 27 named Quaternary faults (Fig. 1; Machette et al., 1998).

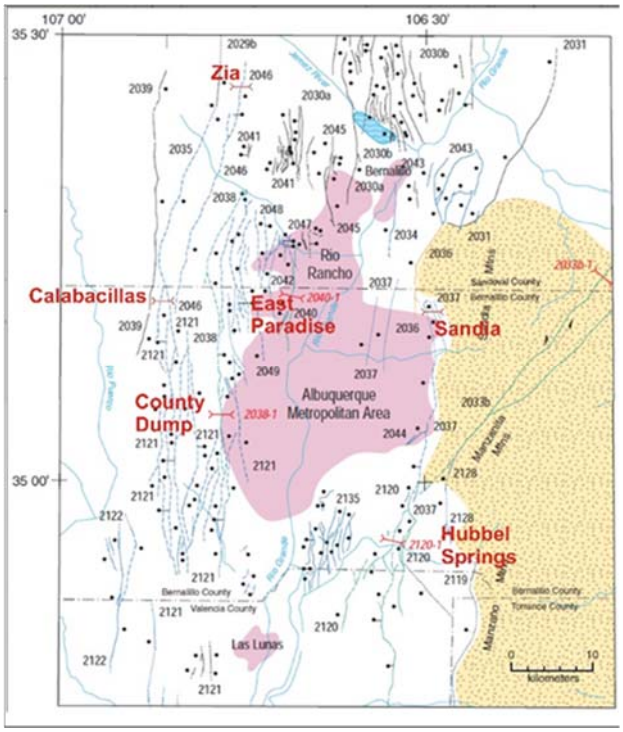

Figure 65: Map of Quaternary faults in and around the Albuquerque Metropolitan area; from Machette et al., 1998. Paleoseismic trench sites are labelled in red.

However, the first of these faults (the County Dump fault) was not trenched until 1996. By 2003 six of the longest faults had been trenched (County Dump, McCalpin et al., 2006; Calabacillas, McCalpin et al., 2011; Zia, McCalpin & Harrison, 2001; Sandia, McCalpin & Harrison, 2006; East Paradise, Personius, 2000; and Hubbell Springs, Olig et al., 2011). In the early 2000s gravity and aeromagnetic surveys revealed the subsurface structure of the basin (Fig. 2), which enabled the surface faulting to be put in a seismotectonic framework.

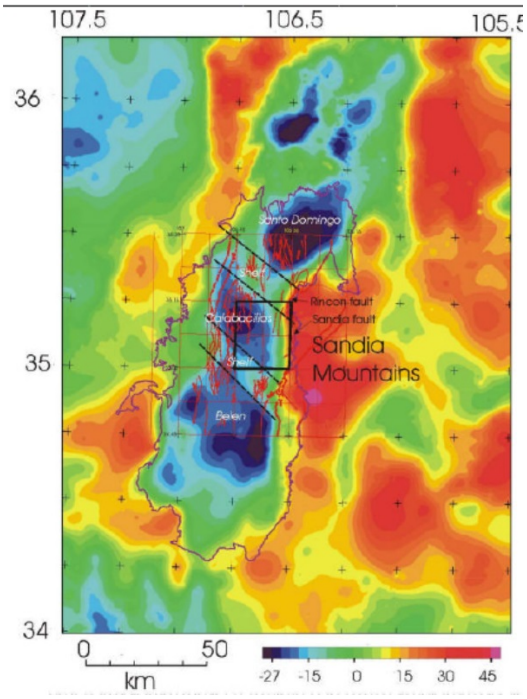

Figure 2: Gravity map of the Albuquerque-Belen basin (values in mgals). Quaternary faults in red. Dark blue colors indicate deep gravity lows in three sub-basins (Santo Domingo, Calabacillas, Belen) separated by higher shelves.

In the central (Calabacillas) sub-basin (metro Albuquerque) the Quaternary fault scarps are on the west side and dip east; these are described first. In the northern and southern (Belen) sub-basins the Quaternary-active master faults are on the east side of the rift and dip west. Strike-slip accommodation faults separate the basins.

County Dump Fault (Calabacillas sub-basin):
The County Dump fault has created a 24 m-high, 800 m-wide scarp (Fig. 3) across the surface of the Llano de Albuquerque (LdA), a ca. 1 Ma abandoned rift valley floor west of downtown.

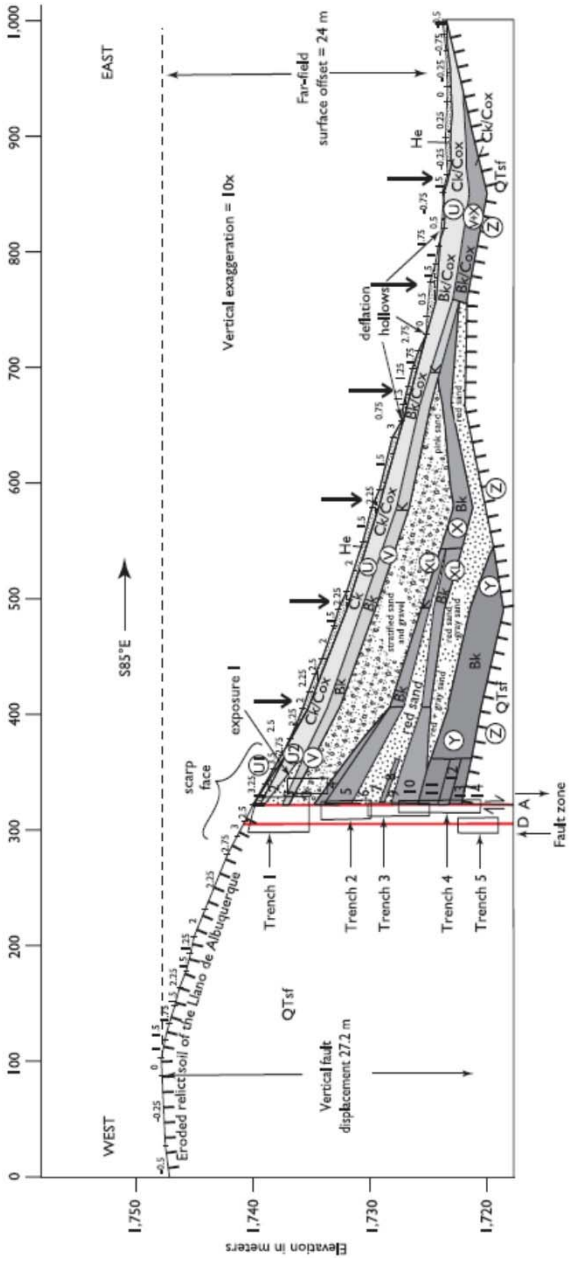

Figure 3: Scarp profile and stratigraphy of the syntectonic depositional wedge. The gross soil stratigraphy of the wedge is based on six measured sections (located below arrows just above ground surface), except adjacent to the fault zone where 14 superposed soils were exposed by our five stacked trenches. Vertical exaggeration= 10x.

We excavated five "half-trenches" along the fault plane as it descended an erosional south-facing slope just on the north side of Interstate Highway I-40 (Fig. 4). The lowest stratigraphy in one trench was also captured in the next trench downslope, exposing a composite stratigraphic section of the syntectonic wedge 26 m thick (Fig. 4).

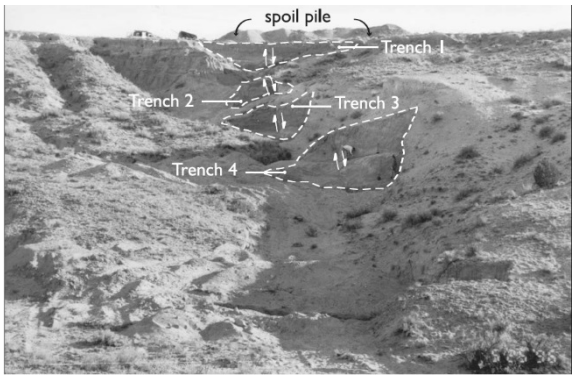

Figure 4:Telephoto of trenches 1-4, looking north. Upper parts of trench walls are outlined with white dashed lines. Note person in the center of Trench 4.

Each of the 13 buried soils was interpreted as forming in a stable hiatus between surface-faulting events, and the thickness of the overlying post-faulting sediment was taken as a proxy for downdrop of the hanging wall. The paleoseismic record extended back to about 750 ka, yielding a mean recurrence interval of ca. 30 kyr.

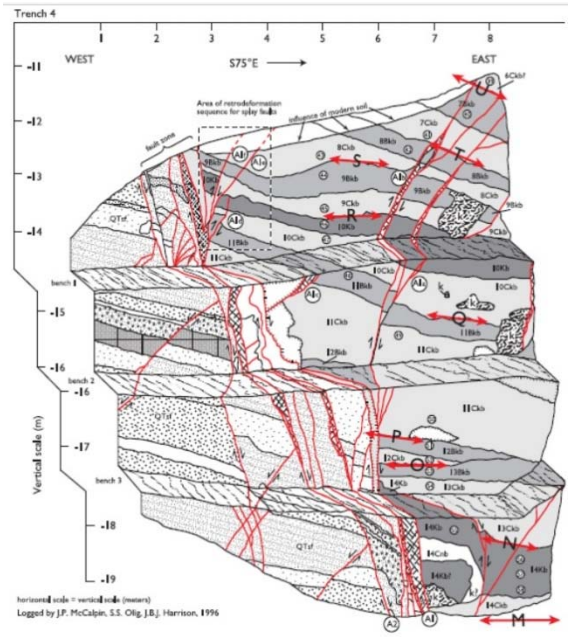

Figure 5: Log of Trench 4. Each of the four vertical faces is 1.5 to 2 m high. Vertical scale at left measures meters below the surface of the Llano de Albuquerque.

Calabacillas Fault (Calabacillas sub-basin):
The Calabacillas fault is a 40-km-long, down-to-the-east normal fault on the western edge of the LdA). In the past ca. 1Ma vertical displacement on the Calabacillas fault has created a 27-m-high, east-facing fault scarp on the western edge of the LdA (Fig. 6), equating to a long-term slip rate of 0.027-0.054 mm/yr. Our two trenches were located ~1 km from the south end of the fault, where a 1-km-wide graben has formed east of the main fault scarp.

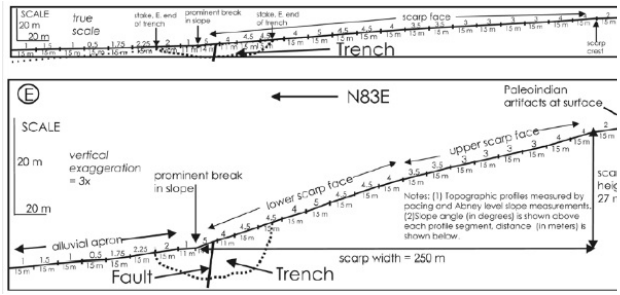

Figure 6: Topographic profiles of the broad fault scarp of the Calabacillas fault. Top, 1:1 scale; bottom, vert. exaggeration= 3x.

The paleoearthquake chronology on the 5.3-m-high antithetic scarp could not be reconstructed in detail because a strong carbonate soil profile had overprinted the entire 3-m-thick colluvial wedge deposit. It appears that numerous submeter displacements created this scarp, but the displacement was partitioned across several faults, so that no single free face was higher than 10–20 cm. Free faces so small did not create distinctive colluvial wedges.
On the 27-m-high main fault scarp, our 60-m-long trench straddled a minor slope break that overlay the main strand of the Calabacillas fault. The upper four soils exposed in the trench could be correlated across the main fault and indicated displacements of 10 cm, 30 cm, 55 cm, and 20 cm in the latest four paleoearthquakes.

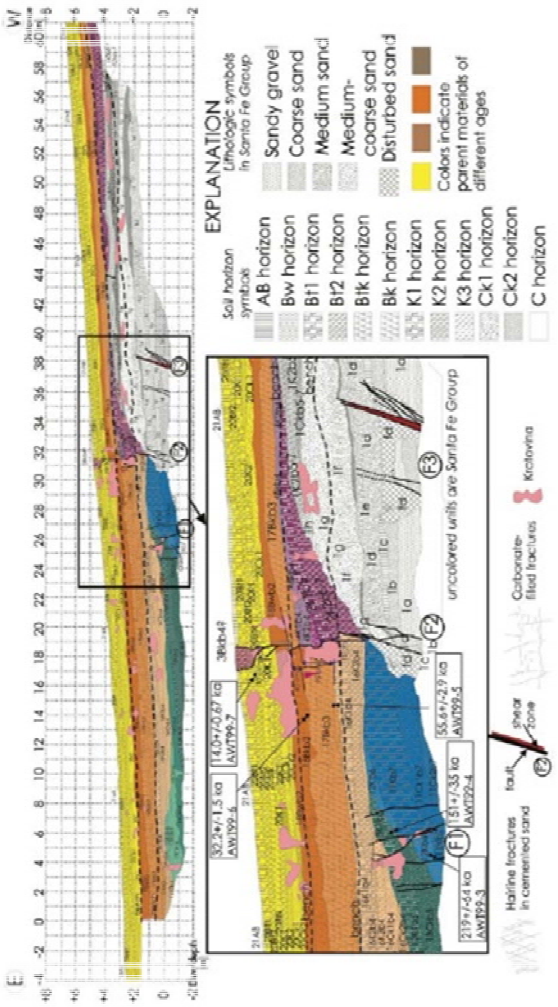

Figure 7: Log of the western trench. Top, entire south wall. Bottom, center part of south wall.

Six infrared-stimulated luminescence (IRSL) dates on eolian sands range from 14 ka at a depth of 0.5 m to 219 ka at a depth of 5 m. The latest four faulting events are dated at ca. 14 ka, 23 ka, 35 ka, and 55 ka. Thus, the displacement and recurrence times increase with increasing age, yielding relatively consistent closed-cycle slip rates of 0.011–0.028 mm/yr (Fig. 8).

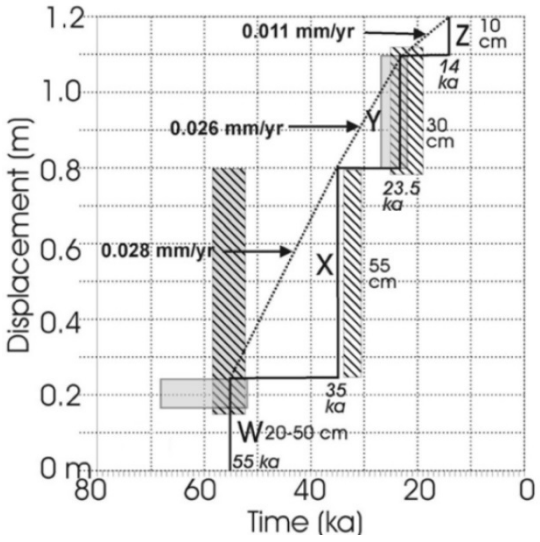

Figure 8: Slip history diagram for the Calabacillas fault.

Zia Fault (Calabacillas sub-basin):
The 40 km-long Zia fault lies 5 km east of and parallel to the Calabacillas fault (Fig. 1). Our trench site was located near the northern end of the fault, where it descends the northern edge of the LdA. A syntectonic wedge similar to that at the County Dump trenches (25 m thick and 600 m wide) underlies the fault hanging wall.

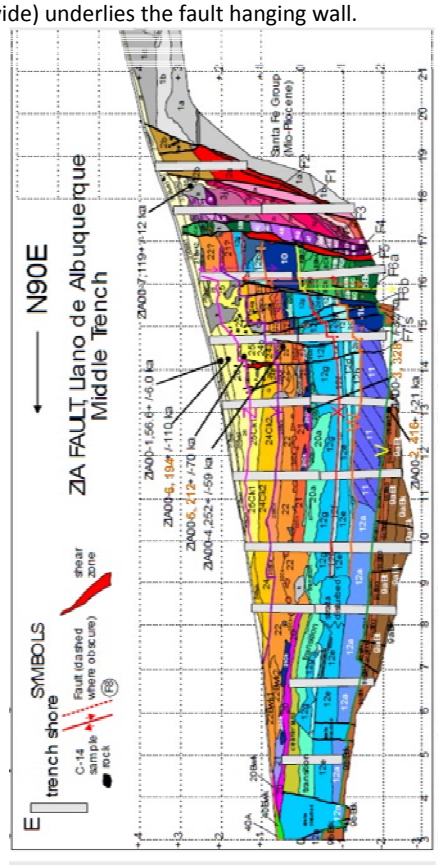

Fig. 9. Log of the south wall of the middle trench, Zia fault. The trench does not expose the entire syntectonic wedge, but the oldest bed dates at 416 ka. The fault zone is 3 m wide and composed of 6 step-faults. Strata between the step faults represent parts of the basal syntectonic wedge that mainly underlie the trench floor, and are older than 416 ka.

Figure 9: Log of the south wall of the middle trench, Zia fault.

The middle trench reveals (Fig. 9) evidence for at least 5 faulting events. Displacement in these events ranged from 0.6 to 2.6 m, with an average of 1.3 m. The 5 events occurred in the past 416 ka, yielding an average recurrence interval of can 80 ka.

Hubbell Springs fault zone [HSFZ] (Belen sub-basin):
The master Quaternary fault in the Belen sub-basin is the HSFZ, which lies on the eastern side of the rift. The HSFZ is 74 km long and up to 18 km wide, and is composed of multiple parallel west-facing fault scarps (Fig. 10) that displace the early-Pleistocene (0.5-1.0 Ma) Llano de Manzano (LdM) geomorphic surface.

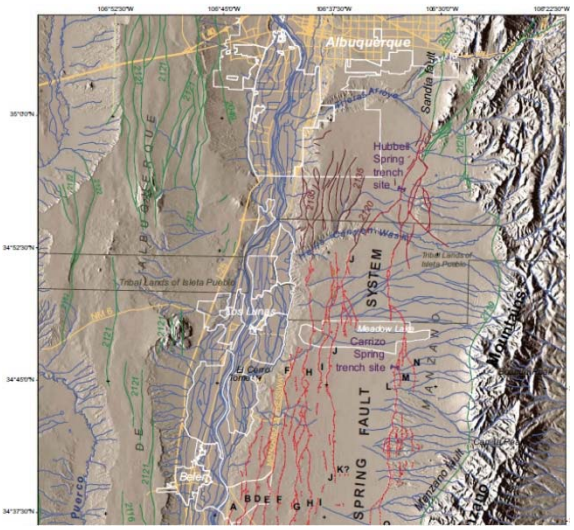

Figure 10: Quaternary fault scarps (red lines) on the LdM geomorphic surface, northern half of the HSFZ. The Rio Grande (blue lines) flows south down the rift axis. From Olig & Zahcariasen, 2010.

Fault scarps form a subparallel, anastomozing and branching pattern, and offset late Quaternary eolian and piedmont deposits down to the west. Vertical surface displacements across individual scarps range from 0 to 31 meters. Displacements in individual events range from 1.7 m to 4.7 m. Paleomagnitude estimates vary from Mw 6.6 to 7.5, depending on the rupture scenario and input parameter (see Discussion).

Trenching on two major fault strands in the zone has identified and dated the latest four displacement events. On the western strand events occurred at 6-15 ka, 27-30 ka, 30-55 ka, and 65-84 ka. Events on the central strand date at 12±1 ka, 29±3 ka, 56 ka, and $\leq$92 ka. Olig et al (2011) considered the event times to overlap, indicating possible multi-scarp ruptures.

DISCUSSION

Fault patterns in rifts pose challenges to seismic source characterization for seismic hazard assessment. First, it is unclear if each fault scarp represents an independent seismic source. This uncertainty, if not resolved by field data, will require numerous rupture scenarios in the beginning of the seismic source logic tree, which will of course increase uncertainty in the output hazard curve of ground motion. There are two indicators of independence of fault strands: (1) the strands does not intersect downward with another fault above seismogenic depths (as imaged by geophysical cross-sections), and (2) the ages of surface-rupturing events on the strand do not overlap with those on adjacent strands. Once the rupture scenarios have been trimmed to a minimum, we input the appropriate values for surface rupture length and displacement per event for each strand. The next issue is whether we can use the above values with empirical scaling relationships to estimate the magnitude of paleoearthquakes. Very few historic normal-fault surface ruptures have occurred in fault swarms such as at Albuquerque. Olig & Zachariasen (2010) suggest that east-west transects of trenches across the entire fault zones would be the simplest way to constrain some of the rupture scenarios.

Until those are performed, however, the expedient approach would be to model the fault zones as containing 4 to 8 parallel distributed faults that rupture randomly in time and space. Unfortunately, such a model will not assign higher rupture probabilities to those fault strands with the longest elapsed times, so cannot support earthquake probabilities based on the earthquake cycle and conditional probabilities.

Acknowledgements: Trenching of the County Dump, Calabacillas, Zia, and Sandia faults was supported by the USGS NEHRP External program. Trench loggers included Susan Olig, Dennis McMahon, Marsha Fronterhouse, Karen Holmes, Martha Eppes, Iain Madin, Paul Wisniewski, Willow Foster, Mike Kulikowski, Deborah Green, and Allen Jones.

REFERENCES

Machette, M.N., Personius, S.F., Kelson, K.I., Haller, K.M. and Dart, R. L., 1998, Map of Quaternary faults and folds in New Mexico and adjacent areas: USGS Open-File Report 98-521.

McCalpin, J.P. and Harrison, J.B.J., 2001, Paleoseismicity of Quaternary faults near Albuquerque, New Mexico: unpublished Final Technical Report submitted to U.S. Geological Survey by GEO-HAZ Consulting, Inc., Contract 99HQGR0056, Aug. 4, 2001, 58 p.

McCalpin, J.P. and Harrison, J.B.J., 2006, Paleoseismicity of the Sandia fault, Albuquerque, New Mexico: unpublished Final Technical Report submitted to U.S. Geological Survey by GEO-HAZ Consulting, Inc., Contract 02HQGR0068, March 14, 2006, 38 p.

McCalpin, J.P., Harrison, J.B.J., Berger, G.W., and Tobin, H.C., 2011, Paleoseismicity of a low-slip-rate normal fault in the Rio Grande rift, USA; The Calabacillas fault, Albuquerque, New Mexico: Geol. Soc. Amer. Special Paper 479, p. 23-46.

McCalpin, J.P., Olig, S.S., Harrison, J.B.J. and Berger, G.W., 2006, Quaternary faulting and soil formation on the County Dump fault, Albuquerque, New Mexico: New Mexico Bureau of Geology and Mineral Resources, Circular 212, 36 p.

Olig, S.S., Eppes, M.C., Forman, S.L., Love, D., and Harrison, J.B.J., 2011, Late Quaternary earthquakes on the Hubbell Spring fault system, New Mexico, USA: Evidence for noncharacteristic ruptures of intrabasin faults in the Rio Grande rift: Geol. Soc. Amer. Special Paper 479, p. 47-77.

Olig, S.S. and Zachariasen, J., 2010, Additional analyses and mapping of the Hubbell Spring and other intrabasin faults south of Albuquerque, New Mexico: New Mexico Bur. Geol. Min. Res, Open-File Report 527, 50 p.

Personius, S.F., 2000, Paleoearthquake Recurrence on the East Paradise Fault Zone, Metropolitan Albuquerque, New Mexico: Bull. Seismol. Soc. Amer., 90(2), p. 357-369.

INQUA Focus Group Earthquake Geology and Seismic Hazards

paleoseismicity.org

Postglacial slip rate variability of the Lastros normal fault (eastern Crete, Greece)

Mechernich, Silke (1), Dahms, Hannah (1), Reicherter, Klaus (2), Papanikolaou, Ioannis (3)

(1) Institute of Geology and Mineralogy, University of Cologne, Zülpicher Strasse 49b, 50674 Köln, Germany, mechernich.s@gmail.com
(2) Institute of Neotectonics and Natural Hazards, RWTH Aachen University, Lochnerstr. 4-20, 52064 Aachen, Germany
(3) Laboratory of Mineralogy and Geology, Agricultural University of Athens, 75 Iera Odos Str., 11855 Athens, Greece

Abstract: *The 11-km-long Lastros fault in eastern Crete forms an impressive bedrock fault scarp indicating active extension in the Hellenic forearc. No earthquakes from historical and instrumental catalogues can be associated with the Lastros fault. We mapped indicators of relative exposure duration along the bedrock fault plane, like colour contrast and fault plane roughness. The data suggests coseismic offsets between 15-35 cm for the last three earthquakes, corresponding to magnitudes of M_s~6.2-6.5. Preliminary modelling of twenty cosmogenic ^{36}Cl samples from an undisturbed site suggest temporal slip rate variabilities with 0.2-0.7 mm/yr during the last 2.9 ± 1.8 kyr (last 3 earthquakes), preceded by a rate of 0.6-1.2 mm/yr from ~2.9-10 kyr. The exhumation of the upper part (0.2-0.3 mm/yr, last ~10-36 kyr) is probably highly influenced by non-tectonic processes.*

Keywords*: Hellenic forearc extension, bedrock fault, coseismic slip, cosmogenic ^{36}Cl concentrations, postglacial fault scarp*

INTRODUCTION

The active extension in the Hellenic forearc results in a complex pattern of normal faults (Figure 1a). In eastern Crete, the Ierapetra fault zone is one of the most prominent geomorphologic and tectonic structures (Figure 1b). Seismicity during the last 15 years shows over 20 shallow earthquakes between magnitude 3 and 4, which could be attributed to the faults of the IFZ (EMSC, 2018). This indicates that although there have been no large ruptures in historical times, strain is released within the seismogenic zone. To date, two studies determined its

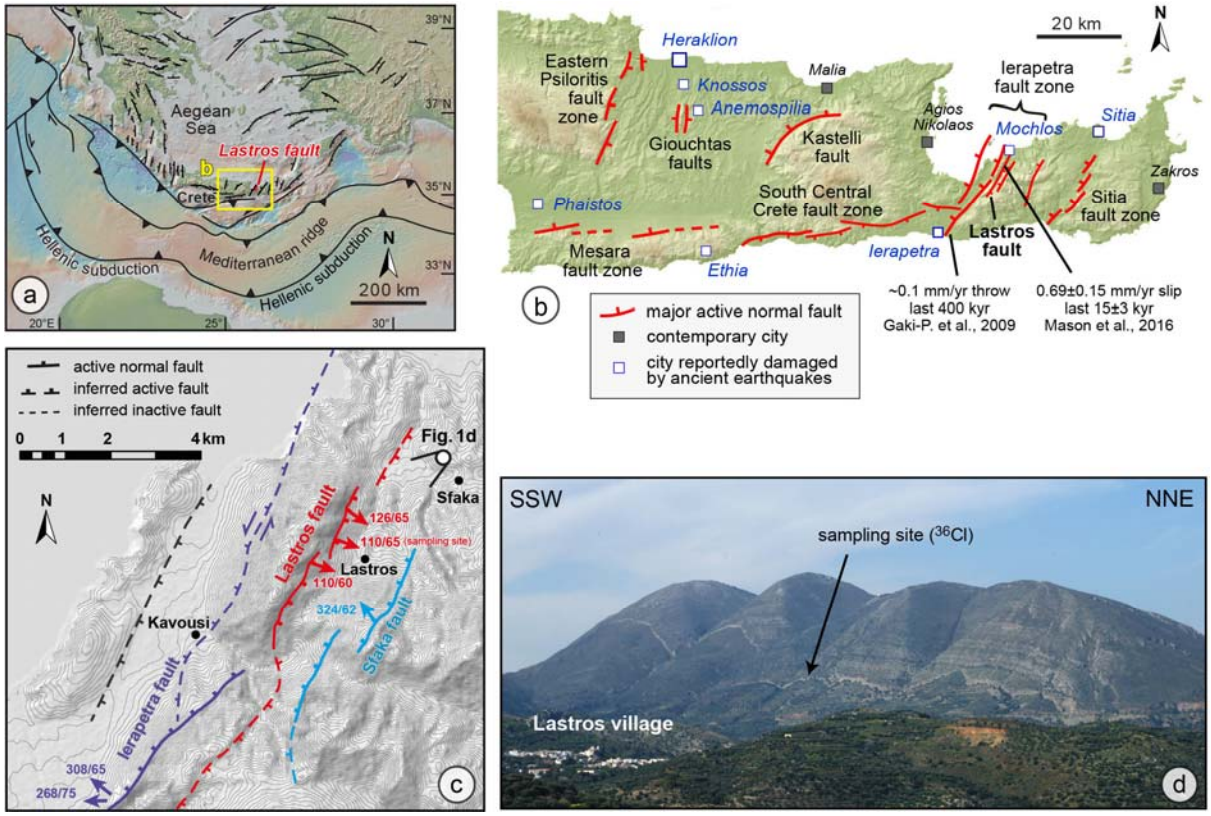

Figure 1: (a) Neotectonic map of SE Europe (faults after Jolivet & Brun, 2010). (b) Eastern Crete with major active faults (after Mason et al., 2016). (c) Major active faults in the western Thripti Mountains. Mapped striations are indicated. (d) View of the Lastros fault.

faulting rates. First, uplifted marine terraces that are displaced by the transtensional Ierapetra fault indicate a throw rate of ~0.1 mm/yr during the past ~400 kyr (Gaki-Papanastassiou et al., 2009) (Figure 1b). Secondly, geomorphic estimations along the Lastros fault suggest slip rates of 0.69 ± 0.15 mm/yr (Mason et al., 2016). This rate is based on the hypothesis that the exposed bedrock fault scarp (Figure 1c,d) was generated during the last 15 ± 3 kyr. So far, no dating was obtained on offset features of the 11-km-long Lastros fault and the amount of past coseismic offsets is unknown.

In this study, we map indicators of coseismic offsets on the bedrock fault plane of the Lastros fault. Furthermore, we use cosmogenic ^{36}Cl analysis to determine the age of the fault scarp, earthquake recurrence intervals and past slip rates.

METHODS

We mapped the Lastros bedrock fault to identify sites that are suitable to indicate past coseismic offsets. Ideally, the fault plane should have only been exhumed by earthquakes and remained exposed since each respective exhumation. Thus, suitable sites should not have been affected by denudation processes (e.g., channel incision, landsliding events, fault scarp degradation), depositional processes (e.g., alluvial or scree deposits) or anthropogenic processes (e.g., terrace formation for agriculture). Furthermore, we avoided locations where cemented colluvium is attached to the fault plane and locations near segment boundaries. Suitable sites are highly limited at the Lastros fault since most locations at the Lastros fault are affected by anthropogenic changes or the occurrence of cemented colluvium (Mason et al., 2016, 2017). At the suitable sites, indicators of relative exposure duration were examined by visual observations on the exposed fault plane (e.g. colour changes, lichen colonization changes, different karstification features; Mechernich et al., accepted). Scale bar measurements revealed the height of the exhumed stripes above the local scarp base. For absolute age constraints, cosmogenic ^{36}Cl samples were taken at the best-preserved site (Figure 2a-c). Therefore we used a battery powered angle grinder, hammer and chisel. At the scarp base, 1.2 m of soil were excavated to allow a precise analysis of the ^{36}Cl pre-exposure concentrations. The ^{36}Cl samples were chemically treated and measured at the University of Cologne using the protocols described by Gromig et al. (2018). The data was analysed with the Bayesian Monte Carlo Makrov Chain (MCMC) modelling code of Cowie et al. (2017) and Schlagenhauf et al. (2010).

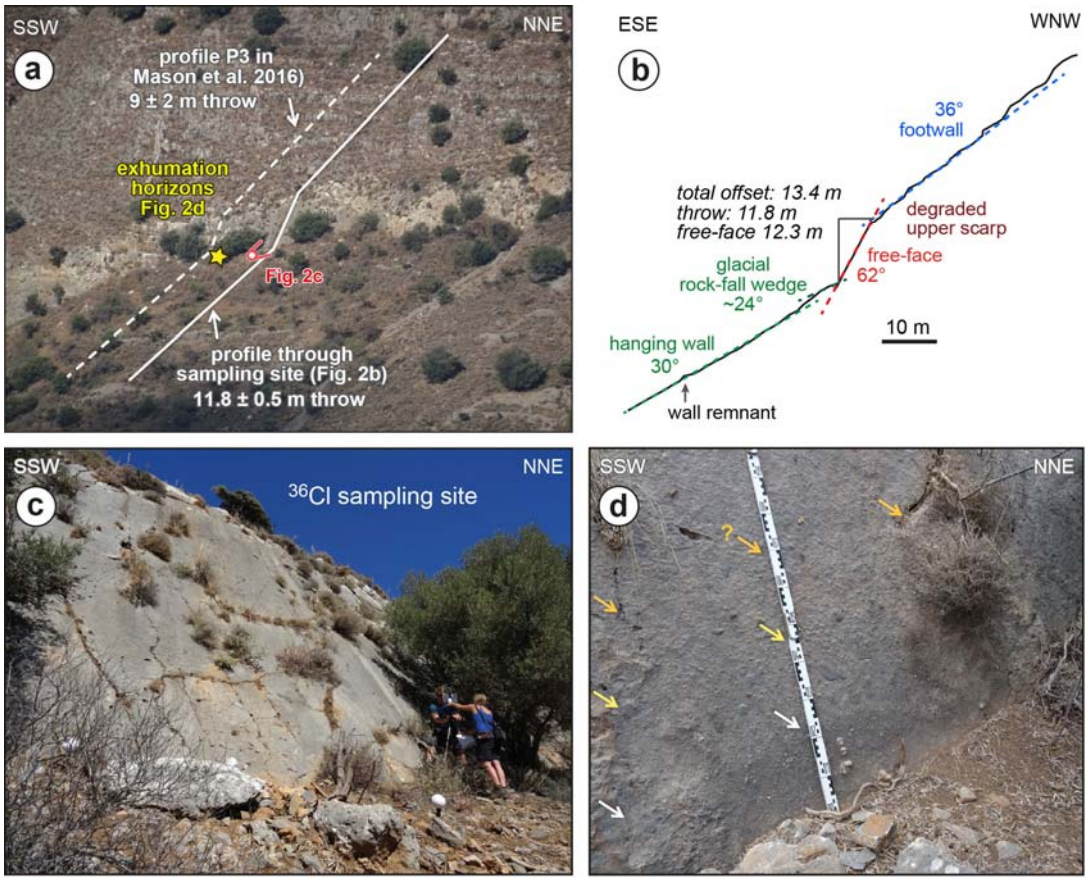

Figure 3: (a) Photographic overview around the sampling site. (b) Topographic profile across the sampling site obtained from measurements with clinometer and scale-bar. The profile reveals the fault scarp height and geometry, which are used as input parameters for the cosmogenic nuclide modelling. (c) Photograph of the sampling site, persons for scale. (d) Relative indicators of fault plane exposure. Horizon EQ1 (~23 cm high, white arrows) was identified by colour differences, horizon EQ2 (~47 cm high, yellow arrows) by a smoother appearance of the fault plane, particularly of outstanding clasts, the possible horizon EQ3 (~70 cm high, orange arrows) is weakly indicated by a terminating solution

RESULTS AND INTERPRETATIONS

The structural mapping revealed an average fault dip of 66° towards 114° with corrugations deviation ±25° from the fault strike. Striations obtained from recrystallized calcite and limonite minerals plunge on average 65° towards 110°, indicating a pure normal faulting character (Figure 1c).

Relative exposure duration observations

At some of the sites with stable hanging wall, horizontal stripes were detected based on different fault plane features. For instance, a darker stripe of 16-30 cm height occurred at three locations (Figure 2d). Above this, a second stripe appears until 45-62 cm height, which is characterized by a smoother appearance of the limestone surface (Figure 2d) and up to 20% coverage with white lichen (up to 2 cm large). The next stripe is characterized by a higher surface roughness and up to 4 cm large white lichen. A significant increasement of lichen colonization occurs in 68-80 cm height at five locations, showing partly complete fault plane coverage. Some solution flutes are ending at this height as well (e.g. Figure 2d).

These differences in surface colour, roughness and lichen colonization are interpreted as indicators of different exposure duration, as introduced by Mechernich et al. (accepted). Since we only used sites with minor non-tectonic surface changes, this suggests coseismic offsets of 16-30 cm for the last earthquake (EQ1), ~15-35 cm for EQ2 and ~20-30 cm for EQ3. Such coseismic offsets equal earthquake magnitudes of M_s 6.2-6.5 (±0.4) according to the empirical formula of Pavlides & Caputo (2004). This is in agreement with the expected magnitude of M_s 6.4 (±0.4) based on a surface rupture length of ~11 km.

^{36}Cl sampling site, age modelling

We sampled a very well preserved site at the central part of the Lastros fault (Figures 1d, 2a,c). The slope gradient is 36° on the footwall and 30° on the hanging wall except for three meters at the base of the fault scarp which are flatter (24°) due to the occurrence of a rock-fall wedge (Figure 2b).

Cosmogenic samples were taken every 30-100 cm from -1 m to 12.4 m scarp height. ICP-OES analyses revealed chemical compositions with ~38% ± 2% calcium. Hence, the majority of the ^{36}Cl nuclides are produced by spallation of calcium. The ^{36}Cl concentrations indicate an overall exponential increase with scarp height (Figure 3a). The parameters for the ^{36}Cl concentration modelling were obtained during fieldwork and they are given in Figure 3a. Modelling of theoretical ^{36}Cl concentrations for scenarios of different quasi-continuous exhumation rates do not result in a good fit of the obtained ^{36}Cl concentrations (Figure 3a). This suggests a temporal variability of the slip rate, which is underlined by 68,000 iterations in the Bayesian MCMC model (Figure 3b). To quantify exhumation rates, we divide the free-face in three parts and used the range of the 100 most likely exhumation scenarios (Figure 3b). According to this, the uppermost part of the free-face (12.4-7.0 m) was exhumed from 36 ± 2 kyr to 10 ± 2 kyr at a constant rate of ~0.2-0.3 mm/yr. A rather fast exhumation (0.6-1.2 mm/yr) occurred for the free-face between 7.0-0.75 m from 10 ± 2 to 2.9 ± 1.8 kyr. The lowermost ~75 cm were probably exhumed at an average rate of 0.2-0.7 mm/yr during three earthquakes in the last 2.9 ± 1.8 kyr.

DISCUSSION

For the fault plane below ~9 m, the obtained exhumation rates can be regarded as slip rates. This is based on the very well preservation of the fault plane and a lack of observed recent slope processes. The data suggest a slip rate variability during postglacial times with a period of highest slip from ~2.9 – ~10 kyr (Figure 3b). The last three earthquakes occurred most likely within the last ~4 kyr, which suggests a millennial earthquake recurrence interval. This agrees with the lack of historical earthquake reports and points to a recent slip deficit. Using the 25-cm of average coseismic offsets from the lower free-face, suggests a significantly shorter earthquake recurrence interval of ~150-400 yrs between ~2.9 – 10 kyr. Alternatively, the occurrence of larger coseismic offsets might be possible as well.

The fault plane exhumation rate of ~0.2-0.3 mm/yr should be regarded with caution during the glacial period since first, the amount of measured ^{36}Cl concentrations is limited, and secondly, a degradation of the upper scarp and sedimentation at the scarp base are expected due to enhanced frost weathering (Mason et al., 2017). Thus, the modelled exhumation rate at >9 m scarp height is most likely related to a mixture of tectonic exhumation and external processes. It appears that the average fault scarp height of the Lastros fault (~10.3 m, Mason et al., 2016) extends already in the last glacial period (~22 ± 2 kyr, *Figure 3b*). This is also the case when accounting for uncertainties of the modelling input parameters, which can result in a shift of ages and slip rates by up to ±15%. These findings suggest that the glacial erosion did not fully erode the Lastros fault scarp.

CONCLUSIONS

Different surface features indicate the relative exposure duration along the Lastros fault and allow the estimation of coseismic displacements for ancient earthquake events. The last three offsets were in the range of 15-35 cm, corresponding to M_s 6.2-6.5 earthquakes. ^{36}Cl concentrations of a well-preserved site reveal that the fault plane exposure can expand beyond the last glacial maximum. Slip rates can only be constrained for postglacial times due to significant erosion during the glacial period. The obtained postglacial slip rate variation of the ^{36}Cl concentration modeling suggests a slip deficit for the Lastros fault during the last 2.9 ± 1.8 kyr.

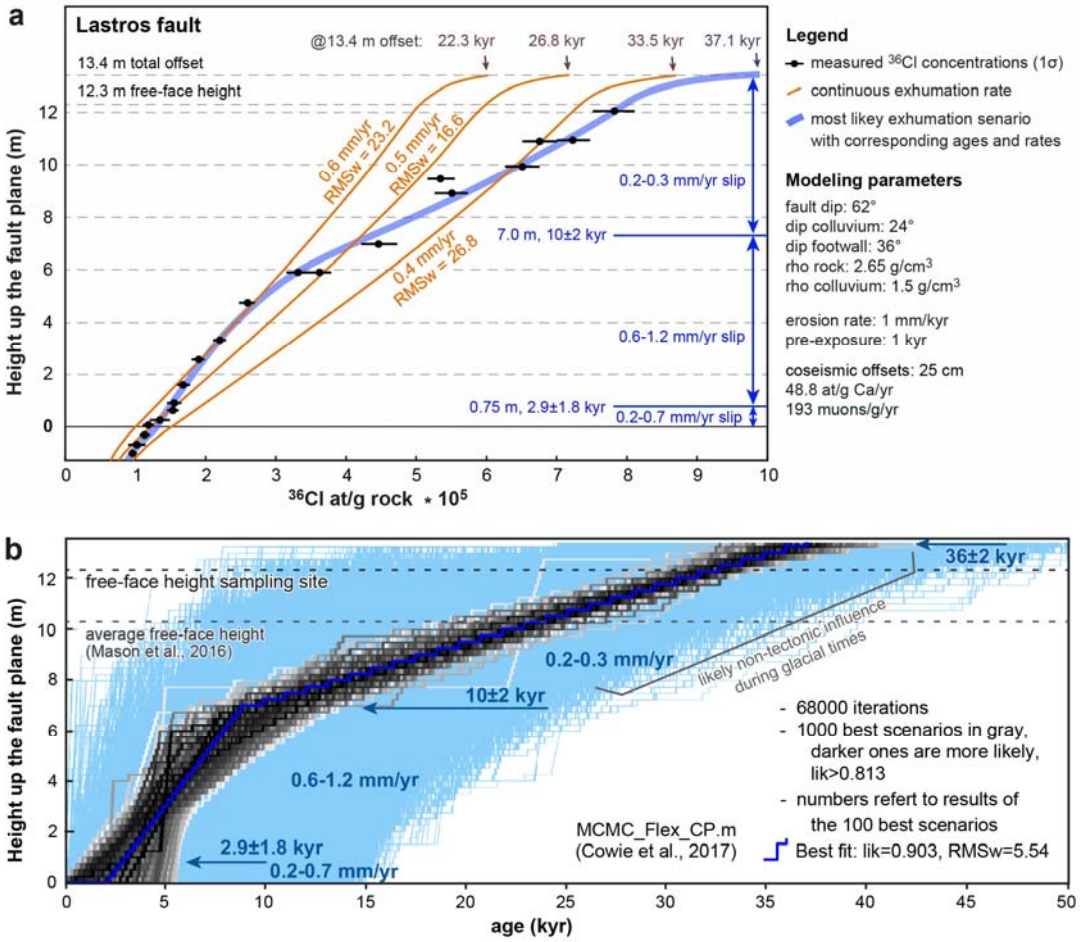

Figure 3: (a) The 20 measured ^{36}Cl concentrations along the Lastros fault plane and scenarios of their exhumation history with quasi-continuous exhumation curves in orange and the most likely exhumation history in blue. (b) Bayesian MCMC modelling of the exhumation history after 68,000 iterations.

Acknowledgements: We highly appreciate the help and discussions with Jakub Surma, George Deligiannakis, Jack Mason and Sascha Schneiderwind during the fieldwork. The financial support of the German Research Foundation (DFG, ME-4212/3-1) is gratefully acknowledged.

REFERENCES

Cowie, P.A., et al., 2017. Orogen-scale uplift in the central Italian Apennines drives episodic behaviour of earthquake faults. *Scientific Reports* 7, 44858.

European Mediterranean Seismological Centre (EMSC), 2018. Available online at: http://www.emsc-csem.org.

Gaki-Papanastassiou, K., Karymbalis, E., Papanastassiou, D., & Maroukian, H., 2009. Quaternary marine terraces as indicators of neotectonic activity of the lerapetra normal fault SE Crete (Greece). *Geomorphology* 104, 38-46.

Gromig, R., Mechernich, S., Ribolini, A., Wagner, B., Zanchetta, G., Isola, I., Bini, M., & Dunai, T., 2018. Evidence for a Younger Dryas deglaciation in the Galicica Mountains (FYROM) from cosmogenic ^{36}Cl. *Quaternary International* 464, 352-363.

Jolivet, L., & Brun, J.P., 2010, Cenozoic geodynamic evolution of the Aegean, *International Journal of Earth Sciences* 99, 109-138.

Mason, J., Schneiderwind, S. Pallikarakis, A., Wiatr., T., Mechernich, S., Papanikoloau, I., & Reicherter, K., 2016. Fault structure and deformation rates at the Lastros-Sfaka Graben, Crete, *Tectonophysics* 683, 216-232.

Mason, J., Schneiderwind, S., Pallikarakis, A., Mechernich, S., Papanikolaou, I., & Reicherter, K., 2016. Hanging-wall colluvial cementation along active normal faults, *Quaternary Research* 88, 39-59.

Mechernich, S., Schneiderwind, S., Mason, J., Papanikolaou, I., Deliginnakis, G., Pallikarakis, A., Binnie, S., Dunai, T., & Reicherter, K., (accepted): The seismic history of the Pisia fault (eastern Corinth rift, Greece) from fault plane weathering features and cosmogenic ^{36}Cl dating. *Journal of Geophysical Research - Solid Earth*.

Pavlides, S., & Caputo, R., 2004. Magnitude versus faults' surface parameters: quantitative relationships from the Aegean Region, *Tectonophysics* 280, 159-188.

Schlagenhauf, A., Gaudemer, Y., Benedetti, L., Manighetti, I., Palumbo, L., Schimmelpfennig, I., Finkel, R., & Pou, K., 2010. Using in situ Chlorine-36 cosmonuclide to recover past earthquake histories on limestone normal fault scarps: a reappraisal of methodology and interpretations. *Geophysical Journal International* 182, 36-72.

INQUA Focus Group Earthquake Geology and Seismic Hazards

paleoseismicity.org

Paleoseismological studies on Hinagu Fault, Kumamoto, Japan

Miyashita, Yukari (1), Azuma, Takashi (1)

(1) Research Institute of Earthquake and Volcano Geology, AIST, Site 7, 1-1-1 Higashi, Tsukuba, Ibaraki, 3058567 Japan, yukari-miyashita@aist.go.jp, t-azuma@aist.go.jp

Abstract: *We conducted 3 paleoseismological trench surveys on the Hinagu fault zone to narrow the width of range of probability of the occurrence of a large earthquake in near future. Hinagu fault zone is one of the longest right-lateral faults in Japan, which is located in central Kyushu. The epicenter of the 2016 Kumamoto earthquake located northernmost part of this fault zone and surface faulting occurred with ca. 7 km length along this fault zone. After this earthquake, seismicity was immediately increased along the middle part of this fault. ERC-HERP (2013) evaluated activity and segmented this fault zone based on the results of trench surveys on 4 sites inland and four site off-shore. However, these value are too wide to judge the urgency of future activity of this fault. Result of our trench surveys indicates that recurrence intervals is rather shorter and collapsed-time-ratio in the middle part is high.*

Keywords*: Active fault, Hinagu Fault, Kumamoto, Trenching survey, Long-term evaluation*

INTRODUCTION

Hinagu fault zone is one of the longest fault zone in Japan, with ca. 80 km in length. This fault zone located just south of the epicenter of the 2016 Kumamoto earthquake in Kyushu island. Along the most northern part of this fault zone, surface ruptures with right-lateral displacement less than 0.5 m appeared with the length of 7 km during 2016 event. Seismicity along this fault zone was rather high in Kyushu island, and it increased after 2016 event.

LONG-TERM EVALUATION OF HINAGU FAULT ZONE

Japanese earthquake research committee in HERP (Headquarters for Earthquake Research Promotions) have published reports on long-term evaluations of major active faults in Japan since 2002, as well as the probabilistic seismic hazard map of Japan. Evaluation report of Hinagu fault zone was published in 2002 and revised in 2013. Revised version includes new segmentation model for Hinagu and Futagawa fault zones. In 2002 version, Futagawa-Hinagu fault zone is consisted of 3 segments, northeast, central and southwest. In 2013 version, Hinagu fault zone was separated from Futagawa fault zone, which was added 2 concealed segment (Uto and Uto Peninsula Northwest coast) based on gravitical anormaly data, and was subdivided into 3 segments, Takano-Shirahata, Hinagu, and Yatsushiro sea. Slip rates of segment are 0.04-0.2 m/ka (vertical) for Takano-Shirahara segment, and 0.7 m/ka (right-lateral) and 0.2-0.5 m/ka (vertical) for Hinagu segment. The timing of the latest fault event of each segment is 1200-1600 cal yBP, 2000-8400 cal yBP, and 360-1700 cal yBP, respectively.

PALEOSEISMOLOGICAL SURVEY BEFORE THE 2016 KUMAMOTO EARTHQUAKE

Takano-Shirahata Segment

Takano-Shirahata Segment includes 3 faults in the previous fault catalogue (Acitive Fault Research Group of Japan, 1991), Takano, Shirahata, and Hinagu faults. This segment has NNE-SSW direction and length of 16 km (ERC-HERP, 2013).

NUPEC (1996) reported result of trenching surveys at Takaki site. They opened 4 trenches and 3 pits and concluded that the latest fault event occurred between (1200-1600 cal yBP) and rihgt-lateral and vertical offset were ca. 2.2 m and 0.3 m, respectively (Shimokawa & Kinugasa, 1999).

AIST (2008) conducted a trenching survey at Wanize site. They reported the latest fault event was occurred in Holocene.

Hinagu Segment

Hinagu segment includes Hinagu, Warabino-Deharu, Shinkai-Sakatani, Koura-Imaizumi and Hatajima-Sotohira faults of Active fault research Group (1991). A part of Hinagu fault is also called as Ono fault. Length of this segment is 40 km.

Kumamoto Prefecture (1997) reported result of trenching surveys at Takatsuka and Kakoi sites. They conducted two-lines of borings survey and 1 trench at Takatsuka site and 2 trenches at Kakoi site. AIST (2008) conducted a trenching survey at Minamibeta site. From these surveys, the timing of the latest fault event was identified between 2000 cal yBP and 8400 cal yBP. Other boring survey conducted by Kumamoto Prefecture (1996) and NUPEC (1996) showed that the vertical slip rate of this fault was 0.2-0.4 m/ka.

Based on the result of trenching surveys, 4 fault events are recognized and those ages are in 2000-8400 cal yBP, 12000-13000 cal yBP, 16000-19000 cal yBP and 30000-35000 cal yBP. Average recurrence intervals are estimated as 3600-11000 years. Average recurrence interval is culculated as 1100-6400 years.

Yatsushiro-oki Segment

Southwestern part of Hinagu fault zone continues into the Yatushiro Sea. This segment consist of several fault traces, that were identified by offshore seismic (sonic) profiling surveys.

From results of seismic profiling surveys and offshore boring surveys by Kumamoto Prefecture (1996) and AIST (2008), the timing of the latest event was identified between 900 cal. yBP and 1700 cal. yBP and the penultimate event occurred between 2800 cal. yBP and 7300 cal. yBP.

PALEOSEIMPLOGICAL SURVEYS AFTER THE 2016 KUMAMOTO EARTHQUAKE

Minamibeta

AIST conducted a trenching survey from January to March in 2017 at Minamibeta site, where a trench and boring surveys were conducted by AIST in 2008. Depth of trench is ca. 5 m. There are several layers of fine sediment in the shallow part and humic silt and gravels in the deeper part of trench. On the trench walls, reverse faults with large strike-slip component and high-angle fault were recognized. Reverse faults were dipping east with 40-50 degrees and cut a layer dated ca. 2,100 cal yBP and overlain by a layer dated ca. 1,200-2,100 cal.yBP.

Amount of offset along the reverse fault was ca. 1 m in the deeper part and ca 0.3 m in the shallow part. We interpreted it as not deference of the accumulation of displacement but decrease of slip toward surface, because structure of fault plane was very simple.

The penultimate event is inferred from flexural deformation of humic silt layer, which produced difference of height in the site, then fine sediments were distributed only in downthrown side of fault. This event occurred after sedimentation of humic silt and before the last event. Range of its age are between 2,100-10,000 cal yBP.

Rather older fault events are recognized from deformation of humic silt layers and gravel layers by high angle faults. We interpreted that two fault events occurred between 10000-20000 cal yBP.

Yamaide

This site is located in the valley of Midorikawa River and in the southernmost area of the surface rupture along Hinagu fault zone related to the 2016 earthquake. Displacement related to 2016 earthquake was very small (< 10 cm in vertical) and accompanied by echelon open cracks, showing right-lateral slip benease the sediments.

Depth of trench was ca. 4 m. Sediments observed on the wall were fine and soft. Several high-angle faults and flexures of leyses were observed on the north and nouth walls. A fault related to the penultimate fault event cut the layer with organic materials dated 800-926 cal yBP and overlain by the layer dated 800-926 cal yBP.

Another trench survey was conducted by Kyoto University group at Takaki on Takano-Shirahata segments.

Kawatamachi-nishi

Acknowledgements: These trenching surveys are part of the project by MEXT.

REFERENCES

Shirahama, Y., Yoshimi, M., Awata, Y., Maruyama, T., Azuma, T., Miyashita, Y., Mori, H., Imanishi, K., Takeda, N., Ochi, T., Otsubo, M., Asahina, D., & Miyakawa, A., 2016. Characteristics of the surface ruptures associated with the 2016 Kumamoto earthquake sequence, central Kyushu, Japan. *Earth, Planets and Space* 68 (191), doi: 10.1186/s40623-016-0559-1.

Earthquake Research Committee, Headquarters for Earthquake Research Promotion, 2013. Long-term evaluation of Futagawa and Hinagu fault zones (in Japanese).

Shimokawa, K., & Kinugasa, Y., 1999. Paleoseismicity and activity study of the Hinagu fault system (in Japanese with English abstract). Interim Report on Active Fault and Paleoearthquake Researches in the 1998 Fiscal Year, Geological Survey of Japan Interim Report no .EQ/99/3, 253-262.

INQUA Focus Group Earthquake Geology and Seismic Hazards

paleoseismicity.org

Changes in land level, gravity and sea level at the 2009 earthquake in Samoa

Mörner, Nils-Axel (1)

(1) Paleogeophysics & Geodynamics, Stockholm, Sweden, morner@pog.nu

Abstract: *The Samoa Islands were significantly affected by the September 29 nearby earthquake of Mw 8.1. We study the effect on the land level by means of GPS monitoring and on ocean level by tide-gauge records. This allows us to wind up a new picture of the interaction of crustal movements, gravitational adjustment and sea level changes. The land level exhibits a co-seismic uplift followed by a post-seismic crustal subsidence. The ocean level records a fall, significantly larger than the uplift and delayed by several months, followed by a significant rise, by far exceeding the crustal subsidence and delayed by several months. This indicates a significant contribution from changes in gravity (geoidal eustasy), besides relative sea level changes due to crustal movements.*

Keywords*: The Samoa Islands, 2009 earthquake, GPS record, gravity changes, sea level changes*

INTRODUCTION

The Samoan Islands are located in the Southwest Pacific just to the NE of the active plate boundary marked by the Kermadec-Tonga subduction zone (Fig. 1). The area has been struck by a number of high-magnitude earthquakes.

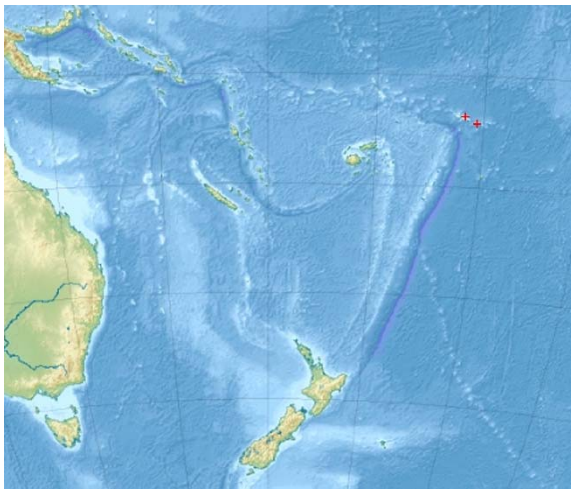

Figure 1: Location of the Samoa Islands (crosses) and epicentre of the 2009 earthquake just at the turn of the Kermadec-Tonga subduction zone.

On September 29, 2009, the Samoa region was struck by an earthquake of magnitude Mw 8.1. The epicentre was located 200 km south of the main Samoan Island chain, and at a depth of about 18 km below the seafloor. The earthquake was not caused by subduction, but by normal faulting in association with the bend of the plate boundary SW of the Samoan Islands (Fig. 1).

Because it was a normal faulting in the seabed, it set up a huge tsunami composed of, at least, 4 separate waves. The maximum tsunami wave height was 11.9 m, which implies that it reached a maximum level in the relation between earthquake magnitude and tsunami wave height (Mörner, 2017).

We investigated (Mörner et al., 2018) the effects of the September 29, 2009, earthquake (M_w 8.1) on the land level (by GPS) and the sea level (by tide-gauges) in the Samoa Islands; the stations on Upolu Island in Samoa and on Tutuila Island in American Samoa (Fig. 2).

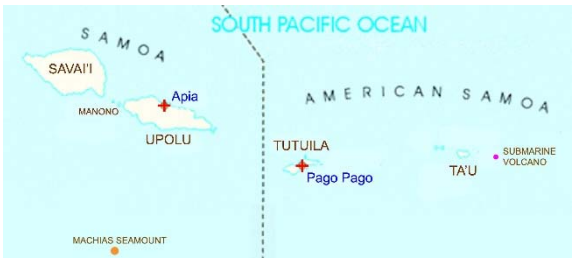

Figure 2: The Samoa Islands with the location of the tide gauge and GPS stations at Apia and Pago Pago,

THE CHANGES IN LAND LEVEL

Continual measurements of changes in the land level by means of GPS are available from Upolu Island in Samoa and from Tutuila Island in American Samoa (Mörner et al., 2018). The records are accessible form the SONEL (2018) and JPL (2018) databases. The SONEL records are more detailed but end in 2014. The JPL records end in 2018, and hence provide a longer record.

The GPS station on Tutuila Island (known as the ASPA station) lies 7 km to the NE of the tide gauge station location at Pago Pago. The GPS record provides a very detailed record of the changes in land level from 2002 to 2014 (Fig. 3). It gives a perfect image of the crustal response to a major earthquake; viz a pre-earthquake period of stability, an instantaneous co-seismic jump of +3.58 cm at the September 29 earthquake of 2009,

followed by a post-seismic subsidence of 9.10 cm in the first 4 years. The post-seismic subsidence decreases exponentially. It represents a crustal relaxation from the earthquake deformation. The rate of subsidence for the last 2 years (2012-2014) was 10.5 mm/yr. The pre-seismic rate is hard to see in the Fig. 3 graph of daily data. A graph of the weekly data from 2002 to 2008 gives a continual mean subsidence of -0.60 ±0.20 mm/yr. This is important, because it suggests that Tutuila Island may be experiencing a weak long-term subsidence.

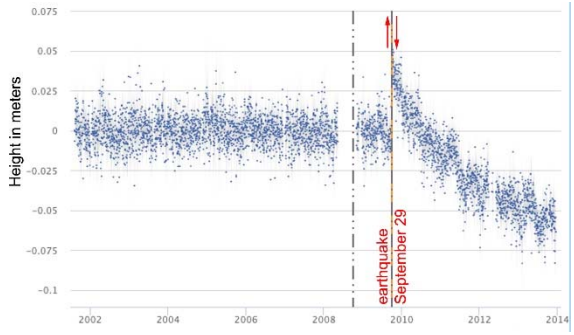

Figure 3: GPS record of the September 29, 2009, deformation at the station SE of Apia on Upolu Island; a co-seismic jump in the order of +2-3 cm followed by a post-earthquake subsidence of 6-7 cm.

The JPL record (2018) covers the period 2002-2018. It shows a pre-seismic period of weak subsidence (0.07 mm/yr), a co-seismic offset of -3.87 cm and a post-seismic subsidence, which for the last 6 years had a mean rate of 10.0 mm/yr. The subsidence has continued for more than 8 years. The GPS station on Upolu Island (at Fagali'i airport) is located 3.5 km the SE of Apia, where the tide gauge station is located. The SONEL record provides a good record of the changes in land level from 2002 to 2014 (Fig. 4), although the record is not as clear as the one from Tutuila Island (Fig. 3). It shows a fragmentary pre-seismic record, a co-seismic jump in the order of 2-3 cm, and a post-seismic subsidence in the order of 6-7 cm.

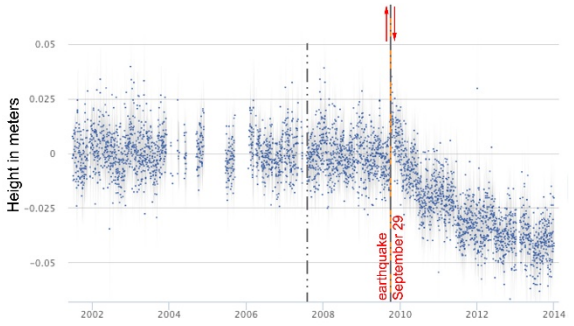

Figure 4: GPS record of the September 29, 2009, deformation at the station SE of Apia on Upolu Island; a co-seismic jump in the order of +2-3 cm followed by a post-earthquake subsidence of 6-7 cm.

The JPL (2018) covers the period 2002-2018. It shows a pre-seismic period of weak subsidence (-1.17 mm/yr), a co-seismic offset of -1.44 cm and a post-seismic subsidence at a rate of -5.89 mm/yr. The subsidence has continued for more than 8 years. The pre-seismic rate of subsidence (-1.17 mm/yr) is important because is suggests that the Upolu Island may be experiencing a weak long-term subsidence.

CHANGES IN SEA LEVEL

There are two tide gauges (PSMSL, 2018; Mörner et al., 2018) one at Pago Pago on Tutuila Island in American Samoa (station 539; PSMSL, 2018) and one at Apia on Upolu Island in Samoa (station 1840; PSMSL, 2018). The location of the stations is marked in Fig. 2.

The tide gauge of Pago Pago on American Samoa is managed by NOAA/NOS. The source of data is PSMSL (2018), station 539. It covers the period 1948-2016 with a completeness of 93% (Fig. 5). Spanning 68 years, this record qualifies for analysis of sea level changes. It records a pre-seismic subsidence of -2.21 ±0.81 mm/y (NOAA, 2018; Mörner et al., 2018), a some-what unclear co-seismic uplift (i.e. sea level fall) of 5-8 cm, and post-seismic subsidence of 19-22 cm with a recovery in less than a year.

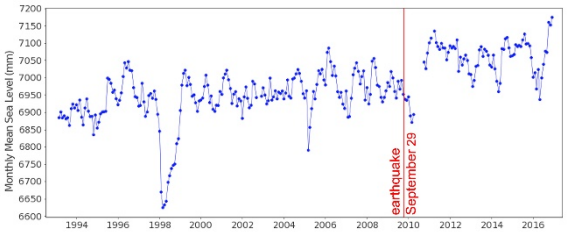

Figure 5: Tide-gauge record from the Apia station recording a pre-seismic subsidence (i.e. sea level rise) of -0.19 mm/yr, a co-seismic uplift (i.e. sea level fall) of 4.55 cm and a post-seismic subsidence of 10.0 cm lasting for 12 months. The 1998 sea level drop refers to the ENSO event.

The Apia tide-gauge station on Upolu Island is, in fact, two separate stations. Station 743 of PSMSL (2018) covers the period 1954-1971 (with a completeness of 82%). It shows a fairly straight trend of -0.19 mm/yr. Much more important is the Apia-B station or station 1840 of PSMSL (2018). It covers the period 1993-2016 with a completeness of 97%. Since 1998, it is a part of the Australian National Tidal Facility SEAFRAME (2018) project. The Apia-B station records a pre-seismic subsidence of 1.99 mm/yr, a co-seismic uplift (sea level fall) of 4.55 cm lasting for 4 months, and a post-seismic subsidence of 10.0 cm lasting for 12 months and followed by semi-stability during the last 6 years (Fig. 5). By comparison with the GPS records (Fig. 4), we can be sure that the signal in 2010 is caused by the 2009 earthquake, and has nothing to do with the ENSO-events recorded in 1998, 2005 and 2016.

The SEAFRAME (2018) data provides an improved picture of the deformation in sea level in association with the 2009 earthquake. It shows separate graphs for the high-tide level (HTL), the mean-tide level (MTL) and the low-tide level (LTL) with a tidal range in the order of 1.35 m. Fig. 6 gives the changes in tidal range from 1993 up to 2017. It shows minor oscillation within a zone of 125-145 cm. Right after the 2009 earthquake, the tidal range experiences very strong swings; viz by +65 cm in mid-January and -80 cm in in mid-June. This can only be understood in terms of significant changes in gravity involved in the post-earthquake changes. This is a novel and important observation, which makes any recalculation of observed relative sea level changes during the first years following the earthquake very complicated, if not impossible.

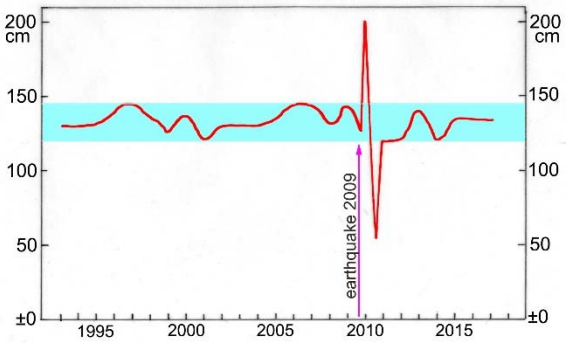

Figure 6: Changes in tidal range recorded at the Apia station. The normal level fluctuates between 125 and 145 cm (marked with a blue zone). Right after the 2009 earthquake, the tidal range increased to 200 cm and then fell to 55 cm, indicating significant changes in gravity in association to the seismically induced crustal movements. This is a novel observation on coastal seismo-tectonics (Mörner et al., 2018).

DISCUSSION AND CONCLUSIONS

The earthquake magnitude (M_w 8.1) and geogra-phical extension reaching far beyond the Samoa Islands imply that direct effects are likely to have affected both land and sea levels in the Samoan Islands. The GPS stations on Upolu and Tutuila Islands both record an instantaneous co-seismic uplift followed by an exponentially decaying subsidence (Figs. 3-4). The tide-gauge station close-by on the same islands both record a sea level fall followed by a sea level rise (Fig. 5). The tidal parameters from the Upolu station (Fig. 6) show large changes in the tidal range; first an increase of 65 cm, then a decrease of 80 cm with respect to the normal tidal range of about 135 cm. This indicates that changes in gravity are connected with the post-seismic changes in crustal and ocean levels. The combined changes in land level (red) and ocean level (blue) recorded at the stations on Tutuila (a) and Upolu (b) Islands are plotted in Fig. 7.

Right at the earthquake, the land levels jumps up by a few cm. This uplift is followed by a subsidence from a slowly relaxing crust, recorded by an exponentially decaying subsidence (continuing for, at least, a decade). The ocean level shows a fall taking a few months to culminate. The falls in sea level by far exceed the amount of uplift. Together with the delay in culmination, this enhanced fall in sea level (with respect to amount of uplift) is indicative of simultaneous gravitational changes deforming the gravitational potential surface (or geoid). The same applies for the subsequent rise in sea level, which, by far, exceeds the post-seismic crustal subsidence. Besides, it is significantly delayed with respect to the crustal subsidence phase.

In conclusion, Fig. 7 records the interaction of crustal movements, gravitational changes and sea level changes. The sea level changes are a combination of relative sea level changes due to tectonics and geoidal eustatic changes in sea level (Mörner, 1976).

The September 29, 2009, earthquake affected the land level of Upolu Island in the Samoan Islands and Tutuila Island in American Samoa by initiating a co-seismic uplift followed by crustal subsidence, and the ocean level at the same islands by sea level fall followed by sea level rise. Even the tidal amplitude was significantly deformed. The effects of the 2009 earthquake observed imply the interaction of crustal deformation, gravitational compensation and changes in sea level.

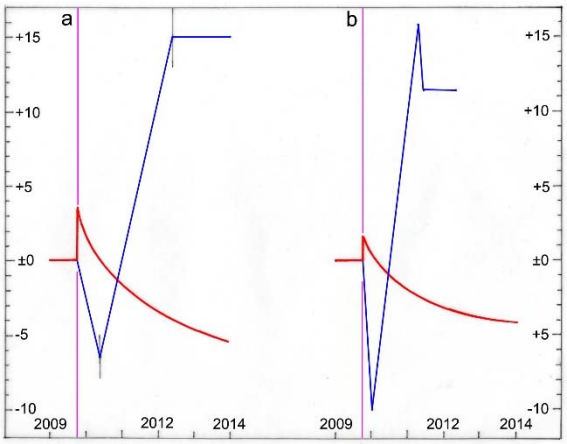

Figure 7: Synthesis of the observed change in land level (red) and sea level (blue) at the stations on Tutuila Island (a) and Upolu Island (b) in association with the September 29, 2009, Mw 8.1 earthquake (purple line).

Only by combining different records of the changes in land and ocean levels was it possible to wind up the complicated geodynamic processes linked to the 2009 earthquake.

The multiple forces interacting in the post-earthquake sea level changes make available tide-gage records from the Samoan Islands quite unsuitable for sea level studies of the post-2009 period.

Removing the earthquake effects on the sea level record, there is no longer any traces of a recent acceleration is sea level rise (Mörner et al., 2018; Parker et al., 2018).

Acknowledgements: This paper represents a summary of an extensive research paper by Mörner et al. (2018). This paper includes additional observational data and references to adequate literature.

REFERENCES

JPL, 2018. GPS data for (SAMOA.html) and (ASPA.html), sideshow.jpl.nasa.gov/post/links.

Mörner, N.-A., 1976. Eustasy and geoid changes. *Journal of Geology*, 84, 123-151.

Mörner, N.-A., 2017. Converting tsunami wave heights to earthquake magnitudes. *Open Journal of Earthquake Research* 6, 89-97.

Mörner, N.-A., Parker, A., & Matlack-Klein, P., 2018. Crustal subsidence induced by the 2009 Samoa earthquake as recorded by GPS and tide-gauge measurements. Submitted.

PSMSL, 2018. Data for stations 539, 743 and 1840. http://www.psmsl.org/data/obtaining/stations/539.php.

Parker, A., Mörner, N.-A., & Matlack-Klein, P., 2018. Sea level acceleration caused by earthquake induced subsidence in the Samoa Islands. *Ocean and Coastal Management*, in press.

SEAFRAME, 2018. http://www.bom.gov.au/ntc/IDO70062/-IDO70062SLI.shtml.

SONEL, 2018. Data for stations 631 (ASPA, American Samoa) and 831 (Samoa). www.sonel.or.

INQUA Focus Group Earthquake Geology and Seismic Hazards

paleoseismicity.org

Seismotectonic markers of the Hockai Fault Zone (East Belgium)

Mreyen, Anne-Sophie (1), Havenith, Hans-Balder (1)

(1) ULiège-University of Liege, 14 Allée du 6-Août, B-4000 Liege, Belgium, as.mreyen@uliege.be

Abstract: *The historic 1692 Verviers Earthquake (M_s 6-6.3) represents one of the most significant events in NW Europe, with its supposed epicentral area being located along the Hockai Fault Zone (HFZ) in East Belgium. This, and other seismic events in the past, characterises the 42 km long HFZ as a seismically active zone of multiple fault segments, which also crosses the entire Stavelot Massif. In this work, we present various geomorphological markers that can be used as proxy indicators to characterise the seismotectonic activity of the area. A special focus is laid on recently discovered geomorphological features in the region of Malmedy, i.e. a tectonic scarp in the orientation of the HFZ adjacent to two ancient slope failures. These features have been investigated by various geophysical techniques.*

Keywords*: geomorphological marker, tectonic scarps, seismic slope failures, geophysical prospection*

INTRODUCTION

Even though NW Europe, and especially Belgium, is not known as textbook example in the field of seismotectonics, East Belgium hosts one of the most important fault zones of the area. The NNW-SSE striking Hockai Fault Zone (HFZ; see location in Fig. 1a) is 42 km long and presents various geomorphological markers such as tectonic scarps, bedrock displacements, river diversion and landslides, that can be used as proxy indicators for its seismotectonic activity.

In terms of seismicity, the zone can be characterised as moderately active. It most likely produced the historical September 18, 1692, Verviers earthquake (M_s 6-6.3; Camelbeeck et al., 2000; Alexandre et al., 2008) in its northern part. The 1692 earthquake predominantly affected the northern Belgian Ardennes, but is also known as the strongest historical seismic event in north-western Europe with effects perceivable from Kent in England, to the Rhineland in Germany as well as to the Champagne in France. Historical records of the epicentral area (Verviers, Soiron, Herve and Montzen) and its surroundings (i.a. Liège, Aachen,–Stavelot and Malmedy) indicate intensity values of VII–VIII on the EMS-98 scale after Alexandre et al. (2008), as well as six aftershocks felt after the main event within a distance of 100-200 km around the epicentre. The high magnitude of the earthquake suggests a rupture of the entire bedrock; however, the origin of the seismogenic fault due to the 1692 event is not clearly established (Camelbeeck et al., 2000).

Since the beginning of the digital instrumental recording of seismic activity, 103 smaller earthquakes with hypocentral depths ranging from 5 to 10 km could be located inside the HFZ: in 1985, a ML 2.9 event occurred in the region of Malmedy; a few years later, between 1989 and 1990, a seismic sequence (with events of M_L=1.0-2.4) was recorded within a 12 km long zone in the North-East of Malmedy (see epicentre locations in Fig. 1b; Camelbeeck, 1993; Lecocq, 2011).

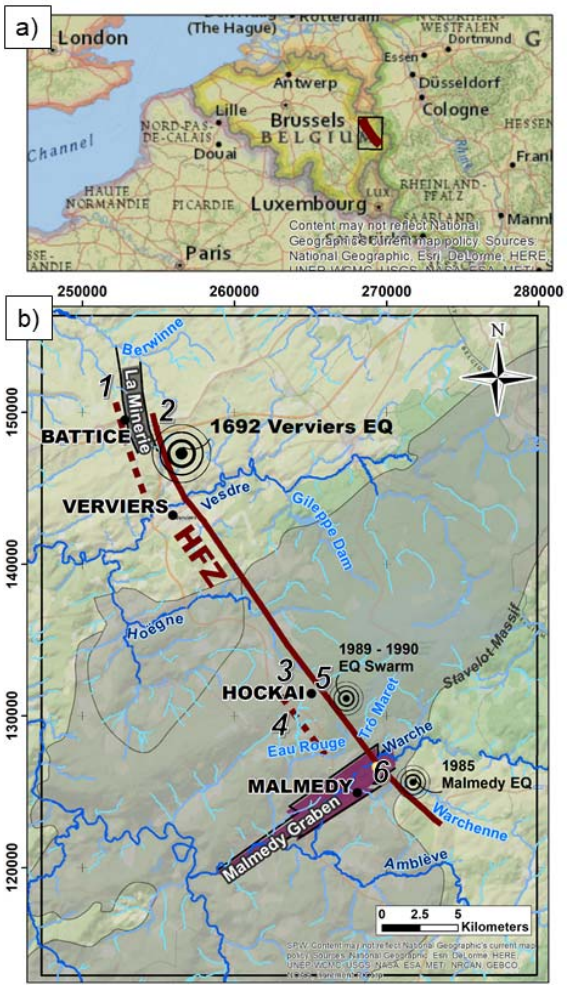

Figure 66: a) Location of study area in East Belgium. b) The eastern border faults of the Hockai Fault Zone (HFZ) marked by the continuous line, the parallel hatched lines refer to parallel supposed tectonic markers (i.e. conjugate faults and scarps). The three epicentre locations along the HFZ are marked by spots; the numbers refer to features explained in the text.

In this work, we discuss the various geomorphological markers along the HFZ and establish their seismotectonic context using geophysical techniques. Our focus is on the northern and a southern parts of the fault zone, i.e. the regions of Battice and of Hockai/Malmedy, respectively. Note that the well-defined segments of the HFZ are especially situated along its eastern border faults. Parallel to that, tectonic alignments and conjugate faults can be found in some areas (i.e. western border faults, see hatched lines in Figure 1b).

NORTHERN PART OF HFZ: REGION OF BATTICE

The northernmost segment of the HFZ is represented by the Minerie Graben ('1' in Fig. 1b), a tectonic depression showing strike-slip and normal displacement components of the local bedrock (Ancion & Ervard, 1957). In the vicinity of this graben, the *Pays de Herve* is affected by slope failure phenomena ('2' in Fig. 1b): at least 15 paleo-landslides developed in the rather favourable geological setting of liquefiable Aachen sands underlying soft Vaals clays (see Fig. 2). The spatial distribution and the probably simultaneous initiation of the Battice slope failures (50-250 AD; Demoulin et al., 2003) suggest combined triggering effects of repeated intense rain falls coupled with seismic events.

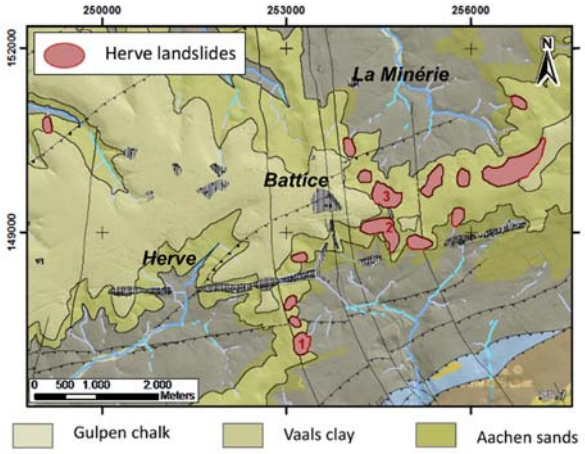

Figure 2: Landslide distribution in the 'Pays de Herve', region of Battice. Areas affected from landsliding (marked in red) show the presence of both, Vaals clays overlying liquefiable Aachen sands.

In 2016-2017, we performed several seismic and electrical tomographies as well as microseimsic H/V measurements, in order to detect the landslide depth or possible impacts of the HFZ passing through the region.

SOUTHERN PART OF HFZ: REGION OF HOCKAI/MALMEDY

The surroundings of the locality Hockai show various geomorphological markers that can be used as proxy indicators for the seismotectonic activity of the region: the assumed surface ruptures of Belheid ('3') and Baronheid ('4' in Fig. 1b; studied by Lecocq, 2011, and associated to the western border faults of the HFZ), as well as the Hoëgne River turn (occurring at the eastern border). Figure 3 shows an electrical resistivity profile that was realised across the Belheid scarp. The tomography clearly indicates a strong lateral resistivity contrast (from ~2000 Ωm to ~100 Ωm), suggesting bedrock rupture in its middle part.

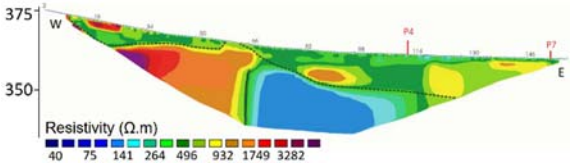

Figure 3: ERT of the Belheid scarp in the vicinity of Hockai (modified after Heeren, 2014).

The Hoëgne turn ('5' in Fig. 1b) of nearly 90° represents a clear marker of the tectonic alteration affecting the region. The river changed its course from a NE-SW orientation to the NNW-SSE striking direction of the HFZ. Other fluvial witnesses of the HFZ's impact are the river turns of the Warchenne and Amblève river (see Fig. 1b), as well as the river captures of the Trô Maret and Warche Rivers in the region of Malmedy (Pissart & Juvigné, 1982; Delvenne et al., 2004; Rixhon & Demoulin, 2018).

Recently, unknown seismotectonic features could be revealed near the southern end of the HFZ trace (Mreyen et al., submitted). In Bévercé, within the Malmedy Graben, a pronounced scarp next to two massive landslides ('6' in Fig. 1b) were discovered during a regional geological mapping project in 2015. The larger of both, here called Bévercé landslide, lies directly next to a NNW-striking steep scarp with a height of ~20 m and a length of ~ 100 m. The analysis of the new LiDAR-DEM of the area unequivocally confirmed the presence of these two landslides and the nearby scarp (see Fig. 4). Note, the landslides developed in the Permian fill of the tectonic Malmedy Graben, i.e. a layered conglomerate of calcareous-argillaceous cementation. Geomorphological analyses in the field revealed a disturbed landslide surface with hummocky structures, graben aperture at the landslide top as well as numerous single blocks that turned over along the slope (marked by changes in the original layer dip). Zones of internal reactivations can be found at the foot of the landslide (probably due to erosion phenomena after recent deforestation of the slope).

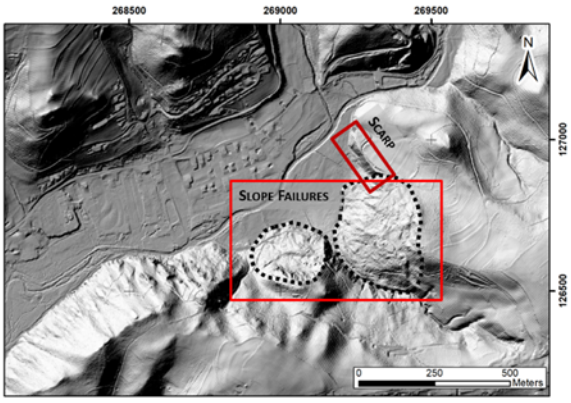

Figure 4: LiDAR-DEM showing recently discovered fault scarp and slope failures in Bévercé, region of Malmedy.

In order to understand the context of the Bévercé features, multiple investigation methods were applied on the big landslide and on the scarp area. Fig. 5 shows results of a geophysical prospection across the scarp in form of a 2D seismic refraction (SRT) and electrical resistivity tomography (ERT) along the same profile section.

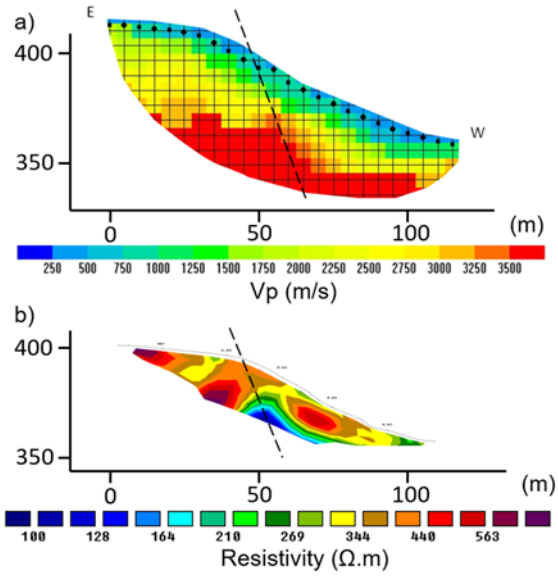

Figure 5: Fault detection along a profile crossing the Bévercé scarp (Malmedy) with hatched line indicating the assumed bedrock displacement. a) SRT. b) ERT.

We interpret the central part of the profile highlighted by laterally changing P-wave velocities (*Vp*) and lower electrical resistivities as a zone of more intense rock fracturing subject to increased groundwater flow, probably due to the presence of a fault. By assigning the higher (> 3500 m/s) *Vp* to the bedrock, we estimate that across this fault the bedrock was downthrown on the western side by about 15 m. These results mark the importance of the tectonic scarp in the seismotectonic context of the region, especially in combination with the adjacent deep-seated slope failures (indicating an energetic trigger event).

DISCUSSION

The Hockai Fault Zone (HFZ) in eastern Belgium has been intensively studied over the past 15 years in terms of geomorphological and seismogenic characteristics. All along the zone, various markers witness its impact on the landscape and geology at local and at regional scale. While the north-western part of the HFZ (region of Battice), as well as the intermediate parts around Hockai have been well established in its geomorphological and seismotectonic characteristics, the south-eastern part of HFZ (region of Malmedy) was exclusively defined by river diversion phenomena. With the recent discovery of the previously unknown geomorphological features, i.e. a tectonic scarp and landslides, new proxy indicators for the seismotectonic activity of the region could be defined. As described in Mreyen et al. (submitted), seismic events would best explain the initiation of the Bévercé slope failures, especially since they 'sit' on the fault, i.e. the prolongation of the tectonic scarp (identified as fault scarp by geophysics). To define the age of the features, however, comparison to the age of the Battice landslides in the north segment of the HFZ are not reliable due to their different geological setting and further studies are necessary.

Acknowledgements: We thank the Fund for Research Training in Industry and Agriculture (FRIA/F.R.S.-FNRS, Belgium) for supporting Anne-Sophie Mreyen with a PhD fellowship.

REFERENCES

Alexandre, P., Kusman, D., Petermans, T., & Camelbeeck, T., 2008. The 18 September 1692 earthquake in the Belgian Ardenne and its aftershocks. *Historical Seismology*, 209-230.

Ancion, C., & Evrard, E., 1957. Contribution à l'étude des failles Monty, Mouhy et d'Ostende dans la partie orientale du Massif de Herve. *Ann. Soc. Géol. Belgique* 80 (B), 477-488.

Camelbeeck, T., 1993. *Mécanisme au foyer des tremblements de terre et contraintes tectoniques : le cas de la zone intraplaque belge*. Unpublished PhD Thesis, Louvain-La-Neuve.

Camelbeeck, T., Alexandre, P., Vanneste, K., & Meghraoui, M., 2000. Long-term seismicity in regions of present day low seismic activity: the example of western Europe. *Soil Dynamics and Earthquake Engineering* 20 (5), 405-414.

Delvenne, Y., Demoulin, A., & Juvigné, E., 2004. L'évolution géomorphologique dans le secteur de l'ancienne confluence Warche-Trô Maret. *Hautes Fagnes* 4, 256.

Demoulin, A., Pissart, A., & Schroeder, C., 2003. On the origin of late Quaternary palaeolandslides in the Liège (E Belgium) area. *International Journal of Earth Sciences* 92(5), 795-805.

Heeren, M., 2014. *Caractérisation de la zone faillée de Hockai et évaluation de son potentiel géothermique*. Master Thesis, Liege University, 103.

Lecocq, T., 2011. *L'activité sismique en Ardenne et sa relation avec la tectonique active*. Thèse de doctorat, Observatoire royal de Belgique.

Mreyen, A., Demoulin, A. & Havenith, H., submitted. Seismotectonic activity in East Belgium: relevance of a major scarp and two associated landslides in the region of Malmedy. *Geologica Belgica*.

Pissart, A., & Juvigné, E., 1982. Un phénomène de capture près de Malmedy : la Warche s'écoulait autrefois par la vallée de l'Eau Rouge. *Annales de La Société Géologique de Belgique* 105, 73-86.

Rixhon, G., & Demoulin, A., 2018. The Picturesque Ardennian Valleys: Plio-Quaternary Incision of the Drainage System in the Uplifting Ardenne. In Landscapes and Landforms of Belgium and Luxembourg (pp. 159-175). Springer, Cham.

INQUA Focus Group Earthquake Geology and Seismic Hazards

paleoseismicity.org

Preliminary Paleoseismic Evidences of Active Faulting along the southern part of Gyeongju city, SE Korea

Naik, Sambit Prasanajit (1), Shin, Hyeonjo (1), Kim, Young-Seog (1), Jeong, SuHo (1), Kim, Taehyung (1), Lee, Jin-Hyun (1), Kyung, Jai Bok (2)

(1) Active Fault and Earthquake Hazard Mitigation Research Center, Dept. of Earth & Environmental Sciences, Pukyong National University, sambitnaik@gmail.com
(2) Department of Earth Sciences, Korea National University of Education

Abstract: *Gyeongju city is situated at the confluence point of a major fault system (Yangsan and Ulsan Fault System) along with several other minor faults. The Gyeongju earthquake (M_L =5.8; 12 September, 2016) is the largest instrumental earthquake in Korea, which has caused moderate damage around the city. Previous studies based on historical seismicity and archeoseismolgy suggest that Gyeongju area has experienced several large earthquakes in historical past around 768, 779, and 1036 AD. Despite having long historical records of earthquake damage, only a few paleoseismic studies have been reported around the Gyeongju city. In this present work, we have carried out detailed paleoseismic investigations along a newly identified active fault near to the southern part of Gyeongju. Though the data presented is very preliminary, needed more age dating and detailed interpretation of the earthquake sequences, this study will help us in understanding the earthquake history around the historical Gyeongju city.*

Keywords*: Active Fault, Paleoseismology, Gyeongju, Yangsan Fault, Ulsan Fault*

INTRODUCTION

Korean peninsula is considered to be seismically stable in comparison to neighbouring countries such as Japan, China and Taiwan (Choi et al., 2015). However, recent Gyeongju (M=5.8; 12 September 2016) and Pohang (M=5.4; 2017) earthquakes raised the concern about the earthquake hazard assessment along Korean Peninsula.

The Gyeongju earthquake was the highest ever instrumentally recorded earthquake in Korean Peninsula and caused moderate structural damages around the city. The historical city Gyeongju is situated at the confluence point of the Yangsan and Ulsan fault system, which is the most active fault system in the southeastern part of the Korean Peninsula. Based on the historical records and archeoseismological evidences reported, the study area has experienced several large earthquakes such as the destructive events occurred in 768 AD, 779 AD, and 1036 AD (Lee, 1998; Jin et al., 2009). From the historical and archeoseismological records, it is inferred that 779 AD and 1036 AD earthquake caused severe damages to the historical buildings like Hwangryongsa pagoda and Bulguksa Temple, which are situated in Gyeongju city.

Despite of having long historical records of earthquake damage, only a few paleoseismic studies have been reported around the city (Kee et al., 2009; Choi et al., 2015). Particularly the southern part of the Gyeongju have not been investigated in terms of active tectonics due to factors like presence of heavy vegetation, highly rugged topography, and human induced modification of landscapes. By keeping in mind historical and modern day seismicity around the city, we have tried to identify the Quaternary faults around the Gyeongju city under the Korean Active Faults Mapping project. In this present study, a new Quaternary fault has been identified and a detailed paleoseismic survey has been carried out for this fault. Though the data presented here is very preliminary after obtaining the ages of the faulting events exposed in the trench, it will help us in understanding the earthquake history of in and around the historical Gyeongju city.

TECTONIC AND GEOLOGICAL SETTINGS

Recently active fault mapping has been carried out along the southeastern part of the Korean Peninsula. It is suggested that the Cenozoic tectonic deformation is mainly associated with NNE-SSW or NNW-SSE trending faults, which were active during the opening and closing of East Sea (Choi et al., 2015). Since Pliocene the stress pattern has changed to E-W or ENE-WSW with dominant strike-slip with minor reverse slip components (Fig.1). The historical seismicity shows (Fig.2) most of the earthquakes in southeastern part of the Korean peninsula are confined along the Yangsan Fault and Ulsan Faults which have generally experienced multiple slips including early normal and strike-slip events (Kim et al., 2004). Fig. 3 shows the major tectonic features along the southeastern Korean peninsula.

The present study area, southern part of Gyeongju city, where historically reported damaged temples are located due to earthquakes (Jin et al., 2009). The study area is rugged mountainous area, mainly composed of Cretaceous Bulguksa biotite granite, Cretaceous shale, and Quaternary deposits (Fig.4). The Quaternary deposits are mainly composed of alluvial terrace and fan deposits. Major

structural feature is the N-S trending fault, which has displaced the alluvial fan surfaces. Though the fault is around 15-20 km long, the faulting mechanism and earthquake history has not yet been studied.

Figure 1: General Tectonic setting around the Korean Peninsula with major fault systems in SE Korea (Choi et al., 2015).

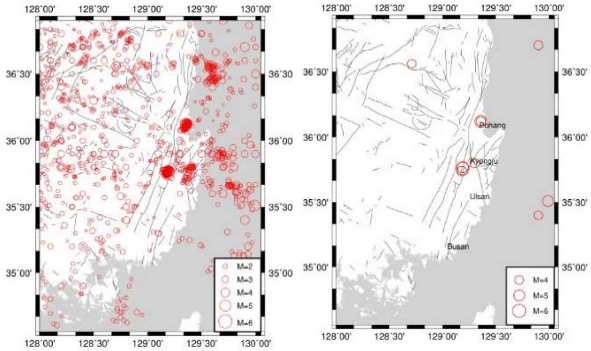

Figure 2: Historical and Instrumental seismicity around the Korean Peninsula and recent 2016~2017 earthquakes along the SE Korean Peninsula.

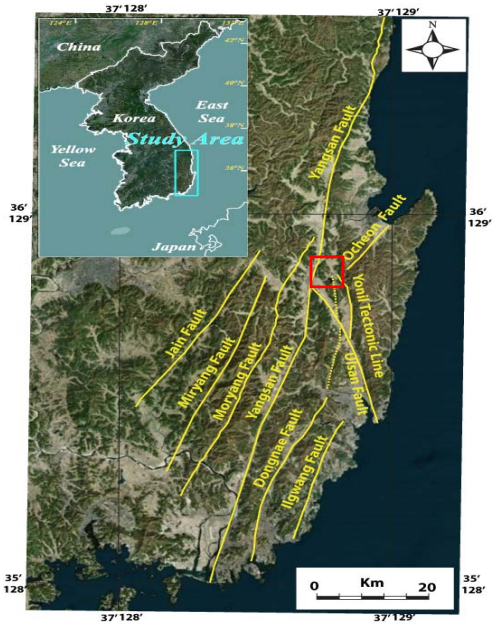

Figure 3: General tectonic map of the study area showing major faults and tectonic lines in the SE Korean Peninsula. Red box shows the area undertaken for present paleoseismic investigations and geological map presented in Figure 4.

LINEAMENT ANALYSIS AND ACTIVE FAULT MAPPING

Lineaments are the surface expression of underlying geological structures. Lineaments can be identified on the basis of geomorphic markers offset by the recent tectonic activity along those lineaments.

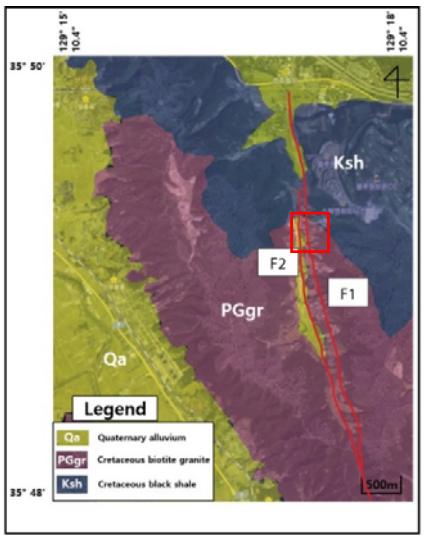

Figure 4: Geological map showing the geological deposits along with the mapped lineament (red box shows the area taken for detailed paleoseismic investigations.

In the tectonic regimes with slow slip rate like Korea, lineament analysis can be very useful in identification of active faults and related landforms. In the present study, we have analysed the lineaments and classified the tectonic lineaments on the basis of tectonic landforms such as linear valley, deflected and offset streams, uplifted alluvial fans and fluvial terraces. From the lineament analysis, it is inferred that most of the lineaments are aligned to the NE-SW direction with some N-S and NW-SE directions (Fig. 4).

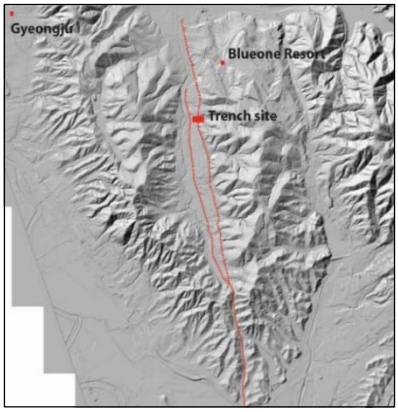

Figure 5: LiDAR derived DEM showing the newly identified lineaments around Gyeongju city, SE Korean Peninsula.

It is well matched with the trend of the major structural features i.e. Yangsan, Ulsan and Dongnae faults around the study area. According to Kim et al. (2004), the maximum principal stress direction of Korean Peninsula is EW which results into the NE-SW lineaments/ faults.

From the LiDAR data and aerial photo acquired by Korean Space Agency in 1954 (Fig.5), we were able to identify two parallel running lineaments in the study area, namely F1 and F2 (Fig. 4 and 5) with strike of almost N-S. The traced length of the lineament is around 10-15 km, which may have caused the formation of alluvial fans and uplifted fluvial terraces around the study area. From the field outcrop, the presence of fault gouge between granitic bed rock and basaltic dikes was firstly observed in the area (Fig. 6).

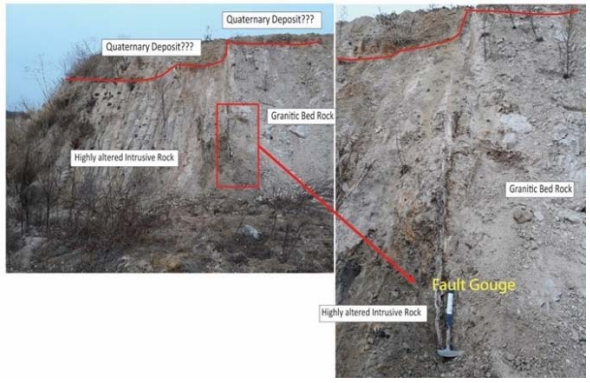

Figure 6: Field photographs showing fault gouge and quaternary faulting along the newly identified fault.

DETAILED FIELD AND PALEOSEISMIC INVESTIGATIONS

On the basis of preliminary lineament and geomorphic analysis, a detailed field survey has been carried out around the study area. In the field along an exposed construction site, we observe basement fault between granite and basaltic dike with presence of 2-7 cm fault gouge and fault breccia, which is covered and displaced the overlying quaternary deposits along F1 (Fig. 4). The fault gouge is mainly clayey gouge with different colours (red, white and grey) with sharp contact with each other, which may indicate the fault has moved multiple times in historical past.

Field photograph showing the fault gouge between granitic bed rock and basaltic dyke displacing overlying quaternary surfaces along F1 is shown in Figure 7. As it can be seen in the field photo, the outcrop has been modified by the construction work. Thus, one trench has been excavated towards south of the outcrop to understand the earthquake history, recurrence interval, and most recent earthquake along this fault on the basis of stratigraphic offset of the quaternary sediments.

A trench with dimension of 8 m length × 2 m wide and almost 7 m deep was excavated across the scarp along F1 (Fig.8). On the basis of rock type, boulder size, sorting, colour or matrix, and underlying as well as overlying surfaces of the quaternary layer exposed in the trench, the exposed section was classified into 10 different units. In the trench, we observed the fault zone comprised two parallel faults F1 and F2 forming a wide deformation zone.

Unit-A is the oldest unit and Unit -J is the youngest unit. Unit-A is mainly highly fractured granite and exposed at the base of the trench in the both side of the fault and is more than 3 m thick. Towards west side of the fault F1, Unit-B makes a typical triangular wedge shape and have sharp contact with the fault plane. Unit B is mainly composed of granite wash deposits containing small pebbles of host granitic rocks. Since the age is not determined now, it is very difficult to say about the age of the granite wash deposits and the first faulting event in Quaternary time. Unit-B is covered by Unit-C, which is composed of rounded pebbles with sand matrix and forms a typical lens/wedge shape and most probably composed of scarp derived materials with sharp contact with the fault. The contact between the Unit-B and Unit-C is irregular, which indicates the Unit-B was exposed to erosion for some time before deposition of Unit-C.

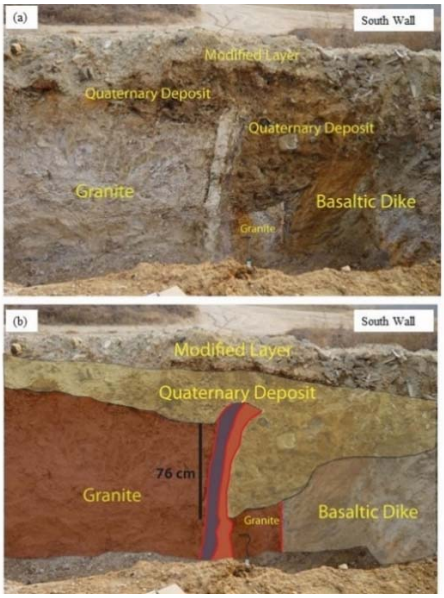

Figure 7: Pit showing the evidences of Quaternary faulting long the lineament 2.

Similarly Unit-D cover the Unit-C and forms another wedge shaped layer. Unit-D is mainly composed of angular pebbles with sand/silt matrix with very sharp contact with the fault. The thickness of this unit is around 1 m near the fault plane and gradually decreases with distance from the fault plane. The Unit-D is covered by Unit-E which is composed of angular pebbles with silty clay matrix and is around 1 m thick. The Unit-E also shaped like a typical wedge, which is mainly formed due to scarp derived material. Unit-E is covered by small patches of sandy deposits with greyish and reddish matrix named as Unit-F and Unit-G, respectively.

From the stratigraphic relationship of underlying and overlying layers, it can be inferred that after the faulting event, which displaced the Unit-E, Unit-F and Unit-G got deposited, but with time it got eroded leaving only the small patches. These units are covered by Unit-H, which is displaced by the fault and cover the entire units below. Unit-H is having few cm thicknesses on the east side of the fault and around 1 m thickness on the west side of the fault, which indicates that the unit got displaced by the fault. Unit-I, mostly organic rich with present day plant roots covering the entire section of the trench, indicates that it is a recent surface. The thickness of the Unit-I is varying through its length but is not more than few cm all along its extent. Above Unit-I, the exposed section is having more than 4-meter-thick landfill deposits and are

deposited due to the ongoing construction work nearby and named as Unit-J.

On the basis of unit exposed in the trench and its crosscutting relationship with the fault, our preliminary interpretation indicates that the fault has experienced at least four Quaternary earthquakes. First earthquake occurred along the Fault F1a which formed a colluvial wedge i.e., Unit-C. Subsequently two more earthquakes occurred along F1a and F2 after the deposition of Unit-C forming other colluvial wedges i.e. Unit-D and Unit-E, respectively.

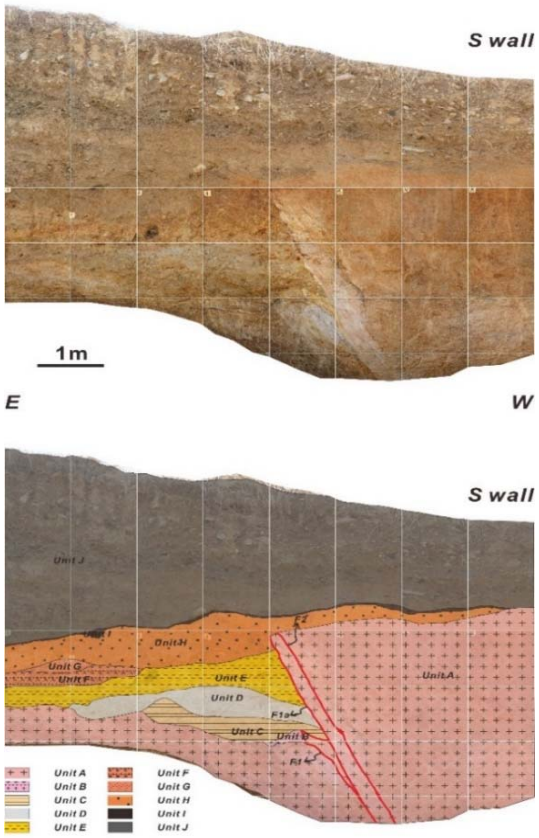

Figure 8: Photomosaic and log of the trench wall.

The most recent earthquake may have occurred after deposition of Unit-H, which is displaced by the fault and covered by the Unit-H. To understand the sequence of faulting and timing of earthquakes, both charcoal and OSL samples have been collected from the Units B, C, D, E, G, and H. The earthquake and faulting sequence will be further enhanced after obtaining the ages.

DISCUSSION

From the Historical records, it is understood that the Korean Peninsula, especially the south-eastern part is continuously facing earthquakes in historical past. Despite of having well documented historical record of earthquakes, there is still lack of proper and regional scale active fault mapping for the Korean Peninsula. Also the timing and recurrence intervals of those earthquakes are not poorly constrained for Korean Peninsula. This may be due to slow slip rate, long recurrence interval of large magnitude earthquakes, very rugged terrain, and rapid urbanisation.

The recent finding of the active fault around the southern part of Gyeongju city, which is close to the epicenter of the 2016 Gyeongju earthquake (M=5.8), may help us understanding the earthquake dynamics and active fault research in and around the area. With combination of advanced techniques such as LiDAR with old tools like aerial photos and adoption of proper age dating techniques may help for identifying more active faults around the area. With identification of more active faults, we will be able to quantify the earthquake parameters such as lengths of the faults, magnitudes of the earthquakes, geological slip rates, and recurrence intervals of large magnitude earthquakes, which will further help in preparing a better seismic hazard assessment for the study area.

CONCLUSIONS

Using aerial photos, geological maps, and detailed field survey, a new active fault of more than 10-15 km long was identified. From the exposed outcrop and the presence of multiple coloured fault gouges, it can be inferred that the fault has moved several times in historical past. On the basis of cross cutting relationship exposed in the trench with fault and presence of multiple colluvial wedges, it can be concluded that the fault has experiences multiple earthquakes in recent past by displacing the quaternary deposits. With more detailed logging and age dating, the timing of earthquakes, its recurrence intervals, and the most recent earthquake along this fault can be discussed in the near future. The present finding with age dating and with the integration of historical data will help us in understanding the earthquake cycle around the Gyeongju city and also around the South Eastern Korean Peninsula.

Acknowledgements: This research is supported by funding from Korean Active Fault Mapping Project funded by Korean Ministry of Public Safety and Security (MPSS).

REFERENCES

Choi, J.H., Kim, Y.S., & Choi, S.J., 2015. Identification of a suspected Quaternary fault in eastern Korea: Proposal for a paleoseismic research procedure for the mapping of active faults in Korea. *Journal of Asian Earth Sciences* 113, 897-908.

Jin, K., Lee, M., & Kim, Y.-S., 2009. Geological study on the collapse of a carved stone Buddha statue in Yeolam valley of Namsan, Gyeongju, Korea. *Journal of the Geological Society of Korea* 45, 235-247 (in Korean with English abstract).

Kee, W.-S., Kihm, Y.H., Lee, H., Cho, D.L., Kim, B.C., Song, K.-Y., Koh, H.J.,Lee, S.R., Yeon, Y.-K., Hwang, S., Park, K.G., & Seong, N.-H., 2009. Evaluation and database construction of quaternary faults in SE Korea. Korea Institute of Geoscience and Mineral Resources, IP2006-047-2009(1) (in Korean).

Kim, Y.-S., Park, J.Y., Kim, J.H., Shin, H.C., & Sanderson, D.J., 2004. Thrust geometries in unconsolidated Quaternary sediments and evolution of the Eupchon Fault, southeast Korea. *Island Arc* 13, 403-415.

Kim, Y.-S., Kihm, J.-H., & Jin, K., 2011. Interpretation of the rupture history of a low slip-rate active fault by analysis of progressive displacement accumulation: an example from the Quaternary Eupcheon Fault, SE Korea. *J. Geol. Soc.* 168, 273-288.

INQUA Focus Group Earthquake Geology and Seismic Hazards

paleoseismicity.org

Using Direct Push *in situ* sensing techniques and geophysical studies for tracing tsunami signatures at the Gulf of Kyparissia (Peloponnese, Greece)

Obrocki, Lea (1), Vött, Andreas (1), Wilken, Dennis (2), Fischer, Peter (1), Willershäuser, Timo (1), Koster, Benjamin (3), Lang, Franziska (4), Papanikolaou, Ioannis (5), Rabbel, Wolfgang (2), Reicherter, Klaus (3)

(1) Institute of Geography, Johannes Gutenberg-Universität Mainz, Johann-Joachim-Becher-Weg 21, 55099 Mainz, Germany, lobrocki@uni-mainz.de
(2) Institute of Geosciences, Applied Geophysics, Christian-Albrechts-Universität zu Kiel, Germany
(3) Institute of Geosciences, Neotectonics and Natural Hazards, Rheinisch-Westfälische Technische Universität Aachen, Germany
(4) Department of Classical Archaeology, Technische Universität Darmstadt, Germany
(5) Institute of General and Environmental Geology, Agricultural University of Athens, Greece

Abstract: *We conducted* in situ *direct push sensing measurements using different techniques (HPT, CPT, seismic CPT) in combination with surface-related seismic investigations in order to trace tsunami landfall along the Kaiafa Lagoon and the former Mouria Lagoon (western Peloponnese, Greece). Based on this new approach, the lateral and vertical variability of tsunami signatures in the local geological record were recognized. Compared to coring, direct push techniques offer a quick and cost-efficient approach to identify and characterize allochthonous tsunami deposits within coastal sedimentary sequences.*

Keywords*: Direct push sensing, geophysics, tsunami deposits, Peloponnese, Greece*

DIRECT PUSH TECHNIQUES USED FOR TRACING TSUNAMI SIGNATURES

The western Peloponnese is known to have been hit by major tsunami impacts during historical times as reported by historic accounts and recorded in historical earthquake and tsunami catalogues. During the past years, geomorphological and sedimentary evidence of repeated Holocene tsunami landfall was found between Cape Katakolo in the north and Kyparissia in the south (Vött & Kelletat 2015). Additionally, neotectonic studies revealed strong crust uplift along regional faults with amounts of uplift between 13 and 30 m since the mid-Holocene (Papanikolaou et al., 2007, Vött et al., 2015).

This study focuses on the detection of historically young tsunami impacts, sedimentary and microfaunal evidence of which were reported from the eastern shore of the Kaiafa Lagoon (Koster et al., 2015) as well as on further Holocece tsunami signatures found in the former Mouria Lagoon near Pyrgos (Willershäuser et al., 2015). Moreover, numerical simulation of tsunami inundation along the central Gulf of Kyparissia are well consistent with field traces of tsunami impact (Röbke et al., 2016).

We conducted detailed surface-based geophysical prospection by means of electrical resistivity measurements (ERT) and seismic studies. These investigations were completed by direct push *in situ* sensing at specific points along geophysical transects. A Nordmeyer drill rig RS 0/2.3 with a mounted Geoprobe pushing device (Fig. 1) was used. In a first step, we carried out direct push electrical conductivity (EC) measurements. In a further step, a hydraulic profiling tool (HPT) was used and cone penetration tests (CPT) were realized, the latter also in the form of seismic CPT. Direct push EC, HPT and CPT data were logged with a vertical resolution of c. 2 cm.

Figure 67: Direct push sensing used to achieve in situ *data characterizing Holocene sedimentary sequences. Geoprobe equipment mounted on Nordmeyer RS 0/2.3 drill rig, University of Mainz.*

Direct push methods helped to analyze *in situ* high-resolution stratigraphic records in search of different kinds of sedimentological and geomorphological indicators of high-energy inundation, such as abrupt increase in grain size and fining upward sequences representing different tsunami inundation pulses. We further coupled surface-based ERT and seismic data with highly resolved vertical datasets obtained by direct push sensing and sediment core characteristics in order to improve the quality of geophysical models. Moreover, direct push data were used to calculate the sand fraction for sites where no sediment cores were drilled based on multivariate linear regression analyses.

We present details of this methodologial approach newly applied in the framework palaeotsunami research and discuss how the obtained results can help to improve tracing tsunami signatures in the sedimentary record and deciphering geomorphological characteristics of past tsunami inundation.

Acknowledgements: AV and FL thank the German Research Foundation for funding our research activities in the western Peloponnese (LA 1183/9-1, VO 938/19-1, project number 270113181).

REFERENCES

Koster, B., Vött, A., Mathes-Schmidt, M. & Reicherter, K., 2015. Geoscientific investigations in search of tsunami deposits in the environs of the Agoulinitsa peatland, Kaiafas Lagoon and Kakovatos (Gulf of Kyparissia, western Peloponnese, Greece), *Zeitschrift für Geomorphologie N.F., Supplementary Issue* 59/4, 125-156.

Papanikolaou, D., Fountoulis, I., & Metaxas, C., 2007. Active faults, deformations rates and Quaternary palaeogeography at Kyparissiakos Gulf (SW Greece) deduced from onshore and offshore data. *Quaternary International* 171-172, 14-30.

Röbke, B.R., Schüttrumpf, H., & Vött, A., 2016. Effects of different boundary conditions and palaeotopographies on the onshore response of tsunamis in a numerical model - a case study from western Greece. *Continental Shelf Research* 124, 182-199. http://dx.doi.org/10.1016/j.csr.2016.04.010

Vött, A., & Kelletat, D., (Eds.) 2015. Holocene palaeotsunami landfalls and neotectonic dynamics in the western and southern Peloponnese. The past as a key to the present and predictor of the future. *Zeitschrift für Geomorphologie N.F., Supplementary Issue* 59/4.

Vött, A., Fischer, P., Röbke, B.R., Werner, V., Emde, K., Finkler, C., Hadler, H., Handl, M., Ntageretzis, K., & Willershäuser, T., 2015. Holocene fan alluviation and terrace formation by repeated tsunami passage at Epitalio near Olympia (Alpheios River valley, Greece). *Zeitschrift für Geomorphologie N.F., Supplementary Issue* 59/4, 81-123. http://dx.doi.org/10.1127/zfg_suppl/2014/S-00209

Willershäuser, T., Vött, A., Hadler, H., Fischer, P., Röbke, B.R., Ntageretzis, K., Emde, K., & Brückner, H., 2015. Geo-scientific evidence of tsunami impact in the Gulf of Kyparissia (western Peloponnese, Greece). *Zeitschrift für Geomorphologie N.F., Supplementary Issue* 59/4, 43-80. http://dx.doi.org/10.1127/zfg_suppl/2014/S-00189

INQUA Focus Group Earthquake Geology and Seismic Hazards

paleoseismicity.org

Unravelling the paleoseismological history of Achensee (Western Austria) combining on- and off-fault sublacustrine signatures

Oswald, Patrick (1), Moernaut, Jasper (1), Fabbri, Stefano (2), Hilbe, Michael (2), De Batist, Marc (3), Strasser, Michael (1)

(1) Institute of Geology, University of Innsbruck, Innrain 52, 6020 Innsbruck Austria
(2) Institute of Geological Sciences, Oeschger Centre of Climate Change Research, University of Bern, Baltzerstr. 1+3, 3012 Bern, Switzerland
(3) Department of Geology, Renard Centre of Marine Geology, Ghent University, Krijgslaan 281s.8, Ghent B-9000, Belgium

Abstract: *First lacustrine geophysical data has been acquired on Achensee in Tyrol, Western Austria, which has – despite its intraplate seismotectonic setting – a remarkably high seismicity due to ongoing Alpine shortening. From preliminary interpretation of reflection seismic profiles, the hypothesis rises that the postglacial Achensee sediments uniquely records both primary (i.e. surface ruptures) and secondary (e.g. multiple mass-transport deposits, megaturbidites) paleoseismic evidence of active seismotectonic faulting. This hypothesis will be tested in an innovative scientific approach using lacustrine and terrestrial geophysical datasets and calibrate them by sediment long coring and structural field mapping of Pleistocene sediments.*

Keywords*: Lacustrine Paleoseismology, Active Tectonics, Achensee, Austria*

BACKGROUND

Short historical and even shorter instrumental seismicity records limit our perspective of earthquake occurrence and maximum magnitude for the European Alps, which are characterized by low crustal deformation rates and thus long recurrence rates of severe earthquakes. Therefore, high-quality paleoseismic data is crucial for reliable seismic hazard assessments. Primary paleoseismic evidence such as surface ruptures or offset horizons is scarcely found in the Alps and only little on-fault geological evidence of post-LGM surface ruptures has been documented (e.g. Ustaszewski & Pfiffner, 2008; La Taille et al., 2015; Fabbri et al., 2017; Hintersberger et al., 2018). The scarceness of such primary paleoseismic evidence is probably attributed to pervasive anthropogenic landscape modification, gravitational slope processes and high erosion rates in the Alpine region. To overcome the limitation of first order evidence in the Alpine region, lacustrine paleoseismology has focused primarily on off-fault paleoseismic evidence,

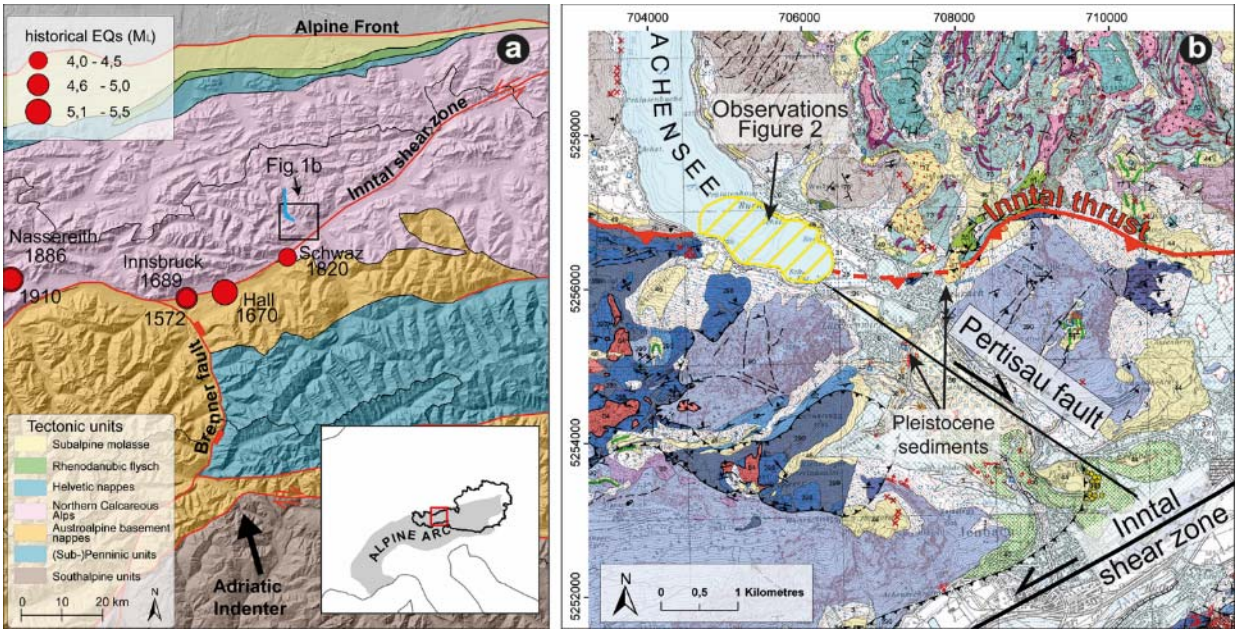

Figure 68: a) Regional tectonic map of the central Eastern Alps including major fault systems and epicenters of historical earthquakes with M_L >4. Tectonic map redrawn after Schmid et al. (2004); earthquakes derived from Hammerl (2017). b) Local geologic map of the southern Achen Valley within the Northern Calcareous Alps nappe stack (modified after Geological Survey of Austria, 2008). Major thrusts, partly crosscutting Achensee, are emphasized. Yellow hatched area in the lake marks the occurrence of potential primary and secondary paleoseismic observations derived from seismic data (see Figure 2).

taking advantage of the continuity of the sedimentary records and their sensitivity to abrupt environmental impacts. Coeval, multiple mass-transport deposits (MTDs), turbidites and in-situ deformation structures in lake sediments became well-established secondary paleoseismic indications documenting past earthquakes and neotectonic activity (Monecke et al., 2004; Kremer et al., 2017; Praet et al., 2017).

STUDY AREA

In the collisional orogenic belt of the Eastern Alps, the NNW-ward pushing of the rigid Adriatic Indenter plays a major role in the Neogene to present tectonic evolution. The seismicity in this area is related to several more than 100 km long major fault systems (i.e. Inntal shear zone, Inntal thrust; Reiter et al., subm.), which are linked to the Alpine basal detachment. The study area is located within this region with enhanced seismicity and comprises the Achensee, Tyrol's biggest and deepest lake (6.8 km^2, 134 m deep) occupying an under-filled glacially-eroded valley in the immediate adjacency of these major fault systems (Fig. 1). In the past, there have been several damaging earthquakes (e.g. Hall 1670, local magnitude M_L = 5.2; Hammerl, 2017) and the area is theoretically capable of a moment magnitude M_W = 6.5 event (Lenhardt et al., 2007). When comparing to an empirical database linking rupture area and displacement with earthquake magnitude, such an event can be expected to rupture the surface (Wells & Coppersmith, 1994). However, there has been no systematic paleoseismic investigation in this region yet, neither on-fault nor robust off-fault paleoseismic evidence of prehistoric earthquakes in Tyrol has been reported in literature.

PRELIMINARY RESULTS / HYPOTHESIS

Preliminary interpretation of the recently acquired geophysical data (reflection seismics, multibeam bathymetry) from Achensee leads to the hypothesis that its postglacial sedimentary infill uniquely records both primary and secondary paleoseismic evidence generated by an active tectonic fault, which is partly located under the lake basin. Observations supporting this hypothesis are:

i) a distinct NW-SE striking linear geomorphic structure in the bathymetric map cross-cutting the general depositional trend of a local alluvial fan (blue arrow in Fig. 2 a);

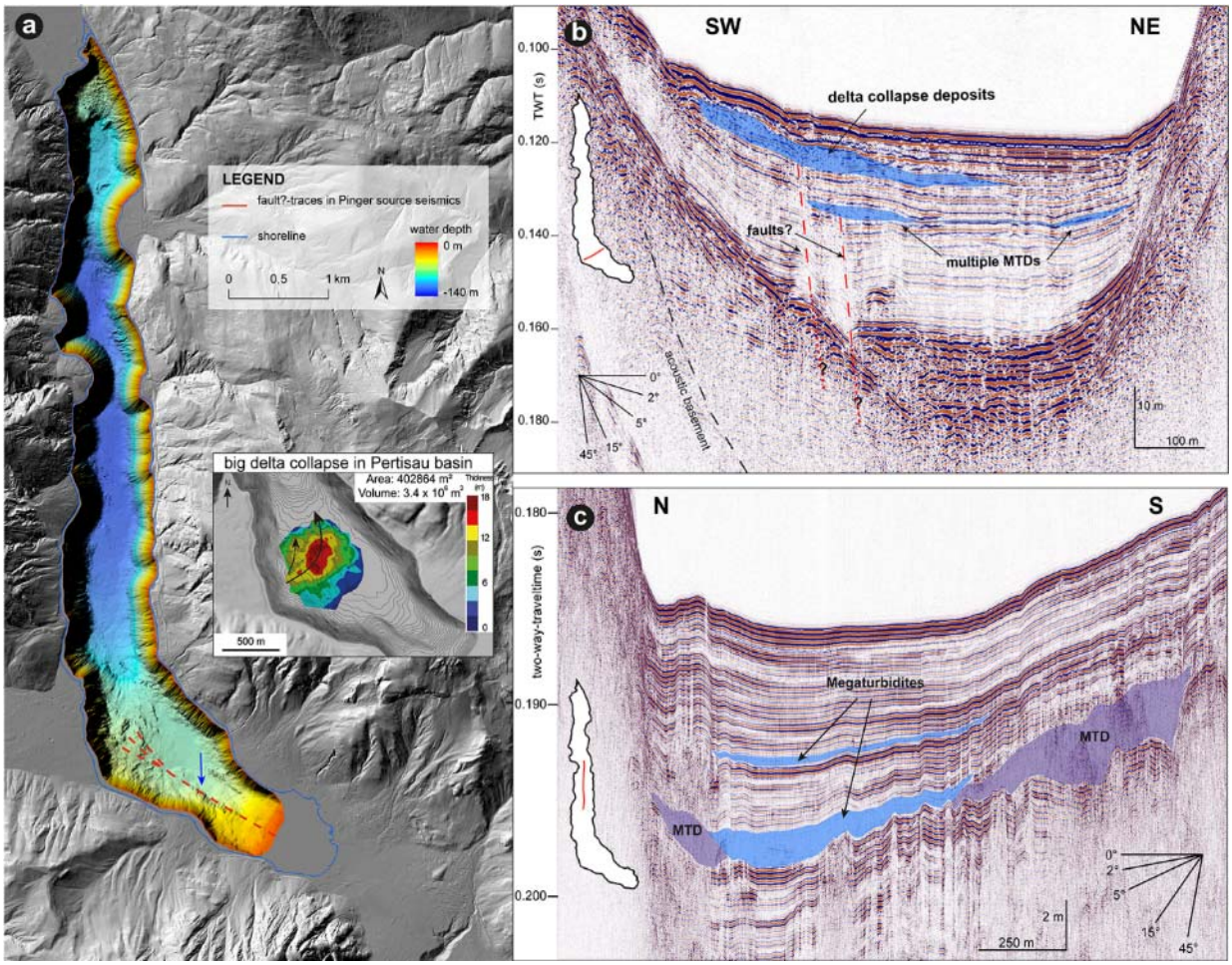

Figure 69: Preliminary interpreted geophysical data of Achensee acquired in 2016 and 2017. a) Achensee bathymetry including possible fault traces and isopach map of a big delta collapse. b) Subsurface cross line in southern basin (Sparker source) completely imaging the whole sedimentary infill down to acoustic basement. The strata is offset subvertically along subvertically dipping faults and respective event-horizons are overlain by multiple MTDs and the big delta collapse deposits. c) Subsurface profile along main central basin (3.5 kHz Pinger source) reveals multiple MTDs covered by two mega-turbidites.

ii) subvertical structures offsetting the lacustrine stratigraphy suggesting faulting (Fig 2. b). Preliminary mapping shows that these offsets can be traced across several seismic lines in the southern part of the lake (red dashed line in Fig. 2 a). They appear to belong to a set of aligned, NW-SE striking structures;

iii) the stratigraphic offsets can be traced downwards to the acoustic basement suggesting the faulting could originate in the bedrock (Fig. 2 b);

iv) an upwards termination of offset structures in large delta-collapse deposits and MTDs indicating that offsets and slope failures occurred simultaneously (Fig. 2 b);

v) coeval, multiple MTDs and co-genetic mega-turbidites occurring in several basins, implying a seismic trigger behind these subaquatic slope failures (Fig. 2 c). Such features have been shown to be a characteristic fingerprint of earthquake shaking of local macroseismic intensities of at least VI - VII (Moernaut et al., 2014; Kremer et al., 2017).

OUTLOOK

We plan to conduct a multidisciplinary amphibious investigation examining the potential primary and secondary paleoseismic evidence to test the hypothesis of recently active seismotectonic faulting in central Tyrol. Therefore, we will systematically map occurrence, geometry, orientation and stratigraphic position of mass movements and offset stratigraphic features in lacustrine geophysical data and complement and calibrate them by sediment long coring and dating of event horizons. Additionally, terrestrial geophysical data (gorund-penetrating radar, geoelectrics) and structural mapping of Pleistocene sediments in incised canyons will verify the occurrence of surface ruptures and the potential activity of seismotectonic faults.

REFERENCES

Fabbri, S.C., Herwegh, M., Horstmeyer, H., Hilbe, M., Hübscher, C., Merz, K., Schlunegger, C., Schmelzbach, C., Weiss, B., & Anselmetti, F.S., 2017. Combining amphibious geomorphology with subsurface geophysical and geological data: A neotectonic study at the front of the Alps (Bernese Alps, Switzerland). *Quaternary International* 451, 101-113.

Geological Survey of Austria, 2008. *Geologic maps (GEOFAST) of Austria 1: 50.000, map 119 - Schwaz*. Geological Survey of Austria, Vienna.

Hammerl, C., 2017. Historical earthquake research in Austria. *Geoscience Letters* 4 (1), 7.

Hintersberger, E., Decker, K., Lomax, J., & Lüthgens, C., 2018. Implications from palaeoseismological investigations at the Markgrafneusiedl Fault (Vienna Basin, Austria) for seismic hazard assessment. *Natural Hazards and Earth System Sciences* 18 (2), 531.

Kremer, K., Wirth, S.B., Reusch, A., Fäh, D., Bellwald, B., Anselmetti, F.S., Girardclos, S., & Strasser, M., 2017. Lake-sediment based paleoseismology: Limitations and perspectives from the Swiss Alps. *Quaternary science reviews* 168, 1-18.

La Taille, C., Jouanne, F., Crouzet, C., Beck, C., Jomard, H., Rycker, K., & van Daele, M., 2015. Impact of active faulting on the post LGM infill of Le Bourget Lake (western Alps, France). *Tectonophysics* 664, 31-49.

Lenhardt, W.A., Freudenthaler, C., Lippitsch, R., & Fiegweil, E., 2007. Focal-depth distributions in the Austrian Eastern Alps based on macroseismic data. *Austrian Journal of Earth Sciences* 100, 66-79.

Moernaut, J., Daele, M.V., Heirman, K., Fontijn, K., Strasser, M., Pino, M., Urrutia, R., & De Batist, M., 2014. Lacustrine turbidites as a tool for quantitative earthquake reconstruction: New evidence for a variable rupture mode in south central Chile. *Journal of Geophysical Research: Solid Earth* 119 (3), 1607-1633.

Monecke, K., Anselmetti, F.S., Becker, A., Sturm, M., & Giardini, D., 2004. The record of historic earthquakes in lake sediments of Central Switzerland. *Tectonophysics* 394 (1-2), 21-40.

Praet, N., Moernaut, J., Van Daele, M., Boes, E., Haeussler, P.J., Strupler, M., Schmidt, S., Loso, M.G., & De Batist, M., 2017. Paleoseismic potential of sublacustrine landslide records in a high-seismicity setting (south-central Alaska). *Marine Geology* 384, 103-119.

Reiter, F., Freudenthaler, C., Hausmann, H., Ortner, H., Lenhardt, W., & Brandner, R., subm. Active seismotectonic deformation north of the Dolomites Indenter, Eastern Alps, Tectonics.

Schmid, S.M., Fügenschuh, B., Kissling, E., & Schuster, R., 2004. Tectonic map and overall architecture of the Alpine orogen. *Eclogae Geologicae Helvetiae* 97 (1), 93-117.

Ustaszewski, M., & Pfiffner, O.A., 2008. Neotectonic faulting, uplift and seismicity in the central and western Swiss Alps. *Geological Society, London, Special Publications* 298 (1), 231-249.

Wells, D.L., & Coppersmith, K.J., 1994. New empirical relationships among magnitude, rupture length, rupture width, rupture area, and surface displacement. *Bulletin of the seismological Society of America* 84 (4), 974-1002.

INQUA Focus Group Earthquake Geology and Seismic Hazards

paleoseismicity.org

Magnitude of the 1920 Haiyuan (China) Earthquake Re-estimated using Geological and Seismological Methods

Ou, Qi (1), Kulikova, Galina (2), Yu, Jingxing (1,3), Walker, Richard (1), Parsons, Barry (1)

(1) COMET, Department of Earth Sciences, University of Oxford, OX1 3AN, Oxford, UK, qi.ou@earth.ox.ac.uk
(2) Institute of Earth and Environmental Sciences, University of Potsdam, Karl-Liebknecht-Strasse 24, Potsdam, Germany
(3) State Key Laboratory of Earthquake Dynamics, Institute of Geology, China Earthquake Administration, Beijing 100029, China

Abstract: *The 1920 Haiyuan Earthquake in Gansu, China is the largest earthquake in the Northeast Tibetan Plateau recorded in the instrumental period. Its magnitude is often cited to be above M 8.5, which is surprisingly large for an earthquake that occurred in the continental interior. This study aims to re-estimate the magnitude of this earthquake using geological and seismological methods. Horizontal offsets were measured from orthorectified high-resolution Pleiades satellite imagery to give M_w=7.8. Historical seismograms were collected, digitised and analysed to give m_B=7.8 and M_S=8.2, suggesting the larger range of previously reported magnitudes were overestimated. This result minimises the uncertainty of the size of the 1920 Haiyuan earthquake and provides an important constraint for future seismic risk assessment in this area.*

Keywords*: Haiyuan, Magnitude, Pleiades, Offset, Seismology*

INTRODUCTION

The size of the largest earthquake of an area is important for regional earthquake occurrence rate determination because of its role in calibrating the Gutenberg-Richter Relationship against the strain accumulation rate (Gutenberg & Richter, 1956; Bird & Kreemer, 2015)

$$N(M) = aM^{-b} \quad (1)$$

and

$$M_{tot} = \frac{ab}{1-b} M_{max}^{1-b} \quad (2)$$

where *a* and *b* are constants. *N* is the number of events with moment equal to or greater than *M* in a given time interval with total moment release M_{tot} and the largest single-event moment release M_{max}.

The NE Tibetan Plateau is undergoing rapid deformation due to the underthrusting of India underneath Tibet. The largest earthquake recorded instrumentally in this region is the 1920 Haiyuan Earthquake which ruptured ~230 km of surface and killed over 220,000 people (Fig.1; Deng et al., 1986; Zhang et al., 1987; Peizhen et al., 2005). However, its size is still poorly determined, with reported magnitudes ranging between 7.8 and 8.7 in various scales (Liu-zeng et al., 2015). Therefore, this study aims to investigate the rupture style and moment release of the 1920 Haiyuan Earthquake using a combined geological and seismological approach to better constrain its magnitude.

Geological study

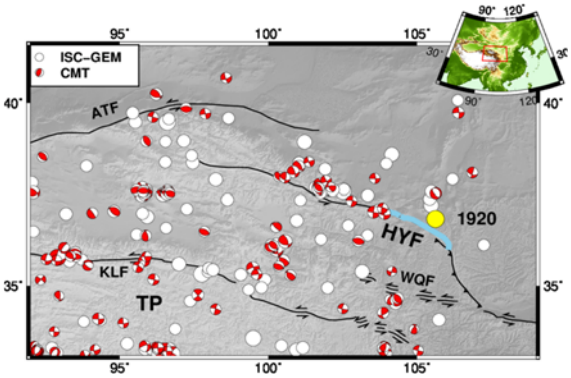

Figure 70: Tectonic map of the NE Tibetan Plateau (TP) showing the Haiyuan (HYF), Altyn Tagh (ATF), Kunlun (KLF) and Western Qinlin (WQF) Faults. The 1920 Haiyuan Earthquake is highlighted in yellow with its surface rupture highlighted in blue.

The moment magnitude M_w is the most reliable magnitude scale for characterising the size of large earthquakes:

$$M_w = \frac{2}{3}(\log_{10} M_o - 9.1) \quad (3)$$

and

$$M_o = \mu DLW \quad (4)$$

with M_w the moment magnitude, M_o the seismic moment, μ the shear modulus of the crust, *D* the average slip along the fault, *L* the length and *W* the down-dip width of the rupture (Aki, 1966; Kanamori, 1977).

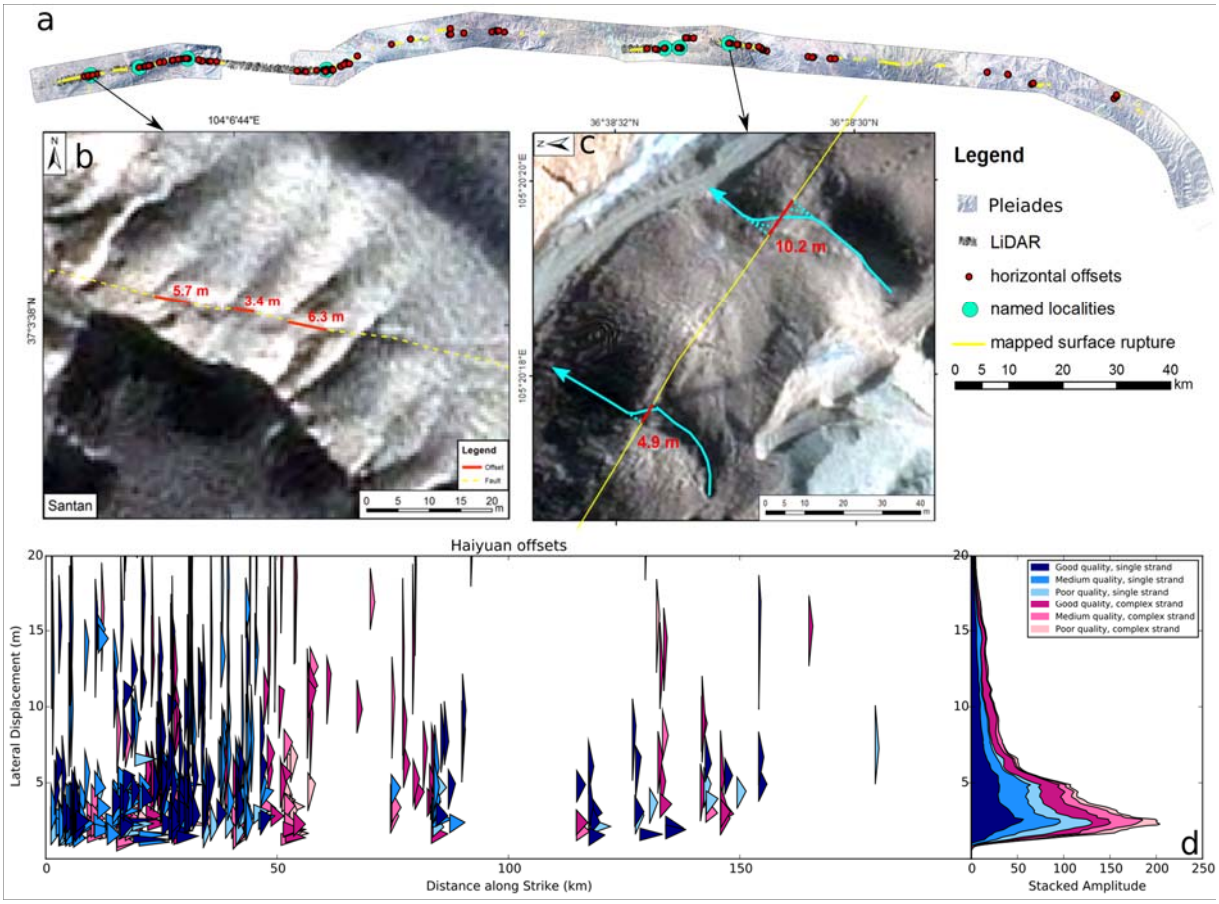

Figure 71: (a) Pleiades data coverage for rupture and offset mapping, with LiDAR data from Ren et al. (2016) (b) Consecutive offsets with varying lengths in Santan area. (c) A site with 4.9 m offset next to the 10.2 m previously identified as the largest 1920 offset.

Trio-stereo Pleiades satellite data were acquired to produce ~0.7 m resolution orthorectified optical imagery to measure horizontal offsets along the entire rupture of the 1920 Haiyuan earthquake (Fig.2a). It is common to map offsets with different sizes within only tens of meters on the same fault segment and the same lithological substrate. This observation suggests that larger offsets in such local systems are most likely recording cumulative slip from multiple events (Fig. 2b,c).

The measured offsets were categorised according to their preservation quality and whether they fall on single-strand or multiple-strand fault segments. Equal area triangles defined by their minimum, maximum and best offset measurements were stacked to show peaks in offset sizes (Fig.2d). The lowest peak averages to 3.4 m which we believe represent the average slip of the 1920 event. Therefore, I agree with (Ren et al., 2016) that the 10.2 m 'largest 1920 offset' identified in field surveys in the 1980s is likely a cumulative offset (Institute of Geology, 1990). Assuming the earthquake was purely strike-slip and completely ruptured the surface, *D* of 3.4 m, *L* of 230 km and *W* of 20 km give an M_w of 7.8.

Seismological study

Earthquake magnitudes can also be determined using the body- and surface-wave magnitude formulae and through waveform modelling. The International Seismological Centre (ISC) calculates magnitudes from amplitude-period pairs recorded in station bulletins. This approach generated nine widely scattered magnitudes between 7.85 and 8.80 for the Haiyuan Earthquake which is not satisfactory. Therefore, it is important to collect the original waveforms to (1) verify and complement the amplitude-period readings from bulletins, and (2) model the waveforms to determine the seismic moment released from this event. This abstract only contains results of the former and the modelling results will be presented in the poster.

44 analogue seismic records from 18 stations in Japan, Indonesia, Germany, Italy, Spain, Sweden, the Netherlands, Mexico, Bolivia and the US were collected and digitised (Fig.3). The curvature and slant of the waveforms due to the mechanical design of the recording instruments, such the Wiechert and Bosch-Omori seismographs, were removed using an inversion algorithm based on instrument geometry (Fig.4; O. Cadek, 1987; Kulikova, 2016). Dimensions of selected historical instruments were measured in museums and archives to check the validity of the inversion results.

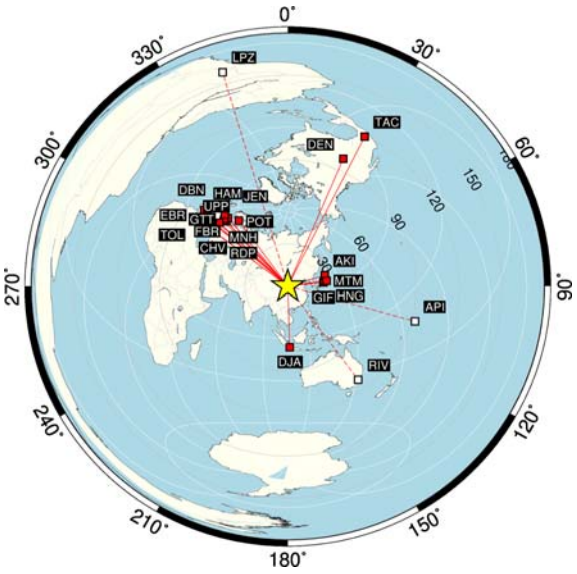

Figure 73: Station distribution. Waveforms from the red stations are already used in this study. More seismograms are expected to arrive from the white stations.

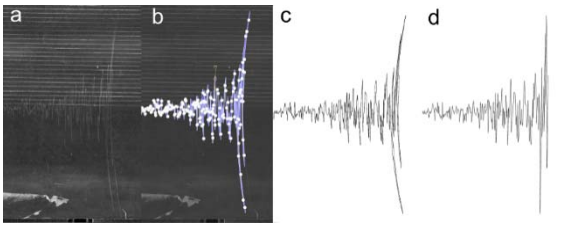

Figure 72: (a) Scanned seismogram from Potsdam Station. (b) Waveform traced as a Bezier curve. (c) Digitised waveform. (d) Curvature corrected waveform.

The amplitudes, *A*, and periods, *T*, of identified phases were measured for the following body- and surface-wave magnitude formulae (Bormann, 2012). Amplitudes within half a wavelength between E- and N-component were vectorially combined to give the true horizontal amplitude, A_H. Historical station latitudes and longitudes from station bulletins were used to calculate the epicentral distances. The hypocentral depth, *h*, was assumed to be 15 km.

$$m_B = \log\left(\frac{A}{T}\right)_{max} + Q(\Delta, h) \quad (5)$$

$$M_S = \log\left(\frac{A_H}{T}\right)_{max} + 1.66\log\Delta + 3.3 \quad (6)$$

Equation (5) is a broadband body-wave magnitude formula that accepts PH, PV, PPH, PPV and SH phase amplitudes with periods between 2 s and 20 s. It saturates at m_B~8.5 instead of the more-familiar narrow-band m_b which saturates at m_b~6.5, hence is more suitable for determining the magnitudes of large earthquakes like the 1920 Haiyuan Earthquake. Equation (6) is the conventional surface-wave magnitude formula.

The resultant m_B and M_S magnitudes from E, N and Z components, as well as the vectorially combined horizontal H components, are plotted in Figures 5 and 6 respectively, with the maximum value from each station highlighted with a blue asterisk. The stations in the horizontal axis are arranged in the order of increasing epicentral distance, with Gifu in Japan (GIFH) at 25.6° and Tacubaya (TACB and TACW) in Mexico at 120.4° from Haiyuan.

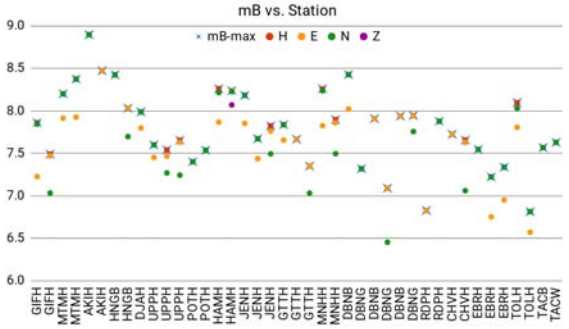

Figure 74: mB plotted against station.

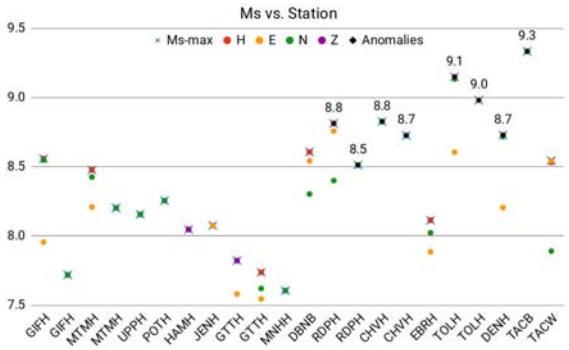

Figure 75: Ms plotted against station.

DISCUSSION

There is good agreement between the moment magnitude, M_w=7.8, and the average of body wave magnitudes, m_B=7.8. The surface wave magnitudes, however, average to a higher value of M_S=8.4.

Some m_B and M_S values obtained are higher than the expected saturation points on the magnitude scales, suggesting further scrutiny is required. One possible reason could be that some waveforms were recorded by instruments not designed for recording long-period waves from large earthquakes. For example, the micrometre used at Akita station in Japan (AKIH) had an instrumental period of 4 s, which would preferentially amplify the high-frequency content to result in a large A/T ratio for the body-wave and hence give m_B=8.9. The Bosch-Omori instrument operating at Toledo (TOLH) station in Spain was not damped, which potentially allowed the stylus to swing wildly upon high-amplitude surface waves, hence the extreme values of M_S~9. The Bosch-Omori instrument at Tacubaya (TACB) was also undamped and the only instrumental parameters found were published in 1917 which could be different from those in 1920. The

components and instrument responses for the Denver (DENH) record were also not found so parameters published in 1931 were used instead. The Agamennone horizontal pendula seismograph in RDPH station are known to have problems with stability and there is also ambiguity in which station the RDP abbreviation refers to, hence less confidence should be placed on these magnitudes. The damping factor of the Stiattesi horizontal pendulum seismograph in Chiavari (CHV) in Italy was not found; our attempt with measuring the oscillatory coda resulted in damping factor ranging between 0.01 and 0.07, thus large uncertainty is expected in the resultant magnitude. If these results are removed from the dataset, the average M_S from remaining stations will be 8.16.

The results show that the higher previously reported magnitudes are very likely overestimated. This could be because early earthquake magnitudes were often reported based on the intensity of shaking inferred from damage to the buildings, which means the poor quality of the buildings in the rural area in western China could easily inflate the estimated magnitude. For the 1920 Haiyuan Earthquake, the first detailed field survey was done 60 years after the event, during which time weathering could have obscured the difference between single-event from multiple-event offsets. There was also no international seismic data sharing schemes in the 1920s. The only Chinese analogue signal for Haiyuan Earthquake, recorded by the Zi-ka-wei station in Shanghai, saturated upon the first P-wave arrival and the recording stylus was dislocated before the S-wave arrived, rendering this record useless for magnitude determination. Therefore, this study is the long overdue re-examination of the magnitude of this 1920 Haiyuan Earthquake thanks to the availability of high-resolution Pleiades imagery and the careful preservation of the old surviving seismograms in various archives. Hopefully, the final step of waveform modelling will better define the magnitude from a seismic moment release point of view and resolve the ambiguity in magnitudes reported in different magnitude scales.

Acknowledgements: Special thanks go to Dr Jingxing Yu and Prof Wenjun Zheng for their advice on geological mapping and to Dr Galina Kulikova for her guidance on the seismological part of the study. I am also grateful to Professors James Dewey, Emile Okal, Josep Batlló, Dr Bernard Dost and Domenico Di Giacomo for sharing their knowledge on historical seismograms and instruments. Many thanks to Alexandra Rose at London Science Museum for showing me the old instruments and to Dr Austin Elliot for the insightful discussions. Finally, none of the seismological studies would have been possible without the support and seismograms from the following institutes: Istituto Nazionale di Geofisica e Vulcanologia (Italy), Royal Netherlands Meteorological Institute, Universidad Nacional Autonoma de Mexico, Svenska Nationella Seismiska Nätet (SNSN, Sweden), the USGS, Instituto Geográfico Nacional (Spain), Observatori de l'Ebre and El Observatorio Fabra.

REFERENCES

Aki, K., 1966. Estimation of earthquake moment, released energy, and stress-strain drop from the G wave spectrum. *Bulletin of the Earthquake Research Institute* 44, 73-88.

Bird, P., & Kreemer, C., 2015. Revised Tectonic Forecast of Global Shallow Seismicity Based on Version 2.1 of the Global Strain Rate Map. *Bulletin of the Seismological Society of America*, 105 (1), 152-166.

Bormann, P., 2012. *Magnitude calibration formulas and tables, comments on their use and complementary data*, Available at: http://gfzpublic.gfz-potsdam.de/pubman/item/escidoc:124248/component/escidoc:321682/Chapter_4.pdf.

Deng, Q., et al., 1986. Variations in the geometry and amount of slip on the Haiyuan (Nanxihaushan) Fault zone, China and the surface rupture of the 1920 Haiyuan earthquake. In *Haiyuan Fault Zone*, 170-182.

Gutenberg, B., & Richter, C.F., 1956. Magnitude and energy of earthquakes. *Annali di Geofisica* 9 (1).

Institute of Geology, 1990. *Active Haiyuan Fault Zone Monograph*, Seismol. Publ. House, Beijing, China.

Kanamori, H., 1977. The Energy Release in Great Earthquakes. *Journal of Geophysical Research* 82 (20), 2981-2987.

Kulikova, G., 2016. *Source parameters of the major historical earthquakes in the Tien-Shan region from the late 19th to the early 20th century*.

Liu-zeng, J., et al., 2015. Variability in magnitude of paleoearthquakes revealed by trenching and historical records, along the Haiyuan Fault, China. *Journal of Geophysical Research: Solid Earth*, 1-30.

O. Cadek, P., 1987. Studying earthquake ground motion in Prague from Wiechert seismograph records. *Gerlands Beitr. Geophysik* 96 (5), 438-447.

Peizhen, Z., et al., 2005. Paleoearthquake rupture behaviour and recurrence of great earthquakes along the Haiyuan fault, northwestern China. *Science in China Ser. D Earth Sciences* 48 (3), 364-375.

Ren, Z., et al., 2016. Clustering of offsets on the haiyuan fault and their relationship to paleoearthquakes. *Bulletin of the Geological Society of America* 128 (1-2), 3-18.

Zhang, W., et al., 1987. *Displacement along the Haiyuan Fault associated with the great 1920 Haiyuan, China, earthquake.* The Society.

INQUA Focus Group Earthquake Geology and Seismic Hazards

paleoseismicity.org

Tectonic movements of the Corinth Isthmus (Greece) during Quaternary

Pallikarakis, Aggelos (1), Papanikolaou, Ioannis (1), Triantaphyllou, Maria (2), Reicherter, Klaus (3), Dimiza, Margarita (2), Migiros, Georgios (1)

(1) Laboratory Mineralogy - Geology, Department of Natural Resources Management & Agricultural Engineering, Agricultural University of Athens, Athens, Greece, agpall@aua.gr
(2) Hist. Geology-Paleontology Department, Faculty of Geology and Geoenvironment, National and Kapodistrian University of Athens, Athens, Greece
(3) Institute of Neotectonics and Natural Hazards, RWTH Aachen University, Aachen, Germany

Abstract: *The tectonic movements of the Corinth Isthmus are studied in detail. Based on the micro- and nanno- palaeontological analysis both in borehole sequences and i surface outcrops at the eastern part of the Corinth Isthmus, a 3-D spatial and temporal distribution of the sediments are described. Furthermore, based on the ages supported by the nannofossils assemblages, the uplift rate of the eastern part of the Corinth Isthmus is re-interpreted following an independent approach compared to existing published rates, adding confidence to existing regional reported uplift rates. Furthermore, in the basis of the ages proposed both from previous corals data and through nannofossils assemblages, the activity of the Kalamaki-Isthmia fault is estimated verifying a relatively low slip-rate but active fault.*

Keywords*: Uplift rate, Slip rate, Calcareous nannofossils, benthic foraminifera*

INTRODUCTION

The Corinth Isthmus is located at the hangingwall and footwall of active normal faults, which either uplift or subside the area such as the South Alkyonides Fault System (SAFS), the Loutraki, the Kenchreai and the Agios Vassileios faults (Fig. 1; e.g. Papanikolaou et al., 1988; Koukouvelas et al., 2017; Deligiannakis et al., 2018). Furthermore, secondary structures such as the normal Kalamaki-Isthmia fault also influence the tectonic processes of the area (e.g. Pallikarakis, 2018) (Fig. 1).

The sum of all the factors, which uplift or subside the area is a 0.3 mm/yr uplift rate at least since MIS 7, (e.g. Collier et al., 1992). The uplift of the area combined with the glacioeustatic sea level changes has influenced the local sedimentation processes resulting in transgressive - forced regressive sequences (e.g. Collier, 1990).

This study aims to estimate the activity of the low slip rate Kalamaki-Isthmia fault located at the eastern margin of the Corinth Isthmus close to the canal and examines the uplift rate of the area following a different and independent methodology, compared with the methodologies followed by previous researchers (e.g. Collier et al., 1998).

MATERIALS AND METHODS

Through detailed mapping (1:5,000) alternations of clayey, sandy to gravely layers of Pleistocene age have been described at the eastern part of the Corinth Isthmus (Fig. 1).

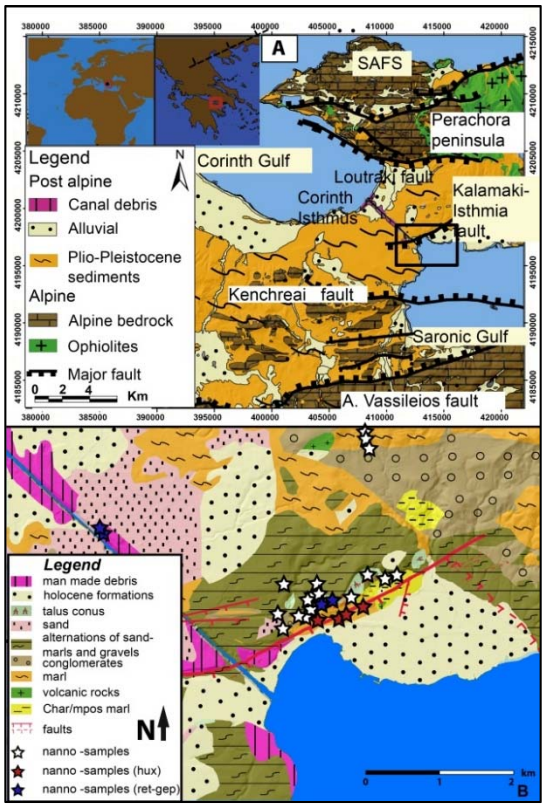

Figure 76: A) Simplified geological map showing the lithology of the area, as well as the major faults of the area SAFS, Loutraki, Ag. Vassileios and Kenchreai faults and the Kalamaki-Isthmia fault (modified from Bornovas et al., 1972, 1984; Gaitanakis et al., 1985; Papanikolaou et al., 1989, 1996). The black box indicates the area where the boreholes were drilled. B) Geological map of the study area (based on Gaitanakis et al., 1985; this study) and the locations of the outcrops where the extracted samples have been analysed for nannofossils.

Samples extracted from sandy, clayey and even gravely outcrops of Pleistocene age corresponding to fluvial to shallow marine facies, as well as samples extracted from eleven drillholes of either side of Kalamaki-Isthmia fault (~ 373 m total length) are micropalaeontologically described, following the standard procedures (e.g. Triantaphyllou et al., 2003; Pallikarakis, 2018; Pallikarakis et al., in press). Furthermore, the magnetic susceptibility of core sediments is measured also to assist interpretation of the paleoenvironment (e.g. Pallikarakis, 2018).

63 samples of fine-grained sediments (32 extracted from surface outcrops and 31 from the borehole cores were examined by Scanning Electron Microscopy (SEM) for their calcareous nannoplankton content following the standard procedures (e.g. Thierstein et al., 1977). The definition of the *Emiliania huxleyi* NN21a biozone (Martini, 1971) (≤ 265 ka) is based on the first appearance of specimens of the species that is the midpoint of the slope of the initial increase of species in counts of 300 coccoliths (e.g. Thierstein et al., 1977).

DISCUSSION

3D visualization and paleoenvironmental interpretation

The paleoenvironmental units in the boreholes are described through hierarchical cluster analysis of the foraminiferal assemblages, correlated with the described lithologies and with the measured MS values (Pallikarakis, 2018; Pallikarakis et al., in press). The lagoonal environment is associated with Group B-Cluster III assemblages (dominated by small sized *A. tepida*, followed by *E. granosum* and *Haynesina* spp). Shallow marine environments are associated with Group A/C-Cluster II assemblages (dominated by full marine species (e.g. *N. terquemi, Asterigerinata* spp., *Discorbis* spp.). Transitional environmental conditions (from shallow marine to lagoonal) are associated with Group B/C-Cluster I (dominated by *A. beccarii, E. crispum*). Based on these divisions different depositional paleoenvironments can be differentiated and therefore a temporal reconstruction of the paleoenvironment is feasible. This analysis clearly demonstrates and confirms that not only lithology but also the depositional environment display significant spatial and temporal variations over short distances.

The vertical stacking of the borehole cores mark five distinct successive sedimentary sequences, indicating an onset of transgressive-regressive (T-R) conditions (Fig. 2) which are better manifested in the deepest borehole (Bh-3). In boreholes Bh-1 and GA-5 (Fig. 2) three successive transgressive-regressive (T-R) sequences can be described. In borehole GA-4 (Fig. 2) three successive transgressive-regressive (T-R) sequences can be described as well. Furthermore, even though no paleoenvironmental description of boreholes Bh-6 and Bh-4 exists, this horizon can be correlated with fine-grained sediments in boreholes Bh-6 (20.70–24.30 m core depth) and Bh-4 (17.50–20.00 m core depth). In cross section Bh-6 / GA-4 a clayey horizon is correlated between boreholes Bh-6 and Bh-4. Notably, this horizon is displaced ~5 m by the activity of the Kalamaki-Isthmia fault. The latter is in agreement with the ~ 5 m offset described in Papanikolaou et al. (2015) between lagoonal horizons in boreholes Bh-3 and Bh-7. This testifies to the Kalamaki-Isthmia fault's activity, considering as well the proximity of these boreholes.

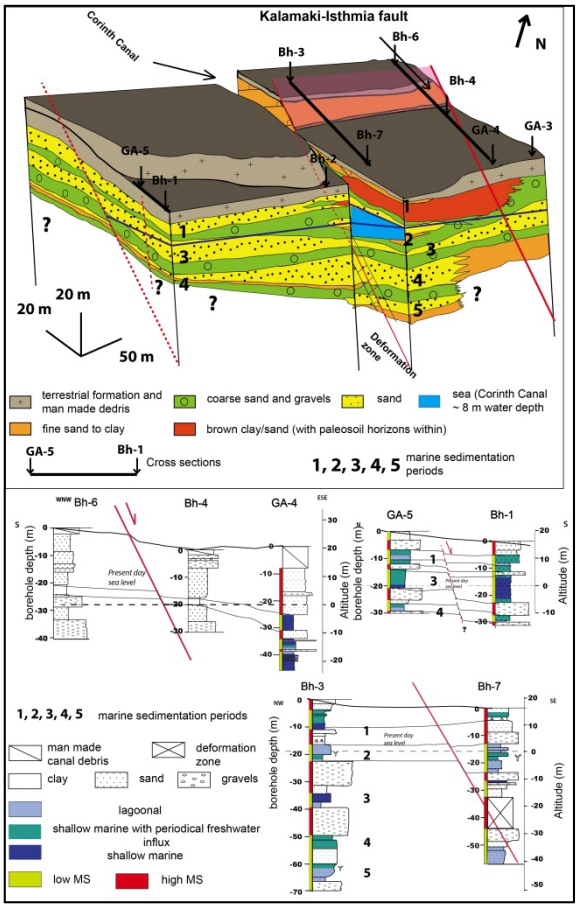

Figure 77: A) 3D sketch of the study area based on the boreholes description. Numbers 1-5 show the correlation among the sediments described at the 3-D sketch with the borehole Bh-3. Cross sections showing the correlation of the stratigraphy and the paleoenvironment between neighboring boreholes.

Uplift rate

The 0.3 mm/yr uplift rate since MIS 7.3 (c. 205 ka) of the Corinth Isthmus was well documented by Collier et al. (1992). Nannofossils though, can also provide an independent methodology for estimating the age and consequently the uplift of the area. In borehole GA-2, at 12.95 m depth the presence of *E. huxleyi* indicates an age younger than 265 ka. Based on the glacioeustatic sea level curve (e.g. Siddall, et al., 2003) and the estimated palaeobathymetry (e.g. Pallikarakis, 2018; Pallikarakis at el., in press), an age between ~125 ka (MIS 5.5) and 265 ka (MIS 7) is suggested and an uplift rate ~0.34 ± 0.12 mm/yr is estimated (Fig. 3). If the examined sediments were younger than 125 ka, then based on the sea level curve a minimum uplift rate ~0.5 mm/yr is calculated. In this scenario the expected paleoenvironment within the boreholes could not be correlated with the borehole data since; instead of alternations of lagoonal and shallow marine facies, relatively deep marine sediments would have been described. Therefore, this scenario is excluded.

Possible ages younger than 125 ka (MIS 5.5) are also excluded since the area was constantly emerged and no marine sedimentation was taken place since MIS 5.5 (Fig. 3).

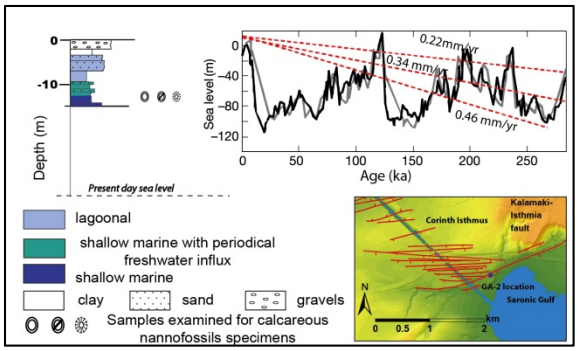

Figure 78: The paleoenvironmental interpretation of borehole GA-2 and the possible range of the estimated uplift rate based on the described calcareous nannofossils from sample GA-2 12.95 m the canal showing how the faults have displaced characteristic horizons.

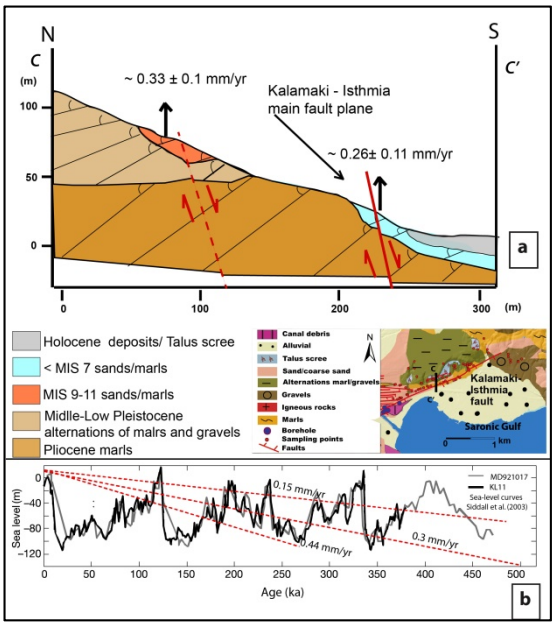

Figure 79. a) The paleoenvironmental interpretation in cross section C-C′ almost perpendicular to the Kalamaki-Isthmia fault trace, showing the estimated uplift rate based on calcareous nannofossils assemblages. b) The possible range of the estimated uplift rate based on the described calcareous nannofossils from surface outcrops.

Furthermore, in surface samples (S.23.9/2, S.25.9./3, S.25.9/2 and S.12/7/3) (Fig. 1) where nannofossils were traced, the presence of *E. huxleyi* also suggests an age between ~125 ka (MIS 5.5) and 265 ka (MIS 7). Nannofossils in samples S.17/7/5 and S.17/7/6 indicate an age in-between MIS 9 to MIS 11. Based on the regional estimated paleodepth (~30 m water depth, Pallikarakis, 2018) in both cases and the altitude in which the samples were extracted, an 0.27 ± 0.12 mm/yr uplift rate on the hangingwall and 0.33 ± 0.12 mm/yr uplift rate on the footwall of the fault is estimated (cross section C-C') (Fig. 4). Therefore following all the above constraints an average 0.30 ± 0.12 mm/yr uplift rate for the units in cross section C-C' is suggested and based also on the results from borehole GA-2 (~0.34 ± 0.12 mm/yr), an average 0.32 ± 0.14 mm/yr uplift rate for the eastern part of the Corinth Isthmus is extracted.

The error of the estimated rates incorporates the uncertainties of the paleodepth and the different highstands where the sedimentation was possible. However, the extracted rates are in agreement with the rates extracted through absolute dating techniques (e.g. Collier et al., 1992) adding confidence to the reported rates.

The Kalamaki - Isthmia fault activity

The ~0.3 mm/yr uplift rate of the area is the result of all the combined factors which subside or uplift the Corinth Isthmus. Collier (1990), Collier et al. (1992), though mentioned a relatively lower uplift rate at the western part (~0.2 mm/yr) than the eastern part (~0.3 mm/yr). Furthermore, the morphology of the western part of the Isthmus is relatively smoother than the eastern part where the Kalamaki-Isthmia fault is the dominant structure (e.g. Papanikolaou et al., 2015), also indicating higher tectonic activity. The cross section of the Canal (e.g. Collier, 1990; Collier et al., 1992) shows significantly more faults at the eastern part (Kalamaki-Isthmia fault zone) than the western part (Fig. 5).

Mapping of the area has also revealed several faults displacing the exposed strata within the Corinth Canal (Fig. 5c, d). It is questionable though whether these displacements were caused only from their activity and/or have been passively ruptured during another earthquake triggered by distal faults, like possible the Kalamaki-Isthmia fault during the 1981 earthquake sequence (e.g. South Alkyonides fault system, Papanikolaou et al., 2015).

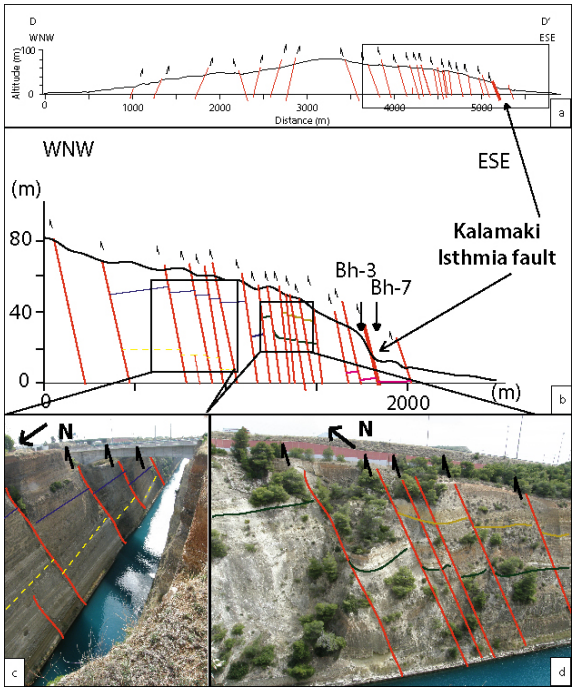

Figure 80: a-b) Cross section of the Corinth Canal (based on Collier (1990) and this study), showing significantly more faults intersecting the eastern than the western part of the Canal. c-d) Photos from the northern part of the canal showing how the faults have displaced characteristic horizons.

Papanikolaou et al. (2015) suggested a ~0.04 mm/yr maximum slip rate since MIS 6.5 for the main trace of the Kalamaki-Isthmia fault, based on displaced lagoonal

horizons in boreholes Bh-3 (footwall) and Bh-7 (hangingwall). In cross section C-C' (Fig. 4) between surface outcrops samples S.17/7/5, S.17/7/6 at the footwall and S.23/9/2 at the hangingwall of the fault, a ~0.06 mm/yr difference between the estimated uplift rates is noticed. Considering of course that the error of the estimated rates incorporates the uncertainties of the paleodepth and the different highstands where the sedimentation was possible, this difference can be interpreted as the offset caused by the Kalamaki-Isthmia fault zone activity (Fig. 5). Furthermore, since cross section C-C' is located approximately at the center of the fault, the difference of the uplift from the footwall and the hangingwall extracts the maximum fault's throw rate at least during MIS 7. Based on the geometry of the fault (~65^{o} dip), a maximum slip rate ~0.07 ± 0.02 mm/yr for the Kalamaki-Isthmia fault zone since MIS 7 is extracted.

Acknowledgements: The Academy of Athens scholarship (Mitsopoulos Fund) is thanked for financial support.

REFERENCES

Bornovas, J., Lalechos, N., & Filipakis, N., 1972. *Korinthos geological map. Athens, Greece,* Institute of Geology and Mineral Exploration, scale 1:50,000, 1 sheet.

Bornovas, J., Gaitanakis, P., & Spiridopoulos, A., 1984. *Perachora geological map. Athens, Greece*, Institute of Geology and Mineral Exploration, scale 1:50,000, 1 sheet.

Collier, R.E.L., 1990. Eustatic and tectonic controls upon Quaternary coastal sedimentation in the Corinth Basin, Greece. *J. Geol. Soc.* 147, 301-314.

Collier, R.E.L., Leeder, R.M., Rowe, P., & Atkinson, T., 1992. Rates of tectonic uplift in the Corinth and Megara basins, Central Greece. *Tectonics* 11(6), 1159-1167.

Gaitanakis, P., Mettos, A., & Fytikas, M., 1985. *Sofikon geological map. Athens, Greece*, Institute of Geology and Mineral Exploration, scale 1:50,000, 1 sheet.

Deligiannakis, G., Papanikolaou, I., & Roberts, G., (in press). Fault specific GIS based seismic hazard maps for the Attica region, Greece. *Geomorphology* 306, 264-282.

Koukouvelas, I., Zygouri, V., Papadopoulos, G., & Verroios, S., 2017.Holocene record of slip-predictable earthquakes on the Kenchreai Fault, Gulf of Corinth, Greece. *J. Struct. Geol.* 94, 258-274.

Martini, E., 1971. Standard Tertiary and Quaternary calcareous nannoplankton zonation. In: Farinacci, A. (ed.), Proceedings of the Second Planktonic Conference. (Roma). *Technoscienza*, pp. 739-785.

Pallikarakis, A. 2018. Quaternary multi-proxy analysis of the paleoenvironment, paleogeography and active tectonics of the Corinth Isthmus. Ph.D. thesis, AUA, Athens.

Pallikarakis, A., Triantaphyllou, V.M., Papanikolaou, I., Dimiza, D.M., Reicherter, K., & Migiros, G., Cor. Proof. Age Constraints and Paleoenvironmental Interpretation of a Borehole Sedimentary Sequence at the Eastern Part of Corinth Isthmus, Greece. *Journal of Coastal Research*. DOI: 10.2112/JCOASTRES-D-16-00191.1

Papanikolaou, D., Lykousis, V., Chronis, G., & Pavlakis, P., 1988. A comparative study of neotectonic basins across the Hellenic Arc: the Messiniakos, Argolikos, Saronikos and Southern Evoikos Gulfs. *Basin Res.* 1 (3), 167-176.

Papanikolaou, D., Chronis, G., Lykousis, V., Pavlakis, P., Roussakis, G., & Syskakis, D., 1989. Offshore Neotectonic Map the Saronic Gulf. Athens, Greece: Earthquake Planning and Protection Organization, National Centre for Marine Research, University of Athens, scale 1: 100,000, 1 sheet.

Papanikolaou, D., Logos, E., Lozios, S., & Sideris, Ch., 1996. Neotectonic Map of Korinthos, Athens, Greece: Earthquake Planning and Protection Organization, scale 1:100,000, 1 Sheet.

Papanikolaou, I.D., Triantaphyllou, M., Pallikarakis, A., & Migiros, G., 2015. Active faulting at the Corinth Canal based on surface observations, borehole data and paleoenvironmental interpretations. Passive rupture during the 1981 earthquake sequence?. *Geomorphology* 237, 65-7-8.

Siddall, M., Rohling, E.J., Almogi-Labin, A., Hemleben, Ch., Meischner, D., Schmelzer, I., & Smeed, D.A., 2003. Sea-level fluctuations during the last glacial cycle. *Nature* 423, 853-858.

Thierstein, H.R., Geitzenauer, K.R., Molfino, B., & Shackleton, N.J., 1977. Global synchroneity of Late Quaternary coccolith datum levels validation by oxygen isotopes. *Geology* 5(7), 400-404.

Triantaphyllou, M.V., Pavlopoulos, K., Tsourou, Th., & Dermitzakis, M.D., 2003. Brackish marsh benthic microfauna and paleoenvironmental changes during the last 6000 years on the coastal plain of Marathon (SE Greece). *Riv. Ital. Paleontol. Stratigr.* 109 (3), 539-547.

INQUA Focus Group Earthquake Geology and Seismic Hazards

paleoseismicity.org

Transverse tectonic zones delimiting seismic segments along prominent rift structures in the South Aegean: The Amorgos 1956 and Kos 2017 events

Papanikolaou, Dimitrios (1), Nomikou, Paraskevi (1), Lampridou, Danai (1)

(1) Department of Geology and Geoenvironment, National and Kapodistrian University of Athens, Panepistimioupoli Zografou, 15784, Athens, Greece, dpapan@geol.uoa.gr

Abstract: *The Kos 2017 earthquake is analysed taking into account the onshore and offshore geological and geophysical data. The resulting image is a 35 km long activated normal fault of E-W direction dipping to the south, occurring along the coastline south of the Bodrum peninsula and east of Kos Island. The overall seismically activated structure is delimited within two subparallel transverse tectonic zones of NW-SE direction which affect the continuity of the ENE-WSW general rift structure observed along 180 km length. Similar transverse segmentation has been described along the ENE-WSW Santorini - Amorgos tectonic zone, where the 1956 Amorgos events have been delimited in another 40 km long segment by NW-SE transverse structures. The transverse segmentation determines the magnitude of the rupture zones along the major rift structures and may contribute to a better understanding of the seismic hazard.*

Keywords*: fault segmentation, rift zone, active faulting, seismic hazard*

INTRODUCTION

Two subparallel rift structures of ENE-WSW orientation are observed within the Cycladic plateau and the north Dodekanese islands, north of the Cretan basin in the Aegean Sea. They are both characterised by a very young Late Pliocene - Pleistocene age and they host active volcanic centres of the modern volcanic arc (Nomikou et al., 2018a and 2018b). These recent rift structures are the result of an extension in the NW-SE direction, observed also by the GPS velocities within the SE part of the Aegean microplate, indicating a 4-5 mm/year rate from the central Cyclades plateau of Naxos, Ios, Amorgos to the southern Dodekanese islands of Rhodos and Karpathos (Papanikolaou & Royden, 2007; Reilinger et al., 2010). The first rift structure runs through the Santorini - Amorgos islands for a length of more than 140 km and includes the Christiana - Santorini - Kolumbo volcanic centres. It includes a number of horsts and grabens with active faults that have given large earthquakes like the maximum 7.3 magnitude 1956 Amorgos event, followed by the strongest tsunami of the eastern Mediterranean (Okal et al., 2009).

The second rift structure is observed in a subparallel zone running south of the islands of Astypalaea and Kos, continuing into the Gulf of Gökova, between the Bodrum peninsula in the north and the Datça peninsula in the south (Fig. 1). In July 2017, a 6.6 magnitude earthquake occurred in the area of Gökova basin east of Kos along a E-W fault running parallel to the southern coast of Bodrum peninsula dipping to the south (Tiryakioğlu et al., 2017; Ocakoğlu et al., 2018; Kiratzi & Koskosidi, 2018). In both cases of Amorgos and Kos the activated faults ruptured a small segment of the entire length of the rift structures. Our studies indicate that the delimitation of the activated segments is made of a systematic development of transverse structures of NW-SE direction, which determine the maximum magnitude of the expected earthquakes.

MATERIALS AND METHODS

Our study is based on the combination of onshore and offshore data in the area of the southern Cyclades, the Northern Dodekanese islands and Gökova area between the Bodrum and Datça peninsulas. The onshore data have been obtained during several years of geological mapping and tectonic analysis together with the relevant geological literature (Papanikolaou & Nomikou, 1998; Görür et al., 1995; Nomikou et al., 2018a and 2018b). The offshore data in the southern Cyclades, the Northern Dodekanese islands have been obtained by systematic marine research with oceanographic vessels including swath bathymetry and air-gun seismic profiling (Nomikou & Papanikolaou, 2011; Iscan et al., 2013; Nomikou et al., 2013, 2017; Hooft et al., 2017; Ocakoğlu et al., 2018; Nomikou et al., 2018a and 2018b). The offshore data in the Gulf of Gökova was collected by the Turkish Navy, Department of Navigation, Hydrography and Oceanography (TN-ONHO) in 2005 and published previously by İşcan et al. (2013) and Ocakoğlu et al. (2018).

RESULTS

The 2017 Kos 6.6 magnitude strong shallow earthquake occurred along the southern coastline of Bodrum peninsula, with an E-W direction and southward dip, corresponding to a normal fault (Kiratzi & Koskosidi, 2018) (Fig.1). This fault is part of the 180 km long ENE-WSW rift zone observed from the area south of Astypalaea Island up to the basins south of Kos and the Gokova Gulf (Fig. 2). It is remarkable that the geological basement in the area of Bodrum in the footwall comprises metamorphic rocks

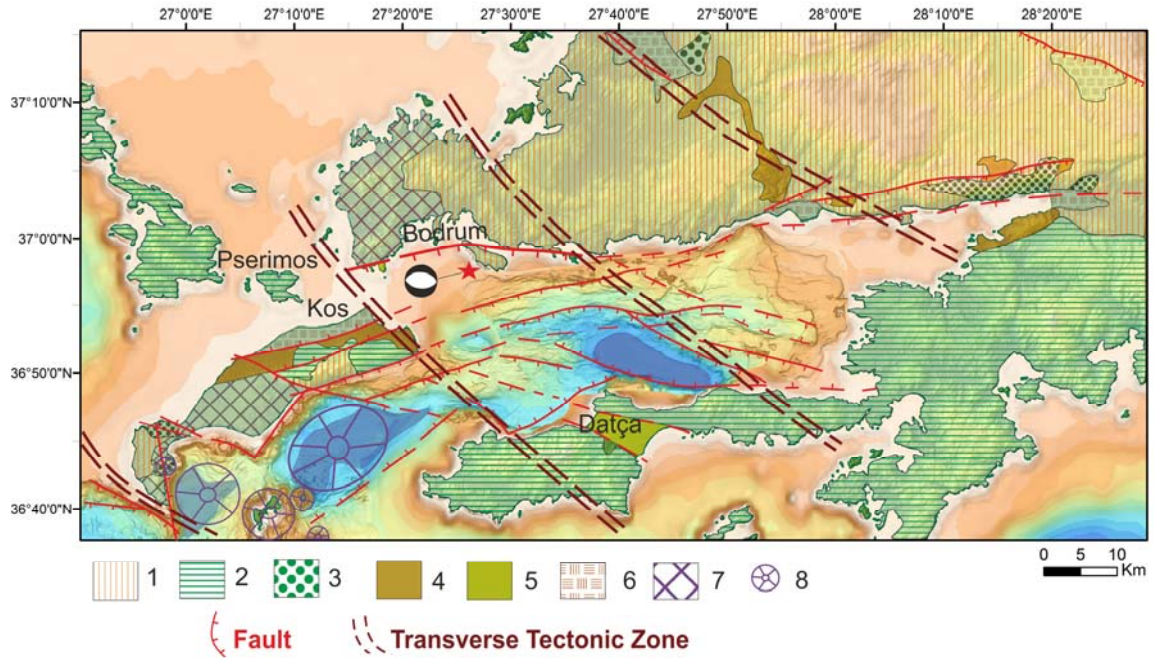

Figure 81: Synthetic map of the Kos - Gökova area combining onshore and offshore structures (from Papanikolaou & Nomikou, 1998; Görür et al., 1995; Nomikou et al., 2018b). Swath data by Iscan et al., 2013; Nomikou et al., 2013; Ocakoğlu et al., 2018; Nomikou et al., 2017; 2018b are plotted above EMODENT bathymetry. 1: metamorphic basement, 2: non metamorphic alpine basement, 3: Lower Miocene marine sediments, 4: Upper Miocene-Pliocene continental sediments, 5: Upper Pliocene-Quaternary sediments, 6: Recent Alluvial, 7: Neogene-Pleistocene volcanics, 8: recent and active volcanic centres.

whereas the basement in the hanging wall observed in the south along the Datca peninsula comprises non metamorphic rocks of the upper nappes. On Kos the metamorphic basement crops out in the form of tectonic windows in Dikeos mt and in Kefalos peninsula in the west. Lower Miocene marine sediments occur on Kefalos peninsula as well as in the easternmost part of the Gokova Gulf. The area has been uplifted and eroded during Miocene with Upper Miocene -Pliocene continental deposits preserved in various localities. However, during late Pliocene - Pleistocene marine sediments have been deposited in some NW-SE basins/grabens, like the basin across the Datca peninsula. Recent volcanic centres are observed only in the basins south of Kos, whereas Miocene volcanic rocks occur in the westernmost part of the Bodrum peninsula without any younger activity east of Kos.

The activated fault segment of the rift zone as defined by the aftershocks of the 6.6 magnitude July 2017 event, is limited within two NW-SE transverse tectonic zones. Towards the west it is limited from the eastern boundary of the Kos horst structure, made of the alpine basement rocks, with the metamorphic relative autochthon of Dikeos mt rising up to 900m of elevation. The Gökova fault zone running parallel to the southern Bodrum coast is shifted by about 18 km to the south in the active fault running along the southern coasts of Kos/Dikeos mt. The NW-SE transverse tectonic zone passes through the eastern coast of Kos and it is terminated towards the NW in the plateau between the Bodrum peninsula and Pserimos Island whereas towards the SE it separates the eastern Kos basin from the Datça basin. A possible continuation of the zone towards the SE may occur across Datça peninsula up to the western coast of Symi island. The eastern transverse tectonic zone occurs at the middle of the Gökova Gulf separating the deep basin (800 m depth) from the shallow part of the gulf towards the east.

More to the west the tectonic segmentation continues with another transverse structure delimiting the Kos horst from the basin separating it from Astypalaea (Fig. 2). However, the Kos horst is further divided in the Dikeos horst to the east from the Antimachia graben/plateau in the centre, formed by the Kos ignibrite of the huge volcanic eruption 145 Ka ago (Allen & Cas, 2001) and the Kefalos horst to the west, where the alpine metamorphic basement is cropping out again (Nomikou et al., 2018b). Thus, two more NW-SE trending faults separate the three neotectonic blocks of the Kos horst, which can be observed also offshore separating the Western Kos from the eastern Kos basin (Fig. 1). It is noteworthy that the tectonic displacement of the Kos horst is much smaller towards the north, where the offshore area between Kos and Kalymnos is shallow and flat in contrast to the southern area where the deep basins of Western and Eastern Kos are developed, hosting also the recent volcanic centres. The overall throw across the E-W faults creating the horst of Dikeos mt is more than 2km from the southern side but only 800m - 1000m from the northern side. The 6.6 magnitude Kos earthquake of 1933 has occurred on this southern Kos fault, where the central and eastern segments of Antimachia and Dikeos were activated but probably not the western segment of Kefalos as indicated by the seismic intensity contours (Ambraseys, 1988; Papazachos & Papazachou, 1989).

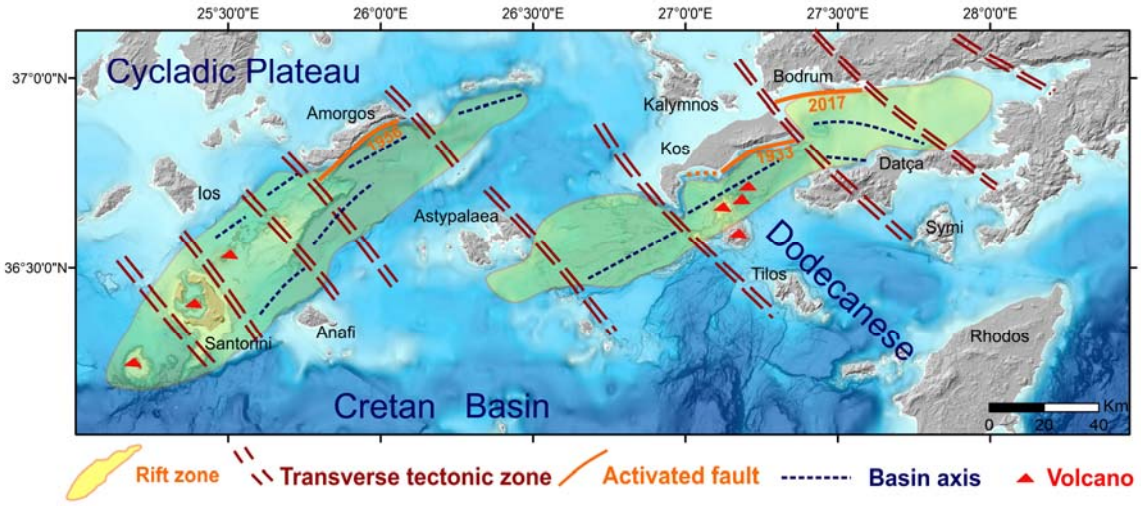

Figure 2: Map of the southern Cyclades - North Dodekanese islands showing the transverse segmentation of the two subparallel rift zones. Swath data by Nomikou & Papanikolaou, 2011; Nomikou et al., 2013; 2017; Hooft et al., 2017 are plotted above EMODENT bathymetry. Triangles indicate volcanic centres.

Similar segmentation has been described in the ENE-WSW Santorini - Amorgos rift zone (Nomikou et al., 2018a) with major differences along strike, such as the Anhydros horst followed by the Amorgos basin (Fig. 2). The 1956 7.3 seismic event of Amorgos was restricted along the Amorgos fault of approximately 40 km length. It is noteworthy that the volcanic centres are also located within certain fault segments along the rift zones whereas they are absent from the adjacent ones like the Kolumbo submarine volcano not observed on the adjacent Anhydros horst to the east or the Yali, Strongyli and Avyssos volcanic centres south of Kos, not observed in the Gökova basin to the east (Fig. 2). The earthquake mechanisms all along the two rift zones show extensional deformation in the N-S to NNW-SSE direction with normal faulting and only minor strike-slip components (e.g. Kitatzi & Louvari, 2003).

The general conclusion is that transverse structures produce in both rift zones a lateral segmentation, which controls the magnitude of the active faults and the expected seismic potential of each segment. Thus: (1) the seismic hazard of the area can be accessed and (2) a relation between intensity of deformation and volcanic eruptions may be correlated in those segments where volcanic activity is going on. The co-existence of the dominant ENE-WSW rift tectonic zones with the transverse NW-SE tectonic zones raise a number of issues, regarding their dynamic and kinematic links within the overall tectonic evolution of the area. It is characteristic that the 800m deep sub-basin of the Gokova Gulf has a NW-SE orientation, parallel to the onshore Datca graben, where Plio-Pleistocene marine sediments have been deposited, although the overall orientation of the gulf remains ENE-WSW. Thus, the resulting geometry may occur from a transitional stage of the evolution of the area, behind the Hellenic arc and trench system. In any case, the along strike stress differences of the rift zones may be accommodated by some transverse structures with complex kinematics, that remain to be further investigated.

Acknowledgements: This work combines two different projects: 1) GEOWARN project (Contract no: IST-1999-12310). The European Commission is acknowledged for their financial contribution to the project. The officers and the crew of the R/V AEGAEO are gratefully acknowledged for their important and effective contribution to the field work, 2) PROTEUS project supported by US National Science Foundation grant number OCE-1548026.We thank the ship captain and crew and science officers of the R/V Marcus Langseth for their indispensable contribution to collecting this dataset.

REFERENCES

Allen, S., & Cas, R.A.F., 2001. Transport of pyroclastic flows across sea during the explosive rhyolitic eruption of the Kos Plateau Tuff. *Greece. Bull. Volcanol*. 62 (6-7), 441-456.

Ambraseys, N., 1988. Engineering seismology. *Earthquake engineering and Structural Dynamics* 17, 1-105.

Görür, N., Şengör, A.M.C., Sakınç, M., Tüysüz, O., Akkök, R., Yiğitbaş, E., Oktay, F.Y., Barka, A., Sarıca, N., Ecevitoğlu, B., Demirbağ, E., Ersoy, Ş., Algan, O., Güneysu, C., & Akyol, A., 1995. Rift formation in the Gökova region, southwest Anatolia: implications for the opening of the Aegean sea. *Geol Mag* 132, 637-650.

İşcan, Y., Tur, H., Gökaşan, E., 2013. Morphologic and seismic features of the Gökova Gulf, SW Anatolia: evidence of strike-slip faulting with compression in the Aegean Extensional Regime. *Geo-Marine Letters* 33, 31-48.

Hooft, E.E.E., Nomikou, P., Toomey, D.R., Lampridou, D., Getz, C., Christopoulou, M-E., O'Hara, D., Arnoux, G.M., Bodmer, M., Gray, M., Heath, B.A., & VanderBeek, B.P., 2017. Backarc tectonism, volcanism, and mass wasting shape seafloor morphology in the Santorini-Christiana-Amorgos region of the Hellenic Volcanic Arc. *Tectonophysics* 712-713, 396-414.

Kiratzi, A., & Louvari, E., 2003. Focal mechanisms of shallow earthquakes in the Aegean Sea and the surrounding lands determined by waveform modelling: a new database. *Journal of Geodynamics* 36, 251-174.

Kiratzi, A.A., & Koskosidi, A., 2018. Constrains on the year source motions of the Kos-Bodrum 20 July 2017 MW6.6 earthquake. *16th European Engineering*. Thessaloniki 18-21 June 2018.

Nomikou, P., & Papanikolaou, D. 2011. Extension of active fault zones on Nisyros Volcano across the Yali-Nisyros Channel based on onshore and offshore data. *Mar Geophys Res* 32, 181-192.

Nomikou, P., Papanikolaou, D., Alexandri, M., Sakellariou, D., & Rousakis, G., 2013. Submarine volcanoes along the Aegean volcanic arc. *Tectonophysics* 597-598, 123-146.

Nomikou, P., Ocakoğlu, N., Işcan, Alp, Y., Lampridou, D., & Papanikolaou, 2017. Morpho-structural setting of the eastern part of the Aegean Sea (Kos-Nisyros-Tilos-Gökova region) revealed by high-resolution bathymetry. *Proceedings of 16st International Conference "Geoinformatics: theoretical and applied aspects"*, SUB ID: 43371, 15-17 May, 2017, Kiev, Ukraine.

Nomikou, P., Hübscher, C., Papanikolaou, D., Farangitakis, P.G., Ruhnau, M., & Lampridou, D., 2018a. Expanding extension, subsidence and lateral segmentation within the Santorini - Amorgos basins during Quaternary: Implications for the 1956 Amorgos events, central - south Aegean Sea, Greece. *Tectonophysics* 722, 138-153.

Nomikou, P., Papanikolaou, D., & Dietrich, V.J., 2018b. Geodynamics and Volcanism in the Kos-Yali-Nisyros Volcanic Field. In: *Nisyros Volcano* (Dietrich, V., Lagios, E., eds), Springer, 13-56.

Ocakoğlu, N., Nomikou, P., İşcan, Y., Loreto, M.F., & Lampridou, D., 2018. Evidence of extensional and strike-slip deformation in the offshore Gökova-Kos area affected by the July 2017 Mw6.6 Bodrum-Kos earthquake, eastern Aegean Sea. *Geo-Marine Letters*, doi: 10.1007/s00367-017-0532-4, GMLE-D-17-00084.1.

Okal, E.A., Synolakis, C.E., Uslu, B., Kalligeris, N., & Voukouvalas, E., 2009. The 1956 earthquake and tsunami in Amorgos, Greece. *Geoph. J. Int*. 178, 1533-1554.

Papanikolaou, D., & Nomikou, P., 1998. The Palaeozoic of Kos: A low grade metamorphic unit of the basement of the external Hellenides terrain. IGCP Project No 276, Newsletter No 6, 155-166.

Papanikolaou, D.J., & Royden, L.H., 2007. Disruption of the Hellenic arc: Late Miocene extensional detachment faults and steep Pliocene-Quaternary normal faults-Or what happened at Corinth?. *Tectonics* 26.

Papazachos, B., & Papazachou, K., 1989. *The Earthquakes of Greece*. Ziti editions, Thessaloniki, 356p.

Reilinger, R., McClusky, S., Paradissis, D., Ergintav, S., & Vernant, P. 2010. Geodetic constraints on the tectonic evolution of the Aegean region and strain accumulation along the Hellenic subduction zone. *Tectonophysics* 488 (1-4), 22-30.

Tiryakioğlu, İ., Aktuğ, B., Yiğit, C.Ö., Yavaşoğlu, H.H., Sözbilir, H., Özkaymak, Ç., Poyraz, F., Taneli, E., Bulut, F., Doğru, A., & Özener, H., 2017. Slip distribution and source parameters of the 20 July 2017 Bodrum-Kos earthquake (Mw6.6) from GPS observations. *Geodinamica Acta* 30 (1), 1-14.

INQUA Focus Group Earthquake Geology and Seismic Hazards

paleoseismicity.org

Paleoseismic trenching and evaluation of the Assiros - Krithia fault and the Drimos fault zone in Mygdonia Basin, Northern Greece

Papanikolaou, Ioannis (1), Dafnis, Pavlos (2), Deligiannakis, Georgios (1), Hengesh, James (3), Panagopoulos, Anestis (2)

(1) Mineralogy-Geology Laboratory, Department of Natural Resources Development and Agricultural Engineering, Agricultural University of Athens, 75 Iera Odos Str., 118-55 Athens, Greece, i.pap@aua.gr
(2) Geoskopio SA - EDAFOMICHANIKI GROUP, 19 Emmanouil Papadaki Str., 141 21 N. Iraklio, Greece
(3) Interface Geohazard Consulting LLC, 20 Plumeria Pl., Lahaina, HI 96761 USA

Abstract: *Paleoseismic investigations were carried out along the Assiros-Krithia fault (AKF) and Drymos fault zone (DFZ), near the city of Thessaloniki, in northern Greece. Both structures were investigated through detailed geomorphological and geological mapping followed by paleoseismic trenching and radiometric dating. The AKF and DFZ form the northern and northwestern boundaries of the Mygdonia Basin, respectively. The AKF was expressed as a single north dipping fault trace with the last event producing 48 cm of vertical displacement around 4540 cal. yrs. BP. The estimated slip rate is 0.15 mm/yr. The DFZ is characterised by distributed deformation across eight major and secondary fault planes. Three possible paleo-events were identified with vertical displacements ranging from 40 cm up to 77 cm. The DFZ has an estimated slip rate of 0.1-0.3 mm/yr. The investigations demonstrate the presence of seismogenic structures at the northern and northwestern margins of Mygdonia Basin.*

Keywords: *Assiros, Drymos, Mygdonia, slip-rate, radiocarbon dating*

INTRODUCTION

Regional tectonic setting

The central Macedonia landscape and geological structure is dominated by large NW-SE trending fault-bounded basins, such as the Mygdonia and Strymon basins. These basins formed during Late Miocene to Pliocene NE-SW directed extension that primarily activated NW-SE striking normal faults (Dinter & Royden, 1993). Since the Quaternary, the stress field has changed and is now dominated by N-S extension and formation of E-W trending normal faults that have reshaped the pre-existing basins (e.g. Lyberis, 1984; Pavlides & Kilias, 1987; Tranos, 2011). The current N-S extension direction also is confirmed by geodetic data (Martinod et al., 1997; McClusky et al., 2000; Müller et al., 2013). These E-W faults are known to be active and have produced historical fault ruptures. Isoseismal data from past earthquakes (e.g. 1902 M=6.6 Assiros, 1932 M=7.0 Ierrisos 1932, M=6.2 Sochos and 1978 M=6.5 Volvi events) indicate that both the NW-SE faults and the E-W trending faults are active (Papazachos et al., 1979; Voidomatis et al., 1990; Papazachos & Papazachou, 1997). Although a limited number of prior paleoseismic investigations have been completed along some of the E-W oriented fault zones in northern Greece (Chatzipetros et al., 2005), none previously have been carried out on the NW-SE oriented fault zones in the region. Two paleoseismic studies were completed to assess the characteristics of the Assiros Krithia fault (AKF) and Drymos fault zone (DFZ) located along the northern and northwestern boundaries of the Mygdonia basin (Fig 1). The AKF is related to an E-W trending, north facing tectonic scarp that has deflected the local drainage system. The alluvial fan north of the fault scarp has a smooth morphological gradient of 1°-2°. The slope on the south side of the fault consists of Pleistocene sediments that have been deformed along the fault zone forming slope gradients of up to 15°.

Two northwest trending linear topographic ridges on the northern basin margin are related to the DFZ. The westernmost ridge is the most prominent. Pleistocene and Holocene alluvial deposits occur east of the fault trace and form a smooth geomorphic gradient. Steeper slopes are observed to the west due to the outcrops of Alpine rocks in the footwall of the fault zone.

General Stratigraphy

The area north of the AKF consists of Holocene alluvial deposits overlying Pleistocene formations that are exposed on the uplifted southern side of the fault. Similarly, Holocene deposits overlie Pleistocene alluvial deposits in the area east of the DFZ. Alpine bedrock formations outcrop to the west (Fig. 1).

METHODOLOGY

Detailed geomorphological, geological and paleoseismic trench investigations were conducted in order to assess the location, geometry, kinematics and past surface displacements associated with these two fault zones. For both faults paleoseismic observations were performed along targeted sections of an existing construction trench.

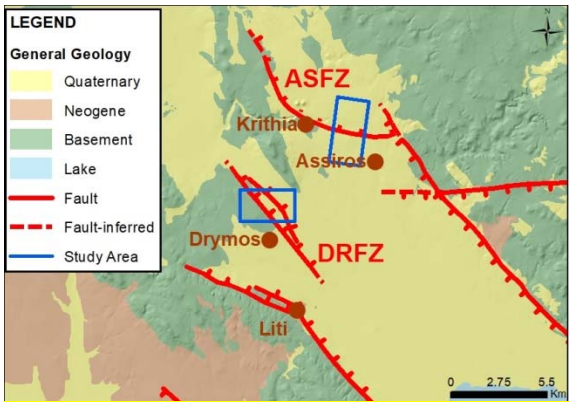

Figure 1: Simplified geological map showing the main faults of the Mygdonia basin.

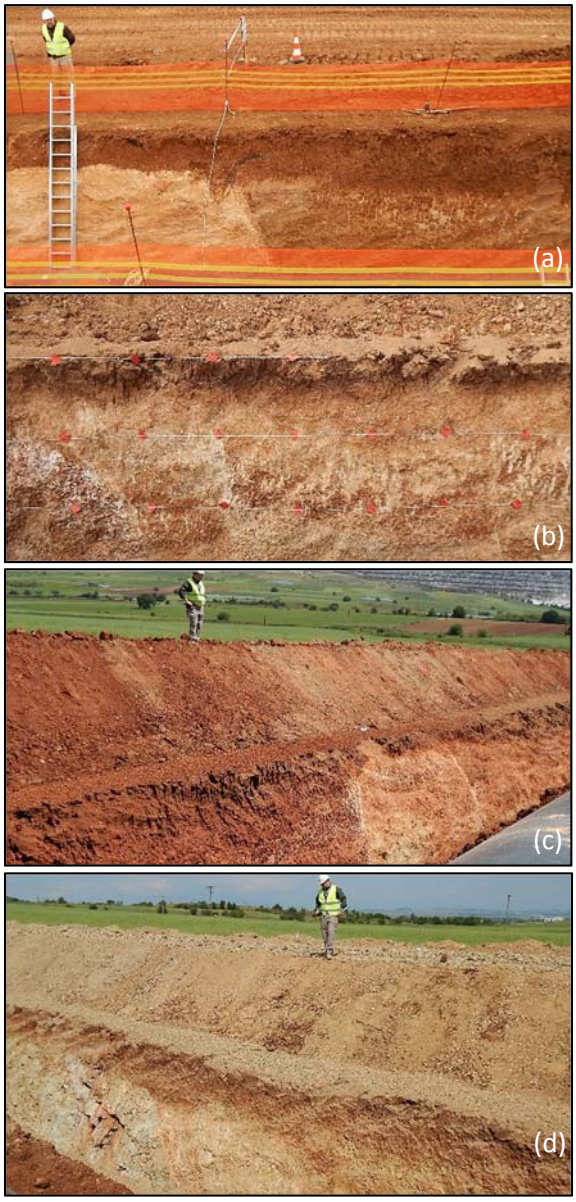

Figure 2: a) Westward view of the trench wall at AKF location. b) Westward view of the cleaned and 1x1m gridded T1 location at DFZ area. Northward (c) and westward (d) view of T3 and T4 locations at DFZ area, respectively.

RESULTS - DISCUSSION

Faults description

The AKF forms an 8 to 12 km long fault trace (Fig. 1) that has produced a north sloping uphill facing topographic scarp in the area of the trench. The fault has a normal, down-to-the-north sense of displacement. The escarpment forms a local drainage divide and controls the middle Pleistocene to Holocene sedimentation processes. A prominent antecedent stream near the eastern tip of the fault is not diverted but has cut through the fault scarp. The position of strath surfaces across the fault projection in this drainage demonstrate that fault displacement could not exceed 3-4 m since the time of strath formation (late Quaternary).

The DFZ is an 8 to 10 km long fault zone (Fig. 1) that comprises two parallel and closely spaced fault splays. Both fault splays have a down-to-the-northeast normal sense of displacement and uplift the area southwest of the fault trace. The faults controlled the middle Pleistocene to Holocene sedimentation processes. The two fault splays are 800 m apart and therefore deform a relatively wide area; the fault splays are possibly linked at depth. The fault traces are mapped following both geomorphological features and geological structure and form the northwestern boundary of the Mygdonia Basin.

Paleoseismic trenches results

The AKF is clearly exposed in both trench walls (Figs. 3 and 4). The main fault plane dips 60˚-70˚ north and strikes ~E-W (095˚) in agreement with the surface expression of the fault. A second splay is located 0.7 m south of the main fault (Fig.3b). The main fault trace has developed a 0.7 to 1 m thick fault deformation zone.

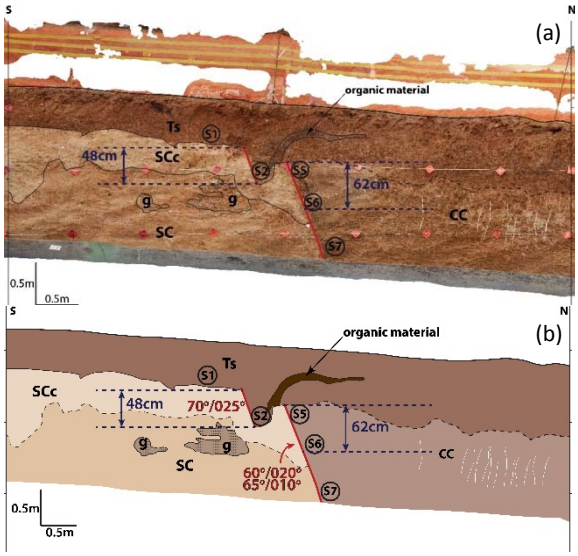

Figure 3: AKF trench logs: a) Interpretation and b) final logging of the west wall of the 9 m long and 3 m deep trench exposure depicting all major boundaries, trench stratigraphy, and radiocarbon sampling locations. Two events with 48 cm (most recent) and 62 cm of vertical displacement are inferred. S1, S2, S6 and S7 represent the sampling locations for radiocarbon analysis.

Two displacement events were recognized: the most recent event produced a 48 cm vertical displacement and the penultimate event produced a 62 cm vertical displacement.

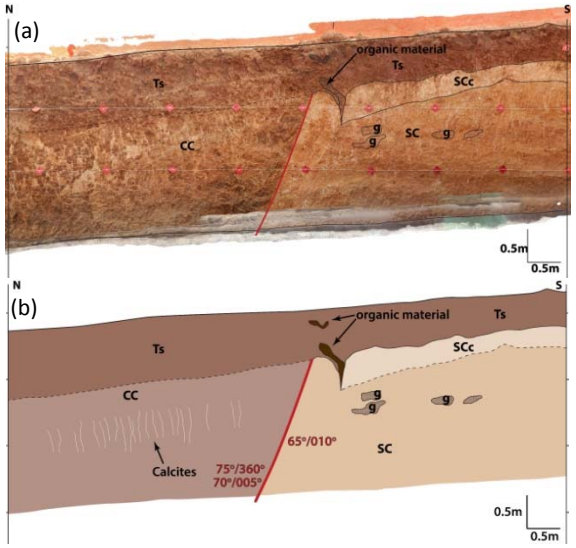

Figure 4: AKF trench log: a) Interpretation and b) final logging of the east (west facing) wall of the 9 m long and 3 m deep trench exposure. Trench logs depict all major boundaries and trench stratigraphy.

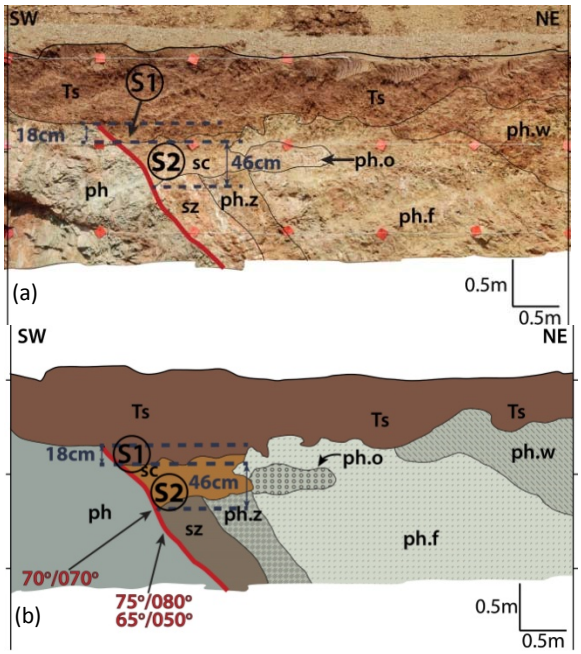

Figure 5: DFZ T4 trench log: a) Interpretation and b) final logging of the 6 m long and 3 m deep north wall of the trench. Log depicts all major boundaries and trench stratigraphy. Two events produced 18 cm (most recent) and 46 cm (penultimate) of vertical displacement. S1 and S2 represent the sampling locations for radiocarbon analysis.

Radiocarbon dates from samples S1 (3000 ± 30 cal. yr. BP), S2 (4540 ± 30 cal. yr BP), S5 (7900 ± 30 cal. yr BP), S6 (19430 ± 50 cal. yr BP) and S7 (18620 ± 50 cal. yr BP) (see Fig.3 for sampling locations) confirm that the fault displaces Holocene to late Quaternary age deposits. We infer that these two events occurred 4540 and 7900 cal. yr. BP, with a recurrence interval on the order of 3360 yrs.

The main fault plane of the DFZ is clearly exposed in both the north and south walls of the T4 trench section. The fault strikes ~NW-SE (140˚) and dips 65˚ NE (050˚). A 2 m thick cataclastic zone is developed along the fault zone (Fig. 5). Overall, the deformation zone for the DFZ is 7 to 10 m wide. A secondary fault is clearly exposed in T1 (Fig. 6). This fault splay strikes ~NW-SE (135˚) and dips 75˚ NE (045˚).

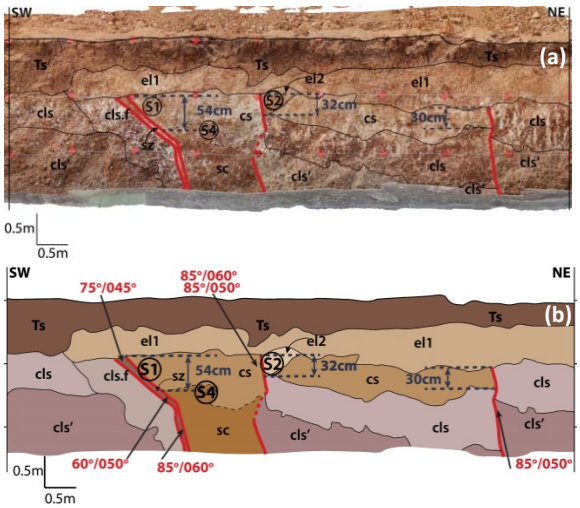

Figure 6: DFZ T1 segment: a) Interpretation and b) final logging of the 9 m long and 3 m deep north wall of trench exposure. Logs depict all major boundaries and trench stratigraphy. 54 cm of vertical displacement is inferred based on the deposition and thickness of the "cs" formation. Two secondary faults have accommodated 32 cm and 30 cm of vertical displacement in the hanging wall. S1 and S2 represent the sampling locations for radiocarbon analysis.

Two fault planes were observed in the hanging wall, 2 m and 6 m east of the main fault in T1 (Fig. 6b). These splays also strike NW-SE (~135˚) and dip ~85˚ ~NE (040°). Considering the northeast dip of the stratigraphy in T1, these two fault planes are inferred to have an antithetic sense of displacement. Based on the disruption of the Top Soil (Ts) at T4, a minimum vertical displacement of 18 cm is inferred for the most recent event. The penultimate event is inferred to have produced 46 cm of vertical displacement of the "sc" formation in T4 and 54 cm of vertical displacement in T1.

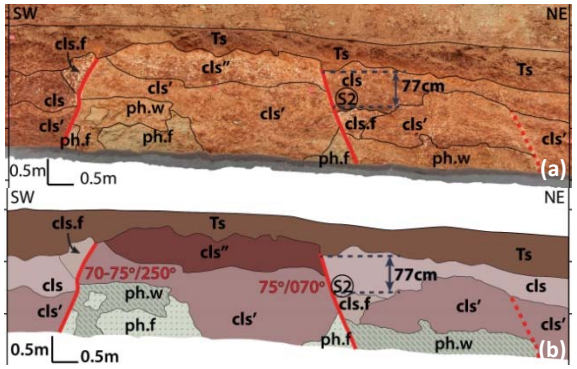

Figure 7: T3 section of DFZ trench: a) Interpretation and b) final log depicting all major boundaries and trench stratigraphy. A 77 cm vertical displacement is inferred, implying one or more paleo-events. S2 represents the sampling location for radiocarbon analysis.

The two secondary faults have accommodated 32 cm and 30 cm of vertical displacement. Additionally, two significant fault related features were identified at T3 between the T1 and T4 sections (Fig. 7). This fault produced a 77 cm vertical displacement of a Holocene deposit (Fig. 7), but it is unclear if this is related to one or more events.

Radiocarbon analyses of samples T4-S1 (4420 ± 30 cal. yr. BP) and T4-S2 (6120 ± 30 cal. yr. BP) (see Fig. 5 for sampling locations) indicate that both events inferred at the T4 location occurred during the mid-Holocene. The recurrence interval is approximately 1700 yrs. Radiocarbon analyses on samples from the T1 location, T1-S1 (6740 ± 30 cal. yr. BP), T1-S2 (6220 ± 30 cal. yr. BP) and T1-S3 (7520 ± 30 cal. yr. BP) (see Fig. 6 for sampling locations), provide evidence that displacement occurred along the main fault plane and the westernmost secondary fault at approximately the same time with the latest displacement occurring around 6740 cal. yr. BP. The age of sample T3-S2 (8890 ± 30 cal. yr. BP) (see Fig. 7 for sampling locations) also confirms that this was a Holocene event. Due to the lack of other dated samples, it is unclear whether the 77 cm displacement (the largest recorded along the Drymos trench) is related to one or more paleo-earthquakes.

CONCLUSIONS

Paleoseismological trenching and dating confirmed that Holocene deformation occurred along both the AKF and DFZ. The AKF is 8 to 12 km long structure that could generate an M_w=~6.0 to 6.4 event, based on empirical relationships from Wells and Coppersmith (1994), Caputo & Pavlides (2004) and Wesnousky (2008). Radiocarbon dates suggest that two events have occurred since the mid-Holocene around 4540 and 7900 years ago. Overall the total displacement over the last 7900 years is 121 cm, implying a 0.15 mm/yr slip-rate, with a recurrence interval of 3360 yrs. The last event (4540 years ago) produced up to 48 cm of vertical displacement. The DFZ is an 8 to 10 km long structure with a slip-rate on the order of 0.1-0.3 mm/yr. Empirical relationships between length and displacement suggest the fault could produce average displacements of 13 to 28 cm and maximum displacements of 24 cm to 40 cm. However, three possible paleo-events with vertical displacements exceeding 40 cm were interpreted in the trench exposures (46 cm at T4, 54 cm at T1 and 77 cm at T3 locations; see Figs. 5 to 7), implying a possible multi-segment rupture scenario including the 20 to 22 km long Gerakarou-Liti fault zone (which is parallel to DFZ with a step over of only 2 km) and the DFZ segment, yielding a potential 32 km long rupture. The Drymos fault is characterized by distributed deformation with eight major and secondary fault planes observed at four different sites (T1 to T4). Dating results confirm that four of these fault planes have produced displacements between approximately 4000 and 9000 ybp.

Acknowledgements: We would like to thank all personnel involved to excavating and cleaning the trenches at the studied segments.

REFERENCES

Chatzipetros, A., Kokkalas, S., Pavlides, S., & Koukouvelas, I., 2005. Palaeoseismic data and their implication for active deformation in Greece. *Journal of Geodynamics* 40, 170-188.

Dinter, D.A., & Royden, L., 1993. Late Cenozoic extension in north-eastern Greece: Strymon Valley detachment system and Rhodope metamorphic core complex. *Geology* 21, 45-48.

Lyberis, N., 1984. Tectonic evolution of the North Aegean trough. *Geological Society of London, Special Publications* 17, 709-725.

Martinod, J., Hatzfeld, D., Savvaidis, P., & Katsambalos, K., 1997. Rapid N-S extension in Mygdonian graben (Northern Greece) deduced from repeated geodetic surveys. *Geophys. Res. Lett*. 24, 3293-3296.

McClusky, S., Balassanian, S., Barka, A., Demir, C., Ergintav, S., Georgiev, I., Gurkan, O., Hamburger, M., Hurst, K., Kahle, H., Kastens, K., Kekelidze, G., King, R., Kotzev, V., Lenk, O., Mahmoud, S., Mishin, A., Nadariya, M., Ouzounis, A., Paradissis, D., Peter, Y., Prilepin, M., Reilinger, R., Sanli, I., Seeger, H., Tealeb, A., Toksoz, M.N., & Veis, G., 2000. Global Positioning System constraints on plate kinematics and dynamics in the Eastern Mediterranean and Caucasus. *Journal of Geophysical Research* 105, 5695-5719.

Müller, M.D., Geiger, A., Kahle, H.-G., Veis, G., Billiris, H., Paradissis, D., & Felekis, S., 2013. Velocity and deformation fields in the North Aegean domain, Greece, and implications for fault kinematics, derived from GPS data 1993-2009. *Tectonophysics* 597-598, 34-49.

Papazachos, B.C., & Papazachou, C.B., 1997. The earthquakes of Greece. Ziti editions, Thessaloniki, 304 pp.

Papazachos, B., Mountrakis, D., Psilovikos, A., & Leventakis, G., 1979. Surface fault traces and fault plane solutions of the May-June 1978 major shocks in the Thessaloniki area, Greece. *Tectonophysics* 53, 171-183.

Pavlides, S., & Caputo, R., 2004. Magnitude versus faults' surface parameters: quantitative relationships from the Aegean Region. *Tectonophysics* 380, 159-188.

Pavlides, S.B., & Kilias, A.A., 1987. Neotectonic and active faults along the Servomacedonian zone (SE Chalkidiki, northern Greece). *Ann. Tecton*. I (2), 9-104.

Tranos, M.D., 2011. Strymon and Strymonikos Gulf basins (Northern Greece): Implications on their formation and evolution from faulting. *Journal of Geodynamics* 51, 285-305.

Voidomatis, Ph.S, Pavlides, S.B., & Papadopoulos, G.A., 1990. Active deformation and seismic potential in the Serbomacedonian zone, northern Greece. *Tectonophysics* 179, 1-9.

Wells, D.L., & Coppersmith, K.J., 1994. New empirical relationships among magnitude, rupture length, rupture width and surface displacement. *Bull. Seismol. Soc. Am.*84, 974-1002.

Wesnousky, S.G., 2008. Displacement and Geometrical Characteristics of Earthquake Surface Ruptures: Issues and Implications for Seismic-Hazard Analysis and the Process of Earthquake Rupture. *Bull. Seismol. Soc. Am.* 98, 1609-1632.

INQUA Focus Group Earthquake Geology and Seismic Hazards

paleoseismicity.org

Paleoseismic trenching and evaluation of the Symvoli - Fotolivos and Tholos - Nea Zichni fault zones in Northern Greece

Papanikolaou, Ioannis (1), Deligiannakis, Georgios (1), Hengesh, James (2), Dafnis, Pavlos (3), Panagopoulos, Anestis (3), Lymperis, Evriviades (4)

(1) Mineralogy-Geology Laboratory, Department of Natural Resources Development and Agricultural Engineering, Agricultural University of Athens, 75 Iera Odos Str., 118-55 Athens, Greece, i.pap@aua.gr
(2) Interface Geohazard Consulting LLC, 20 Plumeria Pl., Lahaina, HI 96761 USA
(3) Geoskopio SA - EDAFOMICHANIKI GROUP, 19 Emmanouil Papadaki Str., 141 21 N. Iraklio, Greece
(4) Edafos Engineering Consultants SA, 9 Iperidou Str, 10558 Athens, Greece

Abstract: *This paper presents the results of paleoseismic investigations at the Symvoli - Fotolivos fault zone (SFFZ) and the Tholos - Nea Zichni fault zone (TNFZ) in Northern Greece. Both fault zones were investigated by detailed geomorphological and geological mapping followed by paleoseismic trenching and radiometric dating of key stratigraphic horizons, which provided evidence of Holocene activity for both faults. Two Holocene surface rupturing events are inferred for the SFFZ with vertical displacements of 75 and 66cm. The displaced stratigraphic units and ages from the SFFZ yield a Holocene slip rate of 0.15±0.1mm/yr and an average recurrence interval of 5700yrs. The TNFZ is a complex structure with several synthetic and antithetic fault planes. Offset measurements and dates for the TNFZ yield a slip rate of 0.2±0.1mm/yr with a recurrence interval of 2500±1000yrs. Our results demonstrate that the NW-SE trending basin bounding faults also can be active in the current N-S extensional stress regime.*

Keywords: *Paleoseismology, Greece, Strymon, slip-rate, radiocarbon dating*

INTRODUCTION

Regional tectonic setting

The Central and Eastern Macedonia landscape and geological structure is dominated by large NW-SE trending fault-bounded basins, such as the Axios, Mygdonia, Strymon and Drama basins (Mercier et al., 1989; Mountrakis et al., 2006; Tranos, 2011). These basins formed during Late Miocene to Pliocene NE-SW directed extensional stresses that primarily activated NW-SE striking normal faults. Since the Quaternary the stress field has changed and is now dominated by N-S extension and formation of E-W trending normal faults that have reshaped the pre-existing basins (e.g. Lyberis, 1984; Pavlides & Kilias, 1987). These E-W faults are known to be active and have produced historical fault ruptures. Isoseismal data from past earthquakes indicate that both the NW-SE faults (e.g. 1902 M=6.6 Assiros and 1932 M=7.0 Ierrisos earthquakes) and the E-W trending faults (e.g. 1932 M=6.2 Sochos and 1978 M=6.5 Volvi earthquakes) are active (Papazachos et al., 1979; Voidomatis et al., 1990; Papazachos & Papazachou, 1997). Although limited paleoseismic investigations have been completed along some of the E-W oriented fault zones in northern Greece (e.g. Chatzipetros et al., 2005), none have previously been carried out on the NW-SE oriented fault zones in the region.

Two paleoseismic studies were carried out to assess the characteristics of the NW-SE trending Symvoli-Fotolivos and Tholos-Nea Zichni fault zones (Fig. 1). The Symvoli-Fotolivos fault zone (SFFZ) is located along the western boundary of Drama basin, near the City of Drama, while the Tholos-Nea Zichni Fault Zone (TNFZ) is located along the eastern margin of Strymon basin, near the City of Serres. The area between the two fault zones consists of Mesozoic metasediments unconformably overlain by late Neogene nearshore fluvial and lacustrine deposits. Along the basin margins both eastward of the SFFZ and westward of TNFZ the basin morphology is generally very smooth with a morphological gradient that ranges from 1° to 3°. However, within the basement uplift between the two fault zones the topography gradually becomes more rugged, with slope gradients approaching 20°. The change in morphology coincides with the positions of the fault zones.

General Stratigraphy

The alluvial plain that lies east of the SFFZ is covered by reddish-brown loams with dispersed round pebbles consisting of red clays, sandy loams with dispersed rounded pebbles (marble, gneiss and quartz) that increase in size towards the lowland. Upslope of the alluvial plain Lower Pleistocene to Pliocene lacustrine deposits outcrop along the basin margins. The slopes immediately above the lacustrine deposits are composed of grey to whitish marble outcrops. West of the TNFZ fault trace, Pleistocene and Holocene alluvial deposits form a smooth geomorphic surface with numerous fluvial terrace risers. To the east of the mapped fault trace and at higher elevations on the up thrown side of the fault, lower Pleistocene to Pliocene fluvio-deltaic deposits are observed (Fig. 1).

METHODOLOGY

Detailed geomorphological and geological mapping and paleoseismic trench investigations were conducted in order to assess the location, geometry, kinematics, and past surface displacements associated with these two fault zones. For the SFFZ a 221 m long and 3 m deep trench was excavated (Fig 2a), while for the TNFZ a 153 m long and 1.5 - 3 m deep trench was excavated (Fig. 2b). Both trenches were excavated using benched trenching techniques to ensure trench stability. Both trenches had 1.5 m high vertical walls and intervening 1.5 m wide benches on each side of the trench. Both trenches were cleaned, gridded, photographed, georeferenced and logged.

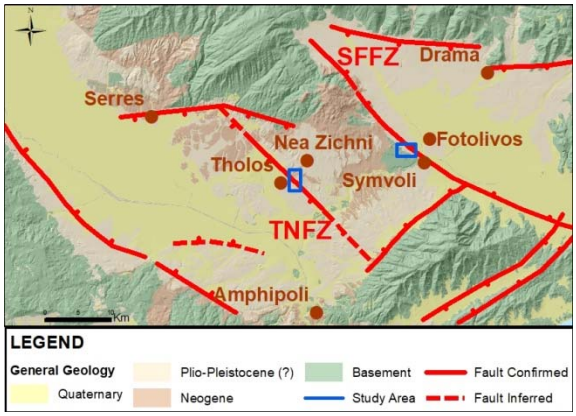

Figure 1: Simplified geological map showing the main faults of the Drama and Strymon Basins.

More detailed photography, logging, and RTK georeferencing were completed where evidence of active faulting was found. Samples also were collected from these locations for radiocarbon dating.

Figure 2: a) Westward view of the 221 m long trench at the SFFZ, b) Westward view of the 153 m long trench at the TNFZ.

RESULTS – DISCUSSION

Fault zones description

The SFFZ is a major NW-SE trending normal fault zone that dips to the northeast and forms the western boundary of the Drama Basin. The fault zone is approximately 53 km long and is divided in several segments. Based on the thickness and distribution of Quaternary deposits within the basin, as well as the present-day sedimentation processes, we infer that the middle and southern parts of the SFFZ are more active and form a 32 ± 2 km long fault structure.

The TNFZ is a major NW-SE trending normal fault zone that dips to the southwest and forms the eastern boundary of the Strymon Basin. Considering the thickness and distribution of Quaternary deposits within the basin, as well as the present-day sedimentation processes and the topography, we infer that the middle part of the zone is more active and forms a 15 km long fault structure. It's prolongation both towards the northwest and southeast could be inferred, but it is based on weaker geological and geomorphological evidence. Due to the difference between the present-day extension direction and the fault strike, a minor horizontal component also is likely. Recent geodetic data (Mouslopoulou et al., 2014) suggest a left lateral component of motion.

Paleoseismic trenches results

At the SFFZ two fault planes were identified. At metre mark 170 from the western tip of the trench a normal fault plane was identified with a 135° strike and 55° east dip. This fault does not offset the overlying Stage IV Pleistocene calcic soil horizon. The strike of this splay is in agreement with the strike of the fault zone identified from surficial geomorphologic mapping. At metre mark 215 (from the western tip of the trench) a normal fault plane was identified with a 135° strike and a 60° east dip. This fault zone offsets the Pleistocene and Holocene soils in the trench. Two events are inferred with vertical offsets of 75 cm (most recent event) and 66 cm (penultimate event) (Fig.3, Fig. 4b-d). The penultimate event involved vertical displacement of the calcic soil "cs" horizon (Fig. 4b). Radiocarbon analysis on samples S14 (5620 ± 30 cal. years BP) and S13 (11350 ± 40 cal. years BP) (see Figs. 3 and 4 for sampling locations) support that both events occurred during the Holocene, with a recurrence interval of ~5700 yrs. Beyond the active and the inactive fault planes, several other secondary ruptures and fissures parallel and subparallel to the fault have been mapped and measured along the trench, predominantly towards the hanging wall.

At the TNFZ several fault related features were observed at 0-16 m and 109-123 m from the eastern tip of the trench. The main fault plane was identified at metre mark 120. The fault strikes N152° and dips 60° SW, in agreement with the strike of the fault zone inferred from surficial geomorphological mapping (Fig. 5). Two major antithetic fault planes were detected at 4 m and 12 m from the eastern edge of the trench. These structures deform and offset the geological formations (Fig. 6). These antithetic faults dip 45° NE (055°) and 70° E (090°), respectively, which contrast markedly to bedding, which dips 27°-40° WSW to W (240°-265°). Based on the disruption of the eluvial

mantle formation (el) we estimate vertical displacements of approximately 49 cm and 68 cm on two distinct antithetic fault planes. Radiocarbon analysis on samples SB3 (6250 ± 30 cal. years BP), SB4 (2780 ± 30 cal. years BP) and SB10 (4850±30 cal. years BP) (see Figures 5-6 for sampling locations) provide evidence that at least 2 events have occurred during the Holocene between 6250 and 2780 years BP.

CONCLUSIONS

Paleoseismological trenching provided geological evidence for Holocene deformation along both NW-SE trending basin bounding fault zones, demonstrating that they can also be active in the current N-S extensional stress regime. The SFFZ has a segment length of 32 km and yields maximum magnitude distributions that range from M_w=6.13 to 6.85 with an average magnitude value of M_w=6.61, based on empirical regressions from Wells & Coppersmith (1994), Caputo and Pavlides (2004), and Wesnousky (2008). The preferred displacement scenario suggests two events with vertical displacements of 66 cm (penultimate event 11350±40 BP) and 75 cm (most recent event ~5620 ± 30 years ago), implying an approximate 0.12 mm/yr throw-rate and 0.14 mm/yr slip-rate, respectively. These data confirm that it is a low slip-rate fault (0.15 ± 0.1mm/yr), with earthquake recurrence intervals on the order of 5700 yrs. No major historical or instrumental earthquakes can be correlated with this fault and this might be due to its long recurrence interval.

The TNFZ has an estimated length that varies from 15-32 km. Geological and geomorphological data strongly support a 15 km long fault segment, which represents the preferred rupture scenario. Paleoseismic trenching revealed that this is a complex fault zone with deformation distributed across several synthetic and antithetic planes. Radiometric dating provides limiting ages of surface displacements along a synthetic fault plane 4950 ± 30 years ago, and along an antithetic fault plane 2840 ± 30 to 6300 ± 30 years ago. Therefore, one or two events appear to have occurred along this fault in the past 6300 years. It is interpreted as a low slip-rate fault (0.20 ± 0.1 mm/yr), with recurrence intervals on the order of 2500±1000yrs.

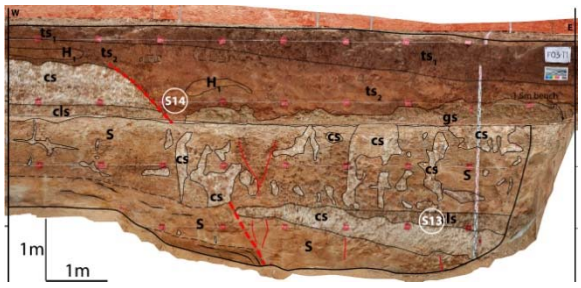

Figure 3: Interpretation on the photomosaic of the 9m long active fault area (from 212 up to 221m) of the SFFZ trench, depicting all major boundaries, trench stratigraphy and sampling locations for radiocarbon dating.

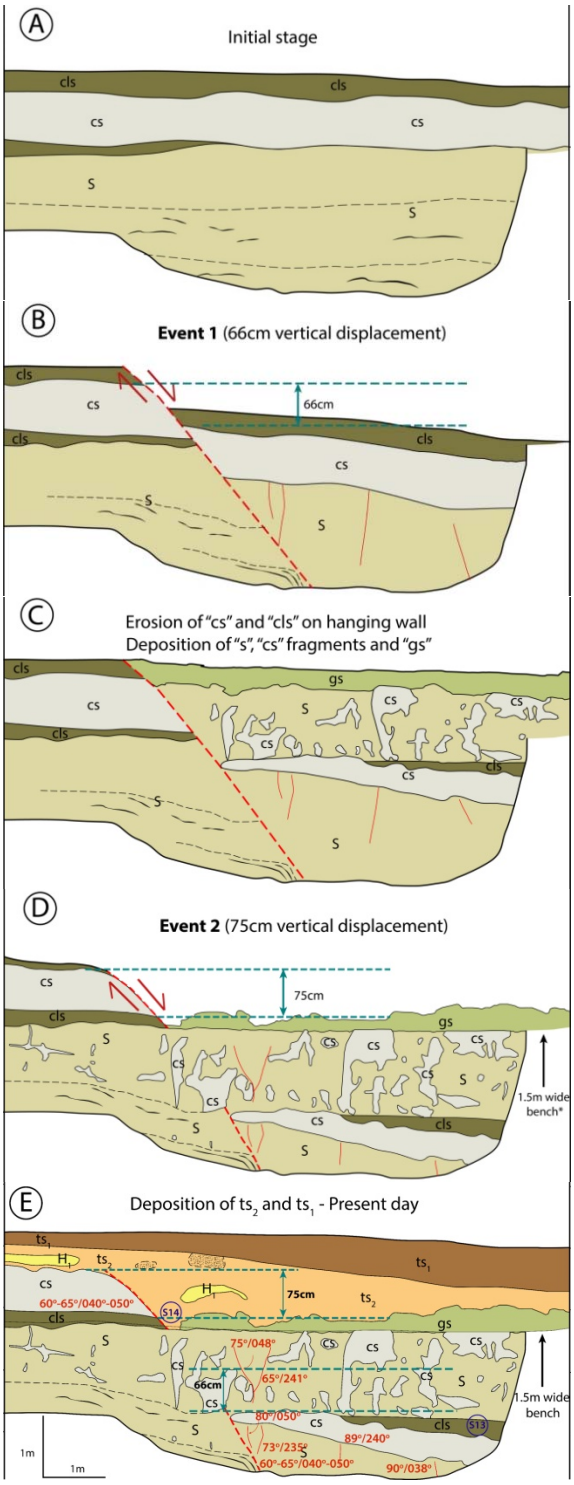

Figure 4: A retrodeformation model for the SFFZ. Model shows the 9m long active fault area, illustrating fault displacement scenarios (A-D) and the final interpretation (E). Two events are inferred with 75 cm (most recent) and 66 cm (penultimate) of vertical displacement. S13 and S14 represent the sampling locations for radiocarbon analysis.

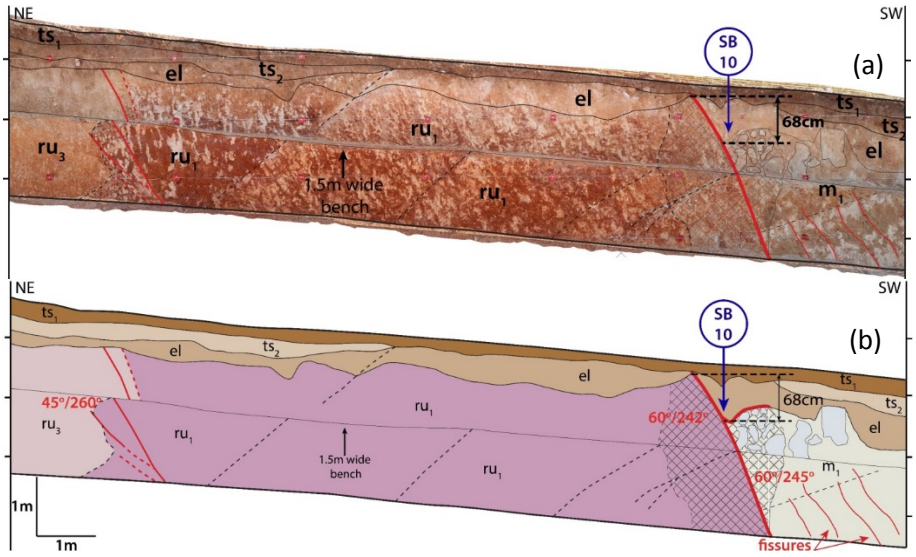

Figure 5: a) Photomosaic of the TNFZ trench from 109 to 123 m, showing the main fault plane. b) Final logging, depicting all major boundaries, trench stratigraphy and sampling locations for radiocarbon dating.

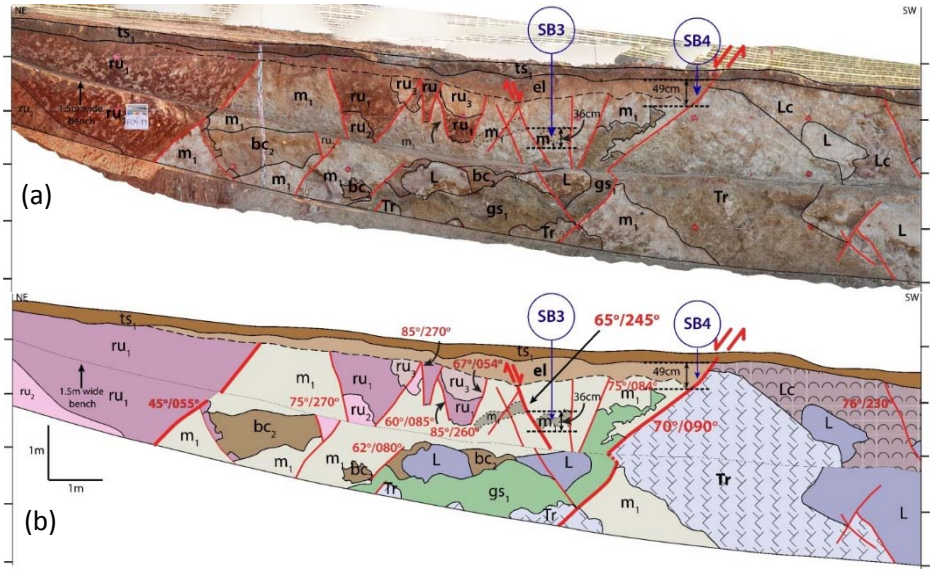

Figure 6: a) Photomosaic of the TNFZ trench from 0 to 16 m, showing the two major antithetic fault planes. b) Final logging, depicting all major boundaries, trench stratigraphy and sampling locations for radiocarbon dating.

Acknowledgements: We would like to thank all personnel involved to excavating and cleaning such long trenches.

REFERENCES

Chatzipetros, A., Kokkalas, S., Pavlides, S., & Koukouvelas, I., 2005. Palaeoseismic data and their implication for active deformation in Greece. *Journal of Geodynamics* 40, 170-188.

Lyberis, N., 1984. Tectonic evolution of the North Aegean trough. *Geological Society of London, Special Publications* 17, 709-725.

Mercier, J.-L., Simeakis, K., Sorel, D., & Vergély, P., 1989. Extensional tectonic regimes in the Aegean basins during the Cenozoic. *Basin Research* 2, 49-71.

Mountrakis, D., Tranos, M., Papazachos, C., Thomaidou, E., Karagianni, E., & Vamvakaris, D., 2006. New neotectonic and seismological data about the main active faults and stress regime of Northern Greece. *Geological Society of London, Sp. Publications* 260, 649-670.

Mouslopoulou, V., Saltogianni, V., Gianniou, M., & Stiros, S., 2014. Geodetic evidence for tectonic activity on the Strymon Fault System, northeast Greece. *Tectonophysics* 633, 246-255.

Tranos, M.D., 2011. Strymon and Strymonikos Gulf basins (Northern Greece): Implications on their formation and evolution from faulting. *Journal of Geodynamics* 51, 285-305.

Papazachos, B.C., & Papazachou, C.B., 1997. *The earthquakes of Greece*. Ziti editions, Thessaloniki, 304pp.

Papazachos, B., Mountrakis, D., Psilovikos, A., & Leventakis, G., 1979. Surface fault traces and fault plane solutions of the May-June 1978 major shocks in the Thessaloniki area, Greece. *Tectonophysics* 53, 171-183.

Pavlides, S., & Caputo, R., 2004. Magnitude versus faults' surface parameters: quantitative relationships from the Aegean Region. *Tectonophysics* 380, 159-188.

Pavlidis, S.B., & Kilias, A.A., 1987. Neotectonic and active faults along the Servomacedonian zone (SE Chalkidiki, northern Greece). *Ann. Tecton*. I (2), 9-104.

Voidomatis, Ph.S, Pavlides, S.B., & Papadopoulos, G.A., 1990. Active deformation and seismic potential in the Serbomacedonian zone, northern Greece. *Tectonophysics* 179, 1-9.

Wells, D.L., & Coppersmith, K.J., 1994. New empirical relationships among magnitude, rupture length, rupture width and surface displacement. *Bull. Seismol. Soc. Am.* 84, 974-1002.

Wesnousky, S.G., 2008. Displacement and Geometrical Characteristics of Earthquake Surface Ruptures: Issues and Implications for Seismic-Hazard Analysis and the Process of Earthquake Rupture. *Bull. Seismol. Soc. Am.* 98, 1609-1632.

INQUA Focus Group Earthquake Geology and Seismic Hazards

paleoseismicity.org

Evaluating the liquefaction hazard in Axios basin, Thessaloniki based on detailed geomorphological mapping

Papathanassiou, George (1), Valkaniotis, Sotiris (2), Koukousioura, Olga (3), Papapetrou, Natalia (3), Marinos, Vasilis (3)

(1) Department of Civil Engineering, Democritus University of Thrace, 67100, Xanthi, Greece, gpapatha@civil.duth.gr
(2) Koronidos 9, Trikala, Greece, valkaniotis@yahoo.com
(3) School of Geology, Aristotle University of Thessaloniki, 54124, Thessaloniki, Greece, okoukous@geo.auth.gr, marinosv@geo.auth.gr

Abstract: *The Thessaloniki plain is the largest deltaic complex in Greece and is situated in the Northern part of Thermaikos Gulf. The plain is surrounded eastwards, near the city of Thessaloniki, by Mount Chortiatis and southwards by the Neogene foothills of Pieria. To the north and west is bordered by Mount Paikon and Vermion respectively, both formed by Mesozoic limestones. This area is mainly covered by Holocene age sediments that are preliminary considered as prone to liquefaction. However, in order to accurately assess the level of susceptibility to liquefaction, a detailed classification of the sediments based on their depositional environment is mandatory. The aim of this research is to assess the liquefaction susceptibility of the area following a detailed geomorphological mapping.*

Keywords*: Liquefaction, Thessaloniki, Axios, geomorphology, susceptibility*

INTRODUCTION

The delineation of areas prone to liquefaction, the evaluation of their liquefaction potential and their detailed mapping represent crucial issues for mitigating the liquefaction risk and especially for minimizing or even avoiding the occurrence of structural damages at buildings. The recently earthquake sequences occurred in New Zealand (2010-2011) and Italy (2012) confirmed the strong influence of depositional environment of the sediments with the liquefaction occurrences. In particular, it was pointed out that the most highly susceptible to liquefaction sediments are the present and former river channels, estuaries and reclaimed land that are underlain by saturated and loosely consolidated fine sand to silt within 10 m of the surface (Bastin et al., 2015; Wotherspoon et al., 2012); accepting that the seismic loading is capable to generate excess pore pressure.

Regarding the earthquake-induced liquefaction phenomena at the Emilia-Romagna region, triggered by the 20 and 29 May 2012 earthquakes (Fig. 1), it has been shown that a strong correlation with the type of geological units also exists. In particular Papathanassiou et al. (2015) and Di Manna et al. (2012), pointed out that numerous and more severe than expected, for these moderate magnitude earthquakes, liquefaction phenomena were induced. In addition, Civico et al. (2015) performed a detailed study within this area using an airborne LiDAR and concluded that more than 50% of the observed liquefaction features were mapped on fluvial landforms; alluvial ridges, levee ridges, crevasse splays and abandoned riverbeds.

Figure 1: Liquefaction phenomena in the area of San Carlo, Italy triggered by the 2012 earthquake.

Thus, it is evident that liquefaction phenomena and the relevant liquefaction-induced failures were not sparsely and randomly distributed on the qualitatively classified as susceptible to liquefaction geological units but they were mainly concentrated within specific zones. Therefore, a further discrimination of the Holocene age sediments following a geomorphological approach could initially provide information regarding the type of sediments, e.g. depositional environment, and result to a more reliable map regarding the susceptibility to liquefaction of the sediments.

The goal of this study is to compile a liquefaction susceptibility map of the Axios basin, Thessaloniki area in order to show that a more detailed classification could be cost-benefit since it decreases the area that should investigated in detail as prone to liquefaction.

GEOLOGICAL AND GEOMORPHOLOGICAL EVOLUTION OF THE AXIOS BASIN

The Thessaloniki plain is the largest deltaic complex in Greece and is situated in the Northern part of Thermaikos Gulf (Fig. 2). The plain is surrounded eastwards, near the city of Thessaloniki, by Mount Chortiatis and southwards by the Neogene foothills of Pieria. To the north and west is bordered by Mount Paikon and Vermion respectively, both formed by Mesozoic limestones. In Thessaloniki plain and Thermaikos gulf, the Axios-Thermaikos tectonic depression was formed during Neogene, with a NNW-SSE trend (Dinter & Royden, 1993). This depression was gradually filled by clastic (conglomerates, sands, clays) and locally calcareous (limestones, marls) sediments. Neogene sedimentation started during Miocene (fluvial deposits, brackish clays, sands and limestones) and deposition successively continued during Pliocene (fluvio-lacustrine sands, silts and lacustrine marly limestones) and Pleistocene (red beds) (Faugères, 1978; Syrides, 1990). The transition from the Younger Dryas deglaciation until the early Holocene (10,000 yr BP) has been recorded at the western part of Thessaloniki plain, where significant surface erosion caused the transport and deposition of fluvial sediments in the plain (Psomiadis et al., 2013).

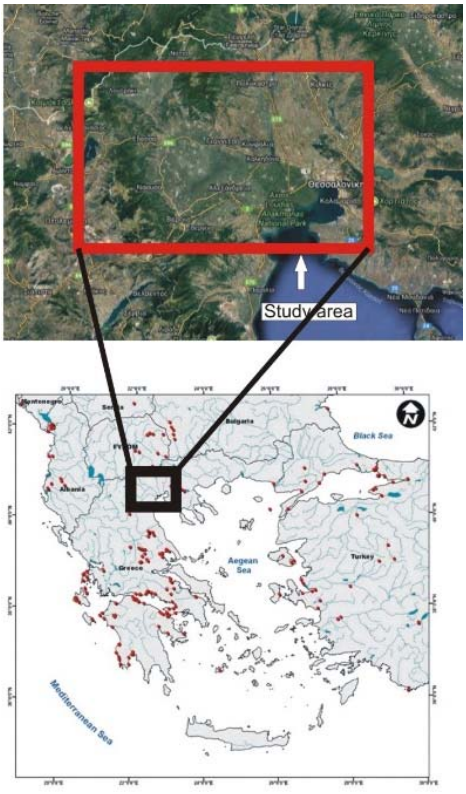

Figure 2: Up) Map shown the study area. Down) spatial distribution of the liquefied sites in Greece (Papathanassiou & Pavlides, 2011).

Intensive tectonic activity during the Middle-Upper Pleistocene severely affected the depression and reshaped the initial basin morphology (Syrides, 1990).

The early Holocene (10,000 yr BP), was recorded only at the western part of Thessaloniki plain, Nea Nikomideia area, and characterized by the establishment of a shallow fresh water lake (Ghilardi et al., 2012). Fluvial sediments rich in carbonates, indicates the presence of very active small streams that discharged into this lake, forming a continuous lacustrine sequence.

The first information about the marine Mid-Holocene sedimentary successions comes from the western/central parts of Thessaloniki plain, where lagoonal conditions are reported (~7,500 yr BP; Ghilardi et al., 2012; Koukousioura et al., 2012). Later at around 6,000 yr BP, the central Thessaloniki plain and its northern margins, Archontiko area, was a large open marine embayment with shallow marine conditions mainly in the western part and deeper waters in the eastern part of the gulf (Fouache et al., 2008; Ghilardi et al., 2008a,b; Syrides et al., 2009), while at the western part of the plain a second freshwater lake occurred (Ghilardi et al., 2012). Since then and between 5,000 and 4,500 yr BP the bay began to fill rapidly with fluvial sediments deposited by the surrounding rivers. This procedure created sandy barriers, behind which, lagoons were formed (Fouache et al., 2008; Ghillardi, 2007; Ghilardi et al., 2008a,b).

After 2,500 yr BP the sea regressed gradually from westwards to south-eastwards and the shoreline was rapidly retreating, changing to shallow marine environment and forming a number of short-lived lagoons (Fouache et al., 2008). Consequently, the shoreline gradually shifted in the same direction until it reached its present-day position. On the other hand, in the westernmost part of the plain a large lake was formed, whose size was gradually decreasing due to lacustrine sedimentation and was probably the ancestor of Giannitsa (Loudias) lake. The alluvial plain continued to prograde and after 2,000 yr BP, the northwest part of the plain was characterized by a brackish to limnic environment (Fouache et al., 2008).

At about 1,500 yr BP the former bay and actually all the plain was filled by alluvial deposits and the northwestern part was disconnected from the lake. A large limnic occupation is attested to the westen-cental part of the plain, displacing from the west to the east. This lake, Giannitsa lake, survived until the beginning of the 20th century at the western part of the alluvial plain until it was drained in the 1930s (Fouache et al., 2008). A final shallow lake phase has also developed at the southwestern part of the plain very recently, probably during the Little Ice Age, gradually becoming an area of shallow swamps during the last two centuries (Ghilardi et al., 2012).

While at the western part of the plain this lacustrine sedimentation occurred, at the lower part of deltaic complex a rapid geomorphological evolution took place. The creation of a series of coastal barriers, due to the alluvial sedimentation, led to the isolation of lagoons and the formations of swamps, although some connections to the

sea still existed (Ghilardi et al., 2010). Because of the rapid creation of the deltaic complex (Axios and Aliakmon lobes) the main rivers shifted gradually south eastwards, to their present position. All the levees created and then abandoned by the rivers, created natural dams which later turned into coastal spits (Ghilardi et al., 2010). After the connections between the deltaic lobes of Axios and Aliakmon Rivers, the Thessaloniki plain was created, taking its final form.

ASSESSING THE LIQUEFACTION SUSCEPTIBILITY

The assessment of liquefaction susceptibility of sediments is considered as the first step towards the evaluation of liquefaction hazard and can be achieved in regional scale by mainly evaluating the depositional environment. In particular, the depositional process affect the liquefaction susceptibility of sediments since fine and coarse grained soils sorted by fluvial or wave actions are more susceptible than unsorted sediments.

The most applied methodologies regarding the regional scale assessment of liquefaction susceptibility have been proposed by Youd & Perkins (1978), the California Department of Conservation, Division of Mines and Geology (CDMG, 1999) and recently by Witter et al. (2006). The selection of one of the above approaches depends on the amount and type of collected data and mainly on the scale of geological maps.

In this study, we were able to apply the Youd & Perkins (1978) method because we could use data provided both by geological map in 1:50.000 scale compiled by IGME (Geological Survey of Greece) and geomorphological one compiled by Ghiliardi et al. (2010), where detailed information regarding age and depositional process of sediments has been defined. These data were used as a base layer for digitizing the spatial distribution of the Holocene age geological units (Fig. 3).

Furthermore, taking into account that a soil layer can be liquefied only when it is saturated, it is obvious that the evaluation of the depth of the groundwater is a crucial issue for the estimation of liquefaction potential. In this study, we assumed that the groundwater table depth is less than 3 meters thus; the degree of liquefaction susceptibility is characterized as high according to Youd & Perkins (1978). This assumption was based on the fact that the groundwater level at many sites fluctuates seasonally and consequently; unsaturated deposits during one season can become saturated the next one and capable for liquefaction. Therefore, it was decided to be conservative regarding the groundwater table at this scale liquefaction susceptibility map. Areas that are characterized as liquefiable should be further investigated in detail using groundwater measurements.

Thus, in order to apply the criteria proposed by Youd & Perkins (1978), we initially grouped the Quaternary sediments, since pre-Pleistocene deposits are classified as very low susceptibility units, and then we further analyzed and assessed their liquefaction susceptibility based on the proposed by the researchers' classification. The outcome of this approach is shown in Figure 4. Using the resulted classification, areas covered by each corresponding susceptibility class were calculated, as well as the cumulative length of main road network crossing Axios basin area (Table 1). OpenStreetMap vector data were used for extraction of the road network, divided in two subsets: highways and main roads. Residential roads, tracks, etc. were removed from the dataset.

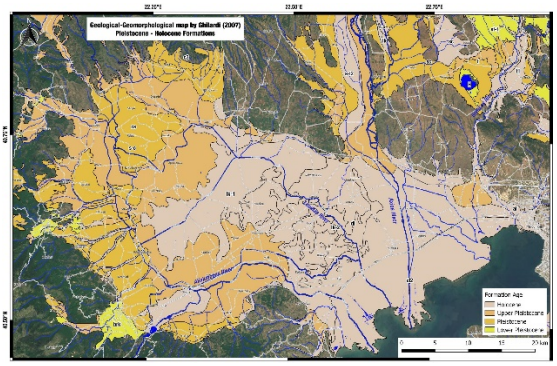

Figure 3: Simplified geological map of the study area (modified by IGME, 1985 and Ghiliardi et al., 2010).

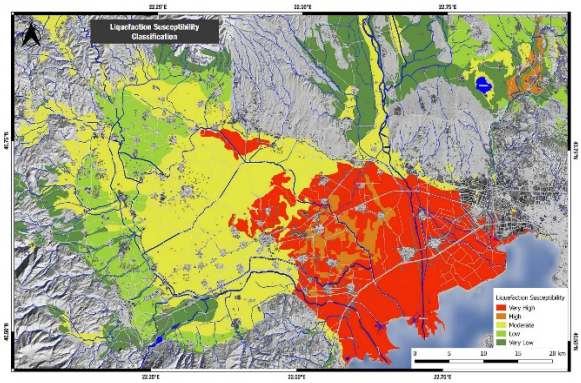

Figure 4: Liquefaction susceptibility map of the study area based on Youd & Perkins (1978) classification.

Table 1: Areas and road network covered by liquefaction susceptibility classes in the study area of Axios basin.

Liquefaction susceptibility	Area (Km2)	Highways (km^2)	Main Roads (km^2)
Very High	892	78	703
High	686	9	59
Moderate	662	116	1355
Low	185	48	472
Very Low	139	47	398

CONCLUSIONS

Existing geological maps were widely used for regional liquefaction susceptibility assessment in Greece. In addition, geomorphological maps can provide a suitable alternative for assessing the liquefaction potential over

large alluvial and fluvial basins, where few data for the distribution of surface material exist.

This study aiming to assess the liquefaction susceptibility of the geological units that were mapped in the Axios basin at the broader Thessaloniki area. In order to achieve this, a well-known published classification was taken into account. In addition, it was decided to use a geomorphological map, instead of a geological one, because the former map provides crucial information regarding the depositional environment of the sediments. As it is shown on the liquefaction susceptibility map that was compiled for the purposes of this study, the very high susceptibility area covers 892 km^2.

REFERENCES

Bastin, S., Quigley, M., & Bassett, K., 2015. Paleoliquefaction in easter Christchurch. New Zealand *Geological Society of America Bullettin* 127, 1348-1365.

Civico, R., Brunori, C.A., De Martini, P.M., Pucci, S., Cinti, F.R., & Pantosti, D., 2015. Liquefaction susceptibility assessment in fluvial plains using airborne lidar: The case of the 2012 Emilia earthquake sequence area (Italy). *Natural Hazards and Earth System Sciences* 15, 2473-2483.

CDMG, 1999. *Guidelines for analyzing and mitigating liquefaction hazards in California, California Department of Conservation, Division of Mines and Geology*, Special Publication 117, p. 63.

Di Manna, P., Guerrieri, L., Piccardi, L., Vittori, E., Castaldini, D., Berlusconi, A., Bonadeo, L., Comerci, V., Ferrario, F., Gambillara, R., Livio, F., Lucarini, M., & Michetti, A.M., 2012. Ground effects induced by the 2012 seismic sequence in Emilia: implications for seismic hazard assessment in the Po Plain. *Annals of Geophysics* 55 (4), 697-703.

Dinter, K.-R., & Royden, L., 1993. Late Cenozoic extension in northeastern Greece: Strymon valley detachment system and Rodope metamorphic core complex. *Geology* 21, 45-48.

Faugères, L., 1978. *Recherches géomorphologiques en Grèce septentrionale: Macédoine centrale et occidentale*. Service de reproduction des thèses de l'Université de Lille 2 vol., p. 849.

Fouache, E., Ghilardi, M., Vouvalidis, K., Syrides, G., Kunesch, S., Styllas, M., & Stiros, S., 2008. Contribution on the Holocene reconstruction of Thessaloniki plain, north central Greece. *Journal of Coastal Research* 24 (5), 1161-1173.

Ghilardi, M., Psomiadis, D., Cordier, S., Delanghe-Sabatier, D., Demorya, F., Hamidi, F., Paraschou, T., Dotsika, E., & Fouache, E., 2012. The impact of rapid early- to mid-Holocene palaeoenvironmental changes on Neolithic settlement at Nea Nikomideia, Thessaloniki Plain, Greece. *Quaternary International* 266, 47-61.

Ghilardi, M., Genç, A., Syrides, G., Bloemendal, J., Psomiadis, D., Paraschou, T., Kunesch, S., & Fouache, E., 2010. Reconstruction of the landscape history around the remnant arch of the Klidhi Roman Bridge, Thessaloniki plain, north central Greece. *Journal of Archaeological Science*, 37 (1), 178-191.

Ghilardi, M., Fouache, E., Queyrel, F., Syrides, G., Vouvalidis, K., Kunesch, S., Styllas, M., & Stiros, S., 2008a. Human occupation and geomorphological evolution of the Thessaloniki plain (Greece) since mid Holocene. *Journal of Archaeological Science* 35 (1), 111-125.

Ghilardi, M., Kunesch, S., Styllas, M., & Fouache, E., 2008b. Reconstruction of Mid -Holocene sedimentary environments in the central part of the Thessaloniki Plain (Greece) based on microfaunal identification, magnetic susceptibility and grain-size analyses. *Geomorphology* 97 (3-4), 617-630.

Koukousioura, O., Triantaphyllou, M.V., Dimiza, M.D., Pavlopoulos, K., Syrides, G., & Vouvalidis, K., 2012. Benthic foraminiferal evidence and paleoenvironmental evolution of Holocene coastal plains in the Aegean Sea (Greece). *Quaternary International* 261, 105-117.

Papathanassiou, G., Mantovani A., Tarabusi, G., Rapti D., & Caputo, R., 2015. Assessment of liquefaction potential for two liquefaction prone areas considering the May 20, 2012 Emilia (Italy) earthquake, *Engineering Geology* 189, 1-16, http://dx.doi.org/10.1016/j.enggeo.2015.02.002.

Papathanassiou, G., & Pavlides, Sp., 2011. GIS-based database of historical liquefaction occurrences in the broader Aegean region, DALO v1.0, *Quaternary International* 242 (1), 115-125, doi: 10.1016/j.quaint.2011.03.049.

Psomiadis, D., Ghilardi, M., Demory, F., Delanghe-Sabatier, D., Bloemendal, J., & Yiu, C., 2014. Late Pleistocene to Mid Holocene landscape reconstruction in the western part of the Thessaloniki Plain, Greece: evidence for environmental changes, and implications for human occupation. *Zeitschrift für Geomorphologie, Supplementbände* 58 (2), 67-87.

Syrides, G., 1990. *Lithostratigraphic, Biostratigraphic and Palaeogeographic study of the Neogene - Quaternary sedimentary deposits of Chalkidiki peninsula, Macedonia, Greece*. PhD Thesis. Scientific Annals School of Geology. Volume I, No 11, 243 p. Thessaloniki (in Greek).

Syrides, G., Albanakis, K., Vouvalidis, K., Pilali, A., Papasteriou, A., Papaefthimiou-Papanthimou, A., Ghilardi, M., Fouache, E., Paraschou, T., & Psomiadis, D., 2009. Holocene palaeogeography of the northern margins of Giannitsa plain in relation to the prehistoric site of Archontiko (Macedonia, Greece). *Zeichrift für Geomorphologie* 53 (1), 71-82.

Witter, C.R., Knudsen, L.K., Sowers, M.J., Wentworth, M.C., Koehler, D.R., & Randolph, C.E., 2006. Maps of Quaternary Deposits and liquefaction susceptibility in the Central San Francisco Bay Region, California, Open file report 2006-1037, USGS, pp. 43.

Wotherspoon, L., Pender, M., & Orense, R.P., 2012. Relationship between observed liquefaction at Kaiapoi following the 2010 Darfield earthquake and former channels of the Waimakariri River, *Engineering Geology* 125, 45-55, doi:10.1016/j.enggeo.2011.11.001, 2012.

Youd, T.L., & Perkins, D.M., 1978. Mapping of Liquefaction induced Ground Failure Potential, *Journal of the Geotechnical Engineering Division* 104, 433-446.

INQUA Focus Group Earthquake Geology and Seismic Hazards

paleoseismicity.org

How does local faulting and geology control the earthquake damage distribution? The Lesvos 2017 earthquake case

Papazachos, Costas (1), Chatzis, Nikolaos (1), Kkallas, Charalambos (1), Anthymidis, Marios (1), Rovithis, Emmanouil (2), Karakostas, Christos (2), Papaioannou, Christos (2)

(1) Geophysical Laboratory, School of Geology, Aristotle Univ. Thessaloniki, PO Box 352-1, Thessaloniki GR54124 Greece, kpapaza@geo.auth.gr
(2) Institute of Engineering Seismology and Earthquake Engineering (OASP/ITSAK), Dasyliou str., PO Box 53, Pylaia GR55102 Greece

Abstract: *While the 2017 M6.3 Lesvos mainshock inflicted limited damage along the southern Lesvos coastal area, significant damage was observed in the historical Vrisa settlement, built on the edge of a Holocene basin. Heavy damage was recorded in masonry houses built in the northern Vrisa, founded on recent (Holocene) sediments. On the contrary, in the southern part of the village (founded on stiff Neogene deposits) limited damage was observed. Since this pattern indicates the presence of strong site-effects controlled by local geology, we used different geophysical data (single station and array ambient noise measurements, active seismic profiles, aftershock sequence seismic records) to define a 3D geophysical/geological model of the area and study the spatial distribution of the soil fundamental frequency and amplification. The data processing allowed to reconstruct the 3D basin structure and assess the spatial distribution of strong ground motions throughout the Vrisa settlement, in very good agreement with the observed damage pattern.*

Keywords*: Holocene sediments, Site effects, Earthquake damage, Urban geology, Ambient noise*

INTRODUCTION

The June 12, 2017 strong (M6.3) earthquake which occurred off the southern coast of Lesvos island (north-eastern Aegean Sea, Greece), inflicted relatively limited damage along the broader Lesvos area, even the neighbouring coastal region. An impressive exception was the case of the historical settlement of Vrisa: Extensive damage was observed for a large number of collapsed masonry houses, mostly in the northwestern part of the village, which was founded on recent (Holocene) sediments. In the southern part of the village, founded on much stiffer Neogene formations, relatively limited damage (even for masonry houses) was reported. In general, a negligible impact on the fewer reinforced concrete modern constructions was observed.

The previous observations suggest that the local geology is responsible for the presence of strong site-effect phenomena on seismic motions and the resulting damage pattern. For this reason, we collected a large number of geophysical data (ambient noise, active seismics, seismic records), in order to recover the uppermost 3D geophysical/geological structure of the Vrisa area, and assess its effect on the spatial distribution of the expected (from the modelling) and observed site effects on seismic motions.

Finally, an assessment of the mainshock expected damage and its correlation with observed damages, in terms of macroseismic intensities, was performed. The obtained results show an excellent correlation between observed (from field survey) and predicted (modelled) damages.

LOCAL GEOLOGY & GEOPHYSICAL DATA

A critical factor for the assessment of site effects on seismic motions is the soil fundamental frequency, f_0, or period, T_0, and the corresponding maximum spectral amplification, A_0. A preliminary assessment of this distribution was performed by the means of a dense grid of ~70 ambient noise measurements, which were employed in order to derive single-station Horizontal-to-Vertical Spectral Ratios (HVSR).

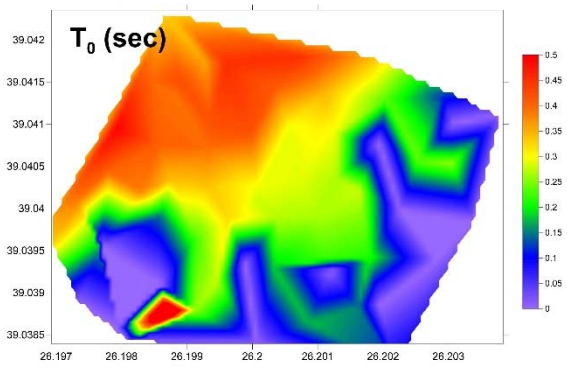

Figure 82: Spatial variation of the fundamental soil period, T_0, in the Vrisa area, as revealed from a dense grid of noise measurements.

The results revealed a strong spatial variation of the soil fundamental period, T_0, as this is approximated by the observed peaks of the recovered HVSR curves. Moreover,

the maximum HVSR amplitudes, A_0^{HVSR}, exhibited values close to one, with almost flat HVSR curves in the southeast Vrisa (Neogene sediments), allowing for its consideration as a seismic bedrock. On the contrary, large A_0^{HVSR} values (locally larger than 4) were determined for the northwestern Vrisa section, located on the Holocene sediments, mainly for periods in the range 0.35-0.45 sec (Figure 1). It should be pointed out that A_0^{HVSR} values are considered to provide a lower estimate of the actual A_0 maximum spectral amplifications (Haghshenas et al., 2008). Therefore, it is expected that the actual mainshock seismic motions were significantly amplified in the Holocene sediments section of the village, with even larger amplifications. To confirm this suggestion, we employed Standard Spectral Ratios (SSR) from aftershocks recorded on both Neogene and Holocene deposits. The obtained results confirmed that the real peak spectral amplifications, A_0, were almost double than the observed A_0^{HVSR} values from the HVSR data, showing an almost identical shape for the SSR and HVSR curves.

To confirm the previous findings, we employed a large number (13) of MASW lines, distributed throughout the broader Vrisa area, complemented by a circular Noise-Array in the area of the thickest expected Holocene deposits. Dispersion curves from the MASW and Ambient Noise array were determined with the use of the f-k method, and were subsequently inverted in order to determine a 1-D shear-wave velocity model for all examined sites. The Rayleigh wave dispersion curve inversion was combined with the inversion of the Rayleigh wave ellipticity information, as obtained from the RAYDEC algorithm proposed by Hobiger et al. (2009). Using this approach, Rayleigh wave dispersion and ellipticity curves were jointly inverted, using an appropriate equal-weight misfit function, with the *Geopsy* software (http://www/geopsy.org). *Geopsy* employs the Monte-Carlo type neighbourhood inversion algorithm, proposed by Wathelet et al. (2008), allowing an efficient model search and parameterization. This joint non-linear inversion scheme improved the recovered Vs-models, mainly by limiting their non-uniqueness.

The final 1D Vs models were used to reconstruct a 3D Vs model of the broader Vrisa basin. This 3D geophysical/geological model confirms the critical role of local geology on seismic motions. More specifically, Holocene sediments in northern Vrisa show a thickness of ~20-25 m over the Neogene sediments, with very low velocities (Vs<300 m/sec, dropping to <200m/s closer to the surface). Neogene sediments exhibit much larger velocities (typically >400m/s), rapidly increasing above 500m/sec and reaching seismic bedrock velocities (700-800m/sec) at relatively small depths (~10-20m). The MASW lines, as well as focussed seismic refraction profiles, suggest that this transition is rather sharp, i.e. it is controlled by a NE-SW trending normal fault which bounds the southern edge of the local Holocene basin and practically crosses through the middle of the Vrisa village.

DAMAGE DISTRIBUTION AND MAINSHOCK SIMULATION

The available post-earthquake survey data (collected by ITSAK-EPPO) showed that most (~60%) class A old masonry buildings with poor construction quality that were located in the Holocene sediments area (northern Vrisa) exhibited heavy damage (grade 5 in the EMS98 macroseismic scale) due to the Lesvos 2017 mainshock (M6.3). On the other hand, the same type of structures presented much lower damage levels (grade 2 or 3 in the same scale) when built on the Neogene formations of the southern part of Vrisa. The previous distribution confirms the control of local geology on site amplifications, as also revealed from modelled (from the final 3D Vs model) and observed (from the SSR) amplifications. To verify this pattern, we have used the comparison between the available HVSR and SSR curves to reduce all 70 observed HVSR measurements into equivalent spectral soil amplifications. The amplifications were used in a finite-fault stochastic simulation of the expected seismic motions, following Boore (2009). The reconstructed seismic motions suggest that the southern part of Vrisa (Neogene deposits) has sustained macroseismic intensities of the order of 6+ to 7 (in the Modified Mercalli macroseismic scale), while for the northern Vrisa section (Holocene sediments) the expected damage levels reached levels between 8+ to 9. The previous results are in good agreement with the observed damage pattern, which suggests EMS98 intensities between 8 and 9 in the Holocene sediments (north) and of the order of 7-8 for the Neogene Vrisa section (south).

Acknowledgements: This work was partly supported through the help of the Greek Earthquake Planning & Protection Organization (OASP), under project 95538 of the Research Committee of the Aristotle Univ. Thessaloniki.

REFERENCES

Boore, D.M., 2009. Comparing stochastic point-source and finite-source ground-motion simulations: SMSIM and EXSIM. *Bull. Seism. Soc. Am.* 99 (6), 3202-3216.

Haghshenas, E., Bard, P.Y., Theodulidis, N., & SESAME WP04 Team, 2008. Empirical evaluation of microtremor H/V spectral ratio. *Bull. Earthq. Engin.* 6 (1), 75-108.

Hobiger, M., Bard, P.-Y., Cornou, C., & Le Bihan, N., 2009. Single station determination of Rayleigh wave ellipticity by using the random decrement technique (RayDec). *Geophys. Res. Lett.* 36, doi: 10.1029/2009GL038863.

Wathelet, M., 2008. An improved neighborhood algorithm: Parameter conditions and dynamic scaling. *Geophys. Res. Lett.* 35, doi: 10.1029/ 2008GL033256.

INQUA Focus Group Earthquake Geology and Seismic Hazards

paleoseismicity.org

Active faults as Seismogenic sources in the Aegean region

Pavlides, Spyros (1), Chatzipetros, Alexandros (1), Sboras, Sotiris (2)

(1) Department of Geology, Aristotle University, University campus, Thessaloniki, GR 541 24, Greece pavlides@geo.auth.gr
(2) Institute of Geodynamics, National Observatory of Athens, Lofos Nymfon, Thisio, Athens, GR118 10, Greece, sboras@noa.gr

Abstract: *In this article review we emphasize the key-role of active faulting in the geodynamic setting of the broader Aegean region. We also describe briefly the transition from active faults to seismogenic sources through the Greek Database of Seismiogenic Sources (GreDaSS), an ambitious project that aims at the homogenization of seismic hazard in this region. This transition relies on various philosophical aspects and criteria in order to fulfil the practical needs of Seismic Hazard Assessment and give answers to scientific questions about the seismotectonic setting of the Aegean. In this context we show some characteristic cases of different types of morphometric features and coseismic surface rupture patterns that occurred in this area of interest.*

Keywords*: Active faults, seismogenic sources, seismotectonics, surface faulting, Aegean*

GEOTECTONIC SETTING

The broader Aegean Region is among the most tectonically active areas of the Mediterranean realm. Its geotectonic evolution started during the Mesozoic, when the discontinuous southwestward migration of the Alpidic orogenic process, characterized by intense collisional tectonics, caused successive subductions of the Tethyan oceanic basins producing a complete stack of several nappes. Today, the Aegean geodynamic setting is controlled by the relative lithospheric plate motions. Either continental collision (Apulia vs Aegean) or convergence (Africa vs Eurasia), along with quasi-oceanic subduction (Mediterranean beneath Eurasia), the Aegean crust undergoes an inner strong deformation which is expressed by intense faulting. Active faults try to overprint their morphological marks on the older Alpidic relief, although sometimes they just follow the older inherited structures. Whether the Alpidic orogenic process has stopped or still goes on in northwestern Greece (where the Apulian continental plate is subducted under the Aegean), the Hellenic Arc keeps its southward retreat and roll-back movement, which started since the Priabonian stage, leaving plenty of space in the back-arc region for crustal extension. As a consequence, all the active procedures above produce intense seismicity in both terms of magnitude and frequency.

The neotectonic period in the Aegean started since the Late Pliocene-Early Pleistocene and continues until Today. During this period, the roughly N-S crustal stretching develops, due to the Hellenic Arc southward migration. The geodynamic regime is rather complex forming a large variety of faults which in turn produce earthquakes of different P/T-axes orientations. It is noteworthy to mention that Greece, like other modern industrialized countries with high concentration of population in large and constructionally complex urban areas, has suffered many human losses and economic damages. The Athens 1999 earthquake alone, caused 143 deaths and $3.0-4.2 million in damage.

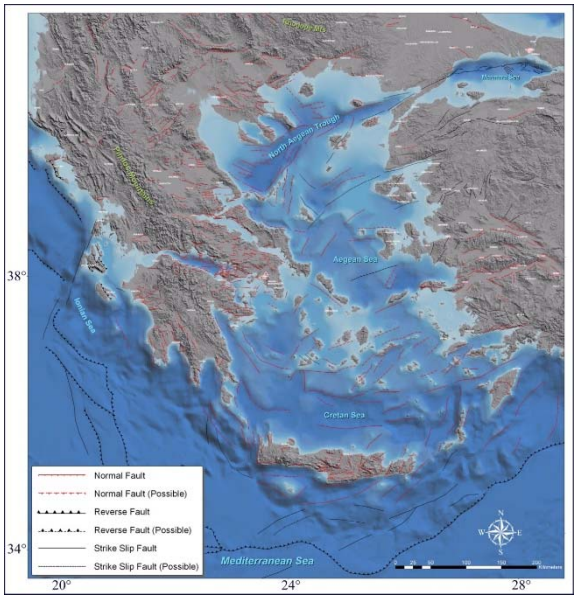

Figure 83: The map of capable faults in Greece, as proposed by Pavlides et al. (2007).

THE GREEK DATABASE OF SEISMOGENIC SOURCES (GreDaSS)

Aiming at a better, reliable and realistic contribution towards seismic hazard assessment, GreDaSS was developed (Sboras et al., 2011; Caputo et al., 2012; http://gredass.unife.it) using the structure and informatics of DISS, a well-tested, time-proven and worldwide acknowledged geodatabase developed by the Working Group of INGV (e.g. Valensise & Pantosti, 2001; Basili et al., 2008). GreDaSS is a continuously updatable open-file built

in GIS environment. Only shallow (crustal) tectonic structures are initially included. Shallow structures are more important in terms of SHA since they are scattered all over the Aegean Region, close to and sometimes even directly affecting inhabited areas. Not only GreDaSS does analyse and combine all kind of information that is hidden in numerous publications, but it also represents a multi-level tool of interconnected data addressing to all kinds of end-users, expertized or not. As a result, the second target of GreDaSS is to help comprehend the complex geodynamic regime of the Aegean.

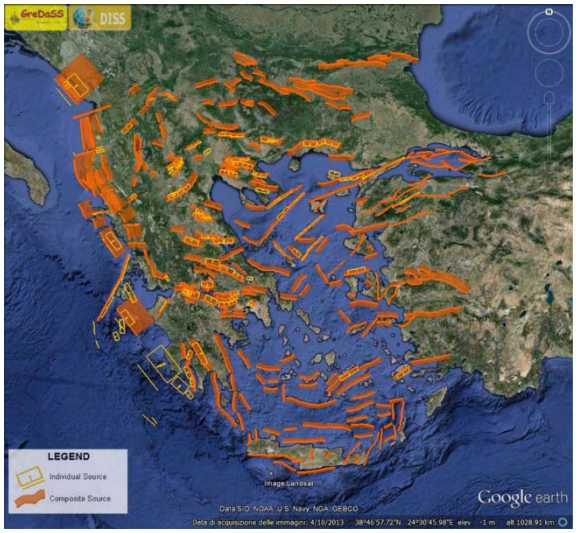

Figure 84: GreDaSS as shown in Google Earth environment.

Terminology varies in literature as long as the definition of active, capable and inactive (?) faults concerns. These terms usually deal with the time window used to describe the latest activity. Herein, the term "active fault" is preferred instead of "capable fault", of producing a future earthquake.

Defining an active fault: Faults have different derivatives, while "fault zone" is either a band of finite width across which the displacement is partitioned among many smaller faults, or the zone of rock bordering the fault that has fractured during faulting". However, a shear zone is defined as the zone of finite width along which displacement is attributed to major shear forces. Thus, the term of active fault is applied when a fault shows evidence of recent reactivation and/or is capable of being reactivated in the future. The definition of recent is quite relative and can be very subjective, but it is always comparable to the seismotectonic regime of the Aegean Region. When an active fault can be safely associated with a specific seismic event, the term "seismic fault" is preferred. Older, pre-historic events, have been identified with the aid of palaeoseismology (Chatzipetros et al., 2005) suggesting that active faults may have been repeatedly reactivated many times in the recent past and could be reactivated again in the near future. Some criteria can be assigned to the active faults, all adapted suitably for the faulting character of the Aegean. These criteria are described by Pavlides et al. (2007).

Active faults in Greece show a large variety at all scales. However, small individual faults are insignificant for the aims of Seismic Hazard Assessment (SHA). For this reason, GreDaSS basically contains seismogenic sources. Based on the definition of Kastelic et al. (2008) for DISS, seismogenic sources are active faults capable of generating M_w > 5.5 earthquakes. The latter definition is also suitable for the case of the Aegean region, given that Pavlides and Caputo (2004) suggest that a magnitude larger than 5.5 is needed in order to have linear morphogenic earthquakes (sensu Caputo, 2005) in the Aegean.

CHARACTERISTIC FAULT RUPTURES IN GREECE

A few cases of active faulting in Greece showing various coseismic ground rupturing patterns and morphotectonic features are listed below:

The Samothraki fault, a segment of the North Aegean Trough, uplifts and hangs the Giali drainage basin also forming triangular facets (Figure 85).

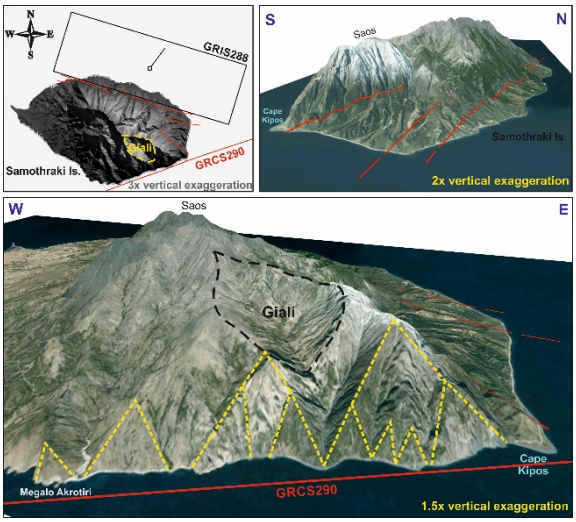

Figure 85: Morphotectonic features on Samothraki Island (uplifted valleys and triangular facets). The seismogenic sources at the North (GRIS288) and South of the island (GRCS290) are also shown. The onshore fault traces (red lines) are the surficial expression of ISS288 source. From Sboras et al. (2017).

In the Mygdonia Basin, where the 1978 (M_w 6.3) Thessaloniki earthquake epicentre is located, the major marginal faults have formed a distinctive curvilinear escarpment, but the co-seismic ground ruptures formed three main bifurcating antithetic lineaments (Figure 86a). Similar complexity also demonstrated the co-seismic ground ruptures of the 1995 (M_w 6.4) Kozani-Grevena earthquake (Figure 86b). The main fault was expressed by discontinuous and scattered surface ruptures, while an older antithetic inherited structure was partially reactivated (Chromio Fault). The most prominent fault escarpment next to the seismic fault (to the east) did not slip at all. Rupture was also complicated at depth, showing moderate dipping angle at deeper depths and steeper at shallower depths. The 1954 strong earthquake (M_w 6.6) near Sophades left ground ruptures that were parallel or sometimes diagonal to the segmented main fault escarpment (Figure 86c). The fault segments had to be breached in order to produce an earthquake of such magnitude. The Kaparelli seismic fault was reactivated during the third strongest shock (M_w 6.2) of the 1981

Alkyonides sequence on March 4. Surface rupture did not prefer the prominent fault escarpment towards the west, but jumped parallelly to the SW forming a relay-ramp in between (Figure 86d). More recently, a hidden or blind seismic fault produced the NW Peloponnesus 2008 earthquake.

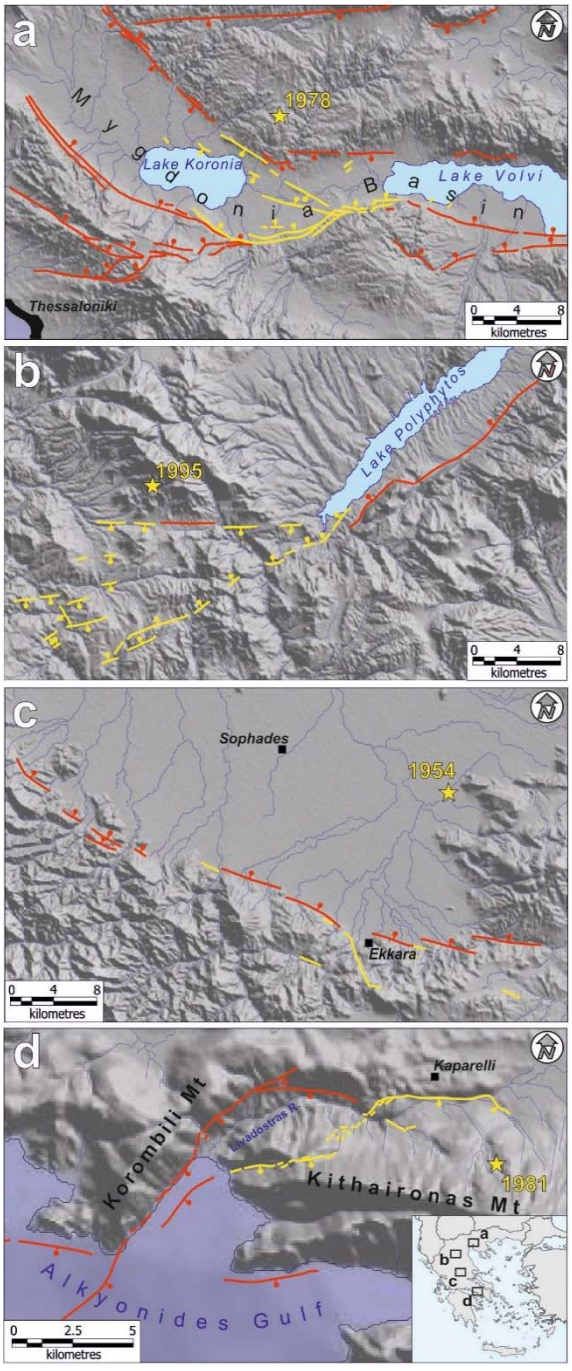

Figure 86: Active fault traces (red lines) and coseismic ground ruptures (yellow lines) for four cases in Greece: a) 1978 Thessaloniki earthquake, b) 1995 Kozani-Grevena earthquake, c) 1954 Sophades earthquake, and d) 1981 Alkyonides Gulf sequence (3rd strongest shock).

REFERENCES

Basili, R., Valensise, G., Vannoli, P., Burrato, P., Fracassi, U., Mariano, S., Tiberti, M.M., & Boschi E., 2008. The database of individual seismogenic sources (DISS), version 3: summarizing 20 years of research on Italy's Earthquake Geology. *Tectonophysics* 453 (1-4), 20-43.

Caputo, R., 2005. Ground effects of large morphogenic earthquakes. *J. Geodyn.* 40, 2-3, 113-118.

Caputo, R., Chatzipetros A., Pavlides, S., & Sboras, S., 2012. The Greek Database of Seismogenic Sources (GreDaSS): state-of-the-art for northern Greece. *Ann. Geophys.* 55 (5), 859-894.

Chatzipetros, A., Kokkalas, S., Pavlides, S., & Koukouvelas, I., 2005. Paleoseismic data and their implication for active deformation in Greece. *J. Geodyn.* 40, 170-188.

Kastelic, V., Vannoli, P., Burrato, P., Barba, S., Basili, R., Fracassi, U., Tiberti, M.M., & Valensise, G., 2008. Seismogenic sources of the Adriatic domain: an overview from the Database of Individual Seismogenic Sources (DISS 3.1.0). *Rendiconti online Soc. Geol. It.* 2, 1-3.

Pavlides, S., & Caputo, R., 2004. Magnitude versus faults' surface parameters: quantitative relationships from the Aegean *Tectonophysics* 380, 159-188.

Pavlides, S.B., Valkaniotis, S., & Chatzipetros, A., 2007. Seismically capable faults in Greece and their use in seismic hazard assessment. In: *4th Int. Conf. Earthq. Geotech. Eng.*, June 25-28, 2007, Thessaloniki, Proceedings, paper n. 1609.

Sboras, S., 2011. *The Greek Database of Seismogenic Sources: seismotectonic implications for North Greece*. Pubblicazioni dello IUSS, 5 (1), 1-274.

Sboras, S., Chatzipetros, A., Pavlides, S.B., Çemen, İ., & Yılmaz, Y., 2017. North Aegean Active Fault Pattern and the 24 May 2014, M_w 6.9 Earthquake. In: *Active Global Seismology: Neotectonics and Earthquake Potential of the Eastern Mediterranean Region* (Çemen, İ., Yılmaz, Y., eds.), *Geophysical Monograph 225*, American Geophysical Union, John Wiley & Sons, Inc., 239-272.

Valensise, G., & Pantosti, D., 2001. Database of potential sources for earthquakes larger than M 5.5 in Italy. *Ann. Geofis.* 44 (4), 797-807.

INQUA Focus Group Earthquake Geology and Seismic Hazards

paleoseismicity.org

The Fira fault (Santorini, Greece) from the French "Expédition de Morée (1829-38)" to modern scientific approach

Pavlides, Spyros (1), Chatzipetros, Alexandros (1)

(1) Department of Geology, School of Geology, Aristotle University of Thessaloniki, Greece, [pavlides, ac]@geo.auth.gr

Abstract: *Fira fault is a syndepositional normal fault that deforms volcanics (lava layers and pyroclastic flows) of the volcanic complex of Santorini Island. This fault is classified as active, as documented by the microseismicity pattern, during the 2011-2012 crisis. The fault has been a prominent feature of Fira cliff and it has been described since the early "Expédition de Morée" survey. Although volcanic material near the uppermost part of the fault appears undeformed, a prominent scarp of the same strike modifies the relief at the fault-line.*

Keywords*: Santorini, normal fault, volcanic complex*

Santorini is a volcanic island of the South Aegean Active Volcanic Arc. It consists of several volcanic centres and lava - pyroclastic layers, as well as domes, dykes and palaeo-calderas. The surficial soft tuff-pumice materials (1 to 40 m thick) are products of the well-known late Bronze age (Minoan) enormous volcanic eruption of the 17th c. BC, that shaped the island complex of Thera/Santorini. The island basement has few outcrops and consists of the Cycladic blueschist Unit, overthrusted by crystalline limestone

Many papers have dealt with the physical volcanology and the evolution of the Island, as well as the volcanic rocks and especially of the prehistoric enormous eruption of the 17th century B.C., but only a few for the structural features of the island (e.g. Mountrakis et al., 1996, Fig. 1) and none with the Fira active fault.

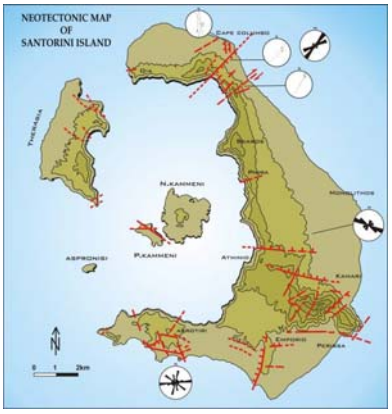

Figure 1: Neotectonic map of Santorini Island group (Mountrakis et al., 1996).

The French Morea expedition (Expédition Scientifique de Morée) is the name given to the land intervention of the French Army in the Peloponnese between 1828 and 1833, at the time after the Greek War of Independence. This mission was linked to the scientific fields of geography and geology, natural history, cartography, archaeology, (Leader: Bory de Saint Vincent, Blouet and Ravoisié, 1831; Bory de Saint-Vincent et al., 1834). In the first volume and the chapter of Geology a sketch clearly shows a discontinuity of the lava and pyroclastic layers (Fig. 2).

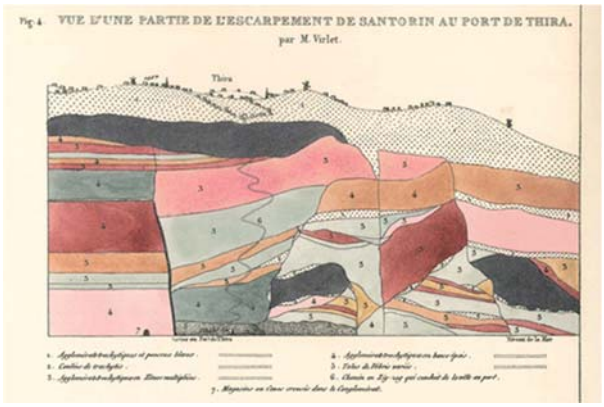

Figure 2: Detail from the first volume of Expédition Scientifique de Morée, where Fira fault is clearly been sketched.

Fira fault is a normal 7Fault trending ENE-WSW (N60°E) with a right lateral oblique slip sense of movement. It shows gradually smaller displacement from the see level to top lava layer (Nomikos Conference Center) (Fig. 3). It affects all the layers from the sea level up to the last volcanic flow, which is 40.000 - 60.000 years old, where typical cooling fractures and tectonic open joinst have been observed. A non-typical fault scarp on the surface volcanics is also observed. It runs subparallel to a longer "fault zone", including the known volcanic centres, known as Kamenes and the 1956 earthquake M7.5 great Amorgos-Santorini fault zone. The Santorini-Amorgos area is a zone of crustal weakness in an overall right-lateral transtensional regime. It represents a major structural boundary.

Figure 3: Overview of Fira cliff and fault.

Figure 4: Colour view of the 3D model of Fira fault outcrop that was constructed using photogrammetry. The fault displacement decreases towards the top.

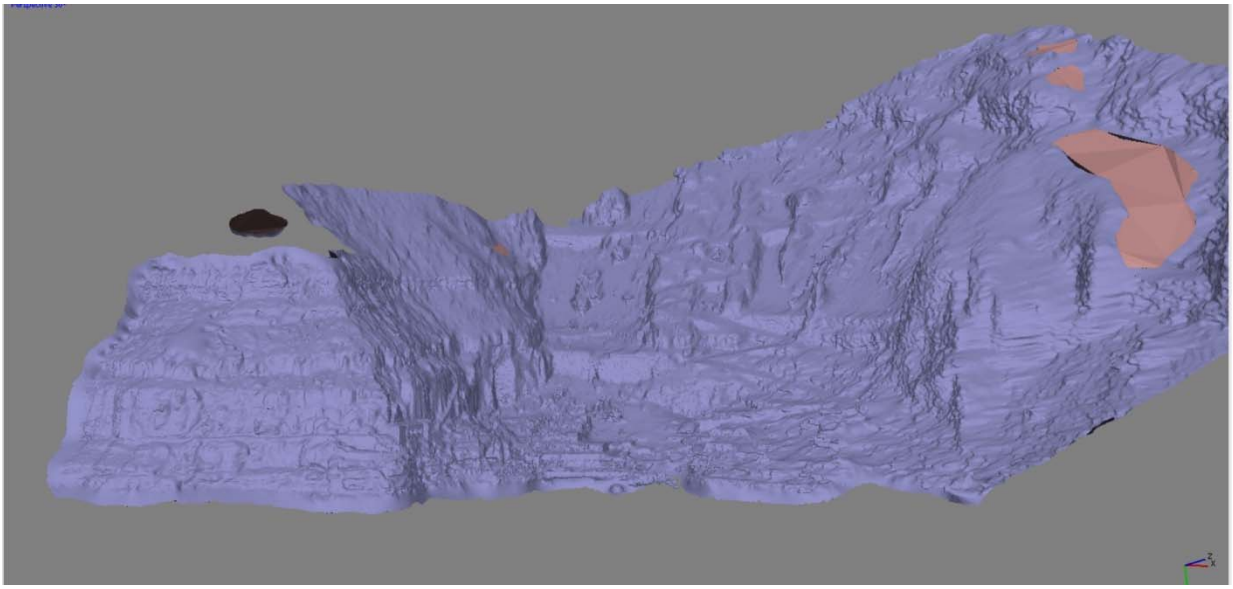

Figure 5: Shaded 3D model of Fira cliff.

The stress regimes in the broader area imply that the Amorgos-Santorini line is attributed to the tectonic stresses related with the well-established Aegean motion towards SSW, whereas the Fira fault, which gives rise to recent microseismicity of the area, is due to a local stress regime attributed to buoyancy forces relating the magmatic processes of the area.

The combination of two stress regimes reflects the competition between the tectonic (lithospheric) and magmatic (local volcanotectonic) forces, in a fault-dynamic regime that could be characterized as an extensional-transtentional field.

During the 2011-2012 volcano-seismotectonic crisis the Kamenes volcanic line - Fira Fault was activated by a series of minor earthquakes M 2.0 to 3.5. The Fira fault segment that was activated during the 2011-2012 crisis is about 6 km long, so its maximum potential magnitude calculated from the empirical relationships (Wells & Coppersmith 1994; Pavlides & Caputo 2004) is less than 5.5.

3D Model

To better understand the geometry and the gradual displacement of the fault, a 3D model was constructed using photogrammetric methods. A set of more than 50 photos was aligned and paired using specialized software. The paired photos were then used to extract a dense point cloud (ig. 4), which in turn was used to construct a uniform 3D model (fig. 5). This can be used to apply quantitative analytic methods to quantify the syndepositional behaviour of the fault.

The 3D model shows that there is a gradual decrease to the fault displacement from 22 m to its lowermost part (where visible) to 0 next to the surface. The decrease gradient is not smooth, but it shows an episodic pattern, which can be interpreted as intermittent periods of activity, possibly related to the volcanic activity rather than the structural pattern.

REFERENCES

Blouet, A., & Ravoisié, A., 1831. Expédition scientifique de Morée, ordonnée par le Gouvernement Français. Architecture, Sculptures, Inscriptions et Vues du Péloponnèse, des Cyclades et de l'Attique, Firmin Didot, 3 volumes.

Bory de Saint-Vincent, J.B., et al., 1834. Expédition scientifique de Morée. Section des sciences physiques., volume II, Géographie et géologie.

Mountrakis, D., Pavlides, S., Chatzipetros, A., Meletlidis, S., Tranos, M., Vougioukalakis, G., & Kilias, A., 1996. Active deformation of Santorini. In: *Proceedings of the 2nd Workshop on European Laboratory Volcanoes, Santorini* (Casale, R., Fytikas, M., Sigvaldasson, G., Vougioukalakis, G., Eds), 2-4 May 1996, 13-22.

Pavlides, S., & Caputo, R., 2004. Magnitude versus faults' surface parameters: quantitative relationships from the Aegean. *Tectonophysics* 380, 159-188.

Wells, D.L., & Coppersmith, J.K., 1994. New Empirical Relationships among Magnitude, Rupture Length, Rupture Width, Rupture Area, and Surface Displacement. *Bull. Seism. Soc. Am*. 84, 974-1002.

INQUA Focus Group Earthquake Geology and Seismic Hazards

paleoseismicity.org

Tracing the origin of load structures induced by permafrost- and seismicity-related processes

Pisarska-Jamroży, Małgorzata (1), Woronko, Barbara (2), Van Loon, A.J. (Tom) (3)

(1) Institute of Geology, Adam Mickiewicz University, B. Krygowskiego 12, 61-680 Poznań, Poland, pisanka@amu.edu.pl
(2) Faculty of Geology, University of Warsaw, Żwirki i Wigury 93, 02-089 Warsaw, Poland, bworonko@uw.edu.pl
(3) Geocom, Valle del Portet 17, 03726 Benitachell, Spain; Shandong University of Science and Technology, Qingdao 266590, China, tvanloon@amu.edu.pl

Abstract: *Load structures like load casts, pseudonodules, ball-and-pillow structures and flame structures are relatively easily recognizable but the responsible trigger mechanism is commonly difficult to establish or - in some cases - not at all. Load structures can be formed in almost all depositional environments, and they are formed under numerous conditions. We deal in the present contribution only with periglacial conditions and seismic activity because Quaternary geologists commonly study cryoturbations but have still insufficient attention for traces of seismic activity. We therefore discuss whether it is possible to distinguish load structures formed by periglacial from those caused by seismic shocks.*

Keywords*: load casts, pseudonodules, soft-sediment deformation structures, seismites, periglacial structures, glacio-isostatic rebound*

INTRODUCTION

The most common genesis of load structures is gravity-induced sinking due to a reversed density gradient, often acting as a Rayleigh-Tayler instability (e.g., Murton & French, 1993; Harrison, 1996; French 2007; Vandenberghe, 2009; Superson et al., 2010; Alexeev et al., 2014; Van Loon & Pisarska-Jamroży, 2014). However, some load structures can be formed due to external factors such as passing earthquake-induced shock waves resulting in strongly deformed layers (called seismites; e.g., Seilacher, 1984; Van Loon, 2014), or by freezing/thawing alternations under periglacial conditions; the latter category of deformations are known jointly as called cryoturbation (e.g., Vandenberghe, 2009).

Load structures develop most easily in water-saturated sediments with a large pore volume, because the frictional strength of unconsolidated dewatered sediments tends to be too high for starting the loading process (Vandenberghe, 2013). Loading is directed downwards because it is caused by gravitation, whereas liquefaction that occurs in a sediment with overpressurized pore water due to the weight of the overburden causes an upward injection that induces - because the resulting space problem must be solved - in the development of load structures in between the injectites. Liquefaction causes temporary loss of strength so that the sediments behave mechanically like a fluid (Allen, 1982; Owen, 1996). Liquefaction is often followed by fluidization: when the sediment strength is lost through moving interstitial fluids buoying the particles, the process is called 'fluidization'.
The nature of the trigger mechanism plays a minor role in the development of load structures, and is less important than the initial sedimentary setting, the driving force and the duration of the deformable state (Vandenberghe, 2009; Owen & Moretti, 2011; Owen et al., 2011). The presence of load structures is consequently not diagnostic for either a periglacial or a seismic setting.

An even much more puzzling situation can arise when (1) sediments affected by a seismic shock become later, due to climate change, positioned in a periglacial setting, (2) sediments with soft-sediment deformation structures formed due to periglacial processes are later affected by seismic shocks, (3) sediments that are being deformed by periglacial processes are simultaneously affected by seismic shocks, and (4) successive deformation phases due to both periglacial processes and seismic activity occurred.

SEDIMENTOLOGICAL FEATURES OF LOAD STRUCTURES FORMED UNDER SEISMIC AND PERIGLACIAL CONDITIONS

Several criteria for the distinction of seismites (and thus of the load structures in them) have been proposed (see Owen & Moretti, 2008; Owen et al. 2011; Moretti & Van Loon, 2014). For the sake of clarity and brevity, we restrict our attention here to macroscopic sedimentological features of load structures developed in only a periglacial or a seismic setting.

The following three parameters can help in distinguishing periglacially- from seismically-triggered load structures:

(1) the vertical distribution of load structures within a deformed sedimentary level,

(2) the horizontal distribution of load structures within a deformed sedimentary level, and

(3) the internal structure of the load structures.

Seismically-triggered load structures

- The load structures are mostly restricted to a single, abundantly deformed layer;
- The primary sedimentary structures in the level with load structures are most commonly strongly deformed and/or not well recognizable;
- The horizontal distribution of the load structures is seems commonly haphazard;
- The internal lamination of some of the load structures does not follow the outer boundaries of load structures;
- The load structures may show truncations and other irregularities that indicate a multi-phase deformation process.

Periglacially-triggered load structures

- The load structures may cross boundaries of layers with non-deformed or differently deformed layers;
- The primary sedimentary structures in the level with load structures can commonly still be discerned;
- The horizontal distribution of the load structures is most commonly fairly regular as they may be related to polygonal fissure patterns;
- The internal lamination of the load structures follows most commonly the outer boundaries of the load structures more or less precisely.

FINAL REMARKS

The mechanisms and processes that allow load structures to develop must most commonly be interpreted on the basis of circumstantial evidence. All features mentioned above can only make a periglacial or seismic origin more likely (or unlikely), but they do not provide proof. On the other hand, if all data point into the same direction, it seems scientifically acceptable to consider this as strong evidence.

Acknowledgements: The work has been financially supported by the GREBAL project from the National Science Centre Poland No. 2015/19/B/ST10/00661 and project No. 2013/09/B/ST10/ 02118.

REFERENCES

Alexeev, S., Alexeeva, L., & Kononov, A., 2014. Cryogenic deformation structures in Late Cenozoic unconsolidated sediments of the Tunka Depression in the Baikal Rift Zone. *Permafrost and Periglacial Processes* 25, 117-126.

Allen, J.R.L., 1982. *Sedimentary Structures: Their Character and Physical Basis*, vol. II. Elsevier, New York, 663 pp.

French, H., 2007. *The Periglacial Environment*. John Wiley & Sons Ltd, Chichester, 458 pp.

Harris, C., Murton, J., & Davies, M.C.R., 2000. Soft-sediment deformation during thawing of ice-rich frozen soils: results of scaled centrifuge modelling experiments. *Sedimentology* 47, 687-700.

Moretti, M., & Van Loon, A.J., 2014. Restrictions to the application of 'diagnostic' criteria for recognizing ancient seismites. *Journal of Palaeogeography* 3, 162-173.

Murton, J.B., & French, H.M., 1993. Thermokarst involutions, summer island, Pleistocene Mackenzie delta, western Canadian arctic. *Permafrost and Periglacial Processes* 4, 217-229.

Owen, G., 1996. Anatomy of a water-escape cusp in Upper Proterozoic Torridon Group sandstones, Scotland. *Sedimentary Geology* 103, 117-128.

Owen, G., & Morreti, M., 2008. Determining the origin of soft-sediment deformation structures: a case study from Upper Carboniferous delta deposits in south-west Wales, UK. *Terra Nova* 20, 237-245.

Owen, G., & Moretti, M., 2011. Identifying triggers for liquefaction-induced soft-sediment deformation in sands. *Sedimentary Geology* 235, 141-147.

Owen, G., Moretti, M., & Alfaro, P., 2011. Recognising triggers for soft-sediment deformation: current understanding and future directions. *Sedimentary Geology* 235, 133-140.

Seilacher, A., 1984. Sedimentary structures tentatively attributed to seismic events. *Marine Geology* 55, 1-12.

Superson, J., Gębica P., & Brzezińska-Wójcik, T., 2010. The origin of deformation structures in periglacial fluvial sediments of the Wisłok valley, southeast Poland. *Permafrost and Periglacial Processes* 21, 301-314.

Van Loon, A.J. (Ed.), 2014. Seismites and their soft-sediment deformation structures. *Geologos* 20 (2), 61-166.

Van Loon, A.J., & Pisarska-Jamroży, M., 2014. Sedimentological evidence of Pleistocene earthquakes in NW Poland induced by glacio-isostatic rebound. *Sedimentary Geology* 300, 1-10.

Vandenberghe, J., 2009. Comment to 'Zur Struktur und Entstehung von Eiskeil-Grossformen in Lieth/Elmshorn (Schleswig-Holstein)' by A. Grube, 2007 (Quaternary Science Journal 56, 283-294). *Journal of Quaternary Science* 58, 107-109.

Vandenberghe, J., 2013. Cryoturbation structures. In: Elias, S.A. (Ed.), *The Encyclopedia of Quaternary Science*, vol. 3, Elsevier, Amsterdam, pp. 430-435.

INQUA Focus Group Earthquake Geology and Seismic Hazards

paleoseismicity.org

Macroseismic intensities assessment of the August 21, 2017 Casamicciola earthquake at the Ischia volcanic Island (southern Italy)

Porfido, Sabina (1), Alessio, Giuliana (2), Gaudiosi, Germana (2), Nappi, Rosa (2)

(1) CNR-IAMC, Calata Porta di Massa, 80133 Napoli (Italy)
(2) INGV Sezione di Napoli, Osservatorio Vesuviano, Via Diocleziano, 80124 Napoli (Italy), rosa.nappi@ingv.it

Abstract: *On August 21, 2017 at 20:57 (Local Time) a very shallow earthquake (ca 1.2 km depth) of M_d=4.0 hit the Ischia island (Southern Italy) heavily damaging the Casamicciola Terme village and also the Lacco Ameno village, causing two fatalities and about 40 people injured. Soon after the mainshock we surveyed the area and collect macroseismic data in order to assess the MCS intensity and the ESI-07 intensity values. We assigned the maximum intensity value I= VIII MCS at Casamicciola Terme on the basis of the damage to buildings and we assessed the epicentral intensity value I= VII ESI-07 on the basis of primary and secondary coseismic ground effects. We point out that the Casamicciola volcano-tectonic earthquake (M_d=4), has had catastrophic consequences on local communities, therefore this study can provide relevant implications for seismic hazard evaluation and land use planning in the Ischia island.*

Keywords*: Volcano-tectonic earthquake, Intensity values, Ischia island, ESI-07scale*

INTRODUCTION

The Ischia Island (Southern Italy) is located at the northwestern side of the Gulf of Naples inside of the Campanian volcanic province that also includes the Campi Flegrei volcanic field. This island is known all over the world for its tourist peculiarities, and since ancient times for its healing thermal waters.

Ischia is the emerged portion of a volcanic complex, active since at least 150 ka. (Vezzoli, 1988). The most impacting event in the island geological history is the caldera forming eruption of the Green Tuff of the Mt. Epomeo occurred 55 ka, that caused the collapse of the island central sector, followed by the resurgence of the Mt. Epomeo block, starting from 30 ka. From 10 ka, the eruptions mainly located in the eastern part of the island; the last effusive Arso eruption occurred in 1302 (Orsi et al., 1991; de Vita et al., 2010).

The uplift of the Mt. Epomeo resurgent block was asymmetric, with maximum displacement on the N flank, controlled by E-W normal faults system well described in the literature (Figure 1) (Vezzoli, 1988; Tibaldi & Vezzoli, 1998; Acocella & Funiciello, 1999; Carlino et al., 2006; de Vita et al., 2010; Nappi et al., 2010). The main faults system bording the Mt. Epomeo consists of NW-SE to N-S striking faults in the western sector and of NE-SW to E-W faults in its northern sector. In the eastern sector of the island, N-S and NE-SW striking fractures and faults control the location of the vents.

The northern flank of Mt. Epomeo is considered the most tectonically active sector, with an estimated total uplift of 920-970 m, inferred from the present height of uplifted marine deposits, eustatic variations and basin subsidence (Barra et al., 1992). The island is also characterized by several strong historical earthquakes (Alessio et al., 1986; Cubellis & Luongo, 1998, Esposito et al., 2006) concentrated mainly in the northern sector of the island, in the same epicentral area of the August 21, 2017 earthquake.

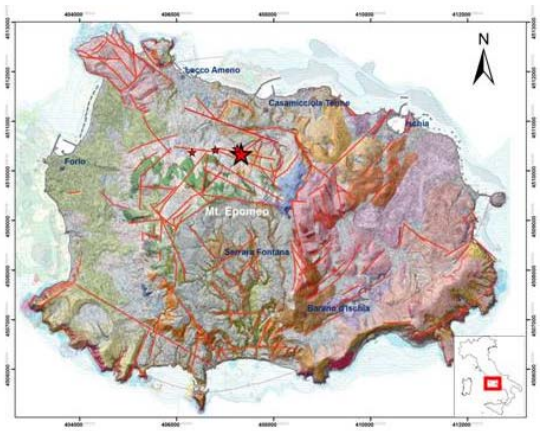

Figure 1: Faults (in red) are from Acocella and Funiciello (1999), de Vita et al. (2010), Vezzoli (1988), Tibaldi & Vezzoli (1998) and geomorphological lineaments from Nappi et al. (2010). The base map is Carta Geologica dell'Isola d'Ischia della Regione Campania in scala 1:10.000, Foglio 464, 2011. The greatest red star is the 21 August 2017 main shock with the main aftershocks.

THE AUGUST 21, 2017 CASAMICCIOLA EARTHQUAKE

On August 21, 2017 at 20:57 (local time) a volcano-tectonic earthquake of M_d =4.0 (Lat. 40.74°, Long 13.90°), with shallow depth (1.2 km, de Novellis et al., 2018), hit the Ischia island heavily damaging the Casamicciola Terme village, the neighboring localities, causing two fatalities and about 40 people injured (Figure 2).

Figure 2: Houses collapsed and heavily damaged by the 21 August 2017 earthquake in the hilly historical centre of Casamicciola Terme (Ischia island). Photos by S. Porfido.

This seismic event was felt throughout the island with extremely different intensities $8<I_{EMS}<3$ (Azzaro et al., 2017). The earthquake was also felt in the nearby island of Procida and in some localities on the coast of the Gulf of Pozzuoli with I≤4 MCS (Figure 3).

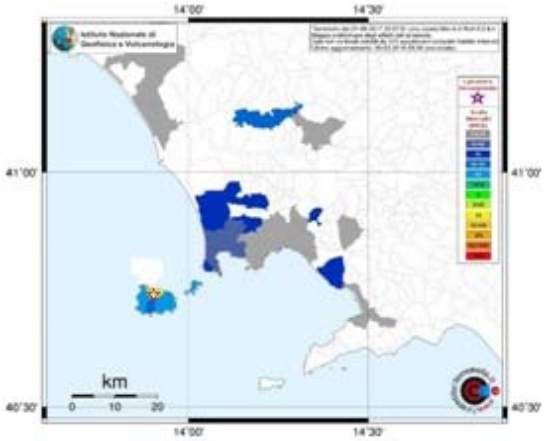

Figure 3: The MCS intensity distribution in the Ischia island and surrounding areas (http://www.haisentitoilterremoto.it/).

It is important to underline that although the island is characterized by high tourist flow, the most common building typology, spread throughout the island, consists of buildings in tufa stone with wooden or steel floor built between the 19th and 20th century. The earthquake caused a few total collapses and some partial collapses, widespread cross and horizontal lesions, which determined in some cases the total inability of the houses. The quake caused serious damage in a limited area of a few km^2: the Casamicciola Terme village with the maximum intensity of VIII MCS at Piazza Maio (the hilly side of the Casamicciola Terme village) and the Fango district (Lacco Ameno village) with the VII-VIII MCS.

Soon after the mainshock we surveyed the epicentral area in order to collect the coseismic ground effects. We mapped more than 100 geological field observations according the standard procedures of EMERGEO W.G. of INGV (http://emergeo.ingv.it/; Nappi et al., 2017; Nappi et al., 2018).

FIELD SURVEY

Although the 2017 Casamicciola earthquake was a moderate size volcano-tectonic event, we observed several ground effects both primary (surface ruptures and permanent displacement caused directly by the seismogenic source), and secondary effects (landslides, hydrological variations etc.) sensu Keller & Pinter (2002) and Michetti et al. (2007).

The most important type of ground effects collected during the field survey, are: ruptures, fractures, landslides, variations in fumarolic activity and dry wall collapses (Figure 4).

Figure 4: Coseismic surface effects: a) and b) surface rupture in Fango (Lacco Ameno); c) surface rupture in via Montecito (Casamicciola); d) e) landslides in volcanoclastic deposits in Casamicciola.

Generally, the whole investigated area showed different fractures on both manufactures and ground, on road and on ground cover, with direction from WNW-ESE to E-W and WSW-ENE (Figure 1), and lengths up to some tens of meters. In addition, some fractures in the soil had 3 cm wide openings, and in some cases a vertical component of appreciable displacement with lowering of the ground Northward.

Widespread sliding phenomena of drywalls, that are locally known as “parracine”, built mainly with green tuff and also with lava materials, were also observed, with a general direction of movement from south to north, as well as modest gravitational phenomena such as small size collapses of several m^3, and small landslides in volcanoclastic deposits, along the northern slope of Mt.

Epomeo (Nappi et al., 2018). Moreover, an increase of steam emission in the Montecito fumaroles was observed soon after the 21 August seismic event, as witnessed and reported by the local inhabitants.

HISTORICAL SEISMICITY OF THE ISCHIA ISLAND

The Ischia island was characterized by strong seismic events in historical time (Mercalli, 1884; Johnston-Lavis, 1885; Cubellis & Luongo, 2018). The seismicity observed in the island is strongly connected to the volcano-tectonic dynamics of the island itself; the earthquake epicenters are located mostly in the northern zone stretching E-W from Casamicciola to Lacco Ameno (North of the Mt. Epomeo), with usually shallow hypocenters (Alessio et al., 1996; Nappi et al., 2018). The observed MCS intensity values range between VII and XI degree, with rapid decrease of intensities versus the distance. The most important historical seismic events that struck the island occurred in the XIX century as the well-known destructive earthquakes of March 4, 1881 with I=IX MCS and the July 28, 1883 with Imax =XI MCS. Both of these strong earthquakes were located in the hilly area of the Casamicciola Terme village and almost completely destroyed it and the surrounding area. The 1881 event caused about 120 casualties and 140 injured, whereas the 1883 earthquake caused 2,300 fatalities and several environmental effects (Alessio et al., 1996; Cubellis & Luongo, 1998; Del Prete & Mele, 1999; Violante et al., 2003; Luongo et al., 2006; Carlino et al., 2010).

On 1762, 1767, 1796, and 1828 other strong earthquakes, with VII≤I_{MCS}≤IX, occurred in the island and caused many victims and damages to the villages built on the northern sector of the Mt. Epomeo. Several landslides (rockfalls and debris flows) detached from the northern flank of Mt. Epomeo, fractures and hydrological changes were also observed, mainly concentrated along the major fault zones, in the northern sectors of the island, which appear as the most disaster prone areas.

DISCUSSION AND CONCLUSIONS

The Casamicciola Terme village was heavily hit by strong earthquakes since historical times, the most important occurred in 1762, 1796, 1828, 1881, 1883, which allowed to recognize a seismogenic area along the northern slope of the Mt. Epomeo resurgent block (Alessio et al., 1996). These strong earthquakes are comparable with the August 21, 2017 seismic event, both for the epicentral zone, besides the macroseismic and environmental effects.

The prompt macroseismic observations of the level of damage distribution to the buildings, allowed us to assess the preliminary epicentral Intensity I=VIII MCS to Casamicciola Terme (hilly area) and I=VII-VIII MCS to Fango (Lacco Ameno). The pattern of primary coseismic ground effects is represented over all by 62% of ruptures and 17% of fractures; the secondary coseismic effects consisted in 14% of drywall collapses; 6% of landslides phenomena; 5% of steam variations in Montecito fumaroles (Figure 5). According to Nappi et al. (2018) the distribution of coseismic effects allowed us to hypothesize the 2 km end to end rupture as primary surface normal faulting, N dipping, of the 21 August 2017, volcano-tectonic seismic event.

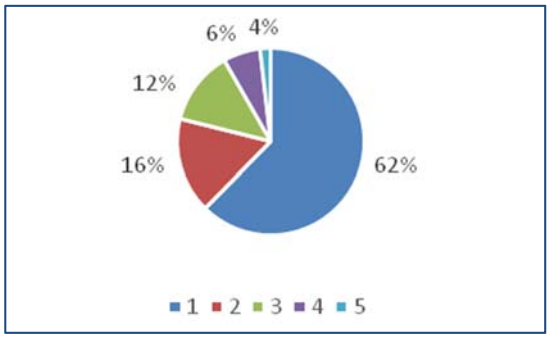

Figure 5: Ground effects induced by the August 21, 2017 Casamicciola earthquake: 62% ruptures (blue); 16% fractures (red); 12% collapse of drywall (green); 6% landslides phenomena (purple); 4% steam variations in Montecito fumaroles (light blue).

Considering the distribution of the primary and secondary coseismic geological data we have assessed the preliminary ESI-07 epicentral intensity; in particular, we have assigned the VII degree of ESI-07 scale by taking into account the total length of the fault segment, ca. 2 km, and the maximum displacement observed, ca. 2-3 cm, as well as the area affected by others secondary coseismic effects, which is only of a few km^2.

In conclusion, , our macroseismic survey pointing out the damaging level and sesimoinduced effects could be used for the reinterpretation of historical earthquakes, and provides new data for understanding the surface faulting mechanism due to a moderate earthquake (M=4.0), for the first time in the Ischia island volcano-tectonic contest.

REFERENCES

Acocella, V., & Funiciello, R., 1999. The interaction between regional and local tectonics during resurgent doming: the case of the Island of Ischia, Italy. *J. Volcanol. Geoth. Res.* 88, 109-123.

Alessio, G., Esposito, E., Ferranti, L., Mastrolorenzo, G., & Porfido, S., 1996. Correlazione tra sismicità ed elementi strutturali nell'isola d'ischia. *Il Quaternario* 9 (1), 303-308.

Azzaro, R., Tertulliani, A., Del Mese, S., Graziani, L., Maramai, A., Martini, G., Paolini, S., Screpanti, A., Verrubbi, V., & Arcoraci, L., 2017. QUEST - Il terremoto di Casamicciola(Ischia) del 21 agosto 2017: effetti macrosismiciiciici e confronto con la sismicità storicica dell'area. *Proc. 36° GNGTS Trieste,* 5-7, ISBN: 978-88940442-8-7.

Barra, A.D., Cinque, A., Italiano, A., & Scorziello, R., 1999. Il Pleistocene superiore marino di Ischia: paleoecologia e rapporti con l'evoluzione tettonica recente. *Studi Geologici Camerti,* 231-243.

Carlino, S., Cubellis, E., Luongo. G., & Obrizzo, F., 2006. On the mechanics of caldera resurgence of Ischia Island (southern Italy). In: *Mechanism of activity and unrest of large calderas. Geological Society Spec. Publications* (Troise, C., De Natale, G., Kilburn, C.R.J., eds), 269, London, 181-193.

Carlino, S., Cubellis, E., & Marturano, A., 2010. The catastrophic 1883 earthquake at the island of Ischia (southern Italy): macroseismic data and the role of geological conditions. *Nat. Hazards* 52, 231-247, https://doi 10.1007/s11069-009-9367-2.

Cubellis, E., & Luongo, G., 1998. Il terremoto del 28 luglio 1883 a Casamicciola nell'Isola di Ischia-Il contesto fisico. In: *Monografia n°1, Pres. del Consiglio dei Ministri, SSN, Istituto Poligrafico e Zecca dello Stato*, Roma, 49-123.

Cubellis, E., & Luongo, G., 2018. History of Ischian earthquakes. Bybliopolis, Napoli, pp. 138 ISBN978-88-7088-652-8.

De Novellis, V., Carlino, S., Castaldo, R., Tramelli, A., De Luca, C., Pino, N.A., Pepe, S., Convertito, V., Zinno, I., De Martino, P., Bonano, M., et al., 2018. The 21st August 2017 Ischia (Italy) earthquake source model inferred from seismological, GPS and DInSAR measurements*, Geophys. Res. Lett.* 45*,* 1-10, https://doi.org/10.1002/2017GL076336.

Del Prete, S., & Mele, R., 1999. L'influenza dei fenomeni d'instabilità di versante nel quadro morfoevolutivo della costa dell'isola d'Ischia. *Boll. Soc. Geol. Ital.* 118, 339-360.

de Vita, S., Sansivero, F., Orsi, G., Marotta E., & Piochi M., 2010. Volcanological and structural evolution of the Ischia resurgent caldera (Italy) over the past 10 ka. *Geological Society of America*, Special Paper 464, 193-239.

Esposito, E., Porfido, S., & Vittori, E., 2006. Earthquake hazard in the Island of Ischia (Campania, Italy). *Proc. EGU 2006*, https://doi: 10.13140/RG.2.2.33895.34722.

Keller, E.A., & Pinter, N., 2002. Active Tectonics - Earthquakes, Uplift and Landscape. Prentice Hall, ISBN 0-13-088230-5, 33-35.

Luongo, G., Carlino, S., Cubellis E., Delizia, I., Iannuzzi, R., & Obrizzo, F., 2006. Il terremoto di Casamicciola del 1883: una ricostruzione mancata. Alfa Tipografia, Napoli, 1-64.

Johnston-Lavis, H.J., 1885. *Monograph of the earthquakes of Ischia*. London-Naples, 1-122.

Mercalli, G,. 1884. L'isola d'Ischia ed il terremoto del 28 luglio 1883, *Mem. Reg. Ist. Lombardo Scienze & Lettere* 3 (6), 99-154.

Michetti, A.M., Esposito, E., Guerrieri, L., Porfido, S., Serva, L., Tatevossian, R., Vittori, E., Audemard, F., Azuma, T., Clague, J., Comerci, V., Gurpinar, A., Mccalpin, J., Mohammadioun, B., Mörner, N. A., Ota, Y., & Roghozin, E. 2007. Intensity scale ESI 2007. *Mem. Descr. Carta Geologica d'Italia*, Roma 74, pp. 53.

Nappi, R., Alessio, G., & Bellucci Sessa, E., 2010. A case study comparing landscape metrics to geologic and seismic data from the Ischia Island (Southern Italy). *Applied Geoma*tics, doi: 10.1007/s12518-010- 0023 z.

Nappi, R., Alessio, G., Belviso, P., Gaudiosi, G., Marotta E., Nave, R., Peluso,P., Siniscalchi, V., Civico, R., Pizzimenti, L., & Porfido, S., 2017. The August 21, 2017 Casamicciola (Ischia Island) earthquake: seismo-geological effects due to a small-size volcano-tectonic event*, Proc. 36° GNGTS, Trieste, 56-60*, ISBN: 978-88940442-8-7.

Nappi, R., Alessio, G., Belviso, P., Gaudiosi, G., Marotta E., Nave, R., Peluso,P., Siniscalchi, V., Civico, R., Pizzimenti, L., & Porfido, S., 2018. The August 21, 2017, Mw 4.0 Casamicciola earthquake: first evidence of surface extensional faulting at the Ischia volcanic island. *SRL, accepted.*

Orsi, G., Gallo, G., & Zanchi, A., 1991. Simple-shearing block resurgence in caldera depression. A model from Pantelleria and Ischia. *J. Volcan. Geotherm. Res.* 47, 1-11.

Tibaldi, A., & Vezzoli, L., 1998. The space problem of a caldera resurgence: An example from Ischia Island, Italy. *Geol. Rundsch.* 87, 53-66.

Vezzoli, L., 1988. Island of Ischia. In: *CNR Quaderni de "La ricerca scientifica"* (Vezzoli, L., ed), 114-10, 122.

Violante, C., Budillon, F., Esposito, E., Porfido, S., & Vittori, E., 2003. Submerged hummocky topographies and relations with land-slides on the northwestern flank of Ischia Island, Southern Italy. In: *Proc. Int. Workshop on Occurrence and mechanisms of flow-like landslides in natural slopes and earthfills* (Picarelli, L., ed), Sorrento, 309-315.

INQUA Focus Group Earthquake Geology and Seismic Hazards

paleoseismicity.org

Geomorphological and geophysical evidences for active faulting in the Upper Rhine Graben

Reicherter, Klaus (1), Hürtgen, Jochen (1), Baize, Stephane (2), Thomas, Jessica (1), Schmid, Gundolf (1), Ritter, Joachim (3)

(1) Inst. of Neotectonics and Natural Hazards, RWTH Aachen University, Lochnerstrasse 4-20, 52056 Aachen, Germany, k.reicherter@nug.rwth-aachen.de
(2) Institut de Radioprotection et de Sûreté Nucléaire, BP 6, 92262 Fontenay-aux-Roses, France, stephane.baize@irsn.fr
(3) KIT, Geophysikalisches Institut, Hertzstr. 16, 76187 Karlsruhe, joachim.ritter@kit.edu

Abstract: *We present new data on our paleoseismological investigations in the Upper Rhine Graben (Germany, France). With the help of LiDAR and remote sensing data, we have evaluated two promising sites along the eastern marginal fault for detailed geophysical studies by ERT and GPR. It seems that tectonic topography of the "seismic landscape approach" is in discordance with present-day instrumental seismicity forming the conundrum of the Upper Rhine Graben.*

Keywords*: Upper Rhine Graben, active tectonics, tectonic geomorphology, Ground Penetrating Radar*

INTRODUCTION

The Upper Rhine Graben (URG) is the central part of the Central European Cenozoic Rift System (ECRIS) and one of the tectonically active regions in Europe. The URG extends from the Jura thrust and fold belt in the South near Basle city (Switzerland) to the Rhenish Massif in the North near Frankfurt and is limited by sinistral strike-slip faults on either sides. Several studies suggested particularly the fault system at the eastern margin to be active, as the Basle earthquake 1356 AD was situated there. Ongoing earthquake activity testifies to active faulting, however, there are many faults and fault strands, many of them are regarded as normal faults, others as reactivated normal faults with a sinistral sense of movement. This is due to a major change in stress direction from SW-NE towards a SE-NW direction in Miocene times.

STUDY AREA

The URG is a low-strain setting with long recurrence intervals of large earthquakes. Moreover, the fault morphological signal is perturbed by anthropogenic land-use, the climate of the area, which is located in the temperate zone, and the erosion and sedimentation of the Rhine River. The eastern margin faults lack any neotectonic and paleoseismological investigations, in contrast to the western border faults that have been examined during the last decades, while the area encompasses critical facilities in a vulnerable region such as, dense population, agriculture, mining, geothermal facilities. Our projects in the frame of an IRSN study and the DFG-SPP AlpArray aim to fill this gap of knowledge in large and infrequent earthquakes, through a paleoseismological investigation of eastern side faults.

METHODS

We used a multidisciplinary approach to improve the input data of seismotectonic models, which include faults and their activity potential in the calculation of seismic hazard assessment and are based on a weak data set at the moment. First results of different locations around Freiburg in the southern URG and around Karlsruhe are presented: the Rhine River fault system about 20 km SW of Freiburg, NE of Freiburg at the eastern border fault system about 10 km. At both sites we used a digital elevation model (DEM) derived from LiDAR-data (5x5m) and together with geophysical measurements performed with ground-penetrating radar (GPR) and electrical resistivity tomography in order to track and identify possible fault scarps. A detailed geomorphological study of the DEM was performed to identify and map superficial expressions of the neotectonic activity of the faults and deformed and offset alluvial terraces and fans. We apply ERT and GPR for imaging the geophysical contrasts at depth, such as faults and stratigraphy in detail. Nevertheless, for the unambiguous verification of these structures and the determination of key fault parameters, such as magnitude, age of last events, slip rate and return periods, additional paleoseismological trenches are needed, which will be the next step of the project.

CONCLUSIONS AND DISCUSSION

Several km s of GPR profiling and 100s of m of ERT section have been evaluated in accordance with commercial seismic reflection profiles and actual seismicity to find possible sits for in-depth paleoseismological investigations. The geophysical studies are underpinned and augmented by tectonic geomorphology by remote sensing methods. Nevertheless, for the unambiguous verification of these structures and the determination of key fault parameters, such as magnitude, age of last events, slip rate and return periods, additional paleoseismological trenches are needed, which will be the next steps of the project.

Acknowledgements: Financial support by DFG Projects RE 1361/31-1 (Spannungstransfer und quartäre Bruchprozesse in nördlichen Alpenvorland) is gratefully acknowledged.

INQUA Focus Group Earthquake Geology and Seismic Hazards

paleoseismicity.org

Late Quaternary paleoearthquakes on the Lijiang-Xiaojinhe fault, southeast Tibet

Ren, Junjie (1), Zhang, Shimin (1), Xu, Xiwei (1), Ding, Rui (1), Li, An (1), Lv, Yanwu (1)

(1) Key Laboratory of Crustal Dynamics, Institute of Crustal Dynamics, China Earthquake Administration, Beijing 100085, China, renjunjie@gmail.com

Abstract: *The Lijiang-Xiaojinhe fault (LXF) is the boundary of Northwest Sichuan and Central Yunnan sub-blocks in the Sichuan-Yunnan block, southeast Tibet. Clear displaced landforms show that the fault has a dominantly left-lateral strike-slip rate of ~3 mm/yr. However there is no large earthquake larger than M 7.0 occurred on the LXF in the historic record. The rupture behavior on the LXF is unclear and it is hard to assess its seismic hazard in the future. In this study, on the base of the interpretation of high-resolution satellite imagery, we choose the middle segment of the LXF and dug four trenches at Muzhuda, Hongxing, Gantangzi, and Runan sites combined with radiocarbon dating and Oxcal modeling. The first three sites are on the middle segment of the LXF, northeast of the Lijiang basin, whereas the last one is on the southwest segment of the LXF, southwest of the Lijiang Basin. The Muzhuda trench shows that at least three events occurred on the middle segment of the LXF at 7750±500Cal BP, 4560±280 Cal BP and 1700±420 Cal BP, respectively. The Hongxing trench indicates that the LXF underwent two events at 4160±960 Cal BP and 1660±440 Cal BP. The Gantangzi trench discovers at least three paleoearthquakes at 31320±13660 Cal BP, 5510±1700 Cal BP and 2040±500 Cal BP, respectively. The events in the Gantangzi trench might be incomplete because of stratigraphic gap. The Runan trench show three events at 5980±560 Cal BP, 1770±1000 Cal BP and 1751AD, respectively. The first three trenches indicate that three events occurred on the middle segment of the LXF in the Holocene at 7750±500Cal BP, 4550±280 Cal BP and 1760±140 Cal BP, respectively. Large earthquakes on the middle segment of the LXF appears to fit the quasi-periodic model with the mean recurrence interval of ~3000 yrs and the estimated magnitude ~7.6. The results on the Runan trench has a poorly correlation with thoes on other trenches, suggesting that the Lijiang basin is probably a step-over as the permament segmentation boundary of the LXF. Given the strong late-Quaternary activity of the middle segment of the LXF and a long elapsed time, we propose that the middle segment of the LXF might have a high seismic hazard in the future.*

Keywords*: Lijiang-Xiaojinhe fault, southeast Tibet, paleoearthquake, trench, recurrence interval*

Acknowledgements: This work was jointly supported by National Science Foundation of China (41572193), the Public Service Funds for Earthquake Studies (201108001), Institute of Crustal Dynamics, China Earthquake Administration Research Fund (ZDJ2017-24).

INQUA Focus Group Earthquake Geology and Seismic Hazards

paleoseismicity.org

Automated detection of surface ruptures associated with the 2016 Central Italy earthquake sequence by Sentinel-1 SAR interferometry data

Roccheggiani, Matteo (1), Tamburini, Andrea (1), Tirincanti, Emanuela (1), Menichetti, Marco (1)

(1) Department of Pure and Applied Sciences, University of Urbino, Campus Scientifico "E. Mattei", Via Ca' le Suore 2/4, Urbino 61029, Italy, matteo.roccheggiani@uniurb.it

Abstract: *Central Italy has been hit during 2016 by a long seismic sequence. Coseismic effects were observed after the main shocks, especially in the Mt. Vettore area and well documented by field surveys. In this work, we exploit Sentinel-1 C-band InSAR data to test the capability of interferometry as a field guide for mapping surface ruptures associated with the sequence main shocks. Some lineaments coincident with known active faults can be already recognized from linear phase discontinuities in interferograms. We proceeded at phase unwrapping and, combining ascending and descending orbits, we retrieved vertical and horizontal components of motion. Afterwards we proceeded with calculate optimized slope gradient maps using vertical displacement values. Even with medium-low data resolution, it was possible to recognize most of the principal fractures already identified by field surveys. Furthermore, new possible ruptures are reported, confirming the value of the method as a valid field mapping support.*

Keywords*: Earthquake, Active faulting, SAR interferometry, Surface rupture, Sentinel*

INTRODUCTION

The detection and the structural analysis of surface coseismic ruptures are essential for characterize the seismogenic structures. A significant sequence of normal-faulting earthquakes occurred in the central Apennines in Italy from August to October 2016. On August 24th, a Mw 6.2 earthquake struck the area close to the towns of Accumoli and Amatrice (Chiaraluce et al., 2017). Several ground ruptures with decimetric offset along SW dipping extensional faults occurred over a distance of more than 10 km. Two months later, on 26 October, another mainshock with Mw 5.9 occurred 25 km to the north, near the town of Visso. On 30 October, the largest shock of the sequence (Mw 6.5) occurred in the area between the epicentres of the previous earthquakes (Fig. 1). These events reactivated many of the existing ground ruptures and produced further NW-SE trending fractures with offsets of more than 1 m with a complex pattern extending over 30 km. In this study, we exploit space borne C-band radar data to test the capability of interferometry as a field guide for mapping surface ruptures associated with Amatrice (Mw 6.2) and Norcia (Mw 6.5) main shocks. Over Italy, Sentinel-1 A/B Interferometric Wide (IW) Swath TOPSAR (Terrain Observation with Progressive Scans SAR) mode offers the possibility of acquiring images with a maximum revisit time of six days. This huge amount of open data is extremely useful for geohazards monitoring such as earthquakes. Interferograms of a moderate-large earthquake show elastic deformation caused by the principal earthquake fault movement. However, Fukushima et al., (2013) and Guerrieri et al., (2010) have shown that phase discontinuities appearing on wrapped interferograms could represent small ground displacement displacements. Price & Sandwell (1998)

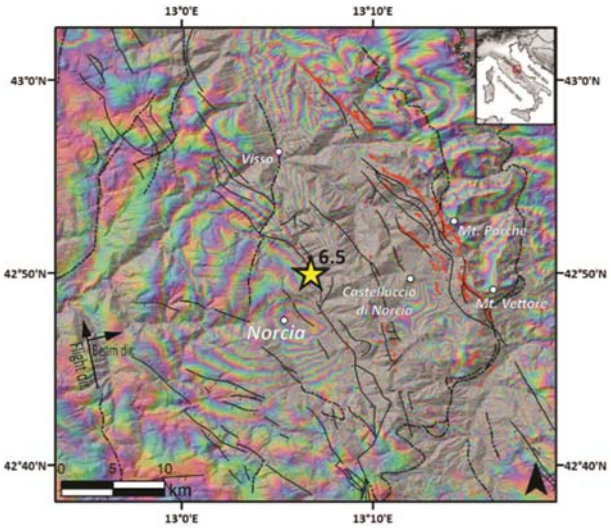

Figure 87: Sentinel-1 wrapped interferogram (ascending orbit 117) showing coseismic displacement of Norcia earthquake (Mw 6.5). Main tectonic lineaments are reported: normal faults (black lines) and thrust faults (dotted lines). The linear ground ruptures detected in the field are shown in red (field surveys of University of Urbino, Menichetti et al., 2017).

used surface displacement gradient maps of complex interferograms to visualize lineaments. Fujiwara et al., (2016) mapped linear surface ruptures of the 2016 Kunamoto earthquake sequence using L-band ALOS-2 SAR interferometry which is advantageous for detecting ground displacements due to its high coherence.

In this study, the adopted working strategy has been creating optimized slope gradient maps of displacement using the vertical motion values obtained combining the ascending and descending unwrapped interferograms.

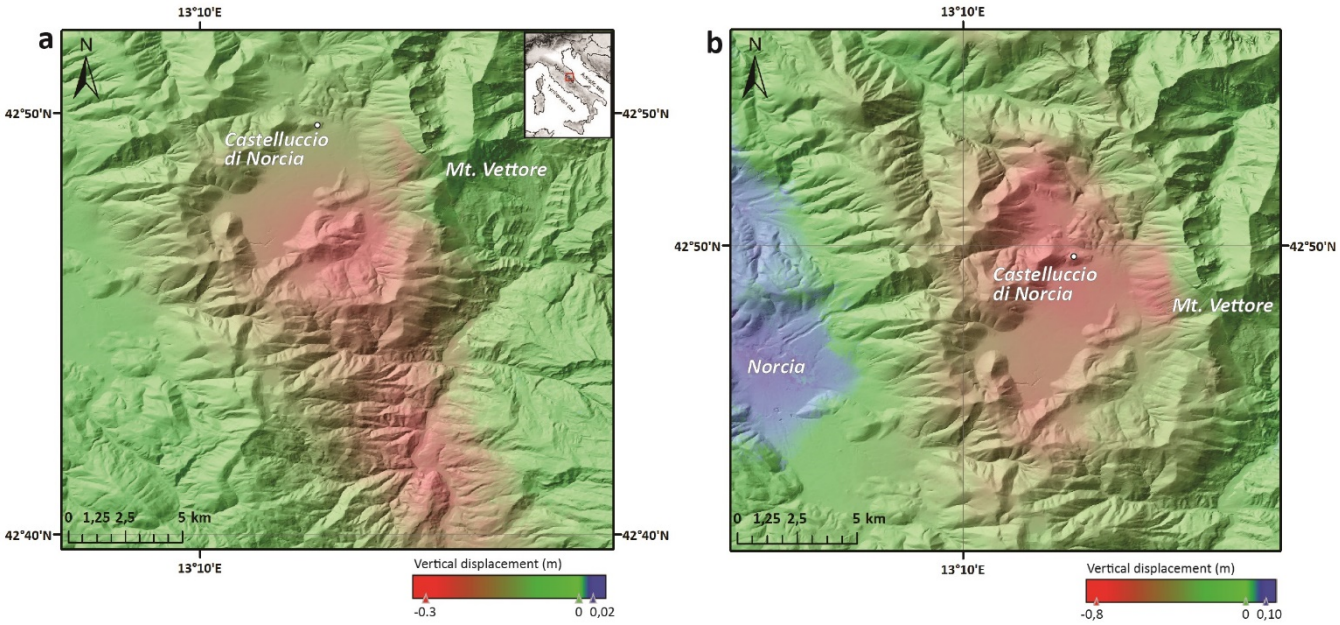

*Figure 2: D-InSAR maps showing coseismic vertical displacement of Amatrice (**a**) and Norcia earthquake (**b**). These maps are produced combining, in GIS environment, ascending and descending unwrapped interferograms.*

GEOLOGICAL SETTING

The Sibillini region is the fourth highest mountain massif of the Apennines after Gran Sasso, Maiella and Velino-Sirente. The area is located along the primary watershed of the central Apennines, between Marche and Umbria regions. The Sibillini mountain chain is a NE verging foreland fold-and-thrust belt, the southernmost part of the Northern Apennines that developed during the late Miocene. The entire region has been experiencing extension since the late Pliocene, expressed by a set of extensional faults which cross cut compressional structures forming several intermountain basins. Active extensional tectonics of about 3 mm/yr plays a key role in the slope morphogenesis of the area (D'Agostino et al., 2011). The thrust related anticlines are constituted by Mesozoic and Cenozoic limestones and marls overlaying a few thousand meters thick Mio-Pliocene siliciclastic sequence with an offset of a few kilometres (Lavecchia, 1985). Mt. Vettore (2476 m a.s.l.) is the highest peak, where Mesozoic limestone outcrops are arranged in a complex folded structure with a N-S trend axes. The entire Mt. Vettore compressional structures, are cross cutted by several SW dipping normal faults. The westernmost of these are responsible for the formation of the intermountain basin of Castelluccio di Norcia and dislocates the Lower Jurassic limestones for more than 1000 m. The fault consists of interlinked segments with NNW-SSE direction over a distance of more than 10 km. Situated on the western side of the chain, the fault has a pronounced morphological feature. A continuous limestone scarp with cataclastic breccia, with a shear zone of a few meters thick, is well documented in the upper slope of the mountain. In the plain area, few steps with decimetric offset extend for few kilometres where debris fan and clastic materials buried other several splays that distribute the fault throw. The extensional faults run toward SE along the Tronto Valley and the western side of the Laga Mountains, linking with the Amatrice and Mt. Gorzano fault systems.

METHODS

We investigated the surface earthquake effects by means of SAR interferometry using the ESA Sentinel-1 satellites acquisitions (C-band). For the InSAR data processing we used the open source Sentinel Application Platform (SNAP) toolbox. The radar data were downloaded from the Sentinel Open Hub (https://scihub.copernicus.eu/). We processed four pairs of Sentinel-1 IW SLC images from descending track 22 and ascending track 117 covering the pre and post seismic period of each main shock. The interferograms were flattened with a flat-earth phase algorithm and the topographic phase was removed based on a 30 m (1 Arc-Second) reference DTM (SRTM). In order to reduce the effects of phase noise a Goldstein adaptive filtering was applied, in addition to multilooking operation to obtain approximately a square pixel interferogram. Phase unwrapping was successfully performed using SHAPHU (Statistical-Cost, Network-Flow Algorithm for Phase Unwrapping) and final results were geocoded at 25 m spatial resolution.

Spaceborne D-InSAR provides an estimation of the relative displacement of the Earth surface in the satellite oblique line-of-sight. Under some assumptions, the acquisitions from different geometries can be combined over the same ground surface in order to measure the vertical and the horizontal component of the ground motion. The unwrapped interferograms, with phase converted do displacement, were imported in a GIS

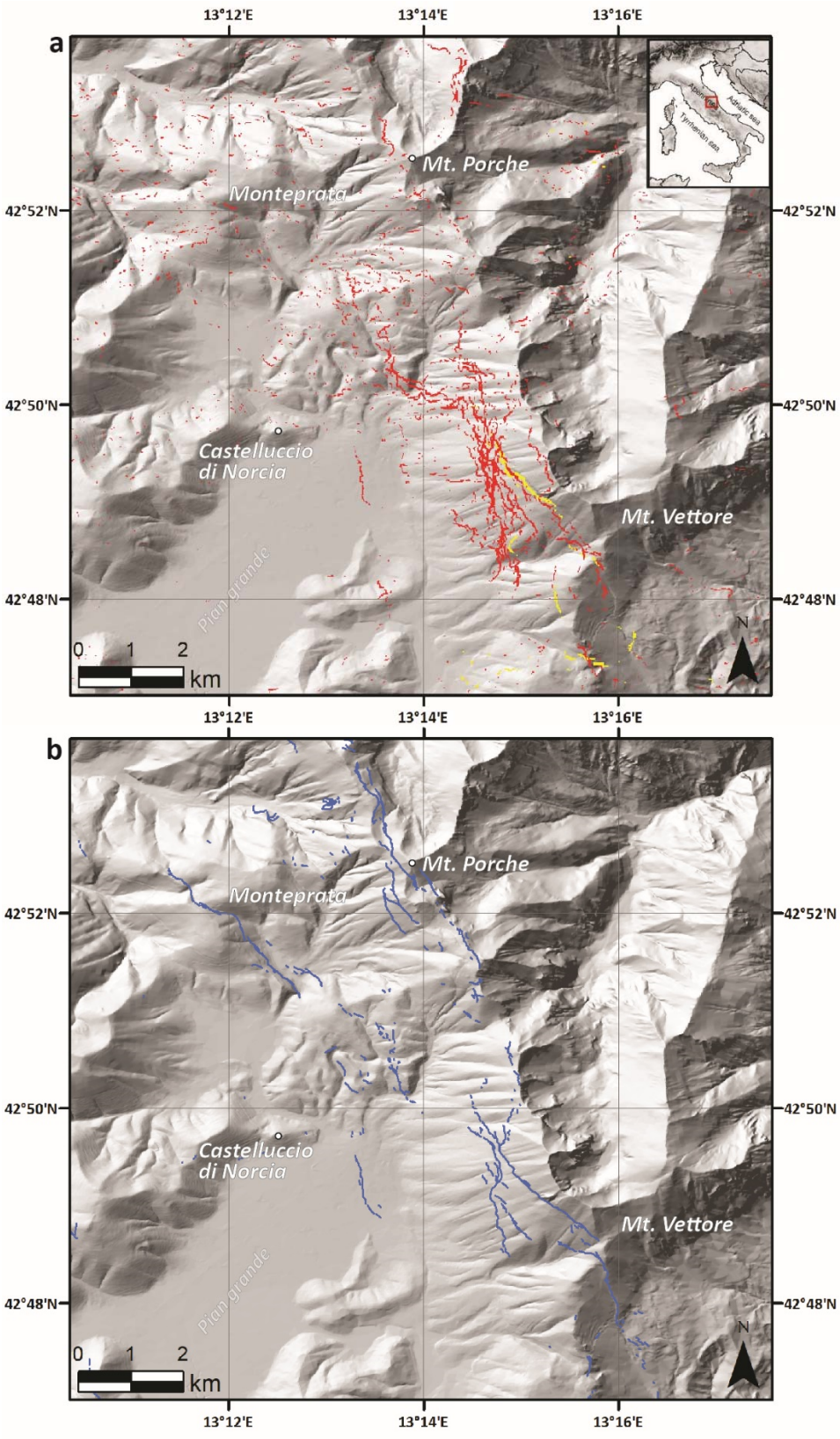

Figure 3: Coseismic ground ruptures of Castelluccio di Norcia and Mt. Vettore area. ***a.*** *Optimized slope gradient map of vertical displacement values. The yellow discontinuities are relative to the Amatrice event while the red ones of Norcia Mw 6.5 main shock.* ***b****. Ground ruptures map, field survey of University of Urbino (Menichetti et al., 2017).*

environment in which we have developed an InSAR motion resolver tool. This raster calculation tool allows, knowing the respective angles of incidence and LOS azimuths, to combine ascending and descending acquisitions very quickly. In this case we focused on the vertical (up-down) component because it better highlights the discontinuities and it preserves better the data of both acquisitions (Fig. 2). At the end, with vertical motion values, a slope gradient

map has been created to detect the possible coseismic ruptures. To limit noise due to unwrapping errors or DTM issues we extracted for the analysis only slope steps greater than 35 degrees (Fig. 3).

DISCUSSION AND CONCLUSION

During the whole seismic sequence, the coseismic effects interested especially the area of Castelluccio di Norcia plains and the Mt. Vettore - Mt. Porche - Mt. Bove sectors. Rupture traces are inferred from the displacement gradient maps taking into account steps with a slope higher than 30-40 degrees. Those are included in the map (Fig. 3a) as yellow and red line coverage. Yellow line are those relatives to the first Amatrice event while the red ones to the Norcia Mw 6.5 event. Rupture traces detected in the field surveying campaigns of the University of Urbino (Menichetti et al., 2017) are plotted with a blue continuous line in the Fig. 3b map. Discontinuities represent both fault rupture and landslide head scarps traces and they are drawn over a hillshaded relief from the TINITALY (Triangular Irregular Network of Italy) 10-m-resolution digital elevation model (Tarquini et al., 2007). The Sentinel InSAR outcomes relative to the Amatrice event highlight quite accurately the well field documented displacement of the Mt. Vettore western flank. Here the geological effect of the earthquake is more than 5 km of ground ruptures along the well-known Mt. Vettore normal fault system. The slope gradient map calculated with vertical displacement values shows clearly a discontinuity which starts from Forca di Presta pass, goes up to the side of Mt. Vettoretto and overcomes, for more than one kilometre, the rocky outcrop known as “Scoglio dell’Aquila”. The same ruptures reactivated during the Norcia major event together with a complex surface faulting pattern composed by subparallel and overlapping synthetic and antithetic fault splays. The slope gradient map clearly highlights the continuous NW-SE alignment of ruptures along the Mt. Vettore western flank and partially, in small segments, those in the northernmost sectors. The slope gradient map of the 30th October event looks noisier than the Amatrice one. That is due to the large deformation and to several minor local deformations such as gravity driven ruptures. We can clearly identify the long rupture at the foot of Mt. Vettore, in the great plain, responsible of a road’s break. The displacements along the “Cima del Redentore” Mt. Vettore complex ridge it’s also well identified as well as a sector of the antithetic splay of Monteprata. Other possible ruptures, corresponding with known tectonic features, are also identified. Results match quite well the field data (Fig. 3b). From a methodological perspective, this approach allows to obtain a quickly preliminary map of the possible ground ruptures and relative branch. Moreover, it demonstrates the effectiveness of the C-band Sentinel-1 open data for this purpose. The methodology could allow to detect the cracks evolution during a seismic sequence characterised by many major events. Also, it can be useful as a field guide to speed up the detailed survey, especially in large or remote areas. In this case study, the best identified surface ruptures with Sentinel-1 C-band are those with throws greater than 10 cm. Improved results could be achieved using a high resolution DTM for topographic phase removal and defining good strategies for filtering and classify results.

Acknowledgements: We thank European Space Agency (ESA) for providing Sentinel-1 satellite acquisition under free, full and open data policy adopted for Copernicus programme.

REFERENCES

Chiaraluce, L., Di Sfefano, R., Tinti, E., Scognamiglio, L., Michele, M., Casarotti, E., Cattaneo, M., De Gori, P., Chiarabba, C., Monachesi, G., Lombardi, A., Valoroso, L., Latorre, D., & Marzorati, S., 2017. The 2016 central Italy seismic sequence: a first look at the mainshocks, aftershocks, and source models. *Seismological Research Letters* 88 (3), 757-771.

D'Agostino, N., Mantenuto, S., D'Anastasio, E., Giuliani, R., Mattone, M., Calcaterra, S., Gambino, P., & Bonci, L., 2011. Evidence for localized active extension in the central Apennines (Italy) from global positioning system observations. *Geology* 39 (4), 291-294.

Fujiwara, S., Yarai, H., Kobayashi, T., Morishita, Y., Nakano, T., Miyahara, B., Nakai, H., Miura, Y., Ueshiba, H., Kakiage, Y., & Une, H., 2016. Small-displacement linear surface ruptures of the 2016 Kumamoto earthquake sequence detected by ALOS-2 SAR interferometry. *Earth Planets Space* 68, 160.

Fukushima, Y., Takada, Y., & Hashimoto, M., 2013. Complex ruptures of the 11 April 2011 Mw 6.6 Iwaki earthquake triggered by the 11 March 2011 Mw 9.0 Tohoku earthquake, *Japan. Bull. Seismol. Soc. Am*. 103, 1572-1583.

Guerrieri, L., Baer, G., Hamiel, Y., Amit, R., Blumetti, A.M., Comerci, V., Di Manna, P., Michetti, A.M., Salamon, A., Mushkin, A., Sileo, G., & Vittori, E., 2010. InSAR data as a field guide for mapping minor earthquake surface ruptures: ground displacements along the Paganica Fault during the 6 April 2009 L’Aquila earthquake. *J. Geophys. Res*. 115, B12331.

Lavecchia, G., 1985. Il sovrascorrimento dei Monti Sibillini: analisi cinematica e strutturale. *Boll. Soc. Geol.Italiana* 104, 161-194.

Menichetti, M., Tirincanti, E., Piacentini, D., Roccheggiani, M., & Tamburini, A., 2017. Geometrical and structural controls on rupture zone fabric: field surveys of the 2016 earthquakes in Sibillini mountains (central Italy) - 36° GNGTS proceedings, Trieste 14-16 nov. 2017, 166-167.

Price, E.J., & Sandwell, D.T., 1998. Small-scale deformations associated with the 1992 Landers, California, earthquake mapped by synthetic aperture radar interferometry phase gradients. *J. Geophys. Res*. 103, 27001-27016.

Tarquini, S., Isola, I., Favalli, M., Mazzarini, F., Bisson, M., Pareschi, M. T., & Boschi, E., 2007. Tinitaly/01: A new triangular irregular network of Italy. *Annals of Geophysics* 50, 407-425.

INQUA Focus Group Earthquake Geology and Seismic Hazards

paleoseismicity.org

Late Holocene earthquake record for the northern Earthquake Valley Fault Zone from a new paleoseismic site at Warner Basin

Rockwell, Thomas (1), Akciz, Sinan (2)

(1) Dept. Geological Sciences, San Diego State University, San Diego, CA 92182, USA, trockwell@mail.sdsu.edu
(2) Dept. Geological Sciences, California State University, Fullerton, Fullerton, CA 92831, USA, sakciz@fullerton.edu

Abstract: *Paleoseismic work was conducted along the Earthquake Valley fault zone in Warner Basin, San Diego County, southern California. Warner Basin is filled with middle Quaternary deposits that contain the 790 ka Bishop Tuff; the main axial channel and margins of the basin are offset about 1.9 km, yielding a long-term slip rate of 2.5 mm/yr. We excavated two trenches in Big Lake, a sag pond, exposing the upper 2.5 m of strata that date to the past 2.6 ka. The upper half-meter contained a 1950's vintage shotgun shell, indicating historical sedimentation. We identified three horizons up to which there is evidence of displacement on many of the fault strands. The uppermost event (E1) breaks up to within 20 cm of the historical horizon and may be the ~M6.5 1890 earthquake. The two earlier interpreted events date to about 800 AD and 0 AD, suggesting a recurrence interval of about 900-1000 years.*

Keywords: *Earthquake Valley fault, Slip Rate, Paleoseismology, Warner Basin*

INTRODUCTION

The Agua Tibia - Earthquake Valley fault zone, hereafter referred to as the Earthquake Valley fault, is considered the eastern strand of the Elsinore fault zone in southern California (Magistrale & Rockwell, 1996). The Earthquake Valley fault is sub-parallel to the Elsinore fault, which is simpler and single stranded to the north of Temecula and south of the Tierra Blanca Mountains (Figure 1). The Agua Tibia-Palomar Mountain uplift is interpreted to be a large pressure ridge system that steps part of the north Elsinore

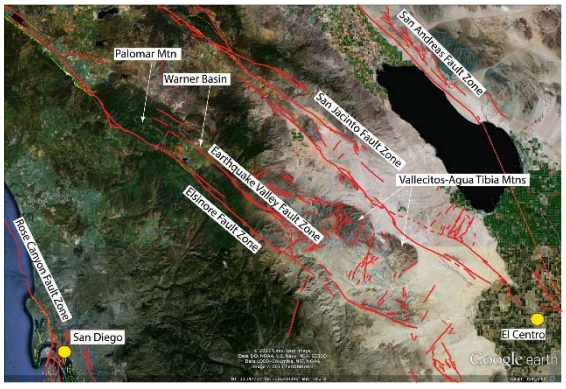

Figure 1: Generalized map of the southern San Andreas fault system in southern California. The Earthquake Valley-Agua Tibia fault is the eastern strand of the Elsinore fault zone.

slip to the southeast onto the Earthquake Valley fault. The Earthquake Valley fault is interpreted to transfer this component of deformation back to the southern San Jacinto fault zone via another restraining step at the Vallecito-Fish Creek Mountains, a topographic bedrock high bounded by deep alluvial fill. In this paper, we describe the offset of Warner Basin and its associated alluvial fill, which we use to estimate the long-term slip rate. We then present our new paleoseismic results on the late Holocene activity of the Earthquake Valley fault at Big Lake in Warner Basin.

Estimation of the Slip Rate at Warner Basin

Warner Basin lies to the southeast of Palomar Mountain (Figure 1) and is more a filled valley than a structural basin. The valley fill deposits are on the order of a few tens of meters in thickness and likely resulted from blockage of the outflow channel, the San Luis Rey River. The age of the valley fill is inferred to be middle Quaternary based on the presence of a tephra that is correlated to the Bishop Tuff (Merriam & Bischoff, 1975). We located an outcrop of the tuff and confirmed its correlation to the Bishop Tuff by ten new zircon ages using Secondary Ionization Mass Spectrometry (SIMS) zircon geochronology (Rockwell et al., 2014).

The valley fill deposits of Warner Basin, along with the axial drainage that bisects these deposits, appears to be offset about 1.9 km in a right-lateral sense (Figure 2). Although the margins of the basin could have exhibited some offset prior to deposition of the valley fill, thereby giving the appearance that the deposits are offset by the full amount, we consider it unlikely that the axial drainage that incises the deposits would show the same amount of deflection unless the 1.9 km of apparent offset represents the actual displacement of the fill. Thus, we interpret the 1.9 km right deflection of the valley fill margins and axial drainage to represent displacement after deposition of the alluvial fill.

Slip Rate

We calculate the long-term slip by taking the inferred offset of 1.9 km and dividing by the 790±26 ka age we determined for the Bishop Tuff in Warner Basin. Using the minimum and maximum age constraints and a ~10% uncertainty for

displacement (1.9±0.2 km) yields a rate of $2.53^{+0.22}/_{-0.45}$ mm/yr, which we round to $2.5^{+0.3}/_{-0.5}$ mm/yr. This rate is a minimum because the tephra is older than the capping surface into which the axial channel is incised, but the age difference is probably well within the stated uncertainties, so we take this as a fair representation of the long-term rate for the Earthquake Valley fault in Warner Basin.

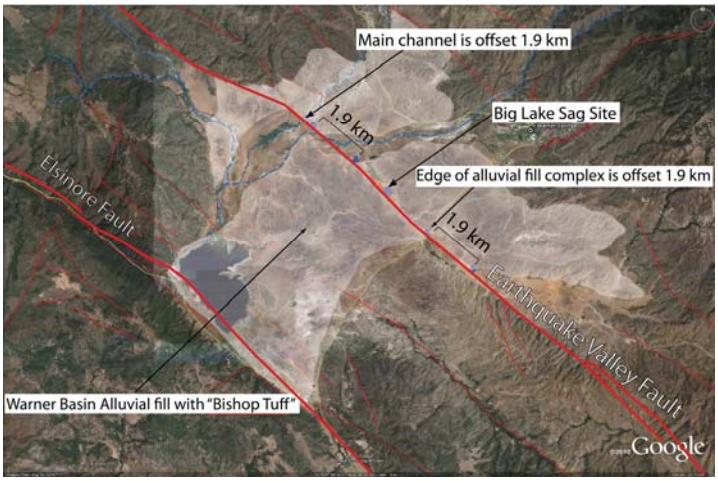

Figure 2: Map of middle Quaternary alluvial deposits in the Warner Basin that contain the Bishop Tuff (780 ka). Note that the SE margin of these basin deposits is offset 1.9 km, as is the major drainage system that flows through the basin deposits. This yields a long-term lateral slip rate of about 2.5 mm/yr.

Paleoseismology at Big Lake

We excavated two parallel trenches across the tonal lineament at Big Lake with the intent of studying the timing of past surface ruptures along the Earthquake Valley fault in Warner Basin. The site was chosen because initial 1 m-deep auger borings indicated the presence of a shallow peat-like horizon, and because the stratigraphy in the upper meter looked promising. The stratigraphy at depth turned out to be less well-stratified than the upper meter, but was sufficient to identify faulted strata and evidence for past surface ruptures. Due to relatively high groundwater, we concentrated our efforts on the trench with the best stratigraphy and clearest faulting relationships, which we designate as trench T-1.

The fault through Big Lake is generally expressed as a broad zone of shattering, with many minor fault strands. A major fault was encountered at about 2 m depth, and apparently was activated during an earlier event, as discussed below, but not in the most recent event. The recent events are represented by numerous small faults that rupture up to two discrete horizons that we interpret as the surface at the time of the rupture. The evidence for each interpreted rupture is described in detail below, after a description of the stratigraphy. We should note that there are also numerous very minor cracks throughout the section that do not appear to have any coherence in terms of event horizons or common rupture levels. These may be do to ground shatter, water withdrawal, or possibly fault creep, although we do not see any other evidence for creep.

Site Stratigraphy - We recognize more than 20 discrete and traceable units in the upper 2.5 m of section at Big Lake. Units 20 and 50 are clayey silt strata that are distinguished by their color and structure. Unit 20 contained a shotgun shell, indicating that it is historical in age and, based on the character of the shotgun shell, likely was deposited in the 1950's. Unit 90 is a dark gray silt horizon that we interpret as a weakly-form A or topsoil horizon based on its color and the presence of abundant fossil rootlets. Unit 100 is an oxidized silt layer with 1-3 mm-sized silt fragments or rip-ups that overlies a 1 cm-thick organic unit that caps unit 110. Units 130 down to 410 are moderately well stratified and laterally continuous and dominated by silt, with some units exhibiting more sand and some with more clay. Altogether, the stratigraphy is reasonably well defined in both walls, and several of the units were distinct enough to allow certain correlation of units from one wall to the other.

Age of Units - We found abundant detrital charcoal fragments distributed throughout the section such that there is some age control on most units and altogether, we submitted 32 for dating, 18 of which yielded dates. Nearly half of the samples did not survive the acid-base-acid pre-treatment. Of the samples that yielded ages, 14 samples were found to be in stratigraphic order from which we constructed the age model shown in Figure 3. The dates indicate that the entire upper 2.5 m of Big Lake strata were deposited in the past 2600 years, yielding an average sedimentation rate of about a meter per thousand years.

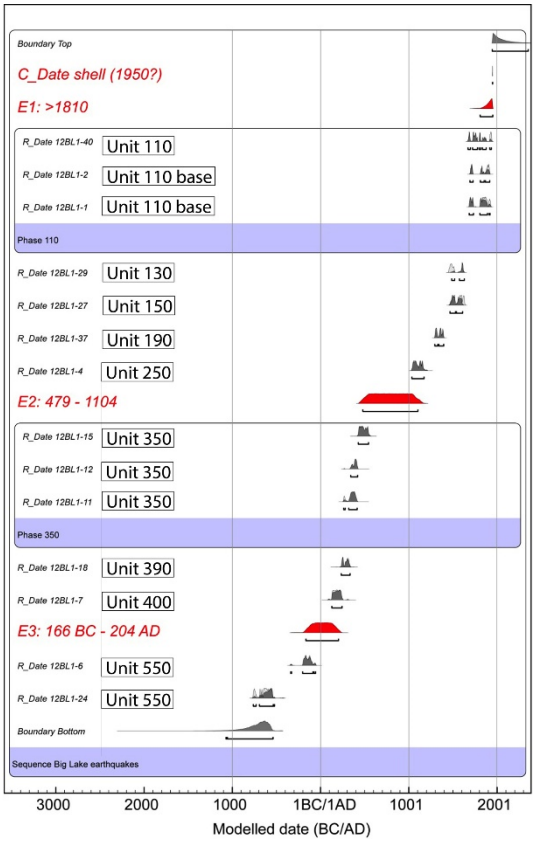

Figure 3: Chronologic model for the sediment history at Big Lake. All radiocarbon dates that do not violate the stratigraphic ordering are shown, as are the ages of the interpreted surface ruptures (in red).

There are two apparent hiatuses or periods of slow deposition, one between units 150 and 190 of about 300 years in length, and one between units 250 and 350 of about 800 years in length. The upper one occurred during the period of accumulation of secondary carbonate in unit 170, and we interpret this to be a generally dry period with little or no sediment deposition during which the secondary carbonate was able to accumulate. The lower hiatus contains unit 300, which we have interpreted as a well-formed buried A or topsoil horizon. It is likely that much of the period of non-deposition is represented by this soil. Periods of non-deposition are potentially significant in that multiple surface ruptures may have occurred for which there is little or no evidence.

Interpreted Surface Ruptures - We have interpreted the occurrence of three surface ruptures at Big Lake over the past 2600 years or so, as recorded in the stratigraphy. The fault zone is distributed, with numerous minor faults breaking the bedded strata. For all three interpreted events, we observed a large number of small faults breaking to a particular level, and then capped by overlying strata. In some cases, faults are observed to break to a level and have an associated filled fissure, which may be rebroken from a subsequent event. For the penultimate event, a scarp formed on a more significant fault strand and was subsequently buried by unbroken strata. The distributed nature of faulting is consistent with Big Lake being a releasing step-over.

Event E1 - Event E1 is represented by many small offsets that break up through unit 90 and are capped by unit 50 (Figure 6). Unit 90 is seen to warp down into fault strands at many locations, and there are filled fissures that we interpret were open cracks resulting from the rupture. Maximum vertical separation on individual faults is on the order of a few centimeters, and there is no significant change in thickness of the overlying unit 50, which suggests that total vertical separation across the entire fault zone is minor or absent.

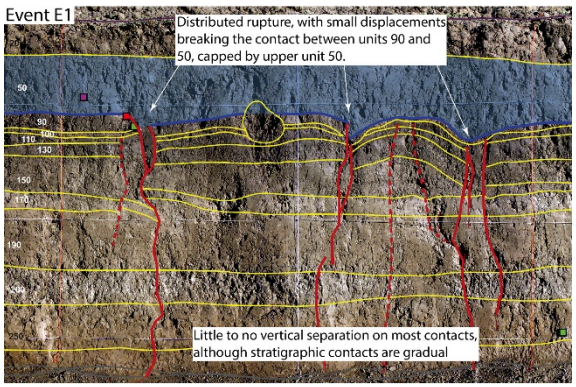

Figure 4: A portion of the NW wall of trench T1 at Big Lake. Many small faults are observed to break up to the top of unit 90 and appear capped by unit 50. Further, there appear to be filled fissures associated with many of these faults that are also capped by unit 50. Based on these observations, the most recent surface rupture is interpreted to have occurred when Unit 90 was at the surface.

The age of event E1 is constrained to be younger than 1810 AD, based on radiocarbon dating (Figure 3). The shotgun shell recovered from the base of unit 20 indicates that deposition has continued into the historical period. These observations suggest that event E1 may be historical in age, and possibly the poorly-recorded ~M6.3-6.5 9 February 1890 or 28 May, 1892 earthquake (Toppozada et al., 1981). If correct, scaling relations (Wells & Coppersmith, 1994) suggest only a few tens of cms of displacement, consistent with distributed cracking at Big Lake.

Event E2 - Rupture interpreted for event E2 is again observed to be distributed across a broad zone, but in this case, there was significant rupture on one of the fault strands, resulting in both significant vertical displacement as well as a mismatch in unit thickness, an indication of significant strike-slip (Figure 5). The rupture breaks up through unit 300 and is capped by unit 280. Unit 300 is interpreted as a buried A horizon and may represent several hundred years of non-deposition. Furthermore, the current age constraints are on units 350 and 250, so the strata that capture the event horizon are not directly dated. Thus, the resulting age constraints on event E2 are poorly constrained to between AD 479 and 1104.

Event E3 - Event E3 is represented by numerous small faults with associated filled fissures that break up through unit 420

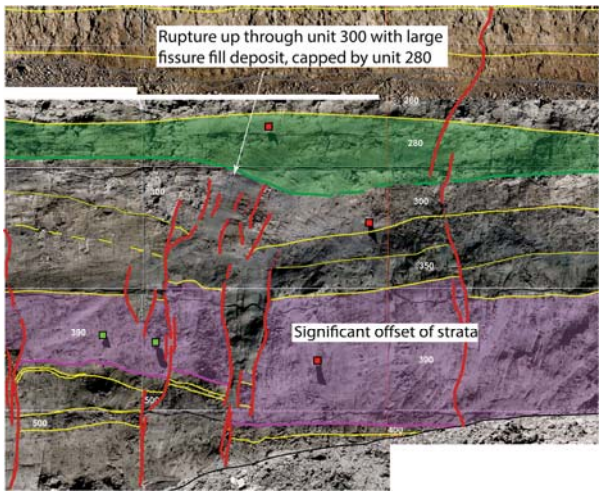

Figure 5: Interpretation of event E2 is based on many faults that disrupt up through unit 300, which we interpret as a buried A horizon, with unit 280 capping the fault. In this figure, units below 300 have significant vertical separations and changes in unit thickness, suggesting significant strike slip occurred in this event. Unit 300 appears fissured down into unit 390, and there is a buried scarp at the top of unit 300, which is buried by unit 280.

and are capped by unit 390, and locally unit 400 (Figure 6). Many of these faults exhibit significant vertical separations of strata below unit 390, whereas unit 390 is either unfaulted by these strands, or if rebroken by a later event, commonly exhibits little or no vertical separation. There is an overall down-to-the-northeast sense of vertical displacement for all units below unit 390, with some lower strata dropping below the base of the trench on the northeast side.

The timing of event E3 is moderately well constrained to between BC 166 and AD 204, placing it close to 0 AD. However, two dates are on units 390 and 400, closely post-dating the event, whereas the highest dated stratum below the event horizon is derived from unit 550. Hence, it is likely that the actual age of event E3 lies towards the younger part of the plausible age range.

DISCUSSION

We have determined a long-term, mid-Quaternary to present slip rate of about 2.5 mm/yr for the Earthquake Valley fault in Warner Basin. This value is about half of the estimated slip rate along the northern Elsinore fault in the Temecula - Murrieta region (Rockwell et al., 2000), and is similar to the inferred slip rate for the central Elsinore fault southeast of Julian (Magistrale & Rockwell, 1996). These observations indicate that south of the Agua Tibia-Palomar Mountain uplift, the slip rate is evenly divided between the Elsinore and Earthquake Valley faults. As the Earthquake Valley fault appears to transfer its slip southeastward to the San Jacinto fault via a restraining step at the Vallecitos-Fish Creek Mountain uplift, this may explain why Fialko (2006) attributed nearly 20 mm/yr to the southern San Jacinto fault, a rate that is similar to that attributed to the southern San Andreas fault. In our model, about 2.5 mm/yr of the Elsinore slip rate is added to the ~14 mm/yr documented for the central San Jacinto fault (Blisniuk et al., 2013), with likely some additional rate distributed among the northeast-striking left-lateral cross faults. This implies that the San Jacinto fault remains subordinate to the southern San Andreas fault in terms of slip on discrete faults.

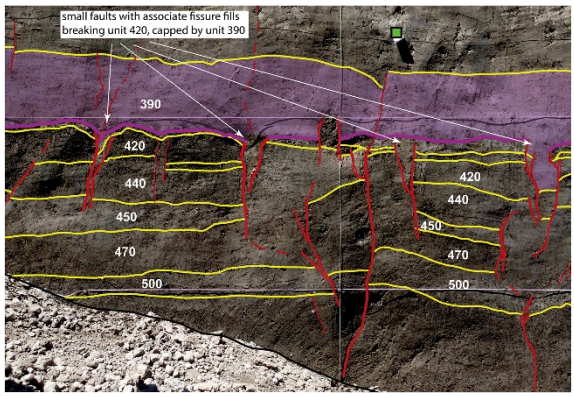

Figure 6: Event E3 is indicated by numerous fault strands that break up through units 420 and are capped by units 390 and 400. Strata below unit 420 show locally significant vertical separations and tilting.

The recurrence interval that we have determined for the Earthquake Valley fault at Big Lake is on the order of about 800-1000 years. This is based on the occurrence of an event at about 0 AD, one at about 800 AD (between 479 and 1104 AD), and one in the past two hundred years. The penultimate two events appear to have produced significantly more vertical separation than the MRE (1890?) so the earlier events may have been larger, although with strike-slip faults, this type of inference can be wrong. For an estimate of average displacement, we assume that each event was similar in size and we also assume that three events are sufficient to accurately represent the average recurrence interval. This last assumption is commonly wrong, as long paleoseismic records almost always show some periods of increased or decreased seismic activity (Rockwell et al., 2014). Nevertheless, if the average recurrence interval is about 900 years, a 2.5 mm/yr slip rate suggests that displacement per event should be on the order of 2.2 m. This value is larger than likely occurred in the 1890 earthquake, which probably had only a few 10's of cms based on the estimated size of the earthquake from very limited damage reports. This argues that the MRE was likely smaller than the prior two events. Further investigations are needed to confirm if the last three earthquakes that ruptured the Earthquake Valley fault were all similar in magnitude and slip distribution or if the MRE was considerably smaller compared to the previous events.

CONCLUSIONS

The Earthquake Valley fault has a slip rate of $2.5^{+0.3}/_{-0.5}$ mm/yr, as determined by 1.9 km offset of the Warner Basin alluvial fill deposits which contain the ~790 ka Bishop Tuff. The fault has produced three surface ruptures in the past 2 ka at Big Lake, with the MRE possibly the 1890 or 1892 earthquake reported for this region by Toppozada et al. (1981), suggesting a recurrence interval in the range of 800-1000 years. Even though the Earthquake Valley Fault lies along the northern continuation of the recent El mayor-Cucapah earthquake surface rupture and was possibly "loaded" by it, our paleoseismic findings suggest that Earthquake Valley Fault is not likely to produce another large earthquake in the near future as it had recently ruptured and released its ~900 year long stress build up prior to the El Mayor-Cucapah quake.

Acknowledgements: We thank Vista Irrigation District for access to the Big Lake trench site, and Eric Gordon for field assistance. This work was funded by USGS Award No. G12AP20070.

REFERENCES

Blisnuik, K., Oskin, M., Mériaux, A-S., Rockwell, T., Finkel, R., & Ryerson, F.J., 2013. Stable, Rapid Rate of Slip Since Inception of the San Jacinto Fault, California. *Geophys. Res. Lttrs*. 40, 4209-4213.

Fialko, Y., 2006. Interseismic strain accumulation and the earthquake potential on the southern San Andreas fault system. *Nature* 441, 968-971.

Fletcher, K.E.K., Rockwell, T.K., & Sharp, W.D., 2011. Late Quaternary slip rate of the southern Elsinore fault, southern California: Dating offset landforms via 230TH/U on pedogenic carbonate. *Journal of Geophysical Research* 116, F02006, doi: 10.1029/2010JF001701.

Magistrale, H., & Rockwell, T., 1996. The central and southern Elsinore fault zone, southern California. *Bulletin of Seismological Society of America* 86, 1793-1803.

Merriam, R., & Bischoff, J.L., 1975. Bishop ash - A widespread volcanic ash extended to southern California. *Journal of Sedimentary Petrology* 45 (1), 207-211.

Rockwell, T., Bergmann, M., & Kenney, M., 2000. Holocene slip rate of the Elsinore fault in Temecula Valley, Riverside County, California. In: *Geology and Enology of the Temecula Valley* (Birnbaum, B., Cato, K., eds), 105-118.

Rockwell, T.K., Akciz, S., & Schmitt, A.K., 2014. Development of a Holocene earthquake record for the northern Agua Tibia-Earthquake Valley fault zone from a new paleoseismic site in Warner Basin. Final Technical Report, US Geological Survey Award No. G12AP20070, 20 pp.

Rockwell, T.K., Dawson, T.E., Young-Ben Horton, J., & Seitz, G., 2015. A 21 event, 4,000-year history of surface ruptures in the Anza Seismic Gap, San Jacinto Fault and implications for long-term earthquake production on a major plate boundary fault. *Pure and Applied Geophysics* 172 (5), 1143-1165, doi: 10.1007/ s00024-014-0955-z.

Toppazada, T., Real, C., & Parke, D., 1981. Preparation of isoseismal maps and summaries of reported effects for pre-1900 California earthquakes. California Division of Mines and Geology Open-File Rept. 81-11 SAC, 182 pp.

Wells, D., Coppersmith, K., 1994. New empirical relationships among magnitude, rupture length, rupture width, rupture area, and surface displacement. *Bull. Seismo. Soc. Am*. 84 (4), 974-1002.

INQUA Focus Group Earthquake Geology and Seismic Hazards

paleoseismicity.org

Deformation and kinematics at the termination of the North Anatolian Fault: the North Aegean Trough horsetail structure

Sakellariou, Dimitris (1), Rousakis, Grigoris (1), Morfis, Ioannis (1), Panagiotopoulos, Ioannis (1), Ioakim, Chrysanthi (2), Trikalinou, Georgia (3), Tsampouraki-Kraounaki, Konstantina (1), Kranis, Haralambos (3), Karageorgis, Aristomenis (1)

(1) Hellenic Centre for Marine Research, 46.7 km Athens-Sounio Ave, 19013 Anavysos, Greece, sakell@hcmr.gr, rousakis@hcmr.gr, gianmor@hcmr.gr, jpanagiot@hcmr.gr, tsampourakik@hcmr.gr, ak@hcmr.gr
(2) Institute of Geology and Mineral Exploration, 1st Spirou Louis St., Olympic Village, 13677, Acharnae, Greece, ioakim@igme.gr
(3) Faculty of Geology and Geoenvironment, National & Kapodistrian University of Athens, Zografou, 15784 Athens, Greece, gtrikalinou@geol.uoa.gr, hkranis@geol.uoa.gr

Abstract: *Swath bathymetry and seismic profiling data show that the current phase of the evolution of the western North Aegean Trough, Greece, reflects the development of a horsetail structure at the western termination of the North Anatolian Fault. The onset of the deformation in the NAT occurred probably in Late Pliocene or Early Pleistocene. Transtensional and transpressional deformation dominates in the western NAT and is accommodated by numerous, curved splay faults that branch from the main NAF zone. The prevailing deformation within the trough indicates simple shear dominated transtension in oblique rifting regime. The western North Aegean Trough (west of Lemnos Island) constitutes a complicated oblique-rifting/shear-zone system with the angle of obliquity decreasing from west to east while the rate of horizontal shearing increases.*

Keywords*: Strike-slip, transtension, transpression, oblique rifting*

INTRODUCTION

When large strike-slip faults die out along their lengths they may terminate either in a zone of plastic strain or, in brittle terminations and their displacement is distributed through several branching splay faults. The splay faults curve away from the main fault and form an open, imbricate fan called a horsetail structure. They display a vertical component consistent with the extensional or compressional character of the fault termination. Large-scale, extensional horsetails may host sedimentary basins (Biddle & Christie Blick, 1985; Cunningham & Mann, 2007; Mann, 2007). The architecture and fault kinematics within the horsetail structures can be very complex (Cunningham & Mann, 2007; Mann, 2007).

The North Aegean Trough (NAT) has developed at the termination of the dextral strike-slip North Anatolian Fault (NAF) in the Aegean Sea. The westernmost segments of the NAF have been correlated with the N40°E trending, steep faulted escarpment along the southern margin of the western NAT by Lyberis (1984), Mascle & Martin (1990) and Roussos & Lyssimachou (1991). The NAF marks the boundary of the deforming "Aegean microplate" to the stable Eurasia continent (Dewey & Sengör, 1979; Lyberis et al., 1984; McKenzie & Jackson, 1986; Mascle & Martin, 1990; Taymaz et al., 1991; Armijo et al., 1999). The NAT encompasses two distinct morphological parts: the western NAT trends N40°E and consists of a series of variably shaped depressions, separated by structural highs and shallower ridges; and the eastern NAT that is a N70°E trending, elongate basin. The western NAT initiated under NE-SW extension in the Oligocene and N-S extension in the Pleistocene (Brun & Sokoutis, 2007). Mascle & Martin (1990) suggested NW-SE extension in the Miocene and NE-SW transtension in the Plio-Quaternary. Thus, the propagation of the NAF into the western NAT in Early Pliocene (Armijo et al., 1996, 1999) or Pleistocene (Brun et al., 2016) is superimposed on a pre-existing basin with up to 6 km thick sediments deposited below the Thermaikos-Sporadhes basin since Middle Miocene.

NE-SW marginal and E-W intra-basin strike slip faults and NW-SE normal faults accommodate the opening of the western NAT under NE-SW extension (Papanikolaou et al., 2002, 2006). The N40°E trending, western NAF fault zone consists of many fault segments while the numerous, curved faults and fault splays branching away from the NAF delineate the horsetail structure developed at its western termination (Sakellariou et al., 2016).

GPS data allowed a quantification of the spatial change of strike-slip motion along the NAT (Müller et al., 2013). Dextral strike-slip motion diminishes from east toward west from 21.2 mm/yr along the eastern NAT to 12.5 mm/yr south of the Chalkidiki peninsula and less than 5 mm/yr at the western termination of the NAF.

MATERIALS AND METHODS

Swath bathymetry data were collected in 2000 (Papanikolaou et al., 2002), 2013, 2014 and 2015 (Sakellariou et al., 2016) with a 20 kHz SeaBeam 2120 (L3 ELAC Nautic), system and were processed at 25m grid. Airgun 5, 10 and 40 ci seismic profiles were shot in 2013, 2014 and 2015 (Sakellariou et al., 2016) (Fig. 1A).

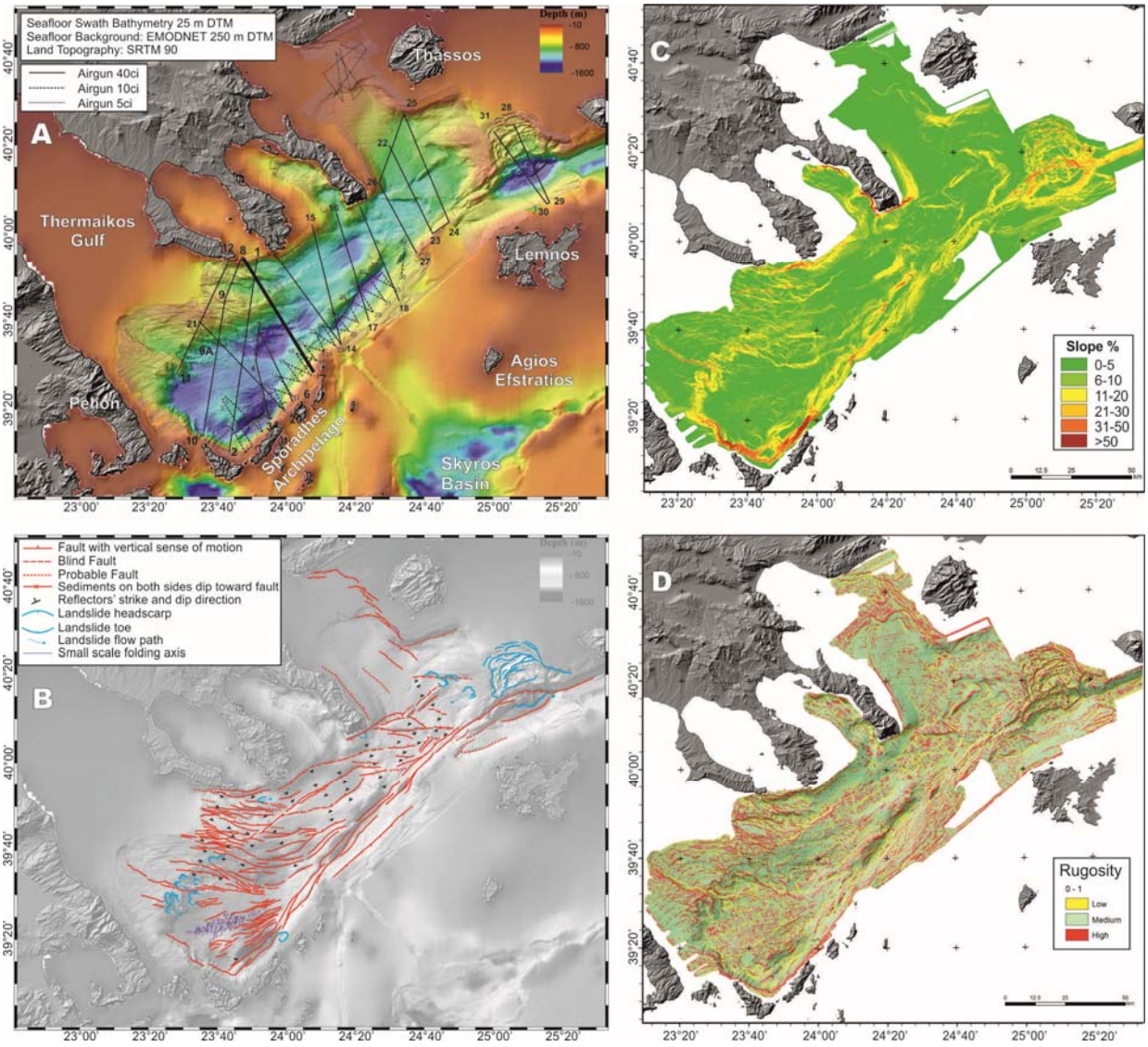

Figure 88: A: Swath bathymetry of the North Aegean Trough and location of the seismic profiles. B: Map of faults, landslides, folds in the NAT. C: Slope Map. D: Rugosity map.

RESULTS

The morphological analysis of the 25 m DTM of the seafloor of the western NAT revealed the detailed characteristics of its relief. The slope map (Fig. 1C) and the rugosity (Fig. 1D) reflect largely the effect of the tectonic, slope stability and sedimentary processes acting below and on the seafloor. The spatial distribution of the steep slopes highlights the following structural elements: (i) the southern composite margin developed along the trace of the NAF; (ii) the steep slopes along the western and northern faulted margins of the NAT; (iii) the spindle shaped Lemnos Deep and the complex amphitheatric slope north of it, which indicate composite slope failure at the junction between the N40^{o}E and the N70^{o}E striking segments of the NAF; (iv) irregularly curved steep, listric slopes indicating multiple slope failures along the southern edge of the Thermaikos Gulf; (v) the numerous, curved, anastomosing morphological scarps that traverse the NAT and imbricate towards W and NW.

The rugosity of the seafloor highlights features that may not be depicted by the slope map. The Sporadhes Basin, north of Skopelos and Alonissos Islands, displays low sloping values (0-5%, Fig. 1C) but is characterized by stripes of high rugosity. The fairly steeply dipping slope east of Athos Peninsula displays rather low (to medium) rugosity indicating thus that sediment deposition processes prevail over instability or tectonic movements.

The processing and interpretation of the seismic profiles revealed a complicated fault network and structure along the NAF and within the NAT. The NAF, which runs along the southern margin of the Trough, consists of many, parallel to subparallel, sinuous and overlapping segments that create multiple restraining (uplifted ridges) and releasing (depressions) bends. The Lemnos Deep is a spindle shaped releasing bend (basin) developed at the bending point between the eastern (N70^{o}E) and western (N40^{o}E) sectors of the NAF. Within the Trough, the numerous seafloor scarps coincide with high-angle, predominantly strike-slip fault splays, which largely initiate from the main NAF zone and curve towards west and northwest (Fig. 2 and 3A). The morphological highs within the NAF represent anticline hinges, fault-uplifted monoclines and pop-up structures. They alternate along and across strike with local depressions and basins. Both, ridges and depressions, develop as tranpressional and transtensional features respectively, with regard to the local fault kinematics (Fig. 2 & 3A).

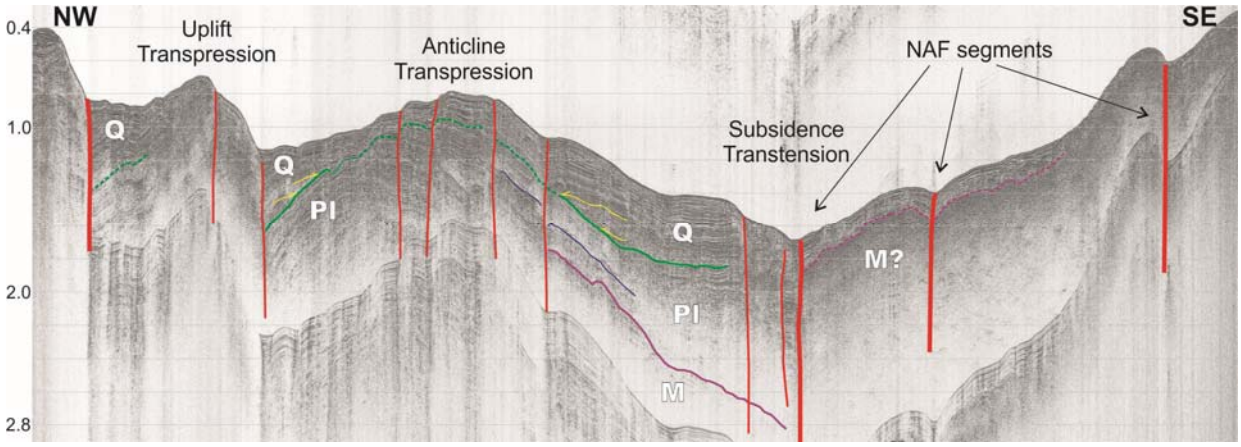

Figure 2: Airgun 40 ci seismic profile across the western NAT. Q: Quaternary. Pl: Pliocene. M: Messinian. See Fig. 1A for location. Note the three segments of the NAF, the anticline, the uplifted monocline and the high-angle, predominantly strike-slip faults within the NAT.

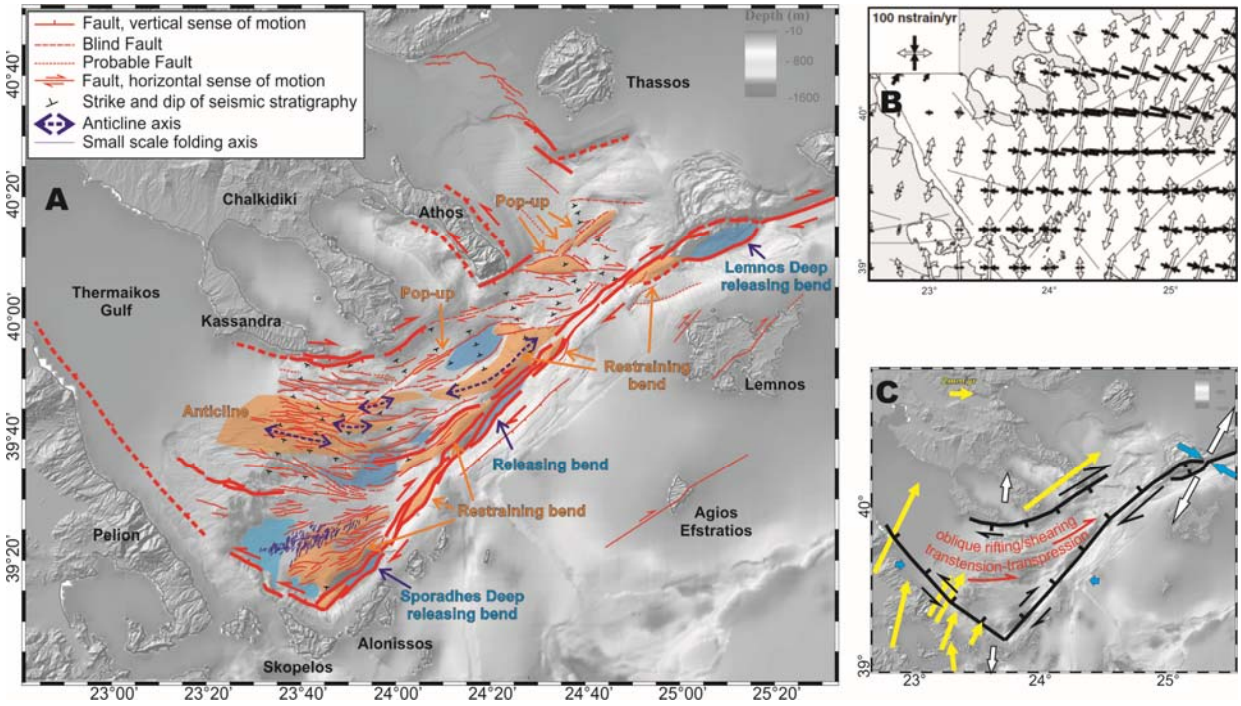

Figure 3: A: Structural map of the termination of the NAF in the western North Aegean Trough. Orange color indicate pressure ridges (pop ups, restraining bends). Blue color marks transtensional depressions and releasing bends. Faults on Lemnos and Agios Efstratios drawn after Chatzipetros et al. (2013). B: Principal strain rates after Mueller et al. (2013). C: Horizontal velocity field (yellow arrows) relative to the southern margin (Skopelos, Alonissos, Lemnos Islands) of the NAT (modified from Mueller et al., 2013). Blue and white arrows show compression and extension directions (extracted from 2B).

DEFORMATION AND KINEMATICS IN THE NAT

The structural map of the NAT (Fig. 3A) shows a characteristic horsetail structure with the deformation at the termination of the NAF accommodated by splay faults that curve away from the main fault and form an open, imbricate fan towards the Thermaikos Gulf. The splay faults in a horsetail structure display vertical component that is consistent with the extensional or compressional character of the fault termination (Biddle & Christie Blick, 1985; Cunningham & Mann, 2007; Mann, 2007).

The NAT horsetail has developed on the northern side of the western termination of the dextral NAF and therefore has to display extensional character. Indeed, the principal strain rates derived from GPS velocities show fast extension in NNE-SSW direction and WNW-ESE directed subordinate compression across the western NAT (Fig. 3B, Müller et al., 2013). The horizontal velocity field relative to the southern margin of the Trough (Skopelos, Alonissos, Lemnos Islands) shows Chalkidiki peninsula moving towards NE, slightly converging with the latter and drifting away from the south-western (Pelion) margin.

Within the NAT, the sense of movement may change along the splay faults. Pure strike-slip movements prevail along the splays which trend parallel or at low angle to the trace of the main fault zone. The vertical component increases away from the main fault as the angle between the latter and the splays increases. However, the vertical sense of movement may switch along the individual splays indicating significant horizontal movement.

Transtensional and transpressional features have formed within the NAT and are related with the kinematic character and the relative position in plan view of the individual splay faults. The transpressional features include (i) pop-up structures squeezed upwards between vertical faults and (ii) anticlines, the hinges of which follow the trend of the splay faults. The seismic profiles across the anticlines provide indirect evidence for the timing of the initiation of the deformation and consequently for the time of the propagation of the NAF. The profile on Fig. 2 shows that the Miocene and Pliocene sediments have been anticlinally folded while the observed unconformities on the flanks indicate folding and updoming evolved synchronously to the deposition of the Quaternary strata. This observation indicates that the deformation associated with the propagation of the NAF may have started in Late Pliocene - Early Quaternary rather than in Early Pliocene.

The hinges of the anticlines in the western part of the NAT, south of Kassandra peninsula, trend roughly in E-W (Fig. 3A). This is in marked contrast to and cannot be explained by the NNE-SSW directed extension derived from the GPS velocities (Fig. 3B). However, the relative movements of the northern, southwestern and southeastern margins of the Trough, as shown on the horizontal velocity field of Fig. 3C, indicate that the NAT undergoes oblique rifting with the obliquity of the rifting with the respect to its margins decreasing from west to east. Extensive shearing along the splay faults accommodates and complements the changing obliquity of the rifting along strike. In this complicated transtensional regime the formation of the anticlines and other compressional features can be explained in terms of simple shear deformation. Strain modeling shows that folds can form in transtension, particularly in simple shear-dominated transtension in oblique continental rifting (Fossen et al., 2013). While folds generated during transpression rotate toward parallelism with the shear zone boundary, transtensional folds rotate toward the direction of rifting between the margins of the rift. This seems to be the case in the NAT as well (Fig. 3A).

CONCLUSIONS

The current phase of the evolution of the western North Aegean Trough represents the development of a horsetail structure developed at the termination of the North Anatolian Fault. Seismic data indicate that the onset of the deformation in the NAT may have taken place in Late Pliocene or Early Pleistocene, considerably later than the proposed (Armijo et al., 1996, 1999) Early Pliocene propagation of the NAF in the Aegean Sea.

Transtensional and transpressional deformation dominates in the western NAT and is accommodated by numerous, curved splay faults that branch from the main NAF zone. The latter consists of multiple, overlapping segments, which strike N40^{o}E along the southeastern margin of the NAT and form restraining (ridges) and releasing (depressions) bends.

Although GPS derived principal strain rates show fast extension in NNE-SSW direction across the NAT, the prevailing transtensional and tranpressional deformation within the trough indicates simple shear dominated transtension in oblique rifting regime. The western North Aegean Trough (west of Lemnos Island) constitutes a complicated oblique-rifting/shear-zone system with the angle of obliquity decreasing from west to east while the rate of horizontal shearing increases.

Acknowledgements: This work builds on the results of the nationally funded "YPOTHER / Aegean Exploration" project that was implemented by the Institute of Geology and Mining Exploration (IGME) and the Hellenic Centre for Marine Research (HCMR).

REFERENCES

Armijo, R., Meyer, B., King, G. C. P., Rigo, A., & Papanastassiou, D., 1996. Quaternary evolution of the Corinth rift and its implications for the Late Cenozoic evolution of the Aegean. *Geophysical Journal International* 126, 11-53.

Armijo, R., Meyer, B., Hubert, A., & Barka, A., 1999. Westward propagation of the north Anatolian into the northern Aegean: timing and kinematics. *Geology* 27 (3), 267-270.

Biddle, K.T., & Christie-Blick, N., 1985. Strike-Slip Deformation, Basin Formation, and Sedimentation. SEPM Sp. Publ. 37, 386 pp.

Brun, J.-P., & Sokoutis, D., 2007. Kinematics of the southern Rhodope core complex. *Int. J. Earth Sci*. 96, 1079-1099.

Chatzipetros, A., Kiratzi, A., Sboras, S., Zouros, N., & Pavlides, S., 2013. Active faulting in the north-eastern Aegean Sea Islands. *Tectonophysics* 597-598, 106-122.

Cunningham, W.D., & Mann, P., 2007. Tectonics of strike-slip restraining and releasing bends. In: *Tectonics of Strike-Slip Restraining and Releasing Bends* (Cunningham, W.D., Mann, P., eds). Geological Society, London, Special Publications, 290, 1-12.

Dewey, J.F., & Şengör, A.M.C., 1979. Aegean and surrounding regions: Complex multiplate and continuum tectonics in a convergent zone. *Geological Society of America Bulletin* 90, 84-92.

Fossen, H., Teyssier, C., & Whitney, D.L., 2013. Transtensional folding. *Journal of Structural Geology* 56, 89-102.

Lyberis, N., 1984. Tectonic evolution of the North Aegean Trough. In: *The Geological Evolution of the Eastern Mediterranean*. *Spec. Publ. Geol. Soc*. 17, 709-725.

Mann, P., 2007. Global catalogue, classification and tectonic origins of restraining- and releasing bends on active and ancient strike-slip fault systems. In: *Tectonics of Strike-Slip Restraining and Releasing Bends* (Cunningham, W.D., Mann, P., eds). Geological Society, London, Special Publications, 290, 13-142.

Mascle, J., & Martin, L., 1990. Shallow structure and recent evolution of the Aegean Sea: A synthesis based on continuous reflection profiles. *Marine Geology* 94, 271-299.

McKenzie, D., & Jackson, J., 1986. A block model of distributed deformation by faulting. *J. Geol. Soc. London* 143, 349-353.

Müller, M.D., Geiger, A., Kahle, H.-G., Veis, G., Billiris, H., Paradissis, D., & Felekis, S., 2013. Velocity and deformation fields in the North Aegean domain, Greece, and implications for fault kinematics, derived from GPS data 1993-2009. *Tectonophysics* 597-598, 34-49.

Papanikolaou, D., Alexandri, M., Nomikou, P., & Ballas, D., 2002. Morphotectonic structure of the western part of the North Aegean Basin based on swath bathymetry. *Marine Geology*, 190, 465-492.

Papanikolaou, D., Alexandri, M., & Nomikou, P., 2006. Active faulting in the north Aegean basin. *Geol. Soc. America, Sp. Paper* 409, 189-209.

Sakellariou, D., Rousakis, G., Vougioukalakis, G., Ioakim, Ch., Panagiotopoulos, I., Morfis, I., Zimianitis, E., Athanasoulis, K., Tsampouraki-Kraounaki, K., Mpardis, D., & Karageorgis, A.P., 2016. Deformation pattern in the western North Aegean trough: preliminary results. *Bulletin of the Geological Society of Greece* L/1, 134-143.

Taymaz, T., Jackson, J., & McKenzie, D., 1991. Active tectonics of the north and central Aegean Sea. *Geophys. J. Int*. 106, 433-490.

INQUA Focus Group Earthquake Geology and Seismic Hazards

paleoseismicity.org

Active faulting and kinematics in the Aegean

Sakellariou, Dimitris (1), Tsampouraki-Kraounaki, Konstantina (1)

(1) Hellenic Centre for Marine Research, 46.7 km Athens-Sounio Ave, 19013 Anavysos, Greece, sakell@hcmr.gr, tsampourakik@hcmr.gr

Abstract: *The detailed review and re-evaluation of the marine geological, geophysical, seismological and geodetic data enabled the systematic mapping of the Plio-Quaternary sedimentary basins and the active offshore faults and led to re-interpretation of the deformation of the Aegean microplate since the Early Pliocene. Back-arc extension is accommodated by extensive shearing along strike-slip zones. The Aegean crust "flows" toward SSW, confined between its northern (North Anatolian and Kephallinia Faults) and southern boundaries (East Hellenic Trench. Dextral shearing along major NE-SW strike-slip zones associated with conjugate NW-SE sinistral and WNW-ESE normal faults dominates over most of the Aegean Region and creates a complex pattern of localized transtensional features and the formation of new basins, along with local transpressional deformation and local uplift. Sinistral NE-SW to ENE-WSW trending shearing prevails in the southeastern Aegean, parallel to the sinistral shear zones of the Pliny and Strabo Trenches.*

Keywords*: Aegean Sea, strike-slip faults, oblique faults, transtension, transpression*

INTRODUCTION

Post-Miocene extension in the Aegean is related to the subduction of the African lithosphere beneath the Aegean, which initiated already in the Eocene (Jolivet et al., 2013; Brun et al., 2016 and references therein) and its interaction with the westward motion of Anatolia along the North Anatolian Fault since Late (?) Miocene to Pliocene (Armijo et al., 1996, 1999; Reilinger et al., 2010 and references therein). Since the seventies numerous surveys were conducted with the aim of defining the major tectonic elements and their kinematic setting in the Aegean Region (Fig. 1). The majority of them focused on seismological and broad scale geological data and GPS campaigns. The progress in studying the seismological and kinematic pattern was much faster than the systematic mapping and detailed study of the offshore geological structure. Compared to the structural complexity of the Aegean, very few systematic marine geological surveys were conducted (e.g. Mascle & Martin, 1990). Recent advances in offshore mapping and thorough analysis and comparison of the proposed kinematic models with the observed geological structures do reveal inconsistencies between them.

The aim of this paper is to present recent progress in swath bathymetry coverage and seismic profiling data, review and reevaluate older data on the geological structure, active tectonics and the seismological regime in the Aegean, to compare them and finally to discuss the different kinematic models proposed so far. New evidence is provided showing that, along with the northern and southern strike-slip boundaries, strike-slip faulting and transtensional/transpressional deformation within the deforming Aegean has played a significant role in its geodynamic evolution during the Plio-Quaternary.

OVERVIEW OF LITERATURE DATA

The first systematic effort to create a comprehensive map of the offshore faulting and the geologic structure of the entire Aegean Sea (Mascle & Martin, 1990) proposed that the Aegean Sea has been progressively affected by NE-SW trending strike-slip zones after the Miocene. It can be considered as a stretching continental domain cut into several NE-SW trending, elongated crustal blocks, which move progressively towards the southwest. Armijo et al. (1996, 1999) proposed that fast extension is localized in the NW Aegean (NAT) and Central Greece (Corinth Gulf) at the termination of NAF, while only slow extension occurs across distinct, arc-parallel zones in the South Aegean and SW Anatolia. Before and especially after the aforementioned works, dozens of local-scale marine geological and geophysical cruises and surveys were conducted and contributed to a significant improvement of the knowledge on the present geological structure. Despite the huge progress during the last decade, there are still many areas either not surveyed or with insufficient data, which prevent a robust understanding of the geological and geodynamic processes which evolved through the time and led to the formation of the present complex structure in the Aegean Region.

GPS data indicate that most of the southern Aegean behaves as a non-deforming block, while deformation concentrates in the North and Southeast Aegean and Central Greece (Kreemer & Chamot-Rooke, 2004; Reilinger et al., 2010; Perouse et al., 2012). Still, seismological data do show significant deformation occurring across the Aegean microplate (Taymaz et al., 1991; Kiratzi & Louvari, 2003; Chatzipetros et al., 2013) (Fig. 1).

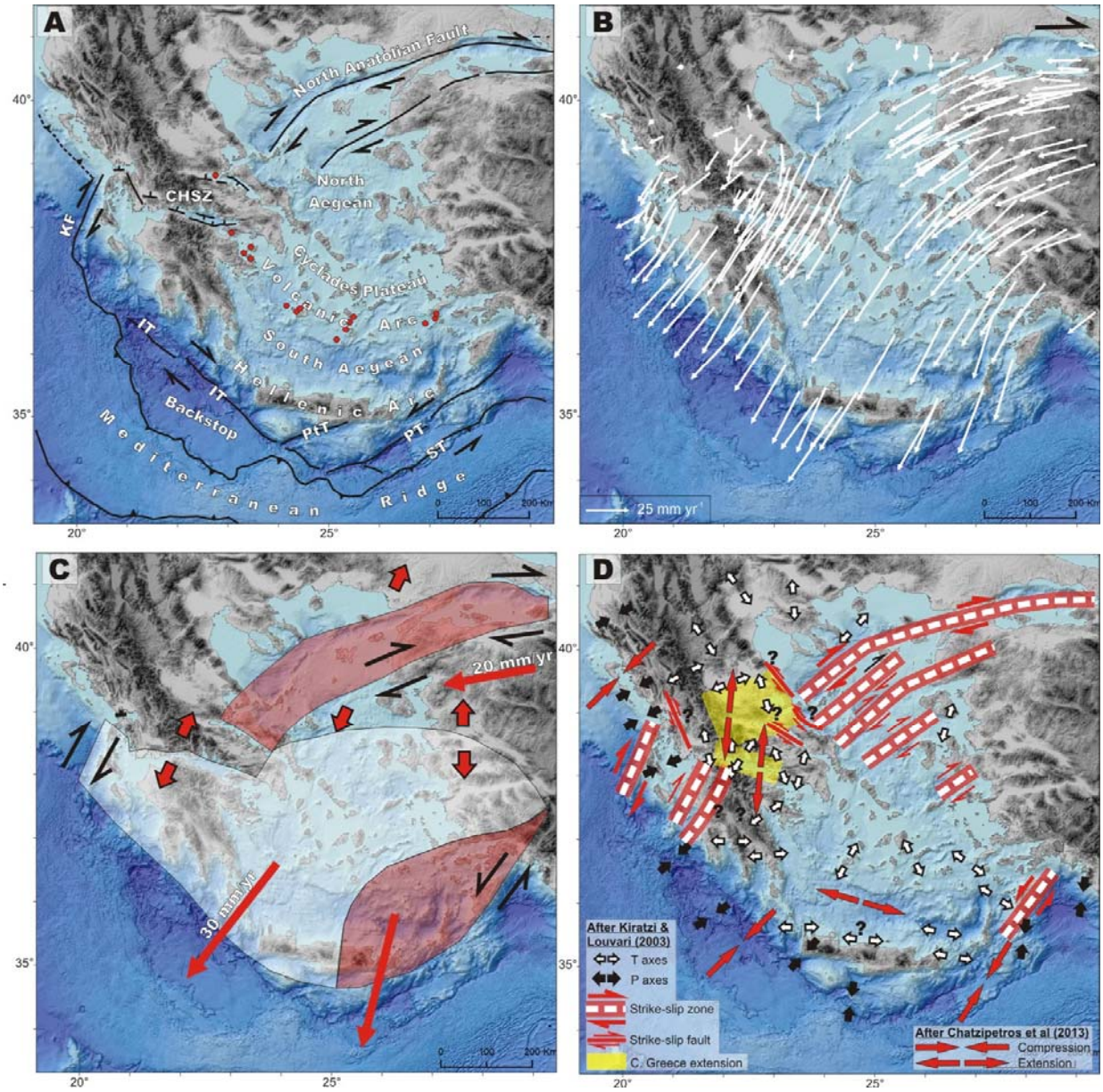

Figure 1: (modified from Sakellariou & Tsampouraki-Kraounaki, 2018). A: Major geodynamic elements of the Aegean Region. White circles represent volcanoes. B: GPS velocities modified after Kreemer & Chamot-Rooke (2004). C: Πresent-day tectonics after Reilinger et al. (2010). The white area translates towards SW with little internal deformation. The reddish areas deform faster. D: P (compression) and T (extension) axes and major geotectonic elements as derived from earthquake focal mechanisms, modified after Kiratzi & Louvari (2003) and Chatzipetros et al. (2013).

OFFSHORE MORPHOLOGY AND ACTIVE FAULTING

Morphological analysis of the most up-to-date, 250 m DTM of the Aegean seafloor (EMODNET Bathymetry project, https://emodnet.eu/bathymetry) revealed the spatial distribution of topographic basins in the Aegean Sea and the Hellenic Trench, categorized according to their depth (Fig. 2A). Most of the basins display a rhomboid, elliptical, trapezoid or spindle shape, their dimensions do not exceed a few tens of kilometers and are aligned predominantly in NE-SW to ENE-WSW, and secondarily in NW-SE to WNW-ESE, directions. The latter two directions prevail over the entire Aegean Sea and coincide with the orientation of the steep, submarine slopes that bound the basins.

Reinterpretation of old and recent, multi- and single-channel, analogue and digital, seismic reflection profiles available at the Hellenic Centre for Marine Research have been reprocessed and re-interpreted and along with the new high-resolution bathymetry led to significantly improved localization of the offshore faults and the Plio-Quaternary sedimentary basins. The morphological basins coincide largely with the main Plio-Quaternary ones. Most of the volcanoes are aligned parallel to the main fault directions and are thus spatially associated with major faults. The faults tend to group in two main directions: (i) NE-SW to ENE-WSW, parallel to or at low angle with respect to the kinematic vectors and (ii) NW-SE to WNW-ESE, perpendicular to or at high angle with respect to the GPS vectors.

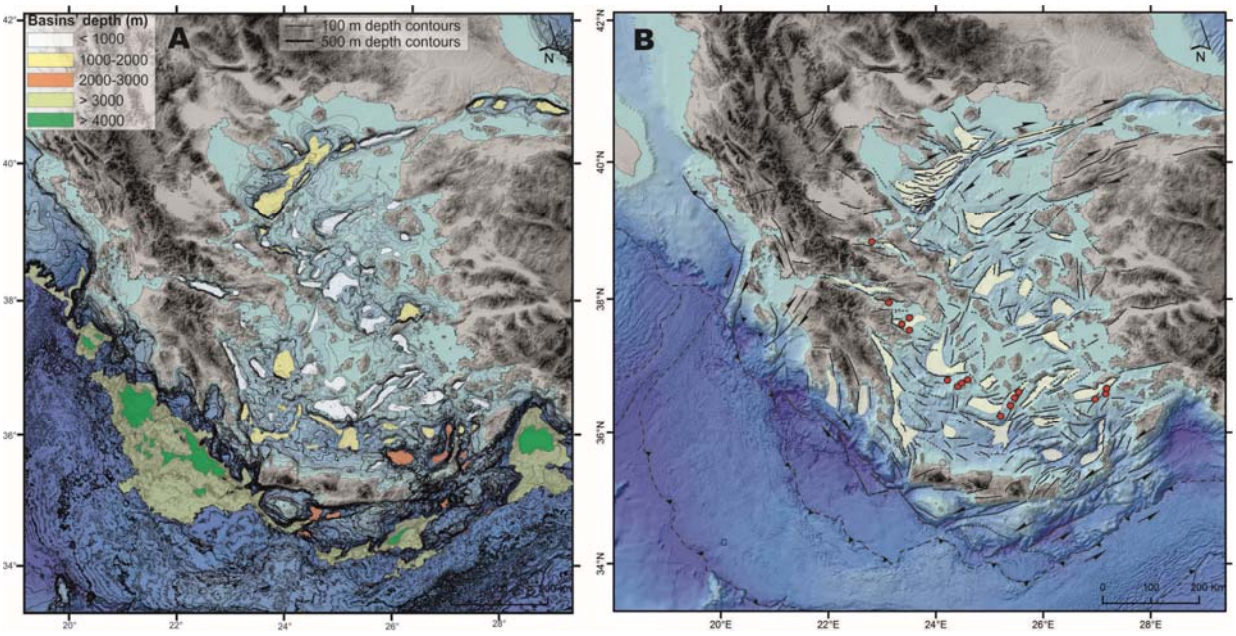

Figure 2: (modified from Sakellariou & Tsampouraki-Kraounaki, 2018). A: Morphological basins in the Aegean Sea and the Hellenic Trench categorized according to their depth. B: Active fault network and distribution of the main Plio-Quaternary basins in the Aegean.

FAULT KINEMATICS AND GEODYNAMIC SYNTHESIS

The integration of the newly described geological structures with the available seismological and geodetic information allows a re-evaluation and re-interpretation of the major geodynamic elements and of the regional and local deformation pattern and kinematic regime (Fig. 3). The value of the angle between the GPS vectors and the fault direction seems to control the kinematic character of the latter. Faults oriented parallel to the GPS vectors are expected to display predominantly strike-slip character (dextral or sinistral), while faults oriented at higher angles may display normal to oblique sense of motion.

The Kephallinia Fault (KF) and the North Anatolian Fault (NAF) constitute the northern dextral boundary of the deforming Aegean crust. Central Greece acts as a relay zone between the opposite tips of the KF and the NAF. The Pliny and Strabo Trenches (PSF) form the eastern NE-SW-trending sector of the Hellenic Trench and represent the southern, sinistral transform-type boundary of the Aegean crust to the Mediterranean Ridge. Between these two, the overriding Aegean crust "flows" toward SW to SSW and is being internally deformed. The resultant SW- to SSW-ward extension is accommodated by major and minor dextral NE-SW to ENE-WSW oriented shear zones and conjugate sinistral strike-slip, oblique and normal faults. These various shear zones create local extension and transtension evolving at rates and following trends which, locally, may differ from the overall extension rate and orientation of the Aegean crust as a whole.

NNE-SSW extension in the North Aegean south of NAT is predominantly accommodated by the NE-SW to ENE-WSW-trending dextral strike-slip Skyros - Biga (SB) and Cavo Doro - Lesvos (CDL) Fault Zones along with NW-SE, sinistral to oblique, conjugate faults and WNW-ESE normal faults. This kinematic pattern is compatible with the Riedel shears model as expected in dextral strike slip zones (Inset A on Fig. 3): the dextral strike slip, NE-SW and ENE-WSW faults represent the P and R shears, the NW-SE sinistral faults the R' shears and the WNW-ESE faults the N faults.

Further south, the dextral Cavo Doro - Lesvos and the Myrtoon - Ikaria (MI) Fault Zones break through the Cyclades Plateau and are associated with NW-SE and WNW-ESE conjugate faults. Note that the two main tectonic directions, NE-SW and NW-SE, can be recognized on the morphological elements of the Aegean Sea including the orientation of the Cyclades and Dodecanese Islands. The Santorini - Amorgos (SA) Fault Zone is the last one toward south displaying dextral sense of motion. It hosts the Santorini volcanic province with its volcanic centers arranged in NE-SW direction (Kameni-Kolumbo Line). The Plio-Quaternary basins have developed either in a transtensional regime on releasing bends, or as pull apart basins, or at the junction between the NE-SW dextral strike-slip and the NW-SE sinistral strike-slip to oblique faults. Oblique rifting along the NE-SW fault zones (Inset B on Fig. 7) is the proposed mechanism to explain basin formation in the Aegean, in particular along the Santorini - Amorgos Fault Zone. The submarine shallow ridges and banks, as well as the islands, represent uplifted blocks, possibly associated with restraining bends.

In the SE Aegean the sense of shear changes to sinistral. The Heraklion - Kos (HK), Kasteli - Nisyros (KN), Ptolemy - Ierapetra (PI) and Karpathos - Rhodes (KR) Fault Zones follow the kinematic character of the Pliny and Strabo Fault Zones. They are associated with NNE-SSW oriented normal to oblique faults, including predominantly normal faults on eastern Crete, which link the ENE-WSW strike-slip zones in southeastern Aegean to the ones running along the troughs south of Crete and east of Gavdos (Inset C on Fig. 3). The spindle-shaped Kamilonisi and the lazy-S shaped Karpathos Basins, the deepest basins of the Aegean Sea, have developed as pull-apart basins along the KN and KR sinistral shear zones, respectively.

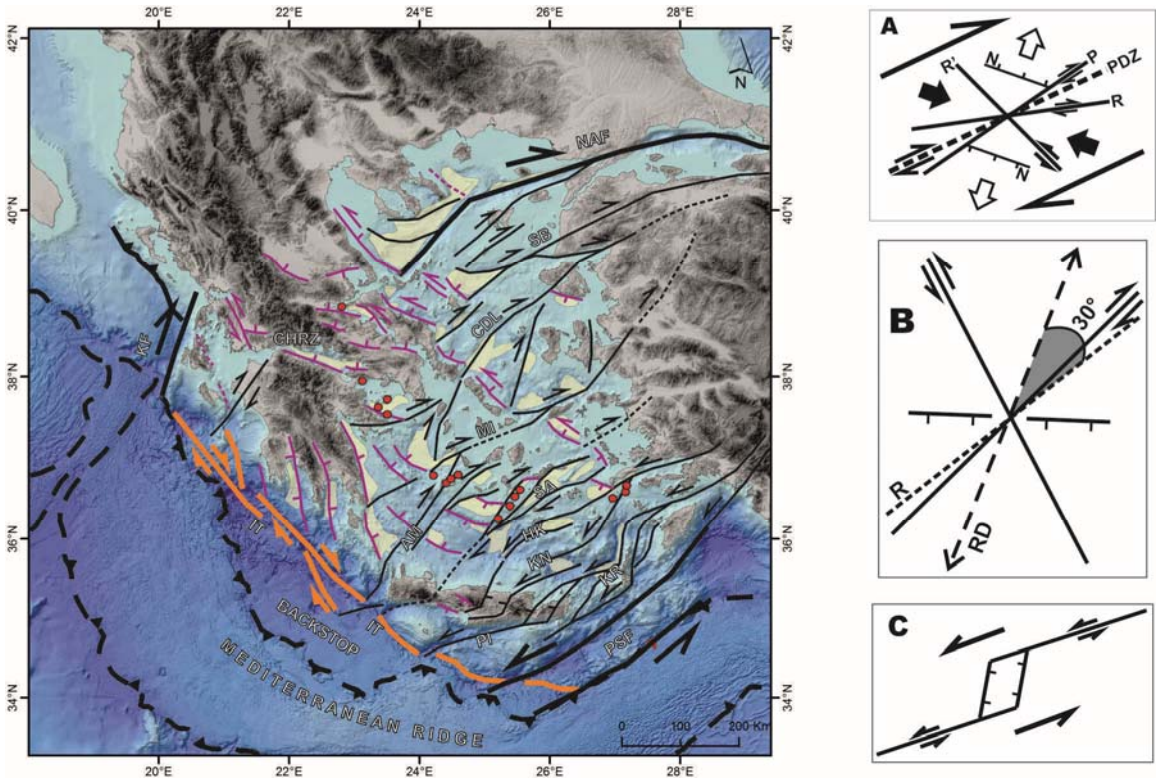

Figure 3: (modified from Sakellariou & Tsampouraki-Kraounaki, 2018): Plio-Quaternary deformation pattern in the overriding Aegean crust. Red dots show volcanoes of the Volcanic Arc. Yellow areas show Plio-Quaternary basins with sediment thickness >500 m. A: Riedel shears (P, R, R', N) and Principal Displacement Zone (PDZ) in a dextral strike-slip deformation zone. B: Kinematics of dextral oblique extension. R: Rift trend; RD: Relative Displacement direction between opposite sides of the rift (modified after Withjack & Jamison, 1986). Inset C: Simplified drawing explaining the kinematic pattern in the southeastern Aegean and East Crete.

The Ionian Trench is a NW-SE-trending geodynamic element. Geodetic data (Kreemer & Chamot-Rooke, 2004) show that the backstop, SW of the trench, belongs to the overriding Aegean crust. Thus the Ionian Trench, which accommodates a considerable amount of dextral strike-slip motion, does not coincide with the outer limit of the Aegean crust. The southeastern part of the Ionian Trench is offset by the three ENE-WSW shear zones (Ptolemy, Pliny, Strabo). The characteristics of the NW part of the trench are less well constrained. It probably represents the surface expression of a diffuse dextral strike-slip zone developed within the upper plate, between the backstop and the arc and may be associated with SW-ward thrusting in the lower upper plate. The NNW-SSE trending normal faults in South Peloponnese may also be related with the kinematics of the Ionian Trench.

REFERENCES

Armijo, R., Meyer, B., King, G.C.P., Rigo, A., & Papanastassiou, D., 1996. Quaternary evolution of the Corinth rift and its implications for the Late Cenozoic evolution of the Aegean. *Geophysical Journal International* 126, 11-53.

Armijo, R., Meyer, B., Hubert, A., & Barka, A., 1999. Westward propagation of the north Anatolian into the northern Aegean: timing and kinematics. *Geology* 27 (3), 267-270.

Brun, J.P., Faccenna, C., Gueydan, F., Sokoutis, D., Philippon, M., Kydonakis, K., & Gorini, C., 2016. The two-stage Aegean extension, from localized to distributed, a result of slab rollback acceleration. *Can. J. Earth Sci.* 53, 1142-1157.

Chatzipetros, A., Kiratzi, A., Sboras, S., Zouros, N., & Pavlides, S., 2013. Active faulting in the north-eastern Aegean Sea Islands. *Tectonophysics* 597-598, 106-122.

Jolivet, L., Faccenna, C., Huet, B., Labrousse, L., Le Pourhiet, L., Lacombe, O., Lecomte, E., Burov, E., Denèle, Y., Brun, J.P., Philippon, M., Paul, A., Salaün, G., Karabulut, H., Piromallo, C., Monié, P., Gueydan, F., Okay, A.I., Oberhänsli, R., Pourteau, A., Augier, R., Gadenne, L., & Driussi, O., 2013. Aegean tectonics: Strain localisation, slab tearing and trench retreat. *Tectonophysics* 597, 1-33.

Kiratzi, A., & Louvari, E., 2003. Focal mechanisms of shallow earthquakes in the Aegean Sea and the surrounding lands determined by waveform modeling: a new database. *J. Geodyn.* 36 (1-2), 251-274.

Kreemer, C., & Chamot-Rooke, N., 2004, Contemporary kinematics of the southern Aegean and the Mediterranean Ridge. *Geoph. Journal International* 157, 1377-1392.

Mascle, J., & Martin, L., 1990. Shallow structure and recent evolution of the Aegean Sea: A synthesis based on continuous reflection profiles. *Marine Geology* 94, 271-299.

Perouse, E., Chamot-Rooke, N., Rabaute, A., Briole, P., Jouanne, F., Georgiev, I., & Dimitrov, D., 2012. Bridging onshore and offshore present-day kinematics of central and eastern Mediterranean: Implications for crustal dynamics and mantle flow. *Geochem. Geophys. Geosyst.* 13, Q09013.

Reilinger, R., McClusky, S., Paradissis, D., Ergintav, S., & Vernant, P., 2010. Geodetic constraints on the tectonic evolution of the Aegean region and strain accumulation along the Hellenic subduction zone. *Tectonophysics* 488, 22-30.

Sakellariou, D., & Tsampouraki-Kraounaki, K., 2018. Plio-Quaternary extension and strike-slip tectonics in the Aegean. In: Duarte, J. (ed), Transform Plate Boundaries and Fracture Zones, ELSEVIER, in press.

Taymaz, T., Jackson, J., & McKenzie, D., 1991. Active tectonics of the north and central Aegean Sea. *Geophys. J. Int.* 106, 433-490.

Withjack, M.O., & Jamison, W.R, 1986. Deformation produced by oblique rifting. *Tectonophysics* 126, 99-124.

INQUA Focus Group Earthquake Geology and Seismic Hazards

paleoseismicity.org

A preliminary note on the macroseismic intensity re-evaluation of the 11 June 1895 central Silesia earthquake, Southwestern Poland

Sana, Hamid (1), Štěpančíková, Petra (1), Szameitat, Annika (1)

(1) Department of Neotectonics and Thermochronology, Institute of Rock Structure and Mechanics, Czech Academy of Sciences, V Holesovickach 41, Prague-18209, Czech Republic, sana@irsm.cas.cz

Abstract: *Although earthquakes in slowly-deforming intraplate regions like Poland are not as frequent or of high intensity as at the plate boundaries. However, few low to moderate intensity earthquakes have been reported to have shaken different regions of Poland in the 19th century. We present a preliminary intensity re-evaluation of one of these earthquakes -the 11 June 1895 mid Silesia earthquake, Southwestern Poland. The intensity revelation in MMI scale was done using detailed reports (in German) collected from different towns and villages of the mid Silesia region soon after the earthquake. The highest intensity on the MMI scale is evaluated to be 7 in two important towns' viz. Strezelin and Ziebice.*

Keywords*: Historical earthquake, Macroseismic intensity, Intraplate deformation*

INTRODUCTION

As opposed to the plate boundaries the intraplate regions deform slowly in space and time. The low shortening rates in intraplate regions are distributed along complex interacting fault systems spread over a large region. So a large earthquake on a fault can increase the strain rate on remote faults in the system. Thus the dormant individual faults can get activated suddenly and result in episodic and spatially migrating earthquakes (Li et al., 2009; Stein et al., 2009; Clark et al., 2012). Central Europe is an intraplate region where the present-day seismicity is attributed to the intraplate Cenozoic deformation due to far-field stresses from the ongoing continent-continent collision in the Alps and Pyrenees, spreading of the Atlantic and the rising of the mantle plumes (Landgraf et al., 2017). As the instrumental earthquake catalogues due to short time span are insufficient to assess the seismic hazard in the intraplate regions. The macroseismic intensity evaluation of historical events and revelation of earthquakes from paleoseismic investigations are useful tools to get an idea of the seismic hazard in the regions with very low shortening rates. We present the macroseismic intensity re-evaluation of an intraplate low intensity earthquake-the 11 June 1895 central Silesia earthquake, Southwestern Poland, Central Europe (Fig. 1). This earthquake is necessarily one of the most significant historical earthquakes in Silesia region of Poland. Not only was it relatively stronger in terms of intensity, it was also felt relatively over a larger area (25000 Km^2) as compared to the 31 January 1883 Silesia earthquake (Leonard & Voltz, 1896).

THE 11 JUNE 1895 MID SILESIA EARTHQUAKE, SOUTHWESTERN POLAND

At 9:27am in the morning on 11 June 1895 a low intensity earthquake struck the central Silesia region of the southwestern Poland. The evening edition of the daily Breslauer Blätter reported that the earthquake had occurred in the foothills of central Silesia on the same day. Soon after Prof. Dr. Frech immediately took the necessary steps to collect as much as possible and accurate reports about this event. A total of 600 (549 positive) reports from 360 administrative districts were collected. The reports and the location names are in German.

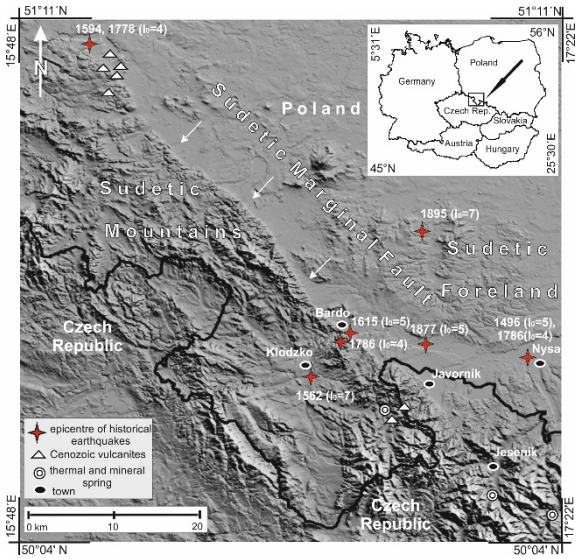

Figure 1: Showing the location of the study region with prominent historical earthquakes.

People have described the earthquake to be, "*like a long distance train passes by the house*, *thunder like, the ground and buildings shook, three shocks were felt with 2-3 second interval, the shaking was also felt outdoors*". Some people have reported aftershocks at 12:05pm but there was a strong thunderstorm at the same time. So maybe people confused the shaking due to thunderstorm as an aftershock. Based on these reports two macroseismic

intensity maps were plotted by Leonard & Voltz (1896) and Dathe (1897). The intensity map of Dathe (1897) is not clear and is unreadable (Fig. 2). However the reports from different areas are elaborate and extensive in Dathe (1897). On the other hand, the intensity map of Leonard and Voltz (1896) is much clearer. But there appears to be a clear conflict in the two intensity maps derived from the same dataset.

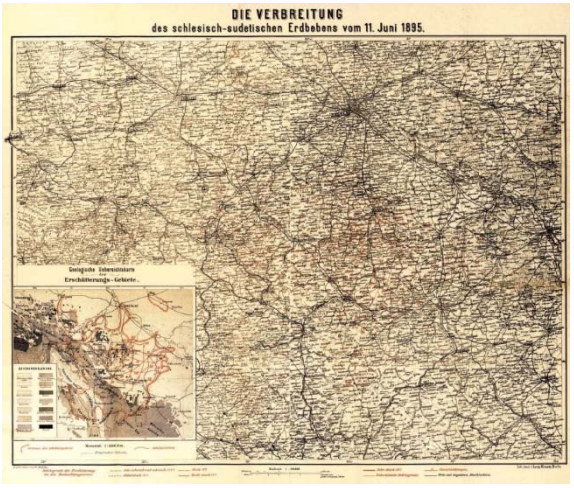

Figure 2: Macroseismic intensity map of the 11 June 1895 central Silesia earthquake, Southwestern Poland by Dathe (1897).

In the detailed unified earthquake catalogue of central, northern, and northwestern Europe (CENEC). This earthquake has been assigned a moment magnitude (Mw) of 4.6, epicentral coordinates of 50.75N and 17.00E with a focal depth of 8km (Grünthal et al., 2009).

RESULTS AND DISCUSSION

In this study, we have assigned present day names (Polish) to towns and villages, which are in German in the original reports. Based on the reports (Leonard & Voltz, 1896; Dathe, 1897) macroseismic intensities of about 100 locations out of about 600 according to the MMI scale have been re-evaluated. An example of 9 locations is shown in table 1. The process of re-evaluating the macroseismic intensities is not complete yet. Only the preliminary results are presented here (Fig 2). The preliminary results show that this earthquake was of low intensity as it was felt within a relatively small area and has been assigned a magnitude (Mw) of 4.5 by Grünthal et al. (2009). The MMI intensities range from 3 to 7 in the study region. The town of Strzelin and Ziebice lie in the maximum MMI intensity of 7 (Fig. 3).

Figure 3: Preliminary MMI intensity map of the 11 June 1895 1895 central Silesia earthquake, Southwestern Poland.

Table 1: Showing the name of locations in German and present day (polish) names with MMI intensity.

German	Polish	Lat	Long	MMI
Alt-Altmannsdorf	Starczow	50.55	16.93	6
Altenburg	Stary Zamek	50.93	16.80	3
Altgersdorf	Stary Gieraltow	50.30	16.92	4
Alt-Grottkau	Stary Grodkow	50.65	17.38	3
Althaide	Polanica Zdroj	50.39	16.51	2
Alt-Heinrichau	Stary Henrykow	50.66	16.97	4
Alt-Liebersdorf	Lubomin	50.80	16.20	3
Alt-Mohrau	Stara Morawa	50.26	16.889	4
Alt-Patschkau	Stary Paczkow	50.45	17.048	4
Alt-Waltersdorf	Stary Waliszow	50.32	16.684	4

Acknowledgements: We would like to thank Institute of Rock Structure and Mechanics, Czech Academy of Sciences, Czech Republic for supporting us through Grant no. 343. We are also thankful to the support of the long-term conceptual development research organisation RVO: 67985891, Czech Republic.

REFERENCES

Clark, D., McPherson, A., & Van Dissen, R., 2012. Long-term behaviour of Australian stable continental region (SCR) faults. *Tectonophysics* 566, 1-30.

Dathe, E., 1897. *Das schlesisch-sudetische Erdbeben vom 11. Juni 1895*. Abhandl. d.k. preuss. geol. Bundesanstalt, Neue Folge, Heft 22, Berlin.

Grünthal, G., Wahlström, R., & Stromeyer, D.J., 2009. The unified catalogue of earthquakes in central, northern, and northwestern Europe (CENEC)-updated and expanded to the last millennium. *Journal of Seismology* 13 (4), 517-541.

Landgraf, A., Kuebler, S., Hintersberger, E., & Stein, S., (eds) 2017. Seismicity, Fault Rupture and Earthquake Hazards in Slowly Deforming Regions. *Geological Society, London, Special Publications* 432, 1-12, https://doi.org/10.1144/SP432.13.

Leonhard R., & Volz, W., 1896. Das mittelschlesische Erbeben vom 11. Juni 1895. *Zeitschrift f. Erdkunde zu Berlin* XXXI, 1-21.

Li, Q., Liu, M., & Stein, S., 2009. Spatial-temporal complexity of continental intraplate seismicity: insights from geodynamic modeling and implications for seismic hazard estimation. *Bulletin of the Seismological Society of America* 99 (1), 52-60.

Stein, S., Liu, M., Calais, E., & Li, Q., 2009. Mid continent earthquakes as a complex system. *Seismological Research Letters* 80, 551-553.

INQUA Focus Group Earthquake Geology and Seismic Hazards

paleoseismicity.org

Epicentral relocation, fault modelling, static stress change distribution and modelled surficial displacements of the July 20, 2017 (M_w 6.6) Kos-Bodrum earthquake sequence

Sboras, Sotiris (1), Lazos, Ilias (2), Mouzakiotis, Evaggelos (1), Karastathis, Vassilios (1), Pavlides, Spyros (2), Chatzipetros, Alexandros (2)

(1) Institute of Geodynamics, National Observatory of Athens, Lofos Nymfon, Thisio, Athens, GR118 10, Greece, sboras@noa.gr
(2) Department of Geology, Aristotle University, University campus, Thessaloniki, GR 541 24, Greece, pavlides@geo.auth.gr

Abstract: *We investigated the strong July 20, 2017 earthquake and its aftershock sequence occurred in SE Aegean Sea. Several secondary ground effects were observed (mainly liquefaction and tsunami), but no primary ground ruptures. We performed a hypocentral relocation of the sequence in order to detect the fault pattern that revealed the existence of three major clusters, one associated with the fault of the mainshock and a second related to neighbouring faults. The majority of the relocated hypocentres does not exceed the depth of ca. 15 km. Based on seismological data as well as morphotectonic and interferometric information, we modelled the source of the mainshock proposing a blind, normal, NNW-dipping fault plane. Using our fault model as a source fault, we calculated i) the Coulomb stress changes for two cases of receiver faults, usually met in this area: similar and antithetic to the source fault, and ii) the surficial horizontal and vertical displacement pattern.*

Keywords*: 2017 Kos-Bodrum earthquake sequence, epicentral relocation, Coulomb stress change, surficial displacement modelling*

LOCAL GEODYNAMIC SETTING

The July 20, 2017 epicentral area lies on the back-arc of the Hellenic Subduction Zone which is the result of the Aegean-Anatolian and African plates convergence. Due to the proximity to the subduction zone, direction of extension locally varies between roughly N-S and NW-SE (e.g. Hatzfeld, 1999; Ring et al., 2017), also controlling local geomorphology. Thus, ca. E-W- to NE-SW-trending horst-and-graben systems have been formed by parallel normal faults respectively. Gökova Gulf is the prevailing tectonic E-W-trending graben in the study area, located between Bodrum and Datça peninsulas, extending for ca. 100 km on an E-W axis with a N-S opening of ca. 25 km.

Both northern and southern margins of Gökova Gulf are bounded by parallel-to-subparallel normal faults that also outcrop onshore (e.g. Gürer & Yilmaz, 2002; Altunel et al., 2003; Duman et al., 2011). Bathymetric surveys have revealed similar tectonic features affecting the seafloor (Kurt et al., 1999; Uluğ et al., 2005; İşcan et al., 2013; Tur et al., 2015; Ocakoğlu et al., 2017). Some authors support the existence of a NE-SW-striking strike-slip fault in the middle of the gulf which plays the role of a transfer fault (Gökova Transfer Fault; Uluğ et al., 2005; İşcan et al., 2013; Ocakoğlu et al., 2017).

Active faulting is also present at Kos Island. The dominating morphological feature is an elongated, ENE-WSW-trending mountain (Mt Dikaeos) located at the eastern part of the island. With a summit at 843 m a.s.l., Mt Dikaeos is the result of ENE-WSW-striking, antithetic, normal faulting that controls both north- and south-side slopes (Nomikou & Papanikolaou, 2010).

Intense tectonic activity in the broader area is evident by the rich strong (M ≥ 6.0) historically and instrumentally recorded seismicity (Figure 1). The oldest event occurred in 412 BC (M 6.8) near Kos Island and the strongest on June 26, 1926 (M 7.6) ca. 45 km SE of Kos Island (Papazachos & Papazachou, 2003).

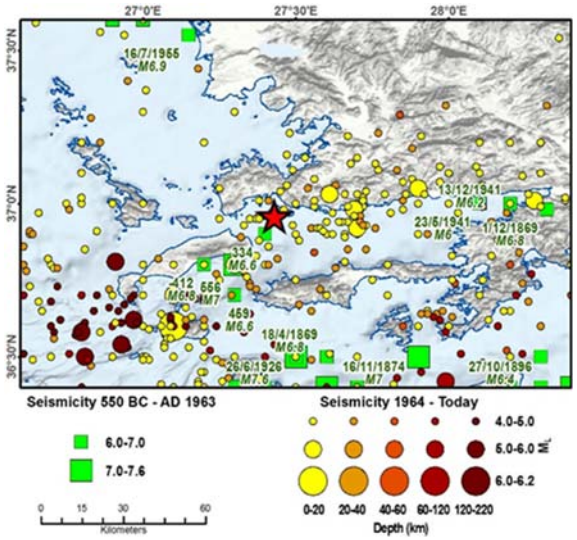

Figure 1: Historically (Papazachos et al., 2000) and instrumentally (NOA) recorded seismicity in the broader epicentral area. The July 20, 2017 mainshock is marked by a red star.

THE 2017 MW 6.6 EARTHQUAKE

Seismic sequence

On 20 July 2017 at 22:31:11.0 (UTC), a strong (Mw 6.6) and destructive earthquake occurred in the border region of Greece and Turkey, between Kos Island, Greece and Bodrum City, Turkey (red star in Figure 2). The focal depth was calculated at 10 km. The proposed focal mechanisms

revealed normal kinematics indicating two nodal planes dipping to the north and south respectively. The mainshock was followed by numerous aftershocks, the strongest of which (Mw 5.3) was recorded many days later, on 8 August 2017, 18 km east of Bodrum.

Ground effects

The consequences of the strong earthquake are imprinted in the wider Kos Island region. At first, the collapse of a building in the city of Kos led to the death of two people, while at least 12 serious injuries were recorded. Modern buildings on Kos Island demonstrated only light damage since they were built according to the Greek seismic code (seismic risk zone II - 0.24 g). Heavier damages were mostly recorded in old buildings (Ottoman era), ancient walls and archaeological sites.

In addition, the port of Kos city was heavily damaged due to extended liquefaction phenomena and was closed down for repair. Landslides and rockfalls were limited, whereas liquefaction phenomena were scattered all over the island. Primary ground ruptures were not observed.

EPICENTRAL RELOCATION

The seismic sequence of Kos has been relocated using combined P- and S- wave phase data from the HUSN (Hellenic Unified Seismograph Network) and the KOERI (Kandilli Observatory and Earthquake Research Institute) networks. During the period of 5/7/2017 to 31/10/2017 more than 11,000 events were recorded in the broader region of the main shock. Our initial dataset consisted of more than 110,000 P and 47,000 S phases recorded by the stations of HUSN and KOERI networks.

The non-linear location algorithm NonLinLoc (Lomax et al., 2000) was used for the event location procedure. The Posterior Density Function (PDF) of the solution is calculated using the equal-differential-time (EDT) likelihood function (Font et al., 2004) with which the travel-time difference between observed and synthetic travel times is calculated for pairs of stations, contrary to typical least squares methodologies. The advantage of this method is that the solution is independent of the origin time, and thus the problem is reduced to a 3-D search over space. Furthermore this methodology makes it possible to identify misspicked data and exclude them from the final location solution. The search for the optimal location is performed throughout the whole space using the Oct-tree importance sampling algorithm (Lomax & Curtis, 2001) which uses recursive subdivisions of a gridded space. This eliminates the issue of location error due to local minima in the PDF.

The relocation procedure was based on the 1-D velocity model proposed by Panagiotopoulos et al. (1985). In our final dataset (Figure 2) we selected all events with more than 15 phases, located with azimuthal gap < 180°, location RMS < 1 s and horizontal and vertical errors < 2.5 km.

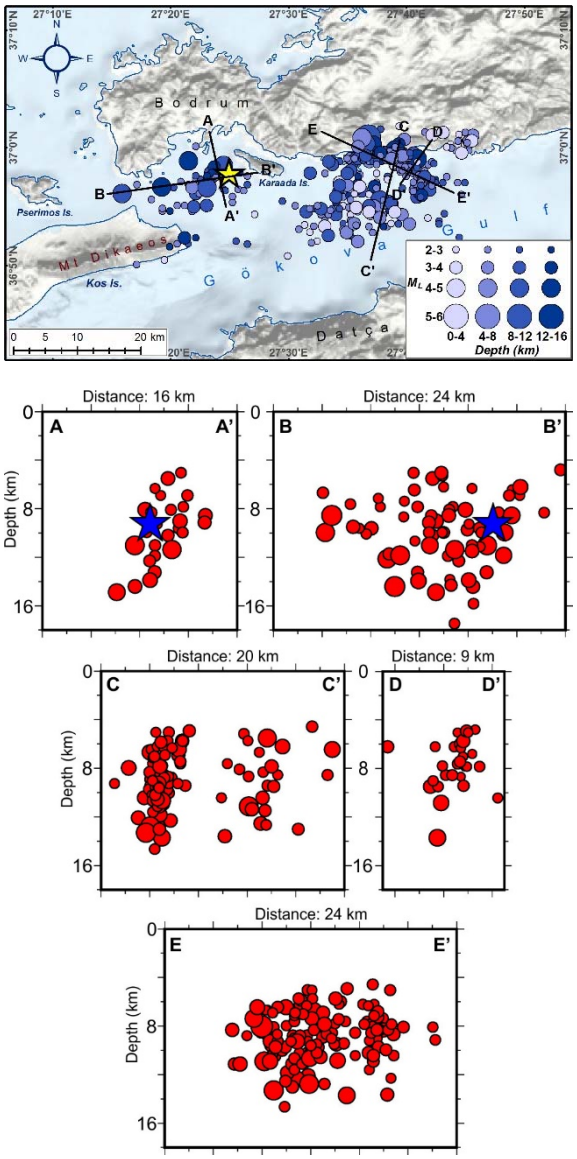

Figure 2: Epicentral relocation of the 2017 seismic sequence. Three clusters can be distinguished: one next to the mainshock, west of the Karaada Is., and two east of the Karaada Is., one northern and another southern. The profile paths are marked in the map on the top.

FAULT MODELLING

In order to calculate the surface deformation and the Coulomb static stress changes we modelled the seismic source of the main event. Based on the scalar relationships of Wells & Coppersmith (1994) the source dimensions (length × width) are estimated at 26 and 15 km respectively. Strike, dip and rake are obtained from NOA's focal mechanism (265:43:-102, respectively). The vertical position of the fault plane relies on the lack of any primary ground ruptures and the vertical distribution of the western cluster which shows that it was restricted approximately between the depths of 4 and 14 km. The relocated hypocentral location of the mainshock also constrained the N-S horizontal positioning of the source. The horizontal positioning depends on i) the horizontal relocated aftershock distribution, and ii) the ground deformation observed on the southeastern edge of Kos Island as revealed by InSAR images (Ganas et al., 2017).

The NNW-dipping fault segment along the northern front of Mt Dikaeos (Kos Island) is probably the surficial expression of the geological fault part of which is the seismic source of the 2017 mainshock. An average slip of 0.68 m is calculated from M0 and the source dimensions after applying the formula of Aki (1966): M0 = μ·u·L·W (μ is shear modulus, u is average slip, L is length and W is width). All modelling parameters are shown in Table 1.

Table 1: Main parameters of the fault model that produced the 2017 mainshock.

Parameter	Value
Strike:	265°
Dip:	43°
Rake:	-102°
Length:	26 km
Down-dip width:	15 km
Minimum depth:	4 km
Maximum depth:	14.2 km
Average slip:	0.68 m

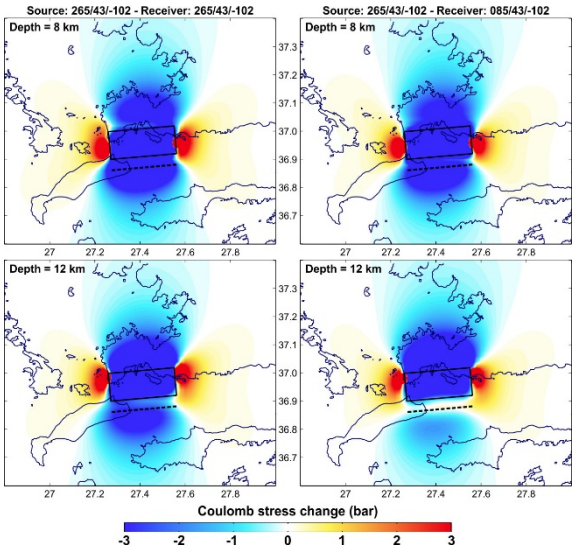

Figure 3: Coulomb static stress change distributions for two receiver fault cases, similar (left side) and antithetic (right side) to the source (modelled) fault, and for two representative calculation depths at 8 (top) and 12 km (bottom). The black rectangular represents the modelled source fault plane and the dashed line the section of the updip fault plane prolongation with the map plane.

STATIC STRESS CHANGES

The calculation of the static stress changes is based on the Coulomb failure criterion. In particular, when the Coulomb stress change receives a value, exceeding the threshold value, slip on fault plane occurs. The aforementioned value is calculated by the following equation:

〖Δσ〗_f=〖Δτ〗_s+μ^'×〖Δσ〗_n

where Δσf is theCoulomb stress change, Δτs is the shear stress change on the failure plane, μ' is the friction coefficient and Δσn is the normal stress change.

We used our modelled fault of the mainshock (Table 1) as source fault and we calculated the stress changes for two cases of fault receivers that are usually met in the study area: i) similar to the source fault, and ii) for antithetic parallel normal faults. For each case we chose two calculation depths: 8 and 12 km. This depth range is representative for possible rupture initiation of crustal earthquakes in this area.

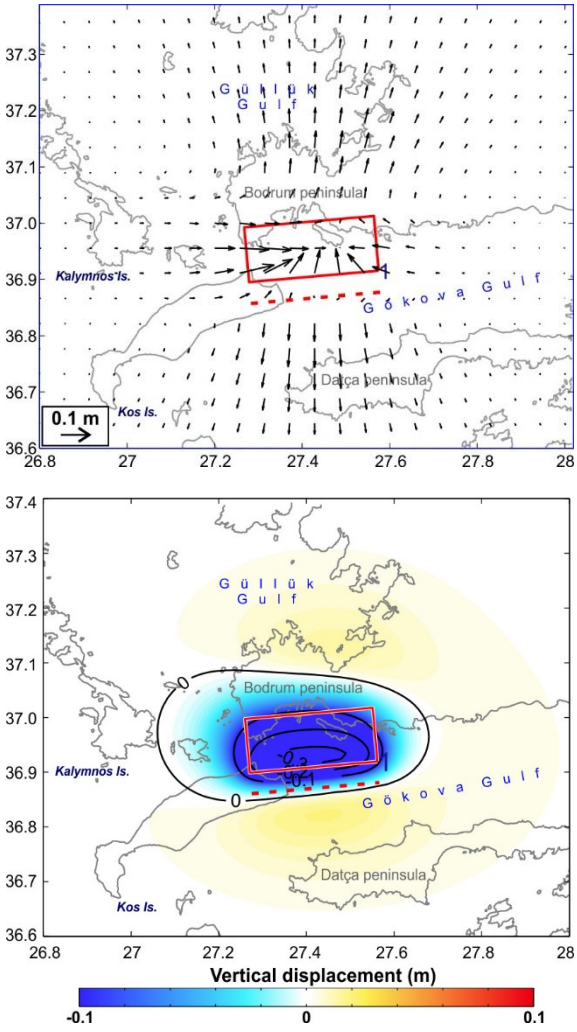

Figure 4: Horizontal (top) and vertical (bottom) displacements of the fault that produced the 2017 mainshock at surface depth.

SURFACE DEFORMATION

The estimation of surface deformation is based on the Okada model (Okada, 1992), including dislocation solutions in a homogeneous, elastic and isotropic half-space. As rupturing fault we used our fault model of the mainshock (Table 1) and we calculated both horizontal and vertical surficial (0 depth) displacements (Figure 4).

RESULTS, CONCLUSIONS AND DISCUSSION

The 2017 seismic sequence epicentral relocation (Figure 2) revealed i) a hypocentral concentration maximum depth at

ca. 15 km, and ii) a horizontal epicentral concentration in three main clusters: a western one, clearly delineating a N-dipping fault plane (profile A-A'), and two eastern ones. The northern cluster of latter two is quite linear in two directions: E-W, along the western half, and NW-SE along the other half. Vertical distribution is also very linear in both above directions (profiles C-C' and D-D'), depicting steeply N-dipping trends probably belonging to two tectonic structures, one striking ENE-WSW and a second striking NW-SE. The southern cluster is rather scattered in both horizontal and vertical sections with no particular dipping trend.

Based mainly on seismological and secondary on morphotectonic and remote sensing data, we modelled the source of the 2017 mainshock proposing a 26 km-long, NNW-dipping fault plane with almost pure normal sense of slip located at depth between 4 and 14.2 km.

Static stress changes, setting our fault model as source fault, were calculated for two receiver fault cases: similar and antithetic to the source fault. Both cases show great similarities at both calculation depths of 8 and 12 km respectively. Stress rises bilaterally along (East-West) and drops across (North-South) fault's strike. This means that faults that run parallel to the northern coast of Gökova Gulf, east and west of the source fault are loaded with stress. An obvious result of the stress rise east of the fault source are the two eastern aftershock clusters.

Horizontal displacements clearly show the distancing between the Bodrum and Datça peninsulas along a N-S axis on the order of 0.1 m. The easternmost part of Kos Island demonstrates an ENE to NE dislocation.

Vertical displacement pattern shows subsidence on the hanging-wall (max. 0.33 m) which is constrained on the southwesternmost part of Bodrum peninsula and the northesternmost part of Kos Island. Datça peninsula demonstrates a slight uplift (< 0.01 m).

REFERENCES

Aki, K., 1966. Generation and propagation of G-waves from the Niigata earthquake of June 16, 1964. 2. Estimation of earthquake movement, released energy and stress-strain drop from G spectrum. *Bull. Earthq. Res. Inst*. 44, 23-88.

Altunel, E., Stewart, I.S., Piccardi, L., & Barka, A.A., 2003. Earthquake faulting at ancient Cnidus, SW Turkey. *Turkish J. Earth Sci*. 12 (1), 137-151.

Duman, T.Y., Emre, Ö., Özalp, S., & Elmaci, H., 2011. 1:250,000 Scale Active Fault Map Series of Turkey, Aydin (NJ 35-11) Quadrangle. S/N: 7, General Directorate of Mineral Research and Exploration, Ankara-Turkey.

Font, Y., Kao, H., Lallemand, S., Liu, C.-S., & Chiao, L.-Y., 2004. Hypocentral determination off-shore Eastern Taiwan using the Maximum Intersection method. *Geophys. J. Int*. 158, 655-675.

Gürer, Ö.F., & Yilmaz, Y., 2002. Geology of the Ören and surrounding areas, SW Anatolia. *Turkish J. Earth Sci*. 11 (1), 1-13.

Hatzfeld, D., 1999. The present-day tectonics of the Aegean as deduced from seismicity. *Geol. Soc. London, Spec. Publ.* 156 (1), 415-426.

İşcan, Y., Tur, H., & Gökaşan, E., 2013. Morphologic and seismic features of the Gulf of Gökova, SW Anatolia: evidence of strike-slip faulting with compression in the Aegean extensional regime. *Geo-Mar. Lett*. 33 (1), 31-48.

Kurt, H., Demirbağ, E., & Kuşçu, İ., 1999. Investigation of the submarine active tectonism in the Gulf of Gökova, southwest Anatolia-southeast Aegean Sea, by multi-channel seismic reflection data. *Tectonophysics* 305 (4), 477-496.

Lomax, A., & Curtis, A., 2001. Fast, Probabilistic Earthquake Location in 3D Models Using Oct-Tree Importance Sampling. European Geophysical Society, Nice (March 2001).

Lomax, A., Virieux, J., Volant, P., & Berge, C., 2000. Probabilistic Earthquake Location in 3D and Layered Models: Introduction of a Metropolis-Gibbs Method and Comparison with Linear Locations. In: *Advances in Seismic Event Location* (Thurber, C.H., Rabinowitz, N., eds), Kluwer, Amsterdam, 101-134.

Nomikou, P., & Papanikolaou, D., 2010. The morpho-tectonic structure of Kos-Nisyros-Tilos volcanic area based on onshore and offshore data. In: Proc. XIX CBGA Congress, Sp. Vol. 99, 557-564.

Ocakoğlu, N., Nomikou, P., İşcan, Y., Loreto, M.F., & Lampridou, D., 2017. Evidence of extensional and strike-slip deformation in the offshore Gökova-Kos area affected by the July 2017 Mw6. 6 Bodrum-Kos earthquake, eastern Aegean Sea. *Geo-Mar. Lett*., 1-15.

Okada, Y., 1992. Internal deformation due to shear and tensile faults in a half-space. *Bull. Seism. Soc. Am*. 82 (2), 1018-1040.

Panagiotopoulos, D.G., Hatzidimitriou, P.M., Karakaisis, G.F., Papadimitriou, E.E., & Papazachos, B.C., 1985. Travel time residuals in southeastern Europe. *Pure Appl. Geophys*. 123, 221-231.

Papazachos, B.C., Comninakis, P.E., Karakaisis, G.F., Karakostas, B.G., Papaioannou, C.A., Papazachos, C.B., & Scordilis, E.M., 2000. A catalogue of earthquakes in Greece and surrounding area for the period 550BC-1999. *Publ. Geophys. Laboratory*, University of Thessaloniki, 1, 333 pp.

Ring, U., Gessner, K., & Thomson, S., 2017. Variations in fault-slip data and cooling history reveal corridor of heterogeneous backarc extension in the eastern Aegean Sea region. *Tectonophysics* 700, 108-130.

Toda, S., Stein, R.S., Sevilgen, V., & Lin, J., 2011.Coulomb 3.3 Graphic-rich deformation and stress-change software for earthquake, tectonic, and volcano research and teaching-user guide. U.S. Geological Survey Open-File Report, 2011-1060.

Tur, H., Yaltırak, C., Elitez, İ., & Sarıkavak, K.T., 2015. Pliocene-Quaternary tectonic evolution of the Gulf of Gökova, southwest Turkey. *Tectonophysics* 638, 158-176.

Uluğ, A., Duman, M., Ersoy, Ş., Özel, E., & Avcı, M., 2005. Late Quaternary sea-level change, sedimentation and neotectonics of the Gulf of Gökova: Southeastern Aegean Sea. *Mar. Geol.* 221 (1-4), 381-395.

Wells, D.L., & Coppersmith, J.K., 1994. New empirical relationships among magnitude, rupture length, rupture width, rupture area, and surface displacement. *Bull. Seism. Soc. Amer*. 84, 974-1002.

INQUA Focus Group Earthquake Geology and Seismic Hazards

paleoseismicity.org

Geomorphic evidence of active tectonic deformation on the SW Gulf of Corinth, resulting from combined onshore and offshore data

Simou, Eirini (1), Nomikou, Paraskevi (1), Papanikolaou, Dimitrios (1), Lykousis, Vasilios (2)

(1) National and Kapodistrian University of Athens, Faculty of Geology & Geonvironment, Greece, erinisim@gmail.com
(2) Institute of Oceanography, Hellenic Centre for Marine Research, POBox 712, 19013 Anavyssos, Greece

Abstract: *According to several geological, geomorphic, geodetic and seismotectonic studies of the past years, the Gulf of Corinth, constitutes a high-strain band, characterized as one of the largest zones of active normal faulting. High levels of extension, which are related to the rift systems, are mainly responsible for the tectonic control on a currently deforming landscape. The main aim of this study has been to examine how the active tectonic deformation, in combination with the attendant fierce erosional and sedimentary processes, has affected the morphology towards the wider SW margin of the Gulf of Corinth. High-resolution multibeam bathymetry in combination with the available land surface data have contributed to accurate submarine and subaerial morphological mapping, revealing a wealth of information with regard to the geodynamic evolution and the tectonic insight.*

Keywords*: Gulf of Corinth, morphotectonics, drainage, erosion, faulting*

INTRODUCTION

The Gulf of Corinth, the northern and most active part of the present-day Corinth Rift, constitutes a natural laboratory for morphotectonic studies as it has been long identified as a site of major importance due to the continuous tectonic deformation. The high rates of concentrated seismicity, the enduring neotectonic activity deforming the coastal region of the NW Peloponnese, the exposal of the well preserved sedimentary sequences and the evidence of the intense geomorphological processes indicate the consequences of active deformation in the Gulf of Corinth. This active deformation, resulting from the high extensional rates (reaching approx. 14±2mm/yr) renders the western part of the Gulf as the most active of the Corinth Rift, arising special interest for understanding the physical model related to fault activity and surface processes. The study area is located at the SW part of the Gulf of Corinth (Lakka - Psathopyrgos fault block - Fig. 1).

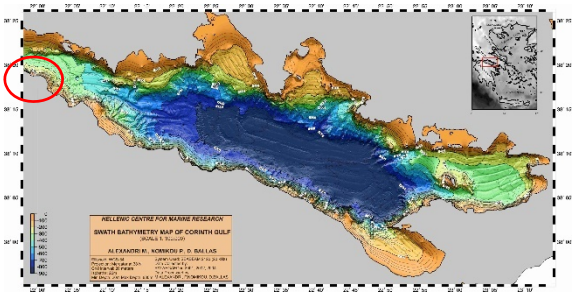

Figure 1: Swath bathymetry map of the Corinth Gulf and the location of the study area (Nomikou et al., 2011).

METHODOLOGY

The construction of a Digital Elevation Model (DEM) has been the basis of the current analysis as it provides a representation of the terrain's surface from which various qualitative and quantitative values may be extracted. These values allowed the evaluation of specific morphostructural elements and the characterization of various processes that affect the landscape.

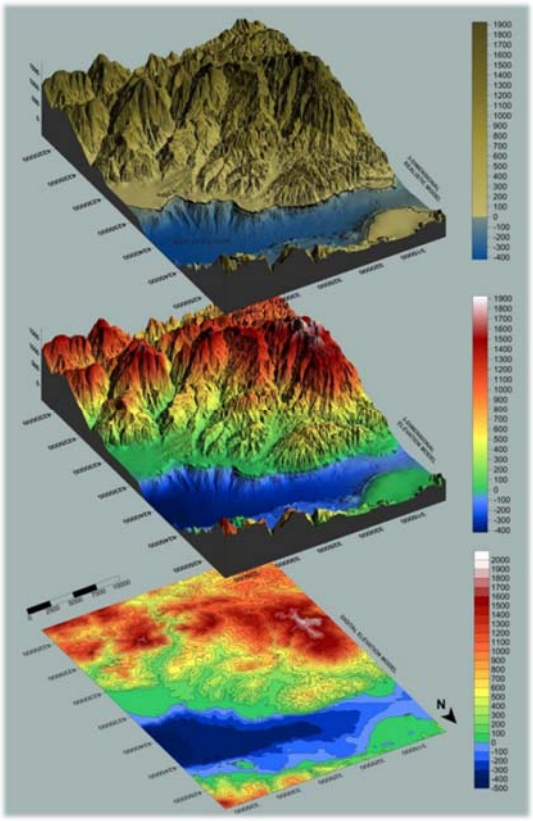

Figure 2: Digital Elevation Model (DEM), 3D Elevation Model and 3D Realistic Model of the combined marine & land surface data, presenting the morphology of the study area.

High-resolution multibeam bathymetry combined with the available land surface data have been primarily used for the construction of a combined DEM (Fig. 2), which is subject to further detection of all those geomorphic features that indicate the on-going active tectonic deformation and the effects of the erosional processes.

DISCUSSION

Drainage basins interplay with the erosional processes as they transport the sediments from the tectonic uplands to the sedimentary basin. The drainage pattern in tectonically active regions reveals the background active processes which are responsible for river incision (extensional faulting related to tectonic uplift in regions such as the Gulf of Corinth), asymmetries of the catchments and river diversions. The submarine drainage system within the study area is characterized by a simple but interesting pattern (Fig. 3); a central E – W trending drainage runoff axis, exceeding 20km in length, accumulating the flow to the east, towards the deepest parts of the Gulf of Corinth. In spite of this simplicity, several results can be extracted as, by taking into consideration the general geological setting, the more active areas can be related to straight and elongated channels with a few or no smaller crossing tributaries while submarine gullies had been developed where activity is less or temporarily ceased (towards east).

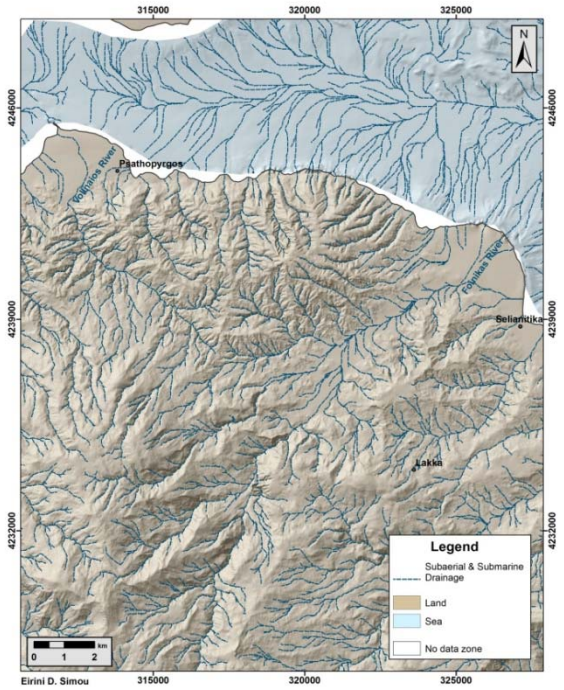

Figure 3: Combined Drainage Map (submarine and on-land) of the study area.

As far as the morphological analysis is concerned, it has been processed from the perspective of slope value distribution and the results have been presented on a Slope Distribution map, which was composed from the combined onshore and offshore datasets. The resulting slope values (ranging between 0° - 65°) have been classified aiming to indicate all those areas, both in the marine and the terrestrial environment, which are characterized by abrupt change of slope values, reflecting the position of the major active tectonic structures (Fig. 4). The combined datasets interpretation shows that the south-western margin of the Gulf of Corinth is characterized by intense coastal relief which passes abruptly to steep submarine slopes. These steep slope values reflect the effects of the most recent brittle deformation, which has occurred towards the currently active Psathopyrgos fault zone.

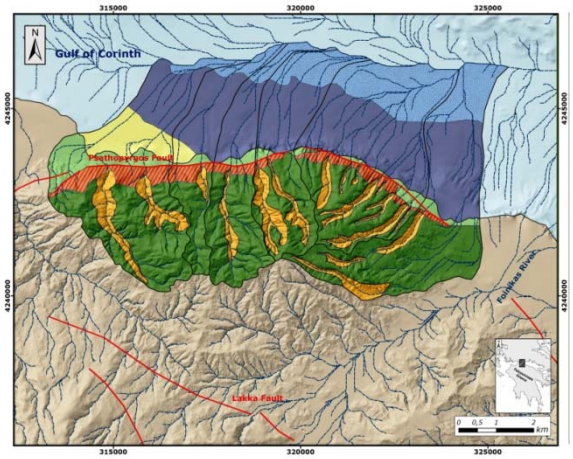

Figure 4: Summarized morphological results presented on the Subaerial and Submarine Morphological Zonation map. The coloured areas represent the slope gradation (light green colour for less steep slope values, red colour for the steepest, related to Psathopyrgos fault zone. In the submarine area, yellow is for the continental shelf, dark blue for the continental slope and part of the basin is indicated by the light blue dotted area).

CONCLUSIONS

Local lithology combined with the steep slope values, the intense seismic activity and the high rates of sedimentation in the coastal region contribute to a high-energy geodynamic environment (Fig. 5), enhancing the possibility of instabilities triggering at the coastal zone. The steep slope values towards the Psathopyrgos fault zone denote the effects of the most recent brittle deformation which are related to limited but sizeable coastal instabilities (e.g. Panagopoula landslide). Conversely, the easternmost less active West Eliki fault is related to less steep slopes at the margins of the basin. Canyons and gullies are extensive and sediment mass failures are identified near the headwalls as retrogressive landslide scars. The indirectly tectonic-induced mass movements evolving near the coastal and shallow marine areas may lead to natural hazards including coastal retreat or slump-induced tsunamis depending on the volumes of the mobilized materials. High-resolution technologies have contributed to accurate submarine and subaerial morphological mapping, revealing a wealth of information with regard to the geodynamic evolution and the tectonic insight.

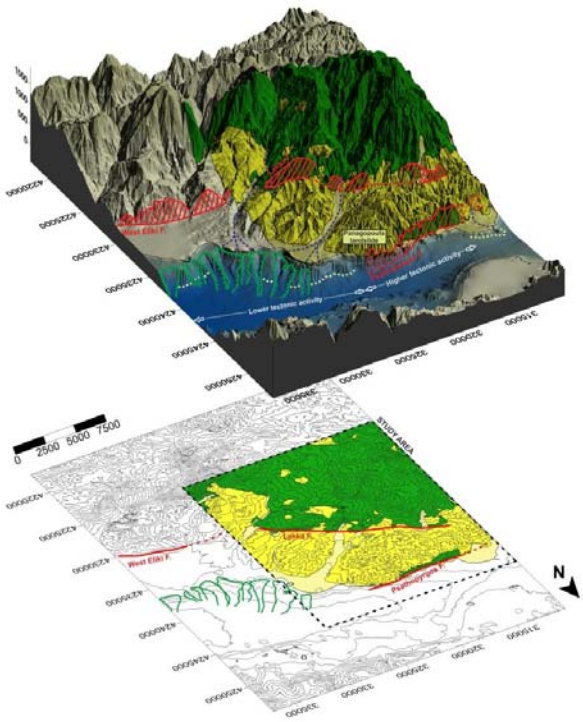

Figure 5: 3D model of the wider study area, including the post-alpine (yellow) and alpine formations (green), the main tectonic features (red lines) and the instabilities (green lines) occurring towards the less active coastal slopes.

REFERENCES

Beckers, A., et al., 2016. Influence of bottom currents on the sedimentary processes at the western tip of the Gulf of Corinth, Greece. *Marine Geology* 378, 312-332.

Beckers, A., et al., 2015. Active faulting at the western tip of the Gulf of Corinth, Greece, from high-resolution seismic data. *Marine Geology* 360, 55-69.

Ford, M., et al., 2012. Tectono-sedimentary evolution of the western Corinth rift (Central Greece). *Basin Research*, 1-23.

Leeder, M.R., & Jackson, J.A., 1993. The interaction between normal faulting and drainage in active extensional basins, with examples from western United States and central Greece. *Basin Research* 5, 79-102.

Nomikou, P., et al., 2011. Swath Bathymetry and morphological slope analysis of the Corinth Gulf. 2nd INQUA-IGCP 567 International Workshop on Active Tectonics, Earthquake Geology, Archaeology and Engineering. Corinth 19-24 September 2011, p. 155-158.

INQUA Focus Group Earthquake Geology and Seismic Hazards

paleoseismicity.org

The Groningen case
When science becomes part of the problem, not the solution

Sintubin, Manuel (1)

(1) KU Leuven, Department of Earth and Environmental Sciences, Celestijnenlaan 200E, BE-3001 Leuven, manuel.sintubin@kuleuven.be

Abstract: *On 16 August 2012 a M3.6 earthquake struck the northeastern province of Groningen, the Netherlands. This earthquake is to date the strongest one of the induced earthquakes caused by the gas extraction in Groningen. While induced earthquakes before this earthquake went quite unnoticed, this earthquake became a tipping point. Since then, the mismanagement of the seismic risk led to a Gordian knot. In this paper I reflect on the role that scientists played in the way the Groningen case was mismanaged. The question is asked if the scientific community failed to properly inform the public to enable them to assess their personal risk perception, and to advice policymakers to allow them to take effective measures. A one-size-fits-all solution for managing risks caused by induced earthquakes does not exist. But at least, lessons can be learned - also from the Groningen case - which can be inspirational for risk management in other cases of induced seismicity.*

Keywords*: Groningen, induced seismicity, risk perception, risk communication, science outreach*

INTRODUCTION

The Groningen case is exemplary of the quest, by both the society and the scientific community, of dealing with induced seismicity. At least since the nineties, the northern Dutch province, situated on top of one of the largest gas fields in the world, is plagued by minor earthquakes, induced by the gas extraction. While at first the impact of the induced seismicity was long time played down and rather seen as a *fait divers*, everything changed on 16 August 2012. That day a minor earthquake of M3.6 rattled the region around the little village of Huizinge. This was - and still is to date - the strongest (induced) earthquake ever recorded in Groningen.

Not only the people living on top of the gas field, but also the local, regional and national policymakers, the operator (the NAM or *Nederlandse Aardolie Maatschappij*), as well as the scientific community, were all taken by surprise. What followed was a downward spiral of distrust and outrage by local communities and people afflicted by damage to their properties, not only towards policymakers but also towards the scientific community. More than 5 years later, a critical assessment can be made on how the science became progressively rather part of the problem, and in no way part of the solution.

Each case of induced seismicity is unique. No universal guidebook exists on how a society has to tackle the issue of induced seismicity. In the end, it remains a continuous learning process for all parties involved. But finally, lessons can be learned, also from the Groningen case, on how earthquake scientists should take on their societal role when confronted with induced seismicity.

THE GRONINGEN GAS FIELD

The Groningen gas field, also known as the Slochteren gas field, located in the northeastern part of the Netherlands, is one of the largest gas fields in the world. It is estimated to contain around 2900 million m^3 (bcm) of gas, of which today some 75% has been produced. After more than 50 years of production, the field is in any case close to the phase of declining production and phasing out.

The reservoir is situated at ~3 km depth in a ~350 m thick, highly permeable, Permian sandstone formation, called the Slochteren Formation, capped by Zechstein salt (de Jager & Visser, 2017). The reservoir is transected by many, predominantly normal faults that are related to a late Jurassic – early Cretaceous rifting event. The faults are to a large extend permeable to gas flow.

The Groningen gas has a high content of nitrogen (~14%), being a low calorific gas. The high dependency of this particular type of gas in the Netherlands, Belgium and Germany for household heating and cooking, makes the Groningen case not only a national problem but also an international issue with respect to future security of supply of low calorific Groningen gas to these countries.

The Groningen gas field was discovered by accident in 1959. Production started in 1963. The early seventies was characterised by a high-rate production (up to 90 bcm/year). Afterwards production was reduced up to 21 bcm/year in 2000. Production increased again up to 54 bcm/year in 2013, the year after the Huizinge earthquake. Since 2014 a systematic reduction of production has been imposed by the regulator in the hope to reduce the induced seismicity. In 2018 the Dutch government decided to definitively phase out the Groningen gas field by 2030, leaving around 10% of the gas in the reservoir. The

operator will be confronted with a stranded asset of more than 50 billion euro, and the Dutch government with a substantial loss of revenue.

INDUCED SEISMICITY

The first induced earthquake - with a magnitude of M2.4 - was recorded in 1991, nearly 30 years after production started. Due to the limitations of the seismic network at that time, it is not known whether or not seismic activity was already present before 1991 (Dost et al., 2017). The first M3.0 earthquake occurred in 2003, the first M3.5 earthquake in 2006. Seismicity rate increased significantly in 2003, seemingly unrelated to physical changes in the reservoir (Dost et al., 2017). In total more than 1200 earthquakes have been recorded since 1991 (1222 on 14 April 2018), of which 12 earthquakes had a magnitude equal or larger than M3.0 and 90 earthquakes a magnitude between M2.0 and M3.0. Nearly all seismic activity has been confined to the reservoir with hypocenters around 3 km depth. Earthquakes with magnitudes of M1.8 and higher are reported to be felt by people, while earthquakes with magnitudes of M2.0 and higher have caused non-structural damage to buildings (e.g. cracks) (de Waal et al., 2017).

While in the beginning of the Nineties the maximum expected magnitude was estimated around M3, this value was systematically raised to about M4 prior to the Huizinge earthquake and M5 after the Huizinge earthquake (de Waal et al., 2017).

It is commonly accepted that the induced earthquakes are primarily the result of the compaction of the reservoir sandstone as a consequence of depletion, causing extra stress on critically stressed faults transecting the reservoir (cf. Bourne et al., 2014). The inferred relationship between production and seismicity led to the believe that the induced seismicity is controllable.

A "DISASTER IN SLOW MOTION"

The combination of the shallow earthquakes, the compaction-related subsidence of land basically at sea level, the weakness of the water-saturated soil and soft sediments in the shallow subsurface, and the high level of fragility of the building stock, largely consisting of unreinforced masonry buildings, turned out to be an explosive mix leading to widespread and serious damage to buildings in the area on top of the gas field. Damage is not only limited to the occasional cracks in walls and floors. Entire buildings are slowly falling apart, seemingly unrelated to any individual earthquake. That's why the Groningen people perceive the progressive deterioration of their build environment as a "disaster in slow motion".

This "disaster in slow motion" has been - whether or not intentionally - mismanaged by both the operator and the authorities. People with damage to their property were confronted with a seemingly endless process, in the first place getting their damage recognized as damage caused by the gas extraction, and in the second place getting the damage repaired and/or compensated. People worried that the value of their property would drop substantially, eventually imprisoning them in an unsellable house full of cracks. This distressingly slow process resulted in a lot of frustration and outrage and an increasing weakened sense of control by the people afflicted. On top of this exhausting battle with the operator and the authorities, comes an increasing sense of insecurity. After the Huizinge earthquake a program of inspection has started to assess the earthquake risk of the buildings in the area, from public buildings such as school, to private dwellings. This inspection programme is the first step in a retrofitting programme. All of a sudden, people received assessment reports, in which they were told that they were living in a seismically unsafe house and that their house would most probably have to be seriously retrofitted or even knocked down and replaced by a newly built house. In the current retrofitting programme, a building is considered seismically unsafe if the risk is high that the building would collapse during a M5.0 earthquake, still considered the maximum possible magnitude by the KNMI (Dost et al., 2017). But because the effective retrofitting is a long-term project, people do not feel safe anymore in their own house, now considered unsafe by the experts. Each new earthquake, no matter how small, causes more distress. This sense of insecurity is furthermore maintained by the lack of effective risk and science communication, leading to an ever increasing perceived seismic risk by the people afflicted.

SCIENTIFIC RESEARCH

After the Huizinge earthquake, the scientific research efforts were boosted, primarily to support the minister of economic affairs to make an evidence-based decision on the future of the gas production in Groningen. Research focused on the relationship between the parameters of the gas extraction (e.g. volume, rate, temporal variability) and the induced seismicity. The most important question - to date still unanswered - was whether or not a "safe" production level exists. Besides a number of scientific institutes (e.g. KNMI, TNO), most of the research has been initiated and directed by the operator, the NAM. This fact alone already raised a lot of suspicion among the public, because the perception persisted from the beginning that "the butcher was inspecting his own meat". The cry for independent research only grew louder through the years. This perception was furthermore fed by politicians and activists, eventually resulting in an overall antiscientific sentiment. Scientists in general, even those not directly involved, are perceived as being "on the wrong side". This antiscientific sentiment will also contribute significantly to the science outreach failure. The extensive research programme primarily focused on the assessment of the seismic hazard and subsequently the seismic risk. Main topics dealt with, were the classical probabilistic seismic hazard assessment (PSHA), the maximum magnitude, and the risk assessment, on which eventually the entire retrofitting programme is grafted.

The scientific understanding of the induced seismicity in Groningen improved significantly since the Huizinge earthquake, but still not to the stage being able to give a conclusive answer to the question whether or not the seismicity can be controlled by managing the gas production. The uncertainties of the models are still too large to allow unambiguous advice to policymakers and transparent information to the public. Again, not being

able to foresee the end of the "seismic terror", only feeds the antiscientific sentiment and the overall distrust and outrage amongst the people afflicted.

SCIENCE OUTREACH FAILURE

In retrospect, a number of examples can be identified, illustrating the failure of the scientific community in communicating both the advances made in the scientific knowledge and the consequences with respect to seismic hazard and risk, to both the policymakers and public.

Probabilistic Seismic Hazard Assessment (PSHA)
The true meaning of a probabilistic seismic hazard map, expressing the annual probability of exceedance of a certain peak ground acceleration (PGA) is very difficult to understand for non-experts. A clear interpretation by experts is crucial. Both the KNMI and the NAM produce seismic hazard maps of the Groningen area, the former following the classical seismological approach on the basis of the (induced) earthquake record, the latter starting from a compaction-based, seismological model (Bourne et al. 2014), in which seismicity is forecast in relation to distinct production scenarios. Through the years, both seismic hazard maps have converged.

Since the Huizinge earthquake in 2012, the KNMI has produced 4 seismic hazard maps (2013, 2015, 2016, 2017). They intent to provide an update every year. All these maps show the PGA that has a 10% chance to be exceeded in a 50 year time period (475 year return period). Comparing the maps, two observations stand out, which make sense to scientists, but only feeds suspicion amongst the public. While the 2013 and 2015 maps show nice elliptical contours, the 2016 and 2017 maps show a more patchy occurrence. This remarkable change is primarily due to an improved GMPE (Ground Motion Prediction Equation), taking into account the details of the shallow subsurface in Groningen. Furthermore, in less than 4 years the highest PGA value decreased for more than 50%, from 0.42g in 2013 to 0.22g in 2017, which indeed reflects the inherently non-stationary nature of the induced seismicity.

While the latter makes perfectly sense for earthquake scientists, people perceived this stepwise decrease in PGA value as a deliberate attempt of compromised scientists to downplay the seismic risk. The situation got only worse when in 2015 the National Coordinator, who is in charge of the retrofitting programme, outlined the so-called "earthquake area" by using the 0.2g contour of the 2015 KNMI seismic hazard map. All of a sudden, this contour became a "hard" static boundary, excluding all people living outside the so-called "earthquake area" from any priority treatment with respect to the retrofitting. The absurdity of this measure quickly became apparent when earthquakes occurred outside the so-called "earthquake area". Moreover, this 2015 0.2g contour was retained in the retrofitting programme, irrespective the subsequent updates of the seismic hazard maps that made the 2015 0.2g contour completely obsolete.

With hindsight, it is incomprehensible that the scientists involved did not confront the policymakers with their misinterpretation and misuse of the seismic hazard map, only giving rise to a lot of confusion, distrust and frustration amongst the public. Although probabilistic seismic hazard maps can be of use in a retrofitting policy, when correctly interpreted, it has become clear that these maps are basically useless in communicating to the public, primarily because people have difficulty understanding probabilities and coping with all the uncertainties involved. Communicating seismic hazard and risk to public and policymakers needs a different approach. An example of such a more communicative approach in the case of induced seismicity has been developed by the USGS, i.e. the One-Year Seismic Hazard Forecast (e.g. Petersen et al., 2016).

Maximum Magnitude
The scientific discussion on the maximum expected and maximum possible magnitude, also turned out having a negative effect on the overall inflated perceived risk amongst the people in Groningen. At first, prior to the Huizinge earthquake in 2012 and the subsequent research programme, no one had any clue of what the maximum magnitude could be. Since 2012 the KNMI considers a maximum possible magnitude of M5.0 (Dost et al., 2017). In 2017 a Senior Seismic Hazard Analysis Committee (SSHAC) – commissioned by the NAM – agreed on a distribution of the M_{max}, ranging from M4.0 to M7.0, with the highest probability attributed to M4.5 and a weighted mean of M5.0 (Bommer & Van Elk, 2017), which is in line with the M_{max} of the KNMI. Zöller & Hohschneider, (2016) calculated a maximum expected magnitude ranging from M3.9 and M4.3.

While the scientists were coping with the uncertainties of their M_{max} estimates, public and policy makers got stuck on the worst-case scenario, a M5.0 "Big One". Also in the communication of the National Coordinator in the framework of the retrofitting programme, emphasis has been put on a M5.0 earthquake. This focus in the retrofitting programme results in a massive operation in which the majority of the buildings in Groningen will need a retrofitting to a certain degree (up to demolition and rebuilding). The impact of the first stages of this massive operation are becoming apparent in villages, where characteristic buildings are knocked down to be replaced by modern, earthquake-proof buildings. Realising the scale of this operation, people are starting to question the retrofitting programme. Remarkably, in the public perception, the fact that the M5.0 earthquake is part of the PSHA, is no longer interpreted as a probability, which may even never occur, but as a certainty, as the "Big One" that one day will or should happen. In this respect, science has again contributed to an inflated seismic risk perception. That both policymakers and scientist play it safe by focusing on the maximum possible instead of maximum expected magnitude, is most probably due to the large degree of uncertainty surrounding the estimates. The consequences are though major, both with respect to the retrofitting programme and the perceived seismic risk.

Transparency & Science Outreach
Both the operator and the scientific institutes take pride in full transparency with respect to the results of their scientific research. All technical reports, scientific studies, peer-reviewed publications, as well as raw data, are made available on their websites. But what is lacking, is the effort

to popularize the science, so that non-experts could understand. The lay public is basically let down. Transparency eventually backfired. By neglecting to interpret the "overload" of scientific information, reports and publications fell victim to cherry picking by non-experts, lacking the basic concepts of earthquake science. An alternative public science was created that eventually took on a life of its own, completely disconnected from the true science. New scientific insights are systematically ignored, in particular when these insights refute aspects of the alternative public science (e.g. seismic hazard, maximum magnitude). This alternative public science excels in simplicity. Moreover, it is inviting to the public by offering certainties, contrary to the true science full of uncertainties and probabilities. And by systematically overemphasizing the worst-case scenarios an "earthquake monster" emerged, only feeding the inflated seismic risk perception amongst the public. Furthermore, the danger exists that politicians, bidding for the public's favour, graft their policy on this alternative science. The scientific community contented itself with so-called transparency, but failed to build a scientifically sound public science, that enables the public to properly assess their personal risk perception, and the policy makers to take relevant decisions. Under the pretext of transparency, the scientific community only generated more suspicion and distrust.

Earthquake Preparedness

Earthquake awareness and earthquake preparedness are crucial in any attempt to keep the seismic risk perception in proportion. Moreover, it gives people a sense of control. Efforts have been made by providing online course material to elementary school in the area to raise children's earthquake awareness (aardbevingswijzer.nl). Authorities have, though, been very reluctant to organise any large-scale public awareness event, such as a ShakeOut earthquake drill, primarily out of fear to spread any panic amongst people that are already fear for the worst. Moreover, people involved are not open to such awareness initiatives, because they basically consider the earthquakes as a problem that the operator should take care of.

LESSONS LEARNED

In Groningen, science has become part of the problem, not the solution. At first, science was not prepared when the Huizinge earthquake took also the scientists by surprise. Since then the scientific community is vainly trying to catch up with events taking place in Groningen. Secondly, science has been – and still is – completely expert-led, focussing on technical and physical aspects related to the induced seismicity. And thirdly, science communication has been a one-way transfer of scientific information, basically talking above people's head.

The Groningen case is exemplary of the concept of social risk, as popularised by Sandman (1989) (Stewart & Lewis, 2017). While scientists view the seismic risk as the product of "hazard x vulnerability", people experience the seismic risk as the product of "hazard x outrage". People in Groningen are indeed outraged because of the way they are treated by the operator and the government. Irrespective of the "real" seismic hazard, people overestimate the hazard because they are outraged. In this context, trying to explain the "real" seismic hazard has little impact on the perceived social risk. Only by taking action to tackle the issues causing the public outrage (e.g. damage settlements, retrofitting), will allow to bring the perceived hazard in line with the "real" - evidence-based - seismic hazard.

The scientific community needs to decide on another risk communication strategy. The conventional "risk message model" (Demeritt & Nobert, 2014), which clearly failed in Groningen, should be replaced by a "risk dialogue model" (Stewart et al., 2017). Dialogues between scientists and public and policymakers should not focus on the "matters of fact" but on the "matters of concern" (Stewart & Lewis, 2017). These "matters of concern" could also become drivers for a bottom-up, community-led research besides the expert-led science (Stewart et al., 2017). Together with the people concerned, scientists should invest in building a public science, of which the public can claim the ownership, and the scientists guarantee the scientific validity. By applying such a participatory approach the scientists, involved in the Groningen case, would associate themselves with the Sendai Framework for Disaster Risk Reduction (SFDDR) (UNISDR, 2015).

REFERENCES

Bommer, J.J., & Van Elk, J.J., 2017. Comment on 'The maximum possible and the maximum expected earthquake magnitude for production-induced earhtquakes at the gas field in Groningen, The Netherlands' by Gert Zöller and Matthias Holschneider. *Bulletin of the Seismological Society of America* 107, 1564-1567.

Bourne, S.J., Oates, S.J., Van Elk, J., & Doornhof, D., 2014. A seismological model for earthquakes induced by fluid extraction from a subsurface reservoir. *Journal of Geophysical Research: Solid Earth* 119, 8991-9015.

de Jager, J., & Visser, C., 2017. Geology of the Groningen field - an overview. *Netherlands Journal of Geosciences* 96 (5), s3-s15.

de Waal, J.A., Muntendam-Bos, A.G., & Roest, J.P.A., 2017. From checking deterministic predictions to probabilities, scenarios and control loops for regulatory supervision. *Netherlands Journal of Geosciences* 96 (5), s17-s25.

Demeritt, D., & Nobert, S., 2014. Models of best practice in flood risk commmunication and management. *Environmental Hazards* 13 (4), 313-328.

Dost, B., Ruigrok, E., & Spetzler, J., 2017. Development of seismicity and probabilistic hazard assessment for the Groningen gas field. *Netherlands Journal of Geosciences* 96 (5), s235-s245.

Petersen, M.D, Mueller, C.S., Moschetti, M.P., Hoover, S.M., Llenos, A.L., Ellsworth, W.L., Michael, A.J., Rubinstein, J.L., McGarr, A.F., & Rukstales, K.S., 2016. Seismic-Hazard Forecast for 2016 Including Induced and Natural Earthquakes in the Central and Eastern United States. *Seismological Research Letters* 87 (6), 1327-1341. DOI: 10.1785/0220160072.

Sandman, P.M., 1989. Hazard versus outrage in the public perception of risk. In: *Effective Risk Communication* (Covello, V.T. ed). Putman Press, New York, 45-49.

Stewart, I.A., & Lewis, D., 2017. Communicating contested geoscience to the public: Moving from 'matters of fact' to 'matters of concern'. *Earth-Science Reviews* 174, 122-133.

Stewart, I.A., Ickert, J., & Lacassin, R., 2017. Communicating Seismic Risk: the Geoethical Challenges of a People-Centred, Participatory Approach. *Annals of Geophysics* 60, fast track 7.

UNISDR, 2015. The Sendai Framework for Disaster Risk Reduction 2015-2030, http://www.preventionweb.net/files/43291_sendaiframeworkfordrren.pdf.

Zöller, G., & Holschneider, M., 2016. The maximum possible and the maximum expected earthquake magnitude for production-induced earhtquakes at the gas field in Groningen, The Netherlands. *Bulletin of the Seismological Society of America*.

INQUA Focus Group Earthquake Geology and Seismic Hazards

paleoseismicity.org

The study paleoseismogenic structures of the southern part of the Khentei-Dauria dome, Mongolia

Smekalin, P. Oleg (1), Imaev, S. Valery (1,2), Chipizubov, V. Anatoly (1), Imaeva, P. Lydmila (1), Radziminovich, Natalya (1)

(1) Institute of the Earth`s crust, Russian Academy of Sciences, Lermontov St. 128, Irkutsk 664033, Russia, imaev@crust.irk.ru
(2) Diamond and Precious Metals Geology Institute, Russian Academy of Sciences, Yakutsk, Russia

Abstract: *In recent years, the Hustai, Gunji, and Kerulen paleoseismogenic structures have been discovered and examined within the Hentey uplift. Their investigations revealed zones of probable earthquake foci, presenting a seismic hazard for Ulaanbaatar - capital of Mongolian republic. We report the first data on the quantitative parameters of prehistoric earthquakes in the Meso-Cenozoic Upper Kerulen basin. The absolute age of two paleoevents determined by radiocarbon dating is within 1152-1702 BC and 5466-7201 BC. Seismogeological study of dislocations made it possible to estimate the type of tectonic stress during the formation of structures within the Hentey uplift and to explain their nature. The horizontal-compression stress is mostly due to endogenous processes, which lead to the enlargement of the uplift area at the expense of the peripheral Mesozoic sedimentary basins.*

Keywords: *paleoearthquake, active faults, Northern Mongolia*

INTRODUCTION

Since 2005, detailed seismological observations with recording of earthquakes, including M < 2 ones, have been performed in the south of the Henteyn uplift (in the areas proximal to Ulaanbaatar) (Fig. 1). The investigations have shown an uneven distribution of their epicenters in space and in time. Earthquakes are localized as isometric spots and linear zones. Recording of a series of M=4.0-4.2 earthquakes at a distance of ≤100 km from Ulaanbaatar in 2008-2009 gave grounds for a comprehensive seismogeological research. Ground works, including ones with trenching, made it possible to relate one of the distinct linear clusters of earthquake epicenters to the Emelt Fault, an outlet of an earthquake focus of Late Pleistocene age. Clustering of epicenters is also observed in the zones of the Hustai, Gunji, and some other faults with seismotectonic activity detected by remote sensing methods. The dislocations of the Emelt, Hustai, and Gunji Faults were studied in detail by a complex of seismological methods involving trenching and geophysics (Demberel et al., 2010; Ferry et al., 2010; Smekalin et al., 2013). The obtained new data on the Holocene activity of seismic processes permit the Henteyn uplift to be considered one of the largest structures assigned by Aprodov (1960) to the western (relative to 108º E) highly seismic half of Mongolia. Probably, the earlier division of Mongolia, when its highly seismic part was limited by the Hangayn uplift in the east, was the cause of the absence of seismogeological studies in the Henteyn area for decades.

In 2010, during the field studies of the Hustai Fault and analysis of the general seismotectonic pattern in the south of the Henteyn uplift, one of the researchers, A.L. Strom (Center of the Geodynamic Survey of Gidroproekt JSC, Moscow), put forward a hypothesis of the presence of traces of seismic ruptures on the northwestern flank of the Upper Kerulen basin. This hypothesis was substantiated by the identical external structural and morphologic features of the Meso–Cenozoic Tola and Upper Kerulen intermontane basins. In 2013, seismogeological investigations in the Upper Kerulen basin revealed fragments of new seismogenic ruptures in the Kerulen Fault, which were genetically similar to the earlier studied ones in the Tola basin. In this paper we present the basic results of these studies.

Seismicity of the southern part of the Eastern Siberia has been assumed to be linked to neotectonic acivity of the Baikal rift basins as well as intermountain depressions of the Mesozoic-Cenozoic age. However, this assumption does not completely correspond to regularities of the epicenter distribution at least for the Southern Transbaikal region and Northern Mongolia. According to seismicity maps for these areas, the epicenters of earthquakes with M>7 are located at the outward parts of the large-scale and long-lived (no younger than Late Paleozoic) geological structures. Among such structures the Khangai upland and Khentei-Dauria dome are distinguished. Earthquakes of their inner parts also pose a certain threat for settlements and industrial facilities, although the seismic hazard here is not so high due to much longer recurrence time for large seismic event which is a few thousand years. Such long recurrence intervals hamper revealing epicenter zones of probable earthquakes. In the past few years we carried out seismogeological investigation in the southern part of the Khentei-Dauria dome. Three paleoseismogenic structures, Hustai, Gunzhin, and Upper Kerulen, were studied by trenching and geophysical profiling. In this paper, general results of the study are described, but before the geological setting of the dome and seismicity for the instrumental observation period will be considered.

GEOLOGICAL SETTING OF THE DOME

The spatial location and boundaries of the Khentei-Dauria dome (Fig. 1) have been determined from results of rock formation analysis of sedimentary and volcanogenic layers, some features of the intrusive magmatism as well as from the

morphological structure (Komarov et al., 1980; Shatalov, 1977). The dome is one of the intracontinental orogen of longtime development resulted from a large granitoid intrusion during the Paleozoic-Mesozoic time.

The foot of the dome or its outer zone surrounds the core and consists of ridges and basins. The latter occupy a significant area of the dome being involved in the uplift. The width of the foot varies from 70 to 330 km. As for the altitude, it is mainly less than 1700 m excepting the Selenga-Orkhon interfluve area and the southwestern part of the dome nearby the Khangai upland where the highest peaks are up to 2100-2200 m respectively.

The core of the dome spatially coincides with the Khentei-Dauria upland that includes Khentei Mnt. and located to the northeast of it the Malkhansky Ridge with the southern flanks of the Chersky and Daursky Ridges. The absolute elevation of the summits exceeds 2500 m reaching up 2800 m in the Khentei. Topography of the upland is sharply dissected with more than 1000 m of the difference between the summit and basal level.

The total area of the dome is about 600,000 km2. In a plane view it looks like an ill formed ellipse with a northeastern strike of the long axis. In the west and northwest, the dome borders with the spurs of the Baikal and Khangai uplands. The area of the contact with these structures in the foot is the most seismically active part of the whole Khentei-Dauria dome (Fig. 1).

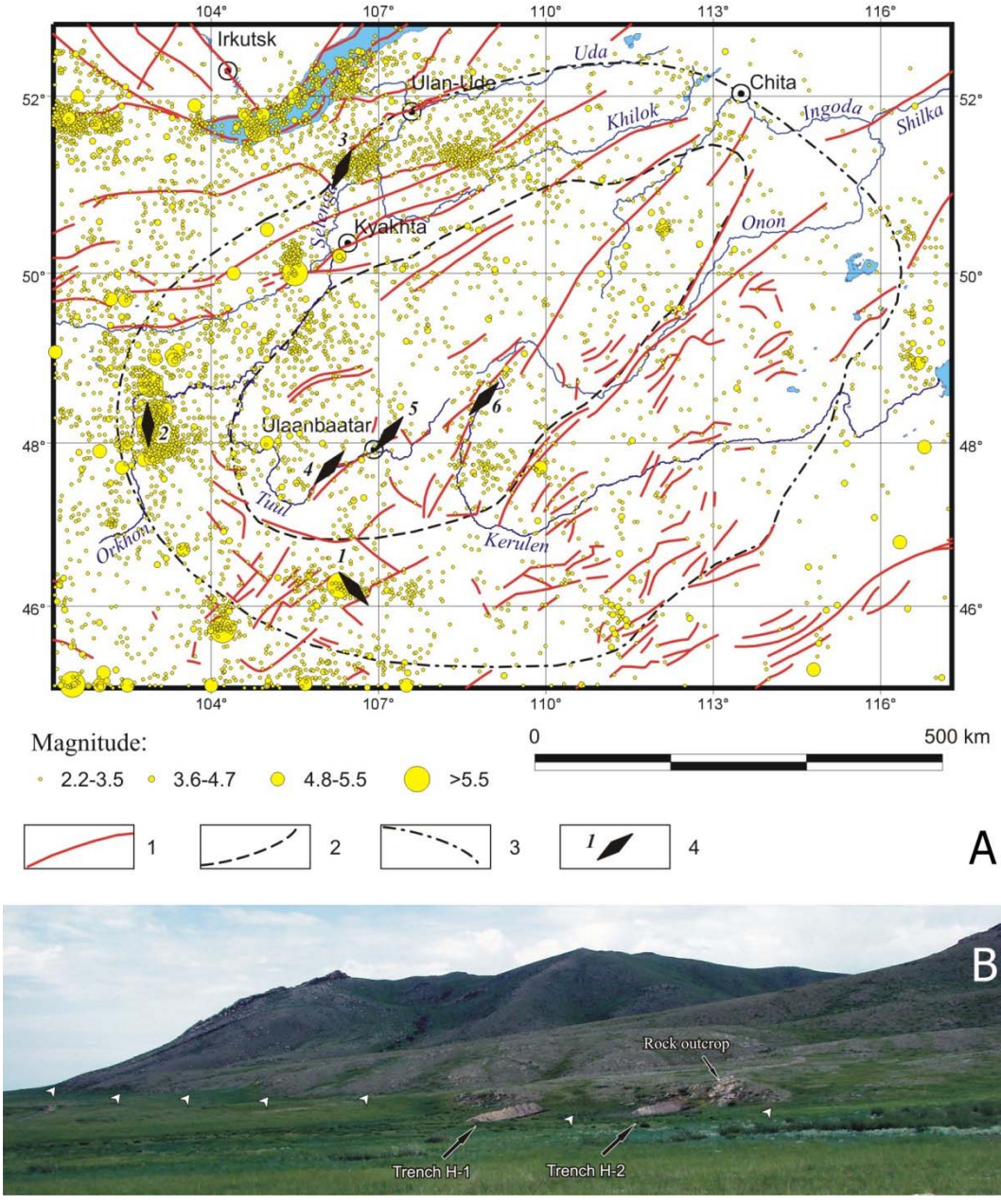

*Figure 1: **A** - Seismicity of the Khentei-Dauria dome for 1913-2014 (from the catalog of the Research Center of Astronomy and Geophysics, Ulaanbaatar Mongolia). 1 - active faults from our data and after Aprodov, 1960; 2 - the boundary between the foot and core of the dome; 3 - the outer boundary of the dome after Shatalov, 1977; 4 - numbers show location of recent and paleoseismogenic structures: 1 - Deren, 2 - Mogod, 3 - Gusinoozersk, 4 - Hustai, 5 - Gunzhin, 6 - Upper Kerulen. **B** - View of the fragment of the Hustai seismogenic structure dissected by trenches. White arrows show the fault scarp basement.*

The central part of the dome began uplifting in the Late Permian after closing the sediment basins of the Khangai-Khentei synclinorium, the rocks of which being heavily dislocated during the Hercynian tectonic cycle compose the core of the present-day dome. For the first half of the Mesozoic, the tectonic activity within the dome resulted in the highly dissected topography as evidenced by the terrigenous sediments of rift-related facies with a total thickness of 3-4 km deposited in the northern part. At the same time some small, elongated intermountain basins like the Tola one and the Upper Kerulen basin were forming mainly in the southern part of the dome. All major structures of the dome in that time, as now, had a northeastern trend. Uplifting of the dome core was against the background of granitoid intrusions. The most active magmatic process occurred in the time period from the Late Triassic to the Late Jurassic. Furthermore, effusive magmatism prevailed in the foot of the dome in contrast to its central part, so that volcanogenic and terrigenous deposits accumulated there in spite of the general uplift of the dome. Tectonic and magmatic activity has been steadily decreased since the Cretaceous (Shatalov, 1977; Yanshin, 1974). It should be noted that formation of granitoid domes and simultaneous destructive processes have largely predetermined the structure of the dome and occurrence of the tectonic events that accompany its development including the present stage. One of these features is seismicity.

EARTHQUAKE EPICENTER DISTRIBUTION

Regularities of the recent seismicity distribution within the Khentei-Dauria dome are mainly predetermined by its geological structure. The most seismically active domains are the southern, western, and northwestern foots of the dome (Fig. 1).

The specific structure and evolution of the Henteyn-Daurian dome should be taken into account on the forecast for seismic processes in its area and on their analysis. The high seismic potential of the dome base is confirmed by the presence of the epicenters of M ≥6.0-7.0 earthquakes and of studied paleoseismic structures. Low seismic activity is recorded in the southern, western, and northwestern sectors of the base (Fig. 1). The earthquakes here are caused by the appearance of new faults encircling the dome core and being often parallel to the dome borders. These faults have been active since Hercynian time and played a particular role in the formation of a net of river valleys and associated Meso-Cenozoic basins.

The number and intensity of seismic events drastically decrease along the boundary between the base and the core of the dome. The existence of this boundary is confirmed by the rounding of the core by the Mongolo-Okhotsk lineament, the most active seismic structure in southern Transbaikalia. Seismic activity in the dome base is recorded not only in the superposed fragment of the Mongolo-Okhotsk lineament but also at other sites. It is expressed, first of all, as groups of earthquakes in the epicentral zone of the 1967 M7.8 Mogod earthquake and 1998 M6.1Deren earthquake and as the epicenters of K = 11-12 earthquakes near the southeastern boundary of the dome. According to instrumental data, the core of the dome is seismically less active and favors the eastward advancement of the E-W striking seismically active structures of end Mongolia. Strong (K ≥11) earthquakes are rare here. The epicenters of weak earthquakes are randomly distributed throughout the core area, except for few clusters tracing active tectonic contacts. The small clusters of such epicenters on the southeastern and western periphery of the core mark the contours of subsided blocks expressed as the dome flanks on the structural scheme proposed by Thomson et al. (Shatalov, 1977). Some weak earthquakes are probably related to stress relaxation in cooling granitoid intrusions on the background of their isostatic “floating”. Komarov et al. (1989) believe that the constant fracturing of granitoids, their decompression, and filling of the fractures with mantle fluids are still one of the reasons for the growth of arched uplifts in northern Mongolia.

A new stage of instrumental observation of seismicity in the southern part of the Khentei dome began in 2005 for monitoring the situation in the vicinity of Ulaanbaatar, the capital of Mongolia. The local seismic station network allows recording earthquakes with magnitude as low as M 2.0. The obtained map of epicenter distribution shows its irregularity both in time and space. Epicenters are clustered in isometric spots and linear zones. As field studies confirmed, one of the most expressed in-line cluster coincides with the Emelt fault. The Hustai, Gunzhin, and Avdarul faults are also characterized by the concentration of epicenters. Some evidences of seismotectonic activity in these fault zones were revealed using remote distance methods. Trenching and subsurface geophysical exploration were performed to study the Emelt, Hustai, and Gunzhin seismogenic dislocations (Demberel et al., 2010; Ferry et al., 2010; Imaev et al., 2012; Smekalin et al., 2013, and others). The new results obtained for the seismic activity during the Holocene cast doubt on the existence of a hypothetical border that according to some researchers (Aprodov, 1960) goes approximate along 108-th longitude and separates the western seismically active part of Mongolia from the eastern one that is less active.

SEISMOGENIC STRUCTURES OF THE SOUTHERN KHENTEI UPLAND

The Hustai, Gunzhin, and Upper Kerulen seismogenic dislocations situated in the southern Khentei upland form a series within a northeast striking system of faults (Fig. 1). The northeast direction is the main trend for structures developing since the Early Paleozoic within the Khentei-Dauria dome. The Hustai and Upper Kerulen seismogenic structures are located at the sides of the Mesozoic-Cenozoic basins and succeed tectonic contacts rooted in the Middle Paleozoic era. Geological structures, folds, dykes, rock fracturing of this area are characterized by a northwestern vergence. The Gunzhin fault is considered as a segment that joins the ends of the Hustai and Upper Kerulen dislocations. The Gunzhin fault succeeds a zone of ancient contact, too; however, its recent activity stage started much later, namely, during the closing of the Tola and Upper Kerulen basins when the heavy Mesozoic sedimentation changed to forming thrusts and reverse faults at the basin sides in the Cenozoic. The development of the commissure between the Hustai and Upper Kerulen faults has been caused by elongation of the Gunzhin fault in a northeast direction. The youth of the Gunzhin fault is evidenced by its indifference to macroforms of the present-day topography.

Linkage of these three faults to the joint suture occurs under sublatitudinal near horizontal compression. The dislocations

of the faults are characterized by the common features of seismotectonic activity; first of all, it concerns kinematics. Displacements on the faults are of thrusts type with some indications of a right lateral component. This fact raises a question on a possible simultaneous rupturing all dislocations that could dramatically increase their seismic potential. The most probable variant is a simultaneous rupturing on the Gunzhin and Hustai faults. The distance between the ends of the surface ruptures of these faults is about 40 km. This interfault segment passes through the Ulaanbaatar territory and Tola valley that prevents revealing seismic dislocations if they really occurred here a few thousand years ago. However, data on the absolute age of the last ruptures of the Gunzhin and Hustai faults testify contrarily their simultaneous rupturing.

Eighteen samples from six trenches in the studied paleoseismic structures were taken for radiocarbon dating (Fig. 2). The samples are mainly humic-rich sand or clay loams whose color varies from light brown to dark brown. In the trench cross-sections of the Gunzhin and Hustai faults we revealed traces for at least two surface-rupturing paleoearthquakes (Imaev et al., 2012; Smekalin et al., 2013), but the age was estimated only for the last ones. For the Upper Kerulen structure (Fig.2) the age was constrained for the two last paleoearthquakes after four samples ^{14}C dating.

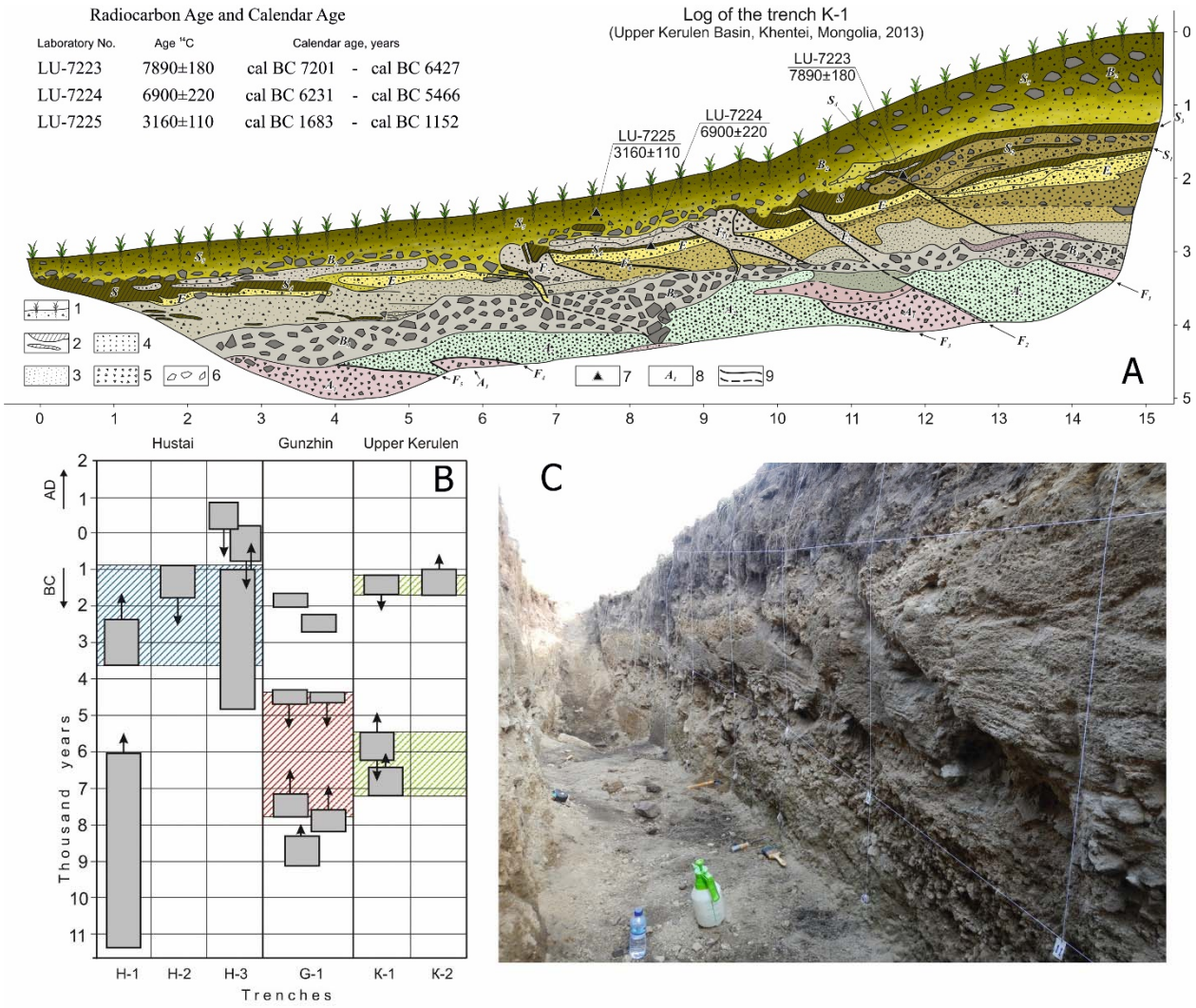

*Figure 2: **A** - Example the log of trench of upper Kerulen basin whith points of samples and paleofaults. **B** - Schematic correlation of calendar (calibrated) ages for the Southern Khentei region. The grey rectangles with arrows show the position of calibrated radiocarbon ages on the time scale. Up arrow marks the sample from the bed deformed during the earthquake, and down arrow marks the sample from the bed overlying seismogenic sediments. Area with diagonal hatching shows the interval age of the paleoearthquake. **C** - Deformations resulted from near-horizontal compression in a trench of the Upper Kerulen seismogenic structure.*

Results of morphometrical analysis, trenching, geophysical profiling, and radiocarbon dating for the Hustai, Gunzhin, and Upper Kerulen dislocations are the following. The length of the ruptures obtained using remote distance methods are 100, 20, and 100 km, correspondingly. Data from morphometry and trenching show that amplitudes of the individual vertical displacements are 2.5 m, less than 1 m, and 1.3 m, correspondingly. In addition, there are clear evidences of the right-lateral movement on the Gunzhin fault. The total amplitude of the shear displacement here estimated on a Z-bending rock-defended terrace edge in the left side of the Undulun River is 25 m. In a trench of the Gunzhin fault we found cleavage fractures with amplitude about 1 m. The dextral strike-slip movement was also evidenced by a structural paragenesis of compression arches and tensile cracks that were confirmed by geophysical data and results of trenching. New results on deformation kinematics allow estimating the maximal value of earthquake magnitude for the studied faults on the basis of an empirical relationship for reverse and strike-slip types of faults deduced by Chipizubov (1998) for platforms involved in seismotectonic activation. The maximal earthquake magnitude is 7.4 for the Hustai fault, 7.0 for the Gunzhin fault, and 7.1 for the Upper Kerulen one.

CONCLUSION

The results of our study show that in spite of the low and moderate level of recent seismicity in the inner parts of the orogenic structures of the Southern Transbaikal region there are seismogenic structures generating M>6.5 earthquakes with recurrence time of several thousand years. These structures are in form of tectonic thrusts in the sides of the Mesozoic-Cenozoic basins. The main cause of the near-horizontal tectonic compression in the Khentei upland is inversion of the vertical tectonic movements in the areas of Mesozoic sedimentation at the periphery (within the foot) of the Khentei-Dauria dome. At the latest stage of development of the former Mesozoic basins in the dome foot turned into the low and medium-altitude mountain topography. Large earthquakes both prehistorical and recorded by seismic networks (e.g., the 1967, 1998 earthquakes) accompany active tectonic processes here. Seismicity zonation of the dome is closely related to its geological setting and tectonic evolution.

Acknowledge: This work was supported by grants of Russian Science Foundation (RSF) N 15-17-20000, which was used for testing the methods of analysis and processing seismotectonical data, funded by RFBR according to the research project № 16-05-00224 and also the project of DPMGI SB RAS (N 0381-2616-0001).

REFERENCES

Aprodov, V.A., 1960. On neotectonics and seismicity of the territory of the Mongolian People's Republic. Byulleten' Soveta po Seismologii. *Voprosy Seismotektoniki Pribaikal'ya i Smezhnykh Territorii* 10, 121-133 (in Russian).

Chipizubov, A.V., 1998. Recognition of one-act and coeval paleoseismodislocations and determination of paleoearthquake magnitudes by their scales. *Russian Geology and Geophysics* 39, 3, 398-410.

Demberel, S., Batarsuren, G., Imaev, V.S., Strom, A.L., Smekalin, O.P., Chipizubov, A.V., Grib, N.N., Syas'ko, A.A., & Kachaev, A.V., 2011. Paleoseismogenous deformations around Ulaanbaatar according to geological and geophysical data. *Seismic instruments* 47 (4), 314-320.

Ferry, M., Schlupp, A., Ulzibat, M., Munschy, M., Fleury, S., Baatarsuren, G., Erdenezula, D., Munkhsaikhan, A., & Ankhtsetseg, D., 2010. Tectonic morphology of the Hustai fault (Northern Mongolia): A source of seismic hazard for the city of Ulaanbaatar. *Geophysical Research Abstracts* 12, EGU 2010-11122.

Imaev, V.S., Smekalin, O.P., Strom, A.L., Chipizubov, A.V., & Syas'ko, A.A., 2012. Seismic-hazard assessment for Ulaanbaatar (Mongolia) on the basis of seismological studies. *Russian Geology and Geophysics* 53 (9), 906-915.

Komarov, Yu.V., Logachev, N.A., & Zhamsran, M., 1980. Orogenic tectonics of Mongolia. *Geologiya I Geofizika* 9, 32-44 (in Russian).

Shatalov, E.T. (Ed.), 1977. *Metallogenic analysis in areas of tectonic activation*. Moscow, Nauka (in Russian).

Smekalin, O.P., Imaev, V.S., Chipizubov, A.V., 2013. Paleoseismic studies of the Hustai Fault zone (Northern Mongolia). *Russian Geology and Geophysics* 54, 7, 713-722.

Yanshin, A.L. (Ed.), 1974. *Tectonics of the Mongolian People`s Republik*. Moscow, Nauka (in Russian).

INQUA Focus Group Earthquake Geology and Seismic Hazards

paleoseismicity.org

Seismotectonic and potential earthquake hazard of pidie jaya and surrounding areas

Soehaimi, Asdani (1), Sopyan, Yayan (1), Sulistiyawan, R. Isnu (1)

(1) Geological Survey Institute, Geological Agency, Ministry of Energy and Mineral Resources, Jl. Diponegoro No.57 Bandung. Indonesia-40122, S.asdani@yahoo.com, yayansopyanst@gmail.com

Abstract: *Seismotectonic of the Kabupaten Pidie Jaya and surrounding areas consist of four seismotectonic zones are Central Aceh (I), Seulemeum (II), Pidie Jaya (III) and Lhokseumawe (IV). These seismotectonic zones as the seismogenetic sources of this region which are generated from the Sumatera active fault and three secondary faults are Lam Teba Baro, Tungkop and Peusang faults. These three secondary faults are the boundaries of four seismotectonic zones of this region. The Lhokseumawe destructive earthquake on April 20th, 1967 located in Lhokseumawe Seismotectonic zone IV and the Pidie Jaya Earthquake on Desember 7th, 2016 located in Seismotectonic zone III. Both of these destructive earthquakes associated with the North Sumatera Back Arc Thrusting. Probabilistic earthquake hazard analyses after Pidie earthquake December 16th, 2016 (after SNI 1726:2012), which is taking into account the north Sumatera back arc thrusting as a new seismic source, shown the Kabupaten Pidie Jaya located at the area of PGA=0,2-0,4 g (base rock/SB, 2 % p.e. 50 years)., PSA=0.45-0.75 g (base rock /SB, 2 % p.e. 50 years, in S_s period of 0.2 second) and PSA=0.25-0.40g (base rock/SB, 2 % p.e. 50 years in S_1 period of 1 second). The damaged areas during the Pidie earthquake mostly located in the coastal zone which is consist of Quaternary deposits (beach sand, floodplain, river channel, swamp and marine near shore deposits). The main cities of this region and its infrastructure located in this zone. The result of this study can be used by local government as a guidance to make low potential risk of earthquake hazard spatial planning.*

Keywords: *Seismotectonic and Potential Earthquake hazard*

INTRODUCTION

Aceh special region of Indonesia, consist of five physiographic zones are West Coastal Range, Barisan Mountains, Banda Aceh Embayment, North Coast Foothills and East Coastal Plain (Bennett et al., 1981). Kabupaten Pidie Jaya, where is the destructive earthquake on December 7th, 2016 taken please, is located in the physiographic regions of North Coast Foothills and East Coastal Plain. Those regions consist of extensive Plio-Pleistocene volcanic sediments, Plio-Pleistocene marine sediments and Holocene coastal sediments.

The settlement of this region mainly concentrated along the main roads in the coastal region. Banda Aceh as the capital city of Aceh Special Region is a main commercial and trade center. In other hand the Sigli, Pidie and Bireun cities which is connected Banda Aceh and Medan as the capital city of North Sumatera Province, develop rapidly as sizeable center.

Pidie earhquake on December 7th, 2016 which is located in the centre of this region caused 429 residences houses, 129 unit department stores, 20 mosques, 1 university campus, 1 hospital and hundred schools damaged, 103 residences perished and 700 residences injured. Total losses is about 1.854 Trillion Rupiah (Media Indonesia, 2016). Geological damaged during this earthquake are surface ruptures, liquefactions and landslides in the steep slopes of this region (Geological Agency, Ministry of Energy and Mineral Resources, 2016).

In order to understand the seismogenetic source and the potential earthquake hazard condition of this region, has been made the preliminary seismotectonic and probabilistic earthquake hazard map of Aceh. The seismotectonic map consist of the geological conditions; tectonic setting, stratigraphy and lithology, structural geology, seismicity and active faults. The probabilistic Earthquake hazard map shown the quantitative of potential earthquake hazard of this region. The result of this studies can be used by local government of Kabupaten Pidie Jaya for urban spatial planning in order to mitigate earthquake risk of this region.

REGIONAL TECTONIC

The southwest plate boundary of Sumatra is part of a long tectonic collision zone between Hindia-Australia Ocenic Plate and Europa-Asia Continental Plate that extends over 8000 km from West Papua in the east to the Himalayan front in the west. The Sumatra-Andaman portion of the collision zone, forms a subduction zone megathrust plate boundary of the Sunda-Java trench, which accommodates oblique convergence between the Hindia-Australia and Sunda plates. The oblique convergence of these plates responsible produces the Sumatera Fault zone which is intense seismicity and volcanism in back bone of Sumatra Island. The Sumatra Fault system is a major transform fault that bisects Sumatra, accommodates the northwest-increasing lateral component of relative plate motion and shown the Right Lateral Strike Slip Fault Mechanism. Continue of oblique convergence activity in western coast of Sumatera Island, also produced the North Sumatera Back Arc Thrusting in eastern coast of Aceh region. In otherwise the plate convergence of the Sunda Trench Arc System also provided the Sunda trench, Sumatera-Jawa fore arc basin and

acrasionary wedge, volcanic arc and the Sumatera Fault, Sumatera back-arc basin, Aceh back arc thrusting and Sunda platform, including Kalimantan (USGS, 2016). The correlation the tectonic setting and seismicity, shown the Aceh region can divided into three main regional seismic source zones are west Sumatera subduction seismic source zone, Sumatera active fault seismic source zone and north Sumatera back arc thrusting seismic source zone. The area of Kabupaten Pidie Jaya located in between Sumatera active fault seismic source zone and north Sumatera back arc thrusting seismic source zone (Figure 1).

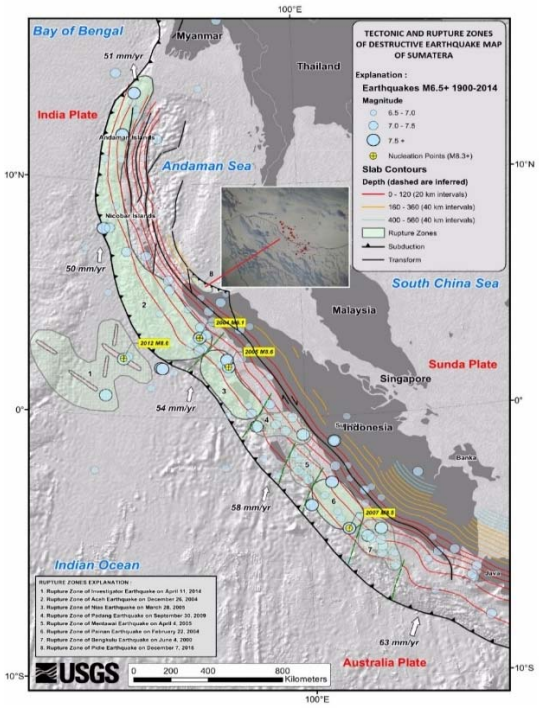

Figure 1: Tectonic Setting and rupture zones of destructive earthquake of Sumatera and Pidie earthquake on 7th December 2016 (modified from USGS, 2016).

STRATIGRAPHY AND LITHOLOGY

Stratigraphy and lithology in Kabupaten Pidie Jaya and surrounding areas belong to East of Geumpang Line (Bennett et al., 1981), from oldest to youngest are Paleozoic and Mesozoic rocks (Woyla Group) consist of slates, marbles, limestone and altered volcanics. Tertiary I, Eocene-Oligocene (Meureudu Group) consist of limestone, sandstones, siltstones, shale, mudstones and conglomerates., Tertiary II, Early-Middle Miocene (Baro Formation) consist of limestone, mudstones and calcareous siltstones. Tertiary III, Middle Miocene-Pliocene consist of calcareous sandstones and conglomerates, limestones. Tertiary III (Plio-Pleistocene) consist of calcareous sandstones and conglomerate, coral rich reef limestone. Lam Teuba and Olim Volcanics (Pleistocene-Holocene) consist of andesitic to dacitic pumiceous tuffs, breccia, agglomerate, tuff and volcanic sandstones. Pleistocene Sediment (Indrapuri Formation) consist of volcanic gravels, sand and clays. Holocene Alluvium consist of gravels, sands, silts, muds in part shelly. The intrusive rock consist of gabro-microgranite with xenolith granodiorite (42±3 m.y). The Pleistocene-Holocene lithology of this region consist of soft physical character rocks and soils. These kind of lithology are vulnerable to earthquake ground shaking.

STRUCTURAL GEOLOGY

Structural geology in Kabupaten Pidie and surrounding areas consist of layering, folding, jointing and faulting. Folding which is found at sedimentary rock in this region shown the east-west directions. The folding in this region caused by regional and local tectonic compressions. Local tectonic compression of folding found in and around regional structure geology such as Sumatera fault, Lam Teuba Baro fault, Tungkob fault and Peusang fault.

Sumatera fault as the main fault of this region travers the Barisan mountain at northwest-southeast direction and shown the right lateral strike slip fault mechanism. This fault divided into three fault segments are Aceh, Lam Teuba Baro and Tripa. There are three branching of Sumatera fault found in this region are Lam Teuba Baro, Tungkob and Peusang faults. The fault branching mainly shown the right lateral strike slip fault, some of them such as the Tungkop and Peusang fault which is shown the normal fault component. Submarine back arc thrusting in this region found in offshore area at the eastern coast line of Aceh and call as the North Sumatera back arc thrusting.

Based on the theoretical aspect of secondary fault (Cheinnery, 1965), the Lam Teuba Baro, Tungkop and Peusang faults is the secondary fault of the Sumatera Regional Fault. The pattern of these secondary fault has similarity with type A mode of secondary faulting. The similarity of this structural pattern found in Alpine fault system in New Zealand.

SEISMICITY AND INTENSITY

The seismicity of Aceh region divided into six seismic source zones are subduction megathrust and benioff seismic source zones, the Sumatera fault seismic source zone, shallow crust seismic source zone, north Sumatera back arc thrusting and magma conduit seismic source zones (Figure 2). Kabupaten Pidie and surrounding areas controlled by the subduction megathrust and benioff, Sumatera active fault (Aceh Segment), shallow crust (Lam Teuba Baro, Tungkop and Peusang fault) and north Sumatera back arc thrusting also magma vonduit seismic source zones. Historical destructive earthquakes caused the serious damaging of infrastructure and casualties in this region. Aceh Earthquake on December 24th, 2004 associated with Subduction Megathrust. Other earthquakes such as Alas Earthquake on September 19th, 1936, Blangkejeren Earthquake on November 15th, 1990 and Bener Meriah Earthquake on July 2nd, 2013 associated with Sumatera Active Fault. Lhokseumawe Earthquake on April 20th, 1967 and Pidie Earthquake on December 7th, 2016 associated with the North Sumatera Back Arc Thrusting.

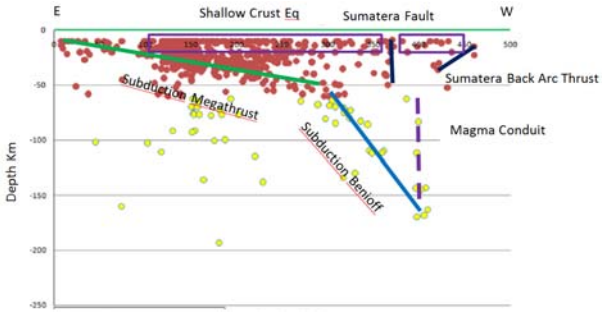

Figure 2: Vertical seismic profiling of Aceh which is shown the seismic source zones.

Base on the geological deformations and the damaging of infrastructures during these destructive earthquakes, can be estimated the maximum intensity caused by the December 24th, 2004 is VIII MMI along the western coast of Aceh between Lhokngah-Meulaboh-Singkil. To the Barisan mountainous the intensity decreasing is VI-VII MMI, in Banda Aceh the intensity increasing become VIII MMI. To the eastern coast of Aceh the intensity decreasing until IV-V MMI. Blangkejeren earthquake 1990, caused by the Sumatera Active Fault. The maximum intensity caused by this earthquake is VIII MMI in Blangkejeren city. Pidie earthquake December 7th, 2016 which is caused by the North Sumatera Back Arc Thrusting has the maximum intensity VII MMI in and around the coastal zone of Kabupaten Pidie.

SEISMOTECTONIC ZONES

Kabupaten Pidie Jaya and surrounding areas consist of four seismotectonic zones are Central Aceh Seismotectonic Zone I which is located at zone of Sumatera fault in western part of Lam Teba Baro fault; Seulemeum Seismotectonic Zone II, located in between Lam Teba Baro fault and Tungkop fault; Pidie Jaya Seismotectonic Zone III, located in between Tungkop fault and Peusang fault and Lhokseumawe Seismotectonic Zone IV, located in between Peusang fault and Lhokseumawe fault.

Central Aceh Seismotectonic Zone I, mainly cover by old rock formations (Pra Tertiary and Lower Tertiary) except northern part of this block cover by unconsolidated river terraces and volcanic rock (Pleistocene). Seulemeum Seismotectonic Zone II, cover by Tertiary Formations (Miocene-Pliocene) and volcanic rock (Pleistocene). Pidie Jaya Seismotectonic Zone III, in southern part cover by Lower-Upper Tertiary Formations (Oligocene-Pliocene) and near coastal line cover by young alluvial deposits (Pleistocene-Holocene). Lhokseumawe Seismotectonic Zone IV, mainly cover by Lower Tertiary Formation (Oligocene) and unconsolidated alluvial fan and alluvial deposits near coastal line (Pleistocene-Holocene).

There are three destructive earthquakes located and associated with Central Aceh Seismotectonic Block I are Alas Earthquake 1936, Blangkejeren Earthquake 1990 and Bener Meriah Earthquake, 2013. Pidie earthquake on December 7th, 2016 and its 89 events of aftershocks located in Pidie Jaya Seismotectonic Block III. The aftershocks in this block shown the propagation distributions from east to west (75 Km length). About 60% of aftershock epicenters distributed in offshore area and riches about 23.5 Km from shore line. Depth of aftershocks 5-15 Km and magnitude < 4.9 Mb (BMKG, 2016).

Base on the depth of main shock hypocenter and the distance of aftershocks epicenter distribution at the boundary line of fault zone, the dip of active fault estimated is 23° and incline the south direction. The main shock of the event shown thrust fault with right lateral slip component (E-W direction) focal mechanism, where is the southern block (hanging wall) move up relative to the northern block (foot wall). Lhoksemawe earthquake on April 12th, 1967 also located in Lhoksemawe Seismotectonic Zone IV). Base on the existing of seismotectonic zone and the historical of destructive earthquakes which are located in each block, shown the Seulemeum Seismotectonic Zone II did not has the historical destructive earthquake epicentres. Therefore the Seulemeum Seismotectonic Zone II is the potential of future earthquake and call as the Seismotectonic Gap Region. Preliminary Seismotectonic and Potential Earthquake hazard Maps of Kabupaten Pidie Jaya and surrounding area shown in Figure 4.

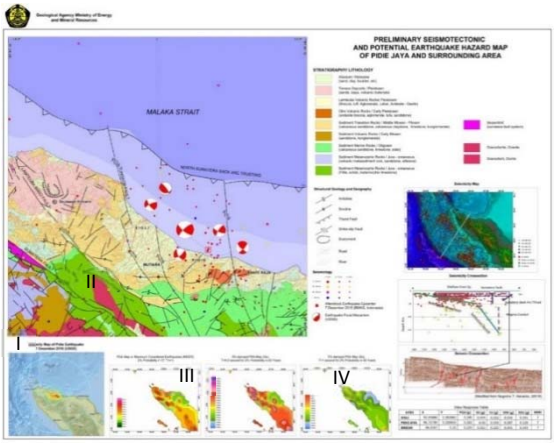

Figure 4: Seismotectonic and Potential Earthquake hazard Map of Kabupaten Pidie Jaya.

EARTHQUAKE HAZARD ASSESSMENT

Earthquake hazard assessment of this region used two approach, first is probabilistic and second deterministic. Probabilistic approach, size and likelihood of each seismic source near the site is evaluated. The estimates of earthquake hazard are base on similar attenuation relationship on the random nature of variables involved. Deterministic approach, the ground motion is derived from the largest event that can result from surrounding seismic sources. The earthquake hazard from the seismic source gets attenuated in accordance with the seismotectonic of the region and distance from the seismic source. The result obtained from these two approach are accelerations as well as the frequency content of the strong motion (SAARC Disaster Management Centre, 2011). Probabilistic earthquake hazard map of Indonesia (SNI 1726: 2012), shown the Kabupaten Pidie located at the PGA=0,3-0,4 g (base rock/SB, 2 % p.e. 50 years). PSA=0.4-0.5 g (base rock /SB, 2 % p.e. 50 years in period of 0.2 second) and PSA=0.15-0.20g (base rock/SB, 2 % p.e. 50 years in period of 1 second).

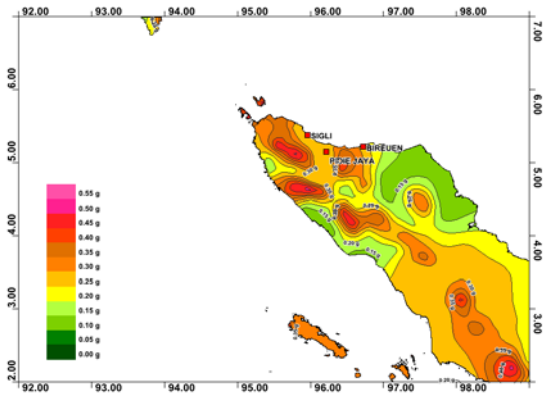

Figure 5: PGA map 2% probabilities in 50 Years.

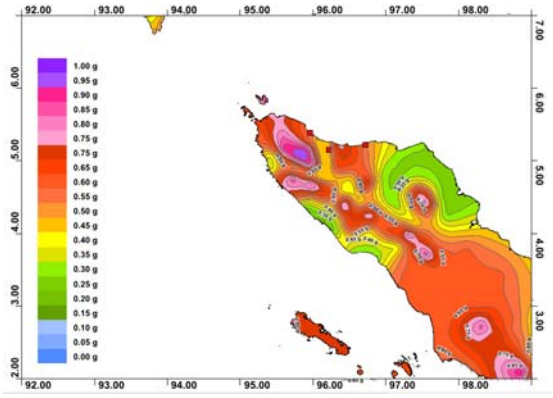

Figure 6: PSA map (Ss T=0.2 second for 2% probabilities in 50 Years).

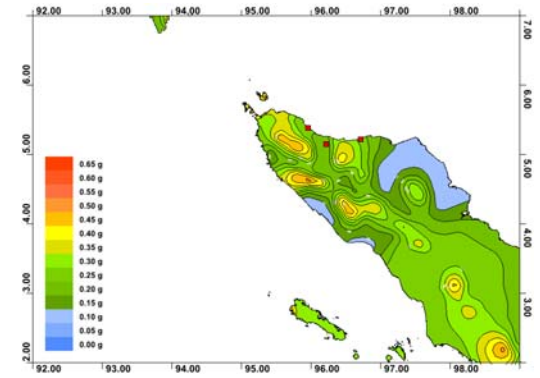

Figure 7: PSA map (S_1 T=1 second for 2% probability in 50 Years).

Seismogenetic analyses after the Pidie Earthquake December 7th, 2016, has defined a new seismic source zone is the North Sumatera Back Arc Thrusting. Based on the new founding of this seismic source, has been calculated the new earthquake hazard map of North Sumatera and Aceh Region (Soehaimi et al., 2017). The result of this analyses shown the Kabupaten Pidie located at the PGA=0,2-0,4 g (base rock/SB, 2 % p.e. 50 years). PSA=0.45-0.75 g (base rock /SB, 2 % p.e. 50 years, in S_s period of 0.2 second) and PSA=0.25-0.40 g (base rock/SB, 2 % p.e. 50 years in S_1 period of 1 second), shown in Figure 5, 6 and 7.

CONCLUSIONS

North Sumatera Back Arc Thrusting is a new seismic source in Aceh region. Consecquaences of existing this new seismic source, the regional probabilistic earthquake hazard map of Indonesia (SNI 1726: 2012) should be reanalyses, which is taking into account the new seismic source of North Sumatera back arc thrusting to probabilistic and deterministic earthquake hazard analyses. The result of reanalyses shown the PGA earthquake hazard has the same value. The PSA earthquake hazard analyses increasing 50 %.

Sumatera, Lam Teuba Baro, Tungkop and Peusang faults are the boundary of seismotectonics blocks of Aceh region. Several historical destructive earthquakes has been occurred in Seismotectonic Zone I, III and IV. There is no evidents of destructive earthquake at Seismotectonic Zone II and this zone predicted as the posibility of the next destructive earthquake of this region (seismic gap).

Damaged areas caused by December 7th, 2016 earthquake located at region of coastal plain, which is cover by Quarternary deposits. In order to mitigate the impact of heavy earthquake ground shaking of this region, need the earthquake hazard microzonation map as a guidance for region urban spatial planning.

North Sumatera Back Arc Thrusting is a tsunamigenic source, therefore early warning of tsunami hazard along the coastal zone of Kabupaten Pidie Jaya is needed.

Acknowledgements: Author wished to thanks to head of Geological Survey Institute, Geological Agency, ministry of Energy and Mineral Resources. Wished to thanks especially to all of my colleague in Quaternary Tectonic, Geomorphology and Quaternary Geology Working Groups of Geological Survey Institute, for yours discussions and contributions during I wrote this paper.

REFERENCES

Badan Geologi, KESDM, 2016. Hasil penyelidikan tim tanggap darurat gempa bumi Pidie 7 December 2016.

BMKG, 2016. Gempabumi susulan Pidie Jaya. Aceh 7 December 2016.

Badan Standardisasi Nasional, 2012. Tata cara perencanaan ketahanan gempa untuk struktur bangunan gedung dan non gedung (SNI 1726: 2012).

Chinnery, M.A., 1965. Secondary Faulting, I. Theoretical Aspect, II. Geological Aspect, *Canadian Journal of Earth Sciences* 3, 1966, 163-190.

Bennett, J.D., Bridge, DMcC., Cameron, N.R., Djunnudin, A., Gaszali, S.A., Jeffery, D.H., Kartawa, W., Keats, W., Rock, N.M.S., Thomson, S.J., & Whandoyo, R., 1981. *Peta Geologi Lembar Bandaaceh*, Sumatera, Skala 1: 250.000, Puslitbang Geologi, Terbit.

Neic USGS, 2016. M 6.5 - 19 Km SE of Sigli, Indonesia.

PVMBG, 2004. *Destructive earthquake catalogs of Indonesia*.

Soehaimi, A., & Teriyanto, 2017. Penilaian potensi bencana gempa bumi daerah Aceh, Unpub. 10 h.

SAARC Disaster Management Centre, 2011. *Seismic Microzonation: Methodology for Vulnerable Cities of South Asian Countries*, New Delhi, India, 2011, 19-20.

USGS, 2016. *Subduction and earthquake rupture zones of Sumatera.*

INQUA Focus Group Earthquake Geology and Seismic Hazards

paleoseismicity.org

Seismological analysis of the low frequencies M_w5.6 earthquake in Sofia Seismogenic zone

Solakov, Dimcho (1), Simeonova, Stela (1), Raykova, Plamena (1), Aleksandrova, Irena (1)

(1) National Institute of Geophysics, Geodesy and Geography, Bulgarian Academy of Sciences , Acad. G. Bonchev St, Bl.3. 1113 Sofia, Bulgaria, dimos@geophys.bas.bg

Abstract: *In seismically active regions of the planet, including Bulgaria, earthquakes and their consequences are the most catastrophic natural disasters. The human necessity of being protected and to respond to the earthquake disastrous consequences moves the seismological science forwards. The effects of earthquakes are function of a number of random factors ranging within broad limits, which should be adequately modelled on the basis of physical considerations, and the available seismic data. An earthquake of moment magnitude 5.6 hit Sofia seismic zone, on May 22nd, 2012. The May 2012 quake was studied using digital data from Bulgarian Seismological Network and available macroseismic information. The results indicate low frequency content of P-waves (maximum at 1.2 Hz), slow release of seismic energy and high mean value (about 280 bars) of the stress drop for S - wave.*

Keywords*: Seismicity, intensity, displacement spectra, seismic moment, stress drop*

INTRODUCTION

The territory of Bulgaria represents a typical example of high seismic risk area in the eastern part of the Balkan Peninsula. The neotectonic movement on the Balkan Peninsula are controlled by extensional collapse of the Late Alpine orogen, and were influenced by extension behind the Aegean arc and by the complicated vertical and horizontal movements in the Pannonian region. Over the centuries, Bulgaria has experienced strong earthquakes. The Sofia seismic zone (outlined by among others in Leydecker et. al, 2008) is located in southwestern Bulgaria the area with pronounced tectonic activity. The capital of Bulgaria - Sofia is situated in the center of the Sofia area that is the most populated (the population is of more than 1.5 mil. inhabitants), industrial and cultural region of Bulgaria that faces considerable earthquake risk. An M_W 5.6 earthquake occurred on May 22nd, 2012 in Sofia seismic zone characterized by a long quiescence (of about 95 years) for moderate events. Moreover, a reduced number of small earthquakes have also been registered in the recent past.

In the present study we first compiled relevant macroseismic information and estimate macroseismic effects caused by the 2012 M_w5.6 earthquake. Than analyze wave form and find spectral characteristics of the main shock and some of the strongest aftershocks. Finally, stress drop σ of the main shock and of the strongest aftershocks is estimated using Brune source model.

SEISMICITY IN THE SOFIA SEISMIC ZONE

Sofia seismogenic zone encompasses the region around the NWW-SEE trending Sofia graben. Complex tectonic faulting processes occurred in the marginal faults of Sofia graben and its surroundings. Prior to the 19th century Sofia was a small town, deeply inside the Ottoman Empire and only few reports on earthquakes felt therein could be found. The available historical documents prove the occurrence of destructive earthquakes during the 15th-18th centuries in the Sofia zone. In the 19th century the city of Sofia has experienced two strong earthquakes: the 1818 earthquake with epicentral intensity I_0= VIII–IX MSK and the 1858 earthquake with I_0=IX–X MSK. The 1858 earthquake caused heavy destruction in the town of Sofia and the appearance of thermal springs in its western part (Watzof, 1902). During the 20th century the strongest event in the vicinity of the city of Sofia was the 1917 earthquake with M_s5.3. The earthquake caused a lot of damages in the city and changed the capacity of the thermal mineral springs in Sofia and the surrounding villages (Kirov, 1952). Almost a century later (95 years after the 1917 earthquake) an earthquake of M_w5.6 hit Sofia seismic zone, on May 22nd, 2012. The earthquake is located in the vicinity of the city of Pernik at about 25 km southwest of the city of Sofia.

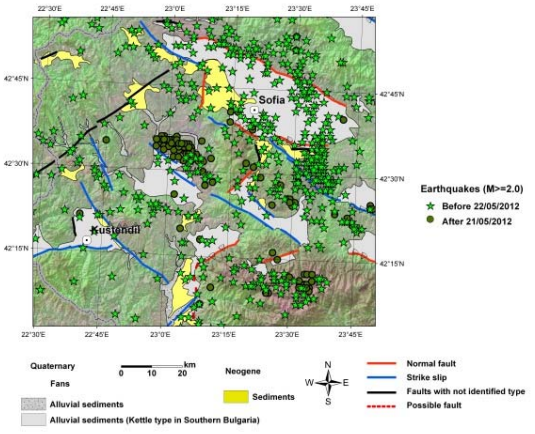

Figure 89: Spatial distribution of recent seismicity (earthquakes generated in the Sofia seismogenic zone during the period 1985-2014); with asterisks are denoted earthquakes occurred before; and with circles-events after the Mw5.6 quake.

The 2012 earthquake occurred in an area characterized by a quiescence (of 29 years) for small to moderate earthquake as it is seen in Fig.1 (Solakov et al., 2016).

The 2012 M_w5.6 earthquake was largely felt on the territory of Bulgaria and neighboring countries: northern Greece, FYROM, eastern Serbia and southern Romania (Fig. 2). No casualties and severe injuries have been reported (Simeonova et al., 2015).

Predominantly moderate (of grade2, Grunatal, 1998) to substantial (of grade 3, Grunatal, 1998) damages (as illustrated in Fig. 3) were observed in the epicentral area (in the cities of Pernik, Radomir and Sofia).

The observed seismic impacts and their consequences are indicative for slow release of accumulated seismic energy, which could be due to slow faulting.

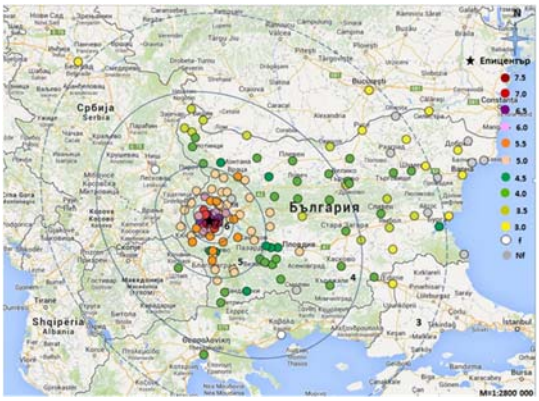

Figure 2: Intensity field of the 2012 M_w5.6 earthquake (based on My Maps Pro).

Figure 3: Damages caused by the 2012 M_w5.6 earthquake.

WAVE FORM AND SPECTRAL ANALYSIS

Wave form (a) recorded at epicentral distance of about 100 km and P wave amplitude spectrum (b) are presented in Fig. 4. The low frequency content of P-wave is well illustrated in the figure. The maxim amplitude of P wave is at 1.19 Hz (Fig. 4b).

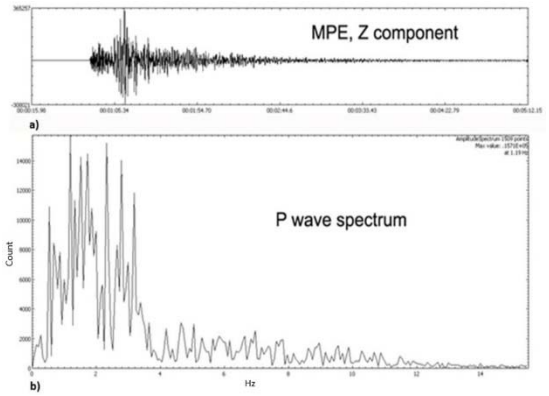

Figure 4: *Wave form (a) and Fourier velocity spectrum of P-wave (b) of the 2012 Mw5.6 quake.*

P-wave displacement spectrum for the 2012 M_w5.6 earthquake and spectra for three of the strongest aftershocks are compared in Fig. 5.

P-wave displacement spectra for the 2012 M_w5.6 earthquake (black line) and three of the strongest aftershocks (the first, M_w4.7- red line; the second m_b4.2 - rose line; and the third M_w4.5 - blue line) are shown in Fig. 5. The presented spectra are based on records at an epicentral distance of about 100 km.

The figure shows low frequency content and not expressed spectrum plateau and corner frequency for the main shock while for the two aftershocks comparatively well outline flat long period displacement spectrum (plateau between 0.7–3.0 Hz) is observed.

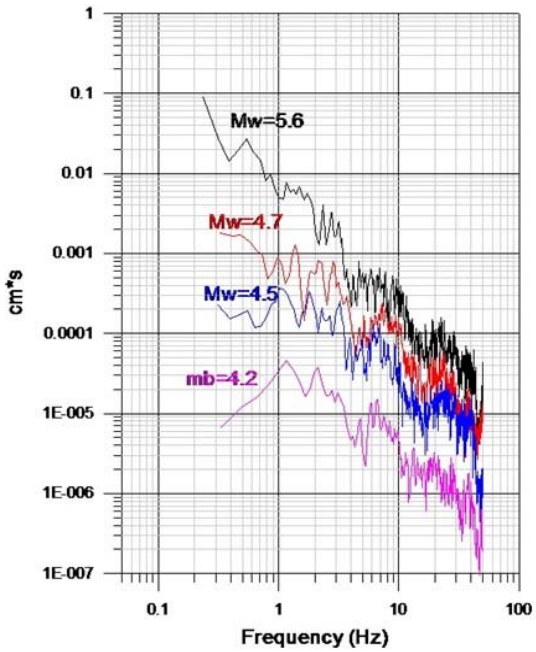

Figure 5: Displacement spectra of P wave for the main event and three of the strongest aftershocks.

The P wave displacement spectrum of the 2012 M_w5.6 earthquake could be assumed as indicative for a very low rupture velocity (Evernden & Thomson, 1985). The low rupture velocity means slow-faulting, which brings to slow release of accumulated seismic energy.

Spectral analysis of seismic waves is one of the most important origin of information for the earthquake sources.

Brune (1970) developed a powerful theory describing the nature of seismic spectrum radiated from the seismic source by considering the physical process of the energy release. The source model relates the corner frequency and low frequency asymptote to source dimension, seismic moment, moment magnitude M_w and stress drop.

For spectral characteristics, the most common seismic source model used is the Brune model. The model has been used extensively and it has been shown that it gives a good agreement with observations from many different tectonic regions and for a large range of magnitudes (see in Chen and Atkinson, 2002). The Brune model predicts the source displacement spectrum, which depends on M_0-the seismic moment, ρ-density, v-velocity at the source (P or S-velocity depending on spectrum), and f_0-corner frequency (Havskov & Ottemöller, 2010). Estimation of source parameters provides significant information for seismicity of a region. The source parameters like seismic moment, source radius, stress drop and moment magnitude of the events are computed following Brune's theory by using the corner frequency and the low frequency asymptote estimated from the spectral method.

Seismic moment M_0 is a direct measure of the tectonic size (product of rupture area time average static displacement) and therefore does not saturate. The seismic moment can be determined by moment tensor inversion or spectral analysis.

Stress drop σ is the average difference between initial and final stress along a fault after an earthquake. This is an important physical parameter associated with movement on a fault. Stress drop is generally thought to be in the range 1-100 bar.

In the present study are generated displacement spectra for P and S waves for 4 earthquakes. Then, following the model of Brune, the stress drop for the 2012 M_w5.6 main event and for three of the strongest aftershocks (the first - M_w4.7; the second m_b4.2; and the third M_w4.5) is estimated using displacement spectra.

Spectra for considered earthquakes are generated on the base of records at the stations situated at a distance of less than 200 km (more details are available in Raykova, 2017). The spectra for the main event with M_w5.6 are generated on the base of records at 14 stations. Displacement spectra for P and S waves based on records at 3 stations are presented in the Fig. 6. The results show that the estimated stress drop values for P-wave vary between 9 bars and 98 bars with mean 53 bars and for S-wave the stress drop values vary between 29 bars and 742 bars with mean 280 bars. The stress drop values estimated for P-wave are within the expected range for moderate earthquakes while for the S-wave stress drop is about 3 times higher than the expected one.

The spectra for the first aftershock with M_w4.7 are generated on the base of records at 12 stations. Displacement spectra for P and S waves based on records at 3 stations are presented in the Fig. 7.

The results show that the stress drop mean value is about 36 bars for the P-wave and approximately 19 bars for the S-wave. For both waves, the stress drop values are within the expected range for moderate earthquakes.

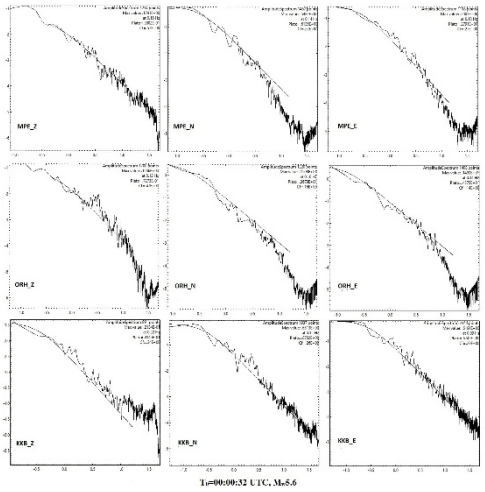

Figure 6: Displacement spectra for P (the most left column) and S waves for main event (with M_w5.6).

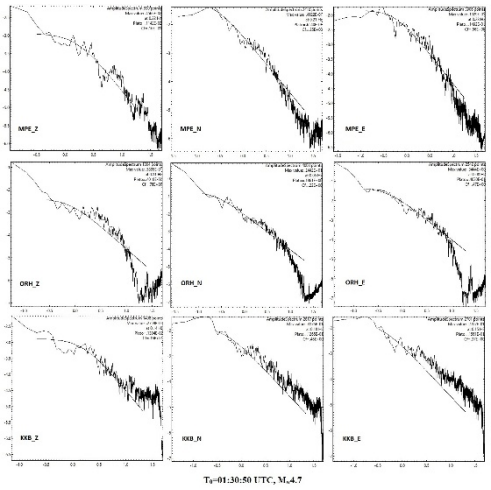

Figure 7: Displacement spectra for P (the most left column) and S waves for the M_w4.7 aftershock.

The spectra for the second mb4.2 (estimated with spectra - M_w4.2) aftershock are generated on the base of record at 11 stations. Displacement spectra for P and S waves based on records at 3 stations are presented in the Fig. 8.

The results show that the stress drop mean value is about 47 bars for the P-wave and approximately 43 bars for the S-wave. The estimated stress drop for P and S waves is within the expected range for moderate earthquakes.

The spectra for the third M_w4.5 aftershock are generated on the base of record at 12 stations. Displacement spectra for P and S waves based on records at 3 stations are presented in the Fig. 9.

The results show that the stress drop mean value is about 74 bars (ranging between 22 bars and 231 bars) for the P-wave and approximately 92 bars (ranging between 7 bars and 361 bars) for the S-wave. For both waves, the stress drop mean values are within the expected range for moderate earthquakes.

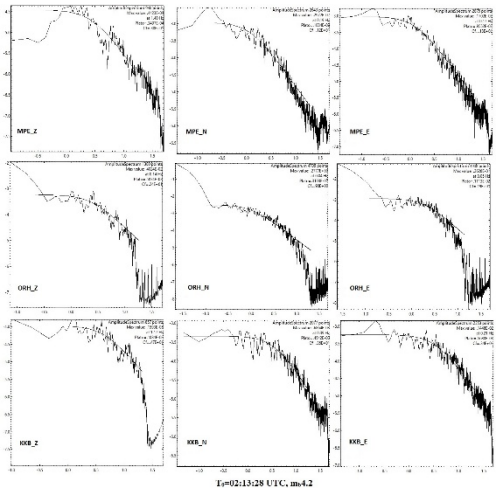

Figure 8: Displacement spectra for P (the most left column) and S waves for the m_b4.2 aftershock.

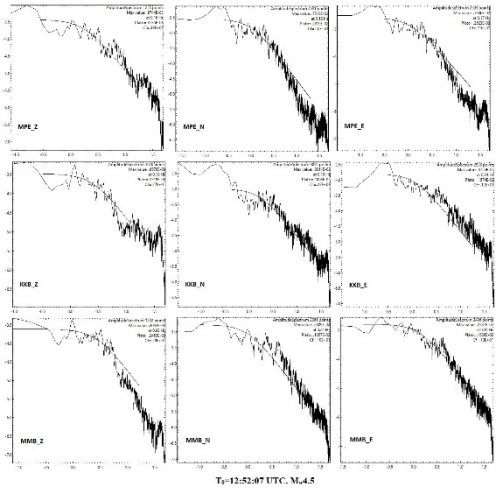

Figure 9: Displacement spectra for P (the most left column) and S waves for the M_w4.5 aftershock.

CONCLUSIONS

On the basis of the analysis the following conclusions can be drawn:

(1) The 2012 M_w5.6 earthquake occurred in the area characterized by 26 years quiescence for small to moderate earthquake;

(2) The quake was largely felt on the territory of Bulgaria and neighbouring countries. No casualties and severe injuries have been reported. Predominantly moderate to substantial damages are observed;

(3) The Mw5.6 earthquake wave form and P wave amplitude spectrum show low frequency content with maximum at 1.2 Hz;

(4) The specific P wave displacement spectral of the 2012 Mw5.6 quake could be assumed as indicative for a very low rupture velocity. The low rupture velocity means slow-faulting, which brings to slow release of accumulated seismic energy;

(5) For 2012 Mw5.6 earthquake the stress drop (about 53 bars) estimated for P- waves is within the expected range for moderate earthquake while for the S-waves (approximately 280 bars) is about 3 times higher than the expected one;

(6) The stress drop values estimated for P and S waves for aftershocks are within the expected range for moderate earthquake.

REFERENCES

Brune, J., 1970. Tectonic stress and the spectra of seismic shear waves from earthquakes, *J. Geophys. Res*. 75, 4997-5009.

Brune, J.N., 1971. Correction (to Brune (1970)), *J. Geophys. Res*. 76, 5002.

Chen, S., & Atkinson, G.M., 2002. Global comparison of earthquake source spectra. *Bull. Seism.Soc. Am*. 92, 885-895.

Evernden, J.F., & Thomson, J.M., 1985. Earthquake hazards in the Los Angeles region- An Earth - Science Perspective, Edt. J.I.Ziony. U.S.G.S. Prof. Paper, 1360, U.S. Gov. Print. Office, Wash., 151-201.

Grünthal, G., edit., 1998. *European Macroseismic Scale*. Conseil de L`Europe, 15, Luxembourg, pp. 99.

Havskov, & Ottemöller, 2010. Routine Data Processing in Earthquake Seismology. ISBN 978-90-481-8696-9, doi 10.1007/978-90-481-8697-6, Springer Dordrecht Heidelberg London New York, 245-282.

Ivanov, J., Nakov, R., Gerdzikov, Y., Radulov, A., 2008. Part 6 Geology. In: *Report Geoph. Ist*.(BAS, S. ed.), (fund NIGGG), 80-113 (in Bulgarian).

Kirov, K., 1952. Contribution to study of earthquakes in Sofia region, *Ann. Main Dep. Geol. and Mining Res*. 5, 407-440.

Leydecker, G., Busche, H., Bonjer, K. P., Schmitt, T., Kaiser, D, Simeonova, S., Solakov, D., & Ardeleanu, L., 2008. Seismic hazard maps for Bulgaria and Romania, *Nat. Haz. Earth Syst. Sci*. 8, 1431-1439.

Raykova, P., 2017. Characteristics of foreshocks, aftershocks and swarm type activity for the territory of Bulgaria and its surroundings, 47 (in bulgarian).

Simeonova, S., Solakov, D., Aleksandrova, I., Raykova, P., & Protopopova, V., 2015. The 2012 Mw5.6 earthquake in Sofia seismic zone and some characteristics of the aftershock sequence. *Bulg. Chem. Comm*. 47, spec. issue B, 397-404.

Solakov, D., Simeonova, S., Raykova, P., Aleksandrova, I., Popova, M., & Protopopova, V., 2016. Seismological Analysis of the 2012 M_W5.6 Earthquake in Sofia Seismic Zone. *Comptes rendus de l'Acad´emie bulgare des Sciences* 69, 1, 67-74.

Watzof, S., 1902. *Earthdquakes in Bulgaria during XIX century, Central Meteor*. St., Imprimerie de I'Etat, Sofia, pp. 93.

INQUA Focus Group Earthquake Geology and Seismic Hazards

paleoseismicity.org

Morphotectonic analysis of Northern Evoikos Gulf

Stefa, Elisavet (1), Nomikou, Paraskevi (1), Lozios, Stelios (1), Antoniou, Varvara (1), Skolidis, Antonis (1), Papoulia, Joanna (2)

(1) National and Kapodistrian University of Athens, Department of Geology and Geoenvironment, Panepistimioupoli Zografou, 15784 Athens, Greece, stefael@geol.uoa.gr
(2) Institute of Oceanography, Hellenic Centre for Marine Research, POBox 712, 19013 Anavyssos, Greece

Abstract: *Northern Evoikos Gulf (NEG) represents an NW-SE elongate active marine basin, between Central Greece and Northern Evia Island. Along the NW-SE long axis of the basin, three distinct basins can be distinguished: the western E-W sub-basin and the south-eastern NW-SE sub-basin, both shallow and flat and the central WNW-ESE deep and asymmetric sub-basin between them. The active seafloor processes, like submarine sliding, erosions, asymmetric sediment deposition, creation of submarine canyons, which diverge in some cases, and the submarine faults define the accumulation of tectonic activity inside the Gulf and coincide with the off-shore neotectonics structures and faults observing on the NE very steep margin of the gulf (along the SW coast of Northern Evia) and the SW normal shelf shaped margin, (along the NE coast of Central Greece).*

Keywords*: Swath bathymetry, Sea bed morphology, Northern Evoikos Gulf, tectonics, Neotectonic Basin*

INTRODUCTION

Northern Evoikos Gulf (NEG) belongs to the central part of the NE-SW transtensional dextral shear zone, bounding the northwestern edge of the Aegean block, known as Central Hellenic Shear Zone (Papanikolaou & Royden, 2007). This tectonically active zone extends from the western prolongation of North Anatolian Fault (NAF) in Northern Aegean Sea to the northern limit of the Hellenic trench and the offshore Cephalonia Transform (Kahle et al., 2000; McClusky et al., 2000; Goldsworthy et al., 2002), crossing the mainland Greece where a system of sub-parallel WNW-ESE basins occur, like the Gulf of Corinth, the onshore basins of Viotikos and Lokris and the NEG (Fig.1).

GPS measurements for central Greece (Biliris et al., 1991) revealed an extensional rate of approx. 1 cm/yr. Crustal studies (Makris & Vees, 1977; Makris et al., 2001) showed that thickness of the continental crust changes rapidly from 30 km onshore Northern Evia to only 19 km below the central part of NEG. In historical times the broader area of NEG experienced strong earthquakes, mostly associated with the Atalanti fault zone (Skouphos, 1894; Papazachos & Papazachou, 1997). The present deformation of NEG however is characterized by moderate seismic activity (e.g. Papazachos & Papazachou, op cited), whereas local seismic arrays (Burton et al., 1991; Papoulia et al., 2006) do not reveal any seismic activity associated with the Atalanti fault zone. The lack of major seismic events is probably due to the successive change of stress field orientation between the NAF and the Gulf of Corinth, resulting to crust fragmentation in relatively small units and fault systems not permitting the generation of strong earthquakes in NEG and surrounding region (Papoulia et al., 2006).The submarine topography of the Gulf is of relatively shallow depth, not exceeding 50m, increasing to 460 m below the central part of the Basin. Recent volcanic rocks are observed in the vicinity of Lichades Island, at the junction of the Northern Evoikos and Maliakos Gulfs.

METHODOLOGY

The multi-beam bathymetric survey presented was carried out in January 2004, in the frame of the "AMPHITRITE" project, with the R/V "AEGAEO" of the Hellenic Centre for Marine Research (HCMR). We used the 'SEABEAM 2120' swath system, which is a fully mounted system operating at 20 kHz at water depths not exceeding 5000 m. The system has an angular coverage sector of 150 degrees with 149 beams, covering a swath width from 7.5 to 11.5 times the water depth for depths of 1 to 5 km, respectively. The maximum swath coverage can reach 9 km at maximum depth and gives a satisfactory data quality with vessel speed up to 10 knots. During this mission, in 4 days, a total track length of 872 km with an average vessel speed of 10.8 knots was surveyed. The total area mapped was about 500 km^2 and the maximum coverage area reached 2 km. The multibeam data were extensively processed by means of data editing, cleaning of erroneous beams, filtering of noise, processing of navigation data and interpolation of missing beams. The maps (2D and 3D) created and presented in this paper were edited through ArcGIS Pro v.2.1 software.

SWATH BATHYMETRY

The resulting slope-shaded bathymetric map was originally compiled at 1:150.000 scale with different colors corresponding to 50 m depth intervals (Fig.1). This map permits the first detailed description of the overall topography of the sea floor as well as the mapping of the major morphotectonic structures within this area.

Along the NW-SE long axis of the Basin, three distinct basins can be distinguished: the western E-W sub-basin (WB) and the south-eastern NW-SE sub-basin (SEB), both shallow and flat, and the central WNW-ESE deep and asymmetric sub-basin (CB) between them (Fig.1). The central basin reaches 460 m depth and it is a wide flat area forming an extensive NW-SE elongated graben.

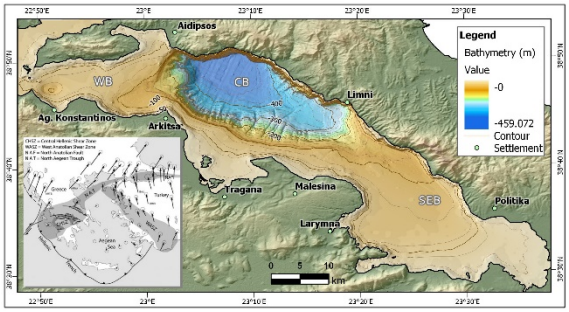

Figure 1: Bathymetric Map of Northern Evoikos Gulf. The relative position of Northern Evoikos within the Central Hellenic Shear Zone (CHSZ) appears in the small scheme from Papanikolaou & Royden (2007).

The continental platform is developed mainly in the southern and western slopes of the Gulf and its depth spans from 80 to 120 m, being the widest at its NW and SE sections. However, the continental platform is absent from the abrupt slopes of the western coast of northern Evia, from Aidipsos up to Limni. This absence is presumably justified by the existence of marginal faults of approximately NW-SE direction along the SE coast and almost E-W along the NW coast, which creates the abrupt slopes.

The southern margin of the NEG, between 150 and 400 m water depth, is scored by numerous small canyons trending NE-SW transversal to the main direction of the Gulf (Fig. 1). In contrast, the northern margin is very steep creating the northern border of the central Basin. The canyons can be categorized into three groups (Fig. 2 & 3): i) the first group is located north of the cape of Theologos, at depths between 150 and 350 m. This group is composed by four elongated-shaped canyons that flow from SSW to the Basin. Counting from east to west, the first canyon is up to 3 km long. Its altitude difference is around 150 m and its width is between 200 and 300 m. The second and the third canyons' altitude difference is up to 200 m, having a length of 6 km and width around 300 m. The fourth canyon's altitude difference is 250 m, its length 4.5 km and width 350 - 550 m on the top of the slope; ii) The second group is located east of the cape Arkitsa and flows from NW to the main Basin. These canyons are shorter than the canyons of the first group, approximately 2 km the easternmost to 3 km the westernmost. Their altitude difference is 200 m and their width varies from 200 to 400 m on the top of the slope; iii) The third group is located south of Aidipsos and flows from west to the main Basin, at depths between 150 and 400 m. These canyons' length is around 2.5 km and their width are 600 m.

The canyons are developed in most of the continental shelf and they do not constitute a continuation of the land river network. The reason of their existence is the morphological discontinuity at the depth of 150 m (Nomikou, 2006).

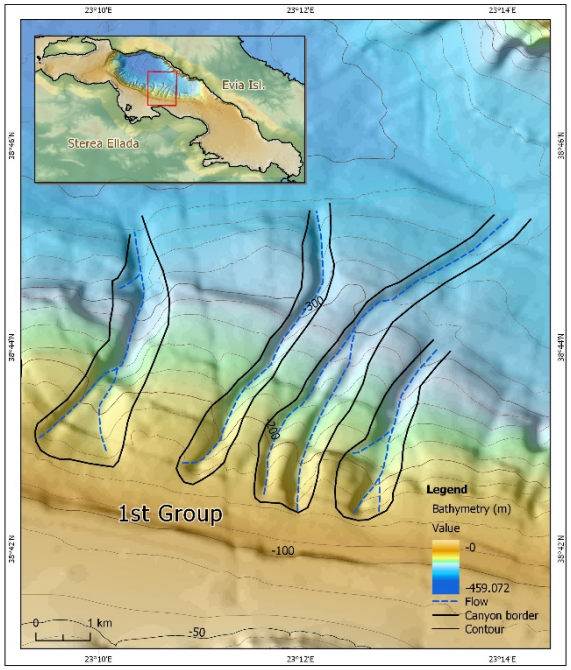

Figure 2: Bathymetric map of the eastern submarine canyons (first group).

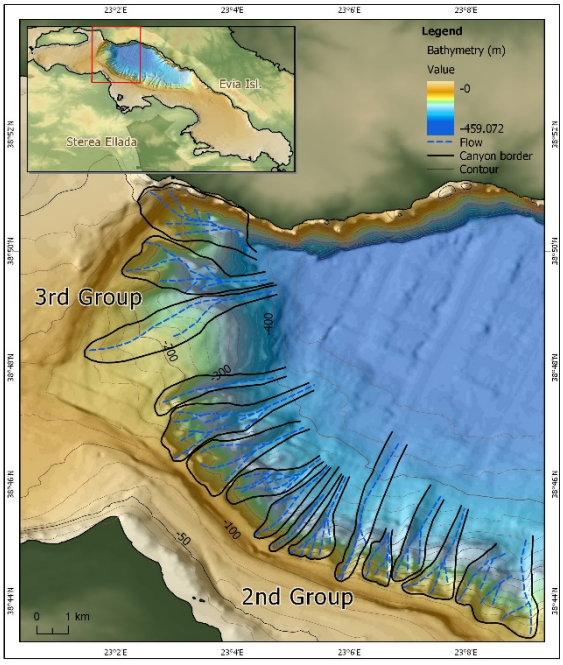

Figure 3: Bathymetric map of the western submarine canyons (second and third groups).

MORHOLOGICAL ANALYSIS

The slope distribution map shows the distribution of slope values within the study area distinguished in six categories: (1) areas of mean morphological slope 0-1%, (2) areas of 1-3%, (3) areas of 3-6%, (4) areas of 6-12%, (5) areas of 12-20% and (6) areas >20%. This classification of the slope magnitude will illustrate the zones where there is an

abrupt change of slope, reflecting possible positions of active tectonic zones in contrast with zones with negligible change of slope, which reflect flat-lying areas such as submarine terraces or basinal areas. The areas with slope value >20% cover only 5% of the overall Basin and reflect the abrupt scarp zones at the NE part of the Gulf, which are probably controlled by active fault tectonics.

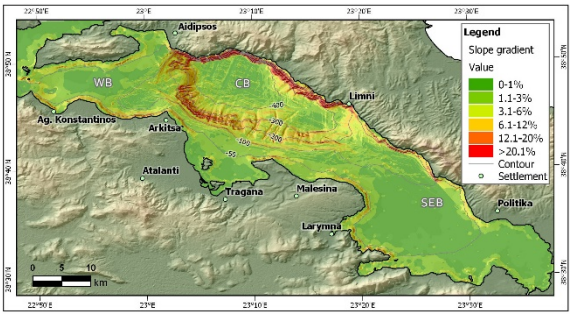

Figure 4: Slope distribution Map of Northern Evoikos Gulf.

DISCUSSION

The NE margin and coastline of NEG is characterized by very steep slopes (both onshore and offshore), which coincide with fault zones, mainly offshore. Three major fault zones can be distinguished from ESE to WNW (Fig. 5) the NW-SE Kandili FZ, the WNW-ESE Telethrion FZ and the E-W Aidipsos and Lichada FZ (Galanakis et al., 1988; Palyvos et al., 2006; Tzanis et al., 2010). In contrast, the SW boundary of NEG is far more inland and normal shelf shaped. This is more complicated and comprises major E-W to WNW-ESE faults and fault zones (like the well-known Atalanti, Malesina, Arkitsa, Melidoni, Agios Konstantinios and Kamena Vourla FZ) that control the first order neotectonic macro-structures of the area. The fault segments arranged en echelon or relay and usually they are overlapping or hard-linked (Tzanis et al., 2010). NE-SW or ENE-WSW transverse or oblique faults and fault zones also occur (Fig. 5), mainly representing transfer zones between the major E-W neotectonic structures (Pavlides et al., 2004; Tzanis et al., 2010) or representing structures that accommodate deformation within a broad NE-SW shear zone that incorporates significant amount of strike-slip deformation and may thus be related to the propagation and diffusion of the North Anatolian and North Aegean fault systems into the Greek mainland (Goldsworthy et al., 2002; Papanikolaou & Royden, 2007; Tzanis et al., 2010).

Preliminary results for the tectono-sedimentary structure of NAG (Sakellariou et al., 2007) shows the existence of three distinct basins (Fig. 5). The shallow E-W striking "western basin" displays southward asymmetry that coincides with the major Kamena Vourla and Arkitsa fault zones at the southern boundary instead of the minor Lichas fault at the northern one. The WNW-ESE striking deep "central basin" show NE-ward asymmetry and is controlled by the marginal Telethrion FZ, which has accommodated a cumulative throw more than 1 km. The NW-SE shallow and flat "southeastern basin" is characterized by a NW-SE morphological long axis and a major fault zone (known as Melouna FZ, Sakellariou et al., 2007) appears along the axis, in the middle of the Basin, separating two parallel sub-basins. The NE one displays a NE-ward asymmetry (similar to the central Basin) and is controlled by the NW-SE marginal Kandili FZ. For the SW sub-basin, the seismic profiles do not reveal any significant fault to the SW margin, although the transition from the sub-basin to the uplifted Malesina peninsula is rather abrupt.

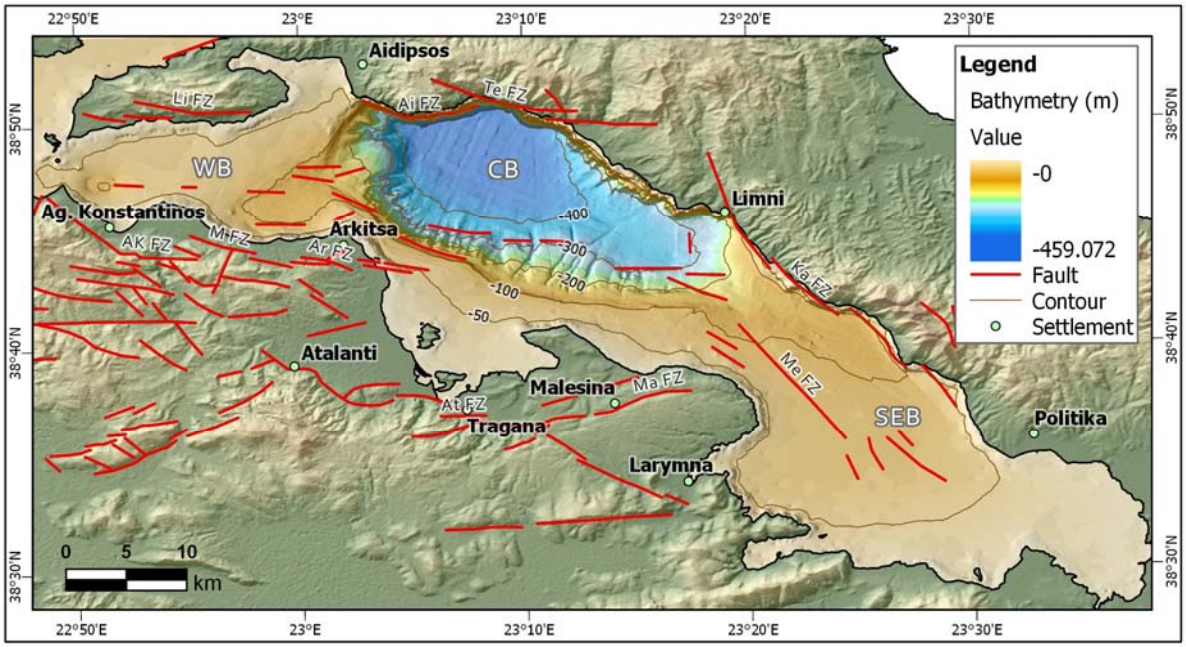

Figure 5: Simplified neotectonic map of Northern Evoikos Gulf. WB: Western Basin; CB: Central Basin; SEB: Southeastern Basin; Ka FZ: Kandili FZ; Ai FZ: Aidipsos FZ; Li FZ: Lichada FZ; AK FZ: Agios Konstantinos FZ; M FZ: Melidoni FZ; Ar FZ: Arkitsa FZ; At FZ: Atalanti FZ; Ma FZ: Malesina FZ; Me FZ: Melouna FZ (Data from Palyvos et al., 2006; Sakellariou et al., 2007 and Tzanis et al., 2010).

CONCLUSIONS

The swath bathymetric survey of the NEG provides insight into morphological expression of the active seafloor processes, like faulting and submarine sliding, erosions and sediment deposition and enables detailed mapping of the offshore structural elements. Canyons prevail the southern margin but are rare on the northern margin of the Gulf. The Basin floor reaches a maximum depth of 460m towards the north. The overall morphology of the sea bottom is controlled by major faults, forming a fault zone in the NE part of the Gulf, and a slope discontinuity, which is located in the SW part of the Gulf (Fig. 4). The creation of the canyons possibly coincides with the accumulation of tectonic activity inside the Gulf and it is revealed by the abrupt change of the slope. Our argument is also strengthened by the fact that a couple of canyons have diverged due to tectonic activity.

Acknowledgements: AMPHITRITE Project was financed by the General Secretariat for Research and Technology of Greece, Community Support Framework III Operational Program.

REFERENCES

Biliris, K., Paradisis, D., Veis, G., England, P., Featherstone, W., Parson, B., Cross, P., Rands, P., Rayson, M., Sellers, P., Ashkenazi, V., Davison, M., Jackson, J., & Ambraseys, N., 1991. Geodetic determination of tectonic deformation in central Greece from 1900 to 1988. *Nature 350*, 124-129.

Burton, P.W., Makropoulos, C., McGonigle, R.W., Ritchie, M.E.A., Main, I.G., Kouskouna, V., & Drakopoulos, J., 1991. Contemporary seismicity in eastern Greece from the Volos netwotk (VOLNET): Fault parameters of major and minor earthquakes. *Brit. Geol. Surv*., Seismology Series, Report WL/91/29, pp. 106.

Galanakis, D., Pavlides, S., & Mountrakis, D., 1998. Recent brittle tectonic in Almyros, Pagasitikos, Maliakos, N. Euboea and Pilio (in Greek). *Bull. of the Geol. Soc. of Greece* XXXII/1, 263-273.

Goldsworthy, M., Jackson, J., & Haines, J., 2002. The continuity of active fault systems in Greece. *Geophys. J. Int*. 148, 596-618.

Kahle, H.-G., Cocard, M., Peter, Y., Geiger, A., Reilinger, R., Barka, A., & Veis, G., 2000. GPS derived strain rate field within the boundary zones of the Eurasian, African and Arabian plates. *J. Geophys. Res.* 105 (23), 353-23, 370.

Makris, J., & Vees, R., 1977. Crustal structure of the Aegean Sea and the Islands of Evia and Crete, Greece, obtained by refraction seismic measurements. *J. Geophys.* 42*,* 329-341.

Makris, J., Papoulia, J., Papanikolaou, D., & Stavrakakis, G., 2001. Thinned continental crust below northern Evoikos Gulf, central Greece, detected from deep seismic soundings. *Tectonophysics* 341, 225-236.

McClusky, S. C., et al., 2000. Global Positioning System constraints on plate kinematics and dynamics in the eastern Mediterranean and Caucasus. *J. Geophys. Res.* 105, 5695-5719.

Nomikou, P., Alexandri, M., Ballas, P., & Papoulia, J., Morphological analysis of the northern evoikos gulf, 8th Panhellenic Symposium on Oceanography and Fisheries, pp. 679-682.

Palyvos, N., Bantekas, I., & Kranis, H., 2006. Transverse fault zones of subtle geomorphic signature in northern Evia Island (central Greece extensional province): An introduction to the Quaternary Nileas graben. *Geomorphology* 76, 363-374.

Papanikolaou, D.J., & Royden, L.H., 2007. Disruption of the Hellenic arc: Late Miocene extensional detachment faults and steep Pliocene-Quaternary normal faults-Or what happened at Corinth? *Tectonics* 26, TC5003, doi: 10.1029/2006TC002007.

Papazachos, B., & Papazachou, C., 1997. *The Earthquakes of Greece*. Ziti, Thessaloniki, pp. 304.

Papoulia, J., Makris, J., & Drakopoulou, V., 2006. Local seismic array observations at north Evoikos, central Greece, delineate crustal deformation between the North Aegean Trough and Corinthiakos Rift. *Tectonophysics* 423, 97-106.

Pavlides, S., Valkaniotis, S., Ganas, A., Keramydas, D., & Sboras, S., 2004. The Atalanti active fault: Re-evaluation using new geological data. *Bull. of the Geol. Soc. of Greece* XXXVI, 1560-1567.

Sakellariou, D., Rousakis, G., Kaberi, H., Kapsimalis, V., Georgiou, P., Kanellopoulos, Th., & Lykousis, V., 2007. Tectono - sedimentary structure and Late quaternary evolution of the north Evia Gulf basin, central Greece: Preliminary results. *Bull. of the Geol. Soc. of Greece* XXXVII, 451-462.

Skouphos, Th., 1894. Two major earthquakes in Lokris on 8/20 and 15/27 April 1894. *Zeit d. Ges. Erdkunde zu Berlin* 24, 409-474 (in German).

Tzanis, A., Kranis, H., & Chailas, S., 2010. An investigation of the active tectonics in central-eastern mainland Greece with imaging and decomposition of topographic and aeromagnetic data. *Journal of Geodynamics* 49 (2), 55-67.

INQUA Focus Group Earthquake Geology and Seismic Hazards

paleoseismicity.org

Neotectonic activity reflected in morphology along the Mariánské Lázně fault and in the adjacent Cheb basin (Bohemian Massif, central Europe)

Štěpančíková, Petra (1), Flašar, Jan (1, 2), Stemberk, Jakub (1), Balatka, Břetislav (2), Kalvoda, Jan (2), Sana, Hamid (1)

(1) Institute of Rock structure and Mechanics, Czech Academy of Sciences, V Holesovickach 41, 18209 Prague 8 Czech Republic, stepancikova@irsm.cas.cz
(2) Faculty of Science, Charles University, Albertov 6, 12843 Prague 2, Czech Republic

Abstract: *The Mariánské Lázně fault (MLF) is a NW-SE striking structure in western Bohemian Massif (Czech Republic), which controls the eastern limit of the Cheb-Domažlice graben at the length exceeding 100 km. To study neotetconic activity of the MLF, we analyzed the related fault scarp and longitudinal river profiles and SL indices of the streams crossing the MLF to identify knickpoints and other anomalies potentially related to activity of the MLF. In addition, we have used morphometric indices such as hypsometric curves, basin elongation ratio, topographic asymmetry, etc. in the Cheb basin to determine whether tectonic or erosional processes have played a dominant role in the development of landscape. Moreover, we mapped and classified the Ohře River Pleistocene terraces within the Cheb basin which appeared to be displaced by the MLF.*

Keywords*: morphotectonics, longitudinal river profiles, fluvial terraces, Mariánské Lázně Fault, Bohemian Massif*

INTRODUCTION

The Mariánské Lázně fault (MLF) is a NW-SE striking, morphologically pronounced structure in western Bohemian Massif (western Czech Republic), which controls the eastern limit of the Cheb-Domažlice graben at the length of about 100 km (Fig. 1). The northern segment of the MLF limits the western mountain front of the Krušné hory Mts towards the eastern limit of the Cenozoic Cheb basin. The Cheb basin is a half-graben filled with Oligocene to Plio-Pleistocene fluvio-lacustrine sediments and volcanoclastics and is famous for Quaternary volcanism, present-day earthquake swarm seismicity (max. ML=4.6) and mantle-derived CO_2 emanations. Moreover, Holocene surface rupturing earthquakes have been recognized recently from in geological record (Štěpančíková et al., 2018). The Cheb basin is superimposed on the western part of the NE-SW trending Eger (Ohře) Rift, the major tectonosedimentary feature of Central Europe, which is an element of European Cenozoic Rift Systems in the Alpine forelands. The Eger Rift is a system of Cenozoic sedimentary basins, high heat flow and voluminous alkaline intraplate volcanism (Malkovský, 1987; Ziegler, 1992; Dezés et al., 2004; Ziegler & Dezés, 2007; Ulrych et al., 2016).

METHODS

In order to identify the trace of the MLF and to assess its activity, the analyses of the relief were performed. Digital elevation models based on LiDAR data (1 point/m^2 resolution) and 2 m contour lines topographic maps were used. Longitudinal profiles and Stream-length (SL) index on water streams crossing the MLF between Nový Kostel and Horšovský Týn (~ 85 km) were performed in order to identify the knickpoints and anomalous values and sudden changes of the SL index. Stream-length (SL) index is a simple, but very strong tool to evaluate the influence of tectonics to the geometry and fluvial style of river systems. It was first used by Hack (1972). The SL index can be counted by the equation $SL=(\Delta H/\Delta L)Ldm$, where $(\Delta H/\Delta L)$ means the stream gradient and Ldm means the length of stream reach between stream source and the middle of the measured part, usually 100 m or 1 km (depends on the length of the stream). The values of SL index react very sensitively to gradient changes of the stream, including lithological, tectonic, hydrological and even anthropogenic influences. Thus, all of the possible controls were considered and analyzed. The anomalous (usually higher) values of SL indexes and particularly sudden changes of the index values indicate the changes in the stream gradient. Origin of these changes can be evaluated with the help of other sources or analyses (e.g. geological maps or morphotectonic analysis). It was also necessary to correct the values of SL index in those places which were heavily influenced by anthropogenic activities (millraces, dams, weirs etc.). The historical maps and historical aerial photographs were used for those adjustments.

In addition, to determine whether tectonic or erosional processes have played a dominant role in the development of landscape in the whole Cheb basin, geomorphic indices like hypsometric curves, basin elongation ratio, topographic asymmetry etc. have been used. Detailed results will be presented on the conference. In addition, the northern segment of the MLF as well as fluvial terraces of the Ohře River in the Cheb basin were mapped in the field. Reconstruction of the river terrace longitudinal profiles crossing the MLF was performed to identify possible anomalies due to activity of the MLF.

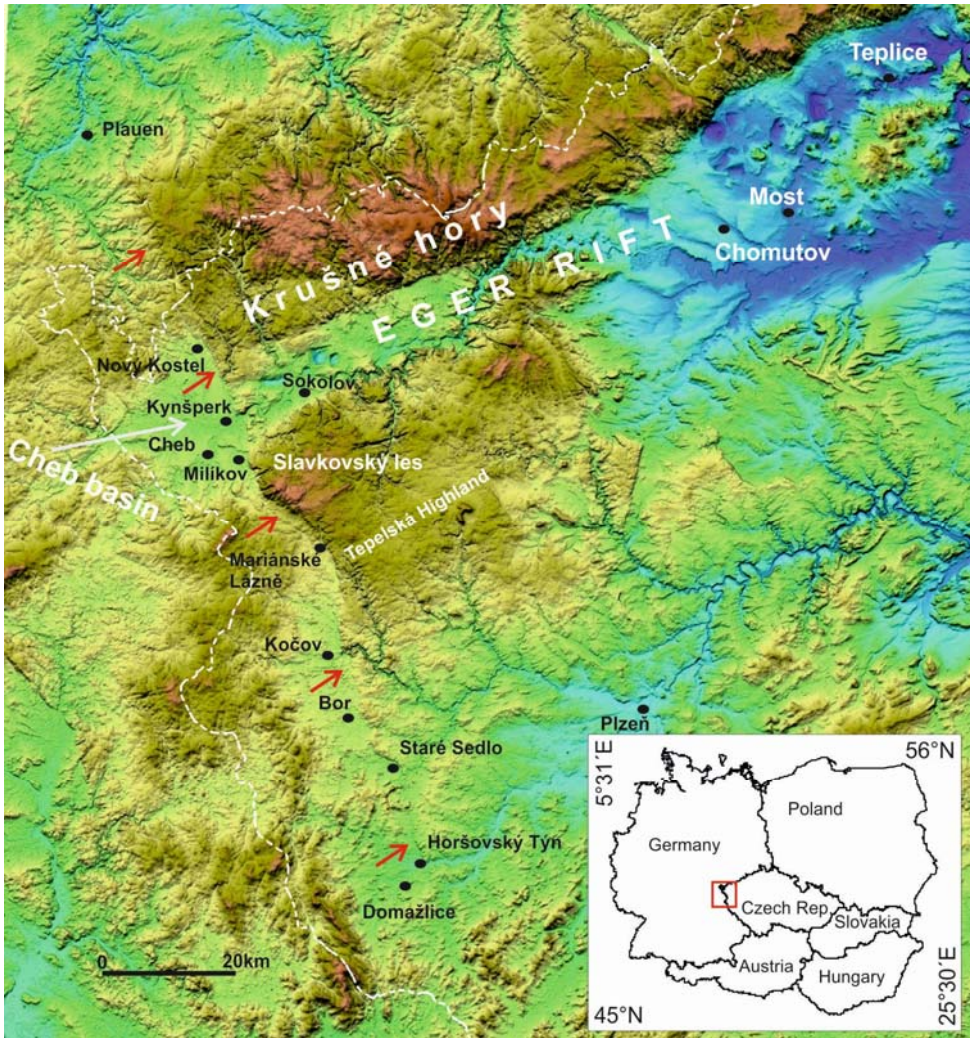

Figure 1: Digital elevation model showing the striking morphology along the Mariánské Lázně fault - pointed by red arrows.

MORPHOLOGY OF THE MARIÁNSKÉ LÁZNĚ FAULT

The MLF is expressed in morphology by more or less pronounced fault scarp at the length of 120 km from Plauen in Germany to Horšovský Týn despite the lack of any fault outcrops (Fig. 1). In the northern part the fault is expressed by a linear arrangement of saddles and by 40-130 m high slope (fault scarp), which divides Smrčiny (Fichtelgebirge) from Krušné hory Mts (Erzgebirge) on the Czech territory. Around Nový Kostel, the fault splays into two scarps, where one is expressed by linear arrangement of places where enhanced headward erosion starts and several valleys change their character or direction, and the second by a steeper slope. This segment is proved also by geophysics and paleoseismic trenching (Fischer et al., 2012; Štěpančíková et al., 2018). From Milíkov the fault is bent and controls the highest elevated area, Slavkovský les by up to 300 m high fault scarp. The scarp is expressed by pronounced trapezoidal to triangular facets. From Mariánské Lázně the fault scarp strikes again NW to NNW and it steps over to the right near Planá, from where is rectilinear to Kočov, where the main river Mže antecedently flows into the fault scarp of about 100 m height. More to the south, almost up to Bor, the fault steps over to the left and is almost N-S striking expressed by two parallel gentle fault scarps, 10-15 m high. This segment seems to be morphologically the youngest one. Near Nová Hospoda (3 km north of Bor) Neogene fluvio-lacustrine sediments are ceased by the fault. From Bor to Staré Sedlo the fault/fault scarp is bending twice from N-S direction to WNW-ESE and reaches the height 15-35 m. From Horšovský Týn, the fault is not expressed in morphology any more.

LONGITUDINAL PROFILES AND SL INDEX

Longitudinal profiles of the brooks which are flowing from the Krušné hory Mts to the Cheb Basin in the study area are highly unbalanced and contain several irregularities such as convex parts of a longitudinal profile or knickpoints. The probable control of increase SL indices is proposed in Fig. 2, such as headward erosion (E), lithological differences (L), occurrence of a fault (F) or anthropogenic effects (A)(e.g. dams, ponds, riverbed regulations, etc.). The MLF segments mainly between Nový Kostel and Kopanina village were marked as possibly active based on SL>100 peaks occurrence. Also other fault segments in Libocký p. brook valley parallel with MLF and Plesná fault zone segments are controlled by fault occurrence, thus possible faulting (Fig. 2).

In central and southern segment of the MLF, the observed knickpoints of shorter, obsequent streams (dissecting the mountain front, controlled by the MLF, down the fault slope, from E to W) can be a sign of the very recent tectonic activity, on the other hand the longer, consequent streams (crossing the fault from W to E, with antecedent valleys due to the MLF activity) can store some indications of older (and regional) tectonic movements in their gradient and SL characteristics (e.g. changes in trends of SL index values). Five consequent streams as well as 82 obsequent streams were analysed in the part of study area (between Kynšperk and Horšovský Týn). The anomalous values of SL index and activity on the central section of MLF has happened earlier than the movements on the northern and southern sections. Further research (geophysics, palaeoseismology) is necessary for proving the hypothesis and validate our obtained results.

RIVER TERRACES OF THE OHŘE RIVER

In the Cheb basin, Pliocene fluvial sediments and 7 levels of Pleistocene aggradational terraces and a Holocene floodplain of the Ohře (Eger) River were mapped and determined. Based on correlation with the published

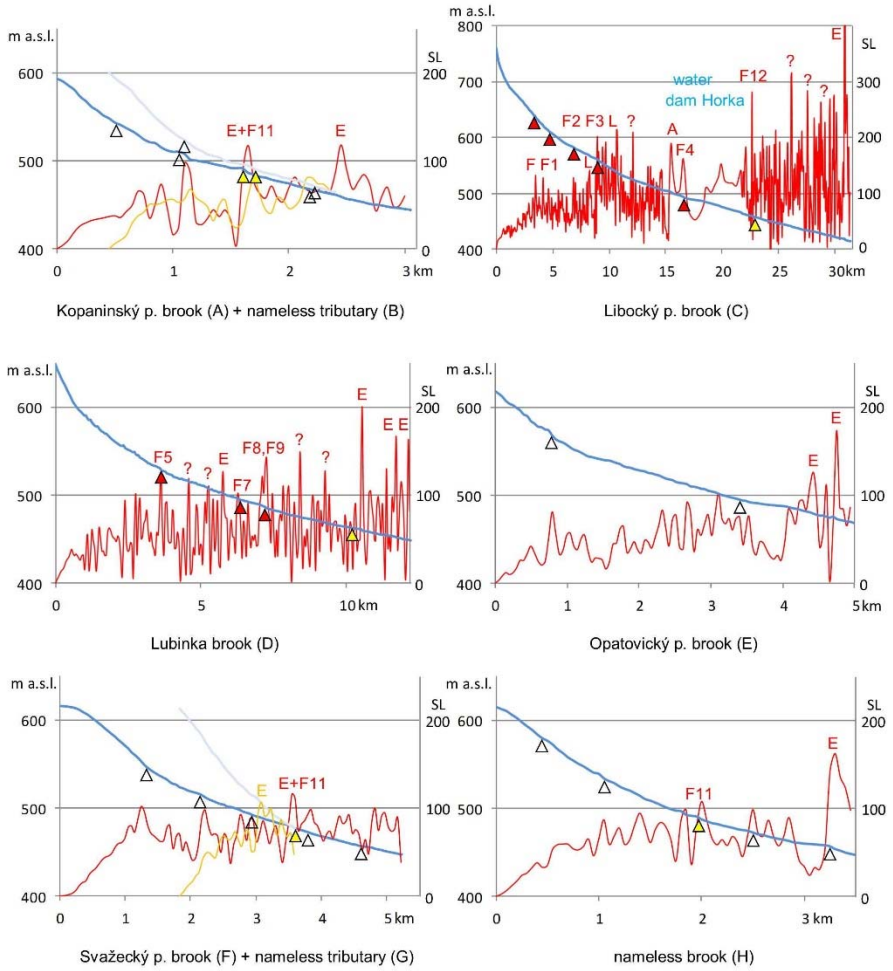

Figure 2: Examples of long profiles and SL indices at streams crossing the MLF in the Cheb basin. White-filled triangle indicates the place where a brook crosses a fault, red-filled triangle shows position of faults which were marked as active based on SL index, and yellow-filled triangle marks the Mariánské Lázně fault. The SL index peaks with identified causes are marked as follows: reach of the headward erosion (E), lithological differences (L), crossing of the fault (F), anthropogenic effects (A); the cause of other SL index peaks is unknown.

sudden changes of longitudinal profiles of Mže River and Kosový potok Brook were found. Those ones can be signs of irregular uplift of the elevated terrain of Tepelská vrchovina Highlands lying eastwards from the MLF. The analyses of the shorter obsequent streams found several promising places (e.g. Nová Hospoda, 3 km north of Bor) with probable very recent, young tectonic activity. On the other hand, we found high values of SL index, but very smooth, hyperbolic longitudinal stream profiles in the area of Slavkovský les. It seems that highly elevated terrain was uplifted earlier than the rest of the Tepelská vrchovina Highlands. It leads to a hypothesis, that the tectonic reconstruction of the central to lower course of the Ohře River terrace flights (e.g. Balatka & Sládek, 1976; Balatka, 1993; Tyráček, 1995), the terrace levels in the Cheb basin were classified according to the current stratigraphic scheme of the Quaternary. The Ohře River terraces originated in complex morphotectonic and climate-morphogenetic conditions that existed during the late Cenozoic evolution of the valley and the terrace system was formed during the period from the Tiglian to the Weichselian stages.

The analysis of the terrace system in the Cheb basin showed that the oldest, highest Pleistocene terrace (I) is uplifted in the Smrčiny Mts about 10 m in relation to its level in the Cheb basin. The two oldest terraces (I, II) are displaced by the MLF and uplifted by 15 m in the Chlumský práh, which is an asymmetric horst dividing the Cheb basin in the west from the Sokolov basin in Eger Rift in the east. Moreover, the youngest Pleistocene deposits of the last glaciation (Weichselian) fill the valley floor and are subsided next to the MLF by 8 m. The details will be presented at the conference.

PRELIMINARY CONCLUSION

The tectonic activity of the MLF is expressed by the present-day morphology of the 140 km long fault scarp with varying strike and height (from 10 to 300 m). The present-day activity expressed in morphology is reflected by the SL indices and knickpoints in the longitudinal profiles of the streams crossing the MLF. Late Cenozoic activity of the MLF and other nearby faults is expressed also by faulted sedimentary infill of the Cheb basin, which reached the maximum thickness up to 400 m with the basin depocenter related to the MLF. Also Pleistocene Ohře river terraces were found to be displaced by the MLF. The Late Cenozoic tectonic movements are also accompanied by volcanic processes and present-day frequent earthquakes swarm activity activity in the region.

Acknowledgements: The project was supported by Czech Science Foundation, project No. 16-10116J, and by the long-term conceptual development research organization RVO: 67985891.

REFERENCES

Balatka, B., 1993. K vývoji údolí Ohře v Doupovských horách. *Sborník České geografické společnosti* 98 (2), 107-122.

Balatka, B., & Sládek, J., 1976. Terasový systém střední a dolní Ohře. *Acta Universitatis Carolinae, Geographica* 11(2), 3-26.

Dèzes, P., Schmid, S.M., & Ziegler, P.A., 2004. Evolution of the Cenozoic Rift System: interaction of the Alpine and Pyrenean orogens with their foreland lithosphere. *Tectonophysics* 389, 1-33.

Fischer, T., Štěpančíková, P., Karousová, M., Tábořík, P., Flechsig, C., & Gaballah, M., 2012. Imaging the Mariánské Lázně Fault (Czech Republic) by 3-D ground-penetrating radar and electric resistivity tomography. *Stud. Geophys. Geod*. 56 (4), 1019-1036, doi: 10.1007/s11200-012-0825-z.

Hack, J.T., 1973. Stream-profile analysis and stream-gradient index. U.*S. Geological Survey Journal of Research* 1, 421-429.

Malkovský, M., 1987. The Mesozoic and Tertiary basins of the Bohemian Massif and their evolution. *Tectonophysics* 137, 31-42.

Štěpančíková, P., Fischer, T., Stemberk, J., Nováková, L., & Hartvich, F., 2018. Active tectonics in the Cheb basin: youngest documented Holocene surface faulting in central Europe? *Geomorphology*, under review.

Tyráček, J., 1995. Stratigraphy of the Ohře River terraces in the Most Basin. Sborník geologických věd, *Antropozoikum* 22, Český geologický ústav, Praha, 141-157.

Ulrych, J., Krmíček, L., Tomek, Č., Lloyd, F.E., Ladenberger, A., Ackerman, L., & Balogh, K., 2016. Petrogenesis of Miocene alkaline volcanic suites from westernBohemia: whole rock geochemistry and Sr-Nd-Pb isotopic signatures. *Chemie der Erde* 76, 77-93.

Ziegler, P.A., 1992. European Cenozoic rift system. *Tectonophysics* 208, 91-111.

Ziegler, P.A., & Dèzes, P., 2007. Cenozoic uplift of Variscan Massifs in the Alpine foreland: Timing and controlling mechanisms. *Global Planet. Change* 58, 237-269.

INQUA Focus Group Earthquake Geology and Seismic Hazards

paleoseismicity.org

Fault rupture and seismic intensities of palaeoseismic events: Evidence from an 18th c. Croatia earthquake

Stiros, Stathis (1)

(1) Dept. of Civil Engineering, Patras University, Patras 26500, Greece, stiros@upatras.gr

Abstract: *Fault ruptures generate accelerations which are modified away from the fault and their effects (mostly intensities) may not be directly indicative of the seismic rupture process. This problem is highlighted in the case of the 1750 Bakar-Rijeka, NW Croatia earthquake, for which two different scenarios have been proposed based on detailed historical and archaeological evidence: A small earthquake (magnitude 5) with locally amplified intensities which implies a rather aseismic Adria-Europe collision front, and alternatively, a large (magnitude ≥6) earthquake which generated moderate accelerations. Observations of coastal notch subsidence permitted to compute a finite fault model of this earthquake, correlate it with a major thrust and recognize a significant co-seismic component in the Adriatic collision front. This example highlights the need to include soil dynamics effects in the study of palaeoseismic events in order to improve our understanding of active tectonic processes and of the associated seismic risk.*

Keywords*: fault model, earthquake intensities, coastal change, soil dynamics, seismic risk*

INTRODUCTION

The sense of earthquakes we acquire reflects a combination ("convolution") of three effects: of the fault geometry and slip (which practically define the earthquake magnitude), of the fault rupture dynamics, and of the radiation and local amplification or attenuation of seismic waves, while their end-effect is usually sampled and sensed mostly as accelerations and seismic intensities (dynamic effects) and more rarely as permanent ground deformation, often masked by local effects. Because of this combination, the effects of earthquakes may be disproportionate to the earthquake magnitude, and no clear geographical correlation between seismic source and geographical distribution of intensities and damages may exist.

As a consequence, back projection of any of the components of this convolution to pre-instrumental seismology periods may predict exaggerated, under-estimated or misplaced events (or series of events). In some cases apparently earthquake-free regions or areas of exaggerated seismicity may be estimated, and this may have serious implications for the understanding of regional tectonics and the assessment of the seismic risk.

A way to overcome this problem is to take into consideration soil dynamic effects, i.e. the engineering aspects of earthquakes, an approach which may help to overcome some problems, but may lead to additional ones. A solution to this problem requires a combination of seismological, tectonic, tectonophysical, geodetic and earthquake engineering approaches leading to finite fault models, models of rupture dynamics and understanding of local modifications of accelerations generated at seismic sources.

THE 1750 CROATIA EARTHQUAKE, A CASE STUDY

The above problems and approaches are highlighted in the case of the 1750 earthquake in SW Croatia, the seismicity of which was till recently poorly understood. Recent historical and archaeological evidence permitted to constrain well the distribution of the intensities of the 1750 earthquake (Herak et al., 2017), which can be interpreted in two ways:

(i) As evidence of a M5 earthquake with locally amplified accelerations (intensities VII-VIII) along a zone ~40 km long (Fig. 1; Herak et al., 2017), too long for an earthquake of this magnitude. This scenario also implies an essentially aseismic compression front between Adria-Europe, while existing evidence indicates a convergence of 2 cm/yr (Serpelloni et al., 2005; Pondrelli et al., 2006) corresponding to about 10 m in the last 500 years, i.e. the period covered by the data of Herak et al. (2017).

(ii) As evidence of a stronger (M≥6) earthquake. The parameters of this earthquake were derived from elastic dislocation modeling of up to 55 cm downward gradual bending of coastal notches for at least 20 km. From this evidence, a finite fault model of the reactivated fault was computed (Fig. 1). Correlation of the predicted fault with the major Bakar-Vinodol thrust and with a quasi-linear zone of high (≥VII) seismic intensities indicates that this earthquake was associated with reactivation of a segment of a major thrust (Fig. 1).

On the other hand, topography and lithology in the meizoseismal area predict some amplification of seismic waves. This implies that the 1750 earthquake was likely associated with a process of relatively slow release of elastic energy and relatively low accelerations at the

source. Such a slow rupture process may be typical for this major fault and it may explain why other historical earthquakes in this area are underestimated or even ignored, but also implies a significant seismic contribution in the Adriatic collision front. Hence this second scenario seems more likely.

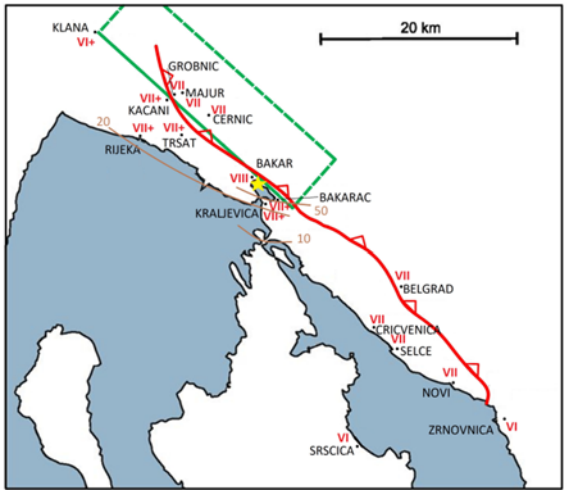

Figure 90: Summary of observations and results discussed. Correlation between (1) the intensities of 1750 earthquake (red Latin numbers), (2) the trace of the Vinodol-Bakar Thrust (red curve, with ticks on the hanging wall), and (3) the horizontal projection of the finite model of the fault (green rectangular; surface trace indicated by a continuous line) derived from elastic dislocation of observations of differential subsidence of coastal notches in the wider Rijeka-Bakar area Yellow star indicates the macroseismic epicenter of the 1750 earthquake. Brown curves represent selected contours of coastal tectonic subsidence (in cm), drawn from data on which was based the proposed finite fault model. After Stiros (2018), summarizing data from various sources.

IMPLICATIONS FOR PALAEISEISMIC STUDIES

Palaeoseismic evidence of seismic intensities and/or of ground deformation of ancient earthquakes is usually limited to sampling of observations of fault geometry and slip and of seismic intensities, and the whole process of release and radiation of seismic energy is not clear. For this reason, scenarios examining the whole process of fault geometry to end effects of earthquakes, including soil dynamics effects may improve our understanding of active tectonic effects and of seismic risk.

REFERENCES

Benac, Č., Juračić, M., & Blašković, I., 2008. Tidal notches in Vinodol Channel and Bakar Bay, NE Adriatic Sea: Indicators of recent tectonics. *Marine Geology* 248, 151-160.

Herak, D., Sović, I., Cecić, I., Živčić, M., Dasović, I., & Herak, M., 2017. Historical Seismologist: Historical Seismicity of the Rijeka Region (Northwest External Dinarides, Croatia)-Part I: Earthquakes of 1750, 1838, and 1904 in the Bakar Epicentral Area. *Seismological Research Letters* 88 (3), doi: 10.1785/0220170014.

Pondrelli, S., Salimbeni, S., Ekström, G., Morelli, A., Gasperini, P., & Vannucci, G., 2006. The Italian CMT dataset from 1977 to the present. *Physics of the Earth and Planetary Interiors* 159, 286-303.

Serpelloni, E., Anzidei, M., Baldi, P., Casula, G., & Galvani, A., 2005. Crustal velocity and strain-rate fields in Italy and surrounding regions: New results from the analysis of permanent and non-permanent GPS networks. *Geophysical Journal International* 161 (3), 861-880.

Stiros, S., 2017. Comment on "Historical Seismicity of the Rijeka Region (Northwest External Dinarides, Croatia)-Part I: Earthquakes of 1750, 1838, and 1904 in the Bakar Epicentral Area" by Herak et al., *Seismological Research Letters* 88 (6), 1534-1536, doi: https://doi.org/10.1785/0220170098.

Stiros, S., 2018. Intensities of ancient earthquakes, earthquake magnitude and soil dynamics effects. Evidence from the 1750 Croatia earthquake. *Geodesy and Geodynamics*, Special Volume edited by A. Korzenkov, in press.

Stiros, S., & Moschas, F., 2012. Submerged notches, coastal changes and tectonics in the Rijeka area, NW Croatia. *Marine Geology* 329-331, 103-112.

INQUA Focus Group Earthquake Geology and Seismic Hazards

paleoseismicity.org

Effect of the completeness of surface ruptures' displacement measurement on the correctness of their characterization

Strom, Alexander (1)

(1) Geodynamics Research Center - branch of JSC "Hydroproject Institute", 2 Volokolamsk Highway, 125993, Moscow, Russia, strom.alexandr@yandex.ru

Abstract: *Analysis of mean displacements (D_{av}), of their ratio with maximal displacements (D_{max}), and of portion of entire rupture length characterized by maximal displacement (L_{max}) based on the database of surface ruptures of modern earthquakes is presented. Reliability of these values estimates depends on a large extent on the completeness of rupture study that can be characterized by number of measurement points and by mean distance between them. Mean D_{av}/D_{max} ratio varies from 0.352 to 0.38 depending on rupture' kinematics, while D_{max} characterizes rather small portion of surface rupture length that, on average, does not exceed 5% of the entire rupture length. It should be taken into consideration for paleoseismic studies planning and for interpretation of their results both in terms of past earthquake magnitudes and of the design displacement values.*

Keywords*: Surface rupture, Maximal displacement, Average displacement, Rupture length*

INTRODUCTION

Most of the statistical relationships of surface rupture displacement with rupture length and earthquake magnitude are based on maximal displacement values (D_{max}) measured for each of surface rupture included in the corresponding database (Bonilla et al., 1984; Slemmons et al, 1989; Wells & Coppersmith, 1994; Strom & Nikinov, 1997; Chipizobov, 1998). However, studying prehistoric surface rupture, either to estimate magnitude of past earthquake(s) or to provide design displacement value for the structure crossed by active fault, we often do not know if the offset measured at any particular point (e.g. in a trench) was really maximal for this event or not. Other important parameters characterizing surface rupture are the mean (average weighted) displacement value (D_{av}), and portion of the entire rupture length (L) characterized by maximal displacement (L_{max}). All these parameters should be analyzed consistently to get more reliable and well-grounded estimate of both paleoearthquake magnitude and of the design displacement value. It was found, however, that relationships between D_{av} and D_{max}, and between L_{max} and L depend on a large extent on the detailedness of rupture's study characterized by number of measurement points and by mean distance between them. An extent of surface rupture study provides some constraints for paleoseismic analysis and for engineering-geological site/route investigations.

MEAN D_{av}/D_{max} AND L_{max} RELATIONSHIPS

According to data on surface ruptures of 67 earthquakes for which slip distribution along ruptures' strike (of net displacement or/and of its vertical or lateral components) could be compiled (Strom & Nikonov, 2000), D_{av}/D_{max} ratio varies from 0.09 to 0.75 with mean values ranging from 0.352 to 0.38 depending on rupture' kinematics. Nearly similar estimates were provided in Strom & Nikonov (1997) and in McCalpin (2009). They, however, differ significantly from earlier estimate of $D_{av}/D_{max}\approx0.5$ made by Wells & Coppersmith (1994).

It was also found that D_{max} characterizes rather small portion of surface ruptures' length that, on average, do not exceed 5% of the entire rupture length (Strom & Nikonov, 1997, 2000). It should be taken into consideration for probabilistic assessment of fault displacement parameters.

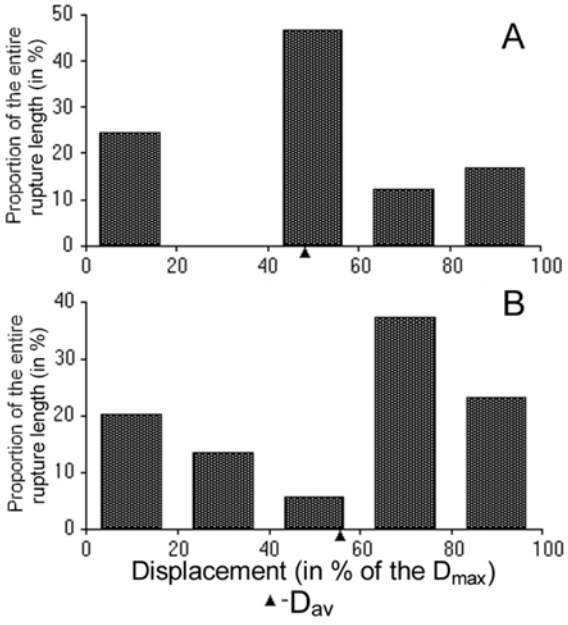

Figure 91: Portions of surface ruptures sections characterized by displacements comprising proportions of the D_{max} values. Black triangles correspond to the calculated D_{av} values. A - rupture of the 06.07.1954 Nevada earthquake (slip distribution according to Tocher, 1956); B - rupture of the 04.03.1981 Corinth earthquake (slip distribution according to Jackson et al., 1982).

It will be interesting to notice that calculated average displacement could be really characteristic of a particular rupture as on Figure 1-A, but could be also just a calculated value that, in fact, can be measured with quite a low probability, as demonstrated by Figure 1-B.

Thus, if we measure displacement in a randomly selected point, we cannot consider it (at least always) as an average value typical of a particular surface rupture. Thus, we cannot simply use the relationships between earthquake magnitude and average displacement such as those proposed by Wells & Coppersmith (1994). We also cannot multiply randomly measured displacement by ca. 2.7 and then substitute the obtained product in the relationships between D_{max} and earthquake magnitude based on much more representative samples. In both cases, some additional analysis is necessary.

EFEECT OF THE NUMBER OF MEASUREMENT POINTS AND OF THE DISTANCE BETWEEN THESE POINTS ON D_{av}/D_{max} AND L_{max}/L RATIOS

Data available on slip distributions along faults' strike are quite uneven. Number of measurement points vary from nearly 10 for some rather poorly studies surface ruptures to more than 250 for longest surface ruptures studied in detail such as, for example, rupture of the 1920 Hayuan earthquake in China (Hayuan, 1990). Besides, distance between measurement points is, first, non-uniform even along the particular rupture, and, second, depends on rupture's length. According to published data it can vary from dozens meters to tens of kilometers. Thus, the problem arises – at what extent D_{av} and L_{max} values and their relationships with D_{max} and L depend on real peculiarities of surface ruptures' formation and at what extent – on the detailedness of their study.

The analysis performed showed that the D_{av}/D_{max} ratio depends neither on number of measurement points (Figure 2), nor on mean distance between them (Figure 3). It demonstrate, from my point of view, that this ratio could really reflect some physically-based peculiarities of slip distribution along surface ruptures that can be determined even if the displacement is measured at a limited number of points - say, about 10-20. It requires, however, that researcher should measure offsets at those points that are typical of rather long fault sections and to fix points where these values change sharply, which is possible for surface ruptures well expressed in the relief only.

L_{max} value, in contrast, decreases regularly with increase of the number of measurement points (Figure 4) and with decrease of mean distance between them (Figure 5). According to these plots slip distribution along surface rupture can be characterized with confidence if number of measurement points is about 50 or more, or if the mean distance between them (better, actual distance) does not exceed ca. 200 m. It means in practice that if we study relatively short rupture we should rely more on the distance between observational points, while studying very long active faults with evidence of surface ruptures we should pay more attention on number of measurements along fault strike, since very frequent offsets measurement along hundreds kilometers long rupture could be too laborious and time-consuming.

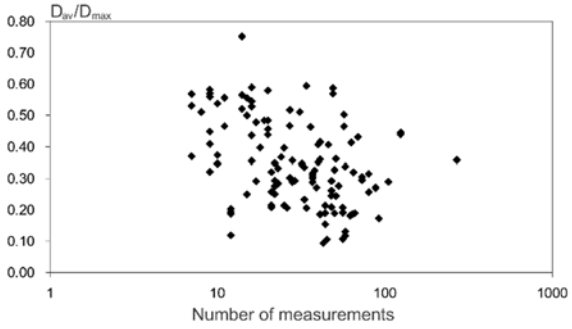

Figure 2: Dependence of the D_{av}/D_{max} ratio on the number of measurement points.

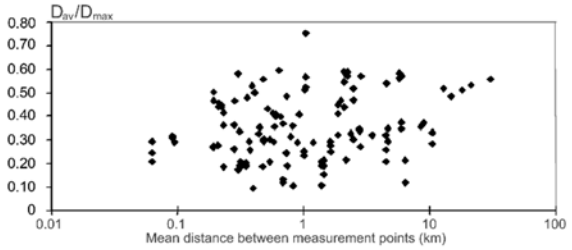

Figure 3: Dependence of the D_{av}/D_{max} ratio on the mean distance between measurement points.

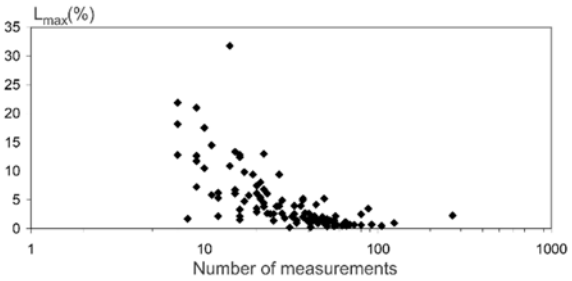

Figure 4: Dependence of the L_{max}/L ratio on the mean distance between measurement points.

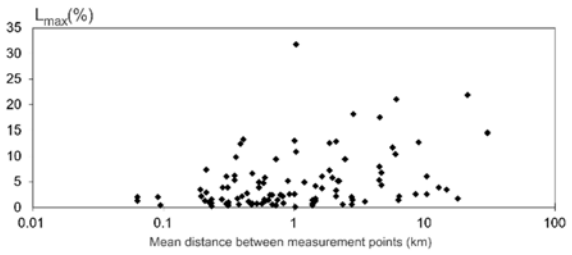

Figure 5: Dependence of the L_{max}/L ratio on the mean distance between measurement points.

It was also found that length of surface rupture section characterized by displacement equal to some percentage of D_{max} (L_D) or exceeding it depends on the number of measurement points and on mean distance between them if $L_D \geq$ 60-70% (Figure 6). It provides some statistical grounds to use 2/3 of the reported D_{max} value as the design displacement value (Figure 7) as it was done for the Trans-Alaska pipeline / Denalli fault crossing (Hall et al, 2003; Haeussler et al, 2004).

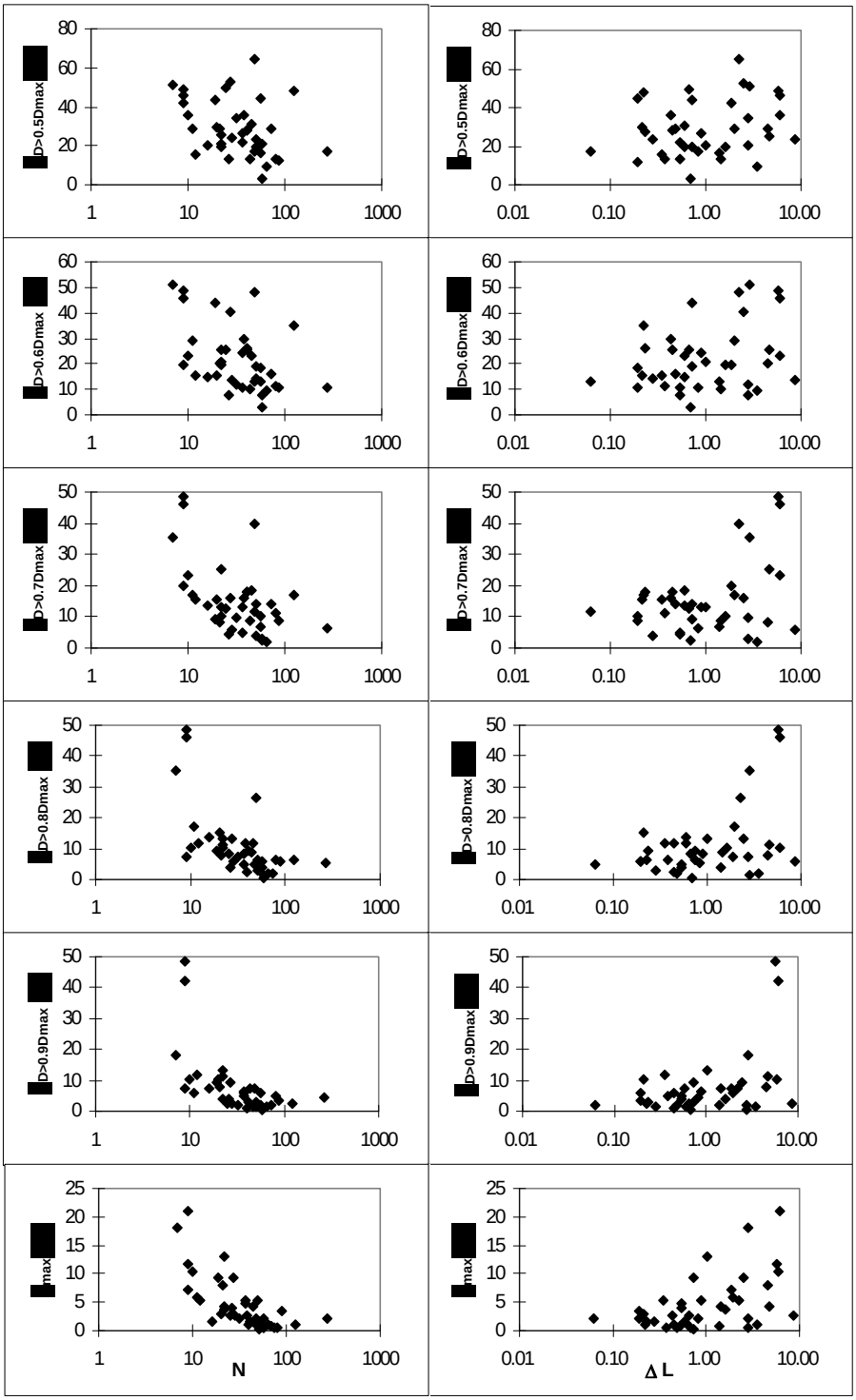

Figure 6: Variation of the portion of rupture length characterized by offsets larger than certain percentage of D_{max} depending on number of measurement points (N - left side) and on mean distance between them (ΔL - right side)

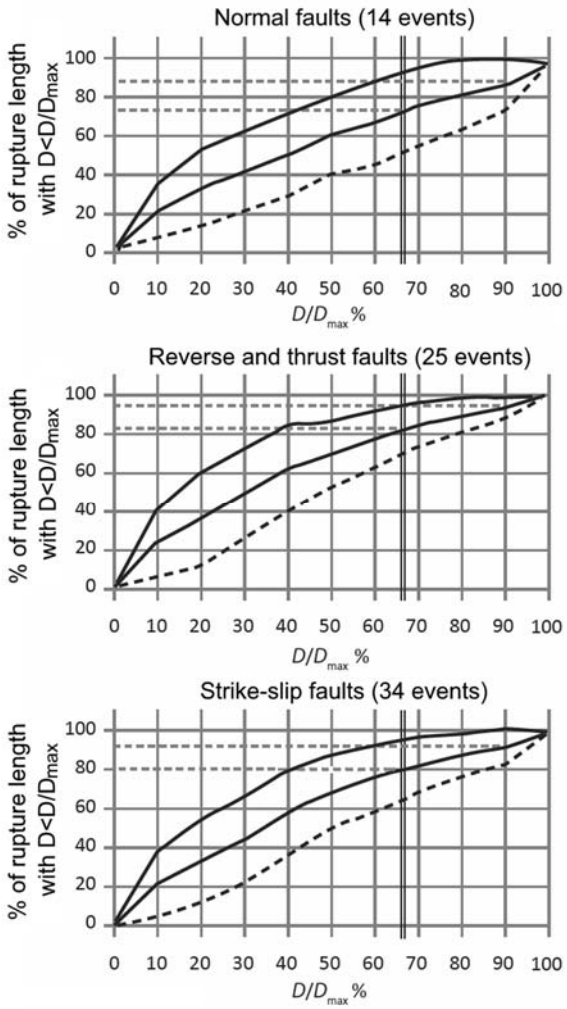

Figure 7. Length of surface fault section with offsets smaller than some portion of a maximal offset. Diagrams are plotted based on the data on displacement distribution along surface ruptures with different kinematics. Mean values and their scatter are shown. Double vertical line corresponds to the 2/3 of maximal offset. Horizontal dashed lines mark length of rupture section at D<2/3 of D_{max} and D<0.9D_{max}

CONCLUSIONS

Relationships between parameters characterizing slip distribution along fault strike and their dependence on the number of measurement points and on mean distance between them should be taken into consideration for planning of paleoseismic studies, and for interpreting of their results both in terms of paleoearthquake magnitude, and of the design displacement values. The latter can be applied for studying faults that cross structures' foundations or lifelines' routes and provide basics for the assessment of risk of surface faulting at construction sites (Strom et al., 2009).

Reliable assessment of slip distribution along fault strike requires regular measurement of displacements either with constant distance between measurement points or at the specific points characterizing long section of surface rupture and sites where offsets change significantly.

Following such recommendation could be rather easy when measuring morphologically expressed landforms such as fault scarps reflecting vertical offsets or evidence of lateral displacements. It could be problematic, however, when quantifying single-event displacements of the penultimate or older events that can be measured in trenches only.

REFERENCES

Bonilla, M.G., Mark, R.K., & Lienkaemper, J.J., 1984. Statistical relations among earthquake magnitude, rupture length and surface fault displacement. *Bulletin of the Seismological Society of America* 74, 2379-2412.

Haeussler, P.J, Schwartz, D.P., Dawson, T.E., Stenner, H.D., Lienkaemper, J.J., Sherrod, B., Cinti, F.R., Montone, P., Craw, P.A., Crone, A.J., & Personius, S.F., 2004. Surface rupture and slip distribution of the Denali and Totschunda faults in the 3 November 2002 M 7.9 Earthquake, Alaska. *Bulletin of the Seismological Society of America* 94 (6B), S23-S52.

Hall, W.J., Nyman, D.J., Johnson, E.R., & Norton, J.D. 2003. Performance of the Trans-Alaska pipeline in the November 3. Denali fault earthquake. *Proceedings of the 6th U.S. Conference and Workshop on Lifeline Earthquake Engineering*, Long Beach, CA, ASCE Technical Council on Lifeline Earthquake Engineering, 2003.

Hayuan active fault zone. Beijing, 1990, 286 p. (in Chinese).

Jackson, J.A., J. Gagnepain, G. Houseman, G.C.P. King, P. Papadimitriou, C. Soufleris, & Virieux, J., 1982. Seismicity, normal faulting and the geomorphological development of the Gulf of Corinth (Greece): the Corinth earthquakes of February and March 1981. *Earth and Planet. Sci. Lett*. 57, 377-397.

McCalpin, J.P. (Ed.) 2009. *Paleoseismology*. International Geophysics Series, 95. Elsevier, 2nd Edition, 613 p.

Slemmons, D.B., Bodin, P., & Zang, X., 1989. Determination of earthquake size from surface faulting events, *Proc. of the International Seminar on Seismic Zonation, Guangzhou*, China, State Seismological Bureau, Beijing, 13.

Strom, A., Ivaschenko, A., & Kozhurin, A., 2009. Assessment of the design displacement values at seismic fault crossings and of their excess probability. Geological engineering problems in major construction projects. *Proceedings of 7th Asian regional conference of IAEG,* 9-11 Sept 2009, Chengdu, China, 139-143.

Strom, A.L., & Nikonov, A.A., 1997. Relationships between seismic fault parameters and earthquake magnitude. *Izvestiya, Physics of the Solid Earth* 33 (12), 1011-1022.

Strom, A.L., & Nikonov, A.A., 2000. The distribution of slip along seismogenic faults and incorporation of nonuniform slip in paleoseismological research. *Volcanology and seismology* 21, 705-722.

Tocher, D., 1956. Movement on the Rainbow Mountain fault in the Fallon Stillwater earthquakes of July 6, 1954 and August 23, 1954. *Bulletin of the Seismological Society of America* 46, 10-14.

Wells, D.L., & Coppersmith, K.J., 1994. New empirical relationships among magnitude, rupture length, rupture width, rupture area, and surface displacement. *Bulletin of the Seismological Society of America* 84, 974-1002.

INQUA Focus Group Earthquake Geology and Seismic Hazards

paleoseismicity.org

Subglacial paleoseismic deformations in central Finnish Lapland

Sutinen, Raimo (1), Ojala, Antti (2)

(1) Geological Survey of Finland, P.O. Box 77, 96101, Rovaniemi, Finland, raimo.sutinen@gtk.fi
(2) Geological Survey of Finland, P.O. Box 96, 02151, Espoo, Finland, antti.ojala@gtk.fi

Abstract: *Airborne LiDAR DEMs have revealed several postglacial faults (PGFs) in the interior of the former Fennoscandian Ice Sheet (FIS). One of them, called as Vaalajärvi-Ristonmännikkö PGF system in central Finnish Lapland, was verified with trenchings. The PGF-trench exhibited indication of multiple earthquake events. Here, we present morphological evidence of subglacial faulting in the area by interpreting the LiDAR-DEMs of the Late Weichselian landforms. Along the SE-trending down-ice transect from the fault, one of the striking feature is irregular groupings of straight or curvilinear and transverse-to-ice flow ridges, which are not comparable to annual or ice-marginal end moraines. We propose that some of the paleo-earthquakes were subglacial and therefore the ice crevassing created pathways for the saturated material to squeeze into the fractured ice system. At 40 km distance from the PGF, a field of arcuate/semi-circular Pulju moraines is associated with transverse-to-ice ridges forming a complex of seismic-induced subglacial landforms.*

Keywords*: PGF, subglacial deformation, squeezing, crevasses, seismic impact*

INTRODUCTION

Fennoscadian shield has subjected to end- or postglacial crustal events (Arvidsson, 1996) contributing to postglacial fault (PGF) systems and subaerial deformations, such as landslides and liquefaction features (Ojala et al., 2017a; Sutinen et al., 2018a; Fig. 1). PGFs eventually have been also a dynamic driver for the subglacial bed deformations, such as the Pulju moraines (Sutinen et al., 2018b).

Transverse-to-ice flow moraines are common in the areas formerly covered by continental ice sheets, yet their morphology, size and shape are highly variable and there are no consensus about the genetic constraints. Some of the transversally oriented moraines, such as Rogen moraine or ribbed moraine are regarded as active-ice subglacial, often polygenetic, landforms (Lundqvist, 1997). Ice-marginal moraines, such as washboard moraines exhibiting crevasse-squeeze features (Ankerstjerne et al., 2015) or De Geer moraines associated with proglacial water bodies (Ojala, 2016), show regular ridge-to-ridge pattern, probably attributed to annual ice recession. Also, small end moraines may exhibit regular pattern of the ridges as a result of ice-marginal oscillations (Ham & Attig, 2001).

As far as we know, the origin of irregular fields of small transversal moraines has not linked to paleoseismicity. It is known, that modern earthquakes/icequakes e.g. in Alaska and Greenland (Ekström et al., 2006) contribute to deformations on subgacial beds. In a similar way, late glacial earthquakes may have contributed to ice-crevassing and subglacial deformations and seen now as transverse-to-ice flow morphologies in the interior part of the Fennoscandian Ice Sheet.

In this paper we provide airborne LiDAR DEM (Digital Elevation Model) information on the group of landforms, such as transverse-to-ice flow moraine ridges and arcuate/winding Pulju moraines with regard to their spatial coexistence with the known Vaalajärvi-Ristonmännikkö postglacial fault (PGF) system in central Finnish Lapland (Fig. 1). The airborne LiDAR DEM data is provided by the National Land Survey of Finland, applying a Leica ALS50-II laser scanner from a flight altitude of 2000 m. The LiDAR data were interpolated to a 2×2 m grid. Last-return data with generally one to three hits per m^2 allows 14-cm-vertical ground resolution.

DISCUSSION

The upthrown block of the Ristonmännikkö PGF (Fig. 2, location in Fig. 1) faces SE. The LiDAR scene exhibits a significant amount of rather chaotic moraine morphologies next to the fault ramp. Further SE some of the moraines, however, exhibit faint transverse-to-ice flow orientation. The ice flow had been from northwest toward southeast. The meltwater erosion channels cross the PGF. We interpret this field of moraines as subglacial deformations induced by PG faulting. The chaotic morphology indicates rather a sudden seismic-induced bed deformation than end moraine processes within the ice-margin oscillations (Ham & Attig, 2001; Sarala et al., 2009) or regular pattern of washboard or De Geer moraines (Ankerstjerne et al., 2015; Ojala, 2016).

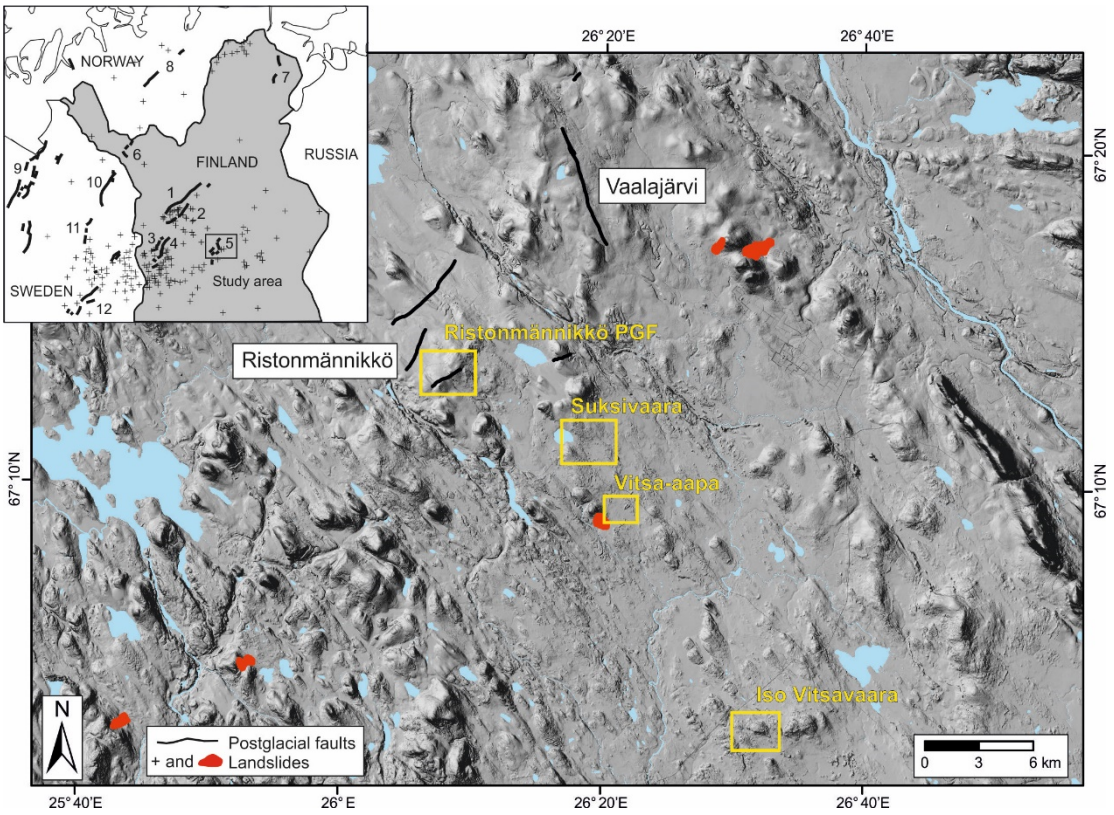

Figure 1: Vaalajärvi-Ristonmännikkö PGF system in central Finnish Lapland (#5 in the orientation map) with subsets Suksivaara, Vitsa-aapa and Iso Vitsavaara on the LiDAR DEM. PGFs and paleolandslides from Olesen et al. (2004), Lagerbäck & Sundh (2008), Sutinen et al. (2014), Mikko et al. (2015) and Ojala et al. (2017a; 2017b). 1. Suasselkä, 2. Riikonkumpu-Isovaara, 3. Venejärvi, 4. Pasmajärvi-Ruokojärvi, 5. Vaalajärvi-Ristonmännikkö, 6. Palojärvi, 7. Sevetti, 8. Stuorragurra, 9.Pärvie, 10. Lainio-Suijavaara, 11. Merasjärvi, 12. Landsjärv.

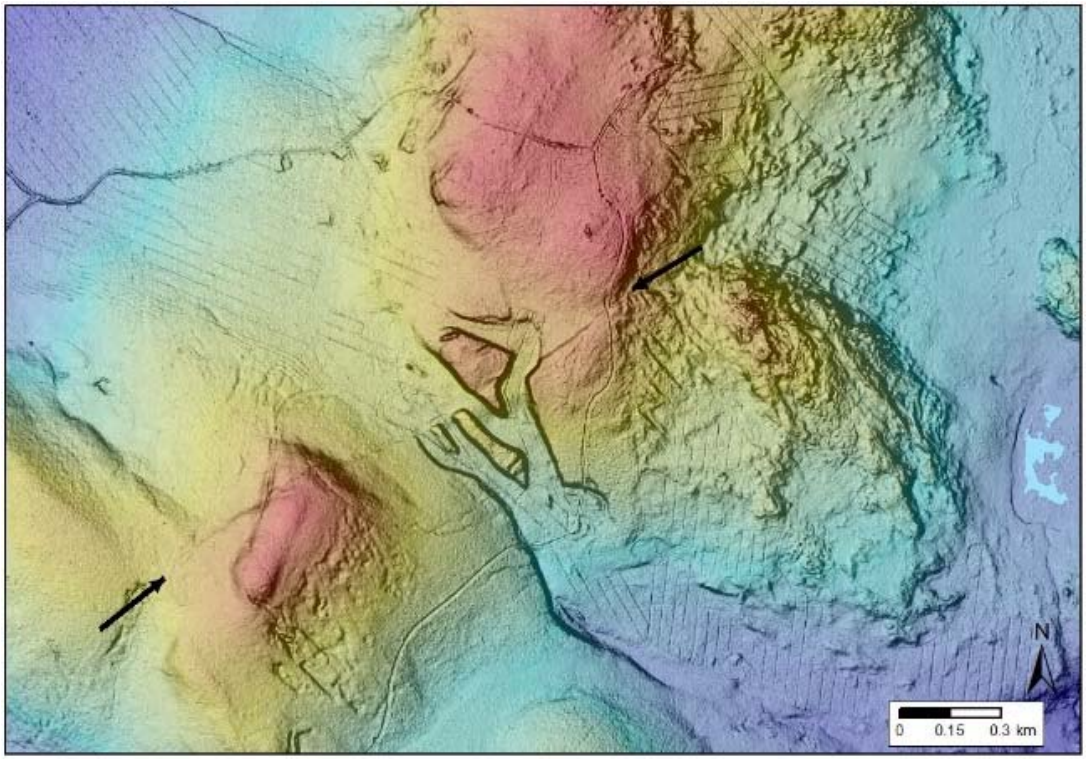

Figure 2: LiDAR DEM showing the Ristomännikkö PGF (indicated by arrows) and adjacent disordered (subglacial) moraine ridge morphology in central Finnish Lapland (location in Fig. 1).

The other example of the transverse-to-ice oriented pattern is given for the Suksivaara site, 8 km from the Ristonmännikkö PGF (Fig. 3: location in Fig. 1). The 1-2.5-m-high ridges are rather randomly spaced, and the

separation between single ridges ranges from 100 to 300 m. Some minor ribbing pattern can be seen between the dominant transverse ridges, particularly in the NE part of the Suksivaara scene (Fig. 3). These minor ridges are 0.5-1 m high are the ridge-to-ridge separation ranges from 10 to 50 m. These transverse-to-ice flow ridges are deforming and/or superimposed on the NE-SE oriented ice-parallel forms, thus indicating the time difference between these morphological assemblages, i.e. the transverse ridges are younger and presumably dating back to late glacial.

Some of the transverse-to-ice flow ridges within the NW-SE transect (Fig. 1) show curvilinear morphologies and with horns bending up-ice direction as shown in the Vitsa-aapa scene (Fig. 4). The tallest ridges reach 2.5-3 m and the ridge-to-ridge spacing varies from 50 to 100 m. In between these ridges small irregular forms, less than 0.5 m, give impression seismic tremor, yet the larger ridges display evidence of the crevasse-squeeze up processes (Hoppe, 1952; Ankerstjerne et al., 2015). We interpret the origin of the crevasses had been subglacial event of the Ristonmännikkö PGF (Figs. 1-2).

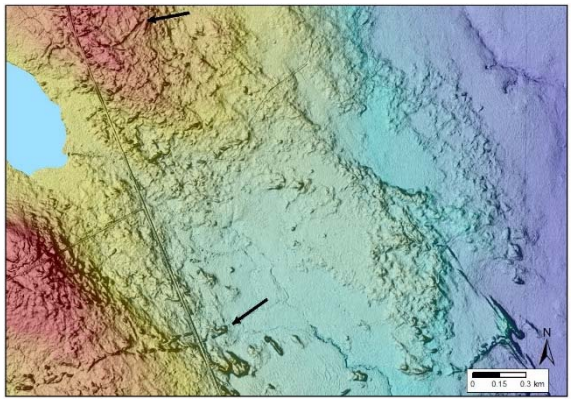

Figure 3: LiDAR DEM over the Suksivaara area in central Finnish Lapland showing irregular ribbing of transverse-to-ice flow ridges deformed and/or superimposed on the NE-SE oriented active-ice forms. Curvilinear ridges (shown by arrows) may reach lengths of 1.5 km.

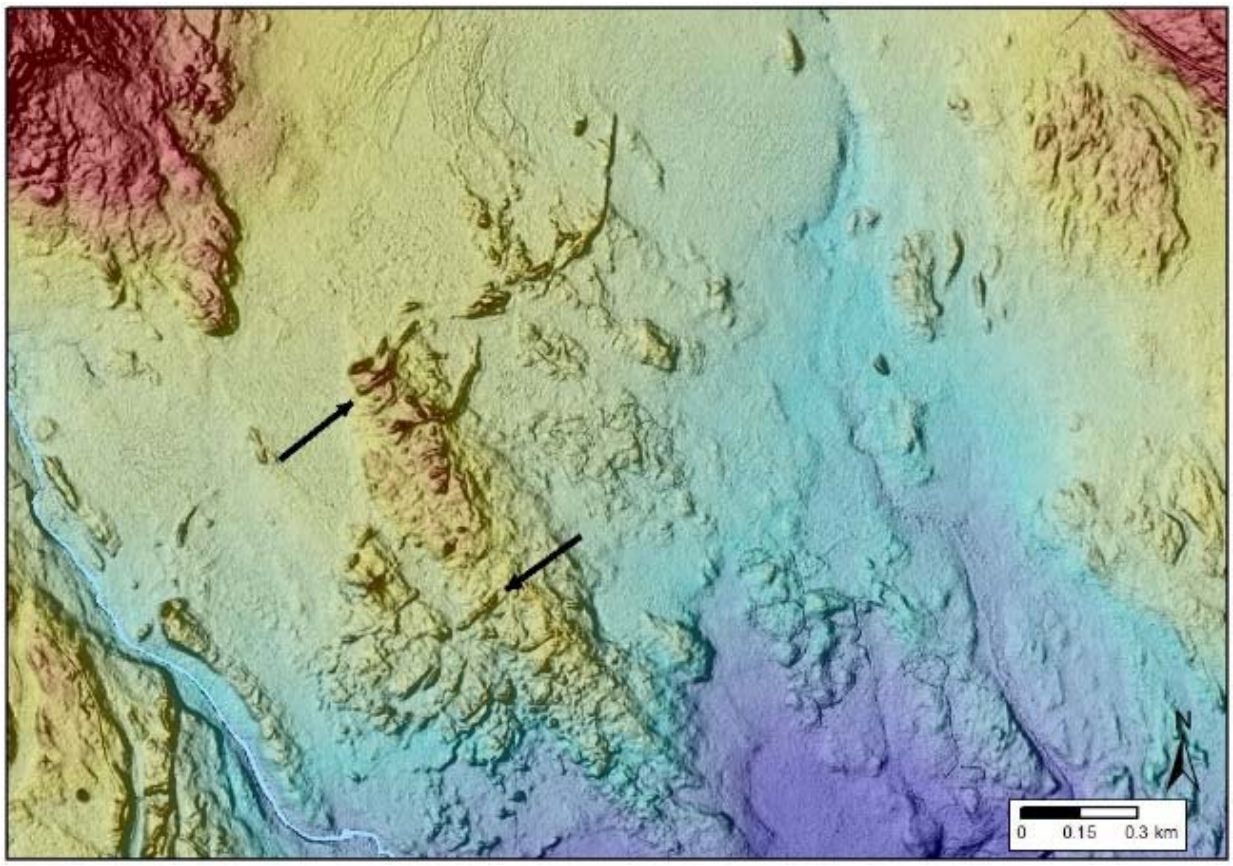

Figure 4: Transverse-to-ice flow ridges (show by arrows) superimposed on or deforming the NE-SE oriented ice-parallel landforms at Vitsa-aapa site in central Finnish Lapland (location shown in Fig. 1).

The Iso Vitsavaara LiDAR DEM (Fig. 5) shows a complex of subglacial landforms constituting transverse ridges and the Pulju moraines (Sutinen et al., 2014; 2018b). As is the case in the other subsets, also here the transverse-to-ice ridges, 2-3.5 m high and with 50-100 m inter-spacing, can be seen covering the local hills with no preference to the elevation. The arcuate/circular Pulju moraine ridges are 1-4 m high and are randomly spaced on the Iso Vitsavaara hill.

According he original squeezing hypothesis for the hummocky moraines in Norrbotten, Sweden by Hoppe (1952), the saturated bed material is forced into cavities by the ice load. We agree with this concept, but in the vicinity of the Ristomannikkö PGF, we postulate that seismic impact(s) primarily contributed to crevassing of the ice and squeezing of saturated bed materials.

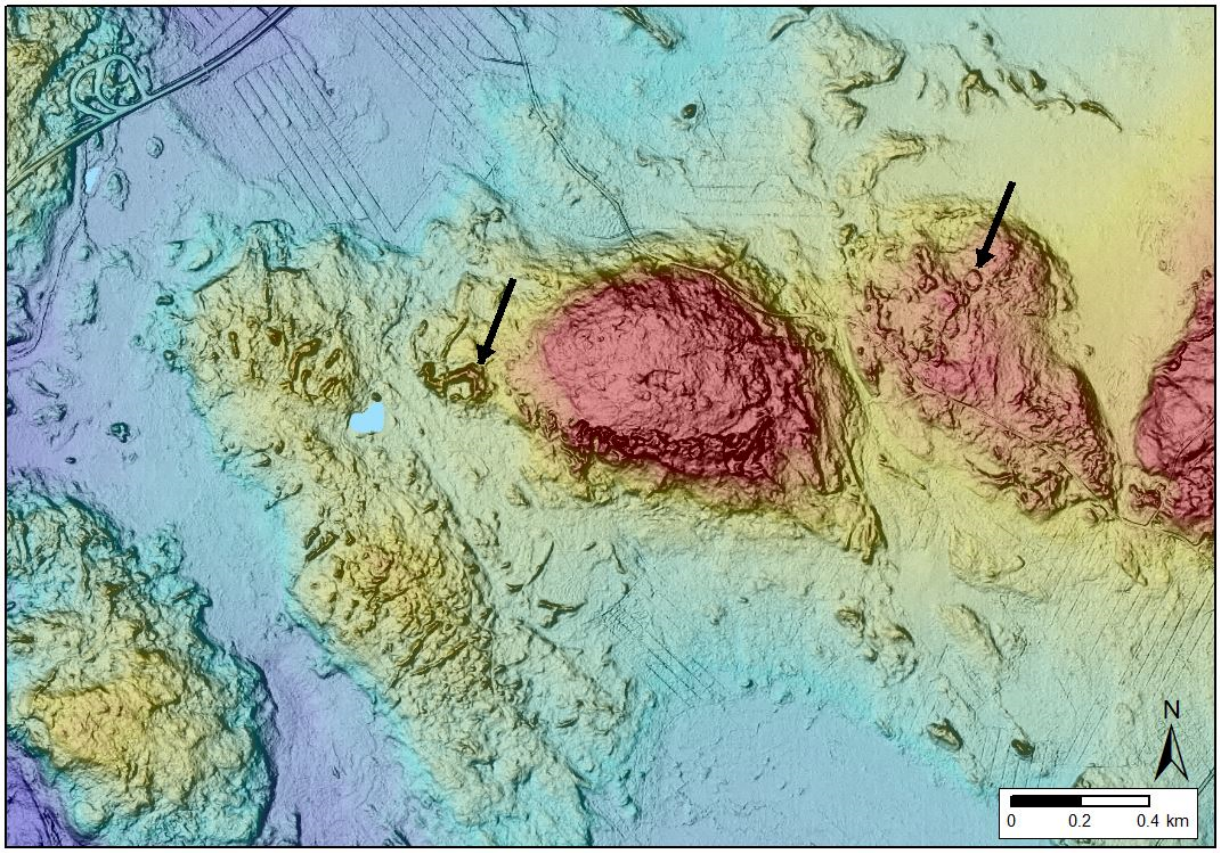

Figure 5: LiDAR DEM showing transverse-to-ice flow squeeze up ridges and arcuate/round shaped Pulju moraines (indicated by arrows) at the Iso Vitsavaara site in central Finnish Lapland (location in Fig. 1).

Acknowledgements: This paper is a part of the project Postglacial faults (#5002-20086) at the Geological Survey of Finland. The Ristonmännikkö PGF was verified by trenching in Sep. 2017 and that data will be reported later by Jussi Mattila and others.

REFERENCES

Ankerstjerne, S., Iverson, N.R., & Lagroix, F., 2015. Origin of a washboard moraine of the Des Moines Lobe inferred from sediment properties. *Geomorphology* 248, 425-463.

Arvidsson, R., 1996. Fennoscandian earthquakes. Whole crustal rupturing related to postglacial rebound. *Science* 274, 744-746.

Ekström, G., Nettles, M., & Tsai, V.C., 2006. Seasonality and increasing frequency of Greenland glacial earthquakes. *Science* 311, 1756-1758.

Ham, N.R., & Attig, J.W., 2001. Minor end moraines of the Wisconsin Valley Lobe, north-central Wisconsin, USA. *Boreas* 30, 31-41.

Hoppe, G., 1952. Hummocky moraine regions with special reference to the interior of Norrbotten. *Geografiska Annaler* 34, 1-72.

Lagerbäck, R., & Sundh, M., 2008. Early Holocene faulting and paleoseismicity in northern Sweden. Sver. Geol. Unders. C836, 80 pp.

Lundqvist, J., 1997. Rogen moraine – an example of two-step formation of glacial landscapes. *Sedimentary Geology* 111, 27-40.

Mikko, H., Smith, C., Lund, B., Ask, M.V., & Munier, R., 2015. LiDAR-derived inventory of post-glacial fault scarps in Sweden. *GFF* 137, 334-338.

Ojala, A.E.K., 2016. Appearance of De Geer moraines in southern and western Finland - Implications for reconstructing glacier retreat dynamics. *Geomorphology* 255, 16-25.

Ojala, A.E.K., Mattila, J., Markovaara-Koivisto, M., Ruskeeniemi, T., Palmu, J-P., & Sutinen, R., 2017a. Distribution and morphology of landslides in northern Finland: An analysis of postglacial seismic activity. *Geomorphology,* http://dx.doi.org/10.1016/j.geomorph.2017.08.045.

Ojala, A.E.K, Mattila, J., Ruskeeniemi, T., Palmu, J-P., Lindberg, A., Hänninen, P., & Sutinen, R., 2017b. Characterization and timing of the Isovaara and Riikonkumpu faults in northern Finland. *Global and Planetary Change* 157, 59-72.

Olesen, O. Blikra, L.H. Braathen, A. Dehls, J.F. Olsen, L. Rise, L. Roberts, D. Riis, F., Faleide, J.I., & Anda, E., 2004: Neotectonic deformation in Norway and its implications: a review. *Norwegian Journal of Geology* 84, 3-34.

Sarala, P., Johansson, P., & Valkama, J., 2009. End moraine stratigraphy and formation in the southwestern Pyhä-Luosto fell area, northern Finland. *Quaternary International* 207, 42-49.

Sutinen, R., Hyvönen, E., Middleton, M., & Ruskeeniemi, T., 2014. Airborne LiDAR detection of postglacial faults and Pulju moraine in Palojärvi, Finnish Lapland. *Global and Planetary Change* 115, 24-32.

Sutinen, R., Hyvönen, E., Liwata-Kenttälä, P., Middleton, M., Ojala, A., Ruskeeniemi, T., Sutinen, A., & Mattila, J., 2018a. Electrical-sedimentary anisotropy of landforms adjacent to postglacial faults in Lapland. *Geomorphology*, https://doi.org/10.1016/j.geomorph.2018.01.008.

Sutinen, R., Hyvönen, E., Middleton, M., & Airo, M.-L., 2018b. Earthquake-induced deformations on ice-stream landforms in Kuusamo, eastern Finnish Lapland. *Global and Planetary Change* 160, 46-60.

INQUA Focus Group Earthquake Geology and Seismic Hazards

paleoseismicity.org

Old raised shoreline relics at the SE part of Cassandra Peninsula, Northern Aegean Sea, Greece: first data and preliminary interpretation

Syrides, Georgios (1), Chatzipetros, Alexandros (1), Vouvalidis, Konstantinos (2)

(1) Department of Geology, School of Geology, Aristotle University of Thessaloniki, Greece, syrides@geo.auth.gr
(2) Department of Physical & Environmental Geography, School of Geology, Aristotle University of Thessaloniki, Greece

Abstract: *Relics of old raised marine shorelines are discovered along the south rocky coast of Cassandra peninsula. Two types of shorelines were identified: raised notches on limestone and old marine coastlines on limestone raised up to 25m asl, accompanied by borings of marine bivalves and cemented coastal clastic sediments. Formation of these raised shorelines can be attributed to the active fault zone along the south coast of Cassandra peninsula.*

Keywords*: raised shorelines, Cassandra peninsula, tectonic uplift*

Cassandra peninsula is the western of the three smaller peninsulas of Halkidiki in northern Aegean Sea. It is an elongated, NNW-SSE trending, peninsula dominated by low hilly terrain (up to 333m altitude). The peninsula consists of mainly soft Neogene sediments (sands & gravels, sandstones, redbeds, and locally fossiliferous limestones) that cover almost the entire area (Syrides, 1990), except the south-east part (I.G.E.Y. 1969) where older (pre-Neogene) rocks are exposing (Mesozoic limestones, ophiolites and locally hard Paleogene sandstones).

Raised marine shorelines in Halkidiki peninsula were unknown a decade ago. In 2009 a first occurrence was observed at the south end of Athos Peninsula (Syrides, 2010). This short paper presents the second instance that raised marine shorelines are identified in Halkidiki.

These raised marine coastlines are located on the Mesozoic limestone exposing for 2 km along the SE coastline of Cassandra peninsula, at the settlement of Loutra Agias Paraskevis. Two types of raised shorelines were identified:

A. Raised marine notches that are situated along the entire 2 km long limestone shore line. They comprise scattered "mushroom" rocks and notches on steep limestone coast. They reveal an open concave horizontal groove ~1m wide; the upper part exceeding up to ~1m above present sea level. Some minor horizontal notches are locally visible inside this raised groove, possibly reflecting small tectonic uplift events.

B. Relics of raised fossil marine coastline located up to ~25m above present sea level (Figure 1). These are identified by holes of boring bivalves on the limestone, relics of fossiliferous sandstones / conglomerates containing marine molluscs and relics of old gravelly sand, with very well rounded quartz pebbles that accompany the raised shoreline. Most of the pebbles reveal a flattened shape indicative of coastal processes.

Figure 1: Example of a raised fossil marine coastline, relics of cemented coastal clastic sediments, (sands and well-rounded flattened pebbles).

The uplifted shoreline is probably associated with a known offshore normal fault zone of WNW-ESE to E-W strike (South Kassandra offshore composite seismogenic source of Caputo et al., 2012). There is disperse low magnitude seismicity in this area, however the quasilinear epicentre distribution of the earthquake sequence of August 2014 (maximum magnitude was M5), shows that this fault is active. Its location is inferred from high resolution seismic reflection profiles (Papanikolaou et al., 2006). The fault zone can be divided into two segments, based on the change of strike (Figure 2). The one associated with the raised shoreline is of WNW-ESE strike and is *ca.* 22 km long, while the entire zone is *ca.* 46 km long, having a maximum expected magnitude potential of M 6.9 (Caputo et al., 2012). Segment 1 of this fault zone is probably also associated with the axial tilting of the southern part of

Cassandra peninsula, first described by Mountrakis et al. (1993).

Figure 2: Extract of the Greek Database of Seismogenic Sources (Gre.Da.S.S., gredass.unife.it), showing the South Kassandra offshore seismogenic source. The entire fault zone can be divided into two segments, based on the change of strike.

Since this is an offshore fault zone, there has been no substantial indications for its rate of displacement up to now. The indicators reported in this paper provide the first field evidence of physical effects of the fault. Research is still in progress.

REFERENCES

Caputo, R., Chatzipetros, A., Pavlides, S., & Sboras, S., 2012. The Greek Database of Seismogenic Sources (Gre.Da.S.S.): state-of-the-art for northern Greece, *Annals of Geophysics* 55, 5, doi: 10.4401/ag-5168.

I.G.E.Y., 1969. Geologic map of Greece 1:50,000. Sheet: Kassandra Peninsula.

Mountrakis, D., Syrides, G., Polymenakos, L., & Pavlides, S., 1993. Neotectonic structure of Axios-Thermaikos tectonic depression in the area of Western Chalkidiki, Central Macedonia, Greece. *Bull. Geological Society of Greece* XXVIII/1, 379-395, Athens.

Papanikolaou, D., Alexandri, M., & Nomikou, P., 2006. Active faulting in the North Aegean basin, In: Postcollisional tectonics and magmatism in the Mediterranean region and Asia (Dilek, Y., Pavlides, S., eds), *Geol. Soc. Am., Special Paper* 409, 189-20.

Syrides, G., 1990. Lithostratigrapical, biostratigraphical and paleogeographical study of the Neogene-Quaternary sedimentary sequence of Halkidiki peninsula. Doctorate Thesis, School of Geology, Aristotle University of Thessaloniki, Thessaloniki, pp. 320 (in Greek).

Syrides, G., 2010. Holocene raised shorelines along Athos Peninsula, Northern Aegean Sea, Greece - first data. GBGA 2010 Thessaloniki, *Abstract volume*, p. 381, http://www.geo.auth.gr/cbga_2010/Documents/CBGA2010_Abstract_volume.pdf.

INQUA Focus Group Earthquake Geology and Seismic Hazards

paleoseismicity.org

Defining subsegments and testing their roles by comparing with actual rupture extent: an example from the Kamishiro fault, Japan

Takahashi, Naoya (1)

(1) Department of Earth science, Tohoku Univ., 6-3 Aramaki-Aoba, Aoba, Sendai, Miyagi, 980-8578, Japan, naoya.takahashi.t1@dc.tohoku.ac.jp

Abstract: *Analysis of paleoseismological and historical records has revealed that a fault segment tends to behave partially or with adjoining segments. Here we defined four subsegments of the Kamishiro fault, the primary segment of the Itoigawa-Shizuoka Tectonic Line active fault system in Japan, based on vertical slip rate, crest profile in a hanging wall, and structural complexity. Inferred subsegments are then compared with co-seismic slip distribution to check whether they play any roles in rupture propagation. The result indicates that a subsegment boundary can behave as a barrier to rupture propagation and we should consider the influences of a stress change caused by surface processes upon secondary faulting and inherited structures in assessing fault segmentation.*

Keywords*: fault segmentation, subsegments, barrier, surface rupture, Itoigawa-Shizuoka tectonic Line*

INTRODUCTION

Earthquake magnitude largely depends on rupture length, and that makes fault segmentation crucial to seismic hazard assessment. Increasing number of earthquake records infers that a fault segment ranging from one deduced from historical rupture extents to static geological and geophysical criteria (McCalpin, 2009) doesn't always behave persistently, thus rupture partially or with adjacent segments (e.g., Lefevre et al., 2018). According to Manighetti et al. (2009, 2015), faults usually contain 2 to 5 major segments, and most of them are subdivided into 2 to 4 secondary (sub) segments. DuRoss et al. (2016) have compiled paleoseismic data for the central Wasatch fault zone to compare with fault segments estimated from geological and geophysical properties and have found that subsegments may control the lengths of the partial and spillover ruptures (Crone & Haller, 1991). Although some subsegments are not long enough to generate a surface-rupturing earthquake by themselves, analyzing subsegments and their boundaries can provide insight into fault segmentation. Here we define subsegments of the Kamishiro fault, the northernmost segment of the Itoigawa-Shizuoka Tectonic Line active fault system (ISTL) in Japan (Fig. 1), based on slip rate, topographic relief (crest profile in the hanging wall) and surface geometry of the fault trace. Then we discuss roles of subsegments by comparing with co-seismic slip distribution during the 2014 Nagano earthquake (Mw6.2, Japan Meteorological Agency, 2014). For the ease of this comparison, the study area is set to where the 2014 Nagano earthquake has ruptured.

THE 2014 NAGANO EARTHQUAKE

On 22 Nov. 2014, two-thirds of the entire Kamishiro fault ruptured to generate the Mw 6.2 Nagano earthquake. Its hypocenter was located at 137˚53.4' E 36˚41.5' N, 5 km

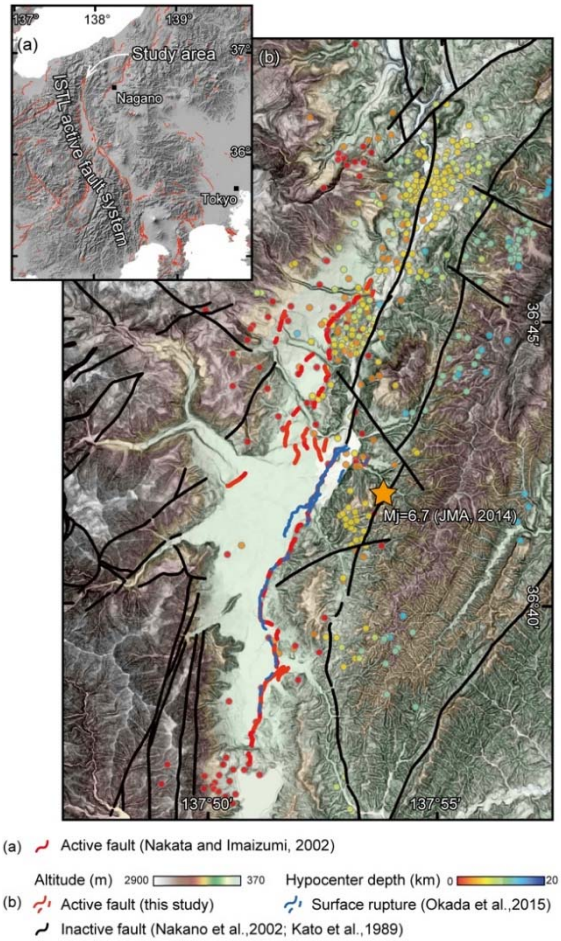

Figure 1: Surface rupture and aftershock distribution (M≧1.0, Nov. 22 to Dec. 31, 2014) accompanied by the 2014 Nagano earthquake. (a) The shaded relief map is offered by Geospatial Information Authority of Japan. (b)The plot of aftershocks is after the Japan Meteorological Agency (JMA) Unified Earthquake Catalogue.

deep, and the focal mechanism showed reverse with left-lateral component (Japan Meteorological Agency, 2014). The ca. 9km of surface rupture was accompanied by the 2014 event, and the maximum displacement was around 80 cm (e.g., Okada et al., 2015). Paleoseismic trenching (e.g., Okumura et al., 2001; Toda et al., 2016; Katsube et al., 2017) and historical records (Usami et al., 2013) has revealed that the penultimate earthquake occurred in 1714 A.D. with the same or a little larger displacement than that of the 2014 event and the anti-penultimate broke multiple segments including the Kamishiro fault in 841 A.D. or 762 A.D. These previous studies have shown the non-characteristic behavior of the Kamishiro fault, and there might be possibility of subsegments controlling a rupture area.

DEFINITION OF SUBSEGMENTS

In defining subsegment, one has to detect discontinuities in the distribution of a geological or geophysical factor along fault strike. These discontinuities usually result from differences not only in tectonic activity but various non-tectonic processes. Therefore, introducing multi-proxy analysis would be helpful to decrease uncertainties caused by non-tectonic processes and define fault segments depending on tectonic activity. To reveal the distribution of vertical slip rate, we identified displaced terraces and measured cumulative offset based on aerial photographs and 1m-meshed digital elevation model (DEM). Then, I calculated vertical slip rate by using tephras and radiocarbon ages shown in the previous studies (Shimokawa and Yamazaki, 1987; Suzuki et al., 2010; Sugito et al., 2015; Niwa et al., 2016; Katsube et al., 2017) (Fig. 2). Although calculated data is not equally distributed along strike, a notable gap of vertical slip rate is observed around 12-13 km (Fig. 2), suggesting this gap corresponds to a subsegment boundary. Despite the fact that crest profile is a function of various factors, such as long-term tectonic activity, river incision and volcanic activity, its profile well reflects cumulative displacement. Manighetti et al. (2009, 2015) have shown that an inter-segment zone coincides with a trough in a cumulative displacement (crest height) profile, so I interpreted five narrow troughs in the observed crest profile as subsegment boundaries (Fig. 2).

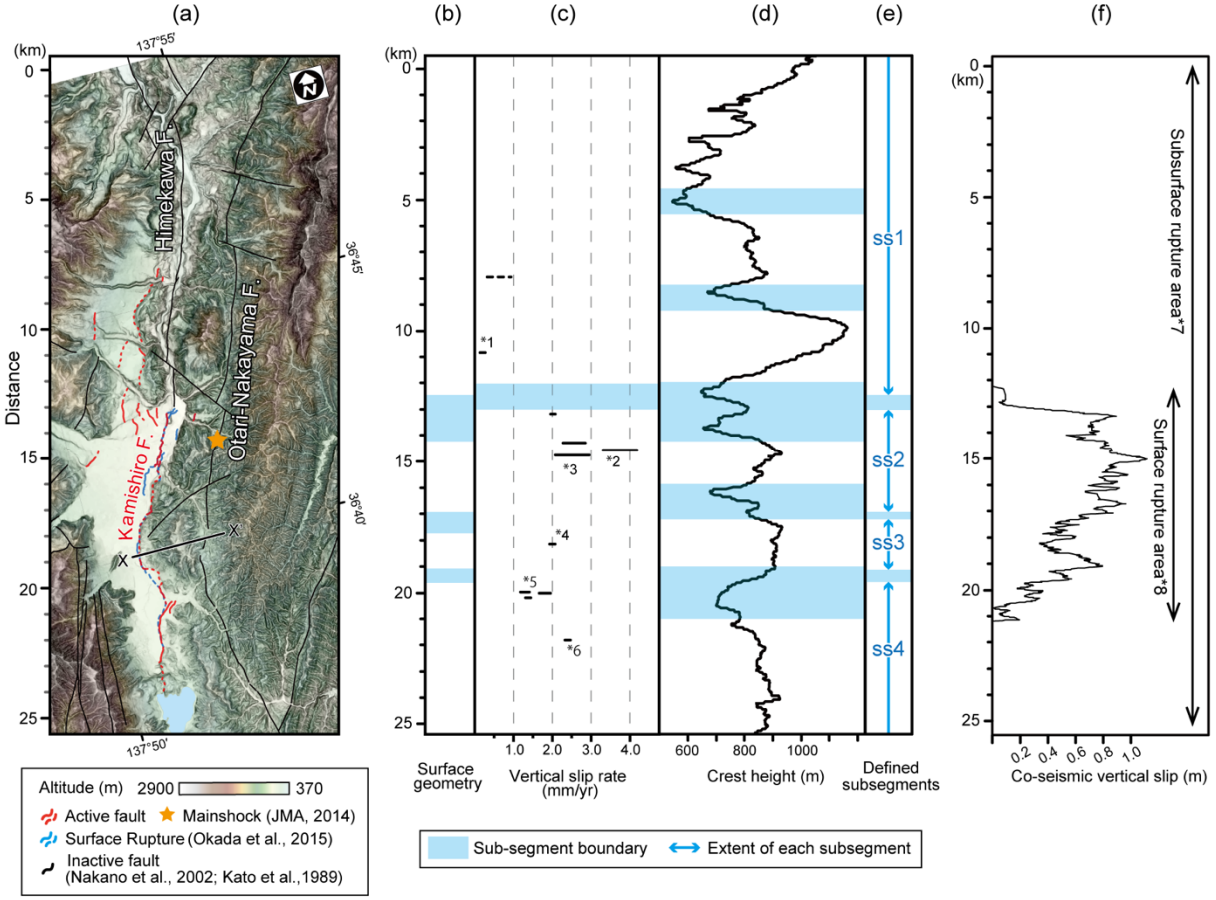

*Figure 2: Definition of subsegments and comparison with the co-seismic vertical slip distribution. (a) topographic map around the Kamishiro fault. (b), (c), (d) Possible sub-segment boundaries based on static geological factors are shown as blue-hatched areas. Terrace ages are estimated from *1 Suzuki et al. (2010), *2 Toda et al. (2016), *3 Sugito et al. (2015), *4 Katsube et al. (2017), *5 Niwa et al. (2016), *6 Shimokawa and Yamazaki (1987). (e) Defined subsegments are named as ss1-4 from the north. (f) In an area around 12-21 km, the clear surface rupture was observed, while in other areas, only minor cracks emerged. *7 is after Kobayashi et al. (in press). *8 is after Ishimura et al. (submitted).*

Analysis of historical rupture endpoints have proved that earthquake rupture often terminates where geometrical complexities, such as bends, branches, and gaps, are observed (e.g., King & Nabelek, 1985; Knuepfer, 1989; Biasi

& Wesnousky, 2017). In the study area, the fault trace shows complexities at three points: one branch around 12.4-14.2 km, two prominent bends (with several hundred meters of step) around 16.9-17.7 and 19.1-19.6 km. Based on discontinuities inferred from each factor, we defined four subsegments; referred to as ss1-4 from the north (Fig. 2). The northern end of ss1 and the southern end of ss4 are estimated to be located outside of the study area because no correspondence of inferred discontinuities is observed at both limits of the study area.

ROLE OF SUBSEGMENTS

Defined subsegments need to be tested whether they play any roles during an earthquake. Here we refer to two results of surface and subsurface co-seismic slip estimation for comparison with defined subsegments; one from a differential LiDAR analysis (Ishimura et al., submitted), and the other from an InSAR analysis (Kobayashi et al., in press). Around the boundary between ss1 and ss2, surface rupture terminated abruptly (Ishimura et al., submitted) while in an area deeper than several kilometers earthquake rupture propagated through this boundary (Kobayashi et al., in press). The same is estimated from the relocated aftershock distribution (Panayotopoulous et al., 2016). Around the ss2-ss3 and ss3-ss4 boundaries, features which are characteristic of rupture endpoints, such as a change in slip sense, tapering and abrupt decrease in co-seismic slip distribution, are not observed. Instead, on the ss3, shorter wavelength deformation occurred compared to adjacent subsegments, and this perhaps reflects the different sub-surface fault geometry.

The comparison shows some subsegments can behave as a barrier to rupture propagation. Considering analyses on historical rupture endpoints (e.g., Knuepfer, 1989; Wesnousky, 2008), one of the key factors to reveal how a segment boundary behaves is the discontinuity of subsurface structure; thus we focus on a subsurface geometry of each subsegment.

According to the relocated aftershock distribution (Panayotopoulous et al., 2016), the Kamishiro fault dips 30°-45° SE at 0-3.5 km depth and converges to the Otari-Nakayama fault, dipping 50°-65° SE, at around 3.5-4.0 km depth. Though this sub-surface geometry is roughly common to all of the defined subsegments, features differentiating with adjacent subsegments are observed in ss1 and ss3. In ss1, several outcrops showing 60°-80° dipping, N-NE striking fault with sinistral displacement are observed along the Himekawa fault, though we are not sure whether this accompanied with the 2014 event. Linear phase discontinuity of the interferogram calculated by Kobayashi et al. (in press) appears along the Himekawa fault. Moreover, an aftershock cluster dipping 80° W and with strike-slip component (Panayotopoulous et al., 2016) exists in ss1. These observations suggest that slip on a steeply dipping fault has been triggered during the 2014 earthquake. The ss3 is characterized by a bow-shaped surface geometry. Two breaks in slope are observed along X-X' (Fig. 3). One corresponds with ~30 m high fault scarp and also with where the 2014 surface rupture has emerged, and the other is found around 1.0 km in X-X' profile and corresponds with a geological boundary between early Pleistocene to Holocene lacustrine deposit and early Pleistocene volcanic rock (Fig. 3). Besides, there is a discrepancy between topographic relief, showing long-term cumulative displacement, and co-seismic vertical slip distribution during the 2014 earthquake (Fig. 3). These observations indicate that the deformation front has migrated westward by ca. 300 meters in ss3. This migration resulted from a stress change in the shallow area due to successive deposition in the footwall (e.g., Rodgers & Rizer, 1981). Considering dipping angle of the Kamishiro fault, migrated fault strand is estimated to diverge from the main strand at shallower than 300m depth.

While at the ss1-ss2 boundary the sense of slip and dipping angle of a fault strand which was activated during the 2014 event changes, at the ss2-ss3 and ss3-ss4 boundaries dipping angle slightly changes only in an area shallower than ca. 300m deep. Though there is no quantitative criterion for determining roles of subsegment boundaries, the difference in subsurface fault geometry shallower than several hundred meters is not enough for the boundary to behave as a barrier.

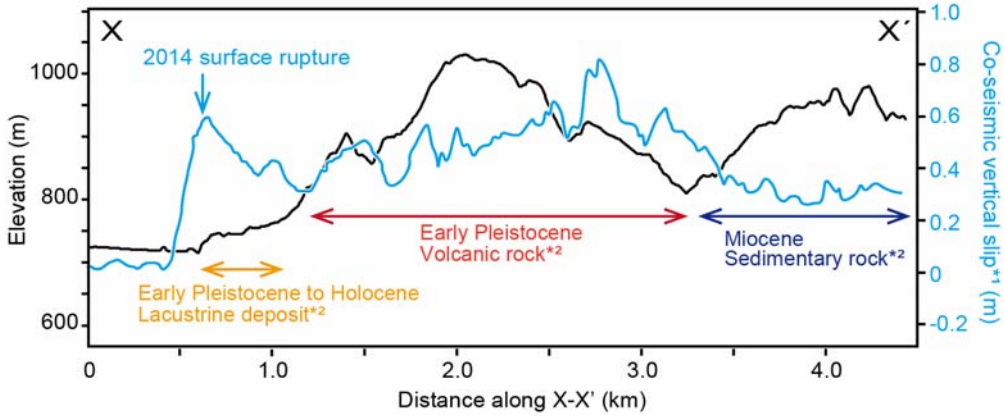

*Figure 3: Topographic and co-seismic vertical slip profile along X-X' line shown in Fig. 2. *1 is after Ishimura et al., (submitted). *2 is after Nakano et al. (2002).*

CONCLUSION

Defining subsegments can be helpful to understand non-characteristic rupture behavior of a fault. Our study confirmed that a subsegment boundary is capable of stopping rupture propagation depending on variation in subsurface structure between adjoining segments. Moreover, the comparison between subsegments and co-seismic slip distribution of the 2014 Nagano earthquake has enabled us to check whether defined subsegments play some roles during an earthquake. Though we only have limited number of examples to verify inferred segments using post-earthquake observation, such fact-checking will help us to tackle issues of fault segmentation.

Acknowledgments: I would like to thank my supervisor, Prof. Shinji Toda, for his kind support and helpful comments on this work.

REFERENCES

Biasi, G.P., & Wesnousky, S.G., 2017. Bends and Ends of Surface Ruptures. *Bulletin of the Seismological Society of America* 107 (6), 2543-2560, doi:10.1785/0120160292.

Crone, A., & Haller, K., 1991. Segmentation and the coseismic behavior of Basin and Range normal faults: examples from east-central Idaho and southwestern Montana, USA. *J Struct Geol* 13 *(*2), 151-164.

DuRoss, C.B., et al., 2016. Fault segmentation: New concepts from the Wasatch Fault Zone, Utah, USA. *J. Geophys. Res. Solid Earth* 121 (2), 1131-1157, doi: 10.1002/2015JB012519.

Ishimura, D., et al., Three-dimensional surface displacement and surface ruptures associated with the 2014 Mw6.2 Nagano earthquake by differential LiDAR data. Manuscript submitted for publication.

Japan Meteorological Agency, 2014. Information about Nagano-ken Hokubu earthquake occurred on 22 November 2014, at 22:08. http://www.data.jma.go.jp/svd/eqev/data/mech/cmt/fig/cmt20141122220817.html.

Kato, H., et al., 1989. Geology of the Omachi district. Quadrangle Series, 1:50,000, Geological Survey of Japan, AIST, 111p.

Katsube, A., et al., 2017. Surface rupturing earthquakes repeated in the 300 years along the ISTL active fault system, central Japan. *Geophys Res Lett* 44 (12), 6057-6064, doi: 10.1002/2017GL073746.

King, G., & Nábělek, J., 1985. Role of Fault Bends in the Initiation and Termination of Earthquake Rupture. *Science 228* (4702), 984-987, doi:10.1126/science.228.4702.984.

Knuepfer, P.L.K., 1989. Implications of the characteristics of end-points of historical surface fault ruptures for the nature of fault segmentation. In: *Fault Segmentation and Controls of Rupture Initiation and Termination* (Schwartz, D.P., Sibson, R.H., eds), *U.S. Geol. Sur. Open-File Report* 89-315, 193-228.

Kobayashi, T., et al., in press. SAR-revealed slip partitioning on a bending fault plane for the 2014 Northern Nagano earthquake at the northern Itoigawa-Shizuoka tectonic line. *Tectonophysics*, doi:10.1016/j.tecto.2017.12.001.

Lefevre, M., et al., 2018. Slip deficit and temporal clustering along the Dead Sea fault from paleoseismological investigations. *Scientific Reports* 8 (1), 4511, doi:10.1038/s41598-018-22627-9.

Manighetti, I., et al., 2009. Self-similarity of the largest-scale segmentation of the faults: Implications for earthquake behavior. *Earth Planet Sc Lett* 288 (3-4), 370-381, doi: 10.1016/j.epsl.2009.09.040.

Manighetti, I., et al., 2015. Generic along-strike segmentation of Afar normal faults, East Africa: Implications on fault growth and stress heterogeneity on seismogenic fault planes. *Geochem Geophys Geosystems* 16 (2), 443-467, doi: 10.1002/2014GC005691

McCalpin, J.P., ed. 2009. *Paleoseismology,* Academic Press.

Nakata, T., & Imaizumi, T., ed. 2002. *Digital Active Fault Map of Japan*. Univ. of Tokyo Press.

Nakano, S., et al., 2002. Geology of the Shiroumadake district. Quadrangle Series, 1:50,000. Geological Survey of Japan, AIST, 105p.

Niwa, Y., et al., 2016. Boring survey, 2015 Report of the Comprehensive Study of the Itoigawa-Shizuoka Tectonic Line Active Fault system (Additional survey). Ministry of Education, Culture, Sports, Science and Technology (MEXT), 60-71 (in Japanese).

Okada, S., et al., 2015. The First Surface-Rupturing Earthquake in 20 Years on a HERP Active Fault is Not Characteristic: The 2014 Mw 6.2 Nagano Event along the Northern Itoigawa-Shizuoka Tectonic Line. *Seismol Res Lett* 86 (5), 1287-1300, doi: 10.1785/0220150052.

Okumura, K., 2001. Paleoseismology of the Itoigawa-Shizuoka tectonic line in Japan. *J. seismology* 5, 411-431.

Panayotopoulos, Y., et al., 2016. Seismological evidence of an active footwall shortcut thrust in the Northern Itoigawa-Shizuoka Tectonic Line derived by the aftershock sequence of the 2014 M 6.7 Northern Nagano earthquake. *Tectonophysics* 679, 15-28, doi:10.1016/j.tecto.2016.04.019.

Rodgers, D.A., & Rizer, W.D., 1981. Deformation and secondary faulting near the leading edge of a thrust fault. In: *Thrust and Nappe Tectonics* (McClay, K.R., Price, N.J., eds), *Geol. Soc. London, Spec. Publ.* 9, 65-77.

Shimokawa, K., & Yamazaki, H., 1987. Fault movement analyzed from deposits of Lake Old Kamishiro. *Association of Japanese Geographers* 17, 92-93 (in Japanese).

Sugito, N., et al., 2015. Slip rate and timing of faulting on the Kamishiro fault revealed at Shinden and Oide, Hokujo, Hakuba Village, central Japan. *Active Fault Res*. 43, 109-118 (in Japanese).

Suzuki, Y., et al., 2010. Prediction of coseismic fault behavior based on slip-rate and slip distributions for the northern part of the Itoigawa-Shizuoka Tectonic Line active fault zone, central Japan. *Active Fault Res*. 33, 1-14 (in Japanese).

Toda, S., et al., 2016. Trench survey, 2015 Report of the Comprehensive Study of the Itoigawa-Shizuoka Tectonic Line Active Fault System (Additional survey). Ministry of Education, Culture, Sports, Science and Technology (MEXT), 72-95 (in Japanese).

Wesnousky, S.G., 2008. Displacement and Geometrical Characteristics of Earthquake Surface Ruptures: Issues and Implications for Seismic-Hazard Analysis and the Process of Earthquake Rupture. *Bulletin of the Seismological Society of America* 98 (4), 1609-1632, doi: 10.1785/0120070111.

INQUA Focus Group Earthquake Geology and Seismic Hazards

paleoseismicity.org

Three-dimensional displacement field of a large co-seismic landslide (2017 Iraq-Iran earthquake) using optical-image correlation and SAR pixel offset-tracking

Valkaniotis, Sotiris (1), Foumelis, Michael (2), de Michele, Marcello (2), Ganas, Athanassios (3), Papathanassiou, George (4)

(1) 9 Koronidos Street, Trikala, 42131 GREECE, valkaniotis@yahoo.com
(2) BRGM - French Geological Survey, Orleans, 45060 FRANCE, m.foumelis@brgm.fr, m.demichele@brgm.fr
(3) Geodynamic Institute, National Observatory of Athens, 11810 GREECE, aganas@noa.gr
(4) Department of Civil Engineering, Democritus University of Thrace, Xanthi, 67100 GREECE, gpapatha@gmail.com

Abstract: *The strong M7.3 November 12 2017 earthquake at the border region of Iraq-Iran activated a massive landslide near Mela Kabod village, Iran. The Mela Kabod landslide was the most significant secondary effect of the 2017 earthquake and of considerable importance, due to its size, for the study and documentation of earthquake environmental effects. Using optical-image correlation and SAR pixel offset tracking, we produced a detailed 3D deformation field of the landslide complex. A multi-sensor analysis using various and multiple processing techniques demonstrated the accuracy of the resulting deformation measurements and the capacity to accurately detect and map earthquake-induced landslides using satellite sensors.*

Keywords*: 3D displacement field, image correlation, earthquake-induced landslide, SAR, Iran*

INTRODUCTION

A strong earthquake on 12 November 2017 (Mw 7.3 USGS, IRSC) occurred in the border region of Iraq-Iran, at the NW part of Zagros range (Fig. 1). The main event resulted in a 90 cm vertical and 50 cm westward displacement on the surface, and a maximum slip of ~3 m (Koyabashi et al., 2018) along a low angle east-dipping thrust fault. No surface displacement was measured or observed around the epicentral area. Slip probably occurred along a fault surface of the Zagros Foredeep Front (Mountain Front Flexure), one of many that comprise a wide fold and thrust belt between the Arabian platform to the west and High Zagros Fault (Main Recent Fault) to the east of the area (Berberian, 1995; Allen et al., 2013). Only minor seismicity has been observed in the epicentral area, with the exception of two historic events of M~6 on 958 and 1150 AD (Ambraseys & Melville, 1982; Berberian, 1995).

Multiple landslides and rock falls were reported in the wider epicentral region, from Darbandikhan to the north up to Sarpol Zahab to the south. The largest landslide activated due to the November 12 earthquake was north of Sarpol Zahab, Iran, near the village of Mela Kabod (Fig. 1 & 2). The displacements induced by the Mela Kabod landslide were not possible to be measured by conventional SAR interferometry (InSAR). The landslide area appears fully decorrelated, low coherence levels, in co-seismic interferograms, due to the large amount of motion involved.

METHODS

In order to measure and map more accurately the co-seismic deformation of the landslide, we used optical satellite image correlation and SAR offset tracking.

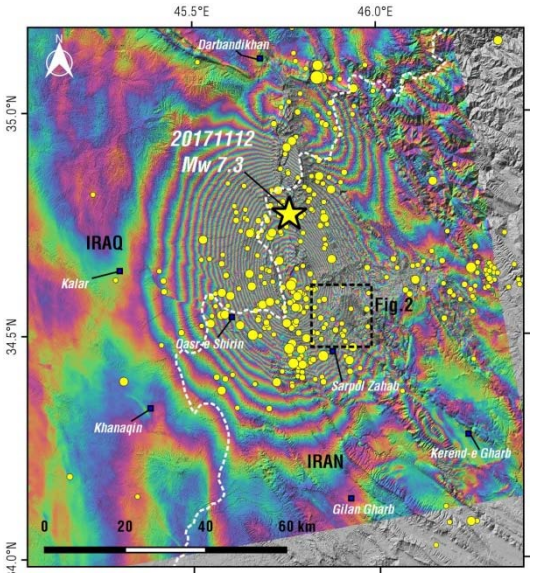

Figure 92: The November 12 2017 M7.3 earthquake (main epicentre with star) at the border region between Iraq and Iran. Sentinel-1 co-seismic interferogram (ascending) between 2017-11-11 and 2017-11-17.Epicentres with M>3 from IRSC.

Utilizing Sentinel-1 IW SLC data the 3D displacement field of the landslide was calculated combining range and azimuth offsets from three independent tracks, one ascending (orbit 72, 20171111-20171117) and two descending ones (orbit 79, 20171112-20171118 and orbit 6, 20171107-20171119). Initially, global offsets were estimated and subtracted. Then, an iterative offset measurement and refinement approach was applied in which search window sizes were reduced at each following step. Finally, range and azimuth offset from both geometries were combined to retrieve the 3D

displacement field of the landslide (de Michele et al., 2010).

For the optical image correlation, we used three different sets of images; Copernicus Sentinel-2A/B medium resolution, ASTER L1A high resolution and TripleSat very high resolution images, with pre- and post-event acquisitions available for each set. Sentinel-2 and ASTER images were processed using the CosiCorr optical correlation software (Leprince et al., 2007) and TripleSat VHR with CIAS (Kääb, 2002; Heid & Kääb, 2012).

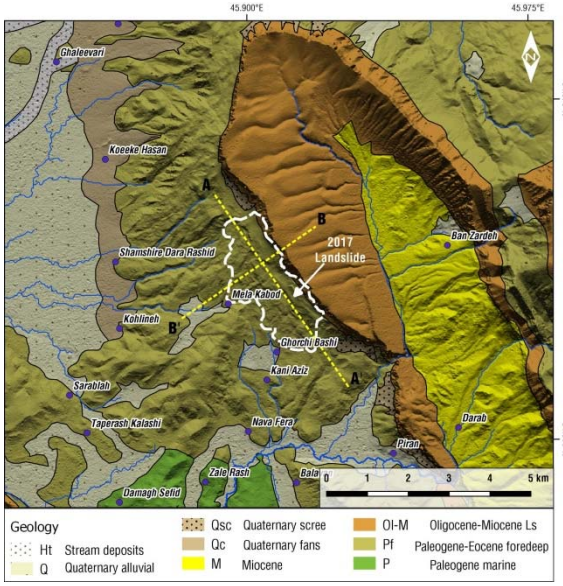

Figure 2: Geological map of the Mela Kabod landslide area. Geological formation interpretation using a detailed DEM and VHR satellite imagery. Stratigraphy from Barwary & Said (1993), Homke et al. (2009) and Sissakian & Fouad, (2012). White line marks the outline of the 2017 co-seismic landslide, traced from VHR imagery. Relief from a 4m DEM extracted from Corona stereo pair.

CosiCorr produces two separate EW and NS displacement grids, and a resulting vector field for 2D displacement. CIAS output is a vector point file with dX, dY, azimuth and total length of displacement vector. The spacing of the output displacement grids is 120, 80 and 10 m for ASTER, S2 and TripleSat, respectively. ASTER and Sentinel-2 results are presented in Fig. 4 & 5. Both CosiCorr resulting displacement fields are quite similar, with minor differences probably due to smaller spatial resolution (15 m for ASTER, 10 m for Sentinel-2A/B) as well as the variation of sensor scan angles for different dates. Absence of dense vegetation and small seasonal variability in land cover in the area of the landslide further enhances the quality of resulting image correlation.

A pair of VHR TripleSat-1 images for the Mela Kabod landslide was made available, with a 2016-06-04 pre-event acquisition and a 2017-11-14 post-event acquisition. TripleSat (BJ-2) panchromatic frames at 0.8 m resolution were orthorectified, resampled at 1 m and then co-registered. A normalized cross-correlation was implemented for pre- and post-event images using the CIAS software. A spacing of 10 m was selected for the final point displacement field, as lower values introduced larger errors and noise, mainly due to image coherence and orthorectification inaccuracies.

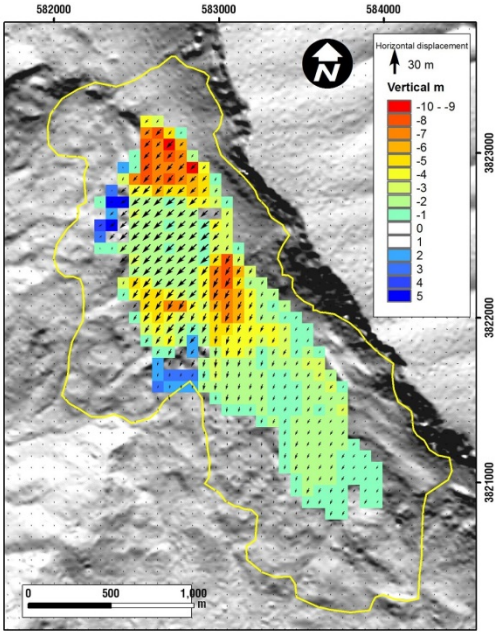

Figure 3: 3D deformation field from Sentinel-1 offset tracking. Arrows represent azimuth and magnitude of horizontal displacement, and colour map for up-down (vertical) displacement.

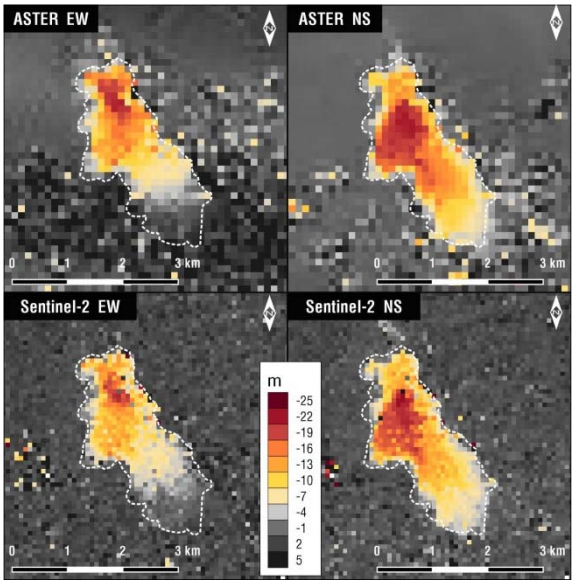

Figure 4: East-west displacements (left) and north-south (right) displacements from ASTER and Sentinel-2 images, using CosiCorr. Positive value towards north and east, respectively.

CIAS results for VHR imagery provides a detailed map of horizontal deformation (Fig.6). Correlation of VHR imagery provides a more accurate landslide boundary delineation, at a mapping resolution of <10 m, close to the one of handheld GNSS receivers. Finer resolution grid enables visualization and mapping of the landslide main block interior deformation. In the case of Mela Kabod landslide, multiple secondary fractures can be traced with localised displacement of more than 10 m.

CIAS correlation of VHR imagery produced a more noisy deformation field, in comparison to ASTER, Sentinel-2 and Sentinel-1. Final point measurements were further improved using a noise reduction filter (REF), although small non-correlated patches remained in the vicinity of the landslide as they correspond to areas with major land cover change between the acquisition dates (agricultural fields and vegetation patches).

DISCUSSION

Examining VHR imagery, local geology and local relief, we assess the area as a large complex of multiple individual paleo-slides, developed on top of a soft rock formation, along the western slope of a syncline (Fig.2). The 2017 re-activation took place mainly inside the older landslide deposits. Yet, no evidence for past activity was found, based on visual interpretation of 1965-1969 Corona satellite imagery.

Image correlation and offset tracking applied to multiple sensors for the Mela Kabod landslide enables us to accurately map the 2D (optical) and 3D (SAR) deformation field of the landslide block. The mapped landslide block covers a total surface area of 4.4 km^2, with a maximum length of 3.8 km and 1.7 km width. The displaced block is estimated to have a volume of >100M m^3 (using a slide surface of at least 20 m deep), corresponding to a value of XI in ESI 2007 scale (Michetti et al., 2007) for the 2017 earthquake.

Analysis of the results from multiple sensors shows a displacement of the landslide block towards SW. The main slide scarp originated at the NE part, at the boundary between overlying limestones and older soft sediments, producing local high-angle scarps up to 20 m height. Two different sub-blocks can be identified inside the landslide area; a western one with high displacement values and internal complexity, and an eastern one with low displacement (Fig.4 & 6). Vertical displacement from Sentinel-1 indicates localized graben formation at the western-central part of the landslide block (Fig.3). We interpret the Mela Kabod landslide as a complex slide with a series of embedded slip surfaces.

Comparing optical and SAR image correlation, results appear comparable with no significant differences. In the comparison profiles of Fig. 5, a narrowing of Sentinel-1 deformation field is observable that we attribute to unfavourable scan angle along the syncline slope as well as to the coarser resolution of SAR outputs (70m). High-resolution optical and SAR imagery can be used for operational detection and mapping of similar co-seismic secondary effects, while VHR imagery correlation enables detailed mapping and characterisation of the features.

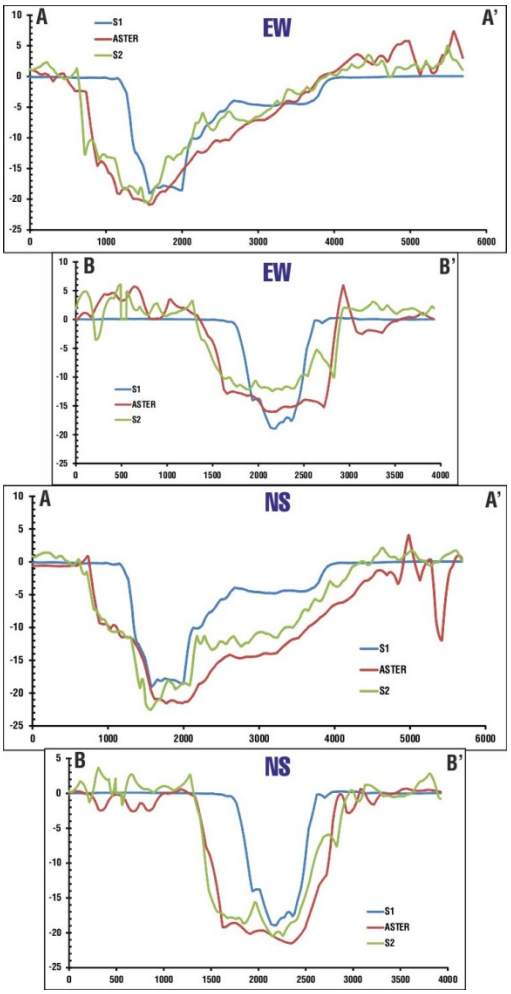

Figure 5: Comparison of east-west and north-south displacements for Sentinel1, ASTER and Sentinel-2. Location of profiles in Figure 2.

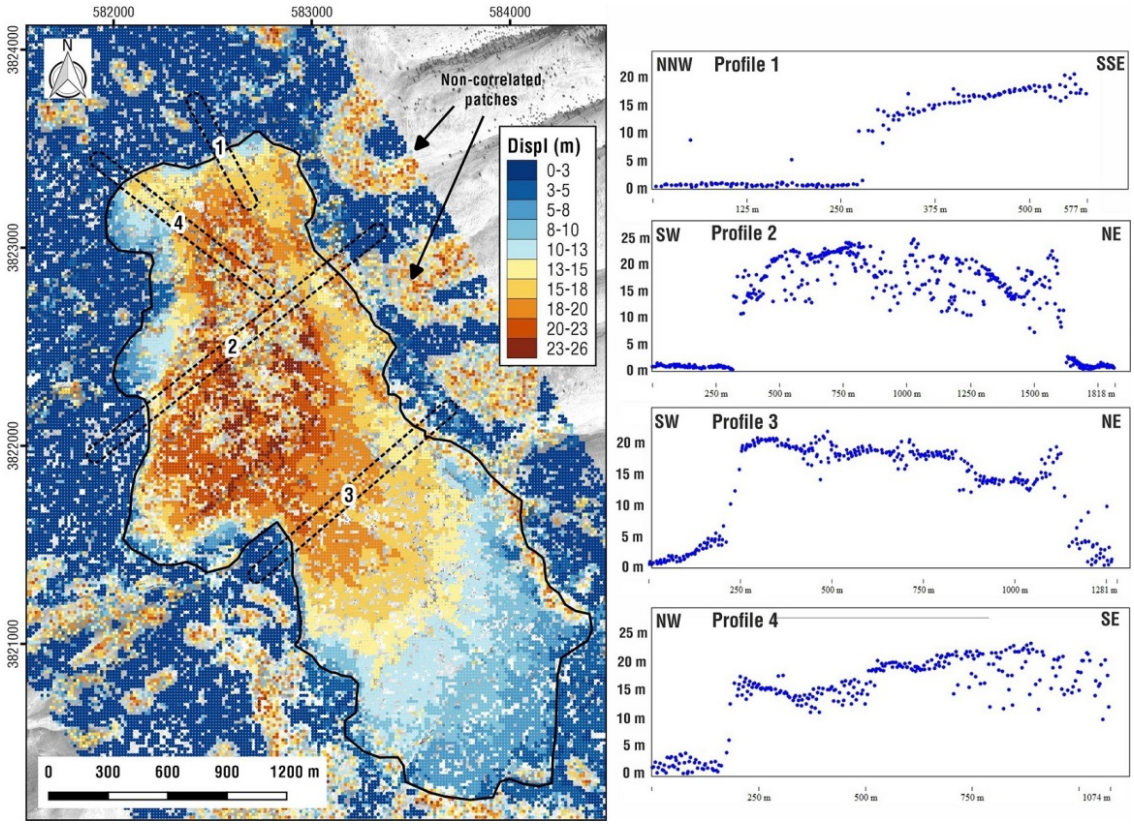

Figure 6: Detailed map of horizontal deformation for the Mela Kabod landslide, using VHR optical imagery. Left: Magnitude of displacement (length in meters) from the CIAS results, in a dense 10x10 m grid of points. Solid line marks the outline of the co-seismic landslide. Right: Swath profiles (40m) showing in details the landslide slip boundary and interior displacement variability.

Acknowledgements: We thank ChinaGEOSS, AOGEOSS and 21AT Co. Ltd for providing pre- and post-earthquake TripleSat data, and ESA for providing Sentinel-1 and Sentinel-2 imagery.

REFERENCES

Allen, M.B., Saville, C., Blanc, E.J-P., Talebian, M., & Nissen, E., 2013. Orogenic plateau growth: Expansion of the Turkish-Iranian Plateau across the Zagros fold-and-thrust belt. *Tectonics* 32, 171-190.

Ambraseys, N.N., & Melville, C.P., 1982. *A History of Iranian Earthquakes*. Cambridge Univ. Press, Cambridge, 219pp.

Barwary, A.M., & Said, F.S., 1993. Report on the Geology of Khanaqin Quadrangle. Sheet NI- 38-37 (GM 15), scale 1:500.000. State establishment of Geological Survey and Mining (Geosurve). Baghdad, Iraq, 23p.

Berberian, M., 1995. Master "blind" thrust faults hidden under the Zagros folds: active basement tectonics and surface morphotectonics. *Tectonophysics* 241, 193-224.

de Michele, M., Raucoules, D., de Sigoyer, J., Pubellier, M., & Chamot-Rooke, N., 2010. Three-dimensional surface slip of the 12 May 2008 Sichuan earthquake (China) from Synthetic Aperture Radar. *Geophysical Journal International* 183, 1097-1103.

Heid, T., & Kääb, A., 2012. Evaluation of existing image matching methods for deriving glacier surface displacements globally from optical satellite imagery. *Remote Sensing of Environment* 118, 339-355.

Homke, S., Verges, J., Serra-Kiel, J., Bernaola, G., Sharp, I., Garces, M., Montero-Verdu, I., Karpuz, R., & Goodarzi, M.H., 2009. Late Cretaceous-Paleocene formation of the proto-Zagros foreland basin, Lurestan Province, SW Iran. *Geol. Soc. America Bull.* 121 (7-8), 963-978.

Kääb, A., 2002. Monitoring high-mountain terrain deformation from repeated air- and spaceborne optical data: examples using digital aerial imagery and ASTER data. *ISPRS Journal of Photogrammetry & Remote Sensing* 57 (1-2), 39-52.

Kobayashi, T., Morishita, Y., Yarai, H., & Fujiwara, S., 2018. InSAR-derived Crustal Deformation and Reverse Fault Motion of the 2017 Iran-Iraq Earthquake in the Northwest of the Zagros Orogenic Belt. *Bull. Geospatial Info. Auth.* 66, http://www.gsi.go.jp/common/000197807.pdf.

Leprince, S., Barbot, S., Ayoub, F., & Avouac, J.-P., 2007. Automatic and Precise Orthorectification, Coregistration, and Subpixel Correlation of Satellite Images, Application to Ground Deformation Measurements. *IEEE Trans. Geosci. Remote Sens*. 45 (6), 1529-1558.

Michetti, A.M., Esposito, E., Guerrieri, L., Porfido, S., Serva, L., Tatevossian, R., Vittori, E., Audemard, F., Azuma, T., Clague, J., Comerci, V., Gurpinar, A., McCalpin, J., Mohammadioun, B., Mörner, N.A., Ota, Y., & Roghozin, E., 2007. Intensity Scale ESI 2007. In: *Mem. Descr. Carta Geol. d' Italia* (Guerrieri, L., Vittori, E., eds)*., Vol. 74*, Servizio Geologico d'Italia - Dipartimento Difesa del Suolo, APAT, Rome, Italy.

Sissakian, V., & Fouad, S., 2012. Geological Map of Iraq scale 1:1.000.000. 4th edition, Iraqi Geological Survey, Baghdad, Iraq.

INQUA Focus Group Earthquake Geology and Seismic Hazards

paleoseismicity.org

The Delphi-Amfissa Fault Zone, central Greece: active extension, morphotectonics and mass wasting at the northern part of Corinth Rift

Valkaniotis, Sotiris (1), Pavlides, Spyros (2)

(1) 9 Koronidos Street, 42131 Greece, valkaniotis@yahoo.com
(2) Aristotle University of Thessaloniki, Department of Geology, 54124, Thessaloniki, Greece, pavlides@geo.auth.gr

Abstract: *The Delphi-Amfissa fault zone (DAFZ) is a large extensional structure north of the Corinth rift in central Greece. The DAFZ is associated with significant landscape features with evidence of post LGM activity and strong historical earthquakes. Large landslides along the Delphi fault are mapped, including possibly the largest known up to date paleo-landslide in continental Greece, near Davlia. Co-seismic ruptures from the 1870 earthquake are attributed to parts of the DAFZ and to secondary faults. Using structural and morphotectonic criteria, we propose a segmentation of the DAFZ. Taking into account the activity and structure of the DAFZ, we interpret it as a boundary structure associated with the Corinth rift.*

Keywords*: normal fault, segmentation, Corinth Rift, landslides, earthquake surface rupture*

INTRODUCTION

The Corinth Rift is a rapidly expanding intra-continental W-E extensional rift, across the Alpine formations of the External Hellenides Geotectonic units of Pindos, Vardoussia, Parnassos and Beotia (Doutsos et al., 1988; Armijo et al., 1996; Nixon et al., 2016; Rohais & Moretti, 2017). The initiation of the rift is estimated at the Late Pliocene (3.3 Ma) and is currently involving extension along segmented and individual normal faults (Figure 1) of W-E to WNW - ESE strike in a broad zone from Patras Gulf to the west up to Beotia and Asopos rift to the east (Taylor et al., 2011; Bernard et al., 2015). Evidence of the active deformation state and rate of the Corinth Rift are numerous; strong historical and recent earthquakes, intense microseismic activity and extension measured by GPS and surveys (Sebrier, 1977; Papadopoulos et al., 1986; Ambraseys & Jackson, 1990; Hatzfeld et al., 2000; Bell et al., 2009; Lambotte et al., 2014). Earlier interpretations of the Corinth Rift as an asymmetrical basin with fault activity concentrated on the southern north-dipping faults are being revised as a more complex basin structure is revealed from recent detailed offshore surveys (Bell et al., 2009; Gawthorpe et al., 2017). In the northern part of the Corinth rift, a series of extensional faults develop parallel to the main rift accommodating the extension between the Corinth Rift and the northern rifts of Kifissos and Sperchios. The most prominent and significant of these structures is the Delphi-Amfissa fault zone.

THE DELPHI-AMFISSA FAULT ZONE

The Delphi - Amfissa fault zone (DAFZ) is a large active extensional structure north of the central part of the Gulf of Corinth along the southern slope of Parnassos Mountain (Péchoux, 1964; de Boer & Hale, 2000; Piccardi et al., 2008; Valkaniotis & Pavlides, 2017). The main Delphi - Arachova segment fault has an orientation of WNW-ESE to WSW-ENE and is dipping south, with a length of about 10 km each (Figure 2). To the west the fault is defined by a large morphological scarp from the Amfissa-Itea plain to the east of Delphi archaeological site with a trend of NW-SE to W-E. The eastern part near Arachova is less accurately defined and mapped, due to the large slope debris and avalances and the erosivity of the flysch basement formation. Fault measurements and morphotectonic features show a complex normal fault zone with an oblique slip and fault lineations 60^0 to the west (Valkaniotis, 2009).

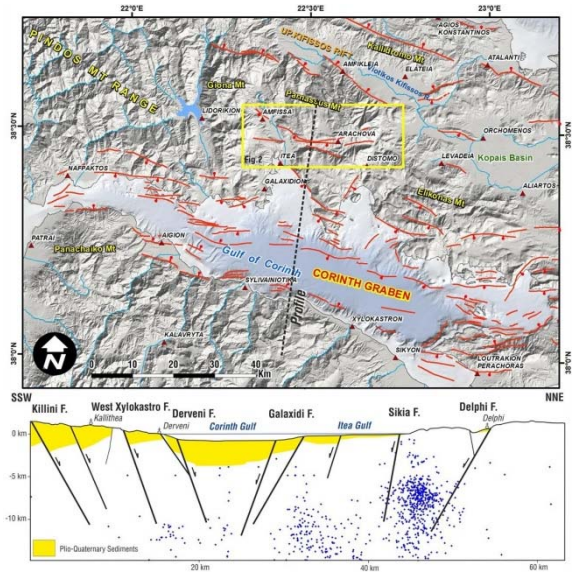

Figure 93: Active onshore and offshore faults of Corinth Gulf and surrounding regions, central Greece. Yellow box marks the position of Fig.2. Structural profile shows the fault architecture across the central part of Corinth Gulf with hypocenters of recent (2008-2018) seismicity with magnitudes M>2. Earthquake data from NOA catalogue.

Overal morphological scarp reaches up to 500 meters in the Plistos Valley, with a post-glacial striated fault scarp of up to 10 meters. The fault zone is distributed with multiple parallel fault scarps along strike converging at a depth to the main fault surface, as is evident in the area of the Delphi Oracle (Piccardi, 2008; Valkaniotis & Pavlides, 2017). The Delphi Oracle site complex is situated inside the fault zone on the hanging wall and is disrupted by at least two historical surface ruptures in 373 BC and 1870 (de Boer & Hale, 2000; Piccardi et al., 2008; Valkaniotis, 2009). The westernmost part of Delphi-Arachova segment is defined by the footwall entrenching of the meander of Skitsa River. After a step of 1.5-2 km the fault zone continues to the west with the Amfissa active fault (Valkaniotis, 2009). We interpret this fault step as a persistent segment boundary and consider the Amfissa fault as a non-linked structure with the Delphi-Arachova segment (Figure 3).

In figure 4, we present a proposed scenario of primary segments and secondary sub-segments for the DAFZ. Sub-segment and segment boundaries are defined using multiple criteria such as topography, along-strike changes in fault strike, fault complexity, relay ramps and steps and the presence of salients (WGUEP, 2016). Total length of DAFZ is up to 33 km. Apart from the Amfissa step, we propose at least two sub-segment boundaries inside the Delphi segment which separate it into three sub-segments with 6, 18 and 5 km length. In figure 4, a profile along the DAFZ was constructed, showing the total footwall throw, using a swath of 1 km width. Almost uniform variation of the footwall throw, especially in the central and eastern part of Delphi segment, is a supporting evidence for the fault origin of the escarpment.

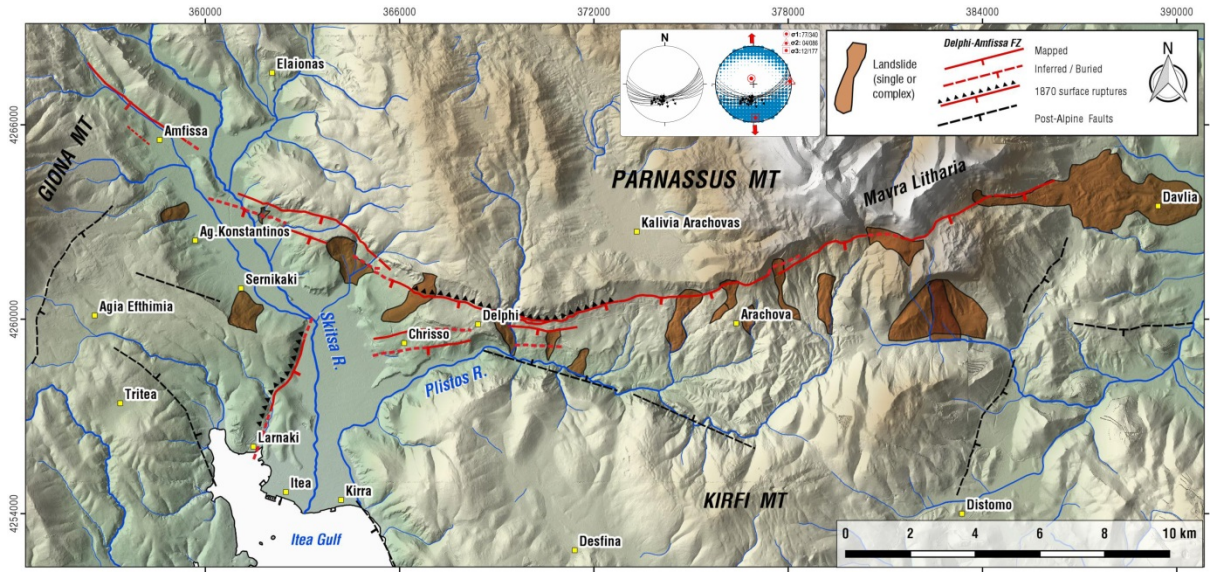

Figure 2: Detailed map of the Delphi - Amfissa fault zone. Large modern and prehistoric landslides along the fault zone are depicted with brown polygons. Inset shows stereographic plots of measured fault plane striations and tensor axis.

Using field data, aerial imagery and detailed DSMs, we mapped a large number of significant landslides along the DAFZ (Figure 2). Estimated age of the landslides is historic or prehistoric and most of them are found along the DAFZ fault trace, in the northern side of Plistos valley. These large landslides are of significant importance to the study of active extension and tectonic structure, as they can mask or displace geologic boundaries, messing with fault and stratigraphic interpretations if not properly recognised. The most important landslide along the DAFZ is the Davlia paleo-landslide (Figure 3). We identified and mapped this giant prehistoric landslide from the distinct surface flow and accumulation features. The Davlia paleolandslide involves a large volume of material (>400M m^3). Part of the DAFZ footwall and Parnassus summits collapsed and was deposited to the east, with a maximum runout distance of ~6 km.

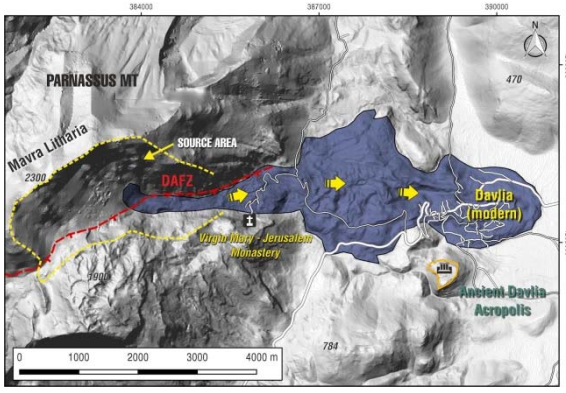

Figure 3: The giant prehistoric Davlia paleo-landslide in the eastern slopes of Parnassus Mt. Displaced and accumulated deposits are marked with purple color. Position of modern and ancient Davlia settlements are marked.

We didn't find any historic reference to this event, and we propose a prehistoric age (Late Quaternary or Early-Middle Holocene) as the surface features are still well preserved. Collapse of the Davlia giant landslide could be triggered by an activation of the DAFZ.

DISCUSSION

Studies of inland active fauls north of the coastline of Corinth Gulf have been limited (Sebrier, 1977; Valkaniotis, 2009; Valkaniotis & Pavlides, 2017). This area between Corinth Rift and the extensional rifts of central Greece to the north (Evoikos, Spercheios) involves some extensional basins (Upper Kifissos; Valkaniotis, 2009) and isolated structures such as the Delphi-Amfissa fault zone. Most of these fault have low or very low slip rates, and accommodate secondary deformation between the major extensional rifts. We propose that a number of these faults are part of the structural complex of the Corinth Rift. The Delphi-Amfissa fault zone is a major normal fault zone with significant historical seismicity (Ambraseys & Pantelopoulos, 1989; Papadopoulos, 2000; Valkaniotis, 2009) and also is associated with significant landscape features. Although the evolution of the fault zone remains unclear, it propably initiated along a pre-existing structure during the early post-alpine deformation period. Activity along the fault zone was increased in the Middle-Late Pleistocene as the orientation of the fault planes was favourable to the N-S extension, and the Corinth Rift was expanding to the north since 0,6-0,4 Ma (Taylor et al., 2011; Gawthorpe et al., 2017). Significant microseismicity patches during the 2008-2018 period are associated with the central fault plane (Figure 1). In the profile of Figure 1, the south dipping Delphi fault is probably the northernmost fault structurally compatible with the main Corinth rift. DAFZ could be a border structure, captured by the extension of the Corinth Rift or partially developed as part of a northernmost expansion of the central part of Corinth rift; High-angle faults are considered to be the dominant strain accommodation mechanism in the upper crust during early rifting (Bell et al., 2017).

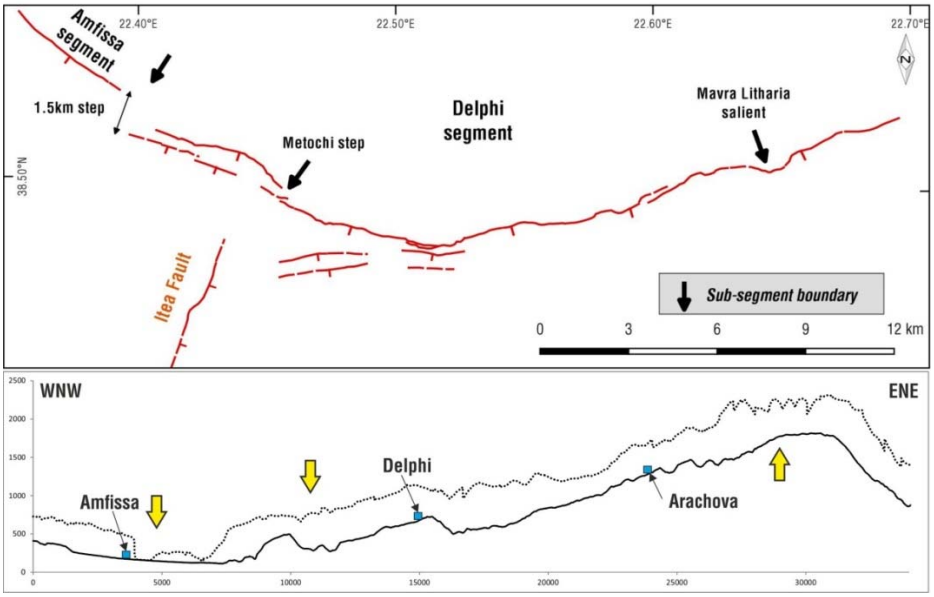

Figure 4: Up; Fault trace of the Delphi-Amfissa fault zone with the proposed primary and secondary segment boundaries. Below; Topographic profile along the DAFZ with elevation of the fault zone (thick line) and the maximum footwall scarp height (dotted line). Yellow arrows mark the sub-segment boundaries from the previous fault map.

The August 1st 1870 earthquake sequence was the most significant and strong recent historical event for both the DAFZ and central Greece area. A foreshock during July 31 was followed by the main earthquake of M 6.7 (epicentre N38.50 E22.60; Papadopoulos, 2000) and a series of strong events, triggered ruptures or strong aftershocks (Ambraseys & Pantelopoulos, 1989). At least 4 strong events during July 31st and August 1 lead to extensive destruction of the area surrounding the DAFZ, with the complete destruction of settlements along the fault zone (Arachova, Chrisso and Kastri - *the predecessor of modern Delphi settlement, then cited on top of the present archaeological site*) and on the Amfissa-Itea valley. Widespread landslides, rock falls and liquefaction were reported around the mesoseismal area (Ambraseys & Pantelopoulos, 1989; Valkaniotis, 2009). It has to be noted that the extent and magnitude of liquefaction phenomena was massive although the earthquake took place in late summer, when the groundwater table is at its lowest. The scarcity of detailed info for the earthquake and its environmental effects is attributed to the period (1870) that predated instrumental seismicity. From contemporary accounts and literature available, we find explicit evidence for surface ruptures for two places (Figure 4): a 4-6km stretch along the DAFZ from west of modern Delphi towards east near Arachova, and a similar stretch in the western slopes of Itea valley between Larnaki and Sernikaki (Ambraseys & Pantelopoulos, 1989; Valkaniotis, 2009). We consider the lack of surface rupture accounts for the rest of DAFZ as due to no proximity to settlements or masking by extensive mass wasting (eastern part). The rupture from Larnaki towards Sernikaki, is interpreted as either large scale liquefaction/lateral spreading or secondary rupture along the Itea east-dipping fault (Figure 2 & 4). The Itea fault (Papanikolaou et al., 2009) is an older structure (Miocene?-Pliocene) related to

the orogen collapse W-E extension. Although the fault is not considered to be active, secondary rupture due to the 1870 sequence could be considered, as the structure fits the description of historical accounts and those types of co-seismic secondary deformation have been reported for strong and complex events. The 1870 earthquake sequence possibly involved complex and multiple triggered fault ruptures along the DAFZ, similar to the 2016-2017 earthquake sequence in central Apennines (Pavlides et al., 2017; Picci et al., 2017).

Acknowledgements: Part of this research was funded by General Secretariat for Research and Technology, Greece in the framework of the PhD of the first author. Discussions and help from Gerassimos Papadopoulos, Theodoros Tsapanos, Athanassios Ganas, George Papathanassiou, Ioannis Koukouvelas, Vassilis Karastathis, Riccardo Caputo and Vassiliki Zygouri has benefited this study. We thank two anonymous reviewers for their comments and help on the final edition of this article.

REFERENCES

Ambraseys, N.N., & Jackson, J.A., 1990. Seismicity and associated strain of central Greece between 1890 and 1988. *Geophys. J. Int*. 101, 663-708.

Ambraseys, N., & Pantelopoulos, P., 1989. The Fokis earthquake of 1 August 1870. *J. Europ. Earthq. Eng*. 3, 10-18.

Armijo, R., Meyer, B., King, G.C.P., Rigo, A., & Papanastassiou, D., 1996. Quaternary evolution of the Corinth Rift and its implications for the late Cenozoic evolution of the Aegean. *Geophys. J. Int.* 126, 11-53.

Bell, R.E., McNeill, L.C., Bull, J.M., Henstock, T.J., Collier, R.E.L., & Leeder, M.R., 2009. Fault architecture, basin structure and evolution of the Gulf of Corinth rift, central Greece. *Basin Res*. 21, 824-855.

Bell, R.E., Duclaux, G., Nixon, C.W., Gawthorpe, R.L., & McNeill, L.C., 2017. High-angle, not low-angle, normal faults dominate early rift extension in the Corinth Rift, central Greece. *Geology* 46 (2), 115-118.

de Boer, J.Z., & Hale, J.R., 2000. The geological origins of the oracle at Delphi, Greece. In: *The archaeology of geological catastrophes* (McGuire, B. et al., eds), Geological Society of London, Special Publication, 171, 399-412.

Doutsos, T., Kontopoulos, N., & Poulimenos, G., 1988. The Corinth-Patras rift as the initial stage of continental fragmentation behind an active island arc (Greece). *Basin Research* 1, 177-190.

Gawthorpe, R.L., Leeder, M.R., Kranis, H., Skourtsos, E., Andrews, J.E., Henstra, G.A., Mack, G.H., Muravchik, M., Turner, J.A., & Stamatakis, M., 2017. Tectono-sedimentary evolution of the Plio-Pleistocene Corinth rift, Greece. *Basin Research*, https://doi.org/10.1111/bre.12260.

Lambotte, S., Lyon-Caen, H., Bernard, P., Deschamps, A., Patau, G., Nercessian, A., Pacchiani, F., Bourouis, S., Drilleau, M., & Adamova, P., 2014. Reassessment of the rifting process in theWestern Corinth Rift from relocated seismicity. *Geophys. J. Int.* 197, 1822-1844.

Nixon, C.W., McNeill, L.C., Bull, J.M., Bell, R.E., Gawthorpe, R.L., Henstock, T.J., Christodoulou, D., Ford, M., Taylor, B., Sakellariou, D., Ferentinos, G., Papatheodorou, G., Leeder, M., Collier, R.E.L., Goodliffe, A.M., Sachpazi, M., & Kranis, H., 2016. Rapid spatiotemporal variations in rift structure during development of the Corinth Rift, central Greece. *Tectonics* 35, 1225-1248.

Papadopoulos, G.A., (ed.) 2000. Historical earthquakes and tsunamis in the Corinth rift, central Greece. National Observatory of Athens, Institute of Geodynamics, Publication No 12, 128 pp.

Papadopoulos, G.A., Kondopoulou, D., Leventakis, G.A., & Pavlides, S.B., 1986. Seismotectonics of the Aegean region. *Tectonophysics* 124 (1-2), 67-84.

Papanikolaou, D., Gouliotis, L., & Triantaphyllou, M., 2009. The Itea-Amfissa detachment: a pre-Corinth rift Miocene extensional structure in central Greece. In: *Collision and collapse at the Africa-Arabia-Eurasia subduction zone* (van Hinsbergen, D.J.J., Edwards, M.A., Govers, R., eds). *Geol Soc Spec Publ* 311, 293-310.

Pavlides, S., Chatzipetros, A., Papathanasiou, G., Georgiadis, G., Sboras, S., & Valkaniotis, S., 2017. Ground deformation and fault modeling of the 2016 sequence (24 Aug.-30 Oct.) in central Apennines (Central Italy). *Bulletin of the Geological Society of Greece* 51, 76-112.

Péchoux, P-Y., 1964. Recherches morphologiques dans la région du Parnasse et du Kiona (Grèce centrale). *Bulletin de l'Association de géographes français* 326-327, 10-28.

Piccardi, L., Monti, C., Vaselli, O., Tassi, F., Gaki-Papanastasiou, K., & Papanastasiou, D., 2008. Scent of a myth: tectonics, geochemistry and geomythology at Delphi (Greece). *Journal of the Geological Society, London* 165, 5-18.

Pizzi, A., Di Domenica, A., Gallovic, F., Luzi, L., & Puglia, R., 2017. Fault Segmentation as Constraint to the Occurrence of the Main Shocks of the 2016 Central Italy Seismic Sequence. *Tectonics* 36. https://doi.org/10.1002/2017TC004652.

Rohais, S., & Moretti, I., 2017. Structural and Stratigraphic Architecture of the Corinth Rift (Greece): An Integrated Onshore to Offshore Basin-Scale Synthesis. In: *Lithosphere Dynamics and Sedimentary Basins of the Arabian Plate and Surrounding Areas* (F. Roure et al. eds), Frontiers in Earth Sciences, 89-120.

Sebrier, M., 1977. Tectonique récente d'une tranversale a l'Arc Egéen, These de Docteur, Academie de Versailles, Universite de Paris XI, 100 pp.

Taylor, B., Weiss, J.R., Goodliffe, A.M., Sachpazi, M., Laigle, M., & Hirn, A., 2011. The structure, stratigraphy and evolution of the Gulf of Corinth rift, Greece. *Geophys. J. Int*. 185, 1189-1219.

Working Group on Utah Earthquake Probabilities (WGUEP), 2016. Earthquake probabilities for the Wasatch Front region in Utah, Idaho, and Wyoming. *Utah Geological Survey Miscellaneous Publication* 16-3, 164 pp.

Valkaniotis, S., 2009. Correlation of Neotectonic structures and seismicity in the broader area of Corinth Gulf (Central Greece), PhD thesis, Thessaloniki Aristotle University, 250 pp.

Valkaniotis, S., & Pavlides, S., 2017. Late Quaternary and Holocene Faults of the Northern Gulf of Corinth Rift, Central Greece. *Bulletin of the Geological Society of Greece* 50 (1), 164-172.

INQUA Focus Group Earthquake Geology and Seismic Hazards

paleoseismicity.org

Aristotle University of Thessaloniki telemetric seismological network (AUTHnet); a brief description

Vamvakaris, Dominikos (1)

(1) Aristotle University of Thessaloniki, Geophysical Laboratory, 54124, Thessaloniki, Greece, dom@geo.auth.gr

Abstract: *The Telemetric Seismological Network of AUTh is a permanent digital network of state-of-the-art instruments, serving as a multi-use scientific facility for 24/7 seismic monitoring, research, and education. AUTh Geophysical Laboratory maintains its own network of seismographs (AUTHnet) to detect local, regional and global earthquake activity. After a strong earthquake in Northern Greece (Thessaloniki, Mw=6.5) in 1978, the first seismological stations established in Thessaloniki and neighbour areas. Today AUTHnet counts 49 stations spread around the country, which are in a permanent real-time communication with the Central Station in Thessaloniki. The network records almost every event (M≥2.0) in Greece. Three local networks connected to the main network were developed to monitor mictoearthquake activity in areas of special interest (Santorini, Nisyros and Ionian islands). Principal aim of AUTH-SS is to keep a permanent interaction with society, not only by informing authorities, media and citizens, but mostly to get people more familiar with earthquakes.*

Keywords*: seismic networks, earthquake monitoring, N. Greece*

INTRODUCTION

A seismic network is the main tool for scientists in order to monitor areas of any seismicity level. Seismic records contribute to solve various geophysical and geological issues, such as active tectonics, study of the earth's interior and geological structure, among others. At the same time, monitoring seismicity is the basic tool for the seismic hazard assessment. For this aim, large earthquakes are not sufficient and smaller ones are strongly useful. The detectability of a network is related to the number of stations and their geographical distribution, apart from other geological and regional settings that affect to records quality. On 20 June 1978 a strong earthquake (M6.5) was occurred near the city of Thessaloniki. Related with a rich foreshock and aftershock sequence (Papazachos & Papazachou, 1997), this destructive earthquake was the first one in the modern history of Greece that occurred in such a big city. This tragic coincidence contributed to the foundation, of the Seismological Station in the Aristotle University of Thessaloniki (AUTH-SS). In the next 2 years, 7 more stations were installed in Central Macedonia (N. Greece) and were connected to the central station in Thessaloniki. That was the initial telemetric seismological network of AUTh which officially started its operation on January 1st 1981. Today (Feb. 2018) it consists of 49 permanent stations covering a large part of the country. This is registered to the International Federation of Digital Seismograph Networks (FDSN) under the code HT, and holds the Digital Object Identifier doi:10.7914/SN/HT.

NETWORK DESCRIPTION

Time Evolution and Geographical Distribution

In 1979 the first seismometer, a 3-component short period S-13 by Teledyne Geotech was installed in the Central Seismological Station of Thessaloniki. By the end of 1980, 7 more stations had already been installed in the central part of Macedonia (N. Greece), on a distance no longer than 100km from Thessaloniki, as shown in Figure 1. Those instruments started recording in a testing mode for some months. On January 1st 1981 the Telemetric Seismological Network of Aristotle University of Thessaloniki (AUTHnet) officially started its operation with 8 stations situated in Thessaloniki (THE), Sohos (SOH), Litochoro (LIT), Griva (GRG), Paliouri (PAIG), Kentriko (KNT), Ouranoupoli (OUR) and Serres (SRS). It is important to mention that this network was the first telemetric network in Greece and also the first seismological network in the broader Balkan area, operating with a computer support. On 1989, the network was reinforced with 4 new stations installed in Igoumenitsa (IGT), Florina (FNA), Alexandroupoli (ALN) and Agios Georgios (AGG). That was the first upgrade that extended AUTHnet towards the north-western and north-eastern edge of Greece, about 250 km far from Thessaloniki, covering now the biggest part of N. Greece, (~5 times bigger area than before). That strategic decision changed the profile of AUTHnet from a local to a regional network, increasing at the same time its detectability. While the continental part of N. Greece was well covered, another region not far from Thssaloniki was practically out of coverage. North Aegean Sea, an area with many catastrophic earthquakes in the last 2500 years, was the next target of AUTHnet. In 1996, 3 stations were installed in Lemnos isl. (LOS), Alonissos isl. (AOS) and Xorichti (XOR) in Pelion Mnt. In 1999, the network extended to western Greece, with the first station installed in Lefkada isl. (LKD) in Ionian Sea, the area with the highest seismicity levels in Greece. In the next 2 years, 2 more stations were installed in W. Macedonia, in Kastania (KTI) and Metsovo (MEV), in order to improve the density of the network in its southwestern part. On 2003 the first special network was established in S. Aegean, far from the existing main network. It was in Santorini (Thira) island, an island of high scientific interest due to its volcano. In collaboration with the Institute for the Study and Monitoring of the Santorini Volcano (I.S.MO.SA.V.), 5 seismological stations were installed (THR1, THR4, THR6 in Thira isl., THR3 in Nea Kameni isl. and THR5 in Thirasia isl.). This local network strongly improved the detectability of smaller earthquakes in S. Aegean and provided important data to scientists. Monitoring of this area is very important, as microearthquake activity could provide reliable information on potential precursory volcanic activity. In the same year, one by

one, all older analog S-13 seismometers are going to be replaced by new digital 3-component broadband CMG-3ESP seismometers by Guralp Systems. Since 2006, there was a continuous try to improve the network, by adding stations in order to extend it, and to have better azimuthal coverage and better density, as well. A new digital station was installed very close to the city of Thessaloniki, in Hortiatis Mnt. (HORT), to support the local activity recordings, as the first one (THE) was situated in an inhabited and noisy area. There was also a spreading of AUTHnet to the central and eastern part of Aegean Sea, another high seismicity area, in the islands of Lesvos (SIGR) and Chios (CHOS), making the network more reliable on detecting events in Aegean Sea, and the NW coastline of Turkey, as well. New stations in Kavala (KAVA), Nestorio (NEST) and THR2 in Thira isl. were installed in 2008, while at the same time LKD2 in Lefkada isl. replaced the older LKD, due to technical problems. Taking advantage of the knowledge derived from the local network of Santorini, a new local network was installed in Dodecanese islands, in order to monitor the potential activity related with the known volcanic center of Nisyros. In collaboration with the regional authorities a station was established in 2008 (NIS1) and 3 more (NIS2, NIS3 and NIS4) in 2009. Due to many technical problems some of these stations stay closed for long periods. In 2010, a new station was added in the local network of Santorini in Fira (THR7). At the same time AUTHnet was extended to the south and the first seismological station of the network was installed in Peloponnesus. A site in Kradini (KRND) was selected, not far from south Aegean where there was a lack of stations. In this way, AUTHnet of more than 30 stations covers the biggest part of the country and is able to detect almost every event in the broader area of Greece. In Figure 1, it is illustrated the geographical distribution of AUTHnet stations in 4 time periods (1981, 1996, 2005 and 2010), showing the spreading and the density of the network as the years pass.

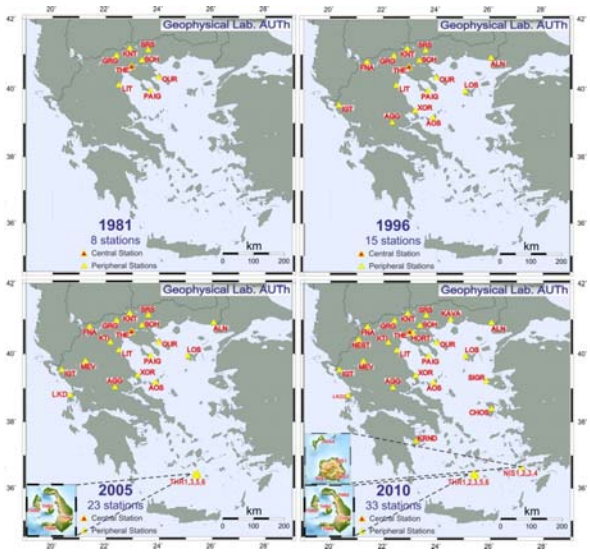

Figure 94: Geographical distribution of AUTHnet stations in the past.

In 2011, a new station was installed in W. Macedonia, located in Kipourio (KPRO) and another in Larissa (LRSO). In Santorini network, at the beginning of 2011, new stations were added in the northeastern part of the island, face to the active volcanic center of Columbo (CMBO), in Athinios (THT1), Monolithos (THR8), Imerovigli (THT2), Akrotiri (THR9) and Taxiarchis (STAX), That decision was very important, while a significant seismic swarm started in January 2011, strongly related with processes showing a volcanic activity (Newman et al., 2012). Thanks to the dense local network (10 stations in ~200km^2), more than 1200 earthquakes of magnitudes M<2.5 were recorded in 2011 in Santorini. In 2012, another station was installed in N. Aegean, in the island of Thassos (THAS), covering the needs of that region. On the other side, in Ionian Sea, 2 new stations were added in Lefkada isl., in Evgiros (EVGI) and Tsoukalades (TSLK). In this way, a new local network is going to be created, in order to monitor the rich seismic activity of the area with the highest seismicity rates in Greece. The recent seismic activity of 2014 (M6.1 and M6.0), pushed this local network to the next step. 2 more stations added in Lefkada isl., in Dragano (DRAG) and Nydri (NYDR), while 2 more stations in Cephalonia isl., in Damoulianata (DMLN) and Pessada (PSDA). This local network was very helpful to the study of the large earthquake (M6.5) in 2015 (Papadimitriou et al., 2017). In 2015 another station was added in E. Macedonia, in Kokkinohori-Kavala (KOKK) and another in Tyrnavos (TYRN) in Thessaly. Last year, in 2017, a new station was established in the eastern part of the network, in Lesvos isl. (LESV) just two weeks after the strong M6.3 earthquake that hit the island. This one is the most recent station connected to the permanent network that counts today 49 stations (Figure 2).

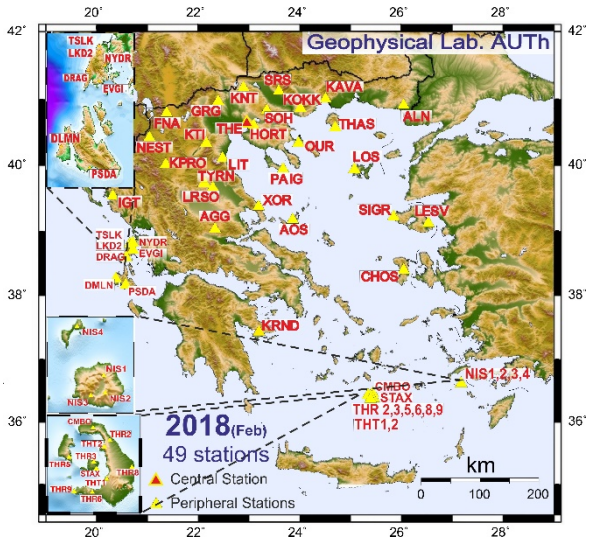

Figure 2: Geographical distribution of the 49 AUTHnet stations in operation today (Feb. 2018). The 3 Local networks are also presented.

Temporal evolution of AUTHnet stations number is presented in Figure 3, where the 3 basic phases of the network upgrade, in 1989, 1996 and 2003 are clearly defined. After that date, the increase of number of stations seems to be continuous. Due to various reasons, 5 stations were uninstalled or relocated.

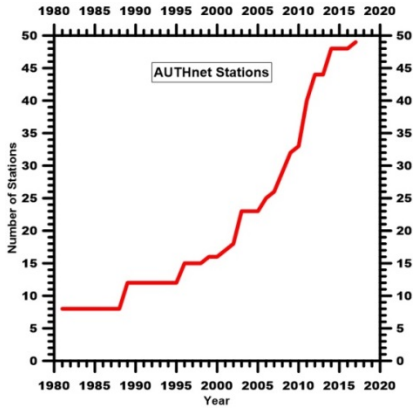

Figure 3: Time evolution of the number of operating stations of AUTHnet.

Network Equipment

The initial network (1981) was equipped with 3-component short-period (1sec) analog S-13 Teledyne-Geotech seismometers (set of 2 horizontals and 1 vertical component), while in some cases only vertical S-13 seismometers were used (many years later). In the Central Seismological Station (THE), a 3-component long-period (20sec) analog SL-220 Teledyne-Geotech seismometer was also installed. Telephone lines were used in order to transmit the analog signal from the first stations to the Central Seismological Station in Thessaloniki. The analog signal was recorded in a set of Teledyne-Geotech RV-301b helicorder drums, but at the same time it was digitized using a 12-bit, 32-channel, AD converter and recorded to 16mm photographic films and magnetic tapes using a develocorder (Teledyne-Geotech). That process was managed by a 16-bit PDP11/34 microcomputer by DEC, making AUTHnet the first telemetric seismological network that was supported by a computer in Balkans. This system was updated in 1989 with a DEC MicroVAX II 32-bit complex instruction set computer, running a VAX/VMS operating system, which was replaced about 10 years later by a DEC microVAX 3100. Since 2003, modern Broadband seismometers were installed in several stations of the network replacing the older short-period S-13. Most of them were CMG-3ESP (100s-50Hz) by Guralp Systems and until nowadays, this is still the most common type of seismometer in AUTHnet stations. Alternatively, CMG-6T (30sec-50Hz) sensors were installed in Nisyros network, CMG-40T (1sec-100Hz and 30sec-50Hz) in Cephalonia-Lefkada network (all by Guralp Systems). Recently, Trillium 120P, 3-component, broadband seismometers by Nanometrics Inc. are preferred in new installations. Last year, a new-type Trillium 120C seismometer was installed in KOKK and LESV station.

A/A	Station	Lat.	Long.	Elev.	Seismometer	Controler	Digitizer	Inst. Year
1	AGG	39.0211	22.3360	625	TRILLIUM 120P	JANUS	TRIDENT	1989
2	ALN	40.8957	26.0497	110	CMG-3ESP/100	JANUS	TRIDENT	1989
3	AOS	39.1654	23.8639	230	CMG-3ESP/100	-	TAURUS	1996
4	CHOS	38.3869	26.0506	854	CMG-3ESP/100	-	CENTAUR	2006
5	FNA	40.7817	21.3836	806	CMG-40T/30	-	HRD-24	1989
6	GRG	40.9558	22.4029	600	CMG-3ESP/100	-	TAURUS	1981
7	HORT	40.5978	23.0995	925	CMG-3ESP/100	JANUS	TRIDENT	2006
8	IGT	39.5315	20.3299	262	CMG-3ESP/100	-	HRD-24	1989
9	KAVA	40.9941	24.5119	95	TRILLIUM 120P	-	CENTAUR	2008
10	KNT	41.1620	22.8980	380	CMG-3ESP/100	-	HRD-24	1981
11	KOKK	40.8178	23.9992	261	TRILLIUM 120C	-	TAURUS	2015
12	KPRO	39.9549	21.3632	837	CMG-3ESP/100	-	TAURUS	2011
13	KRND	37.3830	23.1502	140	CMG-3ESP/100	-	TAURUS	2010
14	KTI	40.3929	22.1165	1329	S-13	JANUS	TRIDENT	2001
15	LESV	39.1074	26.5613	20	TRILLIUM 120C	-	TAURUS	2017
16	LIT	40.1033	22.4892	568	CMG-3ESP/100	JANUS	TRIDENT	1981
17	LOS	39.9330	25.0810	460	S-13	JANUS	TRIDENT	1996
18	LRSO	39.6713	22.3917	78	CMG-40T/1	-	REFTEK-130	2011
19	NEST	40.4147	21.0489	1056	TRILLIUM 120P	JANUS	TRIDENT	2008
20	OUR	40.3325	23.9791	117	CMG-3ESP/100	-	CENTAUR	1981
21	PAIG	39.9363	23.6768	217	CMG-3ESP/100	-	TAURUS	1981
22	SIGR	39.2114	25.8553	92	CMG-3ESP/100	JANUS	TRIDENT	2007
23	SOH	40.8206	23.3556	731	TRILLIUM 120P	-	TAURUS	1981
24	SRS	41.1087	23.5950	314	CMG-3ESP/100	JANUS	TRIDENT	1981
25	THAS	40.6064	24.7194	67	CMG-3ESP/100	-	TRIDENT	2012
26	THE	40.6319	22.9628	132	CMG-6T/30	JANUS	TRIDENT	1981
27	TYRN	39.7110	22.2325	151	TRILLIUM 120P	-	CENTAUR	2015
28	XOR	39.3660	23.1918	541	CMG-3ESP/100	-	TAURUS	1996
SANTORINI LOCAL NETWORK								
29	CMBO	36.4709	25.4056	108	TRILLIUM 120P	-	TAURUS	2011
30	STAX	36.3993	25.4045	20	CMG-40T/30	-	DM-24	2012
31	THR2	36.4469	25.4354	220	S-13	JANUS	TRIDENT	2008
32	THR3	36.4091	25.4008	71	S-13	JANUS	TRIDENT	2003
33	THR5	36.4172	25.3479	180	S-13	JANUS	TRIDENT	2003
34	THR6	36.3562	25.3975	119	S-13	JANUS	TRIDENT	2003
35	THR8	36.4070	25.4788	30	S-13	JANUS	TRIDENT	2001
36	THR9	36.3577	25.3569	54	S-13	JANUS	TRIDENT	2011
37	THT1	36.3858	25.4296	0	S-13	-	SMART-24	2011
38	THT2	36.4351	25.4218	338	CMG-3ESP/120	-	REFTEK-130	2011
NISYROS LOCAL NETWORK								
39	NIS1	36.6023	27.1782	378	CMG-3ESP/100	-	TAURUS	2008
40	NIS2	36.5780	27.1808	400	CMG-6T/30	-	WAVE-24	2009
41	NIS3	36.5742	27.1557	271	CMG-6T/30	-	WAVE-24	2009
42	NIS4	36.6717	27.1314	-	CMG-6T/30	-	WAVE-24	2009
CEPHALONIA-LEFKADA LOCAL NETWORK								
43	DLMN	38.2385	20.3734	370	CMG-40T/1	-	REFTEK-130	2014
44	DRAG	38.6839	20.5746	348	CMG-40T/1	-	REFTEK-130	2014
45	EVGI	38.6210	20.6560	249	CMG-40T/30	-	REFTEK-130	2012
46	LKD2	38.7889	20.6578	485	CMG-3ESP/100	JANUS	TRIDENT	2008
47	NYDR	38.7135	20.6983	212	CMG-40T/1	-	REFTEK-130	2014
48	PSDA	38.1140	20.5841	48	CMG-40T/30	-	REFTEK-130	2014
49	TSLK	38.8249	20.6554	212	CMG-40T/1	-	REFTEK-130	2014

Figure 4: Current (Feb. 2018) station list and instrumentation of the Telemetric Seismological Network of AUTh.

The first years of operation, the network was still pseudo-digital, as the transmitted signal was analog and digitized in Thessaloniki. This situation was changed when the first 24-bit HRD-24 digitizers by Nanometrics were used in some stations, digitizing in-situ the signal and transmitting it to Thessaloniki. Later, some HRD-24 digitizers were replaced by Trident 24-bit digitizers (Nanometrics) that have a typical dynamic range of 142 dB, and works with a Janus-IP communication controller by Nanometrics. Since 2006, modern Taurus digitizers are used very often. Taurus by Nanometrics, is a portable 24-bit digital seismograph, working on 3 channels in a dynamic range of more than 141 dB. In other cases, REFTEK RT130 by Trimble, wave24 by MicroStep-MIS, CMG-DM24 by Guralp Systems, Smart-24 by Geotech Instruments LLC, were used. Lately, modern 24-bit Centaur digital recorders by Nanometrics were obtained. In figure 4, a full list of currently installed instruments is presented for all 49 stations of AUTHnet operating today.

Data Transmission

Typical telephone lines (1020 and 1025) and analog modems (USRobotics and 3Com) were firstly used to transmit the signal from the 7 firstly installed peripheral stations to the central seismological station in Thessaloniki. The next 5 stations used analog and digital Radio Frequency (UHF) transmission. Later, while internet was spreading rapidly and getting faster, PSTN and HellasCom ADSL/VPN lines with suitable routers (RM4 by Nanometrics) for a serial-IP conversion were selected. UHF modems were also used for wireless connections over IP. In the last years, satellite connections (VSAT links) were established. Recently, communications over GSM network were also tested.

DATA ACQUISITION

Data Management, Analysis and Storage

In order to manage all seismological data transmitted to the AUTH-SS, NaqsServer system by Nanometrics is used. That works parallel on 4 acquisition servers (physical and virtual), operating GNU/LINUX. This is a data acquisition system that receives real-time data from digitizers through UDP/IP, distributes the data through TCP/IP, writes the data on ringbuffers, creates and check all the triggers and detect the events. Finally, NaqsServer uses several tools to control the state-of-health for all the stations and to process calibration commands for the controlled instruments. At the same time SeisComP software by GEOFON program (GFZ/Potsdam and Gempa GmbH) is also used. Earthquake analysis is fulfilled by Atlas software for seismic data analysis by Nanometrics Inc. (v. 2.3.6). Appropriate codes prepare and store earthquake parameters and arrival times in the typical GSE2.0 format, creating preliminary bulletins and seismic catalogs. All events analyzed by the 24/7 routine shift are reviewed and final catalogs and monthly bulletins are published. During the earthquake analysis procedure, we calculate local magnitude (ML) adopting the poly-parametric equation:

$M_L = \log A + n\log(R/100) + K(R-100) + c_i$ (Bakun & Joyner, 1984)

where A is the 0-peak (in mm) amplitude on a typical WA seismograph (recorded or synthesized), R is the hypocentral distance (in km), n is the geometrical spreading factor, K is the anelastic attenuation coefficient and c_i is a standard correction. For n and K parameters we adopt the values estimated by Hutton and Boore, 1987 (n=1.11 and K=0.00189), while c_1=3.0. For 0-peak amplitude estimation, peak-peak amplitudes are estimated for each one of two horizontal components and the mean value divided by 2 is adopted. The final local magnitude, M_L, (W-A simulated) is calculated as the mathematical mean value of the individual magnitudes provided by each station used, taking into account 90% confidence limits (+/- 1.65*SD). The earthquake-location

program Hypoinverse (Klein, 1989) is used by Atlas software to estimate the focal parameters of the event with an appropriate velocity model used for the estimation of seismic wave traveltimes. That was based on the two-layer crustal model proposed by Papagiotopoulos and Papazachos, 1985. (d_1 = 18.5km, V_1=6.0 km/sec, d_2=12.5km, V_2=6.6km/sec and V_n=7.9km/sec). Additionally, an upper sediment layer (d_n=1.5km, V_n=5.0km/sec) is also adopted. Raw data are stored in temporary ringbuffers with capacity of about 40-60 days (depending on station), in 100 sample/second. Over 500 channels flow per day in ringbuffers resulting a daily need of about 4GB storage (1.5TB per year). All located events are stored in Earthworm schema database running on multiple Oracle servers, as well as in local hard disks in SEED format. A double back-up of all data is also preserved.

Data exchange and Collaborations

AUTHnet interacts with several institutions. Seedlink servers from GEOFON (Germany), MEDNET (Italy), Turkey, Albania, Bulgaria, FYROM and Serbia exchange data with AUTHnet. This exchange is very useful, mostly in cases of earthquakes outside the network boundaries. Since 2005 AUTHnet participates to the Hellenic Unified Seismological Network (HUSN). According to this project, the 4 Greek institutions monitoring seismic activity (NOA, NKUA, AUTH and UPAT) agreed to share their data, giving to all of them the opportunity to have access to a large, dense virtual network of more than 150 stations.

AIMS AND SOCIAL CONTRIBUTION

Aims and Services provided

AUTHnet operates 24/7 and its main purpose is the continuous real-time monitoring and processing of seismic data. The dense network is able to provide a rapid manual determination (in 15'-20') of the location and magnitude of all earthquakes (M≥2.0) in Greece. Automatic solutions for every event are also immediately available. In case of a distractive event, all available information is disseminating to national and local authorities. This is also a priority for the AUTH-SS staff to provide rapid and valid information to media and public as well. All information is hosted in the web-site (http://seismology.geo.auth.gr/ss) where both automatic and manual locations for the current seismicity are presented. In case of an earthquake with M≥4.0 more details are provided and near-real time moment tensor computations are performed and published, as well. Since 2013, a process for a near-real-time evaluation of the evolution of seismic excitations (Teza, 2011) is also applied and results for seismic sequences are published. Finally, typical seismological maps, preliminary and revised catalogs and monthly bulletins are also available. All information is sent to international seismological centers gathering such data (e.q. EMSC, ISC), while AUTHnet also contributes to the recording of long-distance large earthquakes. The continuous upgrade of the network provides high quality data. The number of recorded earthquakes increases and network detectability is getting better. Practically, all events of M≥2.0 are clearly recorded. In many cases, local networks (e.g. Santorini and Cephalonia-Lefkada networks) are able to provide reliable solutions for events even smaller than M1.0. A typical number of regional earthquakes recorded by AUTHnet and analyzed by scientists for the period 1995 - 2006 was about 1000-1500 events per year, while many earthquakes appeared with insufficient data. In the next years, the annual number of recorded earthquakes shows a continuous increase and in 2015 exceeded 9000. That means approximately 25 regional earthquakes, whose parameters were manually calculated every day. This is a really big number and could be explained with the continuous qualitative and quantitative improvement of AUTHnet mostly since 2004.

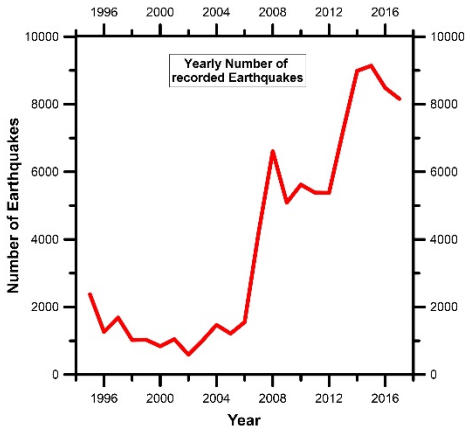

Figure 5: Number of regional earthquakes recorded in AUTHnet, for the period 1995-2017.

AUTHnet contribution in Society

Besides its research profile, AUTh Seismological Station has also an educative mission. Thanks to the seismological network and its data collection, undergraduate students do practice and get involved with seismology, while MSc and PhD students elaborate their theses and work on several projects. In the framework of the continuous information of people, scientists of the AUTH-SS give several lectures to elementary and high-school students who have the opportunity learn about earthquakes and protection measures. More detailed lectures are also carried out for groups of volunteers or rescue teams. In any case, through this permanent interaction with society, the main target is to get people (and especially kids) more familiar with earthquakes and learning how protect themselves.

Acknowledgements: AUTHnet history would be different without the fundamental contribution of Emeritus Professor Basil Papazachos, who had the vision of the network. His help in the scientific and administrative part was priceless. The technical part of installations and maintenance was fulfilled by K. Peftitselis and A. Karamesinis for more than 30 years. Some peripheral station installations were partially supported by local authorities.

REFERENCES

Aristotle University of Thessaloniki Seismological Network, 1981. Permanent Regional Seismological Network operated by the Aristotle University of Thessaloniki. FDSN. Other/Seismic Network. doi:10.7914/SN/HT.

Bakun, W.H., & Joyner, W.B., 1984. The M, scale in central California. *Bull. Seismol. Soc. Am*. 74, 1827-1843.

Hutton, L.K., & Boore, D.M., 1987. The M, scale in southern California. *Bull. Seismol. Soc. Am*. 77, 2074-2094.

Klein, F.W, 1989. HYPOINVERSE, a program for VAX computers to solve for earthquake locations and magnitudes, U.S. *Geological Survey Open-File Report* 89-314, 59 pp.

Newman, A.V., Stiros, S., Feng, L., Psimoulis, P., Moschas, F., Saltogianni, V., Jiang, Y., Papazachos, C., Panagiotopoulos, D., Karagianni, E., & Vamvakaris, D., 2012. Recent Geodetic Unrest at Santorini Caldera, Greece. *Geophysical Research Letters*, doi: 10.1029/2012GL051286.

Panagiotopoulos, D.G., & Papazachos, B.C., 1985. Travel times of Pn-waves in the Aegean and surrounding area. *Geophys. J. R. astr. Soc*. 80, 165-176.

Papadimitriou, E., Karakostas, V., Mesimeri, M., Chouliaras, G., & Kourouklas, Ch., 2017. The Mw6.5 17 November 2015 Lefkada (Greece) Earthquake: Structural Interpretation by Means of the After-shock Analysis. *Pure and Applied Geophysics* 174, 10, 3869.

Papazachos, B., & Papazachou, C., 1997, The Earthquake of Greece, Ziti Editions, 304 pp.

Teza, E., 2011. Automated procedure validating the possible evolution of a seismic excitation. MSc Thesis, AUTh (in greek).

INQUA Focus Group Earthquake Geology and Seismic Hazards

paleoseismicity.org

Ground fissures related to the 2016 Kaikoura (New Zealand) earthquake - a discussion about their enigmatic origin

Van Loon, A.J. (Tom) (1, 2, 3), Belzyt, Szymon (1), Pisarska-Jamroży, Małgorzata (1)

(1) Institute of Geology, Adam Mickiewicz University, B. Krygowskiego 12, 61-680 Poznań, Poland, tvanloon@amu.edu.pl, szymon.belzyt@amu.edu.pl, pisanka@amu.edu.pl
(2) Geocom, Valle del Portet 17, 03726 Benitachell, Spain
(3) Shandong University of Science and Technology, Qingdao 266590, China

Abstract: *The 2016 Kaikoura earthquake caused displacements of several meters, but also other types of deformations. These include fissures that are well exposed at several places along the eastern coast of the South Island of New Zealand. The fissures extend from the surface to a depth of commonly some decimetres, but may occasionally reach larger depths. The origin of these fissures is not clear, as the region has an overall compressional stress regime. It is discussed whether tectonic displacement or earthquake-induced slope process might be responsible for their formation, a combination of these factors, or something else.*

Keywords*: faulting, earthquakes, soft-sediment deformation, Kaikoura, slope processes*

INTRODUCTION

The pre-conference excursion of the foregoing PATA meeting (November 17, 2017) was aimed at showing a wide variety of features related to the 2016 Kaikoura earthquake. Among the various features shown, one was discussed only shortly, and some aspects seem to have remained unrecognized. We here pay more attention to it, hoping to raise a discussion about their origin.

The feature that we discuss here was present at several sites (also during the post-conference excursion), but was particularly well developed and numerous at the site that was indicated in the excursion guide (Upton et al., 2017a) as Stop 4 (Middle Hill Station) (Fig. 1).

Several earthquake-related features were present at the Middle Hill station site, including the 18×10^6 m^3 Seafront Landslide, but we want to deal here with a somewhat less spectacular feature, viz. The presence of a large number of fissures on the slope of a hill that shows a distinct fault scarp (Fig. 2), locally with a throw of up to 10 m (Upton et al., 2017a). All these features have been ascribed to fault activity related to the Kaikoura earthquake, which left it traces in this area in the form of many faults, the most important one being the Papatea Fault.

The fissures (Fig. 3) are intriguing because fissuring points at an extensional regime, whereas the overall tectonic regime of the area is compressional, even though many faults at many places have a strike-slip character. This leaves the question of how they can have originated.

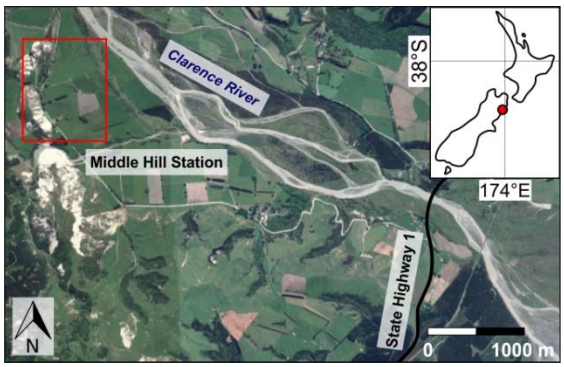

Figure 95: Location of the fissures in the neighbourhood of Middle Hill Station (Clarence Valley, east coast of the South Island).

Figure 2: The fault scarp at Middle Hill Station.

Figure 3: The nature of the fissures is particularly well visible at places where the grass vegetation is absent, such as in a small tree-covered area without shrubs.

DESCRIPTION OF THE FISSURES

The fissures at Middle Hill Station are mentioned but not described or discussed by Upton et al. (2017a), nor are they described in the guide book of the post-conference field trip (Upton et al., 2017b), although similar (and even much larger) fissures are present at more locations. For the sake of clarity, we restrict ourselves here to the fissures at Middle Hill Station.

Figure 4: Most of the area in which the fissures are present is covered by dense grass vegetation.

The fissures at Middle Hill Station have commonly a width of about a decimetre (Fig. 4) and a depth of several decimeters. Occasionally wider fissures are present (up to almost half a meter) and their depths in such cases may reach almost a meter. From place to place, the width of the fissure changes in an apparently haphazard way, and eventually they die out. The fissures show a clearly parallel pattern (Fig. 3), running roughly parallel to the isohypses on the hill side, and they follow commonly a fairly irregular pattern (Fig. 5), without, however, crossing each other.

Because of the dense grass vegetation at most places, it was impossible to check whether the fissures had already been filled up partly by sediments carried over the hill slope after rain; considering, however, that the dense grass hampers both erosion and downhill movement of sediment, it is likely that the depth of the fissures had not changed significantly since the 2016 earthquake.

Figure 5: The fissures do not follow a straight line, but rather an irregular pathway with an overall continuous direction.

ANALYSIS OF THE FISSURES

The fissures developed during the 2016 earthquakes, so there can be little doubt that they are genetically related. As mentioned above, however, fissuring points at an extensional tectonic regime, whereas the overall regime is compressional in the context of a transpressional plate boundary (Clark et al., 2017; Upton et al., 2017b). This seems also the case at this site, as Upton et al. (2017a) mention that the rupture is complex and comprises overlapping reverse and thrust fault traces, which was found also elsewhere (Ceska et al., 2017; Hamling et al., 2017; Wang et al., 2018). It can, however, not be fully excluded that, during the sequence of earthquakes, phases of extension existed at the Middle Hill Station site, even though this seems unlikely. It seems therefore only appropriate to

investigate here first whether a tensional regime might be held responsible.

An origin due to tension tectonics?

It seems likely that, at least locally and temporary, a tensional regime was present at the study site. This is suggested by the shape of the local fault scarp (Fig. 2), and this hypothesis also fits in the framework of the complex nature of the Papatea Fault (Ceska et al., 2017; Shi et al., 2017; Wang et al., 2018).

It seems highly questionable, however, whether fault activity leading to - or related to - the formation of a scarp with a vertical thrust of several meters could also lead to fissures (admittedly parallel to the scarp) without any noticeable vertical displacement. Obviously, the scarp formation and the fissuring might be due to different shocks, but this is not likely either considering the nature of the Kaikoura earthquake: it initiated as a small strike-slip rupture that propagated to the northeast, and the slip on strike-slip faults triggered extensive thrust faulting under the eastern coast of the South Island (Duputel & Rivera, 2017). The unconsolidated sediments at the site do, however, not show any strike-slip displacement, but opening (widening) of the surface material.

These considerations make it unlikely that the fissures have a purely tectonic origin.

An origin due to slope processes?

The position of the fissures on a hill side, and particularly their orientation roughly parallel to the isohypses, suggests that slope processes may have played a role in the formation of the fissures. It should be kept in mind in this context that the area exists of hard rock, but that weathering and slope processes have resulted in a layer of unconsolidated sediment covering the hillside.

Geomorphologists have studied processes on hill sides for a long time. The processes that result in irregular surfaces are mass-wasting processes, such as subaerial slumping. Such processes may locally result in scarps, and occasionally in a fissure, but never have been found to result in extensive, frequent, parallel fissures.
These considerations make it unlikely that the fissures were formed by more slope processes.

A mixed tectonic/slope-processes origin?

Could the surface sediments have become fissured as the result of the joint activity of slope processes and a high-magnitude earthquake? The answer is not easy, as slope processes are complex and the influence of earthquakes on slope processes is still poorly known. If the tectonic activity took place under compressional conditions, it is hardly imaginable that slope processes would result in fissures. Fissuring as a result of strike-slip movement cannot be excluded, but there are no indications at the study site for this type of faulting. This leaves slope processes induced by normal faulting as the only possibility, assuming that a tensional regime may have been present.
Although this option seems the most likely, it is still enigmatic how the fissures must have formed. Similar features have, however, recently been described from China (He et al., 2017). These ground fissures, which were discovered in the Hetao Basin, are located along the frontal margins of the terraces of the Sertengshan piedmont fault. The fissures are 600-1600 m long, 5-50 cm wide, and at most 1 m deep, so fairly comparable with the ground fissures at Middle Hill Station. The Chinese ground fissures rupture newly constructed roads and field ridges; this is a characteristic that is not present at Middle Hill Station, but only because the fissures do not reach such constructions. In contrast to the fissures under study here, the ground fissures in the Hetao Basin developed in an extensional environment, dominated by NE-SW principal compressive shear, involving N-S tensile stress, which has produced ongoing subsidence in the Hetao Basin and continuous activity along the Sertengshan piedmont fault since the late Quaternary. Trenches through the fissures revealed that they are the latest manifestation of the activity of pre-existing faults and are the result of creep-slip movement along the faults.

The above-mentioned characteristics of both the Middle Hill Station and the Chinese ground fissures are comparable in many respects, apart from the extensional tectonic regime in the Chinese example, but - as indicated above - the Kaikoura earthquake resulted in complex fault processes that probably locally and temporarily initiated extensional stress fields. Yet, the Chinese researchers come to a genetic interpretation that seems not to be applicable to the fissures under study. They mention that the groundwater level in the Hetao Basin has been dropping since the 1960s because of overexploitation, resulting in subsidence. When the tensile stress exceeded the ultimate tensile strength of the strata, the strata ruptured along pre-existing faults, producing the ground fissures. They thus consider the Sertengshan piedmont fault planes to be the structural foundation of the ground fissures; eventually groundwater extraction induced the development of the fissures.

As such lowering of the groundwater level did not occur at the Middle Hill Station site, the ground fissures here cannot be explained in the same way, but another mechanism that might explain their formation has not been found as yet, although it seems likely that a combination of fault activity and processes must be held responsible. The origin of the ground fissures at Middle Hill Station thus remains enigmatic for the time being, forming a geological feature that certainly requires a closer look.

Acknowledgements: The 2017 PATA Days, including the pre-conference excursion during which the ground fissures could be studied, were attended in the context of the GREBAL project, which is financially supported by a grant from the National Science Centre, Poland (No. 2015/19/B/ST10/00661).

REFERENCES

Cesca, S., Zhang, Y., Mouslopoulou, V., Wang, R., Saul, J., Savage, M., Heimann, S., Kufner, S.-K., Oncken, O., & Dahm, T., 2017. Complex rupture process of the Mw 7.8, 2016, Kaikoura earthquake, New Zealand, and its aftershock sequence. *Earth and Planetary Science Letters* 478, 110-120.

Clark, K.J., Nissen, E.K., Howarth, J.D., Hamling, I.J., Mountjoy, J.J., Ries, W.F., Jones, K.E., Goldstein, S., Cochran, U.A., Villamor, P., Hreinsdóttir, S., Litchfield, N.J., Mueller, C., Berryman, K.R., & Strong, D.T., 2017. Highly variable coastal deformation in the 2016 Mw 7.8 Kaikoura earthquake reflects rupture complexity along a transpressional plate boundary. *Earth and Planetary Science Letters* 474, 334-344.

Duputel, Z., & Rivera, L., 2017. Long-period analysis of the 2016 Kaikoura earthquake. *Physics of the Earth and Planetary Interiors* 265, 62-66.

Hamling, I.J., Hreinsdóttir, S., Clark, K., Elliott, J., Liang, C., Fielding, E., Litchfield, N., Villamor, P., Wallace, L., Wright, T.J., d'Anastasio, E., Bannister, S.C., Burbridge, D.R., Denys, P., Gentle, P., Howarth, J.D., Mueller, C., Palmer, N.G., Pearson, C., Power, W.L., Barnes, P., Barrell, D.J.A., Van Dissen, R.J., Langridge, R.M., Little, T., Nicol, A., Pettinga, J., Rowland, J., & Stirling, M.W., 2017. Complex multifault rupture during the 2016 M_w 7.8 Kaikoura earthquake, New Zealand. *Science* 356, DOI: 10.1126/science.aam7194.

He, Z., Ma, B., Long, J., Zhang, H., Liang, K., & Jiang, D., 2017. Recent ground fissures in the Hetao basin, Inner Mongolia, China. *Geomorphology* 295, 102-114.

Shi, X., Wang, Y., Jing, L.-Z., Weldon, R., Wei, S., Wang, T., & Sieh, K., 2017. How complex is the 2016 Mw 7.8 Kaikoura earthquake, South Island, New Zealand? *Science Bulletin* 62, 309-311.

Upton, P., Clark, K.J., Langridge, R.M., & Van Dissen, R.J., 2017a. *8th International PATA Days, Blenheim, New Zealand. Fieldtrip guide: northern fault ruptures and landscape impacts of the2016 Kaikoura earthquake, 13th November 2017*. GNS Science. Lower Hutt. 26 pp.

Upton, P., Langridge, R.M., Stahl, T., Van Dissen, R.J., Howarth, J., Berryman, K., Clark, K.J., Kelly, K., & Hammond, K., 2017b. *8th International PATA Days, Blenheim, New Zealand. Three-day post-conference fieldtrip: Northern South Island, Alpine fault and ruptures of the2016 Kaikoura earthquake, 17-19th November 2017*. GNS Science. Lower Hutt. 64 pp.

Wang, D., Chen, Y., Wang, Q., & Mori, J., 2018. Complex rupture of the 13 November 2016 M_w 7.8 Kaikoura, New Zealand earthquake: Comparison of high-frequency and low-frequency observations. *Tectonophysics* (in press).

INQUA Focus Group Earthquake Geology and Seismic Hazards

paleoseismicity.org

Predecessors of the 2015 tsunamigenic M_w8.4 Illapel megathrust and on the potential for large tsunamis in central-northern Chile

Vargas Easton, Gabriel (1), González Alfaro, José (1), Villalobos Claramunt, Angelo (1), Álvarez Ávalos, Gabriel (2), León Cortés, Tomás (1)

(1) Departamento de Geología, Facultad de Ciencias Físicas y Matemáticas, Universidad de Chile, Plaza Ercilla 803, Santiago, Chile, gvargas@ing.uchile.cl
(2) Departamento de Ingeniería en Geomensura y Geomática, Facultad de Ingeniería, Universidad de Antofagasta, Avenida Universidad de Antofagasta 02800, Antofagasta, Chile

Abstract: *On September 2015 the M_w8.3 Illapel megathrust broke the subduction contact between the Nazca and South American plates causing unexpectedly high tsunami waves that strongly impacted the coast along central-northern Chile. Here, from the analysis of pits dug in the area severely impacted by the last tsunami episode, we interpret anomalous sandy layers interbedded between fine alluvial sediments as tsunami deposits. From sedimentological and geochronological results, we identified deposits associated to the last 2015 and to other previous episodes occurred after 3125 ±278 Cal. yrs. BP, with two events dated ca. 1297 ±23 CE and ca. 1454 ±36 CE. According to historical chronicles and previous work the region has been impacted by large tsunamis also in 1730 CE, 1877 CE and 1922 CE. We interpret that tsunami deposits reported here correspond to large megathrust ruptures occurred along central-northern and northern Chile subduction contact segments.*

Keywords*: Megathrusts paleoseismology, tsunami impact, Chilean subduction contact, 2015 Illapel earthquake*

INTRODUCTION

On September 16 2015, the M_w8.3 Illapel earthquake broke the subduction contact between the Nazca beneath the South American plates (Melgar et al., 2015; Ruiz et al., 2016), causing tsunami waves that strongly impacted the region especially in Coquimbo, Tongoy as well as a series of small fishertowns located in front of and in the neighbouring areas of the rupture zone (Melgar et al., 2015; Aránguiz et al., 2015; Fig. 1). According seismic and geodetic observations, this earthquake exhibited a strong directivity from deeper to shallower rupture areas along the plates contact (Ruiz et al., 2016), broking up to the trench (Melgar et al., 2015), then explaining unexpected tsunami heights of 5-6 m a.s.l. as observed in Coquimbo bay and up to 10-11 m a.s.l. in some localized areas (Aránguiz et al., 2015; Melgar et al., 2015), that reached the coast few minutes after the initiation of the earthquake.

Although the region has been impacted by historic tsunamis, the most important events in Coquimbo and La Serena conurbations, which are considered among the most populated and important cities in the country, correspond to the 1877 and to the 1922 tsunami episodes that reached run-ups close to 10 m and 5-7 m in this area, respectively. Both episodes were generated by strong megathrust whose ruptures encompassed the subduction contact located to the north of the Illapel earthquake rupture zone, with estimated magnitudes of ca. M_w8.8 in the case of the 1877 and M_w 8.5 in the case of the 1922 earthquakes, respectively (Abe, 1979; Kausel, 1986; Ruiz & Madariaga, 2018). These megathrusts caused tsunami waves that reached ca. 20 m and 7-9 m of run-ups in the neighbouring areas located in front of each rupture zones, respectively.

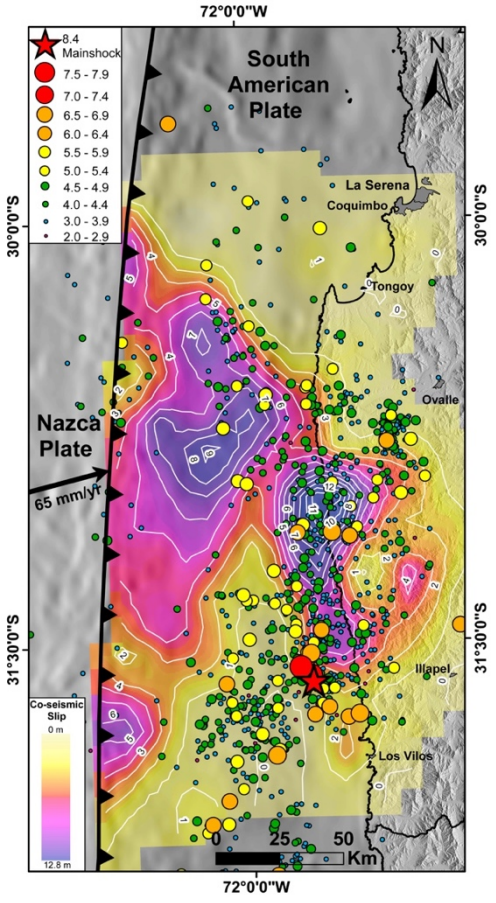

Figure 96: Contour slip distribution and aftershocks of the tsunamigenic M_w8.3 2015 Illapel megathrust occurred in central-northern Chile (after Melgar et al., 2015 and CSN-Centro Sismológico Nacional, Universidad de Chile).

In the Illapel region, previous historic megathrusts occurred on 1880 and on 1943, with estimated magnitudes of 7.5 (Lomintz, 1970; 2004) and M_w7.9 (Beck et al., 1998), according to the critic review of Ruiz and Madariaga (2018). Only minor damages in Los Vilos and eventually an important run-up of sea water in the bay of Coquimbo due to a small tsunami has been reported in the case of the 1943 earthquake (Lomnitz, 1970; Ruiz & Madariaga, 2018).

The most important previous historic tsunamigenic megathrust encompassing the 2015 Illapel earthquake rupture zone occurred in 1730, which ruptured ~1000 km along the subduction contact between the Coquimbo and Concepción regions, with an estimated magnitude of ca. M_w9.0 (28ºS-38ºS; Udías et al., 2012), that caused a strong tsunami of estimated magnitude M9.0 (similarly than for the 1877 earthquake off northern Chile).

Here, we report tsunami deposits observed in Tongoy area, which was strongly impacted by tsunami waves following the 2015 Illapel earthquake (Fig. 2), and we discuss the implications of our findings in terms of previous tsunamigenic megathrust ruptures as well as the potential for large tsunamis in this region.

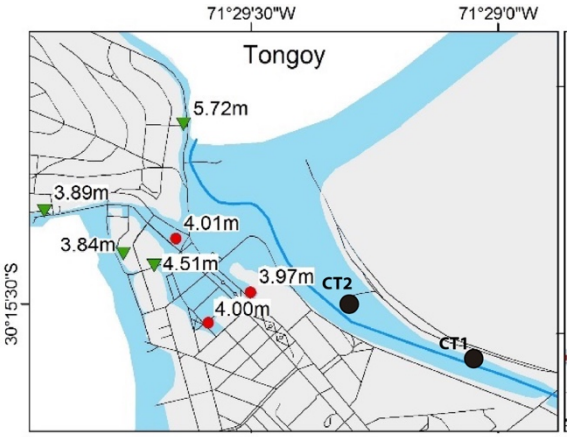

Figure 97: Tsunami inundation area at Tongoy following the 2015 Illapel megathrust (modified from Aránguiz et al., 2015), and location of pits dug for paleotsunami research.

RESULTS

As a result of a post-event survey realized during the days to the weeks after the 2015 Illapel earthquake and tsunami, we observed tiny geomorphological changes associated to vertical movements of the coast (uplift and subsidence), as well as tsunami heights and tsunami deposits along the rupture region. Tsunami deposits exhibited similar sedimentological characteristics than those reported in La Serena and Coquimbo beaches by Bahlburg et al. (2018), with layers of sandy facies overlying previous non-tsunami deposits by an irregular basal contact (Fig. 3).

Pits dug in the area of Tongoy (CT1 and CT2, Fig. 2), shown sandy layers exhibiting similar characteristics than the previously observed tsunami deposits, interbedded in between alluvial deposits constituting a terrace disposed along a small estuarine system (Fig. 2).

Figure 98: Tsunami deposit of the 2015 episode observed in a pit dug in the area of Tongoy (CT2, Fig. 2).

At the location of CT1 the surface of the alluvial terrace is situated at 3-4 m a.s.l., which is close to the limit of the observed run-up of the 2015 tsunami in the area (Fig. 2). The stratigraphic section is constituted by littoral marine sediments of sandy material, with subhorizontal lamination and low angle cross beading at the base, interpreted as intertidal and supralittoral facies (Fig. 4). These deposits are overlaid by subhorizontal alluvial sediments of fine sand to muddy material, with interbedded sandy layers. The distinctive sedimentology of the last deposits, characterized by well sorted material constituted by rounded to subrounded lithic particles, shell fragments and also by small Gastropoda rests and Foraminifera tests, together with their already mentioned irregular basal contact, support their origin by inundation of tsunami waves.

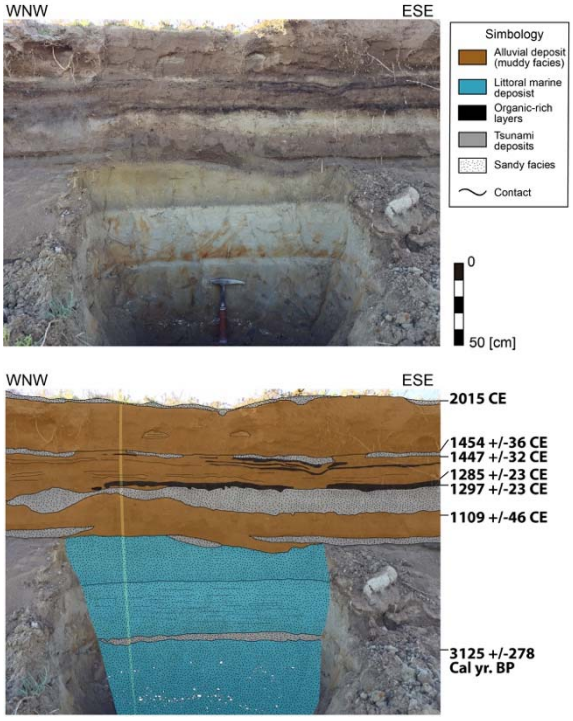

Figure 99: Stratigraphy of tsunami deposits and radiocarbon results (calibrated ages) obtained from a pit dug in the area of Tongoy (CT1, Fig. 2).

Organic rich layers interbedded in between alluvial sediments and tsunami deposits allowed precise radiocarbon determinations, yielding well constrained ages of 1454 ±36 CE and 1297 ±23 CE for the organic rich layers just overlying the two most conspicuous tsunami deposits (Fig. 4). Two other possible tsunami deposits are preliminary dated as occurred between 3125 ±278 Cal. yr. BP and 1109 ±46 CE.

DISCUSSION

The stratigraphic section studied in the area of Tongoy allowed the determination of two, eventually four, prehistoric tsunamis that impacted the area similarly or stronger than the last event driven by the M_w8.3 Illapel megathrust.

Littoral marine and alluvial deposits observed in the studied section together with the embedded estuarine system, most probably reflect a progradation of the alluvial system into the coastal marine basin during the Late Holocene, due to the stabilization of the sea level associated to the current interglacial high stand. This, in the context of the semiarid conditions and limited runoff that characterizes this region. In addition to that, this process would have been accelerated due to the intensification of torrential rainfalls associated to El Niño in the last millennia in the coastal Atacama Desert (Vargas et al., 2006; Ortega et al., 2012). However, conspicuous uplifted marine terraces have been reported also in the area evidencing long-term uplifting of the coast at the scale of the Quaternary (Saillard et al., 2009). In addition, it has been reported that the 2015 Illapel megathrust caused complex coastal vertical movements. While in the Tongoy area these vertical movements would have been close to nil to subsiding, in other areas in front of the rupture zone the coast clearly uplifted according the available coseismic geodetic observations (Melgar et al., 2015; Ruiz et al., 2016). Then, it is not possible to discard that previous massive megathrust ruptures, as in the case of the 1730 M_w~9 event, would have caused -differential- uplifting of the entire coastal zone, including the Tongoy, Coquimbo and La Serena areas which are included in a large embayment (Fig. 1), something that has been previously observed as in the case of the 2010 M_w8.8 Maule earthquake in central-southern Chile (Vargas et al., 2011). All of these could explain the almost absence of sedimentary records after the 15th century in the stratigraphic section studied at Tongoy, neither any traces of the historical 1730, 1877 and 1922 tsunamis that strongly impacted the study region.

From the analysis of laminated sediments in Mejillones bay (23ºS), a paleoseismic event was dated as occurred between the years 1409-1449 CE, which caused an angular unconformity, slumping and loss of material with an associated hiatus encompassing ca. 200 years in the sedimentary record (Vargas et al., 2005). This event closely match our paleotsunami episode dated here as ca. 1454 ±36 CE, as well as the tsunami event reported from historical chronicles that stroke the coast of Japan on September 7 1420 CE, attributed to the Chilean subduction margin by Tsuji (2013). Taking this in consideration, it is most possible that the paleotsunami dated close to 1454 ±36 CE in the Tongoy record, may corresponds to the one reported in the Japanese coast, that was most probably caused by a megathrust rupturing the subduction contact off northern Chile, like in the case of 1877.

There is no sufficient regional observations to correlate the paleotsunami episode dated between 1109 ±46 and 1297 ±23 CE in the Tongoy record reported here. However, considering the thickness of the observed deposit compared with that of the 2015 and 1454 ±36 CE events (Fig. 4), we suggest that this episode could has been originated by a strong megathrust that ruptured the subduction contact probably closer or even in front of the study area, a hypothesis that would need to be better constrained by additional geological observations in the region. For instance, some observations from ongoing research along the coast of northern Chile suggest the occurrence of a probably tsunami event close to such a date, without any traces of a significant megathrust occurred in the region at that time, something that tends support the hypothesis of a megathrust occurred in central-northern Chile as a most possible source for the event dated ca. 1297 ±23 CE in Tongoy area.

The two other possible tsunami deposits dated between 3125 ±278 Cal. yr. BP and 1109 ±46 CE, exhibit similar sedimentological characteristics than the previously mentioned, but need to be better constrained by ongoing geochronological and sedimentological analysis.

It is important to mention that the last 2015 tsunami reached tsunami heights in the order of 6 m in the Coquimbo bay, which is similar to the run up produced by the 1922 tsunami and close to the 10 m estimated run up produced by the 1877 tsunami in the same area, in both of the cases generated by megathrust ruptures occurred northward from the study region. Taking in consideration the thickness of the observed deposits, our paleotsunami record suggests that the paleoevents dated here could has been similar or stronger than the last 2015 episode, especially in the case of the episode dated close to 1297 ±23 CE. Moreover, the consideration for the possibility for a magnitude M~9 tsunami produced by the massive 1730 M_w~9 megathrust in central-northern Chile justify a review of the inundation charts in the area of Coquimbo bay especially, which until now has been mostly focused on the local impact produced by the –distant- 1922 and 1877 tsunamis.

CONCLUSIONS

From sedimentological and chronostratigraphic analysis of natural sections from pits dug in the area strongly impacted by the last 2015 tsunamigenic M_w8.3 Illapel megathrust in central-northern Chile, we identified four tsunami deposits occurred previously, between 3125 ±278 Cal. yr. BP and the 15th century, exhibiting similar textural and compositional characteristics with respect to that produced by the last event in 2015. The two most clear and conspicuous episodes are dated as ca. 1454 ±36 CE and between 1109 ±46 and 1297 ±23 CE. The ca. 1454 ±36 CE event can be preliminary assigned to a strong megathrust occurred in northern Chile and previously reported from the study of offshore sedimentary records there, dated as

1429 ±20 CE (Vargas et al., 2005), with similar or greater estimated magnitude than the 1877 historic episode, and which probably corresponds to the tsunami event occurred on September 7 1420 CE in the Japanese coast (Tsuji, 2013). Because of its greater thickness and continuity of the record, with respect to the 2015 and ca. 1454 ±36 CE tsunami deposits, it is possible that the megathrust causing the tsunami event dated as close to 1297 ±23 CE would has encompassed the study region corresponding to a giant event, eventually similar to that of 1730. Further geological research is needed to better constrain this last hypothesis.

Acknowledgements: This work was funded by project Fondecyt #1161547.

REFERENCES

Abe, K., 1979. Size of great earthquakes of 1837-1974 inferred from tsunami data. *J. Geophys. Res.* 84 (B4), 1561-1568.

Aránguiz, R., González, G., González, J., Catalán, P., Cienfuegos, R., Yagi, Y., Okuwaki, R., Urra, L., Contreras, K., Del Río, I., & Rojas, C., 2015. *Pure Appl. Geohys.*, doi: 10.1007/s00024-015-1225-4.

Bahlburg, H., Nentwig, V., & Kreutzer, M., 2018. The September 16, 2015 Illapel tsunami, Chile - Sedimentology of tsunami deposits at the beaches of La Serena and Coquimbo. *Marine Geology* 396, 43-53.

Beck, S., Barrientos, S., Kausel, E., & Reyes, M., 1998. Source characteristics of historic earthquakes along the central Chile subduction zone. *J. S. Am. Earth Sci.* 11, 115-129.

Kausel, E., 1986. Los Terremotos de Agosto de 1868 y Mayo de 1877 que Afectaron el Sur del Peru y Norte de Chile. In: *Boletin de la Academia Chilena de Ciencias* 3, pp. 8-12.

Lomnitz, C., 1970. Major earthquakes and tsunamis in Chile during the period 1535 to 1955. *Geol. Rundsch.* 59(3), 938–960.

Lomnitz, C., 2004. Major earthquakes of Chile: a historical survey, 1535–1960. *Seismol. Res. Lett.* 75 (3), 368-378.

Melgar, D., Fan, W., Riquelme, S., Geng, J., Liang, C., Fuentes, M., Vargas, G., Allen, R.M., Shearer, P.M., & Fielding, E.J., 2015. Slip segmentation and slow rupture to the trench during the 2015, Mw8.3 Illapel, Chile earthquake. *Geophysical Research Letters* 43, 961-966, doi: 10.1002/2015GL067369.

Ortega, C., Vargas, G., Rutllant, J. A., Jackson, D., & Mendez, C., 2012. Major hydrological regime change along the semiarid western coast of South America during the early Holocene. *Quaternary Research* 78 (3), 513-527.

Ruiz, S., & Madariaga, R., 2018. Historical and recent large megathrust earthquakes in Chile. *Tectonophysics*, https://doi.org/10.1016/j.tecto.2018.01.015.

Ruiz, S., Klein, E., Del Campo, F., Rivera, E., Poli, P., Metois, M., Vigny, Ch., Baez, J.C., Vargas, G., Leyton, F., Madariaga, R., & Fleitout, L., 2016. The seismic sequence of the 16 september 2015 Mw8.3 Illapel, Chile, earthquake. *Seismological Research Letters* 87 (4), 1-11, doi: 10.1785/0220150281.

Saillard, M., Hall, S.R., Audin, L., Farber, D.L., Hérail, G., Martinod, J., Regard, V., Finkel, R.C., & Bondoux, F., 2009. Non-steady long-term uplift rates and Pleistocene marine terrace development along the Andean margin of Chile (31ºS) inferred from ^{10}Be dating. *Earth and Planetary Science Letters* 277, 50-63.

Udías, A., Madariaga, R., Buforn, E., Muñoz, D., & Ros, M., 2012. The large Chilean historical earthquakes of 1647, 1657, 1730, and 1751 from contemporary documents. *Bull. Seismol. Soc. Am.* 102, 1639-1653.

Vargas, G., Farías, M., Carretier, S., Tassara, A., Baize, S., & Melnick, D., 2011. Coastal uplift and tsunami effects associated to the 2010 M(w)8.8 Maule earthquake in Central Chile. *Andean Geology* 38 (1), 219-238.

Vargas, G., Rutllant, J., & Ortlieb, L., 2006. ENSO tropical-extratropical climate teleconnections and mechanisms for Holocene debris flows along the hyperarid coast of western South America (17-24ºS). *Earth and Planetary Science Letters* 249 (3-4), 467-483.

Vargas, G., Ortlieb, L., Chapron, E., Valdés, J., & Marquardt, C., 2005. Paleoseismic inferences from a high resolution marine sedimentary record in northern Chile (23ºS). *Tectonophysics* 399, 381-398.

INQUA Focus Group Earthquake Geology and Seismic Hazards

paleoseismicity.org

Tectonic analysis of the Arakapas and Gerasas faults belts in SW Cyprus

Varnava, Antriani (1), Kilias, Adamantios (1), Chatzipetros, Alexandros (1), Pavlides, Spyros (1)

(1) Aristotle University of Thessaloniki, Faculty of Sciences, 54124 Thessaloniki, Greece, avarnava@geo.auth.gr, kilias@geo.auth.gr, ac@geo.auth.gr, pavlides@geo.auth.gr

Abstract: *The mainly research was focused on Arakapas fault belt and as a secondary on the Gerasas fault belt. The Arakapas fault belt was created at the same period with the Troodos ophiolite, at the Upper Cretaceous, and for that reason nowadays characterized as a "fossil" transform fault. Those fault belts, Arakapas and Gerasa, at Miocene-Pliocene (Neogene) was* operated simultaneously as two strike-slip faults, giving a lateral escape to the area of the Limassol Forest.

Keywords*: Troodos Ophiolite, Arakapas fault belt, Gerasas fault belt*

INTRODUCTION

The ophiolite sequence of Troodos was started to evolve in originated constructive tectonic system in an oceanic basin of Neothys (Smewing et al., 1975), at the Upper Cretaceous (Campanian) (Simonian & Gass, 1978; Smewing et al., 1975).

GEOLOGICAL SETTING

The tectonic evolution of Cyprus (Figure 1) was evolved from Upper Cretaceous (Campanian) to until Pleistocene time.

The Upper Cretaceous (Maastrichtian), older rocks (Mamonia Complex) adhere to the ophiolite sequence of Troodos and are juxtaposed, along transform faults or strike-slip faults (Swarbrick, 1980; Geological Survey Department of Cyprus).

The evolutionary process of the island continued in the Upper Oligocene-Late Miocene and at this period the uplift of the island commences (Robertson et al., 1991).
The end of Miocene, (10 Ma ago) at the northern section of the ophiolite sequence of Troodos, the Range of Keryneia was emplacement.

Then at the period of Miocene-Pliocene the sedimentation was still in process and at the Pleistocene on the area of island of Cyprus the strong uplift took place.

DATA OBSERVATION

First of all, the study area on this work (Figure 2), it was primarily the Arakapas fault belt and then as a secondary the Gerasas fault belt, which is a typical dextral strike-slip fault with an NW-SE strike.

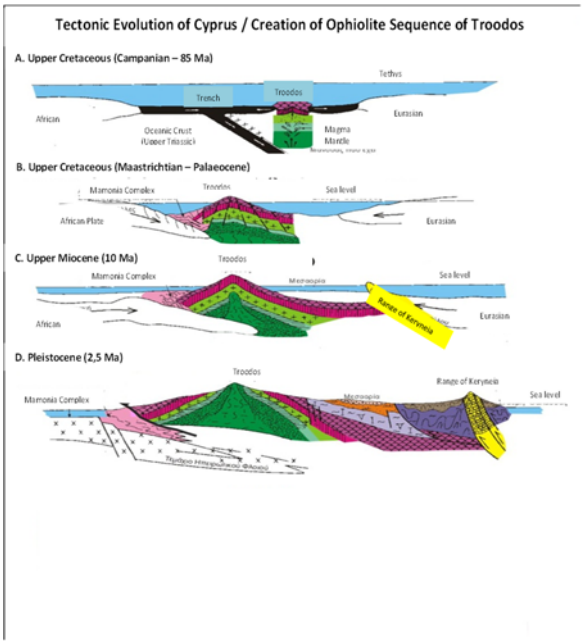

Figure 1: Geotectonic Evolution of the Cyprus (modified after by Geological Survey Department of Cyprus).

The Arakapas fault belt was created concurrently with the ophiolite sequence of Troodos and operated as a transform fault. For that reason nowadays characterized as a "fossil" transform fault (Moores & Vines, 1971; Simonian & Gass, 1978; MacLeod et al., 1990; Scott et al., 2012; Cann et al., 2001). The "fossil" transform fault of Arakapas was extended with an E-W strike, separating the formation of the Limassol Forest from the rest of the ophiolite sequence of Troodos. In our days the Arakapas fault belt extends E-W for almost 35 km and because it is disappearing, at both ends, beneath an underformed cover of Tertiary sedimentary rocks (Simonian & Gass, 1978).

Figure 2: Satellite image of the study area. Source of image: google earth.

Furthermore, the Limassol Forest *(Figure 3)* is bounded by Arakapas fault belt at the north (N) and Gerasas fault belt at the southwest (SW). These faults belts belong to the formation of the Limassol Forest (SW Cyprus).

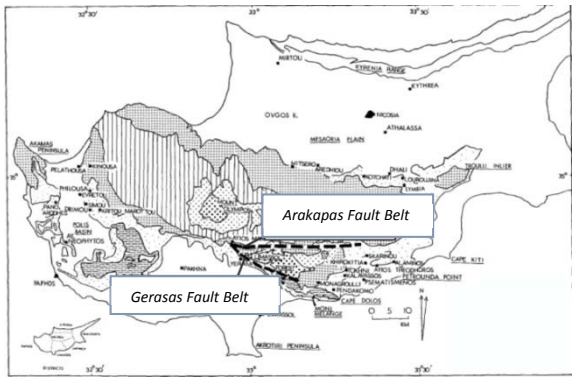

Figure 3: The northern boundary and the SW boundary of the Limassol Forest are the Arakapas fault belt and Gerasas fault belt, respectively (modified after Robertson, 1977).

At the Tertiary period, the Arakapas fault belt received a "tectonic rejuvenation" and began to effect to greater area of the Limassol Forest, as a real sinistral strike-slip fault. At the latest tectonics of the area, two tectonics events were recognized (Figure 4). The black line at the Figure 4, shows the tectonic event, D_1 and the red line shows the recent tectonic event, D_2. The older tectonic event D1 was operated at the Miocene-Pliocene (Neogene) and was evolved from strike-slip faults. Those strike slips faults were created simultaneously normal faults («Riedel» strike slip faults). The recent tectonic event, D_2 is characterized by normal faults with big angles and has operated from Pleistocene (Quaternary) until nowadays.

*Figure 4: The latest two tectonics events, on a fault surface to Arakapas village (*Varnava et al., 2016).

DISCUSSION

At the area of Limassol forest, two tectonics events were recognized. During of the D_1 (Figure 5), Miocene-Pliocene (Neogene) age, those two fault belts of Arakapas and Gerasas was operated simultaneously as two strike-slip faults, giving a lateral escape of the grater area of the Limassol Forest and so that it escape to the SE.

Tectonic Event D_1

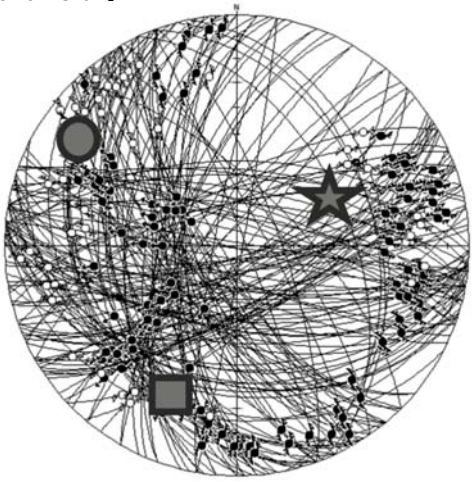

Figure 5: Analysis diagram ($\sigma_1 > \sigma_2 > \sigma_3$) of the Tectonic Event, D_1 (Varnava et al., 2016). σ_1: ★ σ_2: ■ σ_3: ●

Then, during of the Pleistocene (Quaternary), the area was expanded along the N-S axis and the recent tectonic event, D_2 (Figure 6) was recognized. The tectonic event D_2 functions till nowadays (Holocene) and turns out to be the current active tectonic. Therefore, the regime stress at the D_1 and D_2 tectonics events is strike-slip and extension, respectively (Figure 7).

Tectonic Event D_2

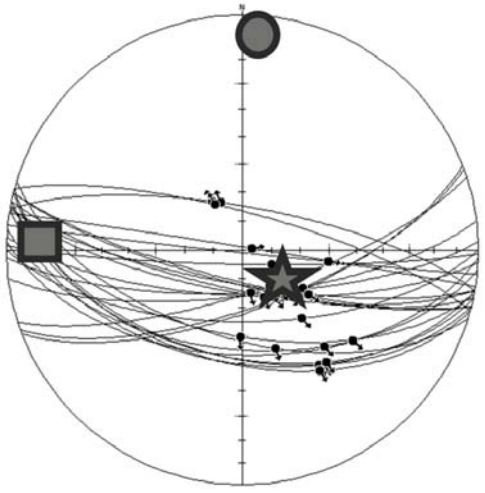

Figure 6: Analysis diagram ($\sigma_1 > \sigma_2 > \sigma_3$) of the Tectonic Event, D_2 (Varnava et al., 2016). σ_1: ★ σ_2: ■ σ_3: ●

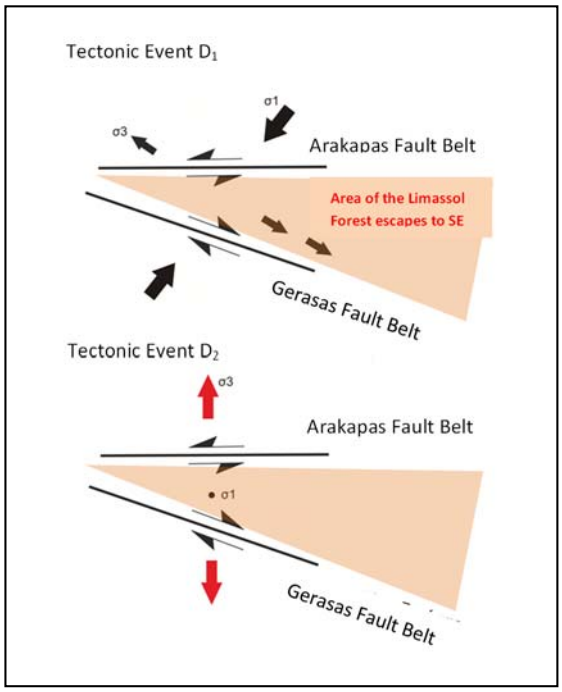

Figure 7: Final Diagrams of the compression and extension, at the each tectonic fact for the wider area of the Limassol Forest - SW Cyprus (Varnava et al., 2016)

REFERENCES

Cann, J.R., Prichard, H.M., Malpas, J.G., & Xenophontos, C., 2001. Oceanic inside corner detachments of the Limassol Forest area, Troodos ophiolite, Cyprus. *Journal of the Geological Society* 158 (5), 757-767.

MacLeod, C.J., Allerton, S., Gass, I.G., & Xenophontos, C., 1990. Structure of a fossil ridge-transform intersection in the Troodos ophiolite, *Nature* 348 (6303), 717-720.

Moores, E.M., & Vine, F.J., 1971. The Troodos Massif, Cyprus and other ophiolites as oceanic crust: evaluation and implications, Philosophical *Transactions of the Royal Society of London A: Mathematical, Physical and Engineering Sciences* 268 (1192), 443-467.

Robertson, A.H.F., Clift, P.D., Degnan, P.J., & Jones, G., 1991. Palaeogeographic and palaeotectonic evolution of the Eastern Mediterranean Neotethys. *Palaeogeography, Palaeoclimatology, Palaeoecology* 87 (1), 289-343.

Scott, C.P., Titus, S.J., & Davis, J.R., 2012. Using field data to constrain a numerical kinematic model for ridge-transform deformation in the Troodos ophiolite, Cyprus. *Lithosphere* 5 (1), 109-127.

Simonian, K.O., & Gass, I.G., 1978. Arakapas fault belt, Cyprus: A fossil transform fault, *Geological Society of America Bulletin* 89 (8), 1220-1230.

Smewing, J.D., Simonian, K.O., & Gass, I.G., 1975. Metabasalts from the Troodos Massif, Cyprus: genetic implication deduced from petrography and trace element geochemistry. *Contributions to Mineralogy and Petrology* 51 (1), 49-64.

Swarbrick, R.E., 1980. The Mamonia Complex of SW Cyprus: A Mesozoic continental margin and its relationship with the Troodos Complex. *Proceedings International Ophiolite Symposium*, Cyprus, 1979, Nicosia, Cyprus, Geological Survey Department, Cyprus.

Varnava, A., Kilias, A., Chatzipetros, A., & Pavlides, S., 2016. Tectonic analysis of the wider area of the Gerasas and Arakapas faults in SW Cyprus. International Conference of the Structural Group of the Geol. Soc. Greece, Athens (abstract).

INQUA Focus Group Earthquake Geology and Seismic Hazards

paleoseismicity.org

Preliminary comparison between paleoseismologically and geodetically determined slip rates in central Greece

Verroios, Sotirios (1), Ganas, Athanasios (2), Zygouri, Vasiliki (1), Koukouvelas, Ioannis (1)

(1) Department of Geology, University of Patras, 26504 Rion Patras, Greece, verroios@upatras.gr, zygouri@upatras.gr, iannis@upatras.gr
(2) Institute of Geodynamics, National Observatory of Athens, 11810 Athens, Greece, aganas@noa.gr

Abstract: *We selected the central Greece as a key area for understanding the rate of deformation based on two promising methods the paleoseismology and the GPS data. We selected four faults showing paleoseismologically determined slip-rates between 0.15 - 1.00 mm/yr and geodetically determined slip- rates between 0.77- 7.90 mm/yr. Given the data presented herein, the geodetic with geological data determine rates that differ by a factor of 1.8-7.9. This is due to several reasons such as a) orientation of baseline azimuth with respect to fault strike, b) deformation occurring without seismic slip on upper crustal faults, c) some transient deformation is present (e.g. post seismic motion), d) baselines sampling extension across multiple active faults due to coarse station spacing.*

Keywords*: paleoseismology, eastern Gulf of Corinth, GPS data, distribution of extension*

INTRODUCTION

The Gulf of Corinth is one of the most active rifts on the Mediterranean. This 130 km long by 30 km wide N120°E trending active structure separates the continental Greece from the Peloponnese to the south. Regarding the tectonic controls on the rifting there are many speculations. The main idea is that it might be the consequence of rifting processes in a back-arc geotectonic setting of the Aegean subduction zone and its enhancement by the westward propagation of the of the North Anatolian fault in the Aegean area (Kokkalas et al., 2006). The rifting is represented by an echelon north and south dipping onshore and offshore fault zone called as the Corinth Gulf Graben (Zygouri et al., 2008). Alternatively the Corinth Gulf graben is evolved along with a crustal scale Mesozoic transcurrent fault dissecting the Apullia east passive margin (Skourlis & Doutsos, 2003). The present study aims to complete the fault map towards the easternmost tips of the Gulf of Corinth and highlight its relationship to the contiguous areas of the South Evoikos comparing the amount of deformation derived from paleoseismology analysis of major faults in the area and the data of GPS permanent stations.

AREAS OF INTEREST

Kenchreai Fault

The 10-km-long E-W-trending Kenchreai Fault (Fig. 1; Tab. 1). Geomorphological data indicate that the E-W trending Kenchreai Fault is an asymmetrical plateau type fault, with maximum displacement towards the west and a rather clear east tip. Paleoseismology data have successfully provided displacement ranging between 0.2-0.5 m/event that is expected for similar earthquakes in Greece and the surrounding area. Slip rate is in the order of 0.15 mm/yr (Koukouvelas et al., 2017).

Pisia-Skinos Fault Zone

The 20-km-long Pisia -Schinos active fault zone forms the onshore surface breaking faults of an echelon set of normal faults that comprise the main Alkyonides Bay bounding fault system (Fig. 1; Tab. 1). Footwall uplift is evidenced by raised Holocene beachrocks, and raised late Pleistocene marine terraces that contribute an average footwall uplift rate of 0.3 mm/yr. During the 1981 earthquake sequence surface ruptures were noticed parallel to the main north dipping fault scarp. Paleoseismological trenches performed in the affected area showed that the average vertical displacement for past events is in the range between 0.4-1.2 m. (Collier et al., 1998). In addition the Holocene vertical slip rate is calculated in almost 1mm/yr (Pantosti et al., 1996).

Livadostras - Kaparelli Faults

The south facing Livadostras - Kaparelli faults forms a series of scarps crossing across the southern flank of the Thiva Basin. The Kaparelli fault is an almost E-W and south dipping fault which ruptured during 1981 earthquake sequence. The Kaparelli Fault shows an almost 10 km long trace that can be divided into two fault segments (Fig. 1; Tab. 1). Morphotectonic analysis for these faults showed an active structure attaining high activity (Tsodoulos et al., 2008). Although, paleoseismological surveys in the Kaparell Fault certified this observation, the derived average slip rate was in the order of 0.3 mm/yr (Kokkalas et al., 2007).

Milesi Fault

The Milesi Fault is an ESE-WNW striking and north dipping fault with a total length of 10km (Fig. 1; Tab. 1). It is located 30 km north of Athens towards South Evoikos Gulf. It is considered a symmetrical active normal fault with fault scarps displaying kinematic indicators. Grützner et al. (2016) suggest a 0.2-0.45 mm/yr slip rate based on

paleoseismological and morphotectonic analysis with recurrence interval similar to the one estimated for Kaparelli fault.

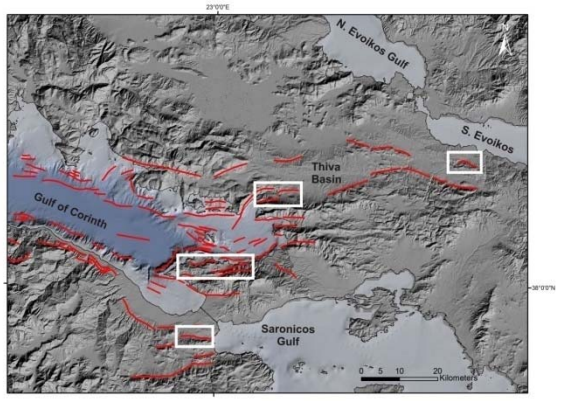

Figure 100: Faults dissecting the easternmost part of the Gulf of Corinth. The white frames highlight the studied faults. From south to north Kenhreai Fault, Pisia-Skinos Fault zone, Kaparelli Fault and Milesi Fault are included.

Studied faults	Kenhreai Fault	Pisia-Skinos Fault zone	Kaparelli Fault	Milesi Fault
Maximum slip rate (mm/yr)	0.15	1.00	0.30	0.45
GPS stations	KORI – SPET	THIV-KORI	THIV-KORI	024A-007A
		ATAL-KORI	014A-007A	025A-008A
Baseline Az	N165°E	N218°E	N218°E	N191°E
		N184°E	N155°E	N193°E
GPS extension rate* (mm/yr)	0.77	4.80	4.80	2.34
		7.90	0.54	1.22
1-D strain (ns/yr)	9.9	89.3	89.3	48.1
		99.9	17.3	23.2
References	Koukouvelas et al., 2017; Copley et al., 2018	Pantosti, 1996; Collier et al., 1998	Kokkalas et al., 2007	Grützner et al., 2016

Table I: Paleoseismological and geodetic estimations of the selected faults. Paleoseismological data in gray shading.

GPS data of the area

The study area undergoes crustal extension that has been well defined from GNSS (Global Navigation Satellite System) data, in terms of both orientation and magnitude. The first results from GNSS (GPS) campaigns were published in 1991 by Billiris et al. (1991) and were enriched by more data published from Clarke et al. (1997) and Briole et al. (2000). Results from continuous GNSS stations were published in 2013 (Chousianitis et al., 2013) and 2015 (Chousianitis et al., 2015). Recently, Marinou et al. (2015) published results from a local GPS network across the Kaparelli fault. The outcome of the geodetic research is the following: a) the deformation decreases from west (Aigion) to east (Oropos) with magnitudes ranging from 300 n/s to 50 ns/yr (dilatation rates; dilatation is the first invariant of the strain rate tensor) b) the ratio of geodetic to seismic moments revealed a large discrepancy with seismic rates being approximately 2 to 3 times smaller than the geodetic in the eastern and western parts of the Gulf of Corinth, respectively (Chousianitis et al., 2015) c) the orientation of extension is N-S to NNW-SSE along the Corinth rift d) the orientation of extension switches to NNW-SSW east of Kaparelli e) there is a clear boundary (separating two crustal blocks) across the Corinth Gulf where station velocities show a sudden jump (increase) in N-S profiles f) the Kaparelli fault marks the location of the continuation of the Corinth rift towards the east as it is characterised by strong strain localization (Marinou et al., 2015). Further east, deformation becomes more diffused with strain localized in sub-parallel normal faults like Avlon and Milesi (Ganas et al., 2004).

The fault slip data are compared to geodetic estimates from Chousianitis et al. (2013). All active faults are crossed by two baselines between continuous GPS stations except for Kenhreai fault that is crossed by the baseline KORI-SPET (extension rate 0.77 mm/yr). The geodetic extension has been determined from GPS stations in central Greece which they were operating for at least three years so that all errors can be modelled and tectonic velocities can be extracted from the raw data. The horizontal velocities of GPS stations in central Greece have been determined rigorously with 1-sigma uncertainties less than 0.5 mm/yr. The strain accumulation can be measured by estimating 1-D strain rates from GPS baseline vectors. Knowing the yearly rate of change between stations and their relative distances (baseline length) it is computed the 1-D strain per year (in ns/yr). The rate of baseline change (in mm/yr) represents the horizontal component of extension rate that is accumulated as strain energy along the active normal faults.

DISCUSSION - CONCLUSIONS

Given the data presented in this study it is interesting that the paleoseismologically determined and geodetically measured deformation rates show remarkable qualitative similarities. However, when comparing the geodetic with geological data it is noticed that the rates differ by a factor 1.8-7.9 (Tab. 1). This is due to several reasons such as a) orientation of baseline azimuth with respect to fault strike (increasing obliquity samples less extensional strain) b) some deformation is occurring without seismic slip on upper crustal faults c) some transient deformation is present (e.g. postseismic motion) d) baselines sampling extension across multiple active faults due to coarse station spacing. The latter reason is the most important and it highlights the need for more geodetic data so that station density can provide baseline lengths less than 50

km (that was during 2007-2013). The overall deformation understanding in this area will be expected to be more precise in the future as more continuous GPS stations are available during the period 2013-2018 and it is envisaged that more baselines will be available across active faults in central Greece. On the other hand more paleoseismological data will provide additional data for the fault slip rate calibration on the active faults of the study area.

REFERENCES

Billiris, H., Paradissis, D., Veis, G., England, P., Featherstone, W., Parsons, B., Cross, P., Rands, P., Rayson, M., Sellers, P., Ashkenazi, V., Davison, M., Jackson, J., & Ambraseys, N., 1991. Geodetic determination of tectonic deformation in central Greece from 1900 to 1988. *Nature* 350, 124-129.

Briole, P., Rigo, A. Lyon-Caen, H., Ruegg, J.C., Papazissi, K., Mitsakaki, C., Balodimou, A., Veis, G., Hatzfeld, D., & Deschamps, A., 2000. Active deformation of the Corinth rift, Greece: Results from repeated Global Positioning System surveys between 1990 and 1995. *Journal of Geophysical Research* 105, 25, 605-25,625.

Chousianitis, K., Ganas, A., & Gianniou, M., 2013. Kinematic interpretation of present-day crustal deformation in central Greece from continuous GPS measurements. *Journal of Geodynamics* 71, 1-13.

Chousianitis, K., Ganas, A., & Evangelidis, C.P., 2015. Strain and rotation rate patterns of mainland Greece from continuous GPS data and comparison between seismic and geodetic moment release. *Journal of Geophysical Research* 120, 3909-3931.

Clarke, P.J., Davies, R.R., England, P.C., Parsons, B., Billiris, H., Paradissis, D., Veis, G., Cross, P.A., Denys, P.H., Ashkenazi, V., Bingley, R., Kahle, H.G., Muller, M.V., & Briole, P., 1998. Crustal strain in central Greece from repeated GPS measurements in the interval 1989-1997. *Geophysical Journal International* 135, 195-214.

Collier, R.E.L., Pantosti, D., D' Addezio, G., De Martini, P.M., Masana, E., & Sakellariou, D., 1998. Paleoseismicity of the 1981 Corinth earthquake fault: seismic contribution to extensional strain in central Greece and implications for seismic hazard. *Journal of Geophysical Research* 103, 30001-30019.

Copley, A., Grützner, C., Howell, A., Jackson, J., Penney, C., & Wimpenny, S., 2018. Unexpected earthquake hazard revealed by Holocene rupture on the Kenchreai Fault (central Greece): Implications for weak sub-fault shear zones. *Earth and Planetary Science Letters* 486, 141-154.

Ganas, A., Pavlides, S.B., Sboras, S., Valkaniotis, S., Papaioannou, S., Alexandris, GA., Plessa, A., & Papadopoulos, G.A., 2004. Active Fault Geometry and Kinematics in Parnitha Mountain, Attica, Greece. *Journal of Structural Geology*, 26, 2103-2118.

Grützner, C., Deligiannakis, G., Schneiderwind, S., Pallikarakis, A., Papanikolaou, I., & Reicherter, K., 2016. New constraints on extensional tectonics and seismic hazard in northern Attica, Greece: the case of the Milesi Fault. *Geophysical Journal International* 204, 180-199.

Kokkalas, S., Pavlides, S., Koukouvelas, I., Ganas, A., & Stamatopoulos, L., 2007. Paleoseismicity of the Kaparelli fault (eastern Corinth Gulf): Evidence for earthquake recurrence and fault behavior. *Bolletino della Societa Geologica Italiana* 126, 387-395.

Koukouvelas, I., Zygouri, V., Papadopoulos, G.A., & Verroios, S., 2017. Holocene record of slip - predictable earthquakes on the Kenchreai Fault, Gulf of Corinth, Greece. *Journal of Structural Geology* 94, 258-274.

Marinou, A., Ganas, A., Papazissi, K., & Paradissis, D., 2015. Strain patterns along the Kaparelli-Asopos rift (central Greece) from campaign GPS data. *Annals of Geophysics* 58, 2, S0219.

Pantosti, D., Collier, R., D'Addezio, G., Masana E., & Sakellariou, D., 1996. Direct geological evidence for prior earthquakes on the 1981 Corinth fault (central Greece). *Geophysical Research Letters* 23, 3795-3798.

Skourlis, K., & Doutsos, T., 2003. The Pindos Fold and thrust belt (Greece): Inversion kinematics of a passive continental margin. *International Journal of Earth Sciences* 92, 891-903.

Tsodoulos, I.M., Koukouvelas, I.K., & Pavlides, S., 2008. Tectonic geomorphology of the easternmost extension of the Gulf of Corinth (Beotia, Central Greece).*Tectonophysics* 453, 211-232.

Zygouri, V., Verroios, S., Kokkalas, S., Xypolias, P., & Koukouvelas, I.K., 2008. Scaling properties within the Gulf of Corinth, Greece; comparison between offshore and onshore active faults. *Tectonophysics* 453, 193-210.

INQUA Focus Group Earthquake Geology and Seismic Hazards

paleoseismicity.org

A comment on finding analogues within Stable Continental Regions (SCR) for use in Seismic Hazard Analysis

Whitney, Beau (1, 2), Clark, Dan (3), Hengesh, James (1, 4)

(1) The University of Western Australia, Centre for Offshore Foundation Systems, Perth, bbwhitney@gmail.com
(2) Geoter SAS-Fugro Group, 3 Rue Jean Monnet, Clapiers, 34830 France
(3) Geoscience Australia. GPO Box 378 Canberra ACT 2601, Australia, dan.clark@ga.gov.au
(4) Interface Geohazard Consulting, 20 Plumeria Pl., Lahaina, HI, 96761 USA, hengesh@igc.com

Abstract: *Probabilistic seismic hazard analysis (PSHA) in regions of low seismicity sometimes utilize the "global analogues approach" for assessing M_{max} and recurrence parameters. In the global analogues approach, seismicity rate and recurrence distributions are generated by amalgamating aerial source zones with limited seismicity data or by drawing on more far-field analogues deemed as having similar seismogenic potential. Since the adoption of the approach three decades ago, the criteria for establishing and substantiating what constitute analogue regions has been refined only slightly and typically analogue regions are defined based on static properties of the crust. The purposes of this comment is to illuminate the need for PSHA analysists to refine the selection of analogue regions by also considering dynamic properties of the crust to delineate active intraplate regions (AIRs) from Stable Continental Regions (SCRs).*

Key words*: SCR, global analogues, PSHA*

Stable Continental Regions (SCRs) (Figure 1) were first defined as part of a seminal study by the Electric Power Research Institute (EPRI) to address two significant challenges faced by earthquake hazard researchers in the intraplate central and eastern United States (CEUS). These challenges included: low confidence in statistics on earthquake occurrence due to the low rates of seismic activity compared to plate boundary settings; and, a paucity of knowledge regarding capable seismogenic structures (Johnston et al., 1994). Despite the low seismicity rates, moderate to large magnitude damaging earthquakes have occurred in the CEUS, and so the EPRI team developed an approach to characterize earthquake occurrence in seismic hazard models for the region.

In order to address these challenges EPRI researchers proposed an ergodic approach, where seismicity data from regions across the globe that met specified criteria for SCRs were aggregated; the so-called *global analogues* approach. Kanter (1994) defined SCRs using the following criteria: (1) must be continental crust; (2) no orogenic activity younger than early Cretaceous; (3) no deformed forelands or orogenic belts younger than early Cretaceous; (4) no major anorogenic intrusions younger than early Cretaceous; and (5) no rifting or major extension or transtension younger than Paleogene (~35 Ma). To avoid circular reasoning, the authors specifically excluded seismicity (or lack thereof) as a defining characteristic of SCRs. The definition is based upon geology, and uses the geological characteristics of the crust of the CEUS as a reference.

Notwithstanding the contributions that the global analogues approach has made to our understanding of intraplate earthquake processes, the SCR designation has limitations-that the EPRI project participants acknowledged. The five criteria are exclusionary. The purpose of SCR designation was to distinguish SCR crust from "active" crust, rather than classifying areas of "stable" crust based on similar seismicity characteristics. That is, to meet the designation as an SCR a region must not have certain tectonic characteristics. Therefore, SCRs are similar only in how they are not something else. They are effectively comprised of regions that do not meet the criteria of being "active."

The initial definition of SCR included subdivisions for extended and non-extended crustal types. The comparison of the seismicity data from these two categories suggested that the seismogenic potential was greater in the extended category; rifted continental margins and interior rifts (see also Mooney et al., 2012). Later analysis of an expanded seismicity dataset suggested that on a global scale, the correlation of seismicity within SCRs and ancient rifts had been overestimated (Schulte & Mooney, 2005). However, the correlation appears to broadly hold true at geological timescales, at least for the Australian SCR (Clark et al., 2014).

For the Australian SCR, variation in fault scarp length, vertical displacement, distances between faults and relations to topography permitted extension of the SCR concept by the division of the continent according to neotectonic characteristics (Clark et al., 2011, 2012) The neotectonic domains model (Clark et al., 2012) places these characteristics into geological context, dividing Australian SCR crust into: 1) Precambrian cratonic; 2) non-reactivated Precambrian orogenic; 3) reactivated Precambrian orogenic; 4) Phanerozoic accretionary; and, 5) extended domains. Analysis of the fault and earthquake data from the

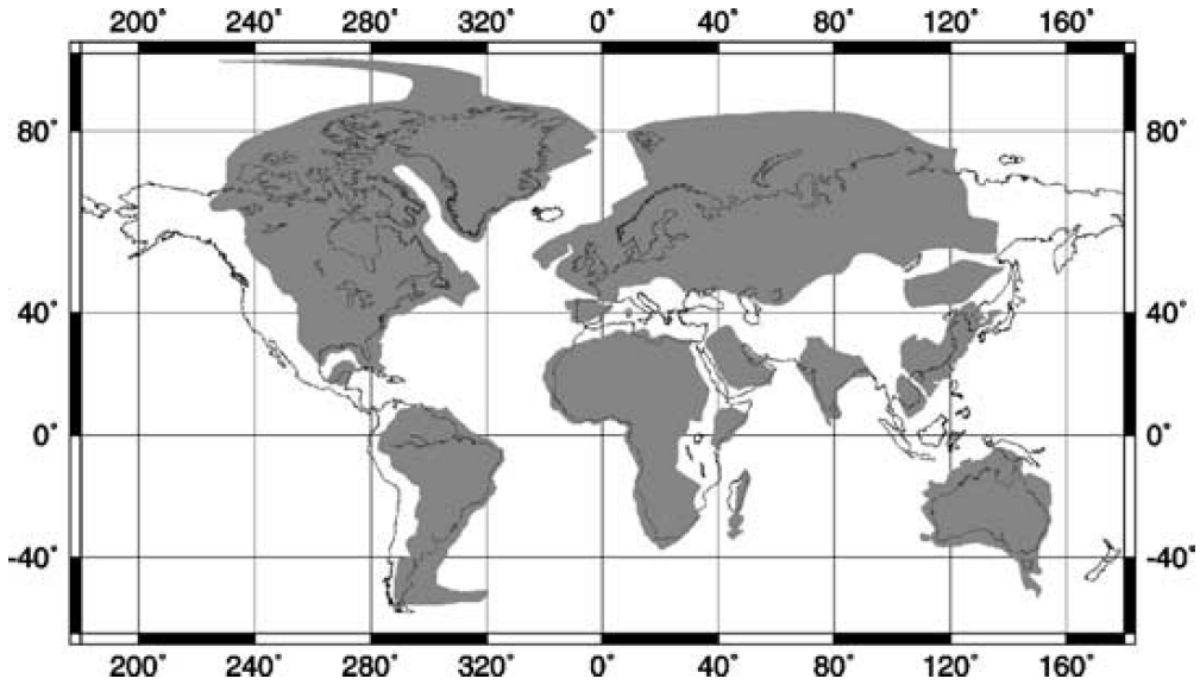

Figure 1: Stable Continental Regions (SCR) (gray polygons) from Schulte & Mooney (2005).

neotectonic domains suggests that they may be useful indicators with respect to earthquake occurrence models, fault geometries, recurrence rates, and maximum earthquake magnitude values (Mmax) (Leonard et al., 2014). However, a limitation of the neotectonic domains model is that intra-plate fault characteristics are not universal in their applicability in global analogue studies (Clark et al., 2012).

In terms of crustal architecture, lithospheric structure, and geological history global analogues for the Australian SCR neotectonic domains may be readily identified. However, the regional geodynamic framework generally is not considered in SCR designation or the neotectonic domains approach developed in Australia. In other words, where the analogue domains fit into the global plate tectonic mosaic is not considered; processes such as underlying mantle dynamics, dynamic topography, heat flow, rates of plate motion, stress, effectively the dynamic processes acting on the crust, are not considered. Therefore, the current method of identifying analogues could be refined by considering dynamic processes that are affecting some regions previously identified as SCRs.

The domains model identifies combinations of crustal architecture and geological history suitable (or not) for seismogenic reactivation, and so provides an indication of seismogenic potential. However, the full seismogenic potential of a region, as evidenced by tectonic geomorphologic features, the paleoseismic record, stress patterns, and seismic activity is the product of larger-scale processes either exploiting or being attenuated by these crustal attributes. Hence, the choice of analogues in assessing seismogenic potential requires the careful consideration of both the crustal domain and the dynamic processes that may be affecting a SCR.

A number of factors are thought to modulate crustal stress (direction and/or magnitude), and hence influence the location and occurrence of intraplate earthquakes (e.g. Talwani, 2014). These factors broadly include thermal influences (e.g., Long, 1988; Celerier et al., 2005; Hillis et al., 2008, Sandiford & Egholm, 2008); structural influences (e.g., Stein et al., 1989; Gangopadhyay & Talwani, 2003; Schulte & Mooney, 2005; Craig et al., 2011); and mechanical influences (Artyushkov, 1973; Sykes, 1973). Dynamic topographic influences relating to underlying mantle processes may also play a role (e.g. Vita-Finzi, 2004). The evolution of plate margin configurations through time, therefore, can make a significant contribution to the seismogenic potential within SCR settings. As such, the identification of analogues requires the careful consideration of both the crustal domain and the nature of the stresses.

An alternate, and not mutually exclusive, school of thought has recently emerged; that fossil stress, accrued under paleo-strain regimes, may influence the frequency and locations of modern intraplate seismicity (e.g., Craig et al., 2016; Calais et al., 2016). This fossil stress may persist in the crust for millions of years. In the absence of appreciable contemporary strain accumulation, a modern catalyst or stress perturbation is required for the fossil stress to be released seismically.

The apparent transient nature of strain and seismicity in SCR crust may be an additional diagnostic indicator to more accurately identify suitable crustal analogues. Earthquake occurrence behavior in SCR settings appears highly variable (Whitney & Hengesh, 2017). Approximately one-third of the faults that have been investigated in areas considered to be SCR do not exhibit evidence for recurrent earthquakes. Applying the domains approach indicates that all of the faults with no evidence for more than one event are within Domain 1 of the Australian model (Clark et al., 2012)-Domain 1 is comprised of Precambrian craton and non-reactivated Proterozoic crust. Elsewhere, faults exhibit long-term

neotectonic activity as indicated by Quaternary tectonic geomorphology and/or displacement of Miocene/Pliocene sediments over Quaternary deposits. Of these, the two that have been investigated at locations suitable for preserving a long record of displacement exhibit evidence for non-periodic recurrence (e.g. Clark et al., 2015), consistent with spatial transience of strain in these areas.

Within the Australian plate far-field plate boundary interactions are thought to have a first order control on the intraplate crustal stress field and seismicity (Cloetingh & Wortel, 1986; Coblentz & Sandiford, 1994; Sandiford & Egholm, 2008; Hengesh & Whitney, 2016; Whitney et al., 2015). For example, the seismotectonic characteristics of the Western Australia Shear Zone (WASZ) (Whitney et al., 2015; Hengesh & Whitney, 2016) is a function of: the paleo-tectonic setting (former extended margin) and associated relic crustal architecture; the nature of the crust (up to 25 km thick Mesozoic sedimentary sequences); the boundary conditions (between Archean cratonic terrains and oceanic crust); and, the current plate boundary stresses that are now affecting these crustal features. The tectonic elements of the WASZ, under a different regional stress regime, would not necessarily behave in a similar seismotectonic manner.

Recent work has challenged the traditional interpretation (e.g. Clark et al., 2012) that this part of the Australian continental should be categorized as an SCR domain (Whitney et al., 2015; Hengesh & Whitney, 2016). Evolving boundary conditions on Australia's northwest margin over the last several million years (Audley-Charles, 2011) have resulted in the selective reactivation of the Australian continental passive margin architecture, by the exploitation of relic structures with a direct linkage to the plate boundary. These reactivated structures extend more than 2,000 kilometres into the Australian plate.

The distinction between SCRs effected by a range of dynamic crustal processes and true SCRs has been recognized for other areas such as the Roer Graben (Europe), New Madrid zone (CEUS), and the Rann of Kachchh (India). A direct structural link to the plate margin appears to be a distinguishing characteristic of active-intraplate regions (AIR). These AIRs have lower strain rates and slip rates than their ACR sisters, contain faults that demonstrate recurrence of large magnitude earthquakes, but have crustal properties more consistent with SCR settings.

THE NEED FOR A MODEL UPDATE

Recently, a new approach has been presented to assist with analogue designation for distinguishing active and stable crust using fuzzy logic to determine "tectonic class based on an "activeness index." The tectonic classes (e.g, SCR, SCR-craton, ACR, subduction) are delineated gradationally based on tectonic and seismological information (Chen et al., 2018). A value of the approach is that it is modular and reproducible. The inputs can be assigned weightings and the results provide a probability of membership for each tectonic class. This provides a framework to address the degree of analogy between regions. Though the use of seismicity-base input parameters (a-values) suffers from the circular reasoning mentioned previously.

A broad range of factors contribute to earthquake occurrence in SCR settings. However, there is no single crustal attribute that provides a reliable predictor of where, when, and how earthquakes in SCR settings are going to occur. Furthermore, there is no clear indication of which aspects of pre-Quaternary history are relevant to the assessment of future seismic hazards (Allen, 1975). However, combinations of attributes may provide a framework with which to better assess seismogenic potential in SCR settings.

The current state-of-practice for PSHA in intraplate settings implements the global analogues approach to improve estimates of magnitude and recurrence parameter values. Wheeler (2009) documented the methods used to estimate Mmax east of the Rocky Mountains. He acknowledged that the adoption of a method for assessing Mmax is fundamentally a matter of choosing the least imperfect of the currently employed approaches and he specifically pointed out the need to establish a meaning for "analogue" regions. Notwithstanding this recognized limitation, the state-of-practice for site-specific PSHA within areas considered SCR crust is to use the global analogues approach and Bayesian analysis for estimating Mmax (Grunthal et al., 2018). This approach is the most frequently cited approach for recently completed PSHA in low seismicity regions (e.g., Youngs, 2011; Bommer et al., 2013, 2015). In this approach *a priori* distributions for all global analogue regions are developed to summarize existing knowledge on SCR earthquakes given the fact that some areal source zones in SCRs contain insufficient data to estimate recurrence parameters.

An *a priori* assumption in the *global analogues* approach is the premise that SCRs comprise seismologically analogous terranes. Recent research in western Australia, Europe, and India demonstrates that some SCRs are being affected by plate boundary forces. Recognizing this distinction may help refine source characteristics for future seismic hazard studies. This may help remove conservativisms embedded in the current analogues approach that could be leading to an over-estimation of hazard for vast regions that truly are stable. Similarly, recognition of these areas may help to more accurately reflect the hazard in "active intraplate regions".

Table 1: Fault attributes in various seismotectonic settings.

Attribute	Interplate	Active Intraplate Region (AIR)		Stable Continental Region (SCR)
Structural linkage to plate boundary	Yes	Yes	No	No or undetermined
Recurrence	10^2-10^3	10^4-10^5		>10^5 or NA
Slip rate	>1.0 mm/yr	1.0-0.01 mm/yr		<0.01 mm/yr or NA
Dominant source of seismicity	Plate boundary stresses	Transmitted plate boundary stresses	Uncertain and/or regionally transient	Paleo, transient, uncertain, or non-tectonic (e.g., hydro-isostatic)
Australian Examples		Western Australia Shear Zone	Flinders/Mt. Lofty Ranges	Tennant Creek

Additional research is needed to refine the definition of analogue areas and focus their application to truly analogous seismotectonic domains. Table 1 presents a brief overview of attributes in three broad seismotectonic divisions (interplate, AIR, SCR). Of particular interest for future analogue research are the AIR of the WASZ of Western Australia and the Flinders/Mount Lofty Ranges of South Australia. These regions lie in orogenic and extended domains of Clark et al. (2012). Faults in these parts of Australia have source parameters intermediate between the 'true' SCR terranes and the active plate boundaries. Slip rates on individual structures tend to vary from 0.01 to 1.0 mm/yr with earthquake recurrence on the order of 104 to 105 years. Given their higher geological activity these regions should not be used as analogues for other SCRs, but could be used as analogues for other AIRs.

Acknowledgements: Thanks mom.

REFERENCES

Allen, C.R., 1975. Geological criteria for evaluating seismicity: *Geological Society of America Bulletin* 86, 1,041-1,057.

Audley-Charles, M.G., 2011. Tectonic post-collision processes in Timor. *Geological Society*, London, Special publications 355, 241-266.

Artyushkov, E.V., 1973. Stresses in the lithosphere caused by crustal thickness inhomogeneties. *Journal of Geophysical Research* 78, 7675-7709.

Bommer, J.J., Coppersmith, K.J., Coppersmith, R.T., Hansen, K.L., Mangongolo, A., Nevelig, J., Rathje, E.M., Roderiquez-Marek, A., Scherbaum, F., Shelembe, R., Stafford, P.J., & Strasser, F.O., 2015. A SSHAC Level 3 Probabilistic Seismic Hazard Analysis for a New-Build Nuclear Site in South Africa. *Earthquake Spectra* 31 (2), 661-698.

Calais, E., Camelbeeck, T., Stein, S., & Craig, T., 2016. A new paradigm for large earthquakes in stable continental plate interiors: Large earthquakes in SCRs. *Geophysical Research Letters*, In Press, September, doi: 10.1002/2016GL070815.

Celerier, J., Sandiford, M., Hansen, D.L., & Quigley, M., 2005. Modes of active intraplate deformation, Flinders Ranges, Australia. *Tectonics* 24, doi: 10.029/2004&C001679.

Chen, Y-S., Weatherill, G., Pagani, M., & Cotton, F., 2018. A transparent data-driven global tectonic regionalization for seismic hazard assessment. *Geophysical journal International* 213, 1263-1280.

Clark, D., McPherson, A., & Van Dissen, R., 2012. Long-term behaviour of Australian stable continental region (SCR) faults. *Tectonophysics* 566-567, 1-30.

Clark, D., McPherson, A., & Allen, T., 2014. Intraplate earthquakes in Australia. In: *Intraplate Earthquakes* (Talwani, P., ed), Cambridge University Press, New York, 8-49.

Clark, D., McPherson, A., & Collins, C., 2011. Australia's seismogenic neotectonic record: a case for heterogeneous intraplate deformation. *Geoscience Australia Record* 2011/11, 100 pp.

Clark, D., McPherson, A., Cupper, M., Collins, C.D.N., & Nelson, G., 2015. The Cadell Fault, southeastern Australia: a record of temporally clustered morphogenic seismicity in a low-strain intraplate region. In: *Fault Rupture and Earthquake Hazards in Slowly Deforming Regions* (Landgraf, A., Kuebler, S., Hintersburger, E., & Stein, S., eds), Geological Society, London, Special Publication Seismicity.

Cloetingh, S., & Wortel. R, 1986. Stress in the Indo-Australian plate. *Tectonophysics* 132, 49-67.

Coblentz, D., & Sandiford, M., 1994. Tectonic stress in the African plate: constraints on the ambient stress state. *Geology* 22, 831-834.

Craig, T.J., Jackson, J.A., Priestly, K., & McKenzie, D., 2011. Earthquake distribution patterns in Africa: their relationship to variations in lithospheric and geologic structure, and their rheological implications. *Geophysical Journal International* 185, 403-434.

Craig, T.J., Calais, E., Fleitout, L., Bollinger, L., & Scotti, O., 2016. Evidence for the release of long-term tectonic strain stored in continental interiors through intraplate earthquakes. *Geophysical Research Letters* 43, 12 p.

Gangopadhyay, A., & Talwani, P., 2003. Symptomatic features of intraplate earthquakes. *Seismological Research Letters* 74, 863-883.

Hillis, R.R., Sandiford, M., Reynolds, S.D., & Quigley, M.C., 2008. Present-day stresses, seismicity and Neogene-to-Recent tectonics of Australia's 'passive' margins: intraplate deformation controlled by plate boundary forces. In: *The Nature and Origin of Compression in Passive Margins* (Johnson, H., Doré, A.G., Gatliff, R.W., Holdsworth, R., Lundin, E.R., Ritchie, J.D., eds), *Geological Society of London Special Publication* 306, 71-90.

Holford, S.P., Hillis, R.R., Hand, M., & Sandiford, M., 2011. Thermal weakening localizes intraplate deformation along the southern Australian continental margin. *Earth and Planetary Science Letters* 305, 207-214.

Johnston, A.C., Coppersmith, K.J., Kanter, L.R., & Cornell, C.A., 1994. The earthquakes of stable continental regions. *Electric Power Research Institute Publication* TR-102261-V1, Palo Alto, California.

Kanamori, H., & Brodsky, E.E., 2004. The physics of earthquakes. *Reports on Progress in Physics* 67 (8), 1429-1496.

Kanter, K.J., 1994. The earthquakes of stable continental regions. *Electric Power Research Institute Publication* TR-102261-V1, Palo Alto, California.

Long, L.T., 1988. A model for major intraplate continental earthquakes. *Seismological research letters* 59 (4), 6 pp.

Leonard, M., Burbidge, D.R., Allen, T.I., Robinson, D.J., McPherson, A., Clark, D. & Collins, C.D.N., 2014. The Challenges of Probabilistic Seismic Hazard Assessment in Stable Continental Interiors. *An Australian Example Bulletin of the Seismological Society of America* 104 (6), 3008-3028.

Mooney, W.D., Ritsema, J., & Hwang, Y.K., 2012. Crustal seismicity and the earthquake catalog maximum moment magnitude (Mcmax) in stable continental regions (SCRs): Correlation with the seismic velocity of the lithosphere. *Earth and Planetary Science Letters* 357-358, 78-83.

Sandiford, M., & Egholm, D.L., 2008. Enhanced intraplate seismicity along continental margins: some causes and consequences. *Tectonophysics* 457, 197-208.

Schulte, S.M., & Mooney, W.D., 2005. An updated global earthquake catalogue for stable continental regions: reassessing the correlation with ancient rifts. *Geophysical Journal International* 161, 707-721.

Stein, S. S., Cloentingh, S., Sleep, N.H., Wortel, R., 1989. Passive margin earthquakes, stresses and rheology. In Earthquakes at North American Passive Margins: Neotectonics and Postglacial Rebound (Gregersen, S., Basham, P., eds), NATO ASI Series C, Boston, MA: Kluwer Academic, 231-259.

Sykes, L.R., & Sbar, M.L., 1973. Intraplate earthquakes, lithospheric stresses and the driving mechanism of plate tectonics, *Nature* 245, 298-302.

Talwani, P., 2014. *Intraplate earthquakes*. Cambridge University Press, New York, 398 pp.

Vita-Finzi, C., 2004. Buckle-controlled seismogenic faulting in peninsular India. *Quaternary Science Reviews* 23, 2405-2412.

Wheeler, R.L., 2009. Sizes of the largest possible earthquakes in the Central and Eastern United States-summary of a workshop, September 8-9, 2008, Golden, Colorado. United States Geological Survey Open-File Report, 2009-1263.

Whitney, B.B., & Hengesh, J.V., 2015a. Geomorphological evidence of neotectonic deformation in the Carnarvon Basin, Western Australia, *Geomorphology* 228, 579-596.

Whitney, B.B., & Hengesh, J.V., 2015b. Geomorphological evidence for late Quaternary tectonic deformation of the Cape Region, coastal west central Australia, *Geomorphology* 241, 160-174.

Whitney, B.B., Clark, D., Hengesh, J.V., & Bierman, P., 2015. Paleoseismology of the Mount Narryer fault zone, Western Australia: A multistrand intraplate fault system. *Geol. Soc. Am. Bull.* 128, 684.

Whitney, B.B., & Hengesh, J.V., 2017. Assessing the Clustering and Quiescence" earthquake occurrence model for Stable Continental Region faults and the implications for Probabilistic Seismic Hazard Analysis. INQUA Focus Group on Paleoseismology and Active Tectonics, 8th INQUA Meeting on Paleoseismology, Active Tectonics and Archeoseismology (PATA), 13-18 September, Korea, 432-436.

Youngs, B., 2011. OPG's Deep Geologic Repository for Low and Intermediate level waste: Seismic Hazard Assessment, Amec Geomatrix, Inc. NWMO DGR-TR-2011-20, 259 pp.

INQUA Focus Group Earthquake Geology and Seismic Hazards

paleoseismicity.org

Urban Geology and Active faulting in the built environment of Thessaloniki

Zervopoulou, Anna (1)

(1) Dr.-M.Sc. Geologist, Thessaloniki, annezervo@gmail.com

Abstract: *Urbanization of areas has shown the need to study the subsurface of the cities or the sub-urban. Urban geology uses different tools to investigate the subsoil due to limited surface geological observation. It is particularly important the construction near or on active seismic faults. These faults raise the need of designing detailed maps for the urban subsoil in cities, as well as the accurate mapping of the active and dangerous faults and also identifying the special building construction zones. This paper will give an initial point of view into urban geology and the tectonic structure or urban tectonic of the Thessaloniki Urban Complex - Megacity. Historical data and maps, drilling data, geophysical surveys and excavations have been used for this research. The resulting faults are categorized according to their activity and their risk, using geological criteria. The thematic maps that arise could help with the earthquake resistance design of the city of Thessaloniki.*

Keywords*: Urban geology, tectonics, active faults, excavations*

INTRODUCTION

The intense urbanization of cities leads to their expansion while occupying larger and larger land areas. The densely-formed environment covers and transforms most of the natural landscapes. The surface is shaped in such a way that can cover the needs of the new city. In the urban environment man is the creator of the landscape or the "cityscape" (Coates, 1976; Bathrellos, 2007), with steep surface levelling and overcoating streams. With the expansion of needs, higher buildings are constructed, while cities acquire a densely populated and crowded centre. In addition to that development, there are created new needs for the management of the natural hazards of the residents and their protection against extreme natural phenomena and seismic events.

EXPLORATION METHODS OF URBAN GEOLOGY AND TECTONICS

a. Urban Geology

To describe geology and tectonics in urban areas, different methods and techniques are used in relation to traditional geology of physical observation. These include the most important study of the geological descriptions of geotechnical drilling logs, as well as information that can be drawn from the hydro-drillings in the urban areas. But borehole drilling, in the already structured environment, is rare and it is often oriented to the needs of the project that finances them. As a result, the choice of drilling positions does not follow a research program. Secondly the description of the formations (strata) also serves the needs of each project. Particularly useful boreholes are drilled for the construction of large sub-urban technical works in cities such as the construction of the Metro line or the public sewer. These large projects organize a drilling program along the construction line.

Another method for exploring the urban subsoil is the geophysical investigations mainly for research programs, with very important information data. Added to this the individual excavations made for the construction of large complex buildings or technical works can provide very important information data about the geology of the suburban, even if they are shallow.

b. Urban Tectonic

Exploring the tectonics of an urban area is even more difficult than the geological formation research. Boreholes in this case can give important information about the existence of an alpine non active fault, but only indications for a neotectonic fault. Particularly useful is the drilling of the boreholes in close proximity to each other. At the same time, in sedimentary environments with repeated sedimentation, it is very difficult to justify a layer changing. This change may be due to the existence of a rupture or fault, but also to a sediment alteration or deposition in lenses.

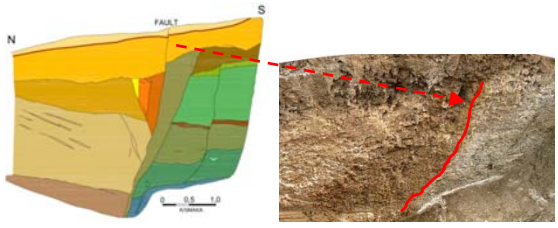

Figure 1: Paleoseismological - Geological trench and photo of Anthemountas Active Fault. Peraia Urban area, suburb of Thessaloniki (Zervopoulou et al., 2007).

A secure estimation method for verifying a fault is to observe it within an excavation. This excavation may be a research paleoseismological trench, which is extremely rare in the urban environment (Fig. 1). Individual excavation for the construction of a technical project can

also provide a large amount of data for a fault, especially when it is a large-scale project (Fig. 2).

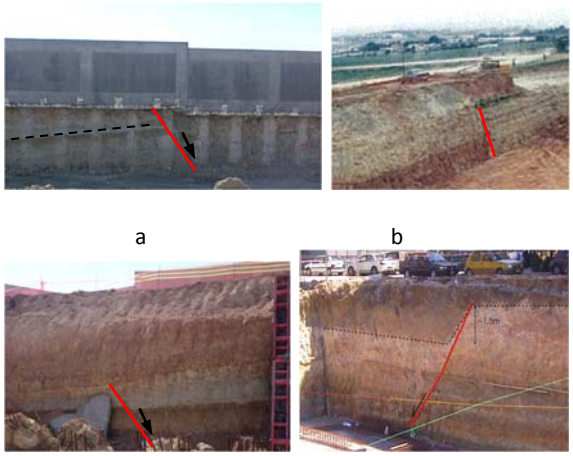

a b c d

Figure 2: Excavations in the urban area of Thessaloniki which showed the existence of faults in eastern Thessaloniki (a,b,c) and (d) in Kalamaria (a,b,c: photo by Zervopoulou d: Chatzipetros A).

At the same time, geophysical investigation can confirm a fault trace in an urban environment. There is also some difficulty in investigation and study them due to the intense city construction and the continuous traffic.

STUDY OF THESSALONIKI CITY

The city of Thessaloniki has been inhabited since 315BC and it counts more than 2.300 years of living. Its area over the years has expanded mainly to the east from about 0,70km^2 to 65km^2 today. Its geology was explored in addition to natural outcrop observation with the study of old photographs and old maps. At the same time, numerous data from the borehole drilling and excavations were used. Many data were complemented and confirmed by geophysical investigations.

a. Geology

The urban complex of Thessaloniki is founded on the rocky basement of the city, consisting of green schist and green gneiss of Mesozoic age. In contact above is the Neogene age Red Clay Series. This series consists of alternations of red color stiff clays, sand and gravel layers and lenses. In contact is the upper Neogene Sandstone-Marl formation Series. This series consists of alternating layers of very dense sand to sandstone with clays and silt of light brown to light green color (Fig. 3).

Above the Neogene formation series are the quaternary deposits which have the highest thickness in the east and west area of the center of the old city. These are deposits of riverine - torrential deposits with cobbles, gravels, sands and marsh - marine or fluvial - deltaic deposits that contains mostly silt and clay (Zervopoulou & Pavlides, 2016). Along the shoreline on the sea front, we find in boreholes the black very soft organic clay with sand, gravel and the presence of shells. Above all these geological layers is located the anthropogenic (man made) or archaeological layer. It is a heterogeneous formation with residential remains and building demolition debris in sand and clays. That formation thickness is reaching up to 15 meters in the historic center of Thessaloniki (Zervopoulou, 2010).

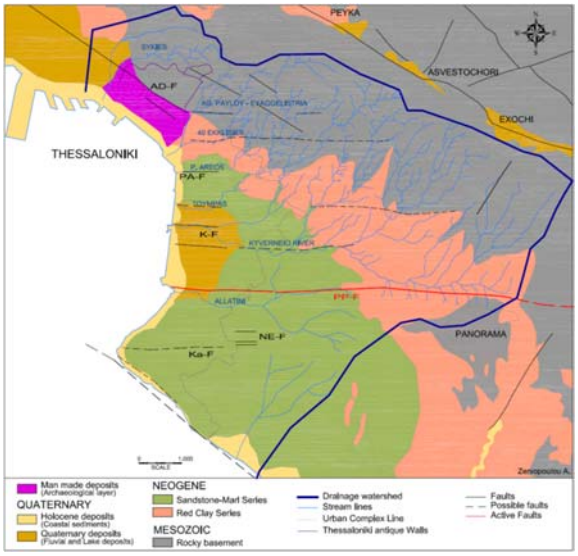

Figure 3: Geological map of the urban complex area of Thessaloniki (AD-F=Agiou Dimitriou fault, PA-F=Pediou Areos fault, K-F=Kyvernio faults, PP-F= Pilea – Panorama fault, NE-F=Nea Elvetia fault, Ka-F=Kalamaria fault).

b. Urban Tectonic - Active tectonic

The city of Thessaloniki is residing in Circum-Rhodope Belt, which has the general direction of NW-SE. Alongside to this direction are extended the oldest inherited faults of the study area. The current active stress field of the area has a N-S direction with normal E-W trending faults lines. The reactivation of older inherited faults also gives a new E-W direction component (Pavlides & Kilias, 1987). Faults appeared in the Thessaloniki urban complex are divided into active, possible active and non-active.

A very impressive fault line is the late Alpine non-active normal fault of Agiou Dimitriou (AD-F) Street (old center city) trending NW-SE and dipping towards to SW. Parallel to this is another normal fault structure along Egnatia Street and probably a third one along Niki's Avenue (coastal street), as is shown the geophysical investigations (Anastasiadis et al., 2001). These are drop normal faults that contributed to the amphitheatrical morphology of the old inner city of Thessaloniki. The Agiou Dimitriou street fault has a natural outcrop exposure while on Egnatia Street the second fault found during boreholes drilling (Fig. 3).

In the eastern part of Thessaloniki city, a number of parallel normal faults have been identified. The faults are oriented to the active stress field of the wider region. Most of them were identified by the borehole drillings and some of them were followed by the streams in the area. Remarkable faults are the possible active normal faults of the Kyverneio Stream (K-F) trending E-W and dipping towards to the South. But the most significant normal fault is a typical urban structure, the Pilea - Panorama Fault (PP-F). It is trending the same direction, E-W and dipping towards to the North. This fault is located along the extensional active tectonic stress field of the area. The extension of the fault in the urban complex of Thessaloniki was identified by boreholes. The fault's length is about

12km divided in to 4 segments. It is extended from the north area of Panorama suburb along Pylea and Nea Elvetia district to the coastline at Depot (Fig. 5).

The Pilea - Panorama fault according to geological criteria (tectonic geomorphology and Asymmetry factor of the main stream basin, Transverse Topographic Symmetry, stream length) is characterized as typical active fault. The data and criteria for their characterization were presented in previous work, such as Zervopoulou 2010, Zervopoulou et al. 2008.

This fault is also associated with microseismicity in the region (Zervopoulou, 2010; Paradisopoulou et al., 2006) (Fig. 4).

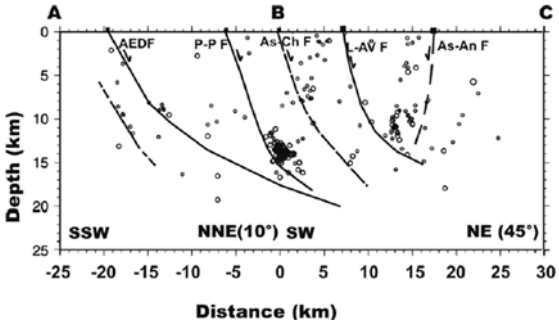

Figure 4: Cross section shows the distribution of the foci of the earthquakes in relation to the geometry of the fault Pilea - Panorama (Paradisopoulou et al., 2006).

The Pilea - Panorama fault crosses a densely populated area with buildings founded on the trace of the fault. In Voulgari Street (Fig. 5), it was found during boreholes drilling and was taken into account in the design of Thessaloniki Metro line construction. Because it is the most significant fault of the city of Thessaloniki it requires further investigations, such as paleoseismological trench. The trench will aims at gathering data such as: details of the fault, the activity and risk of the fault, the width of the rupture zone, the activation in earlier periods and the period of its repetition, the displacement and movement of the formations and soil by seismic event and finally the recurrence time with the aim of geo-dating analysis.

The earthquake maximum magnitude expected for the Pilea - Panorama urban fault segment, using empirical method (Pavlides & Caputo, 2008) is ranging between 5.6 and 6.0 (Deterministic Hazard Analysis D.S.H.A.).

In addition there are normal faults that have been found in the Kalamaria district. These faults affect mainly the Sandstone-Marl series formation and were found in excavations. These are also normal faults. The larger one trending NW-SE and dipping to SW is an Alpine non active normal fault that follows the shoreline in Nea Krini area.

The Kalamaria (Ka-F) and Nea Elvetia (NE-F) faults are normal possible active faults trending E-W to north. These faults are going to be studied further (Fig. 5).

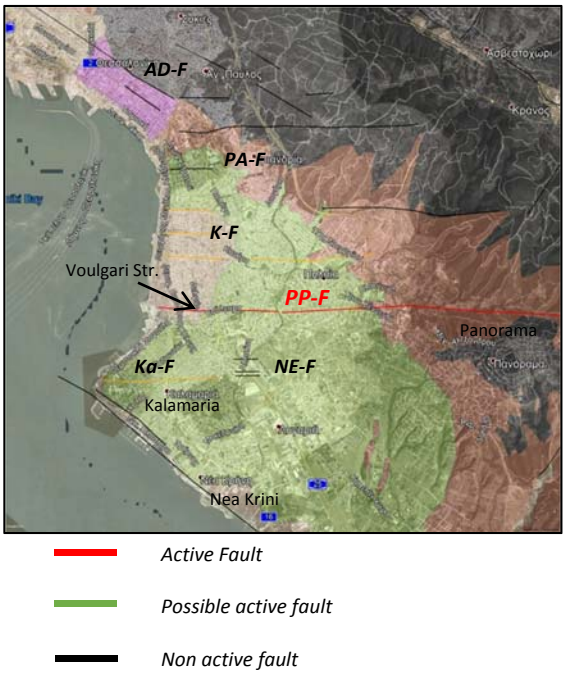

Figure 5: Tectonic map of the Thessaloniki Urban Complex on Google Earth.

DISCUSSION

The city of Thessaloniki is the second largest city in Greece with a prospect of growth in area and population. The recording and study of the active faults that cross the inhabited areas is a matter of major importance for the shielding of the city from the seismic hazard point of view. Urban geology and urban tectonics are at a very early stage in Greece and requires additional study.

In this article we mainly focus on faults that cross the structured grid of Thessaloniki. We recorded the faults and their extensions within the city that were identified in excavations, but also during boreholes drilling. These faults were redesigned and projected on a satellite image background.

We have discriminated the most significant fault for the city of Thessaloniki, Pilea - Panorama Fault, which requires furthermore study by conducting a paleoseismological trench and a monitoring program. The monitoring program investigates aseimic movements with the aim of inclinometers installed on fault plane and a topographic network. In collaboration with engineers, proposals can be made to reinforce existing buildings from disastrous earthquakes, but also to avoid building construction in high risk fault zones.

Acknowledgements: I would like to thank Prof. Spyros Pavlides and Ass. Prof. Alexandros Chatzipetros (Faculty of Geology, Thessaloniki) for their support in the elaboration of this work.

REFERENCES

Alfors, J.T., Burnett, J.L., & Gay, T.E., 1973. Urban geology, master plan for California. Bull 198, California division of mines and geology, Sacramento, California, 138 pp.

Anastasiadis, An., Raptakis, D., & Pitilakis, K., 2001. Thessaloniki's Detailed Microzoning: Subsurface Structure as Basis for Site Response Analysis. *Pure and Applied Geophysics* 158, 2597-2633.

Apostolidis, P.I., 2002. Determination of territorial structure using microtremor. Application to the estimation of dynamic properties and geometry of soil formations in Thessaloniki. (in Greek) Ph.D. A.U.Th.

Bathrellos, G.D., 2007. An overview in urban geology and urban geomorphology. Bulletin of the Geological Society of Greece, Vol.XXXX, 11th International Congress, Athens.

Coates, D.R., 1976. *Urban Geomorphology*. USA geol. Soc. of America.

Kerr, J., Nathan, S., Van Dissen, R., Webb, P., Brunsdon, D., & King, A., 2003. Planning for Development of Land on or Close to Active Faults management planners in New Zealand. Ministry for the Environment.

Legget, R.F., 1973. *Cities and Geology*. McGraw-Hill, N. York.

McCall, G.J.H., De Mulder, E.F.J., & Marker, B.R. 1996. Urban Geoscience. A.A. Balkema, Rotterdam.

Papacharisis, N., & Penelis, G., 1992. Technical Soil profil of path of light «Metro» Thessaloniki. *2nd National Conference of Geotechnical Engineering Thessaloniki* (in Greek), Vol.1.

Paradisopoulou, P.M., Karakostas, V.G., Papadimitriou, E.E., Tranos, M.D., Papazachos, C.B., & Karakaisis, G.F., 2006. Microearthquake study of the broader Thessaloniki area (Northern Greece). *Annals of Geophysics* 49, N. 4/5.

Pavlides, S.B., & Caputo, R., 2008. Earthquake Geology: Methods and Applications. *Tectonophysics* 453.

Pavlides, B.S., 2003/2016. *Earthquake Geology. An Introduction to Neotectonics, Morphotectonics, Palaeoseismology and Archaeoseismology*. (in Greek) University Studio Press.

Pavlides, S.B., Kilias, A., 1987. Neotectonic and active faults along the Serbomacedonian zone (SE Chalkidiki, northern Greece). *Annales Tectonic* I (2), 97-104.

Rozos, D., Chatzinakos, I., & Apostolidis, E., 1998. *Techno - geological map of the wider area of Thessaloniki*. (in Greek) Scale 1:25.000. I.G.M.E.

Stefanidis, P., & Eystratiadis, G., 1985. *Geological - Geotechnical mapping of the Central Sewage Pipeline of Thessaloniki*. (in Greek) I.G.M.E.

Tranos, M.D., Papadimitriou, E.E., & Kilias, A.A., 2003. Thessaloniki-Gerakarou fault zone TGFZ: the western extension of the 1978 Thessaloniki earthquake fault northern Greece and seismic hazard assessment. *Journal of Structural Geology* 25, 2109-2123.

Ulusay, R., Aydan, O., & Hamada, M., 2002. The behavior of structures build on active fault zones: Examples from the recent earthquakes of Turkey. *Structural Eng./ Earthquake* Eng., JSCE 19 (2), 149s-167s.

Valkaniotis, S., Zervopoulou, A., Ganas, A., & Pavlides, S., 2005. Urban Expansion and Seismic Hazard Increase: Athens and Thessaloniki Examples. *1st Scientific Conference of the magazine "Geographies" entitled: Geography of the Metropolis: Aspects of the phenomenon in the Greek area*, (in Greek), Vol.12, Thessaloniki.

Zervopoulou, A., 2010. Neotectonic faults of the broader area of Thessaloniki and foundation on them. PhD Thesis (in Greek) A.U.Th.

Zervopoulou, A., Chatzipetros, A., & Pavlides, S., 2014. Morphological imprinting urban areas and tectonic interpretation. The example of Thessaloniki. *10th International Congress of the Hellenic Geographical Society* (in Greek), Thessaloniki.

Zervopoulou A., Chatzipetros A., Tsiokos L., Syrides G., Pavlides S. 2007. Non -Seismic Surface Faulting: The Peraia Fault Case Study (Thessaloniki, N. Greece). 4th Int. Conference on Earthquake Geotechnical Engineering June 25-28, Paper No. 1610.

Zervopoulou, A., & Pavlides, S., 2016. Geological mapping in urban areas. A case study from the inner city of Thessaloniki, Greece. *Bulletin of the Geological Society of Greece* L, 14th International Conference, Thessaloniki.

Zervopoulou, A., & Pavlides, S. 2008. Neotectonic faults of Thessaloniki urban area. 3th Greek Conference on Earthquake Engineering and Engineering Seismology (in Greek), Athens (Paper 1865).

AUTHOR INDEX


paleoseismicity.org
SCHOOL OF GEOLOGY
AUTH
Hellas GOLD
INQUA
RESEARCH COMMITTEE
ARISTOTLE UNIVERSITY OF THESSALONIKI
GEOTECHNICAL
CHAMBER OF
GREECE
E.P.P.O.
BETA
RADIOCARBON DATING
myolive
Chatzipetrou
REGION OF CENTRAL MACEDONIA
HALKIDIKI Regional Unit